AD 638011

PROCEEDINGS
5th International
SHOCK TUBE SYMPOSIUM

SPONSORED BY THE

DIVISION OF FLUID DYNAMICS

as a Topical Meeting of the

Code 1

CLEARINGHOUSE
FOR FEDERAL SCIENTIFIC AND
TECHNICAL INFORMATION

Hardcopy	Microfiche	
$ 1.50	$ 4.50	1,204 pp

ARCHIVE COPY

PROCEEDINGS
5th International
SHOCK TUBE SYMPOSIUM

SPONSORED BY THE

DIVISION OF FLUID DYNAMICS
as a Topical Meeting of the
AMERICAN PHYSICAL SOCIETY

PROGRAM CHAIRMAN

Z. I. SLAWSKY

ARRANGEMENTS CHAIRMAN

J. F. MOULTON JR.

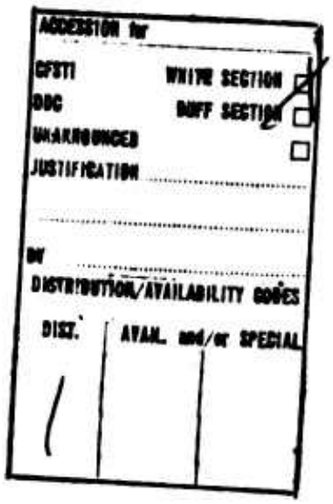
PUBLICATIONS

W. S. FILLER

CONDUCTED BY AND HELD AT THE

U. S. NAVAL ORDNANCE LABORATORY
White Oak, Silver Spring, Maryland

28 - 30 APRIL 1965



PUBLICATION AND DISTRIBUTION

This volume has been published by the U. S. Naval Ordnance Laboratory, White Oak. Reproduction was by photo-offset from text essentially as submitted by authors.

Requests for copies should be addressed to:

U. S. Naval Ordnance Laboratory
White Oak, Silver Spring, Maryland 20910
Attn: Library Division/Distribution

Reprint copies of individual papers are available from authors.

May 1966

FOREWORD

In February 1957, owing to the persistent efforts of Roman R. Birukoff of the Air Force Special Weapons Center (AFSWC), Kirtland Air Force Base, New Mexico, a general meeting on the subject of shock tubes was held at the Massachusetts Institute of Technology. This was the first of what has become a series of shock tube symposia conducted under the auspices of agencies of the Department of Defense and hosted by university, industrial and governmental establishments on an open (unclassified) basis. In 1958 and 1959, the second and third symposia were held at Palo Alto, California, and at Fort Monroe, Virginia, respectively - locations that offered convenient access by way of tours to the extensive shock tube and wind tunnel facilities at Lockheed and Langley Research Centers. As in the first instance, these two meetings were initiated by Mr. Birukoff and sponsored by the Air Force. Dr. T. H. Schiffman, head of the Air Force Shock Tube Facility at the Armour Research Foundation, Chicago, Illinois, was in charge of the arrangements for all three. The fourth symposium, sponsored and hosted by the U. S. Army Ballistic Research Laboratories in 1961, was initiated and arranged by William J. Taylor.

These first four meetings remained congenially small, with the number of papers ranging from 12 to 25 and the number of attendees from about 50 to 150. The papers dealt largely with engineering and applied problems of military interest, though some involved early efforts in fundamental areas that have had an almost explosive growth in recent years. If any topics predominated among the papers of the early symposia, they were, quite appropriately, those concerned with shock tube facilities, techniques, and instrumentation. However, to those who attended earlier meetings as well as the most recent one, it was clearly apparent that in scope and extent of participation the 5th Shock Tube Symposium had taken a rather drastic turn.

In August 1964, when plans for the 5th symposium were being formulated, it was quite clear that shock tube technology and research was no longer dominated by military blast and aerodynamics workers; rather, it was now also the tool of the chemist, the physical spectroscopist, and the plasma dynamicist, tc mention only a few. These circumstances led to contact with the Division of Fluid Dynamics of the American Physical Society. The interest and enthusiasm encountered there provided the basis for the broadened scope of the meeting. This union of sponsoring society and hosting laboratory proved to be an entirely happy one.

BLANK PAGE

SYMPOSIUM NOTES

The 5th Shock Tube Symposium was held at the U. S. Naval Ordnance Laboratory in Silver Spring, Maryland, on 28, 29, and 30 April 1965. The emphasis of the meeting was shock tube development, instrumentation, and technique; those aspects of fluid dynamics that intimately relate to shock tube theory and performance; and the evolution of the shock tube as a research tool in all areas of physics and chemistry.

This meeting also commemorated an important date in the history of shock wave research. For, just 25 years earlier, in March of 1940 W. Payman and W. C. F. Shepherd of the British Safety in Mines Research Board submitted for publication in the Proceedings of the Royal Society a paper which established in a quantitative sense the essential processes occurring in a shock tube. Because of World War II the paper remained unpublished for 6 years and thus did not have the influence on American work that it otherwise might have. The decade and a half of work by Payman and his group in the twenties and thirties presaged the current flowering of shock tube research in chemistry and physics and is excellently described in the first part of J. N. Bradley's commemorative paper in this volume. The rapid growth in the following decade and a half is dealt with in delightful detail by R. J. Emrich in his commemorative paper.

All will recognize the intimate association of shock tube performance and the studies carried out using this technique. Yet, in recent years shock tube technology itself has undergone rapid development as new regimes of high pressure, high temperature, high flow velocity, and low density have been explored. Many novel means for driving the shock, such as magnetic, spark, and combustion methods, and detonation in solids, as well as in gases, have been used successfully. Shock tube surface problems have been given considerable attention as regards thermal effects, boundary layer development, reflections at closed and open ends, and diaphragm effects. Measurement techniques also have been evolving rapidly; not only have long strides been made in the tradiational areas of pressure sensors and optical techniques, but new means have evolved for the measurement of electric, atomic and chemical properties of gases as well as density and temperature. Unusual shock tube shapes and sizes have been developed for various flow studies and applications such as multitubes for shock-on-shock interactions and sector tubes for studying cylindrical and spherical shocks.

How well this meeting succeeded in reflecting the scope and depth of current shock tube research activity, others must judge. We can, however, supply a few, perhaps superficial, statistics. There were approximately 425 attendees including 27 visitors from eight foreign countries. Fourty-two papers were listed on the main program of the meeting and an additional 73 on the supplementary program. Abstracts of all 115 papers, including 15 from abroad, were published in the October 1965 issue of the Bulletin of the American Physical Society.

Below are listed those who shared the distinction of presenting invited papers:

PROFESSOR RAYMOND J. EMRICH, Lehigh University, "Early Development of the Shock Tube and its Role in Current Research"

PROFESSOR JOHN N. BRADLEY, University of Essex at Colchester, "Progress in Shock-Tube Research in England"

PROFESSOR DANIEL BERSHADER, Stanford University, "Atomic Properties of Gases from Shock-Tube Research"

DR. J. GORDON HALL, Cornell Aeronautical Laboratory, "Some Aspects of Nonequilibrium Flows in Shock Tunnels"

PROFESSOR IRVINE I. GLASS, University of Toronto, "Shock-Tube and Shock Wave Phenomena in Earth and in Space"

PROFESSOR EDWIN L. RESLER, JR., Cornell University, "Electromagnetically Powered Shock Tubes"

DR. HAROLD MIRELS, Aerospace Corporation, "Boundary-Layer Effects in Shock Tubes"

DR. PETER H. ROSE, Avco-Everett Research Laboratory, "Applications of Shock Tubes to Hypersonic Flight"

MR. WILLIAM J. TAYLOR, Ballistic Research Laboratories, "Shock-Tube Applications in Defense Research and Engineering"

Seventy-one papers were submitted for publication in this Proceedings volume along with four of the nine invited papers.

It is perhaps inappropriate here to discuss banquet proceedings, but several aspects of that gathering seem particularly worthy of note. First among these was an address by the Honorable (Professor) Donald F. Hornig, Special Assistant to the President for Science and Technology, on some contemporary and vital sociopolitical responsibilities of scientists. Second was an address by Professor Walker Bleakney, Chairman of the Department of Physics, Princeton University, and the "granddaddy" of shock tube research in the U. S., whose remarks threw revealing (if also very humorous) light on the earliest awkward beginnings of the alliance between Government, Science and the Military in World War II. Finally, the audience was privileged to hear the Honorable (Professor Ing.) Hubert Shardin (recently deceased), Director, Bundesministerium der Verteidigung, West Germany, in one of his last talks in this country and to see some of his fascinating and strikingly artistic photographic studies of shock wave phenomena.

The technical success of the symposium was assured in advance by the untiring efforts of Professor R. J. Emrich, who, during the planning stages, was Secretary-Treasurer of the Division of Fluid Dynamics of the American Physical Society. He won the support of the officers of the Division in the joint sponsorship of the symposium that, in turn led to the full cooperation of The American Physical Society. Out of this cooperation, and the patient prodding of Dr. Z. I. Slawsky, grew a broadly representative Program Committee that took on the difficult task of selecting for presentation about one-third of the number of excellent papers contributed. The Committee consisted of Zaka I. Slawsky (Chairman), R. G. Fowler, A. Hertzberg, A. Kantrowitz, O. Laporte, J. F. Moulton, Jr., and A. Roshko, from whose ranks were drawn the Session Chairmen.

Professor R. G. Fowler, taking over the secretaryship of the Division of Fluid Dynamics in January 1965, carried to successful completion the Division's responsibilities to both The American Physical Society and the Naval Ordnance Laboratory. Among the many other details, he arranged for the publication of the abstracts in the Society's "Bulletin."

On the NOL scene to carry out the manifold chores connected with the meeting was an Arrangements Committee consisting of J. F. Moulton, Jr., (Chairman), P. M. Aronson, J. G. Connor, Jr., and LCDR R. E. Goodspeed. The publication tasks were carried out by W. S. Filler. Appreciation is due the many other people and groups within the U. S. Naval Ordnance Laboratory that contributed. However, if any one individual may be credited with literally bringing this meeting to life and and seeing to its successful conclusion, that person is James F. Moulton, Jr., whose peripatetic activity was excelled only by his ubiquitousness.

Solvency of the venture was insured by monetary support received from the Bureau of Naval Weapons, the Office of Naval Research, and the Defense Atomic Support Agency, in addition to the in-house support furnished by the Laboratory. More important to the success of the undertaking than money, however, was the guidance and encouragement generously supplied by the Commander, NOL, Captain R. E. Odening, the Acting Technical Director, Dr. David S. Muzzey, and every member of the Laboratory's Directorate.

To the memory of W. Payman and W. C. F. Shepherd, who founded modern shock tube research, and to Walker Bleakney, who introduced and nurtured shock tube research in the United States, this Proceedings volume is respectfully dedicated.

BLANK PAGE

TABLE OF CONTENTS

Page

Foreword i
Symposium Notes iii
Author Index xv

COMMEMORATIVE PAPERS

EARLY DEVELOPMENT OF THE SHOCK TUBE AND ITS ROLE IN CURRENT RESEARCH
R. J. Emrich, Lehigh University 1

PROGRESS IN SHOCK TUBE RESEARCH IN ENGLAND: RECENT DEVELOPMENTS IN CHEMICAL APPLICATIONS OF THE SHOCK TUBE
J. N. Bradley, University of Essex, Colchester, England 11

INVITED PAPERS

ELECTROMAGNETICALLY POWERED SHOCK TUBES
E. L. Resler, Jr., Cornell University 31

SHOCK TUBE APPLICATIONS TO DEFENSE RESEARCH AND ENGINEERING
W. J. Taylor, Ballistic Research Laboratories 47

CONTRIBUTED PAPERS

SESSION 1 Chairman: OTTO LAPORTE

EXCITATION STUDIES ON THE N_2 (1+) AND N_2^+ (1-) SYSTEMS IN SHOCK HEATED N-N_2 MIXTURES
K. L. Wray, Avco-Everett Research Laboratory 59

EQUILIBRATED SHOCKED PLASMA FROM A LINEAR ELECTRIC SHOCK TUBE WITH SEGMENTED DRIVER
S. M. Hamberger, A. W. Johnson, and R. G. Fowler
University of Oklahoma 81

PLASMA DENSITY AHEAD OF PRESSURE DRIVEN SHOCK WAVES
L. B. Holmes and H. D. Weymann, University of Rochester 93

CONTENTS (Cont' d)

Page

SESSION 2 Chairman: R. G. FOWLER

RADIATIVE COOLING BEHIND STRONG SHOCKS
H. Wong, Lockheed Missiles and Space Company
K. Horn, Stanford University 103

SHOCK TUBE SPECTROSCOPY OF POWDERED SOLIDS
R. W. Nicholls and D. C. Tyte
University of Western Ontario, London, Canada 111

INTERFEROMETRIC MEASUREMENT OF THE VIBRATIONAL RELAXATION TIME IN HYDROGEN-ARGON MIXTURES
E. Wachsler, Cornell University 123

MEASUREMENT OF ELECTRON DENSITY PROFILES USING A MICROWAVE TECHNIQUE (Related paper on pp. 644)
R. Tomboulian, General Applied Science Laboratories, Inc. 135

PRECURSOR IONIZATION IN AN ELECTRICALLY DRIVEN SHOCK TUBE
D. W. Mahaffey, R. I. Schoen, and H. G. Ahlstrom
Boeing Scientific Research Laboratories 145

SESSION 3 Chairman: ANATOL ROSHKO

OPTIMIZED GEOMETRY FOR COUPLING A MASS SPECTROMETER TO A SHOCK TUBE
G. F. Marsters, S. H. Bauer, and E. L. Resler, Jr.
Cornell University 155

SHOCKED GAS TEMPERATURE MEASUREMENTS BY INFRARED MONOCHROMATIC RADIATION PYROMETRY
M. R. Lauver, J. H. Hall, and F. E. Belles
Lewis Research Center 171

NEW VACUUM ULTRAVIOLET AND INFRARED INSTRUMENTS FOR TIME-RESOLVED SPECTROSCOPY
J. C. Camm and R. L. Taylor, Avco-Everett Research Laboratory 183

PRESSURE GAUGE FOR SHOCK REFLECTION STUDIES
D. Baganoff, California Institute of Technology 195

CONTENTS (Cont' d)

Page

GLOW DISCHARGE SHOCK TUBE FOR STUDYING SURFACE CATALYSIS, GAS PHASE, AND CHEMILUMINESCENT REACTIONS
R. A. Hartunian and W. P. Thompson, Aerospace Corporation..... 209

IONIZING SHOCK STUDIES IN AN ELECTROMAGNETICALLY DRIVEN SHOCK TUBE
B. Miller, L. Levine, and R. A. Gross, Columbia University..... 221

PERFORMANCE OF DOUBLE-DRIVER SHOCK TUBE
B. Lemcke, Massachusetts Institute of Technology..... 237

EXPLOSIVE-DRIVEN SHOCK TUBES
R. E. Duff and A. N. Blackwell, Lawrence Radiation Laboratory..... 259

SESSION 4 Chairman: ARTHUR KANTROWITZ

HIGH-PRESSURE SHOCK WAVE EXPERIMENTS IN ARGON AND XENON
R. N. Keeler, B. J. Alder, and M. van Thiel
Lawrence Radiation Laboratory..... 279

METHODS USED IN CONDUCTING EXPERIMENTS IN A WATER-TO-AIR SHOCK TUBE
E. V. Gallagher and F. L. Schuyler, I. I. T. Research Institute..... 291

PRODUCTION OF CARBON PLASMAS
R. W. Rutowski, D. Weimer, and W. C. Marlow
Lockheed Missiles and Space Company..... 307

SHOCK TUBE TECHNIQUES FOR STUDIES OF HIGH TEMPERATURE GAS RADIANCE
J. S. Gruszczynski, W. R. Warren, Jr., and D. A. Rogers
General Electric Company..... 317

CHARACTERISTICS OF THE FREE PISTON SHOCK TUBE
R. J. Stalker, Australian National University..... 339

A FAST INVERSE PINCH SHOCK TUBE FOR PLASMA SHOCK WAVE STUDIES
G. C. Vlases, University of Colorado..... 351

CONTENTS (Cont' d)

Page

SESSION 5 Chairman: ABRAHAM HERTZBERG

VIBRATIONAL RELAXATION OF DEUTERIUM
J. H. Kiefer and R. W. Lutz, Los Alamos Scientific Laboratory..... 369

DETERMINATION OF SHOCK TEMPERATURES FROM SIMULTANEOUS INFRARED EMISSION AND ABSORPTION MEASUREMENTS
G. J. Penzias, S. A. Dolin, and H. A. Kruegle
The Warner and Swasey Company..... 405

SPECTROSCOPIC TEMPERATURE MEASUREMENTS IN SHOCK TUBES UTILIZING EMISSION FROM THE OH VIOLET BANDS
R. Watson, Arizona State University..... 417

SHOCK FRONT CURVATURE AT INITIAL PRESSURES UP TO 700 mm. Hg.
A. T. Mazzella, University of Maryland, and
P. C. T. de Boer, Cornell University..... 439

TURBULENT SPOTS AND WALL ROUGHNESS EFFECTS IN SHOCK TUBE BOUNDARY LAYER TRANSITION
W. P. Thompson and R. J. Emrich, Lehigh University..... 453

ELECTRON BEAM GAS DENSITOMETER FOR SHOCK HEATED GASES
R. Kyracou, E. H. Carnevale, and C. A. Ziegler
Parametrics, Inc.; G. W. Wares, Air Force Cambridge Research Laboratories..... 465

TEMPERATURE AND THERMAL CONDUCTIVITY MEASUREMENTS IN A SHOCK TUBE
E. H. Carnevale, C. Carey, and T. Marshall, Parametrics, Inc. 473

AN ALKALI METAL VAPOR SHOCK TUBE AND THE MEASUREMENTS OF THE CONDUCTIVITY AND ELECTRON CONCENTRATION OF CESIUM IN ARGON
J. F. Louis, Avco-Everett Research Laboratory..... 485

CONTENTS (Cont'd)

Page

SESSION 6 Chairman: J. F. MOULTON, JR.

ON CYLINDRICAL IMPLODING SHOCK WAVES
J. H. Lee and B. H. K. Lee, McGill University, Canada..... 501

A CONICAL SHOCK TUBE NUCLEAR BLAST SIMULATOR
W. S. Filler, U. S. Naval Ordnance Laboratory
Y. Park, Bureau of Ships, and R. E. Pages
General American Transportation Corporation..... 521

THE EQUAL-PRESSURE SHOCK TUBE
H. Reichenbach, Ernst-Mach Institut, Germany..... 543

NOTE ON REFLECTED SHOCK CONDITIONS IN A SINGLE-PULSE TUBE...
H. B. Palmer, E. T. McHale, and G. R. Starkey
The Pennsylvania State University..... 557

THE EXPERIMENTAL STUDY OF THE INTERACTION OF A PROJECTILE WITH A PLANE SHOCK WAVE
J. E. Uppard, R. Burch, and R. Allen
Atomic Weapons Establishment, England..... 571

DETERMINATION OF HOT GAS THERMAL CONDUCTIVITY BY SHOCK TUBE EXPERIMENTS
G. Smeets, Deutsch-Französisches Forschungsinstitut, France..... 587

CONTRIBUTED PAPERS: SUPPLEMENT

INTERACTION OF SHOCK WAVES WITH TAPER SECTIONS
M. Dvir, W. Low, J. Stricker, and S. Maniv
The Hebrew University, Israel..... 593

NF_2 DECOMPOSITION BEHIND SHOCK WAVES
A. P. Modica and D. F. Hornig, Princeton University..... 601

USE OF A MICROWAVE INTERFEROMETER FOR MAPPING ELECTRON DENSITY VARIATION ACROSS THE FLOW FIELD IN A PRESSURE-DRIVEN SHOCK TUBE
J. C. Blackburn and F. L. Tevelow, Harry Diamond Laboratories..... 615

MINIMIZATION OF ERRORS IN SHOCK TUBE INVESTIGATION OF BROMINE DISSOCIATION RATES IN PRESENCE OF NOBLE GASES
M. Warshay, Lewis Research Center..... 631

CONTENTS (Cont'd)

Page

ANOMALOUS ELECTRON-DENSITY PROFILES IN SHOCK-HEATED AIR: EFFECTS OF Na and NaCℓ (Related paper on pp. 135)
M. S. Wecker, T. Baurer, and R. Tomboulian
General Applied Science Laboratories, Inc. 645

THE ASSOCIATION OF CN IN AN EXPANSION WAVE
S. H. Bauer and W. S. Watt, Cornell University..... 655

TWO WAVELENGTH LASER INTERFEROMETER FOR SHOCK TUBE AND PLASMA DIAGNOSTICS
A. B. Larsen, W. B. Johnson, and T. P. Sosnowski
Case Institute of Technology..... 673

RADIATION MEASUREMENT TECHNIQUES
W. A. Menard and G. M. Thomas, Jet Propulsion Laboratory..... 691

OPTIMIZATION OF SHOCK TUBE WAVE SPEED TRANSDUCER LOCATIONS BY A MONTE CARLO TECHNIQUE
A. A. Taylor and R. Watson, Arizona State University..... 727

A MULTIPLEXED SPARK SOURCE SCHLIEREN SYSTEM FOR SEQUENTIAL OBSERVATION OF HIGH-SPEED SHOCK WAVE PHENOMENA
W. M. Robinson, R. Watson, and J. G. Dean
Arizona State University..... 735

DATA DISPLAY AND RECORDING APPARATUS FOR MASS SPECTROMETRIC STUDY OF CHEMICAL REACTIONS IN SHOCK WAVES IN GASES
S. C. Barton, M. A. Di Valentin, and J. E. Dove
University of Toronto, Canada..... 739

SOLID PROPELLANT AS A SHOCK TUBE DRIVER
J. F. Melichar, Ballistic Research Laboratories..... 755

A THEORETICAL ANALYSIS OF THE DRIVER-RESERVOIR METHOD OF DRIVING HYPERSONIC SHOCK TUNNELS
R. F. Flagg, University of Toronto, Canada..... 767

COMBUSTION STUDIES IN THE UTIAS HYPERSONIC SHOCK TUNNEL DRIVER
R. P. Mason and N. M. Reddy, University of Toronto, Canada..... 795

AN MHD AUGMENTED DRIVER SHOCK TUBE
R. L. Leonard and P. H. Rose, Avco-Everett Research Laboratory..... 807

CONTENTS (Cont'd)

Page

A PISTON PROBLEM
T. S. Lee, University of Minnesota 833

NOTE ON A LOW PRESSURE SHOCK TUBE WITH AREA CHANGE NEAR THE DIAPHRAGM
C. A. Kot, IIT Research Institute 843

A 1 MJ ARC DISCHARGE SHOCK TUBE AS A CHEMICAL KINETICS RESEARCH FACILITY
L. L. Presley and G. E. Falkenthal, Ames Research Center
J. T. Naff, MHD Research, Inc. 857

REAL FLOW EFFECTS ON SHOCK ATTENUATION IN SHOCK-TUBE FLOWS
C. S. Kim and C. C. Chang, Catholic University of America
C. Park, Ames Research Center 879

RAREFACTION DISCHARGE LAYER AS A TOOL FOR OBTAINING HIGH SPEED GAS FLOW
J. Rosciszewski, General Dynamics/Convair 915

ANALOGUE NETWORKS FOR HIGH HEAT-TRANSFER RATE MEASUREMENTS IN SHOCK TUBES AND SHOCK TUNNELS
Z. A. Walenta, University of Toronto, Canada 925

CONTACT-SURFACE TAILORING IN REAL SHOCK TUBES
T. A. Brabbs and F. E. Belles, Lewis Research Center 955

LAMINAR BOUNDARY LAYER-INVISCID FLOW INTERACTIONS IN SHOCK TUBES
V. D. Blankenship and P. M. Chung, Aerospace Corporation 969

STRESS JUMP ANALYSIS METHODS FOR SHOCK WAVES
N. Davids, Pennsylvania State University, and
M. Ben-Amoz, General Electric Company 1001

LAMINAR BOUNDARY LAYER BEHIND A VERY STRONG SHOCK MOVING INTO NITROGEN
N. H. Kemp and T. C. Moh, Massachusetts Institute of Technology 1013

CONTENTS (Cont'd)

Page

ELECTRIC ARC-DRIVEN SHOCK TUBE DIAMETER, LENGTH AND ENERGY REQUIREMENTS FOR THE STUDY OF GAS RADIATION PHENOMENA
F. R. Livingston, Jet Propulsion Laboratory..... 1035

DIMENSIONAL ANALYSIS AND KINETIC THEORY OF SHOCKS
L. H. Holway, Jr., Raytheon Research Division..... 1059

PERFORMANCE PREDICTIONS FOR THE WISCONSIN HIGH ENTHALPY SHOCK TUBE
H. N. Powell, W. G. Steenken, R. K. Suri, and C. W. Fisher
University of Wisconsin..... 1065

AIR BLAST SIMULATOR
G. Weigel, Ernst-Mach Institut, Germany..... 1079

A TECHNIQUE FOR STUDYING THE SHOCK-ON-SHOCK PROBLEM
E. A. Brown, Jr. and G. J. Mullaney
Boeing Scientific Research Laboratories..... 1083

A SEVEN FOOT DIAMETER SHOCK TUBE FOR TRANSONIC AND SUPERSONIC AERODYNAMIC TESTING
R. L. Varwig and L. Rosenman, Aerospace Corporation..... 1091

THE GASEOUS-DETONATION DRIVER AND ITS APPLICATION TO SHOCK TUBE SIMULATION TECHNIQUES
M. J. Balcerzak and M. R. Johnson, General American Transportation Corp.. 1111

MODIFICATIONS TO A COMBUSTION DRIVEN SHOCK TUBE FOR USE IN A COUNTERFLOW FACILITY
L. C. Shrout, R. A. Schober, and J. W. Leary, The Boeing Company..... 1129

AERODYNAMIC BREAKUP OF LIQUID DROPS - I - THEORETICAL..... 1145
- II - EXPERIMENTAL..... 1153
W. H. Andersen and H. E. Wolfe, Aeroject-General Corporation

ONBOARD SPECTRAL OBSERVATION TECHNIQUE FOR A MODEL IN A SHOCK TUBE
W. M. Houghton, Langley Research Center..... 1171

AUTHOR INDEX

Ahlstrom, H. G. - 145
Alder, B. J. - 279
Allen, R. - 571
Andersen, W. H. - 1145
Baganoff, D. - 195
Balcerzak, M. J. - 1111
Barton, S. C. - 739
Bauer, S. H. - 155, 655
Baurer, T. - 645
Belles, F. E. - 171, 955
Ben-Amoz, M. - 1001
Blackburn, J. C. - 615
Blackwell, A. N. - 259
Blankenship, V. D. - 969
Brabbs, T. A. - 955
Bradley, J. N. - 11
Brown, E. A., Jr. - 1083
Burch, R. - 571
Camm, J. C. - 183
Carey, C. - 473
Carnevale, E. H. - 465, 473
Chang, C. C. - 879
Chung, P. M. - 969
Davids, N. - 1001
Dean, J. G. - 735
de Boer, P. C. T. - 439
Di Valentin, M. A. - 739
Dolin, S. A. - 405
Dove, J. E. - 739
Duff, R. E. - 259
Dvir, M. - 593
Emrich, R. J. - 1, 453
Falkenthal, G. E. - 857
Filler, W. S. - 521
Fisher, C. W. - 1065
Flagg, R. F. - 767
Fowler, R. G. - 81
Gallagher, E. V. - 291
Gross, R. A. - 221
Gruszczynski, J. S. - 317
Hall, J. H. - 171
Hamberger, S. M. - 81
Hartunian, R. A. - 209
Holmes, L. B. - 93
Holway, L. H., Jr. - 1059
Horn, K. - 103
Hornig, D. F. - 601
Houghton, W. M. - 1171
Johnson, A. W. - 81
Johnson, M. R. - 1111
Johnson, W. B. - 673
Keeler, R. N. - 279
Kemp, N. H. - 1013
Kiefer, J. H. - 369
Kim, C. S. - 879
Kot, C. A. - 843
Kruegle, H. A. - 405
Kyracou, R. - 465
Larsen, A. B. - 673
Lauver, M. R. - 171
Leary, J. W. - 1129
Lee, B. H. K. - 501
Lee, J. H. - 501
Lee, T. S. - 833
Lemcke, B. - 237
Leonard, R. L. - 807
Levine, L. - 221
Livingston, F. R. - 1035
Louis, J. F. - 485
Low, W. - 593
Lutz, R. W. - 369
McHale, E. T. - 557
Mahaffey, D. W. - 145
Maniv, S. - 593
Marlow, W. C. - 307
Marshall, T. - 473
Marsters, G. F. - 155
Mason, R. P. - 795
Mazzella, A. T. - 439
Melichar, J. F. - 755
Menard, W. A. - 691
Miller, B. - 221
Modica, A. P. - 601
Moh, T. C. - 1013
Mullaney, G. J. 1083
Naff, J. T. - 857

Nicholls, R. W. - 111
Pages, R. E. - 521
Palmer, H. B. - 557
Park, C. - 879
Park, Y. - 521
Penzias, G. J. - 405
Powell, H. N. - 1065
Presley, L. L. - 857
Reddy, N. M. - 795
Reichenbach, H. - 543
Resler, E. L., Jr. - 31, 155
Robinson, W. M. - 735
Rogers, D. A. - 317
Rosciszewski, J. - 915
Rose, P. H. - 807
Rosenman, L. - 1091
Rutowski, R. W. - 307
Schober, R. A. - 1129
Schoen, R. I. - 145
Schuyler, F. L. - 291
Shrout, L. C. - 1129
Smeets, G. - 587
Sosnowski, T. P. - 673
Stalker, R. J. - 339
Starkey, G. R. - 557
Steenken, W. G. - 1065
Stricker, J. - 593
Suri, R. K. - 1065
Taylor, A. A. - 727
Taylor, R. L. - 183
Taylor, W. J. - 47
Tevelow, F. L. - 615
Thomas, G. M. - 691
Thompson, W. P. - 209, 453
Tomboulian, R. - 135, 645
Tyte, D. C. - 111
Uppard, J. E. - 571
Van Thiel, M. - 279
Varwig, R. L. - 1091
Vlases, G. C. - 351
Wachsler, E. - 123
Walenta, Z. A. - 925
Wares, G. W. - 465
Warren, W. R., Jr. - 317
Warshay, M. - 631
Watson, R. - 417, 727, 735
Watt, W. S. - 655
Wecker, M. S. - 645
Weigel, G. - 1079
Weimer, D. - 307
Weymann, H. D. - 93
Wolfe, H. E. - 1145
Wong, H. - 103
Wray, K. L. - 59
Ziegler, C. A. - 465

EARLY DEVELOPMENT OF THE SHOCK TUBE AND ITS ROLE IN CURRENT RESEARCH

RAYMOND J. EMRICH
Department of Physics
Lehigh University
Bethlehem, Pennsylvania

1. EVENTS ASSOCIATED WITH THE FIRST SHOCK TUBES AT PRINCETON

The Committee on Passive Protection against Bombing and Division 2 of the National Defense Research Committee were active in Princeton during World War II. After the isotope separation group left for Los Alamos in 1943, the blast and penetration group represented nearly the entire effort of the physics department. The group was concerned with penetration of armor, concrete and other materials, and with structure damage by blast. They worried about blast from bombs exploded in the air, by direct contact explosions and by earth transmitted blast. The measurement of transient pressures was important to much of this work, and various means of recording transient pressures and calibrating the pressure gauges were developed. Walker Bleakney was the leader of the group.

Piezoelectric (quartz and tourmaline) crystals with electrodes and coaxial leads to oscilloscopes were developed by C. W. Lampson and others. Sometime in 1942 George T. Reynolds built a device to which the inelegant name "pot" was applied. The "pot" was about ten inches in diameter and 10 inches deep with a cellophane cover. The gauges to be calibrated were placed inside the "pot" and insulated leads brought through the brass wall and connected to the oscilloscope. The "pot" was evacuated and a knife used to puncture the cellophane diaphragm; a piece of light aluminum foil on the diaphragm was contacted by the knife just before it punctured and this electrical contact was used to start the oscilloscope sweep. An ordinary press type camera was mounted to view the oscilloscope face.

Now in those days one did not have a Tektronix scope in every room in the lab. In fact one had to design and build his own single sweep chassis, and build a high voltage supply to intensify the light on the screen. The single sweep with enough intensity to photograph was an achievement, and one made do with a sweep far from linear.

In discussions of the observed shapes of pressure pulses recorded by the gauges inside the "pot" A. H. Taub and others recognized that one-dimensional waves were being observed. Taub proceeded to calculate the ideal shock tube theory which predicts the strength of the incident shock when a diaphragm is broken between a one-dimensional high pressure chamber and a one-dimensional low pressure chamber.

The first device which can properly be called a shock tube was a brass cylinder of three inches diameter with a flat side of perhaps one and one-half inches width into which various piezoelectric gauges could be mounted to form part of the wall. The tube was approximately 14 feet long overall, the diaphragm being two feet from one end. The low pressure section had an open end so that the tube was noisy. This tube was designed and built by George Reynolds several months before it was first operated. Reynolds remembers that it was only when Abe Taub "threatened" to begin experimental work himself that the first recordings were made. It is an historical fact that, on this first occasion of a shock tube operating at Princeton, Taub moved the diaphragm breaking knife with his own hand and that the shock produced was audible. Lost to history is whether the oscilloscope camera recorded the passage of that first shock. The tube is described in NDRC report A-192 (OSRD 1519) by G. T. Reynolds, "A Preliminary Study of Plane Shock Waves Formed by Bursting Diaphragms in a Tube" (1943).

At some time during this early period, some reports by Payman and Shepherd came to the attention of Bleakney, Taub, Lampson and Reynolds. They apparently arrived, as did much material at that time, from England in photostat form as part of the exchange of information between the groups of scientists doing research in ordnance in Great Britain and the United States. In preprint form these reports did not include the one-dimensional theory and were chiefly concerned with explosions in gaseous mixtures initiated by a shock-wave which was produced by bursting a diaphragm. The work of Vielle (1899) was known, but it is the recollection of all concerned that Taub worked the theory out independently. When Payman and Shepherd published their famous paper in the Proceedings of the Royal Society at the end of the war, they included the shock strength prediction from the initial pressures, attributing the formula to G. I. Taylor. None of the early papers refers to an article by H. Schardin in Physik.Zeits.33, 60 (1932), which existed at the time and was brought to the attention of U.S. workers only some years later by R. N. Hollyer. Schardin's paper refers to an earlier paper by a German engineer who worked out the theory as part of the air brake system in railroad trains. Kobes, K. "Die Durschlags-geschwindichkeit bei den Luftsauge-und-Druckluftbremsen." Z. Osterreicher Ind. Arch.-Ver. 62, 558(1910).

For those of us who came into shock tube work later, a very useful paper was one issued at Princeton by C. W. Lampson, "Resume of the theory of plane shock and adiabatic waves with applications to the theory of the shock tube" dated 27 April 1945 and issued in "dittoed" form as a technical memorandum. The introduction to this document states "the use of a bursting diaphragm in a tube as a method of producing shock waves is covered in a phenomenological report by W. Payman and W. C. F. Shepherd

in 1941. They attribute its earliest conception to P. Vielle in 1899. A calculation of the shock wave pressures to be expected thereby was carried out by A. H. Taub in 1942. Certain experimental work on the tube as a primary standard of blast wave pressures was done by G. T. Reynolds, and extended in a series of quite accurate measurements by W. T. Read who found that the experimental pressures varied about six percent from those calculated from shock tube theory."

This document by Lampson together with the Taylor-Maccoll article in the Durand Aerodynamic Series of books constituted in 1946 the most lucid description of one-dimensional waves and the shock tube theory. There was also a manual on "Shock Waves and Supersonic Flow" written by Courant and Friedrichs and issued by the Applied Mathematics Panel at New York University. Lampson's article was later reissued as Ballistic Research Laboratories Technical Note 139(1950). The manual of Courant and Friedrichs became their well known book. The work done by W. Thornton Read was not written down until 1946 and appears in an OSRD memorandum "Final Report on Shock Tube, Piezoelectric Gauges and Recording Apparatus" OSRD 6321(1946), by J. C. Fletcher, W. T. Read, R. G. Stoner and D. K. Weimer. So far as I can recall (I remember seeing a copy of this report in 1946 but no longer have a copy) these measurements were the earliest and best ones where the velocity of the shock wave in the low pressure section was measured. The measurement used pressure gauges and calibrated sweep times on an oscilloscope face. The measured velocities were compared with the predicted velocities given by the ideal shock tube formula. As you know, the ideal theory gives formulas for all flow variables if the initial pressures in the two sections of the shock tube are known. In Read's work, there were indications of decreasing velocity of the shock waves with distance traveled (attenuation) but the measurements of decreasing velocity were inside the experimental error. At the end of the war, when I ceased shooting bullets at armor plate, and was wanting to do something with shock tubes, this was my starting point, following discussions with Bleakney and Reynolds. Lampson's 1945 report contains an addendum describing experiments he performed to record the reflected rarefaction arrival at gauges placed in the low pressure chamber. The observed arrival times of the rarefaction wave head were compared with the predictions of the ideal shock tube theory. Various lengths of high pressure section were arranged for by insertion of plugs. The 1946 Payman and Shepherd article devotes attention to the wave and front speeds observed in their tube; they studied hydrogen and carbon dioxide as well as air and used pressures as high as 1100 lb/in^2 behind copper diaphragms. Their accuracy of speed measurement was not high and they were not concerned about deviations from predictions of the ideal theory. This brings the shock tube as an instrument to generate shocks for gauge calibration up to 1946. The essential behavior as described in the ideal theory had been demonstrated.

2. DEVELOPMENT OF THE SHOCK TUBE FOR STUDY OF SHOCK WAVE REFLECTIONS.

New types of instrumentation were introduced for these shock tube studies. In 1942, when the first work on shock waves and bomb damage was going on at Princeton, John von Neumann recognized that the reflection of shock waves from the ground was more complicated than in acoustics and at the suggestion of Colonel H. Zornig of the U.S. Army he read the pertinent papers of Ernst Mach which appeared in the Vienna Academy "Sitzungsberichte" vol.72-92(1875-1889). It appears that in turn Colonel Zornig learned of the Mach reflections from discussion with Schardin at the Cranz laboratory in Berlin. Zornig visited Schardin there in 1929. Von Neumann named the kind of reflection Mach had observed Mach reflection and called attention to the fact that the Mach stem would move faster than the incident shock and therefore be stronger than the incident shock. The existence of the Mach reflection in an actual blast wave was observed in 1942 by G. T. Reynolds in some experiments at Princeton using strings of pressure gauges and a small charge set off in the open space behind the Princeton football stadium. The reasoning of von Neumann is recorded in a document "Oblique Reflection of Shocks" Navy Department Bureau of Ordnance Publication, Explosives Research Report No.12 (12 October 1943). In this document he expresses his thanks to those scientists who influenced and assisted him in the course of these investigations. He mentions that the fact that the ordinary scheme of quasi-acoustic reflection is inapplicable to certain shocks was first pointed out to him (that is, von Neumann), by E. Teller in 1940. Quoting further from von Neumann's report: "It will be seen that this breakdown [of acoustic type reflection] is closely connected with that [breakdown] of the flow through an oblique shock at a concave corner. This flow was first analyzed by E. Prandtl and T. H. Meyer in 1908. Its breakdown is equivalent to the detachment of the head wave of a wedge in a supersonic flow. This latter phenomenon follows also from P. Epstein's investigation of the headwave of a wedge, 1931. Very similar conditions exist for the headwave of a cone, as shown by G. I. Taylor and J. W. Macoll, 1933. Of course, these headwave-detachment phenomena are also observed by ballistic photography. The aspect which we wish to stress is, however, the connection with the vicissitudes of shock reflection."

In spite of the theoretical insight of von Neumann and his collaborators R. J. Seeger and P. C. Keanan, both then at the U.S. Naval Ordnance Laboratory, it was apparent that there would be a dependence on experiment for an understanding of what processes would take place in Mach reflection. In view of the practical importance of this Mach reflection problem, basic studies were desirable, and Bleakney proposed the shock tube as a device for studying the problem. Earlier experimental studies, employing the experimental techniques of spherical spark photography and the "soot line" method used long before by Mach, had been carried out by E. B. Wilson, Jr., R. W. Wood, and P. Liebessart. Bleakney tells of interesting discussions in those days among the theoreticians as to whether one could

photograph shock waves in a rectangular tube.

Lincoln G. Smith started, in June 1943, to build the first rectangular cross-section shock tube, which was 2 in by 7 in, and undertook to photograph in a systematic way the angles in Mach reflection and regular reflection at various incident shock strengths. This work was summarized in a report "Photographic Investigation of Plane Shocks in Air. Final Report." NDRC A-350, November 1, 1945 by L. G. Smith. From this report I quote: "The project was started at the suggestions of J. von Neumann and R. J. Seeger of the Navy Department Bureau of Ordnance and has been aided throughout by their very helpful suggestions."

During those years spark photography by shadowgraph of the shocks in front of supersonic bullets was being carried out by A. C. Charters at Aberdeen Proving Ground. The rectangular cross-section shock tube of Smith had large plate glass windows through which both shadow and schlieren photographs were taken of the shock. The photography used first a spark gap designed by Charters and later one "kindly supplied by Colonel P. Liebessart of the French army and lately of Aberdeen Proving Ground." Linc Smith combined information from many sources into a very up-to-date design for his equipment. The spark had to be set off at just the right instant as the shock reached the window of the shock tube. At about this time C. W. Curtis and I, who were using light screens to detect bullet arrivals for measurement of bullet velocity, observed that the light screens were detecting a shock. This was in cases where the gun was firing a subsonic bullet but the blast from the gun overtook the bullet and gave a velocity measurement nearly that of sound as it passed through the light screens. Linc Smith lost no time in installing "light screens" in his shock tube and using a spiral chronograph for measuring his incident shock speeds. The spiral chronograph was a device built at Princeton during the war which measured time intervals to an accuracy of one microsecond by producing a spiral trace on a cathode-ray tube at a known speed of rotation. The trace was started and stopped by the electrical signals to be timed.

There was apparently some not-very-systematic study of diaphragm materials. I recall that George Reynolds used about 18-inch wide Scotch tape with the sticky stuff still on it for his diaphragms in the "pot." Apparently early in the game, people observed that a laminated cellophane with the trade name Red Zip shattered and left little material at the clamp when the experiment was finished and this was the most popular material for a wide variety of shock tubes for quite a few years. The Red Zip cellophane was obtainable only from a company in Cleveland, Ohio; it was made to be cut into narrow strips and used underneath the transparent cellophane covering of a cigarette package, allowing the cellophane cover to be stripped open easily. It was a mark of discovery in the early days of shock tubery away from Princeton to find out how to order this material.

3. SHOCK TUBES AFTER 1946 AT PRINCETON AND OTHER LABORATORIES

While most of the work done on shock tubes during 1942-1946 was not described in the open literature, the essential ideas were presented as contributed papers at the Cambridge, Massachusetts meeting of the American Physical Society on 25 April 1946. Probably the abstract of the paper by Walker Bleakney, Phys Rev 69, 678a(1946) contains the first recorded use in the literature of the words "shock tube." The title of his paper was "Shock Waves in a Tube" but in the body of the abstract he used the words "shock tube".

The first shock tubes built away from Princeton, where the interest can be traced to people involved in or having heard of the studies at Princeton, were at the Ballistic Research Laboratories (Aberdeen), Naval Ordnance Laboratory (Washington) and Langley Research Laboratory. These places were starting work in 1945. Then in 1946 Smith took his shock tube to the University of Michigan and I took to Lehigh parts of a shock tube built at Princeton. Donald F. Hornig, who was at Woods Hole during the war and interested in pressure gauges, saw possibilities in the shock tube as a device for producing and studying shocks. At Brown he and E. F. Greene were starting their studies in chemistry at about this time. In 1947 Hornig told the American Physical Society in a contributed paper how he proposed to measure shock thickness by light reflection, but he did not mention the shock tube in his abstract.

The 1945 activities at Aberdeen and the Naval Ordnance Laboratory were in connection with the Operation Crossroads tests (Bikini). The shock tube was used for the development of the so-called Bikini gauge, or foil meter, a device for measuring blast pressures. The gauge consisted of two brass plates containing several sizes of holes with a piece of aluminum foil held between the two plates. This assembly was bolted to a pot, the purpose of which was to maintain a pressure on one side of the foil at one atmosphere while the other side of the foil was exposed to the blast wave. A strong blast wave made holes in all of the big diameter foils but deformed some smaller diameter foils only by some characteristic amount, while a weaker blast would leave its message on a partly deformed larger diameter foil. All of the foils used in these Bikini gauges were calibrated in the shock tubes at Princeton and at Aberdeen. Shock tube people who carried out these tests include Wesley E. Curtis, Gregory K. Hartmann, Curtis W. Lampson, James F. Moulton, Jr. and W. Thornton Read. Out of these grew two shock tube groups which are still active today. The first large shock tube, 24 in in diameter, was built by Wesley Curtis and Lampson at Aberdeen in 1948. Moulton and Hartmann started a shock tube 4 in by 8 in in cross-section in the spring of 1947. Both the Aberdeen and NOL groups had a continuing interest in gauge calibration, and the Aberdeen tube also performed studies of damage to small structual models, while the NOL tube carried out studies of

shock reflection and diffraction by spark photography and later interferometry.

Gordon N. Patterson, visiting the Princeton Institute for Advanced Study in 1946, attended lectures by von Neumann, Taub and Bleakney on shock waves and fluid dynamics in Palmer Physical Laboratory. The shock tube was discussed then along with other shock wave phenomena. The following year Patterson started shock tube research at the University of Toronto Institute of Aerophysics (later renamed Institute for Aerospace Studies). Under one of Patterson's first graduate students, I. I. Glass, this laboratory quickly became one of the centers of shock tube research. The complete compendium of shock tube design and performance by Irv Glass, W. A. Martin and Patterson, "A theoretical and experimental study of the shock tube" Univ. of Toronto Aerophysics Report No.2 (1953) served to help many become acquainted with the shock tube.

A group at Langley Research Laboratory, started by Arthur Kantrowitz, heard about the shock tube work at Princeton, and recognized the possibilities for studying unsteady flows. P. W. Huber carried out performance studies with the intention of applying the results to pulse jet engines and reported the work in 1949. C. P. Donaldson and R. L. Trimpi were interested in the shock tube as a device for studying flows, and in particular the wall effects (described 1949) and their propagation (1955).

The first studies at Lehigh were also concerned with wall effects and with whether the non-ideal behavior of the shock tube was attributable to wall effects or to the non-instanteous removal of the diaphragm.

In 1946 Lincoln G. Smith left Princeton and went to the University of Michigan. He planned to return to his early love of infrared spectrocopy. He took along his shock tube because nobody at Princeton wanted to use it. Somehow infrared spectroscopy did not engage Linc's undivided attention. At the January 1947 American Physical Society Meeting in New York he was showing his friends some interesting pictures, taken by Michigan graduate students C. W. Mautz and F. W. Geiger, of the mechanism of diaphragm breakage. Smith was proposing to use as a wind tunnel the shock tube he had built in Princeton and taken to Michigan. Although L. G. Smith left Michigan after two years and went to Brookhaven to work in mass spectrometry, never again to make any bangs in shock tubes, Otto Laporte developed an interest in the shock tube and its possibilities at Michigan. In 1949 Laporte presented an invited paper at an A.P.S. meeting in Seattle "Theory and Applications of the Shock Tube." Laporte's group has been one of the most productive - in ideas, in accomplishments, in students trained.

It was also at the 1947 American Physical Society meeting in New York, January 30, 31, February 1 that the nascent Division of Fluid Dynamics made its first public appearance. The Committee on Fluid Dynamics

(R. J. Seeger, chairman) arranged a session on compressible flow. Speakers on the programme were von Neumann, Temple and von Karman. V. Bargmann presented a contributed paper "On Nearly Glancing Reflection of Shocks" which was the first attempt to describe the whole flow field in Mach reflection.

Kantrowitz left Langley in 1946 for the Cornell Aero Department. One of his first graduate students at Cornell was Abraham Hertzberg. These two were interested in the shock tube as a device for producing the elemental flow characteristic of a cyling heat engine such as the Brown-Boveri Comprex. Hertzberg visited Bleakney's laboratory in Princeton in 1947 and learned of the various electronic instrumentation methods in use there. Kantrowitz was also interested in producing high temperature gases. It was his idea at the time to use converging shock waves to create very high temperatures so that he could do plasma studies. The shock tube was used in a study by Perry and Kantrowitz of cylindrically converging shock waves where luminosity was produced. The idea of using the shock tube as a wind tunnel was introduced to the Cornell workers when C. W. Mautz lectured there in 1948. It was about then that Kantrowitz with E. L. Resler and S. C. Lin proceeded with experiments to push the performance of the shock tube to extremes in temperature; they recognized the advantages of high sound speed in the driver gas and employed hydrogen and combustion to achieve very high temperatures.

Without demonstrating any spectacular results of either a fundamental or practical nature, the shock tube used as a wind tunnel spread like wild fire after 1948. In a letter to the editor of Physical Review 74, p.1872(1948), Mautz, Geiger and Epstein gave the criterion for obtaining subsonic, sonic and supersonic flows. R. K. Lobb at Toronto, W. C. Griffith at Princeton and Hertzberg at Cornell Aeronautical Laboratory were authors of early work. R. N. Hollyer, the graduate student following Geiger and Mautz on the 2 in by 7 in Michigan tube, made critical studies of the shock tube as a wind tunnel and was probably the first to recognize the existence of boundary layers growing on the shock tube wall and models. Modification of the shock tube by allowing the shock to expand into a diverging section was proposed by Hertzberg in 1950; he was by then at the Cornell Aeronautical Laboratory in Buffalo. Hertzberg's early work in Ithaca had been originally motivated by the desire to understand wave action in heat engines. When he went to Cornell Aeronautical Laboratory in Buffalo late in 1949, he returned to an interest in heat engines and was calculating a wave diagram in a diverging section when he realized that there was a way to circumvent the Mach number limitation of the straight bore shock tube which had been pointed out by Mautz. The first publication on the hypersonic shock tunnel was a technical report from Cornell Aero Lab in May 1951 "Shock Tubes for Hypersonic Flow." Kantrowitz at Cornell and Henry Nagamatsu at California Institute of Technology began work on hypersonic shock tunnels shortly thereafter, about 1951. Nagamatsu was

assisted by his student Y. A. Yoler and Kantrowitz had S. C. Lin and H. Petschek as student associates. The further development of the shock tubes and shock tunnels leading up to today's proposed 120 in hypersonic shock tunnel is a story in itself about which we will probably hear much at this meeting.

Another story which also starts about 1950, is that of chemical studies in the shock tube. Kistiakowski at Harvard, Kirkwood at Cornell, Norman Davidson at Cal Tech as well as Hornig and Greene at Brown, Griffith at Princeton and Hertzberg at Cornell Aeronautical Laboratory are names which must play a big part in this story.

Another story which begins about 1950 is that of luminous fronts in the shock tube. Richard G. Fowler at the University of Oklahoma was studying spark discharges in glass tubes filled with low pressure gas. A luminous front moving down the side arm of the T-shaped tube was described at a colloquium by Fowler at the University of Michigan in 1950 and Otto Laporte diagnosed this as a shock front. At the same time Laporte was studying the luminosity produced in the Michigan 2 in by 7 in tube when a hydrogen driver was used to produce very strong shock waves in argon. Kantrowitz and Perry had produced luminosity by the converging cylindrical shock wave in 1948 but a way of using this had not been developed. Both Laporte and Kantrowitz had apparently substituted numbers in the ideal theory formulas and were excited to see that such high temperatures could be produced by merely choosing parameters correctly. At the Divisional Meeting of the Division of Fluid Dynamics in Salt Lake City in June 1952, separate papers by Fowler, by Kantrowitz and by Laporte all described the emission of light from high temperature gases produced by a shock wave in a shock tube, although Fowler's shock tube was rather unconventional, having no diaphragm separating high and low pressure sections.

The lines of development that I have mentioned up to this period of 1952 to 1955 have all continued during the past ten years. It is my impression however that no new essential changes have appeared in the last ten years and perhaps the shock tube has reached a certain stage of maturity. At this meeting we shall learn of the most recent developments in all of these areas with the exception of the problem of Mach reflection. This problem which seems to have been the chief motivation for shock tube development at Princeton, has not yet been solved to the satisfaction of everyone. It seems to have been exhausted experimentally; papers in 1949 and 1951 in Rev.Mod.Phys. by Bleakney, Taub, Fletcher review the experimental results. Theorists are in various stages of disagreement as to whether they understand the reasons for the non-applicability of the triple point shock requirements.

In our story we seem to have left Princeton and Bleakney with no workers following the departure in 1946 of Lampson and Smith. Reynolds

was back in Princeton but had transferred his interest to the classical fields of cosmic rays and high energy physics. But Bleakney continued to lead an active group. A succession of young instructors and post-doctoral students included W. C. Griffith, Daniel Bershader and Harry Petschek. A group of eight graduate students earned Ph.D. degrees and fanned out to various labs around the country. Most of the work was carried out in a 4 in by 17-3/4 in shock tube which could be evacuated and filled with experimental gases. Studies of shock wave interactions were carried out by schlieren and shadowgraph and interferometry. This was the first shock tube instrumented with an optical interferometer and considerable work was done in the study of Mach reflections, reflections and transmissions through gaseous interfaces, relaxation and boundary layer studies. This large tube was finally disassembled in 1960 but the interferometer is in use at Lehigh on another shock tube today.

I should like to close by referring briefly to the last meeting of the Division of Fluid Dynamics which was held here at the Naval Ordnance Laboratory. It was a notable occasion both for the Division of Fluid Dynamics and for NOL. It was the third meeting of the Division of Fluid Dynamics; it took place on 30 June and 1 July 1949. It was the first meeting of the Division of Fluid Dynamics separate from the parent society. Highlights of the meeting were: a session on aerodynamics with speakers Hirschfelder, Uhlenbeck, Herzfeld, Lees, Bogdonoff, and P. S. Epstein; a session on shock wave phenomena with speakers Kopal, C. C. Lin, Bleakney, Seeger, Polachek, McMillen; and a session on turbulence with speakers Kampé de Feriet, Batchelor, Chandrasekhar, Squire and Frenkiel. Among the contributed papers were these on the shock tube: Geiger from Cornell Aeronautical Laboratory describing Mautz and Geiger's use of the shock tube for supersonic and transonic flow studies; Patterson, Glass and Bitondo of University of Toronto on calculation of normal shock wave reflection and transmission at a contact surface; Fletcher and Bleakney from Princeton showing the very graphic single fringe interferograms of Mach reflection; and Richard G. Stoner from Penn State describing shock wave refraction in soap bubbles containing helium, carbon dioxide and argon.

I should like to acknowledge corrections and additions to an earlier version of these remarks which have been sent me by the following people: W. Bleakney, C. P. Donaldson, I. I. Glass, E. F. Greene, G. K. Hartmann, A. Hertzberg, R. N. Hollyer, D. F. Hornig, P. W. Huber, A. Kantrowitz, C. W. Lampson, J. F. Moulton, G. N. Patterson, E. L. Resler, G. T. Reynolds, A. Roshko, L. G. Smith, A. H. Taub, R. L. Trimpi, and D. Weimer. I have tried to include all of their suggestions and changes, and I have expanded considerably on the earlier version. I must have included some statements with which they might not all agree. Errors are therefore to be ascribed to me alone.

COMMEMORATIVE PAPER

PROGRESS IN SHOCK TUBE RESEARCH IN ENGLAND: RECENT DEVELOPMENTS IN CHEMICAL APPLICATIONS OF THE SHOCK TUBE

John N. Bradley
University of Essex,
Colchester, England.

As a token of the debt which we all owe to the early workers in this field, I would like to devote the first part of this lecture to a description of the pioneer work on shock and detonation waves carried out by Dr. Payman in England during the pre-war years. During the post-war period, however, it is not really possible to distinguish English contributions from work performed elsewhere since, although certain experimental techniques, for example the use of microwave diagnostics (1), have originated independently in England, the research programmes as a whole have been integrated with concurrent developments in the States. I shall therefore use the second part of the lecture to review recent developments in shock tube technology as applied to problems in chemistry and physics, emphasizing the importance of the experimental techniques rather than the results of their applications. I hope that this approach will prove of particular interest to the non-chemists present.

Dr. Payman entered Government service in 1917 at an experimental station which later became part of the Safety-in-Mines Research Board. Dr. Shepherd, who was Payman's chief collaborator and eventually his successor, following Payman's untimely death in 1946, entered the same establishment only two years later. Both men died "in harness" having devoted the whole of their lives to mining problems, apart from a period during the war when their explosives expertise proved invaluable in other directions. Whilst today we wish to honour their contribution to shock tube research, we should not forget that their most substantial contribution to the welfare of the community at large lay in improving the safety and conditions of those working in our coalmines.

The investigations carried out by Dr. Payman and his collaborators on the properties of shock and detonation waves commenced in about 1925 and continued for a period of over fifteen years. The motivation behind the work is evident: the Safety-in-Mines Research Board was concerned with the dangers attendant upon the use of explosives for blasting operations in coal mines and, in particular, the likelihood of ignition of firedamp. They had previously set up the Explosives in Mines Research Committee to examine the problem and Payman's work was carried out specifically for this Committee. Most of his findings appeared in publications of the Research Board but items of more academic interest were also published in the Proceedings of the Royal Society and the Journal of the Chemical Society. It is always interesting to reflect on the quantity of important scientific information which has ensued from work of a strictly technological nature and it is to Payman's credit that he was continually aware of the wider implications of his findings.

Since Payman was concerned primarily with explosives, it is not surprising to learn that his interests commenced in the detonation field and he was later forced by the very nature of his results into studies on shock waves. It is interesting to record that some subsequent workers have also followed the same progression, though for different reasons. However, before discussing his findings in detail, it is better first to dwell for a while on his most important single contribution to shock wave technology - the development of the wave-speed camera.

At the time he commenced the work, two methods were available for the study of wave phenomena. The method introduced by Mallard and Le Chatelier (2) and developed further by Dixon (3) consisted of photographing the movement of luminous waves along columns of gas on to strips of film attached to the outside of a rotating-drum. The other method was the Schlieren technique which had been developed to the stage where photographs of non-luminous waves could be readily obtained. Both methods were, in fact, extensively used by Payman in his work - the latter technique being adapted to high speed studies by using an intense, short-duration electric spark to provide an instantaneous or kinematographic record of the component parts of the disturbance. Payman simply combined the advantages of the two approaches to obtain a continuous record of the time history of the non-luminous disturbances. (4)

The principle of the method is well-known (Figure 1). A diaphragm at F' serves to allow about one-half of the light passing through any region of interest actually to fall on the film. A density gradient will then refract the light beam so that a greater or lesser amount of light is involved in image formation, a pressure wave thus appearing as a dark or light line on the film depending on its direction of motion. The actual instrument illustrated (Figure 2) was constructed for use at the U.S. Bureau of Mines. In this model the drum had a circumference of 100 cm. and

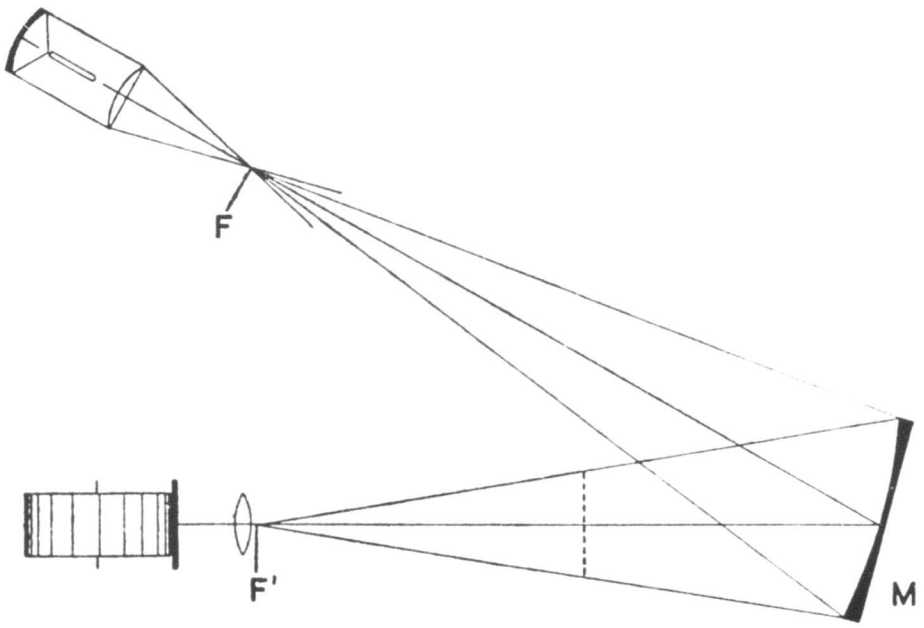


Figure 1.

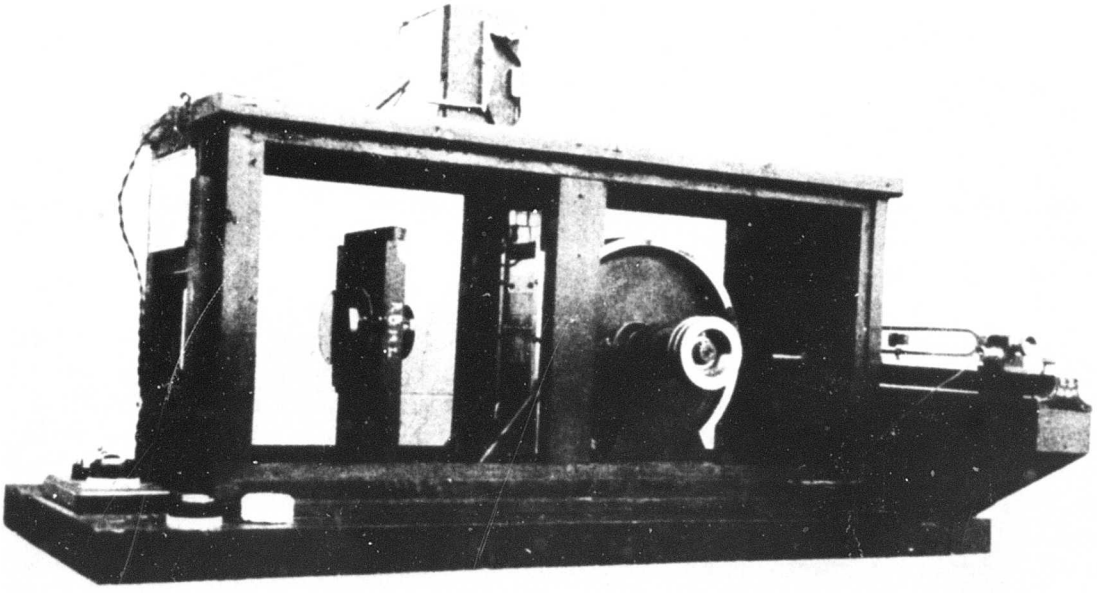


Figure 2.

rotated at 70 revs/sec. so that the linear velocity of the film was about 7000 cm/sec. A falling brass plate constituted the shutter and ensured that light entered the camera only during a single revolution of the drum. The same shutter also made or broke suitable electrical contacts which were used to synchronise the event under observation. The success which was achieved in synchronization is illustrated by the photograph of a moving bullet after leaving the muzzle of a rifle. (Figure 3) The velocity of the bullet was 750 metres/sec. and the shock waves A, B and C can be attributed to (i) gas leakage round the bullet before the rifled section sealed the escape of gas (ii) the piston action of the accelerating bullet, and (iii) the release of the main powder gases.

The first investigations were concerned with the transition between "normal" flame propagation and detonation (5). When a combustible mixture, such as 50% methane in oxygen, is ignited in a long cylindrical tube the initial ("normal") flame travels at about 2 metres/sec. After a period at constant velocity, the flame accelerates rapidly and then settles down to give a detonation wave with a velocity of about 2500 metres/second. In the "normal" flame, chemical reaction takes place because of the transfer of heat by conduction from the hot, burnt gases to the cold, unburnt gas. In the detonation, however, shock or pressure waves initiate very rapid chemical reaction, the energy released serving to maintain the wave. To a first approximation, both will travel at constant velocity, the demarcation between the two being the sound speed of the unburnt gas. Using the techniques referred to above, Payman demonstrated the formation in these flames of "compression" waves whose existence had previously only been postulated. He was able to show that the shock waves responsible for the eventual formation of a detonation do not originate from the initial spark but are generated in the burnt gases due to further chemical reaction. These shock waves then catch up the flame front, leading to an increased amount of reaction and eventually to detonation (Figure 4).

A series of publications then followed which illustrated various aspects of detonation wave formation (6). It will only be possible in the time allotted to give a few examples.

High explosives are normally "set off" by <u>detonators</u> - small capsules of very labile materials which detonate spontaneously on heating - and an investigation was made of the waves and flames which they generated. A considerable amount of information was obtained about the way in which such detonators operate as well as answering the immediate question of their liability to ignite firedamp. During the course of this work, it was inevitable that further knowledge about the properties of shock waves should come to light, in particular, concerning the effect of the temperature and pressure of the gas on the transition, and of interactions between waves themselves and between waves and solid obstacles.

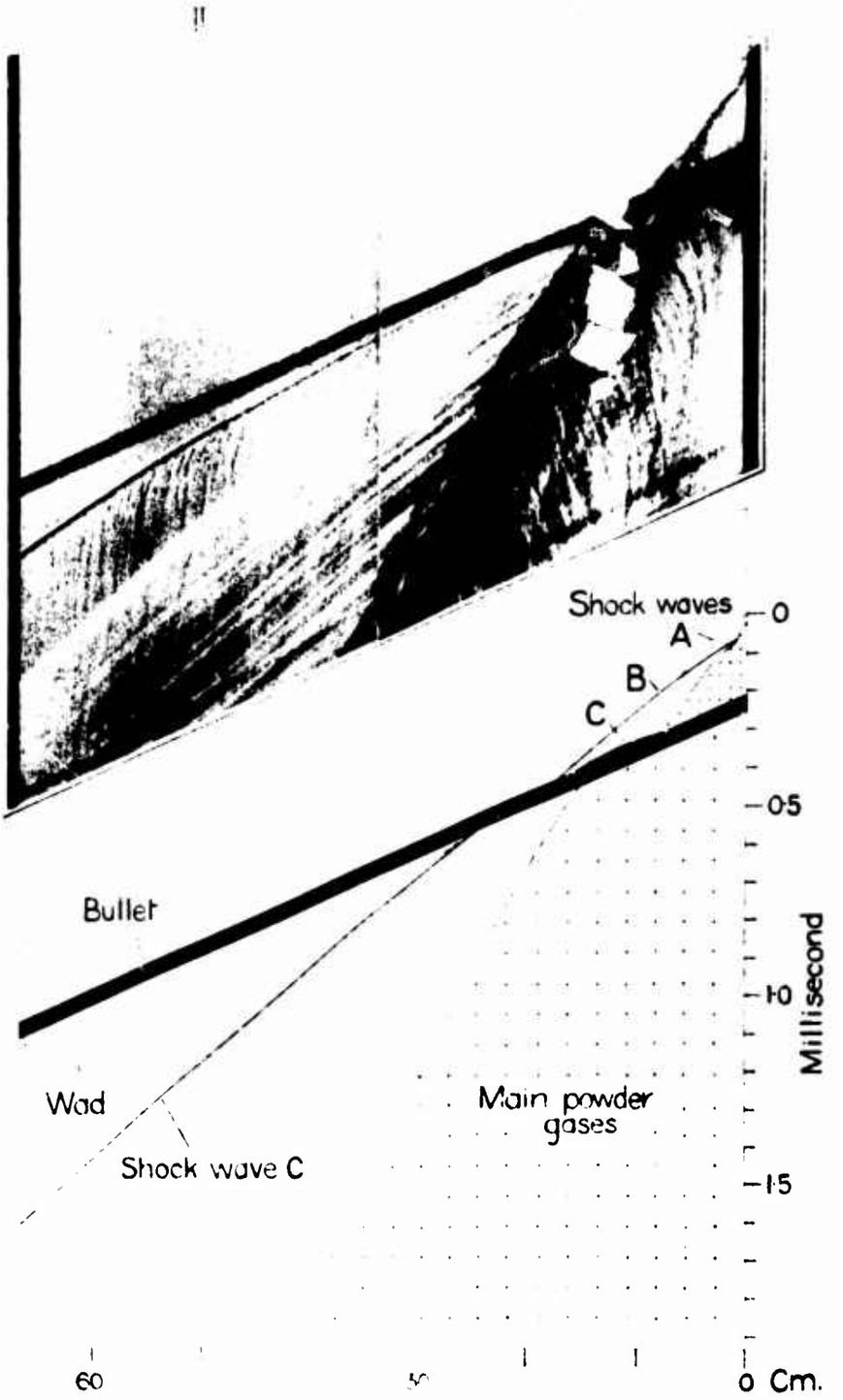

Shock waves
A
B
C
0
0·5
1·0
1·5
Millisecond
Bullet
Wad
Shock wave C
Main powder gases
60
0 Cm.

Figure 3.

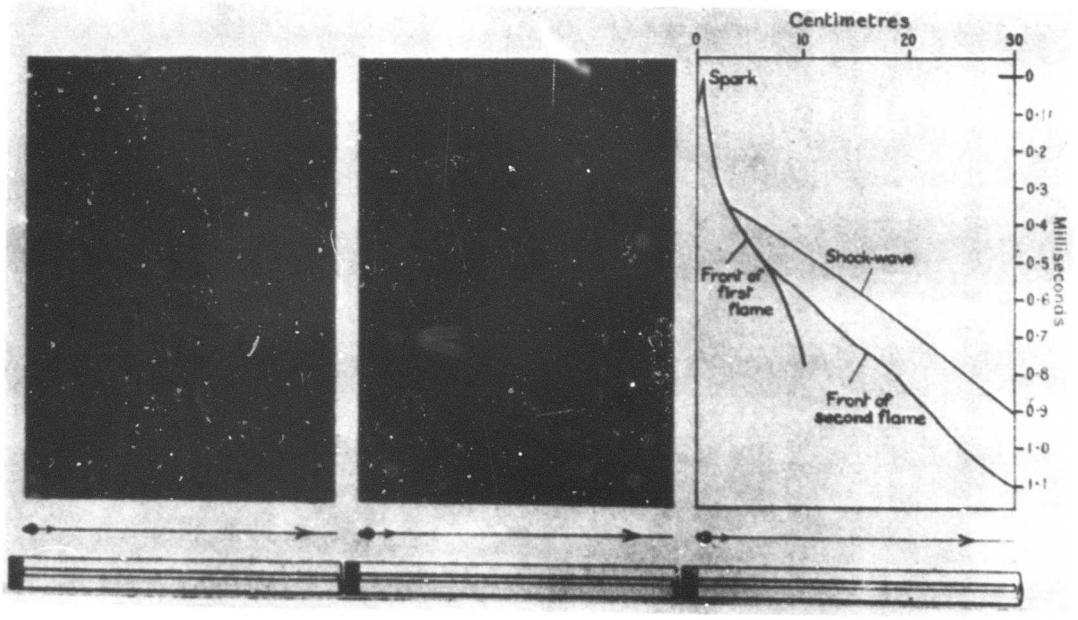


Figure 4.

From the point of view of safety in mines, a particularly interesting observation was that so-called "quasi-detonation" could occur (7). It was established that methane-air mixtures whose composition lay outside the expected range for detonation, due to the presence of the nitrogen diluent, could in fact be made to detonate if a small secondary source of energy were supplied. The importance of this phenomenon as a hazard in mining is clearly apparent and much of the work was carried out at the Bureau of Mines Experimental Station in Pittsburgh as part of a joint programme with the United Kingdom.

Although all this work was performed under Dr. Payman's direction, considerable credit should also go to his co-workers: H. Robinson, W.C.F. Shepherd, whom I have already mentioned, H. Titman, and D.W. Woodhead, several of whom remained with him during the majority of the period.

We now come to what is perhaps the important investigation from our point of view today (8). This describes the study of shock tube behaviour carried out by Payman and Shepherd, using the wave-speed camera. The work was submitted to the Royal Society at the beginning of the Second World War but was not published until 1946, two months after Payman's death.

The bursting diaphragm method of generating shock waves appears to have been first used by Vieille in 1899 (9). Although considerable study of the theory of the shock wave phenomenon was made both before and after that date, it appears that little effort was made to verify the results in the shock tube until Payman and Shepherd's time. The reasons for this are probably that no application for the shock tube had been foreseen and, in any case, until the development of the wave-speed camera, there was no method of verifying with any reliability which of the processes did in fact occur.

Some idea of the kind of result obtained in the work is illustrated in Figure 5, from which the following observations can be made. The first

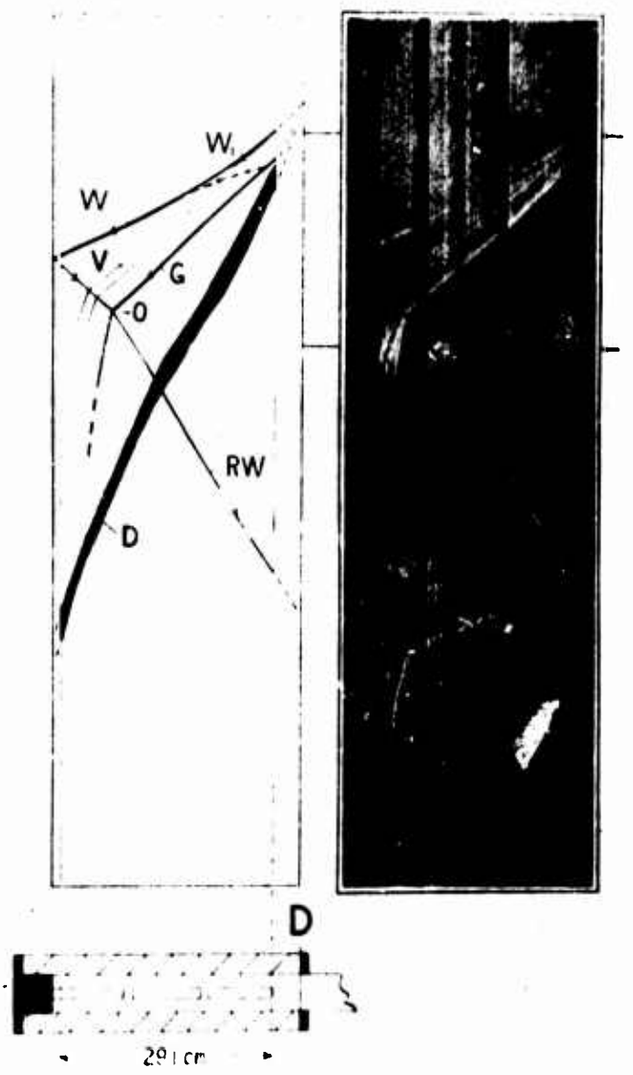


Figure 5.

shock wave is generated by the initial rupture of the diaphragm. It starts off relatively slowly, then accelerates until it reaches uniform speed. This initial wave is due to gas leaking round the diaphragm and is comparatively weak. As the diaphragm travels down the tube it rotates and allows the full compressed gas column to generate the main shock, W, which then overtakes the initial wave. The contact surface, G, is clearly seen, followed by the diaphragm whose varying orientation is shown by the distorted trace, D, on the film. The reflection of the shock at the end-wall, RW, followed by the various interactions with the other waves, is also visible. Similar photographs were obtained of the expansion wave propagating into the driver section.

The authors were able not only to demonstrate the existence of the predicted wave effects but also to make quantitative measurements and hence to establish the validity of the one-dimensional theory. It will only be possible to indicate briefly some of their results:-

(i) It was established that the mode of removal of the diaphragm affected only the initial stages of shock formation and that trapping the moving copper disc did not change the speed of the fully-developed wave.

(ii) Variation in length was found to have no effect on the primary waves, although it did have the expected effect on the time at which subsequent interactions occurred.

(iii) Experiments in which air was replaced by hydrogen or carbon dioxide in either the compression or expansion chambers led to the expected result, that is the shock strength, expressed as the ratio of its velocity to the sound velocity, increased with increased sound velocity in the compression section but was reduced by an increased sound velocity in the expansion section.

(iv) Since both shock and flow velocities could be determined with some certainty it was possible to compare their ratio with that predicted theoretically. Agreement to better than 5% was obtained, thus providing convincing evidence of the validity of shock wave theory. (I should hasten to assure American readers that although Payman and Shepherd assumed an ambient temperature of $0^{\circ}C$, the temperature in British laboratories frequently exceeds this value!) Although they could not measure pressure directly, estimates based on the length of the compressed column of gas at various times gave satisfactory agreement with the predicted values.

(v) The final, and perhaps most convincing, demonstration of the validity of the theory was obtained at Taylor's suggestion by comparing the experimental velocities with those predicted from the bursting pressure ratio.

Over the fifteen-year period, Payman's group had thus developed experimental techniques for following wave phenomena and had moreover

succeeded in demonstrating the validity of essentially all the effects predicted by the one-dimensional theory of the shock tube.

I now wish to jump forward about twenty-five years and make some brief comments on the present state of the art.

The chemist or physicist is less interested in the shock front itself or in the movement of the gas behind it, which can be somewhat of a drawback, and is more concerned with the thermodynamic state of the shock-heated gas. The most interesting variable is the temperature and it is just this variable which has proved most difficult to measure. Conventional thermometric devices are out of the question, owing to their large heat capacities, relative to the hot gas, and their slow response. Measurements of the sound speed have been used with some success in simple gases at lower temperatures but are of little value in systems of chemical interest.

Considerable progress in overcoming this problem has been achieved by Professor Gaydon's group at Imperial College (10,11) using the spectral line reversal method originally developed for the measurement of temperatures in flames. The principle of the method is that a substance will absorb or emit light of characteristic frequency depending on whether its temperature is below or above that of the source. The usual method is to disperse a sodium compound in the test gas and then determine whether it absorbs or emits sodium radiation from a calibrated source. This has provided measurements accurate to within 20°K at 2500°K. One difficulty with the method has been in deciding the meaning of the measured "temperature" when the gas is incompletely relaxed but recent work by Hurle (12) seems to have established beyond reasonable doubt that it is in fact the "vibrational" temperature and vibrational relaxation times for nitrogen obtained on this assumption agree closely with other determinations.

The technique has been used with other substances e.g. chromium, (11,13) from added chromium carbonyl, and C_2 (14), and the results agree closely with those obtained with sodium vapour. Although the technique still leaves much to be desired and new ideas would be welcome, it is outstandingly the most reliable method so far devised.

Pressure is a less important variable of the gas owing to its strong dependence on temperature, but improvements in the measurement of density continue. The Mach-Zehnder interferometer is still the most useful instrument for density measurement and outstanding results on vibrational relaxation using this technique have been produced by Millikan and White at the General Electric Company laboratories (15). Also, by suitable adaptation of laser techniques, the exposure time required to photograph the shock front density profile can now be reduced to 20 nanoseconds (16).

The complementary X-ray densitometric technique appears to have fallen into disfavour, possibly due to instrumental difficulties and to the requirement for a high atomic weight diluent for maximum sensitivity rather

than to dissatisfaction with the results obtained. On the other hand, electron beam densitometry is becoming a powerful tool for density measurements at low initial pressures(17). More will be said about this technique later. In general, the situation regarding the measurement of density appears quite healthy and the limitations now are imposed rather by non-ideal shock tube behaviour than by inadequate instrumentation.

If we assume for the moment that shock tube behaviour is ideal and that translational and rotational relaxation occurs in the front itself, then subsequent relaxation processes may be studied by monitoring the changes which occur as a function of time (or distance) behind the front. Although overall changes in density and temperature are useful, more information can usually be gained by employing techniques which are sensitive to concentrations of particular molecules or even of particular molecular energy states. Thus, the most useful chemical information so far has been gained from measurements of the absorption of ultra-violet or visible light.

A promising addition to the available techniques stems from the development of solid state infra-red detectors which have both the sensitivity and time resolution required for shock tube studies. With their advent, infra-red emission spectrophotometry has become a feasible method of following concentration changes in shock-heated gases. Emission measurements avoid difficulties over source temperatures, line broadening etc. In the ultra-violet and visible regions of the spectrum, emission studies have tended to be less useful because the concentrations of the excited states do not necessarily bear a simple relation to ground state concentrations. However, if one is studying vibrational relaxation, then the populations of the vibrationally-excited states are precisely what are required and, in the case of chemical reaction, vibrational relaxation is usually so fast that a Boltzmann distribution may be assumed in all but the most extreme cases e.g. high temperature dissociation of stable diatomic molecules. Finally, most molecules of chemical interest show an infra-red emission spectrum on heating although they frequently do not possess a characteristic ultra-violet or visible spectrum of appreciable intensity: this is particularly true of hydrocarbon molecules.

Perhaps the best example is provided by the work of Hooker and Millikan on carbon monoxide (18). They followed the fundamental and first overtone frequencies and were able to show that the rate of population of the $v = 2$ level by unit quantum jumps was ten times more efficient than the direct excitation. This was essentially a repeat of a rather less conclusive experiment carried out by Windsor, Davidson and Taylor several years previously (19). Another demonstration of the value of the technique in vibrational relaxation studies is provided by Camac's work on carbon dioxide (20). Camac followed concurrently the total density change by electron scattering and the population of the first excited state of the ν_3 mode by infra-red emission. The fact that both profiles were identical showed that all four vibrational modes relax at the same rate.

Under the more extreme conditions of chemical reaction, the decompositions of NH_3, (21) N_2O, (22) and CO_2 (23) have all been followed by infra-red emission. Of these, the work on carbon dioxide is noteworthy because a number of independent studies were made on the system although it is by no means so encouraging that the separate workers failed to agree about their findings. This is not an uncommon feature of shock tube experiments. Not all investigations have been concerned with decomposition reactions. Since the isotopically-substituted acetylenes C_2H_2, C_2HD and C_2D_2 show different infra-red emission spectra, Kuratani and Bauer (24) were able to follow the exchange reaction of C_2H_2 and D_2, which has particular kinetic significance as a four-centre reaction. The formation of NO in shock-heated air at 2300° - 4500°K has also been investigated by Camac and co-workers (25). Because of the large number of participating reactions the results proved difficult to analyze but satisfactory agreement has been obtained by synthesizing the composition profiles from possible reaction schemes using rate constants which had been proposed independently. The use of trial mechanisms with a high-speed computer to simulate the experimental data is a growing feature of this type of work.

As the most important requirement in a chemical experiment is to follow concentration changes of one species in the presence of several others, selectivity is as important as sensitivity in choosing the spectral range in which to operate. The introduction of infra-red techniques merely extends the spectral range available and the ultra-violet region of the spectrum will continue to be very useful.

The demands of the chemist are even greater in that he is desperately anxious to learn more about the transient species present during a complex reaction sequence. The outstanding advance in this direction was made by Bauer and Schott (26) with their work on absorption by OH radicals and advances continue in this field largely because OH is such an important constituent of oxidation reactions. Some progress is now being made in the use of Lyman-α radiation at 1215.7 Å to detect hydrogen atoms (27), which are probably the most important reactive intermediates in chemistry.

Some results have also been obtained using flash discharge sources and photographic recording to detect transient intermediates (28). Experiments of this type are less quantitative and require considerable repetition in order to obtain comprehensive kinetic records even for a single set of starting conditions. On the other hand, such work can prove very valuable for establishing the mechanisms of reactions.

Undoubtedly, the major advances in simple chemical studies will follow developments in spectroscopic methods for detecting reactive intermediates.

Much important information can be gained if the shock-heated gas is cooled rapidly, after a known time interval, and the products are then analysed in a conventional manner. The simplest way of achieving this is to select the operating conditions so that the reflected shock wave interacts

with the contact surface to give a forward-moving expansion wave (Figure 6b). One investigation has employed this method (29) but it is not satisfactory because the rate of cooling is relatively slow and further wave phenomena will occur before quiescent conditions are attained.

A much more satisfactory technique was developed by Hertzberg and co-workers at Cornell Aeronautical Laboratory Inc. (30). Here the rupture, at the correct moment, of a second diaphragm attached to a large evacuated tank produces a strong rarefaction wave which gives the desired cooling and no further wave interactions occur. (Figure 6c). This has been employed for many investigations and recent developments have minimized some of the difficulties associated with the method i.e. inadequate cooling rates, precise timing of the diaphragm rupture, variation of heating time over tube length (Figure 6d), etc.

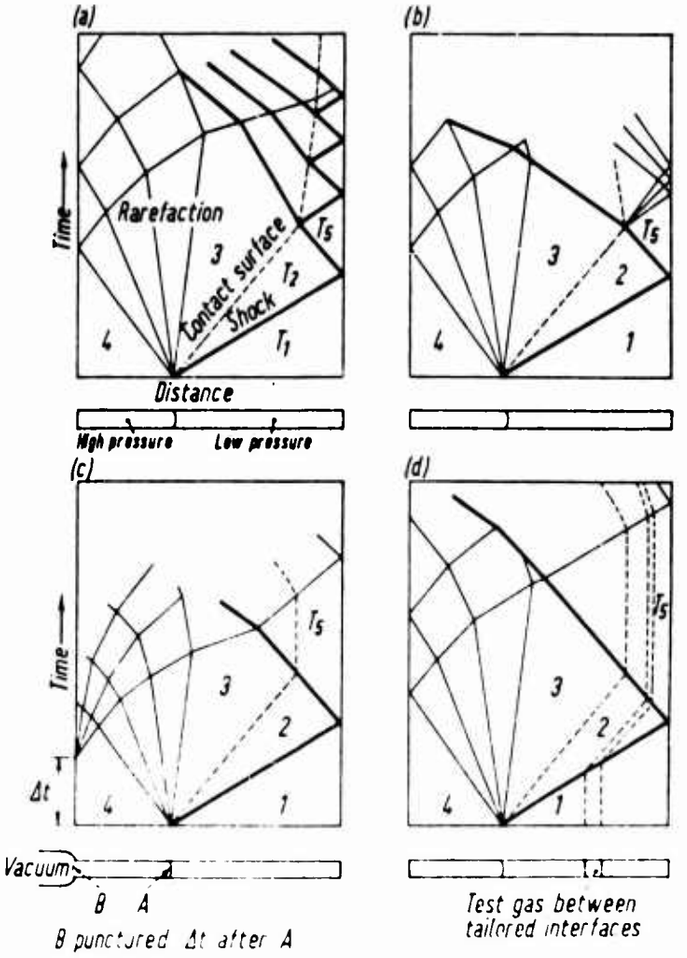


Figure 6.

A novel combination of these two techniques has recently been developed by Lifshitz, Bauer and Resler (31). They employed the cooling wave produced by interaction of the reflected shock with the interface in the same way as Greene and also arranged this to coincide with the arrival of the reflected rarefaction wave. In order to prevent subsequent waves leading to re-heating they placed a dump tank at one side of the shock tube just ahead of the driver section. No diaphragm is needed for its operation, hence avoiding complex timing problems, as it quenches the returning shock without modifying the incident shock. (Figure 7). The importance of this apparatus is its simplicity compared with the CAL single-pulse tube. The gas dynamic aspects of its operation seem satisfactory but it is unfortunate to record that even when the analysis was restricted to a small volume at the end of the tube, an appreciable portion of the gas had not attained the calculated reflected shock temperature.

Yet another method for quenching a reacting gas by rapid expansion has been developed by Jacobs et al.(32). A cylindrical section of the tube close to the end-wall is allowed to open into a vacuum (Figure 8). No attempt was made to collect the expanded gas, the method having been used so far solely to study recombination rates.

The most rapid quenching rates are achieved in expanding nozzle flows and much work is in progress to develop these for chemical studies. Skinner has made considerable progress with such a system for generating molecular beams of high intensity - a typical beam produced in the way having an intensity of 2.4×10^{18} molecules cm^{-2} sec^{-1} and an energy of 1.2 ev. (33). (Figure 9). This technique is presently being examined by ourselves as a method of cooling ionized gases prior to their introduction into a mass-analyzer. The nozzle system is under vacuum and is separated from the tube by a very fragile diaphragm, which ruptures on impact. Starting times of such devices have been studied in the United Kingdom by Schultz and Holder (34).

The same type of device is required in the mass spectrometer detection system used for sampling from reflected shock waves. The gas is allowed to issue from a small orifice in the thin end-wall of the shock tube and it is then open to question whether the sampled gas is representative of the bulk material or of the thermal boundary layer adjacent to the end-wall. Dove and Moulton (35) have improved the method by using a conical projection as a support for the pinhole and claim that the sampling method may be valid for times of the order of 1 millisec. It is clear that any such system must eventually fail as the thermal boundary layer grows with $(\text{time})^{\frac{1}{2}}$ and the hemisphere supplying the gas grows with $(\text{time})^{\frac{1}{3}}$. Despite this difficulty the chemical evidence obtained so far supports the validity of the technique.

Because shock tube operation is gas dynamic in nature, the mean free path must necessarily lie below the minimum dimensions of the vessel and this imposes a lower limit on the densities which can be usefully employed.

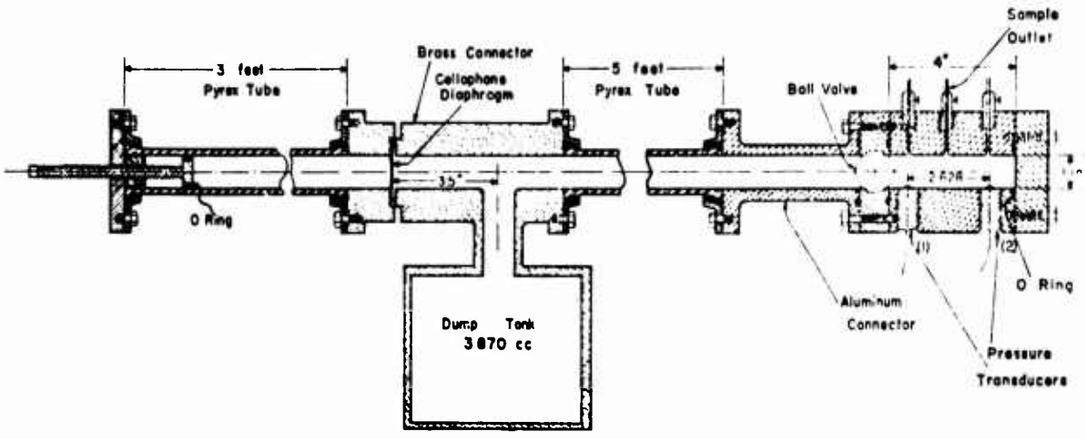


Figure 7.

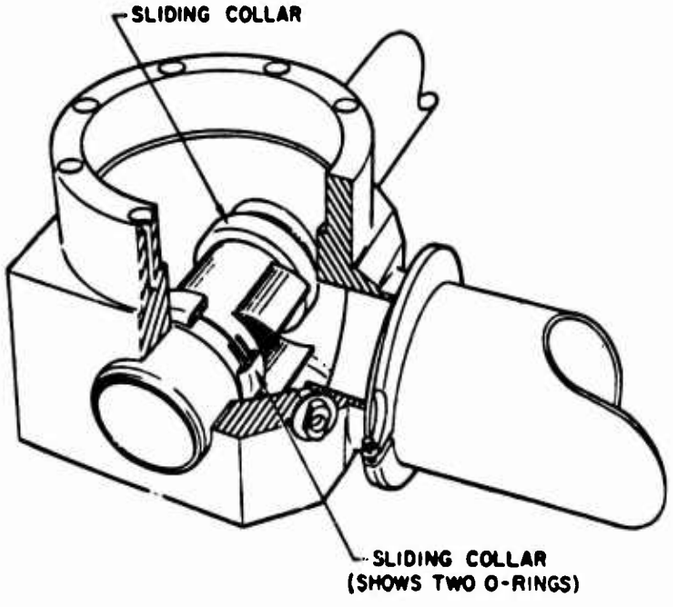


Figure 8.

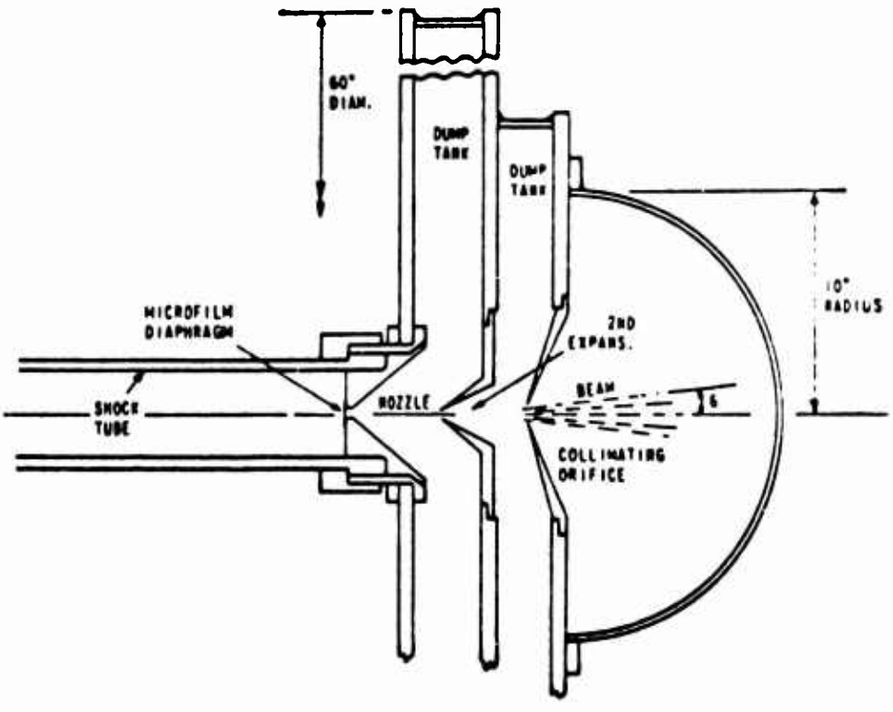


Figure 9.

The 2-foot diameter tube constructed at the AVCO laboratories (37) is thus of considerable interest because it permits experiments to be conducted at densities an order of magnitude below those in conventional systems and hence extends the molecular time scale by a similar factor. Although this produces difficulties with boundary layer growth and shock front curvature, it has enabled relaxation studies to be carried out with much greater resolution, in terms of collision numbers, than in the usual systems. Shock front density profiles have been obtained from electron scattering measurements in this way.(17).

It is worth mentioning that essentially the only property of the shock wave which has proved of interest so far is the increase in temperature and we are presently investigating the high flow velocities behind the shock front with a view to their possible use in chemistry (38). Flow systems are always of value for kinetic work because they permit measurements requiring time resolution to be replaced by those involving distance resolution. For flow velocities corresponding to the unperturbed sound speed, time resolution in the microsecond range can be replaced by distance separations of a millimetre which are readily attained with optical devices. The apparatus under investigation uses a flash-photolysis set-up to initiate a chemical reaction which is then followed by spectrophotometric measurements

downstream. Present indications are that the method is feasible but no outstanding results have been obtained so far.

In discussing instrumentation I have made very little mention of the limitations imposed by deviations from ideal one-dimensional behaviour. Of necessity, the chemist tends to be forced into a "head-in-the-sand" attitude over many of these, minimizing their effects whenever possible and, if they prove unavoidable, justifying his work by the results produced. However, it is worth drawing attention to the most troublesome.

Since the reflected wave region is most convenient for kinetic studies it is extremely irritating to find that ideal behaviour can be relied on, if at all, only in a very narrow region close to the end-wall. In the incident region, work on very strong shocks is being severely hampered by precursor effects - electrical phenomena which are propagated ahead of the main shock wave. Boundary layer growth in the incident shock region is better understood but the adverse effect of trace impurities is very frustrating. Finally, much more searching studies on relaxation processes could be made at lower pressures and it is indeed unfortunate that the shock wave behaviour becomes so complex in this region.

I have made no attempt to indicate the complete range of processes which may be investigated by shock wave techniques, the examples quoted representing only a few of the fields of interest. However, to conclude, I would like to express the opinion that the topic which has so far yielded only limited results yet is apparently particularly amenable to shock tube study is that of thermal ionization. My own impression is that this is due, in part, to a lack of knowledge concerning the precise nature of the ions present and, I might add, my own group, among others, is hoping to assist in solving this problem.

REFERENCES

(1) Hey, J.S., Pinson, J.T. and Smith, P.G., Nature 179, 1184 (1957); 182, 1220 (1958).

(2) Mallard, E. and Le Chatelier, H., Ann. Mines 4, 313 (1883)

(3) Dixon, H.B., Phil. Trans. A200, 315 (1903)

(4) Payman, W. and Woodhead, D.W., Proc. Roy. Soc. A132, 200 (1931)

(5) Payman, W., Proc. Roy. Soc. A120, 90 (1928)

(6) Payman, W., Woodhead, D.W., and Titman, H., Proc. Roy. Soc. A148, 604 (1935)
Payman, W. and Titman, H., Proc. Roy. Soc. A152, 418 (1935)
Payman, W. and Woodhead, D.W., Proc. Roy. Soc. A163, 575 (1937)

(7) Payman, W. and Shepherd, W.C.F., Proc. Roy. Soc. A158, 348 (1937)

(8) Payman, W. and Shepherd, W.C.F., Proc. Roy. Soc. A186, 293 (1946)

(9) Vieille, P., Compt. Rend. 129, 1228 (1899)

(10) Clouston, J.G., Gaydon, A.G. and Glass I.I., Proc. Roy. Soc. A248, 429 (1958);
Clouston, J.G., Gaydon A.G. and Hurle, I.R., Proc. Roy. Soc. A252, 143 (1959)

(11) Gaydon, A.G. and Hurle, I.R., Proc. Roy. Soc. A262, 38 (1961)

(12) Hurle, I.R., J. Chem. Phys. 41, 3911 (1964)

(13) Bauer, S.H., Kiefer, J.H., and Loader, B.E., Can.J.Chem. 39, 1113 (1961)
Kimber, G.M. and Napier, D.H., Combustion and Flame 9, 103 (1965)

(14) Napier, D.H., Nettleton, M., Simonson, J.R. and Thackeray, D.P.C., A.I.A.A. Jnl. 2, 1136 (1964)

(15) Millikan, R.C. and White, D.R., J.Chem. Phys. 39, 98 (1963)
White, D.R. and Millikan, R.C., J.Chem. Phys. 39, 1803 (1963); 39, 1807 (1963); 39, 2107 (1963)

(16) Wachsler, E., private communication.

(17) Camac, M., Phys. of Fluids 7, 1076 (1964)

(18) Hooker, W.J. and Millikan, R.C., J. Chem. Phys. 38, 214 (1963)

(19) Windsor, M.W., Davidson, N., and Taylor, R.L., Seventh Symposium (International) on Combustion, Butterworth, London, p.80 (1959)

(20) Camac, M., Avco-Everett Research Report 194 (1964)

(21) Jacobs, T.A., J. Phys. Chem. 67, 665 (1963)

(22) Fishburne, E.S. and Edse, R., J. Chem. Phys. 41, 1297 (1964)

(23) Jost, W., reported at Army Research Office Symposium, Durham, N.C. (1964)
Steinberg, M., General Motors Defense Research Lab., TR 64-49 (1964)
Davies, W.O., J. Chem. Phys. 41, 1846 (1964)

(24) Kuratani, K. and Bauer, S.H., J. Amer. Chem. Soc. 87, 150 (1965)

(25) Camac, M., Feinberg, R.M. and Ryan, R.J., reported at Army Research Office Symposium, Durham, N.C. (1964)

(26) Bauer, S.H., Schott, G.L. and Duff, R.E., J. Chem. Phys. 28, 1089 (1958)
Schott, G.L. and Kinsey, J., J.Chem. Phys. 29, 1177 (1958)

(27) Myerson, A.L., Thompson, H.M., and Joseph, P.J., CAL Report No. AD-1689-A-3 (1964)

(28) e.g. Gaydon, A.G., Kimbell, G.H. and Palmer, H.B., Proc. Roy. Soc. A279, 313 (1964)

(29) Greene, E.F., Taylor, R.L. and Patterson, W.L., J. Phys. Chem. 62, 238 (1958)

(30) Glick, H.S., Squire, W., and Hertzberg, A., Fifth Symposium (International) on Combustion, Reinhold, New York, p. 393 (1955)

(31) Lifshitz, A., Bauer, S.H., and Resler, E.L., J. Chem. Phys. 38, 2056 (1963)

(32) Jacobs, T.A., Hartunian, R.A., Giedt, R.R. and Wilkins, R., Phys. of Fluids 6, 972 (1963)

(33) Skinner, G.T., Physics of Fluids 4, 1172 (1961)
Skinner, G.T. and Fitz, B.H., Fourth International Symposium on Rarefield Gas Dynamics, Toronto (1964)

(34) e.g. Shultz, D.L. and Holder, B.D., N.P.L. Aero Note/325 (1957)

(35) Dove, J.E. and Moulton D. McL., Proc. Roy. Soc. A283, 216 (1965)

(36) Skinner, G.T., CAL Report No. RM-1396-A-1 (1961)

(37) Lin, S.C. and Fyfe, W., Phys. of Fluids 4, 238 (1961)

(38) Bradley, J.N. and Tuffnell, R., Proc. Roy. Soc. A280, 198 (1964)

BLANK PAGE

ELECTROMAGNETICALLY POWERED SHOCK TUBES*

E. L. Resler, Jr.
Graduate School of Aerospace Engineering
Cornell University, Ithaca, New York

ABSTRACT

The basic factors leading one to undertake the construction of a shock tube in which the shock waves are driven electromagnetically are reviewed. The difference between the performance of the electromagnetically driven tubes and those of more conventional design are discussed. Typical experimental results of phenomena occurring in these tubes are presented, especially those tending to document the interpretation of the operating principles of this type shock tube.

INTRODUCTION

Many and varied are the techniques explored to generate shock waves in order to study their properties or to use to initiate chemical changes in a gas sample. Most of the techniques make use in some manner of an unsteady wave acceleration process. The wave acceleration process is quite general and within this context the ordinary pressure driven and electromagnetic shock tube can be compared. Although electromagnetic drive mechanisms are also abundant they can all be classified in a general way to fit in a theoretical framework that makes their limitations evident.

ORDINARY (PRESSURE DRIVEN) SHOCK TUBES

The operation of this type shock tube depends on a gas piston being accelerated. The gas piston compressing a gas initially at rest, the test

* This work was partially supported by the Mechanics Branch of the Office of Naval Research under Contract Nonr 401(25). Reproduction in whole or in part is permitted for any purpose of the United States Government.

gas, generates a shock wave whose strength is related to the gas piston velocity. For example, consider the physical case depicted in figure 1. The gas piston interface is denoted by the dashed line. The shock wave, denoted by the heavy solid line, is moving from left to right into a gas at rest. The gas at rest is compressed between the shock wave and the piston face and also accelerated to the piston velocity u when the shock passes over it. Hopefully the region between the shock wave and the gas piston interface has uniform properties and is used as a high temperature "test slug" for many purposes. A group of waves, labeled "expansion waves" provide the mechanism to accelerate the driver gas also initially at zero velocity to the gas piston velocity u . The expansion waves are moving through the driver gas from right to left and changing the velocity of the gas from zero to u . The final effect is that the thermal energy of the driver by wave processes is concentrated in the test slug appearing as kinetic and thermal energy of the gas processed by the shock wave. The concentration by wave action of momentum and energy in the test slug of gas is the important feature making possible uses made thus far of the shock tube.

WAVE ACCELERATION PROCESSES

Any wave acceleration mechanism can be described in terms of a force acting in the wave front that accelerates the fluid supporting the wave in accordance with Newton's laws of momentum. Consider the wave depicted in figure 2, which moves relative to the fluid with wave velocity W and in this case from right to left into a fluid with a velocity u . Let the differential force acting across the face of the wave be $d\pi$ then to conserve momentum

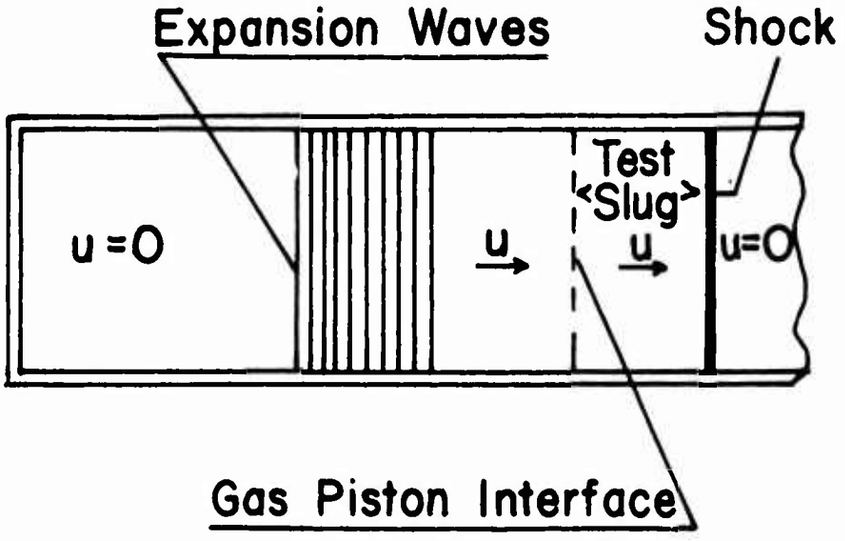


Figure 1

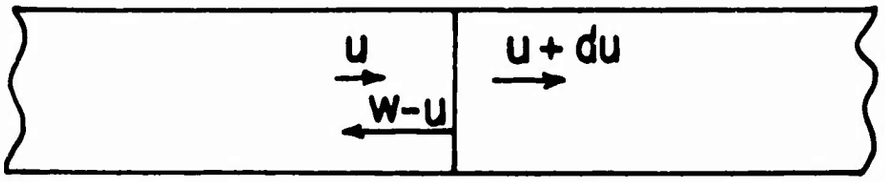


Figure 2

$$d\pi = \rho W\, du \quad \text{or} \quad du = \frac{d\pi}{\rho W} \tag{1}$$

For a pressure driven or thermal shock tube, the description to be clarified below, the wave speed W is the ordinary sound speed a so

$$W = a = \left(\gamma p/\rho\right)^{1/2}$$

and the accelerating force π in this case is the pressure p or $\pi = p$. ρ is the density of the fluid and γ the ratio of the specific heats. The acceleration expected through a group of waves would be the integral through the group, the details of the integration can be complicated but approximating in a general way,

$$u \sim \int du \sim \frac{p}{\rho a} \sim a \sim (T)^{1/2} \tag{2}$$

Thus since the shock Mach number is related to the gas velocity u the pressure driven or thermal limited shock tube has a performance, if performance is measured by shock Mach number, that is determined by the temperature of the driver. Although there are many schemes to heat the driver gas of a shock tube and thus increase its performance ultimately heat transfer to the tube walls, probably by radiation, is faster than the wave process forming the shock wave. When this condition prevails further increase of shock Mach number by driver heating is not possible.

In an electromagnetic powered shock tube any force exerted on the gas by other than gas pressure forces is due to the action of currents j in a magnetic induction field B. The force $d\pi$ acting in this case is

$$d\pi = jBL$$

, L is a typical length and j is a current density so jBL is a force per unit area or has the dimensions of a pressure. Note that if Ampere's law is used so that $j \sim B/\mu L$ that the quantity B^2/μ has the dimensions of a pressure and is usually referred to as the magnetic pressure. μ here is the permeability of the medium. By analogy with the definition of the sound speed, replacing the gas pressure by the magnetic pressure a propagation speed of disturbances c can be defined so that

$$c \sim (B^2/\mu\rho)^{1/2}$$

This disturbance velocity is referred to as the Alfven speed after its discoverer Alfven. This speed is that of waves the fluid can sustain if its elastic properties were entirely due to the presence of the B field. Estimating the velocity u across a group of waves of this type,

$$u \sim \frac{jBL}{\rho B/(\mu\rho)^{1/2}} \sim \frac{jL\sqrt{\mu}}{\sqrt{\rho}} \qquad (3)$$

Note here that there seems to be no natural limit to the possible values of u. That is u can be made as large as desired by increasing j or decreasing ρ. Except for minor differences in actual interpretation of (3) this is true. Electromagnetic drive mechanisms present the exciting possibility of extension without limit within the context of the equations used to describe them.

To help in this discussion it is conventional and convenient to define the magnetic Reynolds number

$$R_m = \mu\sigma uL = \text{Magnetic Reynolds No.} \qquad (4)$$

μ is again the permeability, σ is the scalar conductivity of the medium, u is a typical velocity and L is a typical length. Reorganizing the terms in this definition leads to various equivalent physical interpretations of this number. For example,

$$R_m = \frac{\mu\sigma L^2}{L/u} = \frac{\text{time for } B \text{ field to diffuse a distance } L}{\text{typical time in wave process}}$$

or

$$R_m = \frac{\sigma u B}{B/\mu L} = \frac{B_i/\mu L}{B_a/\mu L} = \frac{\text{wave induced currents}}{\text{currents producing } B_a}$$

B_i is the magnetic field attributable to the induced currents in the plasma and B_a is the field due to currents outside the plasma. In general when R_m is large, it is the magnetic field which controls the bulk modulus of the plasma and thus the wave propagation speed in the fluid. Also if R_m is small, j can be calculated using Ohms law; otherwise (R_m large) j must be calculated using Amperes law.

Consider first the physical circumstances governing the shock tube when one attempts a drive mechanism in the small magnetic Reynolds number range. In these discussions it is assumed that the electromagnetic drive mechanism dominates. In this case $j \sim \sigma u B$ and the wave induced velocity u is then

$$u \sim \frac{jL\sqrt{\mu}}{\sqrt{\rho}} = \mu\sigma u L \frac{B}{\sqrt{\mu\rho}} = R_m \frac{B}{\sqrt{\mu\rho}} \qquad (5)$$

For this estimate it appears that one desires as large an R_m as possible. This expression cannot be used, however, unless R_m is small compared with unity.

For large magnetic Reynolds numbers the same expression for u applies but now j must be calculated from Amperes law or,

$$u \sim j\frac{L\sqrt{\mu}}{\sqrt{\rho}} \sim \frac{B}{\mu L}\frac{L\sqrt{\mu}}{\sqrt{\rho}} \sim \frac{B}{\sqrt{\mu\rho}} \qquad (6)$$

This result can be interpreted in light of our previous result as follows. The final gas piston velocity attainable with electromagnetic drive mechanisms is proportional to the Alfven velocity. For small magnetic Reynolds number cases ($R_m < 1$) the limiting velocity is proportional to the Alfven velocity and the constant of proportionality contains the magnetic Reynolds number as a factor. For large R_m ($R_m > 1$) the magnetic Reynolds number dependence disappears.

Working with the Alfven velocity alone it appears that it could be made any desired large value by decreasing the density and thus any desired shock tube performance would be possible. Actually this is not the case as momentum considerations then limit the performance of the tube. Consider

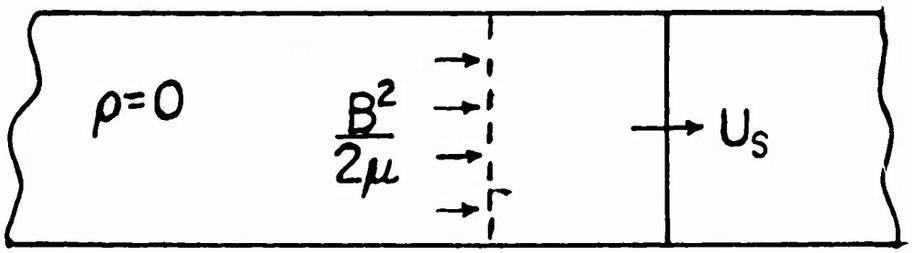


Figure 3.

this case as depicted in figure 3. If $\rho = 0$ in the driver section then the force $jBL \sim (B/\mu_L)BL \sim B^2/\mu$ is just the magnetic pressure acting on the gas processed by the shock wave. This is the case of an expanding magnetic field when the expansion rate is controlled by the gas in the tube processed by the shock wave. In this case the gas pressure behind the shock wave just balances the magnetic pressure or

$$\rho_1 U_s^2 = B^2/2\mu$$

where ρ_1 is the density ahead of the shock wave. The performance of the shock tube is now again determined by an Alfven velocity, namely $B/\sqrt{\mu\rho_1}$, since

$$U_s \sim B/\sqrt{\mu\rho_1}$$

so the shock velocity is finally limited by an Alfven velocity calculated using the density ahead of the shock wave. With these general considerations in mind, one can construct a more rigorous "shock tube theory" and derive a shock tube "equation" which contains not only these limiting cases, but also covers the transitional phases where thermal and magnetic drives are of equal importance.

SHOCK TUBE THEORY

A convenient shock tube theory can be formulated for the case where the driver gas is infinitely conducting, or $\sigma \simeq \infty$, and the magnetic induction B, restrained by the large conductivity to the driver gas, is everywhere perpendicular to the gas velocity vector u. The equations appropriate to this case are then,

$$\rho u = \text{constant} \qquad (7)$$

$$p + \frac{B^2}{2\mu} + \rho u^2 = \text{const} \tag{8}$$

$$C_p T + \tfrac{1}{2} u^2 = \text{const} \tag{9}$$

$$B/\rho = \text{const} \tag{10}$$

$$p = \rho R T \tag{11}$$

Postulate a standing wave in the driver gas as shown in figure 4. Equations (7) through (11) are steady state equations, so inquire as to what velocity ahead of the wave is necessary to render the wave stationary. This velocity is then the propagation speed of the wave. Differentiating (7) and (8) with respect to the density ρ and eliminating the velocity derivative $du/d\rho$ between the resulting equations gives for u and thus W the disturbance speed.

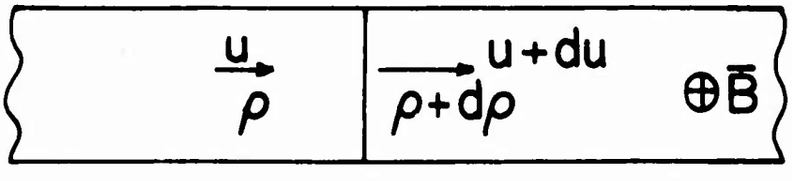


Figure 4

$$u^2 = W^2 = dp/d\rho + \frac{1}{\mu}\frac{d}{d\rho}\left(\frac{B^2}{2}\right) \tag{12}$$

Since (9) implies the flow is isentropic (the joule heating is zero for infinitely electrically conducting fluids) the derivative $dp/d\rho$ for constant entropy is just the ordinary sound speed squared or a^2. Using (10) the derivative $\frac{1}{\mu}\frac{d}{d\rho}(B^2/2)$ is just the Alfvén velocity squared or $c^2 = B^2/\mu\rho$. Thus in this special, though somewhat common, circumstance.

$$W^2 = a^2 + c^2 \tag{13}$$

From equation (8), the accelerating force in this case is obviously $p + B^2/2\mu = \pi$ or the sum of the gas and magnetic pressures. This set of equations now allows one to integrate the relation

$$du = \frac{d\pi}{\rho W}$$

and thus find the quantity that is conserved across these waves. In mathematical terminology, one has found the Riemann invariants of the set of hyperbolic equations where the characteristic directions are $u \pm W$. In standard fashion one can now derive a "shock tube equation."

A physical circumstance described by the above equations is the Magnetic Annular Shock Tube first used by Patrick at the Avco-Everett Research Laboratories and depicted in figure 5. Because of the annular

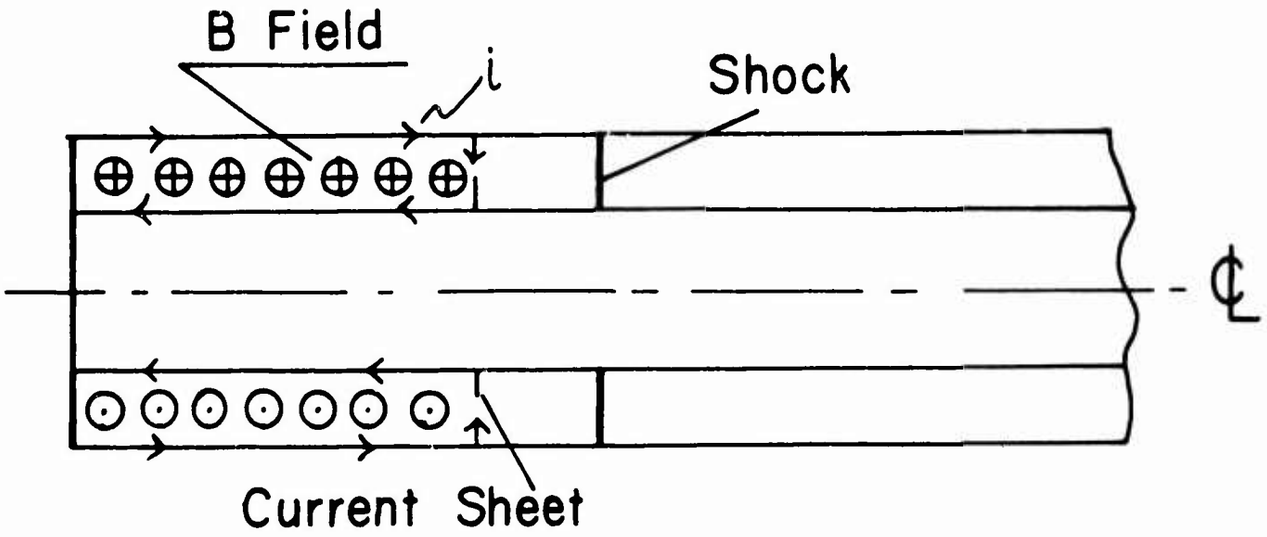


Figure 5

geometry and the current path, the B field is always at right angles to the gas motion along the tube and is circular, closing on itself. This particular geometrical configuration is very economical with respect to magnetic energy density as all the magnetic field (exclusive of that related to the inductance of the leads) is utilized for driving the gas piston generating the shock wave. The tendency of the current loop to expand is the driving force but the gas in the driver being highly conducting mass loads the loop and provides an inertia to the expansion process. Alternatively the loop expansion forces can also be cast into a framework of discussion concerning the action of the magnetic pressure. These two points of view are equivalent in all respects. To estimate the performance parameters and how they affect the final shock wave Mach number, it is reasonable to assume that all the energy that is to be delivered to the tube initially resides in the driver gas, say at time $t = 0$. For example, this optimistically would be the energy in a driving condenser bank, assuming the lead resistances and inductances were not important. Defining the shock tube regions with reference to an idealized wave diagram as shown on figure 6, the appropriate shock tube equation is*

$$\frac{p_4}{p_1} = \frac{\left(\frac{5M_1^2 - 1}{4}\right)}{\left[\frac{1+\pi_4}{\pi_4} X^{2/3} - \frac{1}{\pi_4}\right]^5 \left[\frac{5}{6}(1+\pi_4) X^{2/3} + \frac{1}{6}\right]} \qquad (14)$$

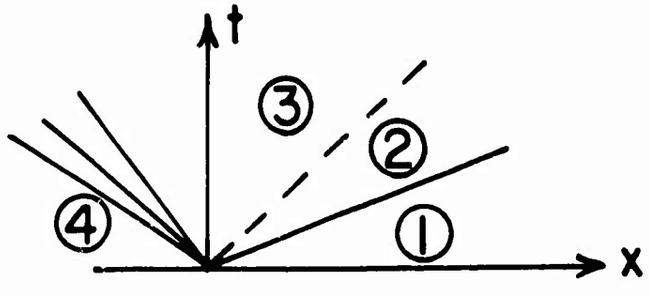


Figure 6

* Plasma Technology, Editor, J. Grey, Addison Wesley, to be published

where $$X = 1 - \frac{3}{8}\frac{a_1}{a_4}\frac{\pi_4\left(M_1 - 1/M_1\right)}{\left(1+\pi_4\right)^{3/2}}$$

and $$\pi_4 = \frac{c^2}{a^2} = \frac{6}{5}\frac{B_4^2/2\mu}{p_4}$$

Expression is for $\gamma = 5/3$ throughout.

This shock tube equation (14) can be solved for M_1 given the initial pressure ratio across the diaphragm p_4/p_1 and the ratio of magnetic to gas pressure in the driver gas. Obviously for zero magnetic pressure this reduces to the familiar ordinary shock tube relation. In the actual operation of a shock tube, there is no diaphragm initially separating the gases in region 1 and 4. However, if the process, e.g., condenser discharge, of adding energy to the driver gas is so fast that the energy addition to the gas occurs before the gas can move from the region, then the heating and magnetic field creation in the gas occurs essentially at constant density. Initially if there were no diaphragm it is also true that $p_4 = p_1$. In this case the shock tube equation (14) reduces to

$$1 = \frac{5/4\ M_1^2\left(\frac{a_1}{a_4}\right)^2}{\left[\frac{1+\pi_4}{\pi_4}X^{2/3} - \frac{1}{\pi_4}\right]^5\left[\frac{5(1+\pi_4)}{6}X^{2/3} + \frac{1}{6}\right]}$$

$$X \simeq 1 - \frac{3}{8}\frac{\pi_4 M_1}{\left(1+\pi_4\right)^{3/2}}\left(\frac{a_1}{a_4}\right) \qquad (15)$$

This equation is also appropriate to describe the many cases where the shock tube currents "crow bar" themselves, short themselves out in the shock tube, thus isolating the current path in the tube from the external circuit, since in this case again one has an expanding current loop. For a description of measurements bearing on this mode of shock tube operation, Keck's* article can be referred to.

Note that equation (14) can be solved for the combination $M_1\ a_1/a_4$ using π_4 as a parameter. In this case two limiting cases are easily discussed; for $\pi_4 = 0$ the equation shows $U_s = 0.599\ a_4$, for $\pi_4 = \infty$, $U_s = 0.52\ c_4$. In both of these limiting cases note that U_s is proportional to $1/\sqrt{\rho}$ and thus this dependence, if verified experimentally, cannot distinguish between a thermal or magnetic drive.

* Keck, J., Phys. Fluids 7, 516 (1964).

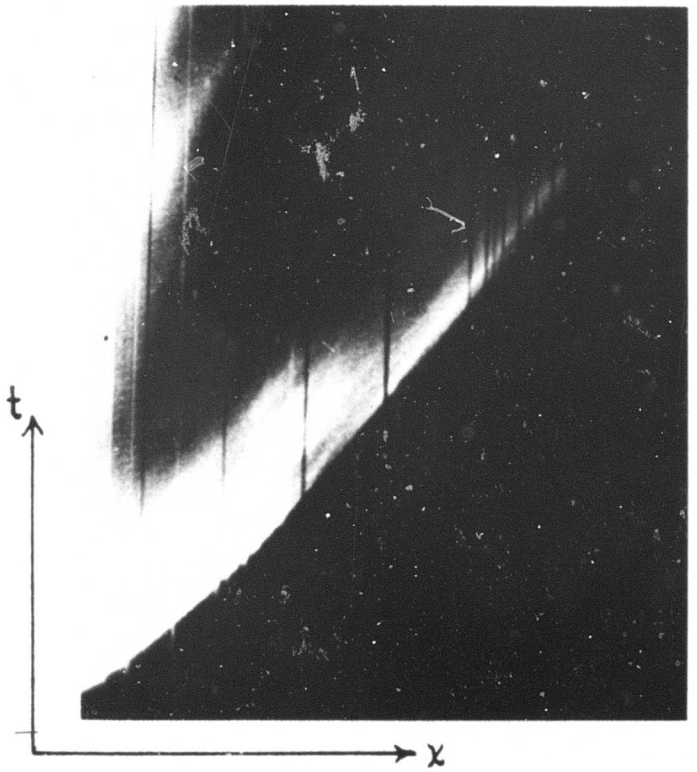


Figure 7

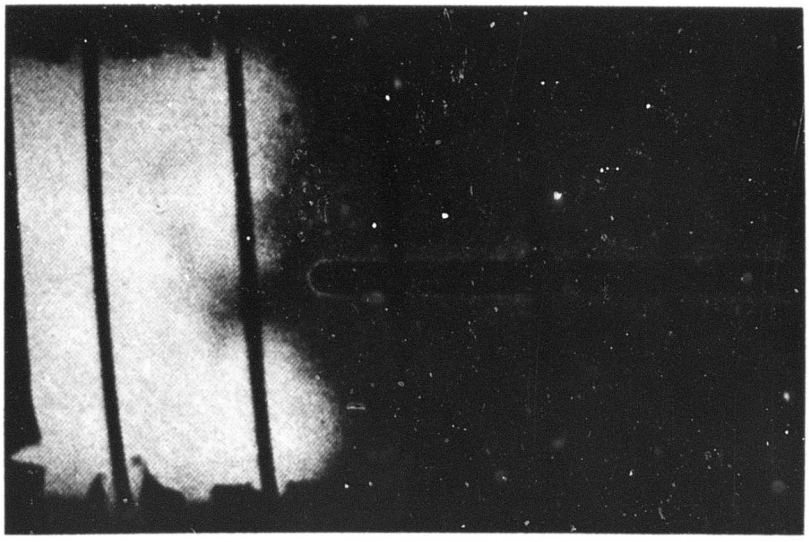


Figure 9

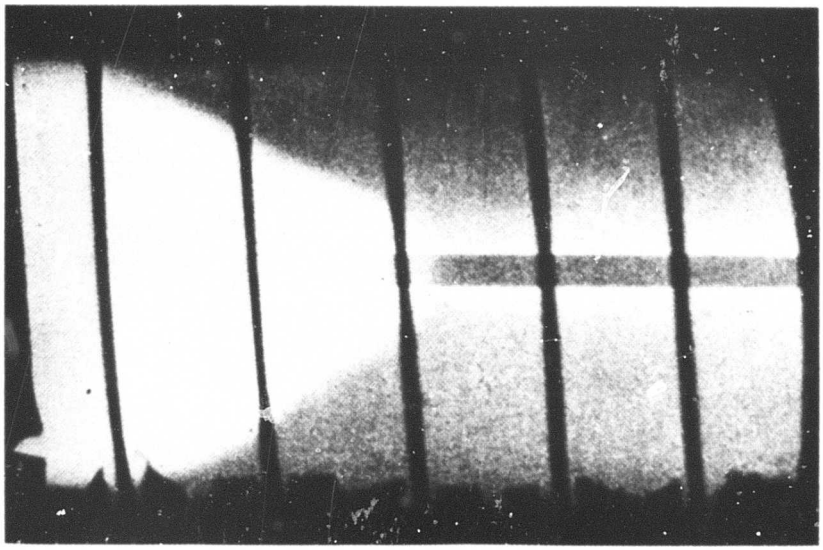


Figure 10

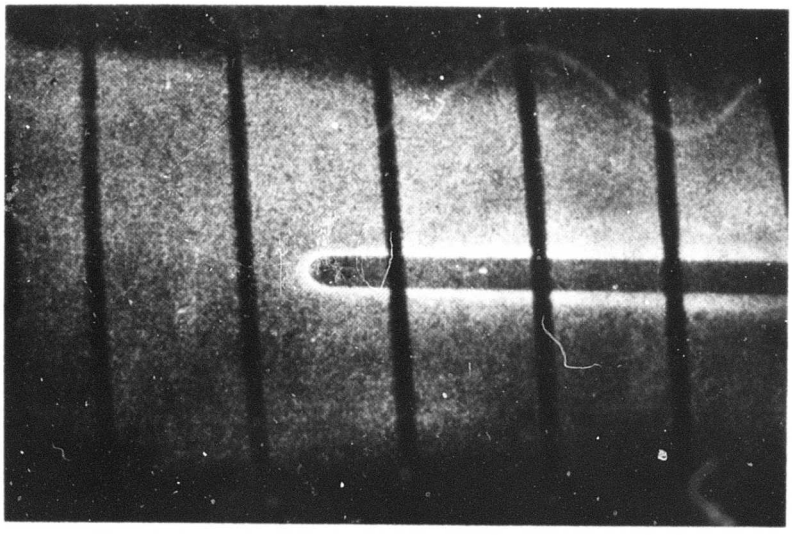


Figure 11

EXPERIMENTAL OBSERVATIONS

The phenomena actually observed in shock tubes of the types described are many and varied. Thus, what is described here should be regarded as a summary of experience with one tube only. One of the easiest measurements to make is to record the position of the shock front in the tube as a function of time with a drum camera or the like. In most cases, approximating the physical situation described here, the shock speed decays with increasing distance along the tube. A drum camera photograph of a shock front progressing down a tube is shown in figure 7.

Since in all cases to achieve high Mach numbers one requires a large wave propagation speed in the driver, it seems appropriate to estimate the decay rate of the shock wave making use of this fact. A high wave propagation speed in the driver implies that no large property differences can exist at any time or the expansion process approaches a simultaneous simple isentropic one for the whole gas. Consider first the case of a thermal drive. Consider the shock position to be given by $\ell = \ell(t)$. Consider also that the density ratio across the shock wave is large enough that no distinction need be made between the shock front and the entropy or contact discontinuity. Since all the mass originally in the driver section with these assumptions occupies at time t a volume proportional to ℓ and if property differences in the driver gas are not important, then $\rho\ell$ = constant = F. For a thermal drive U_s the shock velocity is proportional to the sound speed a of the driver initially, so

$$U_s \propto \frac{d\ell}{dt} \propto a \propto \rho^{\frac{\gamma-1}{2}} \propto \left(F/\ell\right)^{\frac{\gamma-1}{2}} \tag{16}$$

Separating variables in the differential equation

$$\ell^{\frac{\gamma-1}{2}}\, d\ell \propto dt \tag{17}$$

or finally

$$\ell \propto t^{\frac{2}{\gamma+1}} = t^{3/4} \quad \text{if} \quad \gamma = 5/3 \tag{18}$$

So for a thermal drive the shock position should vary with t to the 3/4 power.

Consider now the case for a magnetic drive, again $\rho\ell = F$ but also B/ρ remains a constant say k.

$$U_s \propto \frac{dl}{dt} \propto c \propto \frac{B}{\sqrt{\rho}} \propto k\sqrt{\rho} \propto \frac{k\sqrt{F}}{\sqrt{l}} \tag{19}$$

or

$$\sqrt{l}\, dl \propto dt \tag{20}$$

and thus

$$l \propto t^{2/3} \quad \text{(e.g. } \gamma = 2 \text{ gas)} \tag{21}$$

Note also that for a magnetic drive with $R_m = \infty$, the condition is $B^2 l = K'$ so

$$U_s \propto \frac{dl}{dt} \propto \frac{B}{\sqrt{\rho_1}} \propto \frac{\sqrt{K'}}{\sqrt{\rho_1}} \frac{1}{\sqrt{l}} \tag{22}$$

and again

$$l \propto t^{2/3} \tag{23}$$

The drum camera picture in figure 7 was analyzed and the decay rate plotted and compared with the two decay laws above. The circles in figure 8 are points taken from the photograph. Note that it definitely appears that in this case the magnetic drive mechanism was predominant.

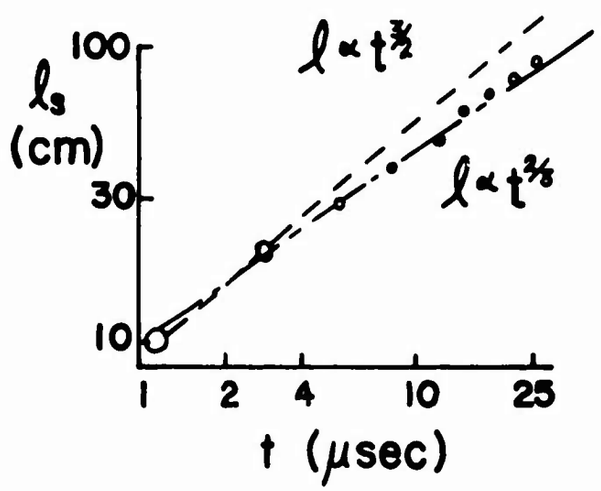


Figure 8

APPLICABILITY OF THEORY

Although the theory accurately ascertains the possibilities inherent in the electromagnetic powered shock tube, there are actually serious shortcomings in practice except where extreme care is taken. For example, in the case of axial symmetry discussed here, the magnetic field is not uniform in the driver section but varies inversely with the radius from the center. Thus the magnetic pressure is never uniform in the radial direction but is more uniform the smaller the annulus spacing compared with its mean radius. Also in presenting the theory it was assumed that the electric current was carried in sheets so that the current density was uniform in the circumferential direction. Although certainly to be desired in many cases, this is difficult to achieve, the current rather choosing to bunch itself into streamers. To insure current sheets, it is common practice to provide an axial bias magnetic field which for radial currents gives a force on the current filaments such that they rotate and thus spread out uniformly, one hopes, in the circumferential direction. Also in actual practice one hopes to study the structure of magnetohydrodynamic shock waves and these are possible with bias magnetic fields on the shock tube such that $J \times B$ forces are important in the shock wave transition itself. Because the theory though straightforward is lengthy, this has not been considered here.

Another topic of current investigation is the mechanism of initial operation and electrical breakdown of the gas in the shock tube. The gas evidently becomes ionized by some mechanism initially ahead of the primary shock. The mechanism of ionization is different for different operating conditions and unfortunately these different mechanisms are all being labeled with the same term "precursor," since the phenomenon precedes the shock wave.

By means of a Kerr cell shutter, one can photograph the front believed to be, or at least called, the shock front. Figures 9, 10, and 11 were photographs taken by Dr. E. Pugh, while at Cornell University. In figure 9 is the shock front as it appeared when there was no axial magnetic field. The blunted cylinder in the photograph is a probe designed to create a shock wave in the "uniform plasma" behind the "plane" shock front. The nearly vertical lines across the photograph are the elements of the coil, which, when energized, create an axial magnetic field. Note the shock jumble is far from what one might describe as plane. The shock tube used in these pictures was not annular but simply cylindrical so that the deviations from the ideal one dimensionality of the phenomena one would expect to be large, as is the case. Figure 10 shows a shock front profile with an axial magnetic field. In this case, the "turbulent" nature of the front is gone but it is far from plane, and the shape seemingly reflects the magnetic pressure variation across the tube one would expect for a drive consisting of an expanding current loop with all the current returning along the axis of the tube. It is interesting to ask oneself when viewing these photographs, where is the uniform test slug of plasma to be used for diagnostic purposes?

In figure 11 a photograph of the probe was taken just after the condenser discharge but well ahead of the shock wave. There seems to be a shroud or glow around the probe presumably due to the "precursor." This phenomenon disappeared when something mechanical isolated the probe. e.g., lucite, thus it is possible the glow is a boundary layer on the probe caused by the motion of the gas due to the passage of the precursor wave. If this glow which had a parabolic growth is interpreted as a boundary layer, then one can make estimates of electron density, etc.* that are consistent with other findings. There certainly are precursors that should accelerate the gas and are distinct waves in their own right. Other diffusive phenomena could affect the energy of the gas but would not be expected to accelerate the gas. Which phenomenon dominates and when has not been sorted out to everyone's satisfaction. Currently at Cornell, Mr. M. Lubin using a radar technique he developed** and also some microwave interferometry has indications that definitely show there is a discrete front to the precursor so that it exhibits many of the aspects of a wave phenomenon.

SUMMARY

In a brief fashion, the general operating characteristics of electromagnetically powered shock tubes have been summarized. The theory very clearly shows limitless possibilities but in practice the desired phenomenon is difficult to control. The possibilities are such, however, that much could be gained by achieving control of shock tube phenomena in this new high Mach number, high temperature range.

* E. R. Pugh, "Studies of the Phenomena Occurring in an Electromagnetic Shock Tube," Rept. Grad. Sch. of Aero. Eng., Cornell Univ. (1962). Plasma Technology, loc.cit.

** M. J. Lubin, "Nanosecond Pulse Technique for Multiple Front Studies in Shock Tubes," Rev. of Sci. Inst. 4, 1408 (1963).

SHOCK TUBE APPLICATIONS TO DEFENSE RESEARCH AND ENGINEERING

W. J. Taylor
Ballistic Research Laboratories
Aberdeen Proving Ground, Maryland

With the detonation of the atomic bomb, blast effects acquired a new significance. Destructive overpressures were experienced at great distances from the detonation, and the long positive phase duration of the blast provided time for targets to respond to dynamic loads. The area of blast damage, when compared to the conventional weapon, had increased by alarming factors and caused the military to become keenly interested in the mechanism of this distruction. In order to understand this,however, and appraise its true potential we would have to conduct experiments.

The first laboratory for these experiments was the Bikini Atoll, which in 1946 played host to a task force of 42,000 men and a large number of experiments. This was Operation Cross Roads, and it would provide answers to such questions as,"what effect would an atomic bomb have on a fleet of Naval vessels", and " is an air burst more lethal than an underwater burst?" It would not, however, answer so directly the questions,"to what extent should accepted principles of ship design be altered in future construction", or "how does one build a blast resistant structure?" To obtain answers to the later would require many experiments. Information would have to be developed on the behavior of the blast wave and the pattern it displays when it interacts with a structure, and we would have to understand the behavior of materials under dynamic loads. We needed this information because it was fundamental to a host of problems that were born with the atomic weapon.

Operation Cross Roads was the first of a long series of nuclear tests, and from the very first experiment we learned that the loading and target response information we sought would come slowly. Making measurements in an environment electrified by an electromagnetic pulse and bathed in nuclear and thermal radiation was to be a challenge in itself. The complexity of this measuring task and the costs of full scale operations focused

attention on the shock tube for studying blast effects. Here was a convenient tool, and we could get a well controlled, reproducible blast wave, without the disturbing attendent effects of a nuclear weapon. We could study many blast problems inexpensively, and the rapidity with which a shock sequence could be produced made it quite feasible to explore newly uncovered areas of interest.

The shock tube could be used for the testing of instrumented models, in much the same way as the aerodynamicist uses the wind tunnel; or it could be used for the testing of certain prototypes. The first efforts, however, were model experiments directed toward developing definitive information on the diffraction process established by the interaction of a shock wave and a rigid target. This type of problem interested the Navy, Air Force and the Army and all three now have their shock tubes and conduct research pertinent to their service requirements.

For the study of shock wave diffraction, rigid, non-responding geometrically similar models are positioned in the shock tube. Mounting them on the side wall of the tube represents the prototype structure in the mach reflection region. The regular reflection region is obtained by mounting them on an angled blind end flange. The test section of the shock tube is positioned at sufficient distance from the diaphragm to give the required length of "compressed gas" testing time and the compression chamber length is varied to produce either a peaked or step shock pressure profile. Most often either of these profiles is suitable for diffraction studies. The step shock represents the infinitely large weapon and gives a maximum diffraction load while the peaked profile with its one dimensional decay is used in the studies dealing with specific weapon yields. Figure 1 shows the comparison of scaled blast waves.

In the figure the pressure profile of the shock tube produced blast wave is compared to the weapon blast in terms of time required for the blast wave to traverse their respective targets - model and prototype. For the average diffraction target only the first few traverse times are important, so for the model in the shock tube the real time of interest is of the order of 1 msec. The time of interest for the prototype will vary as the scale factor and of course during this time the applied pressure will decay. For the average problem in the low overpressure region produced from megaton weapons, this difference in pressure is less than 8% when compared to the step shock wave produced in the shock tube and for larger yield weapons the percentages decrease. Conversely however, as the pressure level increases, the wave form becomes increasingly dissimilar. Another criterian of the time span of interest is the interval required to complete the diffraction on the front face. But for most targets this is about equal to the traverse time.

Studies with the parallel-a-piped models in shock tubes equipped with interferometric instrumentation produced results that were applicable to many full scale structures. The procedures developed for the prediction of

overpressure loads on the roof and walls of structures is predicated primarily on a curve fitting technique with shock tube data providing the basis for the method.

There were,however, the complex structures with re-entrant corners and multiple curved surfaces which did not lend themselves to the generalization of load distribution and this fostered the effort toward the three dimensional model instrumented with high response transducers. This type of testing was restricted to the large diameter shock tubes because of the size of the instrumented model and the necessity of getting information before reflections from the shock tube wall return to the model. Full size structures, designed on the basis of shock tube experiments were exposed to the blast from nuclear weapons and the results verified the model tests. Blast resistant structures were then built with confidence.

The necessity of developing loading information in the high pressure region, where real gas effects become important,imposes new problems. Foremost is the task of producing high pressure shocks in test sections large enough to accommodate instrumented models. The alternate technique of testing at reduced ambient pressure to obtain high shock strengths brings into play a multiplicity of problems, but because of necessity, the technique is used. For instance, the temperature of the gas in the strong reflected shock, the front face of a model, is high enough to cause excitation of the inert degrees of freedom and this will cause the rarefaction wave speed to vary from its initial value to a final speed determined by the equilibrium temperature. The time to reach this equilibrium temperature is a function of the absolute density. Extending the equilibrium attainment times complicates the analysis because they are on the order of the model clearing times. In addition, reducing the absolute pressure in the test section brings about practical experimental limitations with transducers. In order to follow the pressure time history of blast diffraction on a small model, pressure transducers require megacycle response. Piezoelectric gages have suitable response characteristics but exhibit a small signal output which is further aggravated by testing at reduced ambient pressure.

Currently, shock tubes are being used to study diffraction in the 200 psi overpressure region. Evacuation techniques are used when the requirement exceeds 200 psi and fully instrumented model are required. Basic information such as reflection factors as a function of angles of incidence is being obtained in smaller test sections at pressure in excess of 1000 psi but the models for such tests are small and need contain only one gage.

Other types of blast investigations that are of primary importance to the defense posture deal with the structure that is beneath the ground. Here internal loading and differential loads are important. This underground structure may be a compact missile silo or a huge combat operations center. If the shock wave breaks into the structure, it has a volume to fill and the rate at which it fills is goverened by parameters such as: the

ratio of total volume to entrance area, the length of passageways and their geometry, the overpressure and its time history. Problems of this type put more emphasis on obtaining scaled wave shapes in the model experiments because the maximum pressure within the structure may be, at least for the deeply buried structure, more directly a function of the pressure in the applied shock wave at a time many milliseconds behind the front.

Figure 2 illustrates the problems which develop from dissimilar wave shapes. As shown the data obtained in the shock tube show higher maximum pressures at point A because a long duration step shock wave was applied to the model. The long route through the system caused the initial pressure to be a fraction of the maximum pressure and of minor importance to the designer of the door at point A. The pressure of interest is the maximum pressure later in the wave. Corrections must be applied to the data in order to relate the laboratory data to a weapon of specific yield. The investigations involving these filling processes aroused new problems. The testing time had to be long compared to those required for diffraction studies and attention had to be given to wave shape and to Reynolds No. scaling. These shortcomings do not detract from the usefulness of the shock tube in protective structure design; they merely orient the future work.

In these investigations linearly scaled models are attached to the walls or end flanges of the shock tube to represent the traveling wave or overhead burst condition, and pressure-time gages imbeded in the model walls give the pressure-time at selected positions within the model. Very often models are constructed so that the position of a baffle or length of tunnel can be changed with ease, and the effect of these configuration changes can be determined within hours. The wave diagram is a useful tool for analysis of this type, but at late times in a deep complex the technique becomes inadequate.

Small models are more easily adapted to the shock tube than large models, but the degree of miniaturization allowed depends upon the size and positioning of the imbeded transducers. For instance, in order to measure the pressure profile of the shock wave traveling down a circular tunnel, a flat surface gage must be positioned in a curved tunnel wall. This presents a mismatch which grows worse as the model is made smaller. If the structure has a blind corridor, this flat surface is selected as an instrumentation point; and while it may not be a position of prime interest, comparative records at such a position can be used as an index of performance.

It is true that a small model scale is not in the direction of adhearing to Reynolds No. Scaling and this becomes increasingly important for models with long uninterrupted lengths of tunnel. Nonetheless, the similitude relationship is more nearly achieved with this technique rather than working with large models in large test sections and reducing the ambient pressure to attain equivalent shock strength.

In the multiple entrance structure the shock wave coming from one entrance will collide with the shock coming from another entrance and the high pressure zone of interaction will shift as the structure orientation with ground zero changes. Very often it is difficult or impossible to attach a multiple entrance structure to the side wall of a shock tube in more than one direction, but by adding delay routes to the model, orientation changes can be simulated and the zones of interaction can be studied. The ability to produce the same shock wave on either similar or dissimilar models is most helpful to experimenters as is the ability to produce a controlled change in shock pressure so that the movement of reflections within the structure can be traced.

For problems related to Civil Defense, the doorless blast shelter had merit and early nuclear bomb tests included the exposure of instrumented doorless shelters. There was a concurrent shock tube study directed toward the entryway configuration and the positioning of baffles within the shelter to degrade the shock front, retard the filling process and thereby reduce the loads within the shelter. From shock tube experiments it was shown to what degree the arrangement of baffles and area changes could alter the rate of application of load.

On the large military installation, with the complete button-up philosophy, techniques to minimize shock loading become important. Doors, capable of withstanding dynamic loads and large enough to permit truck access must be closed rapidly, and then reopened. The arrangement of baffles and access routes to minimize the blast loading on such doors can mean a substantial financial savings. Thereagain altering access routes can mean additional excavation and these costs must be considered in terms of other techniques for obtaining protection. There are many schemes for entranceway configuration and access routes and the shock tube provides a convenient method of evaluation.

In addition to the access routes within an underground shelter, there is the ventilation system which links the heart of the structure to the outside environment. They are necessary in most blast resistant design because they serve personnel or equipment with uncontaminated air for long periods of time. These systems are relatively simple from an engineering point of view, but most often they contain L and T junctions and the shock wave induced flow through such junctions defies a standard one-dimensional flow analysis. Again, the shock tube has been used effectively to determine the shock pressure transmission through junctions and the results applied to ventilation systems and to the larger cross section access routes that have similar geometry. The pressure pattern in the immediate vicinity of a junction is a diffraction pattern and it is quite complex. Several diameters downstream, the disturbances have subsided and a new peak pressure level can be discerned. Shock tubes have been used to establish the pressure loss through junctions found in normal design and they have been used in the study of blast wave attenuation over streight lengths of tunnel. The combination permits the prediction of shock pressures throughout a system, as the blast wave

progresses in the system. Complicated tunnels defy a good analysis because of the multiplicity of shock wave interactions but results are readily obtained with models.

Most ventilation systems in the underground structure contain filters for separating radioactivity from air, and a valve which is either blast actuated or preclosed on some signal warning of blast arrival. One of the most challenging valve designs is the self-closing or blast actuated valve, because its behavior is not dependent upon any other device. In the process of closing, however, part of the blast wave gets past the valve and into the filter and blower system. A plenum chamber positioned between the valve and filters serves to swamp this blow-by and decrease the pressure differential across the filters to the extent that the sensitive material does not rupture. For the purpose of improved design monitoring instrumentation channels provide data on valve closure time. blow-by pressure and structural response. This area of work has been most rewarding. It has shown for instance, that many valves fail structurally, but that the dedesigned models are structurally sound.

As the desired level of blast protection increased, the protective structure was placed deeper underground. This approach to protection emphasized the need for information on the coupling of the air blast energy to the ground, the characteristics of the blast induced ground shock, and the behavior of a structure buried in this region. For studies related to the mach reflection region ,the traveling wave,a soil box is attached to the underside of the shock tube and this permits the blast wave to traverse the earth medium. Gages imbeded in the soil monitor its behavior,and buried instrumented models respond to the dynamic loads, to yield information on the structure and medium interaction. For studies related to the regular reflection region, vertical shock tubes have been used to produce shocks into different types of soil, and over varying soil condition without the confinement of a soil box. The application of shock tubes to problems of earth shock has aided understanding the soil-structure interaction problem and it has been most helpful in the development of ground shock instrumentation.

Insuring the protection of the underground structure requires giving consideration to many potential problem areas. One such problem is the water system and its behavior if the blast wave fractures a main and transmits its pressure to the water system. For studies of this type shock tubes have been attached to water systems and the system behavior observed directly for easily varied input load conditions.

The shock tube application to problems of protective construction has not been restricted to the large structure suitable for life support. There is, for instance, the problem of protecting the parked aircraft from damage by debris, overpressure, dynamic pressure and motion.

The simply constructed revetment offers protection from debris and, if properly designed, it can minimize blast effects. Simple changes in the geometry of a revetment can produce meaningful changes in the flow pattern

within. Shadowgraphy and interferometry of model revetments in shock tubes have been employed to good advantages in these studies. In addition, a smoke stream technique of measuring gas particle velocity by creating and tracing a multiple stream grid within a revetment has been effectively employed. Figure 3 shows the test apparatus and shock wave interaction with the revetment and grids and illustrates how the effect of geometry changes are readily evaluated. Observing the grid intersection displacement gives velocity and direction and the changes in the area of the region bounded by the intersecting columns yields density. From high speed photographs of the shock grid interaction, aerodynamic parameters are calculated and the efficiency of various shaped revetments determined.

The aircraft in flight as well as the missile in the outer reaches of the atmoshpere are blast sensitive targets and their vulnerability is of interest. Fruitful experiments have been conducted with shock tubes attached to wind tunnels to produce an interaction between a blast wave and simulated moving aircraft. Presently the shock on shock interaction caused by a blast wave interacting with a high speed missile or re-entry vehicle is drawing much attention. This is a challenging problem and the shock tube offers some interesting techniques to assist in the solution.

Consideration has also been given to better protection to the soldier whether he be behind tons of metal in an armored tank or in the hand dug foxhole. The optimum dimensions of a foxhole have been studied in shock tube experiments, and the relation of the occurance in time of reflected shocks is being related to the physiological effects of blast. The frequently asked question "What is the soldier's tolerance to a blast wave?" requires a long complex answer, filled with probabilities and interspecies extrapolations. But the nature of the problem justifies a complex answer, and it is only because of shock tube experiments with animals that we can intelligently discuss the influencial parameters relating to blast biology. These experiments have allowed the development of information that is specific and relatively uncontaminated by integrated effects. For example the effect of rate of pressure rise on the maximum tolerance can be placed in its proper perspective and compared to other influencial parameters such as the effect of incident and reflected pressure and the timing between these loads. Experiments have shown that tolerance is indeed affected by these variables and that thought should be given to dimensions of protective enclosures from a standpoint of the reflections they generate. The duration of the blast load is another important parameter as is the rate at which the load is relieved and for experiments of this type the blast biologist modifies his shock tube with side chambers and sequence valves so that he can exercise a degree of control over the wave shape.

Further, the stamina or lack of it displayed by a single animal specimen requires that the performance of the average specimen be established, and since the experiments relate to man the species and body weights must be varied to assist in the extrapolation from the animal targets to man. It is clearly shown then that blast biology experiments require the repetition and reproducibility that only a shock tube can offer economically.

The translational effects of a blast wave have been studied by observing the whole body motion of anthropometric dummies as they are blown from a large diameter shock tube. These tests show that the position of the soldier at shock arrival time is important to survival. Tests have also been conducted to determine what pressure level renders the gas mask useless by rupturing its filter and at what pressure the mask is pulled loose from the head. In other tests the translational velocity of typical battle field litter is being determined and its wounding potential assessed and related to other incapacitating mechanisms.

Concern for the foot soldier has embraced many facets of defensive mine warfare. The shock tube is being used to reproduced the impulsive load delivered by an exploding mine to the foot of the soldier. In laboratory experiments the shock tube produced blast wave is directed at the feet of cadavers so that the mechanism of the calcaneus fracture, which often requires the leg to be amputated, can be studies. Successful experiments here may result in a new boot design which may save a leg. Conversely, shock waves are directed at buried mines to evaluate their sensitivity to air induced ground shock.

The ability to easily photograph a target under a dynamic load has lead to many experiments, seemingly mundane but actually quite important. For instance, photographing the motion of small objects in a shock tube and evaluating the effect of closeness of space on their translational behavior has assisted in establishing the criteria for the storage of materials or equipment items in tunnels.

It would be remiss not to mention the environmental studies within shock tubes and the role this instrument has played in the routine task of calibrating and developing instrumentation to be used in the real weapons test environment. Much of the weapons test data has been gathered in the somewhat unrealistic environs of Frenchmans Flat, Nevada where thick layers of surface dust are entrained by the blast wave and carried to the target to register high dynamic loads. Elements of such environments have been created in shock tubes to study their effect on blast wave transmission.

Likewise, the water spray system used to wash down ships caught in a radiation fallout, interposes an air water medium between the oncoming shock wave and the ship superstructure and the effect of this water loaded blast wave on such things as antenna have been evaluated. There is a long list of experiments of this type where the shock tube has been used to give quick qualitative and quantitative answers.

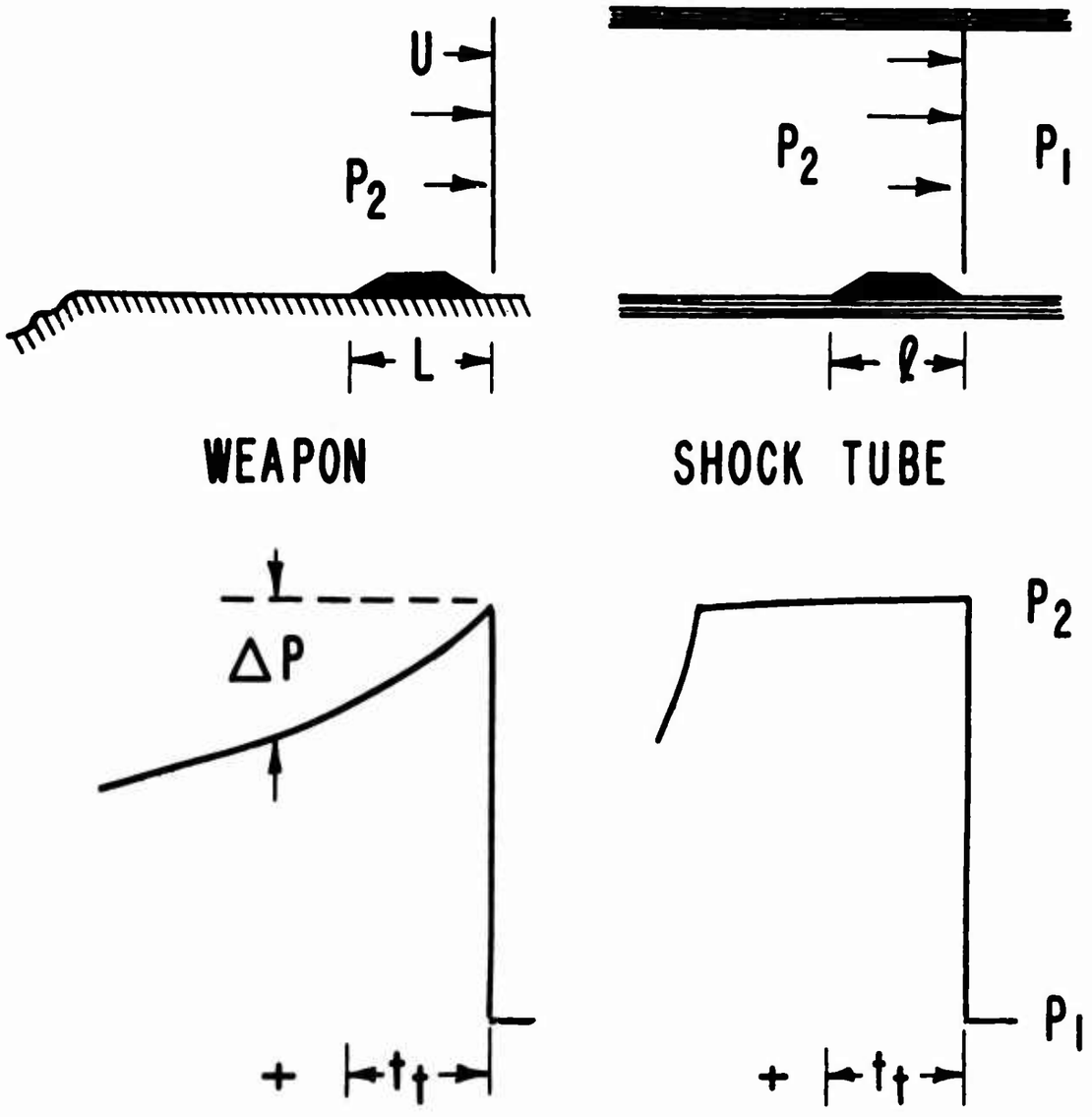
We have seen where the shock tube is used in the ad hoc test and the long range program. In the later, say blast biology or protective design it is a principal tool and work is still in process because either the picture is incomplete or the requirements are changing or both. We still seek, for instance, economical blast protection and this means, among other things, examining the behavior of structures under dynamic loads.

In the past, the full scale nuclear test could be used to assess the progress of laboratory experiments, but now we must rely on theshock tube and on the large scale HE test. Each has its place. On the conveniently executed HE test, say 50 tons of explosive, a target can be exposed without the confines of a tube wall, but there is not enough land area in the region of interest. The area between the 200 and 100 psi levels can be represented by a sector 50 by 800 ft. The same region from a nominal nuclear weapon encompasses over 1 million sq. ft. -- a sector 250 ft by 1 mile.

With the HE test the land area becomes quite competitive and the number of experiments per shot is drastically reduced. Further, these one shot experiments still include scaled experiments because of the comparitively short positive phase duration. In the shock tube the positive phase duration is easily established, but we have the confines of the tube wall.

To progress satisfactorily in the protective design endeavor we must introduce the responding model to the shock tube environment so that we can principally repeat a loading condition. But this brings to focus many problems attendent to similitude scaling. Highlighting these is the non-scaling gravity loads and the realistic joining of structural members. The challange of making valid scale models is being pursued as is the task of producing high pressure long duration shocks in large test sections. The large high pressure test section is not yet a reality, but any progress in that direction will relax the modeling requirement. It will also mean that the shock tube lengths will be thousands of feet instead of the present hundreds of feet.

When an acceptable comprise has been arrived at here, we must attempt to produce a more realistic environment in the shock tube so that we can uncover the problem areas that develop from the interaction of separate phenomonological effects. The early bomb tests introduced such an effect, an integrated effect, the precursor. This anomolie developes as a result of the blast wave interaction with a surface region heated by the thermal output from a nuclear bomb. The precursor was discovered in the real environment. It was subsequently investigated, understood and then put into its proper perspective as a mechanism of distruction. As we reach for a better defense posture, we encroach on a border that was left rather undefined when above ground nuclear testing was discontinued. We must move the shock tube experiments to this border, and test in a simulated real environment so that we can uncover the next problem area.



MODEL SCALE FACTOR L/ℓ	TRAVERSE TIME (MSEC) SHOCK TUBE FIELD		Δ P %	
			t_t	$3t_t$
50	.2	10	1.5	3.5
100	.2	20	2.7	7.5

FIG 1. SCALED BLAST WAVE COMPARISON-
LARGE YIELD & LOW PRESSURE

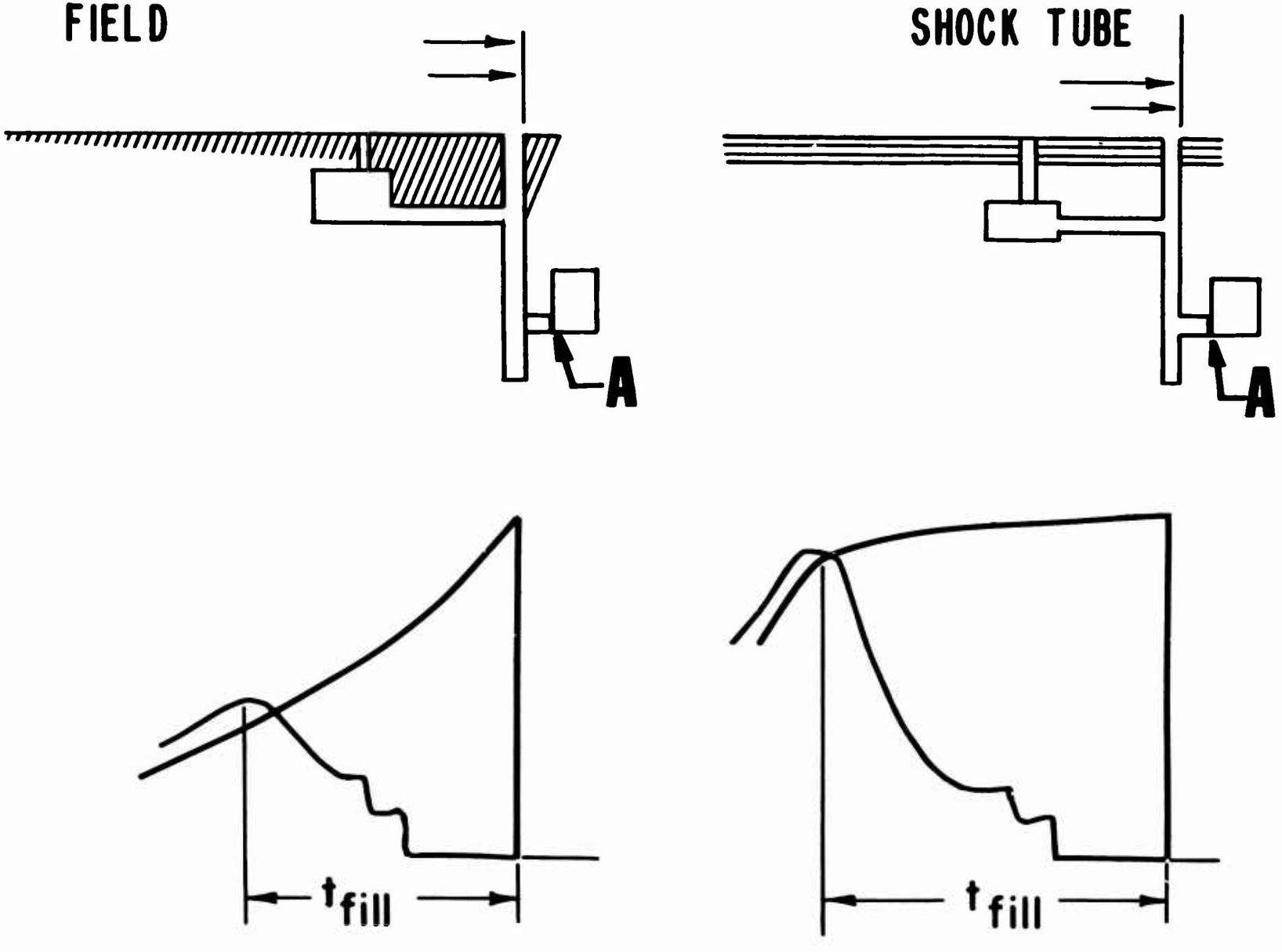
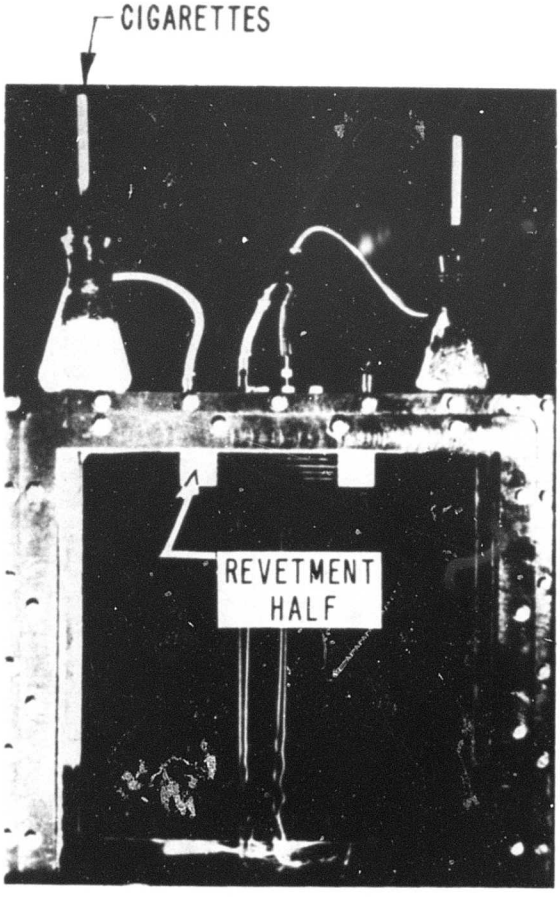
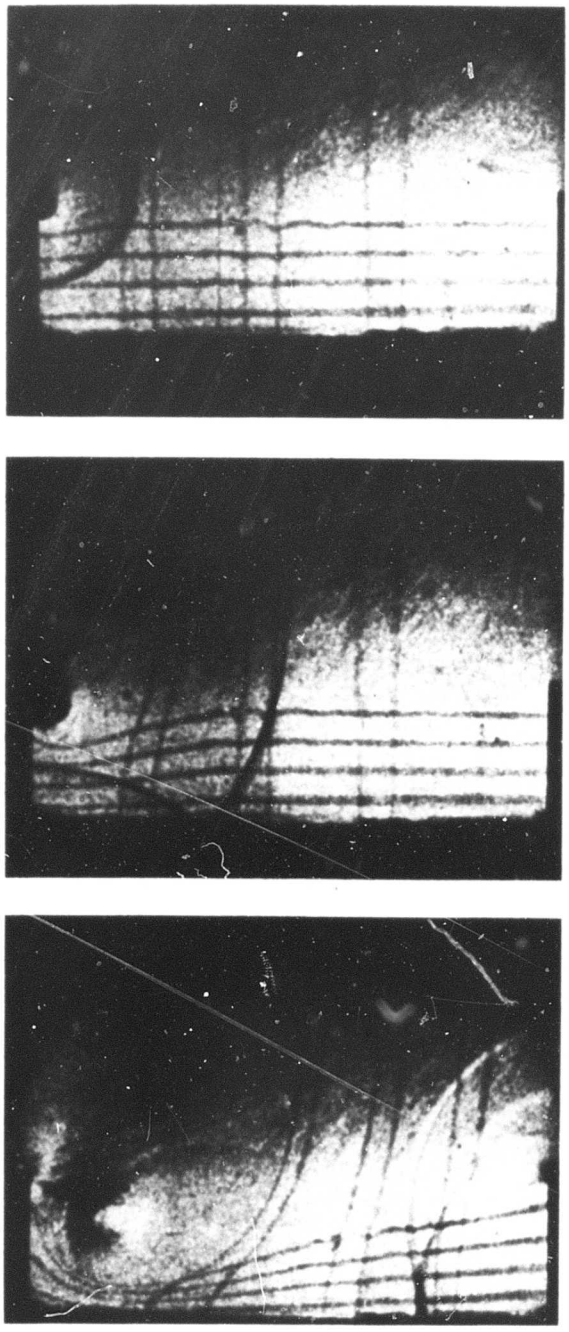


FIG. 2. PRESSURE vs. TIME IN A PROTECTIVE STRUCTURE



SMOKE GRID
APPARATUS



FRAMING CAMERA
SEQUENCE

FIG. 3 — FLOW PATTERNS IN A REVETMENT

EXCITATION STUDIES ON THE $N_2(1+)$ AND $N_2^+(1-)$ SYSTEMS IN SHOCK-HEATED N-N_2 MIXTURES*

Kurt L. Wray
Avco-Everett Research Laboratory, Everett, Massachusetts

ABSTRACT

The rate of excitation of the $N_2(1+)$ and $N_2^+(1-)$ band systems was observed in shock-heated N-N_2 mixtures in which the initial mixtures ratio N/N_2 ranged from 0 to 0.27. A pulsed discharge prior to diaphragm rupture produced the N-atoms; their concentration was determined by monitoring the decay of the Lewis-Rayleigh afterglow for about 50 millisec subsequent to the discharge and up to the arrival of the shock. The shock waves produced temperatures in the range 7000-18 600°K close to the shock front, after rotational relaxation. The radiation intensities from the $N_2(1+)$ (6600 to 8000 Å) and $N_2^+(1-)$ (0, 1) (4272 Å) bands were monitored as functions of time behind the shock front. The initial slopes of the radiation time histories were compared with theoretical slopes. The rate constant expression for exciting ground state nitrogen $X^1\Sigma_g^+$ to the $A^3\Sigma_u^+$ state by collisions with N-atoms was found to be $k_N = 1.9 \times 10^{-6}\, T^{-3/2} \exp(-E_{XA}/kT)$ cm^3/particle-sec, where $E_{XA} = 6.168$ eV. This yields an effective cross section of 2.7×10^{-18} cm^2 at 12 000°K. The analogous rate constant for collisions with N_2 was determined to be $k_{N2} \leq 0.01\, k_N$. These rate constants were found consistent with unsuccessful attempts to obtain Vegard-Kaplan spectra in the discharged but unshocked gas. Attempts to fit the $N_2^+(1-)$ data were not completely successful. It is most probable that the N_2^+ is formed by the associative ionization of a ground state atom and an excited atom.

*This work was supported by Advanced Research Projects Agency, monitored by the Army Missile Command, United States Army under Contract No. DA-01-021-AMC-12005(Z) (part of Project Defender).

I. INTRODUCTION

The primary purpose for this research was to elucidate the mechanisms responsible for the production of the $N_2(1+)$ and $N_2^+(1-)$ band systems in shock-heated nitrogen, and obtain rate constants wherever possible. Of particular interest in the $N_2(1+)$ case were the efficiencies of the nitrogen molecule and the nitrogen atom in raising the ground electronic state nitrogen to the excited state. A preliminary report of this portion of the study has been given.[1] In the $N_2^+(1-)$ case, the pertinent question is how the N_2^+ ion is formed.

These radiation systems are indicated in a greatly simplified potential energy diagram for N_2 and N_2^+ shown in Fig. 1. This figure was prepared from a more complete diagram given by Gilmore.[2] It will be used throughout this paper in discussing the mechanisms responsible for populating the pertinent excited states.

When nitrogen passes through a strong shock wave, the translational and rotational temperatures undergo essentially a discontinuous jump (within a few ambient mean free paths.[3] Then the vibrational degrees of freedom of the nitrogen begin to relax, i.e., the vibrational temperature of the nitrogen climbs from room temperature toward the local translational temperature and simultaneously the translational temperature drops. At low temperatures, this process of vibrational relaxation occurs rapidly compared to the dissociation of the nitrogen molecules into atoms, whereas at high temperatures the vibrational and dissociation relaxation times are comparable and the two processes are strongly coupled.[4] Also occurring within the relaxation zone are the ionization and electronic excitation processes which are of interest to us in the present work.

Among the states populated by the electronic exciation processes is the $N_2(B^3\pi_g)$, the species which, in undergoing a transition to the $N_2(A^3\Sigma_u^+)$, gives rise to the $N_2(1+)$ band system (see Fig. 1). This system has been observed by various workers as a function of time in shock-heated air and nitrogen.[5, 6] The general characteristic of the radiation history is that the light intensity rises rapidly to a peak and then slowly decays to an equilibrium level. In the present experiment, the $N_2(1+)$ system was monitored over a broad band of radiation from 6600 to 8000 Å.

Since the radiating state is a triplet state and the ground state is a singlet state ($X^1\Sigma_g^+$), a spin flip is necessary somewhere in the excitation mechanism. It has been suggested that this transition might be more easily accomplished in an N-N_2 collision rather than an N_2-N_2 collision. If this were true, it would be reasonable to expect that the presence of nitrogen atoms in the gas at the time of the shock wave arrival would significantly change the rate of rise of radiation immediately behind the shock front.

The N_2^+ ion is formed in the shock heated gas. The $N_2^+(1-)$ radiation system arises from transitions between the $B^2\Sigma_u^+$ state and the ground state $X^2\Sigma_g^+$. This system also has been monitored as a function of time in shock-heated air and nitrogen[6, 7] and it displays a time history similar to that

of the $N_2(1+)$ system. In the present experiment the $N_2^+(1-)$ radiation was monitored over a narrow band centered at 4272 Å.

The expected mechanism for producing N_2^+ behind the shock waves in nitrogen is by associative ionization of nitrogen atoms, i. e., $N + N \rightarrow N_2^+ + e$. The reverse of this process has been observed[8] and a rate constant determined; however, the state of the nitrogen atoms thus produced was undetermined. In any case, it seemed clear that nitrogen atoms play an important role in the production of N_2^+.

It was for these reasons that the nitrogen gas in the shock tube was predissociated by means of a pulsed electrical discharge in the present experiments. The atom concentration at the optical station prior to the shock arrival was determined from a measurement of the Lewis-Rayleigh (L-R) afterglow intensity. This afterglow is due to the $N_2(1+)$ system. In this case, the N_2 ($B^3\pi_g$) state is populated from atom recombination via the $^5\Sigma_g^+$ state, which crosses the $B^3\pi_g$ state at about the 11^{th} vibrational level.[9]

Shock waves were run into mixtures having the following nominal compositions: $N/N_2 = 0$, 0.025, 0.070 and 0.27. The $N/N_2 = 0$ case did not involve any discharge. The initial pressure (before the discharge) was always $P_1 = 1$ torr. The shock speed was varied between $U_s = 3.80$ and 6.25 mm/μsec, producing temperatures at the shock front subsequent to translational and rotational relaxation of 7000-18,600°K. The high temperature limit was set by inability to resolve the initial rise of radiation at temperatures above about 18,600°K, whereas the low temperature cut-off was due to the appearance of impurity radiation.

II. EXPERIMENTAL METHOD

The shock tube used in this work had a stainless steel driver section about 2 ft long and 1.5 in. in diameter and the low pressure side was a 10 ft long Corning glass pipe 1.5 in. in diameter (see Fig. 2). Stainless steel ring electrodes whose inside diameters were also 1.5 in. were placed at both ends of this 10 ft length. At the driver end the electrode was insulated from the driver section with a 6 in. length of Corning pipe. At the other end the electrode was insulated from the dump tank by another 6 in. length of Corning pipe. A plastic diaphragm was placed between this pipe and the dump tank.

Nitrogen gas was caused to flow continuously through a liquid nitrogen trap into the test section entering near the dump tank and leaving near the metal diaphragm which separated the test section from the high pressure section. The pressure was monitored with an alphatron at the outlet end. The flow rate of the gas through the test section was approximately 5 ft/sec.

The electronic circuits indicated in Fig. 2 are highly schematic, but will serve to illustrate the sequence of events occurring in a typical run. After the gas flow was started through the test section, the driver section was loaded with a mixture of hydrogen, oxygen and nitrogen necessary to

obtain the desired shock strength. The run was initiated by triggering high pressure air gap switch 1 allowing the capacitor bank across the electrodes on the test section of the shock tube to discharge through the nitrogen gas. Simultaneously, the oscilloscope which monitored the L-R afterglow was triggered. At the same instant, a time-delay generator was activated; after a preset time (about 50 millisec) this fired a trigger box which activated air gap switch 2 thus exploding the coaxial wire in the driver section, and igniting the combustion mixture. Within a few milliseconds the diaphragm ruptured and a shock wave moved into the test gas. A photomultiplier (PM) was used to trigger the oscilloscope which subsequently recorded, on a time-based raster sweep, the arrival of the shock wave at three speed-indicating P.M.'s. Another PM was used to trigger the oscilloscope which monitored the $N_2(1+)$ and $N_2^+(1-)$ band systems.

The optical station was described in a previous publication.[10] The external optical system allowed a 1 mm spatial resolution. Wavelength separation was accomplished with a Bausch and Lomb grating monochromator having a dispersion of 33 Å per mm. The monochromator was set for 4272 Å (total band pass = 66 Å). This wavelength band pass centered on the 0, 1 vibrational transition of the $N_2^+(1-)$ system. This spectral region was chosen because here the $N_2^+(1-)$ radiation is intense while impurity radiation, in particular the CN violet system, is minimized. The radiation was monitored as a function of time with a calibrated 6292 Dumont PM (S-11 surface) mounted behind the exit slit.

A portion of the undispersed beam was intercepted by a mirror inside the monochromator and reflected to an RCA 7326 PM (S-20 response). Three Corning filters (1-60, 2-58 and 4-77) were stacked in front of the PM. This combination isolated a broad band of radiation from 6600 to 8000 Å peaked at 7100 Å. The $N_2(1+)$ bands (2, 0) - (6, 4) should be the main contributors in this wavelength range. This wavelength region is relatively free of impurity radiation. It would have been desirable to work at 10, 420 Å the $N_2(1+)$ 0, 0 band head. Some attempts were made to measure initial radiation slopes at this wavelength using an S-1 surface photomultiplier. However, the relatively poor sensitivity of detectors at this wavelength made it impossible to measure the slopes with necessary accuracy because of the poor signal to noise ratio.

The waiting period of about 50 millisec between the single pulse discharge and the initiation of the shock wave was to allow time for the relaxation of all the undesirable conditions produced in the discharge, i. e. short-lived ionic species and unknown temperature. The electron-ion recombination rates at room temperature for N_2^+, N_3^+ and N_4^+ are sufficiently large[8] so that the concentration of these species (and the electrons) must have dropped to a completely insignificant level by the time of shock arrival - regardless of their initial concentrations. The computed relaxation time for cooling the discharged gas by conduction to the tube walls was 5 millisec. This set a lower limit to the time delay. However, it is clearly desirable to wait as long as possible to allow the gas to cool and to allow time for the ionic species produced in the discharge to re-

combine with the electrons. Of course, during this waiting period the N-atoms are recombining so that the shock could not be delayed indefinitely. Different N/N_2 ratios were obtained by varying both this time delay and the size of the capacitor bank.

Diffusion time from the center line of the tube to the walls was about 2 millisec and hence the gas was uniform across the tube diameter. On the other hand, diffusion time from the optical station to the nearest electrode was 1.7 sec, a time long compared to the 50 millisec waiting period; hence, no impurities produced at the electrode during the discharge could reach the optical station. Furthermore, although the electrodes catalyzed the atom recombination, this long diffusion time ensured that there would be no significant N-atom axial gradient in the observed shocked gas.

The PM's monitoring the $N_2(1+)$ and $N_2^+(1-)$ band systems were calibrated using a tungsten ribbon lamp, with geometric conditions identical to those prevailing during an actual shock tube run. Hence, the signal observed during a shock tube run could be converted directly into spectral intensity (watts/cm^3 ster μ) simply by dividing that signal by the calibration factor and the optical path length (3.81 cm).

The L-R afterglow was monitored with an S-11 surface PM in combination with a 3-66 Corning filter. This combination yielded a band pass centered on 5900 Å with a half width of 400 Å; the region of maximum afterglow.[9]

Noting that the signal S produced by the afterglow monitor is proportional to the afterglow intensity, and that the afterglow intensity is proportional to the rate of recombination of atoms via the L-R mechanism,[9] we can write

$$S = G k_{LR} [N]^2 [N_2], \tag{1}$$

where G is the proportionality constant and k_{LR} is the rate constant for recombination via the L-R mechanism. Differentiation of Eq. (1) yields

$$dS/dt = 2 G k_{LR} [N] [N_2] \, d[N]/dt . \tag{2}$$

Inserting the usual atom recombination expression

$$dN/dt = - k_r [N]^2 [N_2] \tag{3}$$

into Eq. (2), and eliminating [N] by means of Eq. (1), we find

$$\frac{d \frac{1}{\sqrt{S}}}{dt} = \frac{k_r [N_2]^{1/2}}{(G k_{LR})^{1/2}} \tag{4}$$

In deriving this equation, it has been assumed that N and N_2 have the same catalytic efficiency in recombining N-atoms at room temperature and the small effect of changes in the concentration of the catalyst have been ignored.

Therefore, a plot of the reciprocal square root of the afterglow signal (in arbitrary units) against time should be a straight line. The room temperature three-body recombination rate constant is relatively well determined[11, 12] to be $k_r = 3.3 \times 10^{-32}$ cm^6/particle^2 sec. Thus, a measurement of the slope of this line yields Gk_{LR} which can be used in Eq. (1) to calculate the atom concentration corresponding to the signal S.

Such afterglow data curves were obtained and found to be straight lines at early times before wall recombination effects became non-negligible. It should be noted that once Gk_{LR} is evaluated, the atom concentration is given by Eq. (1) independent of the mechanism for atom depletion.

A typical afterglow monitor oscillogram is shown in Fig. 3. For this run, the shock wave arrived at the afterglow monitor (and optical station) about 70 msec after the discharge. At this point the signal goes off scale due to the increased intensity behind the shock wave.

It is known that $A^3\Sigma_u^+$ nitrogen is formed during the recombination of nitrogen atoms. These metastables are destroyed by collisional deactivation in the gas phase, collisional deactivation on the walls and by radiating to the ground state. The last of these three processes leads to the Vegard-Kaplan Band System. (See Fig. 1.) An attempt was made to photograph the spectrum of this system subsequent to the pulsed discharge. For this purpose, the dump tank was removed from the shock tube and the open end was covered with a metal plate fitted with a calcium fluoride window. A single spectral plate was prepared by taking 35 exposures of the L-R afterglow (each of 10 seconds duration). During the discharge proper, radiation was prevented from entering the spectrograph. No Vegard-Kaplan spectrum was seen on the spectrogram.

III. EXPERIMENTAL RESULTS AND THEORETICAL MODELS

In what follows we will use the notation $B \equiv N_2(B^3\pi_g)$, $B^+ \equiv N_2^+(B^2\Sigma_u^+)$, etc. At equilibrium the concentration of molecules in the various states are related by equations of the type

$$[B] = [A]\, Q_{AB} \exp(-E_{AB}/kT) = [A]\, K_{AB} \quad , \tag{5}$$

where Q_{AB} is the ratio of partition functions for the B and A states and E_{AB} is the energy separation between the ground vibrational levels of the two states. Table I gives the values for Q and E required for the present work. Q is actually a function of T but here we have taken the high temperature limit to the partition functions which are good approximations in the temperature range of interest.

Table I

Equilibrium Constant Parameters for N_2 and N_2^+

Process	Q	E(eV)
$X \rightleftarrows A$	6.81	6.168
$A \rightleftarrows B$	1.48	1.185
$X^+ \rightleftarrows A^+$	2.61	1.118
$X^+ \rightleftarrows B^+$	0.85	3.169

A. $N_2(1+)$ System

Typical oscillograms of the $N_2(1+)$ radiation are shown in Fig. 4. for the cases (a) $N/N_2 = 0$ and (b) $N/N_2 = 0.067$. The $N/N_2 = 0$ run was at $U_s = 4.56$ mm/μsec corresponding to temperatures of 10,000°K subsequent to rotational relaxation, but before vibrational and chemical equilibrium. The $N/N_2 = 0.067$ run was at $U_s = 4.54$ mm/μsec corresponding to T = 9850°K. Note that in the predissociation case a slightly higher shock speed would be required to obtain the same temperature as in pure N_2. The manner in which the initial slopes are obtained from the oscillograms is indicated in the figure. The small amount of curvature at the foot is instrumental rise time and is ignored. It is to be noted that initial rate of rise of radiation intensity is about 2.6 times larger in the case where atoms are present at zero time even though the temperature is slightly lower.

The data obtained in the $N_2(1+)$ case are shown in Fig. 5 with separate plots for each of the four nominal N/N_2 ratios. In this figure the initial slopes are plotted in units of (watts/cm^3 ster μ)/μsec against the reciprocal temperature occurring at the shock front subsequent to translational and rotational relaxation.

The solid lines shown in the figures are computed on the basis of the following simple mechanism:

$$N_2(X) + N \xrightarrow{k_N} N_2(A) + N \qquad \text{(R1)}$$

$$N_2(X) + N_2 \xrightarrow{k_{N_2}} N_2(A) + N_2 \qquad \text{(R2)}$$

$$N_2(A) \rightleftarrows N_2(B), \qquad \text{(R3)}$$

where (R3) is fast and is assumed to be in local equilibrium at the translational temperature. (See Section IV for a discussion of these assumptions.) Hence, we can write

$$d[A]/dt = \left\{ k_N [N] + k_{N_2} [X] \right\} [X] - d[B]/dt \quad . \tag{6}$$

At local equilibrium Eq. (5) applies, which upon differentiation at zero time yields

$$d[B]/dt = K_{AB}\, d[A]/dt. \tag{7}$$

The experimental radiation intensity I is the power radiated per unit volume per unit solid angle per unit wavelength in the band pass of interest; it is given by the equation[13]

$$\begin{aligned} I &= C \lambda^{-5} f \langle \phi \rangle T^{-1} [A] \exp(-E_{AB}/kT), \\ C &\equiv 2 \pi r_o h^2 c^3/k \quad . \end{aligned} \tag{8}$$

Here r_o, h, c and k are the classical electron radius, Planck's constant, the velocity of light and Boltzmann's constant, respectively. The oscillator strength f is equal to 8.3×10^{-3} for this system at $\lambda = 7100$ Å [10, 14], and $\langle \phi \rangle$ is given by[10]

$$\langle \phi \rangle = \lambda^6 \int_{\lambda_1}^{\lambda_2} \lambda'^{-6} \phi R \, d\lambda' \Big/ \int_{\lambda_1}^{\lambda_2} R \, d\lambda' \quad , \tag{9}$$

where R is the experimentally determined resolution function of the optical instrument,[10] λ_1 and λ_2 are the extreme wavelengths of the instrument band pass, and ϕ is a dimensionless factor of order unity which gives the details of the vibrational spectrum.[13] ϕ can readily be evaluated from the Franck-Condon factors given the rotational and vibrational temperatures of the radiating molecule. The rotational temperature is taken equal to the translational temperature; in the present work it has been assumed that the vibrational temperature appropriate to the B state is also equal to the translational temperature. Over the temperature range 6000-20,000°K, computed values[15] of $\langle \phi \rangle$ were adequately fitted by

$$\langle \phi \rangle = -0.181 + 0.53 (T/10^4) - 0.058 (T/10^4)^2 \quad . \tag{10}$$

Differentiation of (8) yields

$$(dI/dt)_{t=0} = C\,\lambda^{-5}\, f\, \langle\phi\rangle\, T^{-1} \exp(-E_{AB}/kT)\, d[A]/dt. \qquad (11)$$

Equations (6), (7), and (11) finally yield

$$\left(\frac{dI}{dt_L}\right)_{t=0} = \frac{Cf\langle\phi\rangle}{\lambda^5 T} \frac{\exp(-E_{AB}/kT)}{(\rho_1/\rho_2)} \frac{\left\{k_N[N] + k_{N_2}[X]\right\}[X]}{(1 + K_{AB})}, \qquad (12)$$

where the factor (ρ_1/ρ_2) in the denominator has been introduced to effect the transformation from particle time to laboratory time, t_L.

In order to use Eq. (12) and to provide theoretical curves for comparison with the data, we have expressed the rate constants in the following form:

$$k_N = A_N\, T^{-3/2} \exp(-E_{XA}/kT)\ \text{cm}^3/\text{particle-sec} \qquad (13)$$

and

$$k_{N_2} = A_{N_2}\, T^{-1/2} \exp(-E_{XA}/kT)\ \text{cm}^3/\text{particle-sec}. \qquad (14)$$

These provide good fits to the predissociation runs shown in Fig. 5a-c as long as A_N and A_{N_2} are assigned numerical values such that $k_{N_2} \lesssim 0.03\, k_N$ over the temperature range of the data. Hence, only an upper bound can be put on k_{N_2} from this data alone. The solid curves are for $A_N = 1.9 \times 10^{-6}$ and $A_{N_2} = 1.6 \times 10^{-12}$ corresponding to $k_{N_2}/k_N = 0.01$ at $T = 12,000^\circ$K. The equivalent inelastic cross sections for N-N_2 and N_2-N_2 collisions at $12,000^\circ$K are 2.7×10^{-18} and 6.6×10^{-20} cm^2 respectively.

The above choice of A_{N_2} is based on the data obtained without predissociation. These data are shown in Fig. 5d, along with the solid curve based on Eq. (12) using $A_{N_2} = 1.6 \times 10^{-12}$. The theoretical curve was fitted to the data only at the lowest temperatures, making the assumption that the dominant catalyst is N_2. As the temperature is increased, the experimental dI/dt increases more rapidly than predicted by the above simple theory. A linear empirical fit to the data above 8700°K has been added to Fig. 5d as the dashed line defined by

$$dI/dt_L = 3.8 \times 10^3 \exp(-E^*/kT)\ (\text{watts/cm}^3\text{-ster-}\mu)/(\mu\text{sec}), \qquad (15)$$

where $E^* = 10.5$ eV.

It is obvious from the above discussion that the pre-exponential temperature dependence of $T^{-1/2}$ given for k_{N_2} is not at all determined. We leave the equation in this form only because the theoretical curves in Fig. 5 (in particular Fig. 5d) were computed on this basis. On the other hand, the $T^{-3/2}$ pre-exponential temperature dependence for k_N was determined by the best fit to the data of Fig. 5a-c.

B. $N_2^+(1-)$ System

The radiation profiles for the $N_2^+(1-)$ system are similar to those obtained for the $N_2(1+)$ system (see Fig. 4). The initial slope data obtained for the $N_2^+(1-)$ system are shown in Fig. 6. In this case, the theoretical curves are based on the mechanism outlined below.

$$N + N \xrightarrow{k_i} N_2^+(X) + e \qquad \text{(R4)}$$

$$N_2^+(X) \rightleftarrows N_2^+(A) \rightleftarrows N_2^+(B) \qquad \text{(R5)}$$

$$N_2^+ + N \rightleftarrows N_2 + N^+ \qquad \text{(R6)}$$

In (R4) we assume, for the present, that the nitrogen atoms are in the ground electronic state (^4S). Furthermore, we assume that the excitation reactions indicated in (R5) and the charge exchange reaction (R6) are fast and in local equilibrium at the translational temperature.

Proceeding in a manner analogous to that used above, we find

$$\left(\frac{dI}{dt_L}\right)_{t=0} = \frac{Cf\langle\phi\rangle}{\lambda^5 T} \frac{\exp(-E_{X^+B^+}/kT}{\rho_1/\rho_2} \frac{k_i(N)^2}{1+K_{X^+A^+}+K_{X^+B^+}+K_e(N)/(N_2)} . \qquad (16)$$

In this case,[14, 16] $f = 3.4 \times 10^{-2}$, $\lambda = 4272$ Å, and $\langle\phi\rangle = 0.81$ and is independent of temperature.[15] K_e is the equilibrium constant for (R6), it was computed as a function of temperature from the partition functions.

The rate constant for (R4) used to produce the theoretical curves shown in Fig. 6a, b and c is given by Lin and Teare.[17]

$$k_i = 9 \times 10^{-11} T^{-1/2}(1+1.3 \times 10^{-4}T+3.3 \times 10^{-8}T^2 - 10^{-12}T^3) \exp(-67,300/T)$$

$$\text{cm}^3/\text{particle sec.} \qquad (17)$$

This expression is based on the room temperature measurements of Kasner, Rogers and Biondi[8] who studied the recombination rate for electrons and N_2^+ produced in a microwave discharge. Equation (17) was arrived at by using their results in conjunction with a $T^{-3/2}$ temperature dependence suggested by Sayers,[18] and an equilibrium constant expression for reaction (R4). For details see reference (17).

For the $N/N_2 = 0$ case, the theoretical initial slope is obviously zero according to the above mechanism. Hence no theoretical curve is shown in Fig. 6d. The dashed line shown in this figure is an empirical fit to the data given by the equation

$$dI/dt_L = 1.7 \times 10^4 \exp(-E^\dagger/kT) \text{ (watts/cm}^3\text{-ster-}\mu)/\mu\text{sec}), \quad (18)$$

where $E^\dagger = 12.9$ eV.

IV. DISCUSSION

A. $N_2(1+)$ System

In Fig. 5d, which shows the experimental and theoretical initial slopes for the $N_2(1+)$ radiation for the case $N/N_2 = 0$, the simple theory deviates from the experimental data at high temperatures, It is postulated that the steeper temperature dependence of the experimental data is due to the fact that the N_2 is dissociating and the atoms thus produced increase the rate of rise of radiation. Indeed, it is possible that even at the lowest temperatures the N_2 plays an insignificant role, and that the excitation process does not proceed until atoms are formed by dissociation behind the shock front. If this were the case, the solid line in Fig. 5d would be meaningless, and the above value of k_{N_2} would be only an upper bound. It should be pointed out, however, that the data of Figs. 5a, b and c are adequately fitted by Eq. (12) with A_N unchanged even when $k_{N_2} \to 0$.

The contribution of the time-varying atom concentration cannot be assessed in a simple model which does not take account of the complicated dissociation process. The dissociation rate for nitrogen has been measured over the temperature range $6000 \leqq T \leqq 9000^\circ$K.[19] Extrapolation to higher temperatures is dangerous as it immediately enters the regime where vibrational relaxation times are comparable to dissociation times, hence the coupling of these two processes must become important. There are dissociation measurements for the O_2-Ar system up to $T = 18,000^\circ$K, showing evidence of strong coupling;[20] the details, however, are uncertain, as is, of course, the application of these results to the N_2 system.

The assumption was made above that the A and B states are in local equilibrium. Taylor[21] in a recent shock tube study of collision limiting of radiation in N_2, has established that the cross section for deactivating B molecules by collision with $N_2(X)$ is equal to or greater than 2.6×10^{-16} cm^2. Use of this cross section in the excitation direction yields relaxation

times short compared to the times of interest in the present experiment. Hence this important equilibrium assumption is justified. However, there is a question as to whether this equilibrium should be calculated using the local translational temperature as was done above or the local vibrational temperature of the ground state nitrogen molecules. The only evidence bearing on the subject known to the author is the fact that the electronic temperature of sodium atoms seems to follow the vibrational temperature of nitrogen molecules when a small amount of sodium is observed by means of the sodium line reversal technique in shock-heated nitrogen.[22] But, it is not clear from this one piece of evidence that all systems behave in a similar manner. To put the A and B states in equilibrium according to the vibrational temperature would require a much more elaborate analysis. Of course, the mechanism based on vibrational temperature implies that the initial rise of radiation would be nonlinear; however, it is difficult from the present data to shed much light on this question.

The mechanism given in the previous section for production of the B state molecule is not unique. It could also be postulated that B molecules are produced directly in $N_2(X)$ - N collisions; this mechanism is indistinguishable from the one given on the basis of the present data. On the other hand, the B state cannot be populated by three body recombination of N-atoms as this mechanism yields a temperature dependence much smaller than indicated by the data.

In summary, this experiment has demonstrated that the nitrogen atom is at least 100 times more effective than N_2 in causing the transition X → A. The rate constant expression for this process has been found to be

$$k_N = 1.9 \times 10^{-6} T^{-3/2} \exp(-E_{XA}/kT) \text{ cm}^3/\text{particle-sec} \quad , \qquad (19)$$

leading to an effective cross section of 2.7×10^{-18} cm^2 at 12,000°K.

As was outlined in Section II, an attempt was made to record the Vegard-Kaplan band system in the discharged (but unshocked) gas. The results of this experiment were negative, i.e., no spectrum of this system was found. However, this negative result was used to calculate a lower bound to the cross section for collisionally deactivating the A state at room temperature. This was done by comparing the energy per unit area of film necessary to obtain film darkening with the calculated energy per unit area. It was assumed that the A state molecules were deactivated by collisions with N-atoms and the rate constant for that process was calculated from Eq. (19) and the equilibrium constant K_{XA}. The details of this calculation are given in the Appendix. It was found that k_N (at room temperature)given by Eq. (19) was consistent with the inability to record the Vegard-Kaplan spectrum and a lower bound of $1/20\ k_N$ was established.

This (relatively) high efficiency of the N-atom in coupling the X and A states of nitrogen is in disagreement with estimates of the A state concentration in active nitrogen obtained by the ammonia reaction

technique.[23] (But see Ref. (24) for a criticism of this work.)

B. N_2^+ (1-) System

In deriving Eq. (16), the theoretical expression for the initial slope of the N_2^+(1-) system, the X^+, A^+ and B^+ states have been assumed to be in local equilibrium. The cross section for deactivating the B^+ state by collisions with N_2 has been measured by Brocklehurst[25], Davidson and O'Neil[26], and Taylor[21] and is of the order of 1×10^{-15} cm^2. In some recent work Carleton[27] finds this cross section to be 7×10^{-15} cm^2 and also finds the cross section for deactivating the (A^+) state to be 2×10^{-14} cm^2. These cross sections justify the above assumption. This is identical to the assumption made concerning (R3) and the discussion above as to whether this equilibrium should be governed by the translational temperature or the ground state vibrational temperature applies here also. Reaction (R6) has been put in local equilibrium although the alternative assumption of no reaction at all has but a small affect on the theoretical curves shown in Fig. 6a, b and c.

It has been assumed that the atoms responsible for the associative ionization reaction (R4) are in the ground electronic state (^{4}S). As was pointed out by Gilmore,[2] this is only possible if there is a potential curve originating at N(^{4}S) + N(^{4}S) and crossing the X^+ state. (See Fig. 1.) Furthermore, this crossing potential curve must allow formation of X^+ and an electron without violating electron spin conservation; this eliminates the repulsive $^7\Sigma_u^+$ state. In all probability the singlet and triplet potential curves arising from the ground state atoms do not cross the X^+ curve. Hence, theoretically it seems unlikely that the atoms in (R4) can be (^{4}S). See Gilmore[2] for a more detailed discussion of this subject.

As was suggested by Gilmore,[2] (R4) probably involves one excited nitrogen atom, either the ^{2}D or ^{2}P. Now, if it is assumed that these excited atoms are produced extremely rapidly compared to (R4) and go into local equilibrium, then the theoretical curves shown in Fig. 6 would remain essentially unchanged except for ratios of degeneracies in the equilibrium constant. To put a finite rate constant on the production of the excited nitrogen atoms implies $(dI/dt)_{t=0} = 0$, and once again a more involved analysis of the data is required. Although some efforts along these lines have been made, a meaningful treatment really awaits more experimental or theoretical information on the mechanisms and cross sections for producing excited N-atoms before such detailed calculations are warranted.

Vacuum U. V. radiation emanating from excited nitrogen atoms, the lower term atoms being those of interest, has been observed in shock-heated nitrogen,[28] and it seems feasible to do an absorption type shock tube experiment to elucidate the mechanism and cross sections responsible for the production of the ^{2}D and perhaps the ^{2}P nitrogen atoms.

From the molecular beam results of Utterback and Miller[29] for the single energy ionization cross sections for N_2-N_2 collisions, Lin and

Teare[17] have computed rate constants for the reaction $N_2 + N_2 \rightarrow N_2^+ + e + N_2$. Employing such a mechanism for the production of $N_2^+(1-)$ radiation in our shock tube experiments clearly leads to a finite initial radiation slope. However, these were found to be many orders of magnitude lower than the experiment indicated, except at the highest temperatures where this mechanism just becomes of the same order of magnitude as the experimental data.

ACKNOWLEDGMENT

The author wishes to thank Thomas J. Connolly and Walter I. Fyfe for aid given in the operation of the shock tube and data reduction. He also acknowledges many fruitful discussions concerning this work with his colleagues at Avco-Everett Research Laboratory and with Prof. W.R. Thorson. In particular, the author acknowledges the contributions made to this work by J.D. Teare who was instrumental in producing the many machine calculations needed to analyse the data.

APPENDIX

Here we wish to evaluate the Vegard-Kaplan (V-K) band system energy per unit area of film integrated over the 35 exposures each of 10 seconds duration. We note that

$$E = \frac{\beta P \epsilon}{\Delta\lambda 4\pi} \quad 35 \int_0^{10} [A]\, dt\,, \tag{A1}$$

where β is a geometric factor for the optical system having units ster-cm^2, $\Delta\lambda$ is the wave length interval of the band, P is the number of photons/sec-A molecule in the band of interest, and ϵ is the energy/photon.

Carleton and Oldenberg[30] measured the rate of photon emission from the 0, 6 V-K band to be 1.35×10^{10} photons/sc-sec. At the same time, they measured the $N_2(1+)$ (1, 0) band in absorption and employing an incorrect lifetime for that transition calculated the concentration of A state molecules to be 1.5×10^{11}/cc. The error in the lifetime of the $N_2(B)_{v=1}$ state employed by Carleton and Oldenberg was pointed out by Brennen.[24] Using the correct lifetime[24] of the $N_2(B)_{v=1}$ state (13 μsec) and the data of Carleton and Oldenberg given above, we find $P = 9 \times 10^{-3}$ photons/sec-A particle in the 0, 6 V-K band (λ = 2770 Å). This should be the strongest feature of the V-K system.[31]

To evaluate the integral involved in Eq. (A1) we list the pertinent reactions that can occur subsequent to the discharge:

$$N + N + M \xrightarrow{k_r} N_2\,(\text{total}) + M \tag{RA1}$$

$$N + N + M \xrightarrow{3k_r/4} N_2(A) + M \qquad \text{(RA2)}$$

$$N_2(A) + N \xrightarrow{k_{AX}} N_2(X) + N \qquad \text{(RA3)}$$

$$N_2(A) \xrightarrow{\text{WALL}} N_2(X) \ . \qquad \text{(RA4)}$$

Here we have neglected atom recombination on the wall and have estimated that 3/4 of all the gas phase recombination result in production of A state molecules. We can now write

$$d[A]/dt = (3/4)\, k_r [N]^2 [M] - k_{AX} [A] [N] - \text{wall term} \ . \qquad \text{(A2)}$$

It should be noted that (RA3) is the reverse of (R1), hence

$$k_{AX} = k_N / K_{XA} \ . \qquad \text{(A3)}$$

Using k_N as given by Eq. (19) and evaluating Eq. (A3) at 300°K, we find $k_{AX} = 5.4 \times 10^{-11}$ cm^3/particle-sec which corresponds approximately to the kinetic cross-section. Using this value of k_{AX} and typical values of $[N]$, it is readily seen that the wall term in Eq. (A2) is completely negligible as the diffusion time to the wall is 2 msec.

The loss of N atoms is given by

$$d[N]/dt = - k_r [N]^2 [M] \ . \qquad \text{(A4)}$$

Integrating Eq. (A4) to get $[N]$ as a function of t, substituting this into Eq. (A2) and integrating we find

$$[A] = (3/4) [N_0] (a - 1)^{-1} [(qt + 1)^{-1} - (qt + 1)^{-a}] ,$$

$$a \equiv k_{AX}/k_r [M] , \qquad \text{(A5)}$$

$$q \equiv k_r [M] [N_0] ,$$

where $[N_0]$ is the concentration of N-atoms at t = 0.

The integral in Eq. (A1) can now be found:

$$\int_0^{10} A\,dt = (3/4)\,[N_0]\,(a-1)^{-1}\,q^{-1}\left\{\ell\,n(10\,q+1) + (a-1)^{-1}\,[(10q+1)^{(1-a)}-1]\right\}, \tag{A6}$$

and using $[N_0] = 6.4 \times 10^{16}$ and $[M] = 4.8 \times 10^{16}$, we find $q = 1.1 \times 10^2$ and $a = 3.3 \times 10^4$, hence

$$\int_0^{10} A\,dt = 9.8 \times 10^{10} \text{ particles-sec/cm}^3 \tag{A7}$$

Taking $\Delta\lambda = 10^{-7}$ cm to be the band width over which most of the 0, 6 transition energy is radiated, and evaluating the geometric factor β to be 2.0×10^{-8} ster-cm^2, we find Eq. (A1) yields $E = 3.6 \times 10^{-3}$ ergs/cm^2.

Calibration of the photographic film with a standard tungsten lamp yielded $E = 7.3 \times 10^{-2}$ ergs/cm^2 necessary to obtain a density of 0.3 at $\lambda = 2770$ Å.

These calculations indicate that an increase in light intensity of about a factor of 20 would have been needed to obtain a V-K 0, 6 spectrogram. Considering the numerical values of a and q, it should be noted that Eq. (A6), to a very good approximation, can be reduced to

$$\int_0^{10} A\,dt = (3/4)\,k_{AX}^{-1}\,\ell\,n\,10\,q\ . \tag{A8}$$

Thus, these results are in accord with $k_{AX} = 5.4 \times 10^{-11}$, and set a lower bound to k_{AX} of 1/20 this value.

REFERENCES

(1) Wray, K. L. and Teare, J. D., "Excitation Mechanism for the $N_2(1+)$ Band System in Shock-Heated Nitrogen," Presented at the 3rd International Conference on the Physics of Electronic and Atomic Collisions, London, July 22-26, 1963. Atomic Collision Processes, edited by M. R. C. McDowell, (North-Holland Publishing Co., Amsterdam, 1964), p. 1123.

(2) Gilmore, F. R., "Potential Energy Curves for N_2, NO, O_2, and Corresponding Ions," Rand Corporation Memorandum, RM-4034-PR, June 1964.

(3) Camac, M., "Argon and Nitrogen Shock Thickness," Presented at AIAA Aerospace Sciences Meeting, New York, January 20-22, 1964. AIAA Paper 64-35.

(4) Wray, K.L., "Chemical Kinetics of High Temperature Air," Progress in Astronautics and Rocketry, edited by F.R. Riddell, (Academic Press, New York, 1962), Vol. 7, p. 181.

(5) Allen, R.A., Keck, J.C. and Camm, J.C., Phys. Fluids 5, 284 (1962).

(6) Allen, R.A., Rose, P.H. and Camm, J.C., "Nonequilibrium and Equilibrium Radiation at Super-Satellite Re-Entry Velocities," Presented at the IAS 31st Annual Meeting, New York, January 21-23, 1963. IAS Paper 63-77.

(7) Allen, R.A., J. Quant. Spect. Rad. Transf. 5, 511 (1965).

(8) Kasner, W.H., Rogers, W.A. and Biondi, M.A., Phys. Rev. Letters 7, 321 (1961).

(9) Berkowitz, J., Chupka, W.A. and Kistiakowsky, G.B., J. Chem. Phys. 25, 457 (1956).

(10) Wray, K.L. and Connolly, T.J., J. Quant. Spect. Rad. Transf. 5, 111 (1965).

(11) Wentink, T., Sullivan, J.O. and Wray, K.L., J. Chem. Phys. 29, 231 (1958).

(12) Harteck, P., Reeves, R.R., and Mannella, G., J. Chem. Phys. 29, 608 (1958).

(13) Keck, J., Camm, J.C., Kivel, B. and Wentink, T., Ann. Phys. 7, 1 (1959).

(14) Keck, J.C., Allen, R.A. and Taylor, R.L., J. Quant. Spect. Rad. Transf. 3, 335 (1963).

(15) Allen, R.A., Private Communication. See Ref. 7 for Computational technique.

(16) Wray, K.L., and Connolly, T.J., "Electronic f-number of the $N_2^+(1-)$ Band System," Avco-Everett Research Laboratory Research Report 208, February 1965. To be published, J. Quant. Spect. Rad. Transf.

(17) Lin, S.C. and Teare, J.D., Phys. Fluids 6, 355 (1963).

(18) Sayers, J., Private Communication, September 1958.

(19) Byron, S.R., Private Communication, as discussed by K.L. Wray in Ref. 4.

(20) Wray, K.L., J. Chem. Phys. 37, 1254 (1962).

(21) Taylor, R.L., Private Communication, June 1965.

(22) Gaydon, A.G. and Hurle, I.R., Eighth Symposium (International) on Combustion (Williams & Wilkins, Baltimore, Md., 1962). p. 309.

(23) Dunford, H.B., J. Phys. Chem. 67, 258 (1963).

(24) Brennen, W.R., "Studies in Active Nitrogen," Ph.D. Thesis, Department of Chemistry, Harvard University, September 1964.

(25) Brocklehurst, B., Trans. Faraday Soc. 60, 2151 (1964).

(26) Davidson, G. and O'Neil, R., J. Chem. Phys. 41, 3946 (1964).

(27) Carleton, N.P., Private Communication, June 1965.

(28) Allen, R.A., and Camm, J.C., Private Communication, April 1965.

(29) Utterback, N.G. and Miller, G.H., Phys. Rev. 124, 1477 (1961).

(30) Carleton, N.P. and Oldenberg, O., J. Chem. Phys. 36, 3460 (1962).

(31) Carleton, N.P. and Papaliolios, C., J. Quant. Spec. Rad. Transf. 2, 241 (1962).

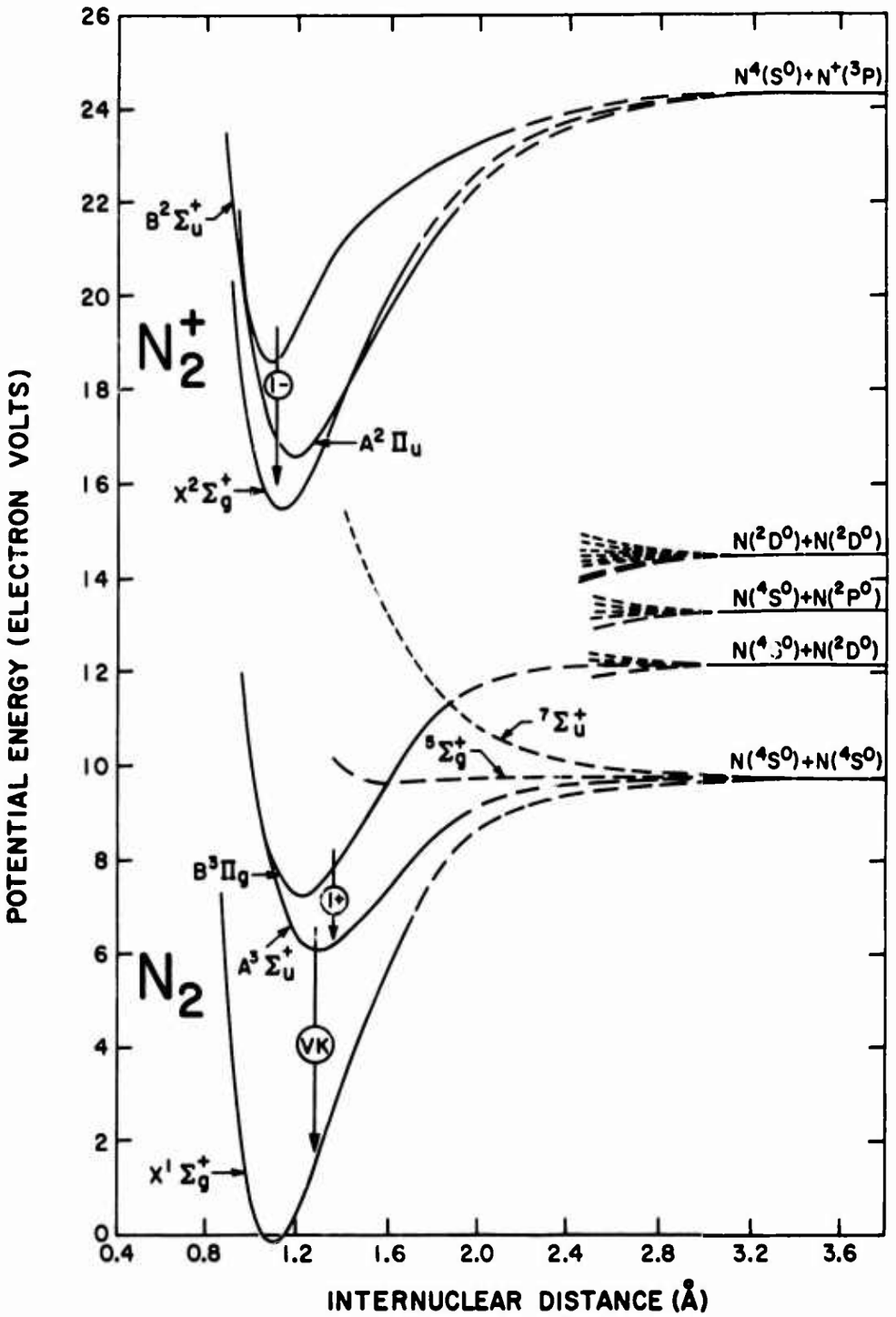


Fig. 1 Simplified potential energy diagram of the N_2 molecule and N_2^+ ion from a more complete diagram given by Gilmore. The radiation bands of interest in the present paper are indicated by vertical lines between the potential curves.

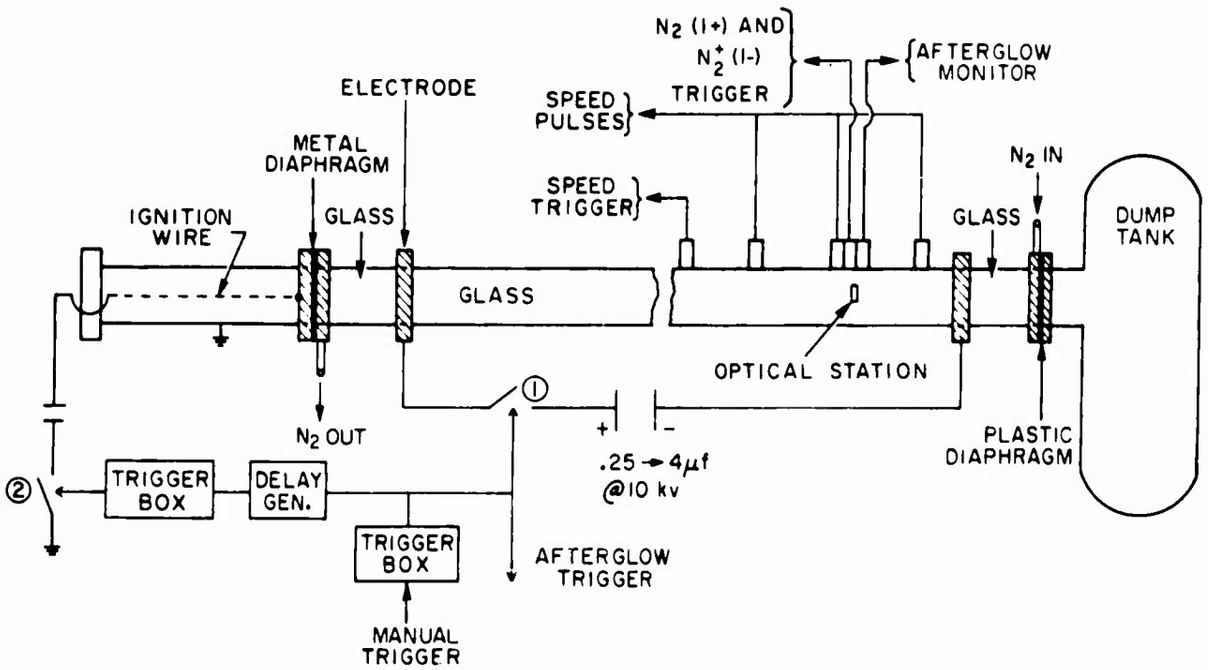


Fig. 2 Schematic diagram of the shock tube, optical measuring devices, and electronic circuitry.

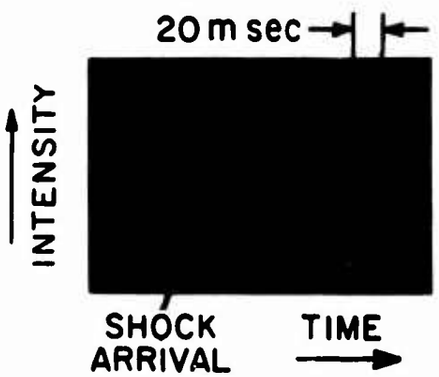


Fig. 3 Typical oscilloscope trace of the Lewis-Rayleigh afterglow. The relative intensity at the time of shock wave arrival at the optical station is used to determine the N-atom concentration.

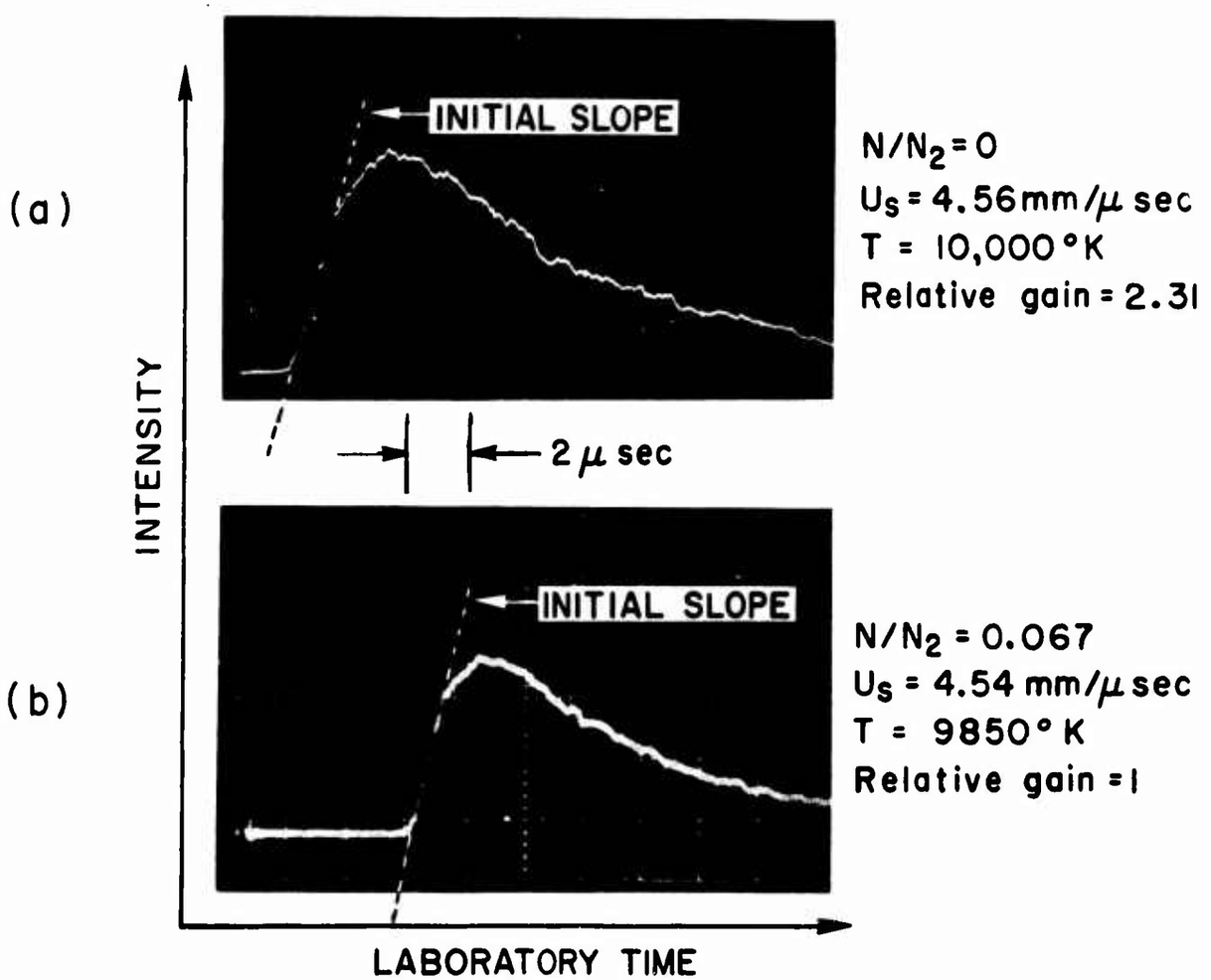


Fig. 4 Typical oscillogram records of the N_2 (1+) band system radiation as a function of time behind the shock wave.

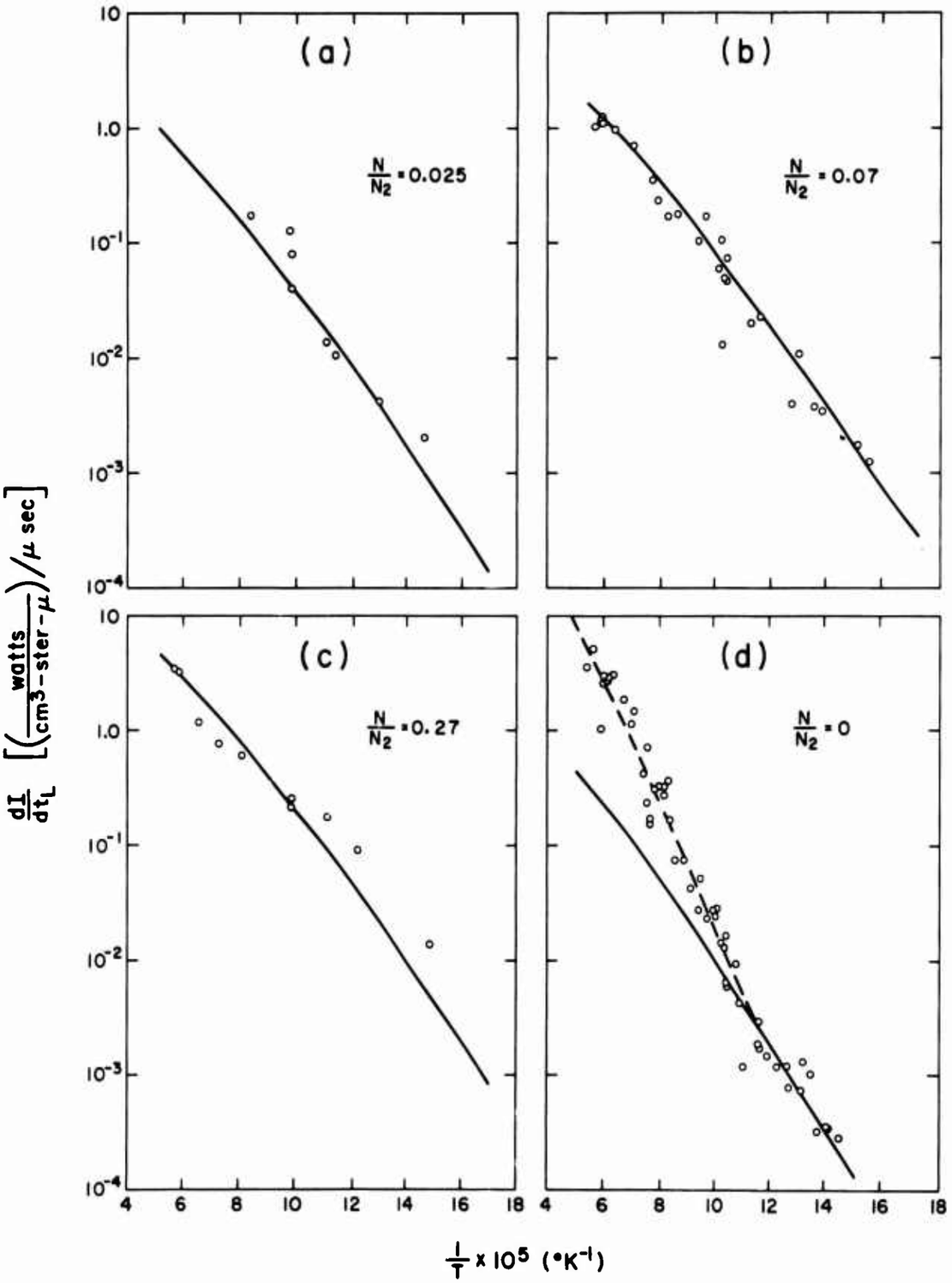


Fig. 5 Initial slopes of the N_2 (1+) radiation profiles plotted against reciprocal temperature at the shock front. The solid lines are theoretical curves which should be applicable only before significant dissociation occurs behind the shock. The dashed line in (d) is a linear empirical fit to the data above 8700°K.

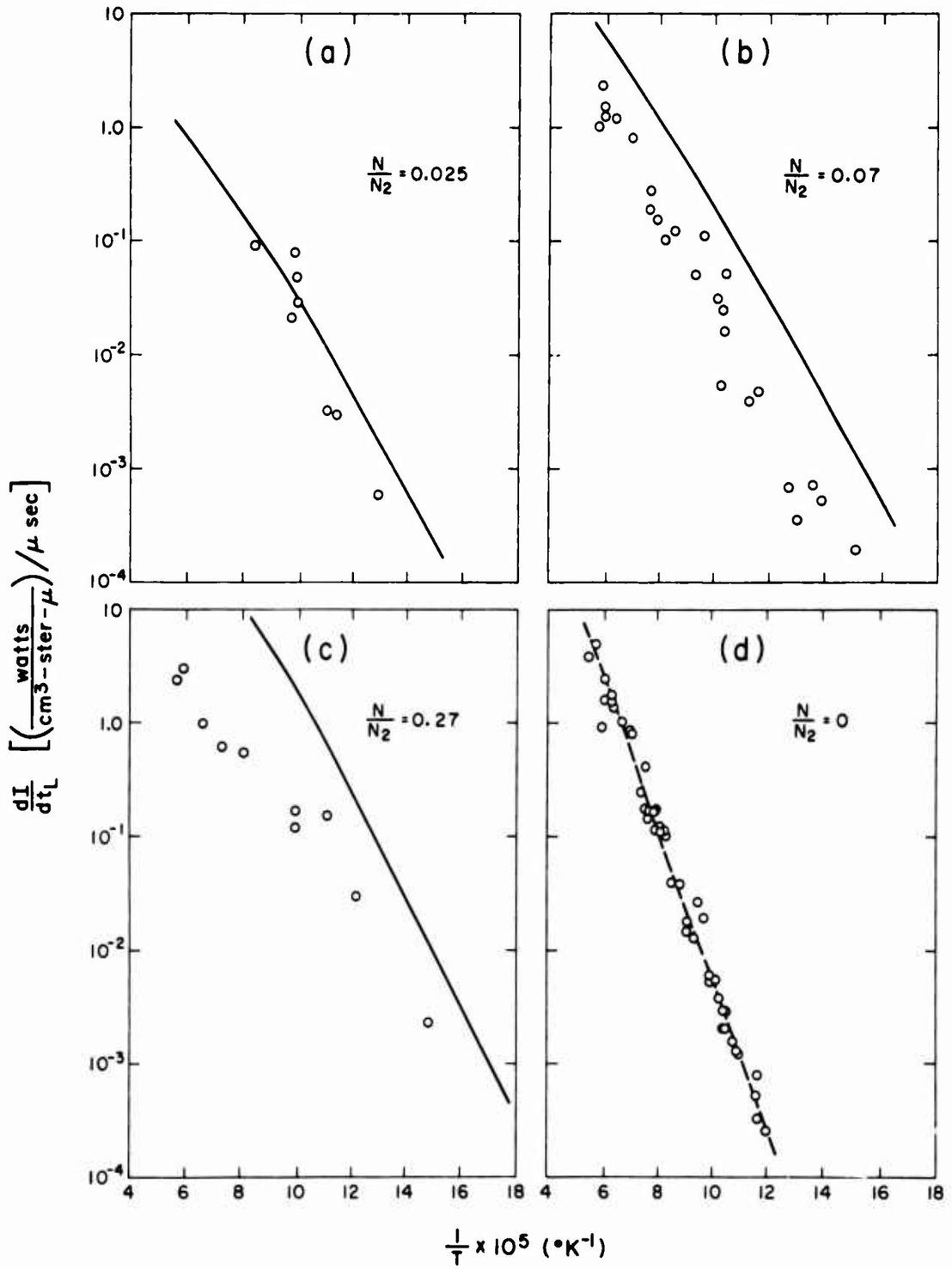


Fig. 6 Initial slopes of the $N_2^+(1-)$ radiation profiles plotted against reciprocal temperature at the shock front. The solid lines are theoretical curves which should be applicable only before significant dissociation occurs behind the shock. The dashed line in (d) is a linear empirical fit to the data.

BLANK PAGE

Equilibrated Shocked Plasma from a Linear Electric Shock Tube with Segmented Driver *

S. M. Hamberger, A. W. Johnson, and R. G. Fowler

University of Oklahoma

Abstract: Absolute time resolved measurements of continuum and line emissions in the shock generated in H_2 by a segmented driver electric shock tube has shown that after a relaxation time of the order of 10^{-6} sec, the absolute magnitude of the continuum at all wavelengths between 8000 and 3000 A, and the absolute intensity of the H_β line are in temperature agreement within 5 per cent. Whether or not this temperature agrees with that which would be expected from the shock equations depends on the extent to which the gas must have been dissociated by the shock. Comparison of this temperature with that which would be expected from the Rankine-Hugoniot equations is made and discrepancies are found.

*Supported by AFSW Center, Kirtland AFB.

EQUILIBRATED SHOCKED PLASMA FROM A LINEAR ELECTRIC SHOCK TUBE WITH SEGMENTED DRIVER

S. M. Hamberger,* A. W. Johnson, and R.G. Fowler
Department of Physics, University of Oklahoma
Norman, Oklahoma

INTRODUCTION

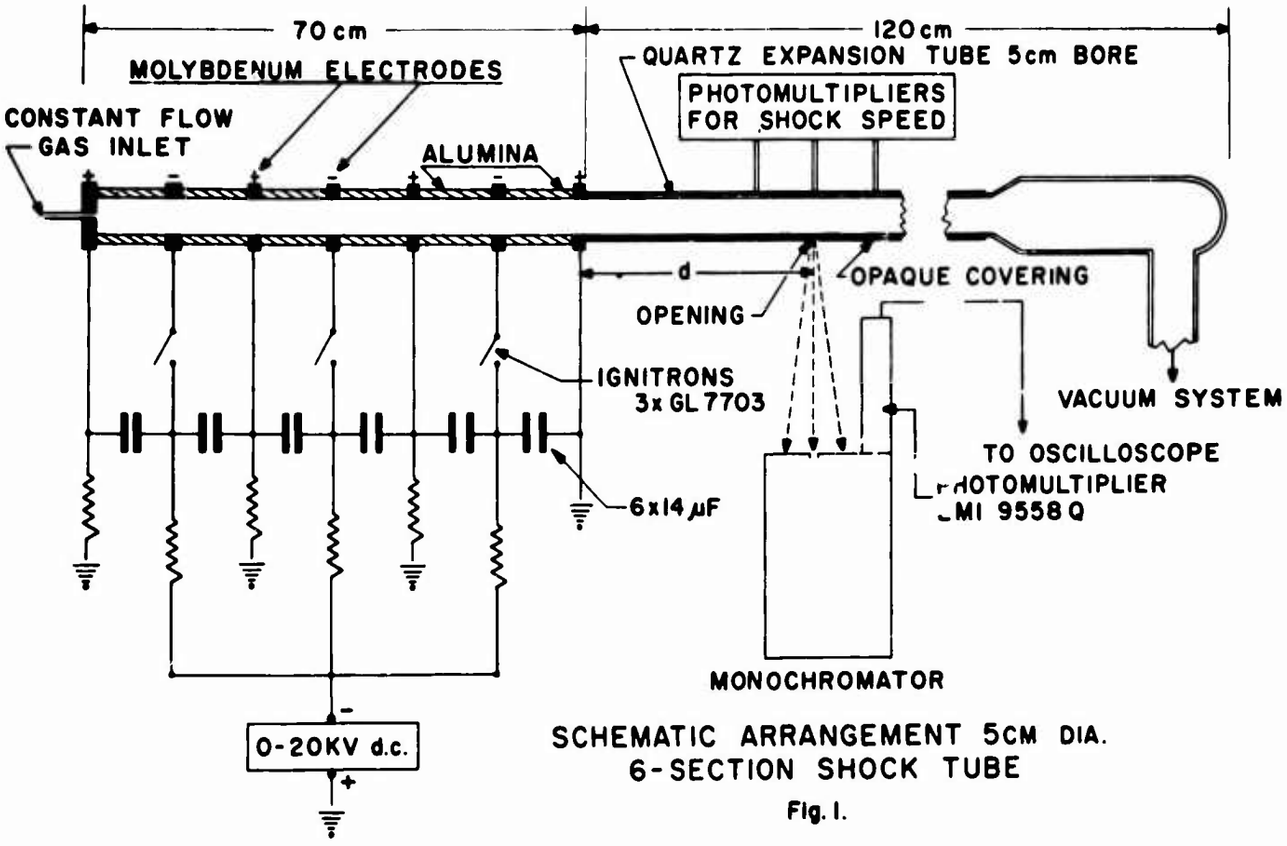
The electrically driven segmented shock tube has become an invaluable tool for the measurement of radiation phenomena of a plasma. (1) Not only does it offer a wide operating range of the plasma parameters, but it also produces a shocked gas that is almost totally free of impurities. Therefore, the electrically driven shock tube is an ideal tool to check some of the theories of radiative recombination. In particular, we used it to look for the attachment continuum of hydrogen, i.e: the recombination or near recombination of an atom and an electron. Some previous measurements have been made on a laboratory plasma in search of this continuum, (2), (3), (4), (5), but none over a wide range of wavelengths with the aid of spectroscopically determined temperatures and particle densities. Comparison of these temperatures with those predicted by the Rankine-Hugoniot equations will also be made.

SHOCK TUBE CONSTRUCTION

The driver section of the shock tube consisted of six ceramic cylinders approximately 10 cm long and 5 cm diameter separated by molybdenum electrodes (Figure 1). Six capacitors, 14 ufd each, charged to approximately 10 KV were discharged through a low inductance circuit with alternating flow vectors from one segment to the next, thus decreasing external fields. One end of the driver section was closed off and the other end was connected, with no change in diameter, to a meter long quartz tube which served as the expansion section of the shock tube. Since the driver is almost a meter long, well defined shock fronts which developed in front of the expanding gas only a few centimeters down stream continued their flow almost the full length of the tube. Higher voltages on the capacitors produced stronger shocks further down the tube.

The down-stream end of the expansion section was connected to an oil diffusion pump with which a base pressure of approximately 10^{-7} mm Hg was obtained. During the discharge of the capacitors, a constant flow of

*Present address: Culham Laboratory, Abingdon, Berks, England



SCHEMATIC ARRANGEMENT 5CM DIA. 6-SECTION SHOCK TUBE

Fig. 1.

hydrogen from a palladium leak was admitted into the tube to produce from 0.5 to 8.8 mm Hg, with a calculated pressure gradient of less than 4% along the length of the tube. Extremely pure hydrogen was thus obtained.

MEASURING INSTRUMENTS

Time and frequency resolution of the radiation was obtained by using an EMI photomultiplier with a Jarrell Ash 0.5 meter Ebert monochromator. The response of the photomultiplier and associated circuitry was checked with the aid of a Kerr cell to be better than 10^{-8} seconds. Wavelength resolution of less than an angstrom was obtained from the monochromator. With the aid of both a carbon arc and a tungsten lamp, absolute calibration of the radiation was obtained. The shock velocity was measured by two methods. The arrival times of the luminous front, which coincides with the shock front in the cases studied in this paper, were measured at two different positions by photomultipliers. From the spatial and temporal separation of these two positions, a velocity was obtained. Also, a Beckman & Whitley wave speed camera was used to measure the velocities for two of the conditions.

MEASUREMENTS BASED ON RADIATION

The processes producing the continuum were expected to be free-free (ff) & free-bound (fb) of hydrogen, negatively charged hydrogen, and H_2 positively charged. Lane (6) performed the calculations of the expected radiation of the H & H^- continua in terms of plasma parameters (particle densities and

temperature). Calculations of the (ff) & (fb) of the H continuum were based on the theory of Unsold (7) for the reduction of ionization potential and on well-known cross sections. The recent work of Geltman (8) and Ohmura & Ohmura (9) enabled the calculations of the (ff) & (fb) of the H^- continuum. For the H_2^+ continuum, the absorption coefficients of Bates (10) were used together with the assumption of equilibrium.

To calculate these continua, the densities of electrons, H^+ and H atoms, and the temperature need to be determined. The electron density, which is also the H^+ density, was determined by the Stark broadening of the H_β line based on the work of Kolb, Griem, and Shen (11). Figure 2 is a plot of one of our H_β Stark broadening lines. The solid line is taken from the cited work, normalized to the peak values. The circles represent the observed values. In this case, as in all of the following cases, a number of shots at each wavelength setting were averaged to get the values recorded.

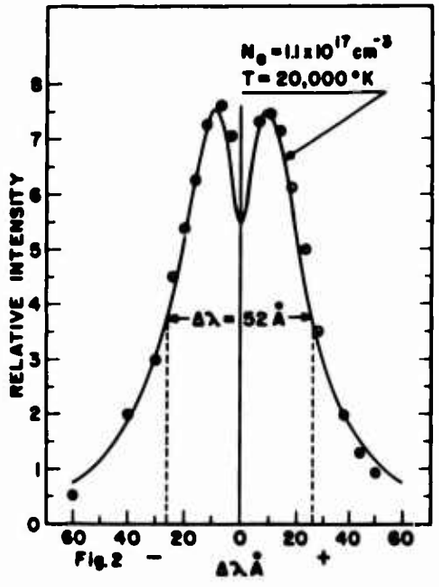


Fig. 2

The temperature was obtained using the Saha-Boltzmann relations. For the conditions of this work, calculations (12) have indicated that the Saha-Boltzmann equation will give the proper temperature if N_4, the density of the atoms in the level with principal quantum number 4, is used in conjunction with N_e, the electron density. N_4 was obtained from the absolute measurement of the radiation of the H_β line together with the spontaneous transition probability.

With the aid of the temperature, the Saha or the Boltzmann equation was used to get the density of the hydrogen atoms, N_1. The assumption that the ground state atoms are in equilibrium with the excited atoms needs consideration. Griem (13) describes in detail the validity criteria for the assumption of local thermodynamic equilibrium. Applying these criteria to the cases measured in this experiment, we expected the excited states of the atoms, the ions and the electrons to be in equilibrium. Furthermore, if the effect of resonance radiation is included in these considerations, the thermal distribution down to the ground state atoms is expected. Consequently, for the conditions discussed in this paper, the assumption that the Boltzmann equation applies to the ground level seems to be reasonable. Indeed, since the H^- continuum radiation is proportional to the number of neutral atoms, (which is very nearly equal to the number of ground state atoms for conditions in this paper), this assumption is consistent within the accuracy of our measurements of the continuum radiation.

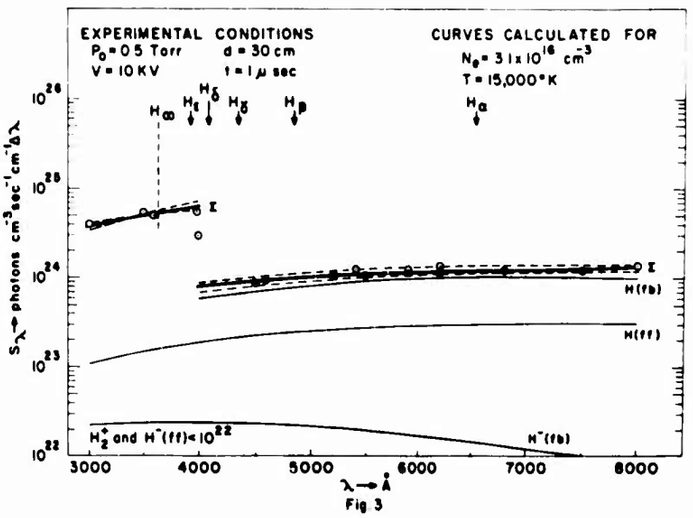


Fig 3

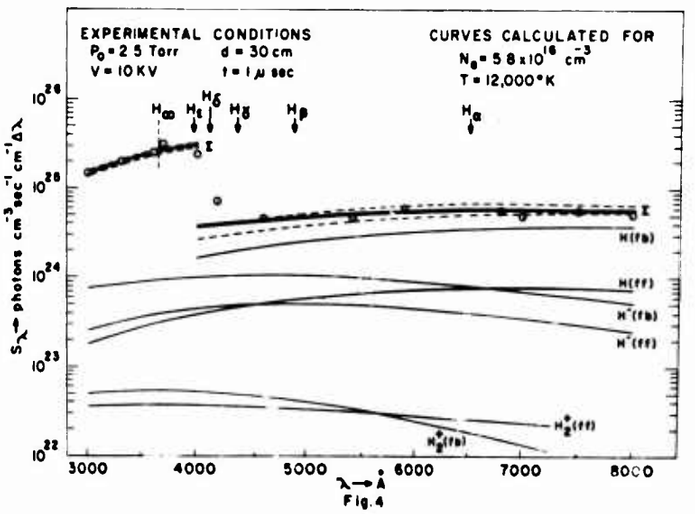


Fig.4

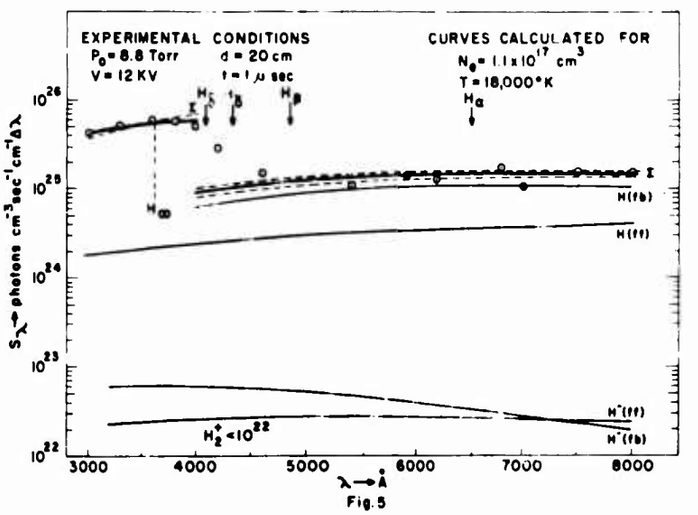


Fig.5

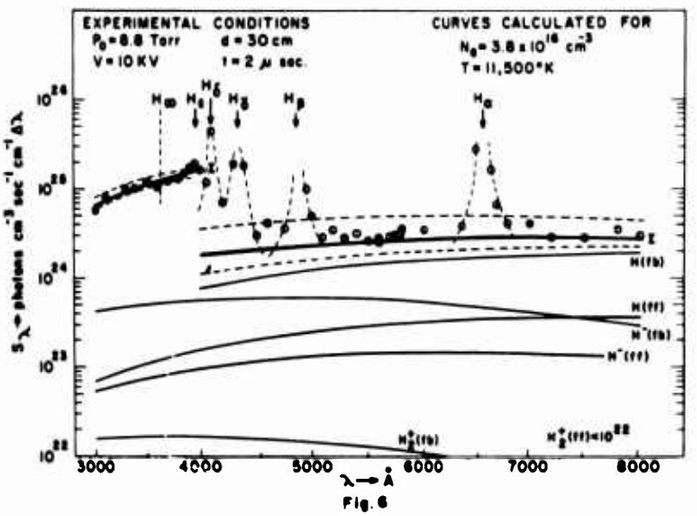


Fig. 6

Figures 3, 4, 5, 6.

EXPERIMENTAL AND COMPUTED SPECIFIC EMISSION COEFFICIENTS

⊙ Experimental Points

Σ Total Computed Continuum Radiation

---- Upper and Lower Limits of Σ for ±5% variations in N_e and N_4

—— Contribution from Individual Processes.

RESULTS OF THE CONTINUUM STUDIES

The measured specific emission coefficients, S_λ, are shown in Figures 3 to 6, in units of photons emitted per cm^3 per second per cm wavelength interval $\Delta\lambda$. All measurements were made with a bandwidth of about 20Å. To exclude obvious wing emission of the highly broadened Balmer lines and weak impurity lines, exploratory photoelectric scans and time-integrated spectrography were imployed. In Figures 3 to 5 the measurement wavelengths were chosen to represent only the true continuous background wherever this was possible. For wavelengths between H_β and the effective Balmer series limit this was not always possible, and some data points represent the minimum intensity between lines whose wings overlap above the continuum. For example, in Figure 4, the point at 4200Å and in Figure 5 those at 4200Å and 4600Å include some line emission. Figure 6 is a more detailed scan, which shows the general behavior of the emission above the unperturbed series limit, H_∞. The lighter dashed lines indicate the approximate positions of the line wings.

Each point in Figures 3 to 6 represents the average of from four to six measurements made, from the oscillograms, at the same instant of time, t, after the onset of luminosity; t was either 1 or 2 μsec in the examples shown. Generally the reproducibility was better at low initial pressures when the fractional ionization was high (as in Figure 3), then to higher pressures where the emission due to the dissociation at the shock front varied slightly and significantly altered the subsequent plasma conditions. Typical shot-to-shot variations ranged from a few percent, (Figure 3) to about 40 per cent (Figure 6). The solid lines represent the components of the continua calculated from the measured and derived quantities, N_e, N_1, T.

MEASUREMENTS BASED ON RANKINE-HUGONIOT EQUATIONS

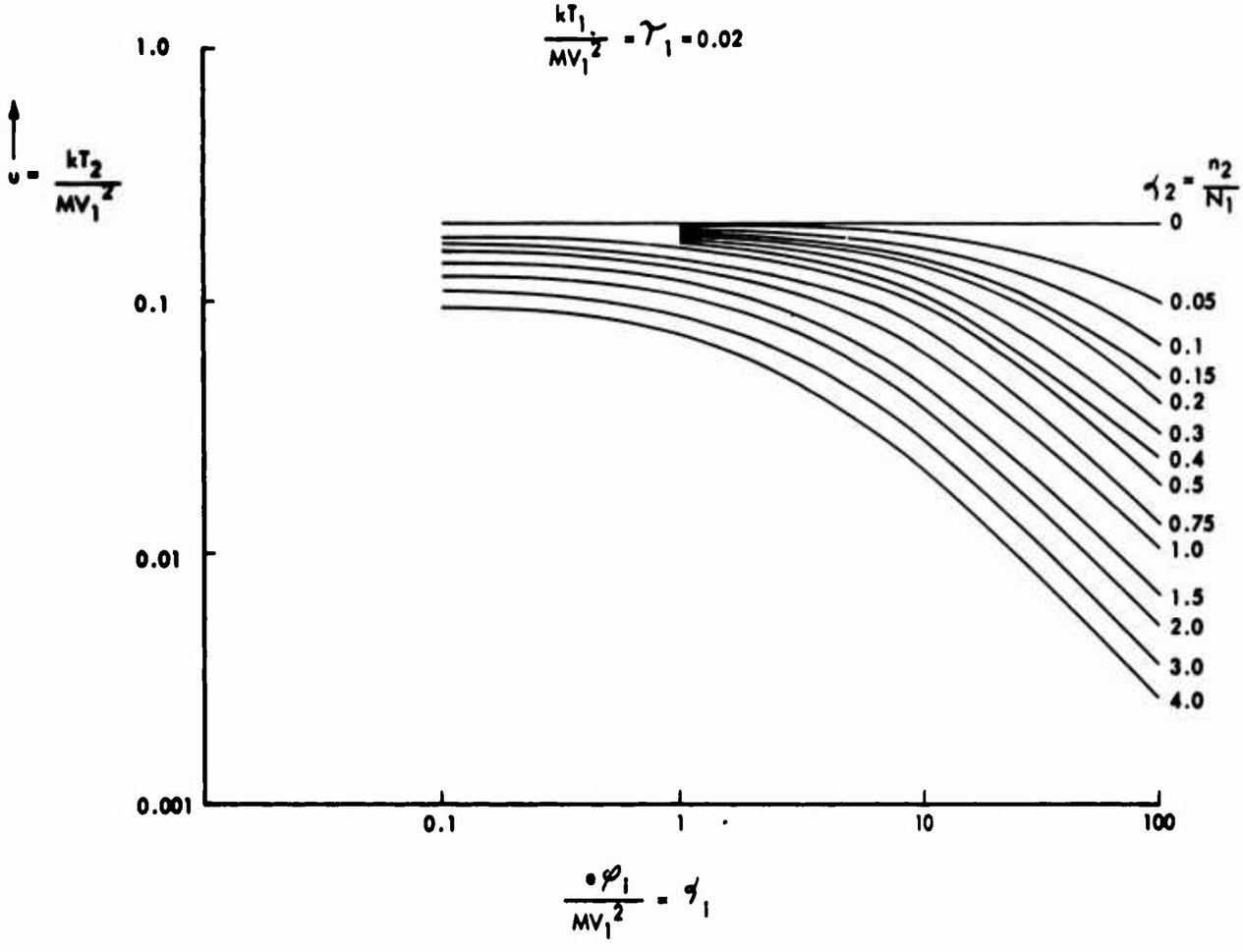
With the information obtained from the previously described spectroscopic measurements, a check may be made on the validity of applying the Rankine-Hugoniot equations to an electrically driven shock tube. With the introduction of suitable dimensionsless variables, a useful new form of these equations may be obtained. Let

$$u = \frac{kT_{II}}{Mv_I^2}, \qquad X = \frac{v_{II}}{v_I}$$

$$\alpha_2 = \frac{n_{II}}{N_I}, \qquad \alpha_i = \frac{e\phi_i}{Mv_I^2}, \qquad \gamma_1 = \frac{kT_I}{Mv_I^2}$$

where the subscripts I and II refer to the regions in front of and behind the shock front respectively. N and n refer to the densities of the heavy particles and the electrons respectively and $e\phi_i$ is the effective ionization energy. M is the mass of the heavy particles and v is the velocity of the particles referred to the shock front. In the cases to be considered, v_I is also the velocity of the shock front in the laboratory frame of reference.

Solutions of the Rankine-Hugoniot equations yield υ and x as functions of α_2, α_1, and γ_1. Figure 7 is a graph of the equation obtained for u with a typical value of γ_1. X, the inverse of the compression ratio, may similarly be graphed in terms of the measurable, dimensionless quantities.



Rankine-Hugoniot Relations for Electric Shock Tube

Fig. 7

Since we were using hydrogen in the shock tube, a modification of these equations is necessary to take into account symmetric diatomic molecules. The graph in Figure 7 may be used if the dimensionless quantities are redefined to be

$$u = \frac{kT_{II}}{2MV_I^2} \quad , \qquad \alpha_2 = \left(\frac{1+\alpha}{2} = \frac{1}{4}\right)\frac{N_{II}}{O_I}$$

$$\alpha_1 = \frac{kT_I}{2M^{v}_{I}{}^2} \quad , \quad \alpha_i = \frac{(e\varphi_i + \frac{1}{2}e\varphi_d)}{M^{v}_{I}{}^2} \quad \frac{1}{\left(\frac{1+\alpha}{2} - \frac{1}{4}\right)}$$

where $e\varphi_d$ is the dissociation energy, 0_I is the density of molecules in region I and α is the fraction of ionization, (n_{II}/N_{II}). It is interesting to note that the limiting case of $\alpha_2 = 0$ produces a temperature for a molecular gas that is twice as large as that for an atomic gas.

In the calculation of the temperatures from the Rankine-Hugoniot equations, the ionization potential was assumed to be 3.4 eV, which implies that the neutral atoms in the shock front which were dissociated principally by molecular impact and subsequently ionized had been excited to the level with principle quantum number n = 2 by photron absorption.

COMPARISON OF RANKINE-HUGONIOT AND RADIATION TEMPERATURES

Table I gives a comparison of the temperatures obtained from the two methods described above. As can be seen, there are some discrepancies. Since the temperatures labeled Saha-Boltzmann are determined from independently measured plasma parameters, they are assumed to be correct. No quantitative reason for these temperature discrepancies may be given at this time, but qualitatively they are reasonable, if the gain and loss of radiation energy is considered.

CONCLUSIONS

For the range of plasma conditions reported in this paper (i.e. electron densities $3 \times 10^{16} - 10^{17}$ cm^{-3}, temperatures 11,500-18,000°K), the continuum between 3000 and 8000Å is adequately described by the existing theories of the H (ff) and (fb) and the H^-(ff) and (fb) radiation. For the conditions examined in this paper, the low intensity of the H_2^+ continuum made no measurable contribution within the accuracy of our observations. Unless care is taken to allow for the effects of the H^- continuum, where this is appropriate, temperature measurement techniques based on continuum measurements may lead to considerable errors; for example, in one case (Figure 6) the measured Balmer step ratio would have indicated T = 15,000°, and H_β line intensity/continuum about 20,000°K, instead of 11,500°K.

Due to the loss and gain of radiation energy in the electrically driven shock tube, the Rankine-Hugoniot equation may not be simply applied. If the radiation from the external region of the plasma under consideration and if the time since the creation of the particular region of the plasma being examined are determined, there is reason to believe that the Rankine-Hugoniot equations could be applied.

TABLE I

Pressure mmHg	Shock Velocity cm/ sec	Rankin-Hugoniot Temperature 10^3°K	Saha-Boltzmann Temperature 10^3°K
0.5	3.6	45	15
2.5	1.9	8.2	12
8.8 (10KV)	0.87	2.5	11.5
8.8 (12KV)	1.1	3.9	18

REFERENCES:

(1) R. G. Fowler, Ad V. Electronics & Electron Physics, 20, 15, (1964).

(2) R. Fuchs, Zeit. Phys. 130, 69 (1951).

(3) W. Lochte-Holtgreven and W. Nissen, Zeit. Phys. 133, 124 (1952).

(4) W. R. Atkinson and R. G. Fowler, Bull. Amer. Phys. Soc. 1, 98 (1956).

(5) O. Weber, Zeit. Phys. 152, 281 (1958).

(6) N. Lane, Ph.D. Dissertation, University of Oklahoma.

(7) A. Unsold, Z. Astrophys. 24, 355 (1948).

(8) S. Geltman, Astrophysics. J. 136, 935 (1962).

(9) T. Ohmura and H. Ohmura, Astrophys. J. 131, 8 (1960); Phys. Rev. 121, 513 (1960).

(10) D. R. Bates, Monthly Notices Roy. Astron. Soc. 111, 303 and 112, 44 (1952).

(11) H. Griem, K. Y. Shen and A. C. Kolb, Astrophys. J. 135, 272 (1962).

(12) D. R. Bates, A. E. Kingston, R. P. W. McWhirter, Proc. Roy. Soc. (London) 267, 297 (1962) and 270, 155 (1962).

(13) H. R. Griem, "Plasma Spectroscopy," McGraw-Hill Book Company, Chapter 5, (1964).

BLANK PAGE

PLASMA DENSITY AHEAD OF PRESSURE DRIVEN SHOCK WAVES

L. B. Holmes and H. D. Weymann
University of Rochester
Rochester 20, New York

BACKGROUND

Many investigators have measured the electrical precursors ahead of strong shock waves. Hollyer (1) was one of the first, in 1957. He investigated precursors with a variety of Langmuir probes.

One of the most spectacular occurrences of a precursor was observed during re-entry of the MA-6 Mercury Capsule in 1962. Lin, Goldberg and Janney (2) observed a plasma halo extending several meters ahead of the bow shock wave. One generally attributes the electrical precursors occurring in shock waves to three basic causes : 1) diffusion of electrons from the shock front, 2) photoemission from the wall, and 3) photoionization of the gas.

In the 1963 Paris meeting on Ionization Phenomena in Gases, Weymann and Holmes (3) presented evidence which showed conclusively that the electron and ion densities occurring ahead of shock waves in experiments with the present shock tube were created by photoionization of the gas. The aim of the present investigation was to get detailed information on the plasma density profiles ahead of the shock and the influence of different parameters.

THE SHOCK TUBE AND INSTRUMENTATION

A schematic of the shock tube and light recording equipment is shown in Fig. 1. The shock tube had a uniform inside diameter of 1 1/2 inches. The low pressure section was made of glass. Welding grade hydrogen and argon were used as the driver and test gas respectively.

The collecting probes used in the present experiment to measure electron and ion densities are a modification of the previously described

probe (3). Fig. 2 shows a schematic of the earlier probe. It consisted of a grid mounted flush with the bore of the shock tube. An electrostatically shielded plate was set 1/8 inch behind the grid and biased with a battery and resistance circuit. Ions and electrons entered the probe by diffusing through the grid. Depending on the polarity, only ions or electrons were attracted to the plate causing an electric current to flow in the circuit. In this probe, direct radiation was incident upon the grid during the entire approach of the shock wave. Photoemission from the grid increased the electron density in the vicinity of the collecting probe. This in turn increased the collected electron current.

A schematic of the modified collecting probe is shown in Fig. 2. There were two collecting plates in each probe formed like half cylinders and set 1/16 inch behind a recessed cylindrical grid. The geometry of the recess was such that the grid of the probe was protected from direct radiation from the shock front until the front was 25 cm from the probe. The main disadvantage was that a region next to the grid was not exposed to direct radiation. Electrons and ions in the shock tube had to diffuse through this region before reaching the grid. Weighing the merits of the two probes, it was decided that better experimental results could be obtained with the recessed grid probe.

The probe arrangement that was used consisted of two of these probes in tandem at one position on the shock tube. By using load resistors that were different by a factor of 100 and by sensing the voltage difference across each resistor with two scope sensitivities different by a factor of 10, currents varying over four orders of magnitude could be measured. The collecting plate bias voltage was set high enough to collect all the incoming particles of the appropriate polarity but low enough to not cause ionization in the probe.

THE COLLECTED CURRENT PROFILES

The variables used to process the data are shown in Fig. 2. The laboratory coordinate is x and the shock velocity is U_s. A coordinate system fixed in the shock front is related to the laboratory system by

$$\xi = x - U_s t$$

where ξ is measured from the shock front, x is measured from the diaphragm, and t is the time. It was found that the shock velocity varied less than 1.5% over the entire duration of one experiment. It will be assumed constant in the following discussion.

In general, the densities measured are a function of both ξ and t. This means that the density profile in ξ develops in time, eventually reaching a stationary state. Because of the experimental arrangement, it is not possible to measure the density profile at a given instant of time. In this experiment both ξ and t vary. One can designate the

instantaneous distance between the shock front and the probe by ξ_o, where ξ_o is defined by the equation

$$\xi_o = x_o - U_s t$$

where x_o is the position of the collecting probe. The measured current profiles were plotted as a function of ξ_o.

Fig. 3 shows the collected currents obtained for an experiment with the collecting probes located 218 cm from the diaphragm. The Mach number for this experiment was 10.2 in argon at 10 mm Hg. pressure. The accuracy with which shock front passage could be determined from the more sensitive probe causeda miss-match of the points from the probes. It was found that the amount of shifting necessary to align the overlapping range of data (this is indicated by the lines through the points) did not exceed our predicted error in evaluating the data.

Notice that the curves for the electron and ion profiles do not coincide. This occurs because there is a drift time involved for the ions to move from the grid to the plate. Therefore the ion signal is delayed relative to the electron signal. If the ion profile is shifted towards the electron profile by a distance corresponding to this delay time it is found that the profiles are identical. This indicates that the ions and electrons are diffusing to the grid ambipolarly, because if free diffusion were taking place, the electron current should be at least 100 times that of the ion current.

Curves like these were used to obtain averaged current profiles. The averaged current profiles are presented in Figs. 4 - 8 in five composite curves with Mach number as a parameter. A comparison of the current profiles obtained with three different probe positions indicates that the current profiles have not reached a stationary state in the time of the experiment or 1 msec. The current profiles obtained with three different initial argon pressures with the collecting probes located 218 cm indicate that the collected currents increase with increasing initial argon pressure.

THE DENSITY PROFILES

What has actually been measured is an electrical current which must now be related to the plasma density created in the shock tube. The collecting-probe-circuit parameters were adjusted so that the collected current would be proportional to the plasma density next to the grid.

The two regions in the probe recess which are separated by the ray shown in the schematic of the collecting probe, Fig. 2, are regions of full shadow and partial shadow. The plasma density was calculated by two methods. First it was assumed that no direct radiation penetrated into the probe recess. This gives an upper limit estimate for the plasma

density. Second it was assumed that the ray separated regions of full intensity and full shadow. This gives a lower limit estimate. Becaus of the reflected radiation from the wall of the shock tube, the actual radiation condition is somewhere between these two, but closest to the second assumption.

Fig. 9 indicates the density profiles obtained by these bracketing estimates for the plasma density based on a particular current profile Curve N_A is obtained by assuming that no direct radiation penetrates into the probe recess. Curve N_B is obtained by assuming that the penetrating radiation is a function of the distance from the shock wave. The two curves approach each other at large distances from the shock wave. The N_F curve is obtained from ion current data from the flush grid probe measurements. There is good agreement between the density measured with the flush grid probe and the N_B curve.

THE PHOTOIONIZATION PROCESS

Having established experimentally that the plasma density profile was created by photoionization it was desired to know the mechanism of the photoionization process. Assuming a one step ionization process, the plasma density distribution was calculated. The theoretically predicted distribution attenuated too rapidly with distance ahead of the shock wave. The one step ionization absorption length is approximately 1/2 cm while the corresponding experimentally determined constant is 50 cm. A two step photoionization process with the resonance state as the first step again leads to an absorption length which is too short. The process that seems most likely at present is a three step process with a longer absorption length for initial excitation to some state above the resonance state. The resonance excitation is trapped because of its very short absorption length. Further absorption of radiation finally ionizes the resonance atoms.

REFERENCES

(1) R. N. Hollyer, Jr., Preliminary Studies in the APL High Temperature Shock Tube, Johns Hopkins University Appl. Physics Lab., Rpt. No. CM-903 (1957)

(2) S. C. Lin, W. P. Goldberg and R. B. Janney, Radio Echoes from the Ionized Trails Generated by a Manned Satellite during Re-entry, Avco-Everett Research Laboratory, Research Rpt. 127 (1962)

(3) H. D. Weymann and L. B. Holmes, Proceedings of the Sixth International Conference on Ionization Phenomena in Gases, Paris 1963, IV pp. 281 - 285.

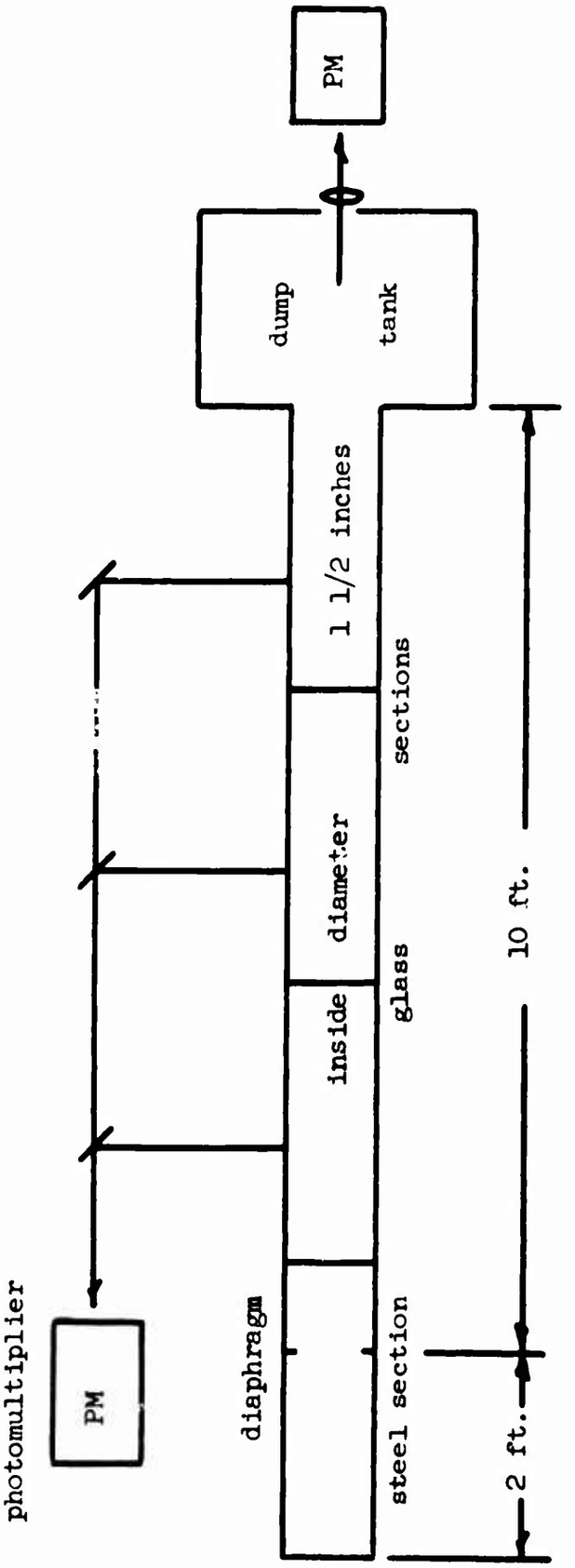


Fig. 1 Schematic of Shock Tube

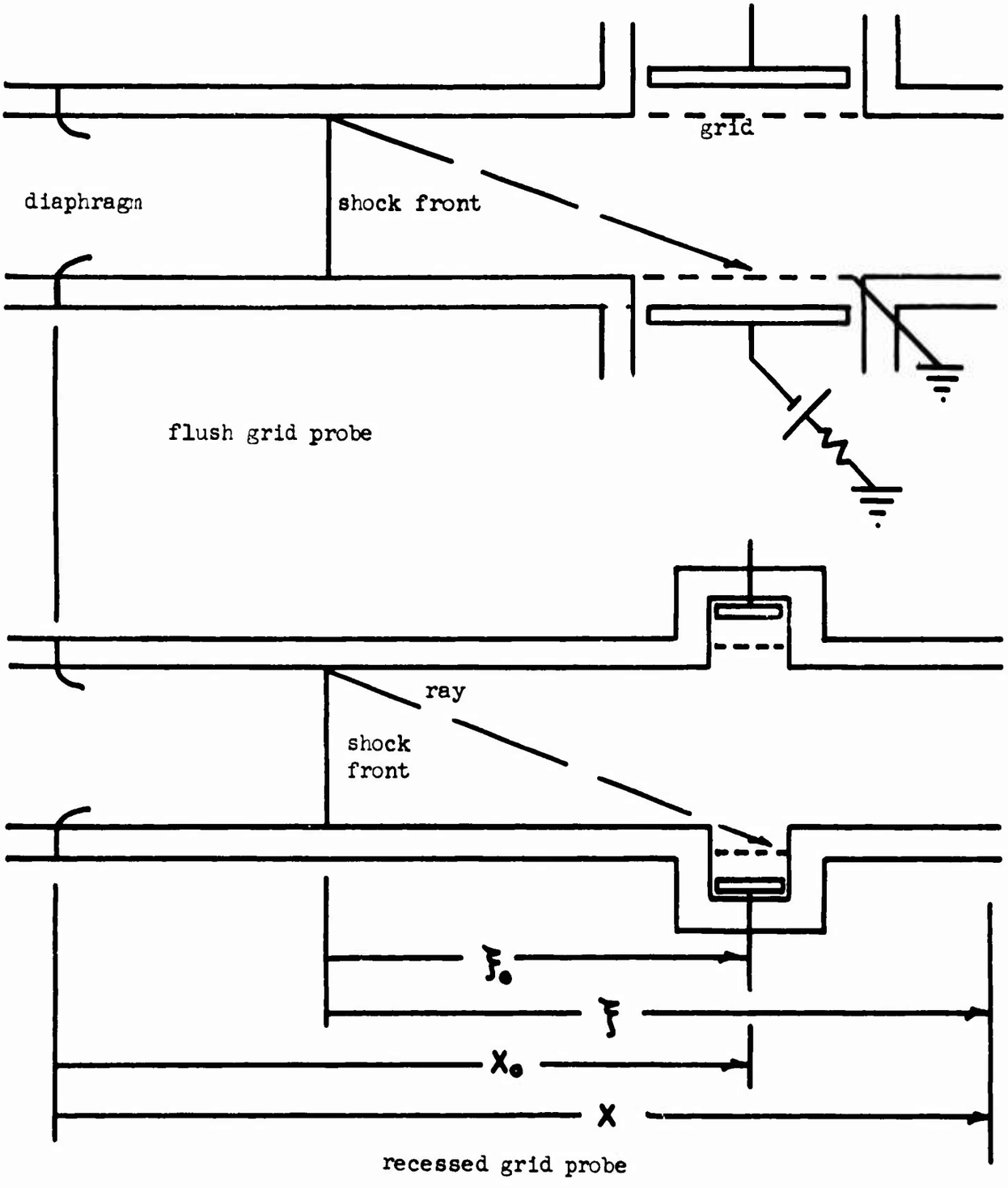
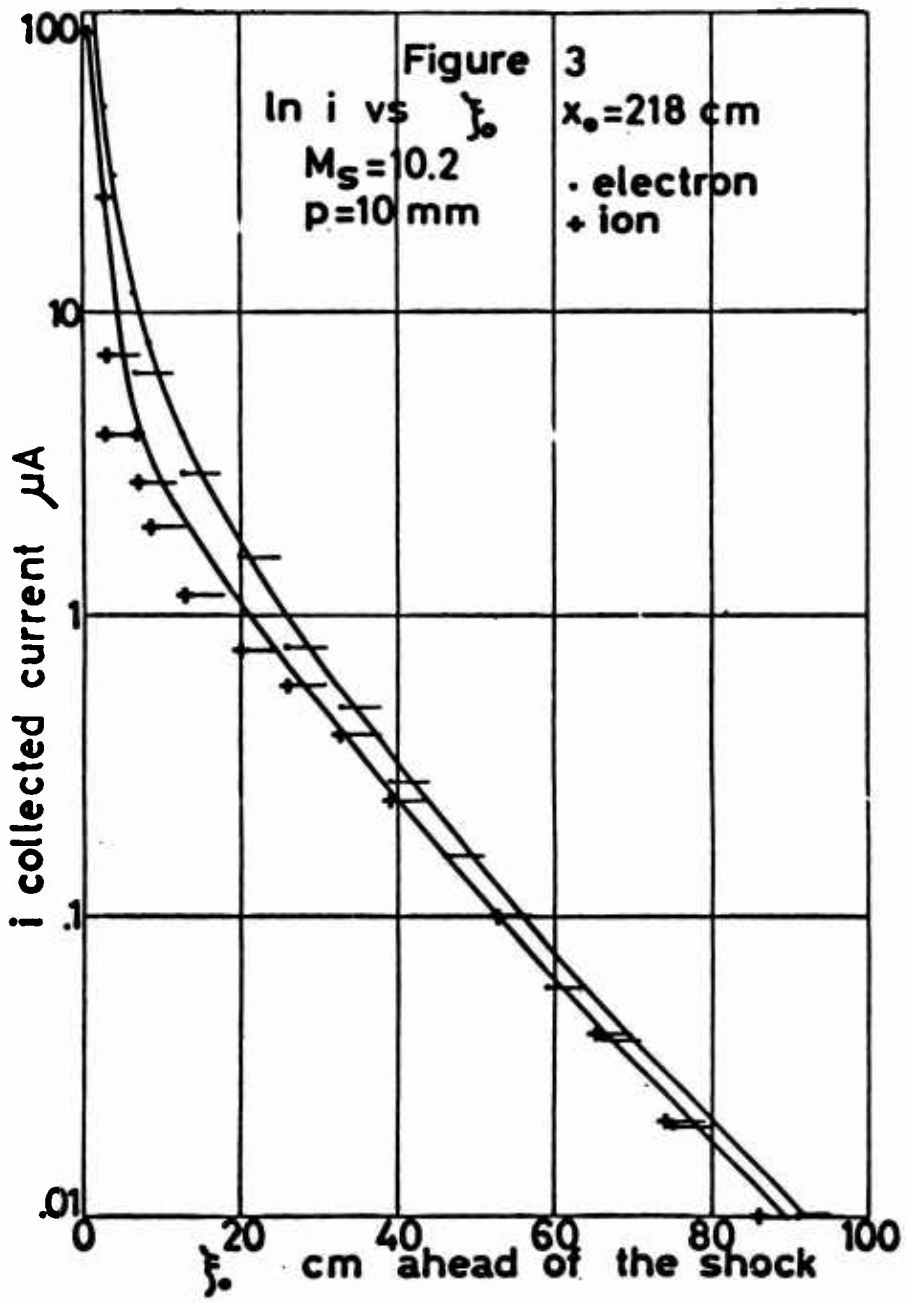
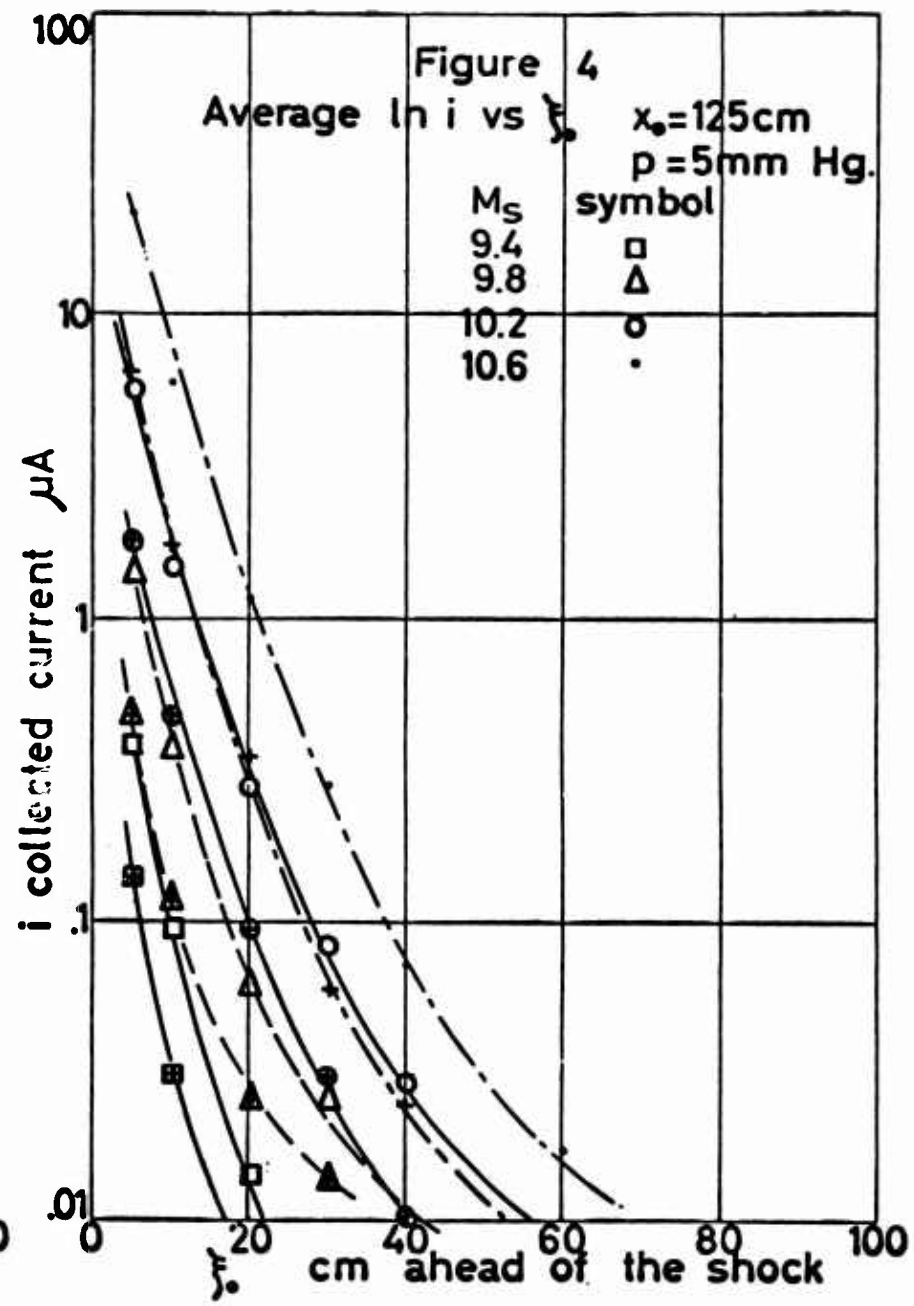
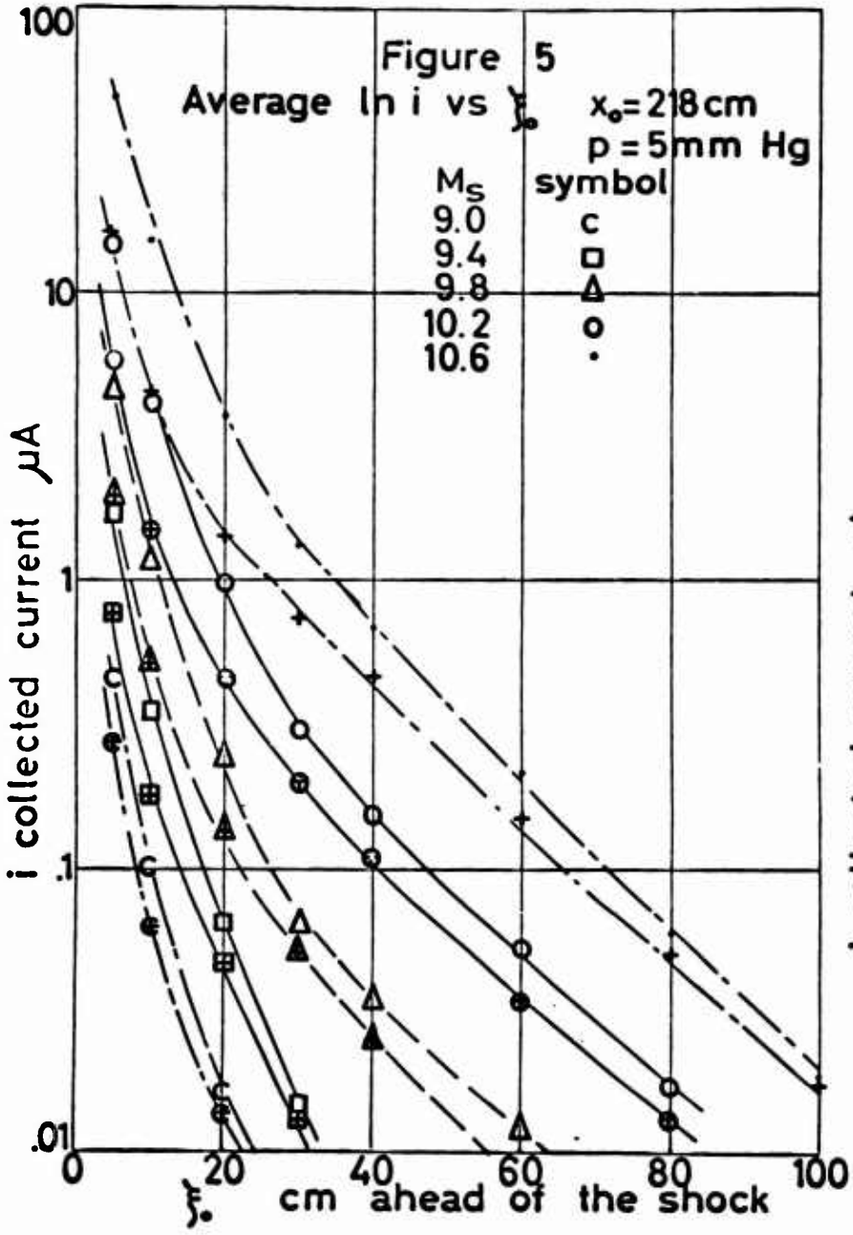
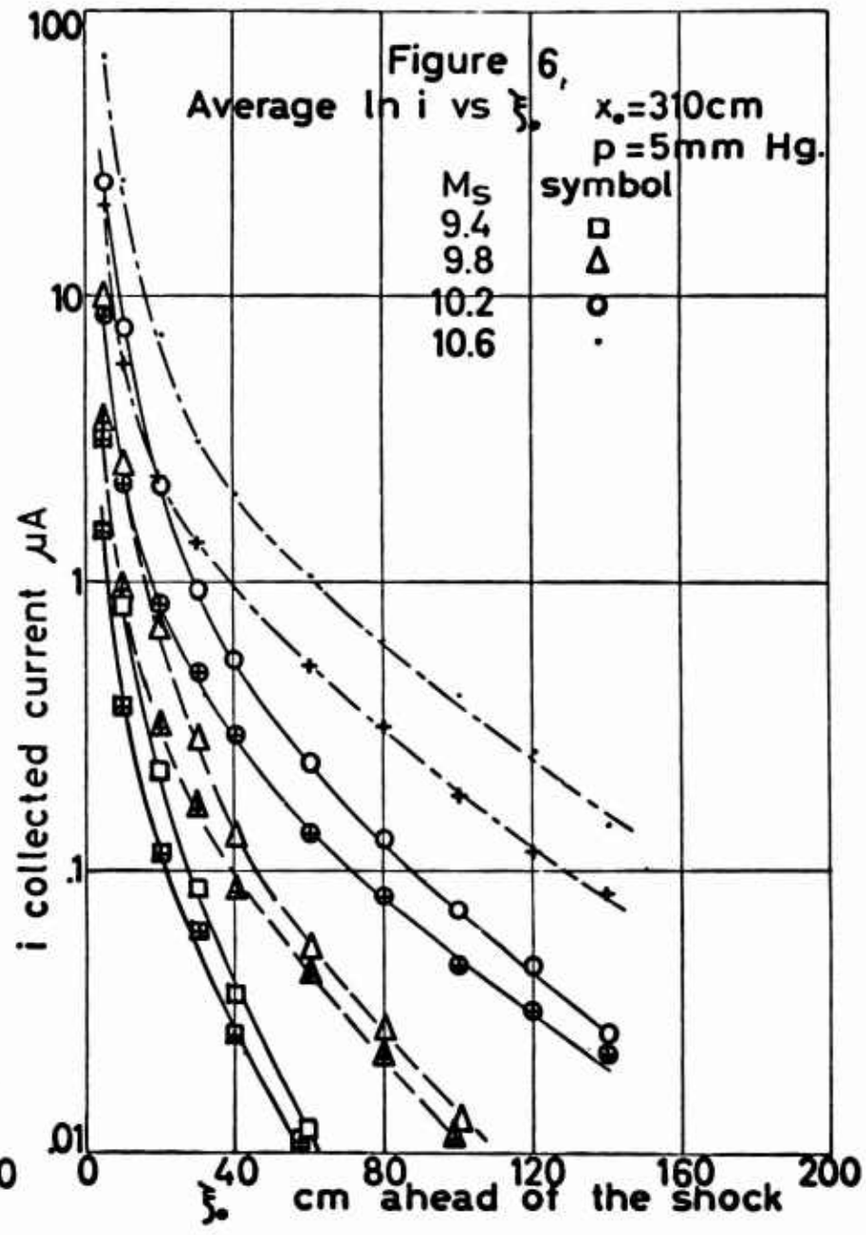


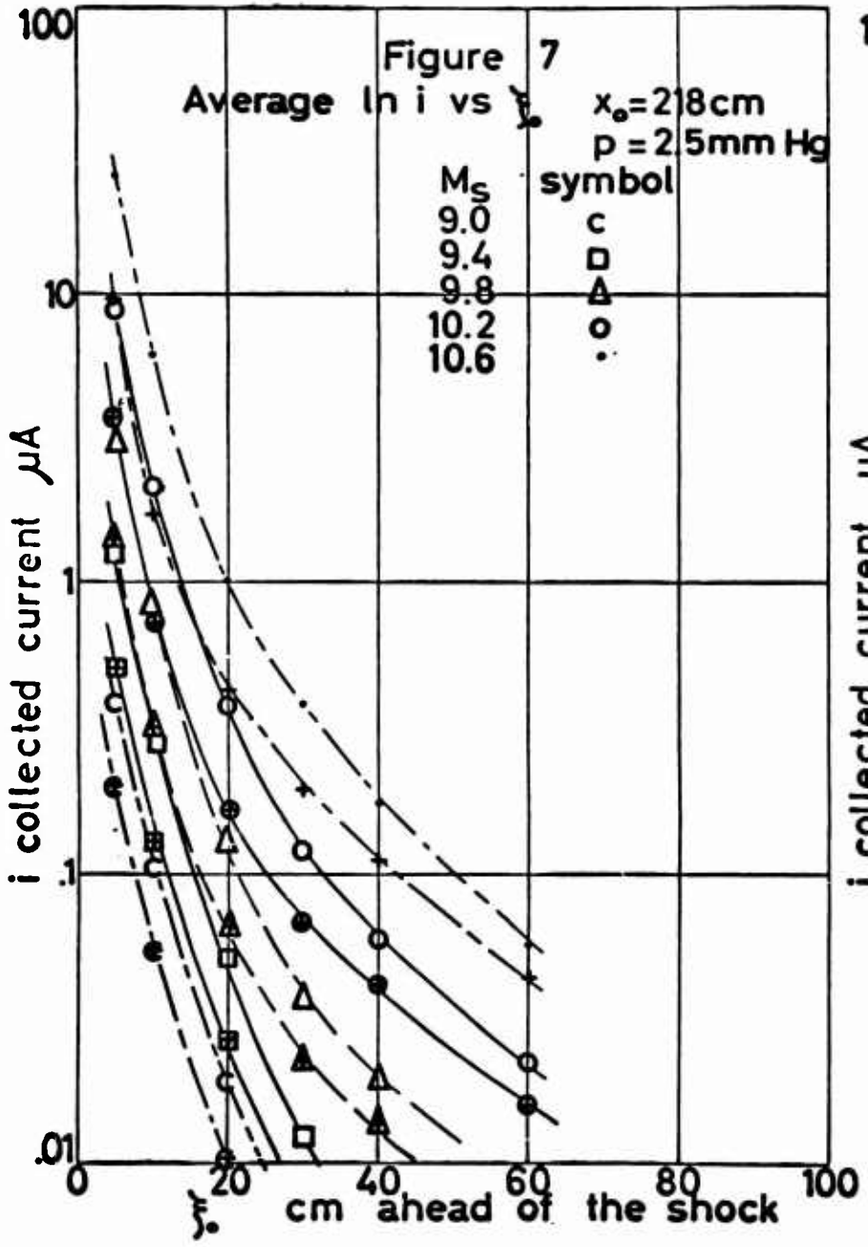
Fig. 2 Schematic of Collecting Probes


Figure 3
ln i vs ξ_0
M_S=10.2
p=10 mm
x_0=218 cm
· electron
+ ion
100
10
1
.1
.01
i collected current μA
0
20
40
60
80
100
ξ_0 cm ahead of the shock


Figure 4
Average ln i vs ξ_0
x_0=125cm
p=5mm Hg.
M_S symbol
9.4 □
9.8 Δ
10.2 o
10.6 ·
100
10
1
.1
.01
i collected current μA
0
20
40
60
80
100
ξ_0 cm ahead of the shock


Figure 5
Average ln i vs ξ_o x_o=218cm
p=5mm Hg
M_S symbol
9.0 c
9.4 □
9.8 Δ
10.2 o
10.6 •
i collected current μA
100
10
1
.1
.01
0 20 40 60 80 100
ξ_o cm ahead of the shock


Figure 6
Average ln i vs ξ_o x_o=310cm
p=5mm Hg.
M_S symbol
9.4 □
9.8 Δ
10.2 o
10.6 •
i collected current μA
100
10
1
.1
.01
0 40 80 120 160 200
ξ_o cm ahead of the shock


Figure 7
Average ln i vs ξ
x₀=218cm
p = 2.5mm Hg
Ms symbol
9.0 c
9.4 □
9.8 △
10.2 o
10.6 •
i collected current μA
100
10
1
.1
.01
0
20
40
60
80
100
ξ cm ahead of the shock

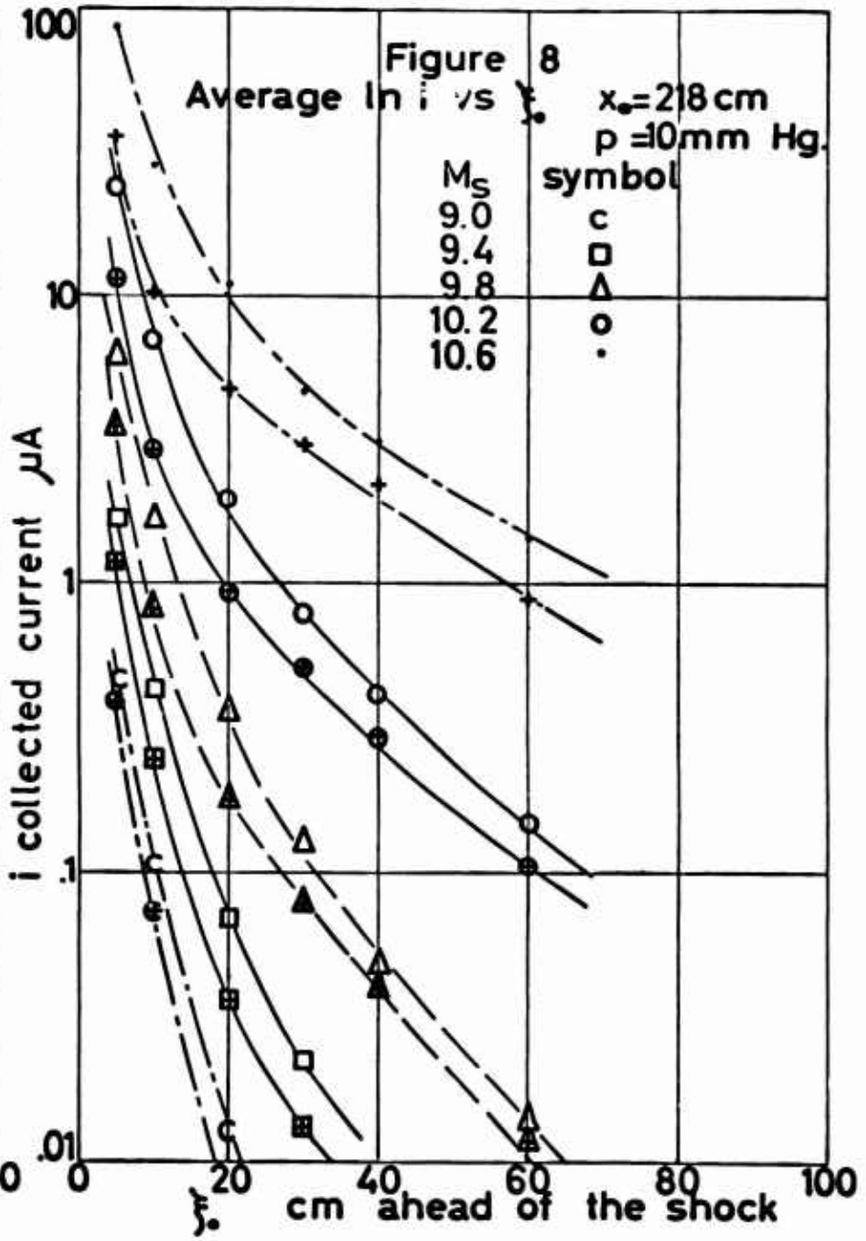
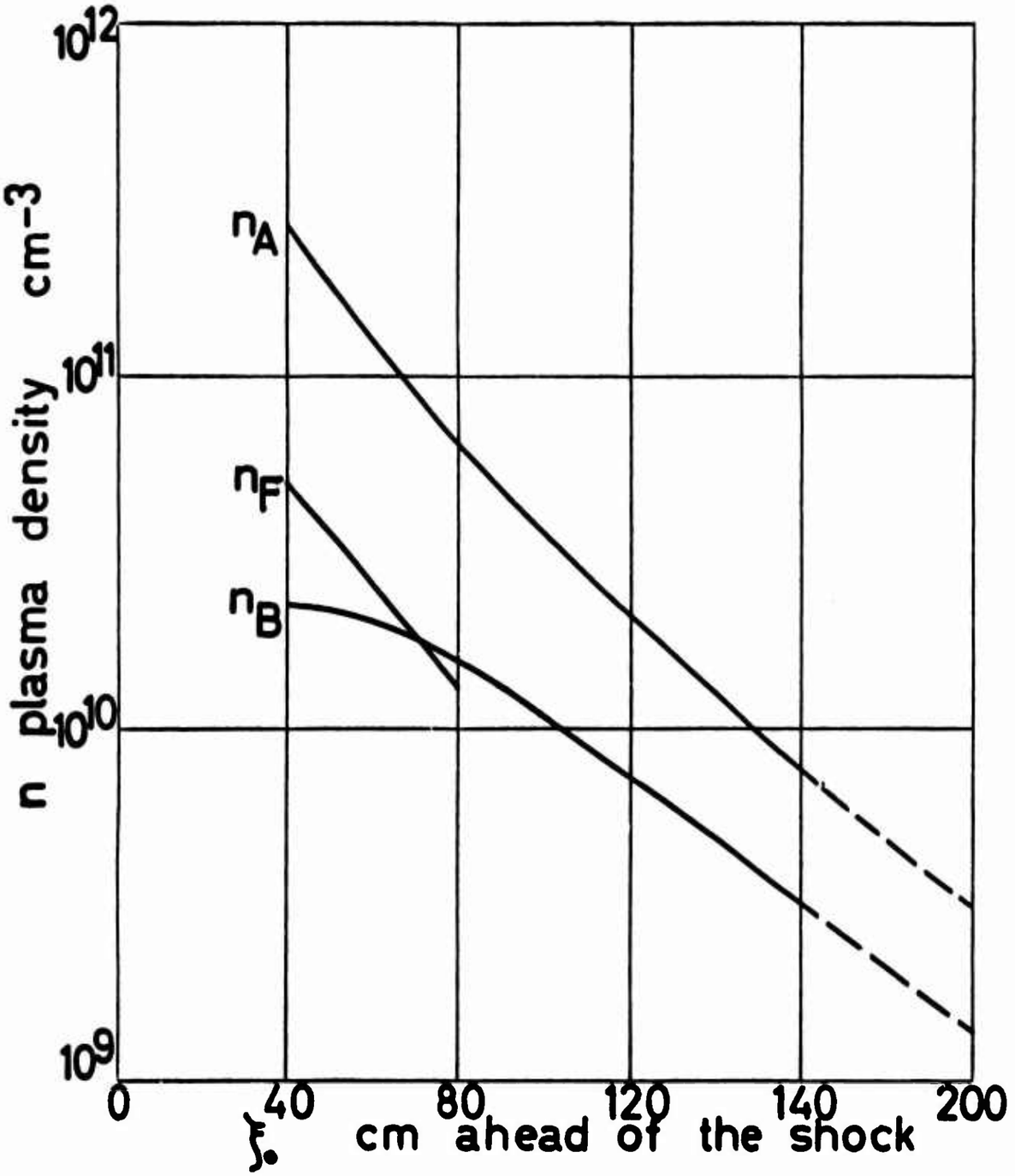

Figure 8
Average ln i vs ξ
x₀=218cm
p =10mm Hg.
Ms symbol
9.0 c
9.4 □
9.8 △
10.2 o
10.6 •
i collected current μA
100
10
1
.1
.01
0
20
40
60
80
100
ξ cm ahead of the shock

Figure 9
PLASMA DENSITY
x_o = 310 cm
p = 5 mm Hg
M_s = 10.2



RADIATIVE COOLING BEHIND STRONG SHOCKS*

Howard Wong
Lockheed Missiles & Space Company
Palo Alto, California

Kenneth Horn
Stanford University
Stanford, California

INTRODUCTION

This study deals with the radiation field associated with thermal ionization of an inert gas, argon. (ref. 1). The ionization is induced by strong normal shock waves generated in a conventional combustion-driven shock tube. The experimental technique employed to study the effect of radiative cooling makes use of a Mach-Zehnder interferometer which monitors both electron and mass densities. This work is an extension of an earlier investigation (ref. 2) on the mechanism of the relaxation phenomena behind strong shocks in argon. The measurements are compared with existing theoretical analysis.

As a strong shock propagates into a quiescent gas, the gas undergoes an extremely rapid increase in enthalpy. As a result the statistical equilibrium is temporarily destroyed, and a relaxation time period exists before the gas species reach a thermodynamic state, predicted by the Saha equation. In the equilibration process it is only during the latter part of the relaxation (as equilibrium is approached) that radiation becomes apparent. As a consequence, the gas cools and does not remain at the Saha equilibrium state (computed from knowledge of the shock speed and initial pressure) under these strong shock conditions for any finite length of time. In shock tube operations there are various processes whereby the gas can cool:

(1) Conduction losses to the wall through the boundary layer.

* Work was supported by the Advanced Research Projects Agency at Stanford University.

This loss will also include the effect of diffusion of charged particles to wall. At present no estimate of the effect of the boundary layer has been made, but from interferograms taken, this effect does not appear to be very large. The density behind the shock is quite high, corresponding to a pressure of about two atmospheres; the observation time is extremely short for any significant boundary layer growth. Diffusion losses due to the charged particles should be minor under these relatively dense plasma conditions.

(2) Effect of shock speed attenuation.

The accuracy of our shock speed measurements over three locations is within 1%. Under these conditions there was no detectable attenuation of the shock speed in the 60 centimeter test section. (The test section was located about 30 feet from the combustion chamber.)

(3) Radiation losses.

RADIATION COOLING

For an emission experiment involving ionized gases there are essentially three effects which will be simultaneously measured:

(1) Free-free transitions, or Bremsstrahlung radiation, which is emitted during encounters of electrons with ions and atoms

$$A^+ + e \rightarrow A^+ + e' + h\nu \quad \text{(predominant)}$$

$$A + e \rightarrow A + e' + h\nu$$

(2) Free-bound transitions which involve radiative recombination resulting in quantilization of the final energy

$$A^+ + e \rightarrow A^* + h\nu$$

$$A + e \rightarrow A^- + h\nu \quad \text{(electron attachment)}$$

(3) Bound-bound transitions

$$A^* \rightarrow A' + h\nu$$

$$A^* + e \rightarrow A' + e + h\nu$$

Both processes (1) and (2) result in continuum radiation. The superscript (*) refers to an excited state.

In the present analysis the gas is assumed to be optically thin and reabsorption of radiation is not taken into account, which in turn ignores optical excitation and photoionization. Bound-bound transitions are also excluded, and hence only continuum radiation is considered. The concept of local quasi-equilibrium is used since collision-induced transitions are predominant over the radiative processes. Thus, the emission of radiation should not lead to any appreciable deviation from equilibrium population among energy states (ref. 3). The conditions of ionization are such that it is reasonable to treat the electron as moving in a pure coulomb potential field. Analytical derivation of the radiative absorption and emission properties of the electrons in a coulomb field has been developed by Sommerfeld (ref. 4), Beth and Salpeter (ref. 5), and evaluated by many investigators (ref's. 6,7,8). A review of the theoretical aspects of the problem has been published by Brussard and Van de Hulst (ref. 8). The following equations will represent their results only.

The combined free-free and free-bound continuum emission/unit time/unit volume for a Maxwellian distribution of electron velocities (equilibrium detailed balancing is invoked) is given by

$$W(T,\nu)d\nu = \left[\frac{16\pi^2 e^6}{3\sqrt{3}\, m_e h c^3}\right] Z^2 N_i N_e \sqrt{\frac{8kT}{m_e}} \left[\bar{g}(T,\nu) + f(T,\nu)\right] d\left(\frac{h\nu}{kT}\right)$$

where Z is the nuclear charge, N_i the ion number density, N_e the electron number density, $\bar{g}(T,\nu)$ the free-free Gaunt factor which is a function of both temperature and frequency, and $f(T,\nu)$ a parameter associated with the free-bound Gaunt factor. The semi-classical derivation by Kramer (ref. 9) differs from the above equation only by the Gaunt factors. This equation has been evaluated for hydrogen and hydrogenic ions, and in applying it to argon we find that no computed values of $f(T,\nu)$ are available. Thus influenced by the fact that the highly excited states are closely spaced, these states are combined with the continuous energy spectrum (ref's 10, 11,12). The total energy emitted per unit volume per unit time is obtained by changing the lower limit of integration to include these "bound" levels. This yields a frequency independent integrand, and the final expression becomes

$$Q = 6.4\times10^{3} \frac{N_e^2}{T} Z_{eff}^2 \bar{g}\, \Delta\nu e^{\frac{\Delta I}{kT}} \text{ ergs/cm}^3\text{/sec}$$

Other implicit assumptions are included in deriving this equation. The possibility of screening effects arising from electron penetration into the ion electron shell is represented by Z_{eff}^2. The Gaunt factor for free-free transitions is assumed to be independent of frequency over the

range considered. The spectral interval for the "bound" states and its corresponding cut-off frequency, $h\Delta\nu$, is chosen to be 3.84 eV. The effect of the lowering of the ionization and charge neutrality are shown respectively by the factors $e^{\Delta I/kT}$ and N_e^2.

Assuming the flow behind the shock to be steady, one-dimensional, constant area, inviscid, and non-heat conducting, the following equations may be written,

mass	$\rho u = \rho_1 u_1$
momentum	$p + \rho u^2 = p_1 + \rho_1 u_1^2$
energy	$u\frac{d}{dx}\left(h + \frac{1}{2}u^2\right) = -\frac{Q}{\rho}$
state	$p = (1 + \alpha)\,\rho RT$
Saha	$\frac{\alpha^2}{1-\alpha^2} = 1.34\left(2 + e^{-\frac{2060}{T}}\right)\frac{T^{5/2}}{p}\,e^{-I/kT}$ (cgs)

This set of five equations plus the expression for Q is solved numerically giving the degree of ionization as a function of time relative to the equilibrium region behind the shock. Subscript 1 refers to conditions ahead of the shock.

EXPERIMENTAL APPARATUS AND TECHNIQUES

The feasibility of using interferometric method for quantitative study of electron production has been shown by Alpher and White (ref. 13). Figure 1 shows a schematic diagram of the interferometer and associated equipment. The light beam, produced by an exploding tungsten wire, passes through the interferometer and the test section, and it is then projected through a vertical slit onto a rotating mirror camera (time resolution of 0.2 microseconds). The tests are conducted in a square aluminum shock tube (5 cm x 5 cm) at initial pressures of p_1 = 3mm and 5 mm Hg. The Mach number ranges from 12 to 18 resulting in a maximum electron density of 2×10^{17} cm^{-3}. Figure 3 shows the fringe shift relative to known conditions ahead of the shock versus Mach number and corresponding electron concentration at equilibrium conditions. The dotted lines indicate partial fringe shift due to different species present in the gas - the argon atoms, the ions, and the electrons; the solid line represents the total fringe shift.

Figure 2 is a rotating mirror camera record of the fringe shift (the shock is moving from the left to the right). At the shock front the fringes are shifted upward due to a sudden increase in density. This initial shift is found to agree with the predicted value where only the

translational modes of the gas are taken into consideration. The subsequent production of electrons causes the fringes to shift rapidly downward. After reaching a maximum negative deflection, which agrees with the Saha equilibrium value, the fringes then begin to slope upward. This indicates a decrease in electron density resulting from radiative cooling. The sudden onset of radiation (as reported by Petschek and Byron (ref. 14)) is also observed.

RESULTS AND DISCUSSION

Figures 4 and 5 show the comparison of experimental results with theory for a shock Mach number of 16.3 but at different initial pressures (5 mm and 3 mm Hg). The degree of ionization is plotted as a function of laboratory time, where t = 0 represents the end of the relaxation period. On each figure there are two theoretical curves corresponding to different values of the parameter,

$$\xi = \bar{g} Z_{eff}^2 \, e^{\Delta I/kT} \frac{\Delta\nu}{(\Delta\nu)_o} .$$

This parameter takes into account the unknown factors in the theory when applied to argon atoms ($\Delta\nu$ is normalized such that $(\Delta\nu/\Delta\nu_o)$ is unity). Although the experimental values indicate a larger radiative loss than predicted theoretically, ξ tends to remain constant with increasing distance from the shock and for different shock conditions. Upon closer examination of this parameter, if $\bar{g}$ is chosen to be unity, ΔI = 0.1 eV (ref's. 15,16), and $(\Delta\nu/\Delta\nu_o)$ = 1, the effective nuclear charge square, Z_{eff}^2, is found to be approximately 2.72 (ref. 17). The exclusion of radiation from bound-bound transitions probably accounts for the lower radiative loss (ref. 18). The figures also show that the relative rate of cooling decreases appreciably with decreasing pressure. The double arrow in the figures represents the experimental uncertainty.

In summary, additional work will be required to investigate some of the basic factors appearing in the radiation theory, such as the Gaunt factor, the effective nuclear charge, and the effect of the lowering of the ionization potential. The addition of bound-bound transitions to the theory will appear in a later paper.

REFERENCES

(1) Petschek, H. E., Rose, P. H., Glick, N. S., Kane, A., Kantrowitz, A., J. of Applied Physics, 26, 83 (1955)

(2) Wong, H., 1st AIAA Annual Meeting, July 1964, AIAA Paper No. 64-376; Wong, H., and Bershader, D., to be published

(3) Biberman, L. M., and Alyanov, Opt. Spectr. XVI, 216 (1964)

(4) Sommerfeld, A. J. F., Atombau und Spektrallinien (New York: Ungar) Vol. 2, Chp. 7 (1953)

(5) Beth, H. A., and Salpeter, E. E., Hab d. Phys., Atome 1 (Berlin: Springer Verlag) (1956)

(6) Karzas, W. J., and Latter, R., The Rand-Corporation Research Memorandum RM-2010-AEC, ASTIA AD/560461 (1957/1958)

(7) Menzel, D. H., and Pekeris, C. L., Notices of the Royal Astronomical Society, 96, 77 (1935)

(8) Brussard, P. J., and van de Hulst, H. C., Rev. of Mod. Phys., 34, 507 (1962)

(9) Kramer, H. A., Phil. Mag., 46,836 (1923)

(10) Unsold, V. A., Ann. Physik, 33, 607 (1938)

(11) Macker, N., and Peters, T., Z. Physik, 139, 448 (1954)

(12) Gaunt, J. A., Proc. Roy. Soc. (London) A126, 654 (1930)

(13) Àlpher, R. A., and White, D., Phys. Fluids, 2, 153 (1959)

(14) Petschek, H. E., and Byron, S. R., Ann. Physics, 1, 270 (1957)

(15) Griem, H. R., Phy. Rev., 128, 997 (1962)

(16) Olsen, H. N., Phys. Rev., 124, 1703 (1961)

(17) Rutowski, R. W., and Bershader, D., Phys. of Fluids, 7, 568 (1964)

(18) Sevastyanenko, V. G., and Yakubov, I. T., Optics and Spectr., XVI, 1 (1964)

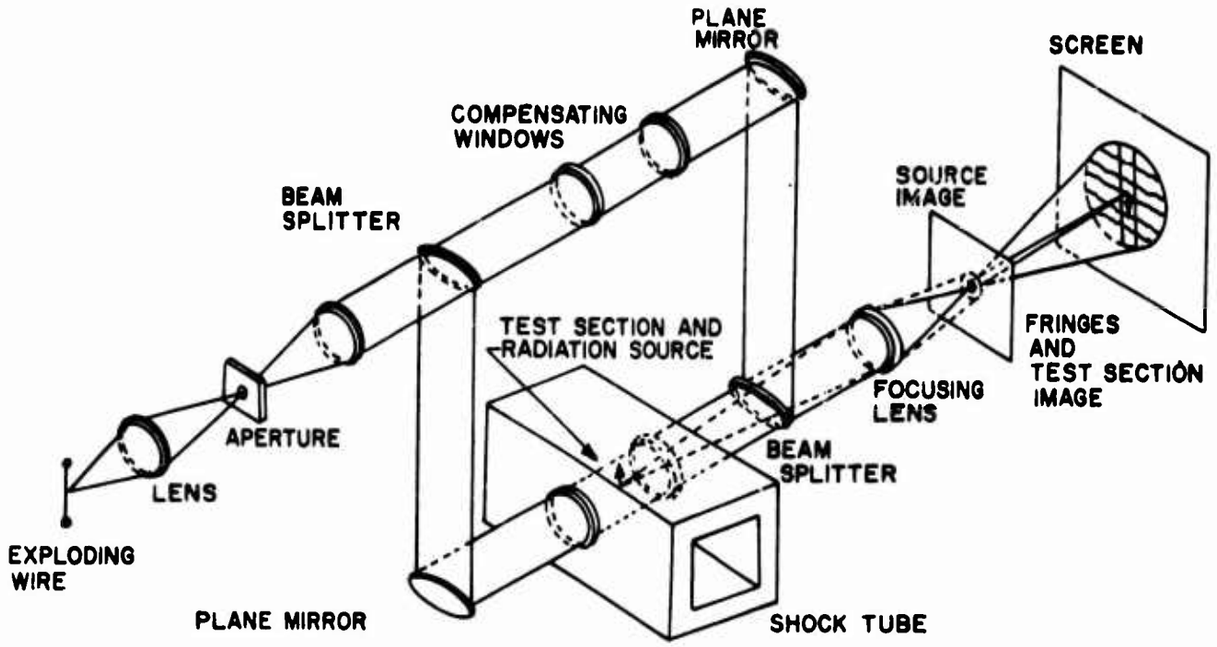
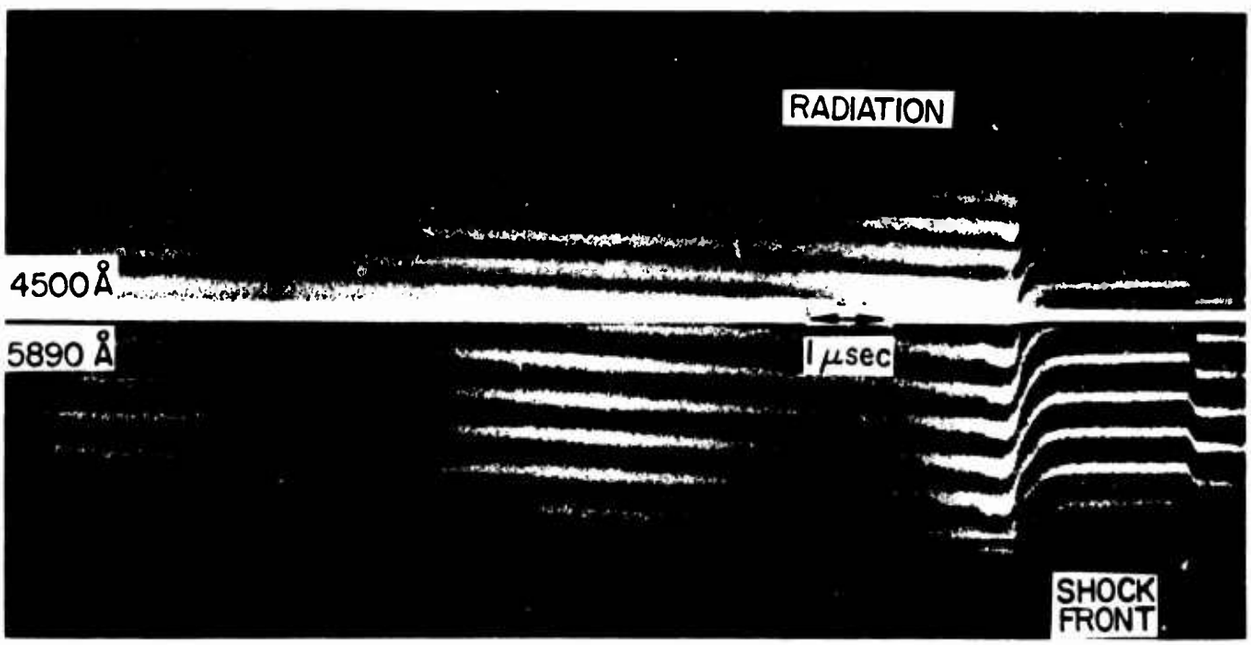


Figure 1 - Schematic diagram of the Mach-Zehnder interferometer and associated equipment.



$P_1 = 0.5\,mm \quad M = 16.3$

Figure 2 - Rotating mirror camera record of fringe shift.

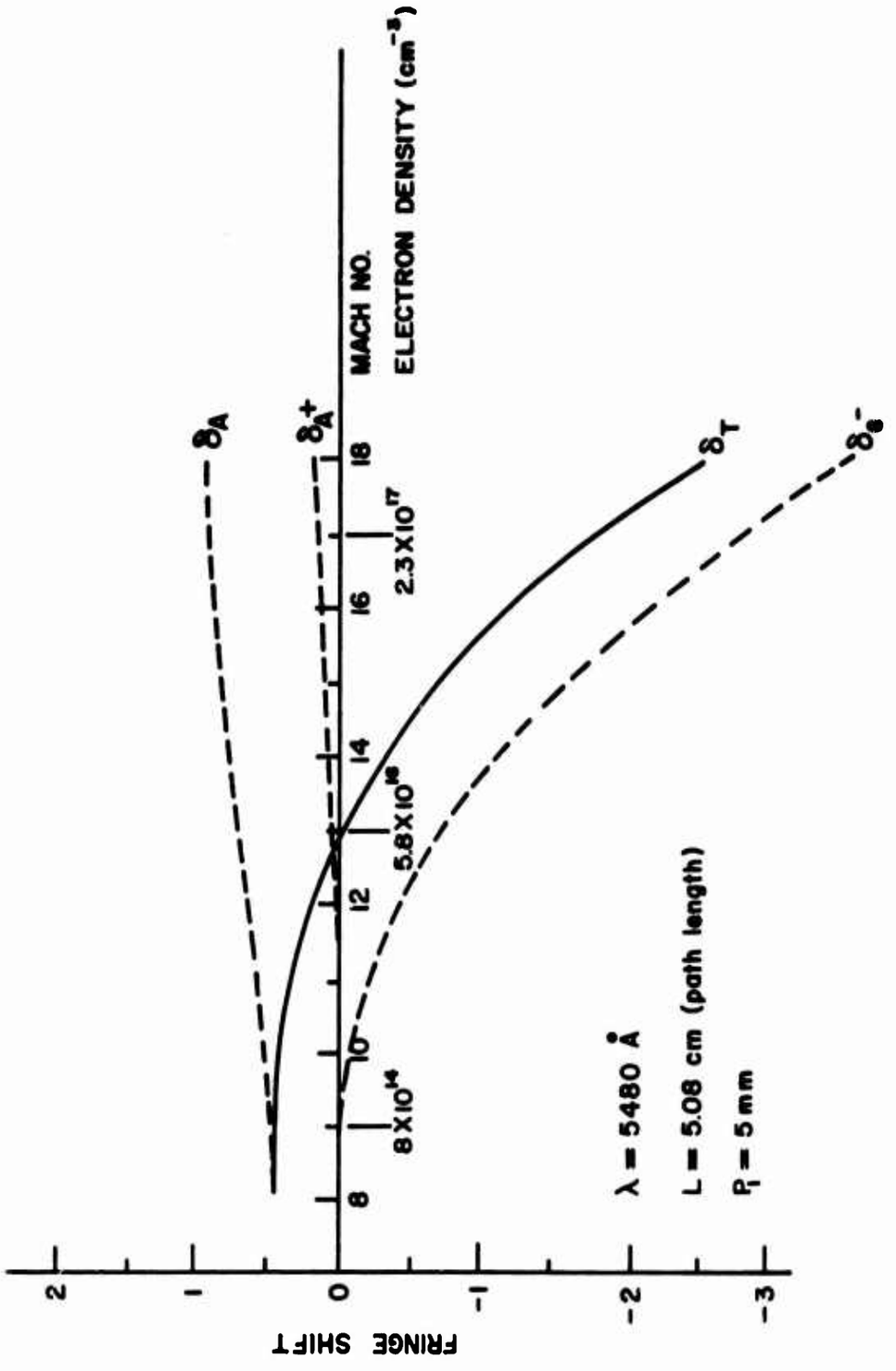


Figure 3 - Fringe shift at equilibrium conditions.

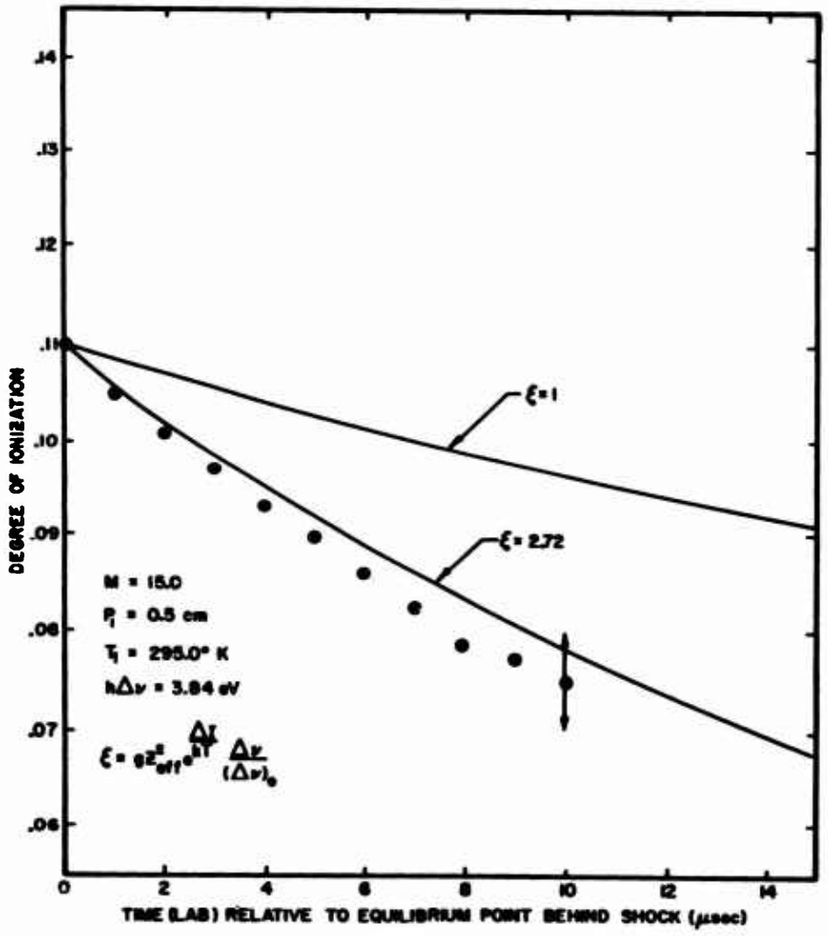


Figure 4 - Radiative cooling behind strong shock.

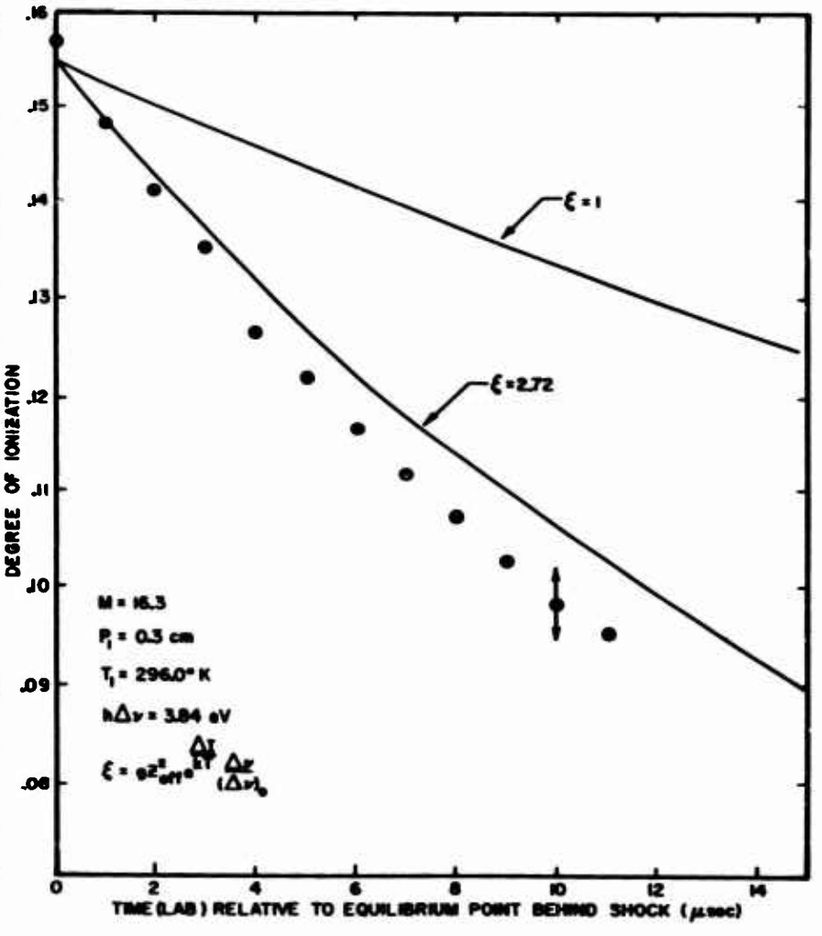


Figure 5 - Radiative cooling behind strong shock

BLANK PAGE

SHOCK TUBE SPECTROSCOPY OF POWDERED SOLIDS

R.W. Nicholls* and D.C. Tyte*
Department of Physics
University of Western Ontario
London, Canada

1: INTRODUCTION

The shock tube has been used for a number of years in physics and chemistry as a means of subjecting gases and powdered solids to controllable thermal environments. Three main areas of research are recognised:

1: Chemical Physics of Hot Gases, Aerothermodynamics
2: Spectroscopic Studies
3: Ablation and Burning of Powdered Solids

Much of the conference has been concerned with aerothermodynamic studies of hot gases. Most of this paper will be concerned with a discussion of some aspects of shock tube spectroscopy. Brief reference will also be made to some work on ablation and the burning of powdered solids.

From a spectroscopic point of view the shock tube is a relatively new and ideal source for the thermal excitation of spectra. Over the past few years the techniques of emission and absorption spectroscopy, (both time resolved and time integrated) have been applied to shock tube research in a number of ways over a wide wavelength range from the vacuum ultraviolet through the ultraviolet and visible to the infrared. Most of this work has been within the two well recognised areas of spectroscopic research:

a) Excitation (or Absorption) of Spectra, Wavelength Measurement, Identifications and Transition Assignment.

b) Quantitative Spectroscopy, the main aims of which are the determination of transition probability parameters, and physical conditions of the source.

Quantitative spectroscopy requires a good knowledge of the thermal state of the gas, and this involves the subsidiary, but important problem of

* Present Address: Department of Physics, York University, Toronto.

accurate temperature measurement. Much quantitative shock tube spectroscopy is laboratory astrophysics, for its motivation has been the provision of basic spectroscopic data needed for the interpretation of astronomical and space observations. Temperatures easily attainable in the shock tube are comparable to those of some stellar atmospheres. The absorption and emission spectral properties of these can thus be simulated in the shock tube. A good example of this is the recent identification of CO Fourth Positive band system in the solar spectrum from a comparison with the absorption spectrum of shock-excited CO (reference 1).

The shock tube is one of the very few spectroscopic sources where unusually high temperatures are easily attainable. It is thus particularly suited to the excitation of spectra of highly refractory materials such as AlO, TiO, WO, ZrO which are of considerable astrophysical importance but which are difficult to excite in more conventional sources.

The easily attainable high temperatures also allow one to study the structure of molecular bands at very high levels of rotational development, where little previous work has been done. Thus perturbations, predissociations, molecular potentials at a higher energy than has previously been obtainable may be studied. High dispersion spectrographs are usually required in such work. One example is the study of the high rotational development of certain N_2^+ bands by Mrs. Jane Gibson (reference 2) supervised by Mrs. Dorothy Buttrey of Lockheed Missiles and Space Company, Palo Alto.

It is the purpose of this paper to illustrate some recent spectroscopic shock-tube studies in our laboratories in the general field of laboratory astrophysics. For a review of the previous work in our laboratories in this field see (reference 3).

2: EXPERIMENTAL

2.1 Shock Tubes

Three conventional shock tubes of one inch, two inch and three inch internal diameter are used in our laboratories. They are of circular cross section, and variable length depending on how many segments are fitted together. Most of the work described below refers specifically to the work with the three inch tube. The shock tube is conventionally driven with hydrogen or helium into argon, and an aluminium or mylar diaphragm is used. Conventional heat transfer gauges are inserted flush with the wall along the length of the tube for measurement of shock speeds.

The window section, usually installed at the end of the tube so that the spectroscopic measurements are made in the T_5 regime, is designed for transverse viewing. When absorption spectroscopy is involved, a triggered auxiliary flash unit is placed behind the window remote to the spectrograph.

The general disposition of apparatus used in many of the experiments is

shown in Figure 1.

The powdered samples are prepared by making finely divided powdered material in a slurry (with a liquid such as acetone or alcohol) which is then spread on a strip (3 cm x 3 mm) of kleenex or mylar. The liquid is allowed to evaporate, and the resultant sample is suspended in the shock channel through a port similar to those used for heat transfer gauges.

In quantitative work, a coloidal suspension from which the liquid has evaporated may also be used. The action of the shock wave is to disintegrate the sample holder (whose spectrum is the Na,D, and the Ca^+, H and K lines) and to transport the powder particles in the gas of the shock wave up the tube to the window region. Some recent time resolved studies of the shape of the light pulse emitted by the incident shock have been interpreted in terms of burning mechanisms for some materials (see 3.3). The hot gas rapidly places the powdered material into the luminous vapour phase. As would be expected, the emission spectrum of the luminous vapour depends very much on the temperature either of the incident, or of the reflected shock wave.

2.2 Quality of Light

Low shock temperatures result in molecular spectra, medium temperatures result in mixed atomic and molecular spectra, and high temperatures lead to entirely atomic spectra (reference 3).

Photographic and photoelectric studies have shown that the luminosity across the window of the shock tube is quite uniform and thus appropriate for quantitative spectroscopy. Further, with the window configuration illustrated in Figure 1, time integrated spectroscopy which produces a spectrum resulting from the whole of the light pulse, can easily be replaced by time resolved spectroscopy, either in emission (with appropriate shuttering) or in absorption (with appropriate delayed flash background continua with or without shuttering). The pulse of light lasts for about 2 milliseconds in the three inch shock tube then for about 1 millisecond in the two inch shock tube. The absorption flash, which lasts for about a microsecond can be inserted, using time delays at a variety of pre-chosen positions. The flash unit most commonly used is that developed by Garton, (references 4, 5).

2.3 Timing Electronics

Synchronization of shock wave and absorption flash is achieved with respect to the output voltage pulse from a phototube viewing the integrated light output of the reflected shock wave. The pulse stimulates a calibrated and pre-set time delay network which produces a voltage pulse to trigger the flash unit.

3: RESULTS

During the past few years many inorganic, and some organic, materials have been studied by shock excitation and a list of the elements involved in this work is given in Table 1. (references 3, 6, 7, 8, 9, 10, 11)

TABLE 1

Compounds of the following elements have been shock-excited

Ag	Al	B	Ba	Be
C	Ca	Cr	Fe	Ge
Li	Mg	Mn	Na	Pb
Si	Sr	Ta	Ti	U
V	W	Zn	Zr	

In recent work the choice of material studied has been dictated by astrophysical interest in specific molecular spectra. Some aspects of this work are illustrated below.

3.1 Excitation of New Spectra

The obvious and most simple spectroscopic application of the shock tube is in its use as a source of new spectra. This is illustrated in Figure 2 where the spectral strips show respectively band systems of WO (from shock excitation of $H_2W_4O_{13}$) and of AlO (from shock excitation of Al_2O_3). The blue-green, red and ultraviolet systems of AlO are recognized.

WO

Analysis of band systems thought to be due to this molecule has been tentative and fragmentry (reference 12). In fact twenty-one bands have been tentatively assigned to six systems. In the original survey of shock excited powdered solids (references 9, 10), powdered metatungstic acid was shock excited, and many of the ''WO'' bands were observed in emission. At the time no new vibrational analysis was attempted. A provisional, and equally tentative vibrational analysis has recently been made of the band heads observed at low dispersion in which all of the bands are all assigned to one system. The provisional Deslandres array is displayed in Table 2.

This analysis is still rather incomplete, and the origin (0,0) of the table has not yet been unambiguously assigned through analysis of the emission spectra. It is noticed in Table 2 that the observed bands lie on broad nested Condon loci in the v', v'' plane indicative of a very large change, Δr_e, of equilibrium internuclear separation (references 13, 14). Provisional ω_e's have been suggested from the analysis. It is hoped to extend the analysis more definitively by absorptinn studies in the near

TABLE 2

Provisional Deslandres Array for WO Band System

v'\v"	n	n+1	n+2	n+3	n+4	n+5	n+6	n+7	n+8	n+9	n+10	n+11	n+12	n+13	n+14	n+15	n+16	n+17	n+18	n+19	n+20	n+21	n+22	n+23	n+24
m(=0?)										5404			5481			5551			5687	5720			5795	5821	5851
m+1						5118				5210			5315			5370			5503	5530				5624	5652
m+2		4878				4969				5064			5141						5338					5437	
m+3						4824				4902						5039									
m+4	4590	4609				4690																	5081		
m+5	4473	4492				4565							4709			4752							4935	4957	
m+6						4444				4522													4806		
m+7		4271				4313				4395															
m+8		4165								4283			4338												
m+9		4028				4110				4182													4414		
m+10																									
m+11										3955															
m+12																									
m+13																							3981		

Notes:

(1) Entries are Wavelengths (Å)

(2) $\omega_e' \sim 600\ cm^{-1}$.

(3) $\omega_e'' \sim 100\ cm^{-1}$.

(4) Δr_e Large

AlO

In a recent series of experiments (references 15, 16, 17), the shock tube has been used as one of the more useful methods of excitation of AlO spectra. The energy level array of AlO is illustrated in Figure 3.

The well known A-X blue-green system is easily excited as is the ultraviolet B-X system. A search was made for the predicted highly complex B-A system, and it was found (reference 18) lying, as expected, in the infra-red. The dotted energy levels in the region of the 40,000 cm^{-1} of Figure 3 are thought to be the upper states of a number of 2500 A band systems which are currently being studied.

This section is illustrative of the use of the shock tube in conventional molecular spectroscopy. Strong band systems are readily photographed in emission using a single shock, though for some weak systems, up to a dozen shocks may be needed. To observe a system in absorption, the number of shocks required depends solely on the intensity of the background continuum. The absorption spectra of some refractory solids have been observed for the first time using shock tubes. The shock tube is particularly useful in the excitation of band system in the infra-red, which when excited in more conventional sources are often seriously obscured by black body continuum originating from hot electrodes or small solid particles.

3.2 Intensities

Intensity measurements in emission and absorption can be made on shock excited spectra and recent work in our laboratories has been concerned with the AlO blue-green system (reference 15) MgH and BeO.

Table 3 is an array of relative band strengths of the AlO system, measured, in part, from shock excited spectra (references 15, 16).

TABLE 3

Smoothed Relative Band Strengths for the AlO ($A^2\Sigma$-$X^2\Sigma$) Blue-Green Band System (reference 15)

v' \ v''	0	1	2	3	4	5	6
0	100	24	2				
1	40	46	33	4			
2	9	51	20	34	6		
3		19	51	7.5	31	7.5	
4			28	46	2.5	28	9
5				33	39		25
6					36	31	
7						38	

Mr. McGregor is currently measuring in absorption intensities of bands of MgH (which occur in the solar envelope) using shock tube techniques.

Recent intensity measurements by Mr. Drake on the BeO C-X system are of particular interest in view of a new technique which has been developed to deal with seriously overlapped band sequences whose rotational structure is not resolved and thus not amenable to established techniques of reduction. Practical reasons prevented the obtaining of high resolution spectra. Intensity measurements were made using a 1.5 m spectrograph. Intensity profiles were obtained by photographic photometry for each (Δv = const) sequence of bands. The profiles of synthetic spectra were calculated for a number of temperatures using well established molecular constants (reference 19) and a computer programme. Simultaneous matches were sought between the synthetic and measured profiles for both the unoverlapped head band of the sequence and the intensity ratio of the observable parts of the P and R branches within each band. This match leads to a temperature determination, and to a knowledge of the contribution to the total intensity in an overlapped part of the spectrum of the section of a band underlying the rest of the sequence. This is subtracted and the procedure repeated for the next band and so on. The results of this work will be published shortly together with a full description of the method.

3.3 Temperatures

Molecular spectra provide, in some circumstances, a very convenient internal temperature standard. It is well known that the intensity distribution within the lines of the band is determined by a rotational temperature of the gas. If one has sufficient dispersion and resolution one can made line by line intensity measurements in absorption or emission to determine the band profile and rotational temperature (reference 20). In such work, particularly using hydrides, one has to be aware of the importance of vibration rotation interaction.

On the other hand if the dispersion is not large enough to resolve individual line components, fractional band intensity techniques can be used (references 21, 22). This approach has been used very successfully on OH (reference 23) by Watson in another paper in this symposium. If the bands are very strongly overlapped, the method of calculation of synthetic band profiles can be employed as discussed for BeO in section 3.2 above.

3.4 Ablation and Burning

Some attempts have recently been made in our laboratory to study ablation in an inert atmosphere of small (40 μ) shock excited particles by sizing them before and after shock treatment. The method had some initial success for Pb and Fe (references 24, 25) but the recent studies on Ni and Al have met with difficulties in the measurement of small changes of radius. Attempts are now under way to extend the work to very small (1 μ) particles where the effect of ablation should be very marked.

The interaction of metal particles with a shock wave through an oxidising atmosphere has also been studied in an attempt to find the best sample introduction and observation stations from the standpoint of optimising the conditions for observing spectra behind the incident shock.

In the case of the wavelength integrated light from the AlO Blue-Green system produced from shock excitation of Al in an A-O_2 mixture, at a shock speed of 0.18 cm/μ sec, the light pulse is displayed isometrically as a function of insertion position and time in Figure 4. The results are best explained quantitatively by a burning mechanism and full details are in preparation of publication elsewhere (reference 26).

ACKNOWLEDGEMENTS

The work described in this paper has been supported in part by research grants from The National Aeronautics and Space Agency (NsG-349), The Air Force Office of Scientific Research (AF-AFOSR 522-64) and the National Research Council of Canada and in part by Contracts with the Air Force Cambridge Research Laboratories (AF 19(628)-4169) and the Defence Research Board of Canada (MM69-40010, Serial 2MM3-351).

REFERENCES

(1) Goldberg, L., Parkinson, W.H., and Reeves, E.M., Astrophys. J. (April 1965) (In Press).

(2) Gibson, Jan, M.S. Thesis, Stanford University (1963).

(3) Nicholls, R.W., Parkinson, W.H., and Reeves, E.M., Applied Optics 2, 919, (1963).

(4) Garton, W.R.S., J. Sci. Inst. 36, 11, (1959).

(5) Garton, W.R.S., Celnick, I.W., Hessberg, H., and Wheaton, J.E.G., Proc. Fourth Conf. on Ionisation Phenomena in Gases, North Holland, p 518 (1959).

(6) Nicholls, R.W., and Parkinson, W.H., J. Chem. Phys. 26, 423, (1957).

(7) Nicholls, R.W., Watson, M.D., and Parkinson, W.H., J. Roy. Astron. Soc. Can. 53, 223, (1959).

(8) Nicholls, R.W., and Watson, M.D., Nature 188, 568, (1960).

(9) Parkinson, W.H., and Nicholls, R.W., ''Shock Excitation of Powdered Solids'', Scientific Report No. 1, Contract AF 19(604)-4560 (1959).

(10) Parkinson, W.H., ''Studies in the Shock Excitation of Powdered Solids'', Ph.D. Thesis, University of Western Ontario (1959).

(11) McGregor, A.T., ''Shock Excitation of Ceramic Materials'', M.Sc. Thesis, University of Western Ontario (1962).

(12) Pearse, R.W.B., and Gaydon, A.G., ''The Identification of Molecular Spectra'' (3rd edition) p 311, 312, Chapman and Hall, London (1963).

(13) Nicholls, R.W., Nature 193, 966 (1962).

(14) Nicholls, R.W., Nature 199, 794 (1963).

(15) Hebert, G.R., and Tyte, D.C., Proc. Phys. Soc. 83, 629 (1964).

(16) Tyte, D.C., and Hebert, G.R., Proc. Phys. Soc. 84, 830, (1964).

(17) Tyte, D.C., and Nicholls, R.W., ''Identification Atlas of Molecular Spectra I: AlO Blue-Green System (1964).

(18) Tyte, D.C., Nature 202, 383 (1964).

(19) Lagerqvist, A., and Westoo, R., Ark. Mat. Astr. Fys. 32A, 10, (1945).

(20) Parkinson, W.H., and Nicholls, R.W., Can. J. Phys. 38, 715, (1960).

(21) Robinson, D., and Nicholls, R.W., J. Quant. Spect. and Rad. Transf. 1, 76, (1961).

(22) Robinson, D., J. Quant. Spect. and Rad. Transf. 4, 335, (1964).

(23) Watson, R., Paper E3 this symposium (1965).

(24) Watson, M.D., ''Physical Studies in Shock Excitation of Powdered Solids'' M.Sc. Thesis, University of Western Ontario (1959).

(25) Nicholls, R.W., Parkinson, W.H., and Van der Laan, H., J. App. Phys. 30, 797, (1959).

(26) Tyte, D.C., (In preparation for publication).

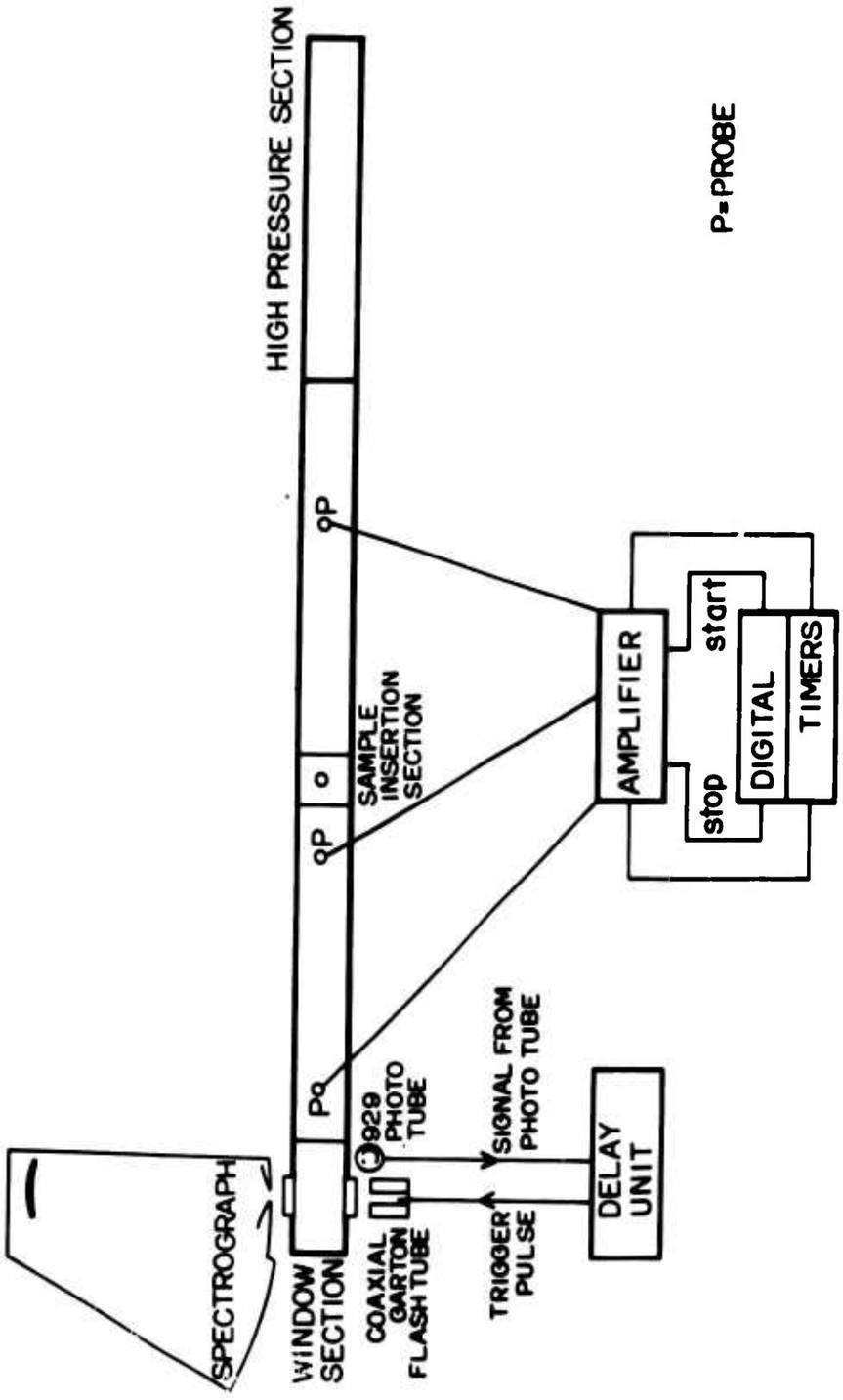


FIGURE 1: Typical Experimental Configuration

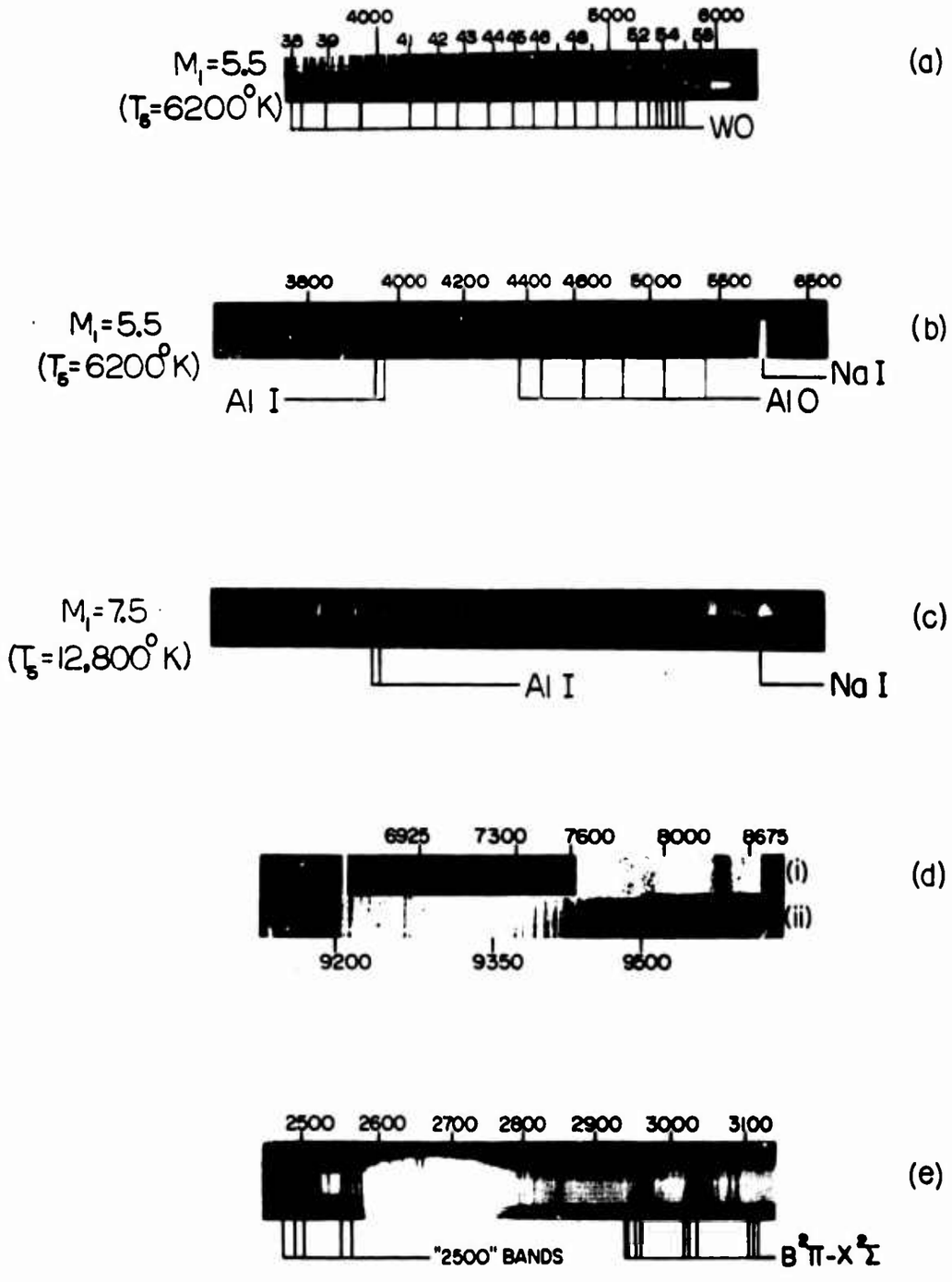


FIGURE 2: Typical Shock-Excited Spectra

a) WO Bands from $H_2W_4O_{13}$ at 6200°K
b) AlO Blue-Green $(A-X)^3$ Bands from Al_2O_3 at 6200°K
c) Al Lines from Al_2O_3 at 12,800°K
d) AlO Red (B-A) Bands: (i) Low Dispersion (ii) High Dispersion
e) AlO Ultraviolet (B-X) and '2500' Bands

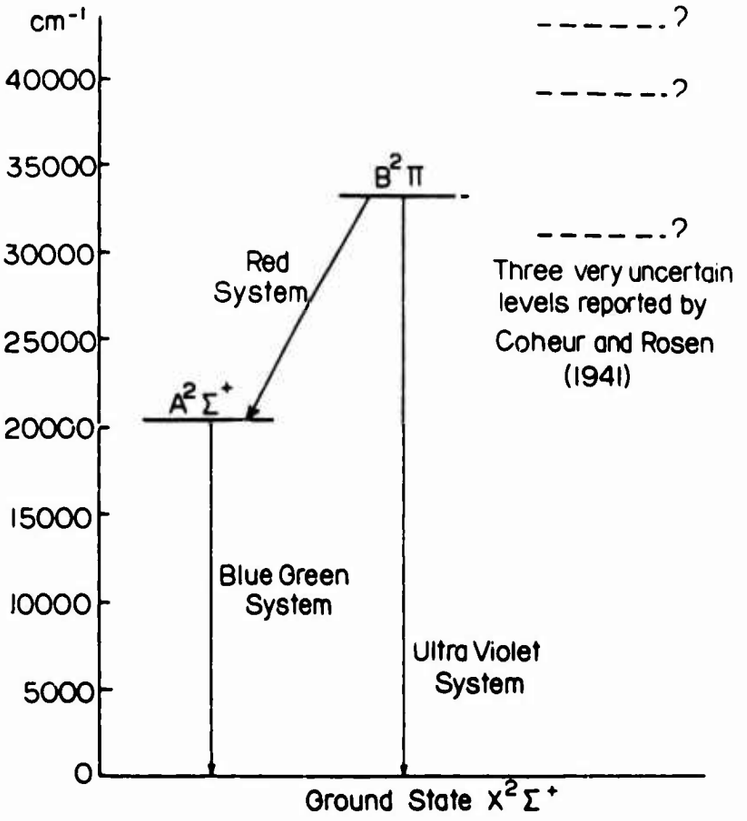


FIGURE 3: AlO Energy Level Diagram

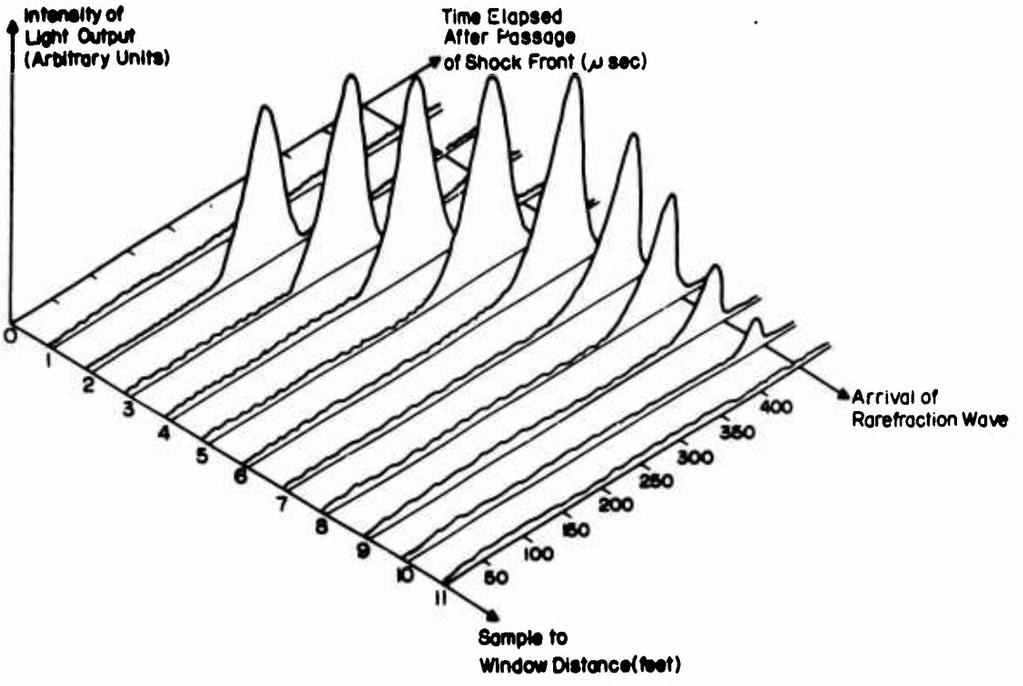


FIGURE 4: Light Pulse from AlO Blue-Green Bands as a function of time and distance between sample and window

INTERFEROMETRIC MEASUREMENT OF THE VIBRATIONAL RELAXATION TIME IN HYDROGEN-ARGON MIXTURES

Emanuel Wachsler
Graduate School of Aerospace Engineering
Cornell University, Ithaca, New York

ABSTRACT

High resolution of the relaxation zone behind an incident shock wave was obtained by the use of a laser light source in conjunction with a Mach-Zehnder interferometer. The experimental setup consisted of a square, pressure-driven shock tube, 15 feet long and 1.654 inches across. The interferometer was set up in a double pass mode. The ruby laser, cooled to liquid nitrogen temperature, produced a continuous light pulse of 200 microsec. duration. A beam splitter was inserted to provide two pictures of the flow field with different time resolutions. A 0.1 microsec. Kerr cell shutter permitted direct photography of the density distribution in the relaxation zone. The image of the test section was also focused onto a 0.001 inch slit and then into a drum camera. The drum camera picture resolved the relatively slow density changes, and permitted us to measure the shock velocity and to check on the presence of disturbances. This setup was developed principally to study diatomic dissociation reactions. The vibrational relaxation time in hydrogen-argon mixtures was measured over the temperature range of 1300-1900 °K. The values obtained for H_2-H_2 collisions, assuming that argon is completely ineffective as a collisional partner, are in good agreement with theoretical calculations by M. Salkoff and E. Bauer.

I. INTRODUCTION

The measurement of high temperature relaxation phenomena in gases has been the subject of much work in recent years. The shock tube has been used because the shock wave processes a gas sample in a known way. Often, the Mach-Zehnder interferometer was used because it provides an absolute measurement of density. However, until recently the interferometer was limited in its ability to resolve high speed phenomena by two conflicting requirements; first, that the light source be small enough so that fringe

contrast would be adequate; second, that the source be large enough so that sufficient light would reach the film to expose it. The necessity for such a compromise was removed by the laser. The laser is a source of parallel light of extreme brightness. Unfortunately, the laser has limitations. At room temperature the light output is neither uniform over the face of the ruby nor continuous in time. The spatial distribution of light depends critically on the quality of the ruby crystal and the cavity design (refs. 1, 2, 3). The phenomenon of "spiking," which occurs at frequencies of the order of 1 Mc., makes submicrosecond time resolution impossible. This problem was essentially eliminated by cooling the ruby to liquid nitrogen temperatures. Another problem is associated with the rather long delay from the triggering of the flash lamp which "pumps" the ruby, to the onset of laser action. This delay, of the order of 300-500 microsec., depends on the capacitor bank characteristics, but it is reproducible so that the usual synchronization techniques can be successfully used.

The density changes behind the shock wave were simultaneously photographed by a drum camera and a Kerr cell. The latter provided a snapshot of the flow field. The former was used to measure shock velocity, relatively slow relaxation phenomena and in particular, to ensure that equilibrium conditions were eventually reached. The desire to check on the existence of a uniform gas sample for each run prompted the selection of the ordinary ruby laser as the light source. The use of the "Q" spoiled laser technique would have provided a light pulse of much greater power and very short duration. However it would have required another light source to monitor attainment of equilibrium for slower reactions.

II. APPARATUS

A photograph of the experimental setup is shown in Fig. 1. The schematic arrangement of the optical setup is shown in Fig. 2. The shock tube consisted of a driver 2.75 inches in diameter and 3 ft. long, a short transition section which acted as a diaphragm catcher, and a driven section. Its internal cross-section was 1.654 in. square and it was 15 ft. long overall. The pressure of helium or hydrogen in the driver was slowly increased, until the scribed copper diaphragms broke. The test section was located sufficiently upstream from the end wall, so that the arrival of the interface limited the test time. The test section consisted of two (sets of) windows 1 inch in diameter, 6.05 inches apart.

The Mach-Zehnder interferometer components rested on a heavy metal plate underlaid by a sheet of foam rubber, which in turn was supported by a sturdy table resting on four air bags. This system of support was found to have good isolation and high damping for all frequencies. All other optical components were mounted on stands which were bolted to the floor and did not touch the shock tube or its supports. The mirrors were 3 inches in diameter and one inch thick, flat to 1/10 wave. The beam splitters were similar and parallel to 3 seconds. The interferometer was

set up in the double pass mode, that is, both the main and the compensating beam passed through the shock tube. This gave us an accurate measurement of shock velocity and a check on the presence of disturbances (ref. 4). The Mach-Zehnder interferometer was aligned with an auxiliary optical system, mounted on the same optical bench as the laser.

The following alignment procedure was used. The mirrors were set at 45° to the shock tube and at the appropriate separation. The usual 2:1 rectangle was chosen because fringe spacing and direction may be changed with only minor changes in fringe focus. The location of the mirrors included the correction for the light beam displacement through the thick beam splitters. Price's procedure (ref. 5), but with a "naked" 6 watt light bulb and a 10X telescope, was used to obtain the initial alignment. Superposition of the multiple images of the light bulb filament could be achieved easily by alternatively slightly rotating one mirror and a beam splitter, while observing the images in the telescope.

Monochromatic fringes now could be seen. By repeatedly defocusing the telescope and rotating one mirror and one beam splitter, the fringe plane could be brought to the test section. At this point the mercury arc was brought to full power, the beam splitter was translated and the fringes periodically brought back to sharp focus. When fringe contrast seemed to be maximum, a pocket spectroscope was placed in the fringe image plane, with its slit normal to the fringe direction and looking back into the light source. In addition to the usual spectral lines, slanted lines of light and dark could be seen. The beam splitter was translated till these lines became horizontal, which corresponded to equal path length (white light fringes).

The ruby laser was 1/4 inch in diameter and 3 inches long. It was 90° cut and a 0.05%Cr. concentration. It was dielectric coated for 90% reflectivity at the "business" end and 99.9% at the other. A thin aluminum spider held the ruby inside a glass tube $\frac{1}{2}$ inch O.D. Cooling of the ruby was achieved by blowing dry nitrogen, cooled to liquid N_2 temperature, through the glass tube. To eliminate frosting, a small flow of dry nitrogen was maintained in the cavity as well. The dry nitrogen was cooled by passing it in a copper tubing coil in an acetone-dry ice bath and then through a copper tubing coil in a dewar filled with liquid N_2. The pumping light source was an EGG FX - 42 flash tube powered by a capacitor bank of 280 microF.(with 180 microH. in series). The cavity consisted of a piece of pyrex pipe 2 inches I.D. and 3 inches long, which was aluminized on the inside and two brass end plates which were polished and aluminized. The ruby was placed at one focus and the flash tube at the other of the stigmatic cavity, thus being one radius apart. The laser was placed 7 feet from the test section, so that the natural beam divergence filled the windows with light. It was typically operated at 1850 volts, which is 40% above threshold and gave a delay of 375 microsec. Light power was around 10 watts and the duration 150-200 microsec. These parameters depended on the matching of the external circuit of the flash tube to the absorption band of ruby. The beam

divergence was still small enough (less than .005 rad.) so that the limitations on spatial resolution were set by other factors. However there was a noticeable fall off in intensity from the center of the windows.

An off axis (2.5° half angle) parabolic mirror 4 1/4 in.in diameter and 45 in. focal length, good to 1/4 wave, focused the image of the test section on the slit for the drum camera and through the Kerr cell directly on the film. The beam splitter had a transmissivity of 0.04 and a reflectivity of 0.83. There was enough light for the drum camera picture even with this very low transmissivity.

The Kerr cell is an electro-optical shutter (of nanoseconds duration) which depends on the rotation of the plane of polarization of light by the application of an electric field. It consists of a polarizer, a cell filled with nitrobenzene and fitted with electrodes, an analyzer and the electronics necessary to provide a high voltage, fast rise, short duration pulse. We used an Electro-Optical Co. system KSC - 51/B, the Kerr cell being fitted with HN - 22 polaroids.

The Kerr constant of nitrobenzene has the usual dispersion relationship. (ref. 6) Hence to get maximum transmissibility at the laser frequency in the far red, the applied voltage was 40.5 KV rather than the usual 35 KV. We had considerable trouble with scattered light but this was eliminated by using a cell whose internal electrodes were blackened. The polarizers were another source of trouble; a small amount of light will "bleed through" even when the polaroids are crossed. The ratio of the light passing through the cell when it is "open" to that when it is "closed" is the figure of merit, called the rejection ratio. The rejection ratio for the HN - 22 polaroids is approximately 12000, which means that equal film density will be obtained by having the Kerr cell open for 20 nanosec. and the light on (bleed through) for 240 microsec. This obviously limits the minimum exposure time or maximum light source duration.

Since the light beam coming from the parabolic mirror was not quite parallel, accound had to be taken of the fact that the Kerr cell is effectively a thick plate and thus caused displacement of the image plane. Kodak High Speed Infrared film was used because it was the most sensitive film available in the far red. A Kodak Wratten filter #25 eliminated the higher frequency visible radiation to which the film was also sensitive. The filter was mounted in the 35 mm. camera which had been fitted with a large shutter (and no lenses). The overall magnification was found to be 1.02.

The image of the test section was also focused by the parabolic mirror on the vertical slit at a magnification of unity. The slit was made by ruling a 0.001 in. clear line on an aluminized glass plate. A camera lens and shutter assembly (f/4.5, focal length 7.5 in.) focused the slit on the film which was wrapped inside the 4 in. diameter drum. Again a Kodak Wratten filter #25 was built in and the Kodak High Speed Infrared film was

used. The overall magnification was 1.053. The drum camera was driven by air from a high pressure supply at approximately 300 cps., which gave the time resolution of 0.5 microsec. The signal from a capacitive pickup was amplified and fed to a 1 Mc.counter. A pulse, simultaneous to the one that triggered the flash lamp, activated the counter which was set to count the number of microseconds in 10 revolutions.

It is clear that there are two images of the slit, one in the main beam and one in the compensating beam. The distance between these virtual slits was measured by placing calipers on either side of the test section and bringing the image of the edge of the jaws into coincidence at the slit plane. This distance, the distance on the film of the shock fringe jumps and the drum camera speed then accurately measured the shock velocity in the interval between the two windows.

Film resistance gauges were used for triggering. The long delay to the onset of laser radiation and the spread in shock velocity caused by the pressure break created problems in "catching" the shock wave on film. These problems were overcome by building two proportional delay generators. The first one triggered the flash lamp so that the laser would go on approximately 50 microsec. before the shock wave reached the upstream window. The second triggered the Kerr Cell when the shock wave was in the middle of the upstream window.

III. EXPERIMENTAL CAPABILITY

Both the capabilities and limitations of the instrumentation are demonstrated in Fig. 3. On the right side is the drum camera picture, whose time scale is set by its RPM and time resolution by the slit width. On the left side is the Kerr cell snapshot (20 nanosec. exposure time) whose time scale is set by the shock velocity, and time resolution by the beam divergence and shock wave curvature. In the middle are shown the calculated positions of one fringe corresponding to the initial, vibrational frozen, vibrational equilibrium, and dissociation equilibrium densities for this run. The information contained in the two pictures is complementary. The Kerr Cell picture resolves the vibrational relaxation zone and the beginning of dissociation. The drum camera picture does not resolve these rapid changes in density, but shows the more gradual approach and attainment of dissociation equilibrium. If we had only the Kerr cell picture, we could not have experimentally checked what equilibrium conditions were eventually reached and thus could not be certain that the gas had been processed in accordance with our calculations.

These pictures also illustrate the advantages and the limitations of the setup. The intensity variation of fringes obtained with the Mach-Zehnder interferometer is sinusoidal. This makes the readings of fractional fringe changes difficult and limits the sensitivity of the instrument. However if the light intensity is sufficiently high, the nonlinear response of the film becomes important and useful. It is clear from the pictures that we have saturated the film almost everywhere except

where the intensity is zero. Thus we can read fringe position more accurately. But it is also clear that the spatial non-uniformity of the laser light (in the Kerr cell picture) and the residual spiking (in the drum camera picture) limit this improvement. Our conclusion is that a bigger ruby and a better cavity would result in sharper fringes in both pictures, i.e., greater ultimate sensitivity.

IV. HYDROGEN VIBRATIONAL RELAXATION - THEORETICAL CONSIDERATIONS

At the time when the instrumentation was completed, there were no experimental data on hydrogen vibrational relaxation except for one inferred value (ref. 7). The reasons for this are very simple; hydrogen vibrational relaxation is an extremely rapid process and, in addition, the low index of refraction of hydrogen makes standard optical techniques of measurement less sensitive than for other gases. The calculation of the frozen and equilibrium density ratios across the shock wave for hydrogen vibrational relaxation brought out an interesting fact. Usually, vibrationally frozen density ratios across the shock waves are calculated by assuming constant specific heat. This procedure is not correct for hydrogen at the relatively low temperatures of interest because of the high rotational and vibrational characteristic temperatures of hydrogen. The neglect of the change in rotational energy implicit in the above procedure results in a slight underestimate of the vibrationally frozen density ratio across the shock wave, but a substantial overestimate of the density change due to vibrational relaxation.

A very simple computer program was carried out, using the thermodynamic molecular constants tabulated by Haar et al (ref. 8) to obtain the proper relaxation density changes. These were discouragingly small, corresponding to a change of only 1/10 fringe for the whole vibrational relaxation zone (a temperature change of 10-50 °K).

An empirical correlation of vibrational relaxation times for other gases has been given by Millikan and White (ref. 9), but was not expected to apply to systems of very low reduced mass, such as hydrogen. A quantum mechanical calculation of the vibrational relaxation time for H_2-H_2 collisions was carried out by Salkoff and Bauer (ref. 10), but its validity was uncertain because of the lack of experimental data. More recently, a bound on H_2 vibrational relaxation times was given by White (ref. 11). More recently still, we became aware of the work of Kiefer and Lutz (ref. 12). They have covered a somewhat wider temperature range, apparently with accuracy higher than that which we could achieve, by using a laser schlieren system.

V. HYDROGEN VIBRATIONAL RELAXATION - EXPERIMENT

Measurements have been made of the vibrational relaxation time in hydrogen-argon mixtures at temperatures from 1300 to 1900 °K and initial pressures from 50 to 150 torr. The gases were mixed in a stainless steel cylinder whose volume was 1/10 that of the driven section. To ensure

proper mixing, magnetic stirring in the cylinder and 15-30 minutes residence time in the driven section were used. The overall leak rate was 10^{-3} torr./minute or less. To document the fact that we were seeing a relaxation zone, we show in Fig. 4 a Kerr Cell snapshot of a shock wave in pure argon. The exposure time for this as well as all H_2-Ar runs was 100 nanosec. The fringes are straight before and after the shock wave as expected. The drum camera pictures were used to measure shock velocity and to monitor the presence of "slow" waves, which indicated poor mixing. A Kerr cell picture of the shock wave in H_2-Ar mixtures is shown in Fig. 5. Here we notice a small, "gradual" rise in the fringe position behind the shock wave, indicating that a relaxation process is going on.

The measured fringe shifts were in agreement with the calculated values. The method of analysis was the standard one given by Blackman (ref. 13). Fringe position and distance behind the shock wave were measured on a 20X optical comparator. The slope of a plot of the log $(\Delta\rho/\Delta\rho_{relax.})$ vs. time (Fig. 6) gave the relaxation time in the laboratory frame. This was then converted to a particle relaxation time at 1 atm. pressure. A summary of the experimental data, as well as the theoretical curve of Salkoff and Bauer (ref. 10) is presented in Fig. 7.

Because the fringe shifts were so small, the accuracy was not sufficient to warrant deducing the relative efficiency of hydrogen and argon as collisional partners. Thus the data in Fig. 6 were reduced with the assumption of zero efficiency for argon as the collisional partner. The excellent agreement of the data with the theoretical calculation was a pleasant surprise. Incidentally, the empirical correlation of Millikan and White (ref. 9) was not successful, the predicted times being too long by a factor of 50.

VI. CONCLUSIONS

We have shown that a standard ruby laser makes possible submicrosecond Mach-Zehnder interferometry, thus extending the usefulness of the instrument to a shorter time domain. Under these conditions, gas dynamic effects such as shock curvature limit the achievable resolving time. The fixed sensitivity of the Mach-Zehnder is another drawback, which can be effectively overcome by having a more uniform light source, or by going to the green and blue lasers which are now becoming available.

ACKNOWLEDGMENT

This work could not have been possible without the help, understanding, and encouragement of Professors E. L. Resler, Jr. and D. L. Turcotte. In addition, many thanks are due to Dave Berkeley and Professor G. J. Wolga, who were the sources of much information on lasers. This work was jointly supported by the USAF Office of Scientific Research and by the Mechanics Branch of the Office of Naval Research. Reproduction in whole or in part is permitted for any purpose of the United States Government.

REFERENCES

(1) Stickley, C. M.,App. Optics 3, 967 (1964)

(2) Ready, J.F., App. Optics 2, 151 (1963)

(3) Roess, D., App. Optics 3, 259 (1964)

(4) Sutton, E. A., J. Chem. Phys. 36, 2923 (1962)

(5) Price, E.W., Rev. Sci. Inst. 23, 162 (1952)

(6) Zarem, A.M., Marshall, F.R., and Poole, F. L., Trans. AIEE 68, 282 (1949)

(7) Goydon, A. G. and Hurle, I.R., Proc. 8th (International) Combustion Symposium, 309-319, The Williams and Wilkins Co., Baltimore (1962)

(8) Haar, L., Friedman, A. S. and Beckett, C.W., NBS Monograph #20 (1961)

(9) Millikan, R. C. and White, D.R., J. Chem. Phys. 39, 3209 (1963)

(10) Salkoff, M. and Bauer, E., J. Chem. Phys. 29, 26 (1958)

(11) White, D. R., J. Chem. Phys. 42, 447 (1965)

(12) Kiefer, J. H. and Lutz, R. W., Presented at 5th Shock Tube Symposium, NOL, White Oak, Maryland, April 27-30, 1965

(13) Blackman, V.H., J. Fl. Mech. 1, 61 (1956)

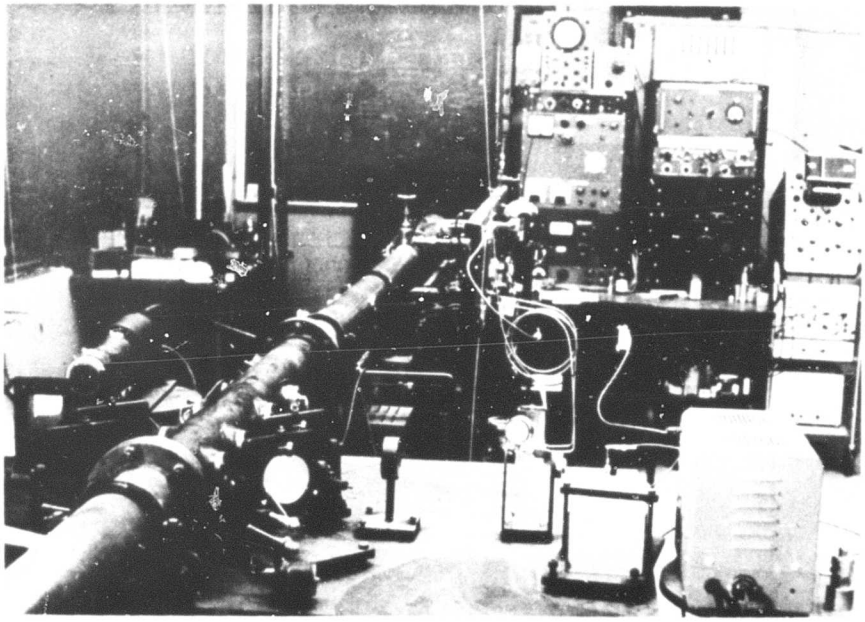


Fig. 1. View of Apparatus

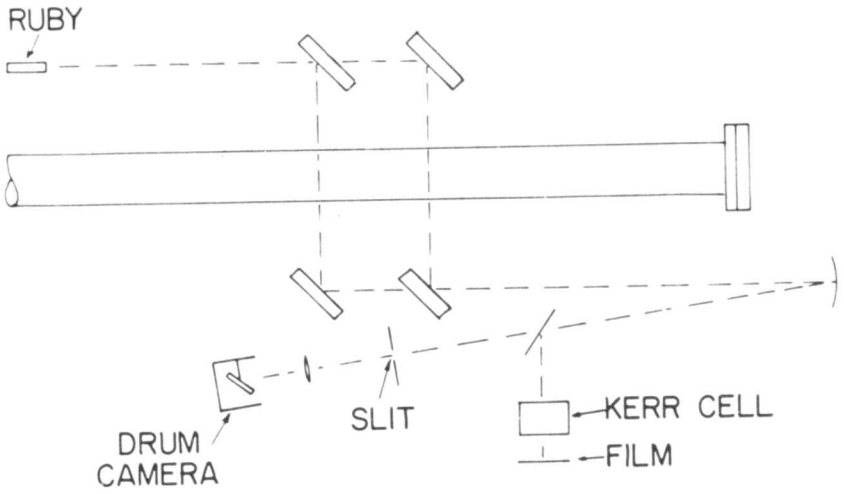


Fig. 2. Optical Setup - Schematic

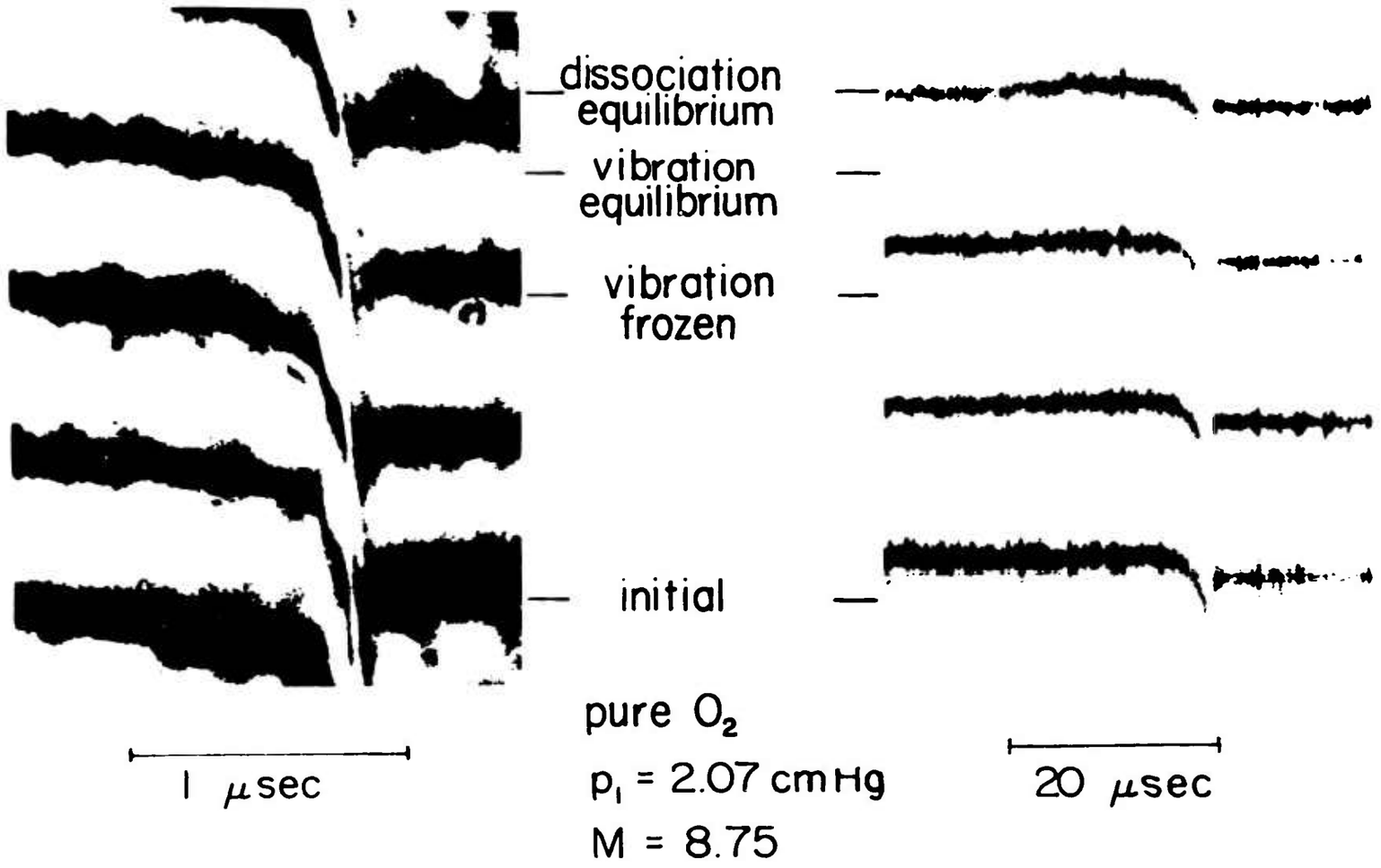
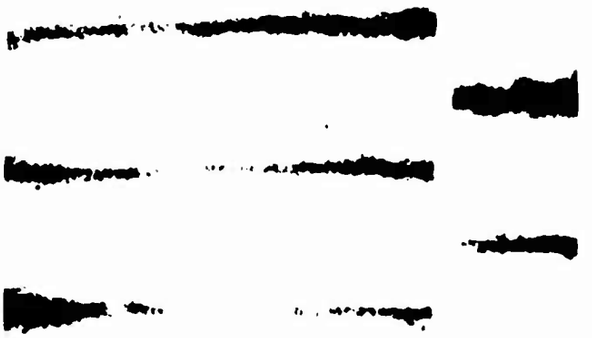
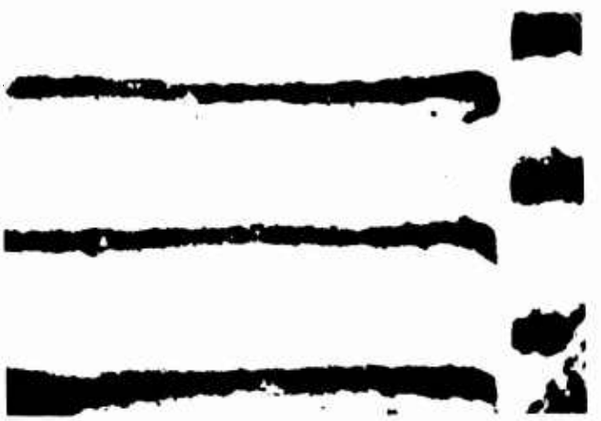


Fig. 3. Kerr Cell snapshot, calculated fringe position and drum camera picture of shock wave moving to the right in oxygen.



Pure Argon
p_1 = 8.65 cm Hg
M = 4.64

Fig. 4. Kerr Cell picture of shock wave moving to the right in pure argon.



0.40 H_2 0.60 Ar
p_1 = 15.67 cm Hg
M = 4.19

Fig. 5. Kerr Cell picture of shock wave moving to the right in H_2-Ar mixture.

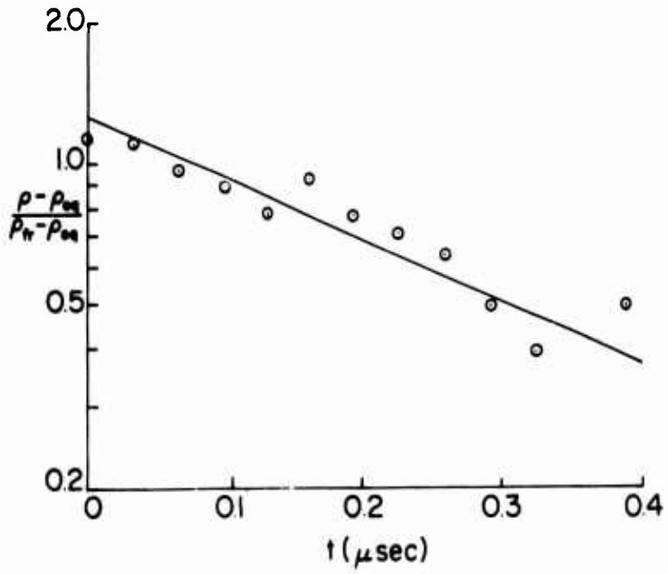


Fig. 6. Log of fractional density relation vs. time for a shock wave moving to the right at $M = 3.94$. The initial conditions were 0.60 H_2, 0.40 Ar and $p_1 = 103.7$ torr.

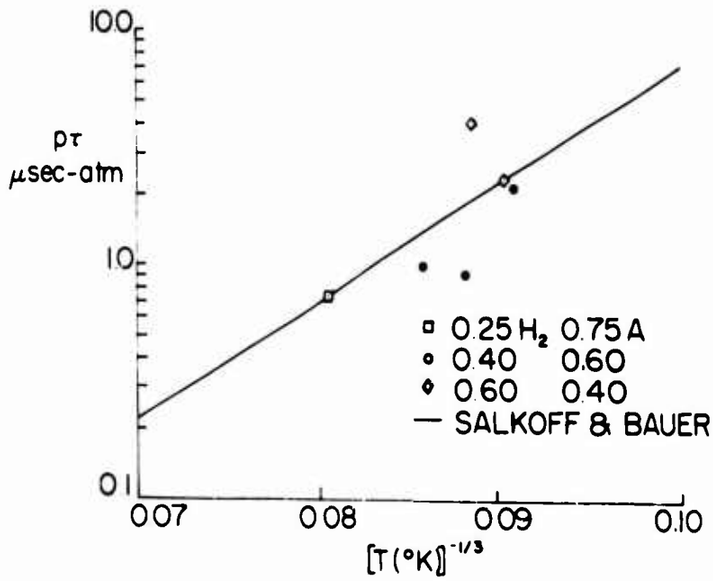


Fig. 7. Hydrogen vibrational relaxation time. Experimental values and theoretical curve.

MEASUREMENT OF ELECTRON DENSITY PROFILES USING A MICROWAVE TECHNIQUE

R. Tomboulian
General Applied Science Laboratories, Inc.
Westbury, L. I., New York

INTRODUCTION

Measurements of the electron density profile behind the shock have been achieved using a microwave technique. It may be noted that for electron densities in the range of 10^{10} e/cc, the conventional microwave interferometer is incapable of spatial resolution better than 10 cm. Since the total phenomena to be observed may occur in a much shorter distance, a technique has been developed which utilizes the shock tube also as a waveguide, and by measuring local field values at the wall, a point-by-point determination of the electron density may be ascertained.

The following is a brief summary of the microwave equipment and the analytical formulations required for determining electron density.

Microwave System

The basic microwave instrumentation system consists of a low power microwave generator, a coupling antenna to the shock tube (waveguide) and, electric and magnetic field detectors. Signals from the detectors together with markers are recorded photographically on a series of oscilloscopes.

A suitable microwave generator is a reflex klystron of about 60 mw output power operating in the 2-4 kmc range for a 3 inch diameter tube. The frequency stability need not be

exceptional but the short term power amplitude variations should be less than 1%. The klystron is coupled to the shock tube through a ferrite isolator. The coupling arrangement to the tube is shown in Fig. 1. In this coaxial to waveguide transition, matching is made by changing the penetration of the antenna and the position of the short circuit piston.

Matching

The matching of the coaxial line to waveguide is very important. All the measurements are based on the fact that the amplitude of the microwave signal coupled into the shock tube is constant. This condition is difficult to obtain because the plasma produces a strong reflection; standing wave ratios of twenty are not unusual. The reflected signal must be absorbed without reflection in the isolator. If reflections take place, they superimpose on the incoming signal with a phase that changes as the plasma moves. This effect is equivalent to a fluctuation of the input signal. The standing wave pattern then becomes a function of the position of the plasma or reflecting surface which is undesired.

A simple check on the matching condition is as follows: A metallic piston is displaced along the shock tube simulating a strongly reflecting plasma. Moving with the piston is a detector picking up the magnetic field near the wall, where it is maximum. The output from this detector gives the fluctuation produced by the mismatch only. Successive adjustments of the antenna to waveguide transition are made attempting to eliminate this fluctuation, thus giving a constant output when the piston moves.

In order to reduce the frequency sensitivity of the antenna, the signal from the generator is altered slightly. The antenna short circuit stub is then adjusted until a minimum change occurs in the output of the piston detector during this frequency change.

The limit of this system of matching comes mainly from incomplete contact between piston and wall. A typical value of the fluctuation after the matching has been performed is 2% but this corresponds to a smaller value when the plasma is reflecting because of the significantly better reflecting properties of the metallic piston.

Detectors

The electromagnetic wave propagated inside the tube has a wavelength λ_g which is a function of the frequency, mode of propagation and diameter of the tube. Some of the radiating energy is reflected from the plasma and the ratio of reflected to incident power is a function of electron density, collision frequency and profile of the plasma. The combination of incident and reflected waves combines to form a system of standing waves along the tube. This pattern has a period of $\lambda_g/2$. When the plasma moves the pattern also moves with the same speed, provided the properties of the plasma remain constant.

Two of the electromagnetic field detectors that have been used are shown in Figs. 2 and 3. Note that the detectors are designed to be flush with the tube wall in order to avoid perturbing the aerodynamic flow. The electric field detector is oriented so that the major axis is in the plane of polarization of the antenna, thus providing the maximum output for the TE_{11} mode of propagation. The outer surface of the probe is connected to a coaxial resonant circuit that provides a match to the impedance of the crystal and short circuits the currents produced by the flow of charges from the plasma to the tube walls. The magnetic field detector is a slot excited by the current flowing in the wall. Because of the relation between magnetic field and current, this slot is equivalent to a loop located in a plane perpendicular to the slot. The signal induced in the slot is coupled to a two line resonant circuit and to a crystal detector. The required field component is tangential H. Hence the H probe is located at right angles to the E detector in the same longitudinal plane and the slot oriented parallel to the tube axis.

For both E and H crystal detectors an output is obtained which is related to the amplitude of the respective field. The characteristics of the crystals cannot be considered either linear nor quadratic and the required accuracy requires that these signals be processed by a compensating network to obtain E^2 and H^2.

ANALYTICAL FORMULATIONS FOR DETERMINING ELECTRON DENSITY

The following is a summary of the analytical expressions used to determine the electron density in the combined shock tube-waveguide. The polarized radiation is introduced in the downstream end of the tube. Probes to detect the radial electric field and the tangential magnetic field are upstream of the antenna, as described earlier. To determine the point by point variations in electron density as the plasma moves past the detector station, expressions are required relating the measured field quantities to the local electron density.

For the TE_{11} mode of propagation, the radial electric field and the tangential magnetic field at the surface of the waveguide are given by,

$$E_r = A, \; J(\gamma,R) \cos \theta u(x) \; e^{i\omega t} \tag{1}$$

$$H_\theta = \frac{i}{\mu\omega} \frac{u'(x)}{u(x)} E_r \tag{2}$$

where γ for the TE_{11} mode is $\frac{1.842}{R}$, R being the tube radius.

The function u(x) is an undefined function which, however, contains the plasma properties. It must be a solution to,

$$u'' + u \left(\frac{\omega^2}{c^2} K - \gamma \right) = 0 \tag{3}$$

where primes indicate space derivatives, and ω is the radiating frequency, with

$$K = 1 + \frac{\omega_p^2}{\omega^2(1-i\frac{\nu}{\omega})} \tag{4}$$

ω_p and ν being the plasma frequency and collision frequency respectively. Assuming the field components are measured at right angles, with the E_r field in the direction of polarization of the radiation, then

$$E_r = A_o u(x) \; e^{i\omega t} \tag{5}$$

$$H_\theta = \frac{i}{\mu\omega}\frac{u'(x)}{u(x)} E_r = \frac{iA_o}{\mu\omega} u'(x)\, e^{i\omega t} \tag{6}$$

Since the values of the fields that are measured, assuming a square law detection, are the square of the real parts of the respective field, the measured quantities are,

$$E_r E_r = A_o^2\, u(x)\, u^*(x) \tag{7}$$

$$H_\theta H_\theta^* = \frac{A_o^2}{\mu^2\omega^2} u'(x)\, u^*(x)' \tag{8}$$

where * indicates the complex conjugate. Solving for K^2 in Eq. (3),

$$K^2 = \frac{c^2}{\omega^2}\left[\gamma^2 - \frac{u''}{u}\right] \tag{9}$$

The solution of K^2 in terms of the field values of Eqs. (7) and (8) can be shown to be,

$$\text{Re } K^2 = c^2\mu^2 \frac{H_\theta H_\theta^*}{E_r E_r^*} - \frac{c^2}{2\omega^2}\frac{\left(E_r E_r^*\right)''}{E_r E_r^*} + \frac{c^2\gamma^2}{\omega^2} \tag{10}$$

and

$$\text{Im } K^2 = \frac{\left[\text{Re } K^2 - \frac{c^2}{\omega^2}\gamma^2\right]\frac{\left(E_r E_r^*\right)'}{E_r E_r^*} + c^2\mu^2\frac{\left(H_\theta H_\theta^*\right)'}{E_r E_r^*}}{\sqrt{4\omega^2\mu^2\frac{H_\theta H_\theta^*}{E_r E_r^*} - \left[\frac{\left(E_r E_r^*\right)'}{E_r E_r^*}\right]^2}} \tag{11}$$

The plasma properties in terms of Re K^2 and Im K^2 are given as,

$$\frac{\omega_p^2}{\omega^2} = (1-\text{Re } K^2)\left[1+\left(\frac{\nu}{\omega}\right)^2\right] \tag{12}$$

and,

$$\frac{\nu}{\omega} = \frac{\text{Im } K^2}{\text{Re } K^2 - 1} \tag{13}$$

The values of the field in the above equations are in MKS units. However, it may be noted that each field quantity appears in a ratio. All that is required for solution in terms of the nondimensional measured quantities are the appropriate scaling ratios.

If the measured values of the field are designated as, E^2 and H^2, then the distance axis scaling needed for the ratios $(E^2)'/E^2$ and $(E^2)''/E^2$ can be determined from the ratio of the measured wavelength $\overline{\lambda g}$ (in units of the elongated trace). That is, if the horizontal (distance axis) coordinate is measured in units of Z and the real coordinate in X, units, then,

$$\frac{\overline{\lambda}_g}{\lambda_g} \equiv S$$

where λ_g is the actual waveguide wavelength (MKS units). Hence to scale the absolute ratios of field values to the measured quantities,

$$\frac{\left(E_r E_r^*\right)'}{E_r E_r} = S\,\frac{(E^2)'}{E^2}$$

and,

$$\frac{\left(E_r E_r^*\right)''}{E_r E_r^*} = S^2\,\frac{(E^2)''}{E^2}$$

To scale the combined ratios of electric and magnetic fields, it may be noted that in the free space region, the ratios of the maximum field values (occurring 180° apart) is given by,

$$\frac{(H_\theta H_\theta^*)_{max}}{(E_\theta E_\theta^*)_{max}} = \frac{4\pi^2}{\mu^2 \omega^2 \lambda_g^2}$$

If the ratio of the same measured quantities is designated by (a), i.e.,

$$\frac{H^2_{max}}{E^2_{max}} = a,$$

then,

$$\frac{H_\theta H^*_\theta}{E_r E^*_r} = \frac{4\pi^2}{\mu^2 \omega^2 \lambda_g^2 a} \frac{H^2}{E^2}$$

Then Eqs. (10) and (11) can be put in terms of measured quantities to give,

$$\text{Re } K^2 = \frac{c^2 4\pi^2}{\omega^2 \lambda_g^2 a} \frac{H^2}{E^2} - \frac{S^2 c^2}{2\omega^2} \frac{(E^2)''}{E^2} + \frac{c^2}{\omega^2} \tag{14}$$

$$\text{Im } K^2 = \frac{\left[\text{Re } K^2 - \frac{c^2}{\omega^2}\gamma^2\right] S \frac{(E^2)'}{E^2} + \frac{c^2 S 4\pi^2}{\omega^2 \lambda_g^2 a} \frac{(H^2)'}{E^2}}{\sqrt{\frac{16\pi^2}{\lambda_g^2 a} \frac{H^2}{E^2} - S^2 \left[\frac{(E^2)'}{E^2}\right]^2}}$$

Hence, the plasma properties can be obtained through the use of Eqs. (12) and (13).

In summary, to calculate the plasma properties at any point behind the shock the following parameters are required.

λ_g	waveguide wavelength
$a = \frac{H^2_{max}}{E^2_{max}}$	taken in the free space region
$S = \frac{\bar{\lambda}_g}{\lambda_g}$	distance scaling ratios ($\bar{\lambda}_g$ measured wavelength on enlarged trace)

$\lambda = \frac{1.842}{R}$ R is tube radius

$\omega = 2\pi f$ f radiating frequency

and E^2, $(E^2)'$, $(E^2)''$, H^2, $(H^2)'$, the field values and derivatives at the wall of the waveguide.

The significant difficulty in this technique is that spatial derivatives of the signals must be obtained. Obviously, if the original E^2, H^2 functions are not extremely accurate, the subsequent derivatives will greatly suffer. Indeed the limiting accuracy of this technique is primarily determined by the validity of the derivatives. To improve these functions, a computer program has been employed to provide self checks and calibration. Typical results of this technique are discussed in the following paper entitled "Anomalous Electron-Density Profiles in Shock-Heated Air, Effects of Na and NaCℓ," by Myron S. Wecker, Theodore Baurer, and Roger Tomboulian.

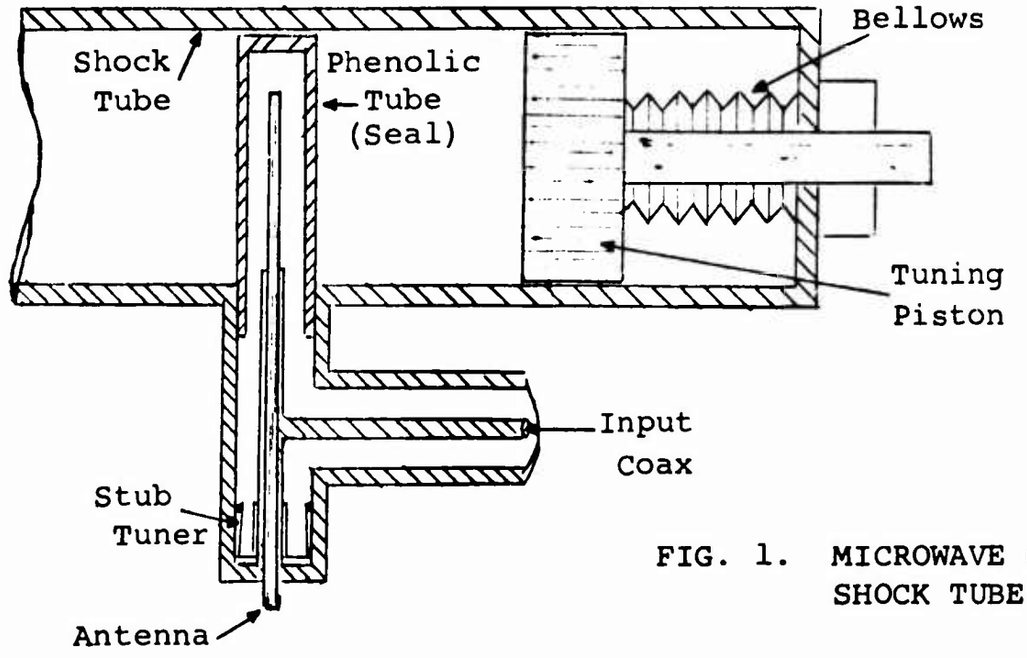


FIG. 1. MICROWAVE COUPLING TO SHOCK TUBE

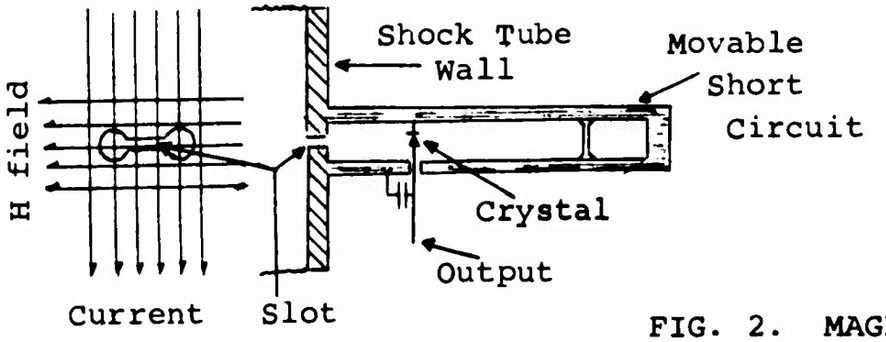


FIG. 2. MAGNETIC FIELD DETECTOR

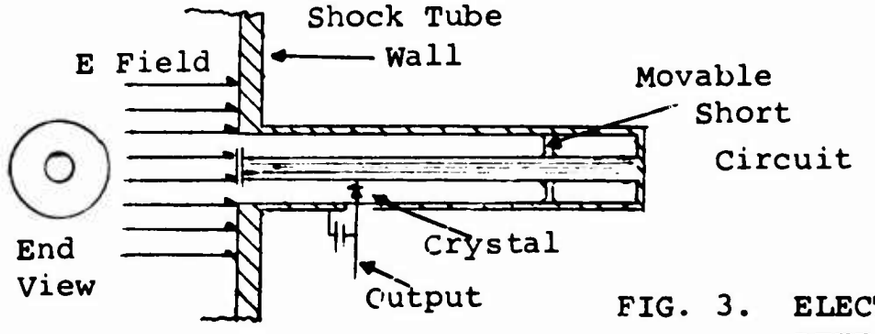


FIG. 3. ELECTRIC FIELD DETECTOR

BLANK PAGE

PRECURSOR IONIZATION IN AN ELECTRICALLY DRIVEN SHOCK TUBE

Derek W. Mahaffey, Richard I. Schoen and Harlow G. Ahlstrom*
Boeing Scientific Research Laboratories
Seattle, Washington

INTRODUCTION

This paper is an account of some experiments which were conducted on a six-inch diameter electrically driven shock tube to investigate precursor and related effects. By precursor effects are meant effects in the gas ahead of the shock or luminous front. The results reported here apply to a particular shock tube. We do not claim that the effects reported here and only these effects will be or have been observed in other tubes. Nevertheless, it would be reasonable to expect the same effects under similar conditions.

The stimulus for this investigation was the observation of light from the tube far in advance of the shock. Observations of similar phenomena have been made by several others. Voorhies and Scott (ref. 1) have observed helium line radiation at 5876 Å from the gas ahead of the electrically driven shock in a He-D_2 mixture. Ionization in and radiation from the region ahead of the shock have been reported by Kolb, Griem and coworkers (ref. 2). Groenig (ref. 3) observed similar effects in a cylindrical shock tube. These investigators agree that the most important cause of precursor ionization is vacuum ultraviolet radiation. Gerardo et al (ref. 4), however, conclude that the precursor ionization which they observed at applied voltages above 8 kV is caused mainly by X-rays. Fowler and coworkers (ref. 5) have reported waves of luminosity propagating ahead of their shocks at speeds of the order of 10^8 cm/sec.

APPARATUS

The electrically driven shock tube is shown schematically in Figure 1.

* Consultant, University of Washington, Seattle

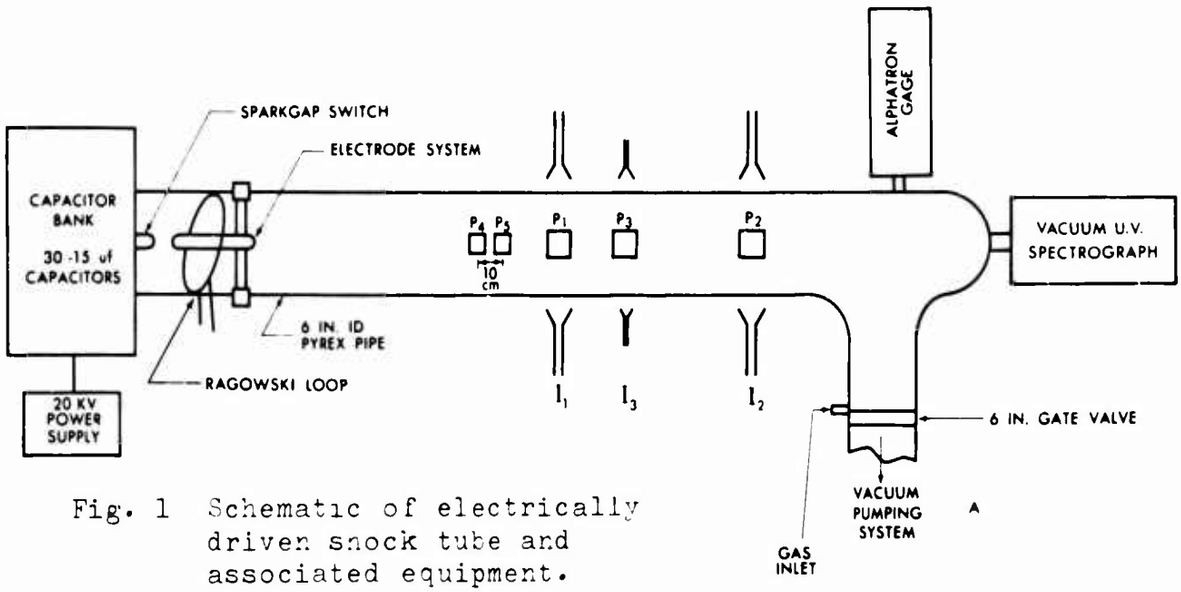


Fig. 1 Schematic of electrically driven shock tube and associated equipment.

A series air-gap switch was used to dump the capacitor energy into the shock tube. The discharge which drove the shock took place between a central copper electrode and a coaxial 6-inch diameter brass ring. The inner electrode was mounted through a hole in 3/4-inch thick plate glass.

The tube itself was made of 6-inch i.d. pyrex pipe. When the tube was sealed off for 24 hours the average leak rate was approximately 1 to 2 $\times 10^{-3}$ mm Hg per hour. A base pressure of less than 1 $\times 10^{-5}$ mm Hg was obtained before any shot was fired.

At various times the following equipment, shown in Fig. 1, was used on the shock tube:

1. Photomultipliers $P_1 - P_5$ were used to measure the rate of propagation of luminous fronts.

2. Three standard microwave interferometers $I_1 - I_3$, two X-band (10 kmc) and one K-band (36 kmc) were placed along the shock tube to measure the electron density ahead of the shock front. Photomultipliers P_1, P_2 and P_3 were located at the sites of the interferometers.

3. A Ragowski loop near the switch was used to measure the discharge current.

4. A 2 m grazing incidence spectrograph aligned to view light from the discharge was used. This instrument could be used either photographically or photoelectrically.

MEASUREMENTS

The initial observations which led us to believe that there were precursor effects in this tube were results similar to those shown in Figure 2. This shows the capacitor bank voltage and a photomultiplier

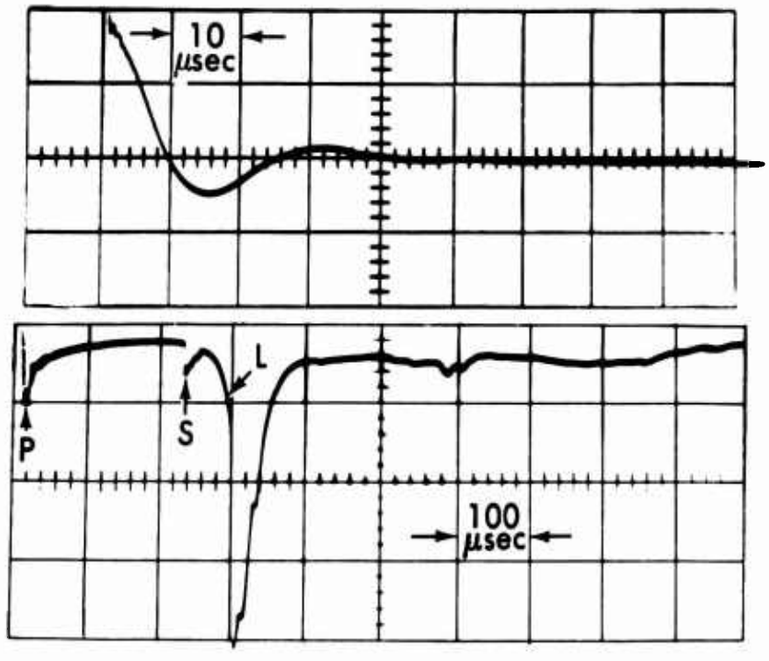


Fig. 2 Upper Trace -- Capacitor bank voltage
Lower Trace -- Photomultiplier output

(P - precursor radiation, S - luminous front, L - contact surface.) Note difference in time scales and starting points of upper and lower traces.

output as a function of time. The photomultiplier was located 3.56 m from the discharge end of the tube. The capacitor bank voltage is a heavily damped sinusoid with a period of approximately 30 μsecs. The photomultiplier output shows a precursor illumination P, the arrival of the luminous front S, and finally the contact surface L, between the shock heated gas and the driver gas. It may be noted that in this case shock separation occurred.

Figure 3 is a schematic of the time variation of the electron density as measured by a microwave interferometer. For convenience in

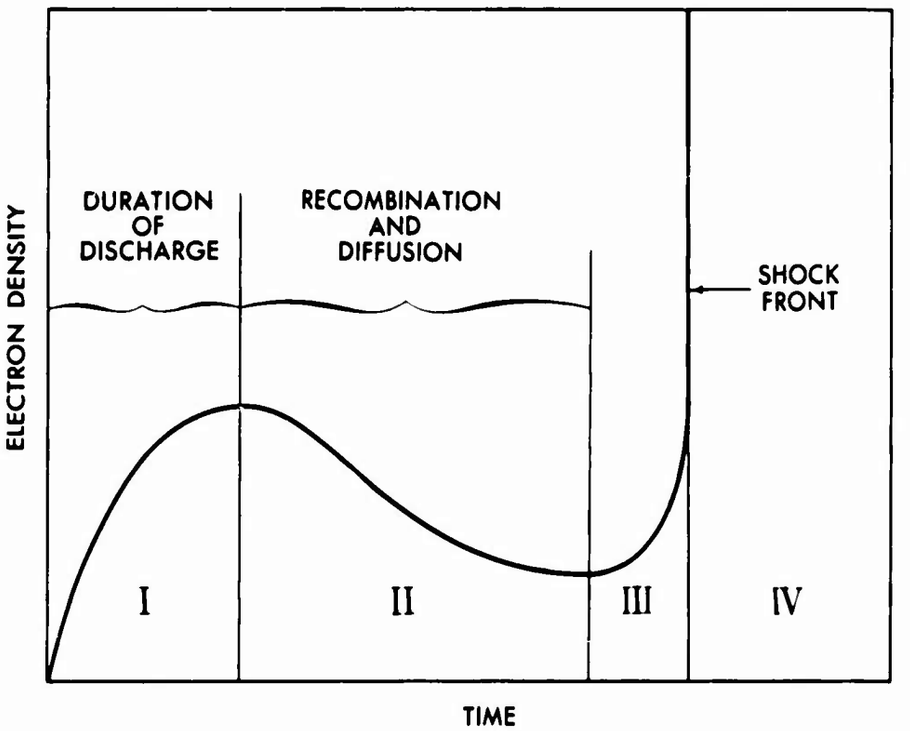


Fig. 3 Schematic of time variation of electron density as measured with a microwave interferometer.

discussion this has been divided into four time intervals:

1. An interval during which ionization appeared throughout the shock tube. The increase in electron density continued for a time which appeared to be no longer than the duration of the first half cycle of the discharge current.

2. An interval of decreasing electron density due to recombination and diffusion after the discharge ended.

3. A transition interval of apparently increasing electron density which was not always observed. This interval may be due to diffusion of electrons from behind the main shock or ionization by radiation from the shock itself (ref. 6), or heating of the electron gas in front of the shock (ref. 7).

4. The arrival of the shock or contact surface front itself.

Similar results were obtained with each interferometer. For an interferometer closer to the electrode system the peak density at the end of interval 1 was higher, but it occurred at the same time. Inter-

val 2 had a shorter duration due to the earlier arrival of the shock front.

No changes were observed when either the polarity of the discharge electrodes was reversed or when all pieces of metal attached to the tube (with the exception of the discharge electrode system) were ungrounded. This reduced the possibility of arcs or streamers down the tube.

The precursor ionization was observed at all pressures used, 0.1 - 5.0 mm Hg in He and A, and at all capacitor bank voltages used, 3 Kv - 15 Kv. The precursor electron density was of the order of $10^{10} - 10^{12}$/cc at the interferometer 3.3 m from the discharge, and was higher at the interferometers closer to the discharge. These figures are for gases with no deliberately added impurities.

There existed no measurable time delay of the arrival of region 1 between any of the interferometers. In particular we observed nothing which could be interpreted as an ionization front of the type reported by Fowler and coworkers (ref. 5) or more recently by Haberstich (ref. 8), who has reported on the presence of potential breakdown waves. A property of such waves is that they may propagate around corners. To determine if these waves were present a curved side tube was added to our main shock tube. A metal probe was placed in the side tube at the end remote from the main tube and no signal was detected on this probe.

DISCUSSION OF PRECURSOR IONIZATION MECHANISMS

Four mechanisms which could cause the observed precursor ionization are considered:

1. Impact ionization by fast ions from the discharge region.

2. Impact ionization by fast electrons from the discharge region.

3. Ionization by X-radiation from the discharge region.

4. Ionization by vacuum ultraviolet radiation from the discharge.

The following discussion is an attempt to isolate one of these as the main cause.

Fast Ions

In all cases there was an interferometer at least 3.3 m from the discharge and precursor ionization was observed at this interferometer. When the gas pressure was equal to or greater than 4.7 mm Hg in argon, electron densities greater than 10^{10}/cc were observed with a capacitor bank voltage of 7.5 Kv maximum. The range of 40 Kv protons is less than 0.1 m in argon at that pressure. Heavier nuclei have

shorter ranges. Thus even if the positive ions achieved energies in excess of five times that available by direct acceleration of singly charged ions in the electric field in the discharge, they would not have the necessary range to cause the observed ionization.

Fast Electrons

Similar range arguments may be applied to electrons, and in addition the application of a 600 - 800 gauss magnetic field transverse to the tube axis between the discharge and the interferometer had no apparent effect on the electron density in the precursor. Such a magnetic field would sweep electrons into the shock tube wall, well short of the position of the observed ionization.

X-Radiation

The fact that precursor ionization was observed with capacitor bank voltages as low as 3 Kv would appear to eliminate the possibility of K X-ray generation in any of the electrode materials. More striking, however, were the results obtained when small amounts of impurity gases were deliberately added to the inert gases. Figure 4 shows the effect on the precursor electron density of introducing small amounts

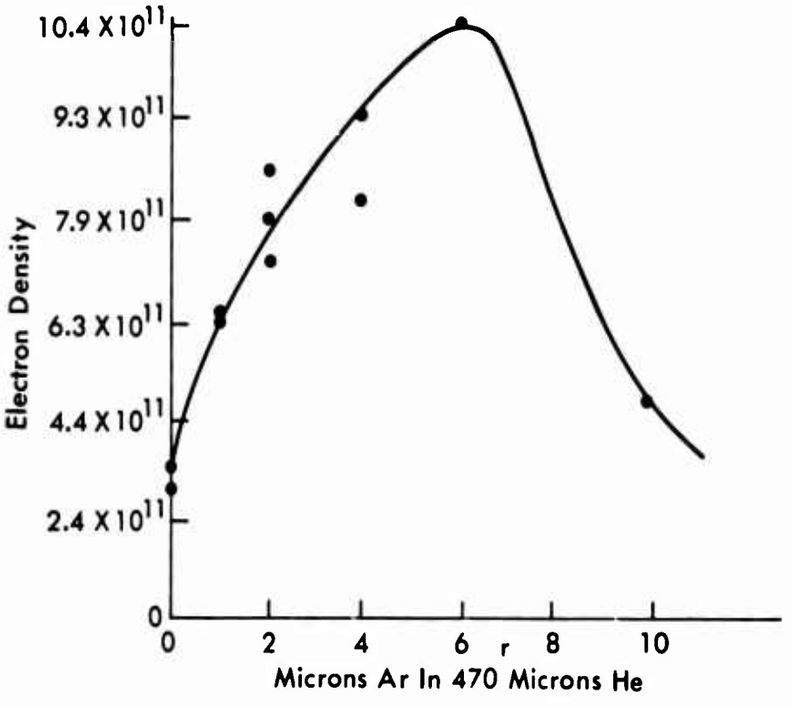


Fig. 4 Variation of peak precursor electron density as a function of the amount of argon added to helium.

of argon into helium. The background pressure of helium was .47 mm Hg. The addition of 1×10^{-3} mm Hg of argon more than doubled the electron density. The addition of 10×10^{-3} mm Hg of argon reduced the density to close to that observed with no deliberately added argon. Similar results were obtained by adding nitrogen to helium. The ionization potentials of nitrogen and argon are less than that of helium.

This rise and subsequent decrease in electron density may be explained if one assumes that the minority constituent was ionized by some radiation which it absorbed in the ionizing proce . Thus a large increase in the minority constituent may cause the radiation to be severely attenuated. Absorption cross sections in the range of 10^{-17} cm^2 are required to explain the results described. Th X-ray cross sections are not large enough to explain this effect. oreover, it was possible to cause a similar increase in the precursor ectron density by adding H_2 into neon. Since the X-ray cross section are expected to be much larger for neon than for H_2 in all parts of the X-ray spectrum, one cannot explain these results on the basis of X-rays.

Vacuum Ultraviolet

The remaining prospective cause of the precursor ionization is vacuum ultraviolet radiation in the wavelength range longer than the ionization threshold of the majority constituent of the shock tube gas. Radiation with wavelengths shorter than the ionization threshold of the main gas in the tube would be absorbed close to the discharge. The ionization observed with no deliberately added impurities is probably due to ionization of impurities included in the tank gases and introduced by leakage and wall outgassing.

The preceding arguments point strongly to vacuum ultraviolet radiation as the cause of the precursor ionization. Some experiments were performed to detect such radiation. Figure 5 shows a grazing incidence vacuum ultraviolet spectrograph which was used for this purpose. The spectrograph was aligned to detect radiation from the discharge and could be used either photographically or photoelectrically.

Photographic detection showed some lines and an apparent continuum in the wavelength range of interest, 500 Å - 800 Å. The time of emission was not defined with photographic detection and it is possible that radiation may have been emitted as hot gas struck the entrance slit to the spectrograph.

The results of photoelectric detection are shown in Figure 6. The upper trace shows the time variation of the discharge current as measured by the Rogowski loop and the lower trace, the vacuum ultraviolet induced photocurrent. The appearance of the ultraviolet during the first half cycle of the current trace may be seen. An indication of some further radiation during the second half cycle could sometimes be

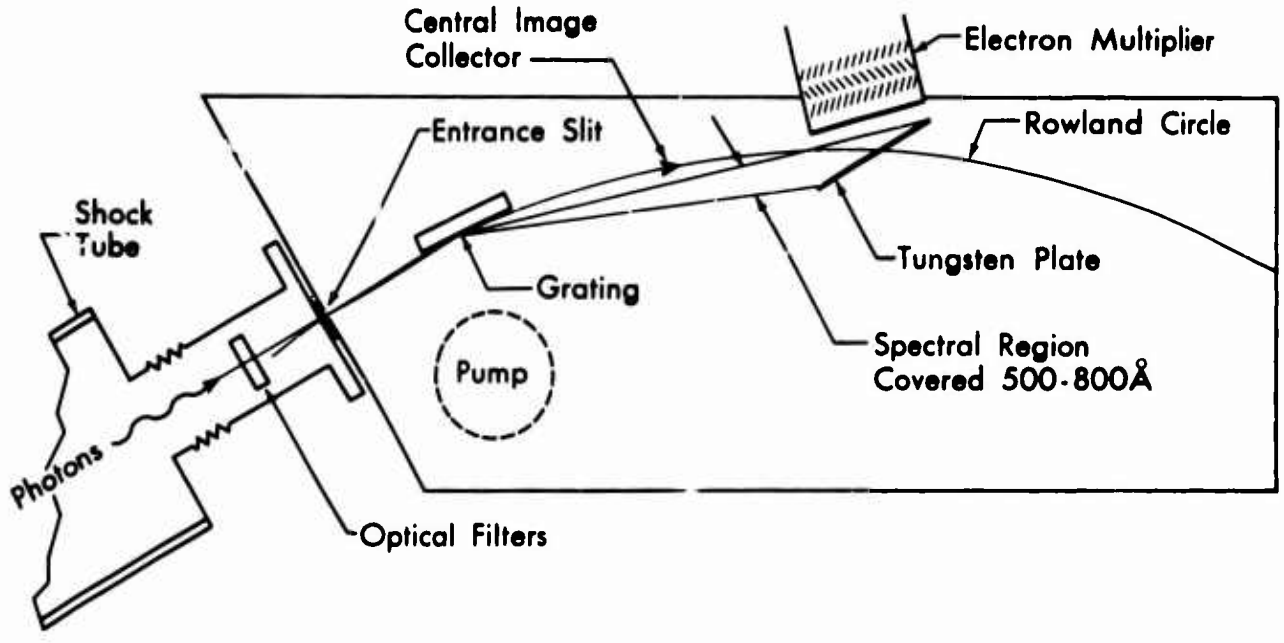


Fig. 5 Vacuum ultraviolet spectrograph attached to shock tube.

seen. The deliberate introduction of impurity gases reduced the radiation as expected.

The possibility that the photomultiplier was responding to scattered radiation with wavelength longer than 1100 Å was eliminated by repeating the experiment with a lithium fluoride window, which transmits only above 1100 Å. No response was obtained under these conditions.

Estimates of the vacuum ultraviolet photon flux were made on the basis of vacuum ultraviolet photomultiplier response and on the basis of impurity ionization. These estimates indicated a flux of more than 3×10^{13} photons per discharge in the spectral range 500 - 800 Å from the 30 capacitors charged to 7.5 kV.

CONCLUSIONS

The conclusions which we draw are similar to those of McLean, et al (ref. 2) and others, namely:

Vacuum ultraviolet radiation, produced in the discharge region, acts on impurities, causing precursor ionization. Therefore, there exists a reservoir of electrons ahead of the shock front which could speed the ionization process as the front passes.

Estimates of the ultraviolet photon flux indicate that there is sufficient energy to raise significantly the enthalpy of the gas close

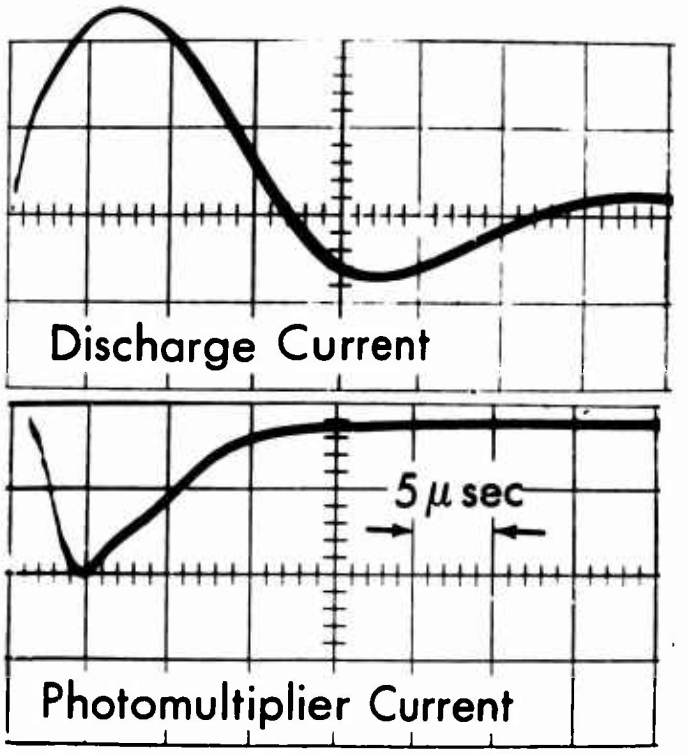


Fig. 6 Upper Trace -- Time variation of discharge current
Lower Trace -- Time variation of vacuum ultraviolet induced photo current

to the discharge, by perhaps as much as 50% within 50 cm of the discharge. Thus calculations based on the Rankine-Hugoniot relations should take this into account.

ACKNOWLEDGEMENTS

The authors wish to express their thanks to L. Sanga and A. LaVigne who assisted with the work at various times.

REFERENCES

(1) Voorhies, H.G. and Scott, F.R., Phys. Fluids 2, 576 (1959).

(2) Kolb, A.C. and Griem, H.R., Atomic and Molecular Processes, edited by D.R. Bates, Academic Press, New York (1962), Chap. 5, Sections 2 and 3;
McLean, E.A., Faneuff, C.E., Kolb, A.C. and Griem, H.R., Phys. Fluids 3, 843 (1960);
Wiese, Wolfgang, Berg, H.F. and Griem, H.R., Phys. Rev. 120, 1)79 (1960); Phys. Fluids 4, 250 (1961);
McLean, E.A., Kolb, A.C. and Griem, H.R., Phys. Fluids 4, 1055 (1961).

(3) Groenig, H., Phys. Fluids 6, 142 (1963).

(4) Gerardo, J.B., Hendricks, C.D. and Goldstein, L., Phys. Fluids 6, 1222 (1963).

(5) Fowler, R.G., Paxton, G.W. and Hughes, H.G., Phys. Fluids 4, 234 (1961);
Fowler, R.G. and Fried, B.D., Phys. Fluids 4, 767 (1961);
Fowler, R.G. and Hood, J.D., Phys. Rev. 128, 991 (1962)
Paxton, G.W. and Fowler, R.G., Phys. Rev. 128, 993 (1962);
for comments see:
Weymann, H.D., Phys. Fluids 4, 1573 (1961);
Fowler, R.G., Phys. Fluids 4, 1574 (1961).

(6) Holmes, L.B. and Weymann, H.D., "Plasma Density Ahead of Pressure Driven Shock Waves", Proceedings of this conference.

(7) Grewal, M.S. and Talbot, L., J. Fluid Mech. 16, 573 (1963)

(8) Haberstich, A. Bull. Am. Phys. Soc. 9, 585 (1964)

OPTIMIZED GEOMETRY FOR COUPLING A MASS SPECTROMETER TO A SHOCK TUBE

G. F. Marsters*, S. H. Bauer** and E. L. Resler, Jr.***
Cornell University
Ithaca, New York

ABSTRACT

The problem of coupling a transient high density source to the ionization section of a mass spectrometer has been attacked recently at many laboratories. Although pin-hole leaks allow the mass spectrometric detection of free radicals generated by shock heating, it would be useful to have a method which might retain the sample integrity more effectively. The in situ composition of the sample could be changed by mixing with boundary layer gas, since the length of molecular diffusion time, from the shock region to the ionizing electron beam, allows the sample to experience many collisions. If it were possible to expand rapidly and thus to cool and quench a portion of the axially located gas to sufficiently low density, fidelity of sampling would be achieved. The coupling section now under construction was designed to generate a high flux but not a well collimated molecular beam for injection into the mass spectrometer ion source. The shock tube is operated in an open ended-mode and defining nozzles are introduced for successively draining off boundary layer gas. Optimization of expansion is achieved by inserting axial sleeves in the end of the shock tube, of diameters appropriate for several regimes of operation. Calculations of sample residence times and total average collision numbers are presented.

---

* Research Assistant, Graduate School of Aerospace Engineering
** Professor, Department of Chemistry
*** Director, Graduate School of Aerospace Engineering

INTRODUCTION

There is ample evidence indicating the usefulness of a constant area shock tube as a tool for chemical kinetics investigations. Using the shock tube, one is able to transfer relatively large amounts of energy to the gas, quickly and cleanly. The passage of a shock wave through a gas results in a very rapid increase in its translational temperature. This is accomplished in less than ten molecular collisions. However, comparatively longer periods are required for the other degrees of freedom of the gas to adjust to the new equilibrium levels of energy. In the event that the energy input is sufficiently large, electronic excitation and/or molecular dissociation will be initiated, and the gas will absorb energy while tending toward an equilibrium concentration of reactant and product species. Still larger amounts of energy input will result in ionization of the gas.

Various methods have been devised for studying the processes outlined above, in which the shock tube plays the role of a pressure wave guide with which one may impart to the gas controlled quantities of energy under reproducible conditions. Many of these methods are discussed elsewhere in these proceedings. Often the technique involves an optical exploration of the conditions existing in the gas after the shock front has passed. A different approach to the diagnostic problem is to extract a sample of gas from the relaxation region behind the shock front, and to measure its chemical composition subsequent to its removal from the shock tube. It is the purpose of this paper to describe such a method currently under development at Cornell University.

The good mass resolution, high repetition rate and the possibility of multiple concurrent m/e recording of the time-of-flight mass spectrometer qualify it as a promising instrument for coupling to a shock tube for the purpose of chemical kinetic studies. Such a union would enable one to detect transient species which appear in the reacting gas. It should be possible to record accurately the relative number densities of the species present, and to observe the time variation of the concentrations of the species of interest. One of the significant problems is the detail of recording the enormous amount of information which is generated in very short times. Indeed, one optimistically may design for a test time in the order of one millisecond per run, during which 100 "readings" are taken for each mass present. The more immediate problem, for this paper, however, is that of coupling the shock tube to the mass spectrometer. One attempts thereby to connect a characteristically high density source, of a highly transient nature, to a detector which requires that the sample be present at a density 10^{-7} to 10^{-9} of that existing in the region behind a shock front. It is essential therefore, to devise an adequate transition which expands the gas from conditions existing within the shock tube behind the shock front, to those compatible with the ion source of the mass spectrometer. In addition, one must

retain the chemical integrity of the sample, that is, the transition ideally should result in quenching of all chemical processes.

In other experimental arrangements in which such a union has been made (1)(2) a pinhole leak or a very small throat-diameter Laval nozzle was used to provide the required transition in density. In this configuration the shock wave is reflected from the end wall of the tube, and the sample effuses from the stagnant hot gas which was processed by both the incident and reflected waves. The diffusion of the cold end wall boundary layer into the gas sample, and the catalytic effects of the cold surface, pose questions for which the answers are not clear. The possibility that integrity of the sample is lost in this particular extraction process warrants a search for alternative methods. The configuration proposed in this work has as one of its chief aims the elimination of the end wall boundary layer problem. The shock tube is used in an "open end mode" which permits the shock front and the relaxation region following it to expand into a dump tank. A slit system within the dump tank and coaxial with the shock tube defines a molecular beam which illuminates the ion source of the time-of-flight mass spectrometer. The rapid expansion into the dump tank effectively quenches the sample, by quickly reducing the temperature (random energy is converted into directed energy) thereby reducing the frequency and "hardness" of molecular collisions, and by quickly reducing the density, which further reduces the collision frequency.

DESIGN CONSIDERATIONS

As pointed out earlier, we were motivated in this work by the difficulties involved in assessing the effects of the cold end wall in the reflected-shock pinhole-leak method of sampling. To illustrate the problem, an order of magnitude type analysis is displayed in Figure 1, where we indicate the growth of the boundary layer and the "sample hemisphere." We assume that the pressure ratio across the orifice is large. The sample which leaks through the orifice in time t_1 must have occupied, at $t = 0$, a hemispherical volume, centered on the orifice. If the orifice is sufficiently small to produce molecular effusive flow, the mass flux through the hole is given by the well known equation

$$\dot{m} = \frac{1}{4} \rho \bar{v} A$$

where ρ is the density in the source region, and $\bar{v}$ is the mean thermal velocity calculated at the temperature of the particles which are within the neighborhood of the orifice, and A is its area. If the flow is hydrodynamic, rather than free molecular, the mass flux is given by

$$\dot{m}^* = k \rho_o c_o A$$

where the asterisk denotes hydrodynamic flow conditions, ρ_o is the density after the reflected shock, c_o is the sound speed after the reflected wave, and A is the area of the orifice. Assuming that the hole is sufficiently small so that it does not disturb the overall conditions in the hot gas region, one finds that the volume which "feeds" the hole grows linearly with time, regardless of whether free molecular or hydrodynamic flow obtains. Hence the radius grows as

$$r \propto t^{1/3}$$

The constant of proportionality is of course dependent upon the type of flow, and its determination may be very complicated. Again, assuming that the overall conditions in the stagnant gas region are not disturbed by the hole, one finds the rate at which the thermal boundary layer diffuses into the stagnation region is

$$\delta \propto t^{1/2}$$

where δ is the thermal boundary layer thickness. A characteristic time is quickly reached where the thermal boundary layer thickness exceeds the hemisphere radius. These arguments were previously presented elsewhere (references 3 and 4). The effects of these growth rates are shown in Figure 1. For illustrative purposes, we have assumed the condition $r_o = 1.5\delta_o$ for $t = t_o$. In addition, to illustrate the comparative growth of the boundary layer and sample radius we included, in Figure 1(b) a qualitative plot of the change with time of the fraction of sample region which is within the boundary layer gas. It appears that only the very early portion of the flow is free from effects of the boundary layer. Furthermore, it is evident that the time available for sampling which is free from end wall effects is dependent upon the size of the orifice. For effusive flow, the sample must come from within a few mean free paths of the wall, and the time available is at best the order of a few tens of mean collision times.

As an alternative to pinhole leak sampling we concluded that the most promising approach was to use the free expansion from an open ended tube and thus to generate a source for a molecular beam. Molecular beams driven by shock tubes have been studied and developed recently by Skinner (3)(5), Oman and Calia(6) and Jones (7). The work of Milne and his collaborators (8) also supported the applicability of molecular beams for mass spectrometric sampling of high pressure sources.

INITIAL FREE EXPANSION

The sequence of events in starting the free expansion from the open end of the shock tube is shown in Figure 2. The flow is initially allowed to expand freely, and thence into a supersonic nozzle, which is shown at the right of the figure in each step of the sequence. Of

course this mode of operation applies only to those cases in which the flow behind the shock front is supersonic. Prior to the run, the entrance of the supersonic nozzle is closed with a very thin collodion diaphragm. On the low pressure side (to the right in the figure) the pressure before the run is about 5×10^{-6} torr, while the pressure upstream of the nozzle is at the initial driven pressure of the shock tube.

For the greatest part of the operating range of this study, the flow behind the shock front will be supersonic. Shock wave Mach numbers of about 2 to 6 are required, and considering a low concentration of sample diluted in argon, one obtains flow Mach numbers in the relaxation region through transonic to about 1.30. In view of these rather low flow Mach numbers, the gas sample is allowed to expand freely until the flow reaches a sufficiently high Mach number to permit the supersonic nozzle to operate satisfactorily. The latter must operate with an attached shock wave, since a shock wave standing in front of the nozzle would represent an undesired additional processing of the sample. The approximate positions of the bounding characteristics are also shown in the figure. The dotted lines represent the locations of the characteristics for the case of steady flow. The initial portion of the expansion, that is, from the open end of the tube to the entrance of the supersonic nozzle, has been investigated using simplified methods described by Lord (9). Since we are interested mainly in the earliest part of the expansion and in the region close to the axis, the following simplifying approximations apply. Essentially, one expands the center line Mach number in a series in x, a dimensionless (with respect to the exit radius) axial distance. Now, retain only the first term of the expansion, so that the Mach number depends linearly upon x. The coefficient of this term varies with the geometry, the Mach number in the exit plane, and the gas properties. To obtain the residence time in this initial portion of the free expansion, the Mach number-distance relations were rearranged to show a velocity in terms of distance, assuming the entropy of any portion of the sample remains constant in the expansion. The following expression results

$$\frac{t}{r} = \tau_{exp} = \frac{K}{G f_1 f_2} \int_{M_p}^{M} \frac{\sqrt{3 + M^2}}{M} \, dM$$

The factors G, f_1, f_2 and K are the geometrical and reference flow parameters; M_p is the Mach number of the flow behind the shock front, and r is the radius of the exit. The integral is easily evaluated, and the ratio of the time in the expansion to radius of exit reduces to an expression in terms of the flow stagnation temperature and the temperature ratio across the shock front. (Note that these calculations are suitable only for the flow region near the exit, and near the axis of the flow.) The gas expands into a region of finite back pressure, but the portion of interest here is well within the confines of the

"shock bottle," and well upstream of the "Mach disc," and thus is not affected by the external ambient pressure.

The computations as outlined above lead to some interesting observations and conclusions. In particular, one notes the requirements for small expansion residence time, τ_{exp}. The only readily controlled variable is the exit radius; all others are either fixed by the gas or by the flow conditions behind the shock front. In Figure 3 we show the curves representing the residence times in the free expansion. Two additional curves, one for Mach number 1.75,the other for Mach number 2.0, are superposed on these curves. The Mach number plots were included since they embrace the region in which the prototype supersonic nozzle has given satisfactory operation. The basic curves represent the variation of residence time in the free expansion with temperature behind the shock front. The dependence of the expansion time upon the radius is readily seen. On the basis of this figure, and the conditions behind the shock front, one can estimate an upper bound to the number of collisions in the free expansion (between the end of the tube and the entrance of the nozzle) and also obtain cooling rates directly by measuring the slopes of the curves. As one might expect, the cooling rates are in general slower for the lower temperature flows, and the time spent in the expansion is correspondingly longer. The cooling rates obtained, (while indicating that in most cases freezing of the sample can be achieved) are sufficiently critical so that one seeks ways of increasing the cooling rate and decreasing the time for free expansion. Since the exit radius is the only parameter which may be adjusted, we propose to introduce a sleeve, mounted coaxially in the dump tank end of the shock tube. This device will be used in the operating regimes where the freezing problem is critical. Flow is established only within the sleeve, since the annular area between the sleeve and the shock tube wall is closed. Such a device carries with it the added advantage of reducing the quantity of the gas which must be handled by the dump tank during the test time. A further advantage is that the sleeve boundary layer is thinner, in all cases, than that which exists in the shock tube itself. However, since the flow cross sectional area is reduced, one must investigate the boundary layer effects carefully. The results of such a study are discussed in the next section.

SLEEVE OPERATION

The operation of the sleeve is shown schematically in a wave diagram, Figure 4. The incident shock wave is reflected from the closed annular area between the shock tube and the sleeve. However, the sample comes from the flow established within the sleeve, so that it is unaffected by the reflected shock. The wave reflected in the annular section traverses the length of the sleeve, and when it reaches the open upstream end of the sleeve, a signal is propagated along the interior of the sleeve. The arrival of this signal at the open end of the sleeve terminates the test, for the gas processed by this wave action from the reflected

shock wave is, for our purposes, an unfit sample. Thus, the sleeve length determines the test time, as shown in Figure 4, where the trajectories of the incident and reflected waves are indicated. The test time shown represents a conservative estimate. Note, however, that one is at liberty to select sleeve lengths and diameters to match conditions of temperature and pressure for desired experimental ranges. The sizes and configurations for such matching will be summarized later.

The boundary layer within the sleeve could result in choking of the flow, since the flow Mach numbers are only slightly greater than unity. Only a small reduction in flow cross sectional area can be tolerated. The problem was investigated assuming the least favorable case, that of the steady flow, after the shock wave has passed out the open end of the tube. The main results are shown in Figure 5. The fraction of cross sectional area which remains "available' to the flow is plotted against temperature ratio across the shock front. The curve labelled "Allowable Area Reduction' represents the area reduction which would result in Mach number equal to unity, and therefore choking of the flow. This line serves as the choking criterion. As the temperature ratio (and therefore the Mach number of the flow behind the shock wave) increases, the fraction of original flow area decreases. Curves for various combinations of initial pressure, p_1, sleeve length, ℓ_3, and sleeve diameter, d, are plotted. Satisfactory operation is to be expected for all points above and to the right of the 'allowable'curve. Points below and to the left of the "allowable" curve represent conditions for choking. Some portion of the range of interest may be made accessible by using slightly conical sleeves. The curves plotted in Figure 5 are based on the assumption of ideal monatomic gases. The presence of endothermic processes in the flow behind the shock front, such as dissociation, in general will lead to lower temperatures, and ultimately to higher flow Mach numbers.

The information in Figure 5 underscores the need to match experimental configurations to the flow conditions of the experiment. Indeed, the case of subsonic flow (temperature ratios less than about 3.5) is not included in Figure 5. The estimates of test times appearing in Figure 5 are conservative, based on sleeve dimensions and shock Mach numbers in the range of interest. Effects of attenuation due to boundary layer are included. The test times are somewhat short, but the detection device used has the capability of producing a significant number of readings over these test periods.

From Figure 5, it can be seen that, in general, one should avoid using a sleeve at low initial pressures and low shock Mach numbers. At high temperatures (high shock Mach numbers) and high initial pressures, the sleeve method should prove satisfactory. The regimes of operation are summarized in Figure 6. Since the conditions which result in subsonic flow behind the shock front represent only a very small portion of the whole range of interest, this case has not yet been treated in

detail. The experiment is designed for studies in the range of temperatures from 800°K to 3000°K, and over the pressure range from 2 to 20 cm Hg. Temperatures in excess of about 1050°K result in supersonic flow in the relaxation region. Included in Figure 6 are estimates of test times and mean numbers of collisions suffered by a particle in traversing the distance from the end of the sleeve to the nozzle entrance. Since no collisions with cold surfaces are permitted, there are no heterogeneous contributions to the reactions. In view of these numbers (which correspond to the case of highest initial pressure and temperature) it appears that the sample will be essentially unaffected by additional dissociation, and three-body recombination is even less likely.

Once the sample passes into the supersonic nozzle, it continues to expand, but now in a region of very low back pressure. Precisely where the flow passes from hydrodynamic to free molecular is not well defined. This will occur somewhere within the second nozzle. Thereafter it is collisionless so that no further energy transfer or essential chemical transformations can be effected. Even though the time required for the sample to traverse the distance from the nozzle to ion source is of the order of tens of microseconds, no significant changes in composition take place. Hence the assembly of particles which arrives at the detector should accurately represent the number densities of species in the gas at various stations in the relaxation region. Also shown in Figure [illegible] possible configurations of the extraction device. These remain to be evaluated.

In summary, the events during a test are as follows. The relaxation region behind the shock front expands from the open end of the sleeve. The sample is subjected to a rapid cooling. When the pressure wave reaches the supersonic nozzle the diaphragm covering it ruptures. The flow then expands into a region of very low pressure. These pressure ratios ensure "perfect starting." (10) A second nozzle skims and collimates the flow; this nozzle operates in the continuum regime at hypersonic flow velocities. At some point just beyond the entrance to the second nozzle the flow becomes free molecular. The beam is further defined by the last collimator; the third slit acts merely as a "skimmer."

DESCRIPTION OF THE APPARATUS

The essential units which comprise the shock tube and coupling section are displayed in Figures 7, 8, 9 and 10.

Figure 7 is a section through the dump tank which shows the arrangement of the collimators. The dump tank consists of "nested" coaxial cylindrical tanks. As a design criterion, the volume required for each section of the system was estimated using the upper level of background density which could be tolerated. The mass flow into the tanks was assumed to be distributed uniformly in the volume, during a nominal test time of one millisecond. For the design of the collimating

system we leaned heavily on the work of Skinner et al (3)(5)(11) at Cornell Aeronautical Laboratory. For general discussions of high flux molecular beams, reference is made to the work of Deckers and Fenn (12), Hagena and Bier (13), and Scott and Drewry (14).

Figure 8 is an isometric view of the external dump tank showing the connections to the pumping system. Continuous pumping during a run would not be effective. However, in Figure 9 we indicate a feature which should minimize the problem of rapidly disposing of large quantities of gas. The walls of the intermediate tank and the nozzle baffles are cryopumping panels. Studies at Cornell University by Bauer and Jeffers (15) indicate that cryosorption pumps are effective for removing large quantities of gas in times of the order of milliseconds. Figure 9 also shows schematically the details of the pumping system, and the locations of the main vacuum components.

SUMMARY

The purpose of this program is to devise a method for coupling a transient high density source to the ionization section of a time-of-flight mass spectrometer so that the fidelity of the sample is retained. A free expansion from the open end of the shock tube is used as the source of a molecular beam. The boundary layer gas is drained off, and a beam formed by a series of nozzles and collimators. The sample arrives at the ion source free from effects of cold surfaces, so that its thermal history is known. Quenching of the chemical processes occurs during the initial expansion. In this design, expansion conditions are optimized by matching the details of the expansion and extraction geometry to the conditions of the experiment.

There remain many problems for which we do not pretend to have solutions. Among these are radial mass separation (ref. 16 and 17), and the "freezing in" of excited vibrational states. The latter will produce a fragmentation pattern in the mass spectrometer which may be quantitatively different from that of the calibrating gas. We are cognizant of these and other problems, and hopefully, solutions will be worked out as the study progresses.

ACKNOWLEDGMENTS

The authors would like to thank Professors Turcotte, Seebass and deBoer for many helpful discussions during the course of this work.

The work was supported by the U. S. Air Force Office of Scientific Research, under the contract number AF49(638)-1448, and by the National Aeronautics and Space Administration, under the contract number NsG 116-61

REFERENCES

(1) Bradley, J. N. and Kistiakowsky, G. B , J. Chem. Phys., 35, 256 (1961).

(2) Diesen, R. W. and Felmlee, W. J., J. Chem. Phys., 39, 2115 (1963).

(3) Skinner, G. T., Cornell Aero Lab Report No. RM1396-A-1, October, 1961.

(4) Sturtevant, B., GALCIT Report ONR Contract Nonr 220-21 Task 21, June, 1960.

(5) Skinner, G. T. and Treanor, C. E., Cornell Aero Lab Report No. AD-1118-A-9, December, 1959.

(6) Oman, R. A. and Calia, V. S., Grumman Research Dept. Memorandum RM-240, September, 1964.

(7) Jones, T. V. "The Design of a Shock Tube Driven Aerodynamic Atomic Beam" Oxford University, Department of Engineering Science, January, 1964.

(8) Greene, F. T., Brewer, J., and Milne, T. A., J. Chem. Phys., 40, 1488 (1964).

(9) Lord, W. T., R.A.E., Farnborough Report No. Aero 2626, July, 1959.

(10) Glick, H. S., Hertzberg, A. and Smith, W. E., Cornell Aero Lab Report No. AD-789-A-3, March, 1955.

(11) Skinner, G. T. and Moyzis, J., Phys. of Fluids, 8, No. 3, 452 (1965).

(12) Deckers, J. and Fenn, J. B., Rev. Sci. Instr., 34, 96 (1963). Fenn, J. B. and Deckers, J., Rarefied Gas Dynamics, edited by J. A. Laurmann (Academic Press, Inc., New York, 1963), vol 1, p. 497.

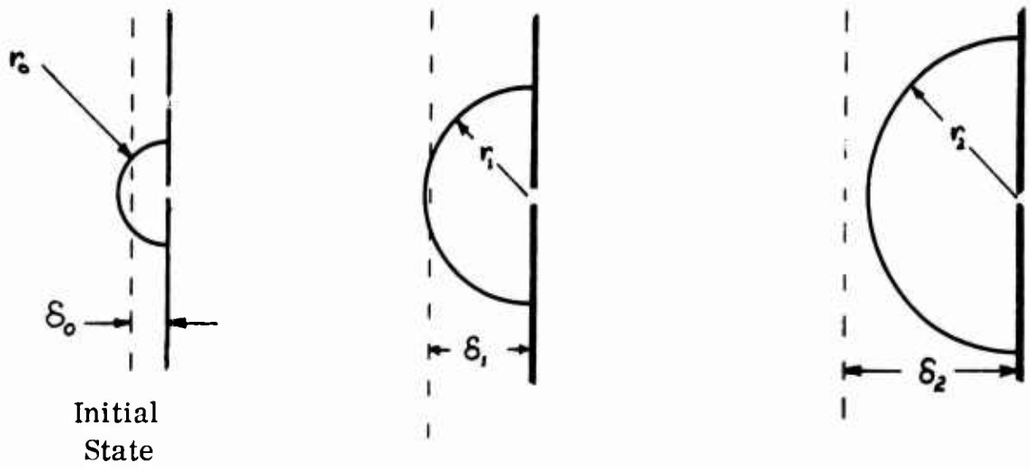
(13) Bier, K., and Hagena, O., Rarefied Gas Dynamics, edited by J. A. Laurmann (Academic Press, Inc., New York, 1963), vol 1, p. 478.

(14) Scott, J. E., Jr., and Drewry, J. E., Rarefied Gas Dynamics, edited by J. A. Laurmann (Academic Press, Inc., New York, 1963), vol 1. p. 516.

(15) Bauer, S. H., and Jeffers, P., Private communication, December, 1964.

(16) Reis, V. H., and Fenn, J. B., J. Chem. Phys., 39, 3240 (1963).

(17) Klingelhofer, R., and Lohse, P., Phys. of Fluids, 7, 379 (1964).



Initial State

$t = t_o$	$t_1 = 10t_o$	$t_2 = 30t_o$
$r_o = 1.56_o$	$r_1 = 3.246_o$	$r_2 = 4.676_o$
$\delta_o = \delta_o$	$\delta_1 = 3.166_o$	$\delta_2 = 5.486_o$

Figure 1(a)

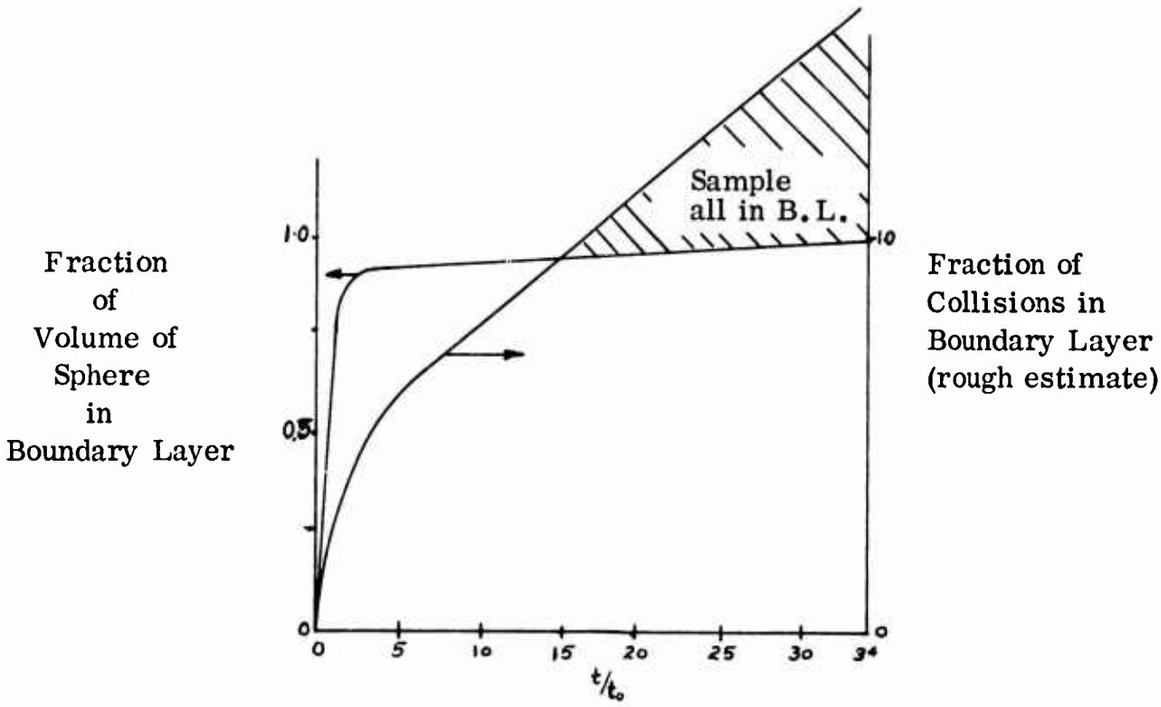


Figure 1(b)

Figure 1 - Effect of Boundary Layer

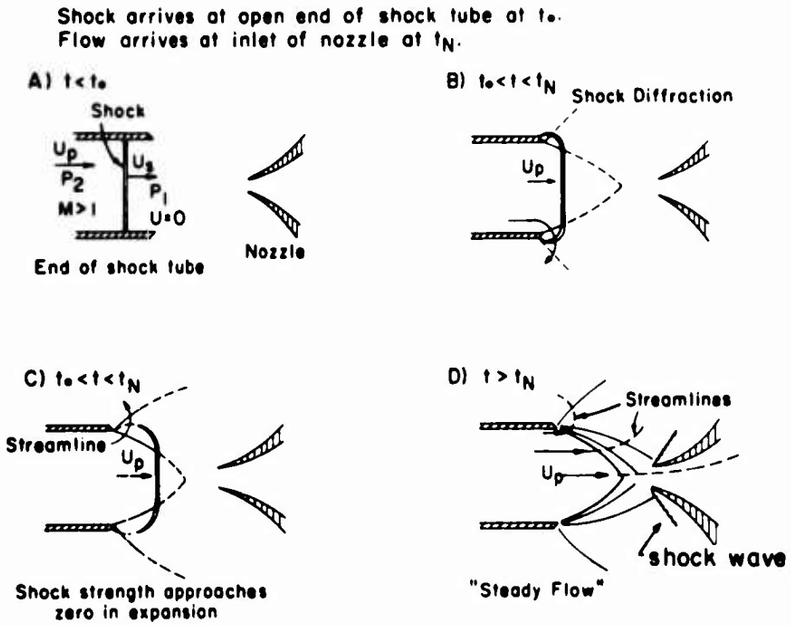


Figure 2 - Initial Expansion

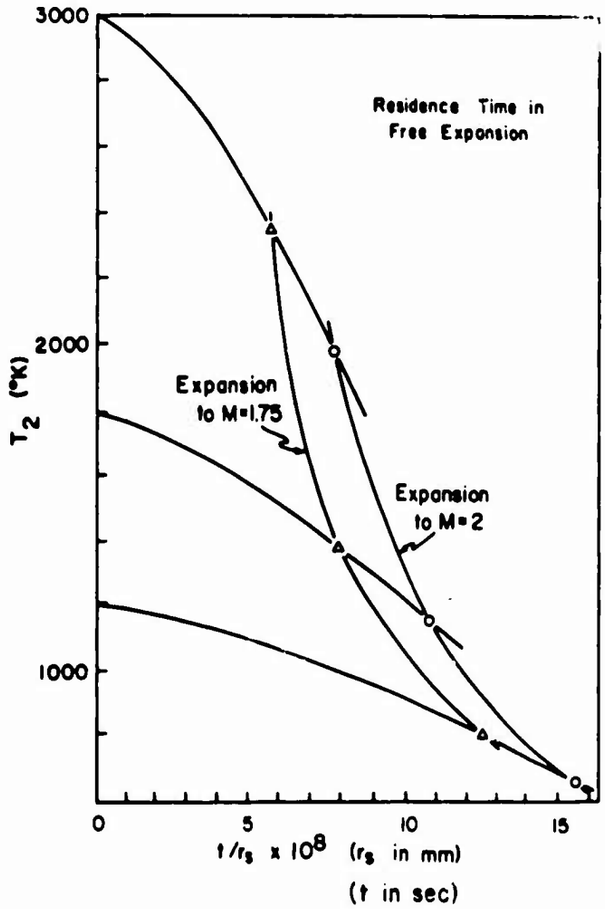


Figure 3 - Residence Time in Free Expansion

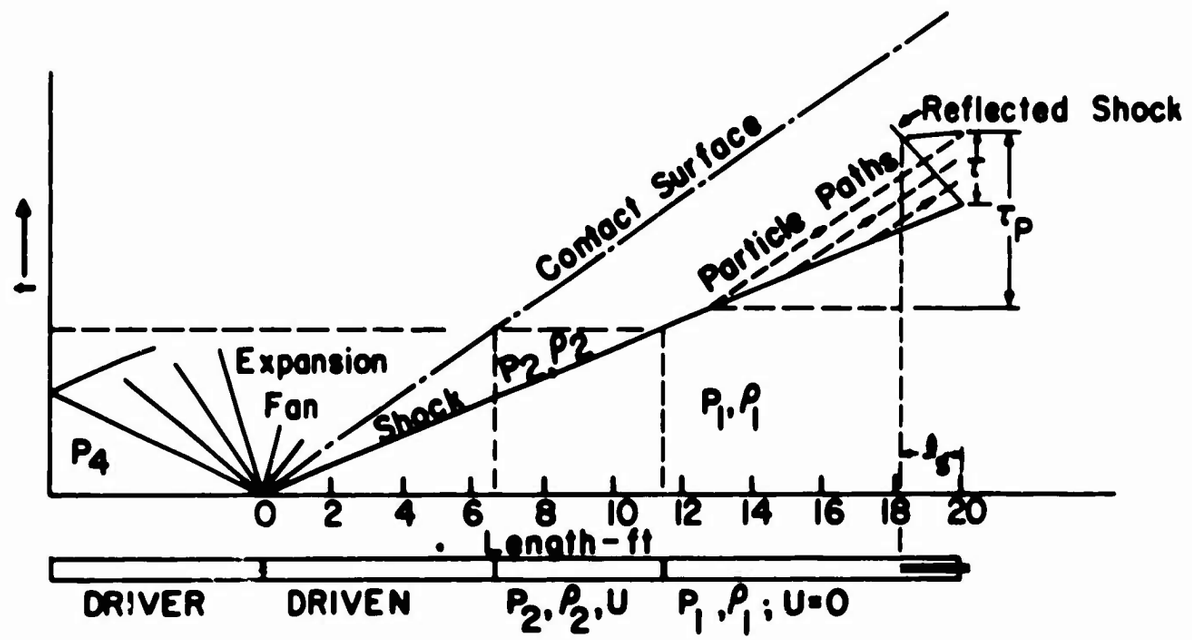


Figure 4 - Wave Diagram

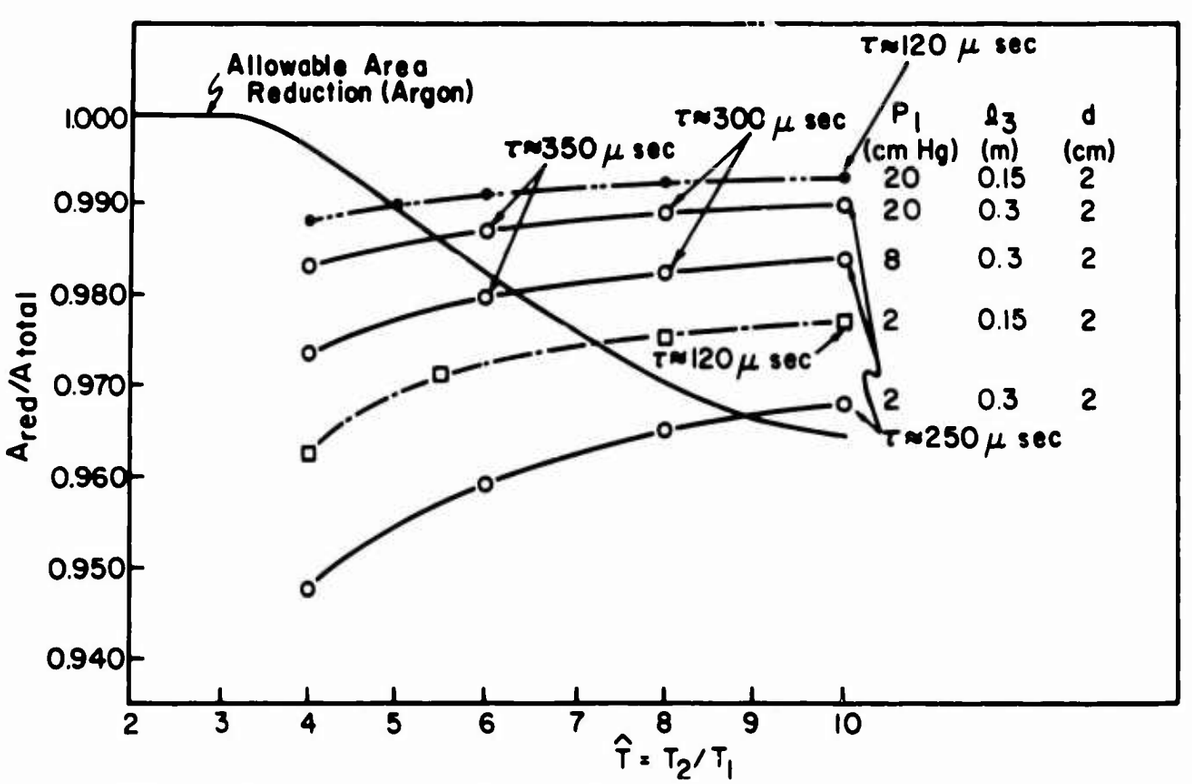


Figure 5 - Results of Sleeve Boundary Layer Calculations

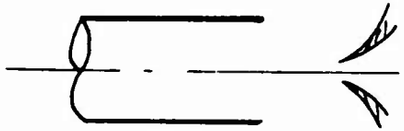
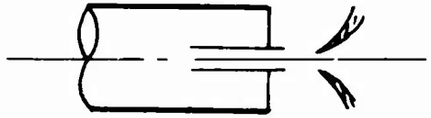
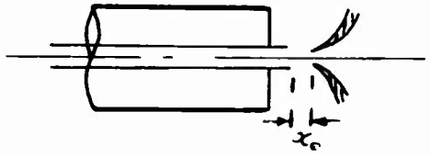
Configuration	x_o	T_2 (°K)	p_1 (cm Hg)	Estimated τ test	Estimated Collisions
	med.	950	2 - 20	1 msec	- -
	large	950 to 1800	2 - 10	500 μsec	3.1×10^3 to 1.7×10^4
	med.	1700 to 2400	2 - 15	300 to 350 μsec	1.5×10^3 to 1.2×10^4
	small	2200 to 3000	> 10	300 μsec	7×10^3 to 1.4×10^4

Figure 6 - Summary of Operating Regimes

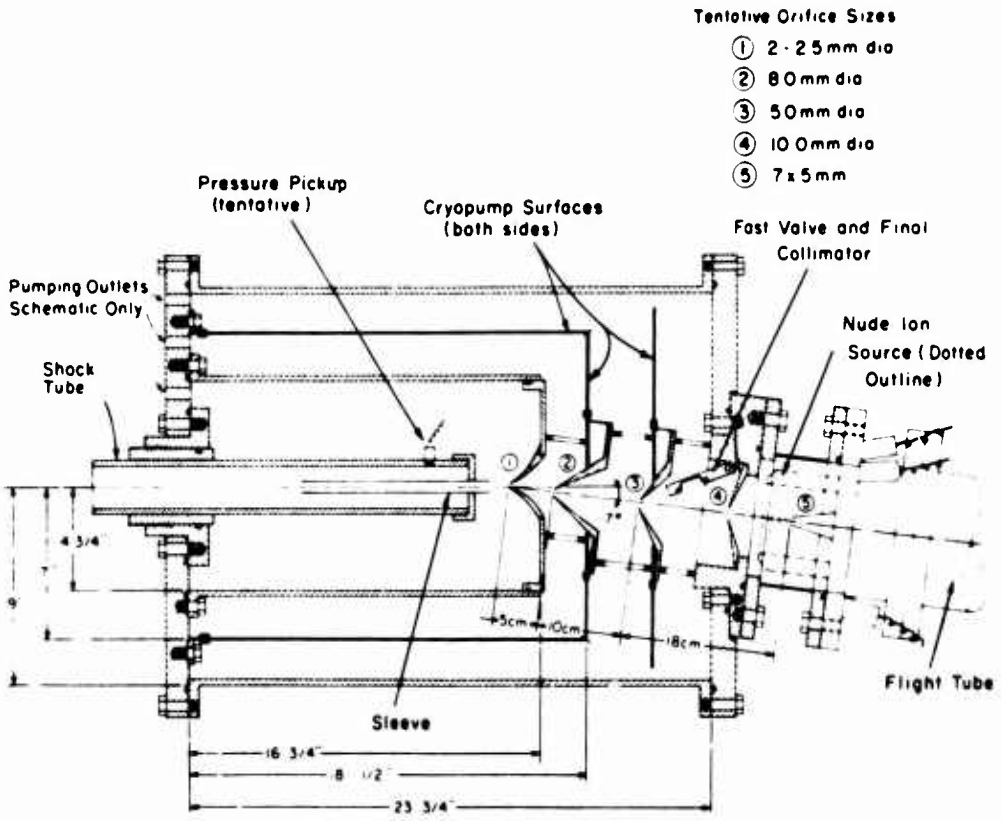


Figure 7 - Section Through Dump Tank

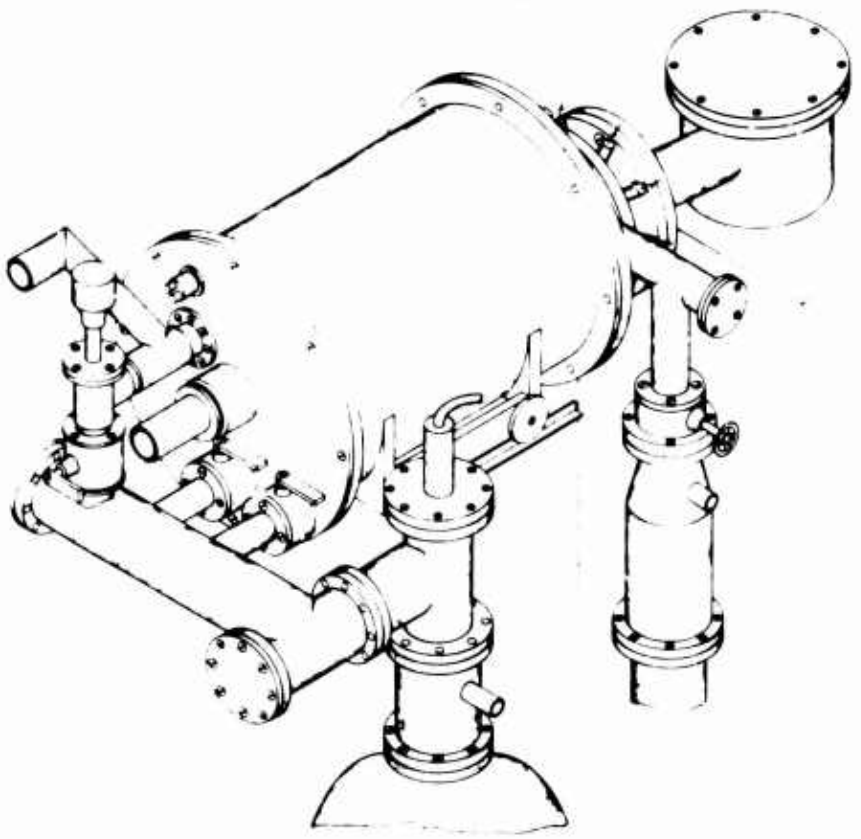


Figure 8 - Isometric View of Dump Tank

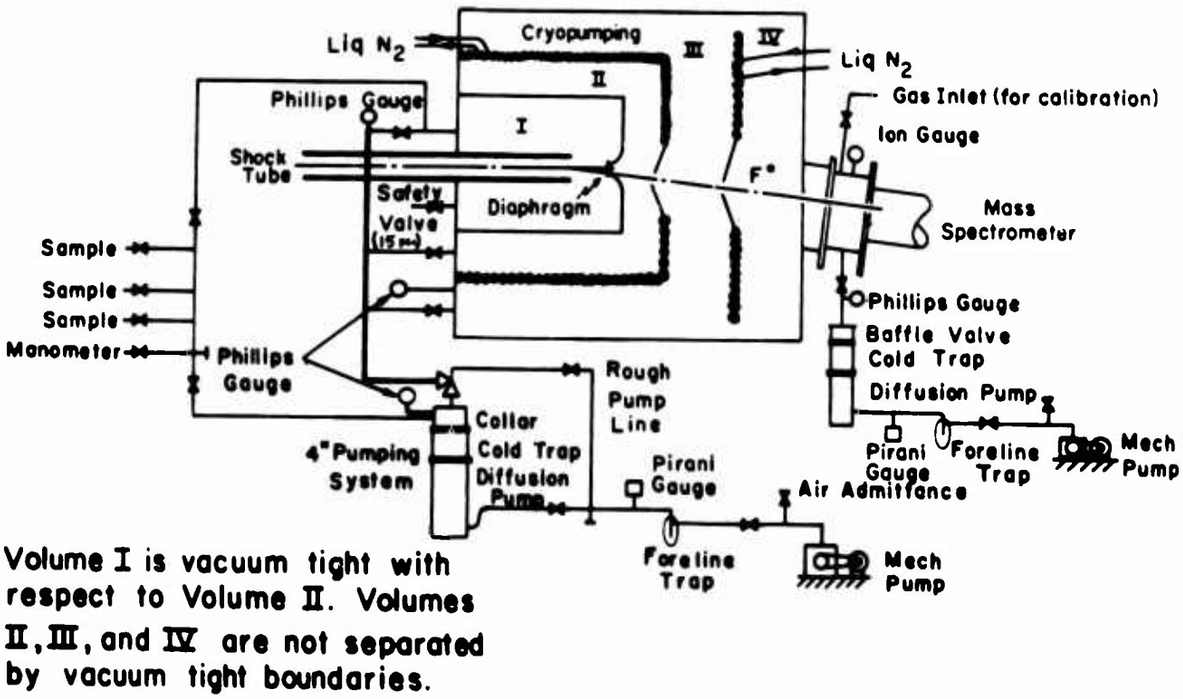


Figure 9 - Schematic of Dump Tank Showing Vacuum System

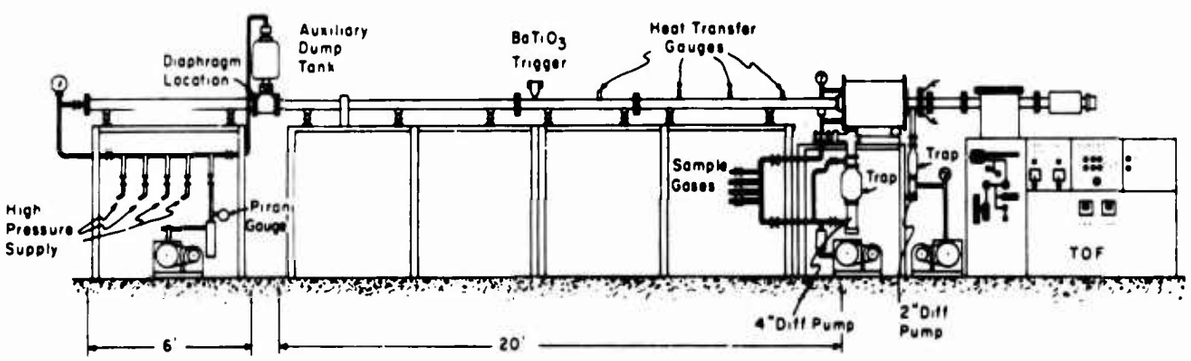


Figure 10 - Arrangement of Shock Tube, Dump Tank and T.O.F. Mass Spectrometer

SHOCKED GAS TEMPERATURE MEASUREMENTS BY INFRARED MONOCHROMATIC RADIATION PYROMETRY

by M. R. Lauver, J. H. Hall, and F. E. Belles
Lewis Research Center
National Aeronautics and Space Administration
Cleveland, Ohio

ABSTRACT

Gas temperature histories in a shock tube were measured by an infrared monochromatic radiation pyrometer technique. A 10 percent carbon dioxide-argon mixture was studied with both incident and reflected shocks. Measured temperatures of 1100° to 3300° K immediately behind the incident shock were in good agreement with the temperatures calculated by one-dimensional wave theory from the shock velocity. Measured temperatures of 1900° to 3550° K behind reflected shocks were in good agreement for short reflection distances with those calculated by one-dimensional wave theory from the incident shock velocity. The relationship between the velocity attenuation and the temperature and pressure rises behind incident shocks was in general agreement with strong shock theory. The change in gas temperature with time behind a reflected shock was adequately calculated from the dissociation rate of carbon dioxide and the measured pressure history of the gas mixture.

INTRODUCTION

The shock tube has found one of its prime applications in the study of high-temperature rate processes in gases. Commonly, these processes have a strong temperature dependence, and it is therefore necessary to know the temperature of the experiment quite accurately. This need can be met nicely so long as incident shock waves are used to heat the gas, because one-dimensional theory, plus the thermodynamic properties of the gas, can be used to calculate the shocked gas temperature from the measured velocity of the wave. Very often, however, it is convenient or even necessary to study processes behind reflected shocks, taking advantage of the higher temperatures and pressures that can be produced without

unduly straining the capacities of conventional shock tubes. In that event, it is no longer so clear that the temperature can be calculated accurately; interactions of the reflected shock with the boundary layer (ref. 1) and with the pressure gradient created by attenuation of the incident shock (ref. 2) introduce complications.

This problem has been widely recognized, and measurements of reflected gas temperature have recently begun to appear in the literature. For the most part they were made by the line-reversal method (refs. 3 and 4), although in one case the rate of a chemical reaction was used as an indication of temperature (ref. 5). The purpose of the present work was to study reflected shock temperatures by a more direct method based on simultaneous measurements of infrared spectral radiance and emissivity. Among the advantages of the infrared method are the following: (1) there is no need to introduce sodium salts or other sources of emission; (2) good time resolution is possible; and (3) a very wide temperature range can be covered, not limited by the available brightness temperature of a light source, as in the reversal method.

This paper reports temperatures measured behind reflected shocks in a gas that is typical of mixtures likely to be used in chemical studies, 10 percent carbon dioxide - 90 percent argon. The temperature range behind reflected shocks was 1900° to 3550° K. A series of temperatures measured at 50 to 200 microseconds after the reflected wave passed the observation station were extrapolated to zero time and compared with values calculated from the velocity of the incident wave. Two detailed temperature-time records are also presented; these show the effects of shock attenuation on both the incident and the reflected shock temperature.

APPARATUS AND EXPERIMENTAL PROCEDURE

Basis of Emission-Absorption Pyrometry

The infrared monochromatic radiation (IMRA) method of gas temperature measurement has been described elsewhere (refs. 6 and 7). It is based on the fact that the radiance of a hot gas depends on the gas temperature and on the number of gaseous entities (molecules, free radicals, or atoms) emitting radiation. Consequently, by measuring the absolute intensity of radiation (spectral radiance) and the relative number density of emitters (spectral emissivity), the temperature of a gas can be calculated. Figure 1 shows schematically the information recorded in a shock-tube experiment and the way in which it is reduced to a temperature measurement.

The measurement of spectral emission is straightforward. The infrared detection system response to the hot gas emission V_g (fig. 1) is compared with its response to a calibrated standard infrared source V_s and converted to absolute units by means of calibration factors. The result is a spectral radiance $N_{\lambda,g}$ in terms of watts steradian^{-1} centimeter^{-2} micron^{-1}

at a specific wavelength. The effect of the number of emitters is accounted for by absorption spectroscopy at the same wavelength. The reduction in signal strength of a chopped transmitted light beam, from V_0 to V volts determines the spectral absorptivity $(1 - V/V_0)$, which is equal to the spectral emissivity ϵ. Kirchoff's radiation law relates the spectral radiance of a hot gas to that of an ideal blackbody radiator. Planck's law relates the spectral radiance of an ideal blackbody radiator to its temperature and emissivity. Combining these laws results in the following relation between the spectral radiance of a gas $N_{\lambda,g}$, its temperature T_g, and its spectral emissivity ϵ:

$$N_{\lambda,g} = \frac{\epsilon C_1 \lambda^{-5}}{e^{C_2/\lambda T_g} - 1} \qquad (1)$$

Thus, inasmuch as C_1 and C_2 are the known Planck radiation constants and $N_{\lambda,g}$ and ϵ are measured at wavelength λ, the gas temperature T_g may be calculated.

Apparatus for Emission-Absorption Pyrometry

A schematic diagram of the shock tube and associated equipment is given in figure 2. A constant intensity of infrared radiation from a glower source is mechanically chopped at 80 kilocycles per second and sent through the sapphire windows of the shock tube into a prism monochromator and a liquid-nitrogen-cooled indium antimonide detector. The shocked gases emit radiation, which passes out of the shock tube into the same radiation detection system. Its output is amplified by a directly coupled circuit providing a measure of the radiance of the gas (the glower radiance is negligible in comparison to that of the gas). The glower signal is selected by a capacitor-coupled, 80-kilocycle tuned amplifier of high gain. With these amplifiers, the detection system uses frequency separation to distinguish between the emitted and transmitted light, although both are presented simultaneously to the one detector, and sends the resulting signals to different oscilloscope beams for recording.

The principle of temperature measurement used in the IMRA technique corresponds to that of the "Two-Path Method with Comparison Source" (ref. 8). An error analysis by Warshawsky (ref. 9) shows large errors for the latter as the gas temperature rises above the glower temperature. The crucial feature of the IMRA apparatus, which minimizes these errors, consists of chopping the glower radiation before it passes through the test gas. This permits the emitted and transmitted components of the radiation to be separated so that each may be amplified independently by the amount required to obtain easily measurable oscillograms. Without chopping, the light from a source that is emitting more weakly than the gas would be swamped by the gas emission.

Calibration of Pyrometer

The IMRA apparatus was calibrated by determining the transmittance of the shock-tube window and the absolute radiance of the internal secondary-standard source (B in fig. 2), which was a tungsten-ribbon lamp.

The window was found to pass 82 percent of 4.5-micron radiation falling on it. This was the wavelength used for the temperature measurements. Although the center of the asymmetric stretching band of carbon dioxide is at 4.3 microns, the longer wavelength is much more desirable. At 4.5 microns, only the hot gas in the shock tube absorbs light, while the cool carbon dioxide in the room and in the shock-tube boundary layer is almost completely transparent.

The internal standard was compared with a source that had been calibrated at the Bureau of Standards. It was found to emit 2.47 watts steradian^{-1} centimeter^{-2} micron^{-1} at 2.2 microns. The relative sensitivity of the optical system and detector at 4.5 and 2.2 microns was then determined by measuring the radiation from a blackbody source of known temperature at the 2 wavelengths.

With the foregoing calibration factors at hand, the absolute spectral radiance $N_{\lambda,g}$, of the hot gas at 4.5 microns is readily determined from the following formula:

$$N_{\lambda,g} = \frac{V_g}{V_s} \frac{1}{R} \frac{1}{t_w} N_{\lambda,s} \qquad (2)$$

where

V_g amplitude of emission signal at 4.5μ, V

V_s amplitude of signal from internal standard source at 2.2μ, V

R sensitivity of the system at 4.5μ relative to that at 2.2μ

t_w transmittance of shock-tube window at 4.5μ

N_s absolute spectral radiance of internal standard at 2.2μ

This formula is valid provided the amplification and the slit width are the same when both V_g and V_s are recorded. If they are not the same, the appropriate correction terms must be applied.

Shock Tube

The shock tube was of rectangular cross section, 37 by 74 millimeters. Two circular sapphire windows, 28 millimeters in diameter, were

flush mounted opposite one another across the longer dimension. The midpoint of the windows was 3.94 meters from the polyester plastic diaphragm that separated this driven section of the shock tube from the driver section. The midpoint of the windows was 179 millimeters from the downstream end wall of the driven section. This distance to the end wall could be reduced to 27 or 78 millimeters by means of close-fitting plugs. The diaphragms were pressure-burst with helium.

Timing, Pressure, and Recording Instrumentation

Four thin-film resistance gauges were mounted upstream of the windows, while one was mounted at the same axial position as the centerline of the windows. These gauges marked the time of incident (and in some cases, reflected) shock arrival at the five positions, relative to the first, or trigger, position. The signals were displayed on one beam of a dual beam oscilloscope. The other beam displayed the output of a quartz pressure transducer. This transducer was also located at a position corresponding to the centerline of the windows. A second dual-beam oscilloscope was triggered to display absorption and emission levels from the gas as measured by the IMRA apparatus. Timing pulses from a crystal-controlled secondary frequency standard were recorded on all four oscilloscope beams for each run. A calibration signal for the emission level interrupted about 1100 times per second for identification and a calibration signal for the pressure were also recorded each time.

Figure 3 shows the oscillograph records of infrared absorption and emission for a single experiment. The important features of this typical record are: (1) The large changes of transmitted and emitted light upon passage of the shock waves, (2) the relatively noise-free signals; and (3) the quick recovery of the tuned amplifier in the absorption channel from the ringing induced by step changes, which permits meaningful readings to be made starting at about 50 microseconds after passage of the shock.

It will be noted in figure 3 that the gas behind the reflected shock in this particular run absorbed almost all of the radiation from the glower source. In many runs of this sort, the portion of the absorption trace after the reflected shock was simultaneously displayed on another oscilloscope at much higher gain, so that the absorptivity could be accurately determined.

Test Gas

A commercially prepared argon-carbon dioxide mixture was used without further treatment. It analyzed 9.9 percent carbon dioxide by volume; the rest was argon. A few tests were made with this gas diluted to 6.7 percent carbon dioxide in argon and with a commercially prepared argon-carbon dioxide mixture that analyzed at 1.1 percent carbon dioxide and the balance, argon.

RESULTS AND DISCUSSION

The results of determinations of gas temperatures behind incident shocks are presented in figure 4, where they are compared with temperatures calculated by simple shock theory from measured shock velocities. The IMRA temperatures were actually measured at several 10-microsecond intervals for each experiment, starting at about 50-microsecond laboratory time when the signals first became readable. Each point in figure 4 was obtained by extrapolating such data back to time zero, the instant when the shock passed the center of the windows. This was done to eliminate effects of shock velocity attenuation on the temperature.

The agreement is good, and as expected, does not seem to be affected by the carbon dioxide concentration over the range studied. Despite this general agreement between measured and calculated incident temperatures, there is nevertheless a good deal of scatter evident in figure 4. Part of this scatter is traceable to contamination of the shock-tube windows, but most of it is due to a drifting type of instability of the infrared detector. From run to run, this instability produced uncertainties as large as 10 percent in $N_{\lambda,g}$. Equation (1) shows that this error results in an uncertainty of only about 30° K at temperatures near 1000° K, but the error grows to nearly 300° K at temperatures near 4000° K.

Inasmuch as the main purpose of the work was to measure reflected shock temperatures at levels above 2000° K, it was desirable to reduce the expected scatter in the results as much as possible. This was done by using the incident shock wave as an internal standard for each run. The temperature calculated from the measured shock velocity at the window position, and the measured emissivity of the gas behind the incident wave, were both assumed to be correct. The value of spectral emission $N_{\lambda,g}$ required to satisfy equation (1) was then calculated. This value, and the measured voltages V_g (incident shock) and V_s, were inserted in equation (2) and used to calculate a lumped instrument factor, $(1/R)(1/t_w)N_{\lambda,s}$.

In each run, then, this individually determined factor was used to convert measured voltages into a series of reflected shock temperatures, starting at about 50 microseconds behind the shock and determined at approximately 10-microsecond intervals. These data were extrapolated to time zero, the instant the reflected shock passed the center of the windows. The resulting measured temperatures are plotted as ordinates in figure 5; the abscissas are the corresponding reflected temperatures graphically (ref. 10) calculated from the velocity of the incident shock as it passed the windows.

Clearly, this means of obtaining calculated reflected shock temperatures for comparison with measured values is rather arbitrary. Its most obvious shortcoming is that it does not allow for the attenuation of the incident wave. However, it is important to see how well the temperatures calculated in this simple way agree with the measured values. Figure 5 shows that they agree surprisingly well. The points obtained with the

end wall at its most remote position, 179 millimeters from the windows, tend to be high, and those obtained with the end wall 78 millimeters away tend to be low. This behavior is not inconsistent with that noted in reference 11, which reported that the reflected shock pressure behaved as if the shock decelerated and then accelerated as it receded from the end wall. But in a grosser sense, the agreement between measured and simply calculated temperatures is very gratifying. Of the 27 measurements shown in figure 5, 14 are within 100° K of the line, and only 4 miss it by more than 200° K. It is, however, believed that deviations larger than 100° K are real and that they reflect actual departures of the shocks from ideal one-dimensional behavior. The two extreme points in figure 5 represent data of which the reflected portions could be accurately measured but of which the incident portions could not. These two points were therefore calculated with the original calibration factors rather than an individually determined factor such as was used for each other point. They are included to extend the temperature range of the reflected data and to indicate that the individual calibration corrections were usually small.

An example of the detail, which it is possible to obtain by the IMRA method, is given in figure 6, where the temperature history of a shock is followed at 10- to 20-microsecond intervals for 700 microseconds after its passage. Measurement of the incident shock wave velocity U at four successive places just before arrival at the test window showed the velocity to be attenuating at the rate of 1.5×10^{-4} (millimeters per microsecond) per millimeter. Therefore, $dU/U = 1.5\times10^{-4}$ for a 1-microsecond interval. Strong shock theory predicts the relation $2\ dU/U = dT/T = dP/P$. Therefore, in the first 200 microseconds after the passage of the incident shock, the temperature would be expected to rise from 1310° K (calculated from shock velocity) to about 1388° K and the pressure P from 1.76 to about 1.87 atmospheres. The IMRA measurements showed this rise approximately, as indicated by their conformity to the incident theory line in figure 6. The pressure rose to 1.90 atmospheres, or $(dP/P) = 3.8\times10^{-4}$, also showing good agreement with the prediction.

Other observers (ref. 2) have noted a rise in pressure behind reflected shocks. This pressure rise, converted into an isentropic temperature change by the equation $T = (P/P_o)^{(\gamma-1)/\gamma} T_o$, corresponds very well with the infrared pyrometer results of figure 6 where γ is the ratio of specific heats and T_o is the reflected shock temperature calculated from incident shock velocity.

A second example of detailed analysis is presented in figure 7. Here the temperature following the passage of the reflected shock tends to rise, because of isentropic compression, and tends to decrease because of dissociation according to the equation

$$CO_2 \rightarrow CO + \frac{1}{2} O_2, \quad \Delta H = 65.8 \text{ kilocalories}$$

(The rate of oxygen atom recombination is sufficiently high so that the concentration of O_2 is much greater than that of O at this temperature.) The following were used to make theoretical temperature calculations: (1) 2.9×10^7 cubic centimeters $mole^{-1}$ $second^{-1}$ $^oK^{-1}$ for the dissociation rate of carbon dioxide, calculated for 3220° K from the expression given in reference 12, and for the subsequent temperatures after the reflected shock-wave passage, (2) the isentropic temperature corrections from the measured pressures, and (3) negligible back reaction of the carbon monoxide and oxygen to form carbon dioxide. As with the simpler case of figure 6, the agreement of theory and results is gratifying. In this case, figure 7, the attenuation comparisons behind the incident shock are $dU/U = 2.6 \times 10^{-4}$, $dP/P = 4.3 \times 10^{-4}$, and $dT/T = 3.4 \times 10^{-4}$.

CONCLUSIONS

1. Infrared pyrometry of a carbon dioxide-argon gas mixture yielded incident shock temperatures in agreement with those calculated from the incident shock speed by common shock theory, from 1100° to 3300° K.

2. A comparison of reflected shock temperatures measured 27, 78, and 179 millimeters after reflection with temperatures calculated from one-dimensional shock theory shows the latter are generally good for short distances after reflection.

3. Attenuation of the speed of an incident shock wave was accompanied by changes in the gas pressure and temperature in the period following the passage of the shock. The relations between these changes were in general agreement with strong shock theory.

4. The change in gas temperature with time after a reflected shock was adequately calculated from the dissociation rate of carbon dioxide and the pressure history of the gas mixture.

REFERENCES

(1) Mark, Herman: The Interaction of a Reflected Shock Wave with the Boundary Layer in a Shock Tube. NACA TM 1418, 1958.

(2) Rudinger, George: Effect of Boundary-Layer Growth in a Shock Tube on Shock Reflection from a Closed End. Phys. Fluids, vol. 4, no. 12, Dec. 1961, pp. 1463-1473.

(3) Napier, D. H.; Nettleton, M.; Simonson, J. R.; and Thackeray, D. P. C.: Temperature Measurement in a Chemical Shock Tube by Sodium-Line Reversal and C_2 Reversal Methods. AIAA J., vol. 2, no. 6, June 1964, pp. 1136-1138.

(4) Hurle, I. R.; Russo, A. L.; and Hall, J. Gordon: Spectroscopic Studies of Vibrational Nonequilibrium in Supersonic Nozzle Flows. J. Chem. Phys., vol. 40, no. 8, Apr. 15, 1964, pp. 2076-2089.

(5) Johnson, Charles D.; and Britton, Doyle: Shock Waves in Chemical Kinetics: The Use of Reflected Shock Waves. J. Chem. Phys., vol. 38, no. 7, Apr. 1, 1963, pp. 1455-1462.

(6) Tourin, Richard H.: Monochromatic Radiation Pyrometry of Hot Gases, Plasmas, and Detonations. Temperature - Its Measurement and Control in Science and Industry. Vol. 3, pt. 2, ch. 43, C. M. Herzfeld, ed., Reinhold Pub. Corp., 1962.

(7) Tourin, Richard H.; Hecht, Maynard L.; and Dolin, Stanley A.: Measurement of Gas Temperatures in Thermal Pulses by Monochromatic Radiation Pyrometry. Pt. 2 of Measurement of Temperatures in Ionized Gases by Means of Infrared Radiation, Warner & Swasey Co., May 1961, pp. 43-68.

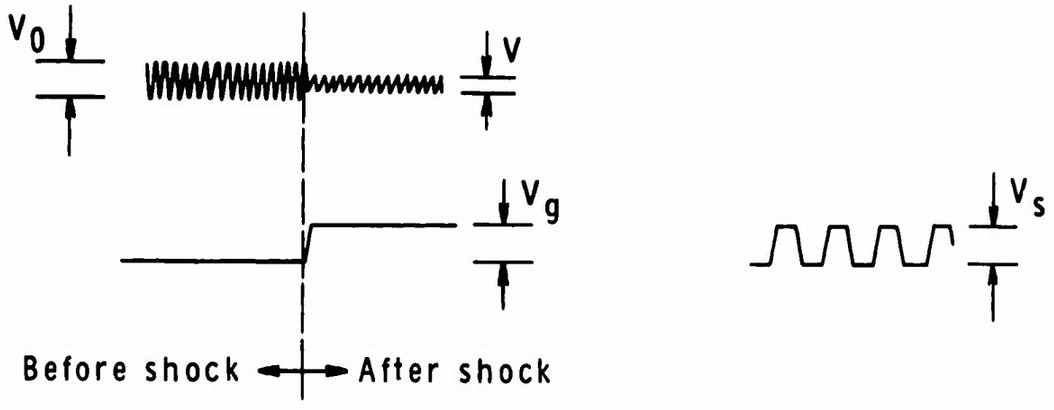
(8) Broida, H. P.: Experimental Temperature Measurements in Flames and Hot Gases. Temperature - Its Measurement and Control in Science and Industry. Vol. 2, Ch. 17, Hugh C. Wolfe, ed., Reinhold Pub. Corp., 1955.

(9) Warshawsky, I.: Measurement of Rocket Exhaust-Gas Temperatures. ISA J., vol. 5, no. 11, Nov. 1958, pp. 91-97.

(10) Markstein, George H.: Graphical Computation of Shock and Detonation Waves in Real Gases. ARS J., vol. 29, no. 8, Aug. 1959, pp. 588-590.

(11) Brabbs, Theodore A.; Zlatarich, Steven A.; and Belles, Frank E.: Limitations of the Reflected-Shock Technique for Studying Fast Chemical Reactions. J. Chem. Phys., vol. 33, no. 1, July 1960, pp. 307-308.

(12) Brabbs, Theodore A.; Belles, Frank E.; and Zlatarich, Steven A.: Shock-Tube Study of Carbon Dioxide Dissociation Rate. J. Chem. Phys., vol. 38, no. 8, Apr. 15, 1963, pp. 1939-1944.



1. Emissivity ε = absorbtivity = $1 - (V/V_0)$

2. Radiance $N_{\lambda,g} = \varepsilon C_1 \lambda^{-5}/(e^{C_2/\lambda T} - 1)$ CS-35672

Figure 1. - Basis of infrared monochromatic radiation pyrometer.

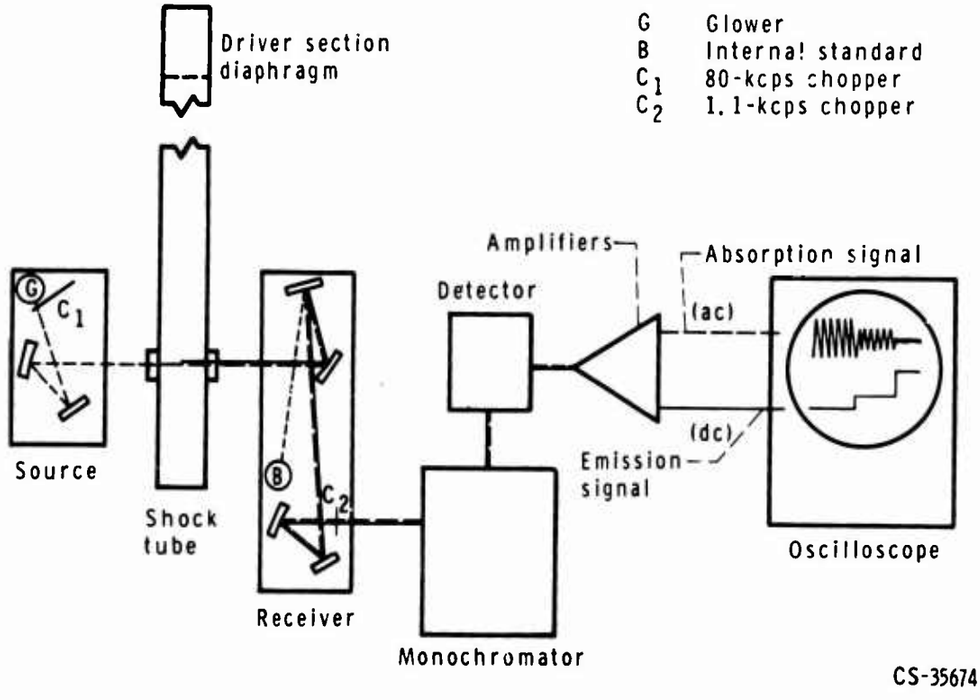


Figure 2. - Schematic diagram of infrared monochromatic radiation pyrometer.

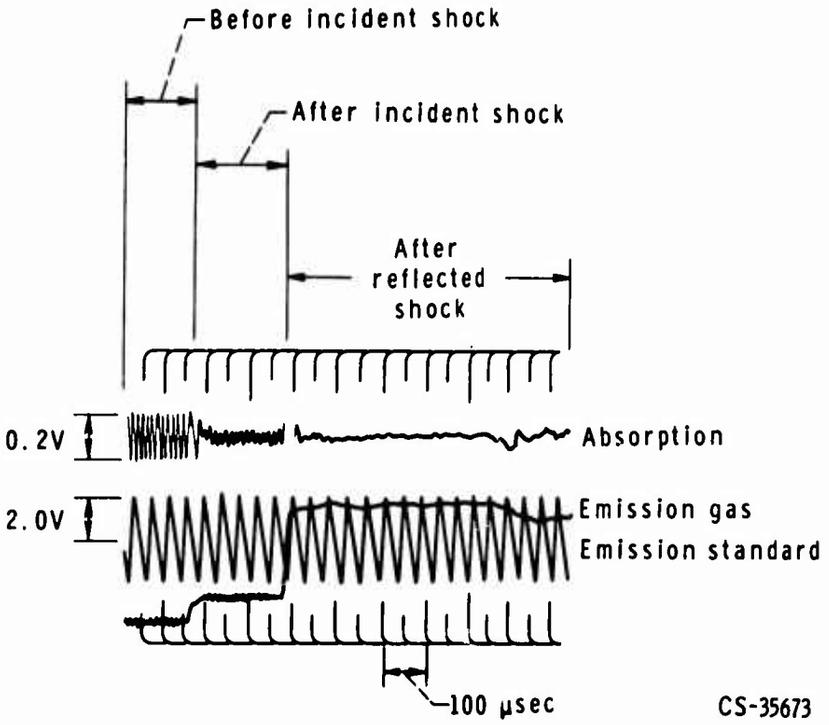


Figure 3. - Typical infrared radiation oscillogram.

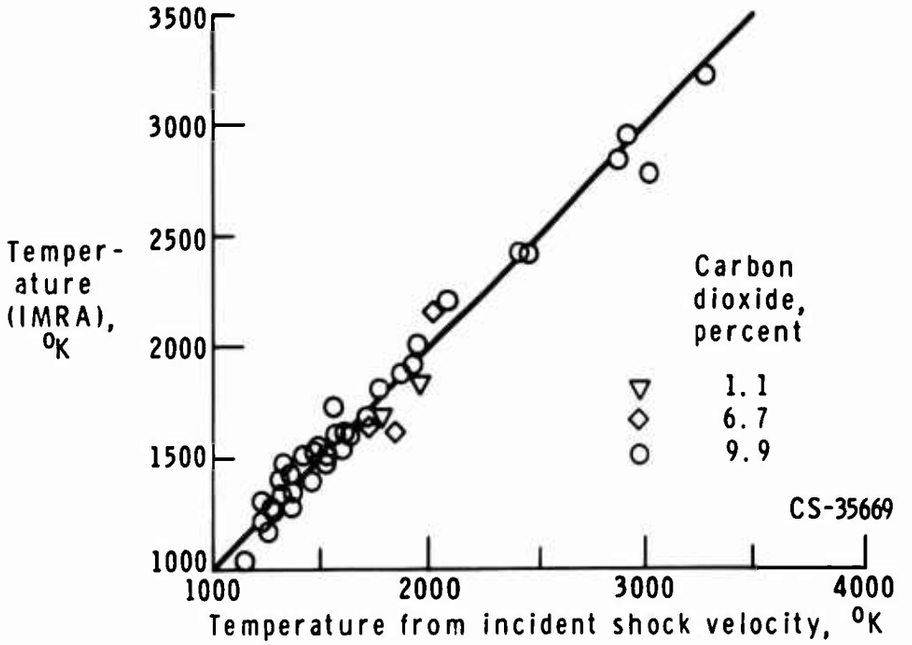


Figure 4. - Comparison of measured and calculated temperatures behind incident shocks in carbon dioxide - argon.

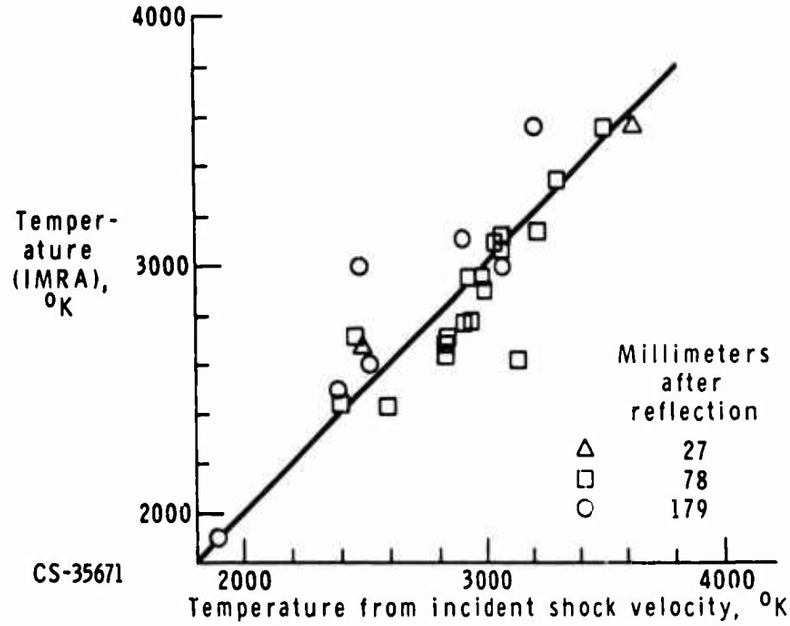


Figure 5. - Comparison of measured and calculated temperatures behind reflected shocks in carbon dioxide - argon.

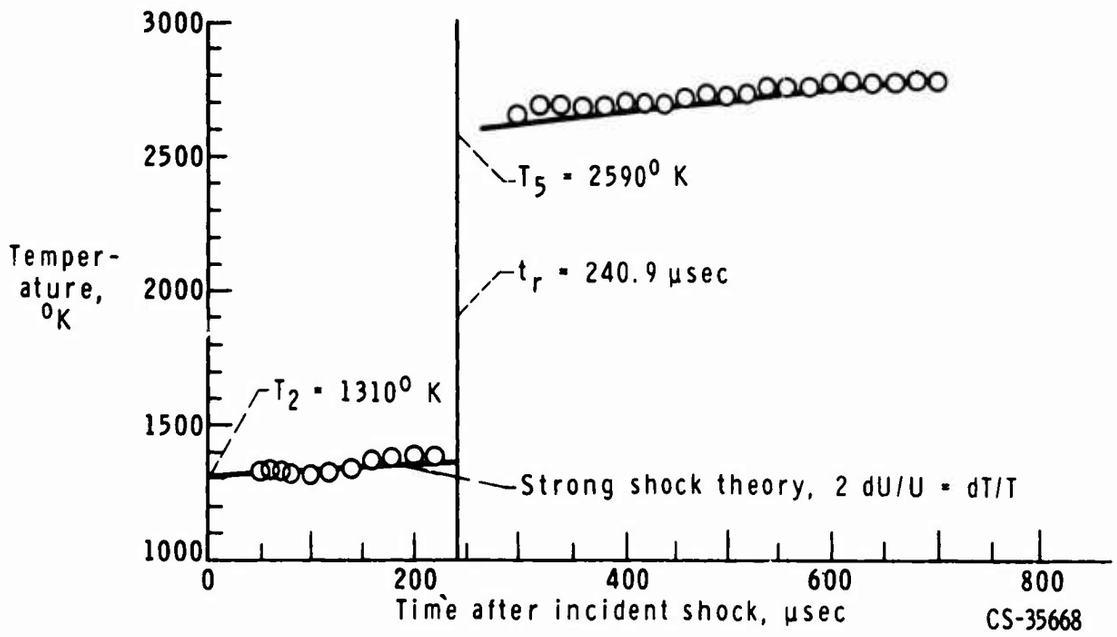


Figure 6. - Experimental and calculated temperatures behind shock waves in carbon dioxide - argon. P_1 = 51.0 Torr; incident Mach number, 3.64.

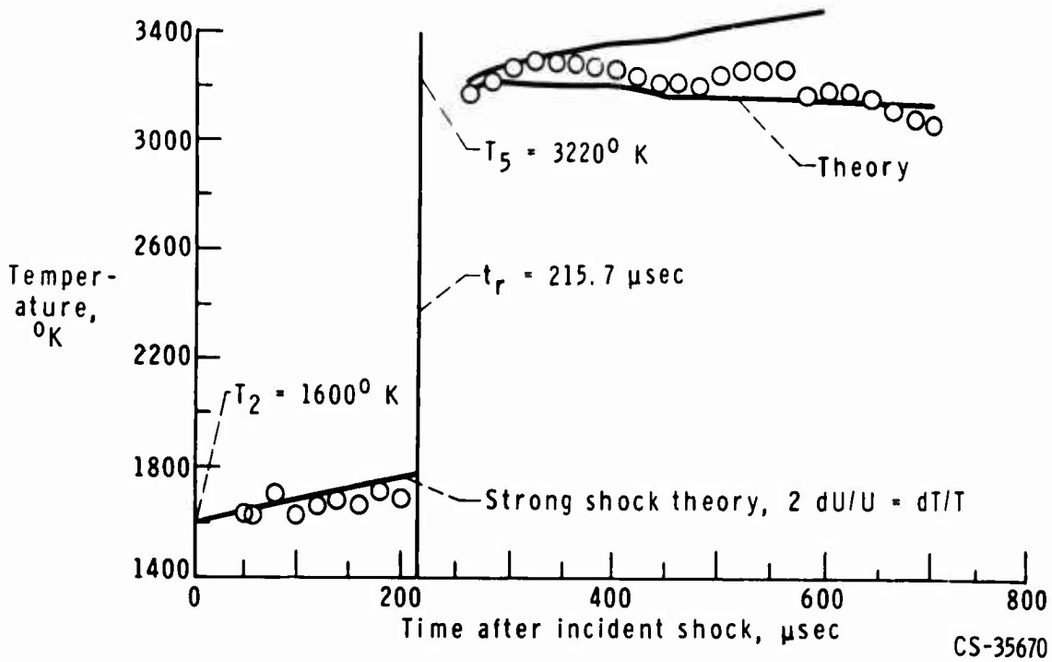


Figure 7. - Experimental and calculated temperatures behind shock waves in carbon dioxide - argon. P_1 = 51.0 Torr; incident Mach number, 4.09.

BLANK PAGE

NEW VACUUM ULTRAVIOLET AND INFRARED INSTRUMENTS FOR TIME-RESOLVED SPECTROSCOPY*

John C. Camm and Raymond L. Taylor
Avco-Everett Research Laboratory
Everett, Massachusetts

ABSTRACT

An Ebert infrared spectrometer has been built which scans a wavelength region of 0.6 μ at a constant scanning rate of .02 μ per μ-sec. The scanning is accomplished by spinning a rotatable aluminum mirror, placed 2 inches before the exit slit, by discharging a capacitor through a coil placed around the mirror. The mirror attains constant angular velocity in 15 μ-sec. Simultaneously with the spectral data, a wavelength scale is obtained from photoelectrically generated signals which indicate the position of the rotating mirror during scanning. The instrument is useful from 1.5 to 5.5 microns using an indium antimonide detector. A vacuum ultraviolet drum camera spectrograph using a concave diffraction grating has also been built. The film is carried on the outside of a drum driven by an electric motor and can attain a maximum speed of .07 mm per microsecond. The 12.7 mm wide film provides a wavelength range of 0 to 4400 Å. The designs, performance, and use of these instruments for shock tube radiation measurements is discussed.

INTRODUCTION

The shock tube has become a powerful tool for the study of the radiation properties of high temperature gases. In such measurements it is usually desireable, if not necessary, to obtain spectra of the shock heated gas in order to identify the radiating species. For identification purposes spectra that are continuous in wavelength are superior to discontinuous spectra such as those produced with a multichannel spectrometer. Furthermore, since test times in high performance shock tubes are often as short

*This work has been supported jointly by Advanced Research Projects Agency monitored by the Army Missile Command and the Air Force Weapons Laboratory.

as 5 μsec, the spectra must be time resolved in order to clearly separate the radiation from the gas under study from the radiation from the driver gas. To provide time resolution spectrographs are equipped either with rotating drum cameras or synchronized high speed shutters. Drum camera spectrographs are usually preferred because they provide spectra continuous in time and need not be synchronized. The advantages of shutters are that they permit multiple exposures for weak sources, and comparison spectra may be placed alongside the shock tube spectrum for qualitative or quantitative purposes.

At the Avco-Everett Research Laboratory spectral radiant intensity measurements in air and its component gases, oxygen and nitrogen, have been made from 0.3 to 7.0 μ using a variety of conventional single or multiple channel spectrometers for quantitative work. For qualitative studies and identification purposes, spectrographs equipped with drum cameras or high speed shutters have been used.[1-5]

In the present paper, two new instruments are described which extend the capability of obtaining time resolved spectra both into the vacuum ultraviolet region and into the infrared beyond the range of current photographic emulsions. These instruments are described, and sample data obtained using these instruments to measure the radiation from shock heated gases are presented.

VACUUM ULTRAVIOLET DRUM CAMERA SPECTROGRAPH

As the interest in re-entry phenomenology has moved to constantly higher flight velocities to provide data for satellite, lunar, and planatary re-entries, the interesting spectral region for air radiation studies has in turn shifted to shorter wavelengths. An instrument to provide such measurements compatible with the appropriate shock tube facility is the drum camera spectrograph shown schematically in Fig. 1. The spectrograph employs a concave grating ruled with 75 lines per mm and blazed at 1000 Å. Mounted on a shock tube as shown in Fig. 1 using a lithium fluoride window, the instrument is useful down to about 1100 Å, being limited by the transmissivity of Li F. The effective speed is f/14, and the plate factor is about 300 Å/mm. With an entrance slit of 10 micron width the spectral resolution of the instrument is about 3 Å.

The film is carried on the outer circumference of a drum by using adhesive transfer tape. This technique has been used successfully at drum speeds up to 200 rps, giving linear film speeds of 0.07 mm/μsec. With a nominal slit height of 0.5 mm time resolution of about 7 μsec has been possible, which is somewhat shorter than the test time expected in the experiments for which the instrument was designed. The drum and its electric motor are both contained within the instrument housing which is purged with a non-absorbing gas such as nitrogen or helium.

As can be seen in Fig. 1, the distance from the focal plane to the grating was made less than the distance from the entrance slit to the grating. The angle of incidence and the angle of diffraction are thereby minimized, reducing the astigmatism. Also seen in Fig. 1 is the shock tube test section used for observation behind the reflected shock. This "cookie cutter" technique has been described elsewhere.(6)

Typical spectrograms obtained using this spectrograph to record the radiation from reflected shocks in a 6-inch diameter electrically driven shock tube are shown in Fig. 2. The initial pressure was 1 torr and the incident shock speed 8 mm/μsec for all the spectrograms. The first three spectra were obtained using a nitrogen purge and the last using a helium purge. The first spectrum is of shock-heated oxygen at an equilibrium temperature of 18,000°K. Several of the radiating species are identified including emission lines from nitrogen impurity. In the last three spectra, which are of shock-heated nitrogen and air, the nitrogen lines appear quite strongly. The Lyman-Birge-Hopfield system appearing in absorption in the first three spectrograms is due to the absorption from the purging nitrogen in the spectrograph. The last air spectrum was obtained using a helium purge; therefore it does not show the Lyman-Birge-Hopfield absorption spectrum common to the other three. In its place we find a continuum and more nitrogen emission lines. On the left edge of the third spectrogram a time scale, which is the same for all spectra, is presented showing time after the first detectable radiation appears. Since the clean test time for these shock conditions is about 10 μsec, the desired spectrum is recorded before the highly luminous driver gas arrives at the window.

This drum camera spectrograph is currently being used to survey the radiation from shock heated air and its component gases in the wavelength region of 1100 - 3000 Å at temperatures of about 12,000 to 20,000°K to identify and evaluate radiating sources.(7)

SYNCHRONIZED HIGH SPEED INFRARED SCANNING SPECTROMETER

Infrared spectra of high temperature gases may be obtained in continuous test facilities, such as arcs, by using simple scanning spectrometers. However, with shock tube sources the short test time available makes it necessary to scan rapidly and to synchronize the scan with the arrival of the shock at the test section. A high speed scanning spectrometer that attains a constant scanning rate 15 μsec after triggering has been built. Used with modern, fast-response infrared detectors and a rather coarse grating, it is possible to scan appreciable portions of the infrared spectral region in times compatible with shock tube experiments.

The synchronized high-speed scanning infrared spectrometer consists of an Ebert-type monochromator with a scanning mirror placed 2 inches before the exit slit, as is shown schematically in Fig. 3. The aluminum scanning mirror is spun by the magnetic field created when a charged capacitor is discharged through a coil surrounding the mirror.

The mirror axis is pre-set at an angle of 45° with the coil axis before the capacitor is discharged. Using a 5.8-cm-square, plane grating ruled with 10 lines per mm and blazed at 3.5 μ, a constant scanning rate of .02 μ per μsec is reached 15 μsec after triggering. The exit slit is defined by the detector element which consists of a Philco indium antimonide detector 0.3 mm wide by 5.0 mm high. The combination of linear dispersion and detector width provide an optical resolution of about 0.07 μ. To provide an optimum signal to noise ratio, the response time of the detector and its associated electronics have been set at about 2.5 μ-sec, consistent with the optical resolution and scanning rate. With the InSb detector the spectral sensitivity of the instrument extends from about 1.9 - 5.5 μ.

A wavelength calibration during each scan is provided by a wavelength calibration signal generator shown schematically in Fig. 4. A line radiation source is focused onto a grid after being reflected twice from the back side of the scanning mirror. As the scanning mirror rotates the image of the line source moves across the grid producing a train of pulses from a photomultiplier positioned behind the grid. The signal from the wavelength calibration signal generator is recorded simultaneously with the spectrometer signal on a dual beam oscilloscope. A typical wavelength calibration oscillogram is shown in Fig. 5 on the middle two traces. The wavelength corresponding to the central peak of the wavelength calibration signal is the nominal wavelength set by positioning the grating, and the wavelength interval between the small peaks is .0224 μ. With this information, we may construct a wavelength scale such as that shown in the figure.

Figure 5 also shows the data obtained in measuring the radiation from a reflected shock in air where the temperature was 7800°K. The lower trace shows the signal from a monitor infrared-sensitive photomultiplier which viewed the reflected shock 2 cm from the end of the shock tube. The monitor trace was triggered 80 μsec before the incident shock struck the end of the tube so as to present a long radiation history. The other three traces were triggered just as the monitor trace brightened and the spectrometer was triggered 3 μsec later. The monitor trace shows that the reflected shock arrived at the test station 32 μsec after the shock struck the end plate. Therefore, we see that the abrupt rise in the scanning signal is due to the arrival of the shock and is not a spectral feature. The remainder of the trace may be reduced to a spectral intensity curve by applying an absolute calibration curve and a correction factor to account for the vignetting caused by the rotation of the scanning mirror.

The absolute spectral sensitivity curve, shown in Fig. 6, was determined using a 1000°K blackbody and a 1.9 μ and a 2.8 μ cut-on filter to eliminate higher orders. The linearity of the detector and electronics were also checked by varying the source temperature. The vignette correction, Fig. 7, was determined in two ways. First, an absolute spectral sensitivity curve was determined with the mirror held fixed at its 45° position, using the blackbody source. This static calibration curve could then be compared with scans of the same source. The ratio of the two signals at the same wavelength is just the vignetting correction. The correction

factor can also be obtained from purely dynamic data by making scans of the same source at slightly different nominal wavelengths. The ratio of the signals at the 45° position of each scan, the central peak of the wavelength calibration signal, to the signal at the same wavelength on another scan where the central peak has been shifted to a new wavelength is again the vignetting correction. As seen on Fig. 7, both of these methods have yielded similar results. The vignetting factor was also observed to be symmetric about the 45° position of the mirror.

In actual experiments using this scanning spectrometer on a shock tube the test time is generally about 30 μsec. It has been possible to synchronize the spectrometer with the shock wave so as to utilize that portion of the scan with the minimum vignetting correction. In actual practice the vignetting correction need not be more than 25-30%, although the correction curve shown in Fig. 7 has been determined out to larger scanning angles.

Results of using this instrument to measure the spectral intensity of air shock heated to 7900°K behind reflected shocks is shown in Fig. 8. Each segment of the broken line was determined from a single scan during a shock tube run. The data have not been normalized and therefore illustrate the scatter caused by the small variation of shock velocity from run to run. The circles are data obtained on a different shock tube with a Perkin Elmer single channel spectrometer where each data point is an individual run. Note that the scanning spectrometer data remove much of the uncertainty of the spectral distribution of the radiation.

The data shown in Fig. 8 were taken with rather course spectral resolution, since the source of the radiation is primarily a continuum. However, better spectral information can be obtained by improving the resolution of the instrument with a resulting loss of spectral coverage during any one scan.

An example of the use of the scanning spectrometer to obtain spectra is clearly shown by the data in Fig. 9. This data was obtained using an Abney-type synchronized scanning spectrometer.[8] A photomultiplier was used as the detector and the entrance slit was 150 microns giving a resolution of 75 Å. The test gas is air shock heated to a temperature of 7600°K. Atomic nitrogen multiplets are easily identified on the trace and furnish excellent reference points for determining the wavelengths of unidentified prominences.

SUMMARY

Spectrographic instruments of simple design have been used to extend the capability of obtaining time-resolved spectra in shock tubes to 1100 Å in the vacuum ultraviolet and to 5.5 microns in the infrared. By suitable selection of the elements of the instruments the spectral range, scanning speed, and resolution can all be controlled, consistent with the source intensity, available test time, and information required. These instruments are currently being used to extend our knowledge of the high temperature radiative properties of air and its component gases.

REFERENCES

(1) Keck, J. C., Camm, J. C., Kivel, B., and Wentink, T., Jr., Annals of Phys. 7, 1, (1959).

(2) Camm, J. C., Kivel, B., Taylor, R. L., and Teare, J. D., J. Quant. Spectr. Rad. Transf. 1, 53 (1961).

(3) Allen, R. A., Camm, J. C., and Keck, J. C., J. Quant. Spectr. Rad. Transf. 1, 269 (1961).

(4) Taylor, R. L., J. Chem. Phys. 39, 2354 (1963).

(5) Allen, R. A., Rose, P. H., and Camm, J. C., "Nonequilibrium and Equilibrium Radiation at Super-Satellite Re-Entry Velocities", Avco-Everett Research Laboratory Research Report 156, September 1962. Published as IAS Paper 63-77.

(6) Lin, S. C., Neal, R. G., and Fyfe, W. J., Phys. of Fluids 5, 1632 (1962).

(7) Quarterly Letter Progress Reports under Contract AF 29(601)-6488, Air Force Weapons Laboratory, Kirtland Air Force Base, New Mexico.

(8) Camm, J. C., "A Synchronized High Speed Scanning Spectrometer", Avco-Everett Research Laboratory Research Note 447, February 1965.

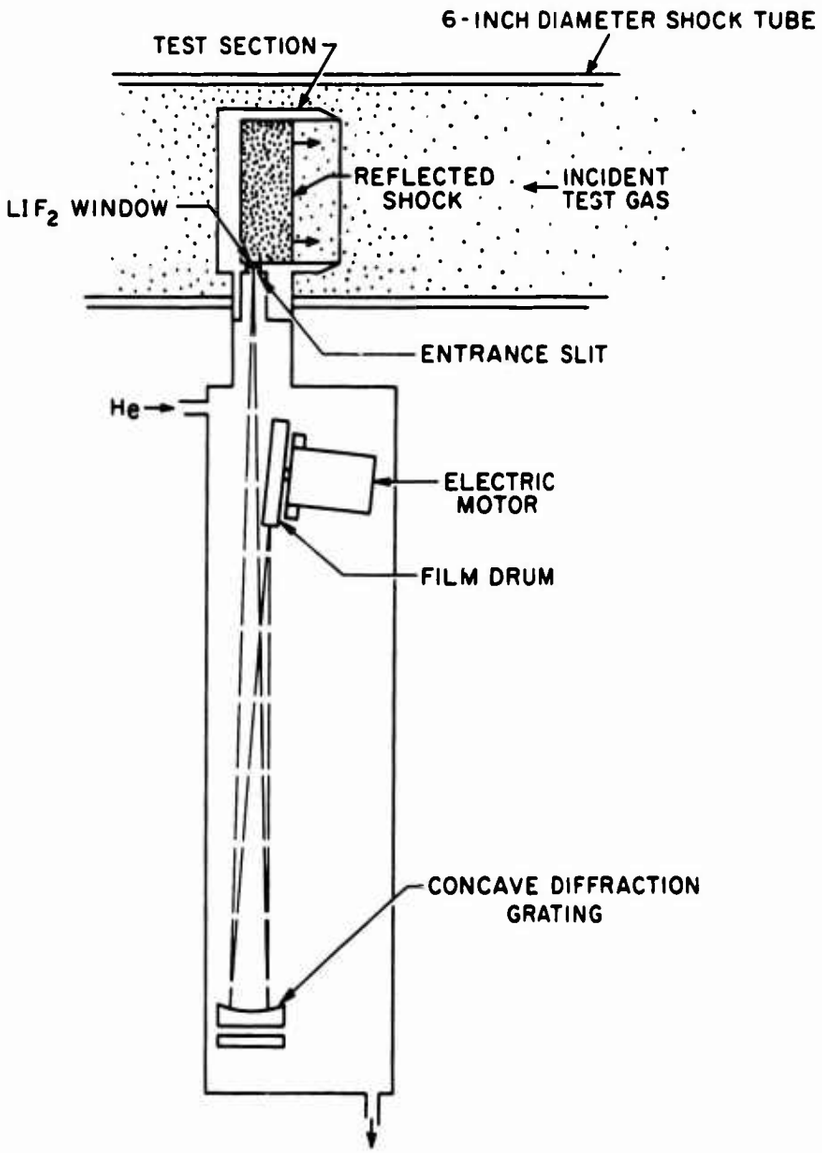


Fig. 1 Schematic Diagram of the Vacuum Ultraviolet Drum Camera Spectrograph Mounted in a Reflected Shock Test Section in a 6-inch Diameter Shock Tube

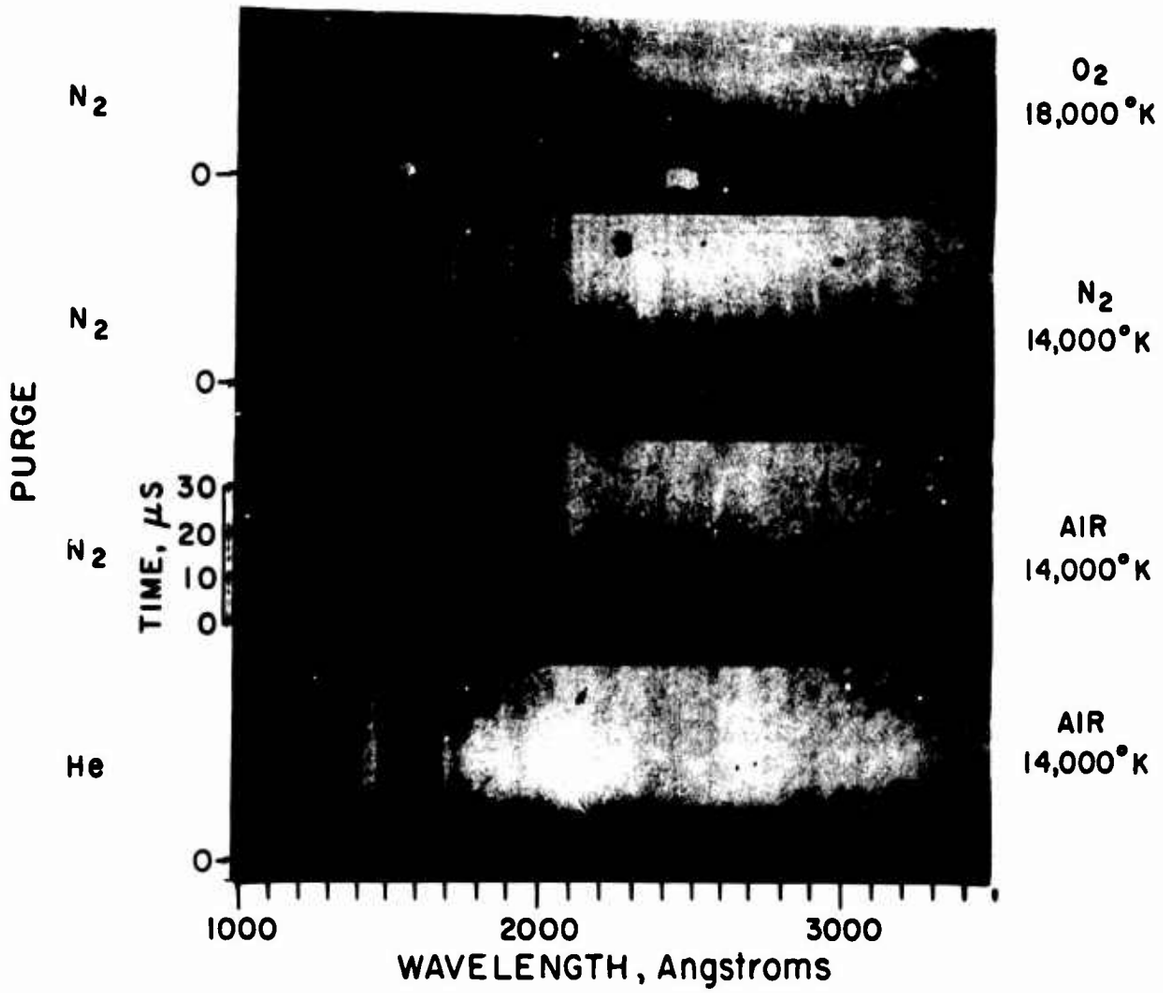


Fig. 2 Spectra Obtained with the Vacuum Ultraviolet Drum Camera Spectrograph

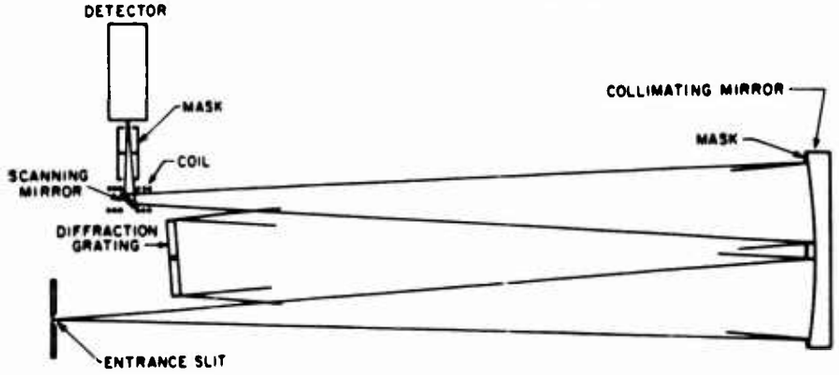


Fig. 3 Schematic Diagram of the Synchronized High Speed Scanning Spectrometer

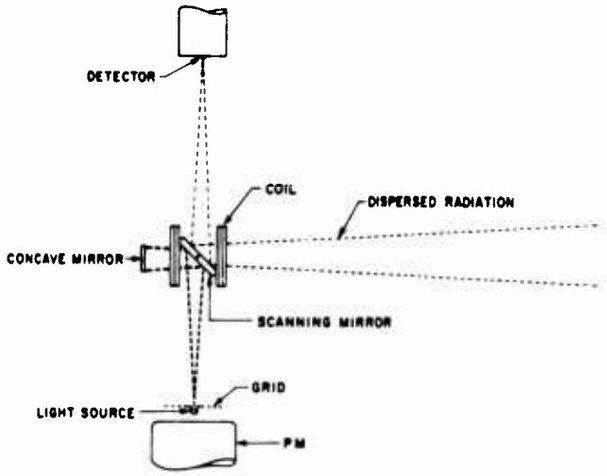


Fig. 4 Schematic Diagram of Wavelength Calibration Signal Generator

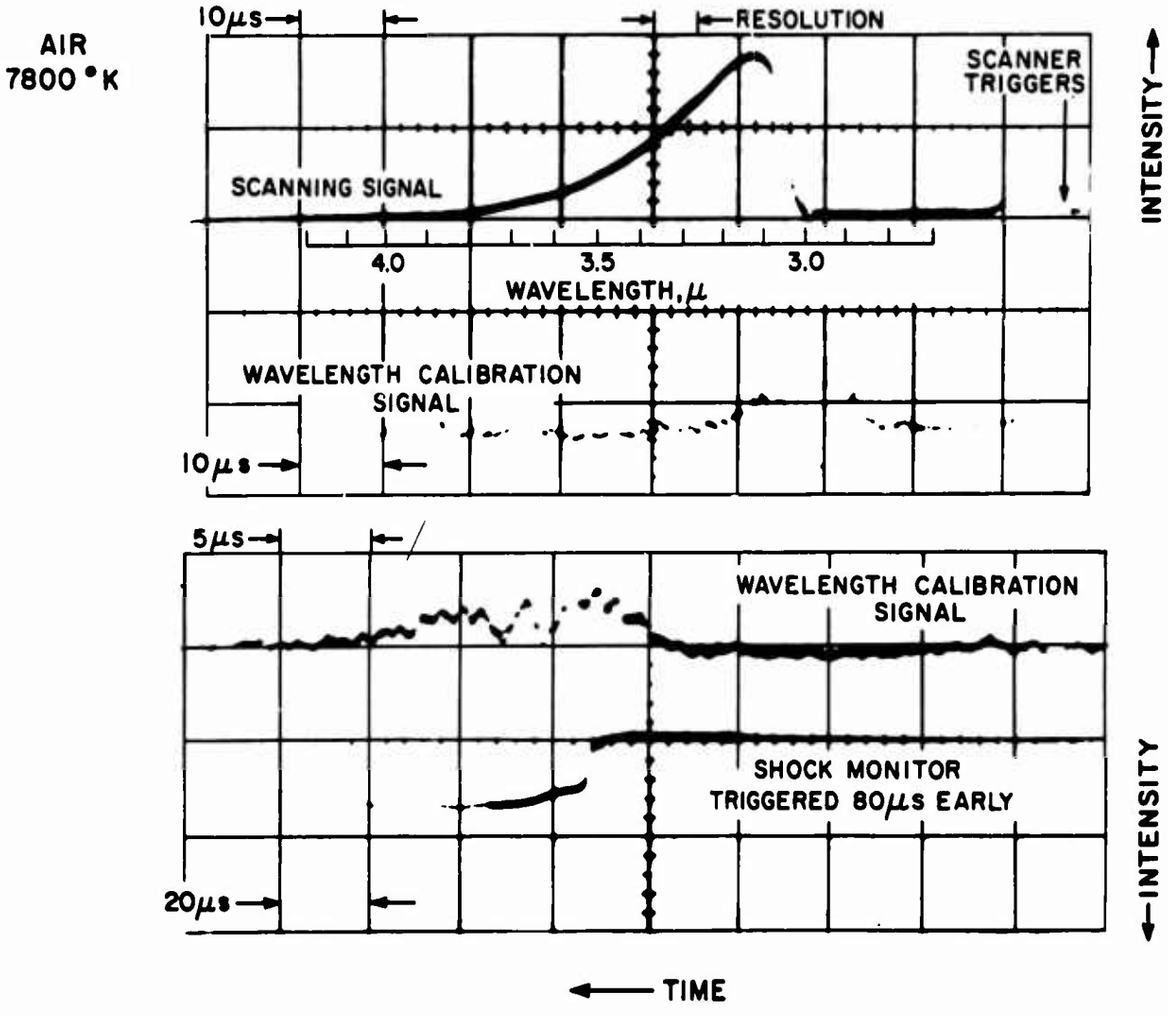


Fig. 5 Oscillograms Showing Scanning Spectrometer Data from a Shock Tube Measurement

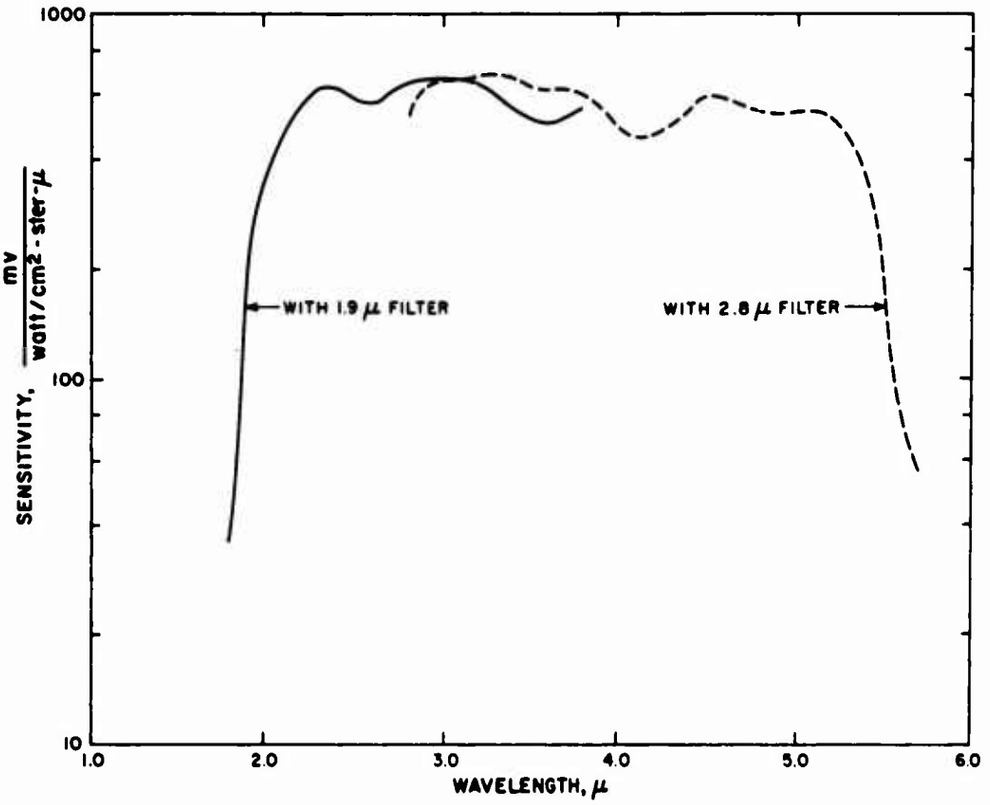


Fig. 6 Spectral Sensitivity of the Scanning Spectrometer

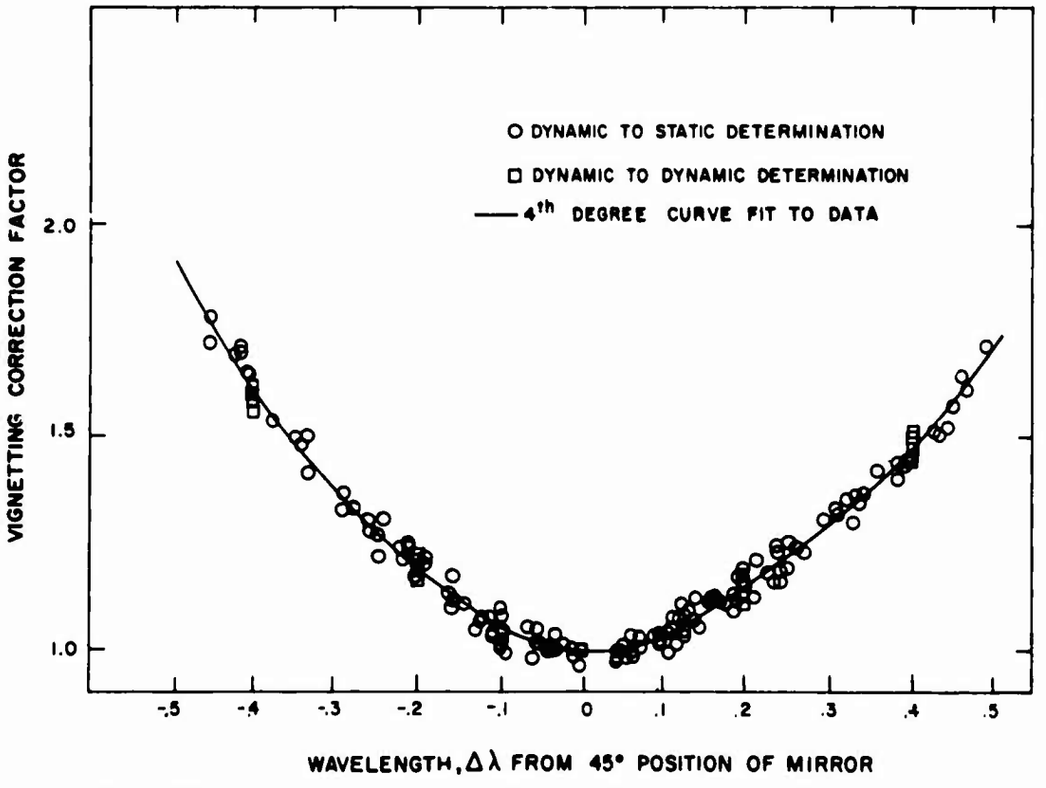


Fig. 7 Vignetting Correction Factor for Scanning Spectrometer

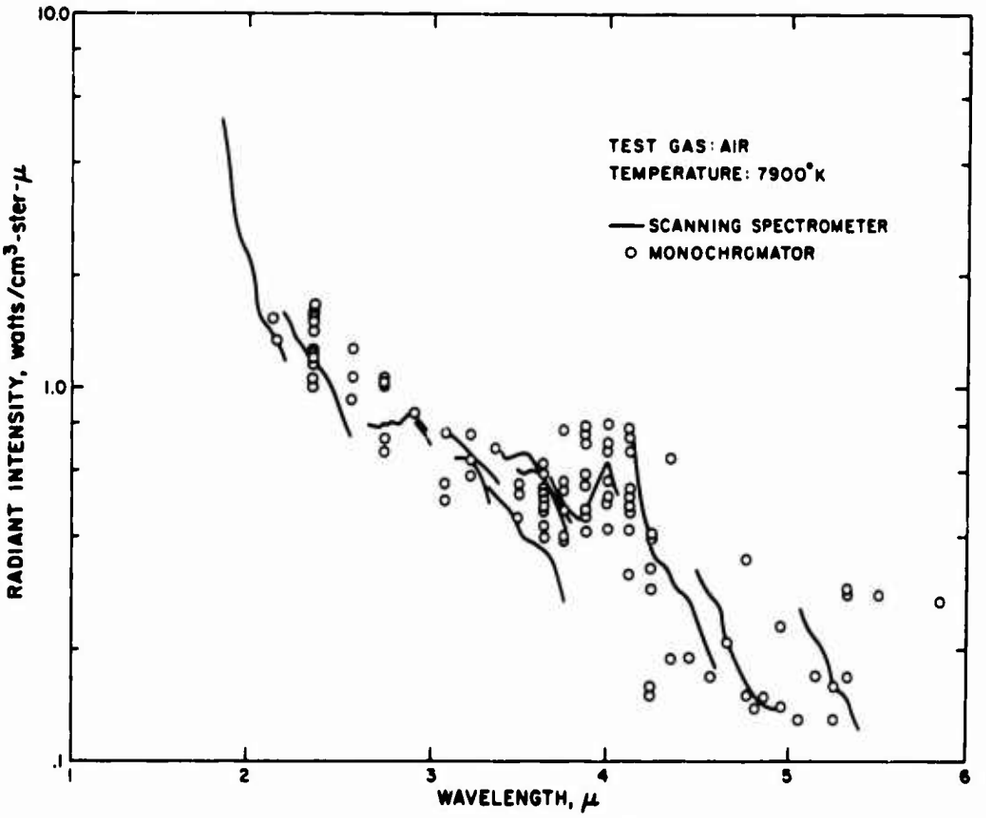


Fig. 8 Spectral Radiant Intensity of 7900°K Air Comparing Monochromater and Scanning Spectrometer Measurements

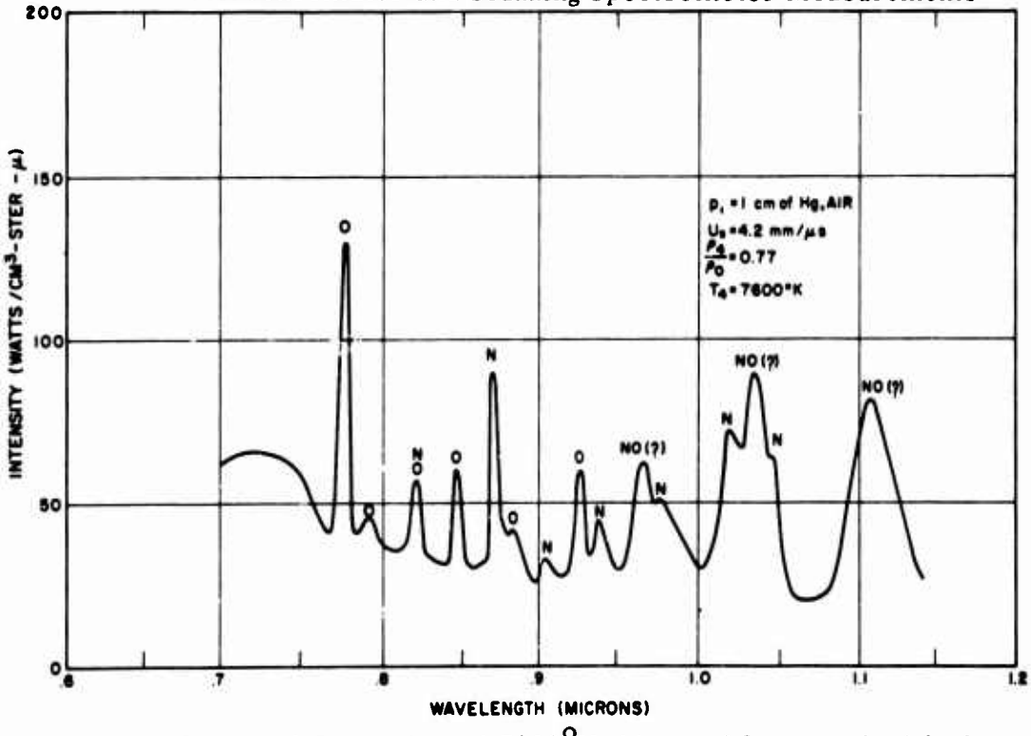


Fig. 9 Spectral Intensity of 7600°K Air as Measured with the Abney-Type Scanning Spectrometer

BLANK PAGE

PRESSURE GAUGE FOR SHOCK REFLECTION STUDIES

D. Baganoff
California Institute of Technology
Pasadena, California

INTRODUCTION

An accurate measurement of the pressure history on the end wall of a shock tube during and immediately following the reflection of the incident shock wave is a useful source of information for the study of the structure of shock waves and its relationship to gas properties. This paper describes a new pressure gauge which was developed for the purpose of studying the pressure history on the end wall of a shock tube in sufficient detail to permit the observation of the reflection of the shock front itself.

As is well-known at standard conditions the thickness of a shock wave is extremely thin. However, with a large diameter low density shock tube, such as the GALCIT 17-in.-diam shock tube at Caltech (ref. 1), relatively thick shock waves (≈ 6 mm) can be produced at an initial pressure of about 50 μ Hg; and this profile passes a fixed observer in several microseconds. Nevertheless, even a pressure signal on a time scale of several microseconds is somewhat beyond the recording capability of available pressure gauges and known techniques. As a result a development program was initiated to try to find a superior method for measuring a weak pressure signal on a microsecond time scale. The degree to which the investigation proved successful is demonstrated in Figure 1 where the response of the present gauge (to a pressure step) is compared with the response of a conventional pressure bar (one of the better of the known methods for measuring fast pressure signals).

The conventional pressure bar consists of an elastic rod and a sensing element, located at a suitable axial station, which gives a voltage output proportional to the average axial strain on the rod cross section; the pressure function to be recorded is applied to one end of the rod. The response of a conventional pressure bar depends on the axial location of the sensing element, the diameter of the rod, and the sound speed and Poisson ratio for the rod material. The pressure bar of Figure 1 consists of a

5 mm diameter brass rod with a 0.13 mm thick ceramic piezoelectric sensing element. For a sensing element located at x/D = 0.3, the figure shows a risetime of about 1 μ sec; and for a sensing element located on the front face of the rod, the risetime is considerably shorter. However, in both cases the response exhibits considerable oscillation.

In contrast to this the response of the present pressure gauge is very flat which allows one to make measurements of absolute pressure levels with a high degree of accuracy. The nearly ideal response of the present gauge was achieved by using a modified pressure bar. A discussion of the modified pressure bar and its use as a pressure gauge is given below.

This paper is divided into two parts; the first part discusses the concept and construction of the gauge, and the second part presents several examples of experimental data obtained with the gauge, to give some idea of the type of work for which the gauge has proven to be useful.

PRESSURE GAUGE

Modified Pressure Bar

Consider a two-dimensional elastic region with coordinates x, z (Fig. 2a). If the face x = 0 were subjected to a pressure step then a plane wave front would propagate into the region with the dilatational speed c_1. The region behind the wave front would be in a state of uniform stress provided we restrain the boundaries z = +b from expanding outward by the application of the lateral stress σ_{zz}. With the application of the lateral stress σ_{zz}, the stress field would remain one-dimensional for all time; however, it would be necessary for the lateral stress σ_{zz} to spread with the dilatational speed c_1 and furthermore, in the general case, to possess the same profile as p(t). Since it would be rather difficult to conceive of providing this boundary condition in practice, let us consider the case of a stress-free boundary. Figure 2b presents a schematic representation of the state of the stress field for a very short time after the application of the negative of the lateral stress considered above. The analytic solution to this problem is very difficult; however, for present purposes, the only information needed is that the wave front also propagates with the dilatational speed c_1 (ref. 2).

The superposition of the two stress fields yields the case of a stress-free lateral surface; and this is depicted in Figure 2c for the case of a circular rod of diameter D. The region near the axis of the rod is in a state of one-dimensional stress up to the time the initial disturbance arrives from the boundary. Therefore, if a small axial strain sensing element were placed on the axis within, say, the indicated cylinder of diameter d then the sensing element would lie in a region of one-dimensional wave propagation until the arrival of the initial waves from the surface of the rod. During this dwell time T, the output from the sensing element would be a close representation of the applied pressure signal p(t), since the sensing element would be sampling the local axial strain of a one-dimensional

non-dispersive strain wave.

This is in contrast to the conventional pressure bar where the sensing element is placed across the entire cross section of the rod and the waves from the rod surface also contribute to the output signal. In the one-dimensional model for the conventional pressure bar, these waves are responsible for the dispersive term that appears in the equation of motion representing the wave process in the rod.

The optimum position of the sensing element for the modified pressure bar is near the front surface of the rod. This position maximizes the dwell time for given rod and sensing element diameters. This configuration is presented schematically in Figure 3a. The response of the modified pressure bar (to a pressure step) is shown in Figure 3b. The risetime τ is determined by the transit time of the strain wave through the sensing element, i.e.

$$\tau = h/c_1 ,$$

and the dwell time T is given by

$$T = (D-d)/2c_1 .$$

The onset of oscillation is due to the arrival of the initial wave front from the corner of the rod. The modified pressure bar possesses a nearly ideal response for the time T and can be used during this time to obtain extremely detailed information on the initial portion of a pressure signal. The imporant characteristics of this configuration are that the risetime can be made very short, fraction of a microsecond, and that the response is very flat. Of course, the gauge is only useful as a pulse device since the output becomes meaningless once the oscillation sets in. However the value of the gauge as a device for accurately recording a pressure signal more than offsets the disadvantage of its limited duration.

Sensing Element

The required characteristics of a sensing element are that the element be elastically indistinguishable from the remainder of the rod and that the element produces a change in some electrical quantity proportional to the instantaneous average axial strain in the element. There are a number of physical principles that could be used: piezoelectric property, strain gauge effect, capacitance change, the reluctance change. However, for the application envisioned in the present work, it was decided to use the effect of the capacitance change; this selection permitted the sensing element to be composed of the same material as the rod and, furthermore, made it possible to minimize the element thickness (a small value of h is desirable for a short risetime).

Figure 3c presents a schematic drawing of the essential elements of the present version of the gauge. Polycarbonate plastic (Lexan) was

selected for the rod material (good electrical and mechanical properties) and electrical conducting epoxy (Eccobond 57c) was used for the internal electrode and center conductor; the external electrode consisted of a sprayed coating of electrical grade silver paint.

During the operation of the gauge, the capacitance change was determined by first charging the sensing element capacitor to several kilovolts and then recording the voltage drop (across a series resistor) produced by the current induced in the circuit by the capacitance change of the sensing element. The maximum voltage applied to the gauge in the present work was about 5 kv; this gave a maximum gauge sensitivity of about 5 mv/psi. The gauge calibration exhibits a linear behavior over a change in pressure of two orders of magnitude (0.2 to 20 psi); consequently, a single calibration constant was sufficient to convert the gauge output to an equivalent pressure.

Discussion

Two different sizes of gauges have been constructed: a 1 3/8 in. diameter gauge having a dwell time of 5 μ sec, and a 5 3/8 in. diameter gauge having a dwell time of 23 μ sec. (Information on the small gauge has been reported in a previous paper and additional details can be found in reference (3).) Figure 4 presents the response of these two gauges to a pressure step. The lower trace for the small gauge shows the characteristic behavior of the modified pressure bar. The trace undergoes a sudden step, follows with a flat response, and then oscillates after the stress waves arrive from the surface of the rod. The upper trace of the same oscillogram gives a detailed picture of the step. The trace shows the dwell time to be about 5 μ sec and the risetime to be something like 0.1 μ sec, with a slight rounding of the upper corner of the step. The oscillogram for the large gauge (lower trace) shows a similar behavior but over a somewhat longer time scale. The risetime for the large gauge is a little longer than for the small gauge, however this is due to a thicker sensing element (three times greater). The large gauge is a more recent construction and incorporates somewhat more sophisticated ideas in the design of the gauge circuit than were used in the small gauge circuit, one of these being a sensing element consisting of three electrodes (thus the reason for the greater element thickness).

Figure 5 is a photograph of the two gauges and indicates their relative size with respect to a 6 inch scale and to each other. The photograph gives a vivid impression of what is required to achieve a dwell time in excess of 20 μ sec. At this point it should be emphasized that the requirement that the pressure signal to be recorded be uniform over the active surface of the gauge is essential to the operation of the gauge. One glance at Figure 5 shows that the gauge cannot be used on the side wall of a shock tube and must be restricted to an end wall application, as was done in the present work. Even on the end wall the active surface of the gauge does not experience a perfectly uniform pressure due to a slight curvature in the incident shock front (ref. 4). However, the curvature of the incident shock

front decreases with increasing initial pressure and it has been found that for initial pressures greater than about 2 mm Hg the full dwell time of the large diameter gauge can be utilized. For low initial pressures ($p_1 = 50\mu$ Hg) where the curvature is quite large, experience has shown that a gauge with a dwell time of about 10 μ sec (or less) seems appropriate for a large diameter shock tube such as the GALCIT 17-in.-diam shock tube.

GAUGE APPLICATION

The following discussion is a short summary of material reported in reference (5) and is presented here to give an idea of the type of wall-pressure data that can be obtained with the gauge. Also, in the interest of brevity, only data collected with the small gauge will be discussed.

Figure 6 presents several examples of wall-pressure profiles for a reflecting shock front. The initial pressure is common (50μ Hg) for the three oscillograms; shock thickness varies inversely with initial pressure but is a weak function of incident Mach number, etc. The traces show that the profiles are about one microsecond in width. From the initial pressure and the incident shock Mach number, one can show that the pressure jump across each profile is roughly one psi. The requirement that a pressure signal, on the order of a psi, be resolved within several microseconds has always been an extremely severe performance criterion for a pressure gauge; consequently, only with the development of the present gauge has observation of shock fronts for reflection shock waves become possible.

The wall-pressure is quite sensitive to changes in the ratio of specific heats γ. This permits one to determine how rapidly a diatomic molecule relaxes rotationally by comparing the experimental wall-pressure jump across the shock with theoretical values for $\gamma = 5/3$ and $\gamma = 7/5$. This comparison is presented in the figure for nitrogen and carbon dioxide. The results show that both molecules are fully relaxed rotationally within the shock front.

A detailed inspection of the traces shows that all of the profiles continue to rise behind the shock front, even for a monatomic gas like argon. This effect can be seen more vividly in Figure 7 where the initial pressure has been increased an order of magnitude to increase the relative amount of the trace that can be seen. The rounding of the upper part of the "pressure step" is due to the thermal layer that develops between the cold end wall and the hot gas behind the reflected shock; this thermal boundary layer depresses the pressure behind the reflected shock momentarily by decreasing the strength of the reflected shock (the thermal layer induces a mass flux towards the cold wall). The small triangle on each oscillogram locates the point in time where boundary layer theory predicts the pressure perturbation to be five per cent of the total pressure jump.

Figure 8 presents several wall-pressure traces for reflected shocks in carbon dioxide and shows the behavior of the wall-pressure history for vibrational relaxation in the test gas. The traces show a "sudden jump"

which corresponds to the frozen jump across the viscous shock front and then a relaxation to a higher pressure level which corresponds to the equilibrium (vibrational) jump across the shock. Quantities of interest from each of these traces are the values of the frozen and equilibrium jumps, the duration of the relaxation process, and the initial slope. Also of interest is the extreme sensitivity of the wall-pressure to a relaxation process in the driven gas.

Figure 9 gives a comparison of the theoretical pressure jump across the reflected shock with the experimental values obtained from the oscillograms; the most striking observation from the figure is the precision with which wall-pressure can be measured.

The last figure, Figure 10, presents some measurements of the vibrational relaxation time for carbon dioxide, as inferred from the wall-pressure traces. (A simple theory can be devised to relate the relaxation time in the flow to the relaxation time exhibited by the wall-pressure history.) The important observation from the figure is that the pressure gauge permits one to obtain relaxation times for carbon dioxide for temperatures higher than those obtainable with a conventional optical interferometer. Using appropriate scaling laws, one can show that this is also true for other gases besides carbon dioxide.

CONCLUSIONS

The original development work on the gauge was motivated by the desire to observe the wall-pressure profile for a reflecting shock front. More recent work with carbon dioxide has demonstrated the usefulness of the gauge for the study of vibrational relaxation and has brought attention to the fact that the wall-pressure is quite sensitive to relaxation processes in general; this introduces the possibility of studying real gas effects in the shock tube by the study of the end-wall-pressure history. Also, the accuracy with which the wall-pressure can be measured with the present gauge presents the opportunity to study the state of the gas in the reflected region by combining the pressure data with data on density and temperature from other measurements.

REFERENCES

(1) Liepmann, H. W., Roshko, A., Coles, D. and Sturtevant, B., Rev. Sci. Instr. 33, 625 (1962).

(2) Miklowitz, J. and Nisewanger, C. R., J. Appl. Mech. 24 ,250 (1957)

(3) Baganoff, D., Rev. Sci. Instr. 35, 288 (1964)

(4) Liepmann, H. W. and Bowman, R. M., Phys. Fl. 7, 2013 (1964)

(5) Baganoff, D., J. Fluid Mech. (to be published)

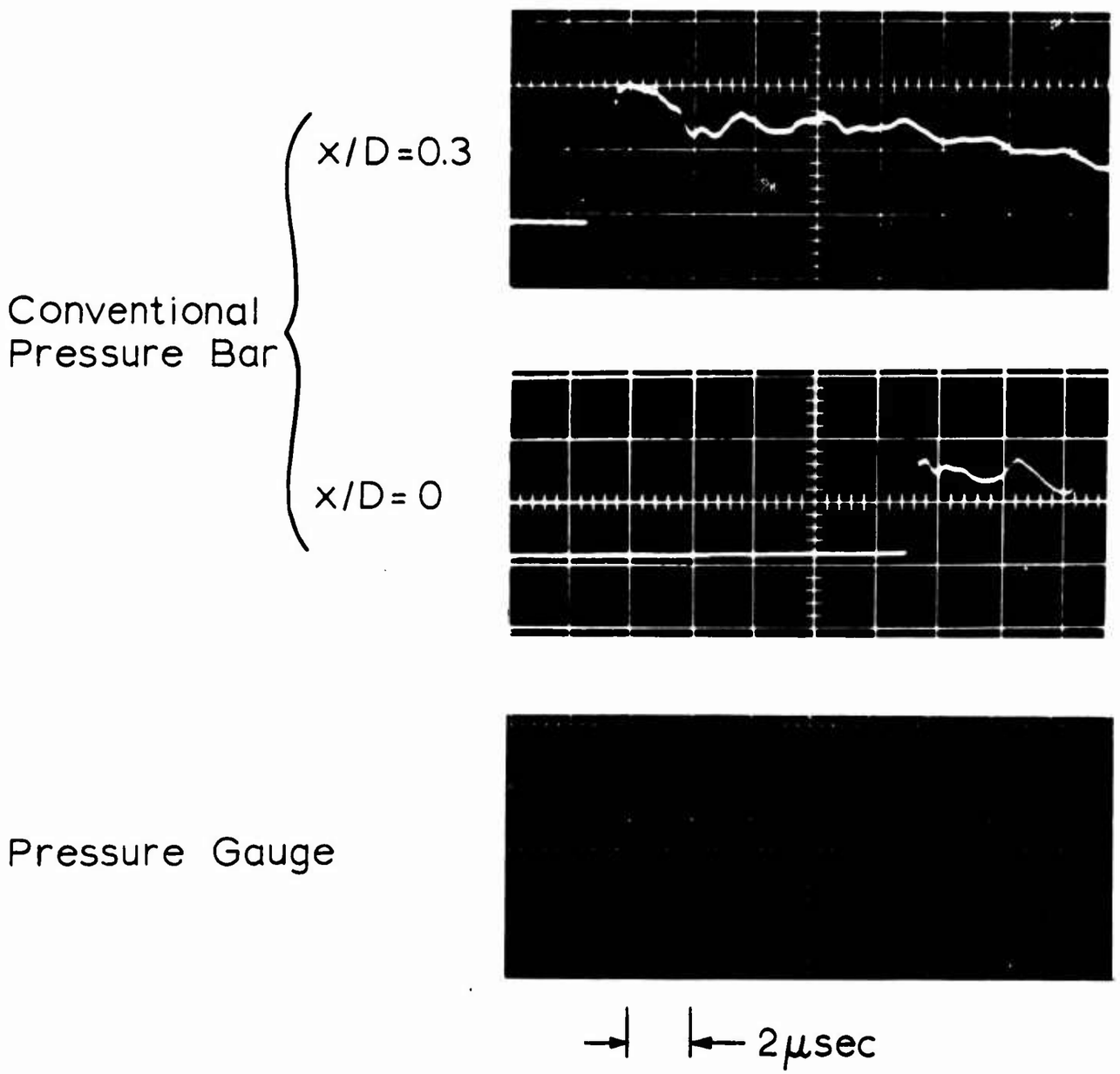


Figure 1. Comparison between the response of the present gauge and a conventional pressure bar.

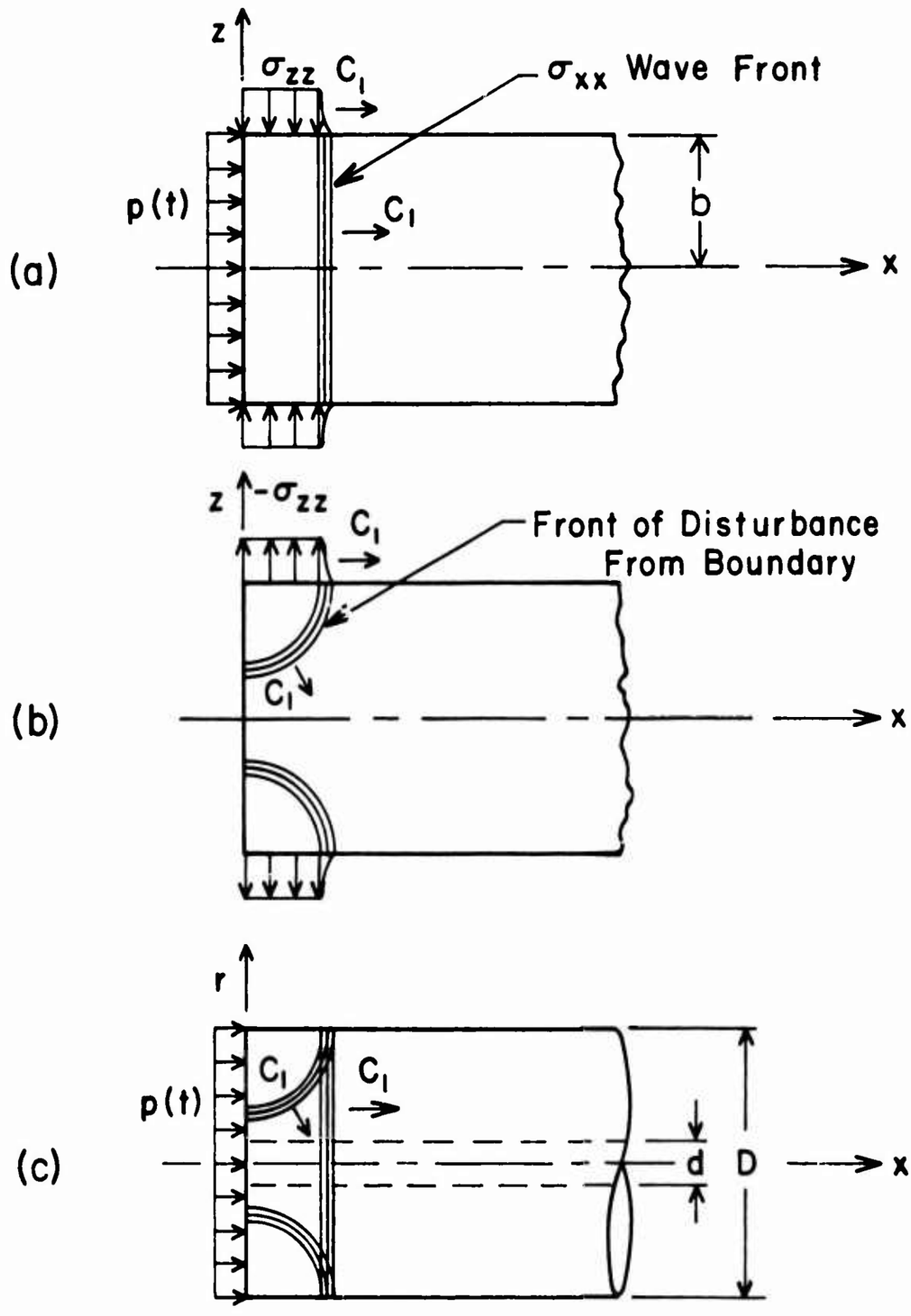


Figure 2. Wave front location in an elastic medium a short time after the application of a pressure signal on a part of the boundary.

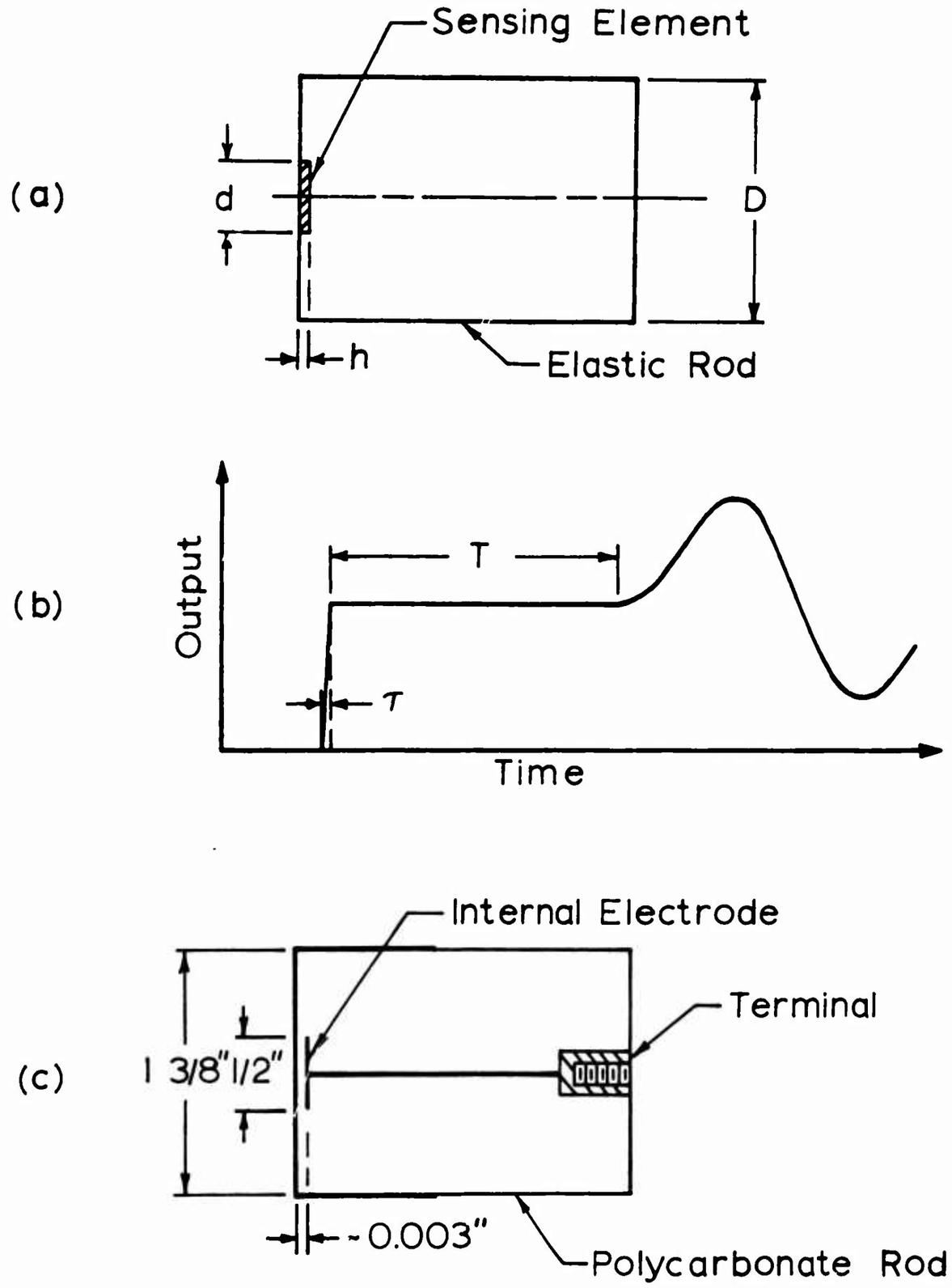


Figure 3. Geometry and response of the modified pressure bar.

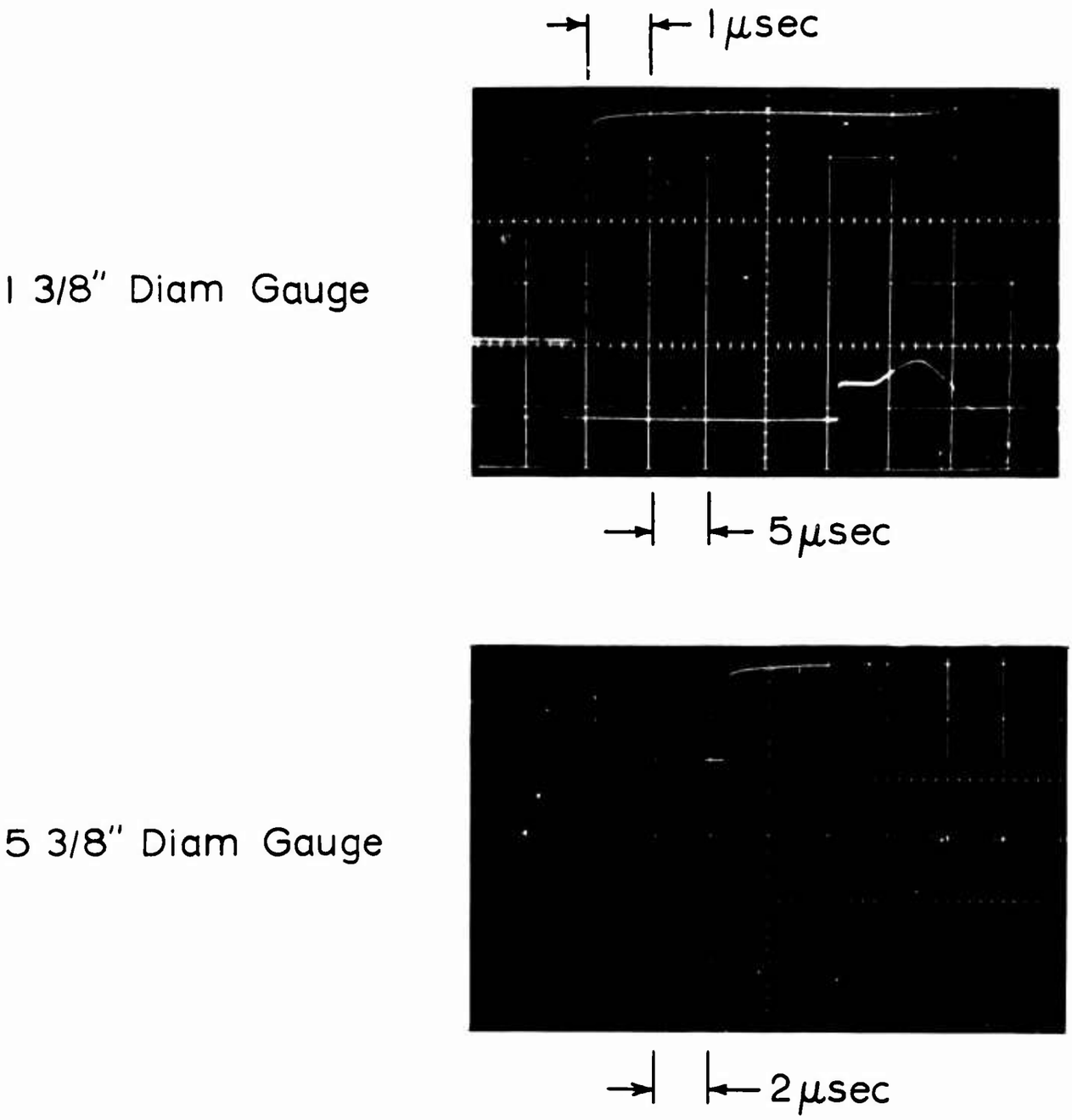


Figure 4. Response of the pressure gauge to a pressure step. The upper trace of the oscillogram for the large gauge should be ignored (heat gauge output).

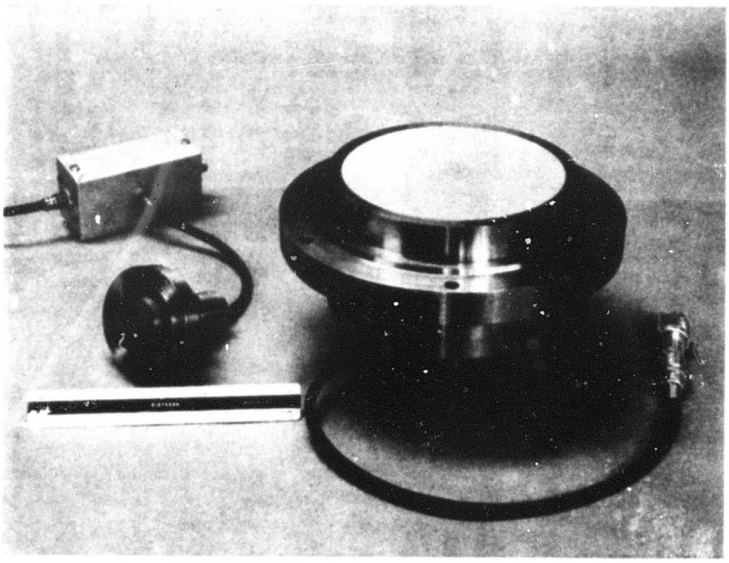


Figure 5. Photograph of two models of the pressure gauge. Small gauge: 1 3/8 in. diameter. Large gauge: 5 3/8 in. diameter.

(a) Argon
$M_s = 7.32$

(b) Nitrogen
$M_s = 6.41$

(c) Carbon Dioxide
$M_s = 8.25$

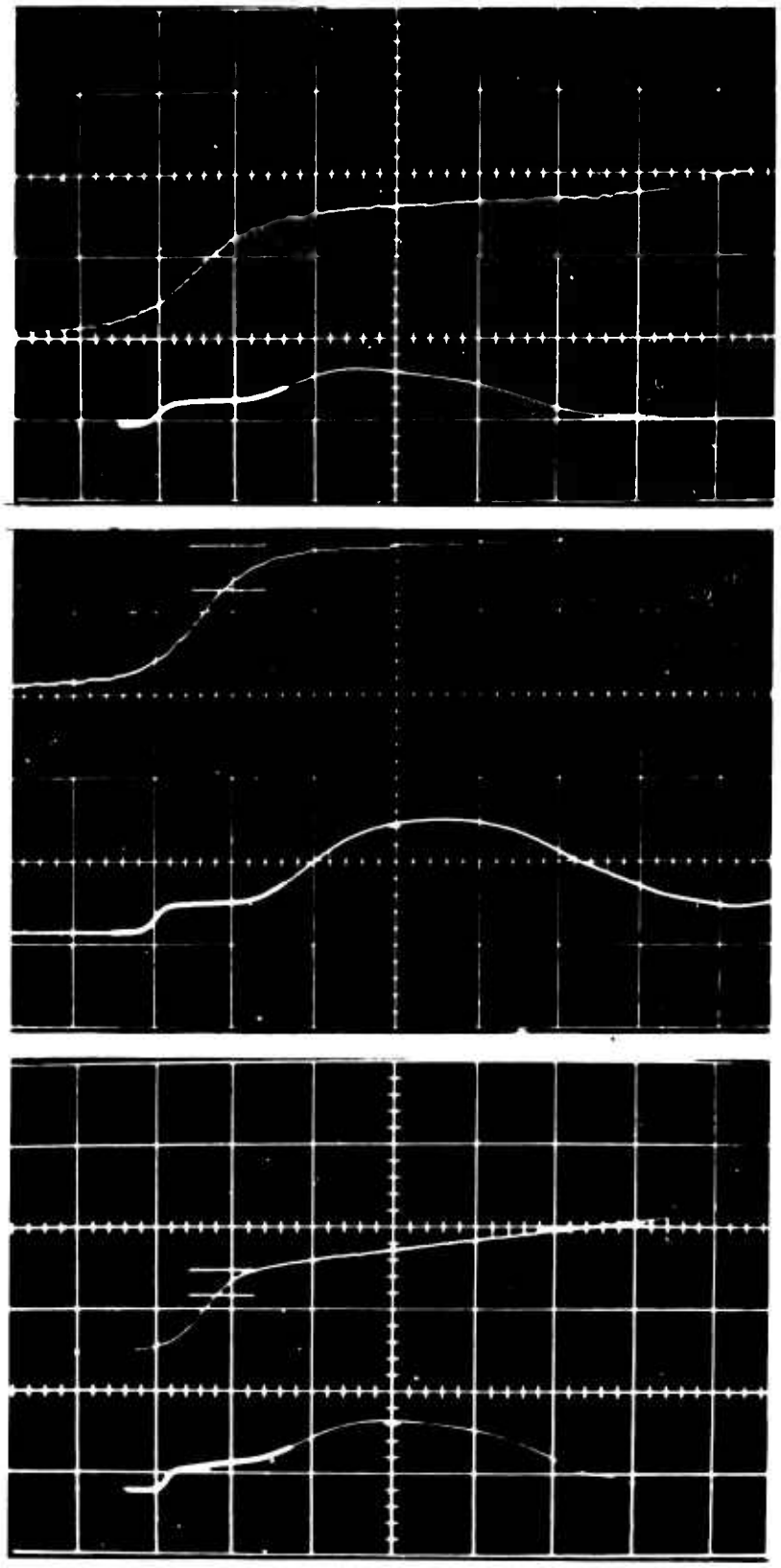
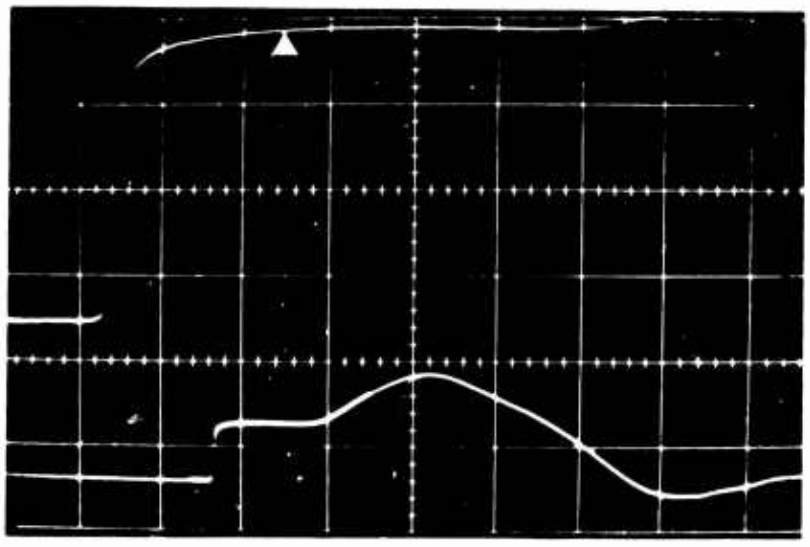


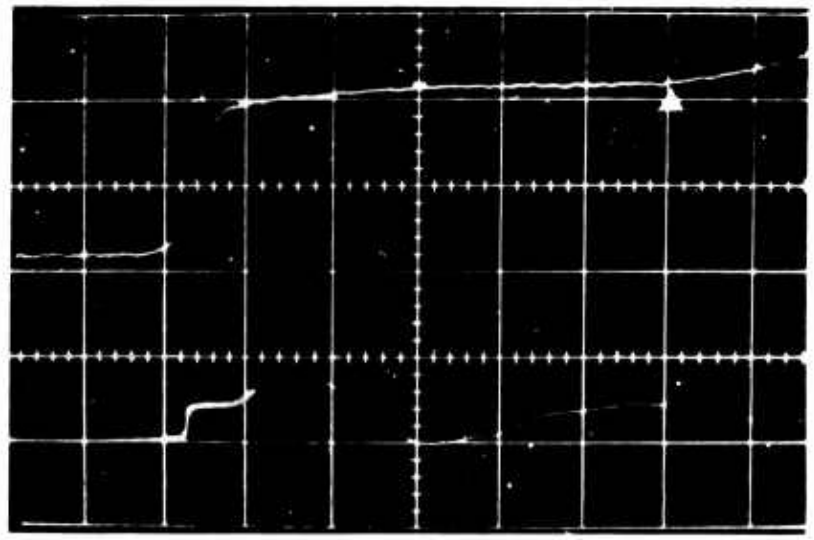
Figure 6. Wall-pressure profiles for a reflecting shock front. $p_1 = 50\mu$ Hg. Each oscillogram: upper, 1 μ sec/div; lower, 5 μ sec/div. Upper mark, $\gamma = 7/5$. Lower mark, $\gamma = 5/3$.

Figu

(a) $p_1 = 1$ mm Hg
$M_S = 5.64$



(b) $p_1 = 0.5$ mm Hg
$M_S = 3.25$



gure 7. Effect of a cold end wall on the wall-pressure history for a reflected shock in argon. Both oscillograms: upper, 1 μ sec/div; lower, 5 μsec/div.

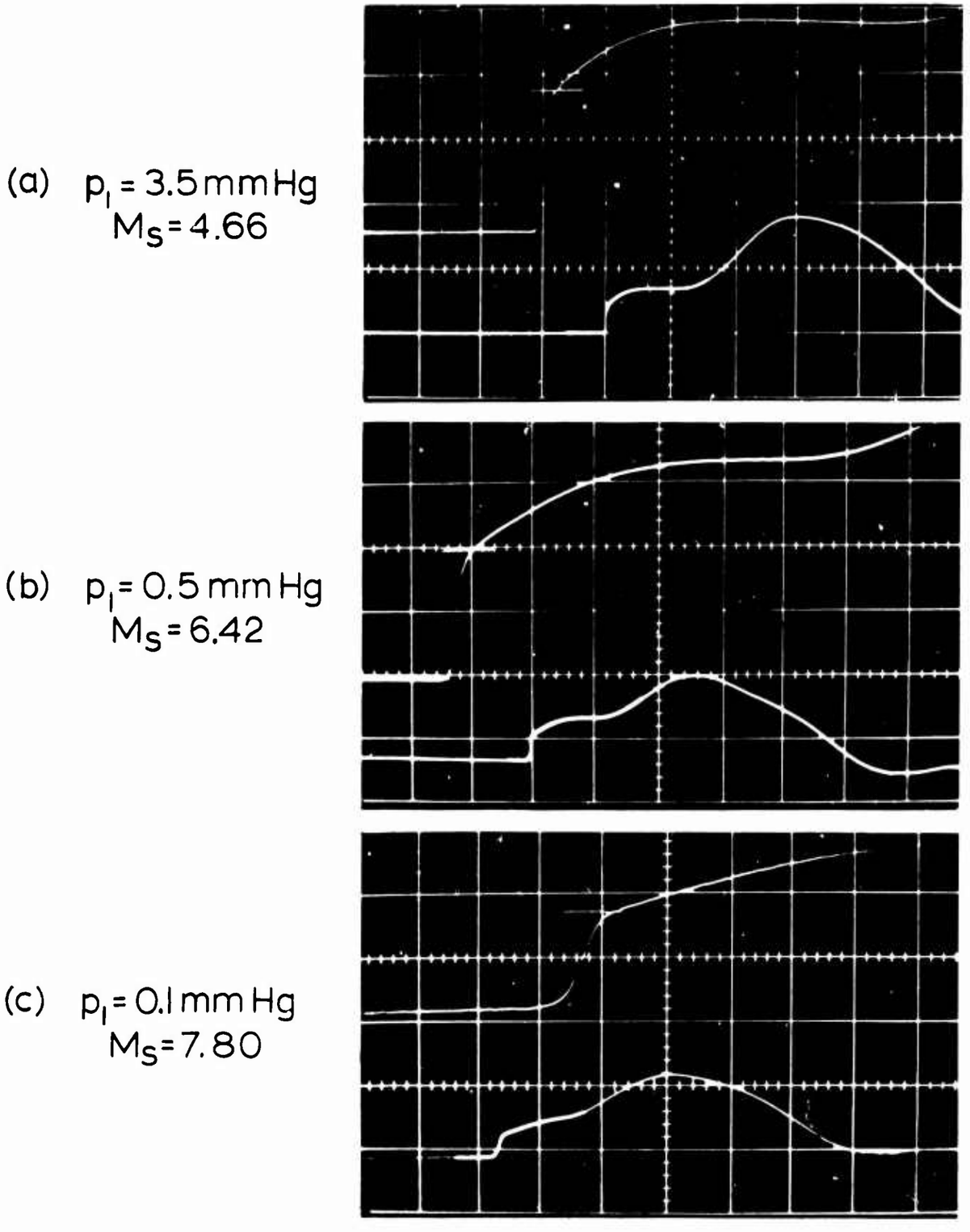


Figure 8. Wall-pressure history showing the effect of vibrational relaxation in carbon dioxide. Each oscillogram: upper, 1 μ sec/div; lower, 5 μ sec/div; M_s based on $\gamma = 7/5$; horizontal mark, frozen jump.

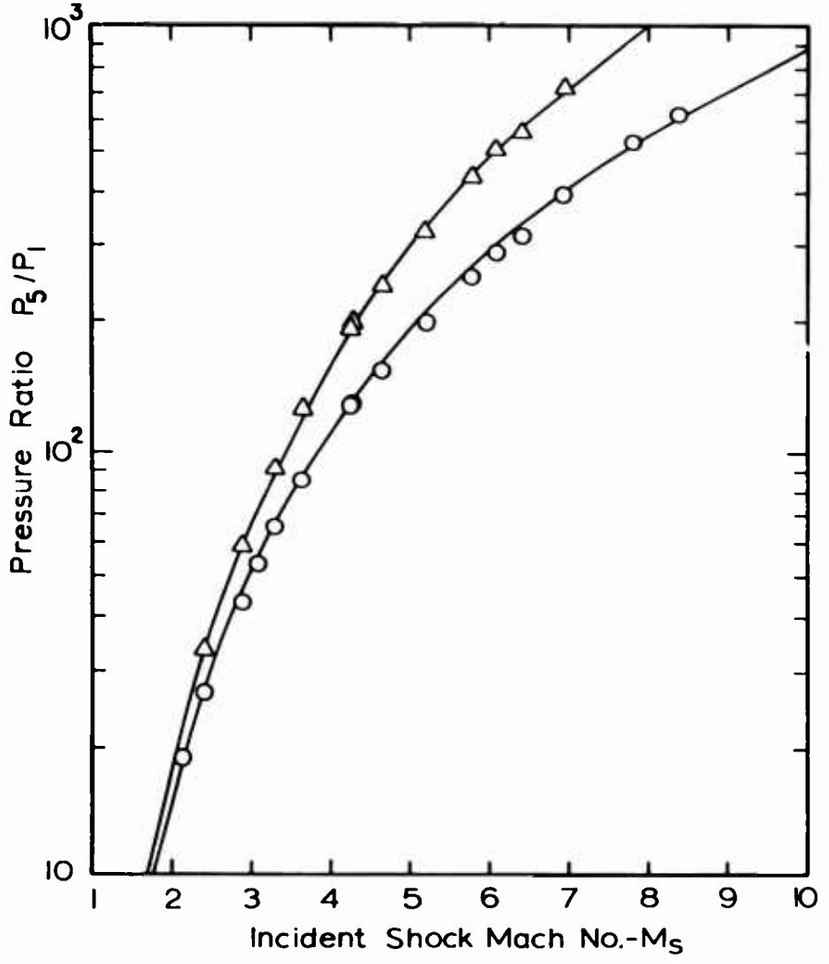


Figure 9. Pressure ratio across a reflected shock in carbon dioxide. M_s based on $\gamma = 7/5$. Data points: O frozen jump; Δ equilibrium (vibrational) jump.

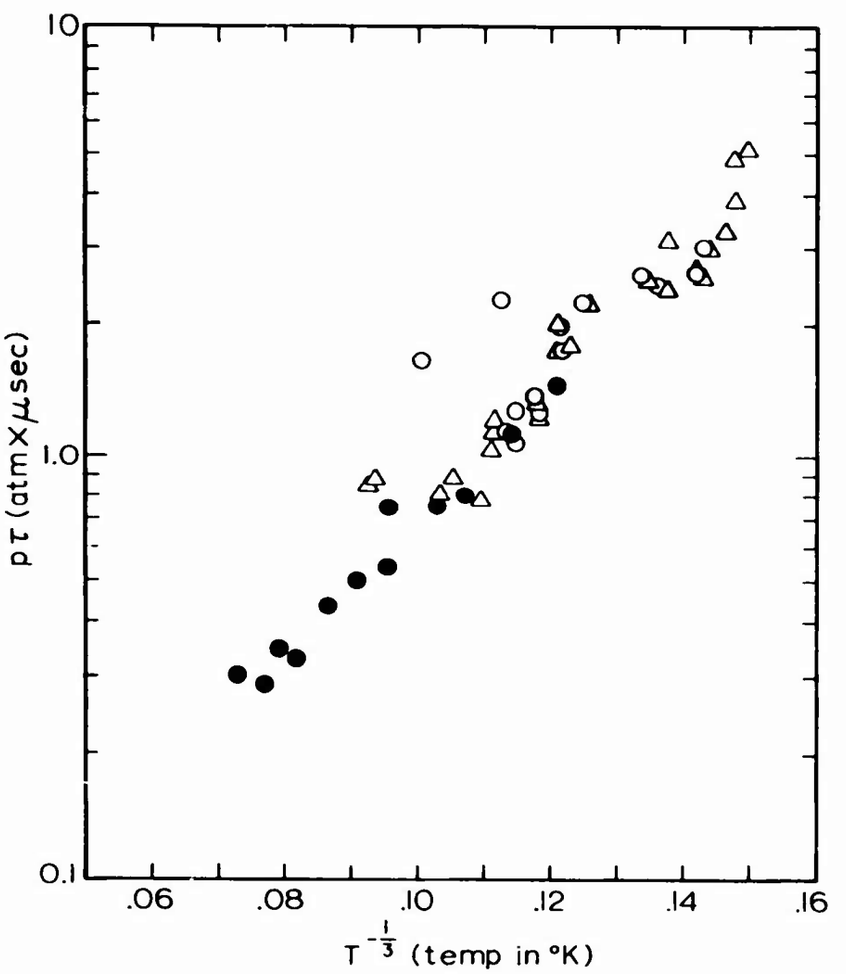


Figure 10. Vibrational relaxation time in carbon dioxide. Data points: ● present results; O Blackman; Δ Griffith et al.

BLANK PAGE

GLOW DISCHARGE SHOCK TUBE FOR STUDYING SURFACE CATALYSIS, GAS PHASE, AND CHEMILUMINESCENT REACTIONS

R. A. Hartunian and W. P. Thompson
Aerospace Corporation
El Segundo, California

ABSTRACT

The ordinary glow discharge tube has been used extensively to study both surface and gas phase recombination rates; typically at room temperature. The combination of a glow discharge flow tube with a shock tube driver to provide a considerable extension of atom fluxes, temperatures, and densities for the study of these kinetic processes is described. In operation, a slow flow is first established, then the RF energy is applied at an upstream point to produce a step function of dissociated (ionized) gas by a driver upstream of the RF region. Typically, the strength is less than that which causes further dissociation. Under these conditions, the effect of the shock is to compress, heat, and accelerate to high speed the pre-dissociated gas. Use of the step increase in atom flux to study the response of a catalytic probe, as well as more generalized application to the study of heterogeneous reactions, is described. Also, the application of this technique to establish the temperature dependence of both chemiluminescent and atom recombination rates is discussed. For the former, results for the $NO + O \rightarrow NO_2 + h\nu$ reaction are given.

INTRODUCTION

In reference (1) we reported on our measurements of heat transfer to a differential catalytic heat gauge in shock tube dissociated flows. The gauge is comprised of two rapid response thin film thermometers mounted adjacent to one another in the stagnation region of a sphere or cylinder; one coated with a material which catalyzes atom recombination and the other a noncatalyst. The differential heat transfer between the two gauges is proportional to the atom concentration in the flow. Although most of the results followed generally expected trends, a new disturbing feature appeared in some of the measurements. Specifically, at the lower initial pressures in the shock tube, the differential heat transfer was found to vary with time

instead of achieving a constant value immediately. At that time we could envisage this effect as being due to either of two possibilities; first, slow dissociation relaxation in the shock layer of our probe or secondly, a slow surface reaction rate at these lower pressures. We had pointed out at other times, and there has been some experimental evidence to the effect, that this latter possibility could be ascribed to submechanisms in the phenomenon of surface catalyzed atom recombination. For example, an atom must be adsorbed onto a surface, it must diffuse to an active site where it awaits another atom to recombine with and then the molecule desorbs. If the time scale for all of these events to occur is of the same order as the delivery rate of atoms in an experiment, it is conceivable that the observed time dependence of the differential catalytic heat transfer measurements could be reconciled. That is, it is conceivable that the catalytic efficiency of a surface might depend on the atom flux.

In our glow discharge experiments (ref. 2), which are used to determine the catalytic efficiency of surfaces of interest, atoms are delivered to the surface at a relatively slow rate (10^{17}/sec), whereas in our shock tube experiments they are delivered on the order of 10^{20}/sec. Shock tunnel flows will deliver atoms to the surface at a rate of about 5×10^{19}/sec. Since one of the major intended applications for our catalytic probe is to measure atom concentrations in hypersonic shock tunnel test sections (ref. 3), in order to establish the nonequilibrium state of the gas flow, it was imperative that we identify the source of the time dependence of our shock tube measurements. It was clear that we needed an experiment in which a known step function of atoms be delivered to our catalytic surface at a rate of the order 10^{19}/sec with a rise time of order 1/2 msec or less (since the shock tube test time was about 1.5 msec). Further, it was essential that no gas phase kinetics be present so as to remove that possibility from causing a time dependent reading of our catalytic probe in these new experiments. To solve this problem we conceived the idea of the Glow Discharge Shock Tube (GDST). This facility was also quickly seen to extend considerably present experimental capabilities in studying both gas phase recombination rates and chemiluminescent reactions. In both of these latter applications, the GDST affords a simple way to measure the temperature dependence of both types of reactions under essentially isothermal conditions. In the following sections, the GDST will be described, the results of experiments related to catalysis of oxygen atoms by a silver oxide surface and the temperature dependence of the air afterglow reaction will be indicated, and a brief discussion of future applications of this technique will be given. It should be pointed out that, unknown to the authors, concepts similar to the GDST had been developed independently by Wray (ref. 4) at Avco and Caruthers at the University of Illinois (as yet unpublished). Wray used the technique to study the excitation mechanism of $N_2(+1)$ radiation, while Caruthers is reported to have used it to study gas phase recombination.

GLOW DISCHARGE SHOCK TUBE

This facility is a combination of the ordinary glow discharge tube and shock tube. In the ordinary glow discharge tube, the gas is flowed steadily

(10-30 ft/sec) down a long glass tube and RF (or microwave) energy is applied at an upstream position, which partially dissociates the gas. The rate at which the atoms recombine in the gas phase as they convect down the tube may be studied or, the atoms may be permitted to impinge upon a probe coated with a catalytic surface to establish the catalytic efficiency of the surface. We have developed, and used extensively, a transient glow discharge technique (refs. 2 and 5) in which we expose catalytic spheres and cylinders to a near step function of atoms convecting down the flow tube. In this method, the steady flow of gas is first established and then the RF energy is suddenly applied at an upstream position to produce a step function of dissociated gas. As this gas convects downstream, the atoms at the front diffuse forward such that upon reaching the probe it takes about 100 milliseconds for the front to cross our probe. The rapid response characteristics of our probe detector made it possible to study surface catalytic reactions on this short time scale. However, as indicated in the Introduction, it was necessary for us to obtain a one-half millisecond rise time of the atom step function in order to identify the difficulty in our shock tube experiments. The GDST concept achieved this purpose. The way this facility works is shown in Figure 1: First, gas is flowed continuously along the ordinary glow discharge tube (4 in. diameter, 17 ft long double tough pyrex) and, at a given time, RF energy is suddenly applied to the gas. When the discharged gas is convected to within a foot or so of the probe, the diaphragm of the driver section is made to burst by a solenoid driven plunger, causing a shock to propagate into the predissociated gas. The strength of the shock employed depends upon the phenomenon under study; for our investigation of surface recombination, weak shocks ($M_s \lesssim 2$) were employed. Under these conditions, the shock wave serves only to compress and accelerate to high speed the RF dissociated gas present in the tube. That is, the density increase is not sufficient to cause atom recombination in the gas phase, nor is the temperature high enough to cause thermal dissociation. To determine the extent to which the atom front is sharpened, consider the trajectory of two particles on either end of the diffused front. When run as an ordinary glow discharge, these particles are about two feet apart, i.e., 20 fps × 100 msec. After they are shocked, these two particles cross our probe in about one-half millisecond. This can be seen in the x-t diagram, where the expression for the ratio of transit times in the shock tube and ordinary glow discharge tube is also presented. Although the major reduction of this ratio is due to the increased convective velocity of the particles, the compressibility factor contributes as well. The various time sequences of the RF pulsing and shock generation as well as their significance to the experiment will be discussed in the following section. Specific results for the oxygen atom-silver surface system will also be given.

In order to follow the oxygen atom concentration as a function of time in this experiment, a trace of NO was added continuously just downstream of the RF coil (Fig. 1). The NO reacts with the oxygen atoms to produce the familiar light green emission of the air afterglow, $NO + O \rightarrow NO_2 + h\nu$. The addition of NO, followed by monitoring of the luminous intensity with a photomultiplier, is a well-known technique for establishing the oxygen atom concentration (ref. 6) in the ordinary glow discharge experiment. The

intensity of the luminosity is proportional to the product of the NO and O concentrations. The NO concentration remains constant due to its rapid replenishment from the reaction $NO + O \rightarrow NO + O_2$ (ref. 6). Accordingly, in the ordinary case, any changes of the luminosity with time during the experiment is attributable to changes in the oxygen atom concentration. However, when the shock wave crosses the photomultiplier, the emitted intensity would be expected to increase as the square of the density (due to the compression of both the NO and O) times a factor due to the temperature dependence of the chemiluminescent reaction. Thus, one would expect a constant output with time from a phototube at any given axial position along the flow tube prior to the arrival of the shock wave, followed by a sudden change across the shock, and finally a new constant output (assuming no gas phase recombination along the tube ahead of or behind the shock wave). In our catalytic probe experiments, we used this technique to establish the atom concentration history. As an immediate product we obtained the temperature dependence for the air afterglow reaction. The results of our measurements with a photomultiplier placed 10 ft from the diaphragm will be given in the following section.

It should be pointed out that the driver section for these experiments was one inch in diameter and five feet long. A conical transition section joins the small driver to the larger glow tube. This area ratio allows weak shocks to be generated with air as a driver gas. The driven section in these first tests was only 10 ft in length. The initial pressure in the flow tube was about 0.6 mm Hg, which, combined with the 4 inch driven tube diameter gave adequate test time. Driver pressures of the order of one atmosphere were used to generate our weak shocks. Shock speed was measured by thin film thermometers placed on the inside of glass spacers mounted between sections of the pyrex flow tube. A considerable amount of attenuation was measured, and is most likely due to boundary layer effects and the shortness of the driven section. The attenuation was of no particular consequence to the objectives of the experiments described in this report. The model, comprised of a silver oxide catalytic gauge mounted immediately adjacent to a silicon monoxide noncatalytic gauge on a small pyrex disc, was placed on the end of a three foot sting mounted on an endplate. The exit to the pump is near the endplate, so that no disturbances due to shock passage over this hole could be fed back upstream to the probe during the useful test time. Finally, the time delay between application of RF energy and diaphragm bursting was achieved by simple relays, whose delayed opening or closing was controlled by variable RC constants.

RESULTS

Typical records from the photomultiplier as well as the catalytic and noncatalytic heat gauges for an ordinary glow discharge tube run are shown in Figures 2a and 2b, respectively. Notice the long time scale of the sweep; 0.2 sec/cm. The photomultiplier records, at the two positions along the tube noted in the previous section, are seen to rise to a peak in about 100 msec. This is due to the diffusion of the atom front (which we have used to independently measure the atom-molecule diffusion coefficient, ref. 2). The

peaking of these records is due to a surge of the RF power supply when it is suddenly turned on. This factor is of no consequence to the present experiments, except to explain one point about phototube records presented below for the GDST runs. When required, in previous experiments, we have eliminated this surging by employing an external pulsing circuit in such a way as to keep the power output tubes in a continuously ready state. The heat transfer records show the characteristic parabolic trace (implying constant heat transfer) for the catalytic gauge and essentially no rise for the noncatalytic silicon monoxide coated gauge, as expected. The early phase of the rise of the catalytic gauge record is due to the diffused atom front, which, of course, results in a time varying atom concentration. This effect correlates directly with the phototube indication of the diffuse front. Now for the GDST runs, we shall present the results in two parts, one dealing with the catalytic probe response and the other with the phototube measurements.

Catalytic Probe Response to High Atom Flux

We have conducted three types of tests using an initial pressure of 600 microns oxygen and a shock Mach number of 2. In the first, we established the gas flow and shocked it, but did not turn the RF discharge on. The resultant heat transfer records to the catalytic and noncatalytic gauges are shown in Figure 3a. Since no atoms were formed, we expect identical records; which is what happened. The slight difference between the two records is due to somewhat different gauge sensitivities. The rise with time of the heat transfer during the useful test time is due to the attenuation of the shock. As mentioned earlier, this attenuation is of no direct consequence to our experiment. In the second experiment, we turned the discharge on and permitted the front of atoms to pass our probe position before firing the shock. In this way, many of the available sites of the silver oxide catalytic surface could be occupied prior to being exposed to the rapid increase in flux of atoms behind the shock wave. If the surface kinetics follows the change in atom concentration instantaneously, on the time scale of this experiment, the heat transfer to the catalytic surface should rise immediately to a higher value than indicated in Figure 3a (when no RF was applied). This is exactly what happened. The catalytic gauge heat transfer jump across the shock with RF is 50% higher than the no RF case (Fig. 3b), while the noncatalytic gauge gives a record identical to that of Figure 3a. The differential heat transfer implies an atom mass fraction of about 3%, which is very close to that which we determine by titration with NO_2 (ref. 6).

Finally, the third experiment times events such that the shock wave arrived at the probe well in advance of the discharged step function gas. In this way we would establish that the rapid response of the surface kinetics was not due to the intentional filling of active sites. For this case, immediately behind the shock, undissociated gas follows so that the initial heat transfer rises should correspond to those indicated in Figure 3a. When the front of atoms is convected across the probe, the catalytic heat transfer should rise rapidly. This is precisely what happened, as indicated in Figure 3c. Again, the noncatalytic gauge in this run remained identical to that in the case with no RF discharge.

As a result of these experiments, we conclude that the surface reactions are rapid enough to follow the sudden changes in atom flux, so that the time dependence of differential catalytic heat transfer observed in our shock tube experiments is not due to slow surface kinetics. With this fact established, and due to the similarity of the atom flux to which the probe has been exposed in these GDST experiments and those to be found in the shock tunnel, we can state that the catalytic probe should behave well as an atom concentration detector in hypersonic shock tunnels.

Temperature Dependence of the Air Afterglow; $NO + O \rightarrow NO_2 + h\nu$

The original intent of our procedure of adding a trace of NO and following the resultant glow intensity with the phototubes was to verify the sharpening of the diffused atom front from 100 msec to about 0.5 msec and to generally establish the absence of atom recombination due to shock compression. The records from the two time sequenced GDST runs described immediately above are shown in Figures 4a and 4b. In the case where the discharged gas has passed the phototube before the shock arrives (Fig. 4a) the record is interpreted as follows. First, notice the zero output baseline at the extreme right of the record, which is due to the arrival of the high pressure air driver gas which extinguished the discharge (hence no glow). Now directing attention to the beginning of the trace at the left, it is seen that some initial glow intensity has been recorded; about 1 cm in amplitude. Then, when the shock arrives, the intensity jumps sharply,as expected, and continues to rise with time until the contact surface arrives and causes a sharp temporary reduction to end the useful part of the test. This contact surface arrival time correlates perfectly with the catalytic gauge indication of its arrival. The rise with time during the test is due to the gradient of atom concentration along the flow tube initially and in some part to shock attenuation. In the latter case, as time increases gas which has been processed by a stronger shock arrives so that the glow intensity, which is proportional to the square of the density ratio, rises accordingly. It might be noted that the second rise is most probably due to the increased density of the mixture of driver and driven gas at the interface. In fact, the extent of the mixing of the gases at the interface can be followed by this method. At still later time, the glow decreases in intensity because the air pressure gets high enough that the discharge extinguishes. All of this later time data (after passage of the contact surface) is of no interest to the present experiments.

With respect to the magnitude of the jump in intensity across the shock, it is clear that the difference between the value expected due to the density ratio squared and the observed value is due to the temperature dependence of the light emitting reaction (assuming the new temperature behind the shock is not high enough to cause dissociation of diatomic or triatomic species). The results of six runs (agreeing within 10% of each other) reduced in this manner gives the extension of Clyne and Thrush's (ref. 7) points to higher temperature indicated in Figure 5. Our data is seen to generally follow the extension of their curve. The simplicity of the present method for

studying chemiluminescent reactions at high temperature is clearly seen.

With respect to the verification of the sharpening of the diffused atom front, this is evident from the glow intensity record of Figure 4b. In this record, which corresponds to the heat transfer record of Figure 3c for the same run, the time sequence of events was such that the shock wave reached the phototube before the atom front. The intensity (hence, atom concentration) is seen to rise to its peak in about 0.75 msec, at which time the contact surface also arrives. The time at which the intensity starts to rise, as well as the rate of rise, correlates directly with the heat transfer record. Further, this rapid rise is to be compared with the 100 msec rise seen in Figure 2a. By these comparisons, we support the conclusion that the catalytic reaction follows changes in atom concentration instantaneously on the time scale of these experiments. It might be noted that the larger peak signal in this run compared to the time sequence of Figure 4a is due to the power supply surge discussed in reference to Figure 2a. That is, in the case when the shock arrives first, the atom front is measured by the phototube with the attendant high amplitude in intensity, while in the other sequence the pre-shock glow intensity has tailed off to the low value seen at the extreme right of Figure 2a.

CONCLUSIONS AND FUTURE APPLICATIONS OF GDST

The feasibility of using the glow discharge shock tube for studies of both heterogeneous and gas phase reactions has been established. Specifically, for heterogeneous reactions, the effects of high atom flux on the process of surface catalysis have been studied on a time scale of a fraction of a millisecond. The GDST thus furnishes the surface kineticist with a new short time scale to study the submechanisms of surface catalysis. For the particular system employed in our experiments, it has been verified that a silver oxide surface; that is, a pure silver surface which has been exposed to a dissociated oxygen flow, responds on a time scale less than that of the experiments time resolution (20 μsec) to a rapid change of atom flux. This information gives us confidence that our differential catalytic probe will perform well in measuring free stream atom concentrations in high enthalpy, hypersonic facilities.

To obtain an independent measurement of the oxygen atom history during a run in the GDST, a trace of NO was added to the flow and the resultant glow intensity observed with phototubes. The atom histories so determined corroborate the sharpening of the diffused atom front by the shocked flow, as well as the detailed histories of the catalytic heat transfer measurements. Further, it has been demonstrated that the GDST provides a relatively simple method of establishing the temperature dependence of chemiluminescent reactions. The present data for the $NO + O \rightarrow NO_2 + h\nu$ reaction at a temperature of 530°K agrees with an extrapolation of Clyne and Thrush's lower temperature measurements.

As for future applications of the GDST, these will follow three paths. First, additional measurements of the air afterglow reaction will be made

over a wide range of temperatures. Similar measurements will be made for the oxygen atom-carbon monoxide system. In general, any chemiluminescent reactions may be studied by this technique. The second general application of the tube will be the study of the temperature dependence of gas phase recombination of atoms. To accomplish this, one would establish the steady discharged flow under conditions that recombination along the tube is small, shock this dissociated gas, and then follow the recombination of atoms behind the reflected shock wave. To provide a plane surface for the end wall of the tube, an automatically actuated gate valve coated with a noncatalytic material would be placed upstream of the pump outlet. This technique will allow the important temperature range between ordinary glow discharge experiments (room temperature, mostly) and the high temperatures of shock tube dissociation experiments to be achieved. The advantages of the GDST approach are that recombination is measured directly, instead of measuring dissociation rates and inferring recombination rates as in most shock tube experiments, and that the recombination takes place nearly isothermally. The latter fact is due to the typically small degree of dissociation in the discharged flow, so that the energy of recombination will not significantly alter the temperature behind the reflected shock. Other techniques by which the recombination rate may be determined directly (refs. 8 and 9) do so with large temperature changes during the recombination, which makes the temperature dependence determination considerably more complicated. The method employed by Wray (ref. 10) to study oxygen atom recombination is an exception. Further, in the GDST situation the third body need not be a diluent as is often the case to simplify data analysis in shock tube and nozzle expansion experiments. Care must be exercised in the GDST experiments to identify any excited states of the molecules or metastables that are characteristic of discharged flows and evaluate the effect they may have on the recombination process.

Finally, the third application relates to studies of surface catalysis on a time scale of a fraction of a millisecond. In these experiments an appropriate pulsing circuit applied to the RF power supply would produce a single square pulse of any time duration which would cross the catalytic surface on the cited time scale. In this way, the surface kineticist is provided with a microscope, so to speak, which allows studies of the mechanisms of catalysis on this time scale. Immediate application of this technique to the studies of the oxidation of pure silver when exposed to oxygen atoms (ref. 11) and the effect of this oxidation on the subsequent catalytic efficiency of the surface is seen. This particular problem will receive attention in our future experiments.

ACKNOWLEDGMENT

The authors are very grateful to Dr. Sidney Benson for many helpful discussions related to the glow intensity interpretation. A special note of thanks is given to Dr. W. Kaskan of General Electric Company. Both he and Dr. Benson pointed out the implication of our phototube measurements across the shock to the temperature dependence determination of the air afterglow. Finally, we would like to acknowledge the assistance of Mr. Carrol Gardner in conducting the experiments.

REFERENCES

(1) Hartunian, R. A. and Thompson, W. P., Preprint No. 63-464 presented at AIAA Conference on Physics of Entry into Planetary Atmospheres, M.I.T., (26-28 August 1963).

(2) Hartunian, R. A., Thompson, W. P. and Solo, R. B., Bull. Am. Phys. Soc. Series II, 8, 494 (1963).

(3) Hartunian, R. A., Phys. Fluids 6, 343 (1963).

(4) Wray, K. L. and Teare, J. D., Proc. 3rd Int. Conf. Physics Electric Atomic Collisions, Univ. College, London, (22- July 1963).

(5) Hartunian, R. A. and Liu, S. W., Phys. Fluids 6, 349 (1963).

(6) Kaufman, F., Progress in Reaction Kinetics, Pergamon Press, (1961).

(7) Clyne, M. A. A. and Thrush, B. A., 9th Combustion Symp., Cornell Univ., Ithaca, New York, (1963) p. 177.

(8) Jacobs, T. A., Hartunian, R. A., Giedt, R. R. and Wilkins, R. L., Phys. Fluids 6, 972 (1963).

(9) Hurle, I. R., Russo, A. L. and Hall, J. G., Preprint No. 63-439 presented at AIAA Conference on Physics of Entry into Planetary Atmospheres, M.I.T., (26-28 August 1963).

(10) Wray, K., Research Report No. 142, Avco, Massachusetts, (September 1962).

(11) Meyerson, A., Research Report No. AF-1412-A-2, Cornell Aeronautical Laboratory, Buffalo, New York (August 1962).

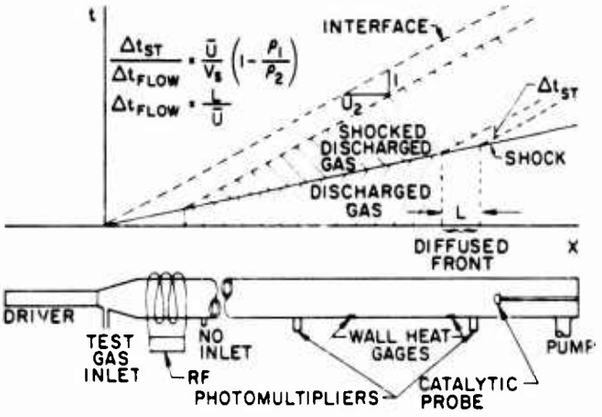
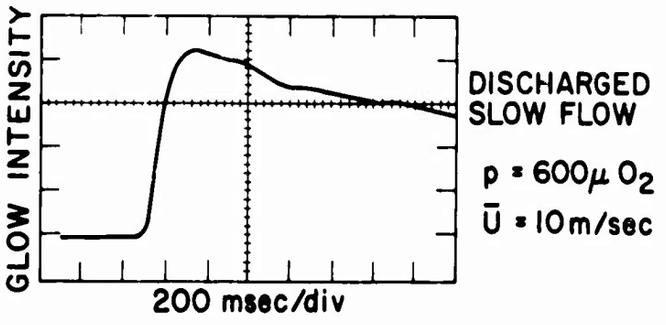
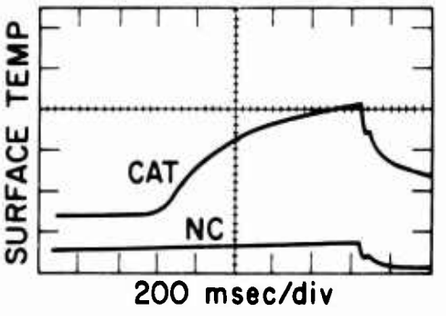


Fig. 1. Glow Discharge Shock Tube: $\bar{u}$ = convective velocity in slow flow; L = length of diffused front in slow flow; V_s = shock velocity; and ρ_2/ρ_1 = shock density ratio

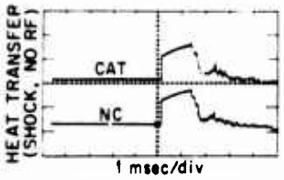


(a) Glow Intensity Record

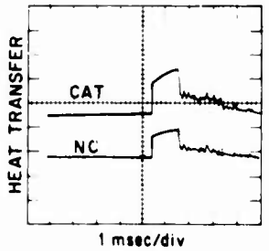


(b) Catalytic (CAT) and Noncatalytic (NC) Surface Temperature Histories

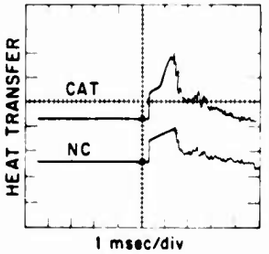
Fig. 2. Typical Records for Ordinary Glow Discharge Run



(a) NO RF DISCHARGE

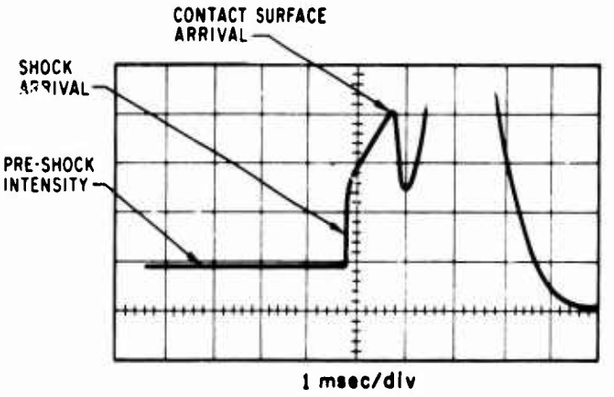


(b) RF ON, DIFFUSED FRONT 1 4 sec AHEAD OF SHOCK

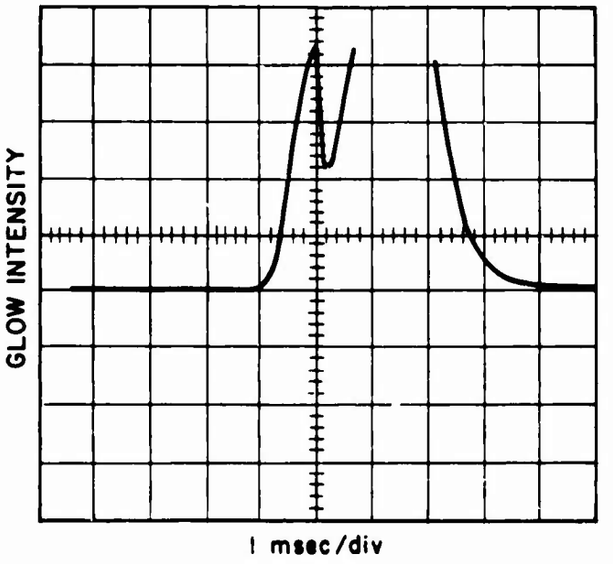


(c) RF ON, DIFFUSED FRONT 0 5 msec BEHIND SHOCK

Fig. 3. Heat Transfer to Catalytic and Noncatalytic Heat Gages With and Without RF Discharge: $M_s = 2$; $p_1 = 600$ μ Hg



(a) Discharged Gas Past Phototube When Shock Arrives



(b) Discharged Gas Arrives after Shock Passes Phototube

Fig. 4. Glow Intensity Histories During GDST Runs

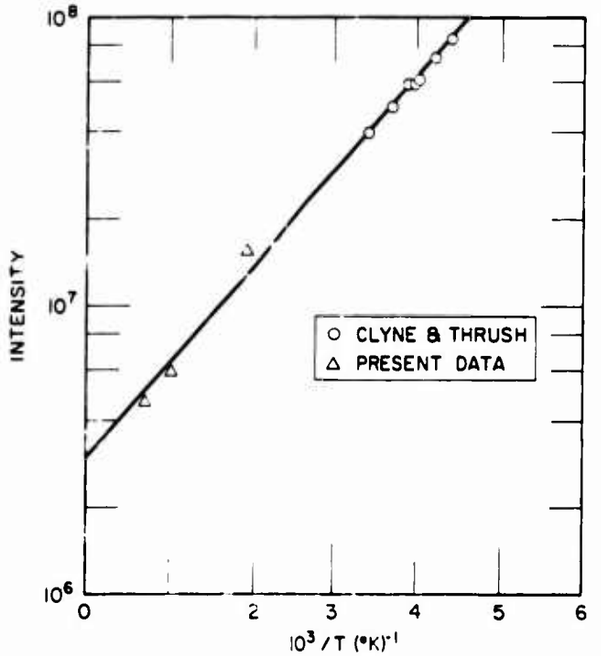


Fig. 5. Arrhenius Plot for Air Afterglow Reaction: $NO + O \rightarrow NO_2 + h\nu$

BLANK PAGE

IONIZING SHOCK STUDIES IN AN ELECTROMAGNETICALLY DRIVEN SHOCK TUBE*

B. Miller, L. Levine, R. A. Gross
Columbia University
New York, New York

At Columbia University we have built a one-meter long coaxial electromagnetic shock tube. It has a mean diameter of 7 centimeters and a one-centimeter annulus. Construction was motivated by our desire to study the formation and the properties of ionizing shock waves propagating through hydrogen. The shock tube described in this paper represents the evolution, through four years, of our understanding of coaxial electromagnetic shock tube technology and of the "normal" ionizing shocks that can be produced by such a device. By an ionizing shock we mean a shock wave propagating into a gas whose electrical conductivity is essentially zero while the gas behind the shock has an appreciable conductivity. "Normal" refers to the situation where the external magnetic field is impressed solely along the direction of propagation. Detailed theoretical studies of such ionizing shock waves, carried out by Robert Taussig at Columbia University,[1][2] have shown that for a pre-shock pressure of approximately 200 microns, shock velocities in the range 2 to 7 cm/μs represent the transition from unionized hydrogen to completely ionized hydrogen.

In keeping with the spirit of the symposium the main body of this paper will be devoted to the technology of the electromagnetic shock tube. However, at the end some of our most interesting experimental results will be presented and examined. Fig. 1 shows the shock tube, which for photographic purposes has been removed from the solenoidal coils used to establish the normal magnetic field. The figure shows the quartz windows for visual and microwaves studies, and various probes coupled both electrically and optically to monitoring stations. Also evident are the magnetic field coils. The capacitor bank which provides the energy for the device is also clearly visible. Fig. 2 is a schematic cross section of the shock tube, (not drawn to scale). The most important features to note are the coaxial geometry; the

* This research is supported by AFOSR 49(638)-1254.

instrumentation ports along the annulus for magnetic and electric field probes, and for photomultipliers; and the knife-edge assembly consisting of:

1) the knife-edge at which the electrical discharge is initiated,

2) the glass backup plate positioned just behind the knife-edge to insure a well-defined boundary condition for the launching of plane shocks, and

3) a coaxial pre-ionizing ring around which a local, 30 Mc/s rf breakdown is established before firing to insure uniform radial breakdown of the gas at the knife-edge. We have found this pre-ionization important in the launching of flat shock waves.

Also note that the knife-edge is about 10 inches away from the main shock tube end wall. This is done so that the knife-edge is located in a region of uniform longitudinal magnetic field.

We will now discuss the shock tube, associated components, instrumentation, and some typical experimental results.

The capacitor bank is a 50-kilovolt, 40,000 joule, shaped-pulse bank consisting of four parallel impedance meshes designed to deliver a maximum of 300,000 amperes into the shock tube. A parallel plate transmission line connects the bank to an air gap switch shown in Fig. 3. The air gap switch is used to hold the bank voltage from the copper feed-through connected to the knife-edge. The figure shows:

1. the parallel plate transmission line from the capacitor bank,

2. the brass anode,

3. the stainless steel cathode, and

4. the teaser electrode insulated from the cathode and used to fire the switch.

Firing is accomplished by initiating a breakdown from teaser to cathode using a .125μf, 10 kv capacitor and a 10 kv, 5 ma power supply. In addition, the figure shows some of the equipment associated with the operation and use of the shock tube, e.g. the magnetic field coils and the shock tube current monitor. The current monitor consists of a carefully shielded rectangular loop that picks up the $\frac{dB}{dt}$ produced by the changing drive current. The output of the probe drives 50-ohm terminated cable which, in turn, is connected to an operational amplifier used in an integrating mode. The output of the operational integrator gives $I(t)$ directly. The advantage of using the operational integrator is twofold. The frequency response is significantly increased compared with the usual RC network and, further, one obtains an increase in sensitivity of at least a factor of 10 over the passive integrator. The next figure (4) shows a detail of the main feed-through and the knife-edge assembly mentioned above. Here we see a close-up of:

1. the knife-edge and the inner conductor,

2. the glass back-up plate that gives the well-defined boundary condition at the launching area, and

3. the approximately 10 inches that the knife-edge is separated from the shock tube end wall.

As mentioned above, the 10 inch separation insures that shocks are launched in a region of uniform longitudinal magnetic field. The magnetic field is a dc field established by using a 600 kw rectifier supplying up to 2200 amperes. All instrumentation ports as well as the knife-edge are within the uniform field region and there is virtually no radial field component throughout the working area. The magnet is capable of providing 500 gauss to 14,000 gauss. Therefore, for a given wave speed we can propagate sub-Alfvenic, trans-Alfvenic, and super-Alfvenic shocks with no difficulty. The Alfven speed is an important parameter since, in the normal shock case, it is the fastest of the three small disturbance speeds.

Diagnostic systems used in ionizing shock studies consist of:

1. photomultipliers for wave speed measurements,

2. magnetic field probes for mapping the self-induced magnetic field in the B_θ direction, and

3. electric field probes for determining the magnitude of the electric field ahead of the shock.

Photomultiplier assemblies are used to measure the propagation velocity of the luminous front associated with the shock. The setup consists of a 1/16th inch hole drilled through the outer conductor wall and viewing the annulus at a particular position. A reflector assembly consisting of a main body and a front silvered mirror is positioned above the 1/16th inch hole. A fiber-optic light pipe is positioned in the reflector assembly and views the port. It is connected to a photomultiplier outside the shock tube. This assembly permits viewing any number of ports along the length of the tube without making any breaks in the magnet.

Fig. 5 shows a magnetic field pickup probe used to monitor the switch-on field behind the ionizing shock. It consists of ten turns of Formvar wire wound into a rectangular form and coated with a layer of clear epoxy to give some structural integrity to the coil. The probe is situated in the annulus and monitors the magnetic field in the θ direction. The output of the coil is carried via the twisted pair to a Cannon connector which mates to a pulse transformer. The output of the pulse transformer is viewed directly on the scope without any prior time integration of the signal. This is an important point and will be discussed later on. Note, also, the large size of the probe. It is roughly 12 millimeters long by 1-1/2 millimeters high. This was done purposely and is intimately related to the reason for eliminating

time-integration of the probe output.

The radial electric field probe is designed to detect a difference of plasma potential between two points in the hot gas by sampling some of the current in the shock and the plasma. The probe is identical in construction to the magnetic field probe except for the bare wires obviously needed to draw current.

In addition to the diagnostic systems just spoken of, three other diagnostic systems, all in the first stages of development, are being brought to bear on the problem. These consist of:

1. a 4-millimeter microwave interferometer for precursor studies, and doppler-shift velocity studies,

2. a laser interferometer for interferometric studies in the main ionizing shock region, and

3. a spectrograph and image converter camera for time-resolved studies of electron temperatures and number densities.

Fig. 6 shows the 4-millimeter microwave interferometer set to monitor the precursor electron density. Here we make use of the quartz windows in the shock tube wall mentioned earlier.

Fig. 7 shows the laser interferometer. The interferometer consists of a cw laser for number density measurements in the range $n_e > 10^{16}$/cc. The method of measurement is, in theory, quite simple. The laser beam is directed through the shock tube, reflects off a mirror and returns. A standing wave pattern is set up along the beam path. A photomultiplier behind the laser views the standing wave pattern. As the shock wave interupts the beam the standing wave pattern shifts and the shift, related to n_e, is monitored directly on a scope.

Fig. 8 shows the time-resolved spectroscopy unit. It consists of a one-meter McPherson spectrograph coupled to an STL image converter camera so that we can study the appearance, time history and the structure of plasma line and continuum radiation and of impurity lines. Preliminary results indicate that even with crude optics the light intensity from the shock tube is sufficient for fast, time-resolved spectroscopy.

This concludes the survey of the experimental apparatus and the equipment. We will now take a brief look at some of the experimental results.

Fig. 9 is an x-t diagram for a shock propagating at an Alfven Mach number of 1.2, i.e. in the middle of the trans-Alfvenic region where we expect to see switch-on shocks. The shock tube was run 10 times at these conditions and photomultiplier outputs monitored at the 25 cm, 35 cm, 50 cm, and 75 cm positions. Note the steady propagation and the very reproducible nature of the several runs. The dashed line represents the acceleration phase of the

shock's propagation. In this region the shock is forming. We will say more about this later.

We now turn our attention to the magnetic field probes. For the conditions specified in Fig. 9, theory[1] predicts a switch-on shock. Fig. 10 is a profile of the magnetic field at the 45 centimeter point for the experimental conditions shown in Fig. 9. Before discussing it, however, it is necessary to make a few preliminary remarks relating to the B_θ probe. In all these experiments we are dealing with shock phenomena and, hence, across the shock we have large gradients in all the measurable variables. One cannot assume that the magnetic field is constant across the probe. For this reason, time integration by electronic means of the EMF produced by the probe may be in serious error. We purposely made our pickup loops large so that B is definitely not constant across the probe width and we did not time-integrate the EMF to yield B_θ. Rather, we used an exact analysis[3] to recover B_θ from the directly observed EMF. The beauty of the analysis we use is that, in principle, its frequency band width is infinite and the only errors introduced are due to the mechanical and electrical characteristics of the probe system. Returning to Fig. 10, the heavy line is the EMF observed by the probe. From the exact analysis B_θ is recovered and consists of the heavy line and the dashed line. To be noted are the shock region, the region of the homogeneous gas sample in which we have a uniform magnetic field, and the expansion fan. The shock thickness and the homogeneous gas sample are both of the order of a centimeter. The expansion fan is of the order of 4 centimeters. This is a real switch-on shock wave.

In all these studies, the importance and the effect of the electric field ahead of the shock must not be minimized. It is responsible for switch-on waves being extended to all slow shocks, to the existence of a limit field beyond which no steady waves can be propagated, and for the fact that there are restricted regimes of steady propagation.[1][2]

The radial electric field at the 35 centimeter point picked up by the electric field probe at $M_a = 1.4$ gives additional evidence that there is a region behind the shock wave and before the expansion fan in which there is little or no current flowing. This is further confirmation of the switch-on shock discussed above.

Fig. 11 shows a study made of shock formation in an electromagnetic shock tube for varying shock strengths. This is done to bring attention to the fact that ionizing shock strength plays an important role in electromagnetic shock tube technology. As in ordinary gas dynamics, the stronger the shock (i.e. higher ratio of wave to signal speed) the faster it forms. This carries over to ionizing shocks as is evident from the figure. For the strong shock, Alfven Mach number $M_a = 2.3$, the shock is well formed at the 20-centimeter point. For the weak shocks, $M_a = .5$ and $M_a > .2$, the shock is not formed at the 20- or 25-centimeter points, but steepens later on, as would be expected.

In conclusion, the electromagnetically driven shock tube described here

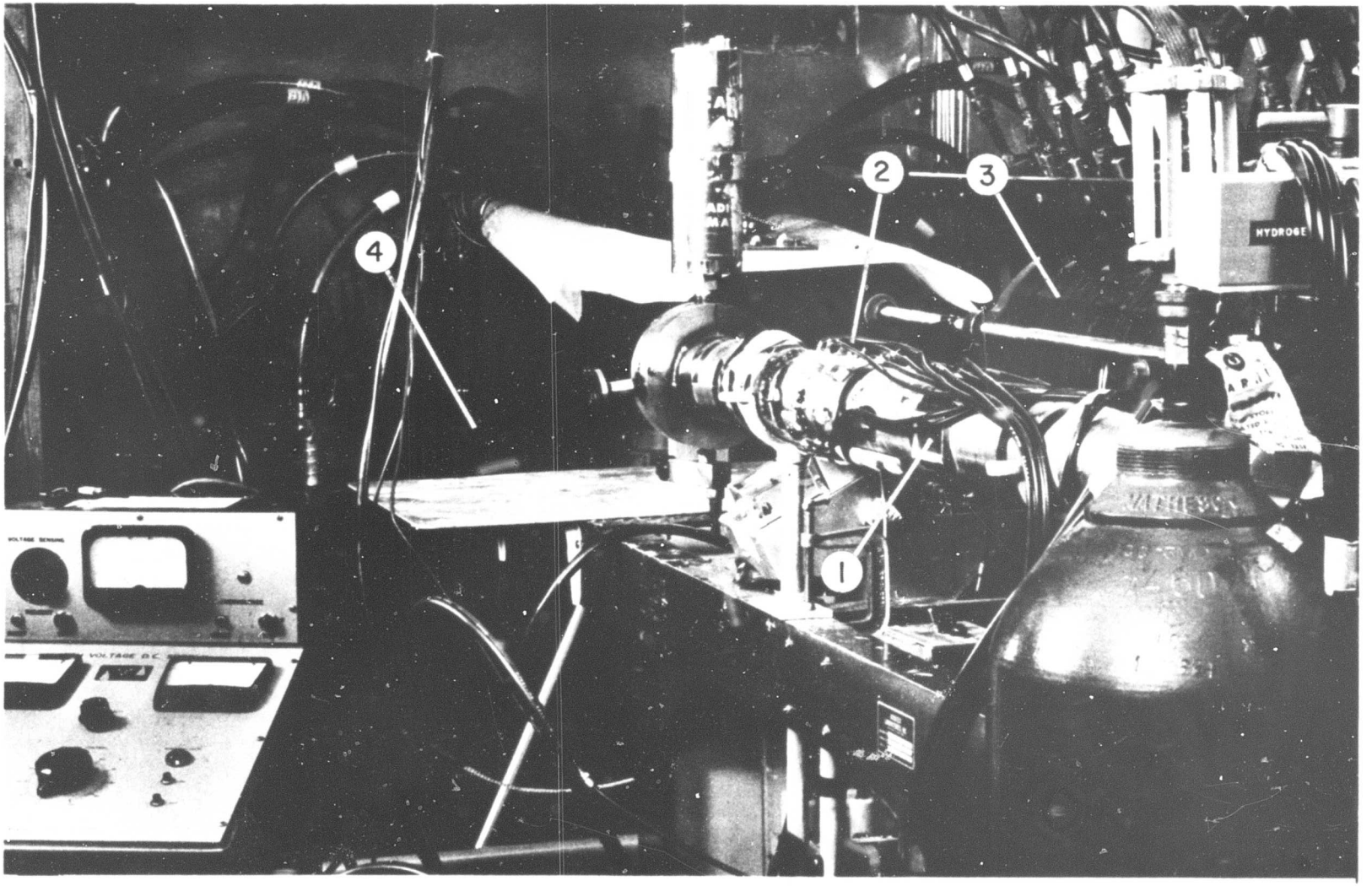
has been found to be a reliable means of generating strong ionizing shock waves and hot dense plasmas.

REFERENCES

(1) Taussig, R., Normal Ionizing Shock Waves, Columbia Univ. Plasma Laboratory Report Nc. 12, July 1964. (To be published - Physics of Fluids).

(2) Taussig, R., Normal Ionizing Shock Waves - The Effects of Equilibrium, Dissociation and Ionization, Columbia Univ. Plasma Laboratory Report No. 14, Aug. 1964.

(3) Miller, B., Columbia University -- Doctoral Thesis; Columbia Univ. Plasma Laboratory Report No. 19, June 1965.



1. Quartz Window
2. Probes
3. Magnetic Field Coils
4. Capacitor Bank

FIGURE 1 OVERALL VIEW OF THE ELECTROMAGNETIC SHOCK TUBE

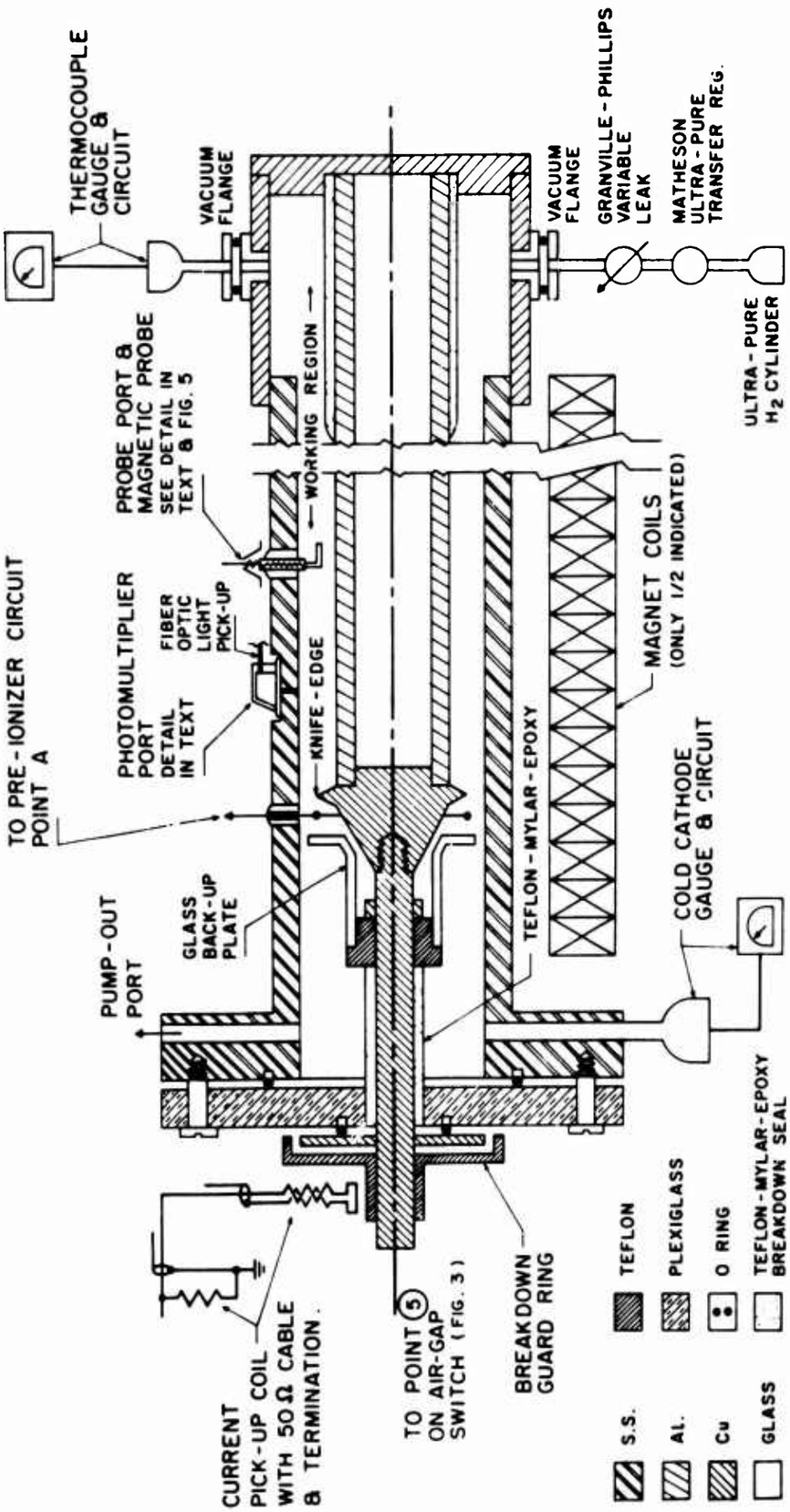
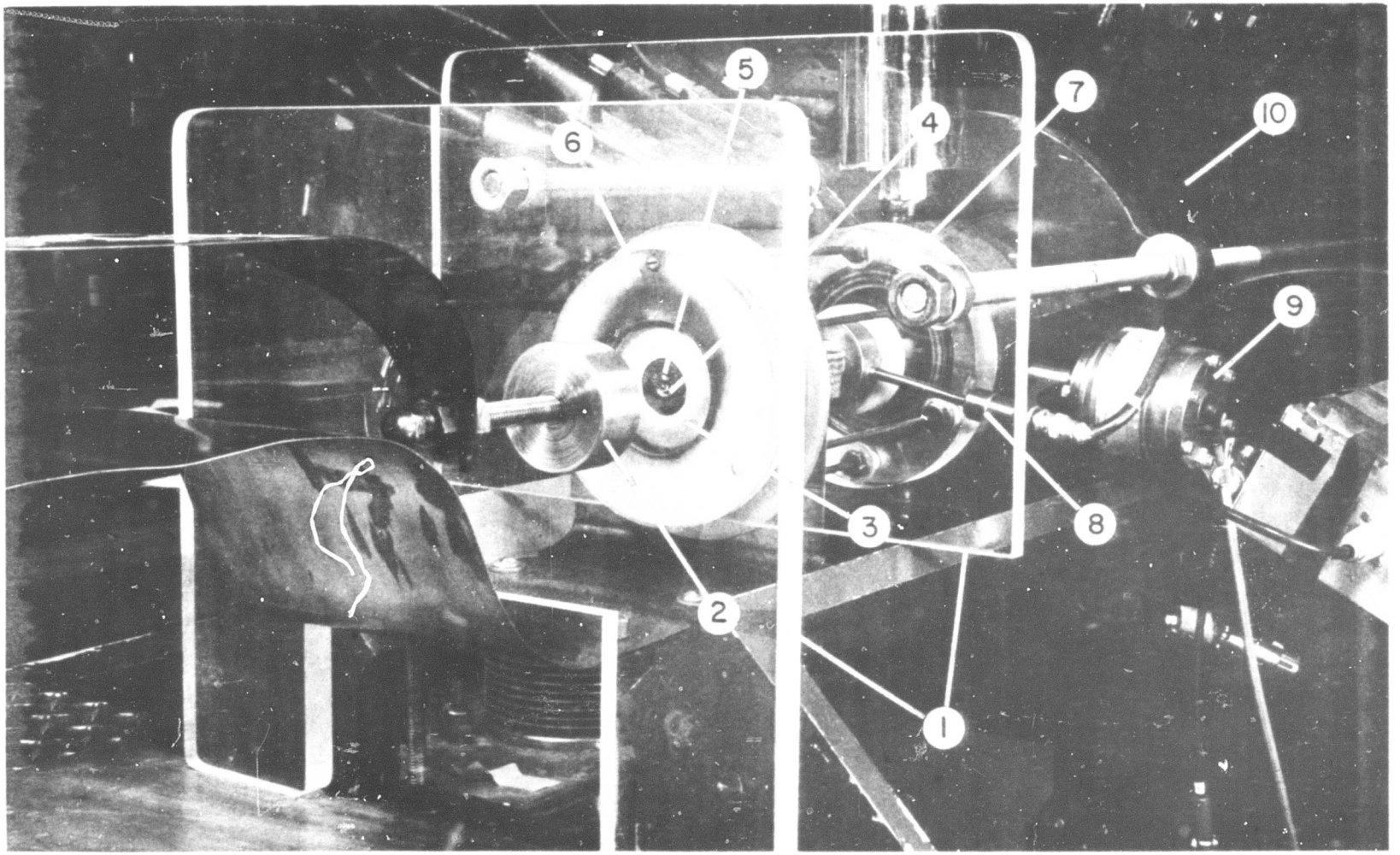
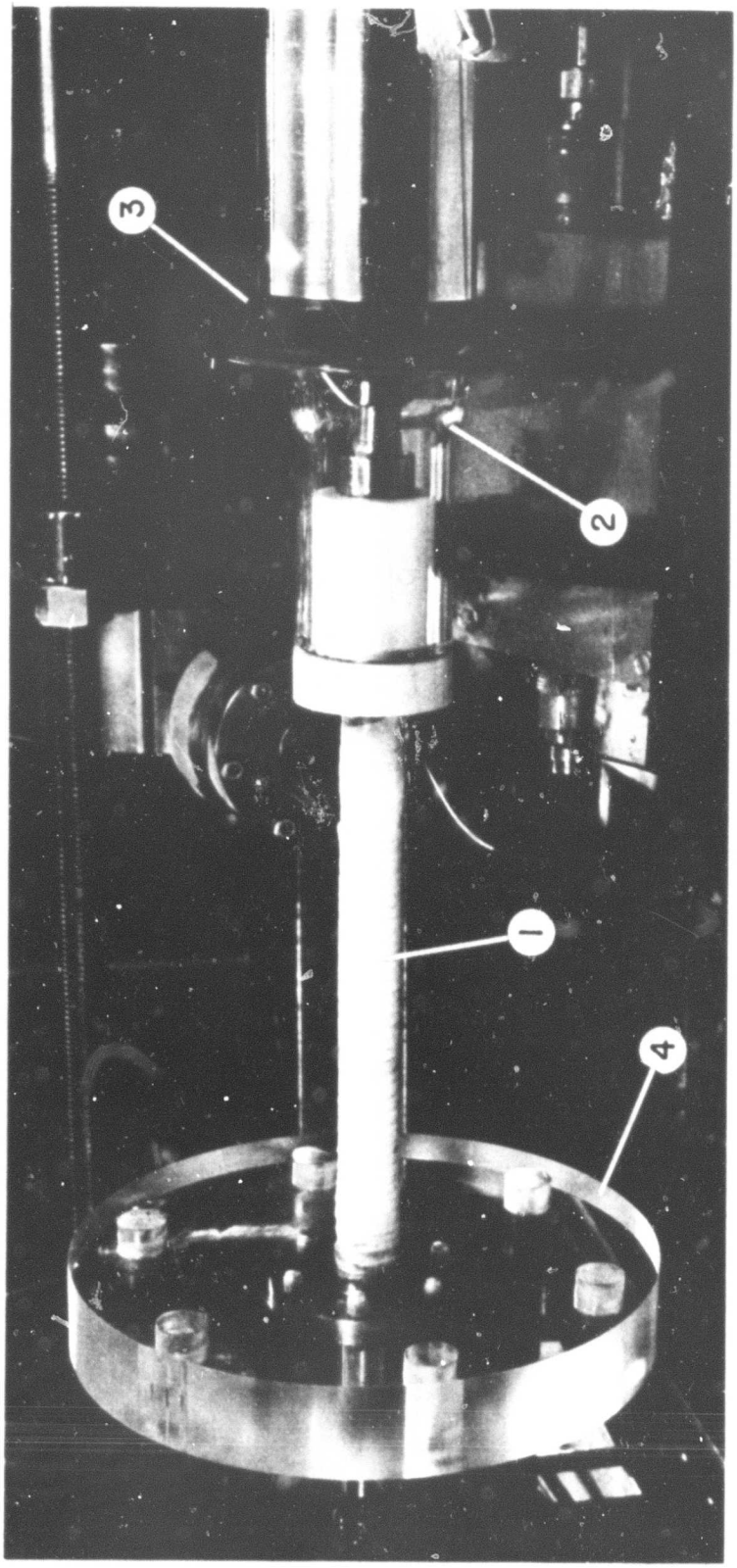


FIG. 2 SCHEMATIC CROSS-SECTION THROUGH SHOCK TUBE. (NOT TO SCALE)



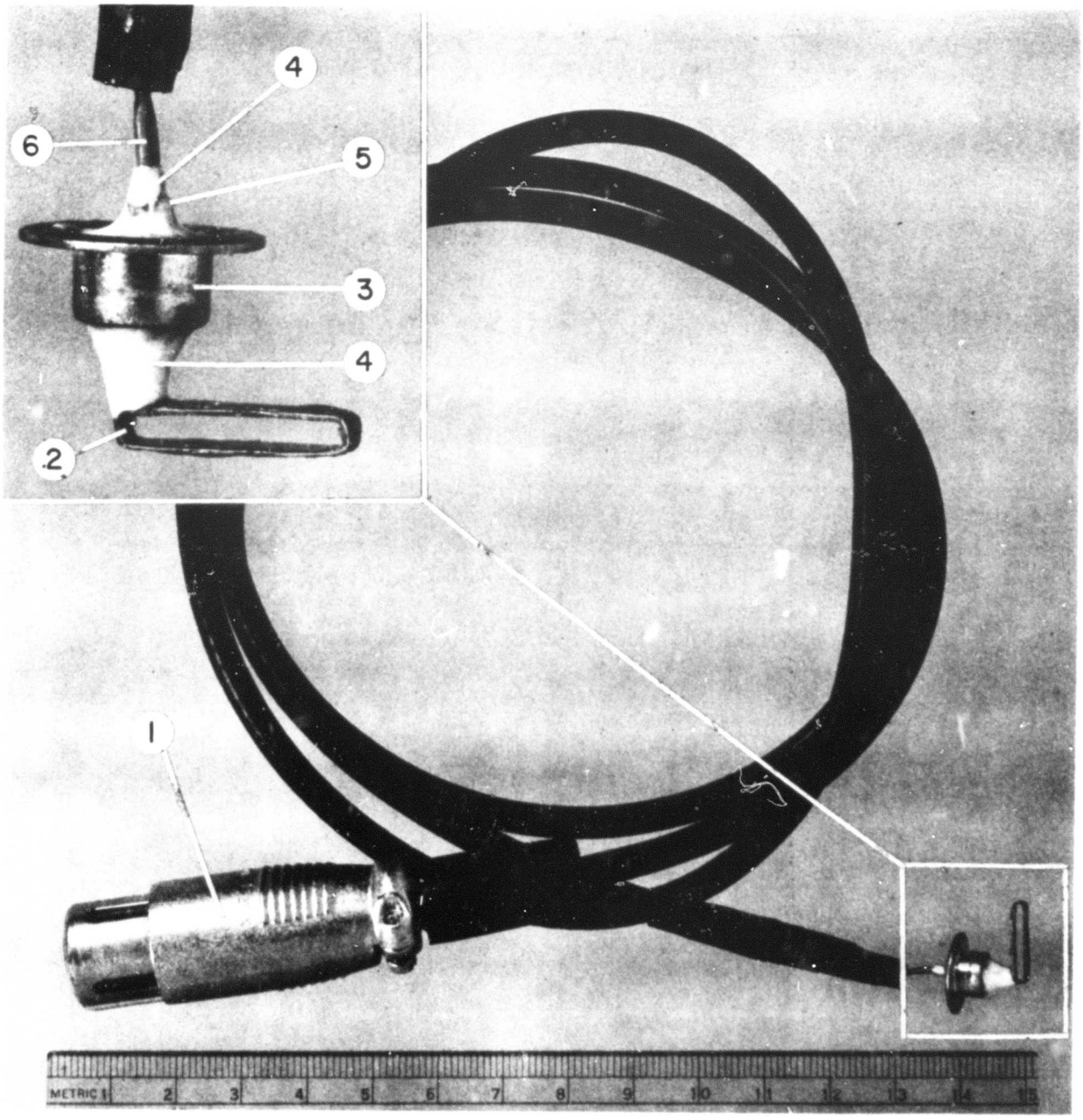
1. Switch Support Plates
2. Anode
3. Teflon Breakdown Guard Ring
4. Teaser
5. Cathode
6. Plexiglas Support
7. Main Body of Shock Tube
8. Current Monitor Probe
9. Cold Cathode Gauge
10. Magnet Coils

FIGURE 3 PARALLEL PLATE TRANSMISSION LINE AND AIR GAP SWITCH



1. Teflon-Mylar Epoxy Breakdown Seal
2. Glass Back-up Plate
3. Knife-Edge
4. Plexiglas End Piece

FIGURE 4 FEED-THROUGH AND KNIFE-EDGE ASSEMBLY



1. Cannon Connector
2. 10 Turn Probe-Epoxy Coated
3. Vacuum Feed Thru
4. Epoxy Seal
5. Glass Sleeve
6. Twisted Pair

FIGURE 5 MAGNETIC FIELD PICKUP PROBE

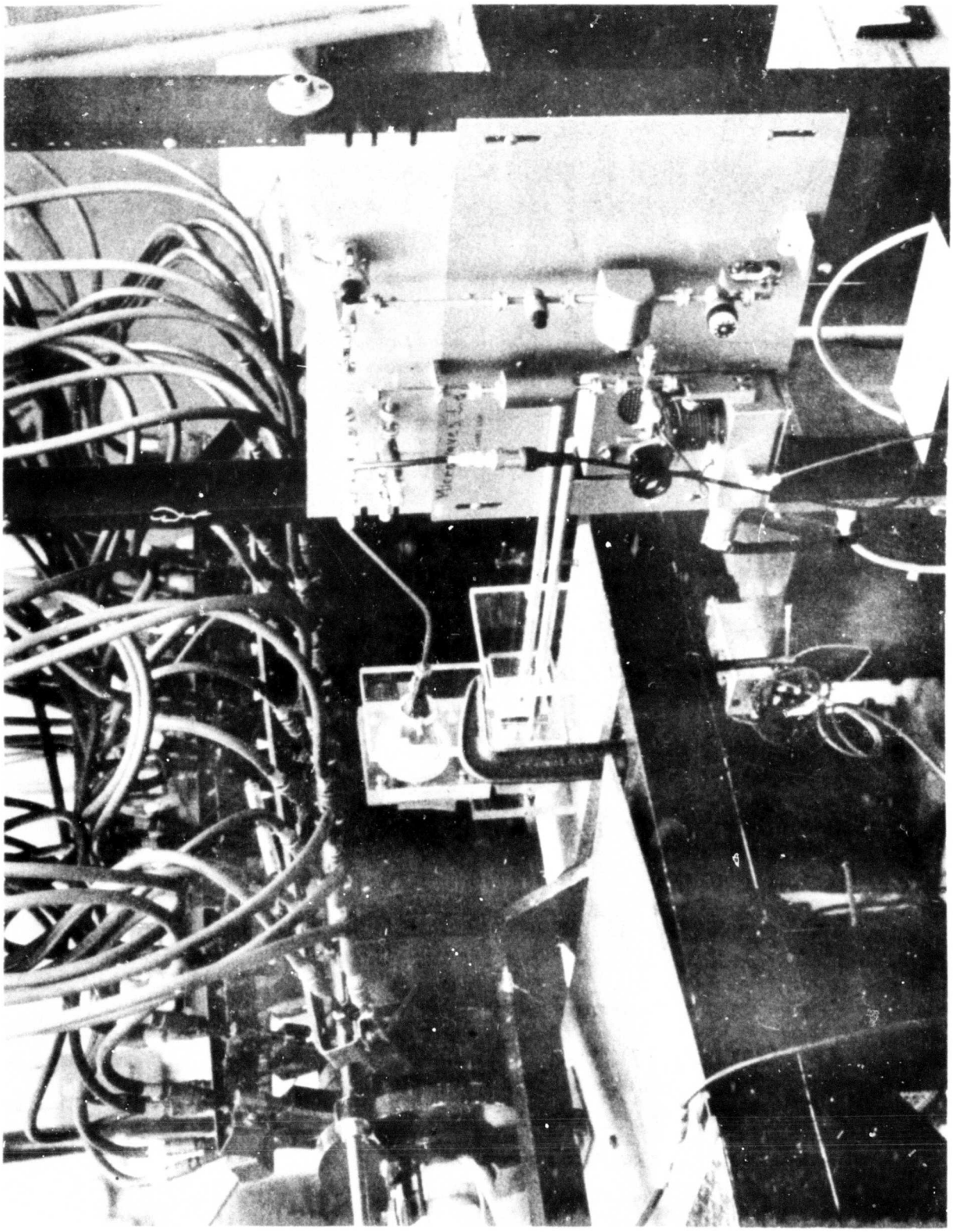


FIGURE 6 FOUR MILLIMETER MICROWAVE INTERFEROMETER

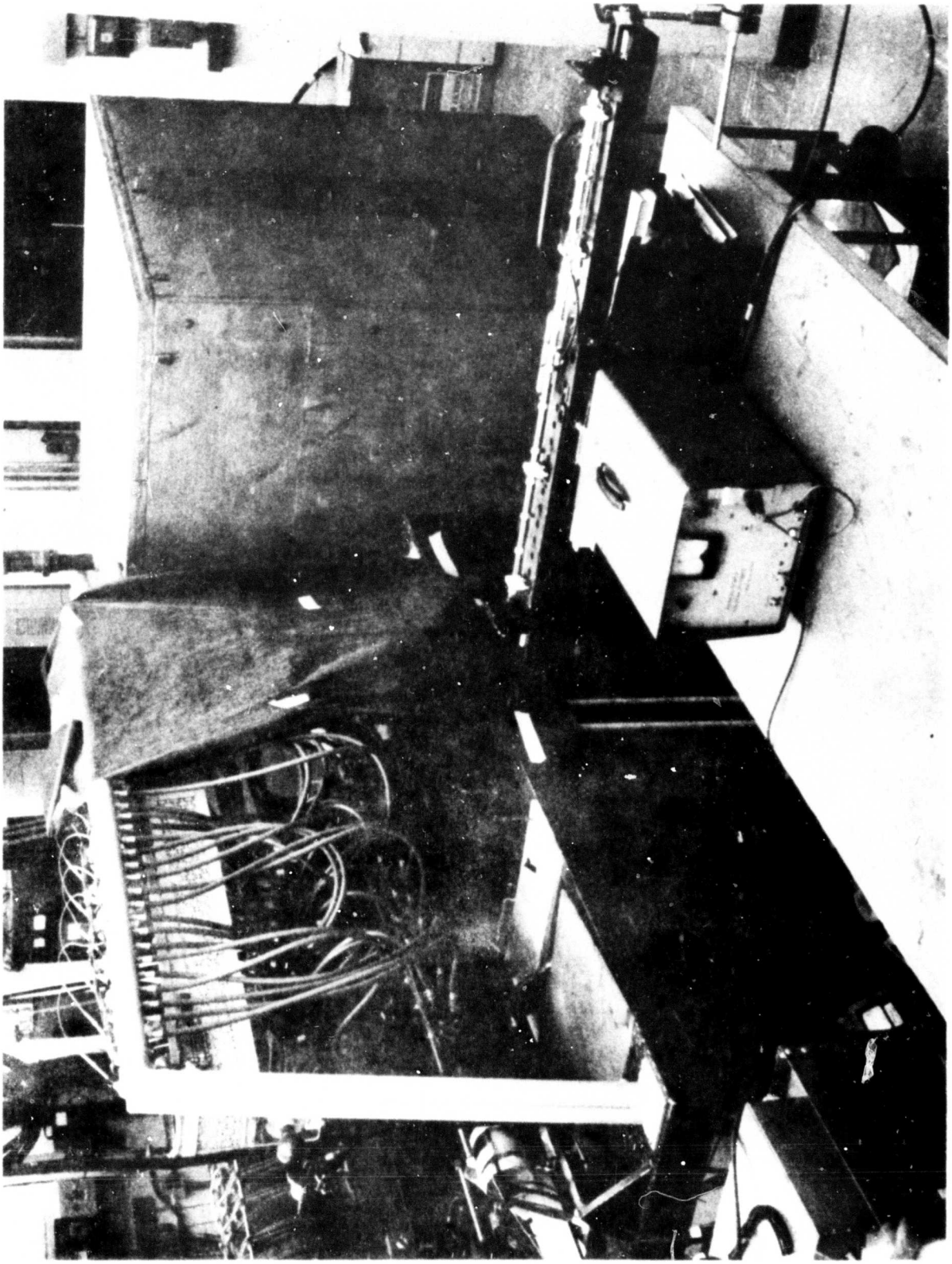


FIGURE 7 LASER INTERFEROMETER

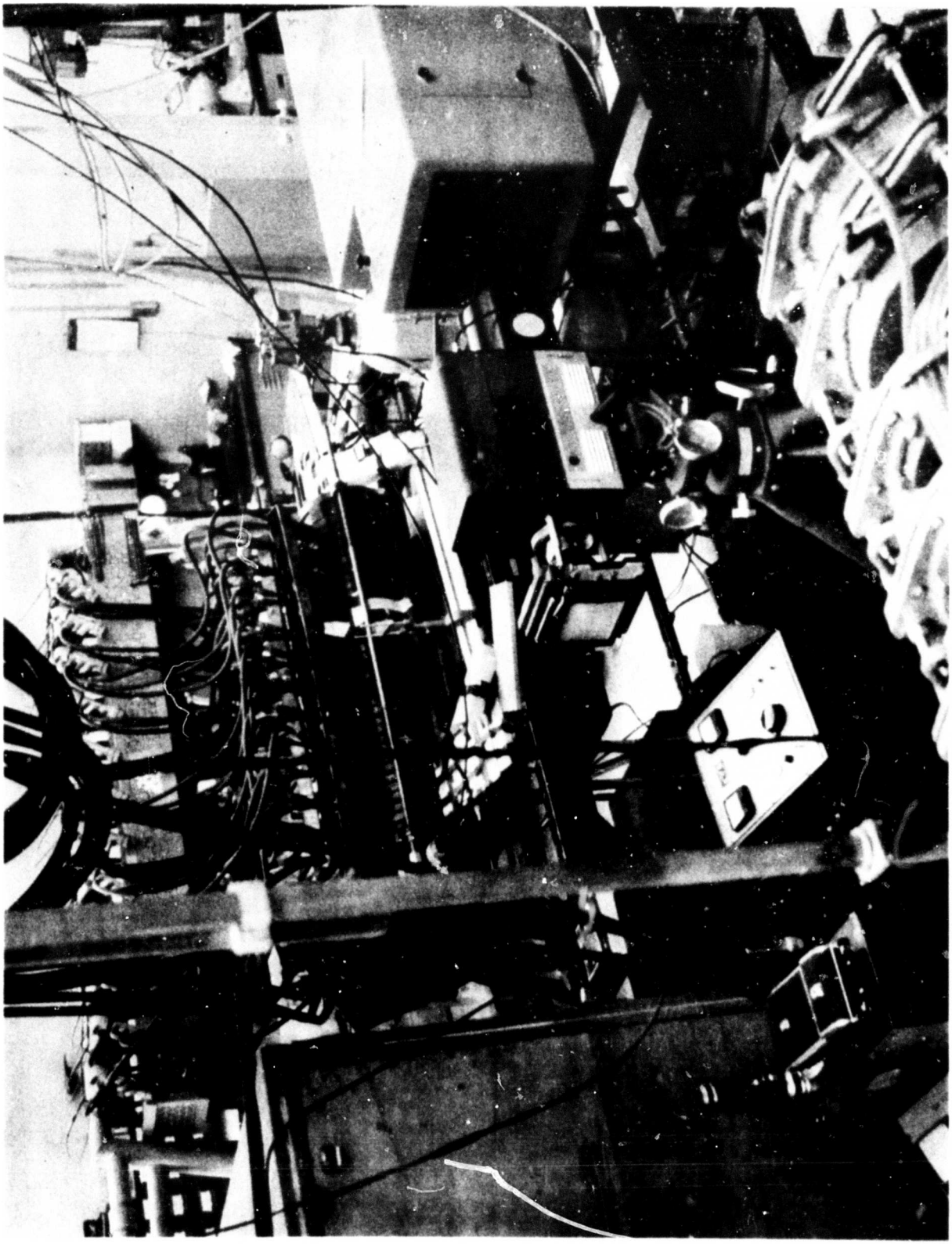


FIGURE 8 GRATING SPECTROGRAPH AND IMAGE CONVERTER CAMERA

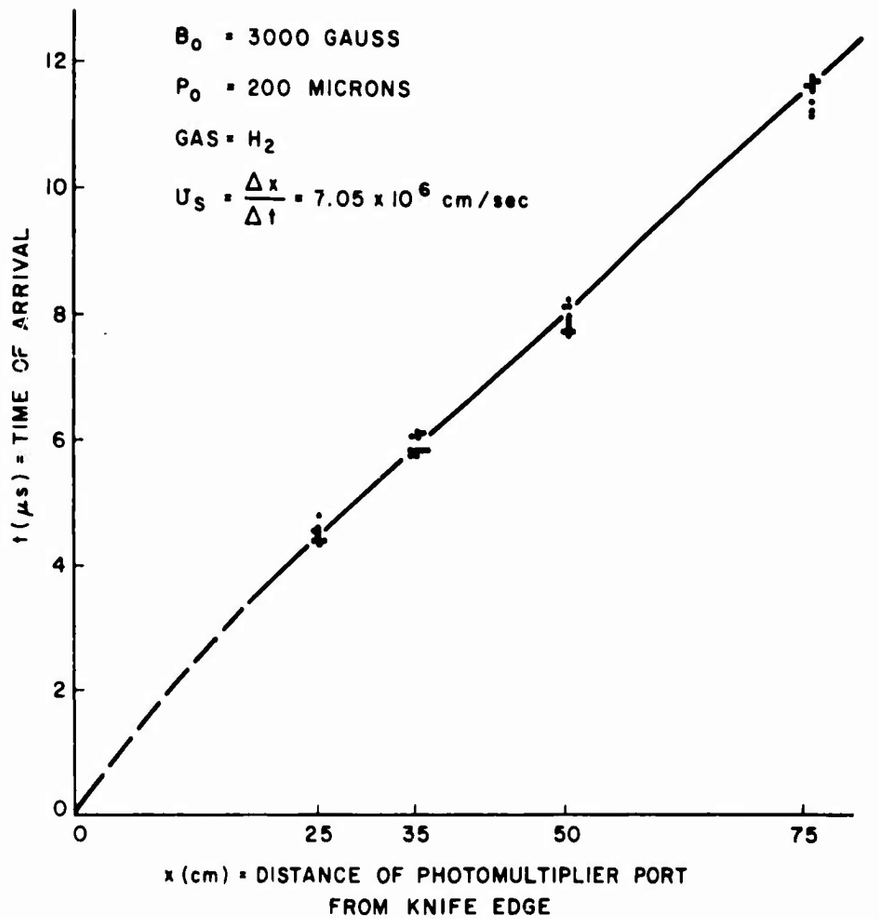


FIG. 9 x - t DIAGRAM FOR SHOCK TUBE

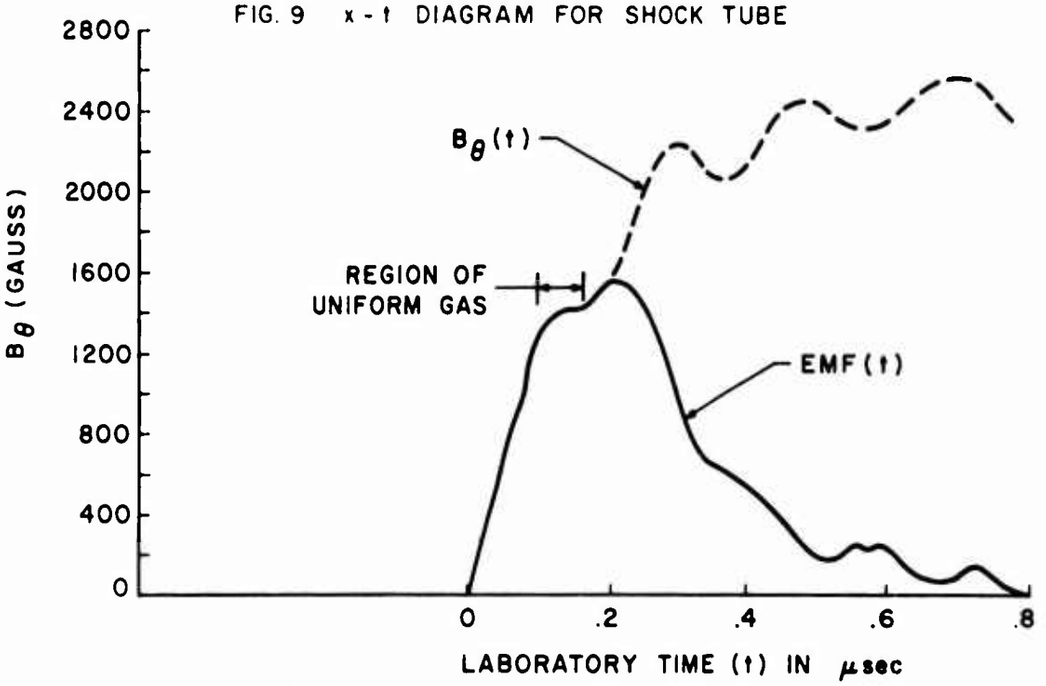


FIG. 10 EMF (t) AND B_θ (t) DERIVED FROM EMF (t).

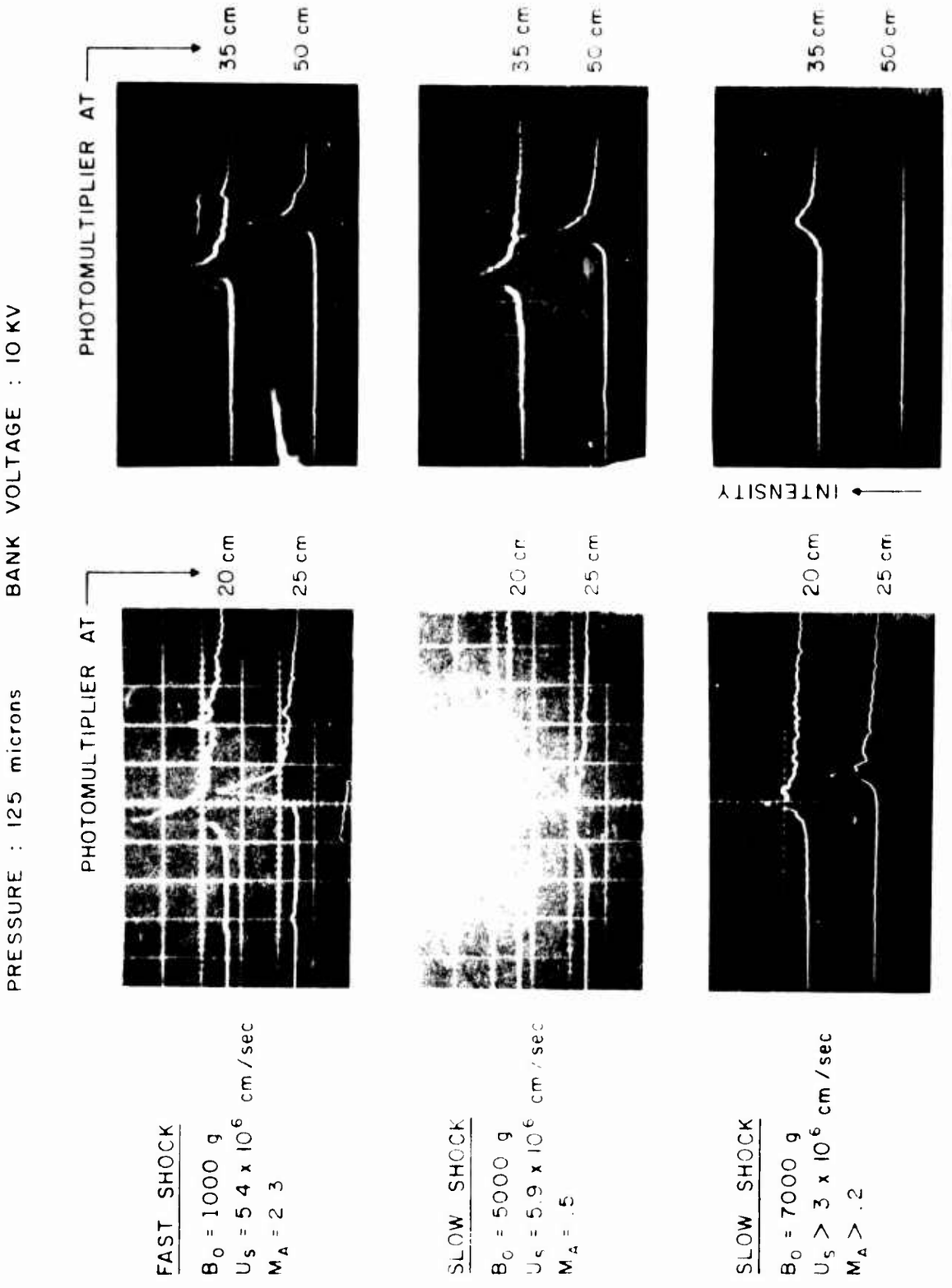


FIGURE 11 SHOCK FORMATION STUDY

PERFORMANCE OF DOUBLE-DRIVER SHOCK TUBE

Bo Lemcke*
Consultant, Massachusetts Institute of Technology
Cambridge, Massachusetts

INTRODUCTION

Blast effects on moving vehicles are currently of great interest. Such problems can arise, for instance, at the interception of a re-entry vehicle by a blast wave from a nuclear explosion, of an airplane by a blast wave from an exploding shell, or the interception of an airplane by the shock wave from a passing supersonic vehicle. For true simulation in the laboratory of the considered problem a method must be found for producing both the ambient flow around the vehicle, or model, and the intercepting blast wave. In reference (1) a method was proposed for producing two consecutive shock waves by employing a double-driver shock tube. The ambient flow around the model would be established behind the first shock wave and then the blast effects could be studied at the arrival of the second shock.

The advantage of a double-driver shock tube is that a well definded flow can be produced and investigated on a fixed model in a facility where the measurement technique is well developed. On the other hand it should be pointed out that the Mach number of the flow around the model is limited to about 3 and that only head-on shock interactions can be achieved. Thus only supersonic (or subsonic) ambient flows can be simulated together with the stagnation region of a blunt body in hypersonic flow. The latter case arises from the fact that the shock layer at the nose of a hypersonic blunt body is virtually established already at a Mach number of about 2.5, see for instance reference (2).

A project under DASA support has been initiated at M.I.T.** to study

---

*Present address: The Aeronautical Research Institute of Sweden (FFA), Bromma 11, Sweden. FFA Contract No. AE-513:1.

**Contract No. DA-49-146-XZ-297

blast effects on a re-entering RV in a shock tube at Cornell Aero. Lab., modified for double-driver operation. While waiting for the preparations at CAL to be completed an in-house program was initiated at the Aeronautical Research Institute of Sweden, to study the basic flow problems in a double-driver shock tube when operated to produce two consecutive shock waves. This program is not yet completed but some significant results of the work done so far will be presented in this paper.

PRINCIPLE OF OPERATION

The principle for the flow in a double-driver shock tube (DDST) when used for producing two consecutive shock waves is illustrated in Fig. 1. The driver and the intermediate driver are separated from each other by diaphragm 2 and the intermediate driver from the expansion chamber by diaphragm 1. The run is initiated by bursting diaphragm 1. A shock wave is propagated into the expansion chamber followed by the contact surface separating the intermediate driver gas from the driven gas. Simultaneously, an expansion wave propagates upstream into the intermediate driver and reflects from diaphragm 2. The pressure drop on the downstream side of diaphragm 2, caused by the reflection of the expansion wave, eventually makes this diaphragm burst and a second shock wave is generated and swept into the intermediate driver and expansion chamber. The second shock overtakes the expansion wave and the contact surface and continues into the driven gas. At the test station, the flow is initiated by the first shock wave, after which the second shock wave follows and interacts with the established flow around the model.

THEORETICAL PERFORMANCE AND SIMULATION CAPABILITIES

To evaluate the performance of a DDST and study the importance of various parameters, a finite-difference solution of the conservation equations for a non-viscous, perfect gas, with the appropriate boundary conditions was programmed for an IBM 7094 digital computer, see reference (3). The output from the computer runs consisted of the location of the second shock wave with time together with thermodynamic and flow properties of the gas at a series of points along the tube. Thus, the strength of the second shock wave was also found at different locations along the tube, for example, by evaluating the ratio between the pressure on either side of the shock.

There are three questions of obvious importance that could influence the performance of a DDST. First, what is the opening time of diaphragm 2, see Fig. 1, compared with typical times in the wave histories? Second, what is the influence on the interaction between the second shock wave and the contact surface from the fact that the contact surface is not a mathematical surface but rather a highly turbulent mixing zone between the driver gas and the test gas? Third, what is the effect on the second shock wave of the interaction between the second shock and the boundary layer

formed on the shock tube walls behind the first shock wave?

In the first question a typical time will be defined as the time for a sound wave to travel through the entire intermediate driver, $t_1 = L_4/a_4$, where L_4 is the length of the intermediate driver, and a_4 is the speed of sound in the intermediate driver. Simple theoretical calculations show that the diaphragm opening time in all practical cases is less than, and in many cases much less than, this typical time, It was felt that no appreciable deviations from the theoretical wave histories would generally occur from the finite opening time of diaphragm 2.

The interaction at the contact surface, or mixing region, depends on the ratio of acoustical impedances across the contact surface and possibly on the variations in flow properties through the contact region. To evaluate the importance of the latter question a simple numerical example was worked out where the contact surface had been replaced by three interfaces separating gases at four different conditions. Assuming perfect gases with the same ratio of specific heats in all the layers, the ratio of acoustical impedances will be equal to the square root of the inverse ratio of the specific volumes. The specific volumes were given numbers in the ratios 2/11/6/15, to simulate a mixing region, as compared to the ratio 2/15 for one interface. A shock wave with a pressure ratio of 15 was then allowed to interact with these interfaces and the transmitted shock strength calculated. With one interface the pressure ratio of the transmitted shock was 5.61 while for three interfaces the ratio was 5.48. Thus a 2.4 % reduction in shock strength was observed in a case where the irregularities through the contact region were made quite large. Based on this result it was concluded that the density variations in the contact region would not produce any additional problems in the performance of a DDST which was confirmed later on by experiments.

Finally there was some concern about the influence of the interaction between the second shock and the wall boundary layer on the pressure history at the shock tube walls as well as the wave histories. To study whether the second shock was essentially plane at the wall through the boundary layer or if it was curved, shock tube runs were prepared for measuring pressure at the wall and at the axis of the tube at the same axial station simultaneously and for making Schlieren measurements. The results of these measurements together with some theoretical evaluations of the observed results will be given below in the section on EXPERIMENTAL RESULTS.

When the DDST is used for simulation of the shock-on-shock interaction at the stagnation region of a hypersonic vehicle a similarity problem has to be solved. In the DDST the conditions in the shock layer can be duplicated but not the strength of the bow shock wave. Thus the following question should be answered: What is the required pressure ratio, p_5'/p_o' of an impacting shock wave on a model in a flow at Mach-number M_o' to produce the same strength of the shock wave transmitted into the shock layer of the

model as would result if the flow was at the hypersonic Mach number M_o and the pressure ratio of the impacting wave was p_5/p_o ? This problem was looked into in reference (4) and the basic result was that for $M_o' < M_o$, then $p_5'/p_o' < p_5/p_o$.

EXPERIMENTAL SET-UP

The experiments were run in an existing shock tube at The Research Institute of the National Swedish Defense, modified for double-driver operation employing air both as driver and test gas. The shock tube consists of a series of interchangeable sections, Fig.2, bolted together. This results in a very flexible system that is well suited for the present test program where the relative length of the different parts has to be changed in accordance with the running conditions. All the sections are mounted on wheeled frames that run on tracks which extend along the full length of the laboratory. Diaphragm station 1 consists of a double-diaphragm system where the pressure between the diaphragms is initially set equal to 0.5 p_4. The run is initiated by releasing this pressure. Thus it is possible to preset all the pressures to the desired values and to initiate the run at will.

The inner diameter of the circular shock tube is 3.94". The test section, however, has a rectangular cross-section, 2.36" by 5.16", having the same cross-sectional area as the circular tube. A constant area transition section followed by an 84" long rectangular tube connects the test section to the circular tube at both ends. This length should be sufficient to damp out most non-uniformities that are created in the transition section. Detailed study of the flow quality in the test section has not been made as yet but is part of the later phase of the test program.

The driving pressure is limited to 860 psi and the best vacuum that has been obtained so far in the expansion chamber is 4 mm Hg. The main source of leakage is the test section, which was built entirely of plexiglass. A new test section is being constructed, however, which should decrease the leakage and also improve the optical quality of the windows which is presently rather poor.

The instrumentation used in the tests consisted of pressure transducers, thin film gages for wall temperature measurements, and a Schlieren system with a spark generator and a drum camera. The spark generator could deliver a series of up to 64 sparks at least 0.25 milliseconds apart with a duration of about 1 μ sec each. The size of the windows was 5.2" x 5.2" and thus a shock wave with a velocity of not greater than 1700 ft/sec could be recorded with 100% probability of success (provided that the spark train was correctly triggered). The window in the new test section will be 10" long and will thus allow shock waves of twice the velocity to be recorded. This will considerably simplify the operation.

A number of pressure transducers and wall temperature gages, but only three oscilloscope channels, were available during the tests. Generally

one pressure transducer was used for triggering and one wall temperature and two pressure histories were recorded. Two different kinds of pressure transducers were used. One was a high frequency response, Kistler 601F, quartz gage, with a rise time of about 2μ sec and with a heavy ringing at the natural frequency when subjected to a step pressure. The other one was a high sensitivity, barium-titanate gage with some overshoot and ringing from a step pressure. The rise-time was measured to be about 8μ sec. To the Kistler gage was made an electric filter to damp the natural frequency of the gage. The filter had a rise-time of 4.5μ sec.and an overshoot of 3%.

A special adapter was made for one of the barium-titanate gages to measure the pressure history on the axis of the shock tube. A pitot tube transmitted the pressure to the transducer which was mounted in the shock tube wall, see Fig.3. Another gage was mounted at the same axial location as the entrance to the pitot tube for measuring the wall pressure. Thus comparisons could be made in terms of pressure history at the axis and at the wall of the shock tube respectively. Due to the difficulties in damping the acoustical ringing in the pitot tube plus the cavity adjacent to the transducer, reliable records were never obtained of the pressure at the shock tube axis. The arrival time of the shock waves could still be accurately determined, however.

EXPERIMENTAL RESULTS

Reflected Expansion Wave

One of the most important factors in the self-timing of the DDST is the pressure drop due to the reflection of the expansion wave from diaphragm 2. A few tests were performed to determine to what extent the observed pressure drop agreed with that theoretically predicted. From equations and graphs in reference (5) it is seen that the reflected pressure can be written as

$$\frac{p}{p_4} = \text{fn}\ \left(\frac{t\ a_4}{L_4}\right) \qquad \text{for} \qquad p \geq p_r$$

where p_r is the terminal pressure after the reflection. The relative pressure drop is thus, at the beginning, only dependent on a dimensionless time and independent of the pressure ratio p_4/p_1. The terminal pressure, p_r, is a function of p_4/p_1, however. The equation above is plotted in Fig.4 together with some experimental values. The experiments were run with different values of L_4 and p_4/p_1. During these tests diaphragm 2 was replaced by a flange containing a pressure transducer mounted flush at the end wall.

From the pressure traces several points were plotted on Fig. 4 and in some cases dashed curves were drawn between the points to show, approximately the pressure history in more detail. Diaphragm 1 consisted of one or two

diaphragms. For the case of one diaphragm the pressure was increased until a natural burst occurred. With two diaphragms the pressures were pre-set and the run initiated by evacuating between the diaphragms.

Fig.4 shows several important facts. If the diaphragm opened properly the pressure drop followed the theoretical curve for a considerable time. For a poor diaphragm opening, that is to say, when the diaphragm did not open to the full tube area, the pressure would level off at far too high a value. When two diaphragms were used there was one initial drop followed by a pressure recovery, corresponding to the burst of the upstream one of the two diaphragms, and then the proper pressure drop followed the burst of the second one of the two diaphragms. Thus the early pressure drop from the reflected expansion wave which is the most important part in these experiments is well predicted by perfect gas theory.

Wave Diagrams

During most of the runs only pressure histories have been measured at two different locations of the tube. Both the thin film gages and the Schlieren system only bacame available towards the end of the test period. The pressure records serve several purposes, however: wave diagrams can be constructed, repeatability of the runs checked, boundary layer effects interpreted to some extent, non-uniformities in the flow established, etc. After several hundred runs, made under sets of different conditions, it can be stated that repeatability has generally been very good. Exceptions have occurred now and then, however, that is to say, some runs have produced results quite different from the normal ones under the present conditions. These anomalies have been attributed to un-even properties of diaphragm 2. More about this will be said later on.

Due to some diffuculties with diaphragm 2 it became apparent at an early stage of the tests that it would simplify the program considerably if only one type of diaphragm was used at station 2. Thus all runs, where results were obtained, have been performed with 1 mm aluminum diaphragms at station 2.

In a number of experimental runs the main objective was to check the theoretical wave histories and to measure the strength of the second shock. Two pressure transducers were located at stations about 7.5 feet and 41 feet respectively from diaphragm 1. The length of the intermediate driver was selected to fit the driving conditions in such a way that the second shock would generally have reached the test gas at the down-stream transducer. Results from these measurements are given in Figs. 5, 6 and 7, for pressure ratios p_4/p_1 of 25, 100 and 1000 respectively. The curves for the shock waves and the contact surfaces were obtained from the computer program, where $p_5 = 2\ p_4$ and $p_s = 0.8\ p_4$, p_s being the pressure in the intermediate driver at diaphragm 2 at its rupture. The experiments were all run with $p_4 = 370$ psi and p_5 ranging from 440 to 720 psi. For $p_4/p_1 = 1000$, p_5 was always larger than 660 psi.

Only a few test runs were plotted, and, as was said earlier, repeatability was generally quite good and very little difference, if any, could be seen in the result from several runs, made at the same conditions. In Fig.7, however, irregularities can be observed in the arrival time of the second shock wave. Again, the explanation can possibly be found in the quality of diaphragm 2.

The locations of the two pressure transducers are indicated with arrows on the x-axis of Figs. 5-7 and labeled P_1 and P_2. Along the history of the second shock wave theoretically obtained values of the pressure ratio across the second shock, σ, are given. In the legend the experimentally measured values are given together with the driving pressure p_5.

It can be noticed that the second shock is stronger if it is generated later. This is because the pressure ratio as well as the speed of sound ratio across diaphragm 2 increases with time due to the pressure drop from the reflected expansion wave. In Figs. 5 and 6 the strength of the second shock, for the appropriate runs, is seen to come very close to the predicted value. Again, in Fig.7, the discrepancy between theory and experiment is larger. It is believed that the discrepancy at this high pressure ratio is not due only to the problems with diaphragm 2.

As was said earlier the interaction between the second shock wave and the contact surface depends on the ratio of the acoustical impedances across the contact surface, $(\rho a)_2/(\rho a)_3$. This ratio ranges between about 0.1 and 1.0 for most practical purposes. In the presented tests values down to 0.33 of this ratio have been obtained at $p_4/p_1 = 1000$. Referring to Fig.7 and the corresponding pressure records there is no evidence of an unfavorable influence of the contact surface on the second shock wave as compared to theory.

Diaphragm Burst

The requirements on the diaphragms at the two diaphragm stations are significantly different. At station 1, where a double-diaphragm system is used, the bursting pressure difference of the diaphragm does not have to be accurately known. The load on each diaphragm is increased by a factor of two when the run is initiated, and it is enough to ensure that failure occurs in that pressure region. At station 2, however, the situation is quite different. Here the accuracy of the burst will dictate the history of the second shock wave and thus the success of the run. In many cases it can be necessary that the burst of diaphragm 2 occurs with an accuracy of a few per cent.

From static pressure tests of a sample of diaphragms (1 mm, soft aluminum), very non-repeatable bursting pressures were obtained. The pressures ranged within ± 30 % around an average value. Interpretation of the wave diagrams, see for instance Figs. 5-7, indicate, however, that in almost all of the runs diaphragm 2 burst at a pressure difference at least equal to the highest one observed during the sample tests. This leads to the

suggestion that the strength of the diaphragms is different under static and dynamic loading conditions. This is a well known property of all materials, but it seems as if in this case it is not a property of the material as such as much as of the product, the diaphragm sheet. Otherwise there should be a fixed ratio between the dynamic and static bursting pressure difference, while here the dynamic strength seems more or less fixed while the static one varies considerably from case to case. It was suggested by Dr. Walter Herrmann, Sandia Corp. (private communication), that "there may not be enough time (like milliseconds) for plastic flow around weak points to develop to the point of instability". This would explain why the material could have basically the same failure load under dynamic conditions and still show irregularities under static testing. Since this problem is of very great importance it is to be studied in greater detail in the future to get a better understanding of the processes involved.

Throughout the test program the problems with diaphragm 2 have, to some extent, directed the course of the experiments. One delivery of 100 very uniform and "well-behaving" diaphragms was received. The runs shown in Figs. 5 and 6 were performed with diaphragms from this delivery. When runs at a pressure ratio of $p_4/p_1 = 1000$ were being prepared the "well-behaving" diaphragms had all been used, however, and diaphragms with the same high quality were not received again. This explains why repeatability was rather poor in Fig.7 and why only a limited number of conditions was used at $p_4/p_1 = 1000$. Efforts will be made to obtain more diaphragms of the same high uniform quality as previously for extending the wave plots to higher pressure ratios, p_4/p_1.

At the very end of the present test program 10 diaphragms were heat-treated after scoring was completed. The results from the tests of these diaphragms look very promising and this method will be further investigated in the future.

Shock-Wave Boundary-Layer Interaction

It would be desirable to make all measurements of the wave histories at the shock tube wall. This would be allowable if the second shock wave was plane across the tube, always moving with the same velocity at the wall as at the axis of the tube. Since the second shock wave is swept down the tube by the established flow behind the first shock wave, except at the shock tube walls where the gas adhers to the walls, it is not obvious that the second shock is plane. It even seems likely that the shock is curved, traveling at a lower absolute velocity at the walls.

To investigate this question the probe shown in Fig.3 was used. Many runs at different driving conditions were performed and the time difference between the first and the second shock waves was measured. The result was that in all cases the time difference at the wall and at the axis of the tube was the same within the accuracy of the measurement. Since the first shock wave is known to be plane the same should also be true for the second one.

There is still a question about the delay time for the pitot pressure due to the time for a pressure disturbance to travel through the pitot tube up to the transducer. If it is assumed that the pressure disturbances from the two shocks in the pitot tube travel with the same shock Mach-numbers as the shocks in the shock tube, and that the speed of sound of the air in the pitot tube after the passage of the first shock wave is equal to that of the air in the shock tube behind the first shock wave it is found that

$$\tau_1 = \frac{\ell}{M_{s_1} \cdot a_1} = \text{traveling time in pitot tube for first shock wave}$$

$$\tau_2 = \frac{\ell}{M_{s_2} \cdot a_2} = \text{traveling time for second shock wave}$$

and thus

$$\Delta\tau = \frac{\ell}{M_{s_1} \cdot a_1} \cdot \left(1 - \frac{M_{s_1} a_1}{M_{s_2} a_2}\right)$$

where ℓ = length of pitot tube, M_s = shock Mach number, a = speed of sound, index (1) refers to first shock, or conditions ahead of the first shock, and index (2) similarly to the second shock. It is further assumed that the second shock has reached the test gas. Typical numbers for a test are ℓ = 70 mm, a_1 = 347 m/sec, M_{s_1} = 2.3, M_{s_2} = 1.3 and a_2/a_1 = 1.4 ; then $|\Delta\tau| \simeq 25\mu$ sec. In no case was the time difference between the two shocks less than one millisecond. Thus the fractional error in determining the time difference between the shocks at the pitot tube was always less than 2.5 % which is about equal to the accuracy of the measurement. An assumed difference in arrival time at the wall and at the axis of 25μ sec would, furthermore, correspond to a distance lag of about one inch for the case above of the part of the second shock that is traveling at the shock tube wall. Thus it seems safe from most points of view to treat the second shock as a perfectly plane shock wave within the running conditions that have been used in this test program.

One immediate consequence of this is that all wave diagrams could be constructed based on measurements done at the shock tube walls. This was done in Figs. 5-7. Another consequence of this flow situation becomes evident when velocity profiles through the boundary layer are plotted with reference to the second shock.

In Fig.8 a) and b) the velocity distribution in the neighbourhood of the wall is shown schematically for co-ordinate systems fixed in the shock tube and on the second shock wave, respectively. For a shock fixed co-ordinate system the velocity entering the shock is seen to increase when the wall is approached. Since the temperature and, thus, the speed of sound is decreasing towards the wall, the shock Mach number increases

towards the wall even more rapidly than does the velocity. From the Rankine-Hugoniot relations, it then follows that the pressure immediately behind the second shock must increase towards the wall. Since the pressure tends to equalize over the cross-section this pressure rise will quickly disappear further behind the shock. Thus, on a wall pressure measurement, a peak should appear at the arrival of the second shock wave.

Examining the pressure records more closely, such peaks also show up quite clearly in many cases. In Figs. 9 and 10, data-sheets are shown from runs at two different running conditions. Wall temperature measurements, as well as pressure measurements, are shown and both display the same spike at the second shock, which is just what could be expected. In Fig.10, at the higher pressure ratio p_4/p_1, it looks as if the pressure spike is followed by several strong pressure oscillations before a steady level is reached. This seems to be confirmed by the wall temperature record.

That the spike behind the second shock is not a dynamic phenomena of the pressure transducer is more clearly shown in Figs. 11 and 12. In Fig.11 is shown two runs performed at identical conditions except that the oscilloscope trace is delayed by 5.5 milliseconds in test no. 326. The presence of the spike is quite obvious. In Fig.12 both of the shock waves are present and again the spike is clearly visible. Fig.12 also includes a determination of the strength of the second shock and its velocity. It is shown, furthermore, that the second shock has overtaken the contact surface.

Fig.8 also showed a calculated pressure variation immediately behind the second shock along the shock surface. The boundary layer was assumed turbulent and approximate distributions of velocity and temperature, as obtained from reference (6), were used. The flow Mach-number ahead of the second shock was assumed to be 1.30 and the temperature 720°K. The pressure ratio across the second shock wave at the axis of the shock tube was 1.80. An impressive peak pressure ratio of 17.2 was obtained at the wall. In the Table below, some peak pressure ratios are worked out for different initial shock Mach numbers and strength of the second shock, in all cases assuming cold shock tube walls and a plane second shock. With these assumptions it follows that $(M_{s2})_{wall} = (M_{s2} + M_2)\frac{a_2}{a_1}$.

Table

of calculated peak pressure ratios at the wall

M_{s_1}	p_7/p_2	$(p_7/p_2)_{wall}$	$(p_7)_{wall}/p_7$
2	2	10.3	5.15
	5	18.0	3.60
	10	30.0	3.00
6	2	100	50
	5	150	30
	10	220	22
10	2	235	118
	5	335	67
	10	570	57

This simple approach to the problem of computing the peak pressure ratio obviously fails when the second shock wave becomes very weak. In the limit, when $p_7/p_2 \rightarrow 1.0$, $(p_7/p_2)_{wall}$ would still have to be > 1.0 to fulfill the requirement of a plane disturbance. For the case of $M_{s_1} = 6$, $p_7/p_2 = 1.0$ the value of $(p_7/p_2)_{wall}$ would be 75. This, of course, is rather speculative and attempts will be made to measure the peak pressures more accurately in the later parts of this investigation to verify to what extent the above calculation of the peak is applicable. Since, in the pressure measurements, the size of the trandsducer was comparable with the boundary layer thickness the hight of the pressure peak can not be expected to show up. The acutal peak value can thus be assumed to be considerably greater than what is seen in Figs. 11 and 12, for instance.

Finally several efforts have been made to take Schlieren pictures of the second shock wave. Since the Schlieren system did not become available until the end of this part of the program and the experimental difficulties were quite large at this time due to the lack of reliable diaphragms, the success has not been very great so far. Only one picture has been obtained and it is hardly worth printing. Since it still illustrates the amount of curvature of the shock it is shown in Fig.13 anyhow. As is seen the shock is almost plane across the tube. It should be pointed out, though, that the boundary layer ahead of the second shock has grown to fill the whole tube in this case. Another feature that is clearly visible on the original picture is the strong density gradients, opposite to those through the shock wave, that are present at the top and the bottom, immediately behind the shock. These regions thus represent areas of strong pressure drop, looking away from the shock, which confirms the other measurements of the peak pressure. Further attempts to take Schlieren pictures are under way.

It is evident that the interaction between the second shock wave and the boundary layer on the shock tube wall is identical to the interaction between a blast wave and the boundary layer on a vehicle. Thus this interaction could be studied in detail in the shock tube.

CONCLUSIONS

The double-driver shock tube has proved to be a useful experimental tool for producing a moving shock wave in a stationary flow field. The performance in terms of wave histories and shock strengths has agreed reasonably well with theoretical predictions, at least under moderate operating conditions. For more extreme conditions no data has yet been obtained.

During the experimental program, the diaphragm separating the two drivers presented a problem. Many times, a large variation between static and dynamic bursting pressure difference caused some unrepeatability, and also difficulties in obtaining the desired starting conditions. Careful selection of these diaphragms seems to eliminate this problem.

The second shock wave was found to have the important feature of being almost plane across the tube through the wall boundary layer. This implies that a pressure peak should occur at the wall immediately behind the second shock. Such a peak has also been noticed on pressure records as well as wall temperature records.

At NOL, reference 7, a method based on the sudden rise of the stagnation pressure of a conventional hypersonic wind tunnel, to produce a blast wave in the test section, showed considerable promise for shock-on-shock studies. A double-driver shock tunnel would thus be a promising extension of both methods to make studies of blast effects at high Mach numbers as well as high enthalpy levels.

REFERENCES

(1) Lemcke, Bo. A Double-Shock Shock Tube for Simulating Blast Loading in Supersonic Flow, JAIAA, Vol 1, Number 6, June 1963, Technical Note, pp. 1417-1418.

(2) Rose, P.H. and Stark, W.I. Stagnation Point Heat-Transfer Measurements in Dissociated Air, JAS, Vol. 25, Number 2, February 1958.

(3) Lemcke, Bo. On the Use of Artificial Viscosity in Finite-Difference Calculations of Nonuniform Unsteady One-Dimensional Flow, Aeroelastic and Structures Research Laboratory, MIT, Report No. ASRL TR 126-1, September 1964.

(4) Lemcke, Bo and Ruetenik, J.R. Double-Driver Shock Tube Experiments for Measuring Strong Blast Loads on a R/V Forebody under Simulated Re-entry Conditions, Presented at the DASA sponsored conference on "Shock-on-Shock Interaction", February 2 and 3, 1965.

(5) Glass, I.I. and Hall, J.G. Shock Tubes, Section 18 of "Handbook of Supersonic Aerodynamics". NAVORD Report 1488 (Vol.6).Dec.1959.

(6) Bernstein, L. Notes on Some Experimental and Theoretical Results for the Boundary Layer Development Aft of the Shock in a Shock-Tube, ARC C.P. No. 625, 1963.

(7) Merritt, D.L. and Aronson, P.M. Study of Blast-Bow Wave Interactions in a Wind Tunnel, AIAA Second Aerospace Sciences Meeting, Jan. 25-27, 1965.

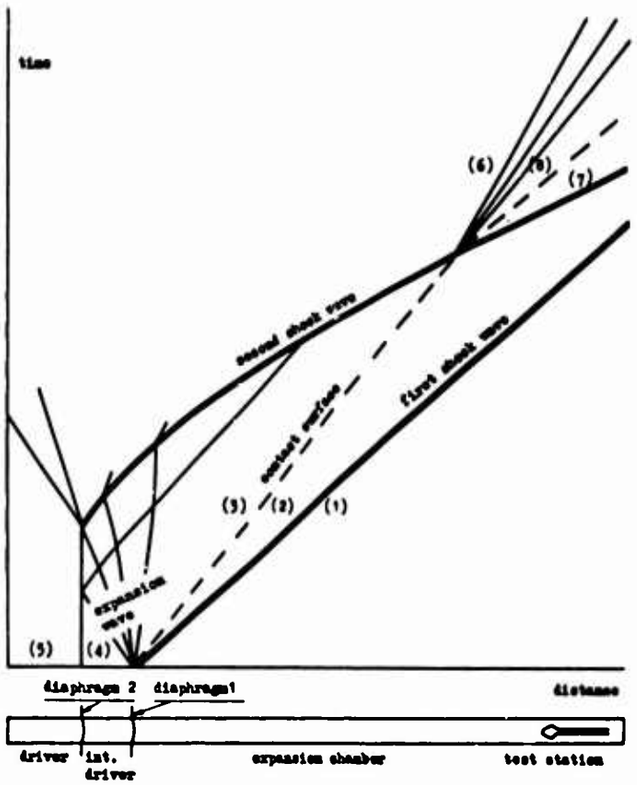
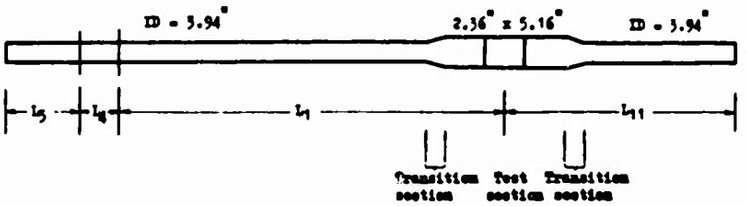


Fig.1. Double-driver shock tube.



L_3 = 3.3' - 13.1': Driver; 3.3' and 6.55' sections

L_4 = 1.3' - 7.9': Intermediate driver; 1.3', 2.0' and 3.3' sections

L_1 = - 96' : Expansion chamber; 3.3', 6.55' and 9.85' *) sections
8' rectangular section connects the transition section to the test section

L_{11} = - 50' : Expansion chamber (end); 5' rectangular section plus 9.85' sections

*) Two of the 9.85' sections contain 5 holes each for instrumentation.
All circular sections are interchangeable

Fig.2. Sketch of shock tube used in experiments.

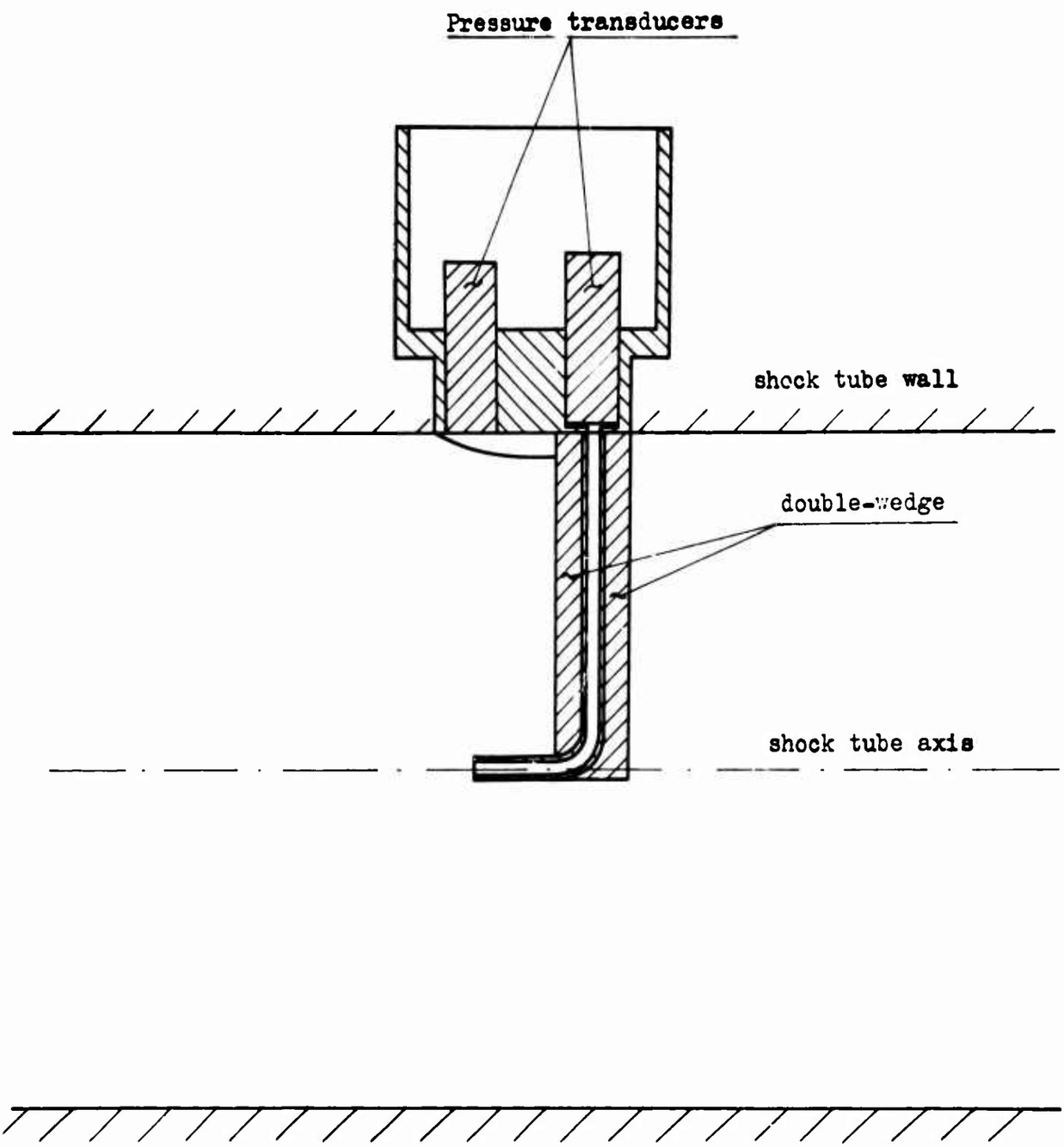


Fig.3. Pressure gages for pitot and wall pressure measurement.

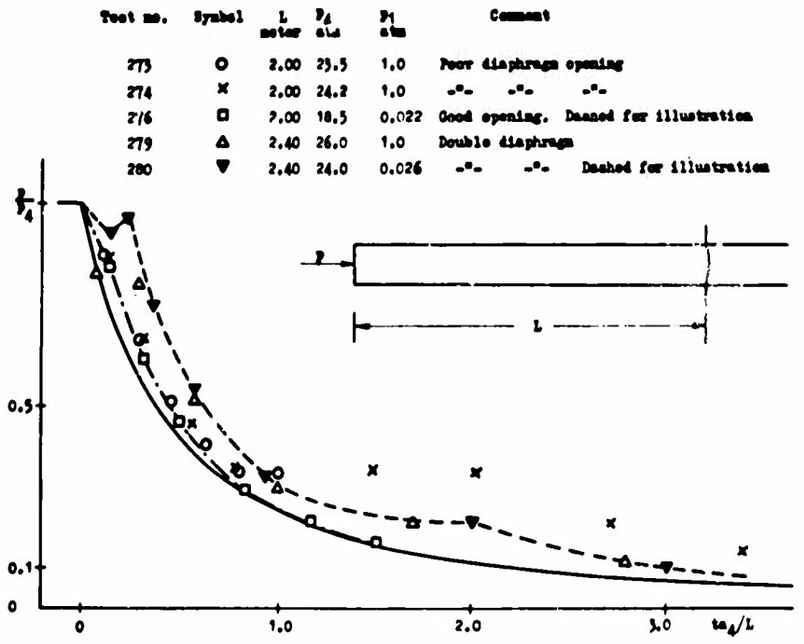


Fig.4. Pressure behind a reflected expansion wave.

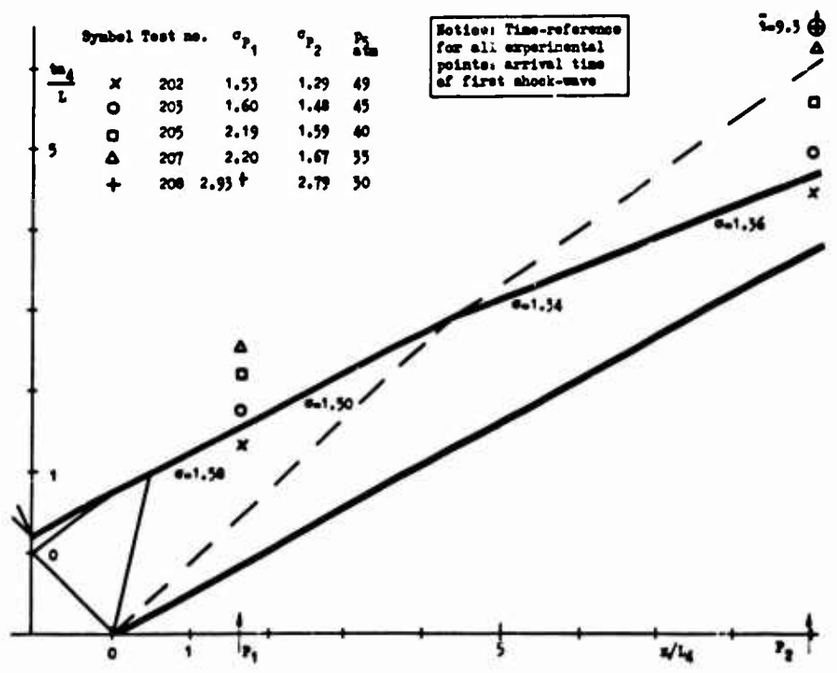


Fig.5. Wave histories for $p_4/p_1 = 25$. σ= pressure ratio across shock wave.

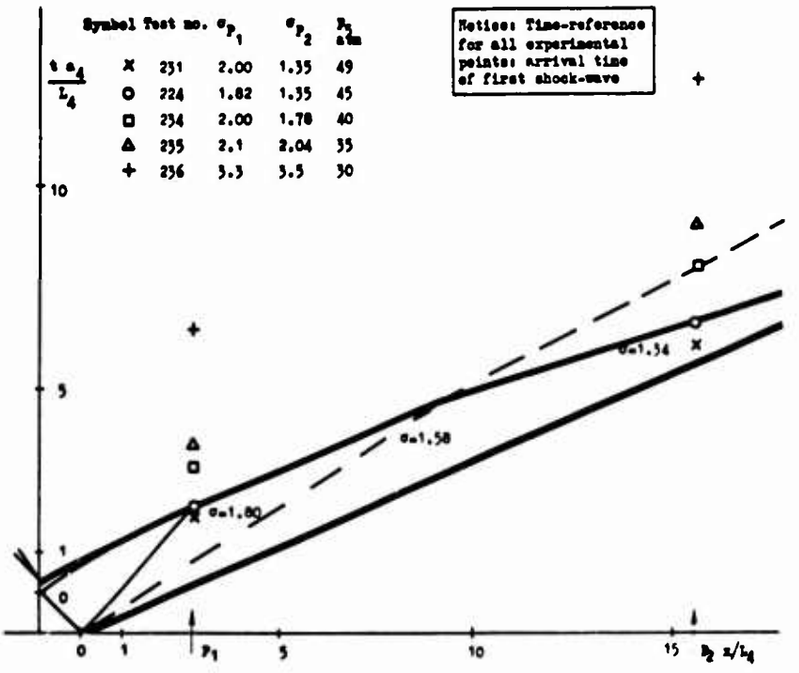


Fig.6. Wave histories for p_4/p_1=100. σ=pressure ratio across shock wave.

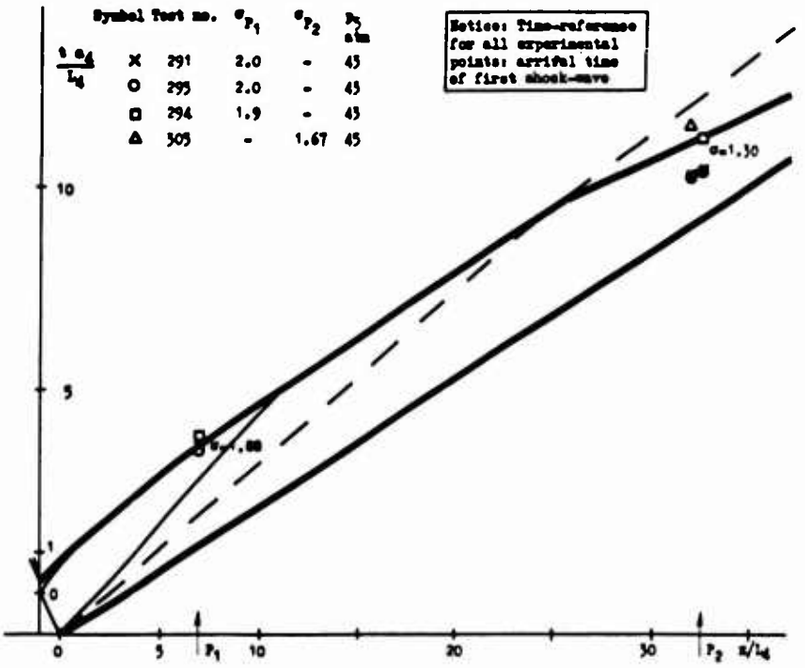
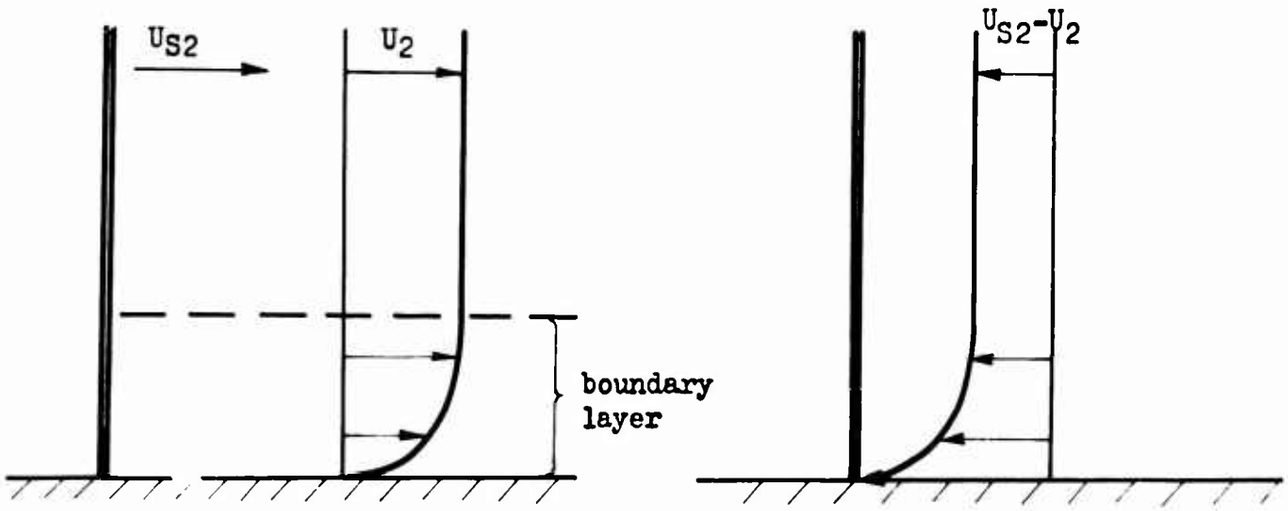
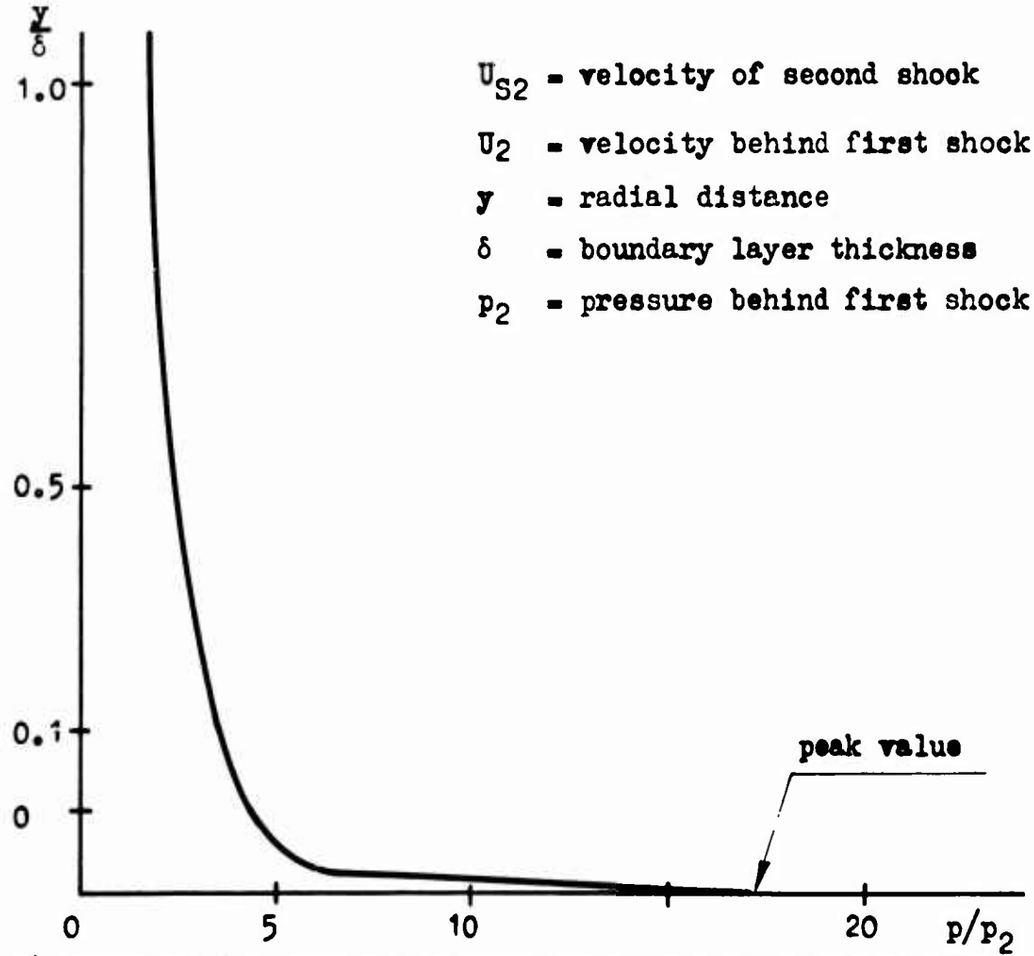


Fig.7. Wave histories for p_4/p_1=1000. σ=pressure ratio across shock wave.



a) Co-ordinate system fixed in shock-tube

b) Co-ordinate system fixed on the shock wave



U_{S2} = velocity of second shock

U_2 = velocity behind first shock

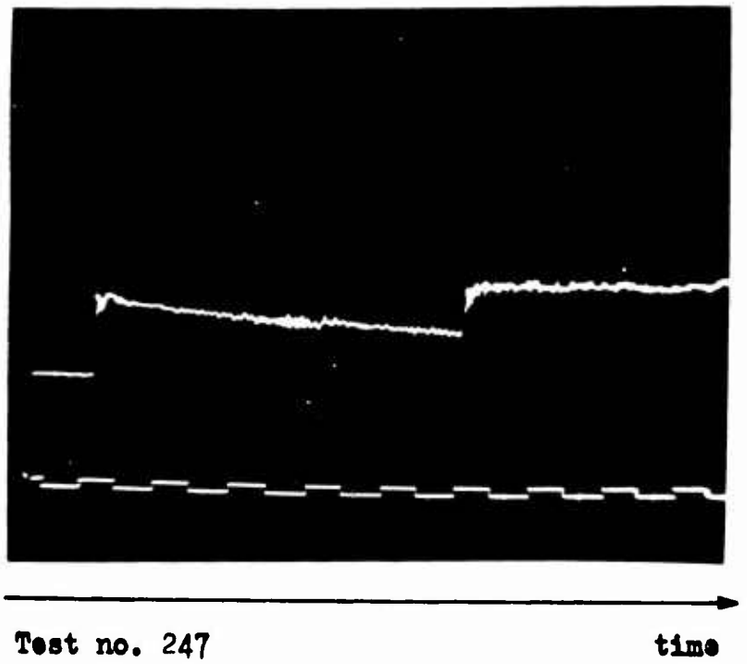
y = radial distance

δ = boundary layer thickness

p_2 = pressure behind first shock

c) Calculated pressure distribution immediately behind a plane second shock.

Fig.8. Interaction between the second shock wave and the boundary layer.



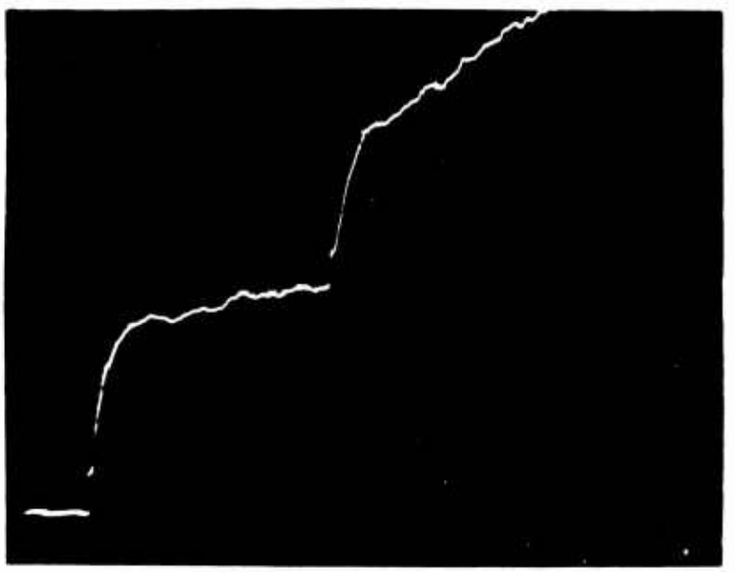
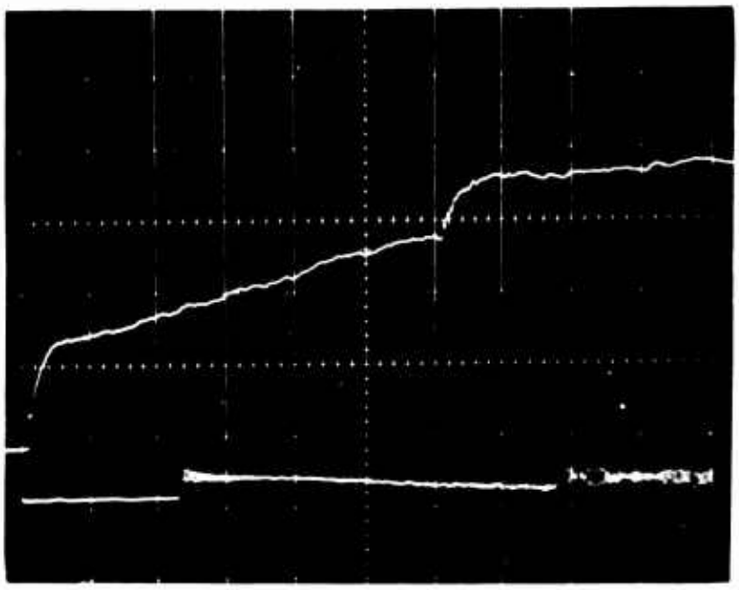


Figure 9. Wall pressure and temperature for $p_4/p_1 = 25$.



Wall temperature

Wall pressure

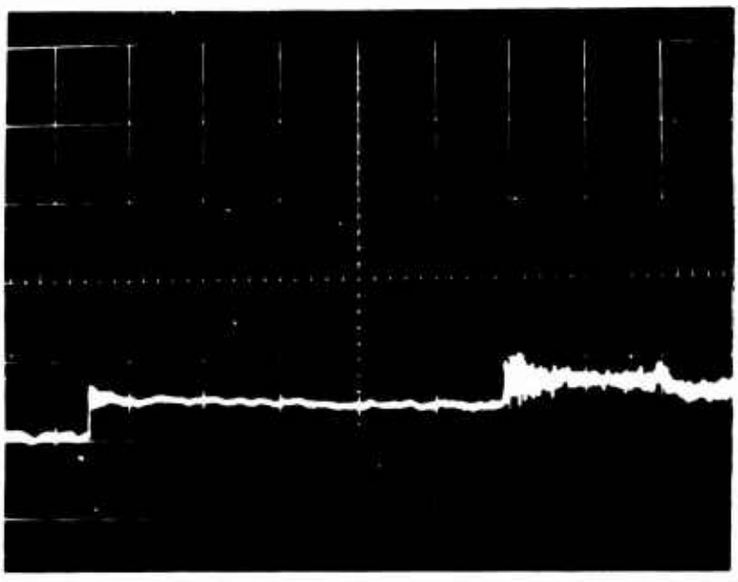
time: 0.5 ms/cm

Test no. 303

p_5 = 661 psi

p_4 = 367 psi

p_1 = 0.367 psi

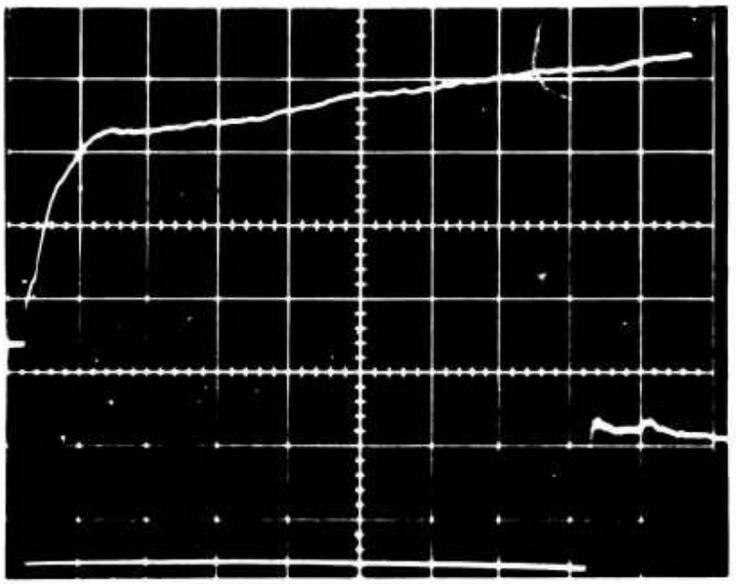


Wall pressure

time: 0.5 ms/cm

Test no. 303

Figure 10. Wall pressure and temperature for p_4/p_1 = 1000.



Wall temperature

Wall pressure

Kistler 601 F + filter

0.2 ms/cm

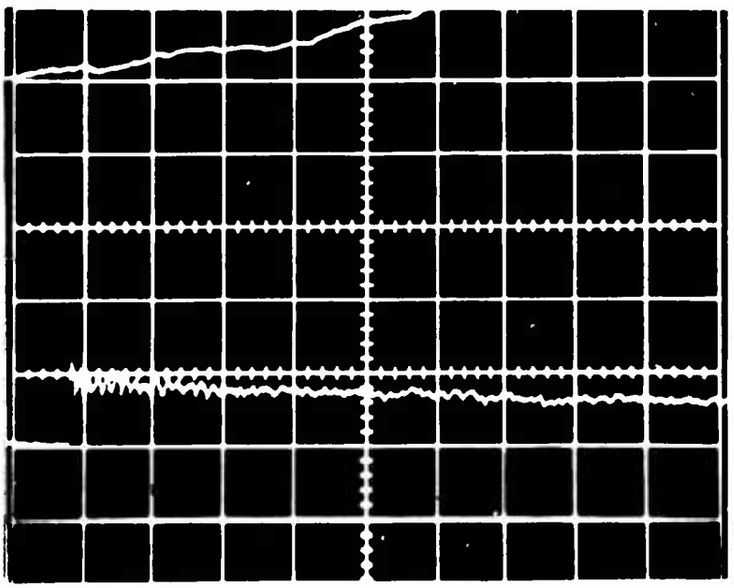
p_5 = 588 psi

p_4 = 367 psi

p_1 = 14.7 psi

Test no. 328

First shock appears on temperature and pressure traces.



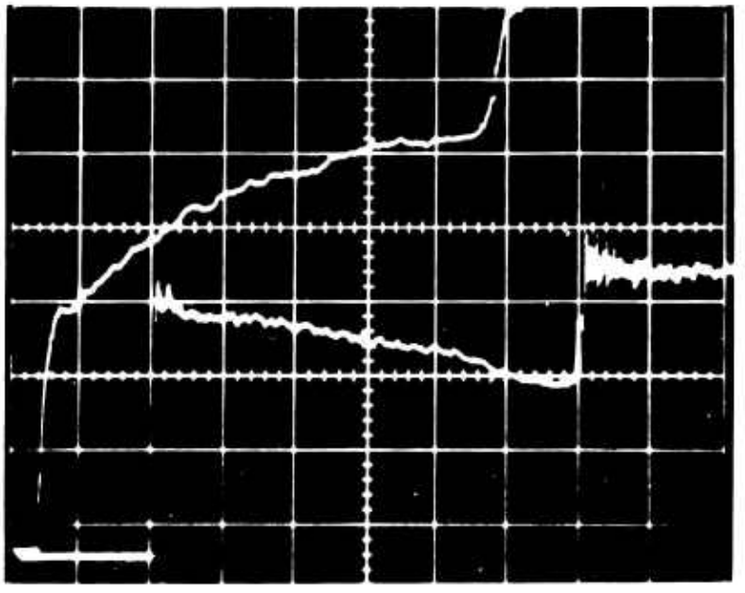
Wall temperature

Wall pressure

Test no. 326. Test conditions as in test no. 328 except that traces are delayed 5.5 ms.

Second shock appears on pressure trace.

Figure 11. Illustration of pressure peak at the second shock wave.



Wall temperature
2 mV/cm

Wall pressure
Kistler 601 F + filter
200 mV/cm
1 ms/cm

p_5 = 588 psi

p_4 = 367 psi

p_1 = 14.7 psi

Test no. 340

Distance between gages = 1.0 meters = 3.28 ft.

Velocity of first shock: $\frac{3.28}{1.62\ 10^{-3}}$ = 2020 ft/sec.

M_{s_1} = 1.79 $p_2 - p_1$ = 38.2 psi

Sensitivity of pressure transducer $\frac{38.2}{0.670}$ = 57.0 psi/V

Velocity of second shock: $\frac{3.28}{1.22\ 10^{-3}}$ = 2690 ft/sec.

Pressure ratio across second shock: 1.45.

Time difference between first and second shock at pressure transducer = = 6.0 ms.

Time difference between first shock and contact surface, from calculated wave history = 9.9 ms. Thus, second shock ahead of contact surface. This is also deduced from the wall temperature record.

Figure 12. Wall temperature and wall pressure record for p_4/p_1 = 25.

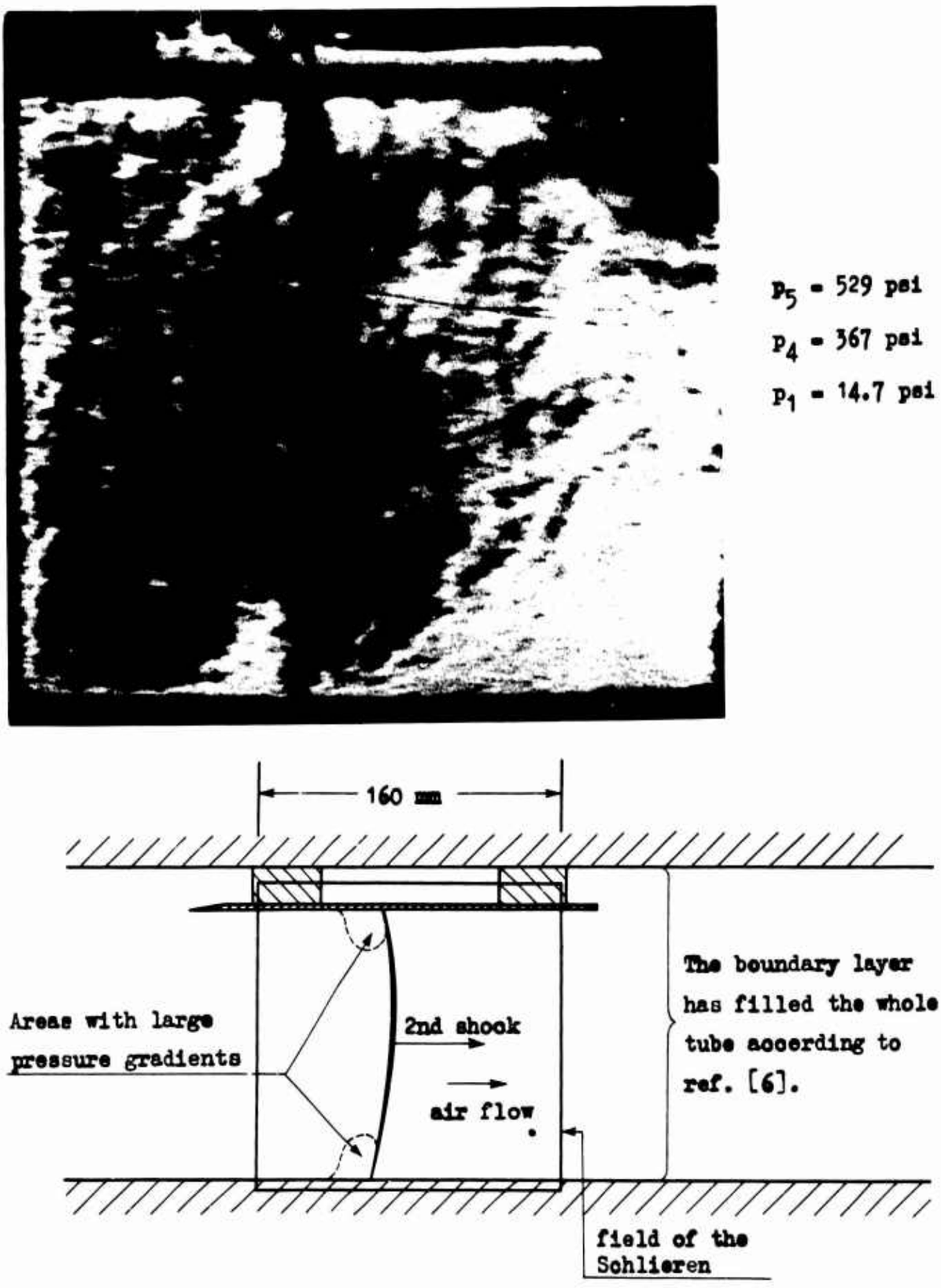


Figure 13. Schlieren picture of second shock wave.

EXPLOSIVE-DRIVEN SHOCK TUBES

Russell E. Duff
Lawrence Radiation Laboratory, University of California
Livermore, California

Arlyn N. Blackwell
Sandia Corporation
Livermore, California

INTRODUCTION

In the past twenty years, the shock tube has developed into a versatile instrument applicable to many classes of problems. In most cases it has been used to heat, compress, and accelerate a gas sample, the properties of which are to be investigated. Relatively little use has been made of the shock tube to generate pressure waves or flows for other purposes. This paper will describe a class of shock tubes driven by high explosives which are intended to provide high pressure gas flows of relatively long duration which are suitable for loading structures placed in the flow. The object is not an investigation of the performance of the shock tube itself or the conditions of the gas in the shock tube; rather the shock tube is used as a blast simulation facility to test structural characteristics of objects. Preliminary discussions of the characteristics of explosive driven shock tubes have been presented before (refs. 1 and 2).

One might well ask why the interest in such a facility. Two answers suggest themselves: First, it is well known that high pressure pulses are generated by large explosions. Military considerations demand that certain structures survive this blast loading. A related problem is the development of components capable of withstanding very large accelerations for durations of the order of milliseconds. These accelerations may have nothing to do with blast conditions. Existing facilities for the simulation of a given blast or for the testing of such components are often limited in the mass which can be accommodated, or in the pulse duration which can be supplied. Explosive-driven shock tubes have application in both of these areas.

Condensed high explosive is used to drive the facility, and in every case the detonation products themselves are used as the primary aerodynamic working fluid. It is, of course, recognized that several investigations in the past have shown that the expanded cold flow of a shock tube is not particu-

larly uniform. These nonuniformities are important if one is interested in the aerodynamics of the flow itself. However, they are relatively unimportant if one is interested in the hydrodynamic loads which the flows will induce on objects immersed in them.

A common feature of the shock tubes to be discussed in this paper is that part or all of the facility is expendable. No effort is made to build structures strong enough to survive explosive pressures. As a result, the facility costs are quite modest, and little, if any, capitalized investment must be made in their construction. Shock tubes will be described which can be oriented at any angle from the vertical to the horizontal. Dynamic pressures from a few hundred psi to tens of thousands of psi can be generated. Flow durations may range from a few hundred microseconds to tens of milliseconds. Accelerations experienced by objects placed in the flow depend upon the ballistic coefficient of the object, but accelerations between a few hundred and tens of thousands of g can be produced on representative shapes. Shock tubes have been built ranging in diameter from two to six feet and in length from ten to fifty feet. The explosive masses involved in a given experiment have varied from a few pounds to almost a thousand pounds.

DESIGN PROCEDURES

Predictions of shock tube performance are made numerically by one-dimensional, Lagrangian calculations of the flow of detonation products and shocked air. The layout of a representative calculation is shown in Figure 1. It will be noted that about two hundred individual zones are used in a calculation. Usually the sizes of the zones used to describe one or more of the materials are geometrically scaled, i.e., each zone is made a given percentage larger than its neighbor. This geometric zoning minimizes the systematic errors made in numerical calculations of this sort when the zone sizes measured in terms of mass or signal transit time change at an interface.

A major problem in calculations of this sort is an adequate description of the equation of state of the several materials involved. In this case, the high explosive is the most difficult material to describe. The explosives of interest in these calculations are bulk density TNT, $\rho \approx 1.0$ g/cc, and cast Composition B, $\rho = 1.715$. Different equation-of-state forms were used for the two materials. The low density TNT was described as suggested by Jones and Miller (ref. 3). They calculated the Chapman-Jouguet isentrope extending from normal detonation conditions down to very low pressures. Their prediction is in excellent qualitative agreement with recent equation-of-state measurements on high density, high performance explosives. The area under this isentrope was integrated to give values of pressure, volume, and energy which were then related by a pseudo-ideal gas equation of state.

$$P = (\gamma - 1)\, E/V \text{ mbars}, \quad \text{for } E \text{ in units of } 10^{12} \text{ ergs/g},$$

where $\gamma = 2.439 - 0.655\ V, \qquad V < 1.5$ cc/g,

$$\gamma = 1.20 + \frac{1}{5.6V - 4.5}, \qquad v > 1.5 \ .$$

Additional constants needed to describe the explosive include the explosive energy $E_o = 0.04682 \times 10^{12}$ ergs/g, the Chapman-Jouguet compression ratio $\rho_{CJ}/\rho_o = 1.421$, and the initial loading density $\rho_o = 1.0$ g/cc. It should be stressed that the gamma which appears in this equation of state is not a ratio of specific heats. It is only a parameter chosen to correctly describe the pressure, volume, and energy relationship for this material. It should also be mentioned that this equation of state describes only the principal isentrope of the material.

A more elaborate equation of state which describes the performance of Comp B under more general conditions was prepared for another purpose;

$$P = 0.01355\eta^{0.4} + 3.646\ (1 - 0.1104\eta)\ e^{-\frac{3.5}{\eta}} + 0.4\eta\epsilon \text{ mbars} \ ,$$

where $\eta = \rho/\rho_o$ and ϵ is the internal energy in units of 10^{12} ergs/initial cc. The additional constants required are $\rho_o = 1.865$ g/cc and $\epsilon_o = 0.08804 \times 10^{12}$ ergs/initial cc. It will be noted that the density 1.865 used with this equation of state does not correspond to that of Comp B. However, the equation is properly calibrated to describe Comp B on an equal mass basis. The results presented later have been appropriately adjusted for this discrepancy in initial density.

The air which is sometimes included in a configuration was described as an ideal-gas, gamma-law material. Values of gamma between 1.2 and 1.3 were used, depending upon the shock strength to be expected in the particular configuration. This simple form of the equation of state was used primarily to save computing time. It is justified because the primary working fluid in each shock tube configuration is the detonation products. The shocked air provides a relatively small part of the total impulse. In addition, one of the calculations was repeated with a more elaborate equation of state which reproduced the known, non-ideal character of air at high temperatures and pressures. No significant differences were observed in the results of the two calculations.

In some of the configurations the high explosive was tamped by a layer of dirt. This dirt was approximated by a simple equation of state based on shock wave measurements of the properties of Nevada alluvium (ref. 4),

$$P = 0.04\mu + 0.1\mu^2 \text{ mbars},$$

where $\mu = (\rho/\rho_o) - 1$ and $\rho_o = 1.8$ g/cm^3 .

The numerical code provided values of the static and dynamic pressures, Mach number, density, and flow velocity for each of the zones at many selected times. Profiles of these quantities could be constructed from this information as desired. Such profiles will be presented during the dis-

cussion of several particular explosive-driven shock tubes. The results presented here are only representative of many more calculations which have been or could easily be run.

SIMPLE SHOCK TUBES

The most elementary explosive-driven shock tube is shown in Figure 2. It consists of a layer of high explosive at the bottom of an air-filled pipe. Bulk density TNT pressing powder was used as the high explosive for this shock tube for several reasons. First, since the explosive density is low, its pressure is low, and therefore the departure from the assumed one-dimensional flow condition is minimized. In addition, the expense and trouble of explosive casting or pressing are avoided, and finally, the use of a bulk material adds to the ease with which various different configurations can be put together. Obviously, one disadvantage of the use of the unconsolidated explosive powder is the requirement that the shock tube be operated vertically.

Calculated profiles of dynamic pressure, static pressure, and Mach number for this simple configuration are shown in Figures 3 through 5. For convenience, the zero of the time scale has been taken as the instant of passage of the contact surface at a given station, and the instant of shock passage is indicated below each profile. The parameter which labels each curve is the ratio of shock tube length to explosive thickness, where the explosive thickness is assumed to be 1 cm. Several points should be noted. The dynamic pressure in the detonation products is calculated to be several times the peak air shock pressure for small values of ξ. This difference, of course, arises because of the relatively more dense nature of the explosive products than the high temperature shocked air. It is well known that the contact surface in a shock tube is not a mathematical discontinuity. Turbulent mixing is almost always observed. Such mixing in this case should tend to smooth out the dynamic pressure profile and generate a more uniform pressure pulse. The static pressure is high in the shocked air and in the explosive products near the contact surface. It is quite low in the remainder of the flow. Finally, the Mach number of the explosive products is calculated to be about 3. However, the mixing of cold explosive products and hot shocked air and the ensuing reaction between the two mentioned above would tend to reduce the anticipated Mach number. It is unlikely, however, that such mixing would make the flow subsonic.

Several experiments have been performed to measure to what extent the predictions of the one-dimensional calculation are verified. These experiments were made in tubes 6 feet in diameter and from 10 to 50 feet long. The explosive layer consisted of 10 g/cm^2 of bulk density explosive. This made a layer about 10 cm thick. The explosive layer was initiated at a triangular array of points at 8-inch intervals. Both branched primacord and individual detonator ignitions systems were used with equal success. In some instances, hard wire instrumentation was used in objects exposed to the flow. Signal cables from these instruments were protected by a heavy, hollow metal pipe as shown in Figure 2.

Shock velocity was measured by an array of foil switches mounted along the outer edge of the tube. The results of several measurements are summarized in Figure 6. It is clear that the shock velocity is about 10% below that calculated.

Arrays of these foil switches have also been arranged perpendicular to the tube axis to measure wave planarity. The switches were supplemented by high-speed cameras for the same purpose. On one shot, 18 switches were distributed uniformily across the mouth of a tube. The shock wave was found to be within ±1 inch of plane and perpendicular to the axis. Actually, the indicated departure from the ideal came from a slight wave tilt. In other experiments where less care was taken in explosive preparation, larger wave asymmetries and even local jetting were observed.

One important measure of the shock tube flow is the total impulse imparted to an object. This impulse was measured in one experiment by an array of six 172-pound steel spheres located in a plane at the mouth of the tube. Each sphere carried a smoke flare so that its trajectory could be observed photographically. Figure 7 is a photograph of these trajectories; the six spheres can be seen near the horizon. The minimum apogee was 390 feet; the maximum was 470 feet; the average was 430 feet. The predicted height was 585 feet. The average observed value was 35% below that predicted, indicating a measured impulse 16 ±5% less than that calculated. This indicates that two-dimensional effects are not a major consideration in such a high-explosive-driven shock tube. This experiment also proved that the impulse is primarily axial and quite uniform across the tube. It is interesting to note that two of the objects that flew highest came from near the outer tube wall.

Flow dynamic pressures have been estimated from surface pressure measurements made on cones and cylinders exposed to the flow and also from stagnation pressure measured by an array of detectors located in a massive steel beam placed across a tube diameter. The beam was 2 inches thick and 24 inches deep. About 2-1/2 tons of lead bricks were piled on each end of the beam to hold it down. Figure 8 shows a dynamic pressure profile calculated from one of the stagnation pressure measurements made in the beam at a distance of 35 feet from the explosive layer. Unfortunately, the stagnation pressure was recorded on magnetic tape, with relatively poor frequency response. Nevertheless, it is clear that the qualitative features of the predicted flow are observed. The dynamic pressure associated with the detonation products is higher than that from the air shock. However, this record, and many others, also indicate that the expected mixing phenomenon did decrease the magnitude of the dynamic pressure associated with the detonation products.

An axial variation in the dynamic pressure associated with the contact surface was observed in the beam experiments. In particular, no second peak was observed from stagnation gages located within a few inches of the tube wall. This means that gages mounted as shown in Figure 2 will record only the air shock dynamic pressure peak. However, the total impulse experiments should be recalled. Objects located at least a foot from the wall of a tube 6 feet in diameter received as much impulse as spheres located near the center.

Reliable static pressure measurements have been difficult to obtain under the rather trying field conditions associated with these experiments. However, the measurements which have been made indicate a pressure somewhat higher than that predicted in the detonation products. Since flow Mach number can be determined from the ratio of static to stagnation pressure, it has been possible to show that the Mach number in the stream is supersonic but significantly below that predicted in the detonation products.

A shock tube test similar to the one described is relatively inexpensive and easy to perform. A rough cost breakdown of the mechanical aspects of an experiment includes the following items:

Site preparation (hole, liner, labor)	$2000
Explosive assembly (container, TNT, detonators, cable, labor)	1500
Engineering and technician labor	1200
Miscellaneous parts and services	500
Total cost	$5200

In every case the metal tube liner was ruptured near the explosive and expanded somewhat. Usually only the upper part of the tube was salvaged for use in another experiment.

MODIFICATIONS OF THE SIMPLE SHOCK TUBE

The dynamic pressure profile shown in Figures 3 and 8 does not provide a good simulation of a blast wave. A profile with a relatively smaller second spike would be more satisfying. Two relatively simple modifications to the shock tube configuration can improve the pressure profile. The easiest of these is simply to space the explosive layer some distance from the bottom of the tube. This leads to a strong rarefaction wave from below which attenuates the explosive product pulse relatively more than it does the air shock. An example of the predicted dynamic pressure for a configuration with an infinite space below the explosive layer is shown in Figure 9. A comparison of this figure with profiles of Figure 3 shows that the amplitude of the second spike has been reduced roughly by a factor of 2. Dynamic pressure measurements made with the beam-carrying stagnation pressure gages, as described above, have verified that indeed the dynamic pressure is reduced as expected.

Instead of attempting to attenuate the dynamic pressure of the detonation products, one could improve the profile by increasing the dynamic pressure of the gas shock. This can most easily be done by substituting a heavy organic vapor for air above the high explosive. Calculations have predicted that Freon gas substituted for air should give a more nearly idealized, single-peaked, blast-wave pressure profile. No experimental verification of this shock tube version has been obtained so far.

VACUUM CONFIGURATION

A particularly interesting variation of the standard shock tube produces a simple triangular dynamic pressure profile by removing the air from the vicinity of the explosive and relying on the detonation products as the sole working fluid. In this configuration one is using a rarefaction flow for aerodynamic purposes. Calculations of the flow expected were made under several sets of assumptions. Both solid Comp B and low density TNT were used as explosives, and both tamped and untamped charges were assumed, i.e., in some of the calculations a thick-layer of dirt was placed behind the explosive to provide hydrodynamic confinement. The results were qualitatively similar in all cases. The solid explosive has the obvious advantage of permitting the shock tube to be built at any inclination, and it also makes leak checking relatively straightforward. Dynamic pressure and Mach number profiles for an untamped, solid Comp B explosive charge are shown in Figures 10 and 11. Note that the time scale for the several profiles in now related to the instant of initiation. The dynamic pressure profile in now an almost ideal shape. The only shortcoming is the relatively slow initial rate of rise of pressure, which is obtained because the flow is not initiated by a shock wave. However, the calculated rate is still comparable to or less than the engulfment time of many objects of interest. A point of greater interest is the engulfment rate itself. It is well known that the velocity of escape of detonation products is comparable to or greater than the detonation velocity. In this case, the engulfment velocity was calculated to be 31,000 ft/sec, a value in excess of orbital speeds.

Peak dynamic pressure and pressure pulse half-width, as a function of tube length for an untamped Comp B explosive, are shown in Figure 12. If hydrodynamic tamping is provided by a thick layer of dirt behind the explosive, the peak pressure is unchanged, but the flow duration is increased by a factor of about 2. This follows from simple, conservation of momentum considerations. These curves should be useful in choosing dimensions to meet particular requirements.

The performance of this shock tube was verified by an experiment designed to produce a flow dynamic pressure of 6000 psi for a half-time duration of 1 msec. Figure 12 indicates and the actual calculations show that these conditions can be produced by a tamped Comp B layer 4 cm thick at the end of a tube about 15 feet long. The configuration tested is sketched in Figure 13. The explosive pad was fastened to the end plate of the tube and it was initiated simultaneously at 560 places. The explosive products expanded into a vacuum chamber 30 inches in inside diameter and 17 feet long. The downstream end of the tube was covered with a 25-mil aluminum diaphragm which was adequate to support atmospheric pressure and light enough to be blown away rapidly. At the time of the experiment, the pressure in the tube was 500 microns. Several feet of dirt were piled over the explosive end of the tube to provide inertial tamping to the detonation products.

Flow characteristics were observed in several ways. One static and two stagnation pressure gages were mounted in each of two heavy, lead-filled

pipes bolted to the tube wall as shown. Kistler 605 and 601 transducers were used. Expansion front velocity was to be measured by several kinds of detectors set in the tube wall at various stations along the length of the tube. Finally, flash x-ray pictures of the motion of four spherical objects were taken to permit unambiguous determination of the dynamic pressure of the stream.

The experiment was successful. Flow-front velocity information was obtained from flush-mounted contact switches. The observed front velocity of 9.5 mm/μsec is higher than the detonation velocity as expected, and is very close to the predicted value of 9.2 mm/μsec.

Two stagnation pressure gages located side by side in the pipe 6 inches from the tube wall gave nearly identical results. The mounting for the other two gages failed after several hundred μsec. The peak pressure recorded by all four gages was 11,800 ± 300 psi.

The ratio of stagnation pressure to dynamic pressure is

$$\frac{P_{st}}{q} = \frac{2\left(\frac{\gamma+1}{2}M^2\right)^{\frac{\gamma}{\gamma-1}}}{\gamma M^2\left(\frac{2\gamma}{\gamma+1}M^2 - \frac{\gamma-1}{\gamma+1}\right)^{\frac{1}{\gamma-1}}}$$

The greatly expanded detonation products were assumed to have $\gamma = 1.4$. For such a γ and at expected Mach numbers this pressure ratio is very close to 2. Therefore, the stagnation pressure measurements were divided by 2 to determine the dynamic pressure. A comparison of the measured and the calculated dynamic pressure is shown in Figure 14. The agreement is good, especially so when one realizes that the empirical equation of state used for this decidedly non-ideal gas had to describe conditions over a pressure ratio of 10,000 and a density ratio of more than 1000. The rise time of the experimental pulse is a bit slower than that calculated, and the pulse width at high pressure is a little larger than expected. Nevertheless, the amplitude, duration, and the integral under the curves agree nicely.

The static pressure transducers did not give good records. Both gages failed during the run, but they both indicated a static pressure at early times of about 500 psi. Therefore, the ratio of stagnation to static pressure was 24. Such a ratio corresponds to a flow Mach number of 4.2 for a specific heat ratio of 1.4 . Theoretically, the initial flow Mach number is infinite, but the calculations summarized in Figure 11 show that the values should decrease to about 10 with a time constant roughly one-half of that which governs the decay of the dynamic pressure pulse. The observed value is lower than predicted, but it is still comfortably supersonic.

Integral and relatively uncontroversial indications of dynamic pressure were obtained from the flight of four solid brass and aluminum spheres ranging in diameter from 1-1/2 to 4 inches. Spheres were chosen because of their obvious symmetry and because the drag coefficient has been found to be independent of Mach number and equal to 1.0 by several investigators. The ballistic coefficient of these spheres varied between 0.82 and 0.12 lb/in^2. The exposures were made by an electron Linac working as a flash x ray machine. The machine gave five pulses of high-energy x rays separated by 500 μsec. One of these x-ray pictures is shown in Figure 15.

The displacements of the spheres were measured. The results were then multiplied by the appropriate ballistic coefficients to facilitate comparison of the trajectories with predictions from the doubly integrated dynamic pressure profiles, both calculated and measured. This comparison is shown in Figure 16. The excellent agreement between the several sets of data is impressive. (It should be mentioned that the calculated curve has been displaced 60 μsec to the right to compensate for the difference in effective zero time indicated in Figure 14.)

The agreement between the trajectories of the several objects and that calculated from the measured pressure profile demonstrates that the flow is uniform across the area of the tube within experimental error.

SUMMARY

This investigation has shown that high explosive-driven shock tubes can make useful blast simulation or acceleration-producing devices. The use of detonation products as the only or, at least, major hydrodynamic working fluid keeps the dimensions of the facility relatively small and the cost modest. The performance of such shock tubes has been shown to be quite close to that predicted by one-dimensional hydrodynamic calculations. The shock front in an air-filled tube can be made plane and perpendicular to the tube axis by careful explosive preparation. The impulse has been found to be uniform across most of the tube diameter, and close to the calculated value. The dynamic pressure in the air-filled case shows a two-peaked profile as calculated, but the magnitude of the second peak has been reduced by turbulent mixing at the contact surface. Similarly, the dynamic pressure profile in the vacuum modification is very close to the predicted triangular shape.

An explosive-driven shock tube similar to those described here can be designed to use any explosive, and the inclination of the tube axis can be varied at will. A facility can be easily tailored to meet specific requirements of diameter and, within limits, peak dynamic pressure and flow duration. It can be constructed quickly and relatively cheaply without the necessity for any investment in a capitalized installation.

One should not conclude that these shock tubes make obsolete all other simulation facilities — they don't. In particular, the calculated dynamic pressure profiles show than a very large ratio of tube length to explosive thickness must be used if low pressure flows are desired. It is also clear

that absolute dimensions must be large to obtain flow durations of many milliseconds. The only apparent way to make the first of these problems less burdensome for short test times is to segment an otherwise very thin explosive layer into a number of compact masses which can be simultaneously detonated. We have not tested this approach. The second problem may not be as restrictive as it might appear at first glance because only the end of the shock tube near the explosive need be destroyed. If a horizontal configuration is used, provision can be made to replace the damaged tube section and reuse the major length of the shock tube for a series of experiments.

Explosive-driven shock tubes as described here are one of very few facilities capable of testing hardened structures, and they have proved to be powerful tools in the development of such structures. Hardwire instrumentation can be used to measure dynamic strains, accelerations, and pressures. Finally, exposed objects can be recovered for post-test inspection.

ACKNOWLEDGMENTS

This work could not have been done without the enthusiastic support of many people at the Lawrence Radiation Laboratory and the Sandia Corporation. It would be impossible for us to adequately list all the contributors to the program, so we simply express our appreciation to our colleagues in both laboratories for their invaluable encouragement and assistance.

REFERENCES

(1) Duff, R. E. and Blackwell, A. N., High Explosive Wind Tunnels for High Altitude Blast Simulation, Trans. Ninth Symp. on Ballistic Missile and Space Tech., Vol II, 419 (12-14 Aug 1964)

(2) Deal, W. E. and Taylor, J. W., Explosive Simulation of Nuclear Blast on Test Vehicles, Trans. Ninth Symp. on Ballistic Missile and Space Tech. Vol II, 359 (12-14 Aug 1964)

(3) Jones, H. and Miller, A. R., The Detonation of Solid Explosives: The Equilibrium Conditions in the Detonation Wave Front and the Adiabatic Expansion of the Products of Detonation, Proc. Roy. Soc. A194, 480 (1948)

(4) McQueen, R. G. and Marsh, S. P., Equation of State of Nevada Alluvium, Los Alamos Scientific Laboratory Report LAMS 2760 (Nov 1961)

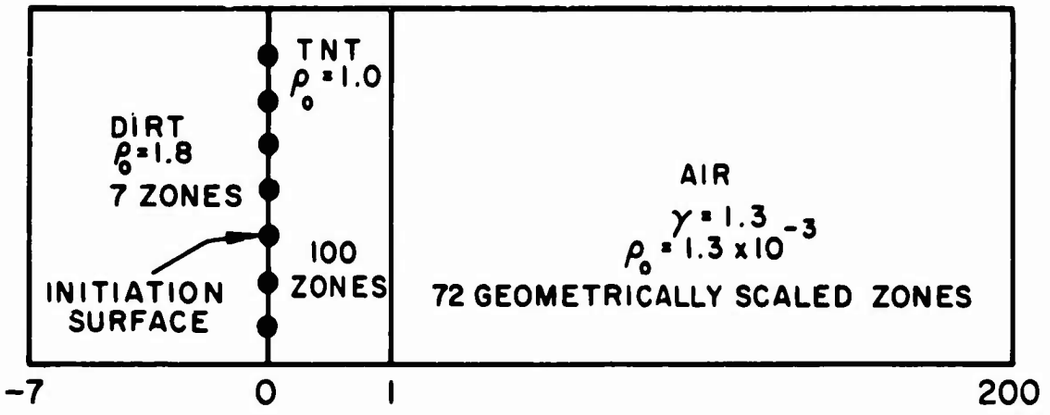


Fig. 1. Configuration assumed in calculation of the flow in an explosive-driven shock tube.

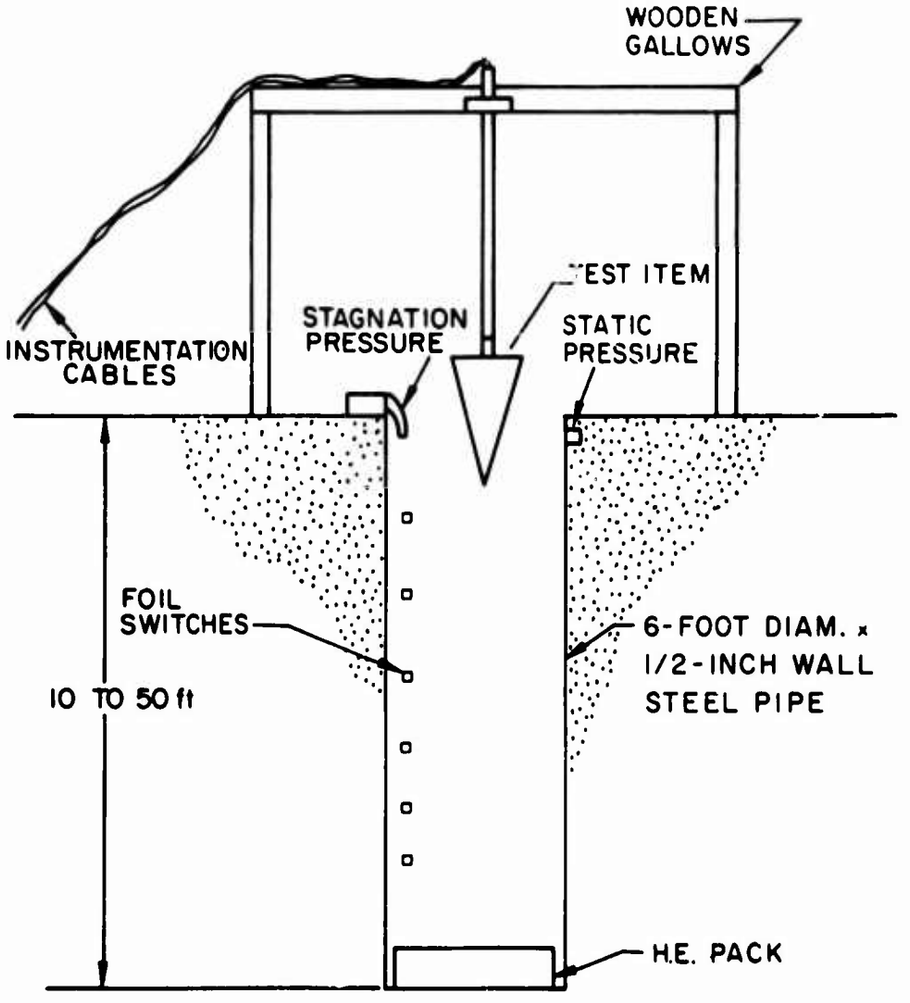


Fig. 2. General test configuration for an air-filled shock tube using low-density explosive.

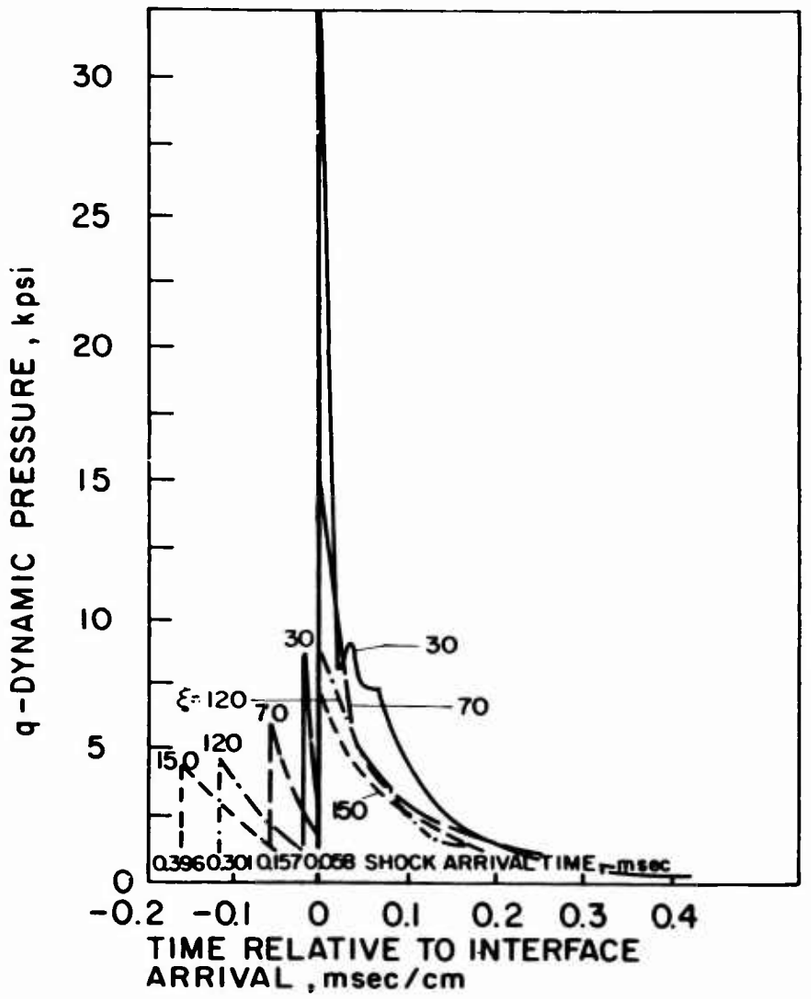


Fig. 3. Dynamic pressure versus time relative to interface arrival at various distances from the charge (1 cm TNT, ρ = 1 g/cc).

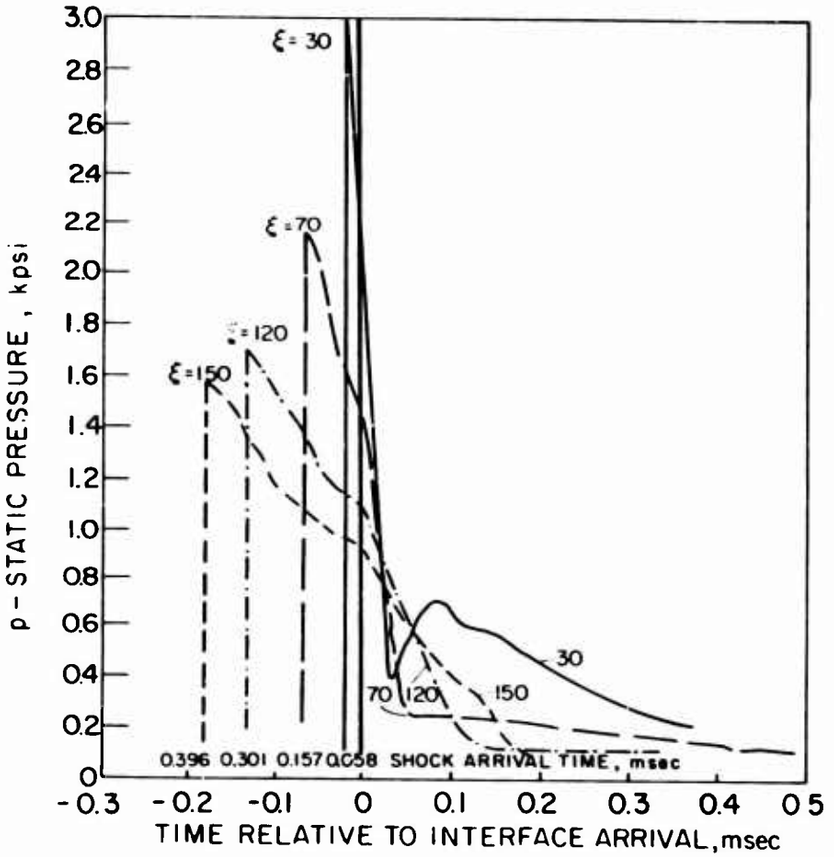


Fig. 4. Static pressure vs time relative to interface arrival at various distances from charge (1 cm TNT, ρ = 1 g/cc).

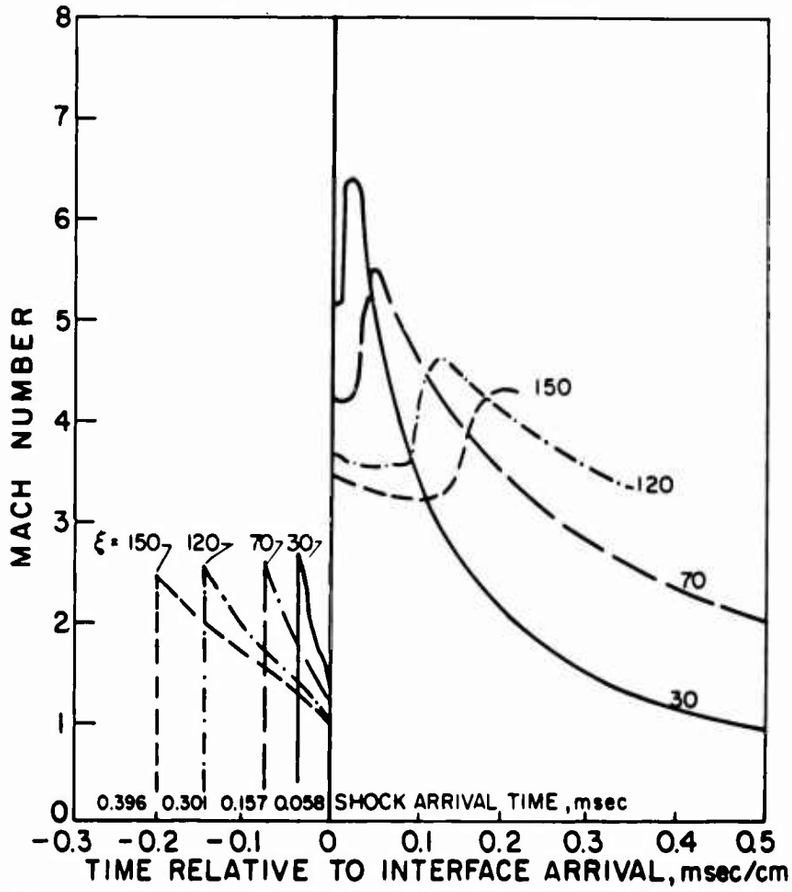


Fig. 5. Mach number vs time relative to interface arrival at various distances from charge (1 cm TNT, ρ = 1 g/cc).

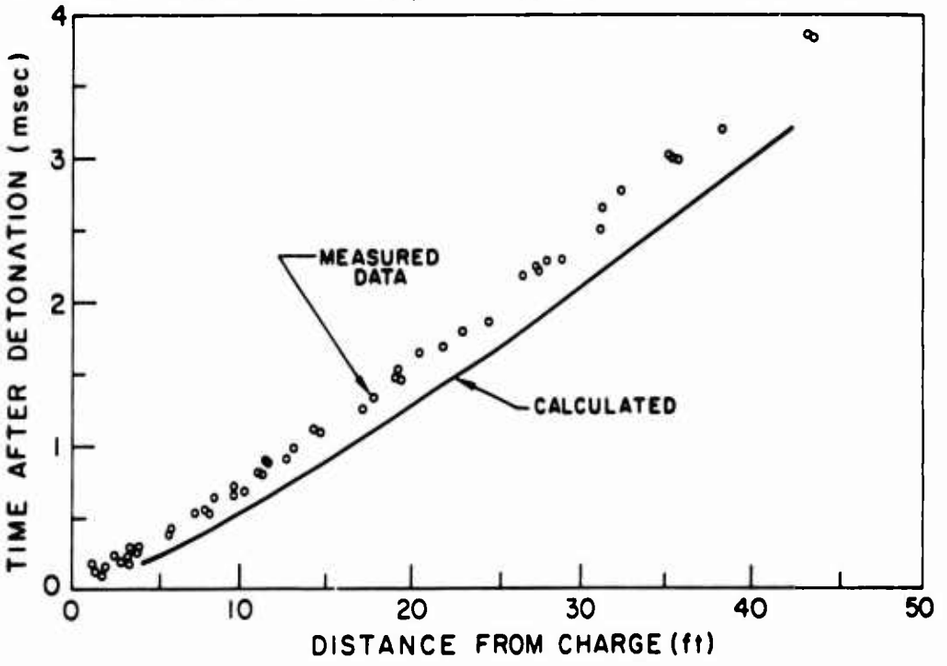


Fig. 6. Comparison of calculated and measured shock front position vs time (10 g/cm^2 TNT, ρ = 1 g/cc).

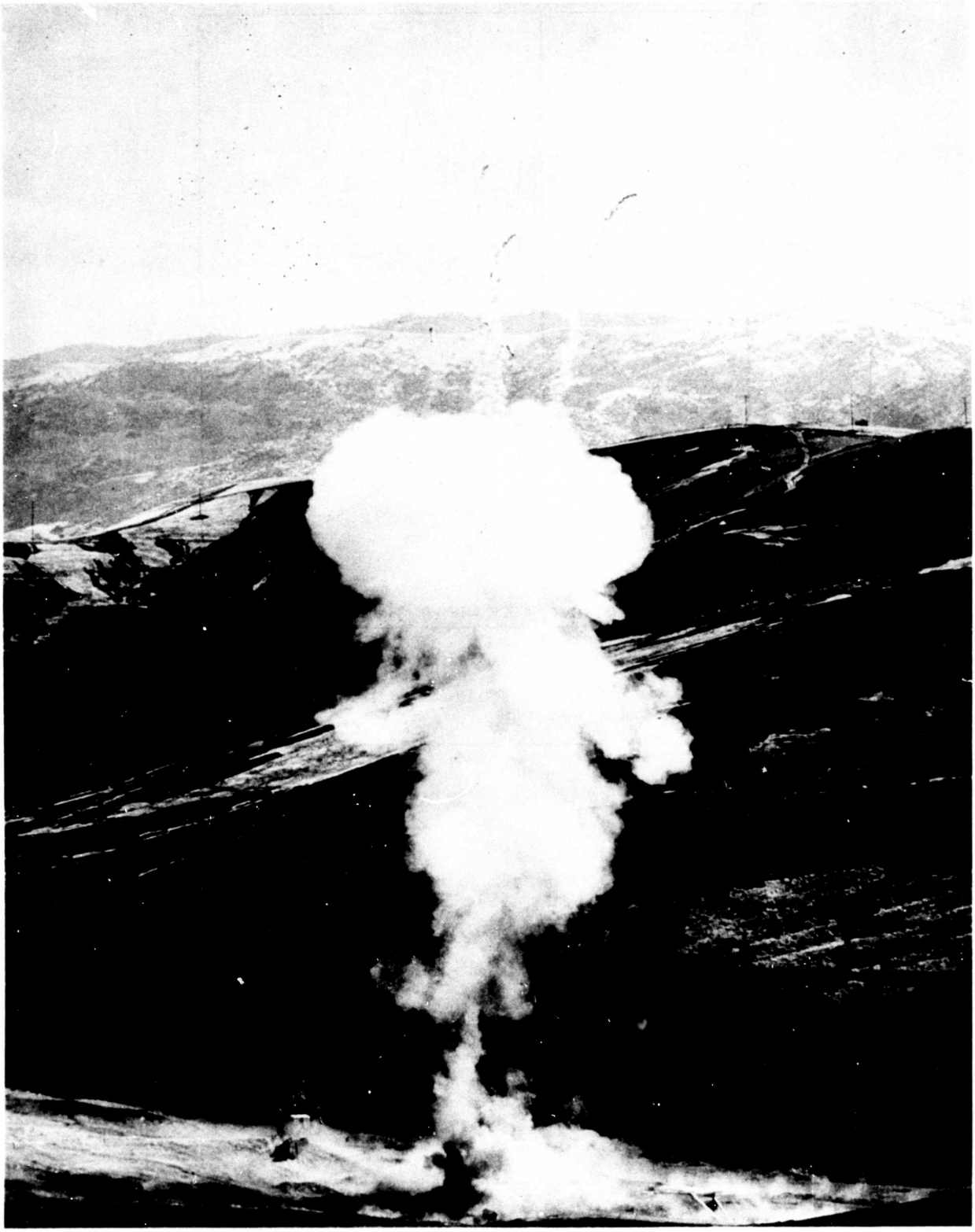


Fig. 7. Trajectories of six solid steel spheres.

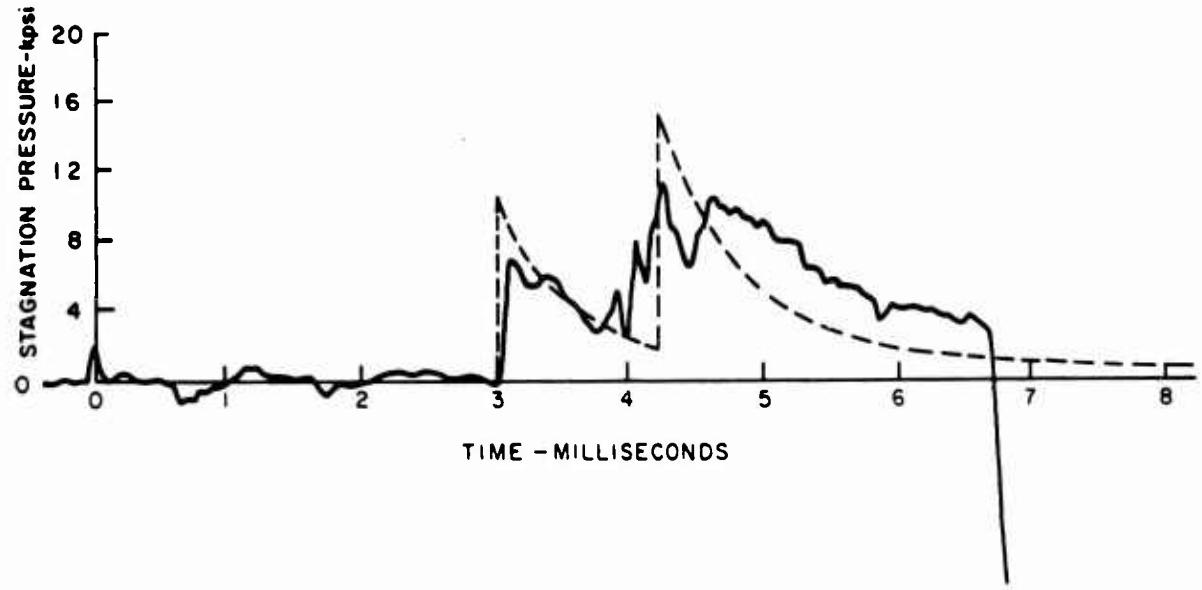


Fig. 8. Comparison of measured and calculated stagnation pressure 35 feet from charge (r/R = 1/2). The theoretical profile was chosen to make the shock arrival time agree with that observed.

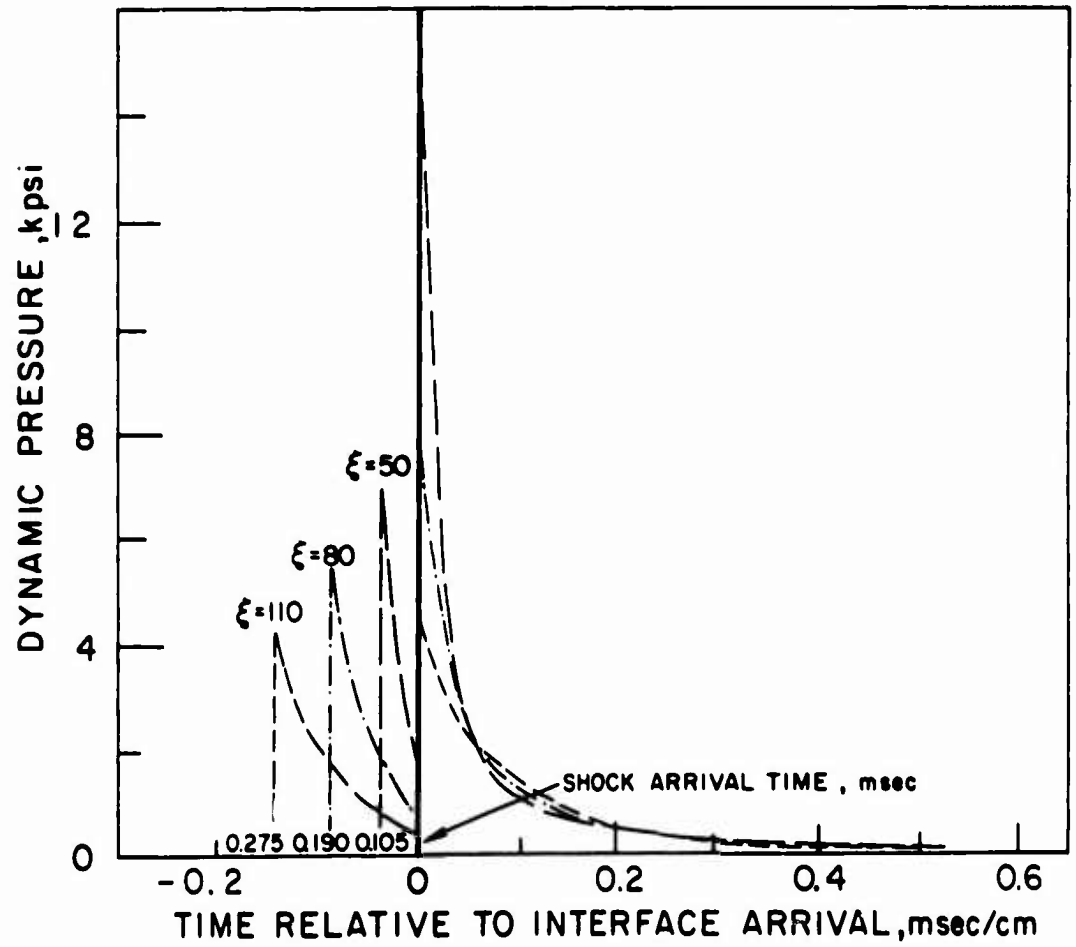


Fig. 9. Dynamic pressure vs time for configuration with void below charge (1 cm TNT, ρ = 1 g/cc).

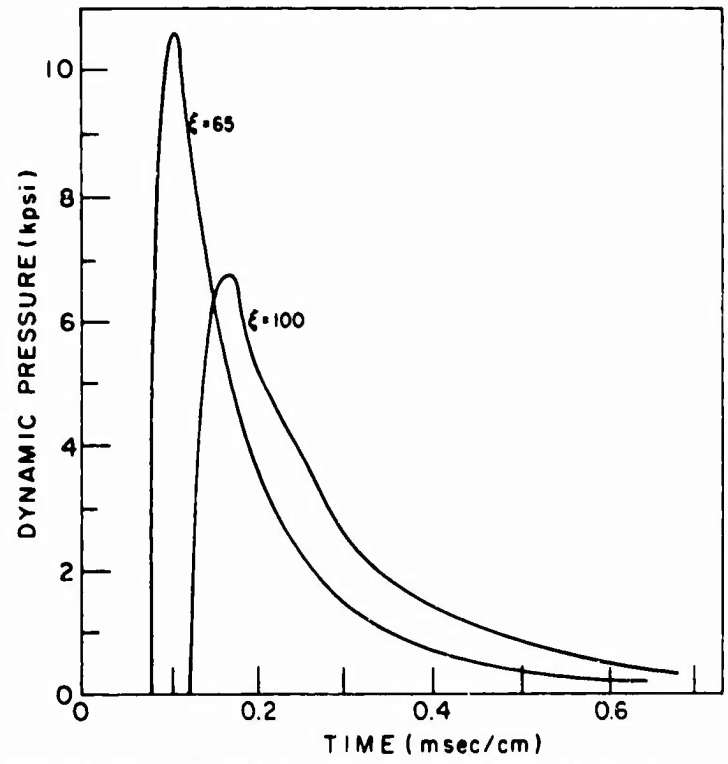


Fig. [illegible]. Dynamic pressure vs time for [illegible] tube for [illegible] tube length to explosive thickness ([illegible] Comp B, ρ = [illegible]).

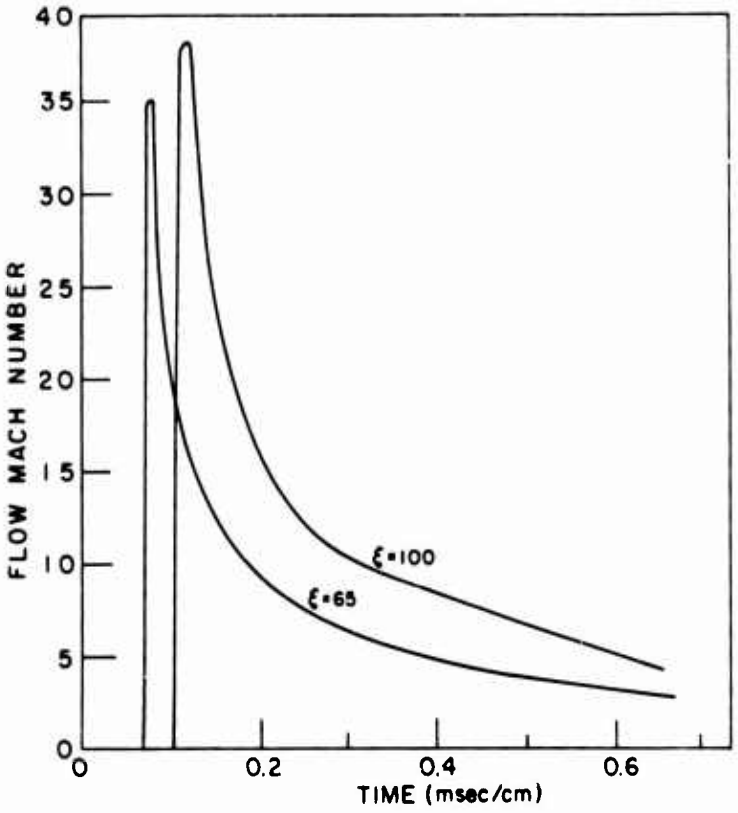


Fig. [illegible]. Mach number vs time for [illegible] tube for [illegible] at the ratios of tube length to explosive thickness ([illegible] Comp B, ρ = [illegible]).

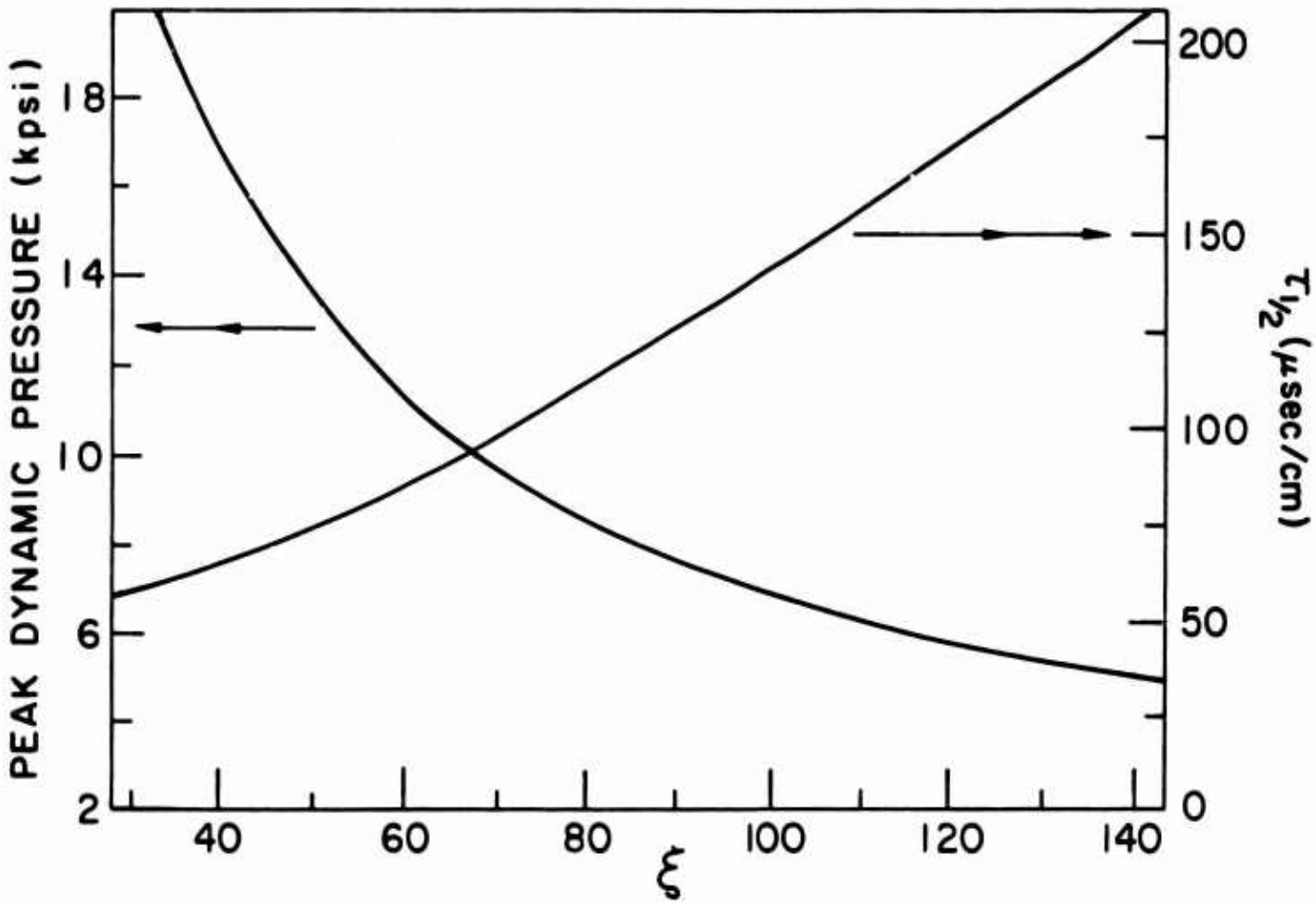


Fig. 12. Peak dynamic pressure and pressure pulse half duration vs ratio of tube length to explosive thickness for an untamped charge (1 cm Comp B, ρ = 1.715 g/cc).

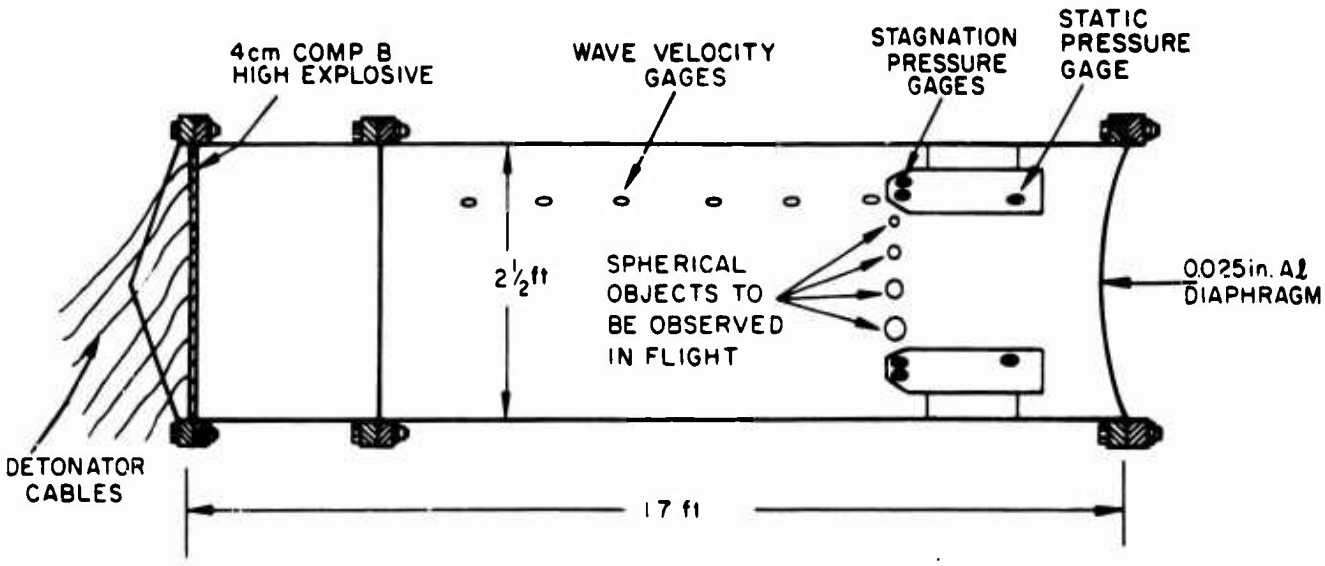


Fig. 13. General test configuration for a vacuum shock tube using solid Comp B explosive.

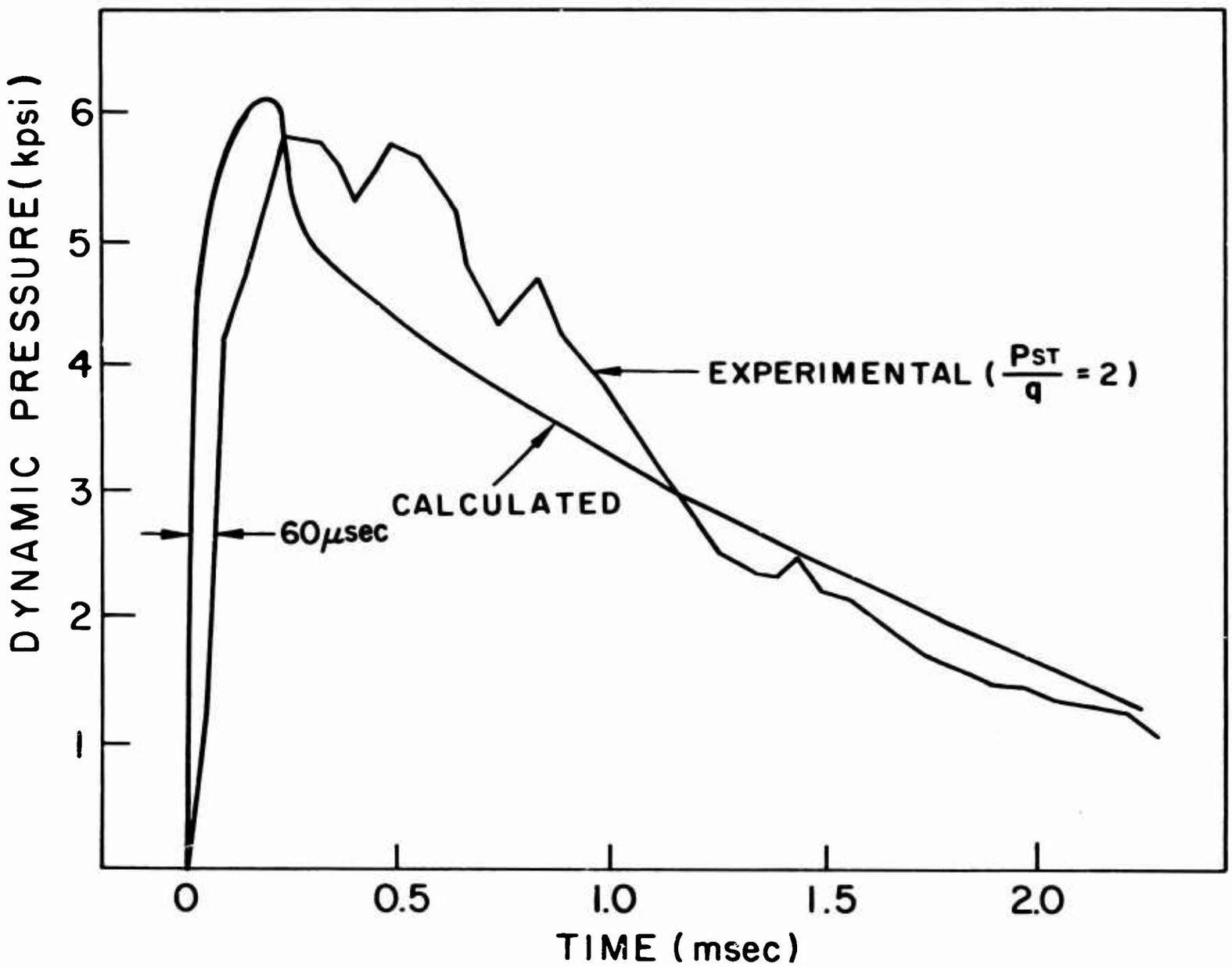


Fig. 14. Dynamic pressure profiles (4 cm Comp B, = 1.715 g/cc).

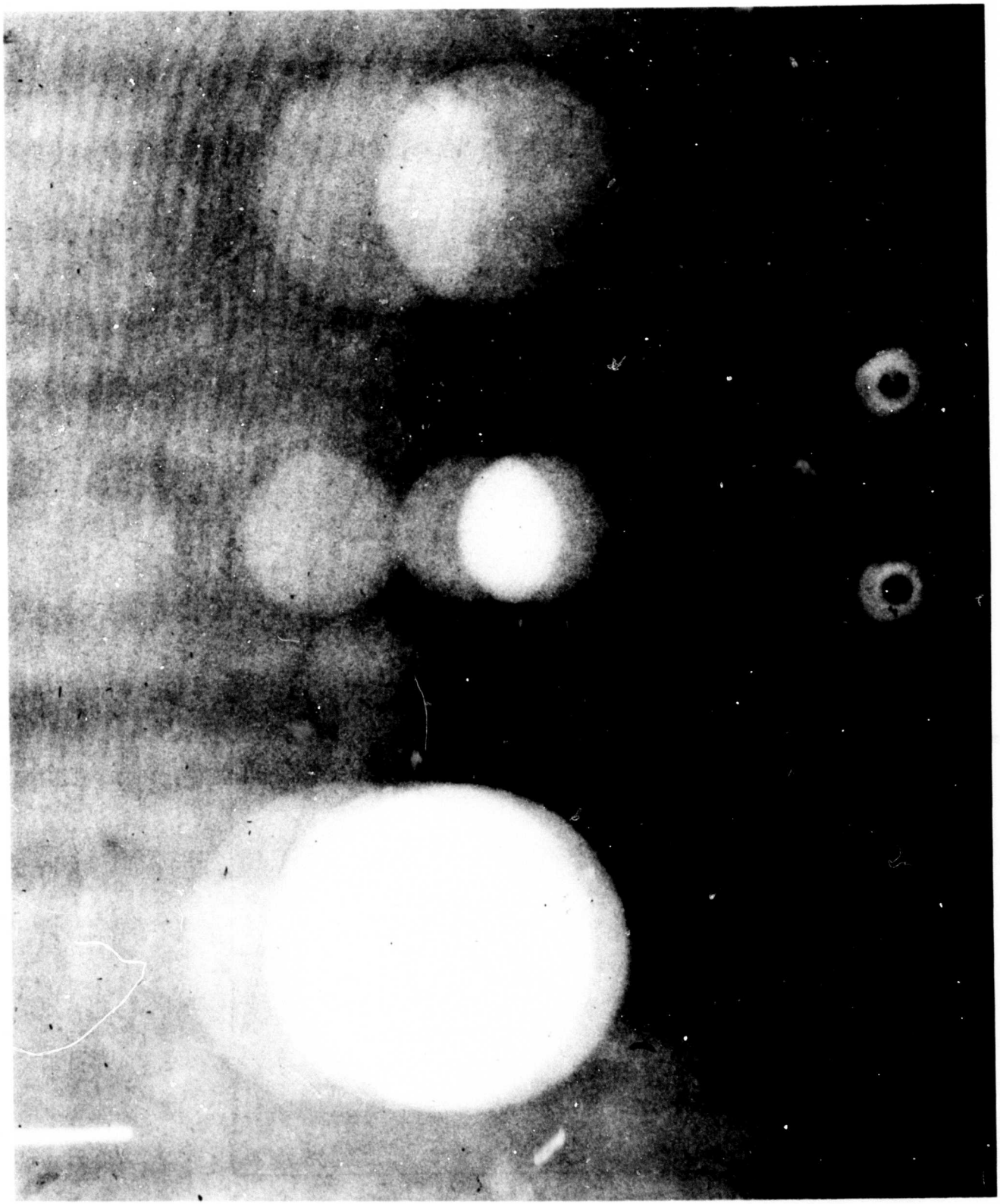


Fig. 15. Flash x ray photograph of the flight of four spheres. The longest sphere is 4 inches in diameter and the time between exposures is 0.5 msec.

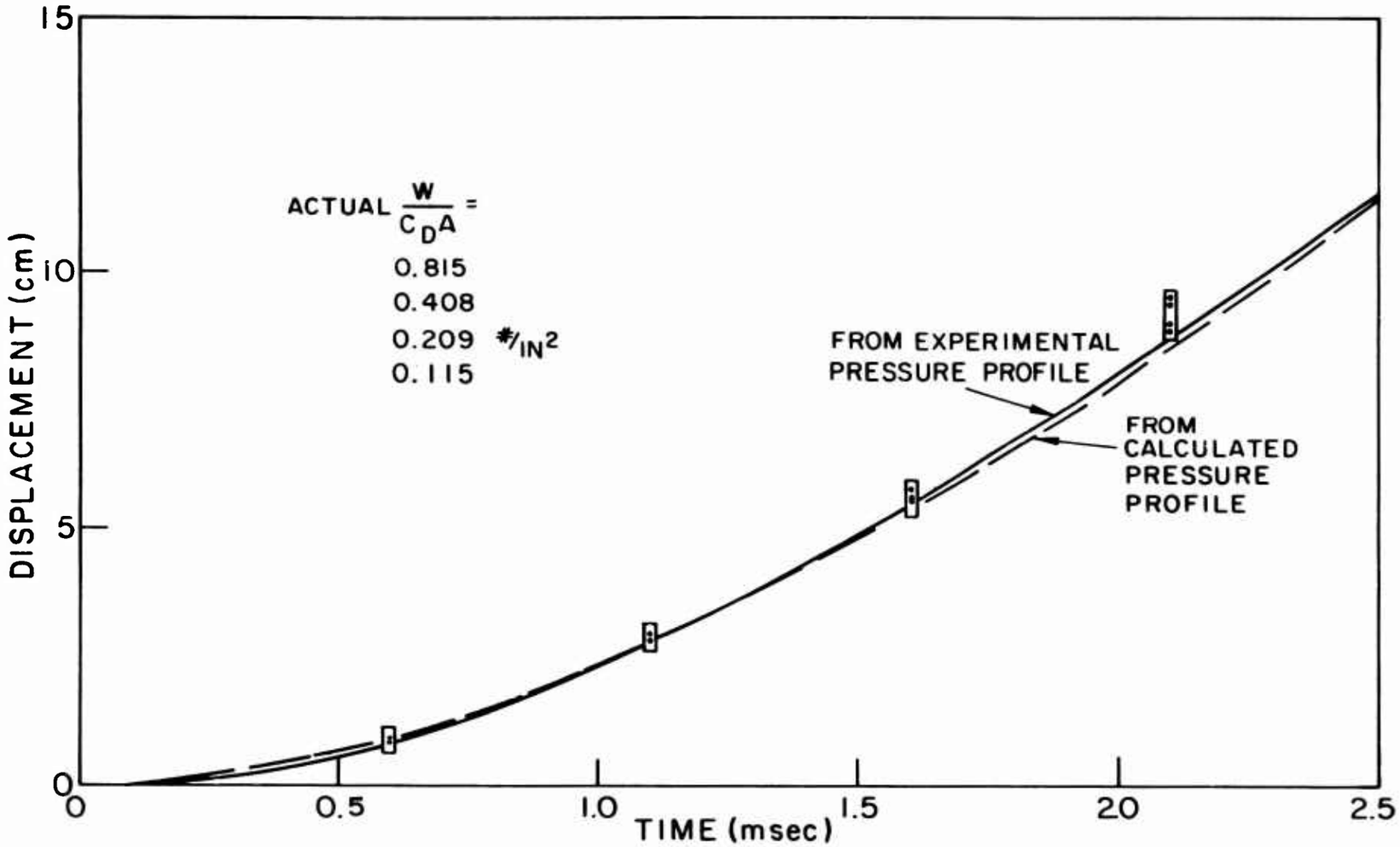


Fig. 16. Trajectories of spherical objects normalized to $\frac{W}{C_D A} = 1$ lb/in^2 .

HIGH-PRESSURE SHOCK WAVE EXPERIMENTS IN ARGON AND XENON

R. Norris Keeler, Berni J. Alder and Mathias van Thiel
Lawrence Radiation Laboratory, University of California
Livermore, California

INTRODUCTION

A significant but little-known area of shock tube physics is the investigation of the properties of dense fluids by means of shock waves generated in expendable cryogenic shock tubes. The same physical ideas are used in shock wave studies of gases and condensed phases; a high pressure and high compression are produced in a material under investigation for a short period of time. The desired measurements are then carried out during this time interval. Although details of construction of these two types of experiment are different, the basic physics is the same in both cases.

In the conventional gas-driven shock tube, the driven gas and driver gas are completely contained at all times, and shock conditions can be sustained for times on the order of milliseconds. On the other hand, the expendable shock tube cannot contain the pressures produced by high-explosive-driven shock waves and the sample and container are destroyed as soon as the shock wave passes. In this system shock wave conditions persist for times on the order of microseconds.

Another feature of shock tube work with gases as compared to work with dense fluids is that almost all the energy expended in compressing the gas goes into raising its temperature; on the other hand, in dense fluids most of the shock energy goes into compression. It should be noted that in our experiments, the initial density of the argon and xenon is of an order of magnitude 10^2 times greater than the initial density of the argon gas in some of the experiments reported in these proceedings.

The working areas in the pressure-volume plane normally covered in shock wave work on gases or condensed materials are shown in Figure 1. Pressures as high as ten megabars, over one hundred million pounds per square inch, have been attained in the Soviet Union (ref. 1) with solid samples. The practical lower pressure limit of this work is ten kilobars. In shock tube

work the initial and final specific volumes are much higher, as is shown in Figure 1.

Because of the density of the media studied and the problem of containment, it is extremely difficult to make accurate measurements of physical properties in shocked dense media. Gas phase measurements have been carried out in shock tubes with great precision and ingenuity. Some of the measurements which have been made, many of them reported in these proceedings, are shown in Figure 2.

Very few sophisticated measurements have been carried out in shock wave experiments in dense media. On many systems the customary volumetric measurements have been made. This involves the measurement of shock and particle velocities, a relatively straightforward procedure.

In the 1950's attempts were made to use flash x-ray densitometry techniques in conjunction with shock wave work (ref. 2). These early results were, in general, suspect because of edge rarefactions.

Several attempts have been made to measure electrical conductivity behind shock waves in dense media. Only one set of even semiquantitatively reliable measurements exist; these are the measurements made in France on sulphur by Joigneau and Thouvenin (ref. 3). The energy gap calculated from these conductivity measurements has been compared with statically obtained energy gaps and the agreement is good. Some of the high temperature conductivity measurements in iodine (ref. 4) appear to be in good agreement with static results. Conductivities have also been measured in the alkali halites (refs. 5, 6, 7). The situation here is most uncertain. Individual investigators cite results which are different by three to four orders of magnitude, for the same materials under the same conditions, and even longitudinal and transverse measurements in these salts have been found to differ by as much as three orders of magnitude. An additional difficulty is that existing circuitry limits the range over which measurements may be taken to resistances between about 0.1 ohm to about 10^5 ohms. Work is currently underway at the Lawrence Radiation Laboratory, Livermore, to extend this range.

Direct-pressure measurements have been made at several high-pressure laboratories (ref. 8) using various types of transducers. The most commonly used is a quartz transducer which is accurate up to about one hundred kilobars. Other investigators have used sulphur transducers which depend on the variation of conductivity with pressure (ref. 9).

A series of advanced solid-state measurements are currently underway at this Laboratory. These are measurements of the shock demagnetization of nickel ferrite, the measurements of the microwave dielectric properties of alkali halides, ultraviolet spectroscopy of the alkali metals, and optical absorption and emission spectroscopy in alkali halides and solid argon. These experiments are in their initial stages, and preliminary results should be forthcoming in a year or two.

The equations used by workers in the shock tube field to calculate state conditions in the driven gas are the one-dimensional, Rankine-Hugoniot equations incorporating an equation of state and a gamma. Since the equation of state of the dense medium under investigation in shock wave experiments is generally not known, the original Rankine-Hugoniot relationships are used to obtain pressure, volume, and energy behind a shock front. These equations are shown in Figure 3. They are simply the equations for mass, momentum, and energy conservation across a one-dimensional shock front and require absolutely no other assumptions in their derivation. In shock wave work in expendable shock tubes the shock velocity is measured directly and the particle velocity is measured indirectly; from these two measured quantities it is possible to calculate the pressure, volume, and energy behind the shock front by use of these relationships.

EXPERIMENTAL TECHNIQUE

A schematic of an experiment is shown in Figure 4, with all its essential parts. The explosive shock is initiated by the detonator and passes into the explosive lens. The lens generates a one-dimensional detonation front which passes into the high explosive and in turn into the aluminum casing and sample. Details of an unassembled casing are shown in Figure 5.

From the one-dimensional Rankine-Hugoniot relationships and three measurements — shock velocity in liquid xenon, shock velocity in aluminum, and free surface velocity in aluminum — the pressure and volume of the xenon behind the shock front are calculated.

The complete apparatus is shown in Figure 6. This stand supports about 40 or 50 pounds of high explosive and the experimental assembly. The high explosive is separated from the cold casing by an insulating board. When the firing switch is depressed, a compressed-air-operated piston forces the insulating board out from between the high explosive and the casing and lifts the explosive into contact with the casing. At this point, two microswitches are closed and the detonator is automatically fired, demolishing the entire experiment in a matter of a very few microseconds.

THEORETICAL BACKGROUND

Some prominent features of the pressure volume plane are shown in Figure 7. As pressure and volume are the state variables which are calculated from experimental measurements, it is customary to plot data in the pressure-volume, or Hugoniot plane. The curve A-B in the dense fluid region is a shock adiabat or Hugoniot, and is defined as the locus of all points which can be reached by shocking a material from a given initial state. The phase diagram of a typical substance is also shown. The solid, liquid, and gas phase are separated by two-phase regions; the liquid gas two-phase region terminating in the gas-liquid critical point. At very high pressures there is a possibility of the existence of a solid-fluid critical point, and in this region pressure and temperature ionization become increasingly important, making it necessary to treat materials shocked to these extreme conditions

from the plasma standpoint. The initial conditions for the experiments in liquid argon and xenon were in the liquid region close to the boundary (liquidus) between the liquid and two-phase region. The Hugoniots for these two substances pass through, out of, and very close to the solid-liquid two-phase region.

The rare gases, argon and xenon, have always been considered interesting subjects for research by physical chemists because they are one-component systems consisting of a single closed-shell atom, and hence are easier to treat theoretically. Because of their simplicity, it is possible to treat these materials by use of the theorem of corresponding states as outlined by Pitzer (ref. 10). Sufficient conditions for two substances to obey the theorem of corresponding states are (1) the substances must exhibit no quantum effects (in the sense that as we confine the molecules to smaller regions the uncertainty in the momentum must increase and the average kinetic energy rises, creating an increase in pressure or volume over their classical value); (2) the intermolecular potential for each substance must be a function of intermolecular separation only and not be angle-dependent; (3) the molecules must be spherical and freely rotating; and (4) the intermolecular potential must have the same functional form for both substances and contain only two characteristic constants, and be written in the form $U(r) = U_o \phi(r_o/r)$ where ϕ is a universal function. If two substances obey corresponding states then their properties, when reduced by the critical properties, fall on the same curve. For example, isotherms plotted in the reduced pressure -- reduced volume plane fall on the same line. Now argon and xenon fulfill the first three conditions for obeying corresponding states; therefore, if their volumetric properties when reduced by the critical constants fall on the same curve, the principle of corresponding states is obeyed and the intermolecular potentials of the two substances are of the same functional form. On the basis of this theorem, experiments were carried out on liquid argon and xenon to determine whether their Hugoniots, when reduced by the critical properties, fell on the same reduced curve.

EXPERIMENTAL RESULTS

The lower part of Figure 8 illustrates that the corresponding states principle is obeyed over a wide range of intermolecular distances. The pair-potential, which fits quite well the equation-of-state data in the gas phase, in the solid phase obtained by static means, in the liquid phase obtained through shocks, as well as the energy of the normal solid, is given by the modified Buckingham potential (ref. 11).

$$U(r) = \frac{\epsilon}{1 - \frac{6}{\alpha}} \left\{ \left(\frac{6}{\alpha}\right) \exp\left[\alpha\left(1 - \frac{r}{r_m}\right)\right] - \left(\frac{r_m}{r}\right)^6 \right\}.$$

The parameters are listed in Table 1. This pair-potential has been introduced in the exact Monte Carlo (ref. 12) method to generate the theoretical Hugoniot given in Figure 8. However, to save calculating machine time, the

Leonard-Jones Devonshire cell theory was used to relate Monte Carlo results for different interaction potentials.

Table 1. Parameters for the Modified Buckingham Potential

	α	r_m, Å	ϵ/k, °K
Argon	13.5	3.80	123
Xenon	13.5	4.45	236

Figure 9 is a comparison of the intermolecular potential obtained in our experiments with the potential obtained in beam scattering experiments and the theoretical Thomas-Fermi potential. Curve I is the intermolecular potential derived from our Hugoniot data, curve II is the intermolecular potential calculated from TFD theory (ref. 13), curve III is the potential obtained from the molecular beam experiments (refs. 14, 15, 16) and curve IV is the Leonard-Jones 12-6 potential, which is seen to be totally inadequate. Thus we have an excellent comparison of our own derived interatomic potential with a potential obtained from a completely independent and different experiment as well as with theoretical calculations.

At the highest pressures, the lack of correspondence observable in Figure 8 can be ascribed reasonably to electronic excitations in xenon. Under the conditions reached in these experiments, these cannot significantly affect the properties of argon, because its energy gap is larger and its temperature is about half that of xenon. The effect of such electronic excitations is to absorb part of the energy imparted to the system by the shock wave so that the temperature, and hence the pressure, do not rise as rapidly as in the absence of such an energy sink.

Very crude conductivity experiments in argon have shown that at the highest pressures the energy gap is close to that of the first excitation level in gaseous argon or the lowest transition found in normal crystalline argon. From the ratio of resistivities the application of simple semiconductor theory leads to a calculated energy gap of 12 eV, somewhat narrowed from the estimated 14.3 eV conduction gap in the normal solid (ref. 17). Even if that ratio were off by a factor of ten, the minimum possible gap of 6 eV would still not affect the argon Hugoniot significantly. In xenon however, temperatures in excess of 2 eV are reached, and the first excitation energies in the gas and solid phase are 8.4 eV (ref. 17). Modifying the Hugoniot conditions only by inserting this energy gap into the internal energy leads to deviation from corresponding states at the experimentally found pressure, as shown by the dotted line in Figure 8. Beyond this initial deviation from corresponding states, as more electrons become excited and the gap narrows further, the system probably must be treated from the metallic point of view. Further conductivity and optical measurements are planned to determine the dependence of the energy gap on density.

It has been found experimentally that there is a linear relationship between shock and particle velocity for Hugoniots which lie within a single phase (ref. 18), $U_s = a + bU_p$. Therefore, it is customary to search for

phase transitions by plotting the experimental data directly in the Us (shock velocity) versus Up (particle velocity) plane. Breaks in the linear relationship are then interpreted as phase transitions. The result for such a plot for argon and xenon is shown in Figure 10. The shock and particle velocities of argon and xenon are reduced by the appropriate combination of the critical constants. The results for argon show a definite break. This is most conveniently interpreted as a phase transition. The argon initially in the liquid state crosses over into the two-phase region at pressures too low to be easily reached by shock techniques. It remains in the two-phase region up to about 45 kilobars and then emerges into the dense fluid region. This crossing of the liquidus corresponds to the break in the reduced shock-particle velocity curve.

CONCLUSIONS

In conclusion, the following have been shown from work in expendable shock tubes: (1) pairwise additivity for argon and xenon holds at close interatomic separations; (2) the repulsive potential for argon and xenon is a universal function; (3) an accurate intermolecular potential for argon and xenon has been derived; (4) deviations from classical behavior due to electronic effects are significant at the highest pressures for xenon; and (5) we have observed what is most conveniently interpreted as the melting transition in argon.

ACKNOWLEDGMENTS

This work was performed under the auspices of the U. S. Atomic Energy Commission. We are grateful to Dr. Marvin Ross for aid in the calculations and Mr. Edward Britton for help with the experiments.

REFERENCES

(1) Altshuler, L. V., Uspekhi Fiz. Nauk, 8, 219 (1965)

(2) Dapoigny, J., Kieffer, J., and Vodar, Boris, J. Rech. Centre Natl. Rech. Sci., Lab. Bellevue (Paris), 31, 260 (1955)

(3) Joigneau, Suzanne, and Thouvenin, J., C. R. Acad. Sci (Paris) 246, 3422 (1955)

(4) Alder, B. J. and Grover, R., Bull. Am. Phys. Soc., II, 6 (1961)

(5) Alder, B. J. and Christian, R. H., Disc. Faraday. Soc., 22, 44 (1956)

(6) Altshuler, L. V., Kuleshova, L. V. and Pavlovskii, M. N., Sov. Phys. JETP 12, 10(1961)

(7) Stanford Research Inst. Report SRI-PGU-4100-FR, (August 31, 1963)

(8) Bradley, R. S., High Pressure Physics and Chemistry vII, p 249 (Academic Press, Lordon and New York, 1963)

(9) Berg, U., Arkiv. Fysik. (Sweden) 25 111 (1963(

(10) Pitzer, K. S., J. Chem. Phys. 7 583 (1939)

(11) Hirschfelder, J. O., Curtiss, C. F. and Bird, R. B., Molecular Theory of Gases and Liquids, p 33 (John Wiley & Sons, Inc., New York)

(12) Wood, W. W. and Parker, F. R., J. Chem. Phys., 27, 720 (1957)

(13) Abrahamson, A. A., Phys. Rev., 130, 693 (1963)

(14) Amdur, I., Jordan, J. E. and Bertrand, R. R., Proceedings of the Third International Conference in the Physics of Electronic and Atomic Collisions, p 934 (John Wiley & Sons, New York, 1963)

(15) Berry, H. W., Phys. Rev., 75, 913 (1949)

(16) Berry, H. W., Phys. Rev., 99, 553 (1955)

(17) Bandini, G., Phys. Rev., 128, 1562 (1962)

(18) Berger, J. and Joigneau, Suzanne, Compt. rend., 249 2506 (1959)

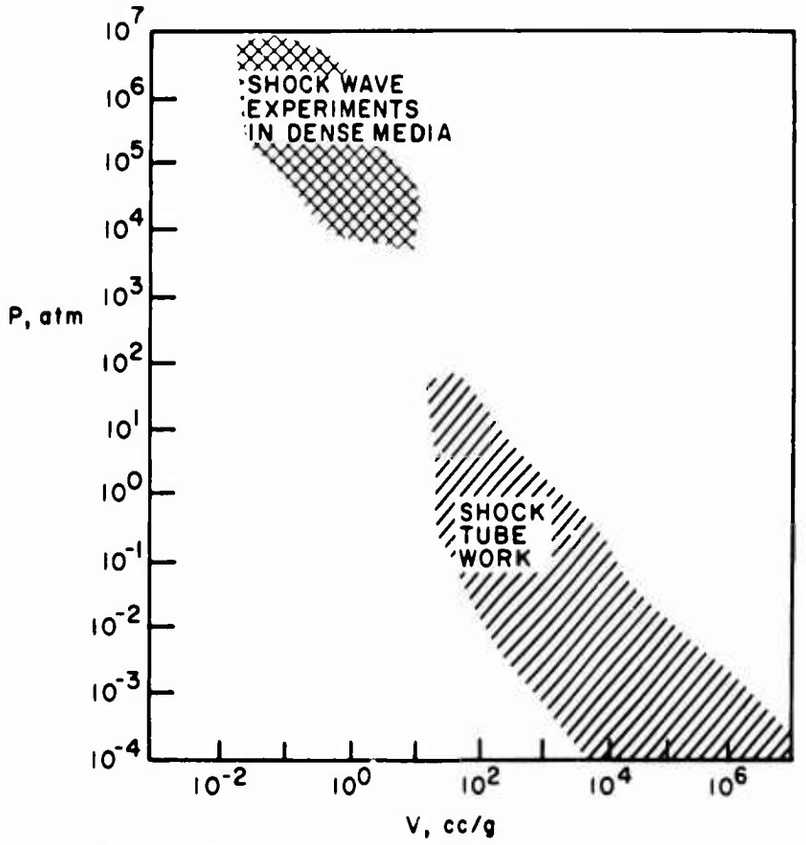


Fig. 1. Working areas in the P-V plane for shock tubes and shock wave work in dense media.

Shock Tube	Shock Wave (Dense Media)
1. Optical Interferometry	1. Volumetric (U_s, U_p)
2. Schlieren techniques	2. Flash X ray densitometry
3. Pressure (direct)	3. Electrical conductivity
4. Heat transfer rates (thermal cond)	4. Pressure (direct)
5. Optical absorption	*5. Magnetic properties (shock demagnetization)
6. Electrical conductivity	*6. Microwave dielectric properti
7. IR, UV, mass spectroscopy	*7. U-V spectroscopy
8. Intensitometry (temperature)	*8. Optical absorption and emissi spectroscopy
9. Microwave (electron density)	
10. Electron beam densitometry	
11. IR absorption and emission	* In initial stages
12. X ray densitometry	

Fig. 2. Measurements made in shock tubes and shock wave work in dense media.

EQUATIONS FOR STATE CONDITIONS BEHIND A SHOCK FRONT

Volume: $$V = V_0\left(1 - \frac{U_p}{U_s}\right)$$

Pressure $$p = p_0 + \rho_0 U_s U_p$$

Energy $$e = e_0 + \frac{1}{2}(P_1 + P_0)(V_0 \quad V_1)$$

U_s = velocity of shock front

U_p = velocity of particles behind shock front

Fig. 3. The one-dimensional Rankine-Hugoniot relationships.

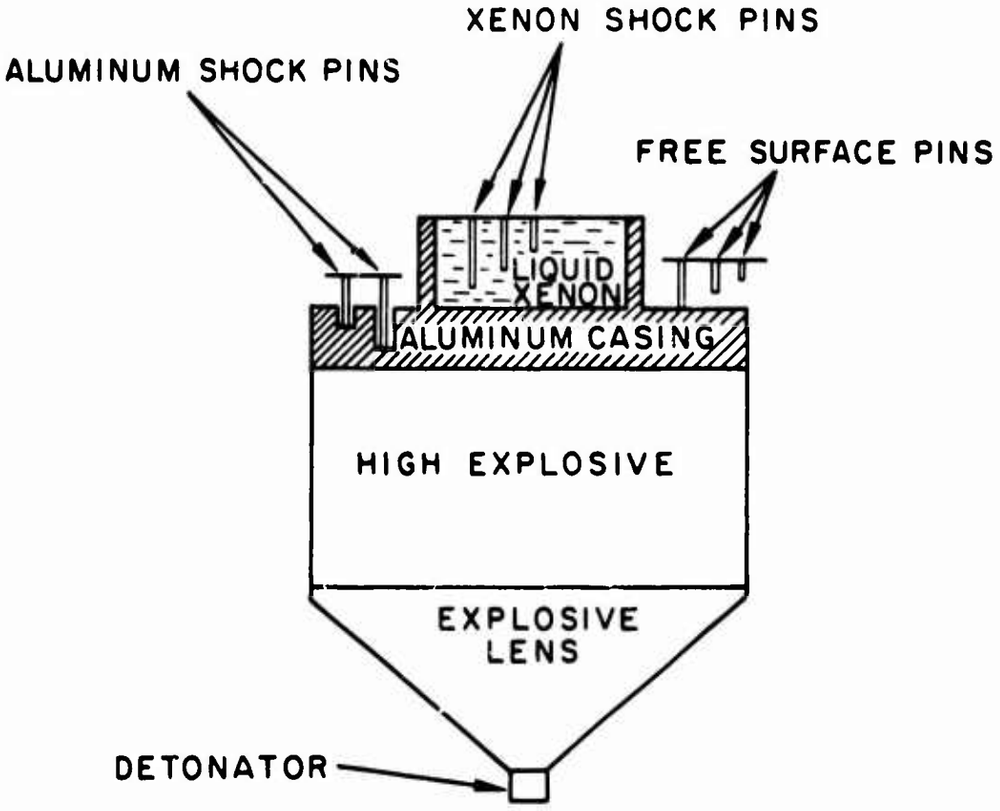


Fig. 4. Schematic of shock wave experiment.

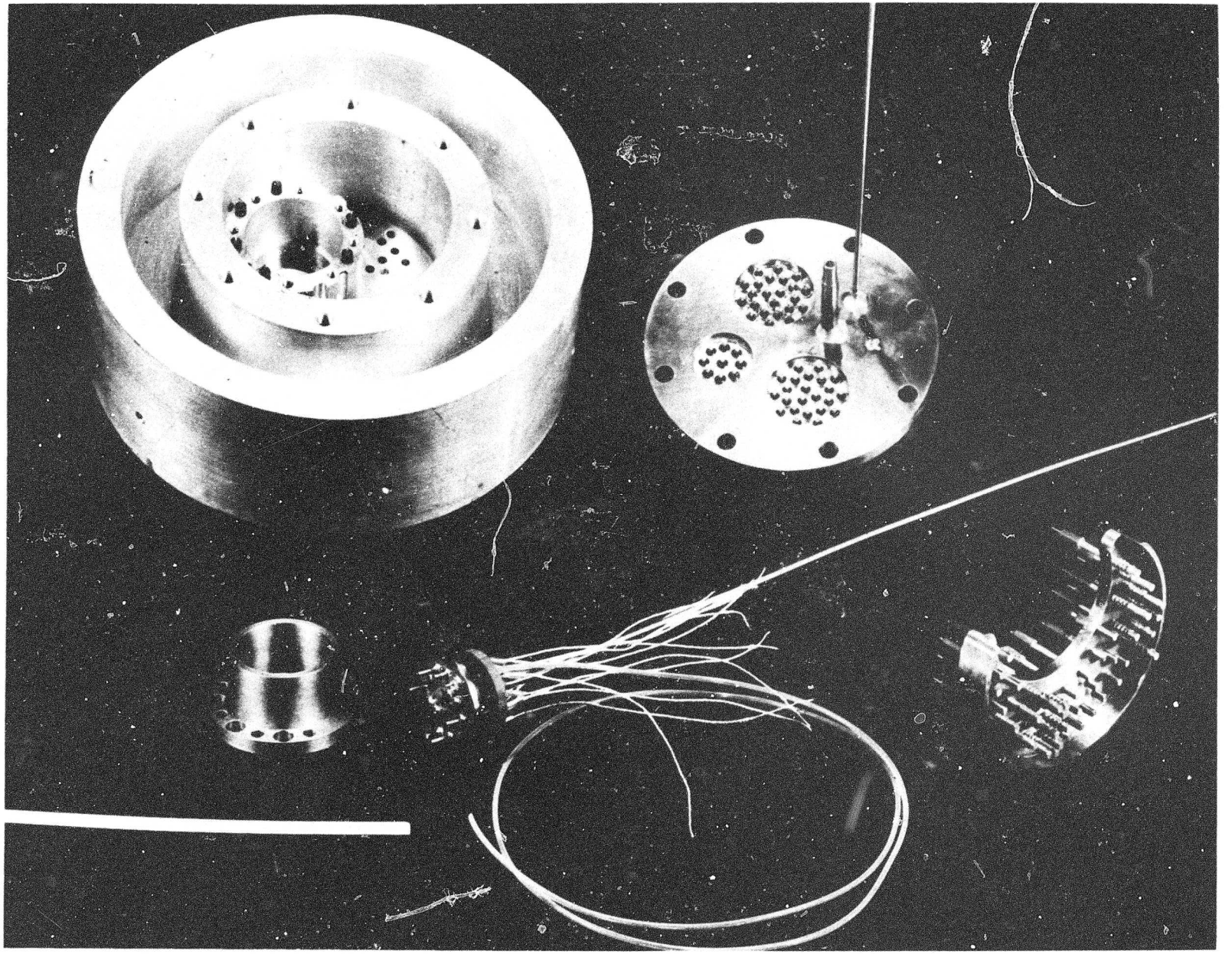


Fig. 5. Details of unassembled experiment.

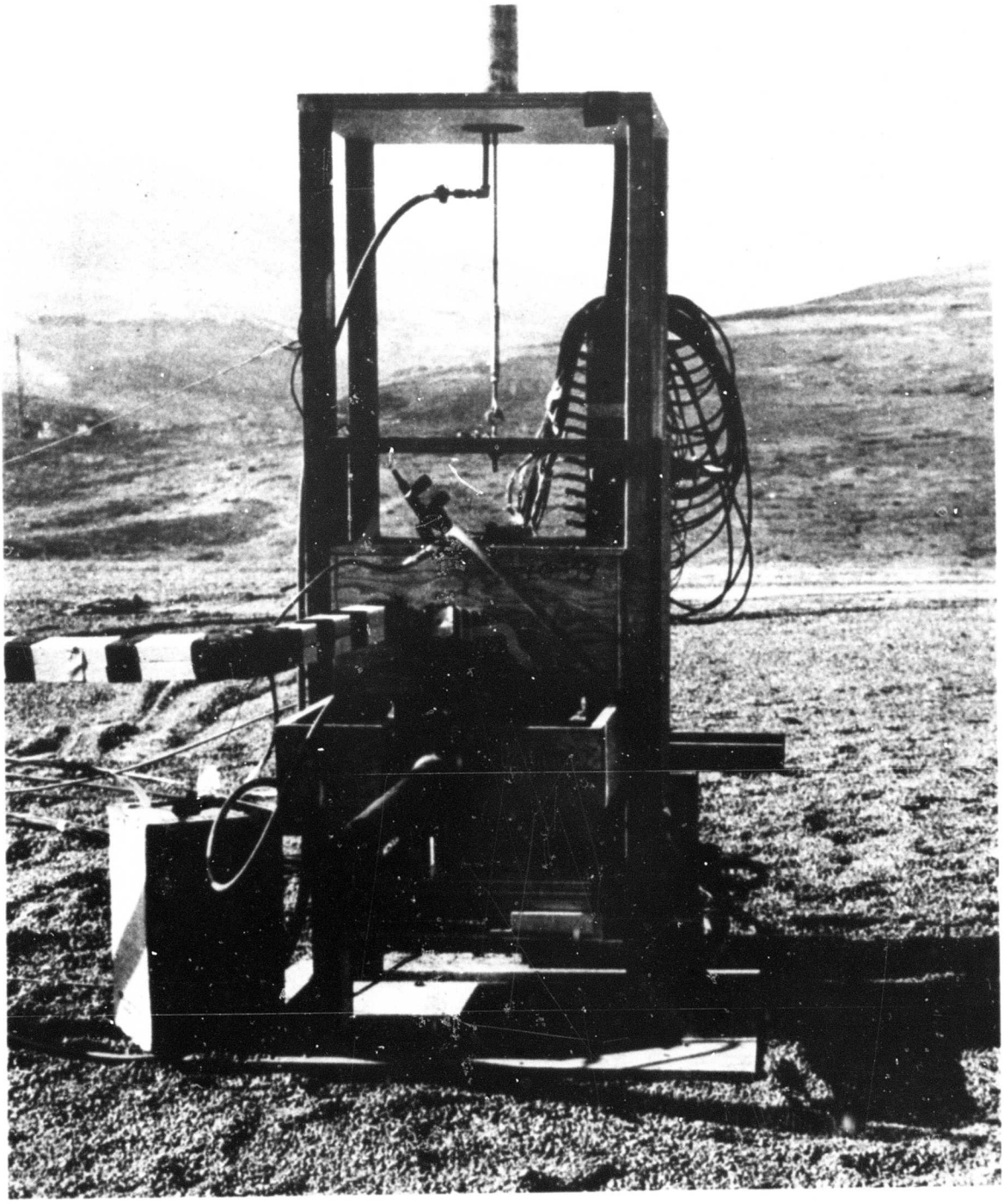


Fig. 6. Assembled experiment at test site.

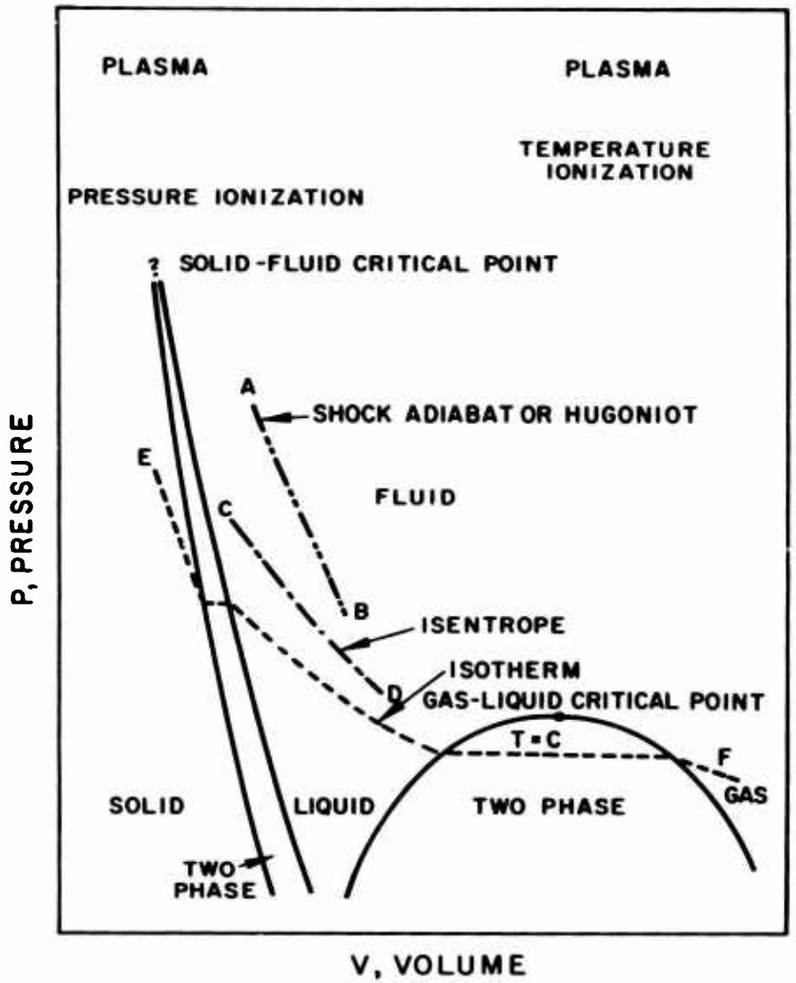


Fig. 7. The P-V plane.

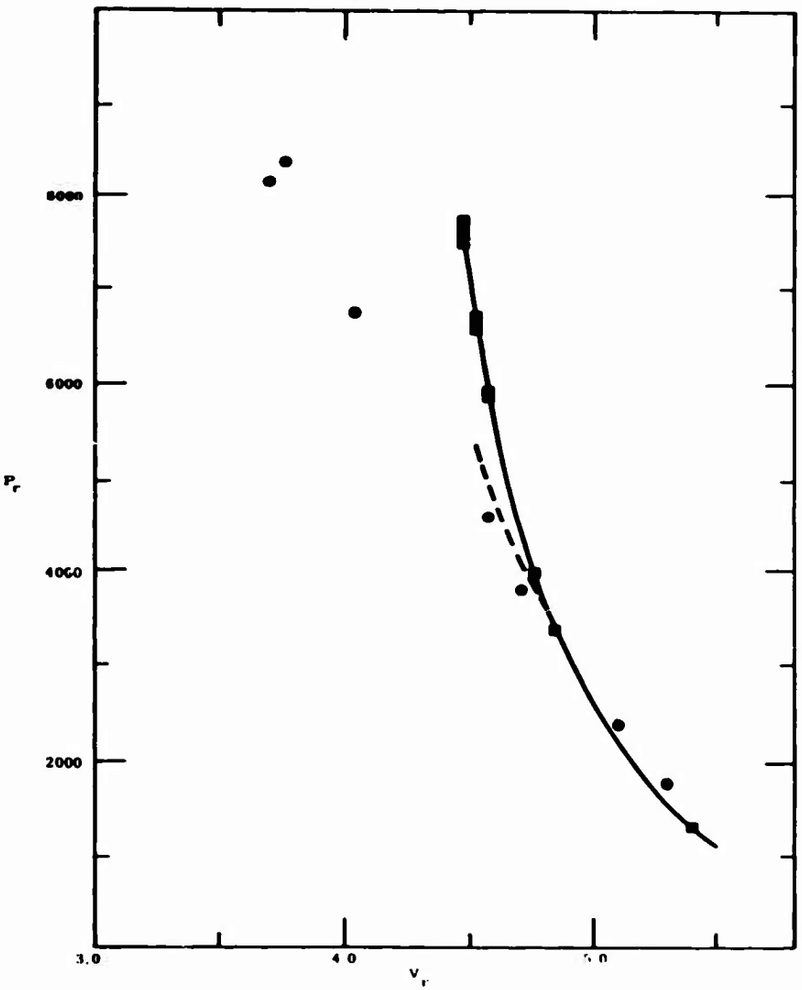


Fig. 8. Reduced Hugoniot of argon and xenon.

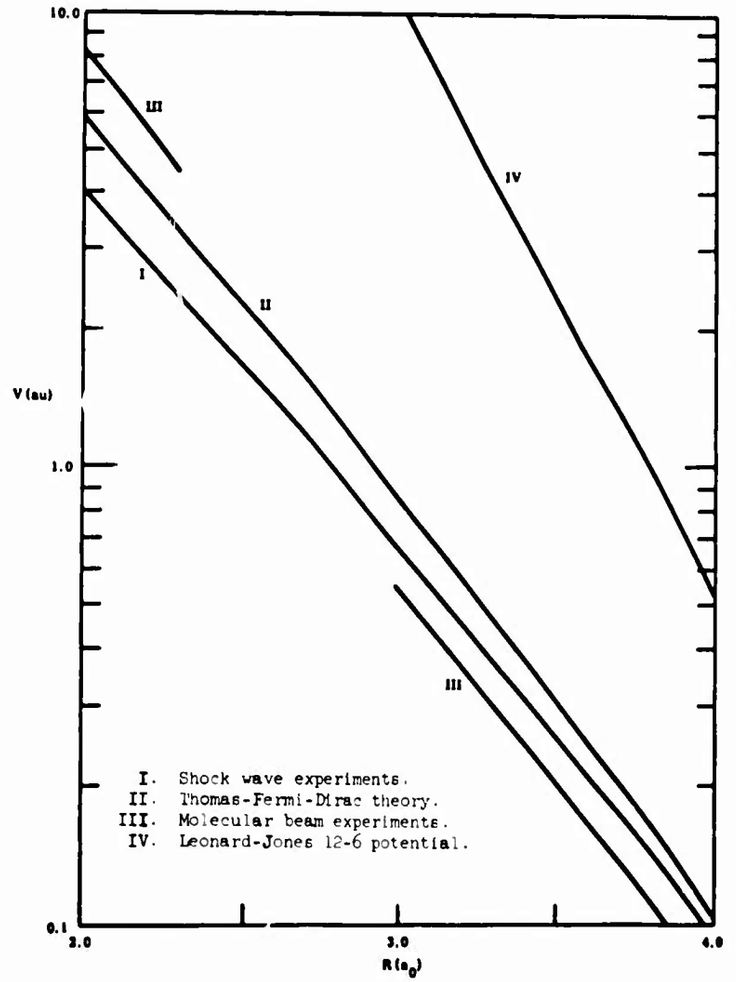


Fig. 9. Comparison of intermolecular potentials for argon (atomic units).

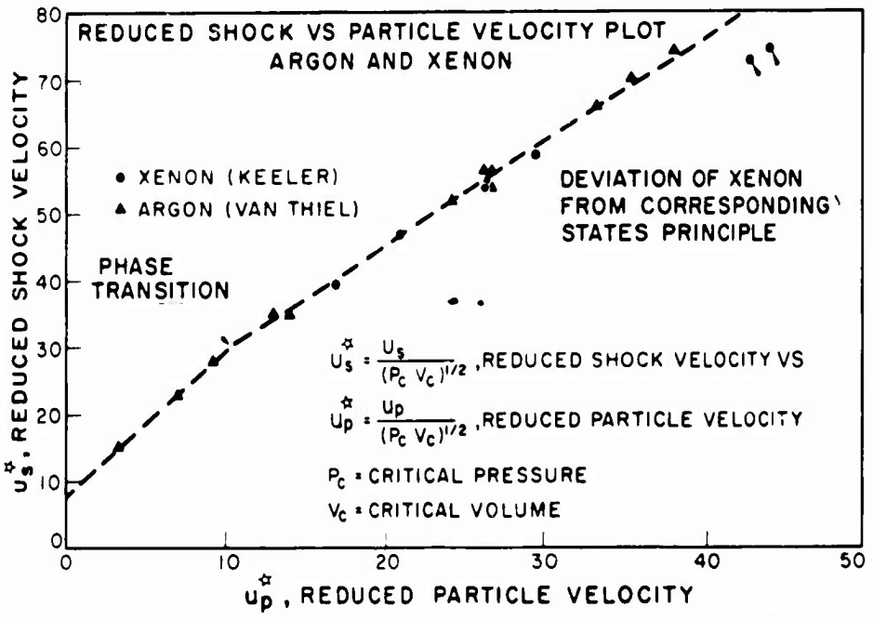


Fig. 10. Reduced U_s - u_p plot for argon and xenon.

BLANK PAGE

METHODS USED IN CONDUCTING EXPERIMENTS IN A WATER-TO-AIR SHOCK TUBE

E. V. Gallagher and F. L. Schuyler
I. I. T. Research Institute
Chicago, Illinois

INTRODUCTION

The purpose of the paper is to present a brief description of the experimental work done and results obtained, using a water-driven shock tube.

Work with the water-to-air shock tube at IITRI was first performed by E. A. Brown (Ref. 1). Brown used water as the driver fluid, at temperatures up to about 212°F and at pressures up to about 25 psia. He used air in the driven section of the shock tube under a partial vacuum at pressures of about 0.5 to 6.0 psia. After Brown, others at IITRI studied water hammer effects in the water-driven shock tube. Terner (Ref.2) and Lieberman(Ref.3) worked with driver water temperatures up to 300°F, and pressures up to 1000 psi. They used air at atmospheric pressure in an open-ended driven section.

Following this earlier work, experiments were conducted by the authors of this paper, using a newly designed shock tube with water in the driver section, at temperatures in the range of 300 to 600°F, and at pressures up to 2000 psi. Results obtained are qualitatively very similar to those of Brown, Terner, and Lieberman. The main differences are quantitative, and result from the higher temperatures of the driver fluid.

The experimental work reported in this paper has been performed at IIT Research Institute under the sponsorship of the United States Atomic Energy Commission, Research and Development Branch, Division of Reactor Development and Technology. Results obtained have been applied to Reactor Containment Analyses.

COMPARISON TO AIR DRIVEN SHOCK TUBE

It is convenient to begin the discussion of the water-to-air shock tube experiments by comparing a simple water-driven shock tube to the familiar air-to-air shock tube. This comparison can be made in terms of wave diagrams, i.e., distance-time plots, and profiles of pressure-versus-distance at some fixed time. These are shown in Fig. 1. The left column of this figure represents the diagrams for the conventional air-to-air shock tube, while the

right column represents the corresponding diagrams for the water-to-air shock tube. These diagrams are only schematic in nature, but illustrate relative magnitudes of velocity and pressure in approximate proportions. In each diagram, the horizontal axis represents distance. The position of the diaphragm separating the driver and the driven sections from one another is arbitrarily selected as X=0. Distance to the right of the diaphragm, i.e., toward the driven section, is taken as positive (+X). Distance to the left of the diaphragm, i.e., back into the driver section, is taken as negative (-X).

When the diaphragm is ruptured flow is from left to right. Four significant regions are indicated as follows, for the air-to-air shock tube. Region 1 represents undisturbed air. Region 2 represents air between the shock front and the contact surface. Region 3 represents decompressed air between the contact surface and the tail of the expansion wave moving back into the driver air. Region 4 represents undisturbed high pressure driver air. A decompression fan separates Region 3 from Region 4. The associated pressure-distance curve is shown below the time-distance sketch, and the distribution of these four regions in the shock tube is shown at the bottom.

In the right-column of Fig. 1, the corresponding features are illustrated for the case of a water-to-air shock tube. In this simple case it is assumed that the driver water is cold, i.e., its temperature is below the saturation temperature which corresponds to a pressure of magnitude, p_1. Thus, when the diaphragm is ruptured, an elastic expansion of the liquid takes place which causes the contact surface to move rightward. This acts as a piston moving against the left end of the air column in the driven section and drives a relatively weak shock into the air.

The strength of the air shock is determined by the motion of the contact surface. Since in the case of no vaporization of the driver water, the contact surface moves very slowly, the shock moving into the undisturbed air in Region 1 is very weak. Thus, the pressure in Region 2, which is between the air shock and the contact surface, is only slightly greater than the pressure in Region 1. As in the air-to-air case, the pressure and particle velocity are continuous through the contact surface. Therefore, Region 3 has the same pressure as Region 2. The decompression wave traveling back into Region 4 of the water travels at a much higher velocity than the shock wave traveling into the air of Region 1, i.e., W_{34} is much greater than W_{12}. Actually there is a very narrow expansion fan between Regions 3 and 4 and this may be approximated by a discontinuity as shown in the pressure-distance curve in the right-hand column. Both the air shock, between Regions 1 and 2, and the decompression wave, between Regions 3 and 4, are acoustic waves. Only a small change in density occurs from Regions 3 to 4 when there is no vaporization of the liquid. This yields a small value of the velocity at the contact surface, and this in turn, combined with the low value of acoustic impedance ratio for air-to-water, results in a very low pressure between Regions 1 and 2.

All important features of the wave motion can be readily calculated for

the case of cold water. The pressure change between regions 4 and 3 (or between 4 and 2) can be taken as approximately equal to the difference in pressure initially between regions 4 and 1. In equation form this is expressed as follows:

$$(p_4 - p_3) \simeq (p_4 - p_1) = \Delta p_w$$

where Δp_w is the pressure drop in the water during the decompression.

The change in velocity of the water at the contact surface, Δu_w, can then be calculated from the momentum equation as follows:

$$\Delta u_w = \Delta p_w / \rho_w c_w$$

where ρ_w and c_w are the density and sound speed of the water. From this, the pressure change in the air, Δp_a, across the shock wave separating regions 1 and 2 can be calculated from the momentum equation as follows:

$$\Delta p_a = \rho_a c_a \Delta u_a$$

where Δp_a represents the pressure change in the air, Δu_a, is the velocity of the contact surface, and ρ_a and c_a are the density and sound speed in the air of region 1 ahead of the wave separating regions 1 and 2. For water at 75°F and 1000 psi, the contact surface velocity is about 15 ft/sec., which results in an air shock overpressure of only about 0.25 psi. The use of the acoustic approximation is therefore, justified.

For the simple case of the water-driven shock tube, in which no vaporization occurs, as depicted in the right-hand column of Fig. 1, the wave motion can be calculated for a given set of initial conditions. Unlike the cold water case, when vaporization of the liquid occurs following sudden rupture of the diaphragm, the resulting wave motion is not easily calculated, since the velocity of the contact surface is not known.

In general, for rapid decompression of a liquid at a high temperature, i. e., when vaporization occurs, the time rate of expansion in flashing to vapor is presently undeterminable. Therefore, the motion of the contact surface is not known and the resulting wave motion, both in the water and in the air, is not known, and can not be calculated without resorting to experiments.

Based upon the above considerations, a series of experiments were planned to study the wave motion which results when high-temperature, pressurized water is suddenly allowed to expand into an air chamber.

TEMPERATURES AND PRESSURES TREATED

In the authors' experiments the initial temperature of the water, i. e.,

the temperature prior to rupture of the diaphragm was in the range of 300 to 600°F. The initial pressures of the water were kept high enough to prevent formation of vapor in the driver prior to diaphragm rupture. In Fig. 2 a plot of saturation pressure-versus-saturation temperature, for water, is represented by the solid curve. For any given value of temperature in the range shown, the water was entirely in the liquid phase, as long as the pressure was kept at a magnitude higher than the solid curve.

From a practical point of view, it was difficult to control the heating of the water so that temperature at all points in the tube would be perfectly uniform. Unfortunately, when temperature non-uniformities would develop during the heating process, local hot spots existed, at which the temperature was as much as 10°F, or more, than that at the nearest thermocouple used to monitor the fluid temperature during heat-up. Under these conditions, vapor could form, unless the driver section was over-pressurized well above the solid curve. The dashed curve of this fighre, obtained by translating the solid curve 10°F to the left, therefore represents a lower limit of the pressure required to avoid vapor formation (if temperatures of the water can be controlled within around 10°F). In many of the experiments the actual degree of over-pressurization was several hundred psi higher than that shown by the dashed curve.

The very earliest shots had studied intensively the possible effects of over pressurization, with the resulting conclusion that over pressurization had no significant effect upon the resulting wave motion. The initial pressurization of the liquid appeared to affect only the elastic expansion, of the water, i. e.. that corresponding to the cold water shock tube discussed in connection with Fig. 1. Thus, 1000 psi water pressure yields about 0.25 psi for the air shock; 2000 psi yields about 0.5 psi, etc. whereas the rate of vaporization and motion of the water-to-air contact surface depends almost exclusively upon the temperature of the water at the time of rupture. In any case the initial pressures up to 2000 psi were used in the experiments near the high end of the temperature range (600°F). At all lower temperatures about 200 to 500 psi overpressurization was used.

DESCRIPTION OF THE EXPERIMENTAL APPARATUS

The driver section (i. e., the water-filled portion of the shock tube) consisted of a two-inch inside diameter by 6-foot long, stainless steel tube. This was clamped to a 6-foot long by 2-inch inside diameter driven section (i. e., air-filled portion). Driven section lengths of 3 feet, and 4 feet were also used on many shots. Although experiments have been conducted using a larger diameter section for the air-filled portion and with diaphragm openings as small as 1/2-inch diameter, in this paper attention is restricted to equal driver and driven cross-sectional areas having a 2-inch diameter, and the same as the diaphragm opening, (i. e., one-dimensional flow).

The shock tube had eight instrumentation stations located at various positions along its length. Five of these were in the driver section and three were in the driven section. Each gage station had three separate gage sockets which could be utilized simultaneously. For most experiments a

single pressure gage and a single thermocouple were operated at any one gage location, while on a few shots an independent check was made of either the temperature or the pressure to determine consistency of the measurements. Not all locations were operated on each shot. At least two locations in the water, and two in the air were used on each shot.

The driver water was heated using electric coils mounted in insulated blocks located on the outside of the tube. About two to three hours was generally required for the heat-up.

The pressure transducers used were all Kistler, model 601 quartz-crystal gages. Since the output of these gages is affected by temperature above 300°F each transducer was mounted in a water-cooled jacket and cool water was continuously circulated around the transducer during the heat-up period and during the experiment.

Two types of thermocouples were used. One type has the junction of dissimilar metals incased in a stainless steel sheath and, therefore, does not have a very high response time but yields useful information for control of initial temperatures during the heat-up. The second type has the junction of dissimilar metals exposed to the flow. This type is made by NANMAC and has a very fast response time. Both the driver section and the driven section were operated with their distal ends closed with steel blind flanges.

The driver section had two 1-1/4" diameter portholes located about an inch upstream of the diaphragm. These permitted visual observation of the flow field using high speed photography, to observe bubble formation. The diaphragm material consisted of tempered glass, ranging in thickness from 1/4" to 3/8". The diaphragm was clamped in place between the driven and driver sections. The glass diaphragm was ruptured at a controlled instant, when all initial conditions in the driver (water-filled) section were as desired. Rupture of the glass was initiated by impacting a small lead pellet with a ball bearing soldered to its front edge. The pellet was fired from a gas gun mounted at the closed end of the air-filled section. The gun was actuated by a solenoid and was designed so that only about one cubic centimeter of gas from the gun entered the air-filled section with the pellet. This prevented any extraneous disturbances in air-filled section which would interfere with, or in any way obscure, the effects of the shock driven by the vaporizing water.

The signal which triggered the oscilloscopes to provide the automatic recording of transient pressures and temperatures was obtained by use of a conductive paint placed on the air side of the glass diaphragm. Other methods of triggering were also used as checks on the method. These consisted of: (1) sensing the stress wave in the steel bolts holding the driver and driven sections together, and (2)triggering from the first drop in pressure on the gage located in the water-filled section nearest to the diaphragm.

In addition to the experiments with all water in the driver section at the time of rupture, some shots, not included in the scope of this paper, were

run with varying amounts of vapor initially present. In Fig. 3, condensing coils are shown which were used to measure the amount of liquid extracted in generating the vapor. The driver section was filled by a hand pump and subjected to a partial vacuum before heating began, to remove dissolved air from the water.

A close-up view of the test section is shown in Fig. 4. The method of mounting the glass diaphragms and the glass porthole windows to prevent leakage, or breakage from clamping pressures, which was critical in these experiments, is depicted in this figure.

RESULTS OBTAINED

Having described the essential features of the experimental apparatus, a brief discussion is now given of some of the results obtained.

First, typical data, representing the type of features observed on the records of pressure in the water-filled section, are given. These are followed by similar information for the air-filled section.

Tracings of the pressure-time history at the closed end of the water-filled section are shown in Fig. 5. These represent data from different shots at the same gage location, where different temperatures (as noted) were used on each shot. In each case the plateau on the left represents the initial value of water pressure prior to rupture of the diaphragm, or more specifically in the case of these records, the plateau at the left represents the pressure level in the water prior to arrival of the decompression wave at the pertinent gage location. At the extreme right of each record there is another pressure plateau which represents the magnitude of the equilibrium saturated pressure value. This saturation pressure level of course, increases with temperature as indicated in Fig. 2. Between the two pressure plateaus there is a very sudden drop in pressure from the initial value to approximately zero pressure for a very short period of time. The pressure then rises toward the level of equilibrium saturation pressure, with some overshoot, before leveling-off at the saturation level of pressure.

Apparently the fluid passes through non-equilibrium, or metastable, states in being decompressed from the initial pressure value to the final equilibrium-saturation value. The duration of this metastable period decreases with elevated temperature for the two records displayed in Fig. 5. The time scale is 1/2 millisecond per division yielding a total time-of-observation of 5 milliseconds for each trace. The pressure scales are respectively 220 psi per cm. division (or 880 psi total for the left trace) and 250 psi per cm. division (or 1000 psi total) for the right trace. The existance of the metastable period indicates that some time is required for the vaporization process to take place. The data indicated that this time can be as high as one millisecond at 400°F and is generally less than 1/2 millisecond at temperatures of 500°F or higher. The decrease in the time required for vaporization to occur is probably associated with the decrease in surface film energy of water with increased temperature, or what is probably equivalent, to the decreased heat-of-vaporization at higher temperatures.

AIR PRESSURE RECORDS

As pointed out earlier, one of the key items of information sought in connection with the experimental program conducted at IITRI, and covered by this paper, is the type of air shock which can be generated by the motion of the water (or vapor)-to-air contact surface. The records obtained from the pressure gages which were mounted in the air-filled section furnished excellent information regarding the air shock development and the motion of the vapor-to-air contact surface.

All of the pressure histories tended to have the same general features. This consisted of: (1) an initial jump in pressure caused by the arrival of the first air shock followed by, (2) a second jump in pressure caused by the passage of the reflected wave returning to the gage position from the closed end of the driver tube. After arrival of this reflected shock the pressure would rise gradually to the equilibrium value.

The manner in which pressure increased to the equilibrium level was influenced by the very complex flow and multi-reflections of various wave fronts, as well as arrival of the vapor itself at the gage location. Primary interest in these records was limited to the time at which the first reflection of the shock arrived at the gage location. Thus, the details of the build-up of pressure to the equilibrium value was not of interest here.

The records from the various gage locations in the air-filled section were quite similar to each other and showed very little qualitative difference from shot to shot, as both temperature and pressure of the driver fluid were varied. As was expected, the time-of-arrival of the wavefront at any given gage location depended on the distance of the gage from the diaphragm and yielded wave velocity information consistent with the magnitudes of the over-pressures observed. Typical pressure records obtained from the gage located one foot from the closed end of the air-filled section are shown in Fig. 6. The arrival of the initial shock, the (first) reflected shock, and the beginning of the buildup toward equilibrium pressure are evident on these records.

The magnitudes of the pressure, both initial and reflected, were plotted as ordinates with initial driver water temperature as the abscissa. Simple empirical variations of the shock pressure magnitudes, as functions of temperature were derived. These are shown in Fig. 7. Initial shock pressures ranged from a low of around 7 psi at a temperature of about 300°F, to a value in excess of 60 psi at the high end of the temperature range (i. e., at about 600°F). The reflected pressures varied from around 15 psi for 300°F driver water to over 200 psi for 600°F driver water. The relationship between the measured reflected pressures and the initial shock pressures checked very well with the calculated values of reflected pressure based upon the equation:

$$p_r / p_i = (6 + 8\xi)/(6 + \xi)$$

where, ξ is the ratio of absolute pressures across the initial shock front.

These results are for a one-dimensional flow. They therefore, represent upper limits of the shock pressures that can be expected if the air-filled section is of larger diameter than the water-filled section, where the initial air shock must expand after being formed, and the contact surface must also expand as it advances. Fig. 6 and 7 were used to construct a wave diagram which represents the over-all wave motion as a function of time along the entire length of the shock tube. The wave diagram is illustrated in Fig. 8.

The schematic wave diagram of Fig. 8 was constructed using time-of-arrival data, and observing the magnitudes to which pressure rose, or fell. The main waves to be considered in the air are: (1) that caused by the liquid expansion (which is a very weak shock), (2) the stronger magnitude shock front caused by the vaporization of the water, and (3) the first reflection of this vaporization shock from the closed end of the tube. The first of these waves (that due to the liquid expansion) was usually less than 0.5 psi. The magnitudes of the second two waves in the air, i. e., the vaporization shock, p_i, and the first reflected air shock, p_r, are much higher. These magnitudes are, as already stated, displayed in Fig. 7 as functions of the initial temperature of the driver water.

In the water, the main waves of interest are: (1) the first expansion wave which consists of a sudden drop in pressure, and (2) the vaporization wave which is a rise in pressure to the saturation value. After this, no other clearly identifiable or important waves can be observed in the water. Once the fluid has vaporized throughout the length of the driver tube, it is filled with a mixture of liquid and vapor which attenuates waves very effectively. This tends to reduce the damage potential of any water hammer effect (which would be observable in cold water).

HIGH SPEED PHOTOGRAPHY

Now, a brief discussion of some of the high speed film results can be given. The aim of the high speed photography was to provide insight into visualization of the flow regimes present. A major problem in describing the nature of two-phase flow, where there can be a mass transfer between the liquid and vapor state, is that of determining both the relative amounts of liquid and vapor present and the manner in which they are mixed with each other.

The layout of the camera and light source, relative to the test section porthole windows, is shown in Fig. 9. The orientation of the camera relative to the shock tube illustrated in this figure is useful in connection with Fig. 10, which shows three individual frames of the high speed film obtained.

In Fig. 10, in the first of the three frames (which is at the top of the figure) no vapor can be seen in the flow field. The absence of vapor is not immediately obvious from inspection of this frame alone but when it was compared to the several frames preceding it, it was evident that all frames are identical, and therefore it is concluded that no vapor has yet been formed. In the top frame, the variations in the light intensity are due to

reflection of the light (which entered the tube at the top of the test section) from the wall of the circular tube. The face of the flush-mounted thermocouple set in the wall of the shock tube is in clear view of the camera.

In the second frame of Fig. 10, which is the first frame on the roll of film differing in appearance from all those preceding it, a region of vapor appears in the center of the frame and three or four much smaller regions appear on the face of the thermocouple. In the third frame of Fig. 10, the vapor region is seen to be larger than the previous frame, and a cloud of vapor appears to be moving very slowly to the right toward the freshly broken diaphragm. On subsequent frames of this film a motion to the right continued as more vapor was formed in the field of view and finally a frothy mixture of liquid and vapor filled the entire field of view.

One important conclusion concerning the formation of vapor near the orifice can be drawn from films of the type illustrated in Fig. 10. In attempting to predict the mass-rate-of-flow through an orifice under transient circumstances similar to those considered in our experiments, it is important to determine whether there is (1) pure liquid flowing through the orifice, or (2) whether a mixture of vapor and liquid flows with partial choking of the flow. The possibility of pure liquid flow to the orifice with all vapor formation occurring further back in the driven section, and no vapor being emitted until all liquid is exhausted from the vessel, must be considered; this case would yield a higher mass-rate-of-flow than the mixed vapor-liquid condition.

The film shown in Fig. 10 was run at 3000 feet per second. Therefore, the time of observation represented in Fig. 10 is approximately 1 millisecond. The initial temperature-pressure conditions for this experiment were 350°F and 1000 psi. On other shots at higher temperatures vapor formed more rapidly and the field of view became filled with a frothy mixture very quickly. Although the onset of vaporization was observable at higher temperatures, the frames presented in Fig. 10 portray the process somewhat better.

The timing of the photography required that the camera be started and allowed to get up to speed by the time that the diaphragm be broken by the pellet. Since the travel time of the pellet from the firing of the gun until rupture of the glass diaphragm varied somewhat from shot to shot, the camera had to be at the proper speeds for a period of time somewhat longer in duration than that actually desired for observation. There was also some variation in the curve of intensity versus time for the photo lamp used. However, the photo lamps had a rated duration of 1.7^{5} seconds, while only a few milliseconds were actually required for observation of the vaporization process. With this amount of overlap the flood lamps could be safely turned on a short time (of the order of about 100 milliseconds) earlier than the diaphragm was expected to break. The time line describing the synchronization of the various events is shown in Fig. 11.

SUMMARY AND CONCLUSIONS

The experiments described in this paper have provided useful information on the behavior of a water-to-air shock tube in the range of temperatures up to about 600°F. The magnitude and shape of the air shock generated in a one-dimensional expansion of the water has been determined and the over-all wave diagram which represents the process, both in the decompressing water and in the compressed air. has been obtained.

The overpressure of the air shock has been observed to depend primarily on the initial temperature of the water, and be almost completely independent of the initial water pressure. The only relation to initial pressure in the water stems from the initial pressure required to keep the driver fluid in the liquid state. This of course is related to the initial temperature of the water and so a certain minimum pressure of the driver water is indirectly associated with any given level of air shock overpressure. But overpressurization of the driver water above this minimum required level does not affect the magnitude of the air shock pressure.

Although not included in this paper, additional experiments have been conducted using a driver section which was filled with a mixture of liquid water and water vapor, stratified so that either the vapor or the liquid was adjacent to the glass diaphragm on a given shot. Other tests have been run using larger-diameter air-filled sections with a smaller-diameter water-filled section. Experiments of this type are still in progress and all results have not yet been fully analysed. In the future when the analysis of these other tests is completed, it will represent an interesting and important extension of the results reported in this paper.

REFERENCES

(1) Brown, E.A., Experiments on the Explosive Decompression of Water, Armour Research Foundation (now named IIT Research Institute) ARF 4132-9, Nov. 1959

(2) Zaker, T. A., Studies of Reactor Containment-Summary Report No. 3 Armour Research Foundation, ARF 4132-14, August 1960.

(3) Zaker, T. A., Studies of Reactor Containment-Summary Report No. 2 Armour Research Foundation, ARF 4132-13, February, 1960.

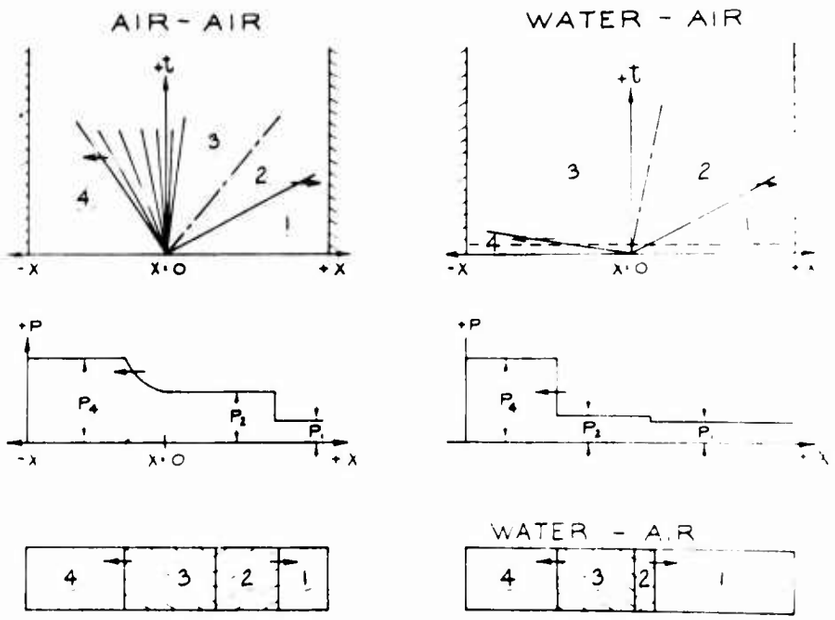


FIG. 1 COMPARISON OF AIR-DRIVEN AND WATER-DRIVEN SHOCK TUBES

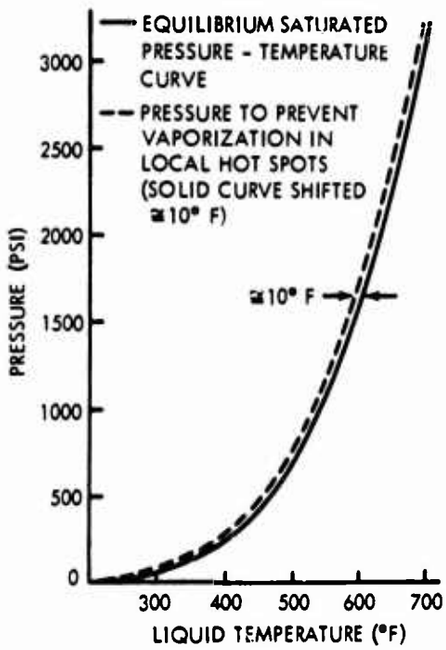


FIG. 2 PRESSURE REQUIRED TO PREVENT VAPORIZATION OF DRIVER WATER

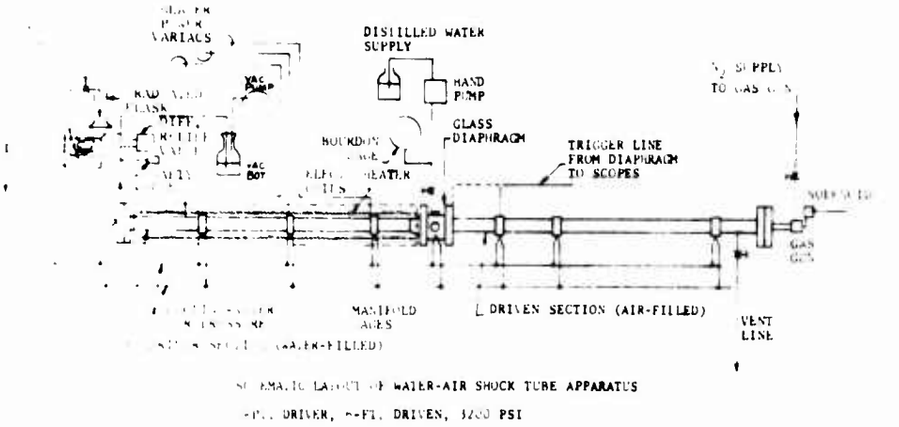


FIG. 3 SCHEMATIC LAYOUT OF WATER-AIR SHOCK TUBE

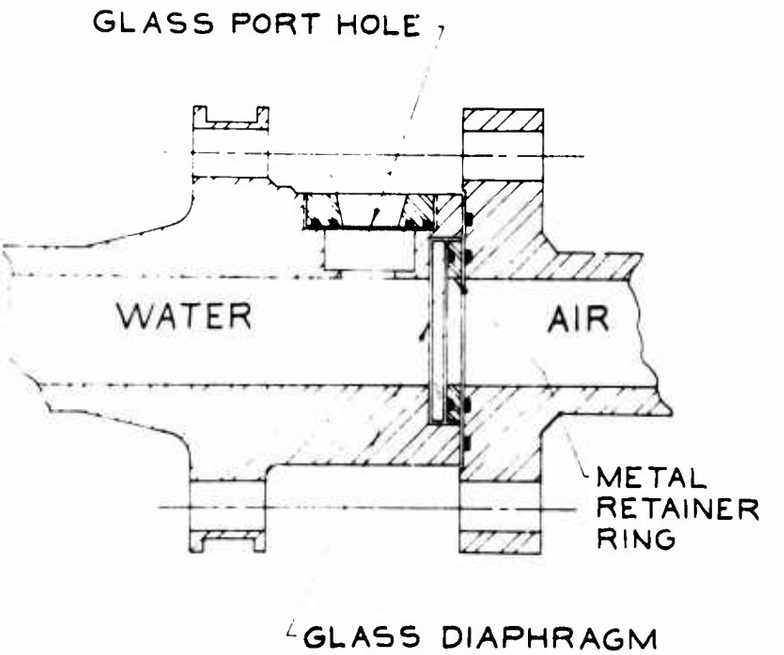


FIG. 4 GEOMETRY OF DIAPHRAGM MOUNT

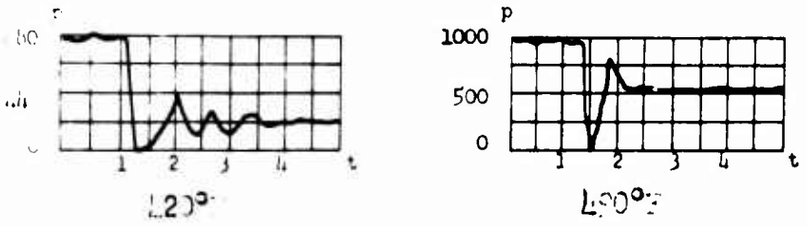


FIG. 5 TYPICAL PRESSURE-TIME RECORDS OF GAGES IN WATER

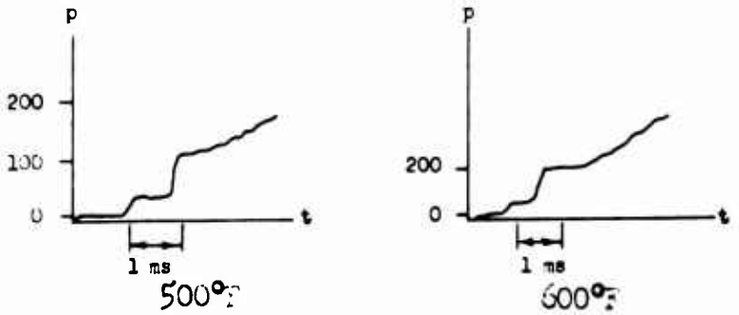


FIG. 6 TYPICAL PRESSURE-TIME RECORDS OF GAGES IN AIR

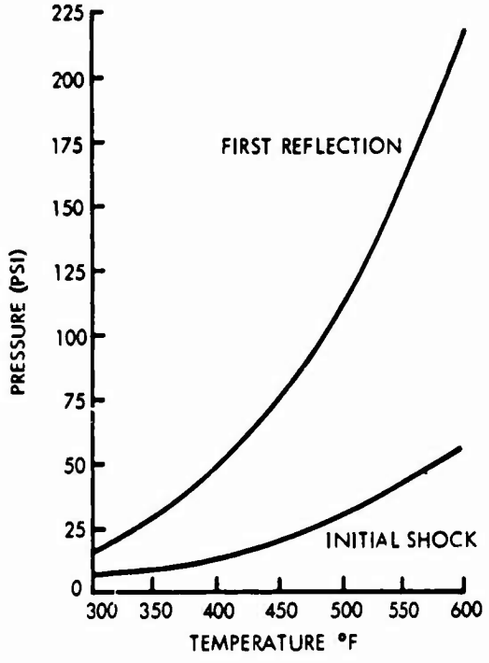


FIG. 7 MEASURED AIR SHOCK PRESSURE VERSUS INITIAL WATER TEMPERATURE

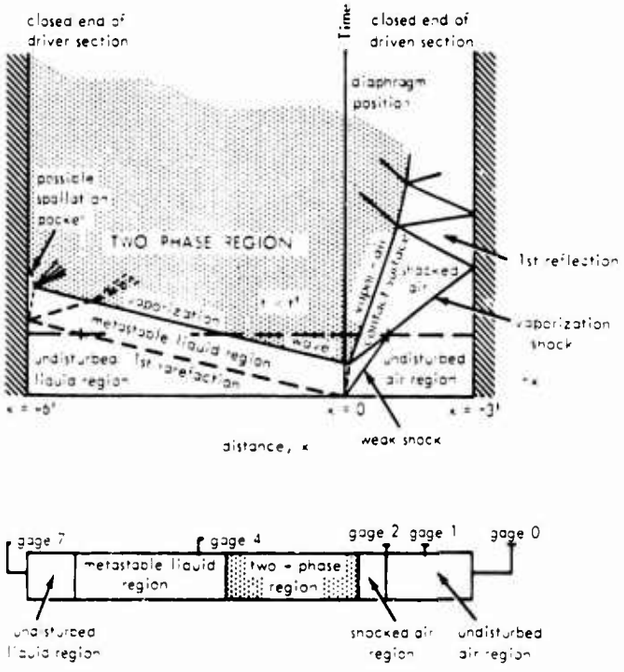


FIG. 8 WAVE DIAGRAM FOR WATER-DRIVEN SHOCK TUBE WITH VAPORIZATION

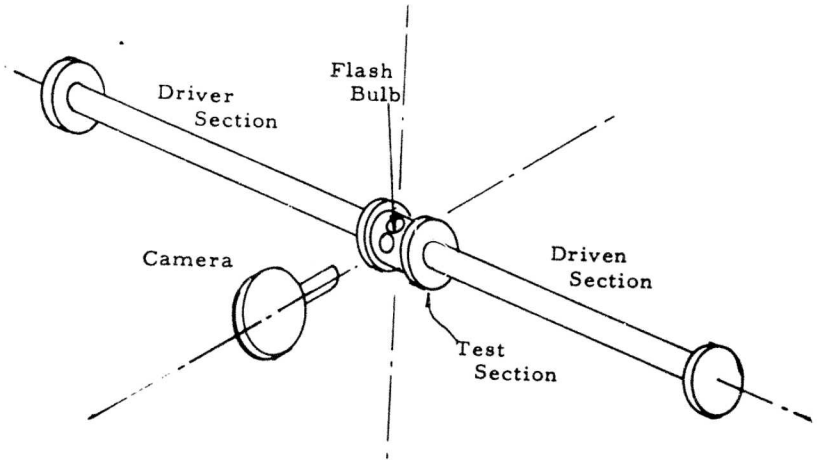


FIG. 9 ORIENTATION OF CAMERA AND SHOCK TUBE

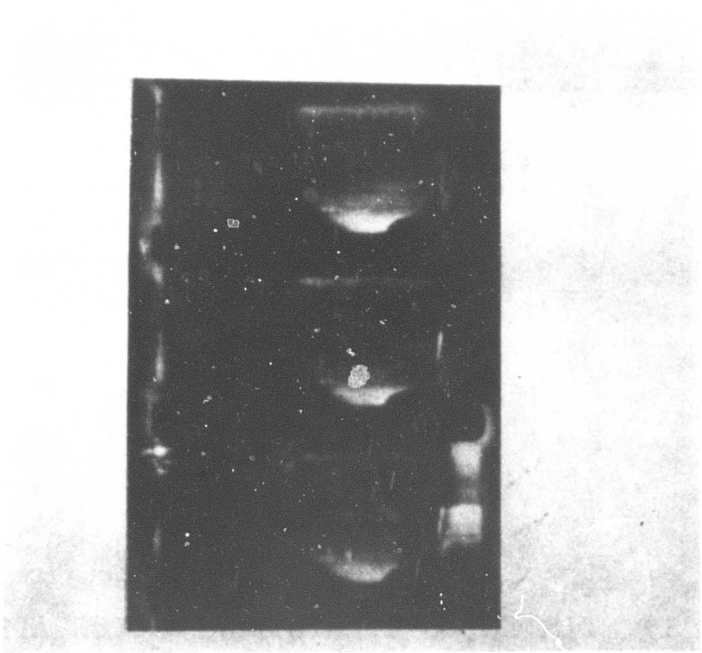


FIG. 10 PHOTOGRAPHS OF VAPOR FORMATION

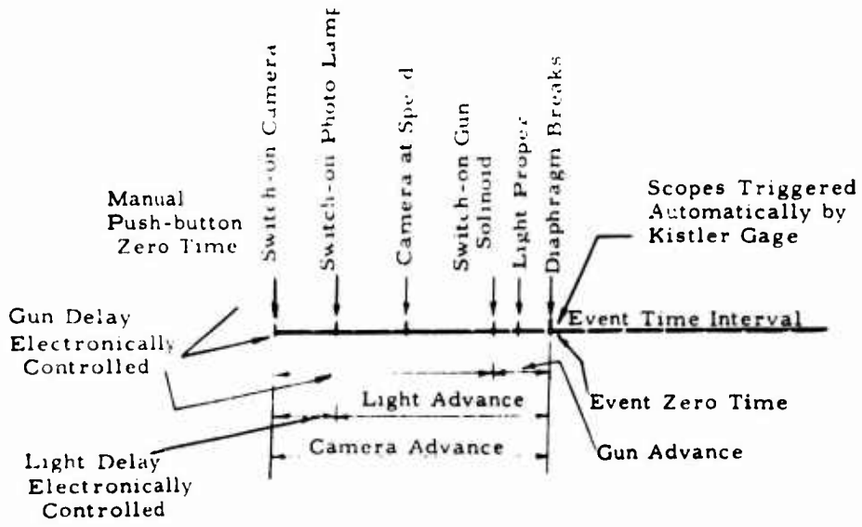


FIG. 11 TIMING OF EVENTS FOR PHOTOGRAPHY

PRODUCTION OF CARBON PLASMAS*

R. W. Rutowski, D. Weimer,** and W. J. Marlow
Lockheed Missiles and Space Company
Palo Alto, California

INTRODUCTION

Experimental techniques for producing dense plasmas utilizing capacitively stored energy have been under investigation at the Lockheed Research Laboratories for some time. The most recent technique to evolve from this program is a method for the production of a dense carbon plasma in a shock-tube-like configuration. Earlier techniques involved a jet-like flow of electrode material ejected from an arc chamber into a large evacuated test chamber. In the shock-tube-like configuration the discharge is directed into a confined geometry, similar in nature to the driven section of a shock tube. The arc chamber itself has undergone a continued development in search of materials and of a design which could endure the extreme temperatures and stress levels generated by the discharge. In the present design the electrode material is carbon. The carbon vaporizes during the discharge and flows into the test section as a dense carbon plasma. This flow is reflected from the end wall of the test chamber producing a reflected shock and a stagnation region behind the reflected shock. It is the carbon plasma in this reflected stagnation region which is of principal interest. The experimental technique, facility, and method of obtaining the plasma properties are described in the following two sections.

EXPERIMENTAL TECHNIQUES

The present facility consists of an arc chamber analogous to a shock tube driver and a test chamber analogous to a shock tube driven section. Both sections are of the same diameter (2.5 cm) and without the usual separating diaphragm. This configuration is shown schematically in Fig. 1.

*Work supported by Air Force Flight Dynamics Laboratory
**Present address: Ohio Northern University, Ada, Ohio

The electrode material is carbon, the inner insulating material is aluminum oxide (Al_2O_3) with an outer sleeve of teflon. A discharge is produced between the carbon electrodes from a capacitor bank storing 120,000 joules at 7000 volts. The discharge is initiated by introducing a low-pressure inert trigger gas into the arc chamber, typically argon at 100 microns. The discharge produces a shock wave in the trigger gas followed by a flow of material from the carbon electrodes. The initial flow problem in the low-density trigger gas is ignored and the high-density carbon plasma flow is treated as if it were the flow behind a shock front. The carbon plasma flows through a pyrex glass observation section into a stainless steel test chamber, impinging on the end wall to produce a reflected shock and a stagnation region behind the reflected shock.

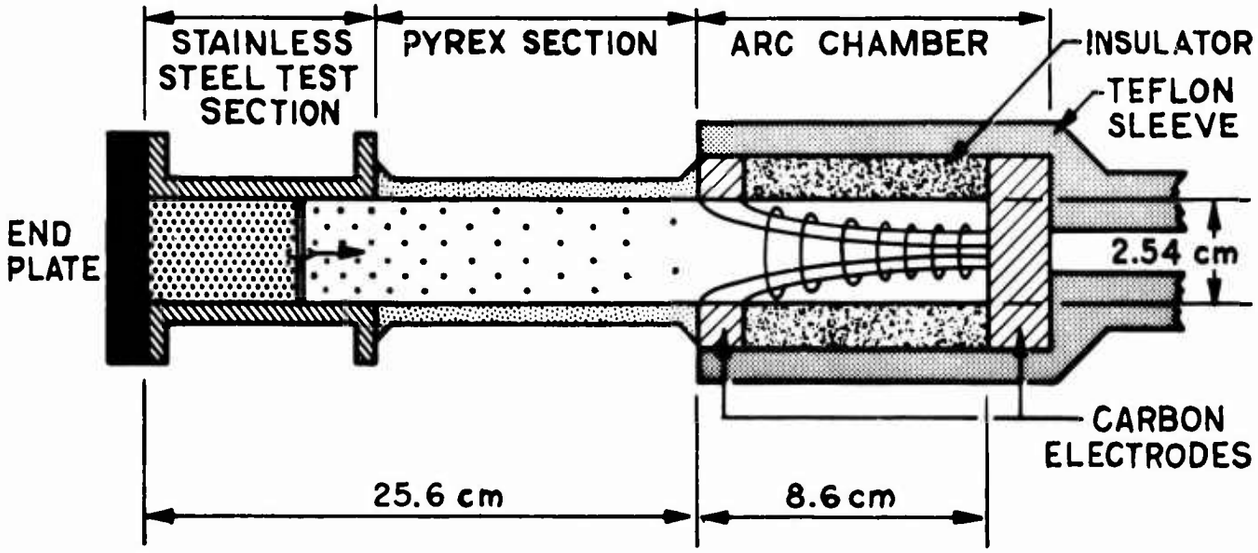


Fig. 1 Schematic view of the shock-tube-like facility for the production of a carbon plasma

Of the original energy stored in the capacitor bank, approximately 45% or 54,000 joules is delivered to the arc chamber. This is determined by measuring the current to and the voltage across the arc. The total energy delivered is then obtained from the integral $\int_0^\infty e \cdot i \cdot dt$. The remaining energy (55%) is dissipated in the bus bars leading to (and from) the arc chamber. Of the energy delivered to the arc chamber approximately 46% (25,000 joules) is associated with the flowing plasma. This is obtained from the expression $\rho_2 [h_2 + \frac{1}{2}(u_2^2)](\pi r^2 u_2 \Delta t)$. The first two factors represent the energy density of the slug of plasma ejected from the arc chamber while the last factor is its volume, where r is the radius of the shock tube and Δt the half width of the power pulse delivered to the arc chamber. The remaining 54% of

the power delivered to the arc chamber is presumably lost in leadin and contact resistance. A consistency check can be made by using the measured properties of the flowing plasma and calculating the Joule heating in the arc chamber. This results in an energy of 37,000 joules which compares favorably with the 25,000 joules associated with the flowing plasma. This calculation was made assuming electron-ion collisions dominate the conductivity of the plasma.

The current and voltage characteristics of the arc are shown in Fig. 2. The initial voltage is about one half of the capacitor bank voltage, indicating that the arc inductance and the bus bar inductance are approximately equal. The current scale is calibrated by integrating the current over time to give the total charge initially stored in the capacitor bank $\int_0^\infty i \cdot dt = CV_0$. The half width of the power curve is noted to be of the order of $\Delta t \sim 75$ μsec.

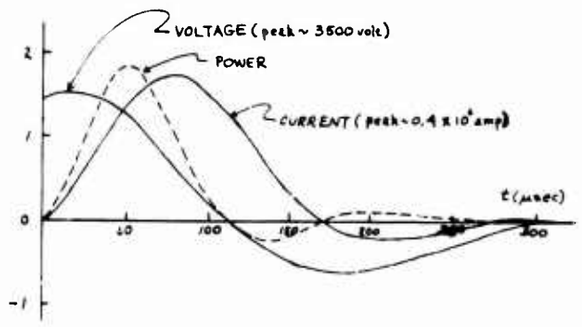


Fig. 2 Voltage, current and power traces for determining the energy delivered to the arc chamber

Fig. 3 shows a streak photograph of the flow from the arc chamber into the pyrex glass section. A nylon plug has been inserted into the pyrex tube so that the reflection of the incident plasma could be observed. This particular test was carried out at a much lower than usual initial energy (~5000 joules) so that the incident shock in the trigger gas would be visible and so the glass tube would not burst. At higher initial energies the radiation from the plasma is so intense that the relatively weak radiation from the initial shock can not expose the film. The reason for the double shock appearance of the shock wave has not yet been determined. The main portion of the flowing plasma seems to last some 50 to 60 μsec, in agreement with the half width of the power trace (Fig. 2). After the main pulse of energy has ended and there is no more material vaporized from the carbon electrodes, the reflected shock accelerates until it is finally reflected from the rear surface of the arc chamber.

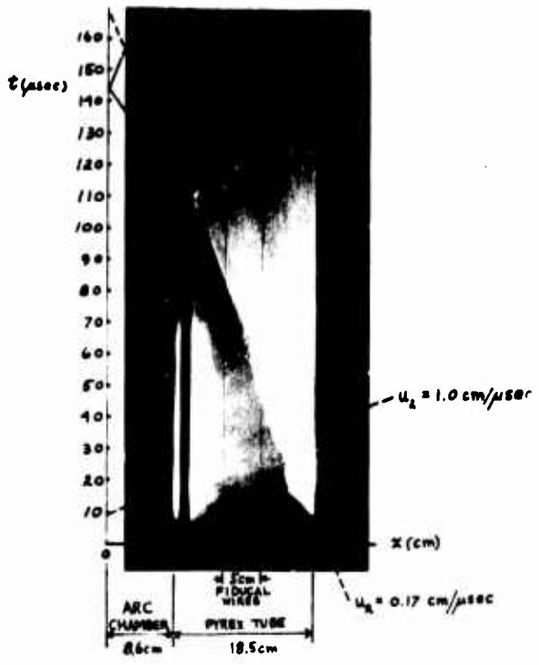


Fig. 3 Streak photograph of the flow of a carbon plasma from the arc chamber into the pyrex observation section

In Fig. 4 a streak photograph of a more typical higher energy experiment is shown. There first appears a relatively cold region behind the reflected shock in the argon trigger gas. This is followed by some nonradiating material from the electrodes which, upon striking the end wall, caused appreciable radiation. Next the hot carbon plasma flows into the reflected shock. At approximately 75 μsec the pyrex glass tube bursts. This relieves the pressure behind the reflected shock and terminates the experiment.

As will be shown in greater detail in the next section, the plasma properties can be estimated from a measurement of the initial flow velocity u_2, the reflected shock velocity u_R, and the reflected shock pressure P_5. A typical bar-gage pressure record is shown in Fig. 5. The pressure pulse as measured with a bar gauge located at the end wall of the stainless steel test chamber (Fig. 1) lasts for 50 to 100 μsec at a level of 700 to 1000 atm. A rarefaction wave, originating when the pyrex glass tube bursts, eventually reaches the end wall and terminates the high-pressure plasma.

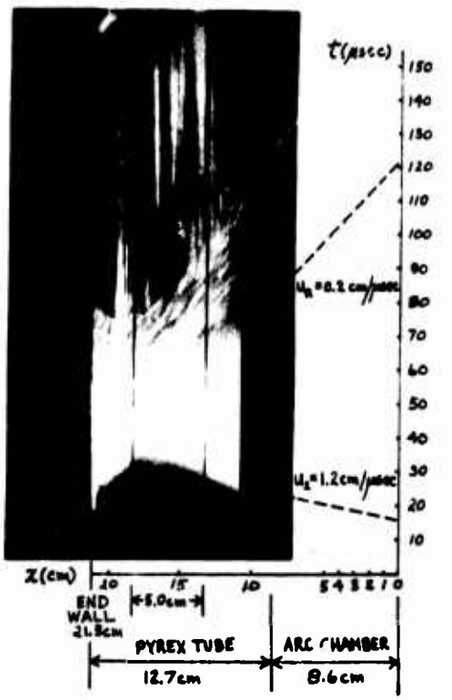


Fig. 4 Streak photograph of the flow for an initial energy of $\frac{1}{2}CV_o^2$ = 124,000 joule, T_5 = 26,000° K, $n_{e5} = 0.8 \times 10^{20}$ cm^{-3}, and P_5 = 800 atm.

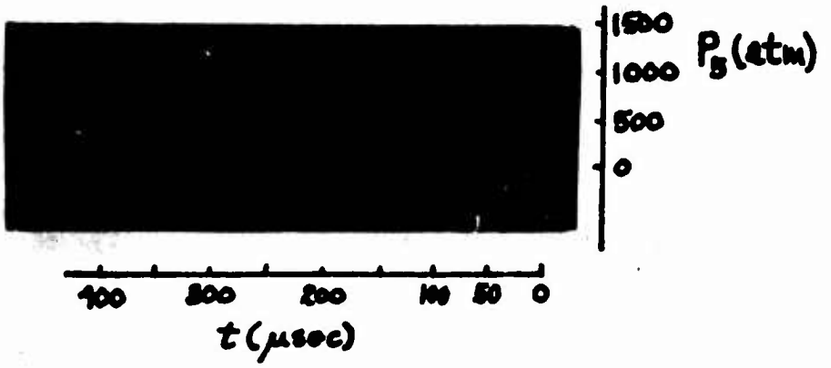


Fig. 5 Typical bar-gage pressure record

Independent temperature measurements of the plasma have been attempted with a radiometer at 5017A calibrated with a tungsten lamp. The measured temperatures are, however, appreciably below the temperature calculated from measurements of u_2, u_R, and P_5. Fig. 6 displays such a temperature measurement for the streak photograph of Fig. 4. The radiometer was focused at a point about 5 mm from the end wall. A peak temperature of approximately 16,000°K was obtained. This was followed by a plateau at about 10,000°K lasting approximately 75 μsec. A number of attempts were made to measure the plasma temperature using various observation points and geometries. None of these attempts produced temperature much over 15,000°K. Presumably these low temperature measurements are due to a cold, absorbing layer between the plasma and the probe which substantially reduces the emissivity of the plasma and subsequently the measured brightness temperature.

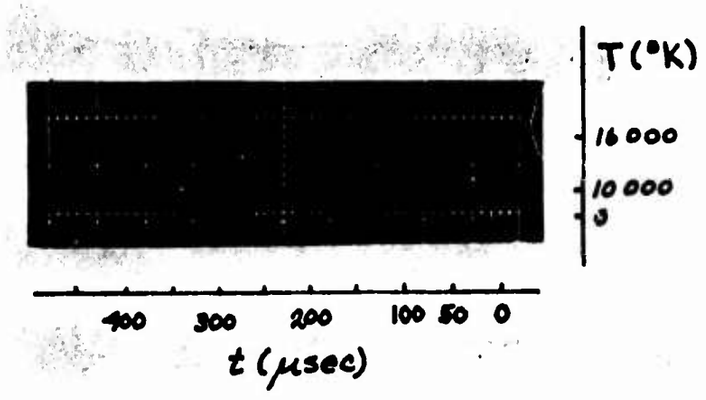


Fig. 6 Brightness temperature measurements with a radiometer at 5017A focussed 5 mm from the end wall in Fig. 4

PLASMA CONDITIONS

In the conventional shock tube three measured parameters are sufficient to determine all incident and reflected shock conditions. These are usually taken as the shock speed, the initial pressure, and the initial temperature. The situation is similar in the present facility. The three measured parameters are the incident plasma velocity u_2, the reflected velocity u_R, and the reflected pressure P_5. Unfortunately, the reflected shock conditions are relatively insensitive to the incident flow conditions, so that errors in the measured reflected shock parameters can produce fairly large errors in the incident flow conditions. However, since it is the reflected shock plasma which is of primary interest, this drawback is not of paramount importance.

As mentioned earlier, approximate values of the temperature and electron density of the carbon plasma behind the reflected shock can be obtained by neglecting the incident shock phenomena in the tenuous trigger gas and treating the carbon plasma from the arc chamber as a gas behind a shock

with velocity u_2. This approximation becomes more realistic as the energy in the carbon plasma is increased. Then, from a measurement of the three appropriate parameters mentioned above, the temperature T_5, and electron density n_{e5} as well as all other conditions can be calculated. The calculation must further assume that the end wall material does not enter into the flow problem. This latter assumption is not true for highly ablative end wall materials. Radiative properties of the plasma are also neglected.

In order to readily understand this calculation it is instructive to calculate the reflected shock temperature and the temperature and pressure of the incident carbon plasma as a function of the measured parameters u_2, u_R, and P_5 for the case of an ideal gas with no ionization. Then,

$$T_5 = u_R (4u_2 + 3u_R)/5R \tag{1}$$

$$T_2 = (u_2 + u_R)(3u_R - u_2)/5R \tag{2}$$

$$P_2 = \frac{(3u_R - u_2)}{(4u_2 + 3u_R)} P_5 \tag{3}$$

Note that, for fixed u_R, T_5 is a linear function of u_2. It is, of course, independent of P_5 since ionization has been neglected. From the equation for T_2 and P_2 it follows that there is a restriction on the reflected shock velocities which are physically realizable. That is,

$$u_R > \frac{1}{3} u_2 \tag{4}$$

Now, if ionization is allowed for, but the neutral carbon gas, ion gas, and the electron gas are each treated as a perfect gas, the condition on u_R becomes

$$u_R > \frac{1}{3} u_2 \left[1 - \frac{2(\alpha_5 - \alpha_2)R\theta}{u_2^2}\right] \tag{5}$$

where α_5 and α_2 are the degrees of ionization for the reflected and incident plasmas, respectively, and θ is the ionization temperature for carbon vapor. The latter restriction admits a larger range of reflected velocity values in the neighborhood of $u_2 \sim 1$ cm/μsec. For very large values of u_2 it reverts to the ideal gas restriction, as it does for small values of u_2, since $\alpha_2 \to 0$. The critical reflected shock velocity is plotted in Fig. 7 for an ideal gas with and without ionization. Clearly, the typical experimental values $u_R \sim 0.2$ cm/μsec $u_2 \sim 1.0$ cm/μsec for $P_5 \sim 800$ atm are allowed when ionization is considered.

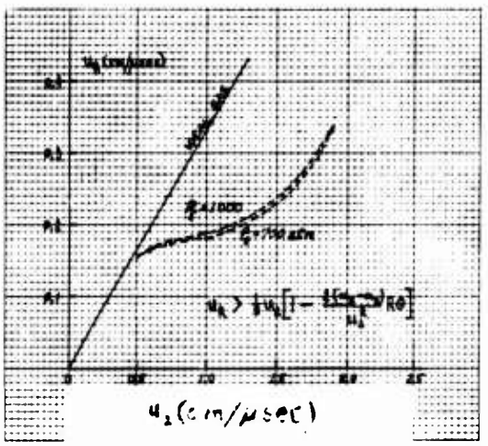


Fig. 7 Critical reflected shock velocities for an ideal gas with and without ionization

A code was developed for more accurate determinations of the plasma conditions from the measured parameters. The code considers real gas effects for the neutral carbon gas and the ion gas. Preliminary estimates of the plasma conditions indicated that second ionization would not be important at the pressures obtained in the reflected plasma. Most probably due to the restriction on the reflected shock velocity as mentioned above, there was only a limited range of values of u_2 where the code was able to find solutions. The most satisfying results from the code were the more realistic values of the incident plasma temperatures, which are very difficult to calculate by hand and, when done without real gas effects, are too low to account for the observed radiation from the flowing plasma. The results of the code for typical measured parameters are given in Table 1.

The Rosseland optical mean free paths given in Table 1 were estimated by a formula due to Raizer. The small values of these optical mean free paths provide the basis for the conclusion reached earlier that the plasma has difficulty in communicating with its surroundings because of an absorbing thermal or velocity boundary layer.

Table 1

TYPICAL PLASMA CONDITIONS

Measured Parameters

$u_2 \sim 1.2$ cm/sec $\quad u_R \sim 0.2$ cm/sec $\quad P_5 \sim 800$ atm

Calculated Parameters

$T_5 = 25{,}300°K \quad \alpha_5 = 0.43 \quad n_{e_5} = 0.7 \times 10^{20}$ cm^{-3}

$\rho_5 = 3.3 \times 10^{-3}$ gm/cm^3 $\quad n_{CI_5} = 0.9 \times 10^{20}$ cm^{-3} $\quad \lambda_{R_5} = 0.034$ cm

$T_2 = 9400°K \quad \alpha_2 = 0.01 \quad n_{e_2} = 2 \times 10^{17}$ cm^{-3}

$\rho_2 = 0.5 \times 10^{-3}$ gm/cm^3 $\quad n_{CI_2} = 2.3 \times 10^{19}$ cm^{-3} $\quad \lambda_{R_2} = 0.84$ cm

$P_2 = 30$ atm

SUMMARY

A device has been described which provides an inexpensive means of producing a relatively high temperature plasma at a high density level and with a life time amenable to study with present day techniques. Although the means used to generate the plasma leads to fairly nonuniform flow and a relatively high contamination level, a plasma with useful properties for many applications is generated. Work is continuing in the study of the properties of the plasma, with particular emphasis on its radiative properties, and in the investigation of plasma flow about, and ablation from, bodies placed in the flow.

BLANK PAGE

SHOCK TUBE TECHNIQUES FOR STUDIES OF HIGH TEMPERATURE GAS RADIANCE

J.S.Gruszczynski, W.R.Warren, Jr. and D.A.Rogers
General Electric Company
King of Prussia, Pennsylvania

1. INTRODUCTION

The problem of radiative heat transfer to the surface of a space vehicle during the entry into a planetary atmosphere gained in importance with the establishment of national programs for lunar exploration and missions to the near planets. The entry velocities for some of these missions will be higher than the earth orbital speed and may reach levels as high as 50,000 ft/sec. At these velocities the flow in the stagnation region of a blunt entry vehicle behind the detached bow shock wave will reach high pressure and temperature levels. Such gas can be expected to emit large amounts of radiant energy characteristic of the chemical species present in the flow. As an example we show in Fig. 1 an altitude-velocity map for earth re-entry on which lines of constant stagnation density, temperature and ion mole fraction (assuming equilibrium thermochemistry) are drawn. Two typical trajectories, one for re-entry after a lunar mission and a second for re-entry from a flight to the planet Mars, are also shown. Stagnation temperatures of more than 11,000°K for the former and more than 14,000°K for the latter will be observed. Higher entry velocities will of course produce more severe stagnation conditions.

The radiance of high temperature gases is a complex phenomena and, although the basic fundamentals have been studied theoretically in some depth, its prediction depends to a considerable degree on approximating assumptions. In considering the contribution of radiative transport processes to the heat transfer experienced by a space vehicle, a distinction can be made between the equilibrium radiation originating in the shock-processed gas, which after passing through the bow wave has relaxed to its thermochemical equilibrium, and the non-equilibrium radiation, which is emitted from the shock front in which the imparted energy has not been distributed among the various degrees of freedom. Non-equilibrium radiation is relatively more pronounced at high altitudes

where, because of the low collision rate, long flow times are necessary for the gas to reach its equilibrium state. Under these circumstances gas molecules will acquire high translational energies and can become thermally excited at effective temperatures higher than the equilibrium value. The emission from such a shock layer is even less well understood than the emission from high temperature gas in thermal equilibrium. It is natural, therefore, to seek experimental techniques for determining the actual radiance from which the radiant heat transfer to the surface of the vehicle can be deduced.

For these purposes the shock tube provides a means for obtaining a sample of high temperature gas representing in composition the atmosphere of interest and simulating the thermodynamic state corresponding to important entry conditions.

Simulation of the conditions corresponding to the hypervelocity environment requires incident shock velocities as shown in Fig. 1. For instance, the thermodynamic state of the gas at the stagnation point of a blunt model in the shock tube flow behind an incident shock wave moving at 29,000 ft/sec is equivalent to flight stagnation conditions at a speed of 40,000 ft/sec.

Producing such high shock velocities is not in itself sufficient since it must be demonstrated that the properties of the gas sample are uniform and that the flow is of sufficient duration to allow the formation of quasi-steady flow around the model and to be compatible with the response time of the instrumentation.

The purpose of this paper is to outline experimental techniques used for studies of equilibrium and non-equilibrium radiative properties of high temperature gases produced in a shock tube. Because of the relatively high temperatures of interest, the UV contribution, extending into the vacuum UV region of the spectrum, will constitute a large portion of the total radiation. For this reason a new technique of measuring this radiation has been developed and will be described in detail.

2. EXPERIMENTAL FACILITY

In the study of radiative properties of high temperature gases representing anticipated planetary atmospheres one is confronted with the problem of producing uniform samples of the gas at the appropriate temperature and pressure for a sufficient duration consistent with the response characteristics of the radiation sensors. In the case of model measurements this must be long enough to allow the formation of steady flow around the model. The simulation of conditions corresponding to hypervelocity entry has become possible with the development of the arc-heated shock tube (1). Such an experimental facility, employed at the GE Space Sciences Laboratory, is shown in Fig. 2. It is essentially a conventional shock tube in which the driver gas remains isolated by means of a metal diaphragm from the test gas in the low pressure driven

section until the heating process of the light gas in the driver - an electrical discharge of capacitor stored energy - is completed. The design features and mode of operation has been discussed in Ref. (2). The driver section has a 6-inch internal diameter and is 31.5 ft. long. A capacitor bank rated at 304,000 joules supplies the energy to the driver. A second capacitor bank with a total stored energy of 768,000 joules can be used when it is desired to obtain high shock velocities at a relatively high initial pressure of the test gas in the driven tube.

With the larger capacitor bank a driver energy density of 550 joules/cm^3 produced incident shock wave velocities in excess of 44,000 ft/sec. In this case the state of the gas in the stagnation region of a blunt model corresponds approximately to stagnation conditions at 60,000 ft/sec. flight velocity. The achievement of such high shock velocities is by itself of little use unless it is followed by a reasonable time of uniform flow of the test gas. Using several auxiliary measurements the duration of the uniform flow behind the incident shock wave moving with 44,000 ft/sec velocity was found to be about 10 μsec. with the end of the test time sharply defined. At lower shock velocities the test time is correspondingly longer.

To assure full validity of the data during each experimental run, the test time is precisely determined by the methods described in Ref. (3). Fig. 3 shows a photograph of the test section of the driven tube together with some of the instrumentation used in the radiation studies;also shown are several instrumentation techniques employed in the determination of shock tube performance and test gas flow quality.

3. SHOCK TUBE PERFORMANCE

Signals from a series of photomultipliers located at various stations along the shock tube, as shown in Fig. 4, are used to measure the shock wave velocity as a function of distance from the diaphragm. From the knowledge of the shock wave velocity and the initial conditions of the gas in the driven tube (initial shock tube pressure is measured with a McLeod gage) all other equilibrium properties such as densities and temperatures behind the incident shock wave and at the stagnation point of the blunt model can be deduced.

The most useful techniques for measuring test time and assessing the quality of the test flow are dependent on observing the radiant emission from the gas behind the incident shock wave and from the flow in the stagnation region of the model. Several techniques of this type are indicated in Fig. 4. Since the emission is a strong function of temperature, the temporal quality of the flow and its duration can be deduced from the steadiness of the emitted radiation and the spatial quality from the image converter photographs.

4. TOTAL RADIATION MEASUREMENTS

The study of high temperature gas radiation requires a measuring technique which is able to measure total radiance, integrated over the whole wavelength spectrum. All photo-emissive devices, such as photomultipliers and phototubes, are sensitive only over a limited range of wavelength. A thin film resistance thermometer gage (4) of the type widely used in shock tubes and shock tunnels for measuring convective heat transfer offers suitable sensitivity and fast response. However, a difficulty arises in the determination of its surface reflectivity which is a function of the surface conditions, the wavelength of the incident radiation and the incident angle.

The gage selected (5) draws on the black body principle for its geometric shape as is shown schematically in Fig. 5. The gage is made in the form of a cylindrical body with the entrance slit set off-axis. The interior of the gage is coated with a thin film of platinum which serves as a fast response resistance thermometer. The radiant energy which enters through the slit is partially absorbed by the platinum film and partially reflected. Because of the chosen geometry the photons will undergo several reflections before they escape back through the entrance slit. However, due to a finite absorption on each incidence, less than 5% of the energy entering the cavity gage will escape if the absorptivity of the platinum film is above 30%. The fast thermal response of the gage is dependent on the film thickness which should be made small relative to the characteristic thermal diffusion depth of the film material. At the same time the film must be made opaque to the incident radiation since its function is to absorb the energy.

The thin film resistance thermometer, the sensor of the cavity gage, is operated at essentially constant current in a circuit also shown in Fig. 5. Each lead is connected through a 1500 ohm resistor to a dry cell battery pack. The gage leads are connected to the inputs of a differential amplifier in order to reject noise pick-up in the gage circuit.

A photograph of the complete gage is shown in Fig. 6. The gage is composed of four quartz cylindrical elements and circular end pieces. All internal surfaces are coated with the thin film, and each section of the gage is connected in a series circuit.

The temperature and density level of the gas under study can cause a wide variation in the spectral concentration of the emitted radiation. In Fig. 7 are shown two theoretical spectral distributions of air radiance, one for air at 7000°K and 1 atm (6) and the other at 14000°K and the same pressure (7). The spectrum at the lower temperature contains mostly contributions from molecular bands in the UV, visible and IR range. Very little emission is expected below 1800Å due to the limitations of the black body radiation. At the higher temperature, however, free-bound, free-free and bound-bound transitions dominate the emission. It can also be noticed that most of the radiation comes from the vacuum UV

part of the spectrum.

All materials normally used for windows in shock tubes have a distinct short wavelength transmission cut-off. This cut-off, as shown in Fig. 7 occurs at wavelengths longer than much of the line and continuum radiation of interest in high temperature gas radiance studies.

Two experimental configurations of the cavity gage system with windows were employed. In the first configuration, the measurements are made of radiation emitted from gas processed by the incident shock wave. This arrangement is shown in Fig. 8. The gage was located behind a set of collimating slits viewing only a narrow layer of the gas across the shock tube. In all recent investigations a fused silica quartz window separated the gage from the radiating gas. Because of the limited temperatures and densities which can be produced in the incident shock flow at a given initial shock tube pressure with the available energy of the driver, the gas radiance at temperatures in the range of 12,000 - 16,000°K was measured using the stagnation region gas ahead of a hemispherical model as the test gas sample. This arrangement of the total radiation cavity gage inside the model is also shown in Fig. 8. A rectangular shaped window 0.1 in. by 0.5 in. and 1 mm thick was used at the stagnation point of the model. The gage itself is located away from the window with its entrance slit parallel to the window aperture. Thus, the gage senses only radiation from a region of the shock layer close to the axis of the model.

During initial operation of the gage, evidence of photoemission from the platinum film was observed. During tests in which the gage was evacuated to a pressure of approximately 3 microns, the photoelectric effect was strong enough to produce partial short-circuiting of the gage. A few runs were made with a glass window under the same flow conditions with no evidence of the photoelectric effect, indicating that the photons with energy corresponding to a wavelength smaller than 3500 Å are required to cause the photoemission. To eliminate this effect, the gage was filled with pure nitrogen at 1 atm. pressure. The presence of nitrogen gas reduced the mean free path of the electrons, causing a space charge to develop close to the surface of the gage which inhibited any further electron emission within a fraction of a microsecond. Nitrogen gas was chosen because of its large cross-section for collision with electrons. A typical trace obtained with a LiF window is shown in Fig. 9.

Use of pure N_2 is satisfactory behind sapphire and quartz windows. However, for studies of vacuum UV radiation, N_2 is not suitable, because of its photo-absorption characteristics. In this case the choice is limited to rare gases, with helium displaying the most desirable optical properties (see Fig. 7). The ability of the model gas to suppress the photoelectric effect was evaluated using a hemispherical model with a LiF window. As a first choice, argon at 2 atm pressure was used. A cavity gage signal obtained from this run is shown in the lower trace of

Fig. 9. The presence of a photoelectric effect which causes the signal to become negative for the duration of the test flow is evident. For comparison a trace of the cavity gage output with the model filled with pure nitrogen found previously to suppress the photoelectric effect is shown in the upper trace. The inability of argon to adequately reduce the electron emission can be explained by referring to Fig. 10 where electron collision cross-section of several gases is plotted as a function of electron velocity. Although argon and krypton display cross-sections for electrons comparable to nitrogen, with electron energy above 4 ev, both noble gases are practically transparent to electrons with energies in the vicinity of about 1 ev. This transparency, known as the Ramsauer-Townsend effect is typical of the heavier rare gases. A gas mixture with equal proportions of Kr, having large cross-sections for energetic electrons, and He, with a reasonable effectiveness for scattering slow electrons, was tried next in the model. A typical trace of the cavity gage response with the LiF window model is shown in Fig. 11. It can be seen that the photoelectric effect is absent and the signal trace is typical of a thin film thermometer response.

As previously mentioned, a windowless gage system is required for sensing vacuum UV radiation. Since a gas mixture within the model is necessary to counteract the photoelectric effect, a problem arises of how to contain this gas inside the model prior to the arrival of the incident shock wave and prevent it from mixing with the test gas. The results obtained earlier indicated that the gas density inside the model must be considerably higher than the shock tube initial pressure for an effective restriction of the movement of photoelectrons. A windowless model as shown in Fig. 12 was therefore developed in which a stretched latex membrane separates the inside gas from the outside. The membrane bursts and uncovers the entrance slit when a pulse of current is passed through a .002 in. wire located along the rectangular entrance slit and in contact with the latex membrane. No combustion of the membrane takes place but the rapid heating weakens the latex to a point where it tears under its own internal stress. The process of the uncovering of the entrance slit of the model takes approximately 15 μ sec. Depending on the gage gas pressure, a delay of about 140 μ sec. between the current pulse and full opening of the slit was observed. This delay was found to be repeatable within $\pm$ 10 μ sec. By using a delayed trigger signal from an upstream station the full opening process can be scheduled to be completed approximately 10 μ sec. prior to the arrival of the incident shock wave at the model station. Analysis of the inflow process in the case when the internal pressure is very much lower than the stagnation pressure showed that an appreciable difficulty will exist in accounting properly for the absorption characteristics of the inflowing gas. If the internal pressure is set equal to the stagnation pressure this effect will ideally be eliminated.

At the instant when the latex membrane breaks, the gage gas issues through the entrance slit into the stationary gas in the shock tube. Since the breaking point of the membrane is timed to occur approximately

10 μsec. before the incident shock arrives at the model only a small amount of the gage gas is able to escape and its penetration is limited to only a few centimeters upstream of the model. This gas is subsequently swept downstream during the first 1-2 μ sec. after the incident shock arrives at the model which coincides with the time taken by the blunt body flow formation. Assuming that the interface between the test gas and the gage gas is stationary, the diffusion of the gases across it was estimated to be negligible during the time corresponding to the test gas flow (20-30 μsec). A typical oscilloscope trace of the gage signal obtained from the windowless model is shown in Fig. 12. In this case the interior of the model was filled with a mixture of equal parts of He and Kr.

Photographs of the shock layer ahead of the blunt model were obtained by means of an image converter camera. These are shown in Fig. 13, with the three consecutive frames taken 5 μ sec. apart. The lower traces in the same figure show the camera monitor and photomultiplier signals. The photomultiplier looks through a window in the sidewall of the shock tube and is focused just ahead of the model stagnation point. The first image converter camera frame was obtained during the flow formation as indicated by the camera monitor. The next two frames were taken during the steady flow corresponding to a uniform shock layer radiance and constant stand off distance. These photographs also indicate that a uniform flow was achieved within the expected time with the end of test gas flow clearly visible, and that the shape of the bow shock wave was not perturbed by the presence of the windowless slit at the stagnation point of the model.

Experimental data obtained with the total radiation cavity gage behind LiF and quartz windows in a hemispherical model is shown in Fig. 14. A few data obtained with the windowless model are also included. These results indicate an important contribution to the total radiation from the vacuum UV region of the spectrum below the LiF window cut-off.

5. MEASUREMENTS OF NON-EQUILIBRIUM GAS RADIANCE

The non-equilibrium radiation can be measured by observing the passage of the incident shock. Since the extent of the non-equilibrium layer is extremely short, the required high spatial resolution of the radiation sensor precludes the use of the total radiation cavity gage. It was found that photomultipliers with their high sensitivity together with an appropriate dispersing optical system can satisfactorily be used in such a study, producing not only the non-equilibrium radiation data but also the spectral distribution of the equilibrium radiance.

Fig. 15 shows the general arrangement of the shock tube, the spectrophotometer and the optical system associated with the incident shock radiation studies. The measurements were made through a quartz window mounted in the sidewall of the tube at a station located at a distance of L/D = 51.5 from the diaphragm. A light trap in the form of a blackened cylindrical cavity was placed

directly opposite the observation window in order to eliminate the effects of internal shock tube reflections.

To measure spectral radiance, a Jarrell-Ash Co. f/6.3 plane grating spectrograph with a dispersion of approximately 40Å/mm was equipped with six photomultipliers mounted in the exit focal plane. Because of the size of the individual detectors, an arrangement as shown in Fig. 15 was necessary so that the radiation in adjacent spectral intervals could be measured simultaneously. A fibre optics package, with each bundle entrance aperture giving 200Å of spectral coverage or a total of 1000Å for the five channels, was used at wavelengths above 4000Å. Five 1P28 photomultipliers were located at the other end of the fibre bundles. For the ultraviolet region of the spectrum a quartz lens reimaged a 255Å wide section of the spectrum from the focal plane of the spectrophotometer directly on the photocathode of a 1P28 photomultiplier. The calibration of the complete optical system above 3200Å was made using a standard tungsten ribbon lamp which was calibrated by the Bureau of Standards. The calibration of the spectrophotometer at wavelengths below 3200Å was made with the use of a pyrometric carbon arc. The arc was assumed to emit as a grey body at a true temperature of 3800°, with an emissivity of 0.97 (8). A check of calibration at a wavelength at which the ribbon filament tungsten lamp could also be used showed good agreement between the two methods.

Typical traces obtained from two of the channels of the spectrophotometer are shown in Fig. 16. The spectral distribution of the integrated non-equilibrium radiation is shown in Fig. 17. In order to obtain the magnitude of the total non-equilibrium radiation it is necessary to integrate over the whole wavelength region.

6. CONCLUDING REMARKS

A method for measuring total emission from a high temperature gas that includes contributions in the vacuum UV region of the wavelength spectrum has been developed and is being employed in the study of air radiance. The total radiation cavity gage, which has been previously used behind windows in the model and shock tube sidewall, was found to be adaptable to a windowless model.

A technique for spectral measurements of equilibrium and non-equilibrium radiation from incident shock waves in the shock tube was described and its application demonstrated.

7. ACKNOWLEDGEMENTS

This work was supported by the Jet Propulsion Laboratory, NASA-Office of Advance Research and Technology and by the General Electric Contractors Independent Research Program. The authors wish to acknowledge the contribution of Mr. H. W. Bousman to the development of the windowless model, and Messrs. F.McMenamin and R.Emsley, who operated the facility.

8. REFERENCES

(1) Warren, W.R., Rogers, D.A., and Harris, C.J.; The Development of an Electrically Heated Shock Driven Test Facility; GE TIS R62SD37; also Proc. 2nd Symp. on Hyp. Tech., University of Denver, Denver, Colo., March 1962.

(2) Gruszczynski, J.S., Warren, W.R.,Jr., and Diaconis, N.S.; Laboratory Simulation of Hypervelocity Heat Transfer Problem During Planetary Entry; GE TIS R64SD73; also Proc. XVth International Astronautical Congress, Sept. 7-12, 1964, Warsaw, Poland.

(3) Gruszczynski, J.S. and Rogers, D.A.; Shock Tube Instrumentation Techniques for Study of Hypervelocity Entry Problems; GE TIS R64SD67; Sept., 1964.

(4) Vidal, R.J.; Model Instrumentation Techniques for Heat Transfer and Force Measurements in a Hypersonic Shock Tunnel; Cornell Aero. Lab. Report No. AD-917-A-1, Feb. 1956.

(5) Gruszczynski, J.S., Harris, C.J., Rogers, D.A. and Warren, W.R.; Fast Response Total Radiation Gage for Measurement of Radiant Emission From High Temperature Gas; GE TIS R63SD11, Jan. 1963.

(6) Nardone, M.C., Breene, R.G., Zeldin, S.S. and Riethof, T.R.; Radiance of Species in High Temperature Air; GE TIS R63SD3, June 1963.

(7) Biberman, L.M., Vorob'ev, V.S., Norman, G.E. and Iakubov, I.T.; Radiation Heating in Hypersonic Flow; Kosmich. Issled., Vol. 2, No. 3, pp 441-454, 1964.

(8) Null, M.R. and Lozier, W.W.; The Carbon Arc as Radiation Standard, Temperature, Its Measurement and Control in Science and Industry; Reinhold Publishing Co., New York 1962.

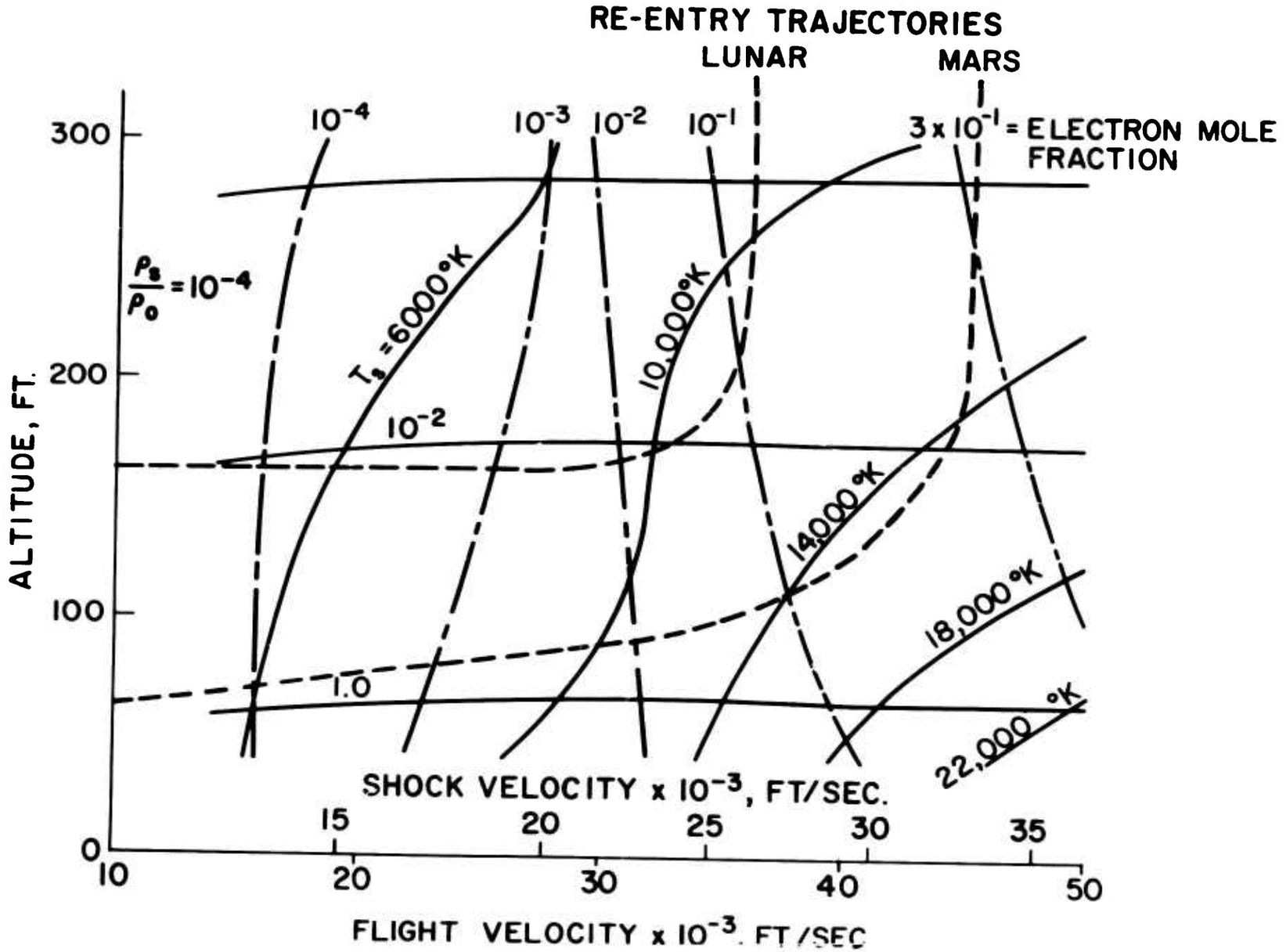


Figure 1 Blunt Body Stagnation Point Equilibrium Gas Properties for Entry into Earth Atmosphere.

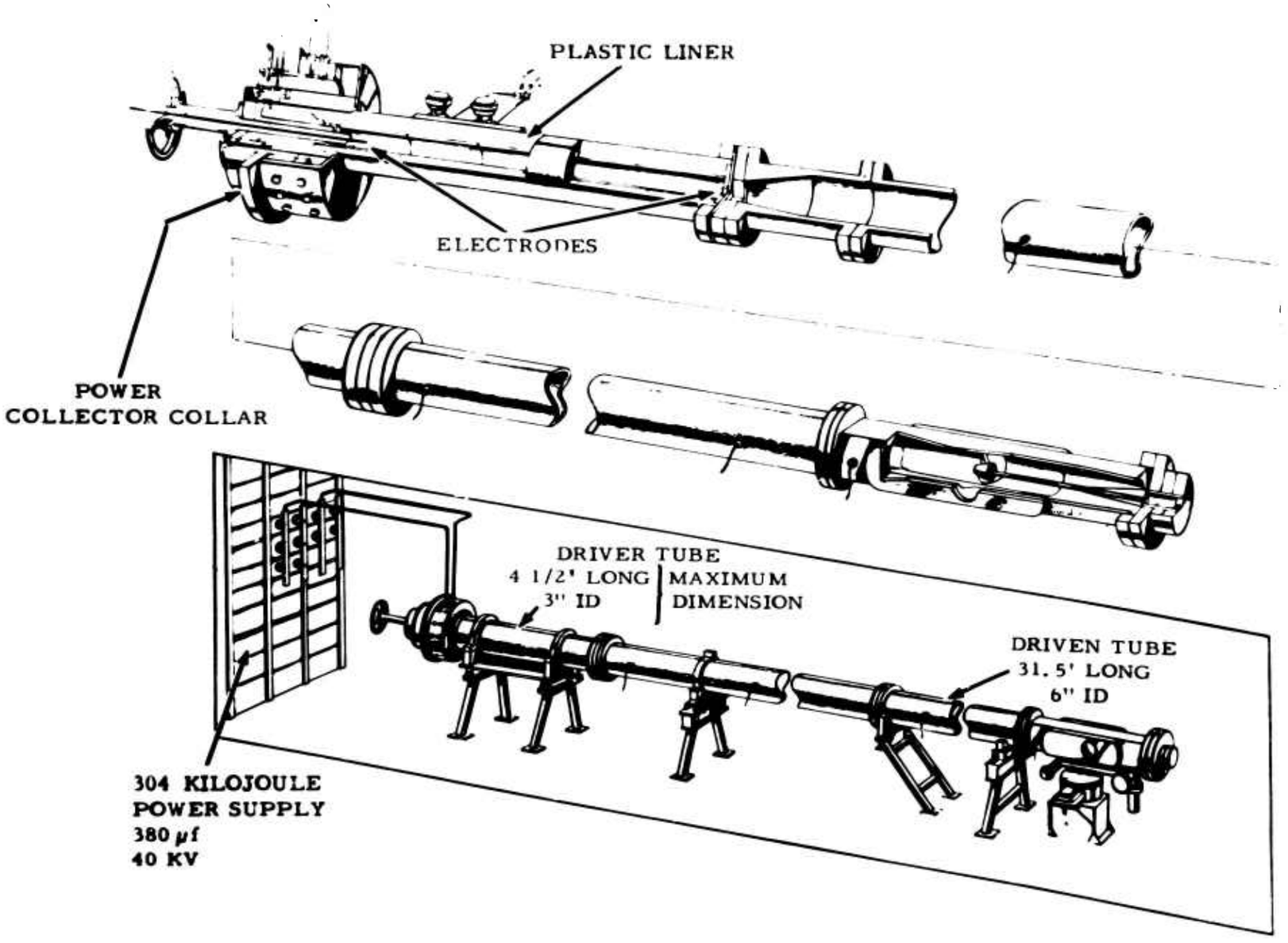


Figure 2 Hypervelocity Shock Tube with Electric Arc Heated Driver.

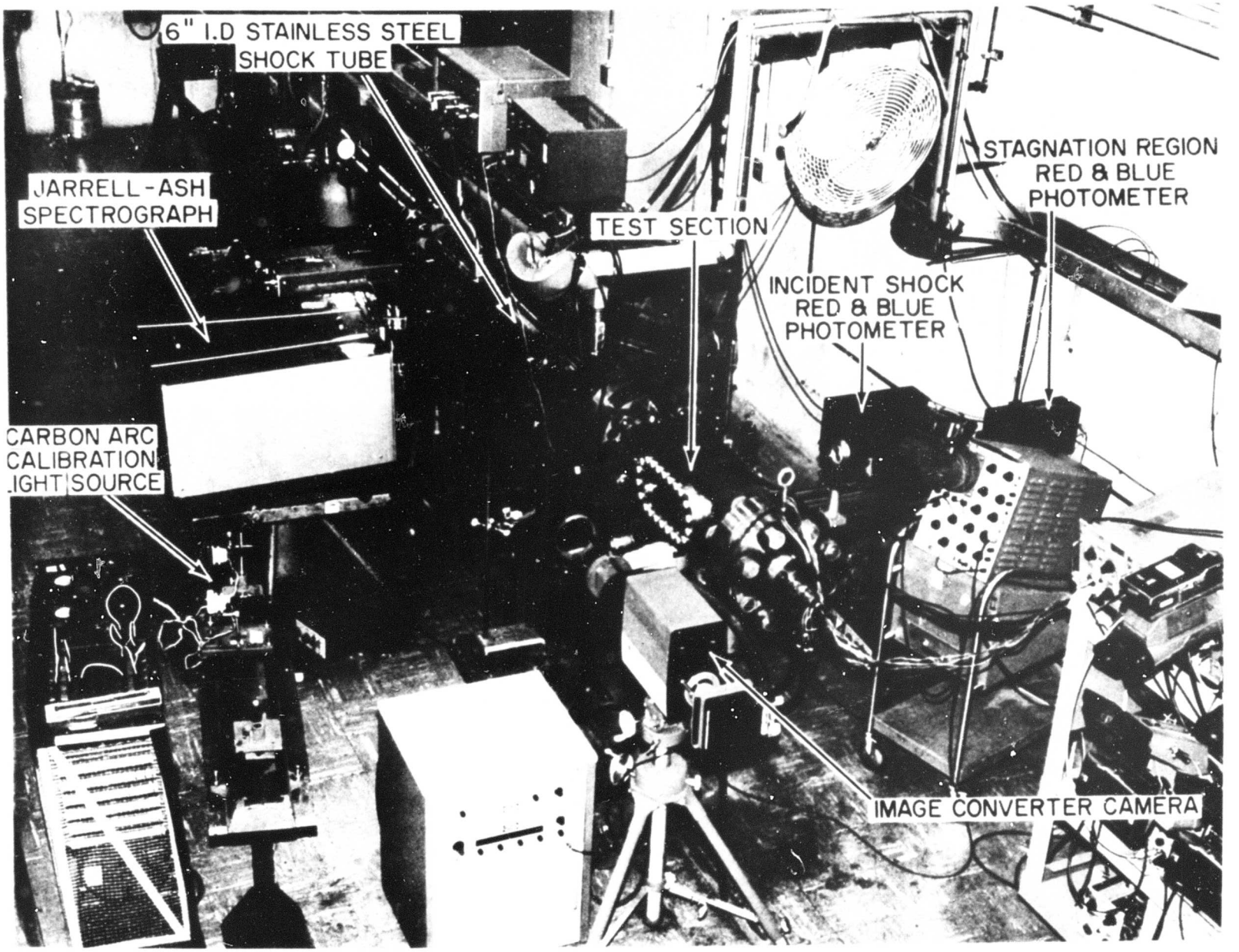


Figure 3 Location of Instrumentation and Test Section End of Driven Tube.

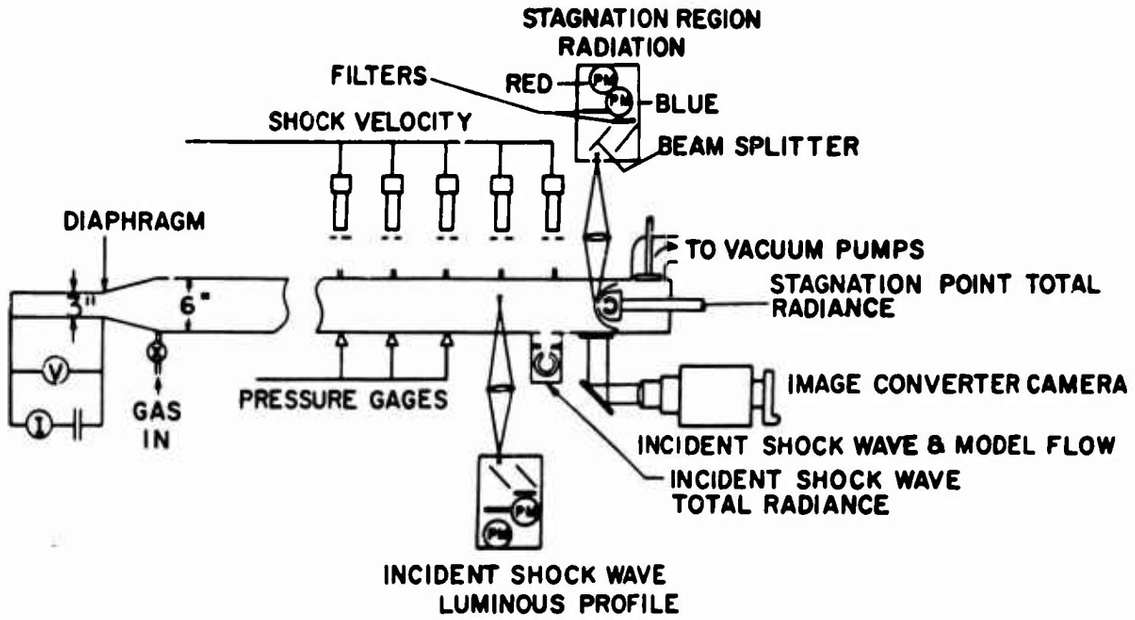


Figure 4 Schematic Diagram of Instrumentation for Study of Gas Radiance. Also Shown Instrumentation Used in Obtaining Shock Tube Performance.

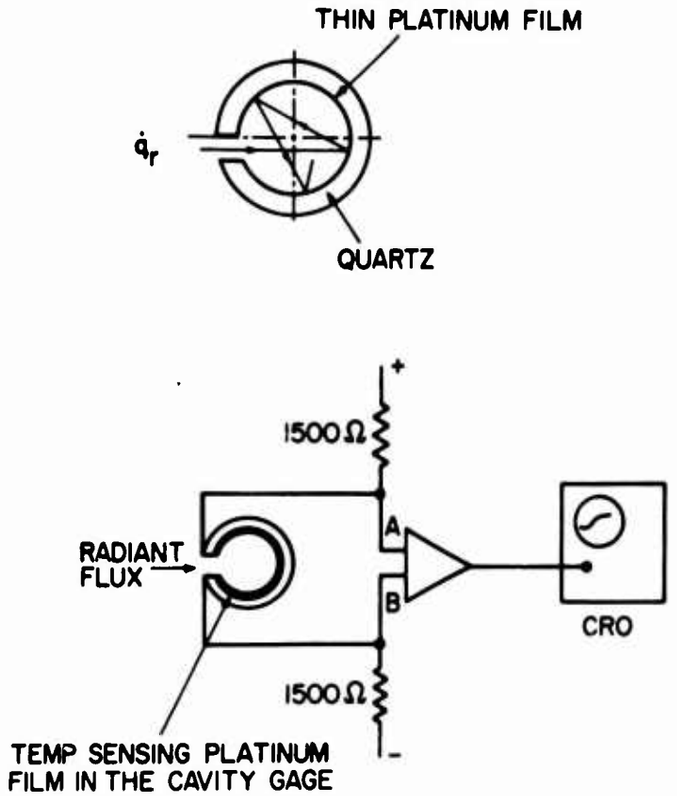


Figure 5 Total Radiation Cavity Gage. Geometry of Cylindrical Section and Schematic of Gage Electric Circuit.

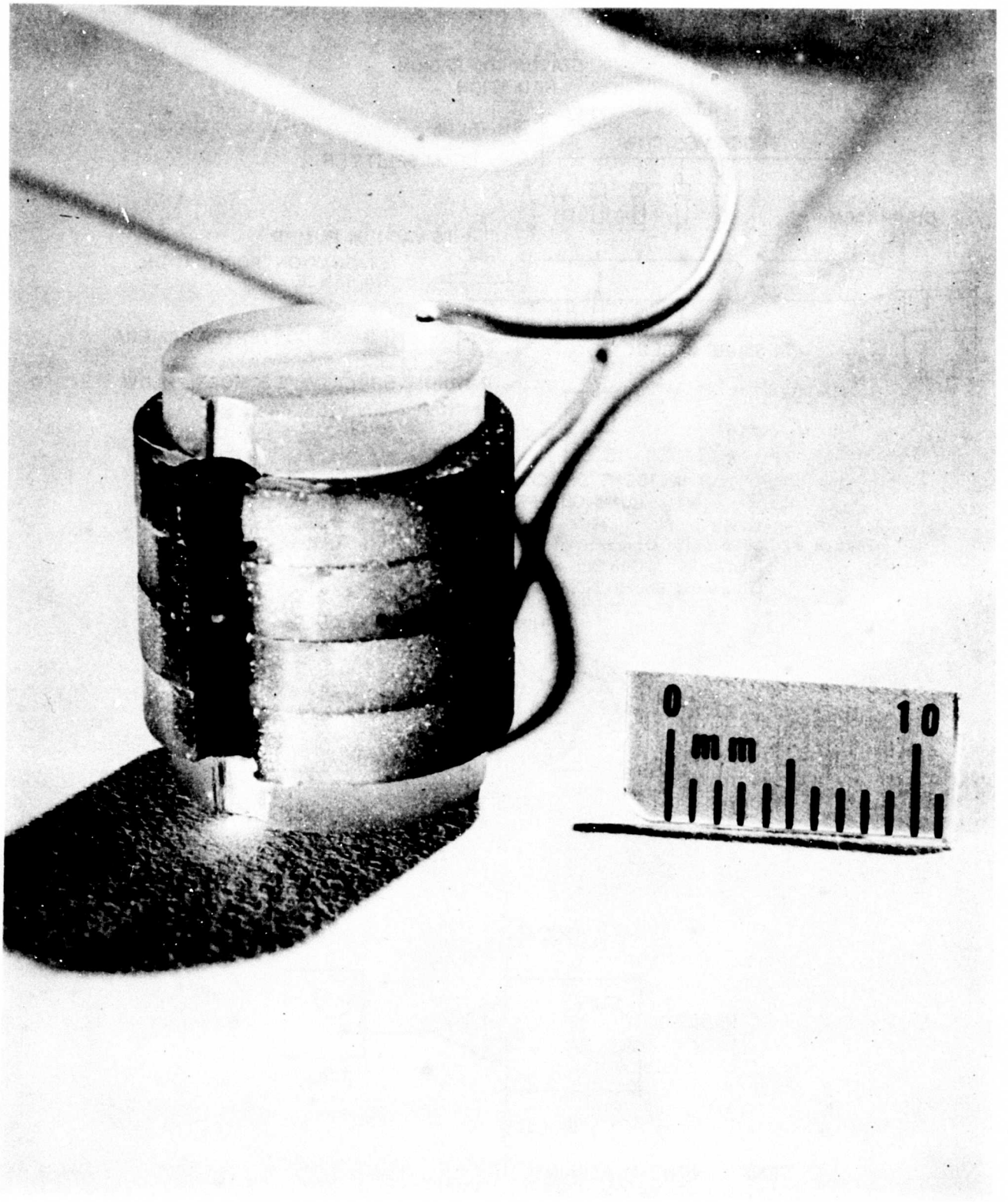


Figure 6 Photograph of Total Radiation Cavity Gage.

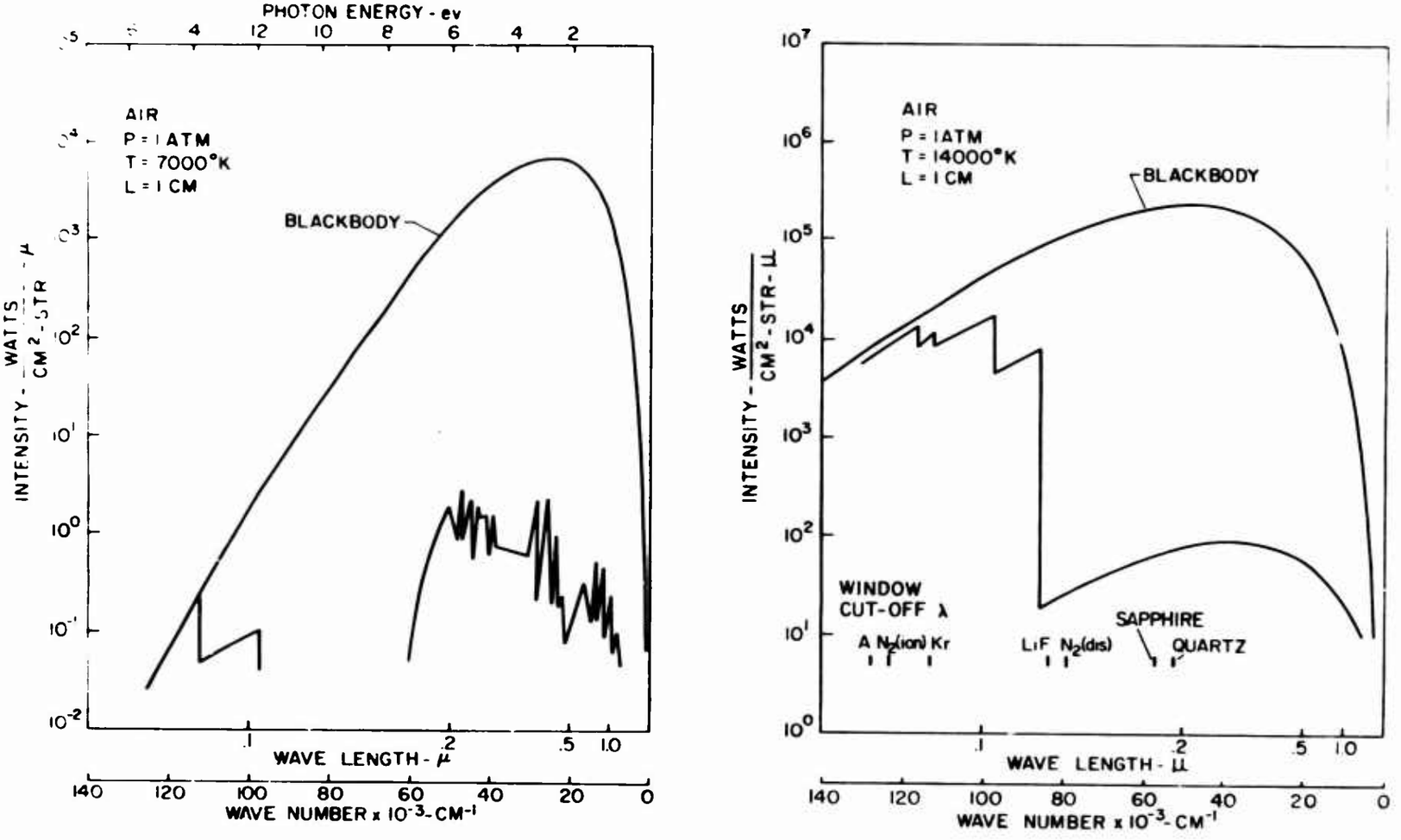
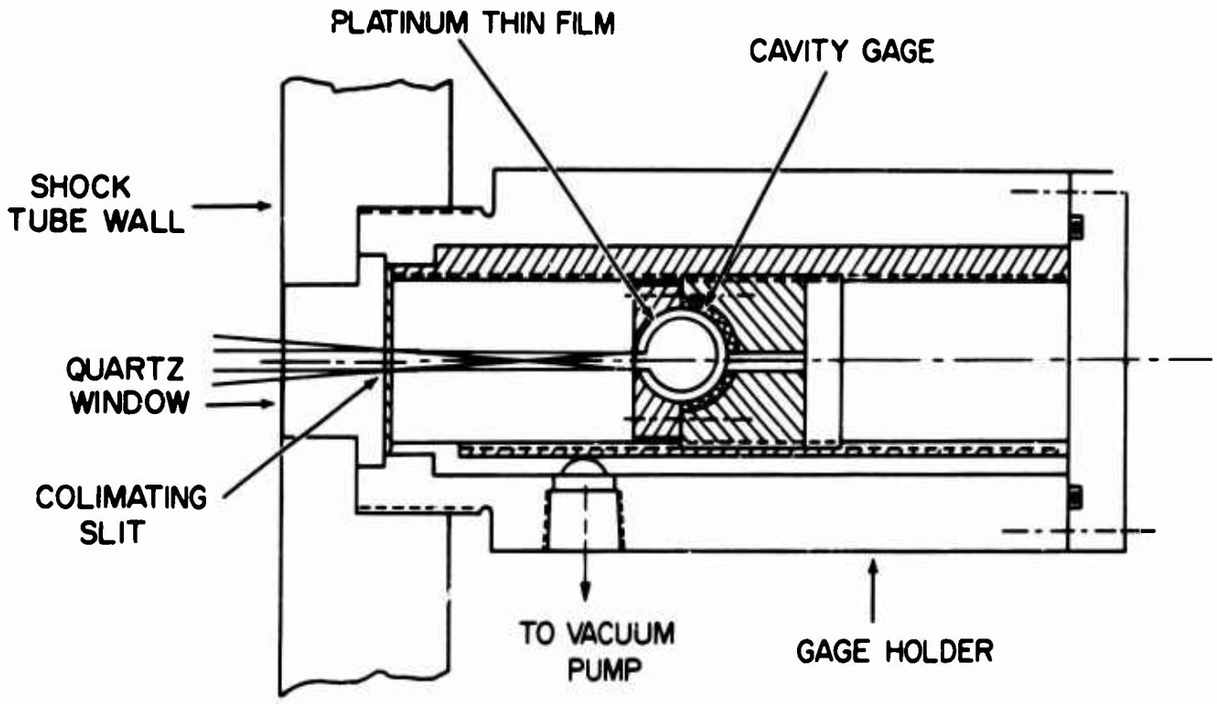


Figure 7 Wavelength and Temperature Dependence of Air Radiation.



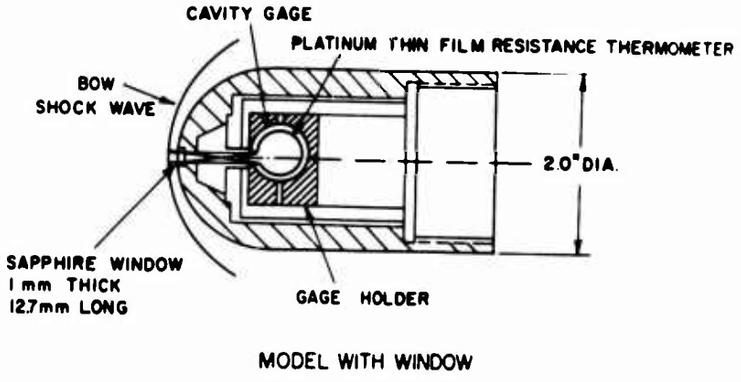
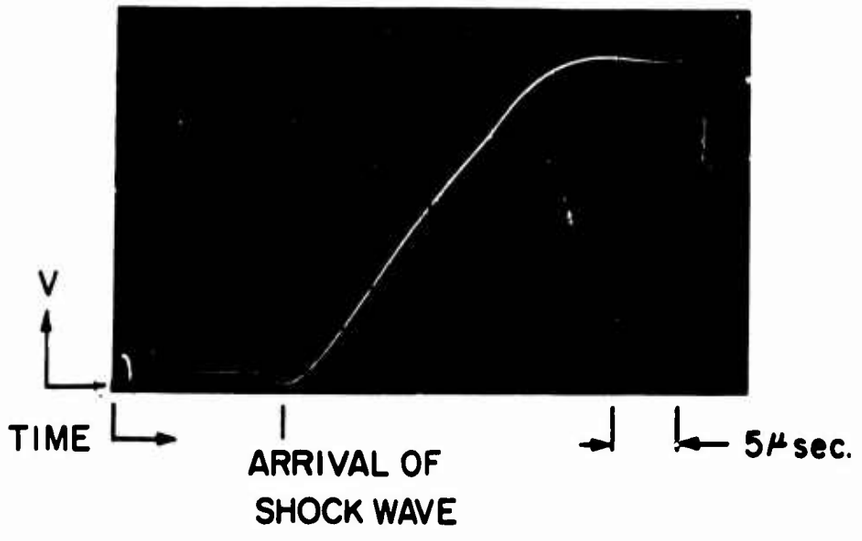


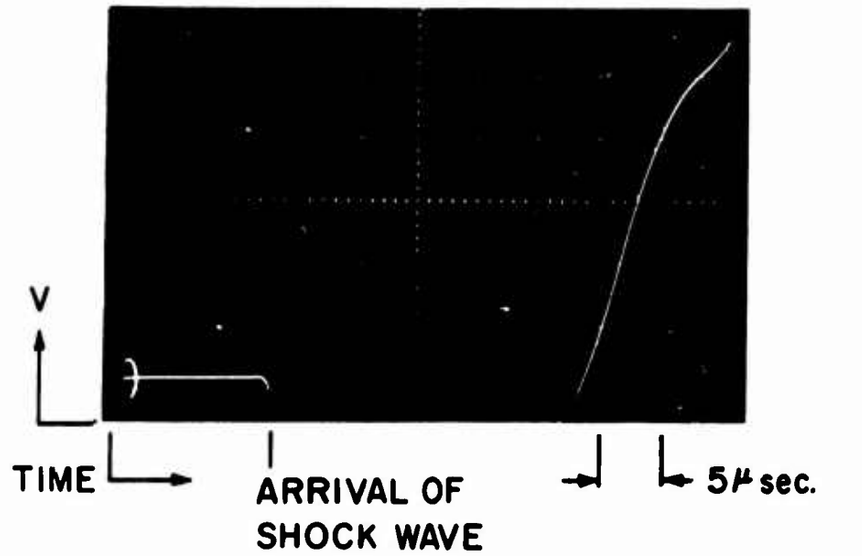
Figure 8 Total Radiation Cavity Gage System Used for Radiation Measurements. Upper Drawing Indicates Side Wall Arrangement. Lower Drawing Shows Stagnation Flow Model Configuration.



P_1 = 0.33 mm Hg U_s = 29,500 ft/sec

CAVITY GAGE WITH LiF WINDOW

MODEL GAS N_2 AT 1ATM PRESSURE



P_1 = 0.33 mm Hg U_s = 31,000 ft/sec.

CAVITY GAGE WITH LiF WINDOW

MODEL GAS – A AT 2ATM PRESSURE

Figure 9 Oscilloscope Traces of Cavity Gage Response with LiF Window. Upper Photograph Shows Model Filled with Pure N_2. Lower Photograph Shows Strong Photoelectric Effect when Model Was Filled with Argon.

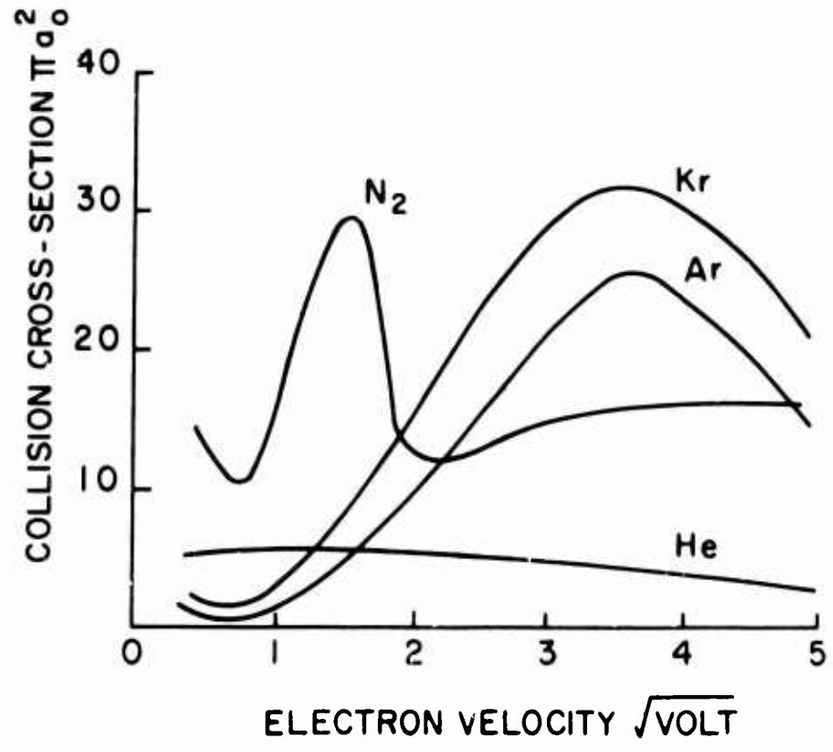


Figure 10 Total Collision Cross-Sections of Several Gases for Electrons with Various Energies.

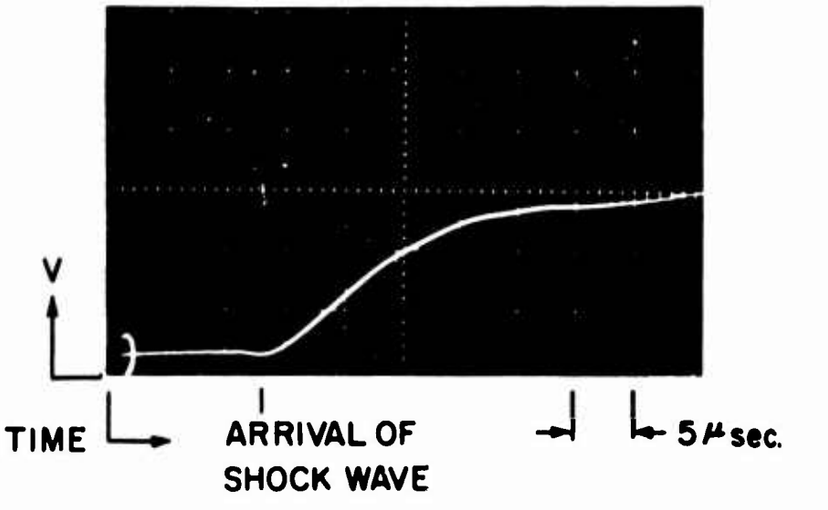
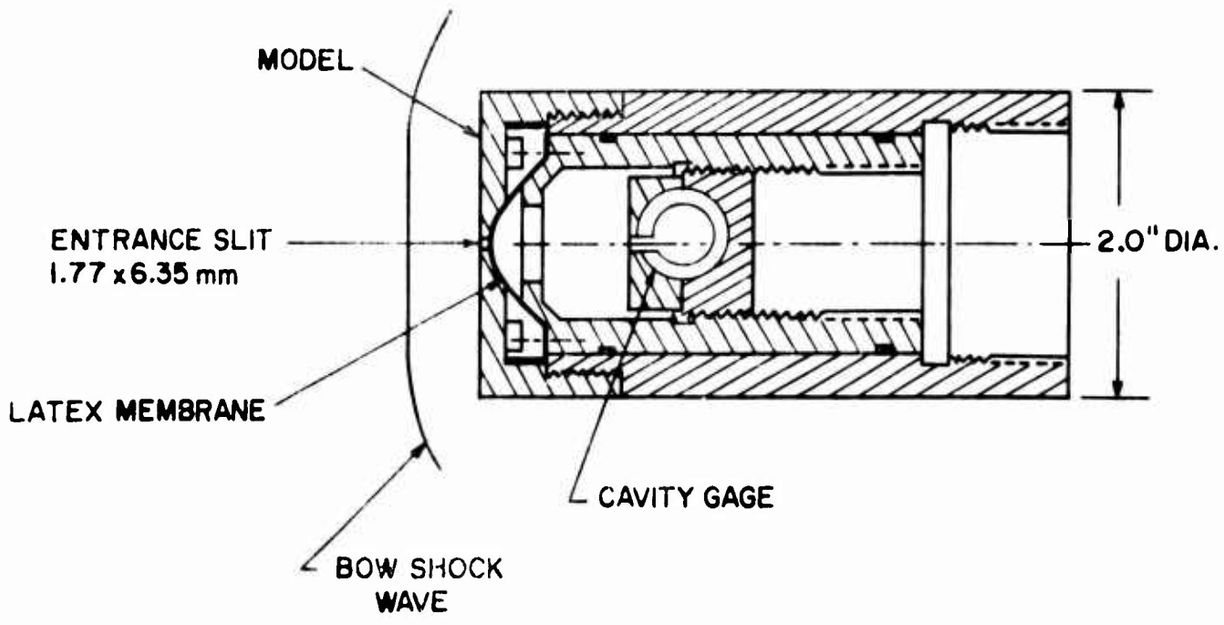


Figure 11 Oscilloscope Traces of Cavity Gage Response with LiF Window. Model Filled with 50% Kr - 50% He Gas Mixture.



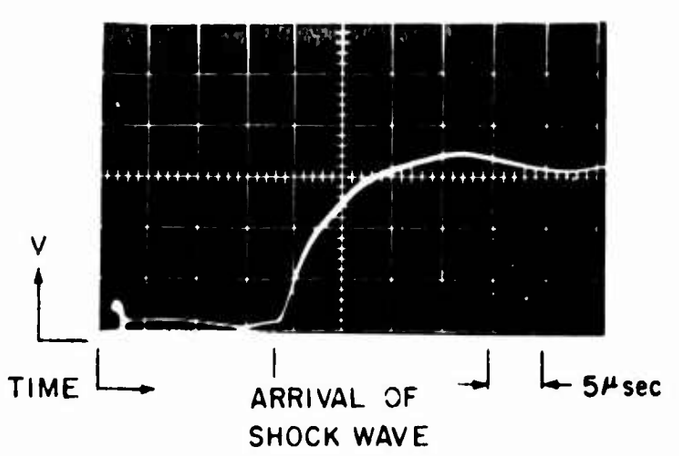


Figure 12 Window-Less Model System and Cavity Gage Response.

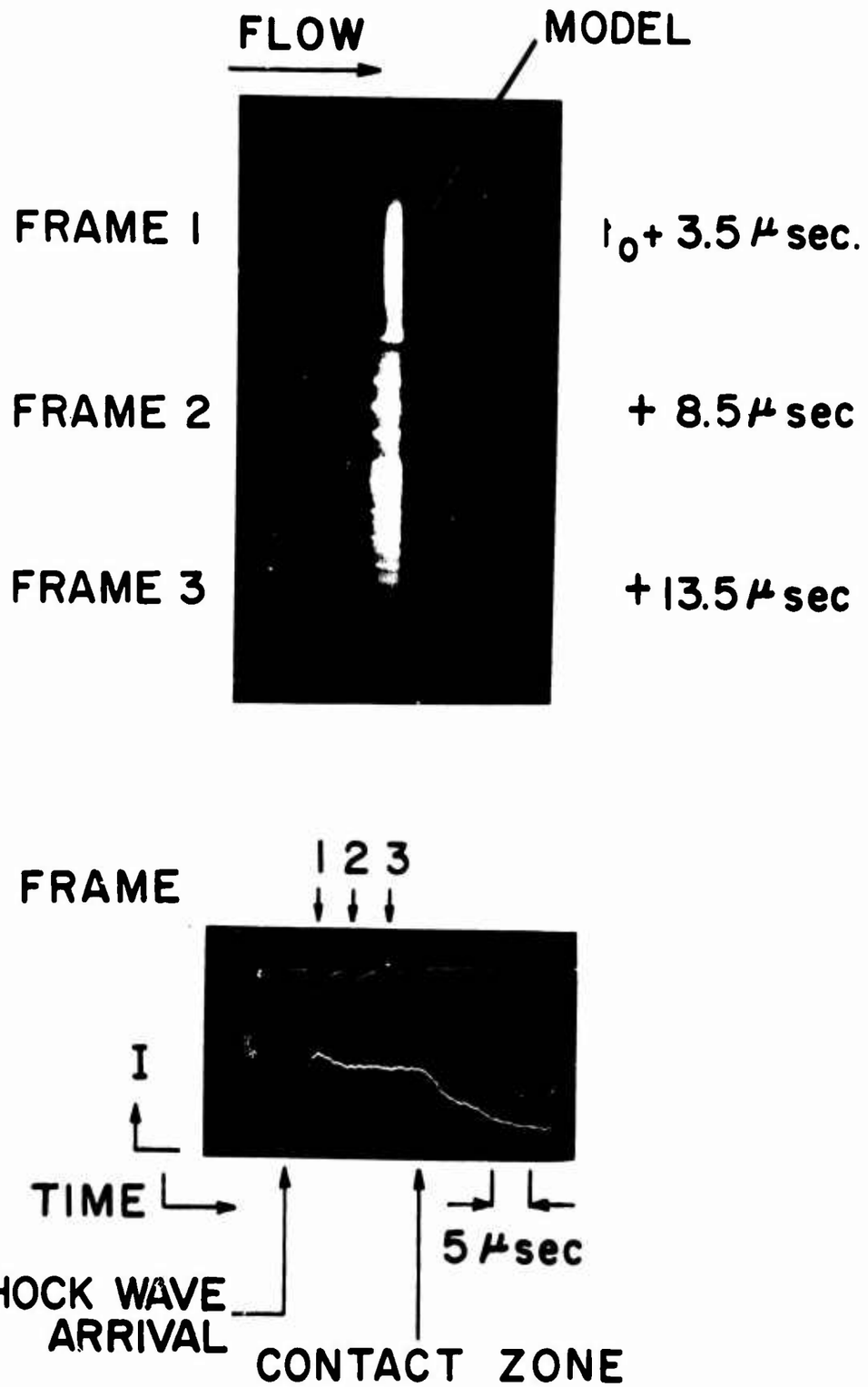


Figure 13 Image Converter Camera Photograph of Stagnation Region Shock Layer. Lower Photograph Shows Trace from Camera Monitor and Photometer Response Viewing Stagnation Region Flow.

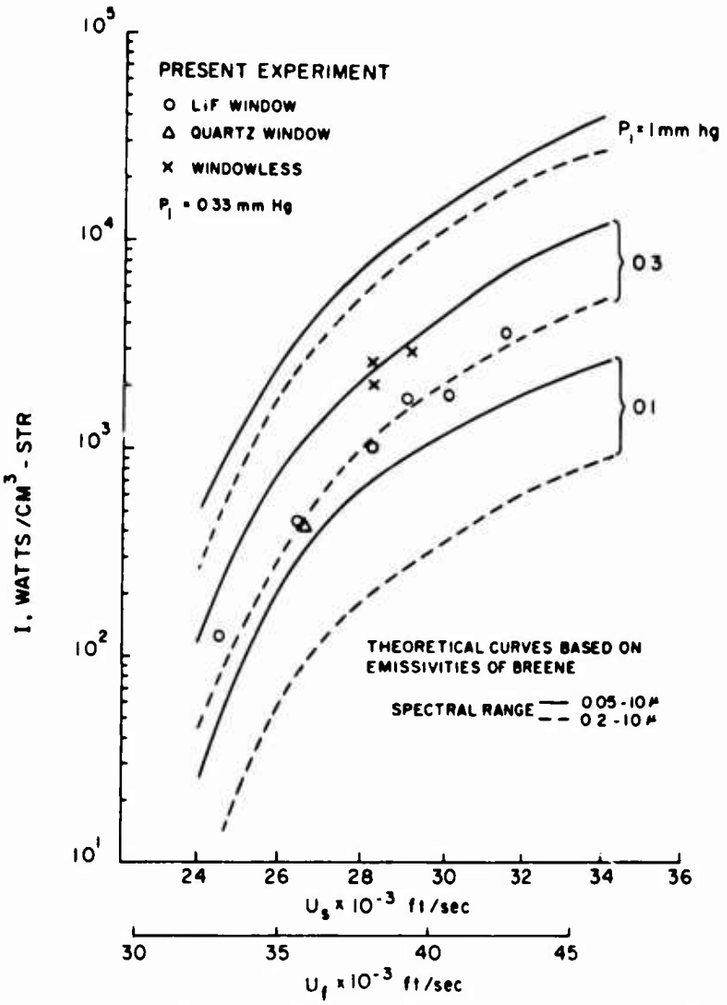


Figure 14 Results of Air Radiation Measurements with Cavity Gage.

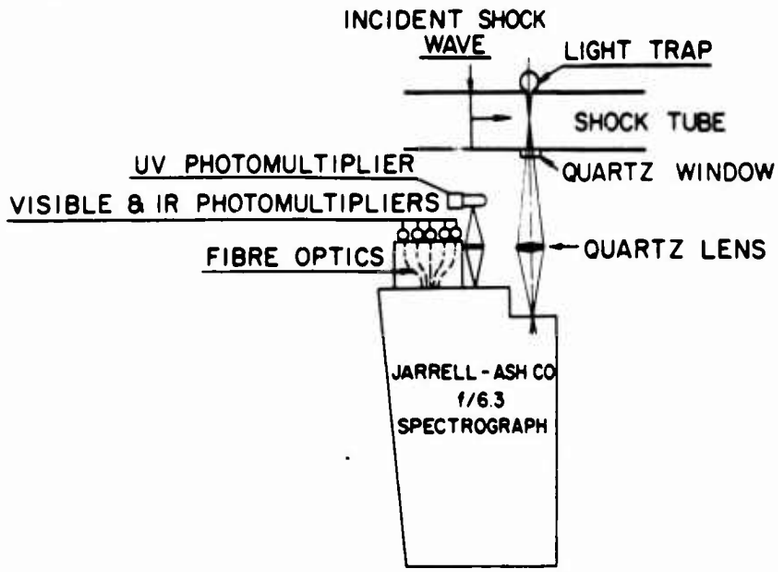


Figure 15 Schematic of Shock Tube Instrumentation for Non-equilibrium Gas Radiance Studies.

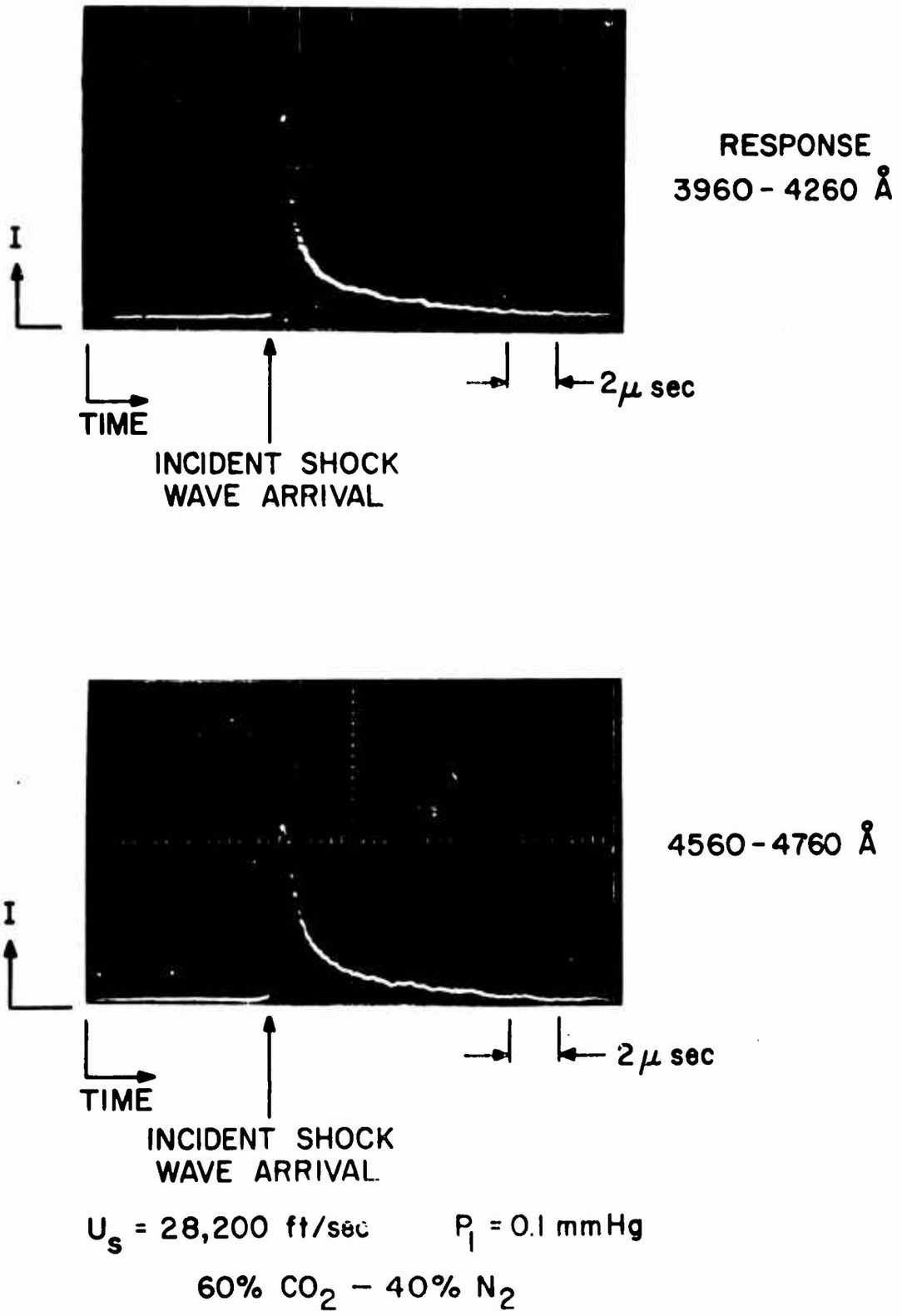


Figure 16 Oscilloscope Traces of Incidence Shock Wave Radiance Obtained with the Modified Spectrophotometer.

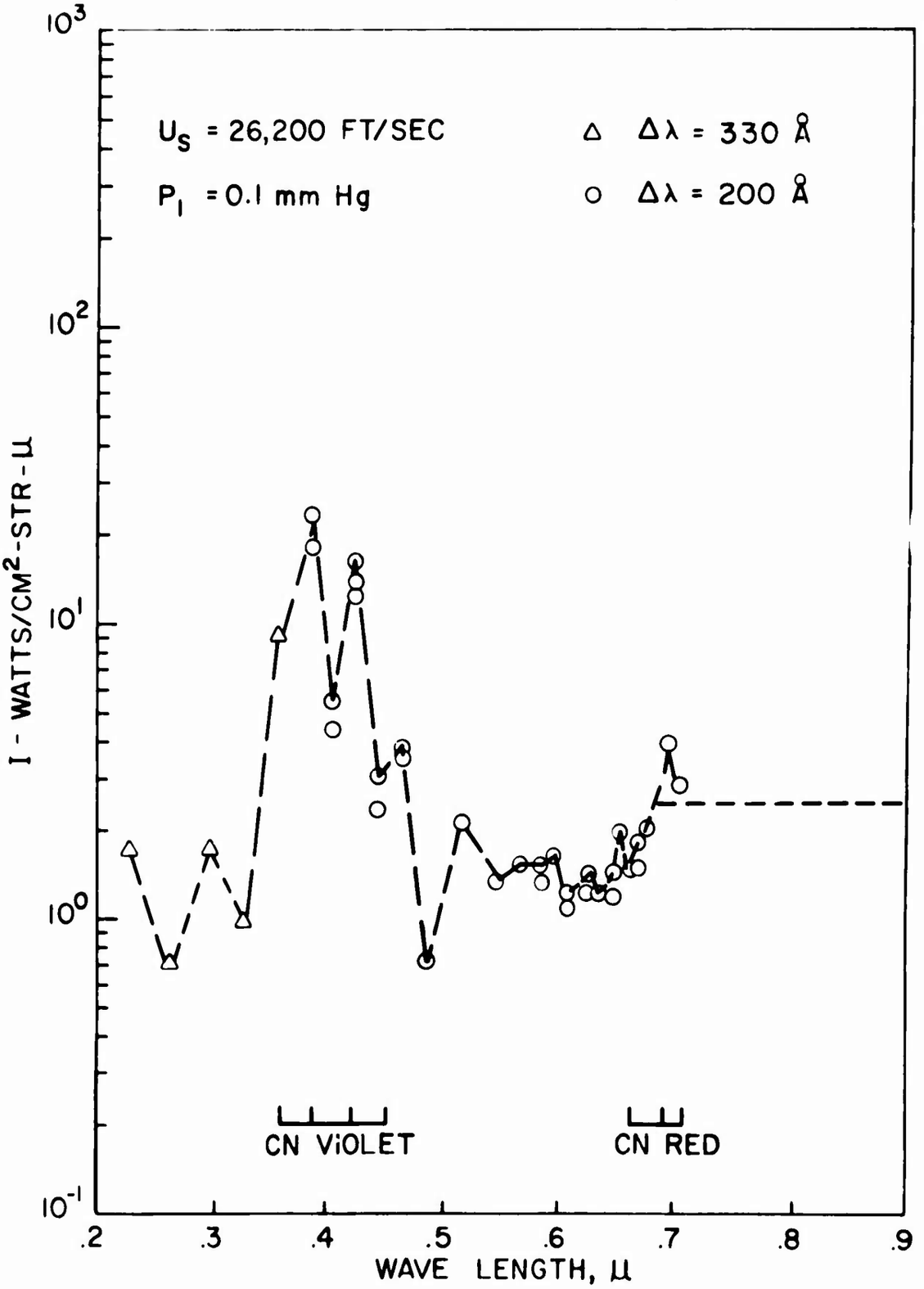


Figure 17 Spectral Distribution of Total Non-equilibrium Radiance from a 26200 ft/sec Shock Wave in 25% CO_2 - 75% N_2 Gas.

BLANK PAGE

CHARACTERISTICS OF THE FREE PISTON SHOCK TUBE

R. J. Stalker
Australian National University

INTRODUCTION

The search for a means of increasing the shock speeds attainable in diaphragm-type shock tubes has been mostly a search for means of controlled and reasonably uniform heating of driver gas of low molecular weight. Considerable effort has been devoted to shock tubes with arc heated Helium driver gas, and these have been developed to the point where a useful test flow is obtained (ref. 1, 2). Heating may also be effected by placing the Helium in a large volume, and using a free piston to compress it into a much smaller volume immediately prior to initiation of the shock tube flow. This method has been studied by the author (ref. 3, 4) and independently by Greif (ref. 5). Present indications are that whilst shock speeds exceeding 10 mm/μsec can be fairly easily achieved, somewhat higher speeds may as readily be obtained with an arc heated driver gas. However, the method does yield a consistently reproducible flow, with very little attenuation in shock speed along the tube, and avoids the problems sometimes associated with use of instrumentation adjacent to high energy electrical discharges. These may constitute reasons commending its use when the stress on highest shock speeds is somewhat relaxed.

Theory of Operation

The method is illustrated by the sketch in fig. 1. The shock tube driver gas is initially contained in the compression tube, at low pressure, when the piston is at i. Upon release, the piston travels down the tube under the action of the reservoir gas, until compression of the driver gas brings it momentarily to rest at m. At this moment, the shock tube diaphragm bursts, and the shock tube flow is initiated.

Compression Process

The use of a free piston to adiabatically compress gas to a high

pressure and temperature is not a new technique, and has been employed in fundamental physical studies of hot, high pressure gases (ref. 6). Its effectiveness stems from the fact that if the initial pressure in the reservoir is a few times larger than that in the driver gas then the piston traverses most of the length of the compression tube before the pressure at its forward face equals the pressure at its rear face. It then has a very considerable kinetic energy, which must be transferred to the compressed gas within the short remaining part of the compression stroke, and this can only be done if high pressures are developed in the compressed gas. Thus, as well as raising the temperature of the compressed gas, there is a large gain in pressure, as the pressure at m is many times that which initially existed anywhere in the apparatus.

For analysis, it is assumed that the compression takes place sufficiently slowly that the pressure is uniform throughout the driver gas at any instant. Also, for convenience, the reservoir is taken to be infinite in volume, and the pressure at the rear face of the piston to be always equal to the reservoir pressure. Then, neglecting heat losses from the driver gas, the compression is isentropic and, when the piston is at m with zero kinetic energy, an energy balance may be written:-

$$P_R \left(V_m - V_i \right) = \frac{P_i V_i}{\gamma - 1} \left(\frac{P_m V_m}{P_i V_i} - 1 \right) \qquad (1)$$

where P_R is the reservoir pressure, P_i and P_m are the initial and peak values respectively of the driver gas pressure, V_i and V_m are the corresponding driver gas volumes, and γ is the driver gas ratio of specific heats. For $V_m \ll V_i$ and $P_m V_m^{\gamma} = P_i V_i^{\gamma}$, equation (1) may be recast as

$$\frac{P_m}{P_i} = \left(\frac{a_m}{a_i} \right)^{2\gamma/\gamma-1} = \left(\frac{V_i}{V_m} \right)^{\gamma} = \left\{ 1 + (\gamma - 1) \frac{P_R}{P_i} \right\}^{\gamma/\gamma-1} \qquad (2)$$

where a_i and a_m are respectively the initial and peak values of the driver gas speed of sound.

Shock Tube Process

The piston is made sufficiently massive that it remains effectively stationary as the head of the expansion wave generated in the driver gas by the bursting diaphragm travels back to the upstream end of the shock tube driver section. Thus, a conventional shock tube flow takes place, as shown in the x - t diagram in fig. 1. A shock is propagated with uniform velocity down the tube, until such time as it is overtaken by the head

of the expansion wave moving downstream after reflection from the end of the driver section. For a particular combination of driver gas and test gas, the shock speed is determined by the diaphragm pressure ratio, P_m/P_1 (where P_1 is the initial pressure in the shock tube), and the speed of sound in the driver gas. As may be seen from equation (2), this latter is determined by V_i/V_m, whence a series of curves may be drawn linking the variation of P_m/P_1 with V_i/V_m for constant shock speed, U_s. Such curves are shown in fig. 2 for Helium as driver and Argon as test gas. Fig. 2(a) is for a constant area shock tube, fig. 2(b) for a shock tube with an increase in cross-sectional area in passing from the driver section to the shock tube.

High driver gas compression ratios must lead to a relatively small shock tube driver section, and this limits the downstream distance, X, at which the head of the reflected expansion wave overtakes the contact surface. For most test purposes this point represents the end of useful flow, and is therefore worthy of special attention. Referring to fig. 1, the ratio of X to L, the length of the driver section, is determined by the contact surface velocity and the path in the x - t plane of the head of the reflected expansion. An analytic expression for this path can be obtained (ref. 7), and leads to an expression for X/L in terms of the ratio of the contact surface velocity to a_m. Since this is determined by the pressure ratio across the expansion, which is in turn fixed, for a particular test gas, by P_m/P_1 and U_s, it follows that curves of constant X/L may be drawn, as shown in fig. 2(a).

Limiting Boundaries

The curves of X/L make it possible to define a boundary of operation imposed by the ratio of the volumes of the compression tube and the shock tube in which tests are to be conducted. Specification of the length, X, and the diameter, D, of the shock tube, together with the value of V_i/XD, and the ratio of driver section and shock tube diameters, implies that for any value of X/L, there is a maximum value of V_i/V_m. A line representing the variation with X/L of this maximum value, for $V_i/XD = 10$, is shown on fig. 2(a). Operation to the right of this line is, of course, impossible.

Another such limiting boundary arises from the ratio of the maximum value permitted for the reservoir pressure to the initial pressure in the shock tube. It is clear from equation (2) that P_m/P_1 is fixed by choice of P_R/P_1 and V_1/V_m, whence a line can be drawn relating values of V_i/V_m and P_m/P_1 associated with a constant value of P_R/P_1. Such a line is shown on fig. 2(a) for $P_R/P_1 = 10^4$. Operation to the left of this line is also impossible.

Thus these two limiting boundaries, together with an upper limit set by the maximum value of the ratio, P_m/P_1, of the peak pressure and the initial pressure in the shock tube, define an area on fig. 2(a) within which the shock tube may be operated. This area should be kept in mind when considering experiments with a free piston shock tube.

EXPERIMENT

Description of Free Piston Shock Tube Assemblies

A free piston shock tube assembly is regarded here as consisting of the reservoir and compression tube. Two such assemblies in operation at the Australian National University are shown in fig. 3.

To the left of the photograph is a small version, with a compression tube 5 ft long and 2" in diameter, which has been used in magneto gas dynamic studies, and for investigation of shock tunnel operation with the free piston technique. The compression tube is a section of drawn stainless steel tubing, used without any supplementary finishing of the internal surface, surrounded by a closely fitting larger diameter mild steel sleeve at the high pressure end. This has been operated consistently at peak driver pressures of 9,000 lb in^{-2}, with driver gas volumetric compression ratios up to 100. For shock tube operation the pistons used have been about 2" in length, machined from a nylon compound. Operation of the shock tube is initiated by bursting diaphragms, which allow the reservoir gas to pass into the compression tube and accelerate the piston.

On the right of the photograph is a larger version, with a compression tube 10 ft long, having an internal diameter bored and honed to 3.000". The reservoir, seen to the left of the large coupling at the left hand end of the compression tube, is 4.2 ft long, 5.5" in diameter, and is designed for use up to 1500 p.s.i. No diaphragms are used between the reservoir and the compression tube. Instead, the coupling incorporates a method suggested by Greif (ref. 5) for restraining the piston prior to firing, in which the piston itself effectively acts as the moving element in a pneumatic valve which can be actuated as required. The high pressure end of the compression tube is enclosed by a close fitting mild steel sleeve with an outside diameter of 9", and in compression tests on Helium, has been operated up to 23,000 p.s.i. with a closed end.

To avoid transmission of large transient forces to the supporting frame, both assemblies are mounted on wooden blocks, and are free to move axially. Thus, in principle, the forward net movement of the piston during operation is balanced by a slight rearward movement of the relatively many times more massive reservoir and compression tube. In fact, this movement tends to be damped by friction.

Results

The success of the method depends on the extent to which the driver gas temperatures theoretically associated with a given volumetric compression ratio are actually realized in the compression process. Studies of the peak conditions produced in this process have therefore been conducted with Helium driver gas in the two assemblies described here, and previously in an assembly involving a compression tube 5 ft long and 3" in diameter at

the National Research Council, Ottawa, Canada (ref. 4). The high pressure end was closed for these studies, and the variation of pressure with time in passing through the peak pressure was recorded. This time variation can be used to obtain the minimum distance of the piston face from the closed end (ref. 4), and thus the peak value of the volumetric compression ratio. The peak temperature was obtained from the initial Helium temperature by assuming isentropic compression of a central core of the gas, and using the ratio of peak pressure to initial pressure. This yielded values which satisfactorily predicted the shock speeds measured subsequently.

The temperatures fell below the values expected from the measured volumetric compression ratios, varying from 55% to 90% of those expected. Closest agreement was obtained with lightweight pistons, when the compression was most rapid. With a given apparatus and piston, and fixed reservoir conditions, there was in general no detectable variation with volumetric compression ratio of the ratio of achieved and expected temperatures. The highest volumetric compression ratio tested was 370, obtained in the 10 ft x 3" compression tube, when the temperature reached 73% of its expected value.

The flow in the shock tube has been investigated in all three of the free piston shock tubes mentioned by taking streak photographs of the luminous, shock heated test gas as it moved down the tube. The reproducibility of the results obtained has been in accordance with that expected in conventional shock tubes. Shock speeds obtained under similar driver and test gas conditions have been the same, within the 2 - 3% accuracy to which velocity can be measured from streak photographs, and the length of the test sample of shock heated gas has been the same at the same distance from the diaphragm. Results of shock speed measurements in air, with a 2.5 cm diameter shock tube attached to the 10 ft x 3" compression tube, are presented in fig. 4. These were obtained with a high pressure diaphragm bursting at 8,800 lb in^{-2}, a volumetric compression ratio of 280, and a peak driver gas temperature, calculated in the above manner, of 8,800°K. Measurements were made between 1 and 1.5 metres from the diaphragm. Shock speeds up to 11 mm/μ sec are obtained and, as mentioned above, agree satisfactorily with those predicted from the calculated temperature.

Photographs obtained during these tests are shown in fig. 5. These were taken with an S.T.L. image converter camera, recording on Polaroid Land Type 47 film (A.S.A. 3000). Fig. 5(a) shows a streak photograph, and displays a uniformity of the shock velocity with distance down the tube which is comparable with that expected in a conventional shock tube. Luminosity apparent in the flow following the shock heated gas may be due to traces of oil in the driver gas. Fig. 5(b) shows two groups of framing photographs taken at a distance approximately 1.5 metres from the diaphragm, with identical shock conditions. These were taken at different camera apertures, to demonstrate different features of the flow, but between the two they illustrate the fact, noted above, that the length of the test sample of shock heated gas is reproducible. The group (i) shows that a plane shock is formed, but there are inhomogeneities evident in the test gas between the

shock and the contact zone. These inhomogeneities do not represent contamination of the test gas by the driver gas, as this would be expected to lead to a consistent gradation of luminosity from the contact zone to the shock, and this is not apparent. Also, group (ii) shows similar photographs, taken with a larger camera aperture, in which the less luminous regions of the contact zone are displayed in more detail. (The distortion of the image which then appears in regions of high light intensity is a characteristic of the camera, and has been evident in other applications.) The irregular nature of the contact zone is apparent, but it is also clear that the length of the zone is much smaller than the length of the sample of shock heated gas.

CONCLUSIONS

Analysis shows that the free piston technique should produce shock tube flow at velocities exceeding 10 mm/μ sec, and this has been confirmed by experiment.

For shock speeds up to 10 mm/μ sec, the technique yielded reproducible shock velocities, with low attenuation along the tube, which were accompanied by a reproducible volume of shock heated test gas. In view of the uniformity preserved in the driver gas by the nature of the compression process, this is not surprising. In a 2.5 cm diameter shock tube, inhomogeneities were evident in the shock heated gas. Although they are not associated with contamination by the driver gas, there is a need to ascertain the existence of these inhomogeneities with shock tubes of larger diameter, and to investigate their nature and causes.

REFERENCES

(1) Rose, P.H. and Stankevics, J.O., A.I.A.A. Journal 1 , 2752 (1963)

(2) Gruszczynski, J.S. and Warren, W.R., A.I.A.A. Journal 2 , 1542 (1964)

(3) Stalker, R. J., A.R.S. Journal 30 , 564 (1960)

(4) Stalker, R. J., National Research Council of Canada, Mechanical Engineering Report MT-44 (1961)

(5) Greif, R., Thesis, Harvard University (1962)

(6) Longwell, P.A., Reamer, H.H., Wilburn, N.P., and Sage, B.H., Ind. Engng. Chem. 50 , 603 (1958)

(7) Lukasiewicz, J., National Research Council of Canada, National Aeronautical Establishment Report 15. (1962)

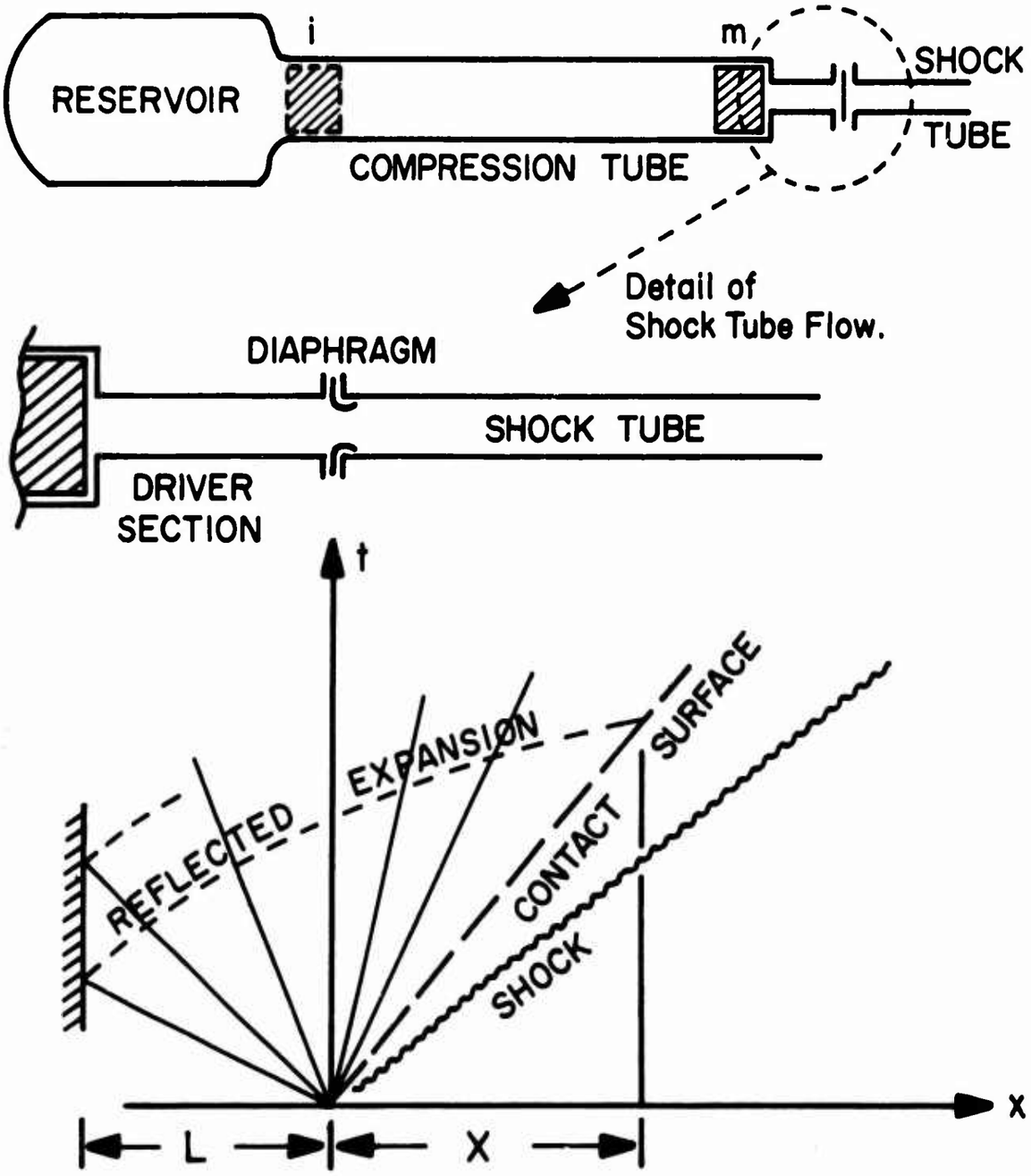
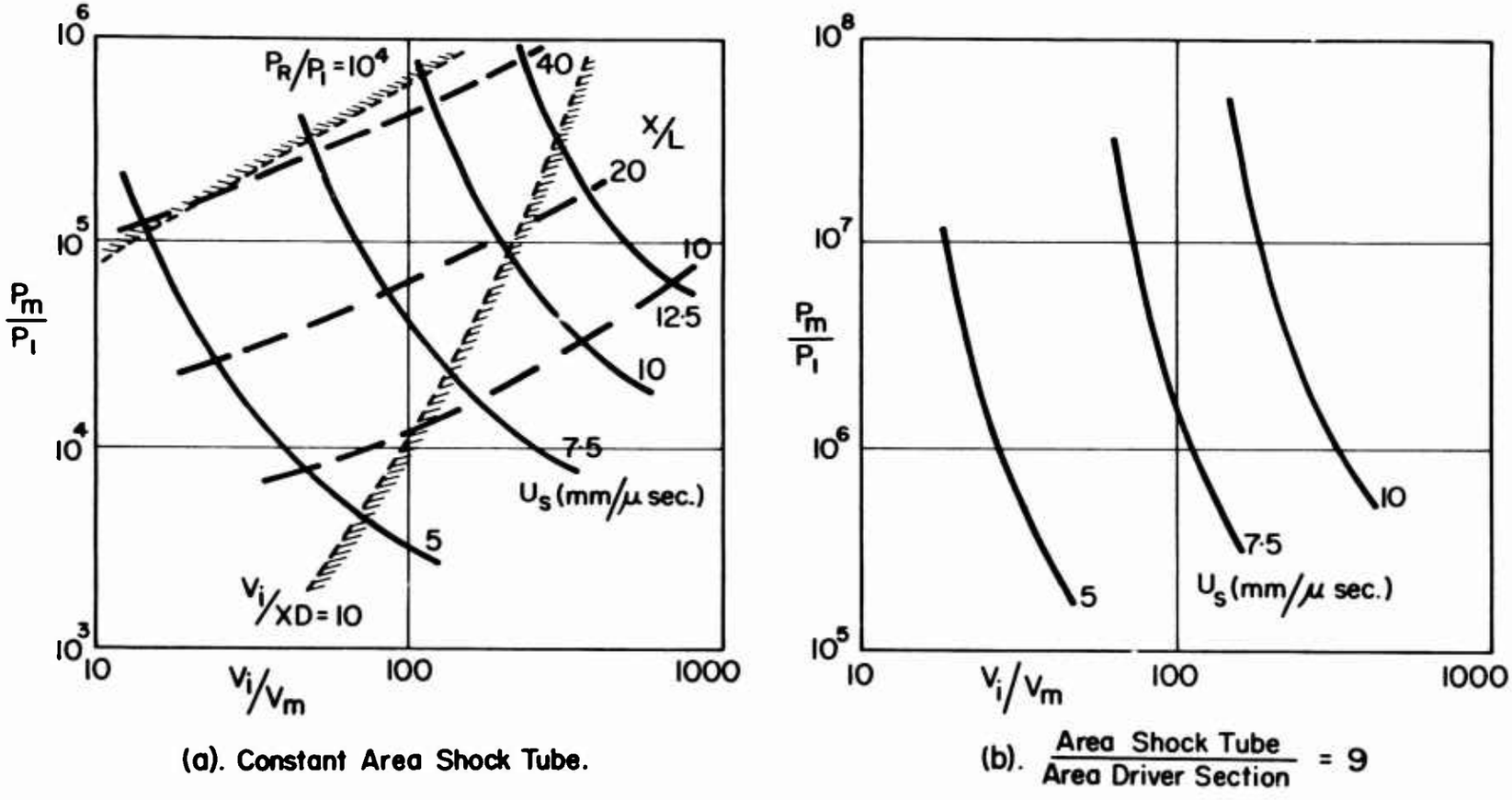


FIG. 1. OPERATION OF FREE PISTON SHOCK TUBE.



(a). Constant Area Shock Tube.

(b). $\frac{\text{Area Shock Tube}}{\text{Area Driver Section}} = 9$

FIG. 2. PERFORMANCE OF FREE PISTON SHOCK TUBE.

Helium/Argon $a_i = 1\ \text{mm}/\mu\ \text{sec.}$

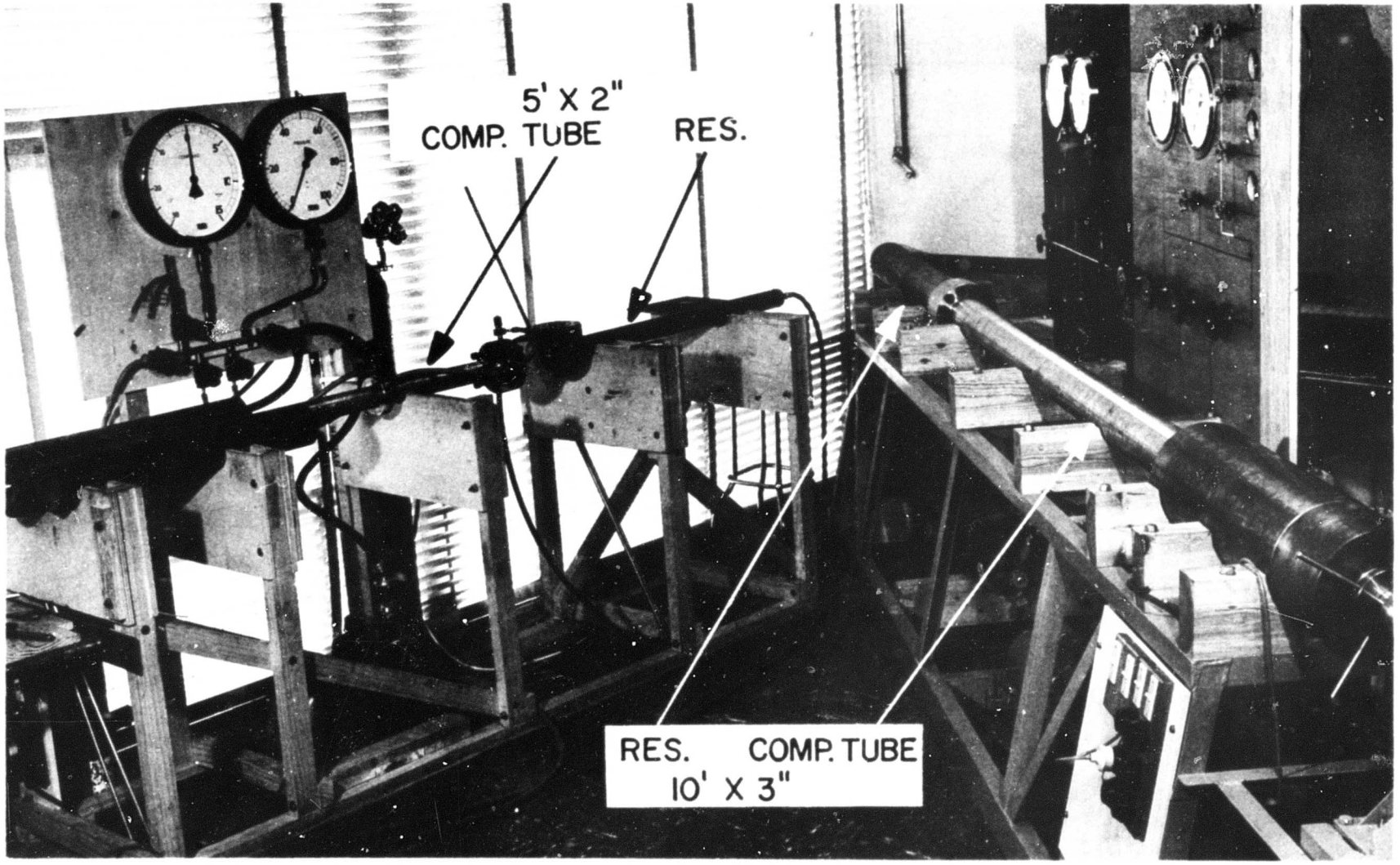


FIG. 3. FREE PISTON SHOCK TUBE ASSEMBLIES.

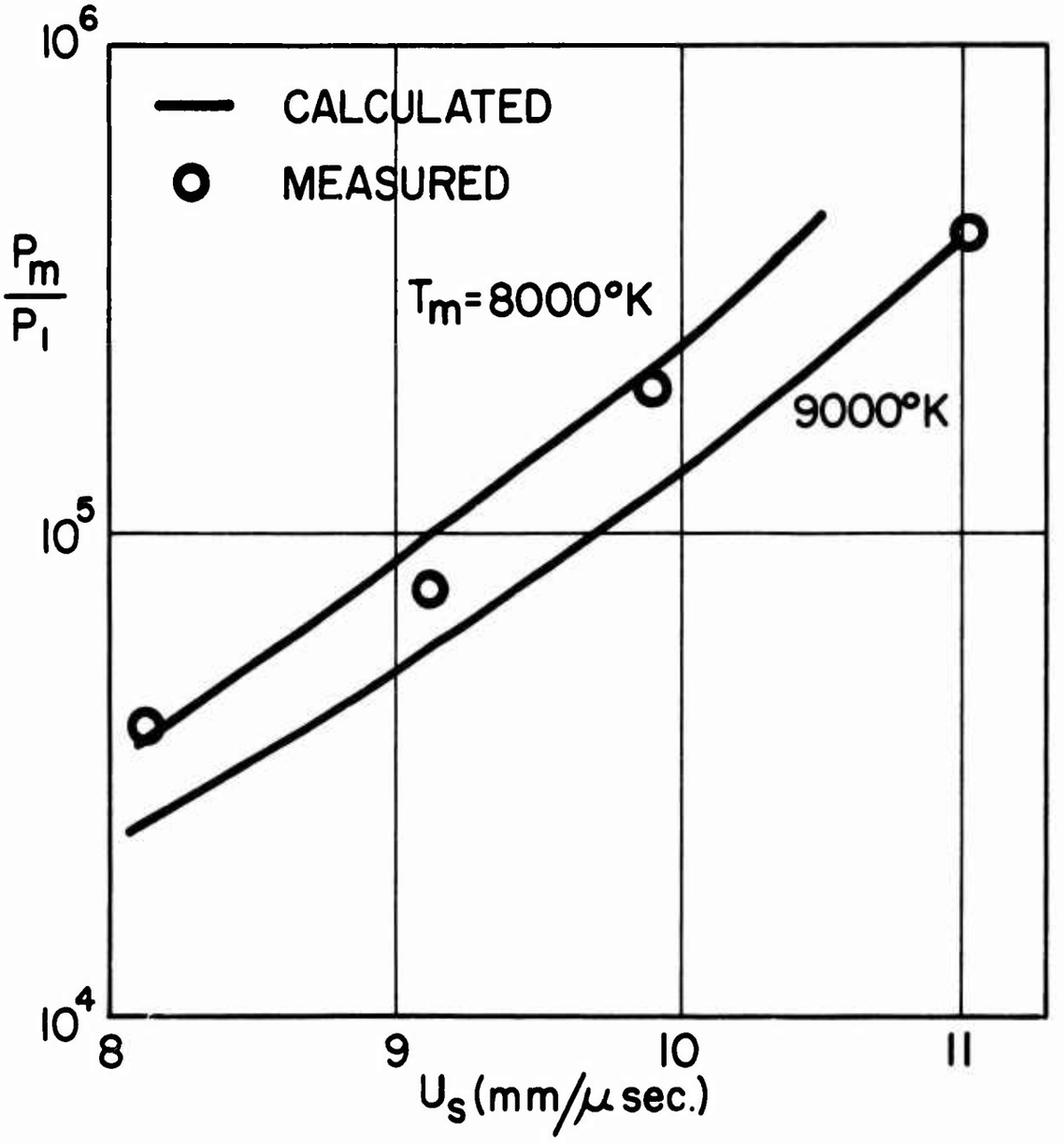


FIG. 4. MEASURED SHOCK SPEEDS HELIUM/AIR.

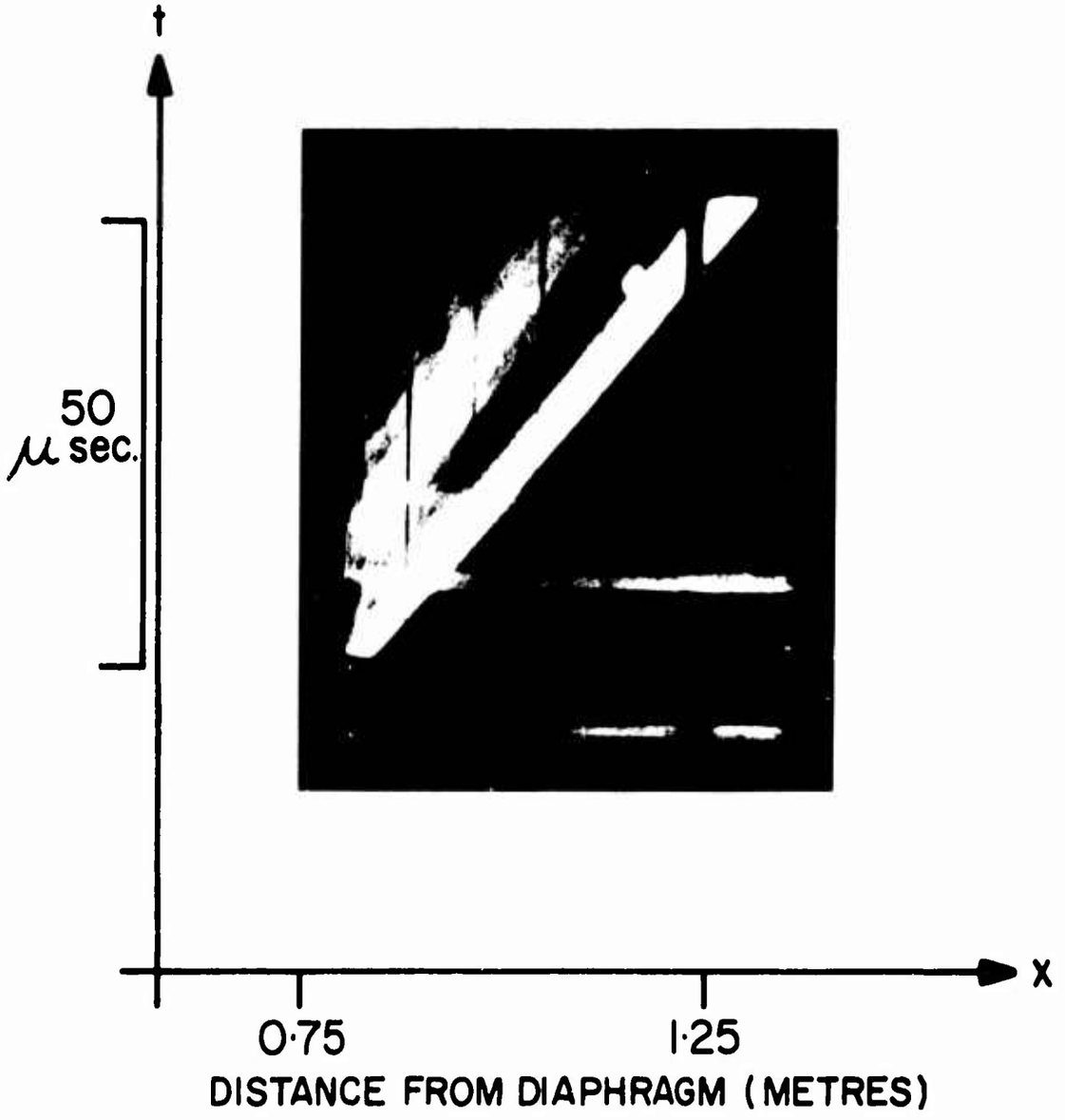
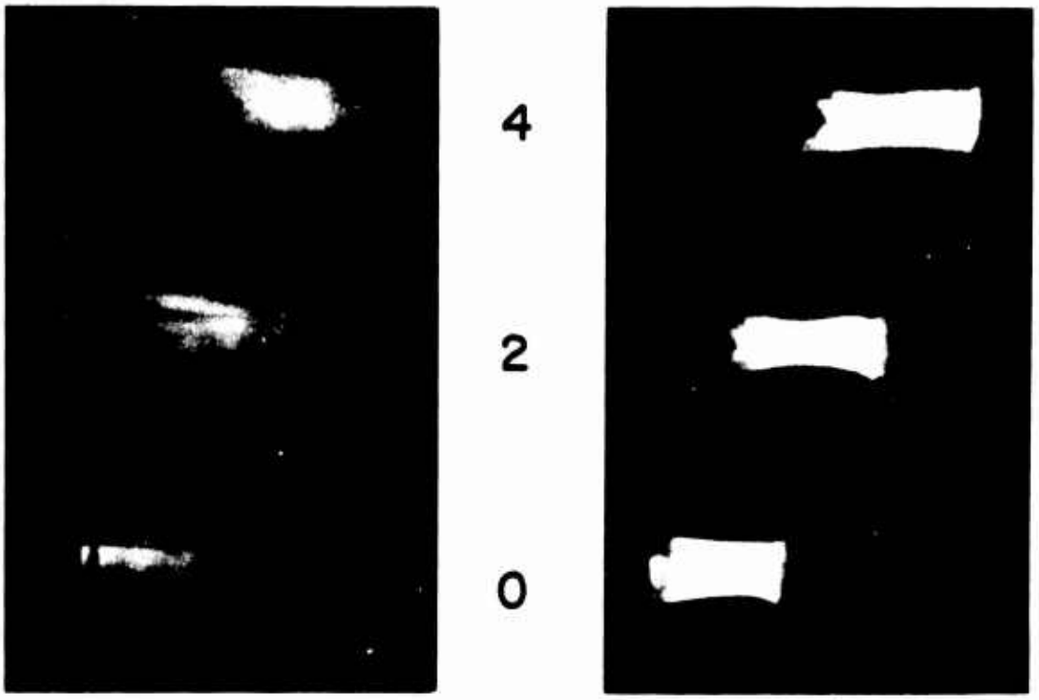


FIG. 5. PHOTOGRAPHS OF SHOCK TUBE FLOW.

(a) STREAK PHOTOGRAPH.

U_s = 9·1 mm/μ sec., P_1 = 5 mm Hg.



(i) FRONT LENS f14. (ii) FRONT LENS f5·6.

FIG. 5. PHOTOGRAPHS OF SHOCK TUBE FLOW.

(b) FRAMING PHOTOGRAPHS. (EXPOSURE 0·02 μsec.)

U_s = 9·9 mm/μ sec., P_1 = 2 mm Hg.

A FAST INVERSE PINCH SHOCK TUBE FOR PLASMA SHOCK WAVE STUDIES

George C. Vlases
Aerospace Engineering Sciences Department
and
Joint Institute for Laboratory Astrophysics
University of Colorado
Boulder, Colorado

INTRODUCTION

An experiment has been designed to study two types of shock waves in a plasma, the ionizing mhd shock and the collisionless shock.

Ionizing mhd shocks are those which propagate into a non-conducting gas containing a magnetic field with sufficient strength to render the post-shock gas conducting. These shock waves, which have no analogy in ordinary fluid mechanics, were first discussed rather briefly by Lyubimov and Kulikovskii (ref. 1) and Zhilin (ref. 2) and have been studied in detail more recently by Chu (ref. 3), Taussig (ref. 4), Kunkel and Gross (ref. 5), and Gross (ref. 6). To date, experimental work on the subject has been sparse. Vlases (ref. 7-9) has reported preliminary work along this line, while Patrick and Pugh (ref. 10) and Miller(ref. 11) have discussed closely related problems.

Ionizing mhd shocks are of interest not only from an academic viewpoint, but also because of their occurrence in electromagnetic shock tubes, pulsed plasma devices, and certain hypersonic mhd flow problems.

Collisionless shocks are those whose thickness is on the order of an ion Larmor radius and is much less than a mean free path for collisions. Possibly the best known example of such a wave is the bow shock associated with the earth's magnetosphere. The theory of such waves, while still incomplete, has been greatly advanced in the last three years. Laboratory experiments in this area are very difficult, however, and to date no clean experiments have been reported.

DESIGN OF THE EXPERIMENT

Required Experimental Conditions.

The ionizing mhd shocks to be studied are limited to the case where the magnetic field ahead of the shock is uniform and parallel to the shock plane. It can be shown theoretically that below speeds of about 4 cm/μsec these shocks will behave as ordinary gas dynamic shocks. Above this speed the wave becomes a "hybrid" displaying features of both gas dynamic and mhd shocks. At very high speeds (above 15 cm/μsec) the wave probably behaves as a pure mhd shock, although this has not yet been firmly established. The range in between these limits is not completely understood. From a mathematical viewpoint the set of jump conditions becomes incomplete when the pre-shock conductivity vanishes. Attempts to pin down the missing condition have concentrated on examining the internal structure of the wave. When this is done, an upstream electromagnetic field is required (ref. 2) which may or may not be compatible with the boundary conditions imposed by the experimental geometry. This dilemna has not yet been resolved either theoretically or experimentally.

The experimental requirements for studying ionizing mhd shocks are straightforward to define, but not trivial to satisfy. One must produce a clean stable shock wave travelling into a non-conducting gas containing a transverse magnetic field at speeds ranging from 5 to 15 cm/μsec, and one must develop instrumentation capable of measuring the quantities of interest.

In order to study collisionless shocks in the laboratory not only these conditions, but some additional ones, must be satisfied. The additional requirements are more conveniently discussed after the section of the paper dealing with the design of the shock tube proper and will be deferred until that point.

The Inverse Pinch Shock Tube.

The high shock speeds required for these studies preclude the use of conventional shock tubes and lead one to the adoption of an electromagnetically driven shock tube. In such a tube a large current is passed through a narrow layer in the gas. The geometry is arranged such that the Lorentz force resulting from the interaction of this current with its self magnetic field accelerates the gas rapidly, acting as a solid piston if the conductivity is sufficiently high. Since there is no inertia-limited driver gas there is in principle no limit (excluding relativistic considerations!) to the shock speeds attainable.

Electromagnetic shock tubes, as a class, have failed to achieve their performance expectations for three principal reasons: (a) the flow is unstable, (b) the flow is not reproducible, and (c) the shock wave is not cleanly

separated from the magnetic piston. One type of tube, however, has been shown by the present author (ref. 7-9) and other experimenters to be very stable and reproducible. This device is shown schematically in figure (1) and has become known as an "inverse pinch". Current from a capacitor bank is fed through a switch (spark gap or ignitrons) to the center rod and up to the top electrode. It returns in a cylindrical arc, which forms initially in the gas adjacent to the center insulator, to the bottom electrode. The Lorentz force is radially outward and produces a shock wave travelling at high speeds. The addition of an axial magnetic field makes possible the study of mhd shock waves.

In addition to its great stability and reproducibility, the inverse pinch possesses several other advantages. Among these are: (a) a constant shock speed for a linearly rising drive current, (b) great accessibility of the advancing front for measurements, (c) reduced wall effects, (d) constant magnetic pressure over the "piston" face, and (e) orthogonality between the shock-compressed field and the field of the magnetic piston, which makes it possible to distinguish between shock and piston on the basis of simple magnetic probe measurements.

It was noted above that electromagnetic tubes have failed for three reasons: lack of stability, reproducibility, and separation of shock and piston. The first two of these drawbacks are not present in an inverse pinch tube operating at reasonably high shock speeds. However, in order to separate shock and piston, great care in the design of the machine must be taken.

The diffusion depth δ of the magnetic field into the plasma, or equivalently the thickness of the magnetic piston is given by (ref. 12)

$$\delta \approx \sqrt{t/\mu\sigma} \qquad (1)$$

where t is the time, μ is permeability and σ is the conductivity of the shocked gas. The ideal separation distance between shock and piston, Δ, is found from conservation of mass to be given by

$$\Delta \approx \frac{r}{2\epsilon} \qquad (2)$$

where r is the shock location and ϵ is the compression ratio across the shock. Since $r \approx u_o t$, where u_o is the characteristic snowplow velocity,

$$u_o = \left\{ \frac{V_o^2}{L^2} \quad \frac{\mu}{8\pi^2 \rho_o} \right\}^{1/4} \qquad (3)$$

the ratio of piston thickness to ideal separation at a radius R is

$$\frac{\delta}{\Delta} \approx \frac{2\eta}{(\mu\sigma u_o R)^{1/2}} \quad . \qquad (4)$$

The requirement for separation of piston and shock is $\delta/\Delta < 1$. Thus one should use a large radius machine operating at high shock speeds (u_o) and using a gas in which the highest conductivity is achieved. The compression ratio, η, is bounded and decreases in the presence of an axial field which enhances separation of piston and shock.

If δ/Δ is not less than one it is very difficult to do really quantitative shock studies. This point is fundamental and has guided the entire design of the present machine.

The present machine is 18" in diameter and is shown in figure (2). It operates at high voltage (30 kv) and was designed for minimum inductance so as to maximize u_o. An axial magnetic field of up to 4500 gauss and uniform to within 5% is provided by a four element corrected coil system of the type suggested by Barker (ref. 13). These coils are powered by a 30 kilojoule capacitor bank. The inside of the chamber consists entirely of Pyrex, alumina, metal, and Teflon so that outgassing is not a problem. The system base pressure is less than 10^{-6} Torr and the leak rate, with a cold trap, is on the order of one micron per hour or less.

The working gas is usually Hydrogen, which was chosen to minimize the ratio δ/Δ. For a given capacitor bank voltage and initial pressure, the use of H_2 leads to the highest shock speed, u_o. More importantly, however, the highest conductivity is also achieved in Hydrogen for this particular device when operated at high shock speeds. This is a result of the fact that a Hydrogen molecule requires less energy for dissociation and complete ionization than any other element. At the initial pressures used in these experiments, the ionization process is complete at a shock speed of about 7 cm/μsec, and above that speed all the energy behind the shock is invested in translational energy. At the speeds theoretically available in this device (up to 12 cm/μsec without an axial field), Helium will not yet be completely ionized (2nd. ionization) and the temperatures will be substantially lower than those attained in Hydrogen. In intermediate speed ranges, however, Helium will give somewhat higher temperatures. The results of sample calculations are shown in figure (3).

Calculations show that with the speeds attainable in this machine, the necessary conditions for obtaining separation should be obtained. Moreover, the range of shock speeds available should be sufficiently wide to explore

the entire "transition region" for ionizing - mhd shocks referred to above.

In order for a collisionless shock to exist, the mean free path must be smaller than the ion Larmor radius throughout substantially all of the wave. This requires

$$\frac{36\pi}{\sqrt{3}} \frac{\epsilon_o^2}{e^3} \frac{(kT)^{3/2}}{nm^{1/2}} B \gg 1 \qquad (5)$$

This implies one should use a low molecular weight gas at low initial densities. The logical choice is again Hydrogen; these requirements are fortunately compatible with those required to produce separation and to study ionizing-mhd shocks.

It is clear that the pre-shock gas must be ionized for the collisionless shock study. As has been recently pointed out by Gerry, et. al. (ref. 14), this is so in order that all cross sections become small rapidly as the temperature increases through the wave. In particular this requires the absence of neutrals so that charge exchange and atom-atom cross sections, which do not have a Coulombic energy dependence, are not important. It is quite difficult to create a uniform pre-shock state in which the temperature is high enough that the inequality (5) is satisfied; however, it is not difficult to obtain a plasma with a temperature of two or three e.v. in which no neutrals are present. The plasma would then be further heated in the front of the wave to the point where collisions are unimportant. In the present device a second capacitor bank firing through the same electrodes is used for preionization. Experience with this technique has been gained previously with a smaller machine using Argon as the working gas (ref. 9).

INSTRUMENTATION

Several diagnostic techniques are being used in these experiments. They include the following:

(a) Detection of pressure pulse arrival by fast-rise piezoelectric transducers (ref. 15).

(b) Magnetic field and current density mapping by magnetic search coils.

(c) Time integrated spectroscopy for impurity analysis.

(d) A six channel photomultiplier readout head fitted to a commercial 1-5 m. grating spectrograph for time resolved line-line and line-continuum relative intensity measurements.

(e) Single-frame image-converter photography for determination of luminous front configuration.

(f) Electric field measurements using probes of the type described by Lovberg (ref. 16) and improved upon by Sorrell (ref. 17).

(g) Measurement of plasma velocity using a sensitive Doppler shift technique similar to the one developed by Hirschberg (ref. 18).

(h) Measurement of time resolved electron density using a modification of a recently developed gas laser interferometry technique (ref. 19-21).

(i) Measurement of shift to width ratio of a linear Stark broadened line via a technique reported by Cooper (ref. 22) which gives the temperature of the free electrons without requiring assumptions of Saha or Boltzmann equilibrium.

(j) Determination of electron density by using a rapid scanning Fabry-Perot interferometer coupled to a monochromator for measuring the line profile (ref. 23).

The first five of these techniques are already in operation. The next three are under development and are essentially ready to be used. Work is just beginning on the last two.

With most of these techniques only one region or point of the test chamber can be observed on each run. Thus the excellent shot-to-shot reproducibility of the inverse pinch is essential for making meaningful measurements.

PRELIMINARY RESULTS

The machine has been in operation in the form shown in figure (1) for about six months. During this period a great deal of data has been gathered on the operation of the device in general and on the ionizing-mhd shock problem. No preionization bank has been used; thus no data on the collisionless shock has been collected.

General Operation

The diameter of the center insulator is presently 1". The resulting inductance is such that the rise to peak current occurs in 3.0 μs, which is greater than or equal to the time required for a wave to traverse the chamber. Shock waves travelling at the speeds predicted by snowplow theory are observed for initial pressures of 200 microns and greater. The shot-to-shot reproducibility of the experiment is shown by the r-t diagram in figure (4) where each data point was obtained on a different run. The overall features of the flow are shown in the image converter photographs of

figures (5) and (6), which were taken through the side and top respectively. It can been seen from these photographs that the symmetry of the discharge, which is quite good without an axial magnetic field, is enhanced by the presence of such a field. The side photographs show further that the light front becomes extremely straight and well defined when the field is present. At initial pressures below 200 μ, the shock speed is somewhat less than that predicted by theory. These pressures are well below the minimum in the Paschen breakdown curve and breakdown becomes more difficult. It is believed that this difficulty in breaking down the gas affects the entire starting process of the flow in such a way as to lower the shock speeds achieved. Support for this viewpoint comes from the fact that more breakdown difficulties were encountered with a larger center insulator (2" diameter) and that shock speeds in this case were no higher than with the 1" diameter rod although the current rise was considerably faster. This difficulty can probably be alleviated by installing a very small preionization bank with sufficient energy to break down the gas in the vicinity of the center electrode without affecting the main body of the gas. Similar techniques have been successfully employed by other experimenters in magnetic shock tubes.

Separation of Shock and Piston

Early results on achieving separation of shock and piston have been encouraging. The fastest shocks in Hydrogen so far studied in any detail have a relatively low speed of 7.2 cm/μsec (M_s = 55) in the absence of a magnetic field. At this speed ionization has just been completed and from figure (3) the equilibrium temperature is about 25,000°K. It can be shown that under these conditions $\delta/\Delta \approx 1$, i.e. clean separation is not to be expected (without a magnetic field).

Simultaneous pressure probe and magnetic probe data shows that in this case the pressure discontinuity is located at the front of the piston, but is not separated from it. The addition of an axial field should decrease δ/Δ. The lowest photograph in figure (7) shows traces obtained from magnetic search coils, at a radius of 19.2 cm, in Hydrogen with an axial field of 1200 gauss. In this case magnetic compression (B_Z) occurs through the shock so that a positive $\dot{B}_Z$ corresponds to the shock wave. The magnetic piston corresponds to a positive $\dot{B}_Z$ deflection, indicated in the upper trace. The negative $\dot{B}_Z$ signal following the shock is caused by the piston "sweeping out" the axial field which is trapped in the shock heated plasma (ref. 7). This oscillogram shows that magnetic compression is nearly complete before the piston arrives or that separation is to a large extent observed.

The middle photograph shows a run made in Helium at the same voltage and initial pressure. Although the shock speed is lower the Mach number has increased to 65 and from figure (3) it can be seen that the equilibrium temperature is around 50,000°K, with a resulting increase in conductivity of a factor of 2.8. Separation should therefore be enhanced over the corresponding case in H_2. It can be seen from the photograph that this is actually the case; magnetic field compression is essentially complete before the magnetic piston arrives. From these early results it appears probable that clean separation will be obtained for higher shock speeds and magnetic field strengths. (The electrical noise on the traces at about the time of piston arrival is characteristic of the machine when operated with a magnetic field and corresponds to the time of maximum drive current. It has been suggested that this results from arcing or an instability in the spark gap, but to date we have not been able to trace the cause. Our photographs show no evidence of instability in the chamber itself occurring at current maximum).

Ionizing MHD Shocks

Preliminary studies have been carried out on ionizing mhd shocks in the "transition" range of shock speeds referred to earlier. Theory predicts no magnetic field compression below about 5 cm/μsec. Figure (8) shows some typical results. In each case an axial field of 1200 gauss was used.

At an initial voltage of 11 kv, with a resulting shock speed of roughly 4 cm/μsec, no magnetic field compression ($\dot{B}_Z$ positive) is observed. At 15 kv, compression is just beginning to occur and at 25 kv, with a shock speed of 7.2 cm/μsec, significant field compression is evident. These results are in accord with the theory.

CONCLUSIONS

A device for studying mhd shock waves has been designed and built. At initial pressures above 200 μ the performance of the machine is essentially that predicted by theory. Below this pressure, the shock speeds have been less than those predicted for reasons believed to be associated with poor breakdown characteristics.

Evidence has been obtained that separation of shock and piston, a primary goal of the experiment, has been achieved for moderate axial magnetic field strengths.

Early experiments on ionizing mhd waves have verified the change in character from ordinary (gas dynamic) behavior to mhd behavior of the wave as evidenced by magnetic field compression beginning at 5 μs/cm. With the achievement of separation and of the transition in ionizing shocks, the prospect for quantitative studies of such waves using the full complement of diagnostic equipment described above appears very bright.

Work is now under way to reduce the inductance of the device and to promote smooth breakdown at low pressures by using a small preionizing discharge in the region of the center insulator. The development of a large preionization bank for the collisionless shock study has also been initiated.

ACKNOWLEDGEMENTS

This work was supported by the Advanced Research Projects Agency under contract number DA-31-124-ARO (D)-139. The author wishes to acknowledge the substantial help of Mr. E. A. Crawford in performing the experiments.

REFERENCES

(1) A. G. Kulikovskii and G. A. Lyubimov, Rev. Mod. Phys. 32, 977, (1960).

(2) Iu. L. Zhilin, P.M.M., 24 543, (1960).

(3) C. K. Chu, Physics of Fluids 8 1349, (1964).

(4) R. Taussig, Columbia U. Plasma Lab Rept., #12 (July, 1964).

(5) W. B. Kunkel and R. A. Gross, U.C.R.L. Rept. #99 36, (1961).

(6) R. A. Gross, to be published in Rev. Mod. Physics, (1965).

(7) G. C. Vlases, J. F. M. 16 82, (1963).

(8) G. C. Vlases, Phys. Rev. Letters 12 43, (1964).

(9) G. C. Vlases, Phys. of Fluids 7 1358, (1964).

(10) R. M. Patrick and E. R. Pugh, Physics of Fluids 8 636, (1965).

(11) B. Miller, Paper #C7, 5th Shock Tube Symposium, N.O.L., (April, 1965).

(12) G. C. Vlases, Ph. D. Thesis, Cal. Inst. Tech., (December, 1962).

(13) J. R. Barker, J. Sci. Inst. 26 273,(1949).

(14) E. T. Gerry et. al., AVCO Everett R. R. 153, (1964).

(15) H. W. Liepmann and G. Vlases, Physics of Fluids 4 927, (1961).

(16) L. Burkhardt and R. Lovberg, Physics of Fluids 5 341, (1962).

(17) F. Y. Sorrell, Ph. D. Thesis, Cal. Inst. Tech., (1965).

(18) J. G. Hirschberg, Princeton Plasma Physics Lab. MATT Dept. 301, (1964).

(19) D.E.T.F.Ashby and D.F.Jephcott, App. Phys. Letters 3 13, (1963).

(20) D.E.T.F.Ashby et. al., Paper presented at 5th Annual Meeting of Plasma Physics Division, A.P.S., San Diego, Cal. (Nov. 1963).

(21) R. F. Gribble, J. P. Craig, and A. A. Dougal, Appl. Phys. Letters 5 60, (1964).

(22) D. D. Burgess and J. Cooper, to be published.

(23) J. Cooper, J. Sci. Inst. 40 433, (1963).

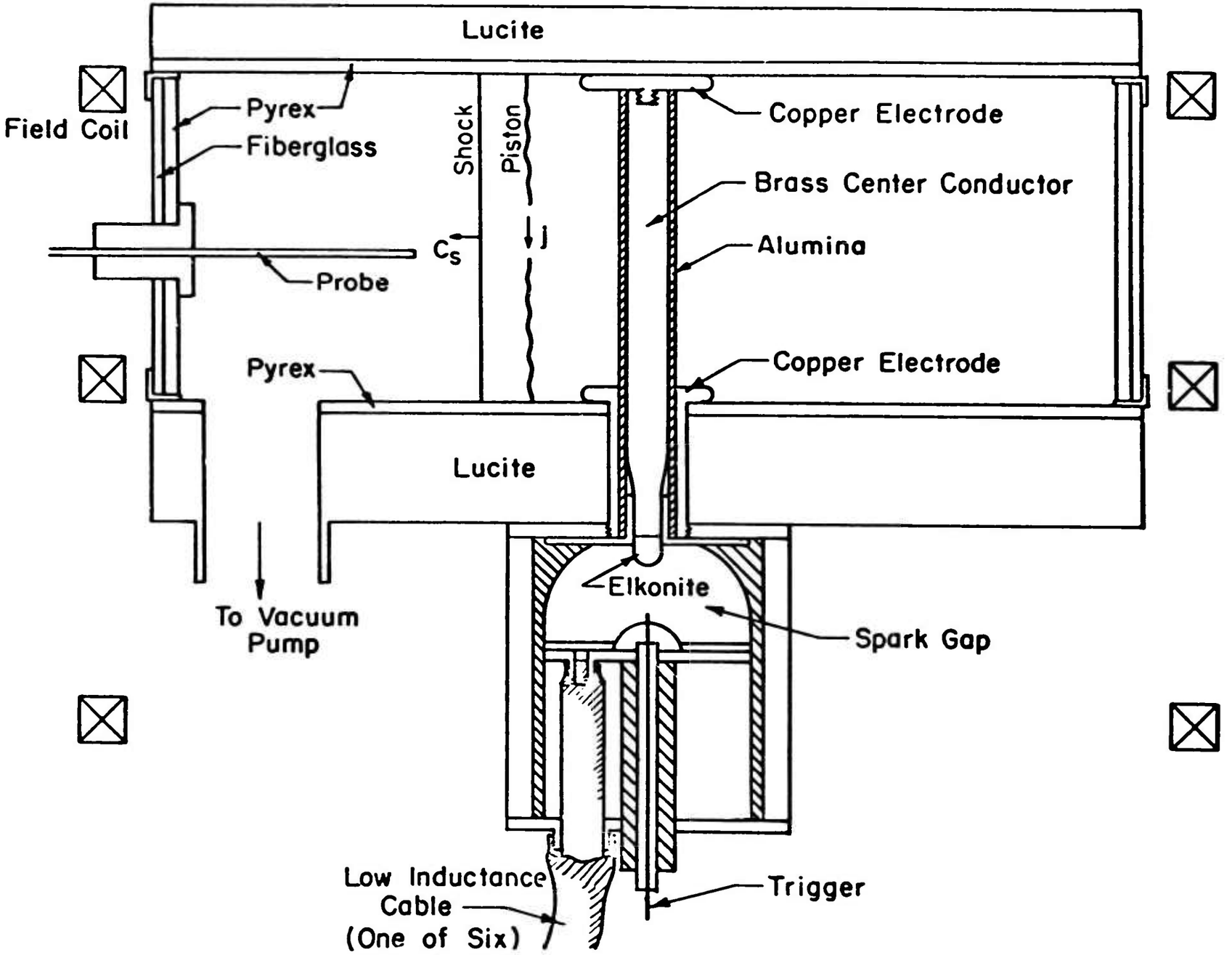


FIG. 1 SCHEMATIC OF INVERSE PINCH MACHINE

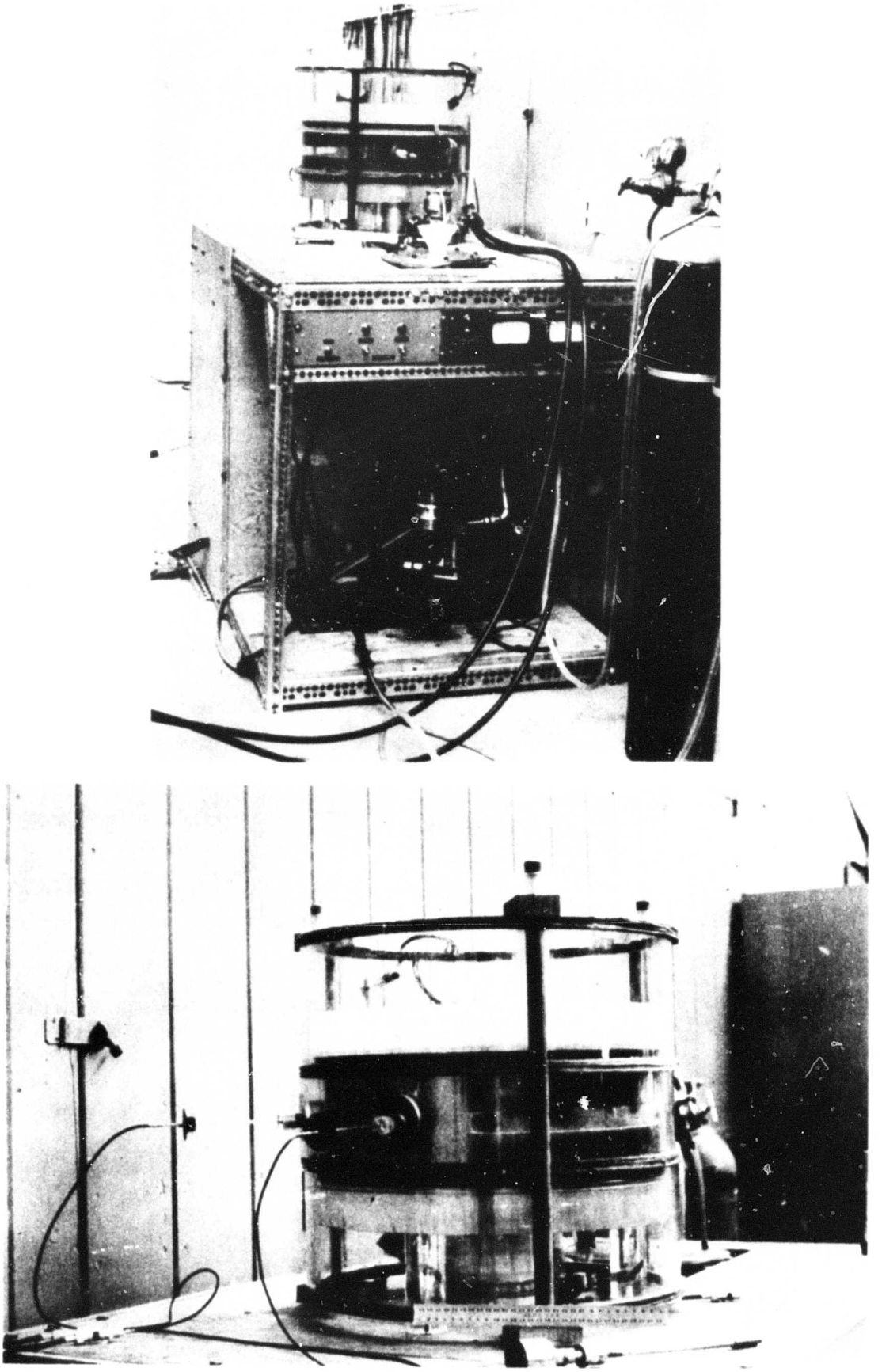


FIG. 2 INVERSE PINCH MACHINE

Equilibrium Temp. Behind Shock Wave vs. Mach Number

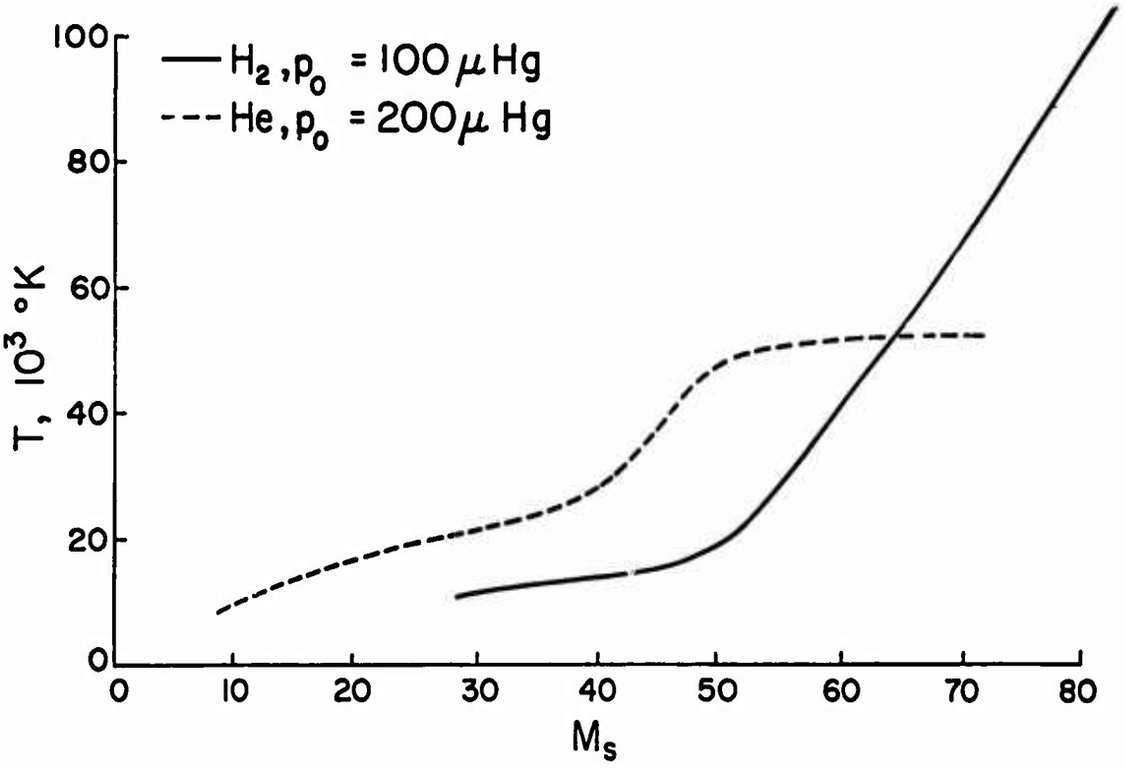


Figure 3

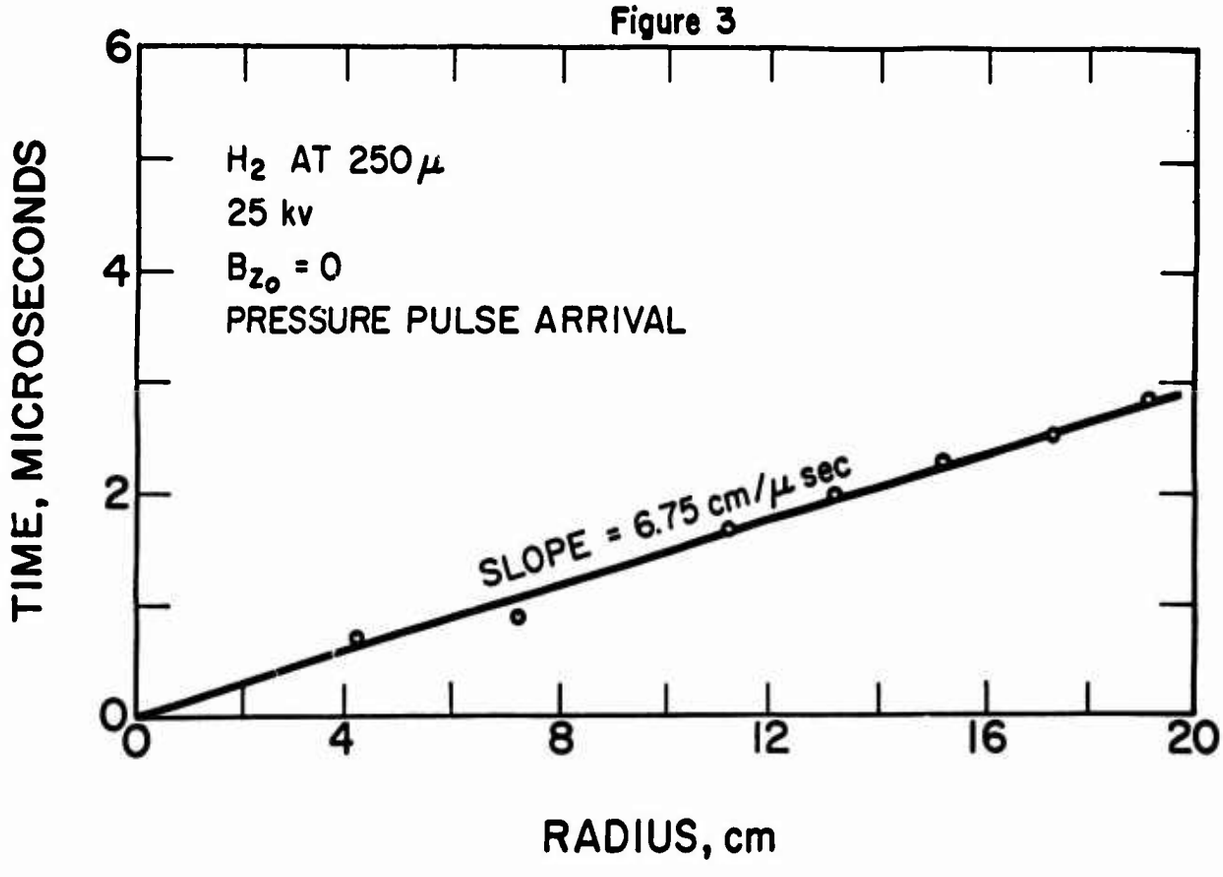
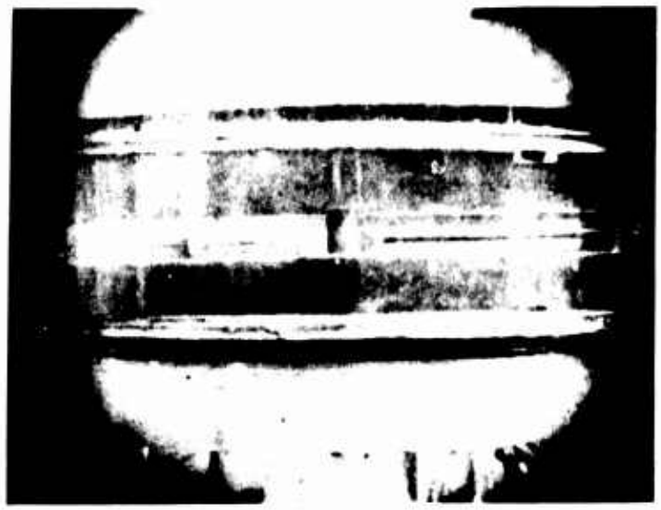
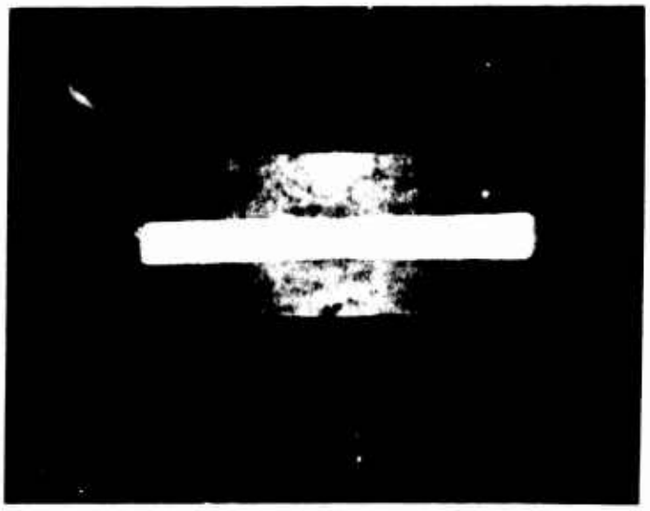


FIG. 4

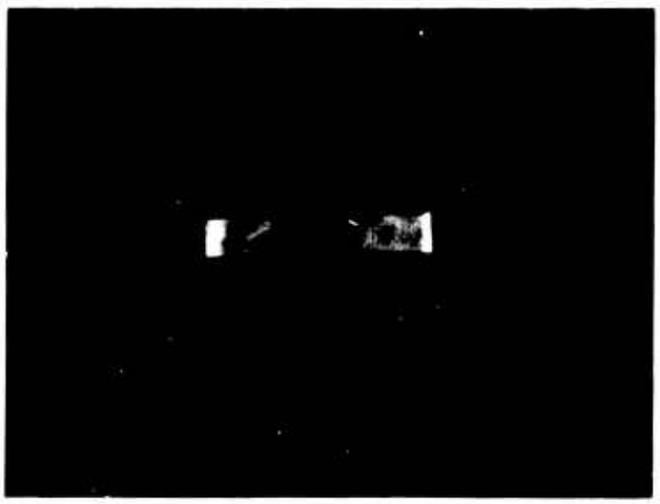
H_2 AT 250μ Hg, 20 kv



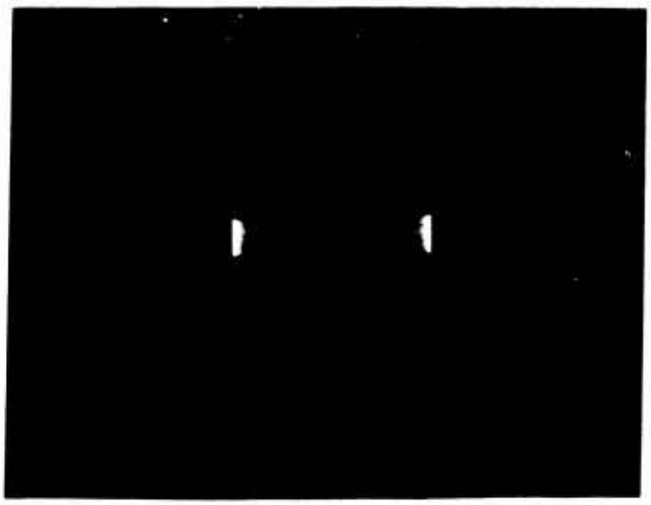
CALIBRATION PHOTO



$B_{z_0} = 0$



$B_{z_0} = 0$



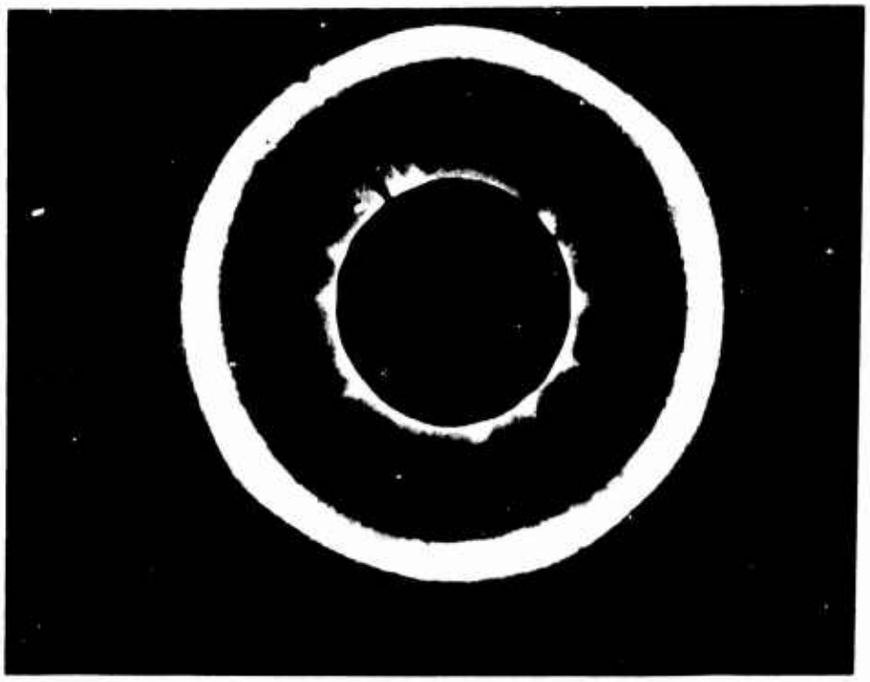
$B_{z_0} = 1600$ g

EXPOSURE TIME : 10 NANOSECONDS

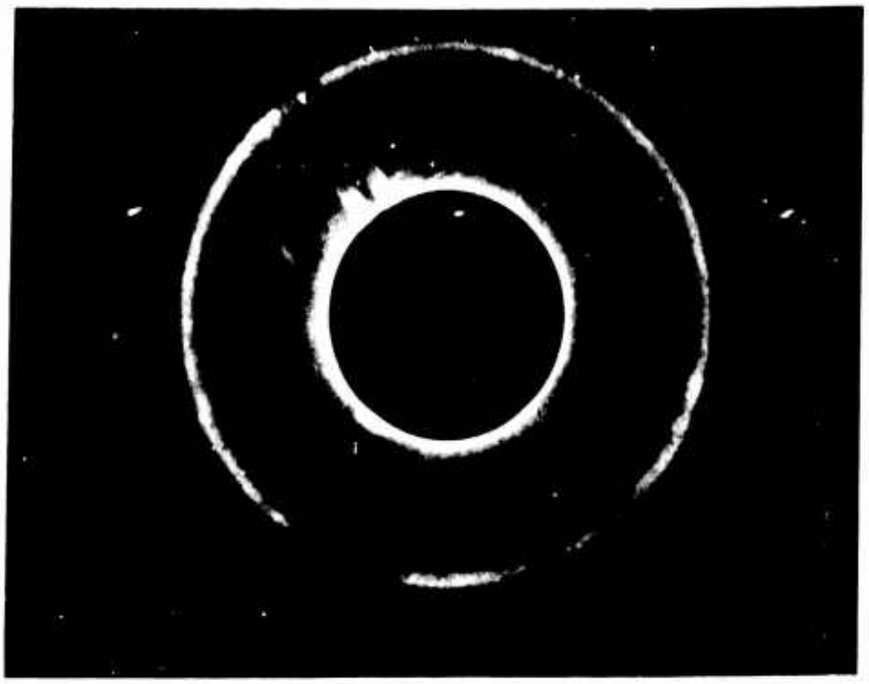
SHOCK SPEED $\approx$ 6 cm/μsec

FIG. 5

H_2 AT 250 μ Hg AND 25 kv



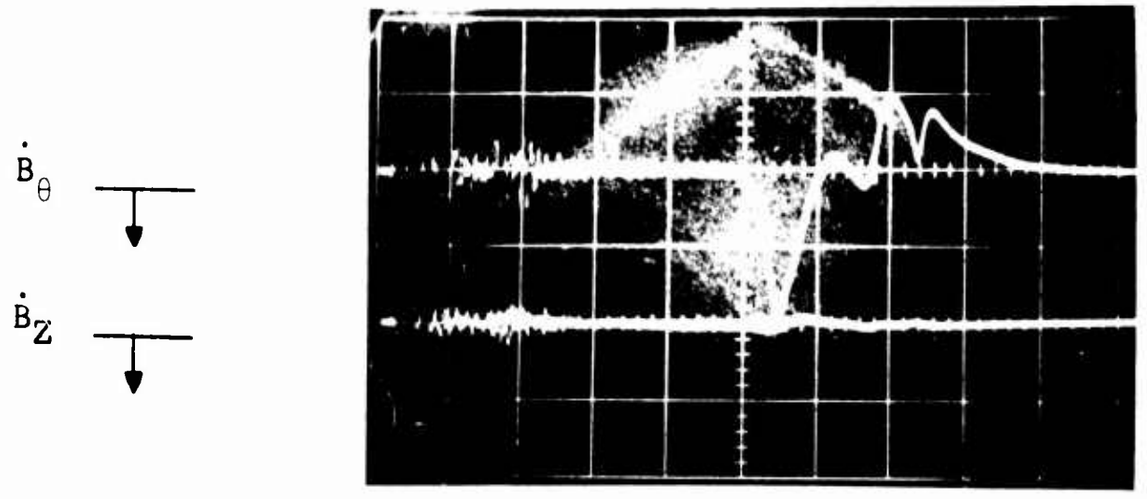
$B_{z_0} = 0$, $r_s = 14.3$ cm



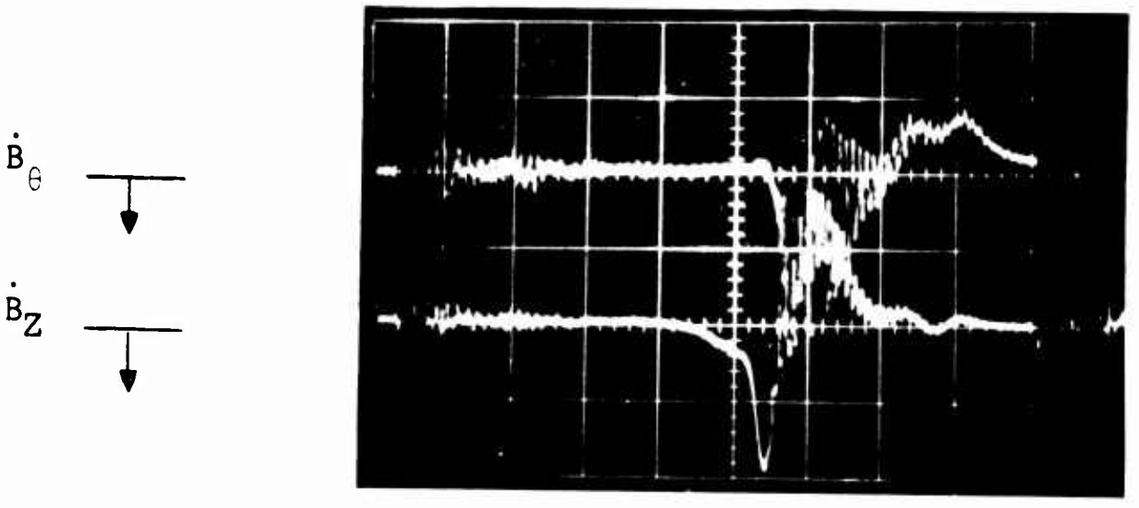
$B_{z_0} = 1600$ g., $r_s = 13.9$ cm

EXPOSURE TIME 10 NANOSECONDS

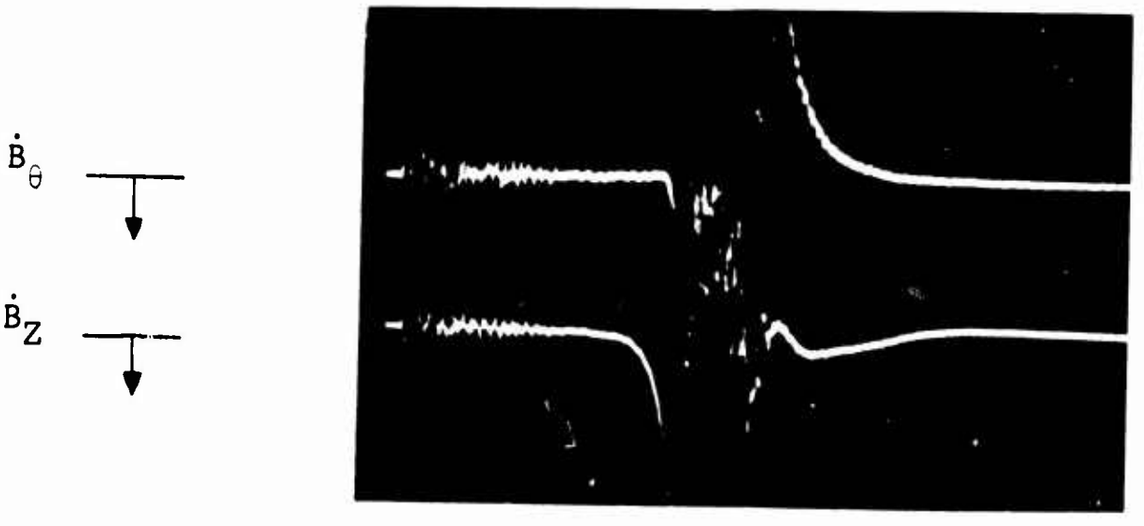
FIG. 6



Helium, $B_{Z_o} = 0$



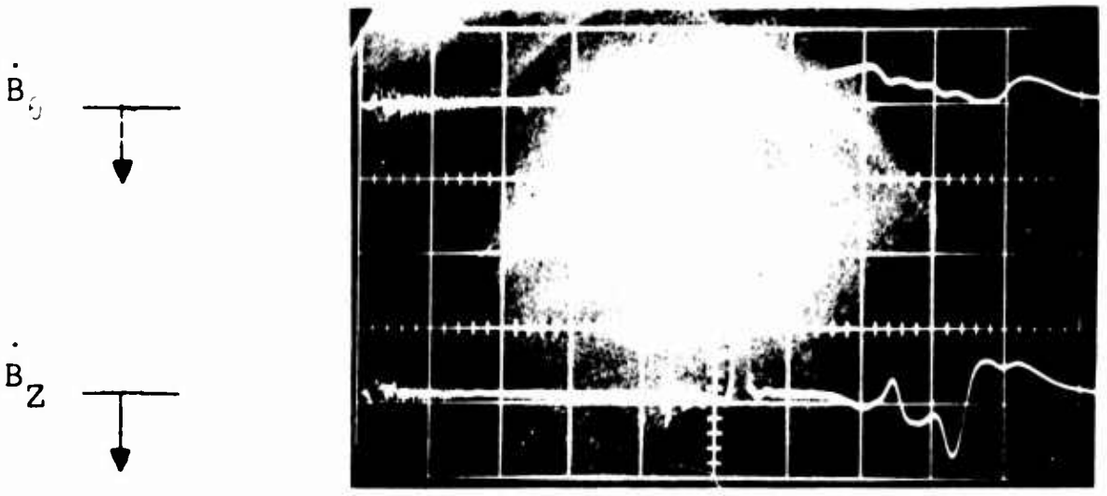
Helium, $B_{Z_o} = 1200$ g.



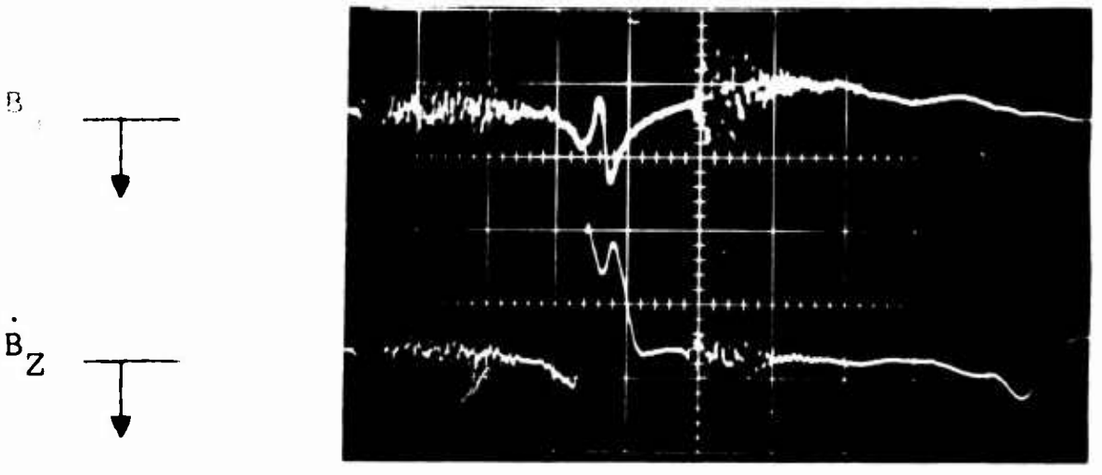
Hydrogen, $B_{Z_o} = 1200$ g.

FIG. 7. SHOCK AND PISTON POSITIONS

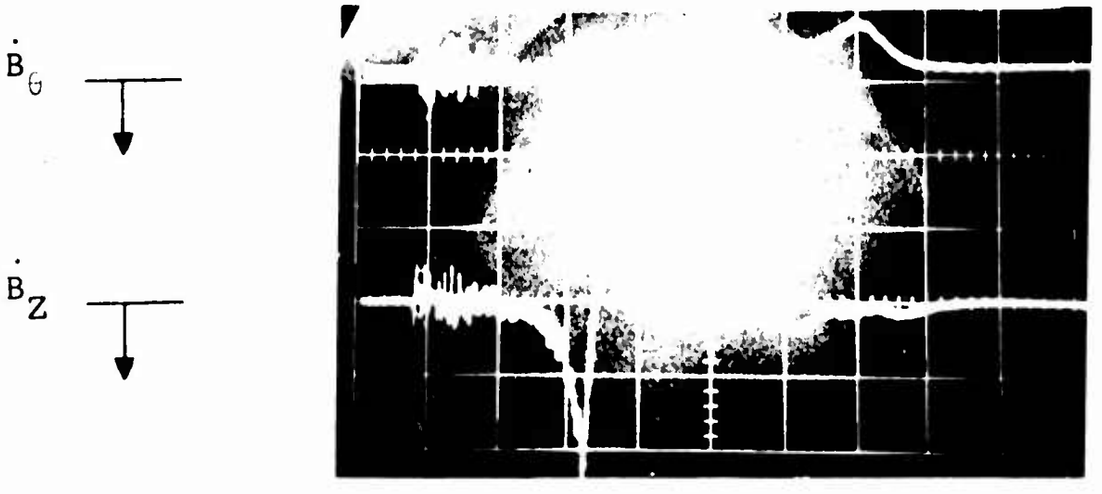
$p_o = 250\ \mu$ Hg; Sweep Rate = 1 cm/μsec, $V_o = 25$ kv



V_o = 11 kv, Sweep = 2 μs/cm



V_o = 15 kv, Sweep = 1 μs/cm



V_o = 25 kv, Sweep = 1 μs/cm

FIG. 8 DEVELOPMENT OF MAGNETIC FIELD COMPRESSION ACROSS IONIZING-MHD SHOCK WAVE

H_2 @ 250 μHg., r = 14 cm, B_{Z_o} = 1200 g.

BLANK PAGE

VIBRATIONAL RELAXATION OF DEUTERIUM*

John H. Kiefer and Robert W. Lutz
University of California
Los Alamos Scientific Laboratory
Los Alamos, New Mexico

ABSTRACT

A quantitative schlieren method is described which uses photomultiplier detection of the deflection of a narrow gas laser beam to obtain a close approximation to a point measure of density gradient. This method is very sensitive to rapid density changes (a gradient of 5×10^{-5} gm/liter-mm can be detected in argon) and laboratory relaxation times as short as 0.2 μsec can be measured in the shock tube. The application of this technique to studies of vibrational relaxation is discussed in detail, and the method is compared with the integrated schlieren of Resler and Scheibe for this application.

This technique has been applied to a shock tube study of the vibrational relaxation of mixtures of D_2 in Ar with the results, in atm·sec:

$P\tau = (2.7 \pm 0.3) \times 10^{-10} e^{(110.5 \pm 1.5)/T^{1/3}}$ (1100 - 3000°K) for pure D_2 and $P\tau = (1.0 \pm 0.7) \times 10^{-9} e^{(118 \pm 10)/T^{1/3}}$ (1600 - 3000°K) for D_2 dilute in Ar. The experimental results are in serious disagreement with both the correlation scheme of White and Millikan and the SSH theory.

*Work performed under the auspices of the U. S. Atomic Energy Commission.

INTRODUCTION

Experiments using the shock tube in conjunction with infrared emission and interferometric measurements have produced vibrational relaxation times of good accuracy over a much greater range of temperatures than is available from other methods[1]. The high temperatures attainable in the shock tube also suggest the possibility of measuring relaxation times densitometrically for infrared inactive species such as hydrogen or deuterium, whose vibrational heat capacities are too small at lower temperatures for detection by ultrasonic or impact tube methods. The results of such an investigation on deuterium in particular should be of chemical interest for their possible relevance to the mechanism of isotopic exchange[2].

White[3] has recently reported a relaxation time of $(4 \pm 2) \times 10^{-6}$ atm·sec for D_2 at 1400°K from a shock tube interferometry experiment. The rapidity of the relaxation, the small density changes in the relaxation zone which result from the low vibrational heat capacity, and the low molar refractivity of D_2 make this measurement very difficult--this estimate of relaxation time was derived from a fringe shift of 0.2 fringes. Accurate measurement of relaxation times for D_2 evidently requires a densitometry technique of greater sensitivity than conventional interferometry.

The authors have described a very sensitive quantitative schlieren method[4] which uses knife-edge--photomultiplier detection of the deflection of a narrow gas laser beam to obtain a close approximation to a point measure of density gradient for one-dimensional flow. The method

is similar to the integrated schlieren of Resler and Scheibe[5], but differs in its use of a laser light source and a narrow beam configuration. The high sensitivity of the present technique is a consequence of the extreme brightness of the laser, and the narrow beam arrangement is advantageous with the laser since it avoids the problems of nonlinear response of schlieren systems with highly parallel light (this behavior has been called saturation by de Boer[6]) without significant loss of sensitivity.

This paper presents an extended discussion of a considerably improved version of the original narrow beam schlieren method[4] and an investigation of the vibrational relaxation of normal D_2 in shock waves using this method.

EXPERIMENTAL

The Shock Tube

The 3 in. shock tube and its associated equipment have been described previously[7][8]. However, some changes appropriate to the present investigation have been made, and these require description.

An entirely new pumping and gas handling facility was installed with all connection to the shock tube now made in the vicinity of the end plate. A Consolidated Vacuum Corp. type PMC 720 diffusion pump with Dow-Corning 705 silicone fluid and a larger forepump allowed more rapid attainment of higher vacua. In the experiments the tube was pumped to below 0.05 μ before introducing the test gas. The leak or outgassing rate was about 0.1 μ/min and the time between filling the tube and initiating the shock wave was kept below 1 minute in all cases.

For the schlieren experiments the section of shock tube containing the x-ray slits was replaced with a new section fitted with 11" x 1/2" glass windows. The windows were installed in the 3" diameter cylindrical tube by milling two opposite parallel flat areas until a slot 11" long by slightly less than 1/2" wide appeared. The slot was opened to 1/2" leaving edges of .010" thickness. Two pieces of optical plate glass 11" x 2" x 3/8" were then cemented to the exposed flat areas with a flexible epoxy adhesive. With this arrangement the upstream edge of the glass plates protrudes less than .010" into the tube. Observation by the laser beam was made 9" from this upstream edge.

Commercial gases were used with some purification. Before purification the gases were subjected to mass-spectral analysis with the result for D_2: 98.58% D_2, 0.31% H_2, 0.92% HD, and less than 0.1% Ar and N_2. The argon showed less than 0.1% impurities, primarily N_2. Mixtures of these gases were prepared manometrically in a glass-lined hot water tank which had been baked out at ~100°C for several days and the mixtures were allowed to stand in this tank for more than 15 hours before use for mixing. The D_2 was admitted to the tank through alumina at liquid N_2 temperature and the argon admitted directly. The shock tube was filled from this tank through the end plate and the initial pressure read with a mercury manometer. Initial temperature was taken to be the tube temperature measured for each experiment. Shock waves were produced by bursting scribed brass diaphragms with hydrogen and helium. All measurements were made on the incident shock. The range of initial conditions employed in the experiments is shown in Table 1.

The Schlieren System

A schematic of the apparatus is shown in Fig. 1. A 6328 Å helium-neon gas laser is the light source. The beam from the laser is reflected by the 25% transmitting, front surface mirror M_1 into a 6/1 demagnifying telescope T_1 before traversing the shock tube through the windows W_1 and W_2. The beam diameter is then about 0.8 mm (distance between e^{-2} points of the Gaussian power distribution) inside the tube. After leaving the shock tube the beam is focused by the 1/1 telescope T_2 onto the knife edge K placed 7 m from T_2. The light passing this knife edge is detected by a photomultiplier and the resulting signal amplified and displayed on an oscilloscope. The change in signal observed by the oscilloscope is then a record of the deflection of the beam and consequently a measure of the density gradient in the shock tube. The energy transmitted by the mirror M_1 bypassed the shock tube and was detected by a second photomultiplier and oscilloscope. This monitor record was then used to correct the base line of the schlieren record for slight variations ($\sim$0.25%) in beam intensity. A more detailed description of the entire system follows.

The Laser and Optical System

The laser was a Spectra-Physics Model 115 supplying a diffraction-limited uniphase beam of 5 mW total power. The beam diameter at the laser is 3.6 mm, (distance between e^{-2} points) and the divergence is about 2.7×10^{-4} radians full angle.

The beam from a uniphase gas laser has a nearly Gaussian power distribution across its wave front. That is, if the z axis is taken

to be the direction of propagation, then the power distribution in the x,y plane is

$$P(x,y) = \frac{P_o}{\pi\sigma^2} \; e^{-(x^2 + y^2)/\sigma^2} \qquad (1)$$

where P_o is the total beam power, and σ is the standard deviation of the Gaussian function.

As the beam traverses the optical system σ varies with z. For example, it is a minimum at the internal foci of the telescopes and a maximum at the knife edge where $\sigma = \sigma_k \sim 2.8$ mm. The 6/1 reduction in diameter accomplished by T_1 increases the beam divergence by the same factor, so that the fractional change in beam diameter across the 10 cm path from T_1 to W_2 is significant. In the present case, further telescopic reduction will actually broaden the beam and the beam used here with $\sigma = \sigma_t \leq 0.30$ mm in the shock tube is essentially the smallest that can be obtained.

Accurate alignment of the beam normal to the shock tube axis is important for good space resolution. The beam was aligned normal to the shock tube windows by superimposing reflections from the windows with the transmitted beam at a distance of several meters. With this procedure alignment in the horizontal plane (the plane of Fig. 1) was kept within 50 seconds of arc of normal, but the beam was slightly misaligned in the vertical plane to avoid detection of the window reflections. For this alignment, the mirror M and the telescope T_1 were provided with finely adjustable kinematic mounts.

The Beam Deflection Detector

The deflection detector is taken to include the knife edge, photo-tube, and associated electronics including the oscilloscope.

The knife edge is a simple straight edge (razor blade) aligned perpendicular to the shock tube axis, initially positioned at the center of the focused beam, and oriented to produce a reduction in transmitted intensity for the deflection generated by an increasing post-shock density. The 7 m path from telescope T_2 to the knife edge produces a large diameter focus on the edge. This facilitates positioning the knife edge at the beam center, and makes a high quality edge unnecessary. The long path also helps eliminate detection of emission from the heated gas in the shock tube and RF pickup from the laser power supply.

The photomultiplier and associated circuitry must respond linearly to high light intensities, have a rapid transient response, and recover accurately from large transients. The following system was constructed to meet these requirements: The photomultiplier was an RCA model 7265, with S-20 spectral response, protected from extraneous light with a 6328 Å interference filter. This photomultiplier was employed in a circuit modified for linear response to high light intensity. In this modification, the signal was taken from the sixth dynode--dynodes seven through fourteen, the accelerating electrode, and the anode were grounded. Circuit potentials were: 200 V between cathode and focusing electrode, 240 V between cathode and the first dynode, and 110 V between succeeding dynodes. All stages were protected with 8 μF capacitors. With this circuit the tube current was 0.7 mA through a 1500 ohm output resistor

for 0.5 mW incident power. The phototube circuit was followed by a cathode follower stage with a gain of 0.85 and a transistorized preamplifier having a gain of ten. The amplified signals were then displayed on a Tektronix 545 oscilloscope with type Z plug-in, and photographed. The preamplifier, designed by Richard Hiebert of this laboratory, has a rise time of 50 nsec and is linear to 1% for output voltages up to 10 V. A maximum output of 7 V is obtained with the addition of a 0.3 neutral density filter in front of the photomultiplier as used here. The overall system rise time is that of the preamplifier.

An identical photomultiplier-cathode follower combination was used to monitor the beam intensity, but in this case the amplifier had a time constant of 1 μsec and the signal was recorded on a Tektronix 515 oscilloscope. In an experiment the two oscilloscopes were triggered simultaneously. Accurate timing correlation was obtained through the use of an earlier, simultaneously triggered display of timing markers.

Component linearity was determined as better than 2% by measuring relative oscilloscope deflections for 1 Kc input square waves of varying amplitude. Photomultiplier linearity was tested by interrupting the beam with a two-slot 3500 rpm chopper wheel which had one slot covered with a 0.3 neutral density filter. The ratio of the signals generated by the two slots was observed and the beam intensity reduced until linear response was obtained. For the present apparatus the full beam intensity at the phototube (0.7 mW with the knife edge inserted) caused saturation, and a 0.3 neutral density filter was placed before the phototube surface to bring the response into a linear region. With this arrangement the

system is linear to within 2% for further reduction in signal. This chopper was also used to determine the magnitude of the unmodulated dc signal.

A separate experiment confirmed that the power distribution at the knife edge was indeed the expected Gaussian function. A rotating mirror was inserted into the beam near the shock tube and the response of the detector observed as the beam swept across the knife edge. The expected integral of the Gaussian power distribution was traced on the oscilloscope within the 2% accuracy of the measurement.

The range of linearity of the beam deflection detector can then be defined in the following way. For a deflection D of the beam initially centered at the knife edge,

$$\frac{\Delta V}{V_o} = -1/2\ \mathrm{erf}(D/\sigma_k) \qquad (2)$$

where $\frac{\Delta V}{V_o}$ is the fractional change in signal (percentage modulation $= \left|\frac{100\Delta V}{V_o}\right|$) and σ_k is the standard deviation of the Gaussian distribution, Eq. (1), at the knife edge. Expanding (2) for small D gives

$$\frac{\Delta V}{V_o} = -\frac{D}{\pi^{1/2}\sigma_k}\left(1 - D^2/3\sigma_k^2 + \ldots\ldots\right) \qquad (3)$$

If it is assumed for the moment without proof that in an actual shock wave experiment the beam is essentially deflected as a unit so that this equation may also be applied to that situation, then for a 15% modulation the non-linear term is 2.2×10^{-2} and as long as the modulation is less than 15%, as in all the present experiments, the deflection detector is linear to about 2%.

Spatial Resolution

The question of spatial resolution with the narrow beam system involves two separate considerations in the present application: (i) the spatial resolution near the shock front, indicated by the distance interval between the front and the first quantitative gradient measurement, and (ii) the resolution of subsequent density variations. It is convenient to discuss (ii) first.

Since the laser beam is of finite width in the shock tube, after the shock front has left the beam the observed change in signal at the knife edge is proportional to an average of the density gradient over the width of the beam. Now the deflection of a single ray of the beam is given by

$$D(x,t) = RLW \frac{d\rho}{dx} \quad (x,t) \tag{4}$$

where R is the specific refractivity of the test gas (Gladstone-Dale constant), L is the distance from the focusing optics (T_2) to the knife edge, W is the internal diameter of the shock tube and $d\rho/dx$ is the density gradient function. x is an axial coordinate fixed in the shock tube, increasing towards the diaphragm, and with its origin at the center of the beam. Using Eq. (4) and the linear form of Eq. (3), a general expression for the post-shock modulation is then

$$\frac{\Delta V}{V_o} = - \frac{RLW}{\pi^{1/2}\sigma_k} \int_{-\infty}^{+\infty} P(x) \frac{d\rho}{dx} \quad (x,t)\, dx \tag{5}$$

where P(x) is a normalized function describing the power distribution across the beam wavefront in the shock tube. P(x) is as yet unspecified and need not be the Gaussian function of Eq. (1).

The important question is to what extent the present apparatus gives a point measure of density gradient. To answer this it is necessary to specify further the density gradient function and to some extent P(x). For a vibrational relaxation process in a shock tube, the density is known to follow closely an exponential variation with time, and an estimate of the deviation from a point measure appropriate to the present investigation can be obtained by assuming an exponential gradient.

Let

$$\frac{d\rho}{dx}\ (x,t) = \frac{\Delta\rho}{U\tau}\ e^{-(t + x/U)/\tau} \qquad (6)$$

in the relaxation zone. Here $\Delta\rho$ is the total change in density, U is the shock velocity, and τ is the apparent relaxation time in laboratory coordinates. Then from Eq. (5)

$$\frac{\Delta V}{V_o} = - \frac{RLW\Delta\rho}{\pi^{1/2}\sigma_k U\tau}\ e^{-t/\tau} \int_{-\infty}^{+\infty} P(x)e^{-x/U\tau}dx = - \frac{RLW}{\pi^{1/2}\sigma_k}\ \frac{d\rho}{dx}\ (0,t - \Delta t) \qquad (7)$$

and the only distortion of the proportionality to density gradient is a shift Δt in the origin of time. This result is independent of P(x) and, of course, the time shift is of no significance if the gradient is truly exponential. The magnitude of Δt depends on the width of P(x) and the values of τ and U. Using the integral over y of the Gaussian function, Eq. (1), for P(x) and Eqs. (5) and (6), $\Delta t = \sigma_t^2/4U^2\tau$ and the largest Δt encountered in the present experiments can then be estimated from this expression as 0.008 μsec. Thus the deviation from a point measure is insignificant for an exponential gradient and this small size also indicates

that the modulation will be closely proportional to the density gradient when the gradient deviates slightly from an exponential. A study of Eq. (5) for nonexponential dρ/dx bears out this conclusion but shows that extreme cases must be carefully considered. It must be emphasized that P(x) need not be exactly Gaussian for the above considerations to apply. The small size of the deviation from a point measure also implies that the beam is deflected essentially as a unit during the observation of the relaxation zone in D_2, which was assumed in the earlier discussion of the linearity of the beam deflection detector.

The above analysis assumes a thin shock with time measured from the coincidence of this shock and the center of the beam. In actuality the shock is not thin and this fact must now be considered. Daen and de Boer[9] have suggested that the effective shock thickness in a schlieren experiment is caused by curvature near the wall; and, in argon and helium, with initial pressures and Mach numbers in the range of the present experiments they found this thickness to vary from 0.15 - 0.4 mm in a 1 in. tube. By assuming that an element of the beam equal to the shock thickness is displaced off the phototube as the shock traverses the beam, this thickness can also be derived by the present technique. Let δ be the shock thickness, then the change in signal as the shock traverses the beam is

$$\frac{\Delta V}{V_o} = - \int_{Ut-\delta}^{Ut} \frac{1}{2\pi^{1/2}\sigma_t} e^{-x^2/\sigma_t^2} dx \qquad (8)$$

where t = 0 is now taken as the coincidence of the leading edge of the shock with the beam center. The result of Eq. (8) will be a sharp spike

in $\left|\Delta V/V_o\right|$ with a distinct maximum at Ut = δ/2. Thus

$$\left|\frac{\Delta V}{V_o}\right|_{max.} = 1/2 \text{ erf } (\delta/2\sigma_t) \qquad (9)$$

Figure 2 shows an example of this schlieren spike for a shock in argon. The values of δ derived from experiments of this kind and Eq. (9) are in agreement with the results of Daen and de Boer when the latter are increased by the square root of the tube diameter ratio[10].

The question of the effective shock thickness in the D_2 experiments is complicated by the presence of rotational and vibrational relaxation. However, a number of experiments in the D_2 - Ar mixtures exhibit the entire schlieren spike (see, for example, Fig. 4), and an estimate of δ from Eq. (9) and these pictures shows that δ probably lies between 0.25 and 0.80 mm in the relaxation experiments.

De Boer[10] has noted that the shock curvature places a fundamental limitation on the spatial resolution of density variations in a relaxation zone. The above discussion shows that for the present experiments this limitation is far more significant than any consequence of the finite beam.

It is convenient and reasonably accurate to take the maximum of the initial schlieren spike as the time origin for the relaxation. This implies that the time in Eq. (6) is probably underestimated by about δ/2U. As will be seen later, this error has no significant effect on the derived relaxation times; however, it can have an important effect on an evaluation of the total change in density. This last point is demonstrated in the subsequent analysis section.

Consideration (i), above, derives from the necessity for waiting until the shock front has effectively left the beam before quantitative gradient measurements can be made. In a relaxation experiment, the first measurement would be made at that point where the modulation caused by the shock, Eq. (8), has become negligible with respect to the modulation from the relaxation. The distance lost to observation, X_L, is then a function of the effective shock thickness and the modulation produced by the relaxation. Thus X_L is different, in general, for each experiment. Without discussing individual experiments, Eq. (8) with the previous estimates of δ and the observed relaxation modulations shows that a maximum estimate of X_L varies between 0.5 and 0.8 mm. These values then represent an approximate description of the spatial resolution near the shock front. With the present shock velocities the time lost to observation lies between 0.15 and 0.5 μsec.

Discussion

In the configuration described above the method is very sensitive to rapid changes in density. The minimum gradient detectable over the statistical noise is less than 5×10^{-5} gm/liter-mm in argon ($|\Delta V/V_o| < 0.001$) and this corresponds to a fringe shift of less than 0.002 fringe/mm from an interferometer observing the same shock tube. The maximum gradient which can be observed before the nonlinearity exceeds 2% is 1×10^{-2} gm/liter-mm, again in argon. Thus the method will respond linearly to a range of more than two decades in density gradient. The upper end of the range can be extended somewhat by numerically solving Eq. (2) for D, but this procedure was unnecessary in the present case, where the modulation always remained less than 15%.

An alteration in the magnification of telescope T_1 or of the specific refractivity of the test gas, for example, will change both the lower and upper limits of the linear range in the same manner. As long as the beam remains sufficiently narrow for the system to respond to density gradient, the factor of 200 between the two limits will be maintained. This ratio of maximum to minimum gradient, in fact, depends only on the detector efficiency and bandwidth, and the useful power at the detector.

A comparison of the narrow beam approach with the integrated schlieren of Resler and Scheibe[5] will serve to define the useful sensitivity of the two methods and explain the choice of the narrow beam technique for the present investigation. The simplest method for making this comparison in an appropriate manner is to consider the signal obtainable from the two methods when both are responding to the same exponential density variation, and when the maximum gradient appearing during this density variation is also the maximum gradient to which both methods will respond linearly. That is, the optics are adjusted so that both techniques have the same upper limit to their linear range. In order to make this comparison meaningful the following additional assumptions are required: (i) R, L, W, and V_o are the same for both (unmodulated signal limited by photomultiplier saturation); (ii) the same laser is used as light source for both which implies identical σ_k since both systems are assumed to become nonlinear for the same gradient.

Eq. (5) still applies to the integrated approach, but P(x) must now be made constant by beam confining slits. This implies

$$P(x) = 1/b \quad \text{from } x = 0 \text{ to } b,$$

and F(x) = 0 outside this range. Thus (5) can be used to give

$$\left(\frac{\Delta V}{V}\right)_{o\ \text{integrated}} = -\frac{RLW}{\pi^{1/2}\sigma_k b}\left[\rho(0,t) - \rho(b,t)\right] \tag{10}$$

If the measurement is to be a complete integration, the beam must be sufficiently wide for point b to be essentially in the region of equilibrium flow throughout the observation. For the exponential variation $\rho(b,t) = \rho_{\text{equilibrium}}$ to 2% (a reasonable requirement) for $b \geq 4U\tau$ (see Eq. (6)). Let $b = 4U\tau$; then using the integral of Eq. (6), Eq. (10) becomes

$$\left(\frac{\Delta V}{V}\right)_{o\ \text{integrated}} = -\frac{RLW(\Delta\rho)}{4\pi^{1/2}\sigma_k U\tau}\ e^{-t/\tau} \tag{11}$$

From Eqs. (6) and (7)

$$\left(\frac{\Delta V}{V}\right)_{o\ \text{narrow beam}} = -\frac{RLW(\Delta\rho)}{\pi^{1/2}\sigma_k U\tau}\ e^{-t/\tau} \tag{12}$$

Thus

$$\frac{(\Delta V)_{\text{narrow beam}}}{(\Delta V)_{\text{integrated}}} = 4 \tag{13}$$

or the narrow beam system affords at least a factor of 4 larger signal for the observation of this exponential gradient. This also implies that the narrow beam system will respond linearly to a factor of 4 larger gradient when both methods are set for the same sensitivity. This result is the principal advantage of the narrow beam, and reason for its use in the present investigation.

Physically, the factor of four in Eq. (13) arises from the confinement of the energy of the beam to the region of highest gradient with the narrow beam. If the unmodulated signal were limited by beam energy rather than photomultiplier saturation, this factor would be considerably larger since the necessity for beam confining slits greatly reduces the transmitted energy with the integrated system.

Because of the greater parallelism and correspondingly smaller σ_k possible with a broad beam, the integrated system is capable of greater sensitivity than the narrow beam system. However, the previous discussion shows that the integrated system will then be nonlinear even for extremely small gradients. For example, if the integrated system should be constructed to have a factor of five greater sensitivity than the narrow beam system for the observation of a relaxation process, it will also necessarily have at least a factor of 20 smaller upper limit to its region of linear response. Certainly the method would then be of very limited applicability since, even for the rather small density changes encountered in the D_2 experiments, the maximum gradients are often near the upper limit of the linear range of the narrow beam system.

A more serious limitation on the usefulness of greater sensitivity is indicated by the observation of shocks in pure argon with high amplification. An oscillogram of such an experiment is shown in Fig. 3. Subsequent to the shock spike an irregular modulation on the order of 0.2% or less can be seen on this record. These schlieren measurements necessarily include the boundary layer, and the above phenomenon is perhaps a result of boundary layer near the shock front. However, regardless of its

origin, in the presence of such an effect it is evident that any increase in the sensitivity of a technique which can already detect a modulation of 0.1% would be useless. The implications of this observation for the D_2 experiments are discussed later.

ANALYSIS AND RESULTS

Figures 4, 5, and 6 show example schlieren records of shocks in D_2 - Ar mixtures. In Fig. 4 the entire spike is clearly visible. In this case the origin of the time axis is taken as the maximum of this spike. In the other two figures this maximum is off scale and the time origin is then estimated as the midpoint of the truncated remnant of the spike that shows on the oscillogram. After the shock front has left the beam (this point can be seen as a distinct break in the slope on the right-hand side of the spike) the subsequent modulation amplitude $h = \left|\Delta V/V_o\right|$ is proportional to the density gradient in the vibrational relaxation zone and the slow fall after the initial spike in all three figures is due to relaxation.

A plot of $\log_{10}(h)$, corrected for monitor variation, is shown for the example of Fig. 5 in Fig. 7. This plot is linear, as expected for a vibrational relaxation process in which the temperature changes are small. In none of the present experiments was any significant deviation from exponential behavior observed and there is thus no distortion of the relaxation data either by limited space resolution or difficulty in placing the time origin.

From the slope (S) of such logarithmic plots an apparent relaxation time can be derived from $\tau_{apparent} = 1/2.303|S|$. To specify conditions in the relaxation zone, state variables were obtained from a computer solution of the Hugoniot equations[11] for each experiment at two points: (a) rotational and translational equilibrium but no vibrational excitation, and (b) complete equilibrium. For the equilibrium calculations, enthalpy data for D_2 were obtained from NBS Monograph No. 20[12]. Functions for the frozen or unrelaxed condition (a) were derived from the equilibrium values by subtracting from these the vibrational enthalpy derived from the partition function,

$$Q_{vib} = (1 - e^{-u})^{-1} \left(1 + \frac{\delta}{e^{u} - 1}\right) \left(1 + \frac{2\theta}{(e^{u} - 1)^{2}}\right)$$

where $u = 4311.1/T$, $\delta = 0.0350$, and $\theta = 92.26/T$ (see pg. 3 of reference (12)). Table 2 shows the range of post-shock conditions employed in these experiments derived by the above procedures.

To confirm that this exponential variation is indeed caused by vibrational relaxation of D_2, a comparison was made of the measured total change in density with the change derived from the Hugoniot computations. The equation

$$\int_{a}^{b} \frac{d\rho}{dx}\, dx = \Delta\rho \qquad (14)$$

where $\Delta\rho$ is the experimental change in density, can be transformed, using Eqs. (6) and (7) with $\Delta t = 0$, to

$$\Delta\rho = -\frac{\pi^{1/2}\sigma_k}{RLW} \left(U\tau_{apparent}\right) \left(\frac{\Delta V}{V_o}\right)_{t=0} \qquad (15)$$

The right-hand side of this equation can be evaluated from an extrapolation of plots like Fig. 7 to zero time, and the values of W, L, σ_k, and R. The derived $\Delta\rho$ can then be compared with $\rho_b - \rho_a$, the change in density obtained from the Hugoniot calculations.

In Table 3 the results of such an analysis are exhibited for six experiments in a 60% Ar - 40% D_2 mixture. These experiments were done specifically for this purpose; careful attention was paid to the value of V_o and σ_k, and the amplification was such that the oscillogram showed the entire spike, as in Fig. 4. For the computation of $\Delta\rho$ by equation (15) the values of W, L, and σ_k were as stated earlier, and the refractivities were taken from Wright[13]. The second column in this table shows the ratio of $\Delta\rho$ calculated from the experimental data and Eq. (15) to the $\Delta\rho$ computed from the Hugoniot equations. The third column shows the values of δ, the axial extent of the shock, estimated from the magnitude of the initial spike, and the fourth column shows the ratio of the two values for $\Delta\rho$ corrected for a zero time error of $\delta/2U$ as previously suggested.

The ratio in the last column is consistently less than one. However, considering the uncertainties in the time origin and the long extrapolation from the actual observations to this origin, the two determinations of $\Delta\rho$ would seem to be in sufficiently good agreement to confirm the interpretation of the observed density change as vibrational relaxation.

An approximate value of $P\tau$ (the relaxation time at one atmosphere total pressure) was obtained from $\tau_{apparent}$ by a process similar to Blackman's[14] method of analyzing interferograms[15]. These values

were then used as trial data for an iterative determination of the relaxation time as defined by the energy equation

$$\frac{dE_v}{dt} = \frac{1}{\tau} (E_v^{eq} - E_v) \tag{16}$$

Here E_v is the instantaneous vibrational energy of the gas, and E_v^{eq} is the instantaneous equilibrium vibrational energy which is a function of the translational temperature. This equation only applies strictly to a two-level vibrator or a harmonic oscillator in the weak collision model[16], however, except at the highest temperatures, the contribution to E_v from levels in D_2 with $v > 1$ is small, and the relaxation time defined by this equation can be considered to give an approximation to the relaxation time of the first vibrational level.

For the above iteration the input data were amplitude readings from the oscillograms h_i at t_i, trial Pr values, state variables at condition (a), and thermodynamic data for the gases. The first requirement was a solution of Eq. (16) for τ, given density gradient data. A breakdown of the right-hand side of (16) can be written

$$(\frac{dE_v}{dt_g})_i = (\frac{dE_v}{d\rho})_i (\frac{d\rho}{dx})_i (\frac{dx}{dt_\ell})_i (\frac{dt_\ell}{dt_g})_i \tag{17}$$

where t_g is molecule time and t_ℓ is observer or oscilloscope time. Now $(\frac{d\rho}{dx})_i = h_i/c$ where c is a constant, $(\frac{dx}{dt_\ell})_i = U$ the shock velocity, and $(\frac{dt_\ell}{dt_g})_i = (\frac{\rho_o}{\rho})_i$ where ρ_o is the density of the unshocked gas. Thus

$$\left(\frac{dE_\nu}{dt_g}\right)_i = \left[\frac{hU}{c\rho/\rho_o}\left(\frac{dE_\nu}{d\rho}\right)\right]_i \tag{18}$$

From (16),

$$\frac{d}{dt_g}\ln\left(\tau\frac{dE_\nu}{dt_g}\right) = \frac{d}{dt_g}\ln(E_\nu^{eq} - E_\nu) = -\frac{1}{\tau}\left(1 - \frac{dE_\nu^{eq}}{dE_\nu}\right) \tag{19}$$

and combining (18) and (19)

$$(P\tau)_i = -\frac{P_i\left(1 - dE_\nu^{eq}/dE_\nu\right)_i}{\frac{d}{dt_p}\ln\left[\left(\frac{dE_\nu}{d\rho}\right)\frac{h\tau}{\rho}\right]_i} \tag{20}$$

The quantities P_i, ρ_i, $(dE_\nu/d\rho)_i$, $(dE_\nu^{eq}/dE_\nu)_i$ and also T_i, the translational temperature, were obtained from a Runge-Kutta integration of Eq. (16) with the trial $P\tau(T)$, the integration being started from condition (a). The denominator of Eq. (20) was evaluated from a least squares fit of the quantity in brackets to a polynomial in t_p. In the D_2 experiments a linear function was adequate. The results of Eq. (20) were then compared with the trial values for $P\tau$, and the process repeated until agreement was obtained. This procedure converges rapidly--in the present study the trial data were sufficiently close to require only one iteration for agreement to 1%.

As is evident from Table 2 the translational temperature is not constant during the relaxation--it can, in fact, vary by almost 10%. This variation in temperature implies a variation in $P\tau$ during a single experiment. However, this variation is smaller than the experimental error, so that only one value of $P\tau$ was selected for plotting from each experiment.

This value and the corresponding gas temperature were taken from measurements near the front where the modulation amplitudes are large.

Landau-Teller plots of the $P\tau$ values obtained from the above calculations are shown in Figs. 8 and 9. In both of these the ordinate is the relaxation time reduced to 1 atm <u>total</u> pressure. The two lines drawn on Fig. 8 are least square fits of the usual expression:

$$P\tau = Ae^{B/T^{1/3}} \tag{21}$$

That this functional form is quite successful in correlating the data is evident from the graphs. The only significant deviation from Eq. (21) is in the highest temperature 80% Ar points where dissociation of the D_2 is involved. The question of the effect of dissociation on the observed relaxation time is outside the scope of this paper, and the four points with T > 3200°K have been ignored in the least squares fit.

The fits shown in Fig. 8 have the following analytic expressions:

$P\tau_{30\%\ Ar} = (3.5 \pm 0.4) \times 10^{-10}\ e^{(111.2 \pm 1.5)/T^{1/3}}$ (1100-3000°K) and

$P\tau_{80\%\ Ar} = (6.6 \pm 2.1) \times 10^{-10}\ e^{(114.2 \pm 5.1)/T^{1/3}}$ (1600-3000°K) in atm·sec.

From these two expressions relaxation times for pure D_2 ($P\tau_{D_2\text{-}D_2}$) and D_2 infinitely dilute in Ar ($P\tau_{D_2\text{-}Ar}$) were obtained by solution of the equation

$$\frac{1}{P\tau} = \frac{X_{D_2}}{P\tau_{D_2\text{-}D_2}} + \frac{X_{Ar}}{P\tau_{D_2\text{-}Ar}} \tag{22}$$

where X_G is the mole fraction of constituent G. The results of this analysis are:

$$P\tau_{D_2\text{-}D_2} = (2.7 \pm 0.3) \times 10^{-10}\, e^{(110.5 \pm 1.5)/T^{1/3}} \quad (1100\text{-}3000^\circ K) \text{ and}$$

$$P\tau_{D_2\text{-}Ar} = (1.0 \pm 0.7) \times 10^{-9}\, e^{(118 \pm 10)/T^{1/3}} \quad (1600\text{-}3000^\circ K) \text{ in atm·sec.}$$

The line in Fig. 9 shows the relaxation times for the 60% Ar mixture derived from the above expressions. The agreement is sufficiently close to confirm the essential validity of Eq. (22). Here again the highest temperature points are affected by dissociation.

The few experiments with added H_2 shown in Fig. 9 indicate that the effect of small amounts of H_2 on the deuterium relaxation is slight, showing that the presence of the very small H_2 impurity in the D_2 used for these experiments can be ignored.

The error figures quoted in the above expressions are standard deviations derived from the least squares procedure. The cause of the scatter in these data is apparently not limited sensitivity or spatial resolution but rather uncertainties in the temperature caused by inaccuracies in the shock velocity measurements, and/or the presence of the irregular modulations noted in the previous discussion of Fig. 3. These irregularities evidently increase in magnitude with the post-shock pressure, and the lower temperature limit of the relaxation measurements is enforced by this magnitude becoming comparable to the relaxation effect. Depending on the mixture, the high temperature limit is imposed by either dissociation or excessively fast relaxation.

CONCLUSIONS

The present D_2 investigation demonstrates the utility of the narrow beam laser schlieren technique for the detection of rapid vibrational relaxation. The results for pure D_2 in particular show a greater self-consistency than is usually obtained from shock tube relaxation studies.

The results agree with the single determination of White[3], the only previous investigation of this process.

The experimental relaxation times are a factor of 7 shorter than would be predicted by the correlation scheme of White and Millikan[1], although the temperature dependence given by the scheme is close for pure D_2. The results for pure D_2 have also been compared with the theory of Schwartz, Slawsky, and Herzfeld (SSH) as given in Herzfeld and Litovitz[17]. With the values for the D_2-D_2 potential parameters taken to be: σ = 2.928Å and ϵ/k = 37°K, this theory predicts relaxation times almost two orders of magnitude smaller than the experimental values.

ACKNOWLEDGMENTS

The authors would like to express their appreciation to Charles W. Hamilton for his help with the numerical computations, and to Richard E. Johnston and James L. Young for their assistance with the experiments.

References

(1) A summary of data from shock tube studies of diatomic molecules is contained in D. R. White and R. C. Millikan, J. Chem. Phys. 39, 3209 (1963).

(2) A. Lifshitz, C. Lifshitz, and S. H. Bauer, J. Am. Chem. Soc. 87, 143, (1965).

(3) D. R. White, J. Chem. Phys. 42, 447 (1965).

(4) J. H. Kiefer and R. W. Lutz, Phys. Fluids 8, 1393 (1965).

(5) E. L. Resler and M. Scheibe, J. Acoust. Soc. Am. 27, 932 (1955); Ind. Eng. Chem. 47, 1182 (1955). See also: W. J. Witteman, Rev. Sci. Instr. 32, 292 (1961) and references 6 and 9 below.

(6) P. C. T. de Boer and J. M. Burgers, Technical Note BN-258, Institute for Fluid Dynamics and Applied Mathematics, U. of Maryland (September, 1961).

(7) J. P. Rink, H. T. Knight, and R. E. Duff, J. Chem. Phys. 34, 1942 (1961).

(8) J. H. Kiefer and R. W. Lutz, J. Chem. Phys. 42, 1709 (1965).

(9) J. Daen and P. C. T. de Boer, J. Chem. Phys. 36, 1222 (1962).

(10) P. C. T. de Boer, Phys. Fluids 6, 962 (1963).

(11) P. F. Bird, R. E. Duff, and G. L. Schott, Los Alamos Sci. Lab. Report LA-2980 (1964).

(12) L. Haar, A. S. Friedman, and C. W. Beckett, "Ideal Gas Thermodynamic Functions and Isotope Exchange Functions for Diatomic Hydrides, Deuterides, and Tritides", NBS Monograph 20 (1961).

(13) J. K. Wright, Shock Tubes, (Methuen, London, 1961).

(14) V. Blackman, J. Fluid Mech. 1, 61 (1956).

(15) The original abstract submitted for this meeting (Bull. Am. Phys. Soc., to be published) contains results based on preliminary experiments and the Blackman solution which are superseded by the present more refined measurements.

(16) J. F. Clarke and M. McChesney, The Dynamics of Real Gases, (Butterworths, London, 1964).

(17) K. F. Herzfeld and T. A. Litovitz, Absorption and Dispersion of Ultrasonic Waves, (Academic Press, New York, 1959).

Table 1. Range of Initial Conditions

Mixture Designation	Actual Composition (The remainder in each case is D_2)	No. of Experiments	P_o(cm Hg)	T_o(°K)	U(mm/usec)
30% Ar	30.20% Ar	28	0.42 - 21.89	300.8 - 303.8	1.738 - 3.265
80% Ar	79.80% Ar	16	0.52 - 6.31	297.5 - 302.0	1.295 - 2.594
60% Ar	60.14% Ar	17	0.53 - 6.79	299.9 - 303.5	1.597 - 2.853
60% Ar + H_2	58.45% Ar 2.55% H_2	5	2.54 - 11.94	299.0 - 299.5	1.479 - 2.257

Table 2. Range of Post-Shock Conditions

Mixture Designation	Mean P(atm)	Mean ρ/ρ_o	$T_{condition\ a}$(°K)	ΔT_{a-b}(°K)	$\Delta\rho_{b-a}$ gm/l	$T_{apparent}$(usec)
30% Ar	.2688 - 4.4578	4.0319 - 5.2104	1091 - 3129	16 - 253	.00187 - .01733	.378 - 1.706
80% Ar	.4693 - 1.8728	3.6956 - 4.3951	1621 - 4899	20 - 339	.00384 - .01064	.303 - 1.649
60% Ar	.5160 - 1.3345	4.0101 - 4.8207	1560 - 4373	34 - 374	.00465 - .01478	.286 - .963
60% Ar + H_2	1.3638 - 2.7131	3.8300 - 4.2383	1344 - 2762	20 - 131	.01034 - .01474	.231 - .375

Table 3. Comparison of Measured and Calculated Density Changes

Experiment No.	$R = \frac{\Delta\rho \text{ (Equation (15))}}{\Delta\rho \text{ (Hugoniot)}}$	Axial Shock Extent δ(mm)	R corrected for time error of $\delta/2U$
1	0.47	0.34	0.57
2	0.66	0.46	0.91
3	0.61	0.47	0.80
4	0.68	0.54	0.88
5	0.57	0.58	0.74
6	0.63	0.48	0.80

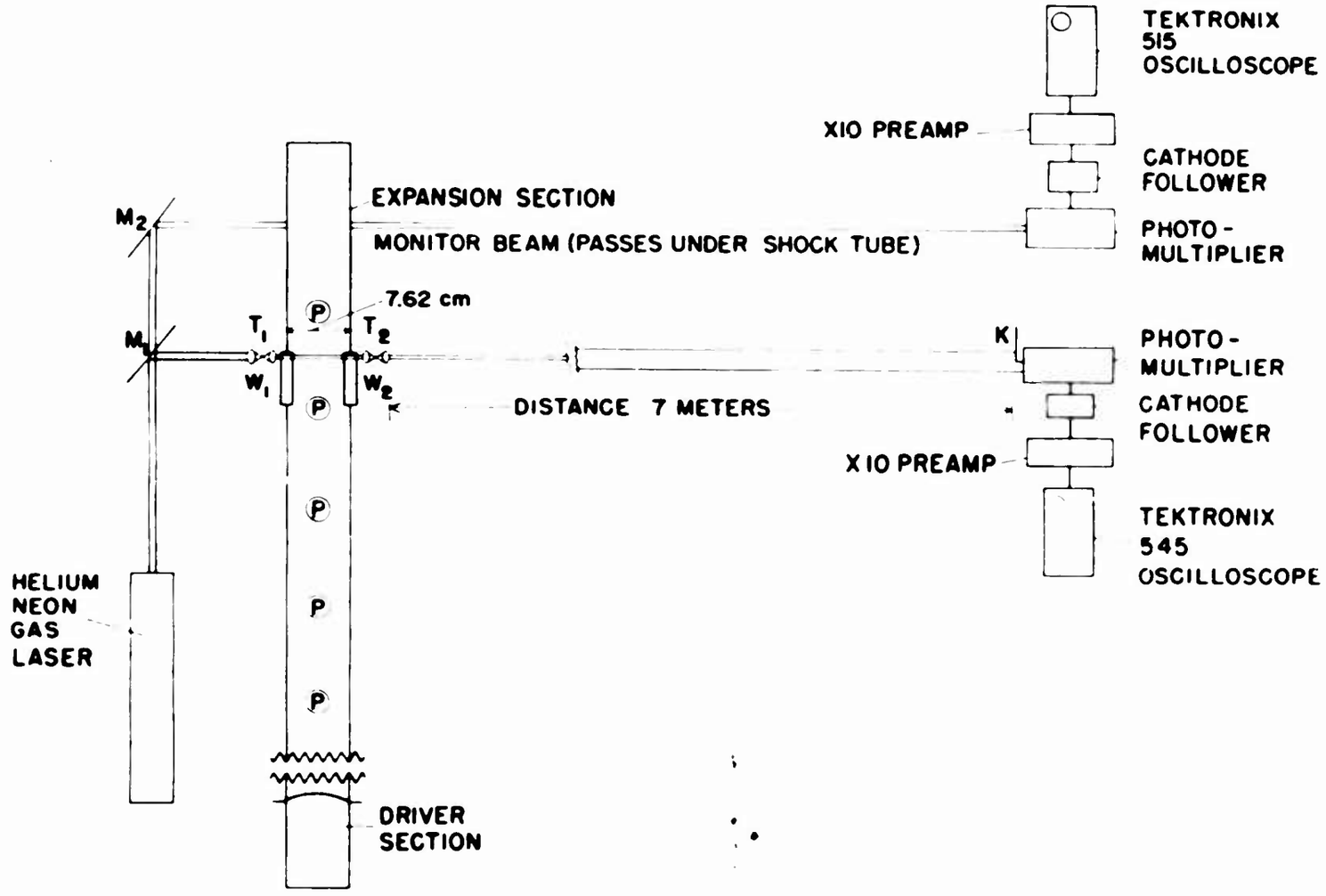


FIG. 1 SCHEMATIC OF THE SCHLIEREN APPARATUS. (P) DESIGNATES PIEZOELECTRIC GAUGES FOR THE MEASUREMENT OF SHOCK VELOCITY.

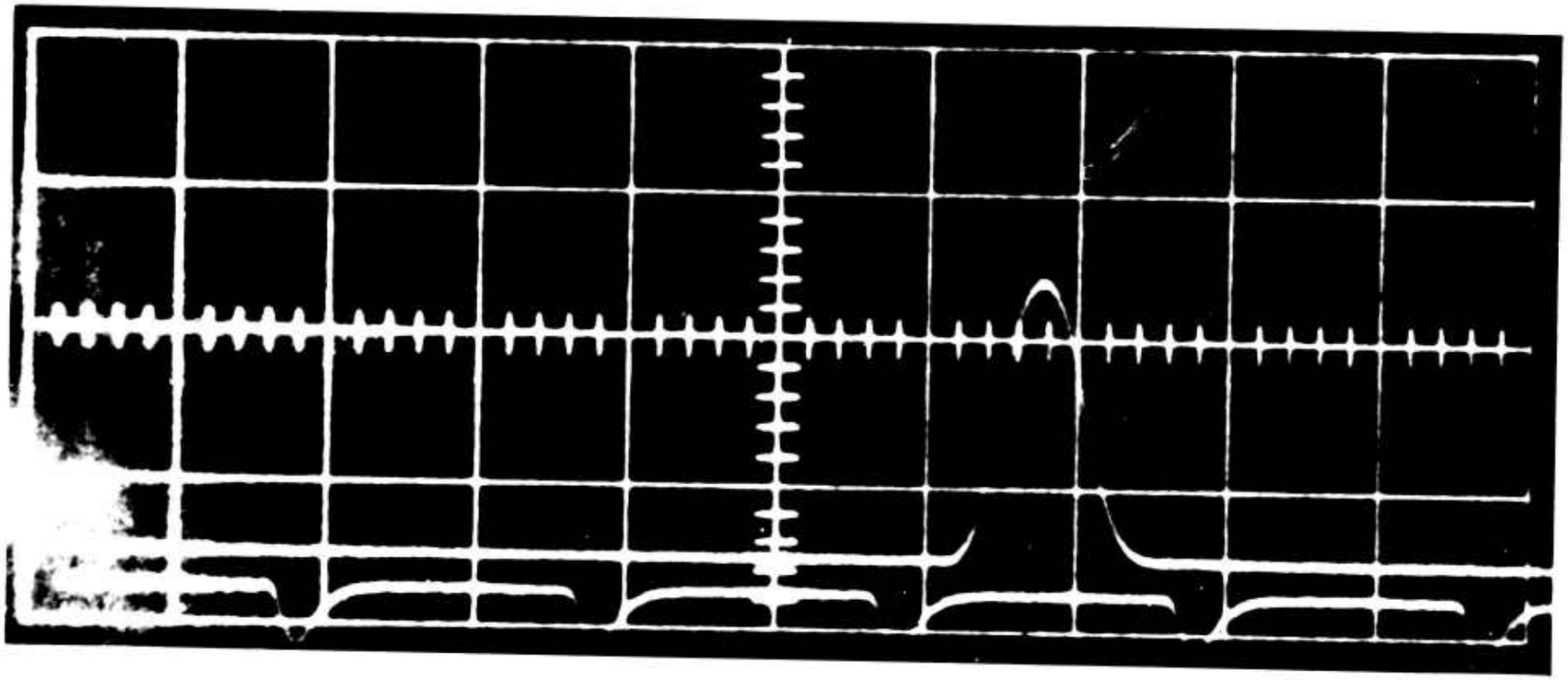


FIG. 2 SCHLIEREN RECORD OF A SHOCK IN PURE ARGON. THE EXPERIMENTAL CONDITIONS WERE: U = 1.905 mm/μ sec, AND P_o = 0.97 cm Hg. THE BOTTOM SWEEP CONTAINS 1μsec TIMING MARKERS, THE TIME INCREASING FROM LEFT TO RIGHT. VERTICAL AMPLITUDE IS PORPORTIONAL TO $\left|\frac{\Delta V}{V_o}\right|$, THE PEAK MODULATION OF THE SPIKE BEING 30%.

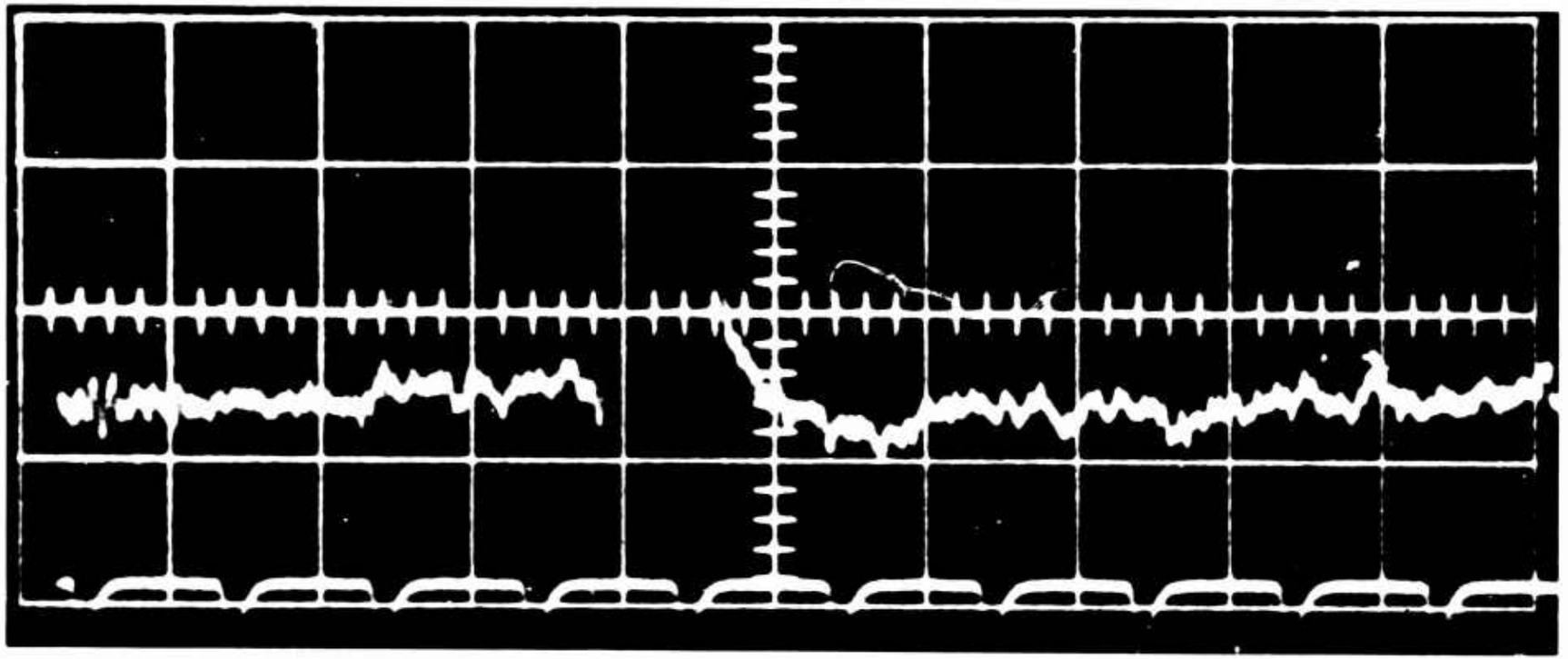


FIG. 3 SCHLIEREN RECORD OF A SHOCK IN PURE ARGON WITH HIGH AMPLIFICATION. THE CONDITIONS ARE SIMILAR TO THOSE OF FIG. 2 . HERE ONE VERTICAL GRATICULE DIVISION REPRESENTS A MODULATION OF 0.36%. THE BOTTOM SWEEP CONTAINS 1μsec TIMING MARKERS, THE TIME INCREASING FROM LEFT TO RIGHT.

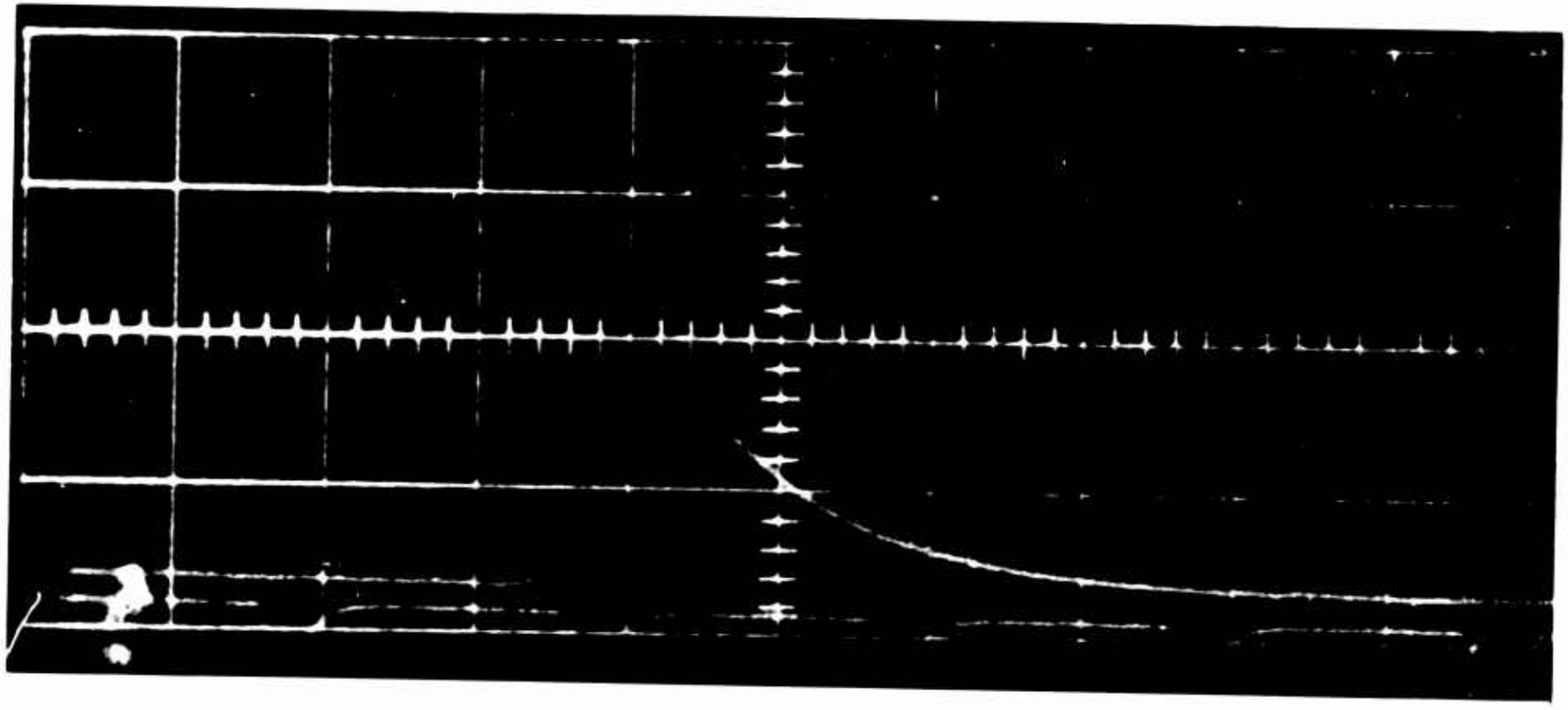


FIG. 4 SCHLIEREN RECORD OF A SHOCK IN 40% D_2 - 60% AR SHOWING THE ENTIRE MODULATION. THE CONDITIONS WERE: U = 1.719 mm/μsec, P_o = 7.08 cm Hg, T_a =1720°K, AND τ_{lab} = 0.504 μsec. ONE GRATICULE DIVISION REPRESENTS A MODULATION OF 7%. THE BOTTOM SWEEP CONTAINS 1 μsec TIMING MARKERS, THE TIME INCREASING FROM LEFT TO RIGHT.

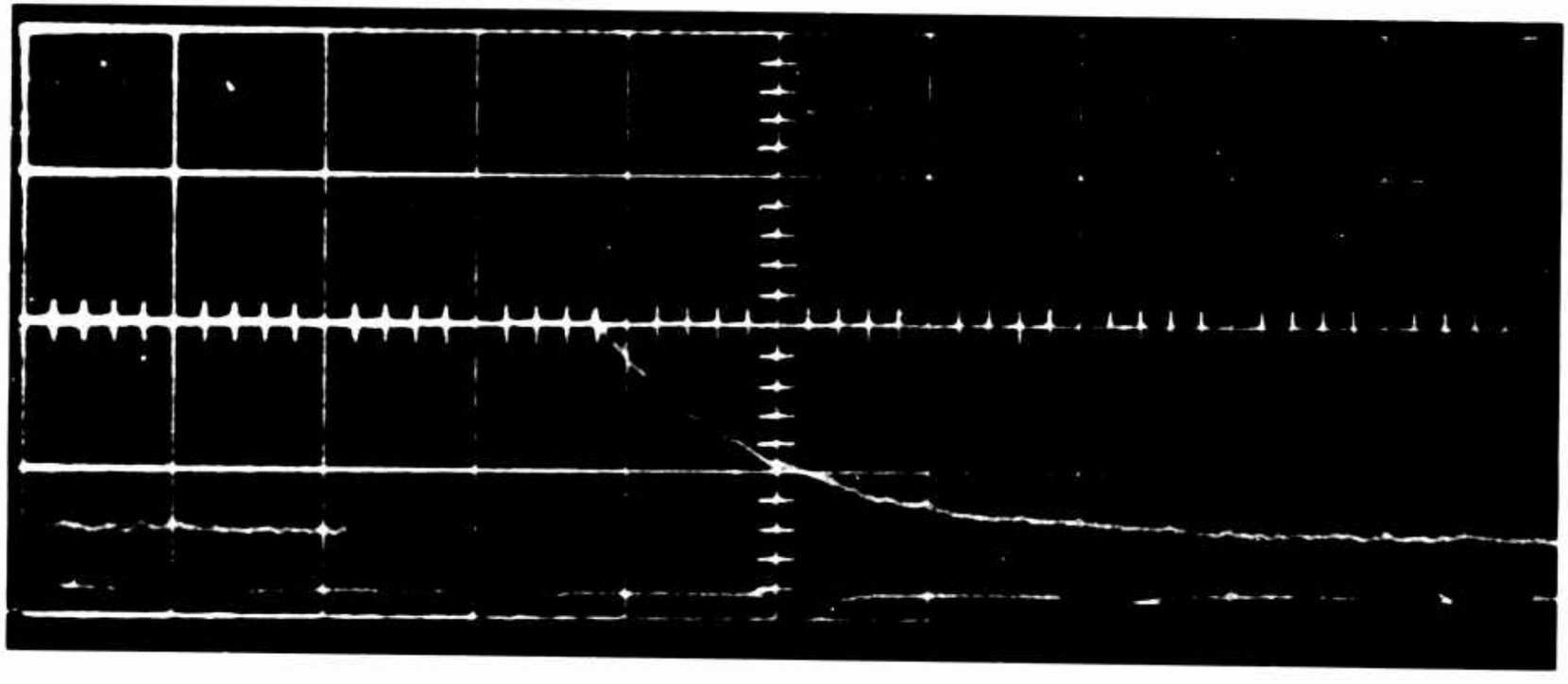


FIG. 5 SCHLIEREN RECORD OF A SHOCK IN 70% D_2 - 30% AR. CONDITIONS WERE; U = 2.397 mm/ μsec, P_o = 3.06 cm Hg, T_a = 1821°K, AND τ_{lab} = 0.549μ sec. ONE GRATICULE DIVISION REPRESENTS A MODULATION OF 1.7%. THE BOTTOM SWEEP CONTAINS 1μ sec TIMING MARKERS, THE TIME INCREASING FROM LEFT TO RIGHT.

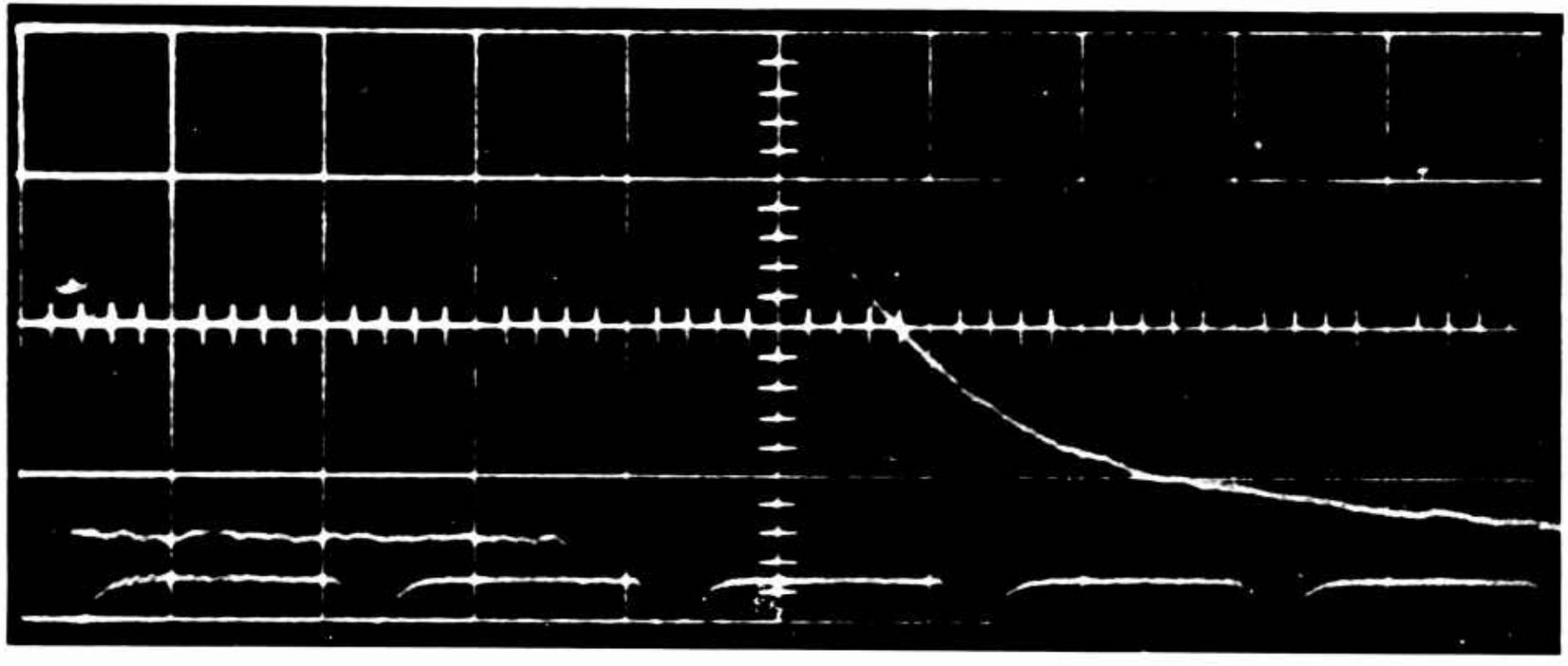


FIG. 6 SCHLIEREN RECORD OF A SHOCK IN 20% D_2 - 80% AR. CONDITIONS WERE: U = 1.686 mm/μsec; P_o =4.00 cm Hg, T_a =2224°K, AND τ_{lab} = 0.662 μsec. THE AMPLIFICATION IS THE SAME AS IN FIG. 5. THE BOTTOM TRACE CONTAINS 1 μsec TIMING MARKERS, THE TIME INCREASING FROM LEFT TO RIGHT.

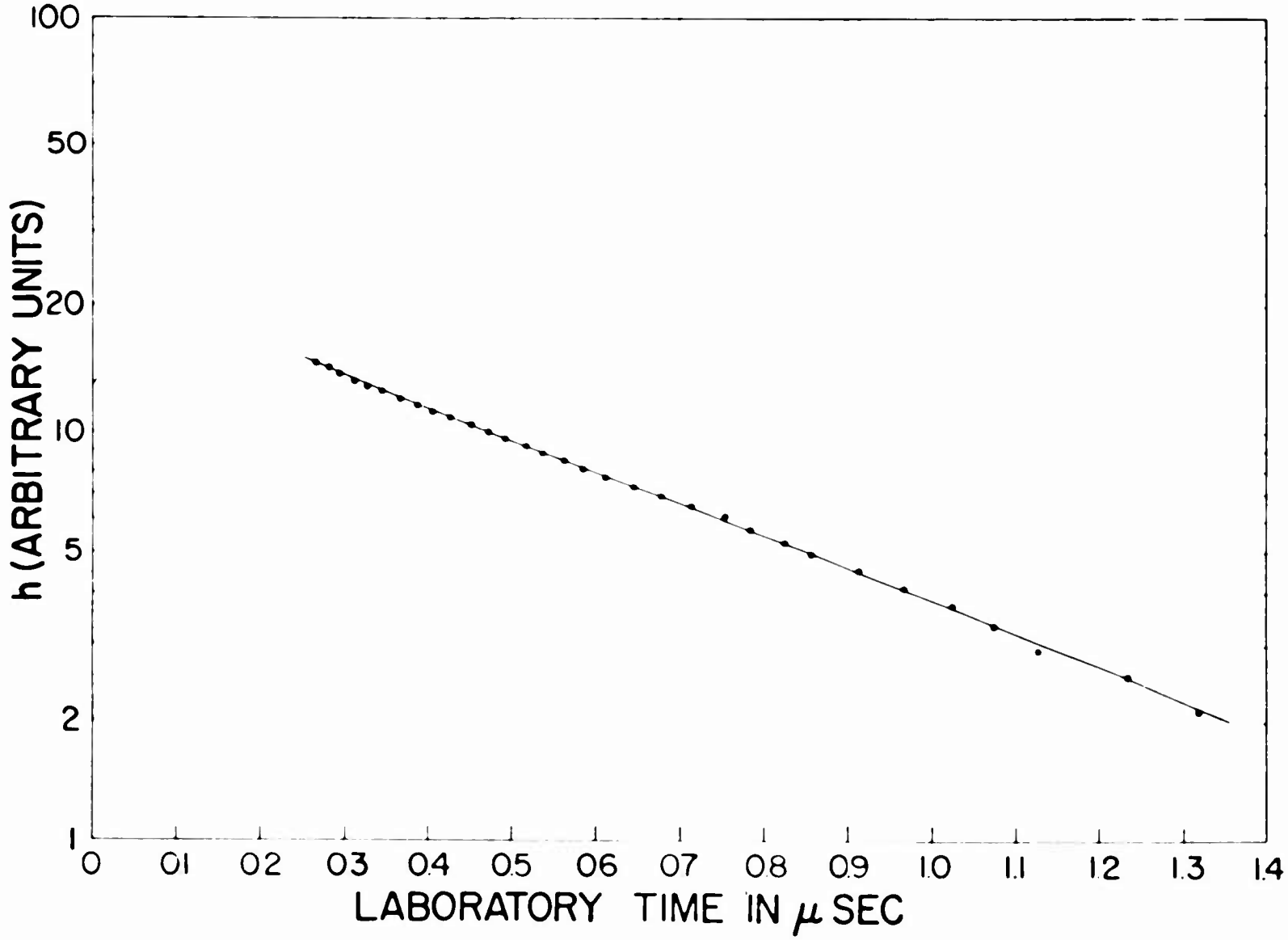


FIG. 7 PLOT OF LOG_{10} h VS LABORATORY TIME FOR THE EXPERIMENT OF FIG. 5.

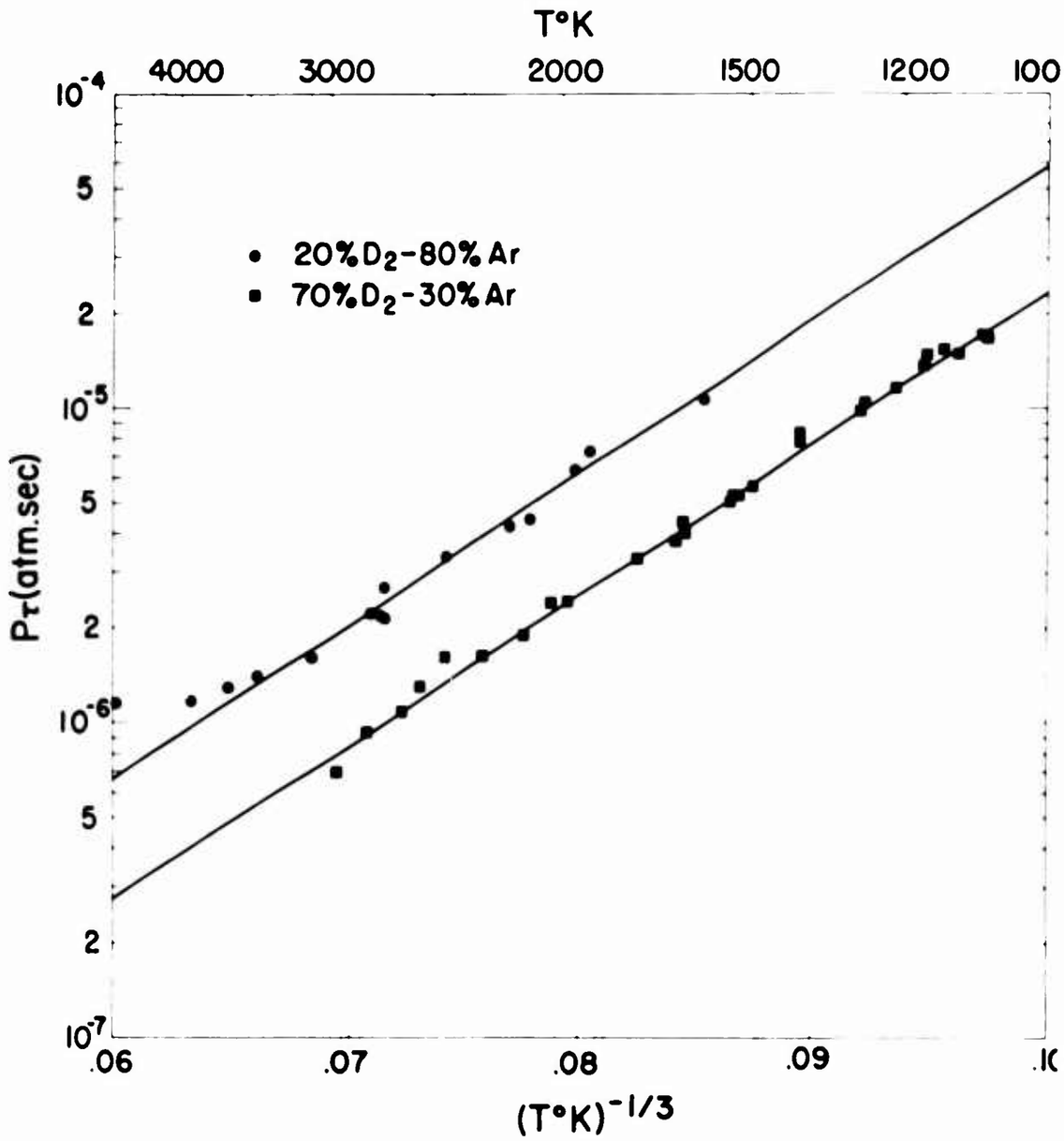


FIG. 8 LANDAU-TELLER PLOT OF RELAXATION TIME DERIVED FROM EXPERIMENTS IN 70% D_2 - 30% AR AND 20% D_2 - 80% AR. THE ORDINATE IS THE RELAXATION TIME REDUCED TO 1 ATM TOTAL PRESSURE.

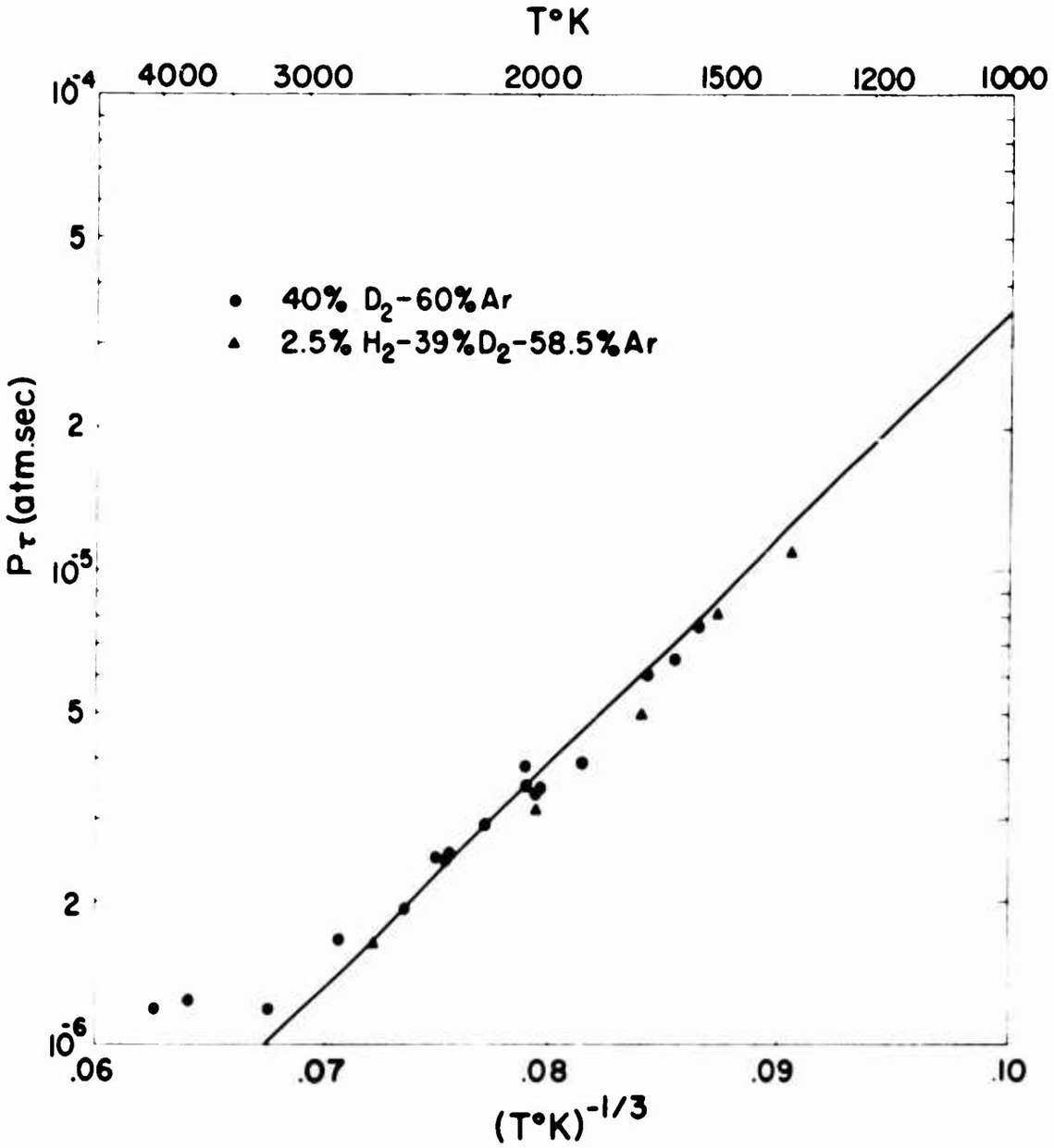


FIG. 9 LANDAU-TELLER PLOT OF RELAXATION TIMES DERIVED FROM EXPERIMENTS IN 40% D_2 - 60% AR WITH AND WITHOUT ADDED H_2. THE ORDINATE IS THE RELAXATION TIME REDUCED TO 1 ATM TOTAL PRESSURE.

BLANK PAGE

DETERMINATION OF SHOCK TEMPERATURES FROM SIMULTANEOUS INFRARED EMISSION AND ABSORPTION MEASUREMENTS*

G. J. Penzias, S. A. Dolin, and H. A. Kruegle
The Warner & Swasey Company
Control Instrument Division
Flushing, New York 11354

ABSTRACT

Gas temperatures in shock-heated CO_2-N_2 mixtures were determined by simultaneously measuring the infrared spectral emission and absorption of hot CO_2 at 4.40-μ. By Kirchhoff's law, the ratio (emission/absorption) equals the Planck blackbody emission, from which the temperature is easily found. The instrument consists of a source and receiver placed on either side of the shock tube at a viewing port. A high speed chopper (to 165,000 cps) modulates the source emission; the emission of the shock-heated gases is unmodulated. This permits discrimination between source emission and gas emission, and yields simultaneous outputs of gas emission and gas absorption. The measured incident shock temperatures agreed with values calculated from the measured shock velocities. The infrared technique can also be used where it is difficult to accurately calculate the gas temperature, as in reflected shocks or where exothermic reactions occur.

INTRODUCTION

The shock tube provides a useful tool for studying gaseous systems at high temperatures and pressures, under uniform conditions. The usual procedure is to calculate the temperature and pressure from a knowledge of the initial conditions in the tube and the readily measurable shock velocity. Under certain shock tube operating conditions, these calculations are not straightforward, and it may be desirable to obtain the temperature from a direct measurement.

* Supported in part by the NASA Lewis Research Center.

We have employed the infrared emission-absorption method (ref. 1) to obtain direct measurements of gas temperatures in incident shock waves. In this method, the spectral emittance and spectral absorptance of the hot gas are measured in a selected narrow infrared band. Gas temperature is then determined by means of Kirchhoff's Law

$$\frac{N_\lambda(T)}{\alpha_\lambda(T)} = N_\lambda{}^b(T) \qquad (1)$$

and the Planck radiation law,

$$N_\lambda{}^b(T) = C_1\lambda^{-5}\,(e^{C_2/\lambda T} - 1)^{-1} \qquad (2)$$

where $N_\lambda(T)$, $\alpha_\lambda(T)$, and $N_\lambda{}^b(T)$ are respectively the spectral radiance of the gas at an infrared wavelength λ, the spectral absorptance of the gas at the same wavelength, and the spectral radiance of a blackbody at that wavelength; T is the absolute temperature; C_1 and C_2 are constants. Measurements of $N_\lambda(T)$ and $\alpha_\lambda(T)$ determine $N_\lambda{}^b(T)$ and T is then easily obtained from Eq. (2).

To use the infrared optical method to determine the temperature of the hot gases generated in the shock tube, the spectral radiance and spectral absorptance must be measured simultaneously and through the same optical path, because of the short time duration. This is accomplished by modulating only the source emission at sufficiently high speed as compared to the duration of the transient shock phenomena.

The instrument used to simultaneously measure the infrared emission and absorption is described in detail and results of measurements of gas temperatures in shock heated CO_2-nitrogen mixtures are presented.

EXPERIMENTAL

Infrared Instrument

General Description

The Warner & Swasey M301 high-speed spectroradiometer capable of simultaneously measuring the infrared spectral emission and absorption, consists of a source unit and a receiver

unit located at the shock tube viewing section. A schematic diagram of the instrument is shown in Fig. 1. The source unit generates a beam of infrared radiant energy modulated at frequencies up to 165,000 cps, which is directed through the viewing windows of the shock tube to the receiver unit. When the shock wave passes by the viewing section, the heated gases absorb some of this modulated radiation. This reduction of intensity of the modulated infrared beam from the source unit is a measure of the gas absorption $\alpha_\lambda(T)$ of Eq. (1).

The modulated radiation beam from the source and the unmodulated radiant emission of the shock heated gases are collected by the receiver unit, which contains a grating monochromator set at a particular wavelength where the gas absorbs. The radiant energy within the infrared beam passed by the monochromator is focused on an infrared detector. The detector converts the radiation signal to an electrical signal which is amplified and displayed on an oscilloscope. Since the source emission is modulated and the emission of the shock heated gases is unmodulated, it is possible to discriminate between them and separate them electrically, thereby yielding simultaneous outputs of gas emission and gas absorption. The optical and electronic systems are described in detail below.

In order that the temperature values obtained from the measurement will correspond to the International Practical Temperature Scale, the measuring system must be calibrated. This is accomplished by calibrating the instrument with a primary radiation standard (blackbody). For convenience a tungsten strip lamp is incorporated in the monochromator unit as a secondary standard. The radiation emitted by the tungsten strip lamp, at a measured voltage, is also calibrated against a blackbody.

Optical System

To measure temperature by the infrared emission-absorption method, the emission and absorption measurements must be made through identical optical paths (ref. 2). This requires that the optical path be carefully matched throughout the entire optical train, from the radiating source in the source unit to the detector in the receiver unit, so that the optical throughput is constant. (For a given throughput, the ratio f number/magnification must remain constant.) The optical design was restricted to the use of first surface mirrors since we wanted to cover a broad wavelength region in the infrared and also be able to accurately align the system with visible light. Another instrument requirement was that the optical beam from the source unit be modulated at high frequency.

To produce a high frequency modulated beam, the source radiation was mechanically interrupted by a slotted disk driven by an air turbine. Mechanical stress considerations dictated that the chopper wheel be small in diameter. Accordingly, a cassegrainian optical system, mirrors M_1 and M_2 shown in Fig. 1, was used to image the source on the chopper slot. The size of the chopper blades dictated a 3:1 demagnification of the globar and to maintain the throughput, an f/1.8 optical system was used to illuminate the chopper blade. The f number of this system is based on the requirement of an f/5 beam from the source unit to fill the receiver field stop (12 x 2 mm entrance slit). Plane mirror M_3, mounted on the air turbine, directs the energy to the chopper blade. The air turbine can be operated at a maximum speed of 110,000 rpm. The chopper has 90 slots, yielding a maximum chopping rate of 165,000 cps. The chopping frequency can be varied by varying the air flow to the turbine.

Cassegrainian optical system mirrors M_4 and M_5 restore the source image to proper size and relay this image to the measurement region between the source and receiver units. To avoid vignetting, which would result from such an optical arrangement, a field lens was placed close to the intermediate focal plane at the chopper, which, in combination with mirror M_1, imaged the surface of M_2 through mirror M_4 onto M_5. With M_2 and M_5 optically conjugate and M_4 made large enough to receive the full beam diameter from the source, all the energy falling on M_2 from the source is imaged in the sample area, minus the transmission and obscuration losses of the cassegrainian systems.

To insure that the optical paths for both emission and absorption are matched, an aperture stop was placed at the image of M_5 formed by the cassegrainian optical system mirrors M_6 and M_7 in the receiver unit. All the energy entering the monochromator section of the receiver unit is limited by this common stop. It should be noted that in cassegrainian optical systems there is both an inner and outer stop. The inner stop, corresponding to the central obscuration, was also optically matched in the same manner as the outer stop, described above.

Cassegrainian optical system mirrors M_6 and M_7 in the receiver unit collect the modulated source radiation and the unmodulated radiant emission of the shock heated gases and focus the energy on the entrance slit S_1. The monochromator section of the receiver unit utilizes a conventional grating

Littrow arrangement. The radiant energy within the infrared band passed by the monochromator is focused on an infrared detector by plane mirror M_{10} and a combination of a plane mirror and an ellipsoid, schematically represented as M_{11} in Fig. 1. Details of the detector optical system are shown in Fig. 2. The diagonal plane mirror intercepts the diverging beam from the exit slits and illuminates the ellipsoidal mirror. The image size is reduced by six to one and the energy focused on the sensitive area of the detector by the ellipsoid. The obscuration of the detector collecting optics does not entail an additional loss of energy as this obscuration coincides with the obscurations of the cassegrainian optics in the source and receiver.

Electronic System

A schematic diagram of the electronic system is shown in Fig. 3. The infrared detector in the receiver unit converts the radiation signal to an electrical signal, proportional to the sum of the modulated radiation from the source unit and the unmodulated radiation from the shock heated gases. Instead of amplifying the combined electronic signal from the detector with a single amplifier, two transistor amplifiers, connected in parallel, are used because there is generally a large amplitude disparity between the modulated source emission and the unmodulated gas emission. Processing the electrical signals in this manner improves the data presentation by permitting separate amplification of the two signals and also simplifies the reduction of the data.

The modulated information from the source unit is amplified by a narrow band amplifier, capacitively coupled, and tuned to the chopping frequency of the source unit. This AC amplifier has a gain of 1000 at the modulation frequency and selectively amplifies the globar signal. The use of a narrow band amplifier for the absorption channel results in an improved signal to noise ratio. Following the AC amplifier is a differentiating circuit. The RC differentiator shifts the modulated signal from a varying emission base line, to a zero base line. This allows the peak-to-peak amplitude of the modulated signal to be measured more conveniently. After the differentiator, the output is connected to one of the input terminals of a dual beam oscilloscope.

Since the unmodulated radiation from the phenomena contains components from DC to several hundred kilocycles, this information is amplified by a wide band amplifier having a response from DC to one megacycle and a gain of 100. The output of this amplifier is connected to the second trace of the dual beam

oscilloscope. The oscilloscope was equipped with a Polaroid Land camera for recording the oscillograms. A typical oscillogram is shown in Fig. 4. The upper modulated trace represents the absorption and the lower trace represents the spectral radiance of the gas.

The indium antimonide infrared detector used in the system is unique in that it is used in the DC mode and has been designed for long term stability. The photovoltaic indium antimonide flake is mounted in a special vacuum dewar with a two-hour liquid nitrogen holding time. The indium antimonide cell is back-biased to a few tenths of a volt using low noise mercury batteries. This biasing technique, along with the stable DC amplifier, results in very small drift at the output of the DC amplifier. To prevent any electrical interference from surrounding equipment from contaminating the detector signal, mercury battery power supplies are used for the AC and DC amplifiers.

Data Reduction

Referring to Fig. 4, the dual beam oscilloscope used to record the phenomena is triggered shortly before the arrival of the shock wave at the viewing section. This provides a measure of the initial modulated source emission (upper trace) and establishes a zero level (lower trace), from which the gas emission is measured. When the shock wave passes the windows, the hot gases radiate resulting in the signal increase of the lower trace. Simultaneously, the modulated signal on the upper trace is diminished as the heated gases absorb some of the source radiation. With the arrival of the contact surface, the gases are cooled and the signal on the lower trace gradually decreases to the zero emission level and the upper modulated signal increases toward its initial value.

The absorptance is obtained by measuring the peak-to-peak amplitude of the modulated source emission before the arrival of the wave (I_o) and the peak-to-peak amplitude of the decreased modulated signal during the steady hot flow portion (I). The ratio of I/I_o equals the gas transmittance. One minus the transmittance equals the absorptance $\alpha_\lambda(T)$ of Eq. (1). The increase in voltage in the lower trace corresponds to the gas emission which is converted to absolute units, $N_\lambda(T)$, using the blackbody calibration. The gas temperature is then readily determined from Eq. (2).

Shock Tube and Related Systems

A conventional, single-pulse, shock tube system was employed. The shock tube and instrument are shown in Fig. 5. The shock tube low-pressure section, consisting of several flanged lengths of 2.25" i.d. stainless steel tubing, had a completely assembled length of 15 feet. The driver section was a 4.5" i.d. stainless steel tube, 4 feet long. The driver and driven sections were connected by a converging transition section containing a 2" valve to permit rapid evacuation of the shock tube. Aluminum or mylar diaphragms, held at the transition section, were ruptured by increasing the driver gas pressure. The shock tube viewing section, which contained two sapphire windows mounted in line, was located 13.5 feet from the diaphragm.

Platinum thin film resistance probes (ref. 3), flush mounted along the shock tube, were used to measure the shock velocity. The probe outputs were displayed on an oscilloscope modified for raster sweep operation. The raster sweep was timed using a time-mark generator with pulses every 10 microseconds. The shock velocity measurements were accurate to within $\pm$ 0.5%. The signal generated by one of the thin-film resistance probes was also used to trigger the dual beam oscilloscope used to record the emission-absorption measurement.

RESULTS AND DISCUSSION

Gas temperatures in shock heated CO_2 and CO_2-nitrogen mixtures were determined by simultaneously measuring the infrared spectral emission and absorption of hot CO_2 at 4.40-μ. The CO_2-nitrogen mixtures were prepared by the method of partial pressures in a mixing chamber and were allowed to stand for 24 hours before use. The shock tube was evacuated to a pressure of a few microns before filling, and the shock tube system had an overall leak rate of less than 1-μ Hg per minute. Initial pressures in the low pressure section were measured with a mercury monometer using a double reduction technique (ref. 4), which permitted the initial pressure to be measured with an experimental error of less than 0.25%. The infrared emission-absorption temperature measurements were made in the incident shock and were compared with values calculated from the measured shock velocities using the method suggested by Gaydon and Hurle (ref. 3), assuming a chemically frozen and vibrationally equilibrated state behind the incident shock. The results are shown in Table I. The error in the calculated temperature due to the accuracy of the velocity measurement corresponds to 15°K under the conditions measured.

The agreement between the measured temperature and the temperature calculated from the measured velocity is good. The maximum difference was 100°K, approximately 4%. This is within the experimental error.

Table I

Comparison of Incident Shock Temperatures

TEMPERATURE °K	
Measured[a)]	Calculated[b)]
2129	2038
2122	2091
2118	2207
2248	2325
2284	2390

a) From infrared emission-absorption of hot CO_2 at 4.40-μ.

b) From shock velocity by method of Gaydon & Hurle (ref. 3).

The comparison made above between measured and calculated values were for incident shocks in the absence of chemical reaction. Under these conditions, the calculated velocity may appear to give more accurate results than the infrared spectral measurements. However, this may not be true for all conditions. Under circumstances where the gas temperature cannot be calculated accurately, as in reflected shocks or where exothermic reactions may be occurring, the infrared technique should prove useful.

REFERENCES

(1) Tourin, R. H., Temperature, Its Measurement and Control in Science and Industry, Vol. III, C. M. Herzfeld, editor, Reinhold, New York (1962), Part 2, Chap. 43.

(2) Babrov, H. J., J. Opt. Soc. Am. 51, 171 (1961).

(3) Gaydon, A. G. and Hurle, I. R., The Shock Tube in High-Temperature Chemical Physics, Reinhold, New York (1962).

(4) Babrov, H. J., Ph.D. Thesis, University of Pittsburgh (1959); also available as AFOSR TR 59-207 (1959).

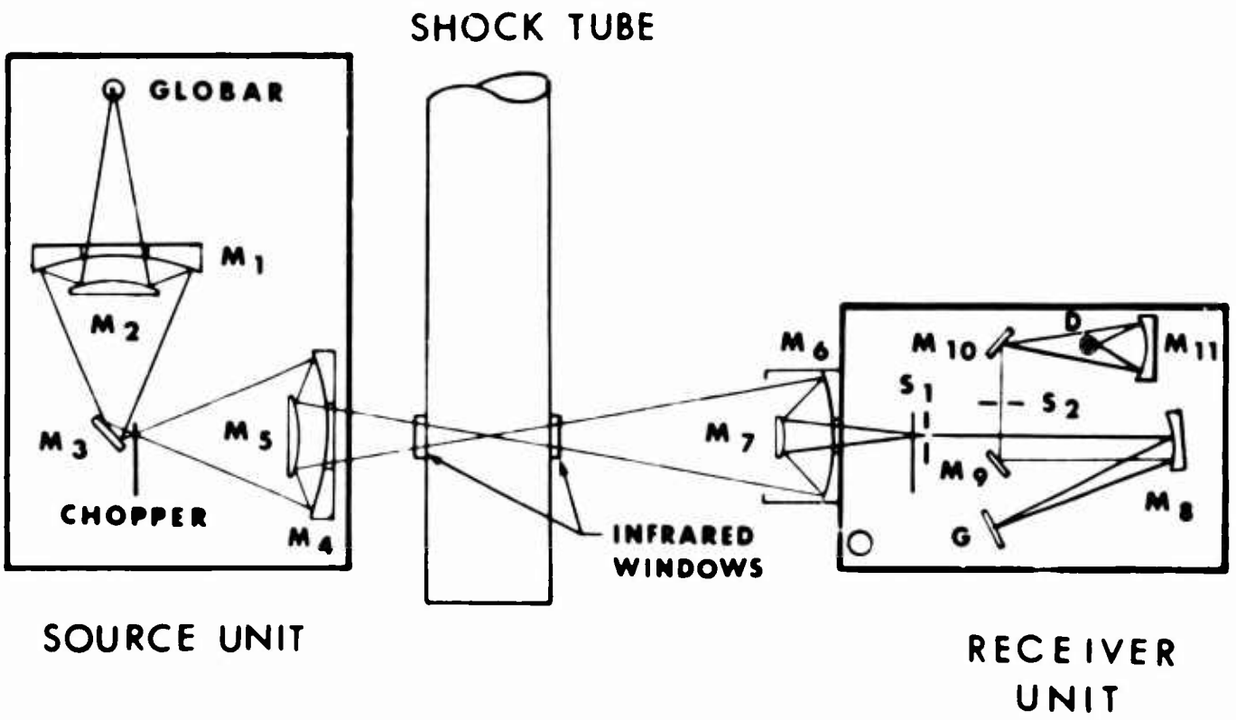


FIG. 1 SCHEMATIC DIAGRAM OF THE WARNER & SWASEY M301 HIGH SPEED SPECTRORADIOMETER.

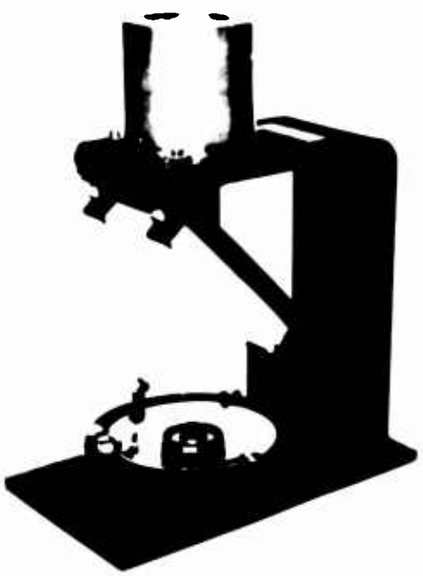


FIG. 2 InSb DETECTOR OPTICS.

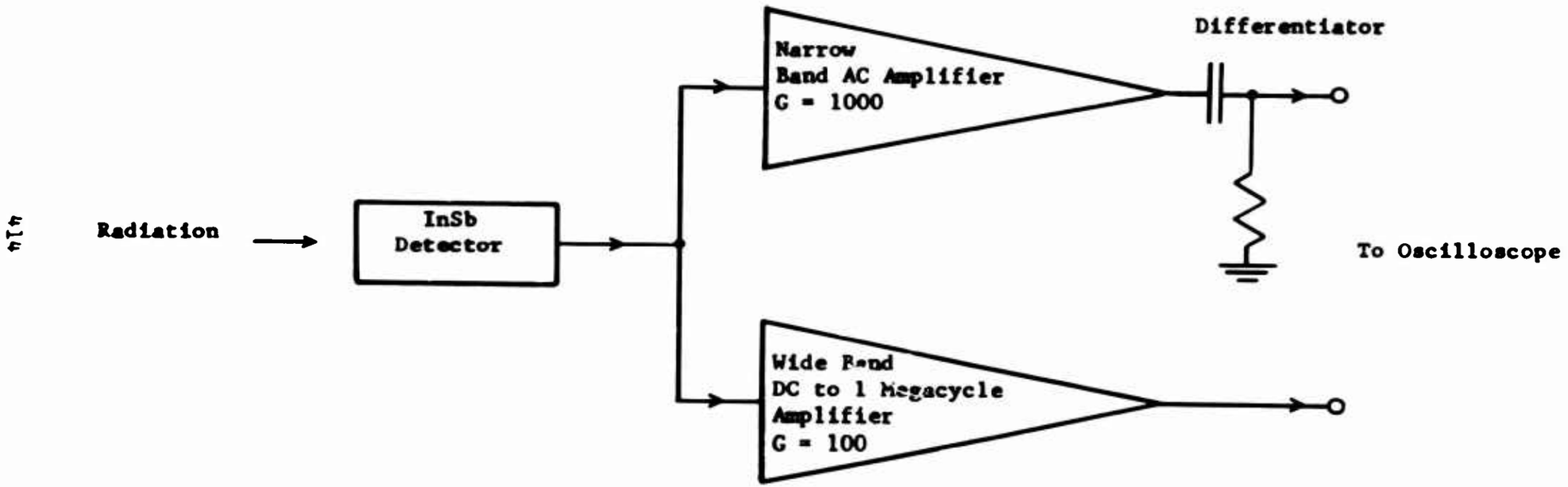
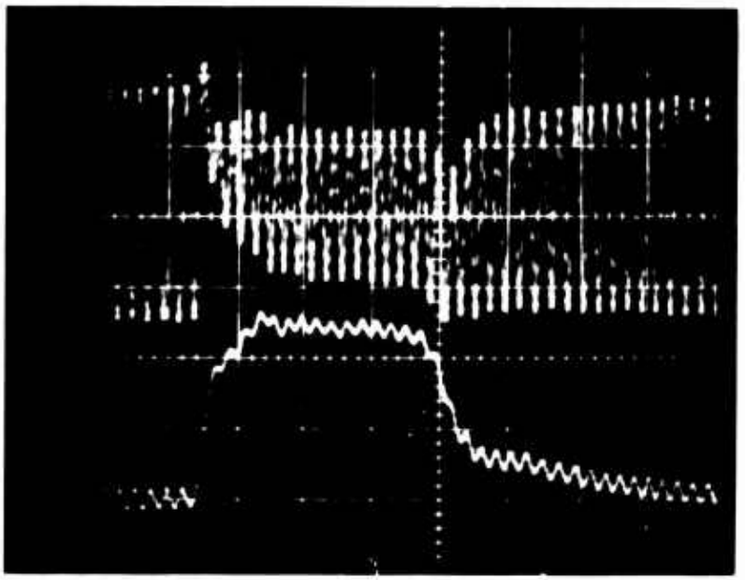


Fig. 3. Schematic diagram of electronic system used to amplify the emission and absorption signals.

$\lambda = 4.40 - 11$



1cm 50 MICROSECONDS (LAB. TIME)

FIG. 4 TYPICAL OSCILLOGRAM OBTAINED WITH HIGH SPEED SPECTRORADIOMETER. UPPER MODULATED TRACE REPRESENTS ABSORPTANCE. LOWER TRACE CORRESPONDS TO SPECTRAL RADIANCE.

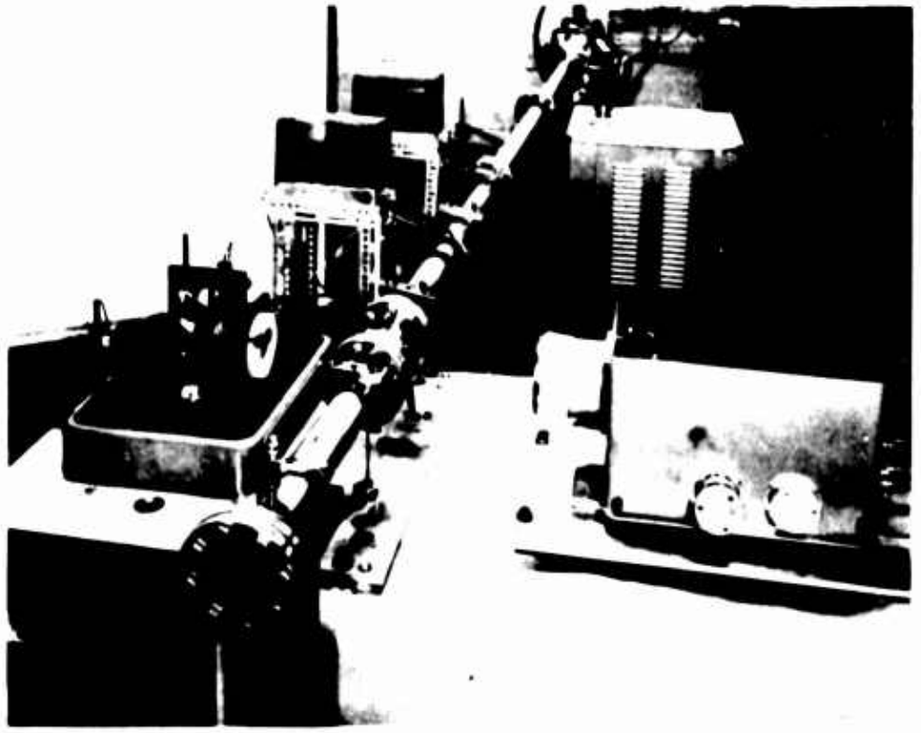


FIG. 5 SHOCK TUBE WITH HIGH SPEED SPECTRORADIOMETER AT VIEWING SECTION.

BLANK PAGE

SPECTROSCOPIC TEMPERATURE MEASUREMENTS IN SHOCK TUBES UTILIZING EMISSION FROM THE OH VIOLET BANDS*

Ronald Watson**
Engineering Center
Arizona State University
Tempe, Arizona

Abstract--The technique for utilizing wide-band emission from a large number of spectral lines in the OH $^2\Sigma - ^2\pi$ electronic band system to obtain spectroscopic temperature measurements in a shock tube is described. Application of the method to the experimental determination of temperatures in the reflected wave region in the range near 3500°K is discussed, and a comparison is made of the measured spectroscopic temperature to the calculated (gasdynamic) temperature based on shock wave speed. The effects of vibration-rotation interaction are calculated using Learner's data (1) for the appropriate Franck-Condon factors and the results show that interaction is not important for the v'=v vibration bands at 3500°K.

I. INTRODUCTION

The extensive use of shock tubes for chemical kinetics investigations, absolute emission measurements, and various high enthalpy flow studies (see for example Refs. 2-6) is primarily due to the fact that the kinetic energy of the shock wave adds thermal energy to the test gas and raises its temperature uniformly and almost instantaneously to a thermodynamic state that is in principle readily determined from the conservation relations of fluid mechanics (7,8). Thus, the shock wave compression produces a sample of test gas in a homogeneous condition whose temperature can greatly exceed the highest attainable in steady-state devices such as furnaces, etc. Many observers have utilized the region behind the reflected shock wave to obtain very high gas temperatures, without being forced to use heated hydrogen driver gas or excessively high driver pressures.

*Part of the work discussed here was supported under Air Force Grant No. AFOSR-176 at the California Institute of Technology.
**Present address: Heliodyne Corporation, Los Angeles, California

Although conditions in the shocked gas may be calculated from one-dimensional gasdynamic relationships, questions concerning equilibrium (9, 10), boundary layer effects (11), wave interaction (12), etc. persist in all shock tube work; this is particularly true in experiments performed at relatively low pressures where the gas particle collision frequency is low. Direct measurements of the properties of the shocked gas are therefore desirable.

It is relatively straightforward to measure the pressure, the usual technique involving the use of a piezoelectric transducer with time responses of the order of microseconds or better (13). Density measurements may be performed with devices such as X-ray densitometers or electron beams (14). The measurement of temperature presents a more difficult problem however, with present technology appearing to preclude any approach other than optical determinations.

It is the purpose of the present paper to describe the theoretical basis for a method of obtaining test gas temperatures by a spectroscopic technique; experimental results are given in later sections. The procedure described here is based on wide-band emission from a large number of spectral lines in two separate wavelength regions of the OH $^2\Sigma \rightarrow {}^2\Pi$ electronic band system. The emission is measured photoelectrically, the signals being generated by a narrow core of hot gas in the shock tube. The ratio of the intensity per unit optical depth in the two spectral regions is a unique function of the temperature for the case of an equilibrium, optically thin gas. If measurements are performed with an optical system looking axially up the tube behind the reflected wave, the linearity of the detector signal can provide a verification of the equilibration and transparency of the test gas. A schematic diagram of the experimental apparatus is shown in Fig. 1.

By employing an admixture of small amounts of water vapor to the principal test gases, the method described here may be used as a "standard" technique in shock tube work in the 2500-6000°K range. The procedure is somewhat analogous to the two-color technique for obtaining the brightness temperature of a grey body (e.g., metal parts in a heated furnace) by a comparison of the spectral intensity emitted from the body at two wavelengths (Ref. 15, Chap. 16).

Other optical techniques for measuring gas temperatures in shock tubes, e.g., the line reversal method, plasma spectroscopy, etc., are discussed elsewhere in the literature, see for example Ref's. 16-18.

II. THEORETICAL CONSIDERATIONS

In this section, the contribution to the flux incident on a detector (in the exit focal plane of a monochromator) emitted by individual spectral lines from the hot gas is obtained; summing over all of the lines passed by the monochromator yields the total flux and hence the voltage signal produced by the detector system observing radiation from the shock tube.

A. Theoretical Calculation of Line Intensities

The "intensity" (the energy emitted per unit time per unit volume) of a spectral emission line of wavenumber $\omega_{vv'JJ'}$ within a molecular band system is given by (see Ref. 19)

$$I_{vv'JJ'} = N_{vJ}\, hc\omega_{vv'JJ'}\, A_{vv'JJ'} \tag{1}$$

where N_{vJ} is the population of the upper state and $A_{vv'JJ'}$ the Einstein transition probability for spontaneous emission from the state vJ to the state v'J'. In terms of $|R_{vv'JJ'}|^2$, the square of the matrix element for the dipole moment of the particular transition, equation (1) may be written as

$$I_{vv'JJ'} = \frac{64\pi^4}{3}\, c\omega^4_{vv'JJ'}\, \frac{N_t}{Q_{int}}\, \exp(-E_{vJ}/kT)\, \left|R_{vv'JJ'}\right|^2 \tag{2}$$

where N_t is the total number of emitting molecules, Q_{int} is the partition function for the internal degrees of freedom, and E_{vJ} is the energy of the upper state. Note that equation (2) assumes a Boltzmann distribution.

At any temperature, the right hand side of equation (2) determines the total intensity emitted (in all directions) from the particular spectral line if the value of $|R_{vv'JJ'}|^2$ is known. Conversely, equation (2) implicitly defines the temperature if the absolute intensity is measured and $|R_{vv'JJ'}|^2$ is known. The temperature-intensity relationship thus depends on the evaluation of the matrix element term, which will be referred to here as the total transition probability. While absolute values of $|R_{vv'JJ'}|^2$ are seldom well known for molecular systems, it will be shown later that a knowledge of the relative values is sufficient for temperature determinations, essentially by using the intensity ratios of various bands.

B. Detector Response to Optical Radiation

In the shock tube experiments, a monochromator (see Fig. 1) allows the photomultiplier detector to respond to radiation from only the desired region of the OH violet spectrum. If the optical-detection system has an overall sensitivity of K' (volts/watt of light input; assumed to be constant over a narrow spectral interval), then the resulting detector signal output from the hot gas emission is

$$V_g = K'F$$

where F is the light flux incident on the detector. Since each jth spectral line emits a flux F_{ω_j}, the detector signal may also be written as

$$V_g = K' \sum_j F_{\omega_j} \,. \tag{3}$$

The monochromator serves as an optical filter and has a non-uniform response to incident light of different wavelengths because of the slit function.† In terms of the total intensity emitted by the jth line, equation (3) becomes

$$V_g = K' \, LA_e \, \frac{\Delta\Omega}{4\pi} \sum_j I_{\omega_j} \, g_{\omega_j} , \qquad (4)$$

where LA_e is the volume of the hot gas radiating into the exit optics (L is the length of the narrow core of hot gas within the shock tube and A_e is the exit window effective area), $\Delta\Omega/4\pi$ is the fractional solid angle subtended by the optical system, and g_{ω_j} is the normalized slit function response at the wavenumber ω_j . Equation (4) assumes self absorption is negligible, so that the signal voltage increases linearly as the length L grows with time.

The detector signal voltage resulting from the flux of all the lines within the slit function base $2\Delta\omega^*$ is

$$V_{g,\omega_o} = KL \, \frac{16\pi^3}{3} \, c \, \frac{Nt}{Q_{int}} \left[\sum_{vv'b\,i} \nu_i^4 \exp(-E_{vJ}/kT)_i \left| R_{vv'JJ'} \right|^2_i g_{\omega_i} \right]_{2\Delta\omega^*} \qquad (5)$$

where the factor K now includes the effect of the solid angle and the effective size of the emitting window area observed by the optical detection system. The subscript $2\Delta\omega^*$ in equation (5) signifies that the summation extends over all rotational lines (i), in all branches (b), in all bands (v,v'), where the slit function g_{ω_i} is non-zero; hence, in a given experiment V_{g,ω_o} depends on the monochromator wavenumber setting ω_o and the slit opening.

Equation (5) forms the basis for quantitative emission measurements and may be used to obtain spectroscopic temperatures if the $|R_{vv'JJ'}|^2$ values are known (the temperature being defined implicitly in equation 5). Alternatively, if the gas temperature is known, values of emission oscillator strengths (which depend upon the $|R_{vv'JJ'}|^2$ values) may be obtained from equation (5).

C. Spectroscopic Temperature Determination

Because of uncertainties in the total transition probabilities and the difficulty in obtaining an accurate determination of the absolute sensitivity factor K, the direct application of equation (5) would generally result in low accuracy. These problems may, however, be circumvented by

†The slit function response represents the spectral transmission characteristics of the monochromator and is triangular in shape with a total band pass of $2\Delta\omega^*$ for a well adjusted prism instrument (see Fig. 2). With the monochromator set at ω_o, all spectral lines outside the range $\omega_o \pm \Delta\omega^*$ are cut off by the instrument.

measuring the ratio of the voltage signals from two spectral regions identified by the subscripts 1 and 2, respectively, belonging to the same band system. The resulting signal voltage ratio is

$$\frac{V_1}{V_2} = \frac{K_1}{K_2} \frac{\left[\sum_{vv'} \sum_{b} \sum_{i} \omega_i^4 \exp(-E_{vJ}/kT)_i \left| R_{vv'JJ'} \right|_i^2 g_{\omega_i} \right]_{2\Delta\omega^*_1}}{\left[\sum_{vv'} \sum_{b} \sum_{i} \omega_i^4 \exp(-E_{vJ}/kT)_i \left| R_{vv'JJ'} \right|_i^2 g_{\omega_i} \right]_{2\Delta\omega^*_2}} \quad . \qquad (6)$$

The $\left| R_{vv'JJ'} \right|^2$ terms in equation (6) need only be determined on a relative basis, and the ratio of K_1/K_2 may be determined by a relative intensity calibration (which is experimentally much easier to perform than is an absolute calibration). On this basis, equation (6) may be written as

$$\frac{V_1 K_2}{V_2 K_1} = \phi(T) \qquad (7)$$

where $\phi(T)$ represents the calculable ratio of the summations appearing in equation (6). Note that equation (6) does not depend on the number density of the emitting molecules, so that an accurate knowledge of the OH concentration is not required as long as it is optically thin (further discussion of this is given in Section V on Experimental Results).

In order to obtain reasonable detector signal outputs (V_1/V_2) with the OH radical, it is required that the monochromator band pass $2\Delta\omega^*$ cover an interval of the order of 100A. This means that the summations in $\phi(T)$ will include many rotational lines (i) from different vibration bands in the $^2\Sigma \rightarrow {}^2\Pi$ violet system. Hence the temperature defined implicitly by equation (7) is a combined vibrational-rotational temperature, and it is assumed here that equilibration of all internal energy states is achieved.

D. Relative Transition Probabilities for OH: No Vibration-Rotation Interaction

The calculation of $\phi(T)$ depends on the evaluation of the $\left| R_{vv'JJ'} \right|^2$ terms. In the case of negligible interaction among the internal energy states, the total transition probability is separable into independent terms in the form

$$\left| R_{vv'JJ'} \right|^2 = \left| R_{el} \right|^2 p_{JJ'} q_{vv'} \quad . \qquad (8)$$

In equation (8), $|R_{el}|^2$ is an average value for the electronic transition moment (see for example Chap. 7 of Ref. 15). The data of Nicholls (20), show that $|R_{el}|^2$ may be taken as a constant for all of the v'= v bands with which the present calculations are concerned (since these bands have much stronger emission than the v'= v±1 bands). The $p_{JJ'}$ term is the rotational transition probability and $q_{vv'}$ is the Franck-Condon factor or the square of the overlap integral.

For this case, the $|R_{el}|^2$ terms cancel in the numerator and denominator of equation (6) and the expression for the (calculable) temperature function $\phi(T)$ becomes

$$\phi(T) = \frac{\left[\sum_{vv'} q_{vv'} \sum_{b} \sum_{i}^{4} \omega_i \exp(-E_{vJ}/kT)_i \, p_{JJ';i} \, g_{\omega_i}\right]_{2\Delta\omega^*_1}}{\left[\sum_{vv'} q_{vv'} \sum_{b} \sum_{i}^{4} \omega_i \exp(-E_{vJ}/kT)_i \, p_{JJ';i} \, g_{\omega_i}\right]_{2\Delta\omega^*_2}} \quad . \qquad (9)$$

Data for the relative values of $p_{JJ';i}$ and $q_{vv'}$ for OH are available in the literature (21,22).

E. Relative Transition Probabilities for OH: With Vibration-Rotation Interaction†

Learner (1) has calculated relative transition probabilities for the main branches of OH by applying Pekeris' (24) wave equation solutions using a Morse (25) potential. In this case, the total transition probability may be written as

$$|R_{vv'JJ'}|^2 = |R'_{el}|^2 \; p_{JJ'} \; q_{vv'JJ'} \qquad (10)$$

Here, $|R'_{el}|^2$ has a weak temperature dependence (an increase of about 1% from 2000-6000°K), but has the same value for the v'= v bands at a given temperature (see Ref. 23). The rotational transition probability terms are again as given in Ref. 21. The Franck-Condon factors $q_{vv'JJ'}$ are not calculated on the basis of the rotationless case (as are the $q_{vv'}$ in equation 8) since they now include the vibration-rotation interaction.

---

†A more extensive discussion of the effect of vibration-rotation interaction on both spectroscopic temperature measurements and absolute emission strengths of OH is given in Ref. 23.

As for the previous case, the $|R'_{el}|^2$ terms cancel in equation (6) and the temperature function with vibration-rotation interaction becomes

$$\phi'(T) = \frac{\left[\sum_{vv'} \sum_{b} \sum_{i}^{4} \omega_i \exp(-E_{vJ}/kT)_i \; p_{JJ';i} \; q_{vv'JJ';i} \; g_{\omega_i}\right]_{2\Delta\omega^*_1}}{\left[\sum_{vv'} \sum_{b} \sum_{i}^{4} \omega_i \exp(-E_{vJ}/kT)_i \; p_{JJ';i} \; q_{vv'JJ';i} \; g_{\omega_i}\right]_{2\Delta\omega^*_2}} \quad . \quad (11)$$

III. NUMERICAL CALCULATIONS FOR OH

Detailed calculations for the temperature function were performed on computing machines using the data of Dieke and Crosswhite (21) for the relative rotational transition probabilities, line locations, and energy levels, and the data of Nicholls (22) and Learner (1) for the Franck-Condon factors. The slit function was taken to be an isosceles triangle centered at ω_o and normalized to a peak value of 1.0 as shown in Fig. 2. The wavenumber interval $2\Delta\omega^*$ was chosen to be 1049 cm^{-1} which corresponds to 100A at 3100A near the band head of the OH violet system for the Perkin-Elmer Model 98 monochromators used in the experiments.

From Ref. 21, it is seen that only the (0,0)-, (1,1)-, (2,2)-, and (3,3)- bands contribute appreciable radiation in the wavenumber interval from 29,000 to 33,000 cm^{-1}. The calculations and experiments were therefore restricted to this interval and these bands.

The effect of wavenumber setting on the relative light flux passed by the monochromators may be seen in Fig. 3, which shows the variation of the relative intensity term

$$I_{rel} = \left[\sum_{vv'} q_{vv'} \sum_{b} \sum_{i}^{4} \omega_i \exp(-E_{vJ}/kT)_i \; p_{JJ';i} \; g_{\omega_i}\right]_{2\Delta\omega^*} \quad (12)$$

with wavenumber at typical shock tube operating temperatures.

Consideration of the data shown in Fig. 3 leads to some conclusions regarding the choice of wavenumbers that should be used for the two monochromator settings to obtain $\phi(T)$. Since the maximum intensity occurs near ω_o = 32,250 cm^{-1} at all temperatures and is relatively insensitive to small errors in monochromator setting, this value is an obvious choice for ω_{o1}. In order to obtain high sensitivity in the temperature measurements, the ω_{o2} setting for the other channel should be as far removed from

32,250 cm^{-1} as possible. The lower limit on ω_{02} is governed by the signal-to-noise ratio available at low wavenumbers; also, it is seen that for a given error in monochromator setting (e.g., $\pm\frac{1}{2}$A), a greater percentage variation occurs in the signal at lower wavenumbers, thus leading to a greater uncertainty in the temperature.

In view of these factors, a choice of wavenumbers was made which allowed reasonable signal strengths to be attained (based on previous experimental experience), and $\phi(T)$ was then calculated as a function of temperature for various values of ω_{02} (see Fig. 4, which is calculated from transition probabilities assuming no vibration-rotation interaction).

From Fig. 4 an estimate may be obtained of the error in the spectroscopic temperatures produced by errors in monochromator settings alone.† The maximum error occurs for ω_{02} = 31,000 cm^{-1} and low temperatures ($\sim$3000°K); errors due to uncertainties in ω_{01} are essentially zero since this setting corresponds to the peak of the curves in Fig. 3. If ω_{02} can be set within 5 cm^{-1} (which corresponds to an experimental accuracy of about $\frac{1}{2}$A), the temperature uncertainty contributed by this factor is ΔT = 25-30°K.

In order to minimize the uncertainty in temperature produced by inaccuracies in the monochromator setting while maintaining a reasonably sensitive indication of the temperature near 3500°K, the experiments were conducted with ω_{02} = 31,000 cm^{-1} (this choice corresponds to the top curve in Fig. 4).

Uncertainties in the monochromator slit width openings do not affect the accuracy appreciably since the intensity term in equation (11) is relatively insensitive to small changes in $2\Delta\omega^*$ for the slit widths considered here.

Figure 5 shows a comparison of the temperature functions $\phi(T)$ and $\phi'(T)$ calculated respectively without and with vibration-rotation interaction. From these curves, differences in measured spectroscopic temperatures which would result from the use of total transition probabilities with and without vibration-rotation interaction may be obtained. These differences are also shown on Fig. 5.

Although appreciable differences exist for temperatures greater than about 5000°K, near 3500°K where experimental data were gathered, the difference (about 70°K) is within the total experimental uncertainty of $\pm$75°K. Over the range of 3500-6000°K, the effect of vibration-rotation interaction would be to raise the observed spectroscopic temperatures from

---

†Note that the total error in the experimental measurements is greater than this because of additional errors in measuring the signal ratio V_1/V_2 and the relative sensitivity ratio, K_2/K_1. See Section V for an estimate of the total experimental error.

about 2-3½% over those that would be obtained by reducing experimental data on the assumption that vibration-rotation interaction did not exist. It should be noted that this relatively small correction is a consequence of utilizing emission from wide spectral regions covering all branches of the main v'= v vibration bands. By observing all branches simultaneously, the interaction effects are minimized since increases in intensity in some branches tend to be offset by decreases in others as shown in Table I for the (0,0)-band.

The effect of interaction would be much stronger if observations were made in the v'= v±1 bands (Ref.'s 26 and 27). These bands lie outside the wavelength region considered in this study however, and in addition have very weak emission compared to the v'= v bands.

IV. EXPERIMENTAL FACILITIES AND PROCEDURES

Detailed descriptions of the experimental apparatus have been reported previously (28-30), however, some features of the equipment that are especially pertinent to the temperature measurements are described in this section of the present paper. A schematic diagram of the essential components of the equipment is given in Fig. 1 and a photograph of the dual monochromator arrangement is shown in Fig. 6.

A. Optical System

Apertures in front of the quartz lenses limit the exit optics systems to observations in a narrow core of gas in the center of the shock tube about 1 cm in diameter and essentially cylindrical in shape with an included divergence angle of less than $\tan^{-1}(0.04)$. Thus, side wall boundary layer effects and light reflections from the inside of the shock tube walls are avoided, and the volume of gas emitting radiation into the optical system grows linearly with time as the reflected shock wave moves up the tube. Viewing emission axially behind the reflected shock allows an experimental check to be made on the assumptions that the gas is transparent and in equilibrium if the increase in the axial emission is linear with time (see Fig. 7).

B. Gas-handling System

The OH was generated by the dissociation of small amounts of water vapor diluted with argon in the shock tube, the initial test gas total pressures all being near 50 mm Hg. In order to achieve the optical transparency required in the theoretical analysis, it was necessary to use very low initial water vapor concentrations; namely about ½ per cent by mole fraction.

The dilution was attained by a continuous flushing operation with dry argon being bubbled through a series of bulbs containing degassed water.

The resulting partial pressure of water vapor was that of saturated vapor at the temperature of the flushing system, which was controlled in the range of 2-10°C (29).

While it is not necessary to know the precise concentrations for the spectroscopic temperatures (see equation 6), the calculated equilibrium temperature based on shock wave speed is sensitive to the amount of initial water vapor since H_2O has a relatively high heat of dissociation. Thus, in order to obtain a proper comparison of the measured temperatures with calculated values, an accurate knowledge of the initial concentration was required.

C. Determination of the Relative Sensitivity Ratio, K_2/K_1

The ratio of relative sensitivities of the two optical systems was obtained directly from shock tube experiments with both monochromators monitoring emission from the same wavelength interval. The resulting signal ratio was the desired factor, K_2/K_1. The calibration records were similar to Fig. 7, except with ω_{O_2} set at ω_{O_1}.

V. EXPERIMENTAL RESULTS

A typical oscilloscope trace of emission from the two wavelengths, 32,250 cm^{-1} and 31,000 cm^{-1}, is shown in Fig. 7. The initial slopes of these records represent the emission per unit length of test gas and together with the K_2/K_1 factor permit determination of the spectroscopic temperature of the OH by utilizing the calculated values of $\phi(T)$. In Table II, the results derived from a number of experiments are compared to the temperatures calculated from the measured shock velocities and equilibrium gasdynamics considerations.

The comparison between the measured spectroscopic temperatures and the calculated equilibrium temperatures in Table II is based on a transition probability assuming no vibration-rotation interaction. This assumption was used since the calculated corrections based on the interaction are normally within the estimated accuracy of the experiments (see the following section). The excellent agreement between the spectroscopic and gasdynamic temperatures in Table II lends support to the neglect of the interaction effects.

A. Estimate of Accuracy

The estimated accuracy of the spectroscopic temperature measurements was about ±75°K. Contributions to this total error come from (a) errors in monochromator settings, (b) errors in the K_2/K_1 calibration, and (c) errors in determining V_1/V_2 from oscilloscope records. As discussed previously in Section III, the error due to uncertainties in the monochromator settings is about 25-30°K. Errors in both K_2/K_1 and V_1/V_2 are associated with errors in determining the slopes of oscilloscope records. This error was about 3 per

cent so that contributions of $\pm 30^{\circ}K$ arise from uncertainties in both K_2/K_1 and V_1/V_2.

The difference between the spectroscopic and equilibrium temperatures shown in Table II varies by more than $\pm 75^{\circ}K$ in some cases, presumably because of some uncertainty in the shock tube performance data (e.g., measured shock velocities, initial mixture temperature, etc.).

B. Temperature Measurements in Other Laboratories

A number of temperature measurements in the incident shock wave region have been made by Gaydon and his coworkers, using line-reversal techniques (31); the results agree within about $\pm 30^{\circ}K$ of the calculated equilibrium values in the range of 2000 to $2800^{\circ}K$.

The line-reversal technique was also used by Lapworth (32) to get $\pm 50^{\circ}K$ agreement behind reflected shock waves up to about $2500^{\circ}K$, and by Charatis (33) with 3 per cent agreement up to $7800^{\circ}K$ behind reflected shocks. Wurster and Treanor's results (34) using oxygen ultraviolet absorption in the reflected wave region agreed with the calculated values within $\pm 100^{\circ}K$ from 1500 to $4000^{\circ}K$. Lauver, Hall, and Belles (35) measured simultaneous absorption and emission from CO_2-Ar mixtures to obtain reflected shock region temperatures near $2500^{\circ}K$ in good agreement with calculated values, and Carnevale, Carey, and Marshall (36) obtained agreement with calculated reflected shock wave temperatures in the 3000-$9000^{\circ}K$ range using ultrasonic measurements in argon.

C. Relaxation Effects

It should be noted that the spectroscopic temperatures described in the present study are based on the assumption that equilibrium exists among the states from which the emission is observed. If a region of non-equilibrium exists in a test gas, the signal from axial observations behind the reflected shock wave will initially exhibit either an under-or-overshoot depending on whether the radiating states are under-or-over populated. However, if an equilibrium zone exists, the slope of the observed signal will reach the proper value required to define the equilibrium temperature, i.e., as in equation (6). This effect was demonstrated in the OH experiments where an apparent relaxation time ($\sim$25 microseconds) was required for the emission of the (2,2)- and (3,3)- bands to become equilibrated with the emission from the (0,0)- and (1,1)-bands (see Fig. 7).

VI. CONCLUDING REMARKS

The experimental records indicate that thermal equilibrium in the OH $^2\Sigma \rightarrow {}^2\Pi$ system was achieved behind the reflected shock wave. The spectroscopic temperatures obtained by the procedures described here were in good agreement with calculated equilibrium temperatures based on measured

shock velocities; this indicates that the wide-band, dual wavelength emission method may be adapted to measure hot gas temperatures in shock tubes, if conditions correspond approximately to those presented in this paper.

The advantages of the method described here are that no external, calibrated light sources are required, and by using wide wavelength regions for the observations, high spectral resolution is not necessary. In addition the technique as adapted to the reflected shock wave studies allows experimental verification of the equilibrium state of the gas.

Some limitations on the method are that it requires the addition of small traces of water vapor (which depresses the gas temperature), and since the technique depends on emission from molecules it is useful only from a lower temperature of about 2500°K to an upper limit of perhaps 6000°K depending on the available signal; no attempts have been made to check the upper limit experimentally, however.

In all cases, due care should be exercised to establish that an equilibrium situation exists in order that the method be valid.

Although many questions remain concerning conditions behind the reflected shock wave, a number of experimental temperature measurements of this region have been reported (see Section V-B) with results in agreement with the calculated gasdynamic value. From these measurements, it would appear that some of the criticism of the suitability of the reflected wave region for quantitative experiments is unwarranted; this is particularly true if the test gas is primarily a monatomic gas, so that bifurcation effects are not important.

VII. ACKNOWLEDGEMENTS

The author is indebted to Professor S. S. Penner for helpful advice and discussions during the experimental work, and to Capt. W. R. Ferguson for calculations concerned with the vibration-rotation interaction.

REFERENCES

(1) R. C. M. Learner, Proc. Roy. Soc. 269A, 311 (1962).

(2) T. Carrington and N. Davidson, J. Phys. Chem. 57, 418 (1953).

(3) C. E. Treanor and W. H. Wurster, J. Chem. Phys. 32, 758 (1960).

(4) J. C. Keck, J. C. Camm, and B. Kivel, J. Chem. Phys. 28, 723 (1958).

(5) R. Watson, J. Quant. Spectr. Radiat. Transfer 4, 1 (1964).

(6) T. D. Wilkerson, Ph.D. Thesis and University of Michigan Department of Physics Report No. 02822-3-T, June 1961.

(7) E. L. Resler, S. C. Lin, and A. Kantrowitz, J. Appl. Phys. 23, 1390 (1952).

(8) I. I. Glass and J. G. Hall, Handbook of Supersonic Aerodynamics, Section 18, Shock Tubes, NAVORD Report 1488, U. S. Govt. Pr' Office, December 1959.

(9) C. E. Treanor, Reprint No. 65-29. 2nd Aerospace S ces Meeting of the AIAA, New York, January 1965.

(10) W. L. Shackleford, Ph.D. Thesis, California Institute of Technology, 1964.

(11) A. Roshko, Phys. Fluids 3, 835 (1960); H. Mirels, "Boundary Layer Effects in Shock Tubes", presented at the American Physical Society 5th Shock Tube Symposium, Washington, D. C., April 28-30, 1965.

(12) A. Hertzberg, W. E. Smith, H. S. Glick, and W. Squire, Report AD-789-A-2, Cornell Aeronautical Laboratory, March, 1955.

(13) D. Baganoff, Rev. Sci. Inst. 35, 288 (1964).

(14) W. T. Knight and D. Venable, Rev. Sci. Inst. 29, 92 (1958); M. Camac and R. M. Feinberg, "Density Measurements with an Electron Beam", presented at the American Physical Society 5th Shock Tube Symposium, Washington, D. C., April 28-30, 1965.

(15) S. S. Penner, Quantitative Molecular Spectroscopy and Gas Emissivities, Addison Wesley, Reading, Mass., 1959.

(16) A. G. Gaydon, "Temperature Measurement and Relaxation Processes in Shock Tubes", Proceedings of the International Symposium on Fundamental Phenomena in Hypersonic Flow, J. Gordon Hall, ed., Cornell University Press, Ithaca, New York, 1965.

(17) H. R. Griem, Plasma Spectroscopy, McGraw-Hill, New York, 1964.

(18) S. S. Penner, "Spectroscopic Methods of Temperature Measurements" in Temperature, Its Measurement and Control in Science and Industry, Vol. 3, Part 1, pp. 561-574, Reinhold Publishing Corporation, New York, 1962.

(19) G. Herzberg, Spectra of Diatomic Molecules, Second Edition, D. van Nostrand Co., Inc., New York, 1950.

(20) R. W. Nicholls, Proc. Phys. Soc. (London) A(GB) A69, 741 (1956); R. W. Nicholls and W. R. Jarmain, A69, 253 (1956).

(21) G. H. Dieke and H. M. Crosswhite, J. Quant. Spectr. Radiat. Transfer 2, 197 (1962).

(22) W. R. Jarmain, P. A. Fraser, and R. W. Nicholls, Astrophys. J. 118, 228 (1953).

(23) R. Watson and W. R. Ferguson, J. Quant. Spectr. Radiat. Transfer (in press).

(24) C. L. Pekeris, Phys. Rev. 45, 98 (1934).

(25) P. M. Morse, Phys. Rev. 34, 57 (1929).

(26) W. G. Zinman and S. I. Bogdan, J. Chem. Phys. 40, 588 (1964).

(27) S. A. Haycock, Live Intensities in Diatomic Electronic Spectra, M. S. Thesis, University of Western Ontario, London, Canada, 1963.

(28) R. Watson, J. Quant. Spectr. Radiat. Transfer 3, 255 (1963).

(29) R. Watson, Rev. Sci. Instr. 10, 1113 (1962).

(30) R. Watson, Appl. Spectr., 16, No. 5, 164 (1962).

(31) J. G. Clouston, A. G. Gaydon, and I. I. Glass, Proc. Roy. Soc. 248A, 429 (1958); J. G. Clouston, A. G. Gaydon, and I. R. Hurle, Proc. Roy. Soc. 252A, 143 (1959); A. G. Gaydon and I. R. Hurle, Proc. Roy. Soc. 262A, 38 (1961).

(32) K. C. Lapworth, "Temperature Measurements in a Hypersonic Shock Tunnel," from AGARD Meeting on High Temperature Aspects of Hypersonic Flow, Brussels, April 1962.

(33) G. Charatis, Ph.D. Thesis, University of Michigan, June 1961.

(34) W. H. Wurster and C. E. Treanor, "Spectroscopic Technique for Temperature-Density Measurements in Oxygen-Bearing Flows," Cornell Aeronautical Laboratory Report No. AD-1118-A-10, Buffalo, New York, December 1959.

(35) M. R. Lauver, J. H. Hall, and F. E. Belles, "Temperature Measurement in a Shock Tube by Monochromatic Radiation Pyrometry", presented at the American Physical Society 5th Shock Tube Symposium, Washington, D. C., April 28-30, 1965.

(36) E. H. Carnevale, C. Carey, and T. Marshall, "Temperature and Thermal Conductivity Measurements in a Shock Tube", presented at the American Physical Society 5th Shock Tube Symposium, Washington, D. C., April 28-30, 1965.

Table I. THE EFFECT OF VIBRATION-ROTATION INTERACTION ON BRANCH INTENSITIES IN THE (0,0)-BAND OF OH AT 3000°K (from Ref. 23)

Branch	Relative Branch Intensity with No Interaction	Relative Branch Intensity with Interaction	%Change in Branch Intensity due to Interaction
P_1	5.31013	5.36922	+1.11
Q_1	8.43656	8.42902	-0.09
R_1	3.38225	3.34509	-1.10
P_2	4.10792	4.15437	+1.13
Q_2	7.27937	7.28114	-0.02
R_2	3.13703	3.11097	-0.83
all satellite branches	3.00420	3.00420	- - -
Total for all branches	34.72874	34.69401	-0.10

$$\text{Branch Intensity} = \left[\sum_{i}^{4} \omega_i \exp(-E_{vJ}/kT)_i \left| R_{vv'JJ'} \right|_i^2 \right]_{\text{branch}} \text{(arbitrary units)}$$

where $\left| R'_{e1} \right|^2 = 1.013 \left| R_{e1} \right|^2$ at 3000°K.

Table II. TABULATION OF EXPERIMENTAL RESULTS

Initial H_2O concentration (per cent)	Incident shock velocity (mm/μs)	Measured spectroscopic temperature (^oK)	Calculated equilibrium temperature (^oK)	$\Delta T = T_{spect} - T_{equil}$ (^oK)
0.50	1.314	3520	3583	-63
0.50	1.299	3550	3510	+40
0.30	1.329	3710	3775	-65
0.30	1.292	3710	3580	+130
0.30	1.299	3680	3620	+60
0.30	1.306	3685	3650	+35
0.29	1.303	3510	3630	-120
0.30	1.337	3800	3840	-40
0.30	1.281	3530	3510	+20
0.30	1.326	3740	3750	-10
0.30	1.299	3600	3615	-15
0.31	1.303	3580	3625	-45
0.29	1.299	3595	3625	-30
0.33	1.232	3385	3280	+105
0.33	1.246	3490	3350	+140
0.33	1.416	4250	4270	-20
0.33	1.314	3620	3690	-70

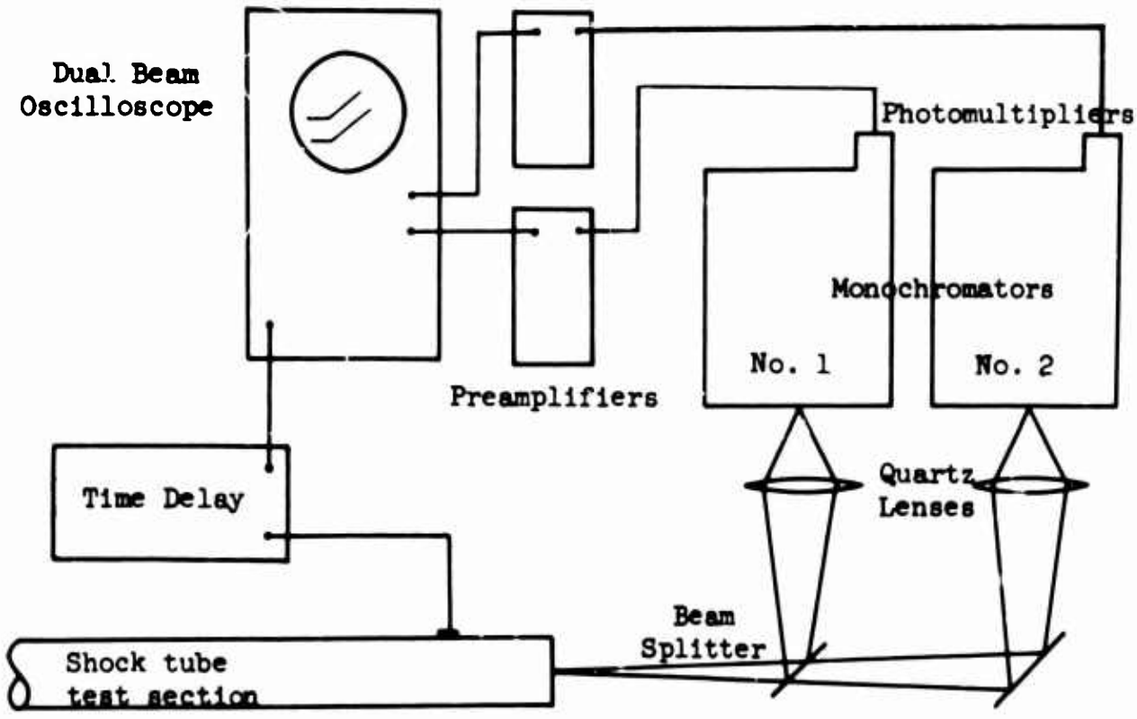


Fig. 1. Schematic diagram of experimental apparatus.

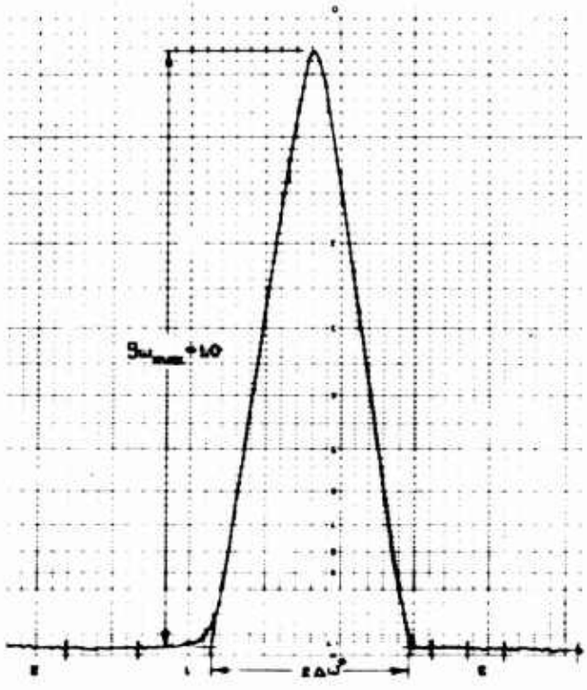


Fig. 2. The monochromator slit function as determined by scanning the 3341.48 Hg line with a thermocouple; the monochromator slit width setting is 1.0 mm.

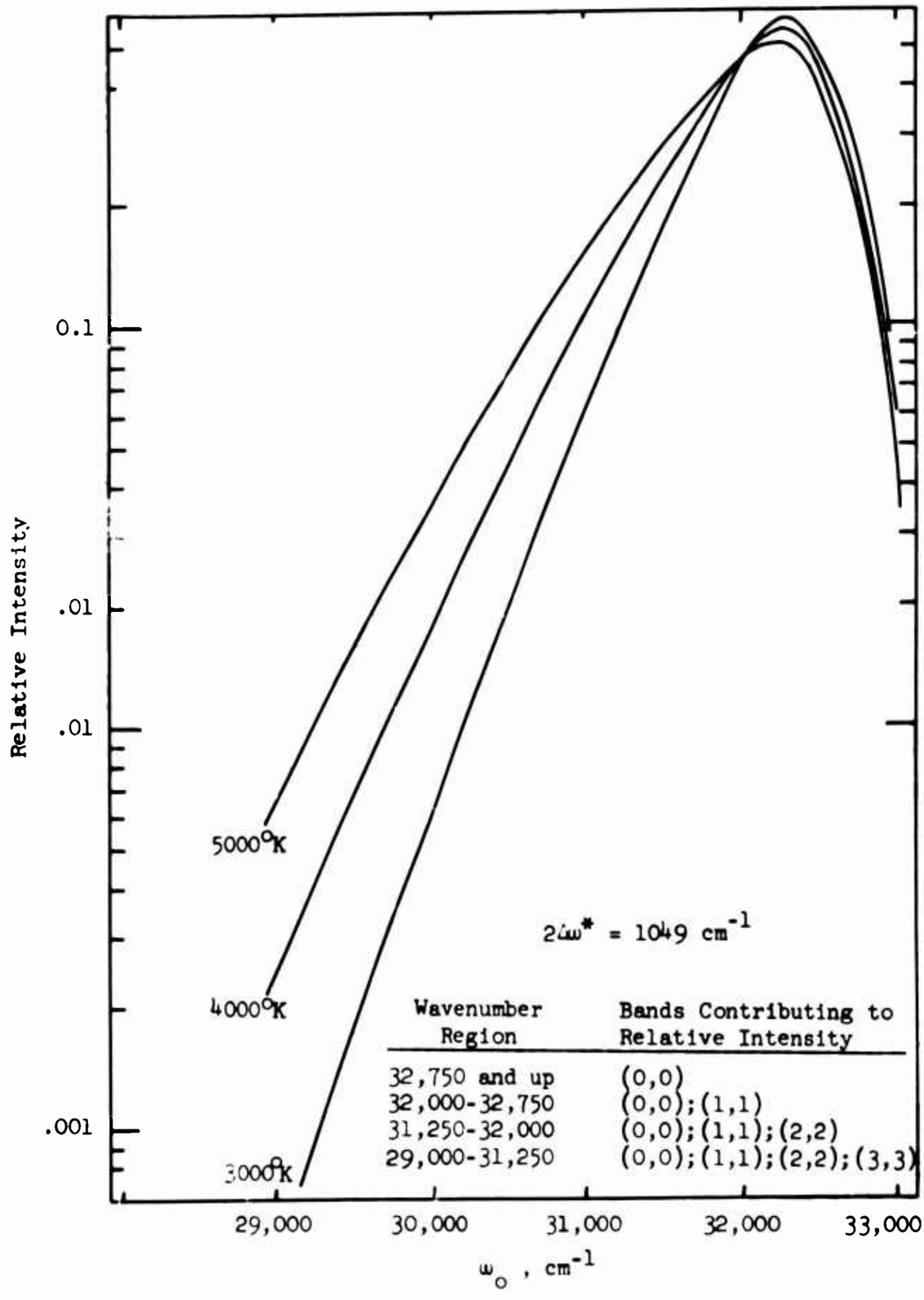


Fig. 3. Relative intensity vs. wavenumber setting for a monochromator with $2\dot{\omega}^* = 1049$ cm^{-1} and a triangular slit function.

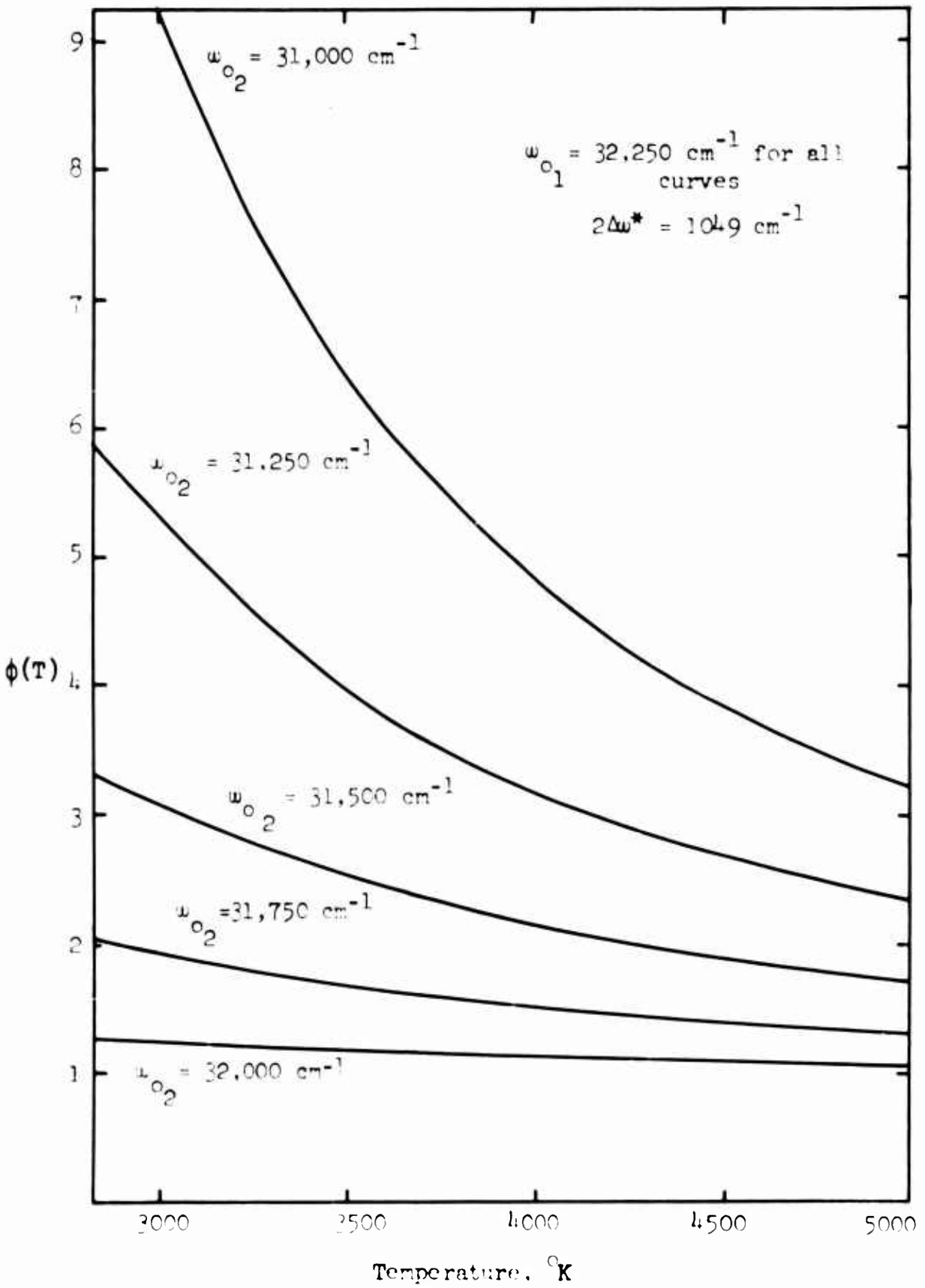


Fig. 4. The intensity ratio, ϕ (T), as a function of temperature for ω_{o_2} from 31,000 to 32,000 cm^{-1}.

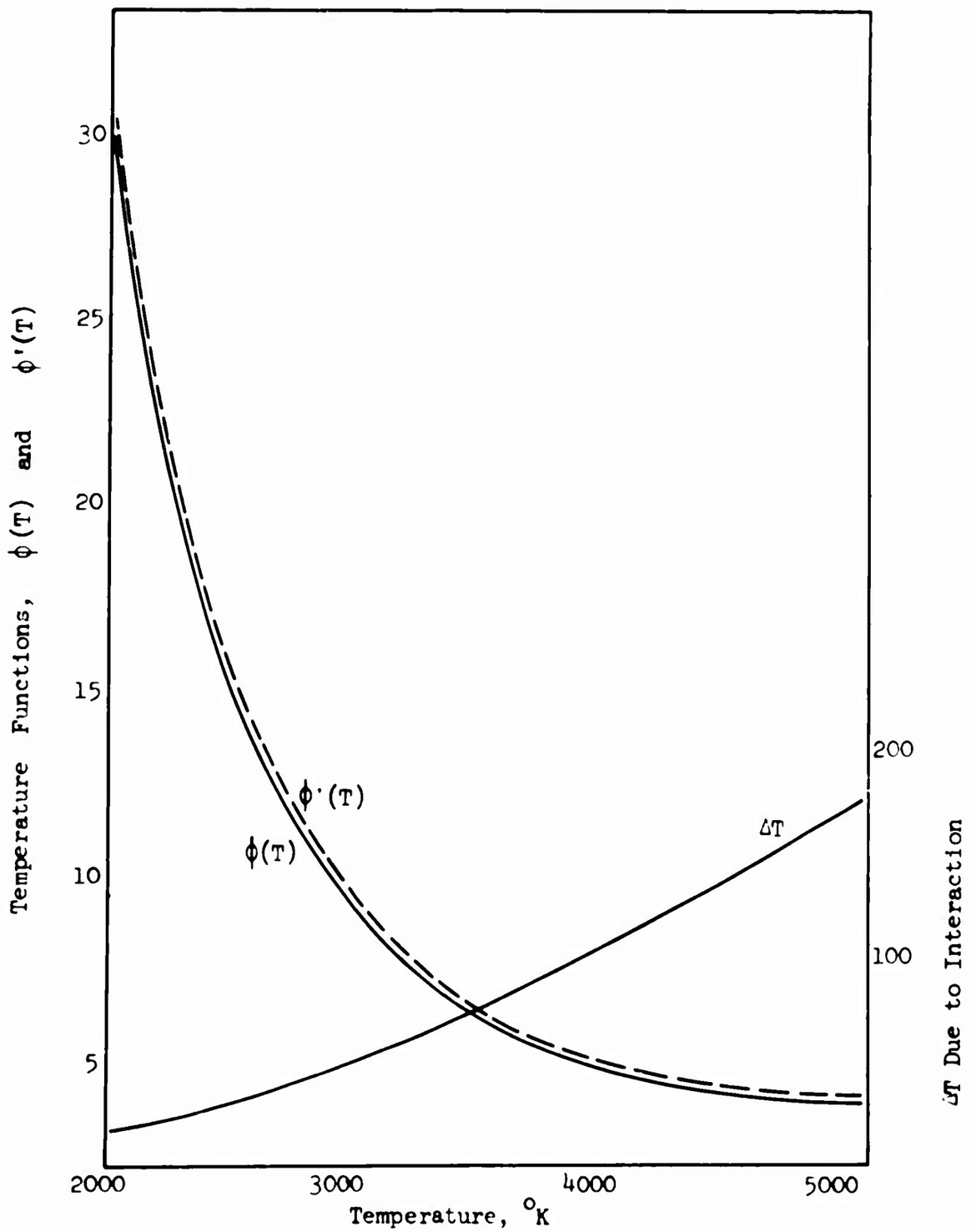


Fig. 5. A comparison of $\phi'(T)$ without vibration-rotation interaction and $\phi(T)$ with interaction, as a function of temperature and the temperature difference ΔT due to vibration-rotation interaction.

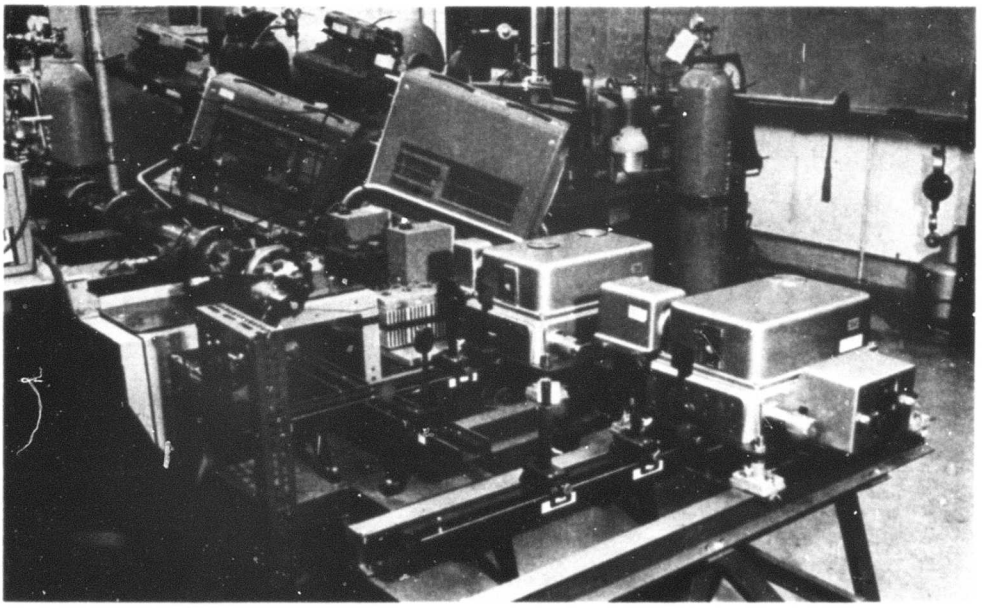


Fig. 6. Dual monochromator system showing the optical system for viewing emission from the shock tube in the axial direction.

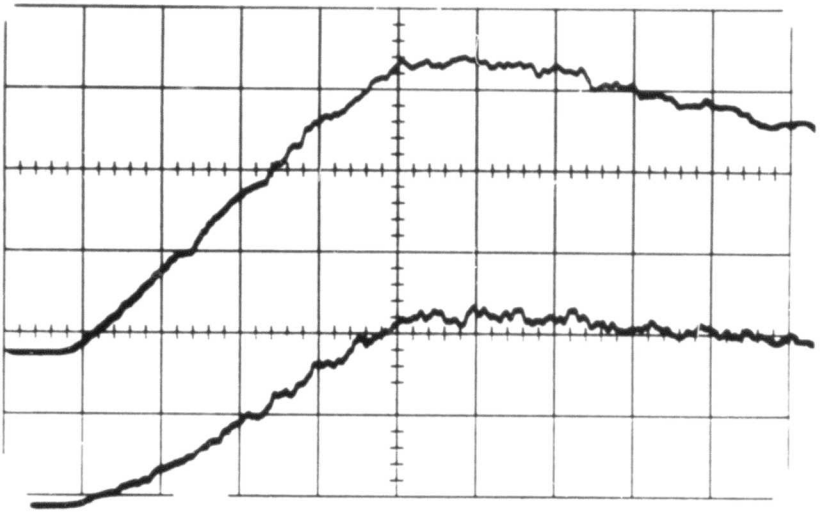


Fig. 7. A typical oscilloscope record from a shock tube test with observation of the OH emission in the axial direction behind the reflected shock wave. Sweep speed = 50 microseconds/cm. The upper trace is for 32,350 cm^{-1} at 10 mV/cm; the lower trace is for 31,000 cm^{-1} at 5 mV/cm. The initial H_2O concentration was 0.30 per cent.

SHOCK FRONT CURVATURE AT INITIAL PRESSURES UP TO 700 mm Hg.*

A. T. Mazzella
Institute for Fluid Dynamics and Applied Mathematics
University of Maryland, College Park, Maryland

and

P. C. T. de Boer
Graduate School of Aerospace Engineering
Cornell University, Ithaca, New York

ABSTRACT

Axial extents of curved shock fronts in argon were measured using thin film heat transfer gauges mounted on a plate perpendicular to the axis of a 1½" diameter shock tube. In interpreting the data, use was made of the theoretical shock shape. This shape was determined from previously derived formulas which apply when the boundary layer behind the shock is either laminar or turbulent, and which account in an approximate way for the influence of the flow at the foot of the shock. At low initial pressures the experimental data obtained agree well with theory and with results of other investigators. For initial pressures above 100 mm Hg the data showed appreciable scatter, which is taken to indicate that the shock is oscillating in curvature. The scatter has the order of magnitude which follows from Freeman's theory for the damping of perturbations in shock shape, with the assumption that somewhere near the diaphragm the shock is strongly curved. Variations in shock tilt were generally less than 0.003 radian.

I. INTRODUCTION

For shock tube measurements of high resolution it is of importance to know the curvature and shape of the shock front. Previous experiments on

* Work supported by the U.S. Air Force Office of Scientific Research and the Office of Naval Research. Reproduction in whole or in part is permitted for any purpose of the United States Government.

shock curvature have been reported by various investigators. Lin and Fyfe (ref. 1) measured the transit time of the shock through a narrow beam of ultraviolet light traversing the shock tube. Duff and Young (ref. 2) and Johnson (ref. 3) mounted piezo-electric pressure detectors at the end wall of their shock tube and measured the differences in arrival time. Liepmann and Bowman (ref. 4) and Gruat and Rieutord (ref. 5) did similar measurements with thin film heat transfer gauges instead of pressure detectors. Indirect measurements of shock curvature based on the deflection of light by the shock were reported by de Boer (ref. 6). A theory for shock front curvature near a wall arising from the influence of the boundary layer along the wall was given by R. A. Hartunian (ref. 7). This theory was extended to flow in rectangular and circular tubes by de Boer (ref. 8), who also considered modifications arising from the finite length of the boundary layers, and from the special character of the flow at the foot of the shock.

At low initial pressures, theory and experiment appear to be in good agreement. The present investigation was undertaken in order to see if this agreement also exists at higher pressures. As in the work of refs. 4-5, thin film heat transfer gauges were mounted on a plate perpendicular to the axis of the shock tube. The differences in arrival time of the shock at these gauges provided information about the axial extent of the curved shock.

II. EXPERIMENTAL DETAILS

A stainless steel shock tube with circular cross section of 3.757 cm inside diameter was used. The inside of the tube had been honed to a 20 micro-inch finish. The distance between the diaphragm and the shock curvature detector was 516 cm (= 138 tube diameters), and the length of the driver section was 137 cm. The driver gas was helium, the test gas argon. The diaphragms consisted of Alcoa Co. number 1100 - 0 aluminum, with thicknesses of 0.016, 0.032, 0.040, 0.050, and 0.060 inches. Two perpendicular grooves of $1\frac{1}{2}$" length were cut into the diaphragms with a milling machine. The depth of these grooves varied from 0.006" for the 0.016" thick diaphragm, to 0.010" for the 0.060" diaphragm. More than 90% of the diaphragms were found to open up to at least 80% of the shock tube cross section. The possible influence of the breaking of the diaphragm on shock curvature is discussed in Section III.

The shock curvature detector consisted of a rectangular quartz bar of $\frac{1}{2}$" x $\frac{1}{2}$", the ends of which were ground to fit the inside diameter of the shock tube (Fig. 1). There were three films applied across the width of the bar. The two outer films had a radius of curvature of 1.66 cm, which was equal to the distance from their centers to the axis of the shock tube. The inner film was straight, and at the center of the plate. The films had a width of 0.6 mm. They were painted on using Hanovia liquid bright platinum paint 05, and baked for about 20 minutes at 660°C. The resulting film resistances were 180, 420, and 280 Ω , respectively.

With the aid of an optical flat giving rise to interference fringes, the film thicknesses were found to be approximately 820A before baking. After baking the thicknesses had decreased still further, while the quartz was found to be flat to better than 0.0025 mm from measurements using a surface indicator. A total number of 253 runs could be made with the detector, after which a piece containing the connection to one of the thin films broke off the side of the quartz plate. The thin films themselves were still in excellent condition.

The electronic circuit connected to each of the films consisted of a 22.5 Volt transistor battery and a 2200 Ω resistance in series with the film in order to obtain approximately constant current (see Fig. 2). Two double beam Tektronix oscilloscopes were used to compare the signal from the center film with that from each of the outer films. The time needed for each signal to achieve 63% of its approximate final value was about 0.03 microsec. An optical comparator was used to measure the time difference between the signals of the upper and lower traces. The base line and a line along the steepest part of the trace were used to define a starting point of the signal, in analogy with the procedure described in ref. 2 (see Fig. 3). A time difference of about 0.004 microsec could be resolved with this technique. By applying a voltage pulse taken from a square wave generator across the three films, the recording circuits were tested for differences in delay time. These differences were found to be at most 0.003 microsec, and were taken into account in the interpretation of the data obtained.

The velocity of the shock could be measured with two additional thin film gauges at the side wall of the shock tube. These films were baked onto glass rods, the ends of which were ground to a radius of 3/4" in order to make them flush with the shock tube wall. The glass rods were tightly fitted into lucite holders with copper strips serving as the electrical contacts. The films were at distances of 172 and 350 cm from the diaphragm, respectively.

Measurements were made of the times which the shock needed to travel from the first to the second film, and from the second film to the shock curvature detector at 516 cm. The average velocity over the second distance was smaller than over the first one. The difference amounted to less than 3% at the lower pressures and to less than 10% at the higher pressures, and was taken into account by linear interpolation in determining the shock Mach number of each experiment.

Further details on the experimental work may be found in ref. 9.

III. EXPERIMENTAL RESULTS

Experiments were carried out with shocks of Mach number 1.8 to 7.3 moving into argon at initial pressures from 5 to 700 mm Hg. At the higher pressures the largest shock Mach number obtained was 3.3, while at the

lowest pressures the Mach numbers were above 4.6. For given diaphragm thickness and initial pressure, shock Mach numbers were reproducible within 10%.

The two differences in arrival time measured in each experiment at the curvature detector were averaged in order to find the axial extent of the shock between the outer films. The results are plotted in Fig. 4. It is seen that on the average x_{sh} decreases as the initial pressure increases. There is appreciable scatter in the data. The dependence of on shock Mach number M_s is not indicated in Fig. 4, but is discussed below. A measure of the shock tilt was obtained from the difference in arrival time at the two outer films. In general, the shock tilt amounted to less than 0.003 radian, although in a very few cases a tilt as large as 0.006 radian (0.34°) was observed.

The outer films of the curvature detector were located along a radius $r = 0.89\,h$, where h is the shock tube radius. Actually, the quantity of greatest interest in specifying shock front curvature is the total axial extent Θ of the curved shock. In order to convert the data obtained into values for Θ, use was made of the results for the theoretical shock profile given in the Appendix. For a laminar boundary layer behind the shock the appropriate equation is (A5). For the conditions of the experiments the correction factor given in square brackets in (A5) was always close to one, and $\Theta / x_{sh} = 1.72 \pm 0.03$. The results for Θ are shown in Fig. 5. In view of the large scatter found especially at the higher pressures average values have been plotted, together with bars indicating standard deviations. The number of points used to obtain an average value in general was about 10. In some cases this number was only three, so that not all of the averages and standard deviations are very meaningful. Also shown in Fig. 5 are theoretical results based on the work of Ref. 6, for fully laminar and fully turbulent boundary layers behind the shock front. Furthermore, approximate theoretical results are indicated for a partially laminar, partially turbulent boundary layer. In calculating these results use was made of the following expression for the transition distance x_t:

$$x_t = \frac{\eta_2}{\rho_1 \, a_1 \, M_s} \left(\frac{\rho_2}{\rho_1} - 1 \right)^2 Re_t \qquad (1)$$

where η is the coefficient of viscosity, ρ the density, and a the velocity of sound; subscripts 1 and 2 denote conditions in front of the shock and in the free stream behind the shock, respectively. Re_t is the transition Reynolds number, which was taken to be 10^6. From a comparison with published data (ref. 10) it appears that this value is a lower limit and that the actual transition Reynolds number in a tube with smooth walls may be a few times larger. The minimum value of x_t found from (1) for the conditions of interest is about

0.9 cm (for p_1 = 700 mm Hg and M_s = 3.3). Since the shock front curvature is essentially determined by the part of the boundary layer within half a tube radius (= 0.94 cm) from the shock front (compare ref. 8 and Fig. 6), we conclude that for the present experiments the turbulent part of the boundary layer cannot be expected to exert a significant influence on the curvature.

It is seen from Fig. 5 that at low initial pressures p_1 there is reasonably good agreement between theory and experiment. While the theory predicts that θ should be practically independent of the shock Mach number at these pressures, the experimental data indicate that θ is somewhat larger for the higher Mach numbers. At high initial pressures, the average curvature found experimentally is much larger than predicted, and there is a large amount of scatter. The major part of this scatter did not arise from measurement errors. Similar scatter has been reported by other investigators (refs. 2 and 4). It appears as if the shock wave is influenced by phenomena connected with the breaking of the diaphragm, and is oscillating about an equilibrium shape. The damping of such oscillations has been investigated by Freeman (ref. 9). He found that the amplitude of oscillation decays as x^{-n}, where x is the distance from the diaphragm. The exponent takes on the value 3/2 for weak shock waves, and the value 1/2 for strong shocks. Assuming that at a distance x from the diaphragm equal to the tube diameter of 3.75 cm the axial extent of the shock is 1 cm, we find that at the shock curvature detector this perturbation has reduced to 0.06 mm for weak shocks, and to 0.85 mm for strong shocks. Although these calculations are quite approximate, it is of interest to note that the scatter in the data falls within these limits. The influence of the diaphragm breaking on the shape of the shock at a distance equal to 60 tube diameters from the diaphragm has recently been demonstrated convincingly by Liepmann and Bowman (ref. 4).

In conclusion we note that at low initial pressures the theory of ref. 8 predicts the shock front curvature with satisfactory accuracy. At high initial pressures the curvature is much larger than predicted by this theory, and apparently is determined by phenomena connected with the shock formation process. The resulting perturbations will be damped out only at very large distances from the diaphragm.

APPENDIX A. SHAPE OF THE CURVED SHOCK

In this appendix we give formulas and numerical results for the shape of the curved shock, applicable when the boundary layer behind the shock is either fully laminar or fully turbulent, and when the shock travels in a gas between two parallel plates or in a circular tube. The formulas given are based on the work of refs. 6 and 8. In the same reference it is shown that the curvature of the shock front in a rectangular tube simply is the superposition of the curvatures obtained for the corresponding two cases of two parallel walls.

a) Two parallel walls.

It follows from equations (10), (15), (9) and (17) of ref. [6] that the shape of the shock front between two parallel walls, as determined by the displacement thickness of the boundary layers on these walls is given by

$$\frac{x_{sh}}{\Theta} = \frac{1}{2\,(2^{s+1}-1)\,\zeta(-s)\,(-s-1)!}\int_0^\infty \frac{\cosh(\varrho\, y/h) - 1}{\varrho^{s+1}\sinh\varrho}\, d\varrho \qquad (A1)$$

Here x is the distance measured in the direction of the flow in the frame of reference in which the shock is stationary, Θ the total extent of the curved shock in the x-direction, y the distance from the centerplane, and h half the distance between the walls. ζ is the Riemann ζ-function. The boundary layer displacement thickness is given by

$$\delta^* = -A\,x^s \,. \qquad (A2)$$

For small y/h it is useful to expand (A1) as follows

$$\frac{x_{sh}}{\Theta} = \frac{1}{(1-2^{s+1})\,\zeta(-s)}\sum_{k=1}^{\infty}\left[-\binom{s}{2k}(1-2^{s-2k})\,\zeta(2k-s)\,(y/h)^{2k}\right], \qquad (A3)$$

while for y near h, setting $h - y = y_o$,

$$\frac{x_{sh}}{\Theta} = 1 - \frac{1}{2\,(1-2^{s+1})\,\zeta(-s)}\left[\left(\frac{y_o}{h}\right)^s + 2^{s+1}\sum_{k=1}^{\infty}\binom{s}{2k}\zeta(2k-s)\left(\frac{y_o}{2h}\right)^{2k}\right] \qquad (A4)$$

For a laminar boundary layer we have $s = \tfrac{1}{2}$, and (A3) becomes

$$\left(\frac{x_{sh}}{\Theta}\right)_L = 0.3552\,(y/h)^2 + 0.1056\,(y/h)^4 + 0.0541\,(y/h)^6 + 0.0341\,(y/h)^8 + \sum_{k=5}^{\infty} a_k\,(y/h)^{2k}$$

$$\text{with} \quad a_k \approx a_{k-1}\,\frac{k - 0.75}{k}\,\frac{k - 1.25}{k - 0.5}\,, \qquad \text{(A3L)}$$

while (A4) goes over into

$$(x_{sh}/\Theta)_L = 1 - 1.3154\,(y_o/h)^{\frac{1}{2}} + 0.3037\,(y_o/h)^2 + 0.0102\,(y_o/h)^4 + 0.0012\,(y_o/h)^6 \ldots \qquad \text{(A4L)}$$

The last two formulas give results identical to better than 0.1% over a wide range of values of y/h. Numerical values for $(x_{sh}/\Theta)_L$ for various y/h are given in Table I.

For a turbulent boundary layer $s = 0.8$, and we obtain

$$(x_{sh}/\Theta)_T = 0.3140\,(y/h)^2 + 0.0604\,(y/h)^4 + 0.0261\,(y/h)^6 + 0.0150\,(y/h)^8 + \sum_{k=5}^{\infty} a_k\,(y/h)^{2k}\,,$$

$$\text{where} \quad a_k \approx a_{k-1}\,\frac{k - 0.9}{k}\,\frac{k - 1.5}{k - 0.5}\,; \qquad \text{(A3T)}$$

or

$$(x_{sh}/\Theta)_T = 1 - 1.6512\,(y_o/h)^{0.8} + 0.6430\,(y_o/h)^2 +$$

$$+ 0.0074\,(y_o/h)^4 + 0.0007\,(y_o/h)^6 \ldots\ldots$$

(A4T)

These two formulas again give results identical to a fraction of a percent over a wide range of values of y/h. Table I also lists numerical values for $(x_{sh}/\Theta)_T$.

y/h, r/h	0.1	0.2	0.3	0.4	0.5	0.6	0.7	0.8	0.89	0.90	0.95
$(x_{sh}/\Theta)_L$	.0056	.0224	.0509	.092	.146	.217	.307	.424	.567	.587	.707
$(x_{sh}/\Theta)_T$	.0083	.0335	.0756	.135	.213	.310	.428	.570	.725	.745	.851
$(x_c/\Theta)_L$	.0057	.0231	.0525	.095	.151	.223	.314	.432	.576*	.596	.714
$(x_c/\Theta)_T$	.0084	.0338	.0762	.136	.214	.312	.430	.573	.728	.747	.853

Table I. Shape of the curved shock for fully laminar and fully turbulent boundary layers along 2 parallel walls and in a circular tube.

As discussed in Ref. 8, the results just given are invalid close to the wall, since the theory breaks down in that region. In order to account for this breakdown an approximate correction was proposed, which is of some importance at very low initial pressures. After some calculations the corrected shock shape is found to be

$$\left(\frac{x_{sh}}{\Theta}\right)_L \approx \frac{\Theta'}{\Theta} - 1.315\,(y_o/h)^{\frac{1}{2}}\left[1 - 1.16\,(a/\beta\, y_o)^{\frac{1}{2}} + 0.5\,(a/\beta\, y_o)\right]$$

(A5)

where Θ' is the corrected total extent of the shock in the x-direction given by

$$\Theta' \approx \Theta\left[1 - 1.52\,(a/\beta\, h)^{\frac{1}{2}} + 0.8\,(a/\beta\, h)\right] .$$

(A6)

* As was already noted in ref 4, the corresponding number given in footnote 10 of ref. 8 is in error.

The quantity a/β is of the order of the mean free path in front of the shock. A detailed expression for a/β is given in Ref. 6. For argon at the shock Mach numbers of 1.5-6 the results are fitted with sufficient accuracy by the empirical relation $a/\beta = 0.07\ (p_1 \text{ in mm Hg})^{-1}(M_s-1)^{-2}$ mm. Equation (A5) is applicable when $h \gg y_o \gg a/\beta$, and essentially consists of the first two terms of (A4L) with appropriate correction factors.

b) Circular Tube.

The formula for the shock shape in a circular tube corresponding to (A1) is (see ref. 8)

$$\frac{x_c}{\theta} = \int_0^\infty \frac{I_0(\varrho\, r/h) - 1}{\varrho^{s+1}\ I_1(\varrho)}\, d\varrho \Big/ \int_0^\infty \frac{I_0(\varrho) - 1}{\varrho^{s+1}\ I_1(\varrho)}\, d\varrho \qquad \text{(A7)}$$

where r is the distance from the axis, and $I(\varrho)$ the modified Bessel function. No series developments equivalent to (A3) and (A4) are available for this case. Equation (A7) was therefore evaluated for various values of y/h with the aid of a computer. The results are included in Table I, and are seen to be quite close to the corresponding results for x_{sh}/θ

Near the walls, the same breakdown of the theory occurs as for the case of two parallel walls. With some confidence we can apply (A5) and (A6) also to the present case.

Fig. 7 shows a comparison of the present theoretical results with the experimental data of ref. 2. The agreement is seen to be satisfactory. The measurements were not sufficiently accurate to distinguish between the uncorrected theoretical curve and the corrected curve obtained with the aid of (A5) and (A6). Higher accuracy of measurement was achieved by Liepmann and Bowman (ref. 4), who found good agreement with the theoretical uncorrected curve for initial pressures between 30 and 170 micron Hg. Their measurements at initial pressures of 5 and 10 micron Hg show deviations from the uncorrected curve, which are qualitatively analogous to the corrected shape given by (A5). Equation (A5) can be made to agree with their measurements by taking $a/\beta = 0.09\ (p_1 \text{ in mm Hg})^{-1}$ mm. Finally, Gruat and Rieutord (ref. 5) report good agreement with the uncorrected theoretical curve for initial pressures of 0.196 - 3.7 mm Hg in a shock tube with a diameter of 16.42 cm.

REFERENCES

(1) Lin, S. C. and Fyfe, W. I., Phys. Fluids 4, 238 (1961).

(2) Duff, R. E. and Young, J. L., Phys. Fluids 4, 812 (1961).

(3) Johnson, D.S., Thesis, California Institute of Technology (1962) (unpublished).

(4) Liepmann, H.W. and Bowman, R.M., Phys. Fluids 7, 2013 (1964)

(5) Gruat, J., and Rieutord, E., Acad. Sc. Paris, 259, 1619 (1964).

(6) de Boer, P.C. T., Ph.D. Thesis, University of Maryland (1962). (University Microfilms, Ann Arbor, Mich., 63-7137).

(7) Hartunian, R. A., Phys. Fluids 4, 1059 (1961).

(8) de Boer, P.C. T., Phys. Fluids 6, 962 (1963).

(9) Mazzella, A. T., Technical Note BN-381, Institute for Fluid Dynamics and Applied Mathematics, University of Maryland (1965).

(10) Hartunian, R. A., Russo, A. L., and Marrone, P. V., J. Aerospace Sci. 27, 587 (1960).

(11) Freeman, N. C., J. Fluid Mech. 2, 397 (1957).

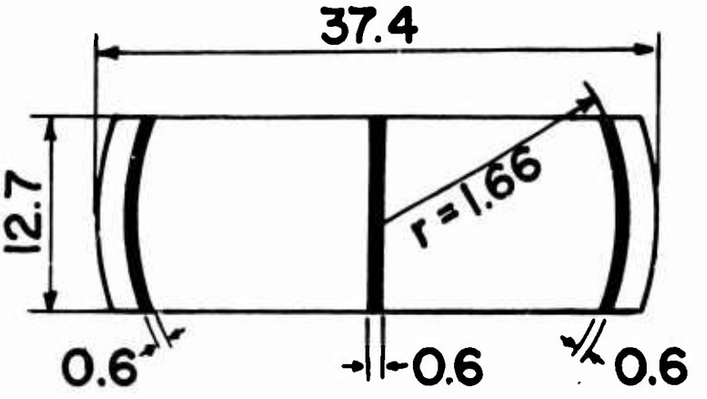


Fig. 1. Sketch of curvature detector, with dimensions in mm.

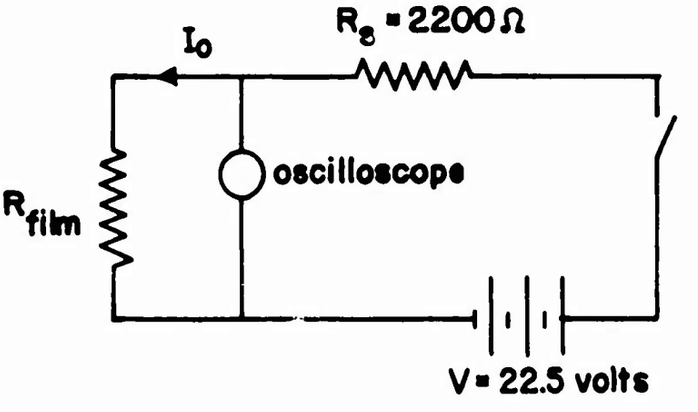
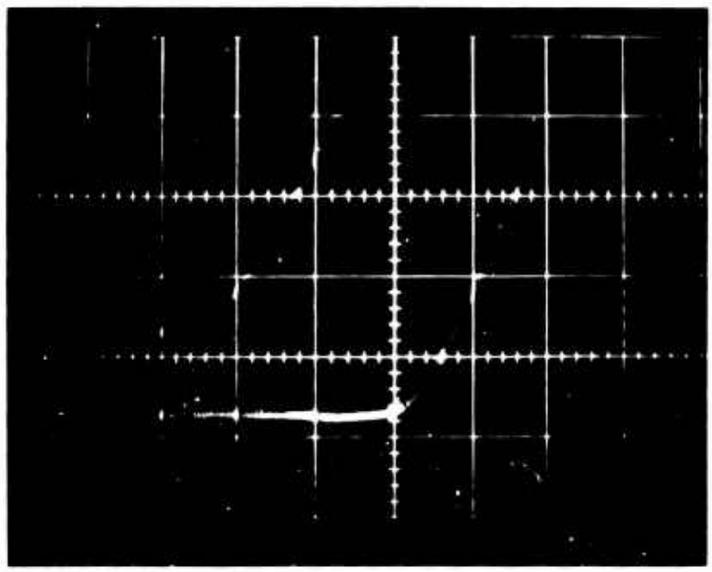


Fig. 2. Electronic circuit used. $R_s \gg R_{film}$, $I_o \approx V/R_s \approx 10$ mA.



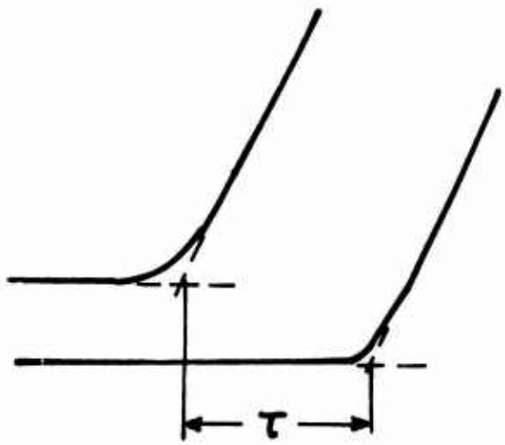


Fig. 3. Representative photograph of records obtained (p_1 = 700 mm Hg, M_s = 3.3). Horizontal scale is 0.04 microsec/division, vertical scale 5 mV/division. The sketch illustrates how the difference in arrival time of the shock at the center and outer film was determined.

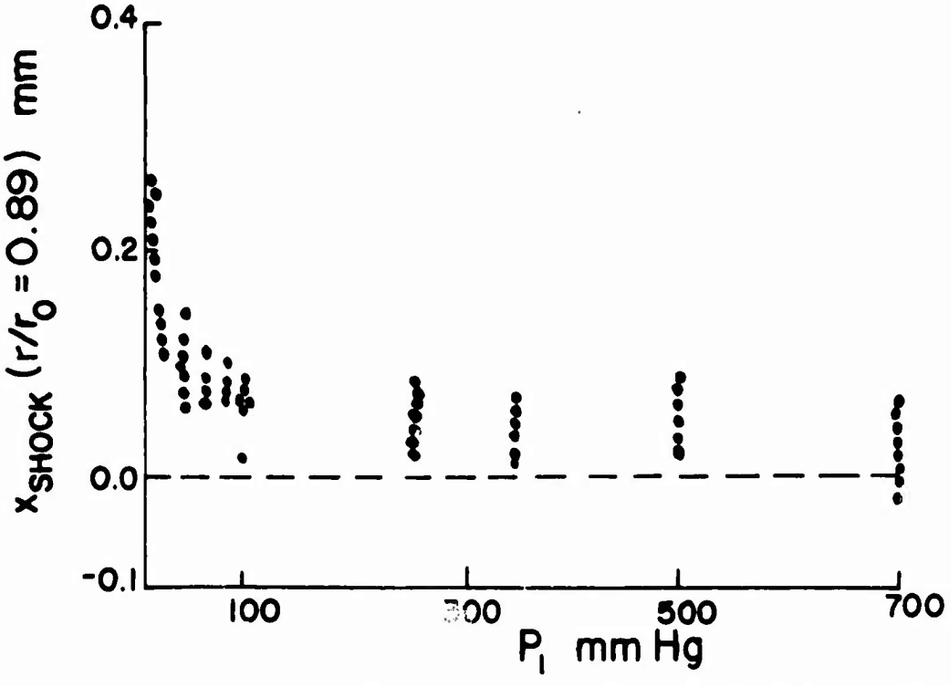


Fig. 4. Measured axial displacement x_{sh} of curved shock at $r/r_o = 0.89$ as a function of initial pressure p_1. (Not all data could be shown).

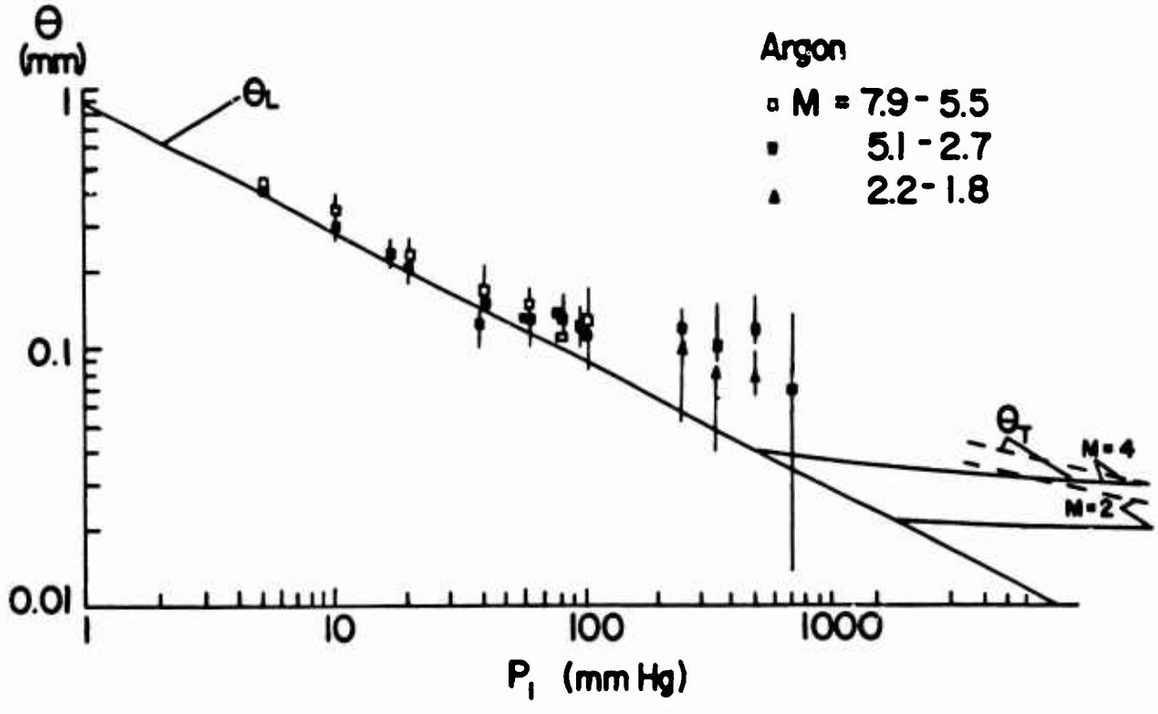


Fig. 5. Total axial extent of curved shock calculated from the data also shown in Fig. 4, as a function of initial pressure p_1. Lines are theoretical results for fully laminar boundary layer (θ_L), for fully turbulent boundary layer (θ_T), and for partially laminar, partially turbulent boundary layer (curved lines). Vertical bars indicate standard deviations.

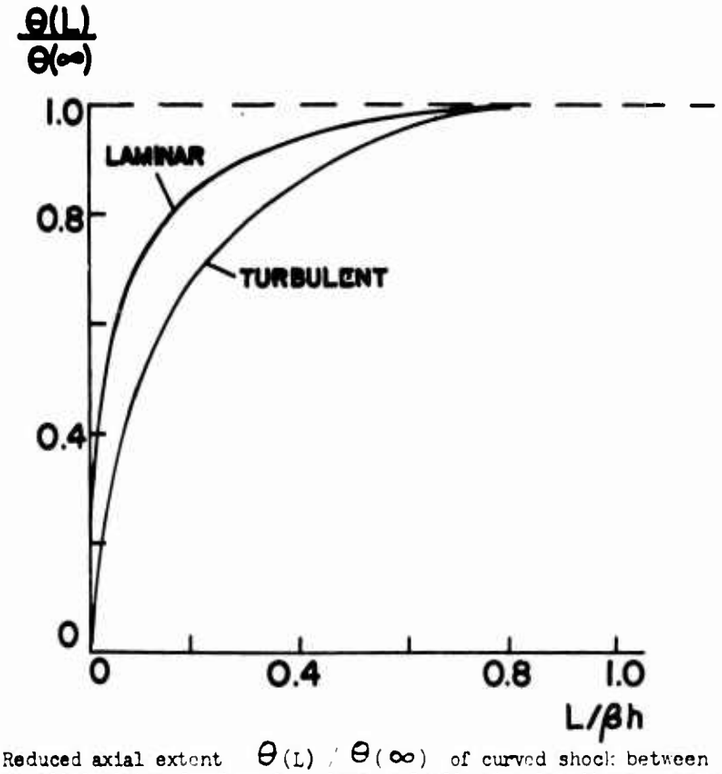


Fig. 6. Reduced axial extent $\theta(L) / \theta(\infty)$ of curved shock between parallel plates for boundary layer of effective length L, as a function of $L/\beta h$ for laminar and turbulent boundary layers. Results are based on equations (26a) and (26b) of ref. 8. ($\beta = (1 - M_2^2)^{\frac{1}{2}}$, where M_2 is the Mach number of the flow behind the shock in the frame of reference of the shock.)

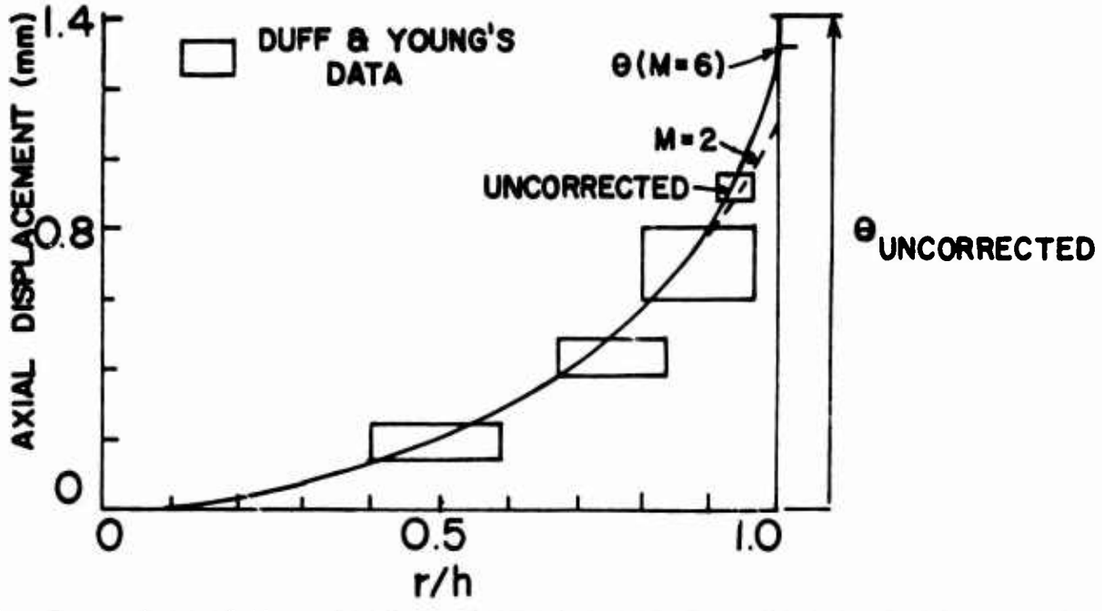


Fig. 7. Comparison of theoretical profile of curved shock with Duff and Young's data for shocks of Mach number 1.83 to 6.33 going into argon at an initial pressure of 0.335 mm Hg, in a circular tube of 18.6 mm inner diameter.

TURBULENT SPOTS AND WALL ROUGHNESS EFFECTS IN SHOCK TUBE BOUNDARY LAYER TRANSITION*

W. P. Thompson† and R. J. Emrich
Lehigh University
Bethlehem, Pennsylvania

INTRODUCTION

There have been many recent experimental studies (ref. 1-6) of the laminar to turbulent transition in shock tube boundary layer flow. Detailed investigations of boundary layer density profiles (ref. 2) and heat transfer rates (refs. 4,6) have amply supported Mirels' theoretical solution of the laminar boundary layer development behind the shock (ref. 7). Based on this solution of the boundary layer structure, Ostrach and Thornton (ref. 8) have developed a theoretical solution for the stability of the boundary layer in the presence of infinitesimal disturbances. The existing transition data are in serious disagreement with the current stability theory, and one aim of the investigation reported here was to relate transition phenomena more closely to the presumed mechanism of flow breakdown and instability.

We shall employ the following nomenclature to characterize the shock and transition parameters: u_w/u_e, wall-to-free-stream velocity ratio in shock-fixed coordinates; u_2 or $\bar{u}_e$, free stream velocity in laboratory coordinates; ν_e, free stream kinematic viscosity; Re_x, Reynolds number based on the distance a particle has moved since started in motion by the shock (ref. 7); and Re_δ, based on boundary layer thickness at $u = .99\ u_2$.

In previous investigations, conveniently summarized in reference (6), transition was seen to occur quite abruptly and reproducibly at a characteristic time behind the shock. This implies that the transition point moves over the wall at shock velocity. In the present experiments, however, the transition is observed to be much more random in time, and turbulent gas is

*Work supported in part by National Science Foundation

†Present address: Aerospace Corporation, El Segundo, California

seen always to move over the wall at the free stream velocity behind the shock. Our current results can be shown to agree with the earlier work in an average sense, however. Further, a study of the influences of finite perturbations on transition has yielded an empirical correlation between the observed transition phenomena and theories of boundary layer stability. A more detailed discussion of these current studies appears in reference (1).

EXPERIMENT

The experiments covered a shock Mach number range from 1.06 to 2.34, at initial pressures from 39 to 5760 mm Hg in air. The shock tube has 3/8 x 4 inch internal dimensions, with a 50 μ inch wall finish. At the test section, 2.5 meters from the diaphragm, polished glass plates 12 x 4 inch were inset flush with the walls. Thin film heat transfer gages were painted and baked on these plates as shown in Figure 1. By suitably distributing the gages, both axial and transverse propagation of transition phenomena could be followed.

In Figure 2 we show a typical record of wall temperature and heat transfer during transition. At shock arrival, the wall temperature jumps to a steady value characteristic of laminar flow. At the time of boundary layer transition, the wall temperature rises suddenly, in an approximately parabolic shape, indicative of the arrival at the gage of fully turbulent boundary layer gas. The heat transfer, obtained by integration of the wall temperature signal, also shows the expected laminar and turbulent behavior. This sort of experimental record is typical of those seen by other investigators, with one significant difference. Whereas others' measurements give a transition time of about 200 μsec at this flow condition, our boundary layer remained laminar for more than 500 μsec. Moreover, the transition shown is not a "natural" transition, but can be attributed to the arrival at the gage of gas which was tripped into turbulence by the wall discontinuity at the upstream edge of the glass plate. Hence the "natural" transition time is even longer than the measured time.

The most significant new feature appearing in our studies is shown in the wall temperature record of Figure 3. The wall temperature is seen to rise linearly, to peak, and to decay back to the laminar value. At a later time, the arrival of fully turbulent, tripped gas from the plate leading edge is seen. We interpret this transient phenomenon as the passage of a turbulent spot over the gage, preceded and followed by laminar flow. The spot leading edge arrives at the first deviation from the laminar temperature plateau, and the trailing edge passes at the peak of the wall temperature bump. (The subsequent decay is a result of the thermal lag at the surface of the wall after removal of the higher turbulent spot heat transfer rate.)

In general, the appearance of turbulence in the boundary layer occurs in successive steps as M_s is increased. 1) At the lowest M_s, no distinct turbulent spots were seen, and laminar flow was limited by the arrival of leading edge tripped gas. 2) As M_s is increased, turbulent spots appear on an increasing fraction of the runs. The spots may be detached (preceded and

followed by laminar flow) or may have merged with other spots or with the tripped turbulent front. Raising either M_s or p_1 serves to increase the frequency of spot occurrence, at $M_s \approx 1.4$. Maximum observed laminar flow time is still determined by leading edge tripping on some portion of the runs at a given flow condition. 3) At higher M_s, no detached spots are seen, and the tripped gas arrival is obscured by merged spots. Transition is still characterized by a linear wall temperature rise appropriate to the leading edge of a turbulent spot. 4) At $M_s > 2$, no turbulent spot phenomena can be distinguished, and the transition occurs with the abrupt, parabolic wall temperature rise seen by other investigators. We shall first consider the tripping process induced by wall roughness elements, and the propagation of the turbulent front. Then we shall discuss the origin and growth of turbulent spots.

Wall Roughness Effects

The motion of the tripped turbulent front gas could be followed along the wall, as shown in Figure 4. Two features should be noted. First, the fully turbulent front is always observed to move over the wall at free stream velocity. Second, the first gas particles to become turbulent are not those immediately behind the shock, but rather those which have flowed for a characteristic time τ_K behind the shock before passing over the roughness element. This delay time, τ_K, is defined graphically as shown in Figure 4, by the intersection of the turbulent front path with the wall discontinuity at the plate leading edge. Many experiments with gages as close as .25 inch behind the leading edge showed this behavior always to be the case.

The line discontinuity at the plate leading edge is a step down in the wall surface, of about .001 inch height. A further experiment was tried using 1 mm wide strips of scotch tape .0025 inch high, forming flat ridge roughness elements. Typical results are shown in Figure 5. Again the characteristic delay time τ_K is seen. Surprisingly, the delay time is the same for tripping by the leading edge or the tape strip, despite their considerably different nature. We conclude that it is the stability of the boundary layer, and not the nature of the 2-dimensional roughness element, which controls the tripping process. If the times τ_K are used to derive a transition Reynolds number Re_δ, then this Reynolds number has a characteristic value of about 1700 for all our tripping experiments. The boundary layer appears to be stable in the presence of finite disturbances until it has achieved this Reynolds number.

Turbulent Spots

We turn now to the turbulent spots. In a large number of subsonic and supersonic flow environments, the generation and growth of turbulent spots has been established as the mechanism of boundary layer transition. Infinitesimal perturbations are amplified in the boundary layer above a minimum critical Reynolds number. When these waves have grown sufficiently large, they cause a point generation of turbulence in the flow. Turbulent spots then grow and propagate downstream from these randomly occurring point

sources. A determination of turbulent spot shape and propagation geometry made in incompressible flat plate flow (ref. 9) is shown in Figure 6. In the shock tube, we have established the following spot characteristics: the leading edge and trailing edge move over the wall at velocities u_2 and 1/2 u_2, respectively. The spot shape is approximately triangular as shown, with a vertex angle between 11 and 18 degrees, in fair agreement with Schubauer's (ref. 9) value of 15.3°. The wake-spreading angle α could not be determined in the shock tube. Note that by extrapolation backward of the growth envelope, the origin of the spot may be located.

Naturally occurring turbulent spots were found to arise at quite random times and positions behind the shock, on successive shock tube runs. At two flow conditions where spot occurrence was most frequent, a statistical analysis of the transition times was performed (ref. 1). An example appears in Figure 7. The function $P(\tau)$ is the probability that the first deviation from laminar flow will occur at time τ. The function $\Gamma(\tau)$ is the probability that the first deviation (i.e., transition) will have occurred prior to time τ. For comparison, the range of transition times found by Chabai (ref. 3) is shown as τ_c. Several conclusions are suggested by these curves. Comparison of the intermittency function $\Gamma(\tau)$ with the similar curves of Narasimha (ref. 10) provides strong evidence that shock tube transition does occur by amplification of small disturbances, leading to turbulent spots. Further, $P(\tau)$ shows a clearly preferred transition time, in fair agreement with others' measurements as typified by τ_c. A possibly more meaningful comparison, specifically with Chabai's work, can be arrived at in the following way: Our present gages are 1/2 inch long, whereas Chabai's gages were 4 inches long, spanning the entire tube. If we assume Chabai's gage to be made up of 8 independent 1/2 inch segments, then we can compute the probability Γ_8 that transition will have occurred somewhere across the tube width by time τ. It is seen from Figure 7 that when the transition probability Γ_8 averaged across the tube reaches a value 0.3-0.6, it agrees very closely with the transition time measured by Chabai. Hence it appears that in this range of flow conditions, where transition occurs by random, point breakdown of the flow, it makes a considerable difference whether measurements are made with localized detectors or by averaging across the tube as was done in references (2-4).

In order to study more carefully the propagation of turbulent spots from a known point source in space and time, it was decided to introduce sparks into the boundary layer. The experimental arrangement is shown in Figure 8. Sparks could be generated at any desired time after the shock passed the thin film spark gap, and the propagation of turbulent spots from this disturbance could be followed by gages downstream.

A schematic x-t plot of the growth of such artificially generated spots is shown in Figure 9. At time τ_s after the shock has passed the spark gap, the spark is fired. The disturbance convects downstream, eventually causing flow breakdown at x_o, τ_o. The turbulent spot can be seen to grow from this origin, with leading and trailing edges moving at u_2 and 1/2 u_2, followed eventually by the fully turbulent front from leading edge tripping. The positions x_o, τ_o of spot origin, as a function of the introduction time of the

spark τ_s, were determined for a large range of τ_s at several flow conditions. Results at $M_s = 1.24$, $p_1 = 760$ mm are shown in Figure 10. The spark disturbance moves downstream at 1/2 u_2, but will not cause flow breakdown or initiation of turbulent spot growth until it has reached a local Reynolds number in the boundary layer given by τ_{CRIT}. Regardless of the strength of the disturbance or its time of introduction, it will not generate a spot until this critical time or Reynolds number is reached. When $\tau_s > \tau_{CRIT}$, breakdown occurs immediately at the spark gap. At lower M_s, for very short τ_s, it was found that spark disturbances would damp out completely, never causing flow breakdown. This is entirely in accord with the presumed Tollmein-Schlichting mechanism of amplification of small disturbances which has been so well verified in other boundary layer flows.

DISCUSSION

The transition data are summarized in Figure 11 and Table I. In Figure 11, the customary transition Reynolds number Re_x is plotted vs the shock strength parameter u_w/u_e. The range of earlier measurements, as summarized in reference (6), is shown by the dotted lines. The range of transitions at each flow condition from the present work is superimposed for comparison. Our earliest transitions, occurring by the random turbulent spot mechanism, fall within the range of others' observations. The maximum observed duration of laminar flow, limited by leading edge tripping, is far in excess of the values seen by others, however. Also shown in the upper left is the theoretical limit of shock tube boundary layer stability (ref. 8), below which disturbances should not be amplified. As was apparent from previous measurements, all the observed transitions fall in the supposedly stable region.

In Table I are shown the critical Reynolds numbers, below which the boundary layer will not become turbulent in the presence of finite disturbances, as determined from wall roughness and spark perturbations. Both disturbance sources give a best correlation in terms of $Re_\delta = 1.7$ or 1.8×10^3. This number then empirically defines the critical Reynolds number for stability of the shock tube boundary layer. Also included in Table I is the minimum transition Reynolds number observed at each flow condition for naturally occurring turbulent spots. As might be expected, $Re_{MIN} > Re_{CRIT}$, since presumably some disturbance amplification must occur in the natural transition case.

SUMMARY

We draw three major conclusions from these studies.

1) For weak shocks at initial pressures near one atmosphere, transition occurs by an intermettent turbulent spot mechanism quite similar to that familiar in steady flat plate flows.

2) The duration of laminar boundary layer flow can considerably exceed that observed in earlier studies.

3) There exists a minimum critical Reynolds number for the shock tube boundary layer, below which the boundary layer is stable even in the presence of finite disturbances.

REFERENCES

(1) Thompson, W. P., "An Experimental Study of Turbulent Spots and Wall Roughness Effects in Shock Tube Boundary Layer Transition," Technical Rept. No. 16, Lehigh University, Institute of Research (June 1963).

(2) Asbridge, J. R., "An Interferometric Study of Shock Tube Boundary Layers," Technical Rept. No. 14, Lehigh University, Institute of Research (April 1959).

(3) Chahi, A. J., "Measurement of Wall Heat Transfer and Transition to Turbulence during Hot Gas and Rarefaction Flows in a Shock Tube," Technical Report No. 12, Lehigh University, Institute of Research (September 1958).

(4) Martin, W. A., "An Experimental Study of the Turbulent Boundary Layer Behind the Initial Shock Wave in a Shock Tube," J. Aero/Space Sci. 25, 644 (October 1958).

(5) Mark, H. and Mirtich, M. J., Jr., "Transition in Shock Tube Boundary Layers," Phys. of Fluids 5, 251 (February 1962).

(6) Hartunian, R. A., Russo, A. L., and Marrone, P. V., "Boundary Layer Transition and Heat Transfer in Shock Tubes," J. Aero/Space Sci. 27, 587 (August 1960).

(7) Mirels, H., "Boundary Layer Behind Shock or Thin Expansion Wave Moving into Stationary Fluid," NACA TN 3712, (May 1958).

(8) Ostrach, S. and Thorton, P. B., "Stability of Compressible Boundary Layers Induced by a Moving Wave," J. Aero/Space Sci. 29, 289 (March 1962).

(9) Schubauer, G. B. and Klebanoff, P. S., "Contributions on the Mechanics of Boundary Layer Transition," NACA Report 1289 (1956).

(10) Dhawan, S. and Narasimha, R., "Some Properties of Boundary Layer Flow During the Transition from Laminar to Turbulent Motion," J. Fluid Mech. 3, 418 (January 1958).

TABLE I

SUMMARY OF TRANSITION DATA

Flow Cond.	u_w/u_e	u_e/ν_e cm^{-1}	Roughness Re_x at τ_k	Roughness Re_δ at τ_k	Natural Re_x Min.	Natural Re_δ Min.	Spark Re_x crit	Spark Re_δ crit
		$\times 10^5$	$\times 10^6$	$\times 10^3$	$\times 10^6$	$\times 10^3$	$\times 10^6$	$\times 10^3$
1	1.10	1.85			.733	3.02		
2	1.15	.385	.12	1.21			2.22	1.64
3	1.18	3.56			.747	3.0		
4	1.23	1.59					4.15	2.20
5	1.24	.679	.271	1.78			2.85	1.83
6	1.40	3.22						
7	1.40	1.07	.185	1.41	1.41	3.9	3.7	2.00
8	1.57	3.17			.496	2.2		
9	1.60	1.68	.495	2.22	.964	3.1	3.5	1.97
10	1.86	.770	.26	1.60				
11	1.86	.770	.23	1.49	1.63	4.0		
12	1.86	.953	.236	1.52			1.72	1.30
13	1.86	1.17	.56	2.33				
14	1.86	1.17	.56	2.33				
15	1.86	2.53	.23	1.51	.911	2.8	2.86	1.68
16	1.97	2.90	.38	1.81	.906	2.7		
17	2.24	1.11	.45	1.86				
18	2.27	1.15	.54	2.03	1.57	3.45		
19	2.32	4.15			.870	2.54		
20	2.57	5.17			1.63	3.32		
21	3.00	.337	.46	1.57				
22	3.14	.366	.50	1.63				
23	1.82	2.33	.16	1.19				
			Mean = 1.7		Mean = 3.1		Mean = 1.8	
Ref. 6	1.1 - 3.0	.16 - 1.8			0.6 - 1.8 $\times 10^6$	2.1 - 4.4 $\times 10^3$		

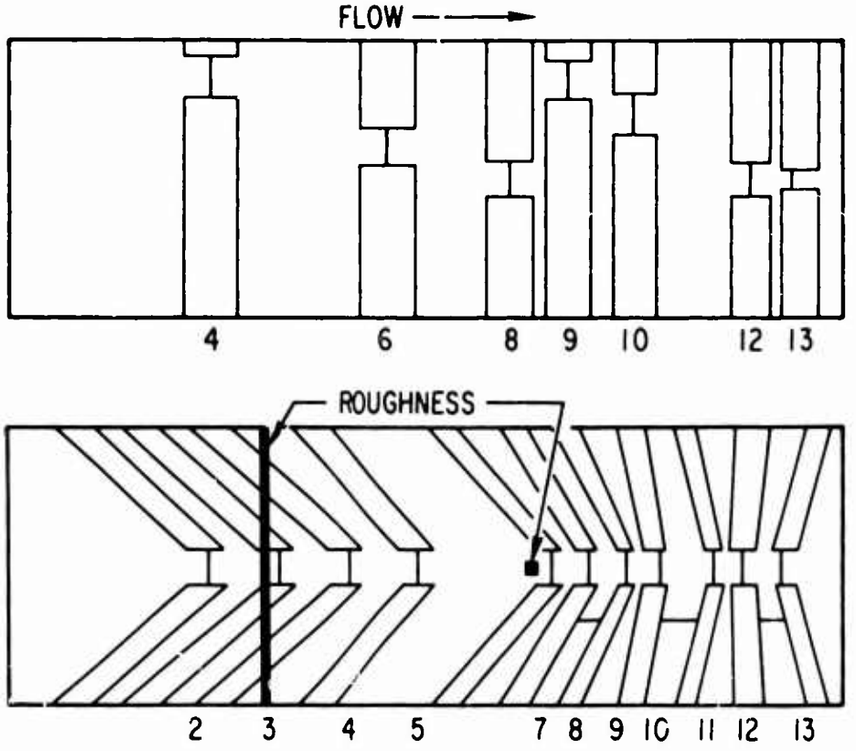


FIG. 1 HEAT TRANSFER GAGE PLATES

TURBULENT FRONT TRANSITION AT $M_s = 1.55$, $p_1 = 760$ mm

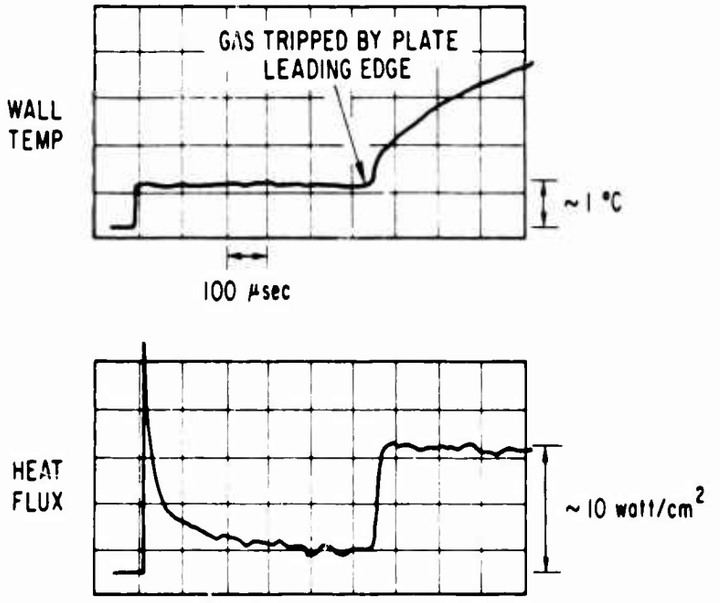


FIG. 2

TYPICAL RECORD SHOWING LAMINAR OSCILLATIONS, TURBULENT SPOT, TURBULENT FRONT: $M_S = 1.33$, $p_1 = 760$ mm Hg

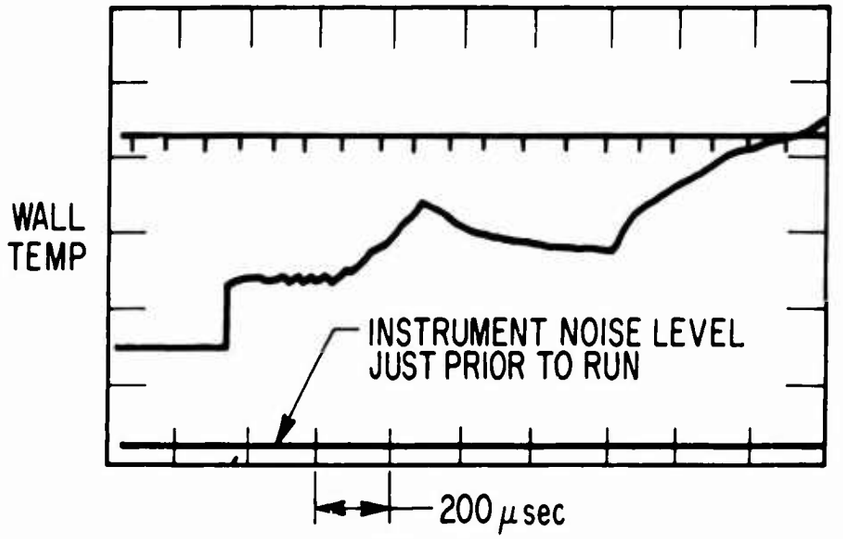


FIG. 3

TYPICAL x - t PLOT OF TURBULENT FRONT MOTION

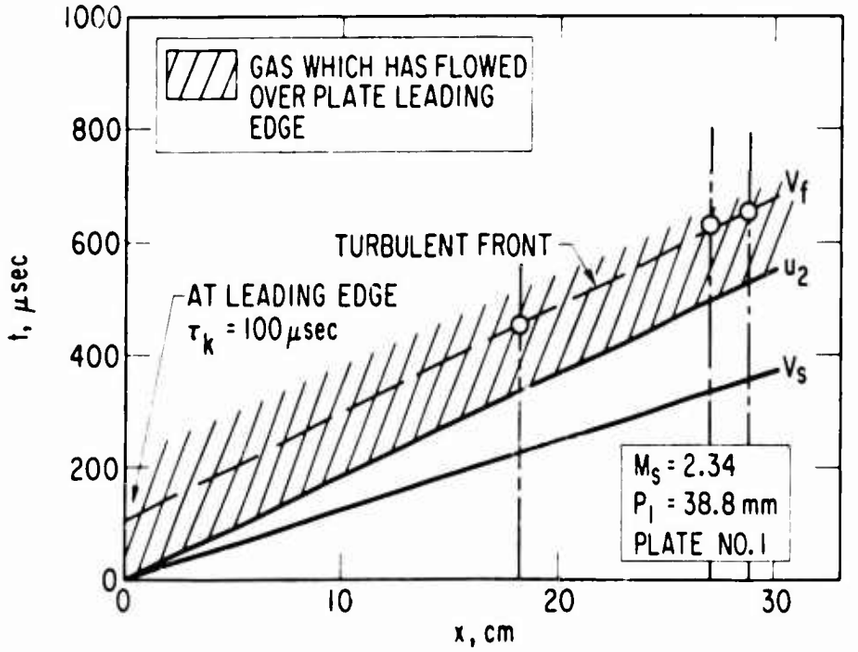


FIG. 4

TRANSITION PRODUCED BY 2-DIMENSIONAL ROUGHNESS

0.0025 IN FLAT RIDGE

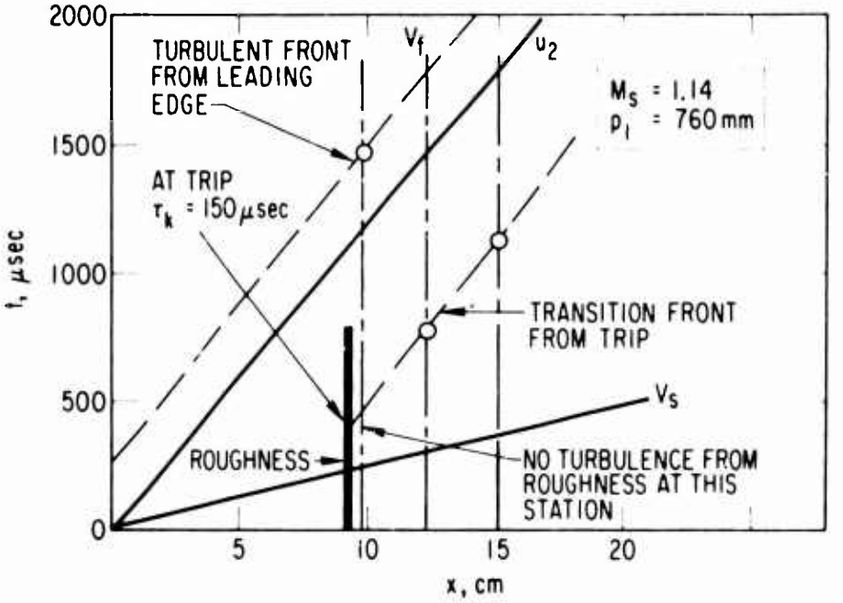


FIG. 5

TURBULENT SPOT GROWTH IN INCOMPRESSIBLE FLAT PLATE FLOW, SCHUBAUER AND KLEBANOFF

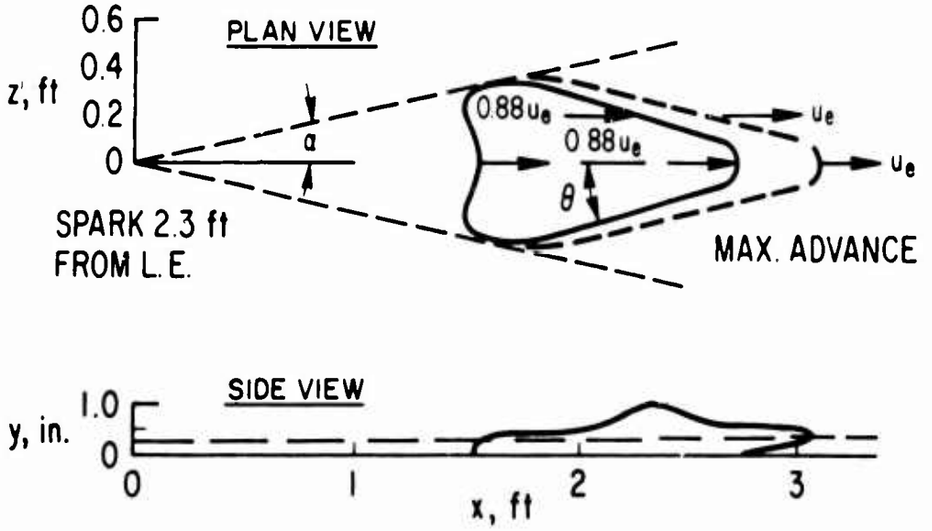


FIG. 6

TRANSITION PROBABILITY FUNCTIONS COMPARED WITH CHABAI

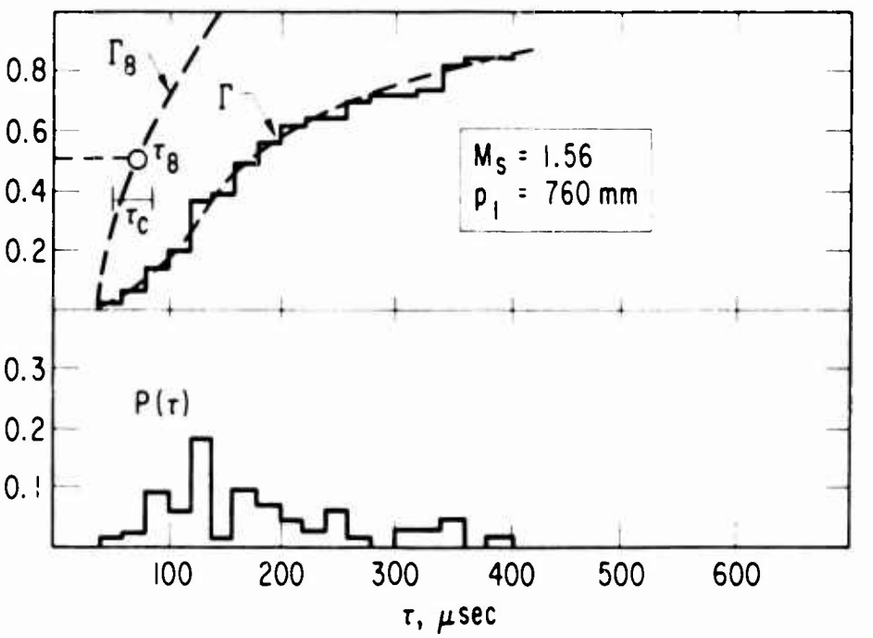


FIG. 7

SPARK GAP PLATE

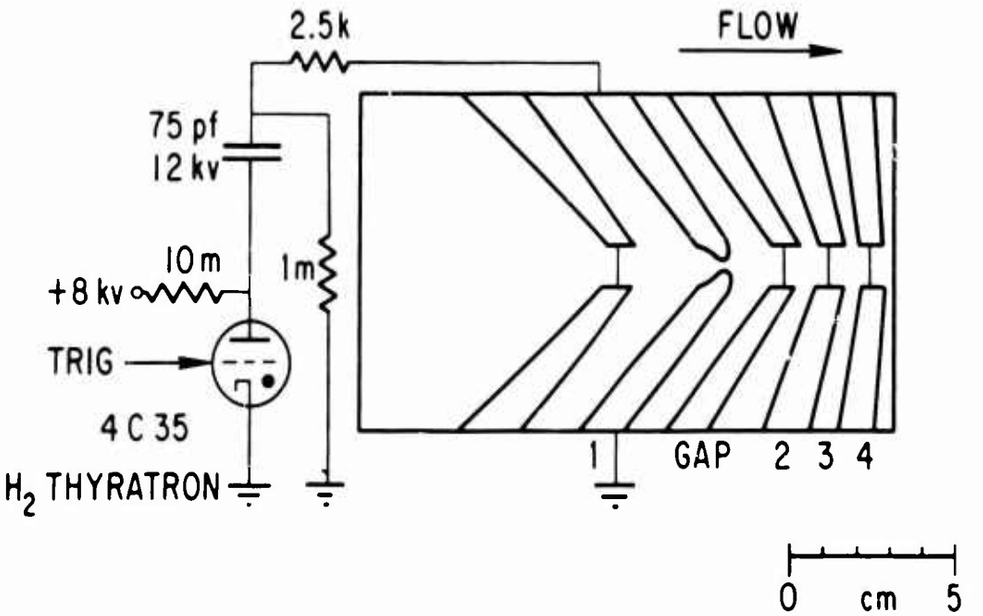


FIG. 8

TYPICAL SPARK-GENERATED SPOTS AND SCHEMATIC x-t DIAGRAMS

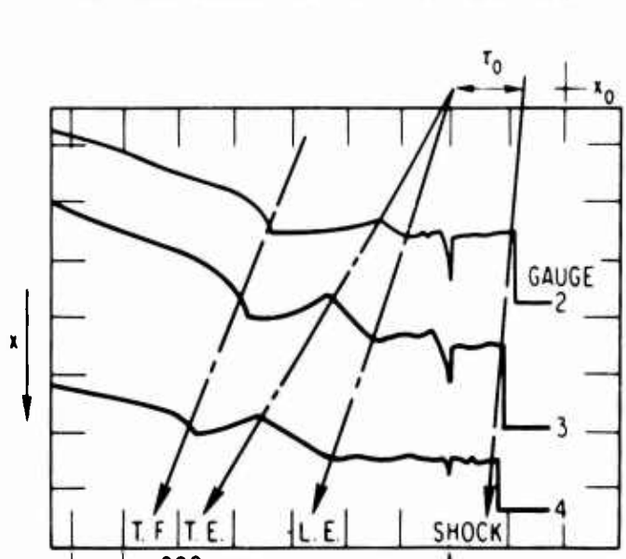


FIG. 9

TURBULENT SPOT ORIGIN FROM SPARKS

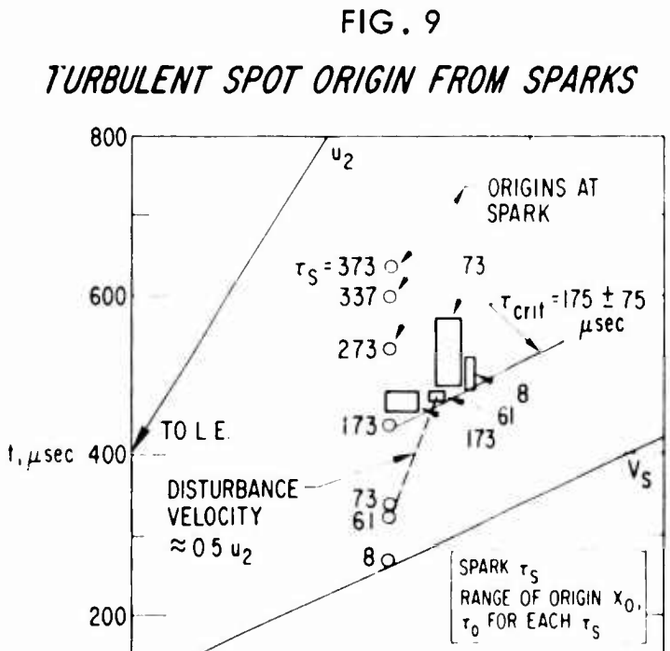


FIG. 10

RANGE OF OBSERVED TRANSITIONS

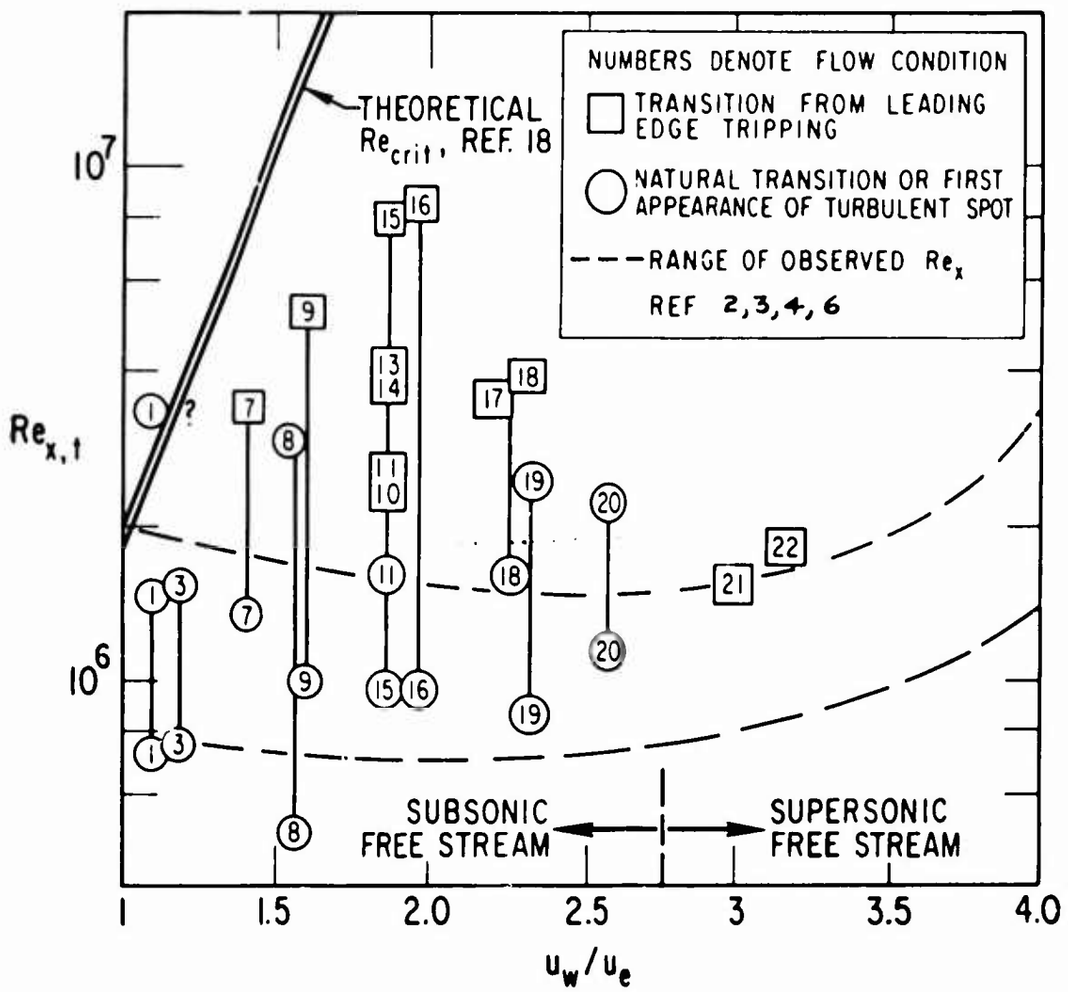


FIG. 11

BLANK PAGE

ELECTRON BEAM GAS DENSITOMETER FOR SHOCK HEATED GASES

R. Kyracou, E. H. Carnevale and C. A. Ziegler
Parametrics Inc., Waltham, Massachusetts
and
G. W. Wares
Air Force Cambridge Research Laboratories
Bedford, Massachusetts

INTRODUCTION

The electron beam technique of density measurement in the shock tube has been used for some time by such investigators as Venable and Kaplan (ref. 1), Ballard and Venable (ref. 2), Duff (ref. 3), and Camac (ref. 4). The measurements here were performed basically to obtain quantitative information on shock front thicknesses. So far, the electron beam technique has been relegated to low initial shock tube pressure ranges, below one Torr. The objective of this work was to extend the experimental range so that density determinations could be obtained under the more severe conditions usually encountered in shock tube research. In order to achieve the greater density measurement range, an electron beam attenuation experiment was decided upon rather than observing the scattered electrons.

The sensitivity of optical methods for gas density measurement (e. g. interferometry) becomes unsuitable for use below about 10^{-4} gm/cm^3. The scattering of electrons from an electron beam by gas atoms at these densities can, however, be an extremely sensitive process provided that electrons of the proper energy are used. An electron beam can be made to pass through an aperture in a shock tube wall with minimum perturbation to the inner wall of the test section. Separation of the electron gun from the test section by a thin metallic window allows exotic and/or corrosive gases at a variety of pressures to be used in the shock tube without affecting the performance or stability of the gun. In the experiment described here the density of gas behind a reflected shock wave was

measured by observing the attenuation of an electron beam caused by scattering.

The scattering process is primarily Rutherford scattering. An electron is scattered by a gas atom because of the mutual electrostatic repulsion. The number of electrons scattered from a beam, N_s, depends on the initial number of electrons, N_o, incident on a volume element of target atoms; on the number of atoms encountered (ρx; density and distance); and on the cross section of the electron-atom encounter (a function of atomic charge, mass, geometry, and electron energy). For simple scattering, the relationship between density and the number of electrons scattered may be written:

$$N_s = N_o (1 - e^{-\alpha \rho x})$$

where α is proportional to the scattering cross section. The experimental procedure is to measure the ratio of the electron beam intensity before and after the arrival of the shock wave and to relate this ratio to the density ratio by means of a calibration curve.

EXPERIMENTAL PROCEDURE AND APPARATUS

The apparatus consists basically of an electron gun with independent vacuum system, the shock tube test section, and a scintillation detector to measure the electron beam intensity. The basic system is shown in Figure 1a. The electron gun is a type SE7N tetrode of the television projection type which is operated in this experiment at 50 kilovolts. The gun has an independent vacuum system which maintains the pressure at 10^{-6} mm Hg. The shock tube test section is separated from the electron gun system by a thin (. 05 mil) nickel window stretched over the . 031 collimating aperture. This thin nickel window is strong enough to survive the pressure pulse of the shock wave yet attenuates the electron beam by only 40 percent.

In operation when the shock wave arrives, the beam is swept once across the collimating aperture and nickel window (as in Fig. 1b) by the action of the magnetic deflection coil. This is to eliminate the possibility of burning a hole through the window which might occur if the beam were continuously incident on it. The result of this sweeping is a square wave pulse of electrons (Fig. 4a). During calibration the beam is swept repetitively across the aperture so that continuous readings may be made.

The electron beam is detected by a scintillation detector which fits flush with the shock tube wall. A detailed drawing of this detector is shown in Figure 1c. The thin aluminum foil (. 3 mil) over the scintillator

plastic is used to prevent light from the shock heated gases from entering the photomultiplier. The foil attenuates the electron beam about 40 percent. The scintillator is a thin (10 mil) sheet of Pilot "B." It is thin enough to allow any X-rays produced by electron interactions with the gas or parts of the apparatus to pass through with minimal excitation of the scintillator yet thick enough to stop the electrons. The light from the scintillator is sent through a light pipe to a multiplier phototube which is terminated by a resistor-capacitor load into an oscilloscope.

DETERMINATION OF GAS DENSITY - RESULTS

The electron beam densitometer may be calibrated merely by filling the shock tube with the test gas at various pressures and observing the height of the calibrating signal (Fig. 4a). A plot of signal height versus density is obtained (Fig. 2) which in turn can be normalized to a plot of voltage ratio versus density ratio (Fig. 3) by dividing by the density and signal height for the initial conditions being used.

In the experimental determination of density, the shock wave proceeds down the tube and is reflected in the test section close to the electron beam exit. The resultant scattering of the electrons gives rise to the oscilloscope trace of Figure 4b. The large negative signal represents the unshocked gas condition; the small signal represents the higher density in the reflected shock wave region. The ratio of the two signals may be converted to a density ratio by using the curve of Figure 3.

A number of shock tube runs were made with an initial pressure of 10 mm Hg of neon and an average Mach number of 4.70. The theoretical density ratio for the reflection of a Mach 4.70 incident shock is 8.32. The average of five data points obtained with the Electron Beam Densitometer is 8.84 with a standard deviation of 1.5. This represents a difference from theoretical of 6.5 percent.

CONCLUSIONS

Measurements have shown that density variation of gases in the shock tube may accurately be obtained with an electron beam attenuation technique. It is planned to further increase the experimental sensitivity and range by optimizing the electron beam energy. Time response has already been improved over the data presented in this report to within 5 μs with promise of still further improvement by increasing the beam current. Increasing the electron beam current has an additional advantage of improving the experimental accuracy through the electronic signal to noise ratio.

REFERENCE

(1) Venable, D. and Kaplan, D. E. , J. Appl. Phys. 26, 639 (1955)

(2) Ballard, H. W. , and Venable, D. , Physics of Fluids 1, 225 (1958)

(3) Duff, R. E. , Physics of Fluids, 2, 207 (1959)

(4) Camac, M. , AVCO Research Report 172 (1963)

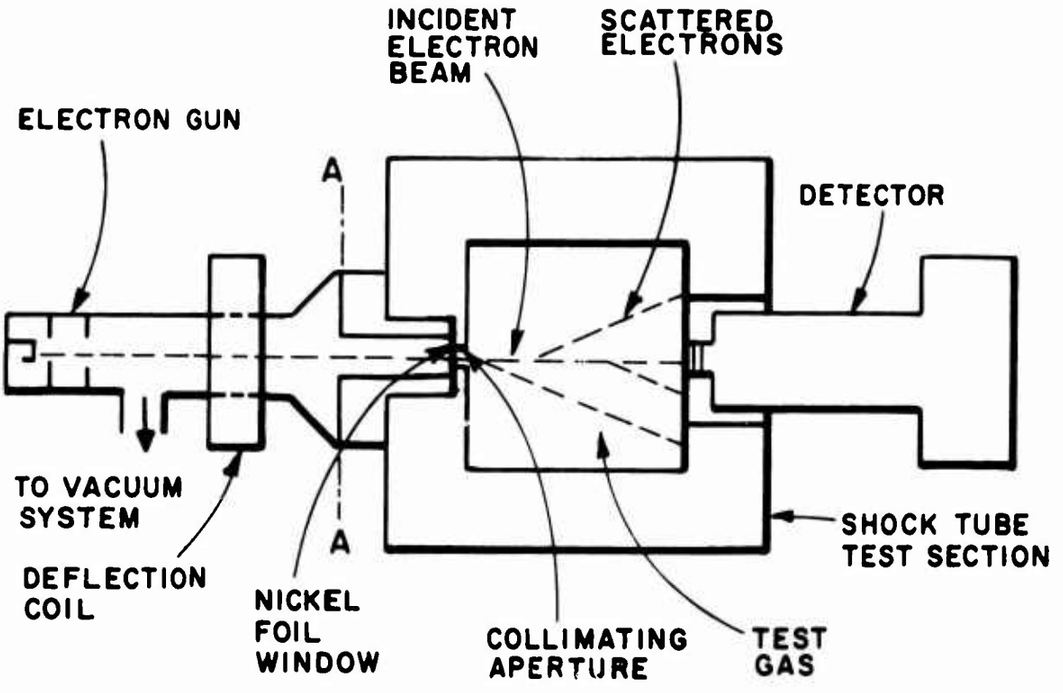


FIG. IA: ELECTRON BEAM DENSITOMETER

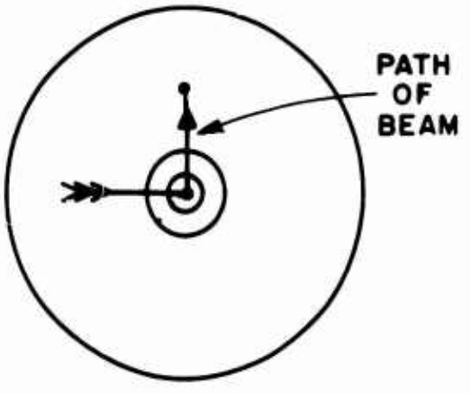


FIG. IB: SECTION A-A OF FIG. IA

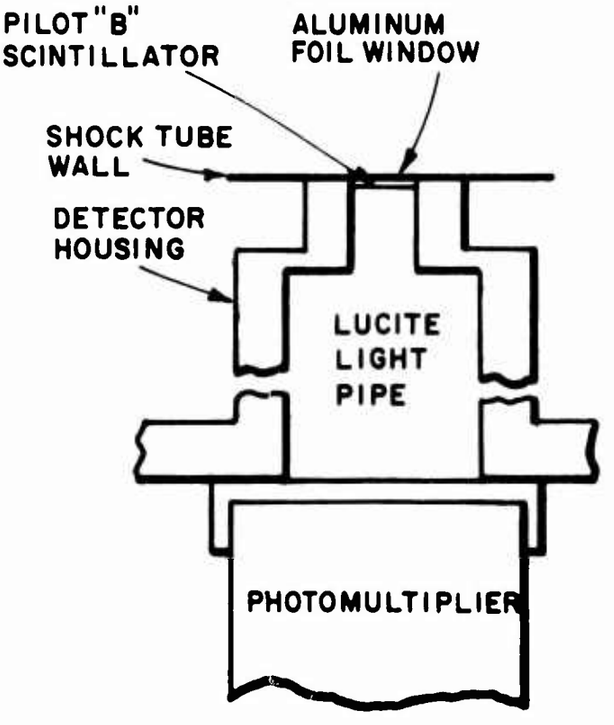


FIG. IC: BEAM DETECTOR

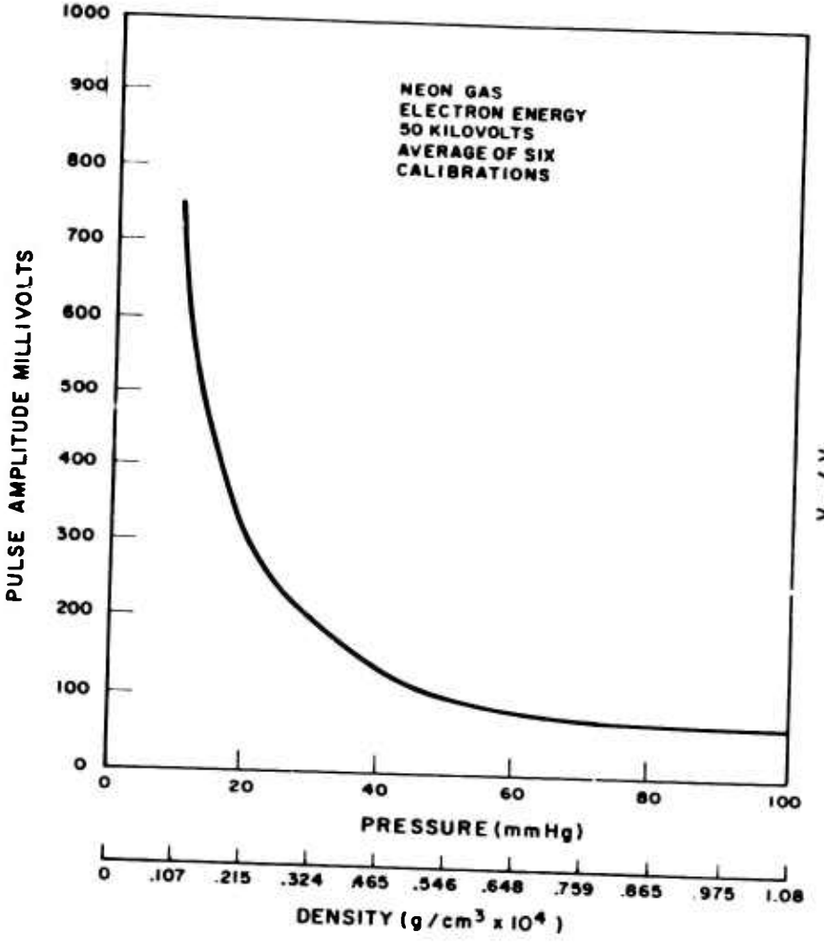


FIG. 2: STATIC CALIBRATION OF ELECTRON BEAM DENSITOMETER

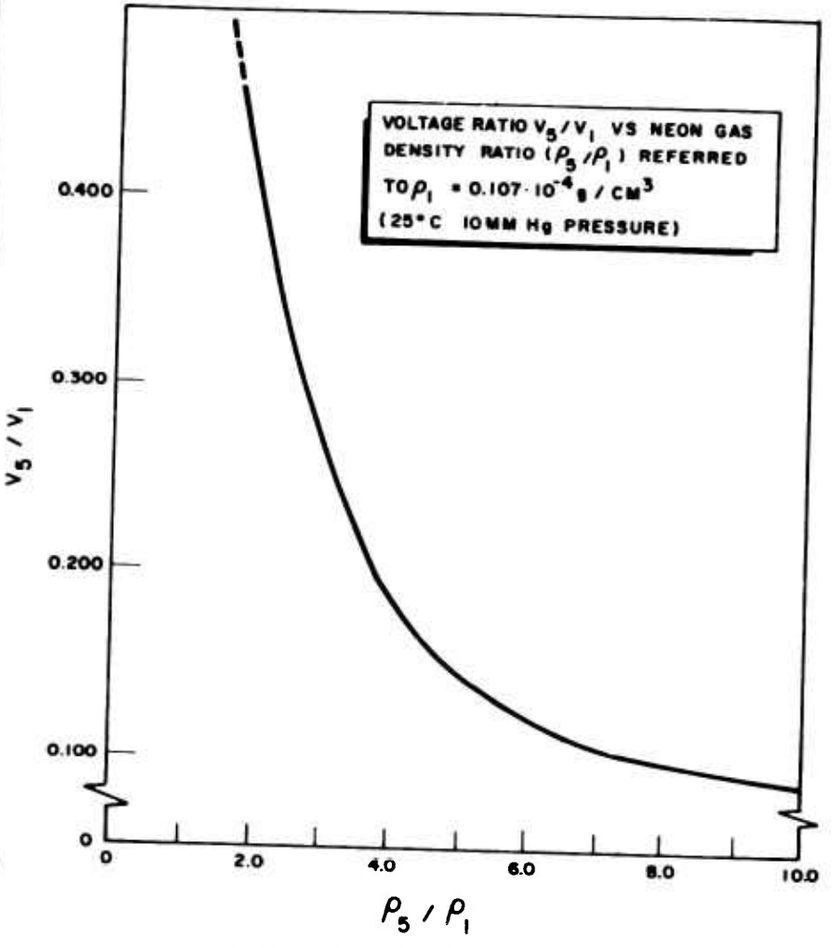


FIG. 3: DENSITY RATIO CURVE

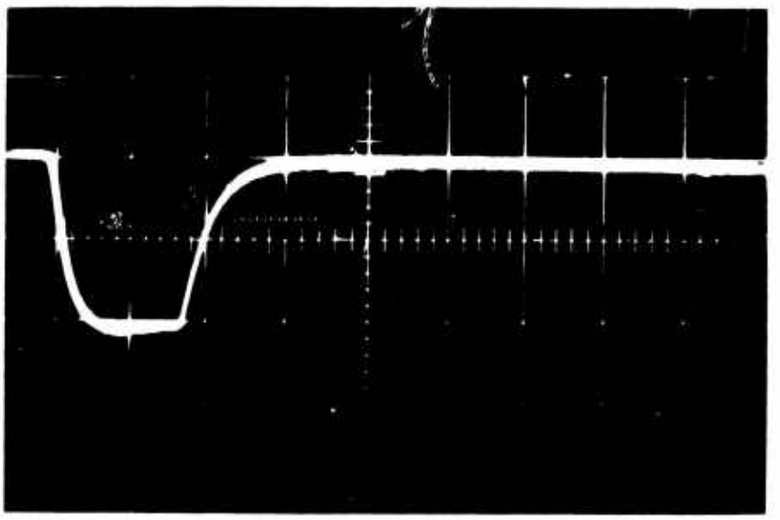


Fig. 4a. Calibration Pulse
Sweep Speed L-R 500 Microsec/cm

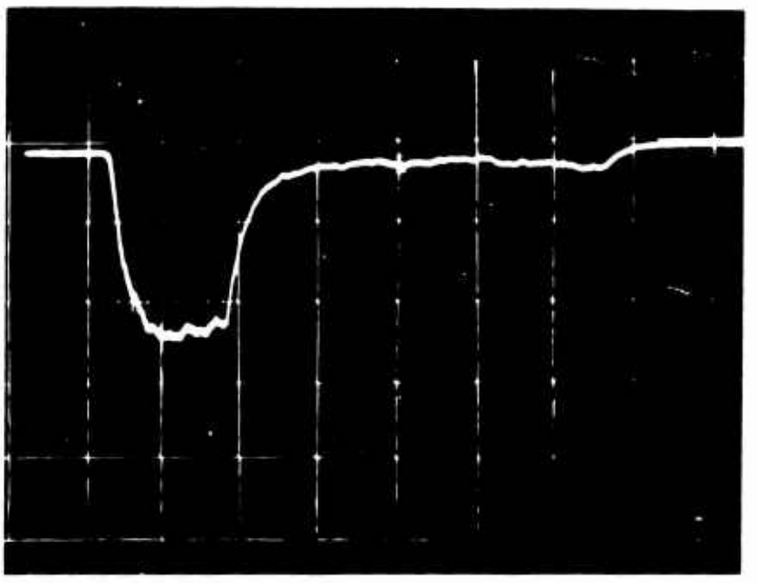


Fig. 4b. A Photomultiplier Record of Electron Beam Attenuation by Shock and Reflected Shock.
Sweep Speed L-R 200 Microsec/cm

BLANK PAGE

TEMPERATURE AND THERMAL CONDUCTIVITY MEASUREMENTS IN A SHOCK TUBE*

E. H. Carnevale, C. Carey and T. Marshall
Parametrics, Inc., Waltham, Massachusetts

INTRODUCTION

One of the largest uncertainties encountered in hypersonic flight is the prediction of heat transfer rates to re-entry vehicles. This is primarily due to uncertainties in the theoretical predictions of transport properties of gases at high temperatures. Relatively little experimental data has been obtained so far on the transport properties of high temperature gases. The techniques which have been utilized include spectroscopic (ref. 1), optical flow line (ref. 2), molecular beam scattering (ref. 3), heat transfer (refs. 4, 5, 6) and ultrasonic (refs. 7, 8).

The present paper discusses the application of the ultrasonic and the heat transfer methods in shock tubes for the determination of transport properties of gases at elevated temperature. It further describes the use of the ultrasonic method in the determination of the temperature of a gas (ref. 9). The high temperature source consists of a shock tube which is ideally suited for both ultrasonic and heat transfer requirements. Ultrasonic temperature measurements have been obtained in the reflected region of shock heated argon in the temperature range from 4000-9000°K. Heat transfer measurements have been obtained from oxygen, nitrogen, carbon dioxide and argon. Specifically thermal conductivity determinations of oxygen from the heat transfer measurements are reported.

*This research was supported by the Air Force Materials Laboratory, Research and Technology Division, Air Force Systems Command, United States Air Force.

EXPERIMENTAL APPARATUS

The principles of shock tube operation and characteristics are to be found in numerous references, for example, Bradley (ref. 10). The shock tube used for these studies is a square cross section seamless stainless steel tube eighteen feet long with 5/16 inch wall thickness. The driver section is from the same stock tubing, six feet long. Pressure burst diaphrams used throughout the present work were of 0.008 to 0.026 inch thick aluminum and were cross scribed for uniform petaling and burst strength. Helium and air were used for the driver gas depending upon the driven gas pressure and shock wave velocity sought for a particular experiment.

The shock tube has proven to be an ideal source for the production of high temperature gases for short periods of time. In this work the reflected shock wave region has been used as a high temperature stationary gas reservoir for ultrasonic and end wall heat transfer measurements. Concurrent stagnation point and side wall heat transfer studies are also in progress at this laboratory for obtaining further transport property data. The stagnation point and side wall heat transfer are of interest because of the dominance of convective processes and hence viscosity dependence. The end wall, reflected shock zone, heat transfer measurement in contradistinction is dominated by thermal conduction.

ULTRASONICS

The temperature of an ideal gas can be determined from its sound speed by the well-known relationship (ref. 11).

$$v = (\gamma RT/M)^{1/2}$$

where v is the sound velocity, γ is the ratio of specific heats, R is the gas constant, T is the temperature and M is the molecular weight. In the case of monatomic gases for temperatures up to about $8000^{\circ}K$, $\gamma R/M$ is constant and known.

Although the use of sound velocity for temperature determinations has been suggested over 100 years ago (ref. 11) and successfully demonstrated over many years, it has not been until recent times that the use of sound absorption for transport property determinations has been suggested* and demonstrated (refs. 7, 8).

*Suggestion of E. Bauer private communication.

In a monatomic gas, an expression for the sound absorption is given by (ref. 11)

$$a = \frac{2\pi^2 f^2}{\gamma P v} \left[\frac{4}{3} \mu + \frac{(\gamma - 1) k}{c_p} \right]$$

where a is the sound absorption coefficient, P is the pressure, f is the sound frequency, c_p is the specific heat at constant pressure, μ is the viscosity and k is the thermal conductivity which is equal to $2.5\, c_p \mu \gamma^{-1}$. Hence a measurement of the sound absorption and sound velocity at a given sound frequency and pressure will provide a determination of either the viscosity or the thermal conductivity since γ and c_p are known. It should be noted that in polyatomic gases the above expression does not completely account for the sound absorption. As a result, relaxation mechanisms have been postulated to account for this difference (ref. 12).

A block diagram of the experimental arrangement is shown in Figure 1. Shock speed measurements are obtained from thin film heat transfer gages. One of the heat transfer gages is also used to simultaneously trigger an r-f pulse (~1 mc/sec) generator and an oscilloscope. The pulse wave train is converted to an ultrasonic pulse by a lead-zirconate-titanate transducer. The sound is transmitted across the shock tube and is received by an identical lead-zirconate-titanate transducer which converts the sound wave back into an electrical signal. The signal is amplified and displayed on an oscilloscope.

Sound velocity and hence temperature are simply determined from a measure of the transit time required for the sound wave to traverse the two inch gas path across the shock tube.

Sound absorption and thus transport properties can be determined from a measurement of the sound amplitude attenuations across two different known path lengths, preferably obtained simultaneously. Hence a rectangular test section or shock tube is required.

It should be noted that considerable effort is required in order to minimize the difficulties associated with the acoustic transducer probe. There are in general three problem areas. Noise is continuously coupled into the walls of the shock tube. The impulsive pressure jump across the shock wave causes the acoustic transducers to resonate. Finally, there are high levels of acoustic pressure variations riding on the homogeneous pressure rise behind the shock wave. The acoustic probe shown in Figure 2 was designed to eliminate each of these problems. The side wall noise is eliminated by using a teflon holder (teflon has high acoustic attenuation) which has minimum contact with the test section walls. Isolation is im-

proved by screwing the transducer into the teflon holder on a threaded nylon rod so that there is no physical contact between the transducer and the teflon holder. The ringing due to the passage of shock waves is reduced by putting a short circuited crystal behind the active crystal to trap and damp large oscillations. The acoustic noise level behind the shock must be overcome by introducing sufficient acoustic power to give a useable signal to noise ratio. Flush mounting of the active transducer and quarter wave epoxy matching layers provide sufficient signal to make measurements with the lead-zirconate-titanate transducers used in this experiment.

Figure 3 shows a reference ultrasonic pulse which has been transmitted across helium at room temperature and atmospheric pressure. Also shown in Figure 3 is an ultrasonic pulse which has been transmitted through argon during the time the gas is in equilibrium in the reflected region of the shock tube. It should be noted that this signal is obtained after the initial noise disturbances which have been discussed above have subsided. A measurement of the transit time, the time from the start of the trace to the first received signal is obtained from the trace and a determination of sound velocity and thus temperature is readily obtained. The measurement of the amplitude of the received signal across two different paths would provide the sound absorption measurement. Sound absorption measurements have been successfully obtained across a two inch and one and one-half inch gas path for shock heated argon. The measurements are still in process.

Ultrasonic temperature determinations which have been obtained in argon in the temperature range from 4000°-9000°K are shown in Figure 4. The solid line is the temperature calculated from measured Mach numbers. The points are experimental determinations of temperature from the ultrasonic measurements and are within 2% of the calculated values. It appears that for the particular shock tube utilized in this program that a measure of the shock speed will provide an accurate determination of the temperature of the shock heated gas in the reflected region of the shock tube. Furthermore it has been demonstrated that sound propagation measurements can be obtained across two different paths and that these measurements provide a sound absorption value which in turn will determine transport properties.

HEAT TRANSFER

Heat transfer studies are being performed to obtain high temperature transport properties in laminar boundary layers. The basic procedure is diagrammatically shown in the flow chart of Figure 5. Given the thermodynamic properties of the test gas as a function of temperature and the

fluid dynamic equations which govern the boundary layer, the transport properties determine the heat transfer through the boundary layer. Thus, assuming a set of transport properties and comparing measured heat flux rates from the shock tube with theoretically predicted heat flux rates, the real transport properties of the gas may be found.

Since the heat flux through a laminar boundary layer depends on the integral of the transport properties over the entire temperature range of the boundary layer, significant information demands two considerations. First, in order to obtain a unique determination of transport property variation versus temperature, the initial experiments are performed under free-stream conditions where the transport properties are already well-known. The comparison between theory and experiment must then be carried out in a piecewise manner as successively higher free-stream temperature experiments are performed. Second, the heat flux rate is more sensitive to the temperature behavior in the boundary layer than to that at the boundaries. Thus, for example, to obtain significant information about the transport properties at 8000^{o}K, measurements and theory at free-stream temperatures up to 10,000^{o}K must be used.

End wall heat transfer measurements in oxygen, nitrogen, argon and carbon dioxide have been made. The oxygen data are compared to the theoretical heat flux computations in the temperature range 400^{o}-6000^{o}K. The energy equation for the end wall boundary layer is

$$\phi'' \; \eta \; \frac{P_r}{C} \; \phi' \; = \; 0$$

for

$$g\,(o) \; = \; 1 \text{ and } g\,(\infty) \; = \; 0. \tag{1}$$

The independent variable in Equation (1) is the parameter

$$\eta \; - \left(\frac{\rho_w}{\mu_w t} \right)^{1/2} \int \frac{\rho}{\rho_w} \; dy \tag{2}$$

where y is the distance from the end wall, ρ_w the gas density at the wall and μ_w is the gas viscosity at the wall. The heat flux potential ϕ is defined in terms of the viscosity parameter C and Prandtl number P_r as

$$\phi = \int_1^g \frac{C}{P_r} \, dg \tag{3}$$

where g is the ratio of local enthalpy to wall enthalpy.

The end wall temperature jump may be written in terms of the gage calibration $(\pi / \rho \overline{c_p k})^{1/2}$, the derivative of the heat flux potential at the wall ϕ'_w, and the gas properties at the wall (h_w, ρ_w, μ_w) as:

$$\Delta T = h_w \left(\frac{\rho_w \mu_w}{2} \right)^{1/2} \left(\frac{\pi}{\rho c_p k} \right)^{-1/2} \phi'_w \tag{4}$$

where h_w is the enthalpy at the wall.

Using an analysis due to Kemp, (ref. 12), the derivative of the heat flux potential at the wall becomes proportional to the integral of a function of the transport properties over the enthalpy range in the boundary layer. The expression is:

$$\phi'_w = a \left(\int_1^{g_e} \int_1^g \frac{C}{P_r} \, dg' \, dg \right)^{1/2} \tag{5}$$

where a is 1.13.

The wall surface temperature was measured using a thin film platinum (Hanovia - 05.x) heat transfer gage on a pyrex substrate. The gage was calibrated using Equations (4) and (5) with low Mach number, end wall, heat transfer experiments. At higher Mach numbers ϕ'_w was obtained from Equation (4) and compared to predictions using Equation (5) and theoretically computed transport properties.

The oxygen heat transfer data is plotted in Figure 7. The data points are ϕ'_w versus free-stream enthalpy ratio. The solid line is the theoretical prediction for free-stream temperature. Below 1500°K an extrapolation based on Hilsenrath's tabulation of gas properties (ref. 13) is used,

$$k = 1.40 \, \mu_w c_p g^{0.722} \text{ for } T < 1500^\circ K \text{ (Ref. 14).}$$

Above 1500°K the solid line was constructed using the transport properties of Yun, Weismann and Mason (ref. 14),

$$k = 1.67 \mu_w c_p g^{0.598} \text{ for } T > 1500^{\circ}K \text{ (Ref. 15).}$$

The measurements are in reasonable agreement with the thermal conductivity versus enthalpy function, thus showing that thermal conductivity data as a function of temperature can be extended through the 6000°K range by shock tube methods.

CONCLUSIONS

An ultrasonic probe which is operating in the environment of the reflected region of the shock tube has been developed. Ultrasonic temperature measurements in reflected shock heated argon have been made in the temperature range of 4000° to 9000°K. The measured temperature ratios agree with constant γ shock jump computations to within 2% (rms).

End wall heat transfer measurements in oxygen are presented which corroborate the theoretical calculations of Yun, Weismann and Mason. Both ultrasonic and heat transfer experiments in the shock tube are capable of yielding transport property information of high temperature gases.

REFERENCES

(1) Maecker, H., Z. Physik 141 (1955) 198.

(2) Wienecke, R., and Ahlbara, B., 2 Physics 165 (1961) 491.

(3) Amdur, I., and Mason, E., Physics of Fluids 1 (1958) 370.

(4) Hansen, C. F., Early, R. A., Alzofon, F. E., and Witteborn, F. C., NACA TR-27 (1959).

(5) Hartunian, R. A., and Marrone, P. V., Physics of Fluids 4 (1961) 535.

(6) Camac, M., and Feinberg, R. M., Journal of Fluid Mechanics, 21 (1965) 673.

(7) Carnevale, E. H., Larson, G. S., and Lynnworth, L. C., J. Acoust. Soc. Amer. 35 (1963) 1833: Ultrasonic Determination of Properties of High Temperature Gases, APS Meeting, Div. Fluid Dynamics, Pasadena, Calif. (Nov. 1964).

(8) Tempest, W., and Parbrook, H. D., Acoustica 7 (1957) 354.

(9) Aronson, P., and Marshall, T., Shock Tube Wind Tunnel Research at the Naval Ordnance Laboratory, Second Shock Tube Symp., March (1958).

(10) Bradley, J. N., Shock Waves in Chemistry and Physics, Methuen, London (1962).

(11) Herzfeld, K. F., and Litovitz, T. A., Absorption and Dispersion of Ultrasonic Waves, Academic Press, New York (1959).

(12) Kemp, N. H., AVCO Everett R. R. 137, (1962). Also Fay, J. A., and Kemp, N. H., J. Fluid Mech. 21 (1965) 659.

(13) Hilsenrath, J. et al., Tables of Thermodynamic and Transport Properties, Pergamon, New York (1960).

(14) Yun, K., Weissman, S., and Mason, E. A., Physics of Fluids, 5 (1961) 672.

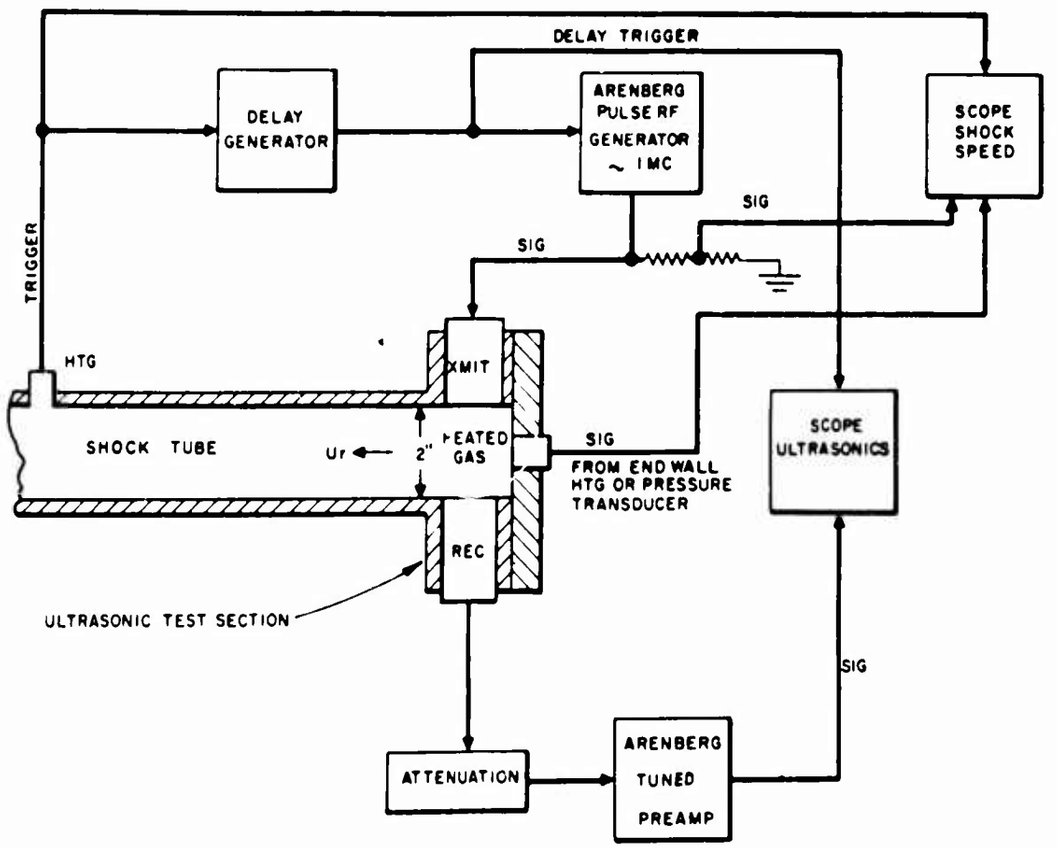


FIG. 1 EXPERIMENTAL ARRANGEMENT

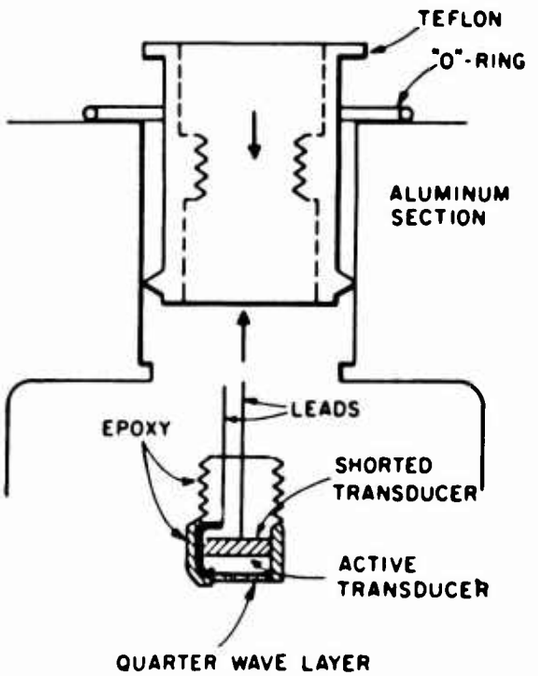
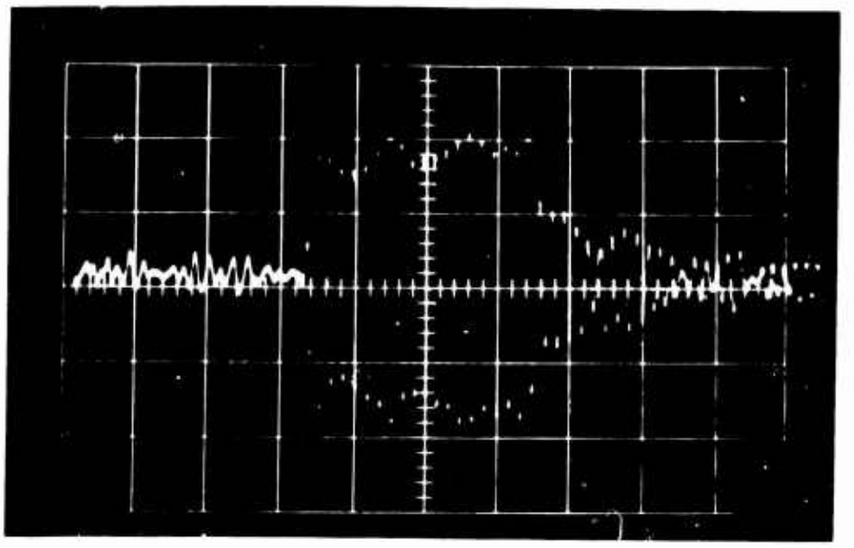
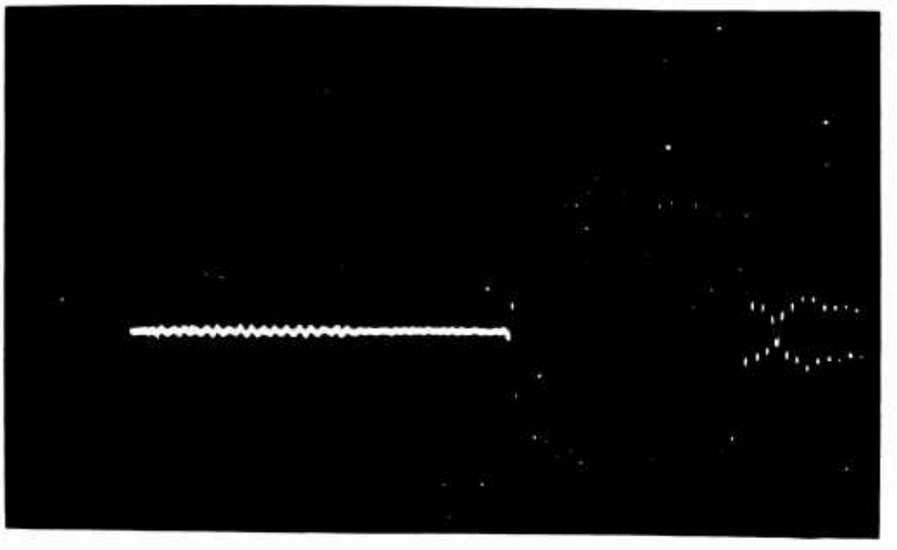


FIG. 2 THE ACOUSTIC PROBE



PULSE THROUGH ARGON BEHIND THE REFLECTED SHOCK
1.6 ATM 8300 °K



PURE HELIUM REFERENCE PULSE
1 ATM 300 °K

FIG. 3

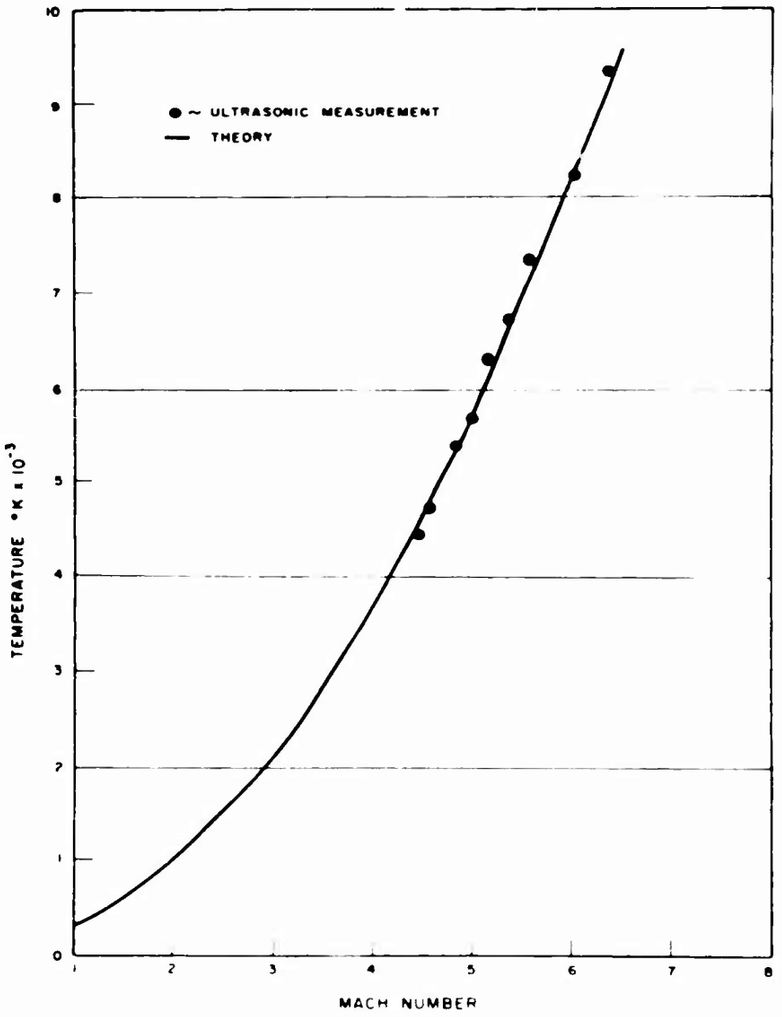


FIG. 4 ULTRASONIC TEMPERATURE DETERMINATION BEHIND ARGON SHOCKS

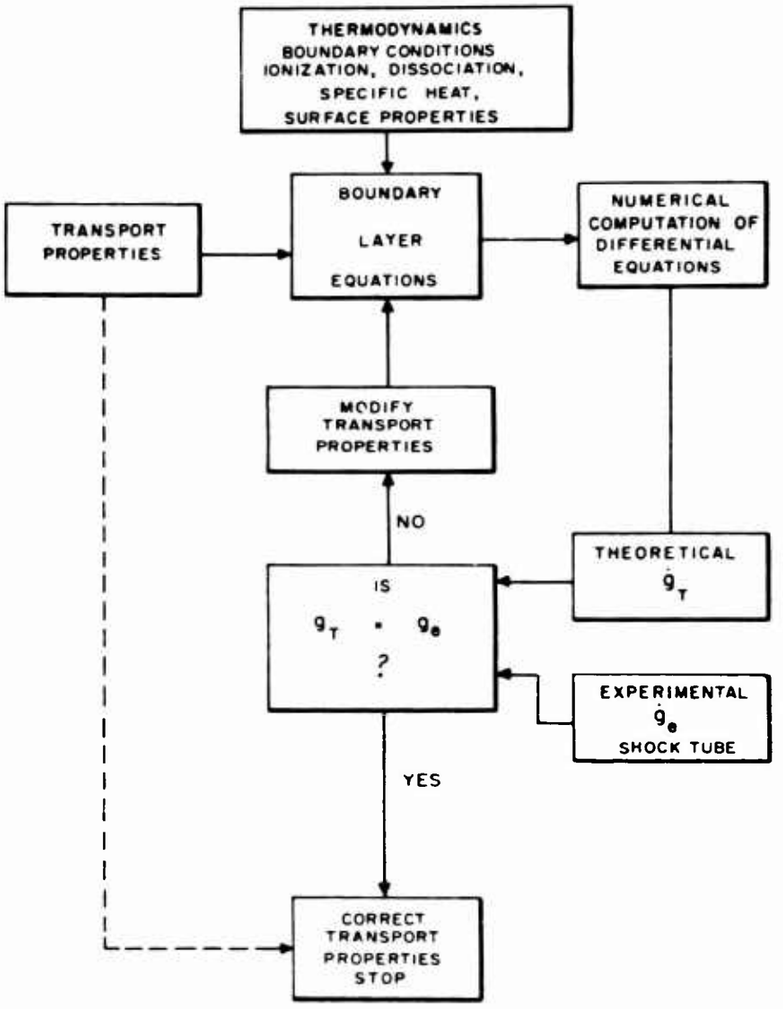


FIG. 5 TRANSPORT PROPERTY DETERMINATION USING HEAT TRANSFER MEASUREMENTS

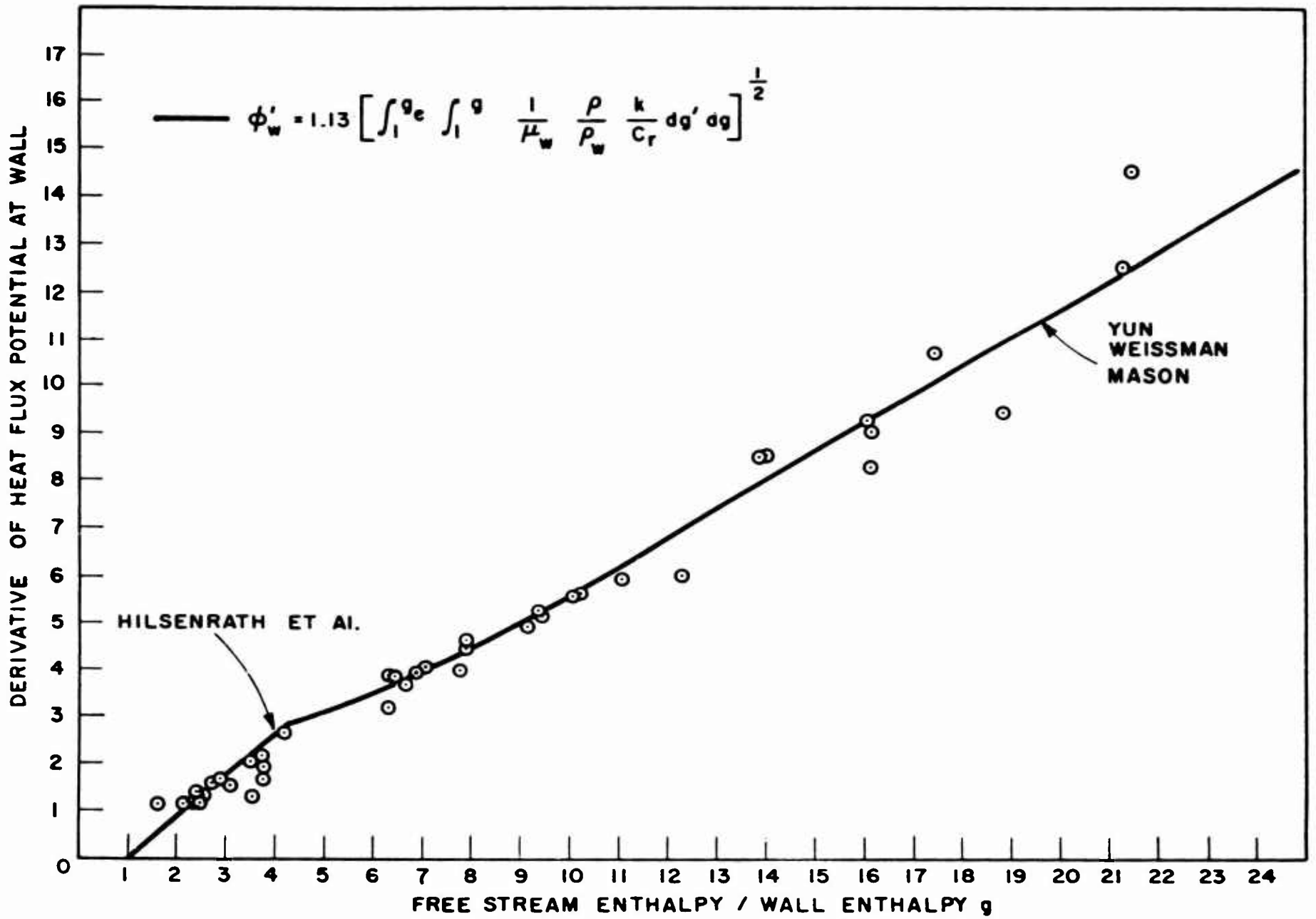


FIG. 6. END WALL HEAT FLUX POTENTIAL MEASUREMENTS

AN ALKALI METAL VAPOR SHOCK TUBE AND THE MEASUREMENTS OF THE CONDUCTIVITY AND ELECTRON CONCENTRATION OF CESIUM IN ARGON

Jean F. Louis
Avco-Everett Research Laboratory
Everett, Massachusetts

A. INTRODUCTION

The kinetics of alkali metal is of interest in re-entry physics, thermionics and MHD devices. At the present time, most of the work has been done in apparatus of small size where the walls and ionization plates often plan an important role, as shown by von Goeler.[1] Experiments in a large diameter (6 inches) shock tube can offer substantial advantages by making wall effects negligible and providing great flexibility in the choice of operating pressure and temperature.

There are two different methods of seeding a shock tube with an alkali metal. The ideal way is to introduce the seed in a vapor phase in the tube. This necessitates uniform heating of the driven section up to the temperature required by the vapor pressure and an oven has to be constructed around the tube. Optical measurements are made difficult by the alkali liquid phase existing on the walls. The hot shock tube technique also raises problems concerning purity and materials since the alkali metal is highly reactive and corrosive. Haught[2] has described the difficulties associated with this type of shock tube and its lack of flexibility. Despite these efforts and those of others, the hot shock tube has not become a useful and flexible research tool.

The alternative is to introduce a cloud of very small solid alkali particles into the shock tube. The present work applies this method to pure alkali and examines the problems of uniform suspension, evaporation of particles in the shock front, and the use of such a shock tube to study kinetics of alkali metal. Experiments show that a uniform slug of gas can be obtained at a short distance behind the shock. The electron concentration in cesium-argon mixtures at various Mach numbers is measured by different methods. A discrepancy between edge and volume measurements is found which can be explained by the existence of an electron temperature profile due to the escape of radiation in the collision broadened resonance line.

B. SHOCK TUBE SEEDING WITH SMALL PARTICLES

1. Solid Particles and Their Suspension in a Carrier Gas

Powder of various substances have been introduced on the walls of shock tubes or on thin secondary diaphragms (Nichols[3]) to study the spectra of these selected materials. Gaydon[4] introduced Na Cl as a suspension of solid particles in a theoretical gas to determine the temperature of the gas by the sodium D-line reversal technique. A similar seeding technique was also used by Lau:[5] a jet of gas, directed onto the surface of a liquid compound, carries a given amount of smoke into a chamber separated from the shock tube by a valve. After the required amount has been fed into the chamber, the valve is opened and the smoke fills the shock tube to the required pressure. The conductivity measurements were found to be dependent on the delay between the opening of the valve and the break of the diaphragm. This phenomenon is most likely to result from settling of the particles on the wall. Settling is the critical problem associated with Lau's method. In the present study, pure alkali metals, as opposed to Na Cl and Cs2 Cl are to be used. The use of alkali metal eliminates the problem of the nature of the dissociation of the ionic molecules and of the electron affinity of the chlorine.

2. Particle Settling

The uniformity of the test slug will depend on the uniformity of the suspension of particles prior to being shocked, which in turn depends on the importance of the settling. The velocity of settling is determined by the balance between the gravitational force (which is a volume effect) and the drag on the particle in its motion relative to the gas (which is a surface effect). Therefore, by making the surfact to colume ratio very large and the total suspension time very small, the influence of the settling can be made negligible. Since the particle size is of the order of, or smaller than the mean free path, Stokes' law has to be corrected for slip. The settling velocity can be written[6]

$$V_s = \frac{2}{9} \frac{\rho_L r^2 g}{\mu} (1 + A\ell/r)$$

where ρ_L is the density of the particle, r its radius, μ the viscosity, A is Millikan's constant, and ℓ the mean free path.

Figure 1 shows the settling velocity as a function of radius for spherical cesium particles in argon gas at 5 cm Hg of pressure. From this figure, one sees that settling is negligible for particles a few tenths of a micron in size in a flow system where the carrier gas moves at a velocity of the order of 1 m/s. Other effects such as thermophoresis can influence the settling, and as a rule gas temperature has been kept 5° C cooler than the walls. Such a flow would be laminar and the diffusion of aerosols to the walls, using Leveque's[7] formula, would be 10^{-4}. Further,

if one uses the expression of Nolan[8] for sedimentation in a horizontal channel under conditions of laminar flow to the specific tube under consideration (6 inches in diameter and 25 feet long with a pumping speed of 2 ft/s), the total fraction lost to the wall is found to be less than 1% for particles less than 0.3 μ radius; a uniform two-phase flow could be obtained for the conditions chosen of 5 mm Hg or for any higher pressure.[11] Lower pressures would require particles of smaller controlled size.

3. Aerosol Production

Sodium chlorides have been prepared by several investigators using aspiration techniques, the hot wire generator, evaporation, sublimation, and cathode discharge. These homogeneous nucleation techniques produce rather uniform size smokes, but the size distribution is not as narrow as those obtained by heterogeneous nucleation. In the latter method, the material condenses on very small nuclei of foreign matter and the size of the particles is determined by the ratio of condensable matter divided by the number of nuclei.

The preparation of alkali metal aerosols is not described in the literature and to eliminate any impurity effect, homogeneous nucleation was chosen. The aerosols were prepared in the following way (Fig. 2): cooled inert test gas is blown over a pool of liquid alkali metal, the quenching of the alkali fog results in the formation of small particles or aerosols which are convected by the test gas. The vapor pressure at the surface of the pool or its temperature determines the concentration of alkali metal convected. The evaporating surface is 10 cm^2 which allows concentrations up to a few percent by weight to be achieved.

From the oven, the two phase flow enters a cyclone separator which serves two purposes: 1. mixing to obtain the required gas mixture at room temperature, and 2. centrifuging of particles larger than 1 μ.

Using the formulas developed by Smoluchowski[9] and knowing the total flow time, one finds that the particles will grow from 4×10^{-7} cm to around 10^{-5} cm.

To determine the particle size distribution, the particles were deposited on a carbon grid and electron micrographs were taken by Dr. Duff of AVCO/RAD (Fig. 3). The micrographs (Fig. 4) indicate that the particles were < 0.3 μ in size and therefore should have very small settling velocity. Unfortunately, the sample had to be exposed to air in its introduction in the electron microscope. This most likely resulted in a surface reaction which probably changed the particle shape and size.

To verify the uniformity of the suspension, pencil beams of light have been shone vertically and horizontally through the shock tube. As shown in Fig. 5, the 90° scattering from this vertical beam is found to be of uniform intensity. Not shown on this black and white photograph is the color of light which varies uniformly from blue to white to gold as the

concentration of the suspension is increased.

This view also indicates that indeed the particles are small for the increased concentration of 1% by weight; were the particles 1 μ, the fog would be opaque and the beam would be occluded.

4. Particle Evaporation Time

Because of its inertia, the particle will take a finite time to acquire speed behind the shock while it is evaporating. Therefore, to determine the total evaporation time, the equations of momentum and energy have to be solved simultaneously, noting that the flow is free molecular as the particle size is smaller than the mean free path. The conservative assumption is made that the particle is spherical. The drag coefficient is given by Schaaf and Chambre[10] or Holt,[11] the heat transfer coefficient by Sauer.[12]

The following equations are derived neglecting the radiation energy and the energy stored which are small relative to the sublimation energy. The following equations were used:

$$\text{Momentum: } \frac{r}{V^2}\frac{dv}{dt} = \frac{3}{8}\frac{\rho}{\rho_p} U_\infty \; G(v)$$

$$\text{and Energy: } \frac{dr}{dt} = -\frac{a}{8}\frac{p_\infty}{\rho_p h_\rho} U_\infty \; V \; F(v)$$

where r is the particle radius, U_∞ free stream velocity, ρ gas density, ρ_p particle density, p_∞ free stream pressure, a accomodation coefficient and $V = \frac{U_\infty - U_p}{U_\infty}$, where U_p is the particle velocity, T_∞ and T_p free stream particle temperature h_p the latent heat of sublimation with $Z = M_\infty V\sqrt{\gamma/2}$.

$$F(v) = (2Z^2 + 5)\left[\frac{e^{-Z^2}}{Z\sqrt{\pi}} + \operatorname{erf} Z\right] + (2Z^2 + 3)\frac{\operatorname{erf} Z}{2Z^2}$$

$$\frac{-4T_P}{T_\infty}\left[\frac{e^{-Z^2}}{Z\sqrt{\pi}} + \left(1 + \frac{1}{2Z^2}\operatorname{erf} Z\right)\right]$$

$$G_v = \frac{\operatorname{erf}(Z)}{2Z^2}\left[4Z^4 + 2Z^2 - 1\right] + \frac{e^{-Z^2}(1 + 2Z^2)}{Z^3\sqrt{\pi}}$$

$$+ \frac{2\sqrt{\pi}}{3Z}\sqrt{\frac{T_w}{T_\infty}}$$

These relations determine an evaporation time roughly linear with the initial radius (Fig. 6), Mach number, and the size of the particles in argon. The evaporation time can be seen to be extremely small compared to the test time. Further, the ambipolar diffusion time for a separation distance of 100 microns is about one microsecond. Consequently, a uniform test slug can be obtained at a short distance behind the shock. However, if chemical kinetics measurements are to be performed behind the incident shock, the particle evaporation kinetics should be taken into account. As mentioned above, it will take a finite time for the particles to reach the translational velocity of gas; and during this time atoms and molecules evaporating from the surface can, through collision , reach a temperature higher than the translational temperature of the g Further, the concentration of alkali close to the evaporating parti s is extremely high compared to its diluted partial pressure. For th two reasons, the particle evaporation kinetics may be a source of n nequilibrium. Therefore, it would seem more desireable to make kinetic studies behind the reflected shock using the uniform gas sample prepared by the incident shock.

C. STEADY STATE MEASUREMENTS - CONDUCTIVITY AND ELECTRONS CONCENTRATION

Steady state measurements were performed behind the incident shock for the following reasons:

1. to calibrate the seeded shock tube,
2. to determine the best measurement methods for the study of the ionization kinetics,
3. to determine the influence of the radiation loss (broadened resonance line).

Since the alkali metals have a low ionization potential, the studies have to be done at relatively low Mach numbers and temperatures between 1500-3000°K. Because the seed is a small fraction of the gas atomic concentration (10^{-3}), the total electron concentration is small.

1. Methods of Measurement of Electron Concentration and Conductivity

Different methods can be used to measure the electron concentration: Langmuir probes, continuum radiation, interferometry, line broadening due to Stark effects, Q coil, microwave transmission, and reflection.

The cesium concentration being small (0.1%-1%), and the temperature relatively low (1500-3000°K), the electron concentration is small. Therefore, optical interferometry and the line broadening method would be marginal in determining the rate of ionization. The interpretation of Langmuir probe potential measurement has been found to be ambiguous in

shock tube experiments.

The cross section given by Mohler, [13] and the calculations of Lutz, [14] indicate that a measurement of the free bound continuum near the 6 P limit (5000 Å) could be performed for densities of 10^{-2} particles/cm^3 and larger, using a narrow bandwidth (50 Å) interference filter and a photomultiplier with a S_{11} surface. The intensity of the radiative recombination is proportional to the product of electron and ion densities and $T_e^{-1/2}$, where T_e is the electron temperature. This variation with temperature is small compared with the experimental variation of the electron density with temperature. This measurement is a volume measurement of the electron density.

Since the work of Haught[15] indicates a long ionization time, the microwave reflection technique at frequencies of 16.0 and 35 k MC, should have enough time resolution and be applicable to a range of electron density from 5×10^{11} - 2×10^{13} electrons/cm^3. The Q coil method developed by Koritz and Keck[16] can be used for equilibrium measurements, but lacks resolution for rate measurements. The latter two methods measure the electron density at the edge of the gas sample. The Q coil response is proportional to σr^4 and the microwave interacts with the plasma within a wave length. Therefore, volume and edge determination of electron density could differ if a radial electron temperature profile existed.

The microwave probe technique has been described by Lin.[17] The edge of the probe is inserted 0.5 cm into the shock tube to reduce the effects of the aerodynamic boundary layer. To minimize the aerodynamic disturbance due to the probe, a flat rectangular end plate with knife edges is introduced at the end of the probe.

The measurement of the continuum is done at 4950 Å; the optic uses a 4 inch focal length lens focused on the center of the tube, plus collimators and baffles. The photomultiplier used is a Dumont 6292. The system is calibrated against a black body source at 1000°C.

2. Measurements

For each run, prior to the gas being shocked a sample of the gas is taken at the end of the shock tube and the amount of cesium therein is determined by both flame photometry and gravimetric methods.

The shock tube uses a pressure break to maintain a high level of purity. The shock velocity is measured from the response to the shock front of thin film gauges equally spaced ahead of the test section. Figure 7 shows the traces obtained from the continuum and the line intensity. They show good indication of axial uniformity. The response from the Q coil is shown on Fig. 8 which also shows uniformity behind the shock.

Lutz[14] has applied the formulation of Aller[18] for hydrogen to cesium to calculate the continuum absorption. He determines the effective quantum

number of the lowest contributing level for each frequency and then sums over-all higher levels. Using these results, the emissivity of the gas in the continuum at a given frequency for a given concentration of neutral cesium can be calculated. The frequency corresponding to 4950 Å was chosen for maximum intensity or sensitivity which occurs near the 6 P limit at 5000 Å.

Figure 9 compares the results of these calculations with experimental results and good agreement is found. This indicates that the electron density in the volume of the gas follows the concentration as determined from the Saha equation using an electron temperature equal to the argon temperature as determined from the shock velocity.

Figure 10 compares the results of the electron density as measured from the microwave reflection at 365 kmc/s with the expected concentration as determined from the Saha equation. It can be seen that an increasing discrepancy with decreasing temperature exists. This would indicate that the electron temperature close to the probe (one wavelength or 1 cm) is lower than the argon temperature. Line reversal techniques applied to sodium and potassium[19] in argon have indicated similar discrepancies.

The same discrepancy is found in the measurements of conductivity (Fig. 11) which also measures the edge of the plasma.

The electron density being low, around 10^{12} electrons/cm^3, and the argon gas being almost transparent to the electrons, a radiation loss could depress the electron temperature (the energy gained by elastic collisions is small). The existence of an important radiation loss can be determined from the spectrum (Fig. 12) which shows that the resonance line is black, well broadened (300 Å), and self absorbed in its center, indicating a colder electron temperature close to the wall.

Lutz has calculated the radiation incident to the wall for a cesium-argon mixture by calculating the contribution from the different lines. A fraction of this radiation is absorbed by the wall and is an energy loss for the electrons. If this energy loss is balanced against the energy gained by the electrons through elastic collisions with the argon atoms, or

$$\frac{m_e}{m_a} \nu_c n_e (T_a - T_e) = a Q_r,$$

the discrepancy between electron and atom temperature can be explained (δ is the energy loss parameter, m_e and m_a the electron and atom mass, T_e and T_a the electron and atom temperature, ν_c the collision frequency, n_e the electron concentration, and $a Q_r$ the fraction of the radiation incident on the wall which is absorbed).

For $a = 0.25$ and Q_r the value determined by Lutz, the results of both the microwave and the Q coil agree with the results obtained from the

above equation in the range of Mach numbers investigated. Therefore it appears that the radiation loss to the wall for cesium in argon is important enough to produce a radial electron temperature profile and depress the electron temperature markedly at the wall surface.

D. CONCLUSION

This work indicates that the seeding of a shock tube with aerosols is feasible if a flow system is used. The control of the settling of the particles is the initial problem which can successfully be managed by suitable particle size control. Up to now, a very simple method of seeding has been used and is very adequate for pressure above 1 cm Hg. For lower pressure, a better control of the size should be achieved by control of the nuclei such as heterogeneous condensation. The experimental results indicate that uniform conditions can be obtained at a short distance behind the shock with alkali metals. The measurements also indicate that for cesium in argon, a radial electron temperature profile exists which results from radiation loss in the pressure broadened resonance lines.

REFERENCES

(1) von Goeler, S., Phys. Fluids 7, 463 (1964).

(2) Haught, A. F., Phys. Fluids, 5, 1337 (1962).

(3) Nichols, R. W., Parkinson, W. H. and Reeves, E. M., Applied Optics, 2, 919, 1963.

(4) Gaydon, A. G. and Hurle, I. R., Eighth Symp. on Combustion, 1962, Williams and Wilkins Co., Baltimore 309.

(5) Lau, J., Canadian Journal of Physics, 42, 1598, 1964.

(6) Fuks, N. A., The Mechanics of Aerosols, 1955.

(7) Leveque, M., Ann. Mines, 13, 276 (1928).

(8) Nolan, J. J. and Nolan, P. T., Proc. Roy. Irish Acad. 45, 361 (1938).

(9) Smoluchowski, M. von, Z. Phys. Chem., 92, 129 (1918).

(10) Schaaf, S. A. and Chambre, P. L., Fundamentals of Gas Dynamics, Section H, p 687, Princeton University Press (1958).

(11) Holt, A., J. Aero Sci., 11, 95 (1949).

(12) Sauer, F. M , J. Aero Sci., 18, 353, 1951.

(13) Mohler, F. L., J. Research Natl. Bur. Stds., 19, 447 (1937).

(14) Lutz, M. A., "Radiant Energy Loss from a Cesium-Argon Plasma to an Infinite Plant Parallel Enclosure," Avco-Everett Research Laboratory Research Report 175, September 1963.

(15) Haught, A. F., Phys. Fluids, 5, 1337 (1962).

(16) Koritz, H. E., and Keck, J. C., Avco-Everett Research Laboratory Research Report 167, September 1963.

(17) Lin, S., Neal, R. A. and Fyfe, W., Avco-Everett Research Laboratory Research Report 105, 1960.

(18) Aller, Lawrence H., Astrophysics: Atmospheres of the Sun and Stars, The Ronald Press Company, New York City, 1953.

(19) Cool, T. A. and Zukowski, E., Fifth Symposium on Engr. Aspects of MHD, April 1965.

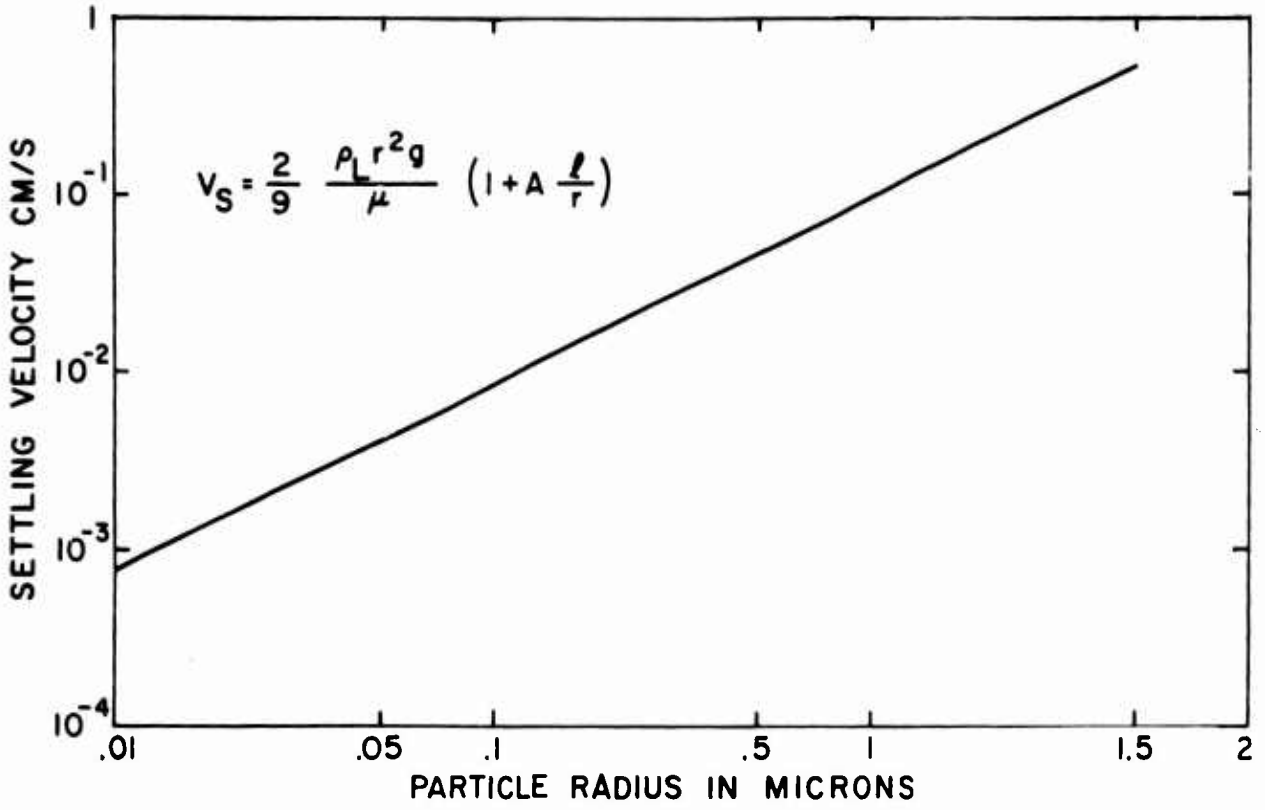


Fig. 1 Settling Velocity as a Function of Particle Radius.

ALKALI VAPOR SHOCK TUBE

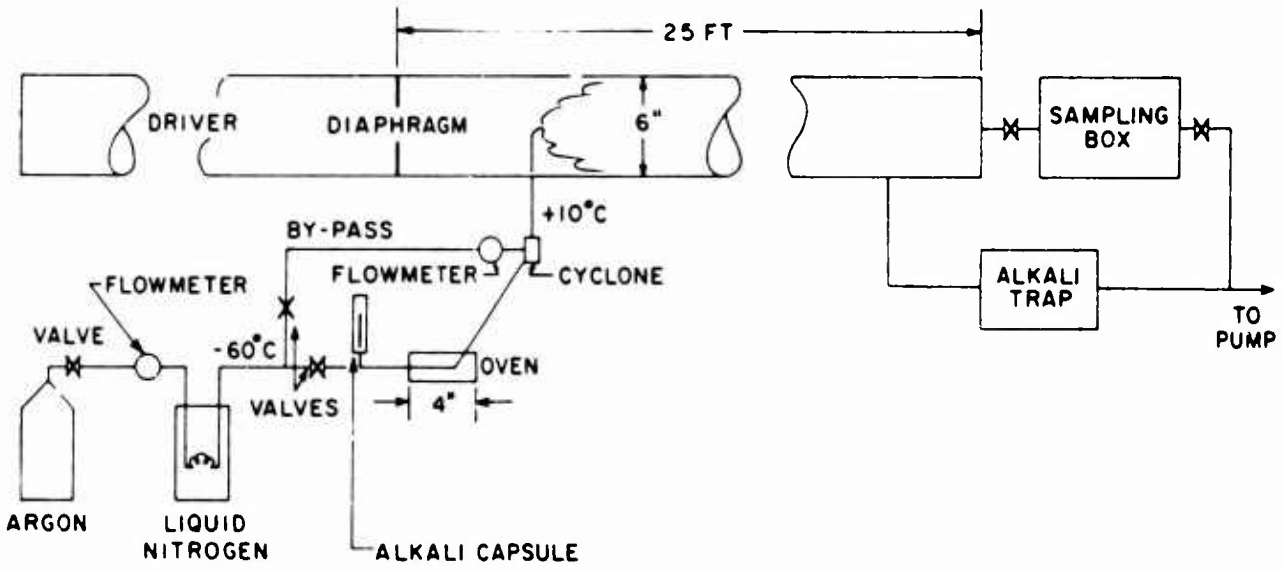


Fig. 2 Alkali Vapor Shock Tube Diagram.



Fig. 3 Electron Micrograph of Particles - Magnification 15000.

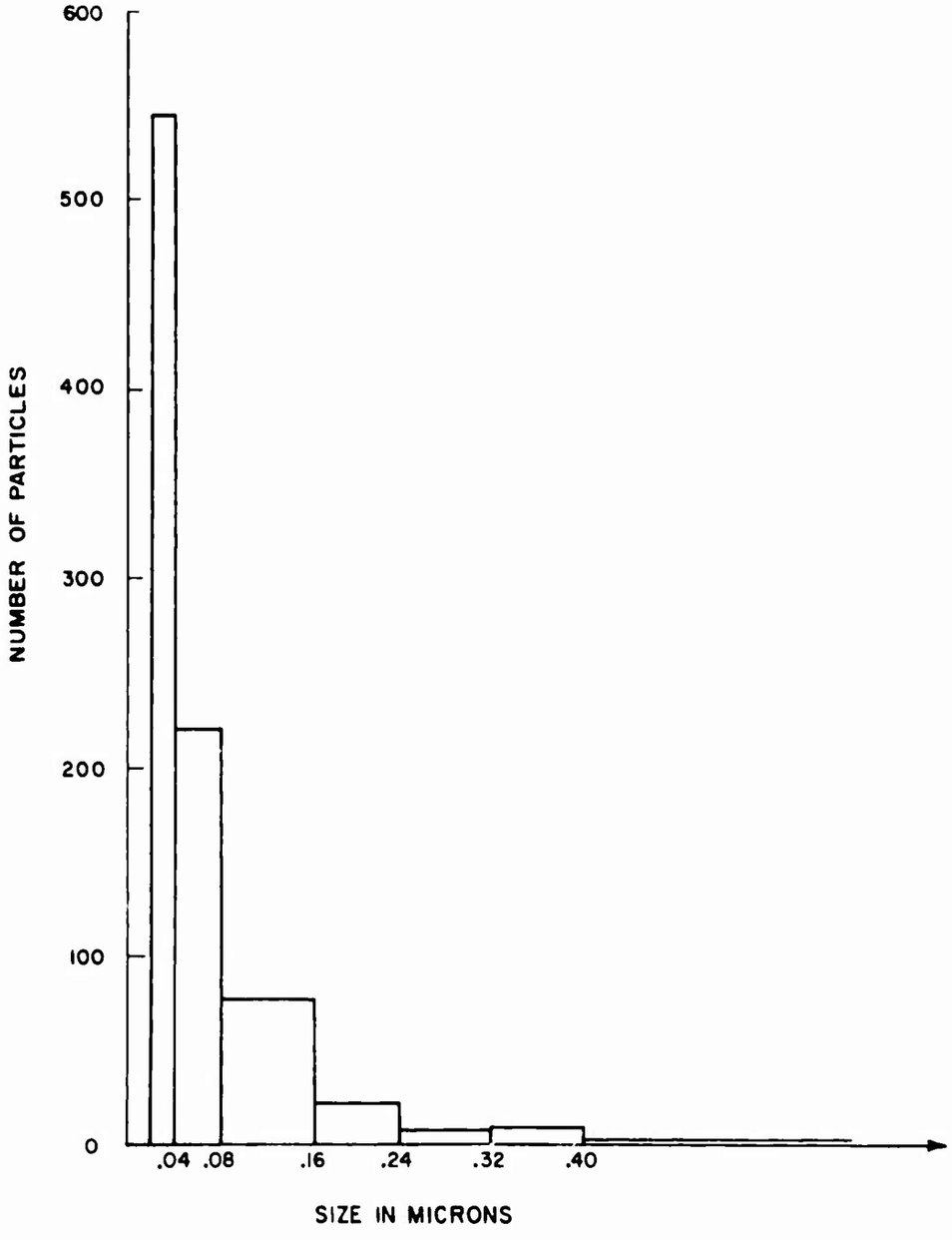


Fig. 4 Size Distribution of Particles.

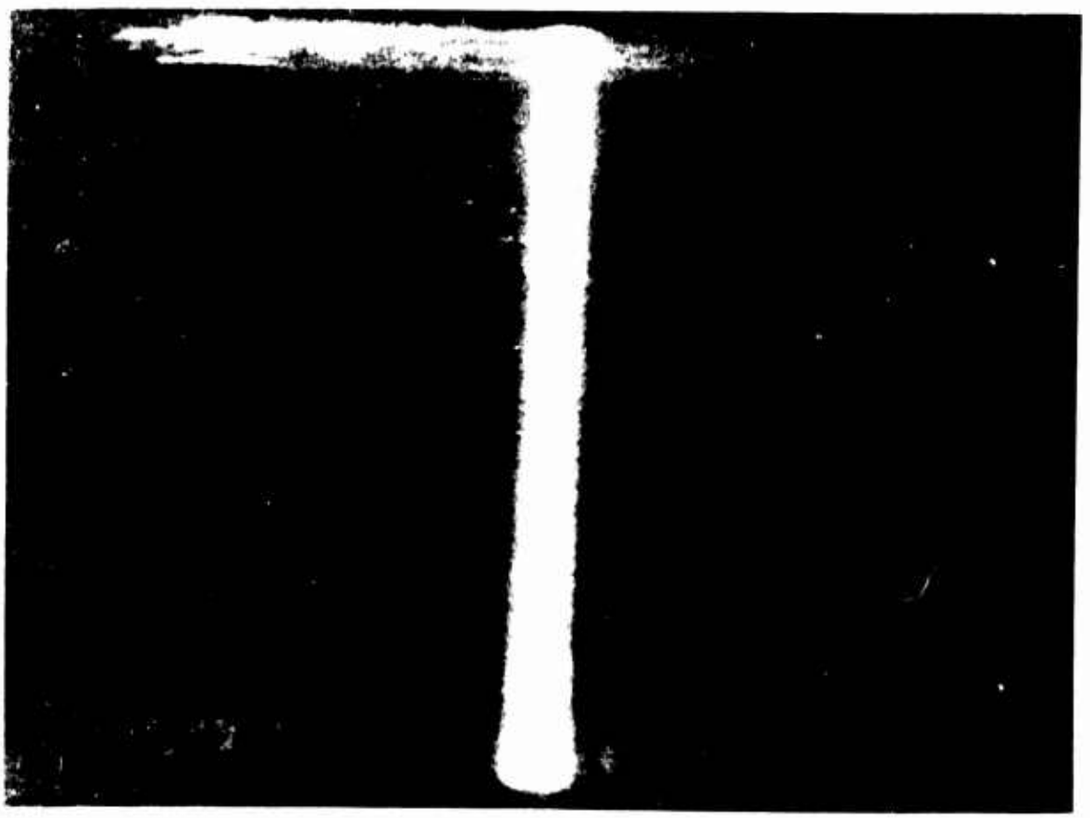


Fig. 5 90^{o} Light Scattering from Vertical Pencil Beam.

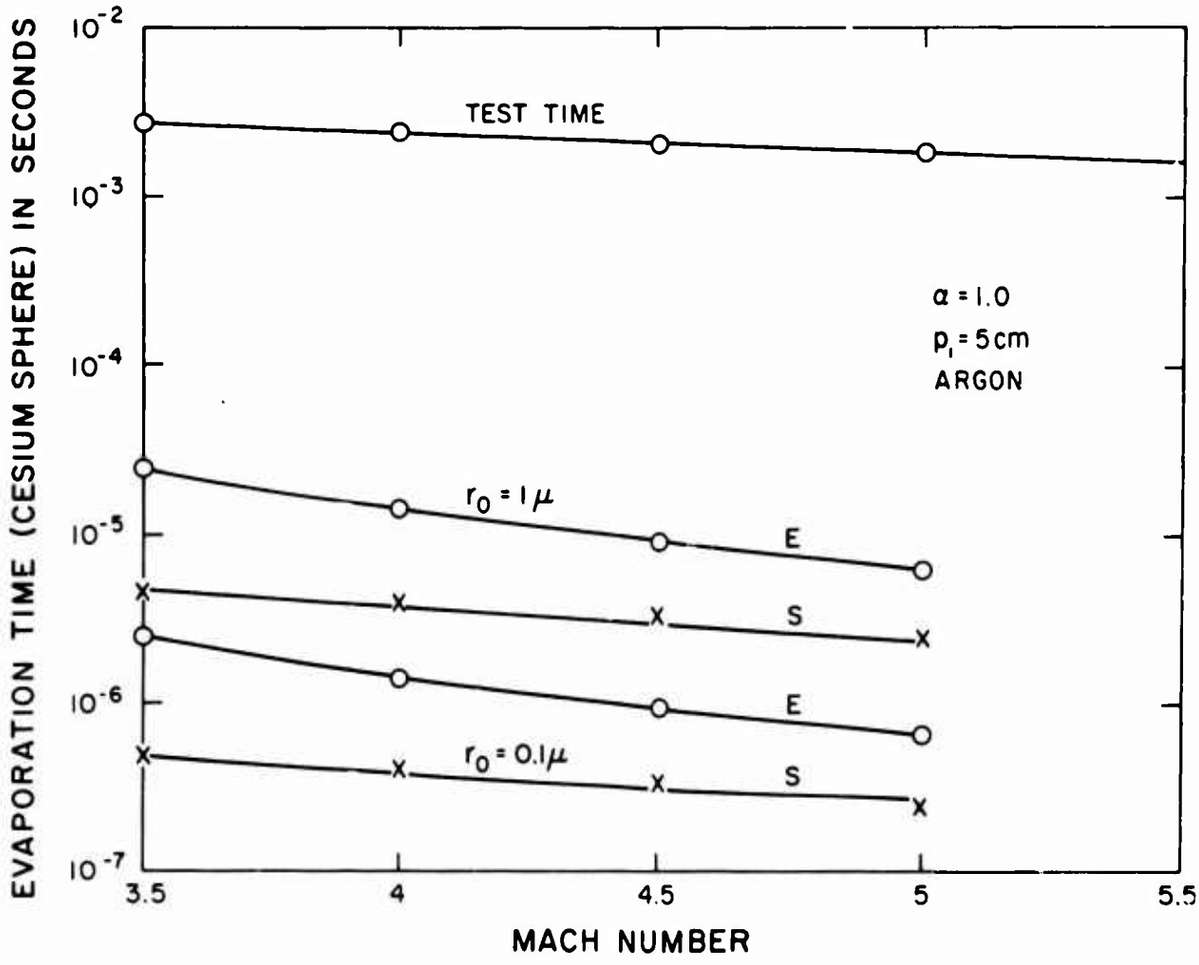


Fig. 6 Evaporation Time as a Function of Particle Radius.

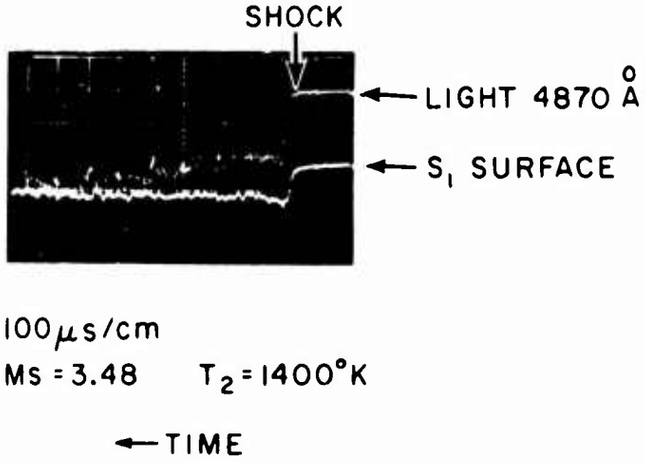
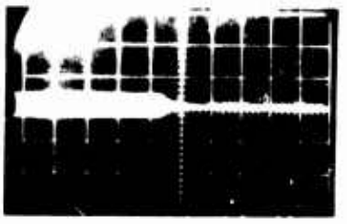


Fig. 7 Photomultiplier Traces:
Upper Trace: Light at 4870 Å with a 50 Å bandwidth.
Lower Trace: Light with the bandwidth response of S_1 phototube surface.



200 μs/cm 50 mV/cm

Ms = 3.48 T_2 = 1400°K

← TIME

Fig. 8 Signal from Ω coil; proportional to gas conductivity.

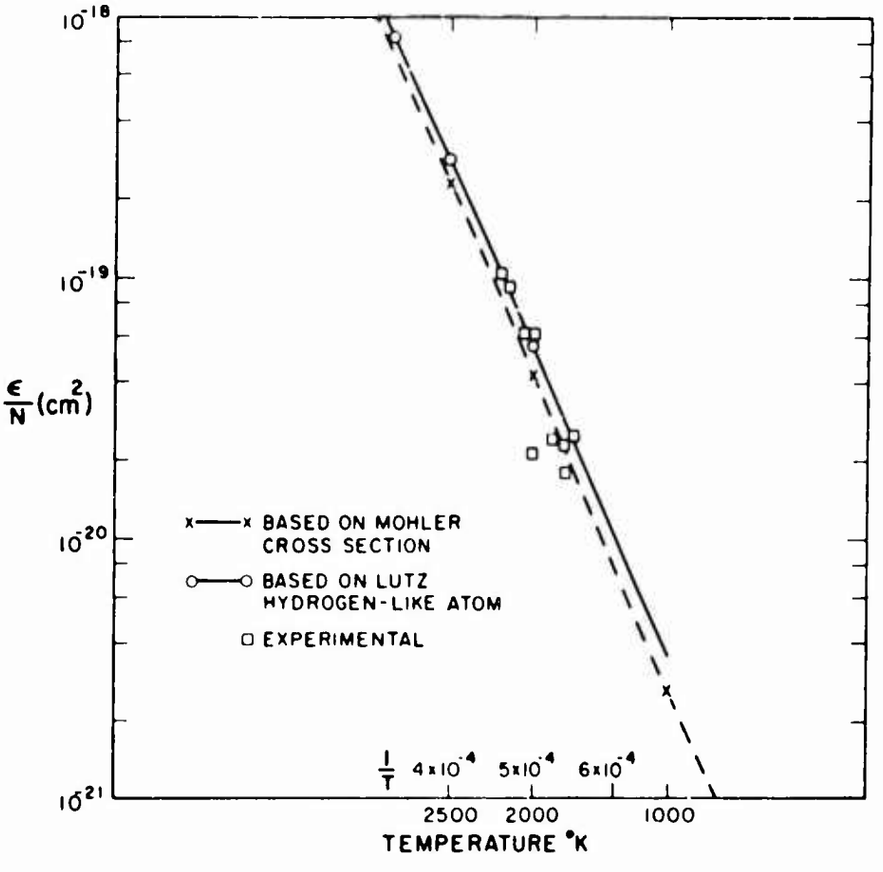


Fig. 9 Comparison of theoretical and experimental free-bound continuum radiation ratio as a function of temperature where ϵ/N is the gas emissivity divided by the number of atoms in the optical path.

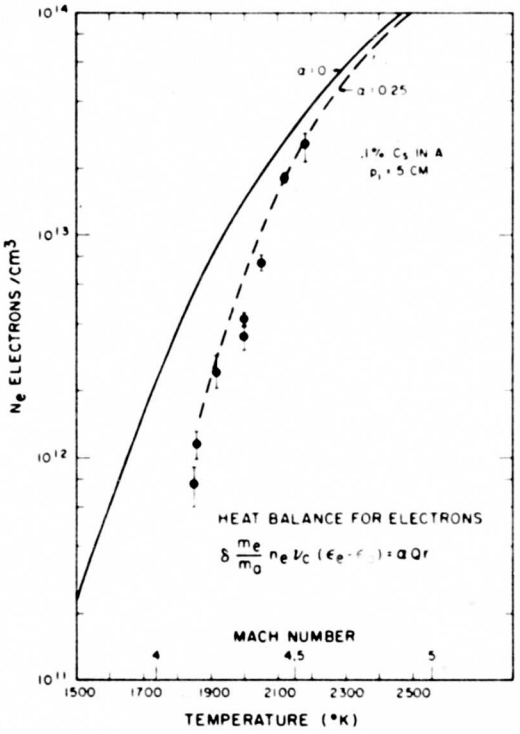


Fig. 10 Measurement of electron concentration attained by microwave probing compared with results of Saha equation without (α=0) and with radiation loss (α = 0.25).

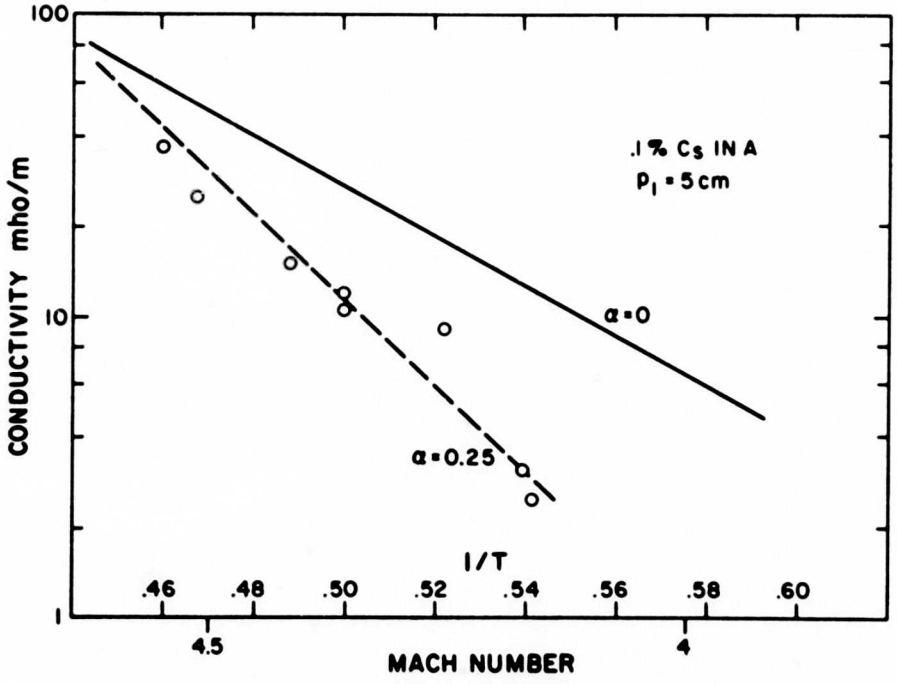


Fig. 11 Measurements of conductivity compared with theoretical results without (α = 0) and with radiation loss (α = 0.25).

Fig. 12 Spectra of cesium shot, cesium and mercury lamps.

BLANK PAGE

ON CYLINDRICAL IMPLODING SHOCK WAVES

J.H. Lee* and B.H.K. Lee*
McGill University
Canada

INTRODUCTION

In a cylindrical or spherical imploding detonation wave, the combustion products flow in the direction of decreasing radius. As a result of the decrease in the flow area, the reaction products are compressed adiabatically and the pressure behind the detonation wave is increased to a value above its normal Chapman-Jouguet value. An imploding detonation wave will therefore be increasingly overdriven as it converges towards the center of symmetry. In the limit, a strongly overdriven detonation wave approaches a strong shock wave when the energy released at the wave front due to chemical reactions becomes negligible as compared to the pressure energy in driving the wave. This self-amplification nature of the imploding detonation waves was first pointed out by Zeldovich (ref. 1). As indicated by the similarity solution of Guderley (ref. 2), the final stages of the propagation of imploding shock wave are independent of its initial conditions. Hence, it appears that imploding shock waves can be achieved near the center of symmetry through an imploding detonation wave.

According to the classical Chapman-Jouguet theory, the propagation of a C-J detonation wave is independent of the conditions in its wake. Hence, the diffraction problem for detonation wave is less severe than that for shock waves and the initiation of imploding detonation waves experimentally should present less difficulties. In this paper the results of an experimental study of cylindrical imploding detonation waves in acetylene-oxygen mixtures are presented.

* Present address: Dept. of Mechanical Engineering, McGill University Canada.

METHOD OF INITIATION

The present method used in the initiation of cylindrical imploding detonations is essentially similar to that used by Perry and Kantrowitz (ref. 3). A cylindrical exploding detonation wave is used to initiate the imploding wave. A schematic of the apparatus is shown in Fig. 1. The bomb consists of a steel cylindrical vessel of 50.8 cm inside diameter and 7 cm wide. It is separated into two chambers, the explosion chamber A and the implosion chamber B, by a steel center plate 50 cm in diameter and 1 cm thick. The center plate is held in position concentric with the cylindrical bomb wall by 8 bolts onto the back wall of the bomb. The bolts are enclosed in double-wedged airfoils to minimize the flow disturbances as the exploding detonation wave propagates by. The steel front plate of the bomb can be replaced by a 1-1/2" thick plexiglas plate for photographic observations of the implosion processes.

To prepare for an experiment, the bomb is first evacuated and filled with the explosive mixture at the desired initial pressure. A cylindrical diverging detonation wave is initiated in the explosion chamber A by an exploding wire or spark discharge. The center plate prevents the ignition of the mixture in the implosion chamber B until the diverging wave reaches the annular opening connecting the explosion and implosion chambers. A detonation wave is then initiated in chamber B which then implodes towards the center.

Equi-molar mixtures of commercial acetylene and oxygen were used throughout the present studies and all the experiments were performed at sub-atmospheric initial pressures ranging from 50mm Hg to 200 mm Hg.

RESULTS AND DISCUSSION

Using the method of initiation described, symmetrical imploding detonation waves are obtained in equi-molar acetylene-oxygen mixtures at initial pressures above 150mm Hg. A typical streak record taken across a 1mm horizontal diametral slit of a stable cylindrical imploding detonation wave is shown in Fig. 2. Detonation velocities measured from these streak records are found to be similar to the corresponding Chapman-Jouguet velocities of that particular mixture. A slight acceleration of the detonation wave can be observed near the center of convergence. However, the changes in the wave velocity are too small to enable meaningful quantitative results to be obtained. An indication of the high temperatures attained at the center of convergence can be observed from the luminosity pattern on the streak record shown in Fig. 2.

To show the symmetry of the imploding wave, streak photographs are taken of three diametral slits simultaneously. The three slits are arranged as follows; one horizontal diametral slit and the remaining two at 45 degrees to it. Using this method of streak photography, the imploding wave can be observed through six radial slits. With the wave velocity determined from the horizontal diametral slit, the instantaneous position of the imploding wave can be calculated. A typical three slit streak record of an imploding wave is shown in Fig. 3. Within the accuracy of this method, the imploding detonation wave was found to be symmetrical about the center.

Since relatively large changes in the location of the Chapman-Jouguet point on the equilibrium Hugoniot curve make only second order changes in the detonation velocity, a more sensitive parameter such as the pressure was measured to study the propagation of the imploding detonation wave. Quartz transducers (Kistler model 603) were spaced at different radii to determine the imploding detonation pressure. The transducers are calibrated and are linear within the pressure range of the experiment. Typical pressure profiles taken at different radii are shown in Fig. 4. The variation of the peak detonation pressure with radius determined experimentally is shown in Fig. 5. The pressure of a planar C.J. detonation wave at the same initial pressure as the imploding detonation is used as the reference pressure. Also plotted in Fig. 5. are the pressure variation with radius for a strong imploding shock wave based on Guderley's similarity solution, and for an imploding detonation wave based on the Chester-Chisnell-Whitham method. Details of the analysis of imploding detonation waves using this method are given in the Appendix. As shown in Fig. 5 extremely good agreement between theory and experiments is obtained. Near the center of convergence, the imploding detonation wave approaches a strong shock wave and the detonation pressure measured is about 18 times that of a planar detonation wave under similar initial conditions.

Below an initial pressure of 150mm Hg, symmetrical imploding detonation waves cannot be obtained using the present method of initiation. Possible reasons for this are: i) Non-symmetry and instability of the exploding detonation wave at low initial pressures, ii) Distortion of the diverging detonation wave by the wedge-shaped airfoils in its path, iii) Diffraction of the detonation wave as it propagates around the annular gap to the imploding chamber.

In a previous investigation (ref. 4), symmetrical diverging cylindrical detonations in equi-molar acetylene-oxygen mixtures were obtained for initial pressures as low as 30mm Hg by exploding wire discharge. The critical ignition energy required for direct initiation was increased significantly at low initial pressures. A regular stable multi-head spin structure was observed. However, the spinning wave was found to be symmetrical about the ignition point.

To investigate the distortion and the diffraction of detonation waves at low initial pressures, the real multi-head structure must be taken into consideration. Perhaps the most direct method to study the diffraction problem is by observing the changes in the regular multi-head structure of the detonation wave as it diffracts around the airfoils and the annular gap between the two chambers. The open-shutter technique was used to observe the diffraction processes of the multi-head detonation wave. This technique consists of focusing the detonation apparatus through a transparent window onto a stationary photographic film. The aperture of the camera is adjusted so that the extremely luminous ignition heads are recorded. A typical open-shutter record of the interaction of a multi-head diverging detonation wave with a double-wedged airfoil is shown in Fig. . As can be observed, the detonation wave regains its regular multi-head structure in a distance about half the total length of the airfoil. For higher initial pressures, the effect of the wedge on the detonation structure becomes insignificant. Six radial slits streak records have also been taken of a cylindrical diverging detonation wave propagating past the wedge-shaped airfoils. No changes in the symmetry of the cylindrical detonation wave were observed.

Typical open-shutter records of a detonation wave turning around a bend are shown in Fig. . As shown in Fig. a, the regular multi-head detonation structure is appreciably distorted as the wave propagates around a sharp bend. The decay of the detonation wave is indicated by the reduction in the number of ignition heads per unit length of the detonation front. The regular structure appears again further downstream. The decay of the detonation wave as it propagates round the bend is perhaps the nominal factor in the failure to initiate symmetrical imploding detonations at low initial pressures. As the initial pressure increases the attenuation of the detonation wave becomes less severe (Fig. b). An indication of the effect of the attenuation of the detonation wave by the bends on the generation of symmetrical imploding detonations is shown in Fig. . The experiments were performed in a flat channel simulating a diametral section of the imploding apparatus. The location of the line of collision of the two detonation waves indicates whether or not symmetrical implosions can be achieved. In Fig. a, the line of collision is displaced from the center of symmetry. At higher initial pressures (Fig. b) the collision occurs at the center of symmetry indicating that the attenuation of the detonation wave by the bends did not affect the initiation of a symmetrical imploding detonation wave.

The diffraction of the detonation wave can be greatly reduced if the bends are provided with a radius of curvature. In Fig. a, a smooth turning is achieved with very small changes in the detonation wave structure. The initial conditions for Fig. b are similar to Fig. a, and the attenuation due to a sharp corner is clearly illustrated.

CONCLUSIONS

With the present method of initiation, symmetrical cylindrical imploding detonation waves can be produced in equi-molar acetylene-oxygen mixtures at initial pressures above 150mm Hg. Pressure measurements indicate the self-amplification characteristics of imploding detonation waves. Good agreement between the Chester-Chisnell-Whitham method and experiments is obtained. With careful design of the channel leading from the explosion to the implosion chamber, symmetrical imploding detonation waves can undoubtedly be produced at even lower initial pressures.

REFERENCES

(1) Zeldovich, Ya. B., Soviet Physics JETP 36, 550 (1959)

(2) Guderley, G., Luftfahrtforschung 19, 302 (1942)

(3) Perry, R.W. and Kantrowitz, A., J. Appl. Phys. 22, 878 (1951)

(4) Lee, J.H., The Propagation of Shocks and Blast Waves in a Detonating Gas, McGill University Publication Rept (·5-1 (19·5)

(5) Whitham, G.B., J. Fluid Mech. 4, 337 (1958)

APPENDIX

Symbols:

A - area
c - speed of sound
D - C-J detonation velocity
M_s - detonation Mach number
p - pressure
Q - chemical heat release per unit mass
R_s - instantaneous detonation radius
r - space co-ordinate
t - time
u - particle velocity
ρ - density
γ - ratio of specific heats

Following the analysis of Whitham (ref. 5), equations for C^+ characteristics are:

$$\frac{dr}{dt} = u + c \tag{1}$$

$$dp + \rho c\, du + \frac{\rho c^2 u}{u+c}\,\frac{dA}{A} = 0 \tag{2}$$

Instead of expressing u, p, and ρ as functions of the two independent variables r and t, it is more convenient to express them as functions of ξ and M_s, where

$$\xi = \frac{r}{R_s} \tag{3}$$

In the transformed co-ordinates, u, p, and ρ can be expressed as:

$$u = \dot{R}_s\, \phi(\xi, M_s) \tag{4}$$

$$p = \rho_0 \dot{R}_s^2\, f(\xi, M_s) \tag{5}$$

$$\rho = \rho_0\, \psi(\xi, M_s) \tag{6}$$

where ϕ, f, and ψ, are functions of ξ and M_s.

Along the detonation front, $\xi = 1$, and equation (2) can be expressed as:

$$2f\, d\dot{R}_s + \dot{R}_s\, df + \sqrt{\gamma f \psi}\,(\dot{R}_s\, d\phi + \phi\, d\dot{R}_s) + \frac{\gamma f \phi \dot{R}_s}{\phi + \sqrt{\frac{\gamma f}{\psi}}}\,\frac{dA}{A} = 0 \tag{7}$$

The boundary conditions to be satisfied at the detonation front are those determined from the Rankine-Hugoniot equations across an exothermic wave. Using equations (4) to (6), and neglecting terms containing $1/M_s^2$, they can be written as:

$$\psi(1, M_s) = \frac{\gamma+1}{\gamma(1-\alpha)} \tag{8}$$

$$f(1, M_s) = \phi(1, M_s) = \frac{1+\gamma\alpha}{\gamma+1} \tag{9}$$

where $$\alpha = \frac{1}{\gamma}\sqrt{1-(\gamma^2-1)\,\frac{2Q}{c_o^2}\cdot\frac{1}{M_s^2}} \tag{10}$$

For frozen equilibrium, the C-J detonation velocity is

$$D = c_o\sqrt{(\gamma^2-1)\,\frac{2Q}{c_o^2}}$$

Therefore α can be written as:

$$\alpha = \frac{1}{\gamma}\sqrt{1-\left(\frac{D}{R_s}\right)^2} \tag{11}$$

At the detonation front, ϕ, f, and ψ depend on M_s alone. Making use of equations (8) to (11), equation (7) can be written as:

$$\frac{1+\gamma\alpha+\gamma\sqrt{(1+\gamma)(1-\alpha)}}{(1-\gamma\alpha)(1+\gamma\alpha)^2}\left\{1+\gamma\alpha+\sqrt{\frac{1+\gamma\alpha}{1-\alpha}}\right\}d\alpha + \frac{dA}{A} = 0 \tag{12}$$

If at any radius R_i, a C-J detonation is initiated, the term dA/A is

$$\frac{dA}{A} = j\,\frac{d(R_s/R_i)}{R_s/R_i} \tag{13}$$

where $j = 1$ for cylindrical waves
$j = 2$ for spherical waves
R_s/R_i varies from 0 to 1, and
$\alpha = 0$ when $R_s/R_i = 1$
$\alpha \to 1/\gamma$ when $R_s/R_i \to 0$

When $R_s = R_i$, the C-J conditions can be applied and they are

$$\psi_i = \frac{\gamma+1}{\gamma} \tag{14}$$

$$f_i = \phi_i = \frac{1}{\gamma+1} \tag{15}$$

For any values of α different from zero, the particle velocity, pressure, and density with reference to those at R_i can be expressed as:

$$\frac{u}{u_i} = \frac{(1+\gamma\alpha)}{\sqrt{1-\gamma^2\alpha^2}} \tag{16}$$

$$\frac{p}{p_i} = \left(\frac{1}{1-\gamma\alpha}\right) \qquad (17)$$

$$\frac{\rho}{\rho_i} = \left(\frac{1}{1-\alpha}\right) \qquad (18)$$

In the numerical solution, the area is varied and the corresponding α is determined from equation (15). Once α is known, then the non-dimensional particle velocity, pressure, and density can be determined from equations (16) to (18).

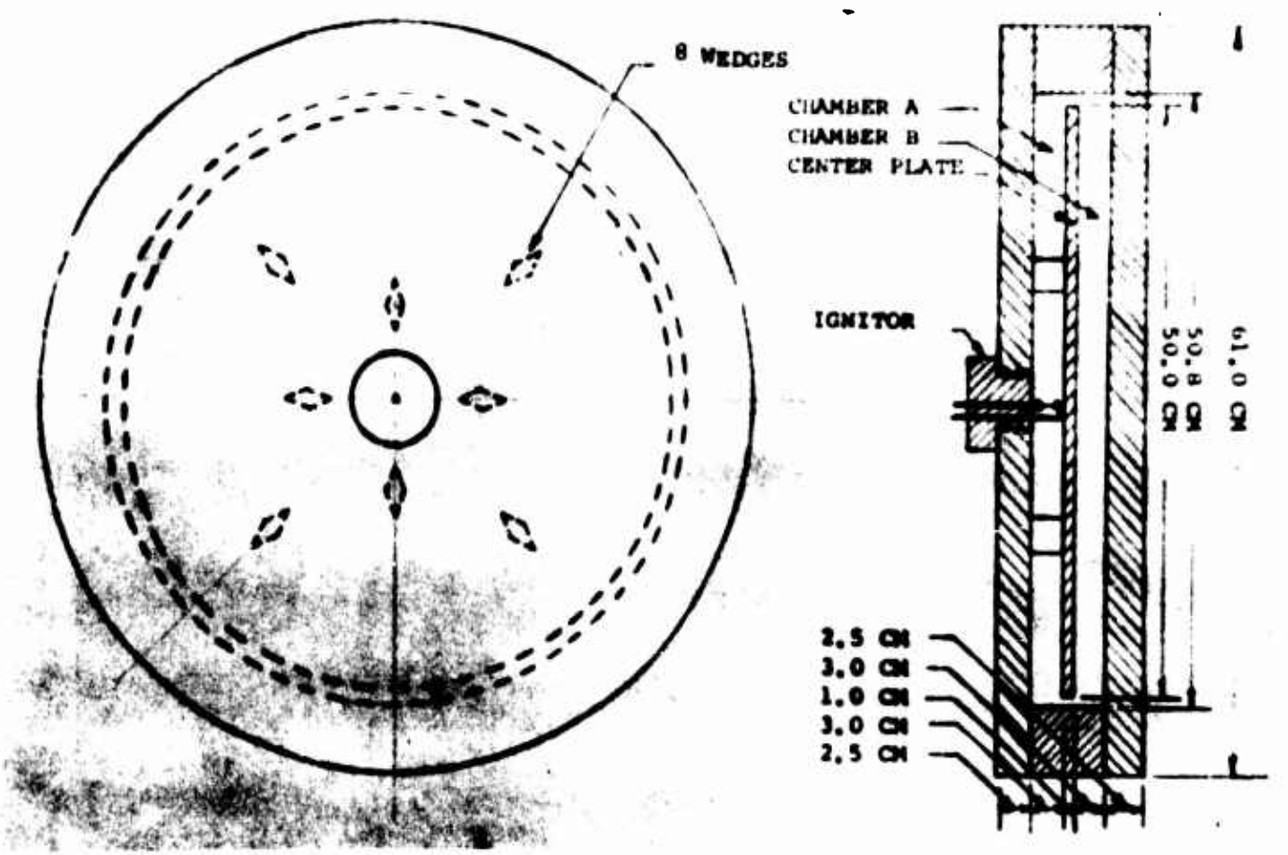


FIG. 1 SCHEMATIC OF THE CYLINDRICAL BOMB.

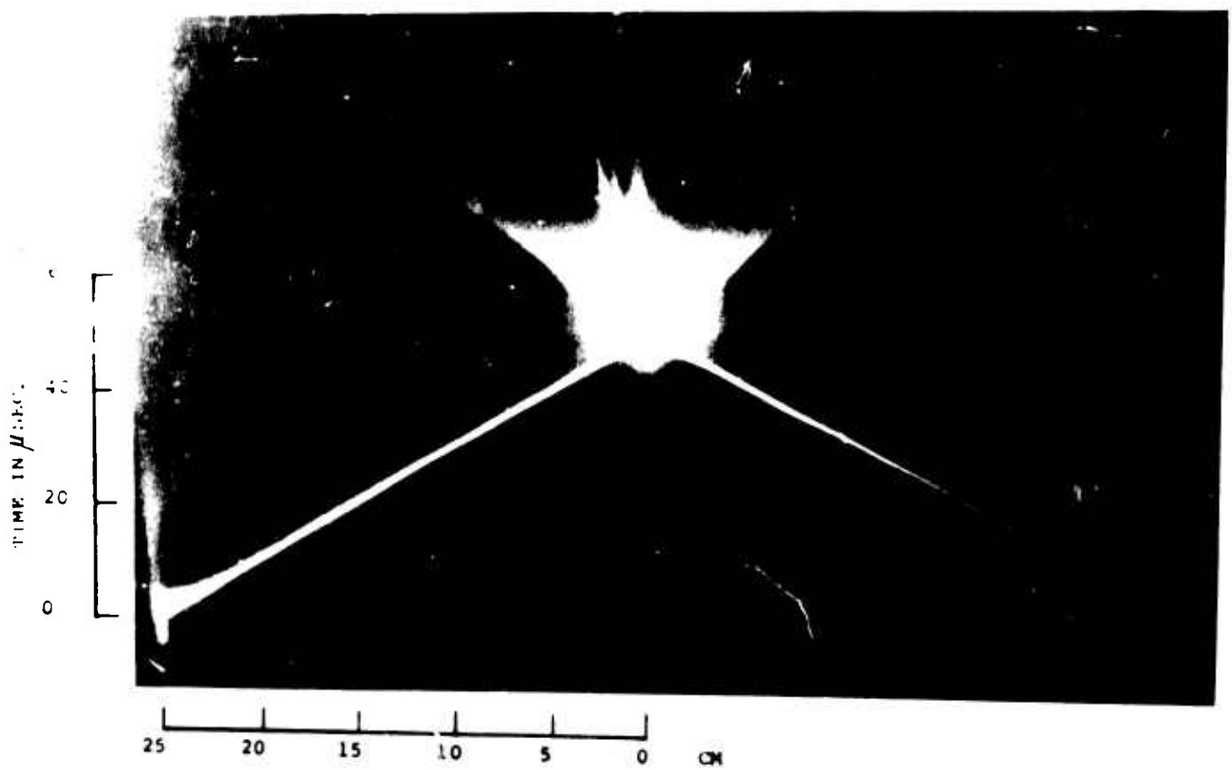


FIG. 2 TYPICAL STREAK PHOTOGRAPH OF A CYLINDRICAL IMPLODING DETONATION IN EQUI-MOLAR ACETYLENE-OXYGEN MIXTURE AT AN INITIAL PRESSURE OF 190 mm Hg.

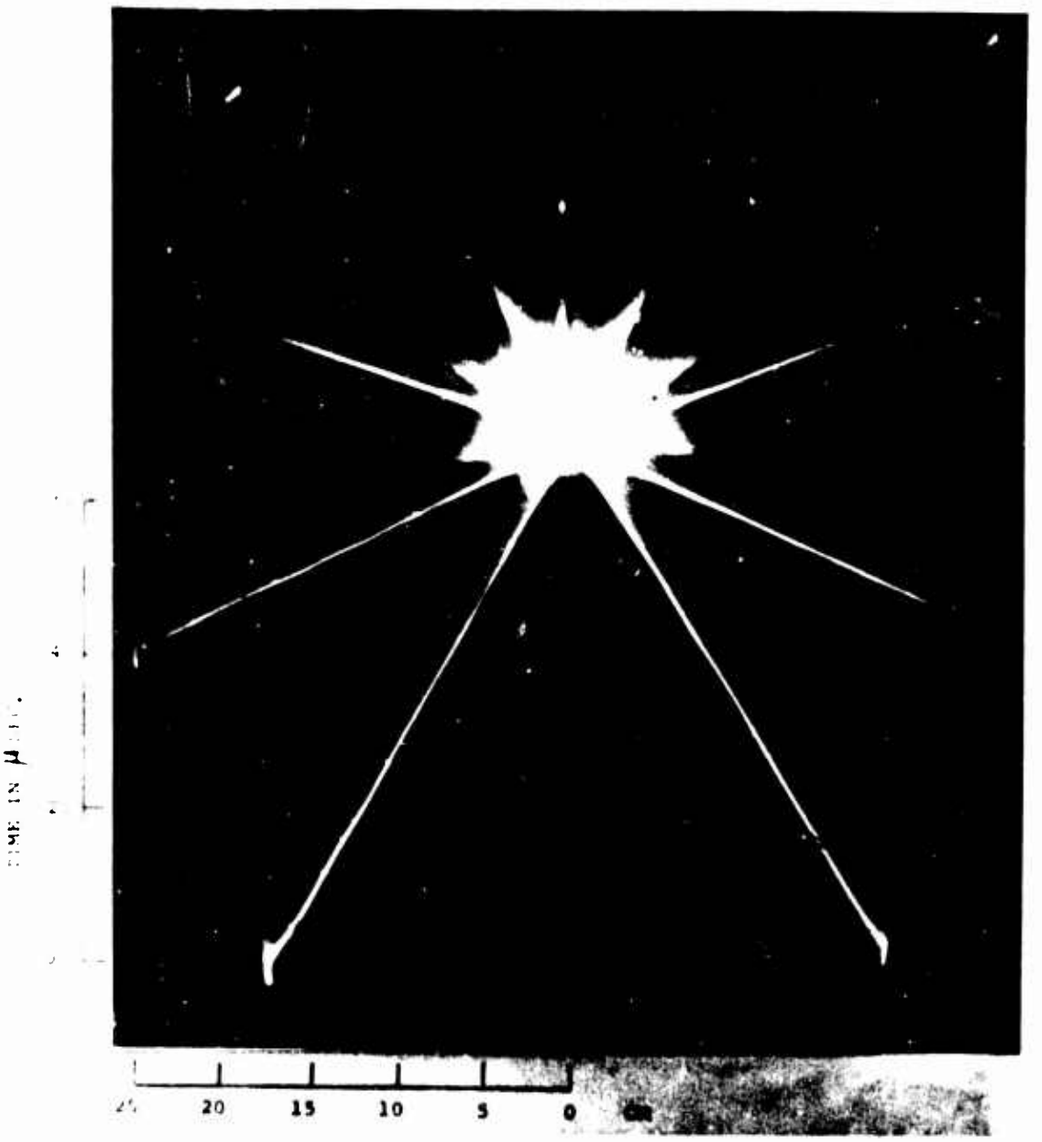


FIG. 3 TYPICAL THREE-SLIT STREAK PHOTOGRAPH OF A CYLINDRICAL IMPLODING DETONATION IN EQUI-MOLAR ACETYLENE-OXYGEN MIXTURE AT AN INITIAL PRESSURE OF 190 mm Hg.

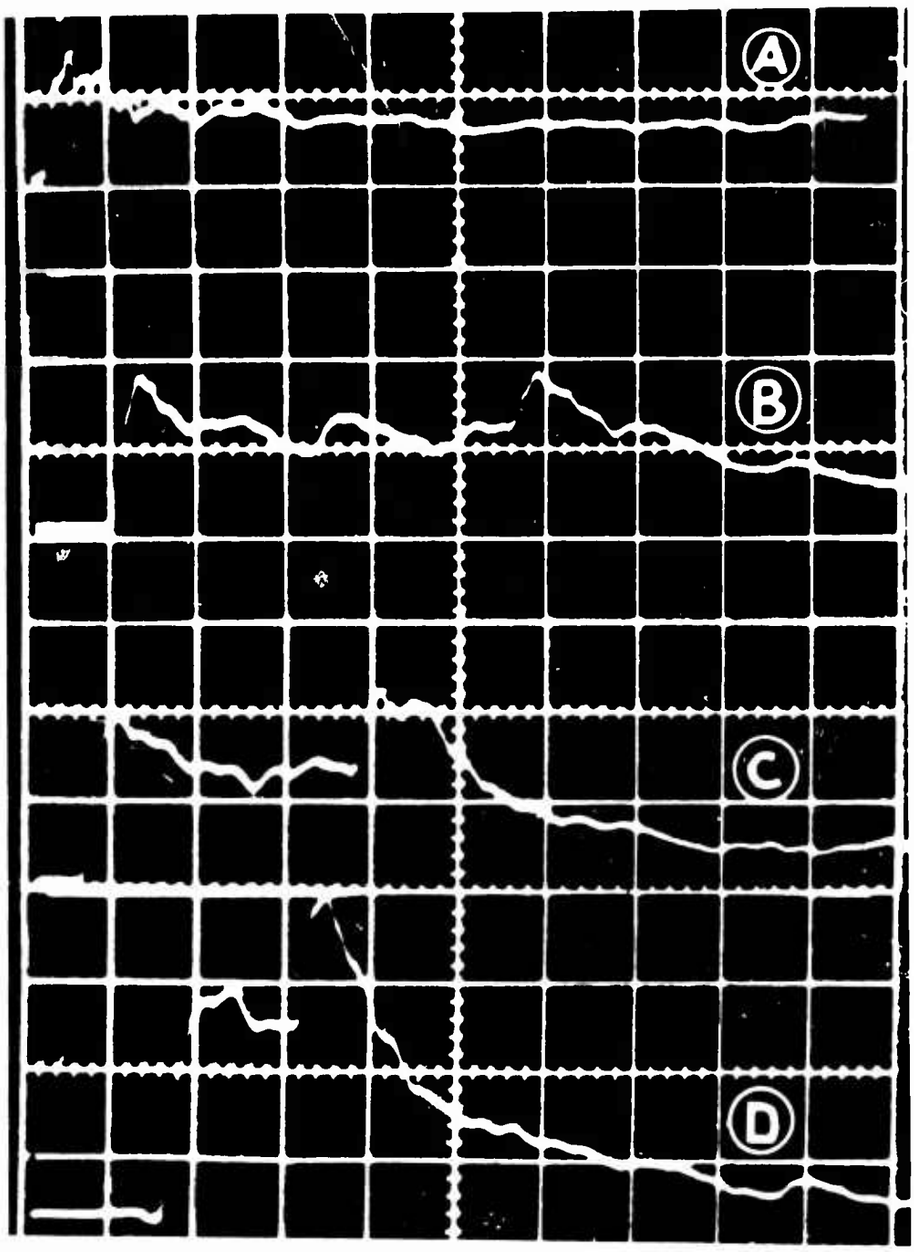


FIG. 4 PRESSURE-TIME PROFILES BEHIND A CYLINDRICAL IMPLODING DETONATION; MIXTURE: EQUI-MOLAR ACETYLENE-OXYGEN AT AN INITIAL PRESSURE OF 190 mm Hg.
TRACES: (A) AT r = 25cm, (B) AT r = 12cm, (C) AT r = 8cm, (D) AT r = 4cm
HORIZONTAL SCALE: 10 μ SEC./cm

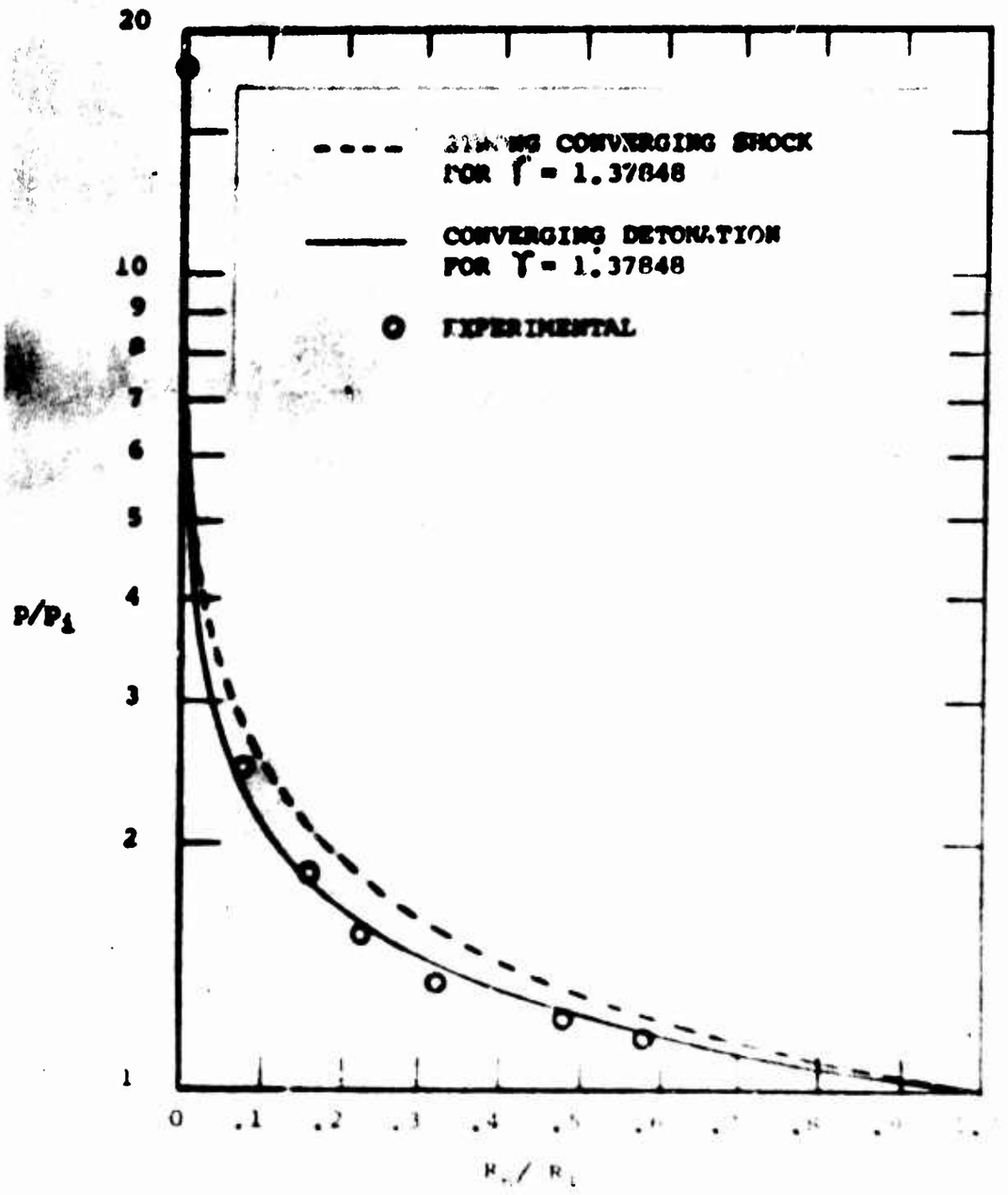


FIG. 5 VARIATION OF DETONATION PRESSURE WITH RADIUS FOR A CYLINDRICAL IMPLODING DETONATION IN EQUI-MOLAR ACETYLENE-OXYGEN MIXTURE AT AN INITIAL PRESSURE OF 190 mm Hg.

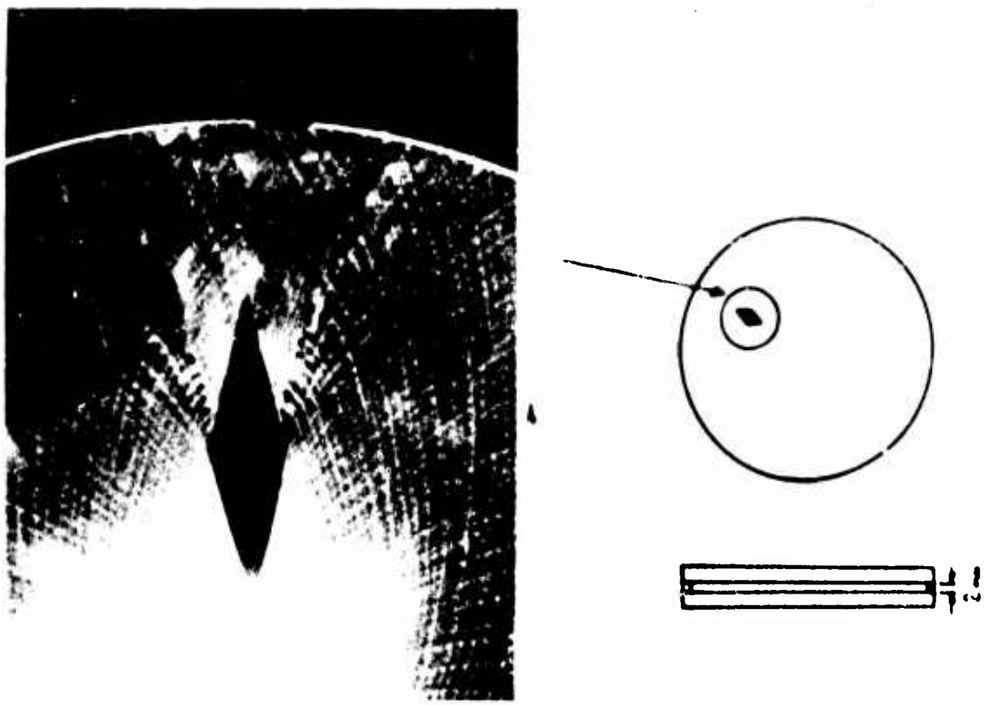


FIG. 6 OPEN-SHUTTER RECORD OF THE INTERACTION OF A MULTI-HEAD DIVERGING DETONATION WAVE WITH A DOUBLE-WEDGED AIRFOIL. THE CYLINDRICAL BOMB IS 2mm THICK. EQUI-MOLAR ACETYLENE-OXYGEN MIXTURE AT AN INITIAL PRESSURE OF 50 mm Hg IS USED.

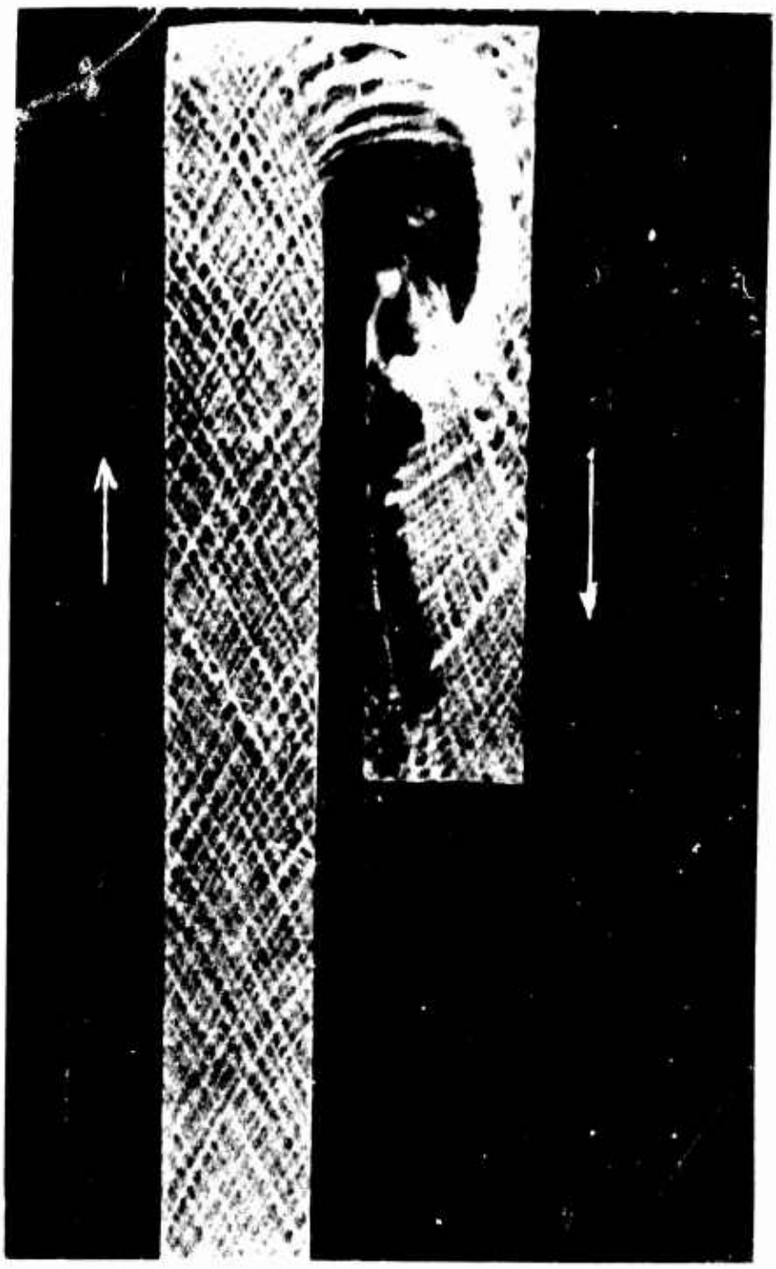


FIG. 7a OPEN-SHUTTER RECORD OF A DETONATION WAVE TURNING AROUND A SHARP BEND. EQUI-MOLAR ACETYLENE -OXYGEN MIXTURE AT AN INITIAL PRESSURE OF 60 mm Hg IS USED.

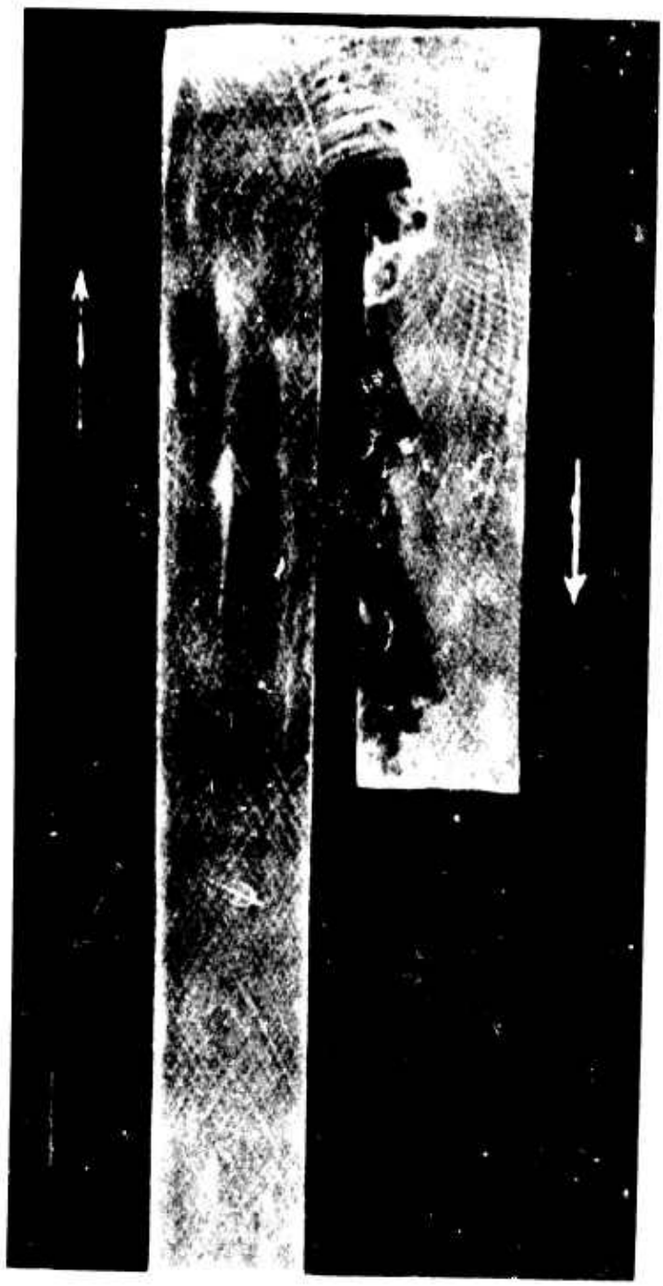


FIG. 7b OPEN-SHUTTER RECORD OF A DETONATION WAVE TURNING AROUND A SHARP BEND; EQUI-MOLAR ACETLENE -OXYGEN MIXTURE AT AN INITIAL PRESSURE OF 80 mm Hg IS USED.

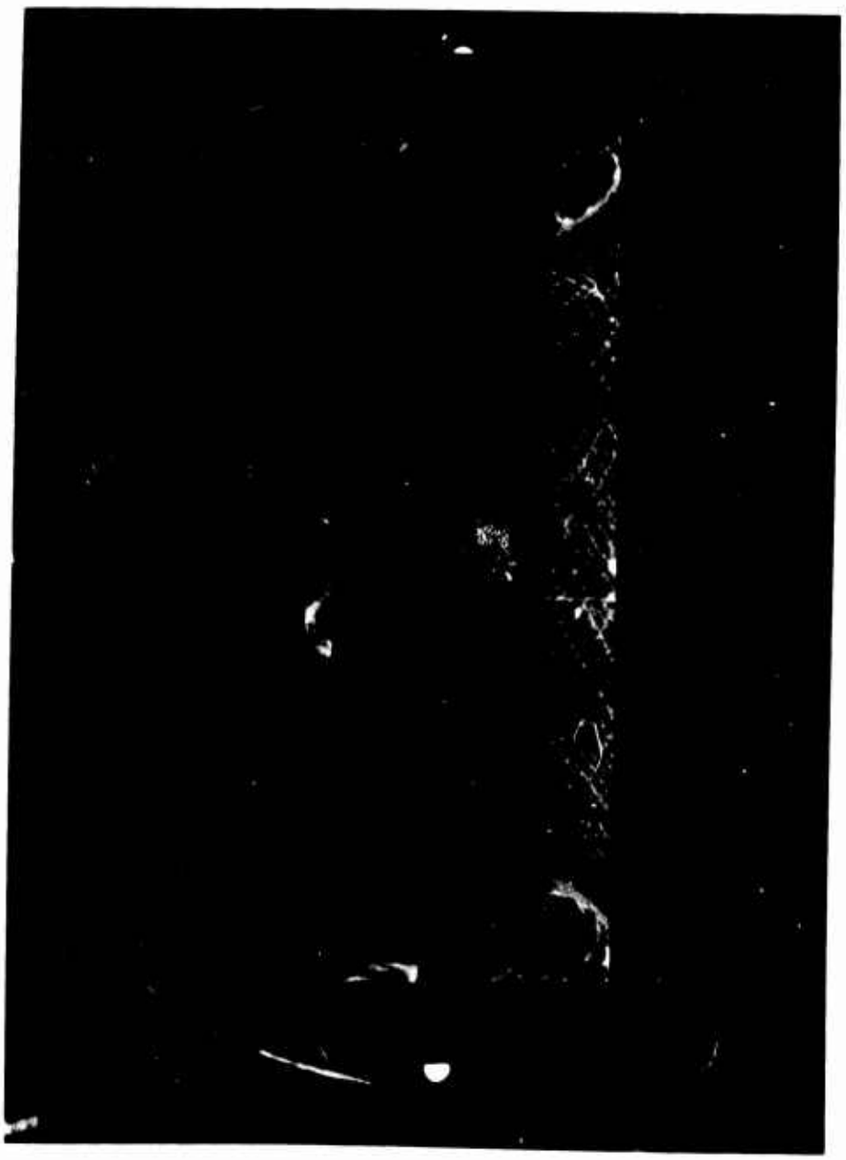


FIG. 8a PROPAGATION OF A DETONATION WAVE IN A FLAT CHANNEL SIMULATING A DIAMETRAL SECTION OF THE CYLINDRICAL BOMB. EQUI-MOLAR ACETYLENE-OXYGEN MIXTURE AT AN INITIAL PRESSURE OF 80 mm Hg IS USED.

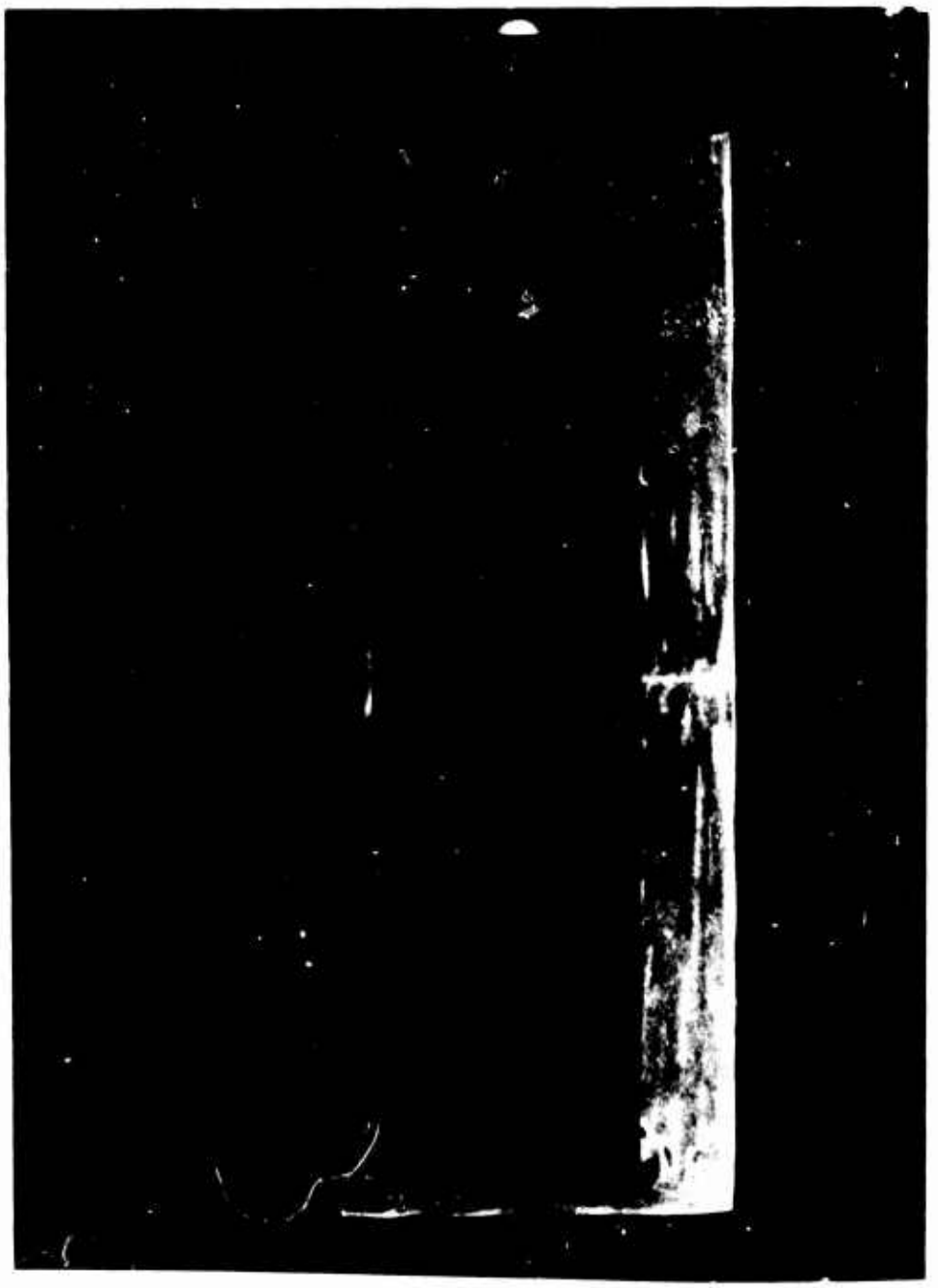


FIG. 8b PROPAGATION OF A DETONATION WAVE IN A FLAT CHANNEL SIMULATING A DIAMETRAL SECTION OF THE CYLINDRICAL BOMB. EQUI-MOLAR ACETYLENE-OXYGEN MIXTURE AT AN INITIAL PRESSURE OF 100 mm Hg IS USED.

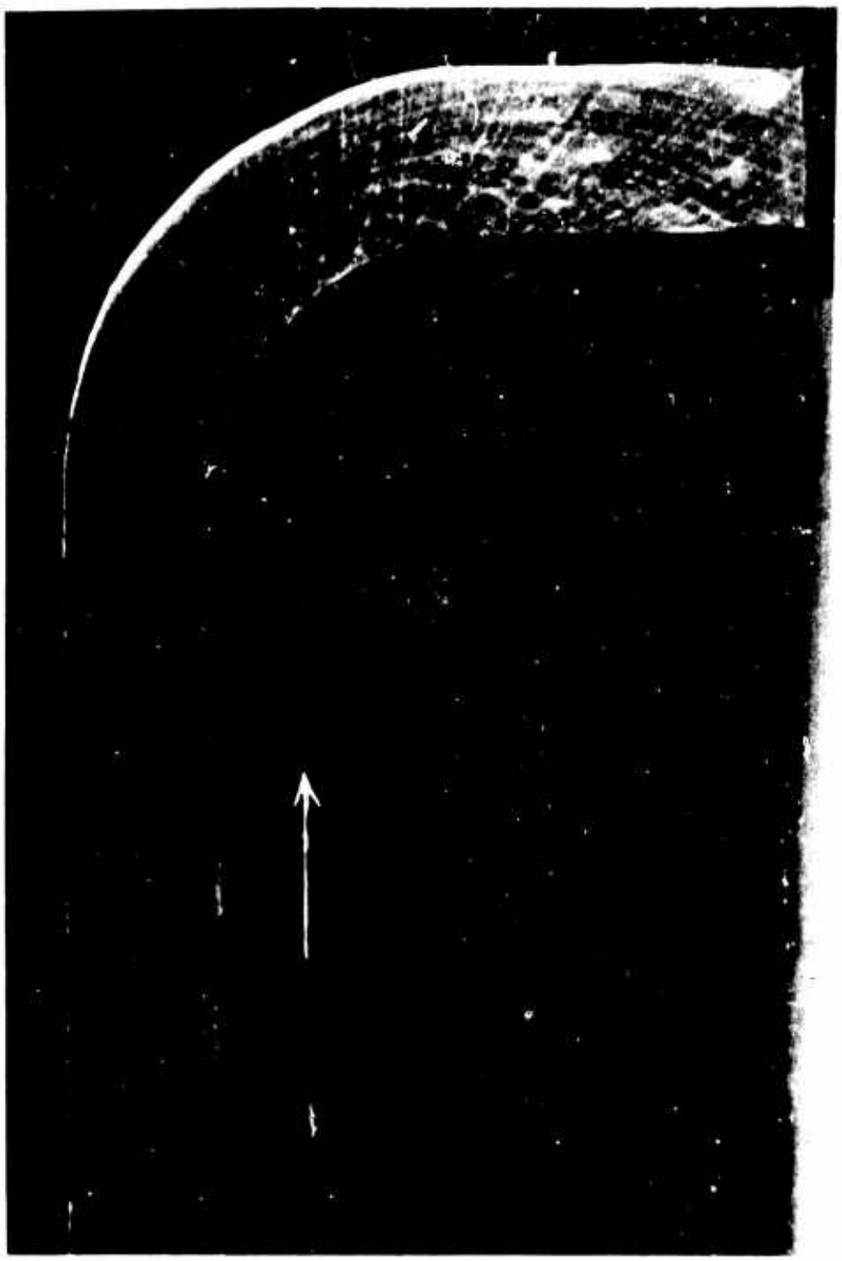


FIG. 9a PROPAGATION OF A DETONATION WAVE AROUND A BEND WITH A RADIUS OF CURVATURE OF 1-1/2 INCHES. EQUI-MOLAR ACETYLENE-OXYGEN MIXTURE AT AN INITIAL PRESSURE OF 60 mm Hg IS USED.

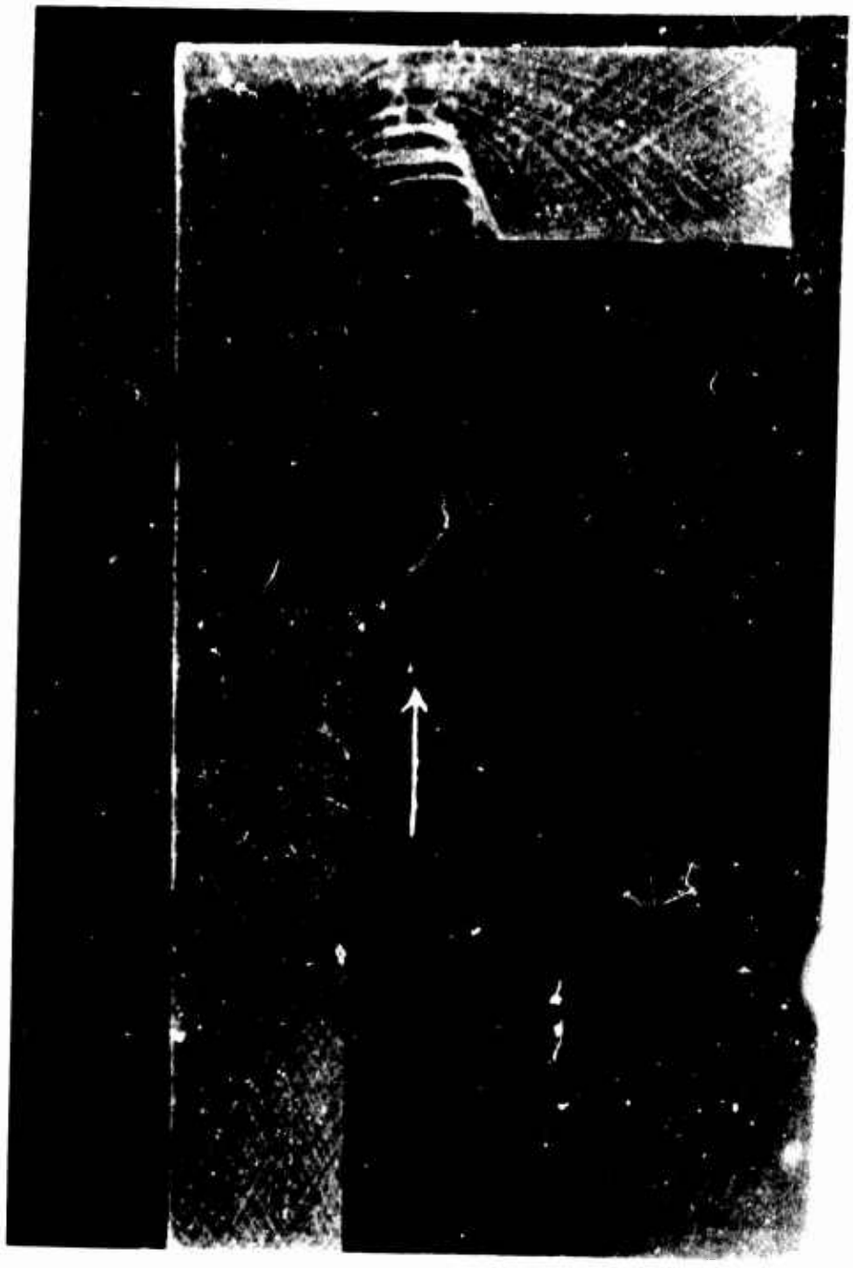


FIG. 9b PROPAGATION OF A DETONATION WAVE AROUND A SHARP CORNER. EQUI-MOLAR ACETYLENE-OXYGEN MIXTURE AT AN INITIAL PRESSURE OF 60 mm Hg IS USED.

A CONICAL SHOCK TUBE NUCLEAR-BLAST SIMULATOR

W. S. Filler
U. S. Naval Ordnance Laboratory
White Oak, Silver Spring, Maryland

Y. Park
Bureau of Ships
Washington, D. C.

R. E. Pages
General American Transportation Corporation

ABSTRACT

A conical shock tube with a maximum diameter of 24 ft and driven by a contained detonation of up to 1000 lb of high explosive has been designed. Based on studies with shock tubes of 1/1000, 1/100, and 1/10 scale, it is expected that, with the maximum charge, blast-wave parameters along much of the nearly half-mile of tube length will closely simulate those for a free-air nuclear explosion equivalent in energy to 20 kton of TNT. The driver chamber consists of four 16-in. naval gun barrels in tandem, within which the high explosive in the form of a long thin cylinder will be fired. The portion of the tube from the firing chamber to the 12-ft-diam section may be closed off by diaphragms and evacuated to 8 mm Hg. Supports for structures tests are integral with and located at the 10-, 15-, and 22-ft-diam sections. The tube is segmented in lengths of 100 ft or less that are free at one end to expand or contract under thermal and elastic influences. Except for an axial force component resulting from the blast wave in the cone itself, the tube is free from firing recoil.

INTRODUCTION

In April 1965 the Department of Defense awarded a contract for the construction of the Defense Atomic Support Agency Conical Shock Tube Facility, which, for short, is to be called DASACON. This sector-type shock tube was developed to simulate, and thereby make more convenient, the study of the blast effects of nuclear explosions with immediate application to the relatively low 10 to 100 psi pressure region.

Compressed-gas-driven sector shock tubes have been described in the literature by Campbell[1] and Cole.[2] If, in place of compressed gas, a high explosive is used in a contained manner as the driving means in a conical tube, a spherical sector blast wave will propagate down the tube.

A series of experiments conducted at the Naval Ordnance Laboratory[3,4] indicated that in a conical tube with a small spherical angle a relatively small quantity of explosive is required to generate a blast wave typical of an enormous amount of high explosive. This is a direct result of the geometry, since, in effect, a small conical sector of a full spherical explosion is isolated within the cone, as illustrated in Figure 1.

These experiments led to interest on the part of the Bureau of Ships in the possibility of nuclear-blast simulation by this means, and a pilot facility 180 feet long and approximately 1/10th full scale was constructed to evaluate the technique.[5] This device, built at the Naval Ordnance Laboratory, proved highly successful and led finally to the design of a full-scale facility to be built at the Naval Weapons Laboratory, Dahlgen, Virginia.

The cone of this full-scale facility has been designed with a taper of 1 foot per 100 feet of length (plane angle of 0.571°). The solid angle of a sphere, 4π steradians, is 160,000 times the solid angle of this cone and this is what we call its amplification factor. Two hundred and fifty pounds of high explosive multiplied by such an amplifying factor equals 20 kilotons. Since about three quarters of the energy is lost in the early phase of the expansion, 1000 pounds of high explosive will actually be required to produce such a blast wave.

It has been well established that over much of its propagation history the blast wave from a chemical high explosive does not differ substantially from that generated by a nuclear explosion where the energy contributed to the blast is equal in both cases. (Although there is some difference in the space-time coordinates with respect to the start of the explosion for the two waves.) As a consequence, the explosive-driven conical shock tube is expected to provide excellent simulation of nuclear blasts in the kiloton range.[6]

HIGH EXPLOSIVE DRIVER

One of the principal problems in the development of this shock tube was the containment of the explosion in the driver section. A pressure of several millions of pounds per square inch exists, for short times, at the detonation front in solid high explosives. In order to avoid plastic deformation, direct contact between the explosive and the walls of the chamber must be avoided. Yet, for explosives spaced reasonably close to the chamber walls, only limited information was available on which to base an efficient design. A number of investigations, empirical as well as theoretical, were made to improve this situation. It would be useful at this point to outline the processes that are involved.

The sequence of events in the firing chamber begins with the detonation wave that moves down the cylinder of high explosive from the closed end of the chamber. The expanding gas behind the detonation front shocks the air in the adjacent space. This shock reflects at the wall and subsequently undergoes successive reflection. The time scale is on the order of tens of microseconds.

A few milliseconds after the start of this process a reasonably uniform distribution of explosion energy has occurred within the chamber space. This may be observed as a pressure that is hydrostatic in character, and is maintained for the time it takes the gases to leave the open end of the firing chamber.[7] This time is on the order of tens of milliseconds and is approximately a linear function of the length of the charge, other variables being constant (Figure 2, columns t_1 and t_d).

The hydrostatic pressure for the proposed firing chamber configuration has been calculated[8] and measured,[7] with good consistency between the two results. For a 16-inch gun with a 4-inch diameter charge, a value in the range of 10,000 psi was determined. This value is only about one third the maximum operating pressure for normal shell firing usage. While this pressure determines the recoil force and the load requirement for recoil absorption (to be discussed later in this report) it does not control the maximum weight of charge that may be used in the gun. It is, rather, the early shock wave processes that play the dominant role in that regard.

A computer calculation of the early shock wave pressure on the inner surface of the gun barrel was made, using an available hydrodynamics code for detonation in solids and shock waves in gas. It was found that with a one to six charge-to-hole diameter ratio the initial peak reflected shock wave pressure loads on the wall were just about at the yield value for the gun barrel, but lasted for only a few microseconds. However, an actual determination of the conditions for yielding under intense shock loading involves the interplay of the elastic and plastic behavior of steel. Unfortunately, means for combining these regimes in a computer code were not available. While the computation pinpointed the early shock wave phase as the chief loading problem, it could not provide specific information on response.

As a result, in the main, empirical tests were relied on to provide actual operating criteria. These tests were intended to determine the critical ratio of charge-to-hole size for plastic deformation of a thick-walled cylinder with a wall thickness approximately equal to the hole size. A systematic investigation using progressively larger explosive charges in expendable naval gun barrels was conducted. Charges supported on rigid foam and varying in weight from gram quantities in brass blocks, through 5-pound charges in 6-inch gun barrels to 240-pound charges in 16-inch gun barrels were used. The results with the 16-inch gun were in surprisingly good agreement with results on the smallest scale and the critical charge-to-hole size ratio for plastic deformation was determined to be about one to four.

A guide to the durability of gun barrels under repeated high explosive firing has also been obtained. A World War I 6-inch gun has been operated at charge-to-hole diameter ratios up to about one to five as the driver of the 180-foot conical shock tube for many hundreds of shots over a period of several years without apparent deterioration except for an occasional need to replace the seal in the breech block.

Although it did not come to our attention until after our testing program was completed, it is a matter of practical interest that around the turn of this century C. E. Bickel developed, for certain test purposes,[9] a technique that involved detonation of a high explosive in a completely closed, thick-walled cylinder. For the maximum quantity of explosive used, a cylindrical configuration would have required a 1-inch diameter charge in a 5-inch hole. Such devices were used for many thousands of firings.

PROPERTIES OF THE BLAST WAVE IN THE CONICAL SHOCK TUBE

Blast wave properties in three small-scale experimental cones have been examined by recording pressure-time histories at various points along the tube, for various charge weights. Some of the physical characteristics of these shock tubes are given in Table 1 along with the projected data on the DASACON. In each of the successive cone designs the charge weight fired was increased (Column 2) as well as amplification (Columns 3, 4), through the use of smaller cone angles (Column 5). The combined effects was to increase the quantity of charge simulated by three orders of magnitude from one cone to the next (Column 6).

For conical shock tubes covering the same range of peak pressure the weight scaling law for high explosives implies that the shock tube length must increase by an order of magnitude for each three orders of magnitude increase in the simulated quantity of high explosive. The shock tubes in these experiments did have in common a shock peak pressure of 40-30 psi at the end of the cone (with maximum charge load) and did increase in length by approximate order of magnitude steps (Column 7). Also, since positive phase duration of the blast is, to a rough approximation, a linear function of distance from the explosion, this also increased in approximately decade steps from one cone to the next (Column 8). The experimental cones are illustrated in Figures 3, 4, and 5. Figure 6 shows related pressure-time histories.

Experiments with Cone III have included a study of wave characteristics and explosive efficiency at pressure simulated altitude. The shock tube has been evacuated and operated at ambient pressures corresponding to altitudes as high as 100 kft.[12] It was found that good pressure-time histories are obtainable, as may be seen by the two records displayed at the bottom of Figure 6. However, the cone efficiency was found to drop.

From these measurements of the peak shock overpressures and positive phase durations it has been established that within the conical shock tube (1) the wave decays in a manner typical of free-air spherical explosions, (2) once an efficiency factor is established, the weight scaling law for high explosives is applicable for varying weights of charge used to drive the cone. The duration of the blast wave, however, although consistent from cone to cone, has been found to be somewhat longer than is to be expected.

From these results it was established that the design of a full-scale nuclear blast simulator could be soundly based on a direct scaleup of one-pound, TNT, peak-pressure distance data.[10] An efficiency factor of 25% (nearly that of Cone III) was assumed. Figure 7 shows the side-on shock pressure loads, calculated on this basis, that the DASACON wall would have to withstand. It is necessary, however, to apply a correction to the small end of the cone, due to the practical requirements of the charge arrangement in the firing chamber. The muzzle end of the real charge will be 68 feet closer (for a maximum load) to the gun-cone junction than an ideal spherical sector. For conservative design purposes blast pressures were determined using distances that are reduced by 68 feet.

Although boundary layer effects as such are not expected to be a disturbing factor for structures tests, secondary reflections from the shock tube wall surface adjacent to a target will need to be considered. This will require careful attention to tube diameter in relation to the target size, shape, location, and the response information that is being sought on each test.[11]

STRUCTURAL AND OPERATIONAL FEATURES OF THE FACILITY

The essential elements of the DASACON facility are illustrated in Figure 8 They consist of a recoil mass, a recoil transfer column, a detonation chamber, a conical expansion chamber, and a control center In addition, within the expansion chamber, are three areas for mounting and observing large-scale models and a 1,069-foot section which can be evacuated to simulate high-altitude pressure conditions. A rail spur and access road provide easy access to the facility and the test areas.

The detonation chamber is composed of four "retired" 16-inch naval guns forming a 186-foot 5-1/2-inch long chamber The muzzles and breeches of the guns have been modified with filler plugs and sleeves to provide a continuous 16-inch diameter tube sealed against internal pressure.

The driving charge consists of a cylindrical HE charge which could be up to 160 feet long. To load the charge, a trough is mounted at the breech end of the chamber and the muzzle is plugged with an inflatable bladder (Figure 9). The chamber is then flooded with water to a level slightly below the center of the bore. Rods of HE set on styrofoam trays are then pushed into the breech end and connected together to form a continuous charge. The water is then drained out and the trays settle slowly into position with the charge centered in the bore.

After the bladder and trough are removed, a recoil transfer column is brought into position. Its end is tapered so that it can be aligned and moved into the breech of the chamber using hydraulic jacks. It is moved far enough into the chamber to allow installation of a "foot pad" between it and the bearing plate on the recoil mass. Then the jacks are used to press it against the bearing plate to avoid "slap" when the charge is detonated. The free position of the recoil transfer column in the tube allows for the force of the explosion to be transferred directly into the recoil mass without placing any axial stress in the gun tube. An estimated 2,600,000-pound force acts for a total time of 58 milliseconds. The recoil mass is designed to resist this force with sliding friction and to have less than 1/4 inch of elastic soil deformation.

To avoid separation of the guns due to forces developed between seals and temperature effects, three 3-1/2-inch diameter pretensioned cables, connected to collars on each end of the chamber draw the guns together. The forward end of the chamber is held in a fixed position by a steel pedestal.

The expansion chamber is a conical-shaped steel tube 2,268 feet long. The diameter increases 1 foot per 100 feet. It is constructed in sections varying in length from 37 feet to 100 feet and, in diameter, from 16 inches to 24 feet. The sectional construction was adopted so that narrow, relatively easily sealed temperature expansion gaps could be used between sections, and to allow the use of any number of "fixed" positions for test models without having to provide for temperature expansion between the model mount and the wall of the tube. Sectional construction will also simplify possible future alterations for new test areas since only the individual section involved need be modified rather than the entire tube.

The walls of the expansion chamber were designed (Figure 10) for the hoop tension due to the internal pressure, the longitudinal bending due to the moving wave and the axial thrust due to the rearward unbalanced component of the internal pressure. Each section was designed to be supported on a ring stiffener at each end. The smaller end is supported on a moveable joint and the larger fixed to either a cantilever beam embedded in the foundation or an embedded anchor.

Three areas are provided for mounting and observing models. They are located at the 10, 15, and 22 foot diameter points along the cone.

Each test area was designed to withstand the anticipated pressures on a model mounted at the centerline of the section with a frontal area 1/3 that of the tube cross section. The forces on the foundation were assumed to be generated by two sources: a) a reflected pressure on a flat circular plate decaying linearly, and b) the overpressure plus the drag forces for a long cylindrical body. The force history used to design the foundations and base plate are shown in Figures 11, 12, and 13.

Each test area contains a heavy, 2-inch thick, curved, model mounting plate which forms the bottom of the section, several 8-inch ports for lighting and observation, a personnel access hatch, instrumentation conduit and a section that can be removed to provide access to the area for a fully assembled test object. The test area foundations are massive concrete structures designed to resist all forces by friction with the soil below.

A portion of the cone was designed to have a capability for simulating high altitude blast effects. Provisions were made for the introduction of two expendable mylar diaphragms mounted on removable cone sections. One diaphragm is freely suspended at the smallest part of the cone near the detonation chamber. The other, more than 1000 feet away down the cone at the 12-foot diameter section, is hemispherical and supported by a permanent steel grill. The expansion joints in the part of the cone between the diaphragms are fitted on the outside with inflatable seals. The resulting closed space, comprising a volume of 45,000 cubic feet, can be evacuated to a pressure of 8 mm of mercury or a pressure-simulated altitude of 100,000 feet in 3 hours by means of three large mechanical vacuum pumps. The test area at the 10-foot diameter section is within the evacuated region and will be used for structure studies at the simulated altitudes.

Central control for the facility will be maintained from an explosion-proof building near the 10-foot diameter section. Instrumentation can be permanently located in this building or in portable trailers located in shelter areas adjacent to each test area and monitored from the central control building. The Naval Weapons Laboratory at Dahlgren also has complete facilities for instrumenting and mounting models and for recording and reducing data.

This facility, when completed, will provide a wide variety of observations of reproducible tests, never before practical except in difficult and costly field tests using actual weapons or huge quantities of chemical high explosives.

REFERENCES

(1) Campbell, R. G., J. Appl. Phys, 29, 55 (1958)

(2) Cole, A., A Study of Cylindrical Shock Waves in a Sector Shock Tube, University of Michigan Ph.D. Thesis, 1961

(3) Filler, W. S., Phys. Fluids 3, 444 (1960)

(4) Filler, W. S., Design Characteristics of a Conical Shock Tube for the Simulation of Very Large Charge Blasts, U. S. Naval Ordnance Laboratory, White Oak, NAVORD Report 6844 (1960)

(5) Filler, W. S., NOL Model Nuclear Blast Simulator, 4th Shock Tube Symp. Proc., BRL Report 1160, 1 (1962)

(6) Moulton, J. F. Jr., Final Report of the Conical Shock Tube Advisory Committee, U. S. Naval Ordnance Laboratory, White Oak, NOLTR 61-169 (1961)

(7) Culbertson, W. D., An Investigation of the Recoil Forces Produced by Detonation of High Explosives in the 16"/45 Cal Gun, U. S. Naval Weapons Laboratory, Dahlgren, Virginia, Technical Memo T-3/62, (1962)

(8) Balcerzak, M. J., American Machine and Foundry Company Tech. Note MR 1208, (Aug. 1962)

(9) Bichel, C. E., New Methods of Testing Explosives, Trans. A. Larsen, Charles Griffin and Co., Ltd., London (1905)

(10) Explosion Effects Data Sheets, U. S. Naval Ordnance Laboratory, White Oak, NAVORD Report 2986, (1955)

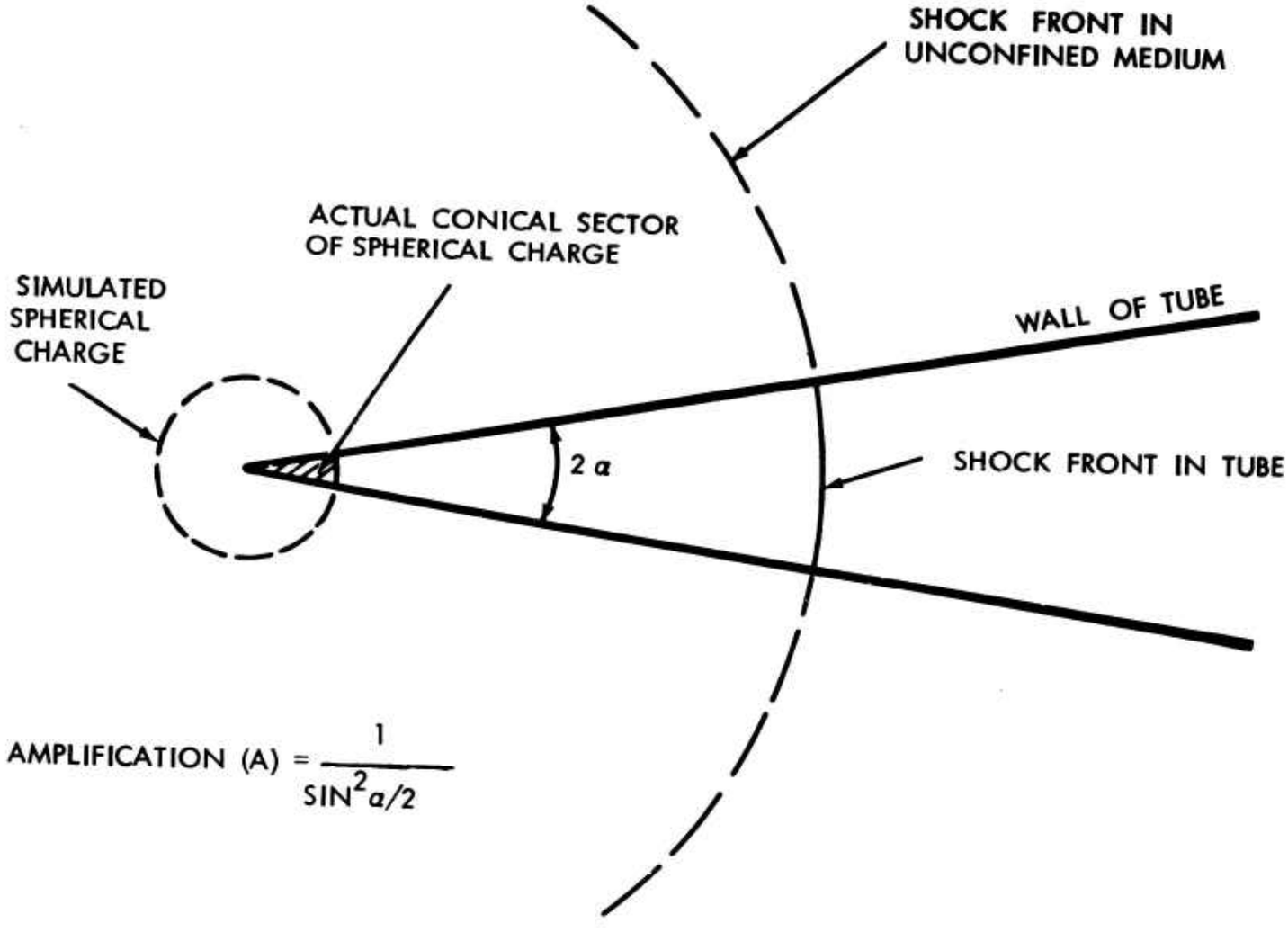
(11) Blockage Effects and Dimensions of a Conical Shock Tube for Model Tests on Naval Structures, David Taylor Model Basin, Washington, D. C., Tech. Note SML-740-2, (1961)

(12) Anderson, T. O., Simulation of Airblast at Altitude in a Conical Shock Tube, U. S. Naval Ordnance Laboratory, White Oak, NOLTR 64-112, (to be published)

TABLE 1. SUMMARY OF SPECIFICATIONS AND TEST RESULTS FOR ALL CONICAL SHOCK TUBES IN THIS PROGRAM

1. Cone	2. Charge Wt Fired (Max) (lbs)	3. Amplification Ideal	4. Amplification Real	5. Plane Angle (degrees)	6. Charge Wt Simulated (lbs)	7. Overall Length* (ft)	8. Max Positive Duration (msec)	9. Efficiency (%)
I	0.001	110	60	22°	0.06	3.75	0.5	55
II	0.015	10,000	3,000	2°	45	18	3.5	33
III	5.0	129,600	30,000	0.637°	150,000	225	40	23
IV	1,000	160,000	40,000**	0.571°	40,000,000**	2400	450**	25**

* From cone apex
** Estimated



$$\text{AMPLIFICATION (A)} = \frac{1}{\text{SIN}^2 \alpha/2}$$

FIG.1 EXPLOSIVE AMPLIFICATION EFFECT IN A CONICAL SHOCK TUBE

TEST	CHARGE WEIGHT LBS.(1)	CHARGE LENGTH IN.(1)	$\bar{P}$ PSIG	t_1 MS	t_d MS	$\int_{t_o}^{t_d} P\,dt$ PSI - MS	$\Delta S/\Delta T$ max IN/SEC	F max LBS	t_s MS	t_F MS
1	75.32	103.49	7800	2.9 ± 0.25	23	57,900	12.0 ± 2.5	0.570×10^6	36	34.5
2	151.05	207.02	9000	6.0 ± 0.5	36	112,000	24.0 ± 2.5	2.09×10^6	26	23
3	247.82	340.00	$\frac{9500^{(2)}}{12,000^{(3)}}$	9.5 ± 0.25	76	$\frac{182,100^{(2)}}{208,400^{(3)}}$	39.0 ± 2.5	3.80×10^6	25	23.5

DATA SYMBOLS ARE DEFINED AS FOLLOWS:

NOTES:
(1) DOES NOT INCLUDE BOOSTER
(2) EXPANDING TUBE PRESSURE CELL
(3) DIAPHRAGM PRESSURE CELL

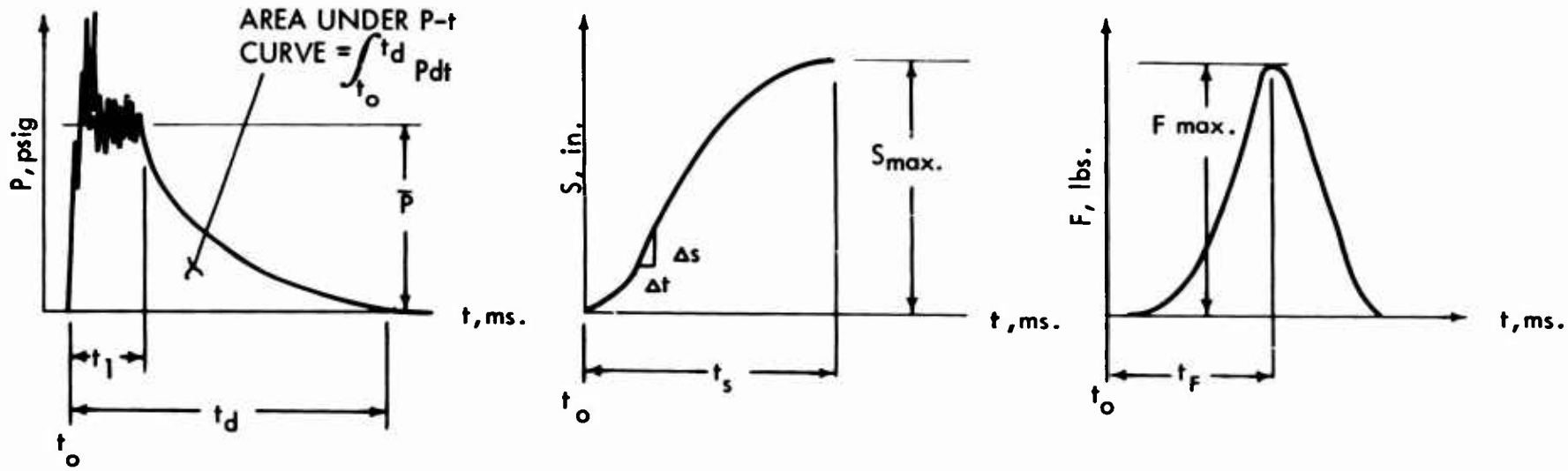
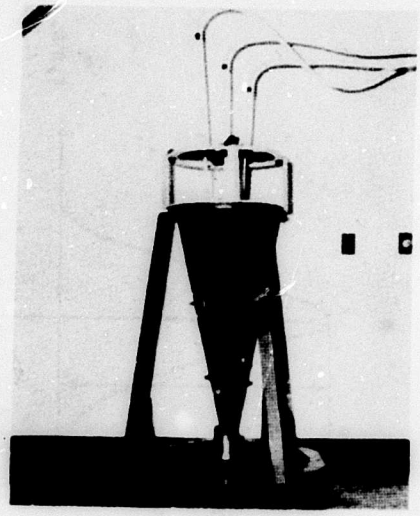
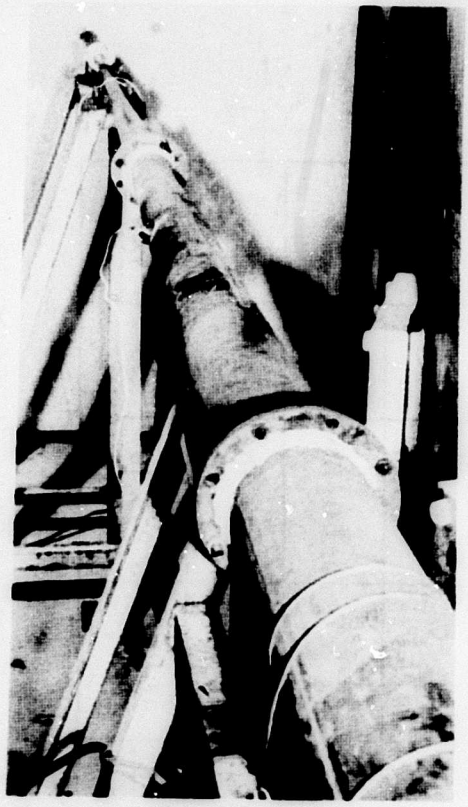


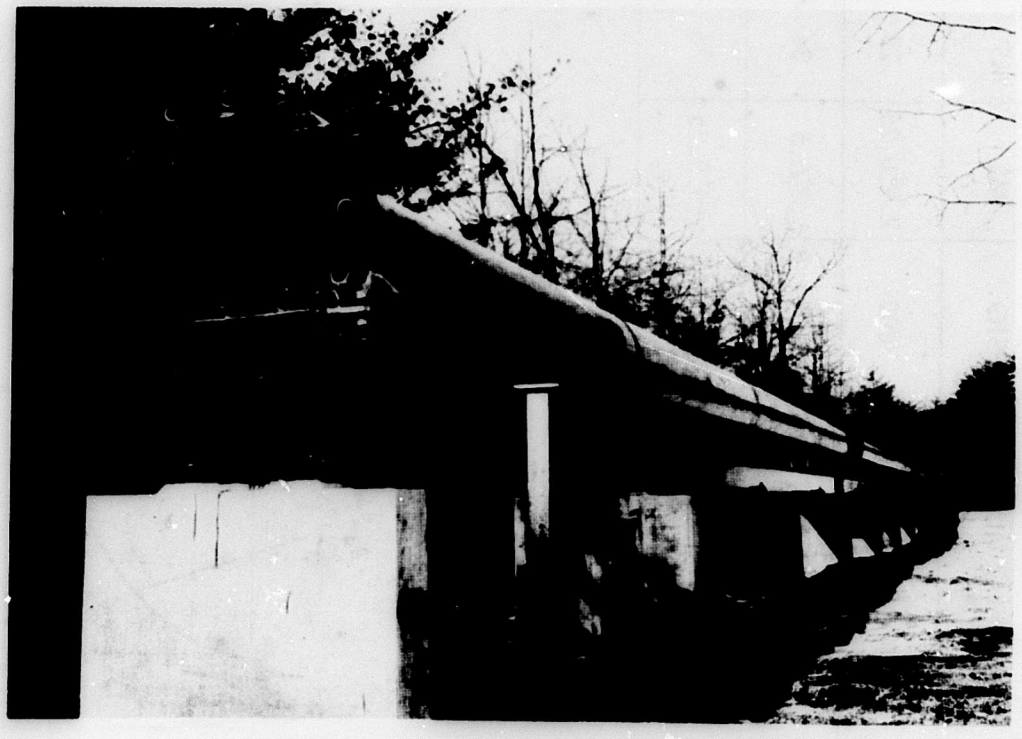
FIG. 2 SUMMARY OF TEST DATA FOR FIRING CHAMBER (FROM REF.7)



CONE I

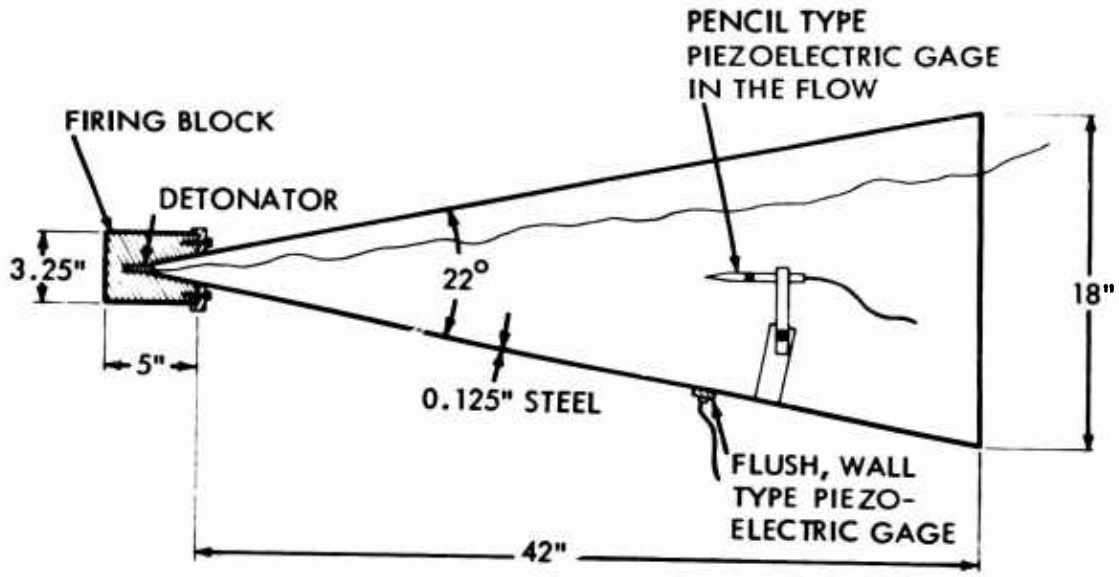


CONE II

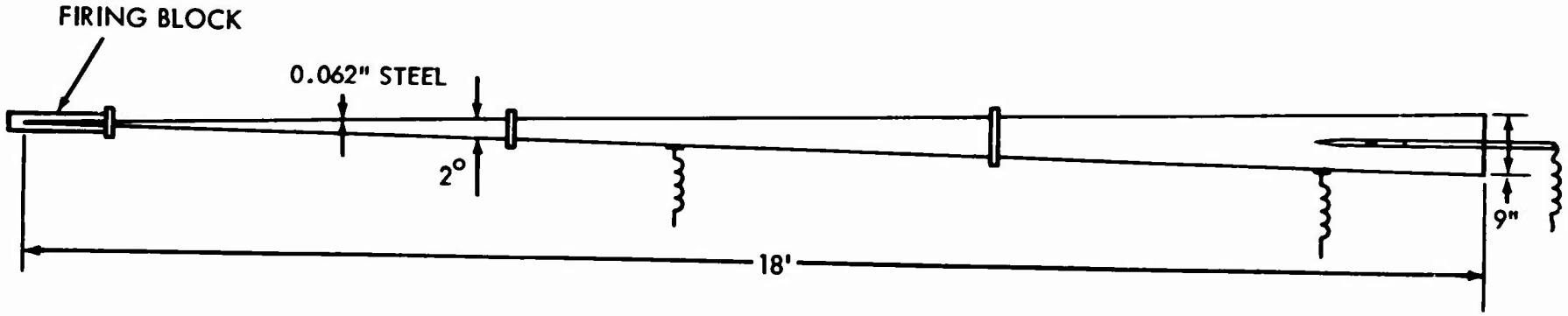


CONE III

FIG. 3 PHOTOS OF EXPERIMENTAL CONES (FOR CHARACTERISTICS SEE TABLE 1.)

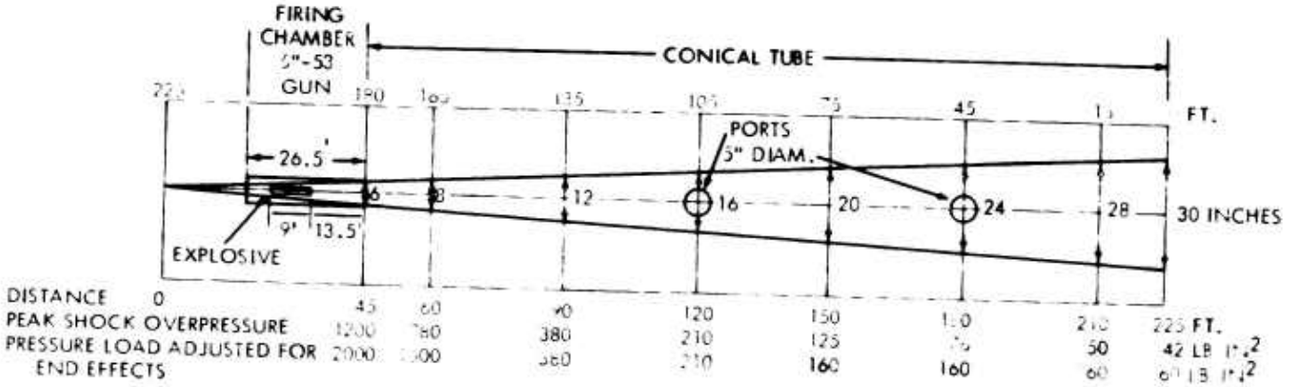


CONE I



CONE II

FIG.4 DIAGRAMS OF CONES I & II



DESIGN DATA SKETCH

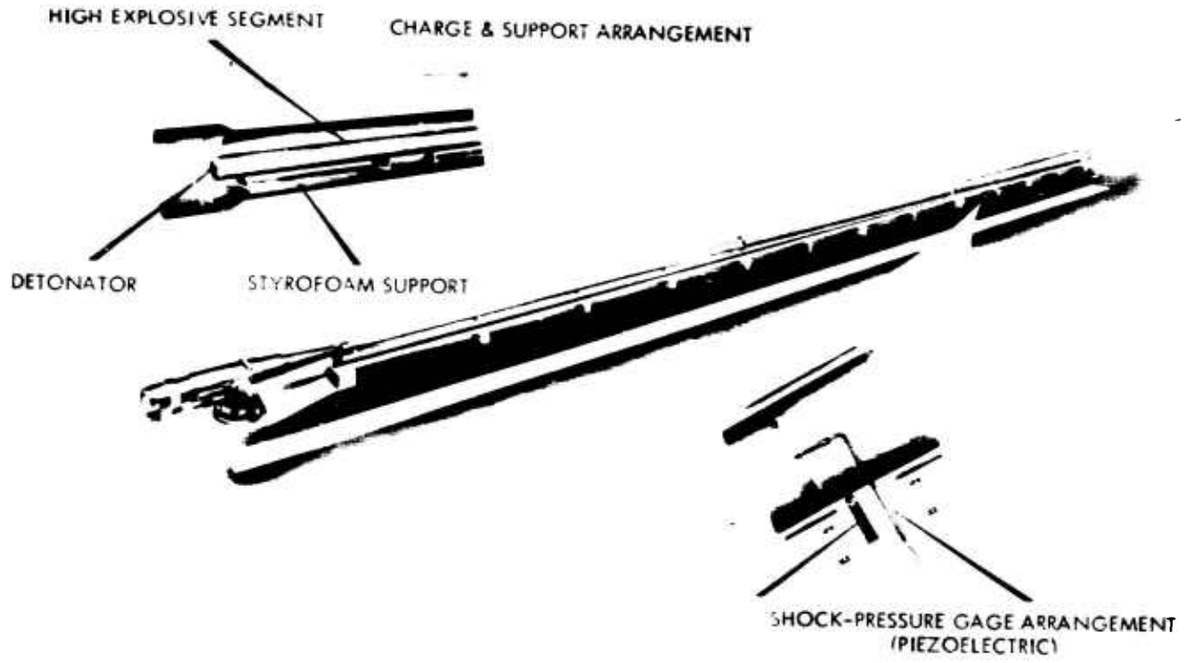


FIG. 3 DIAGRAMS OF CONE III

CONE	DISTANCE (FT)	PEAK SHOCK OVER PRESSURE (PSI)	POSITIVE DURATION (MSEC)
		LOW PRESSURE	
I	2.0	35.0	0.5
II	16.0	40.0	3.5
III	180.0	27.1	42.3
		HIGH PRESSURE	
II	8.0	200.0	1.5
III	120.0	246.5	15.1
		SIMULATED ALTITUDE	
III	40K FT 93.5	18.7	27.0
III	80K FT 93.5	5.8	20.0

NOTE: TIME BASES VARY

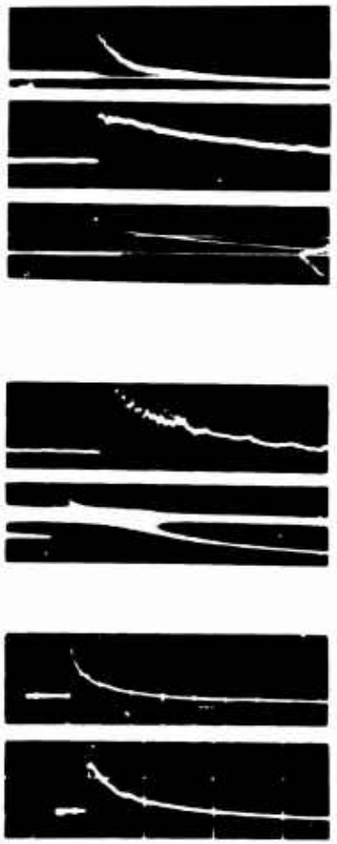


FIG.6 TYPICAL PRESSURE-TIME RECORDS FROM EXPERIMENTAL CONES

DISTANCE FROM APEX (FT)	0	133	200	300	400	500	600	800	1000	1200	1400	1500	1600	1700	1800	1900	2000	2100	2200	2300	2400	2600
DIAMETER (FT)	0	1.33	2		4		6	8	10	12	14		16		18		20		22		24	26
20-KT BLAST PRESSURE (LB/IN^2); WITH END CORRECTION		2575 5320	1680 2600	1030	690 900	480 610	350 430	195 240	118 138	72	48	41	34.5	30	26.5	23.8	21	18.8	17.2	15.6	14.3	12.2
DURATION OF POSITIVE PHASE (MSEC)									~200			~300							~450			

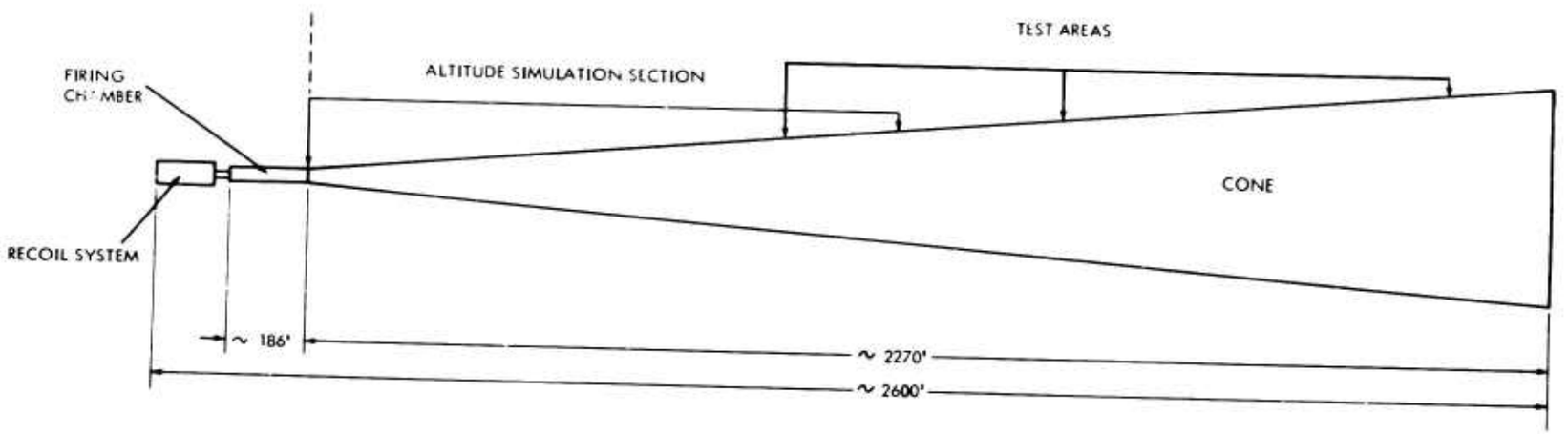


FIG.7 DESIGN PRESSURE DATA AND GENERAL ARRANGEMENT DIAGRAM FOR NUCLEAR BLAST SIMULATOR (DASACON)

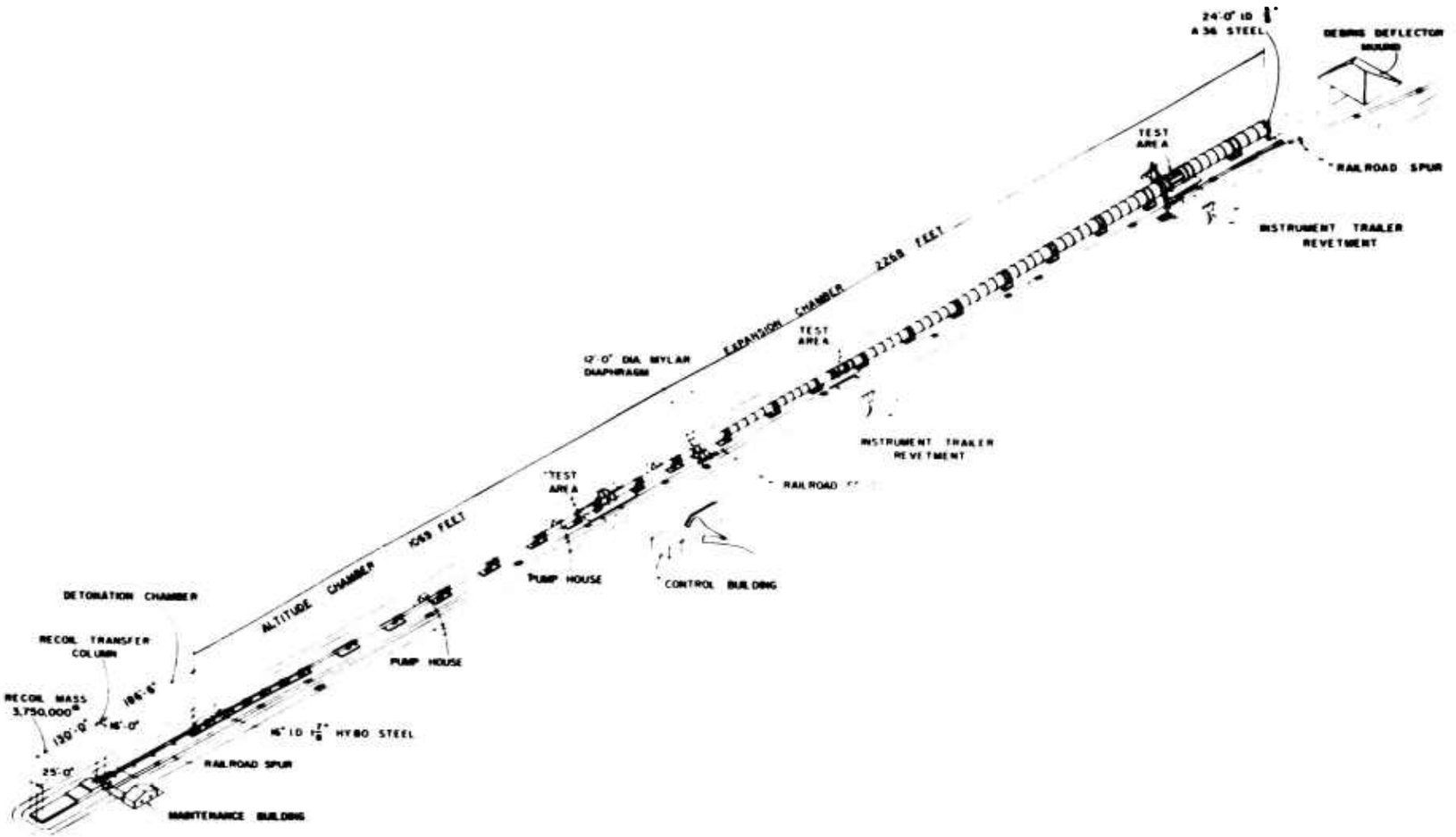


FIG.8 GENERAL ARRANGEMENT OF DASACON FACILITY

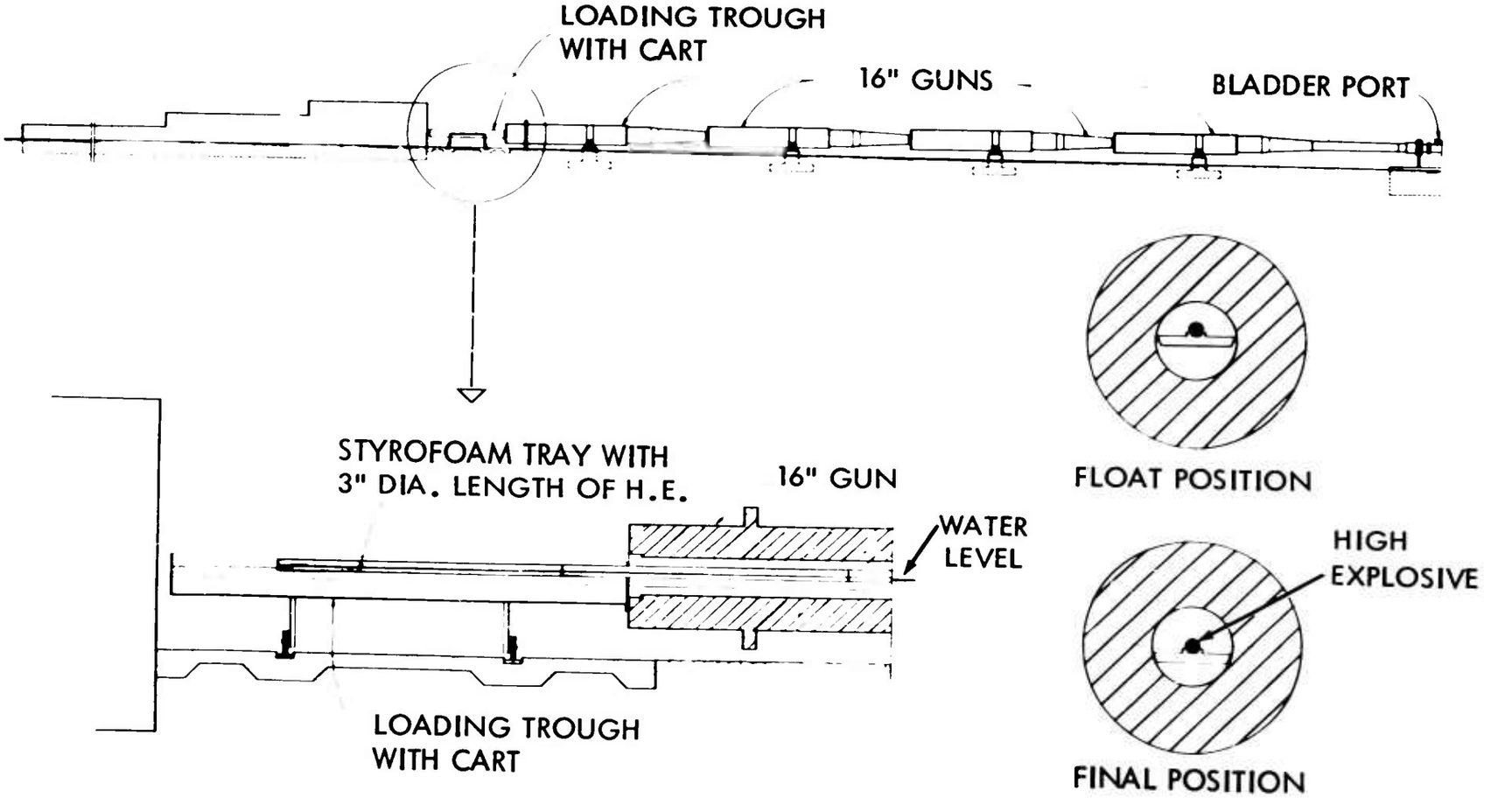


FIG.9 FIRING CHAMBER — LOADING METHOD

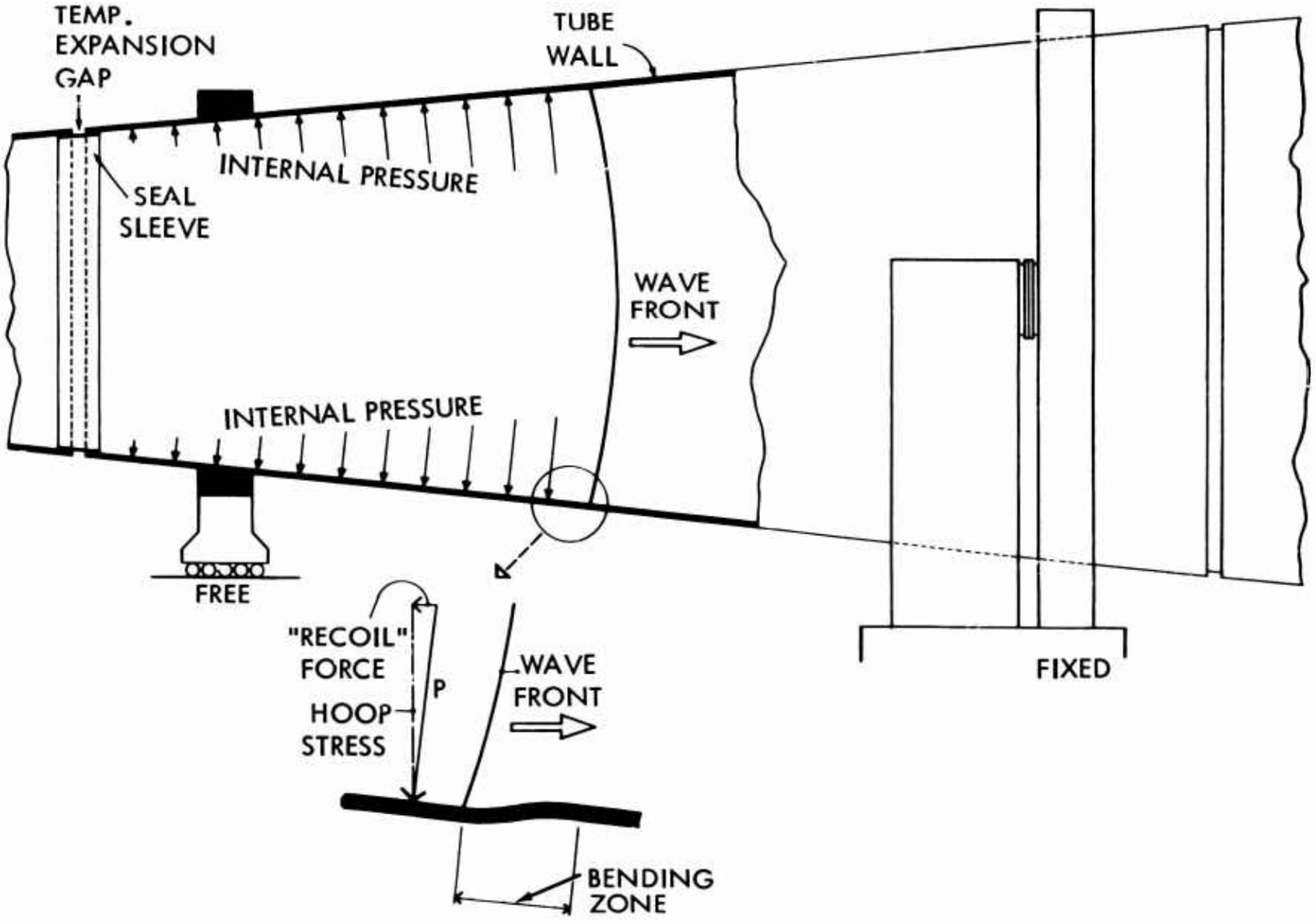


FIG. 10 DESIGN ELEMENTS OF A CONE SECTION

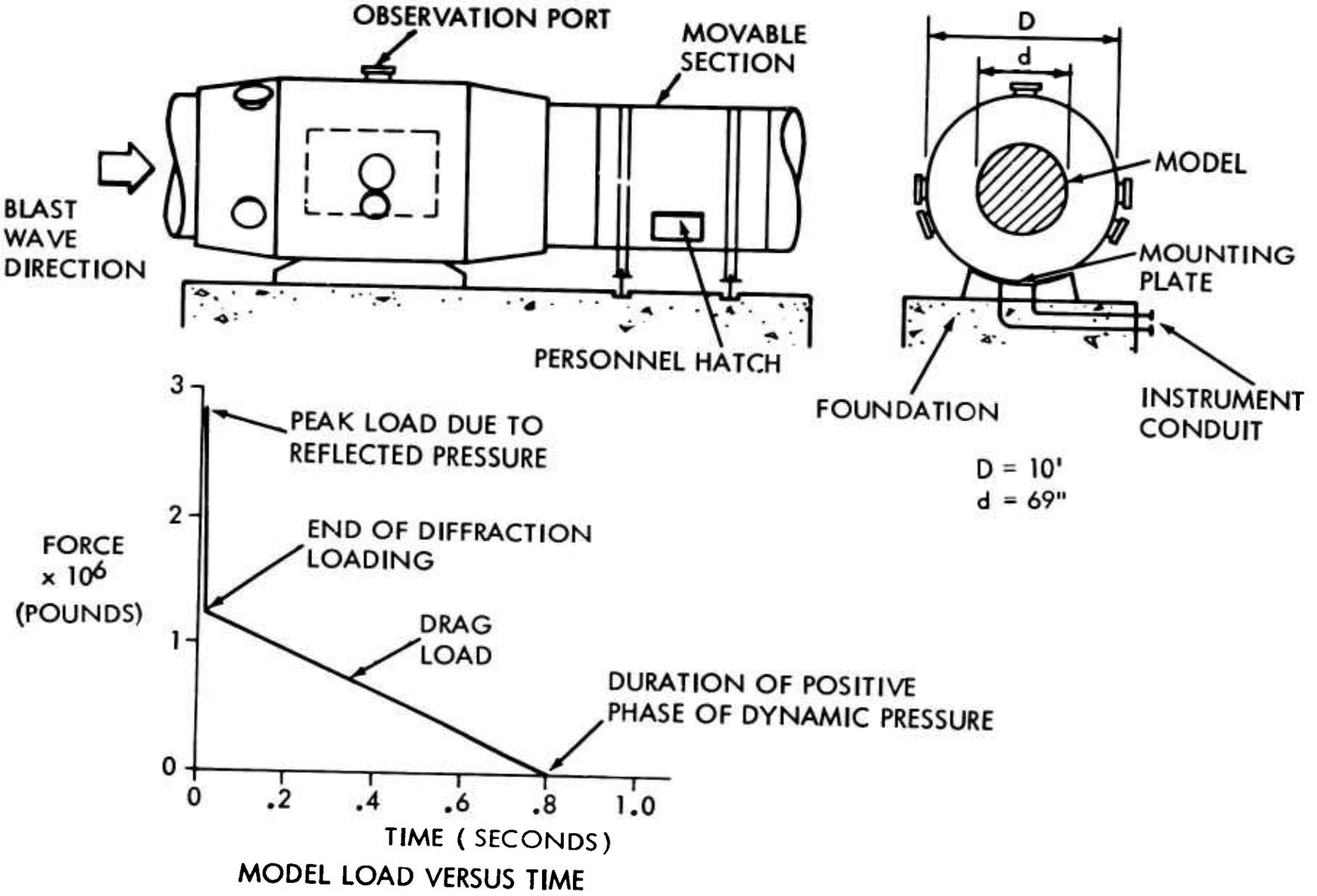


FIG. 11 TEST AREA NO. 1

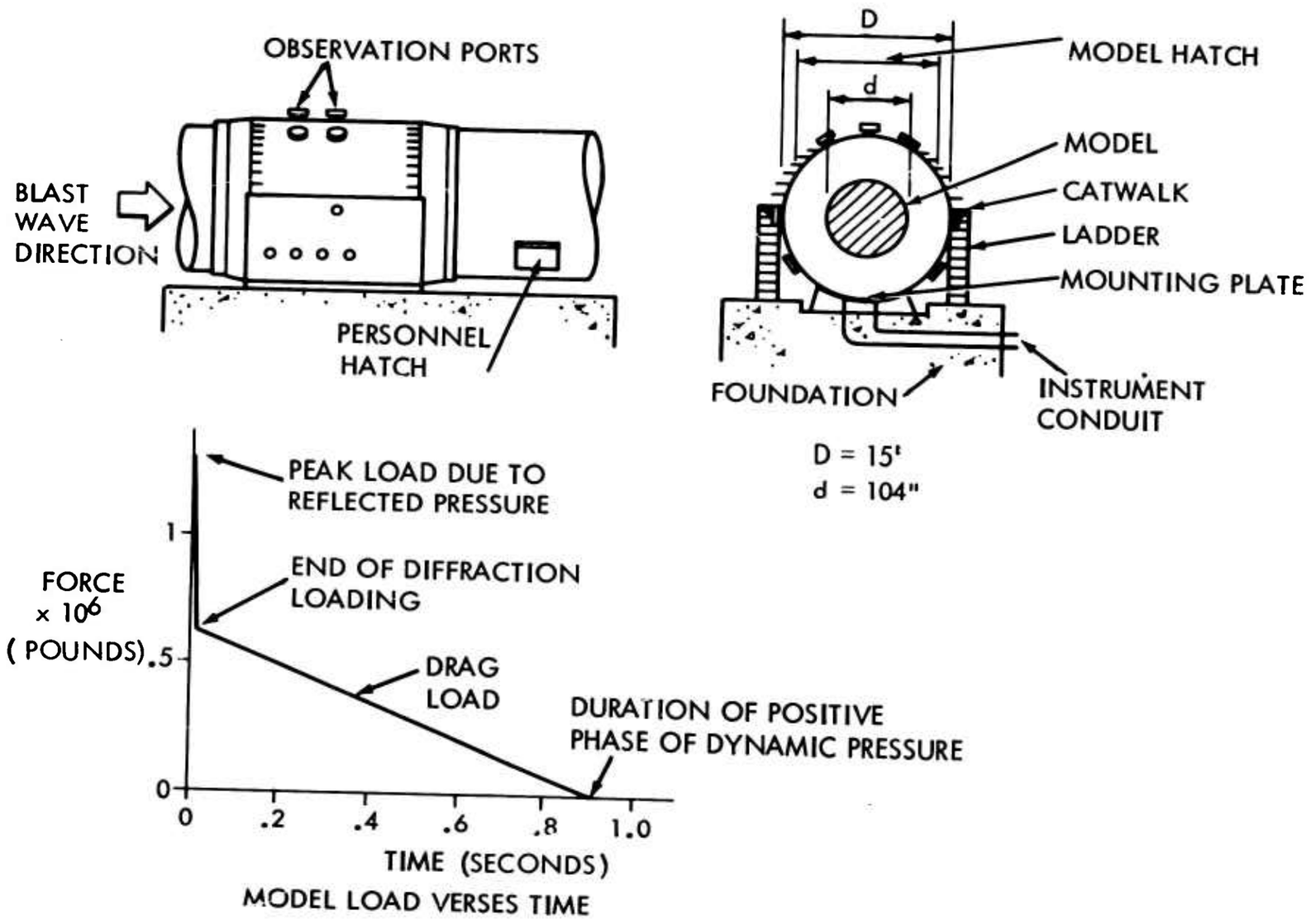


FIG. 12 TEST AREA NO. 2

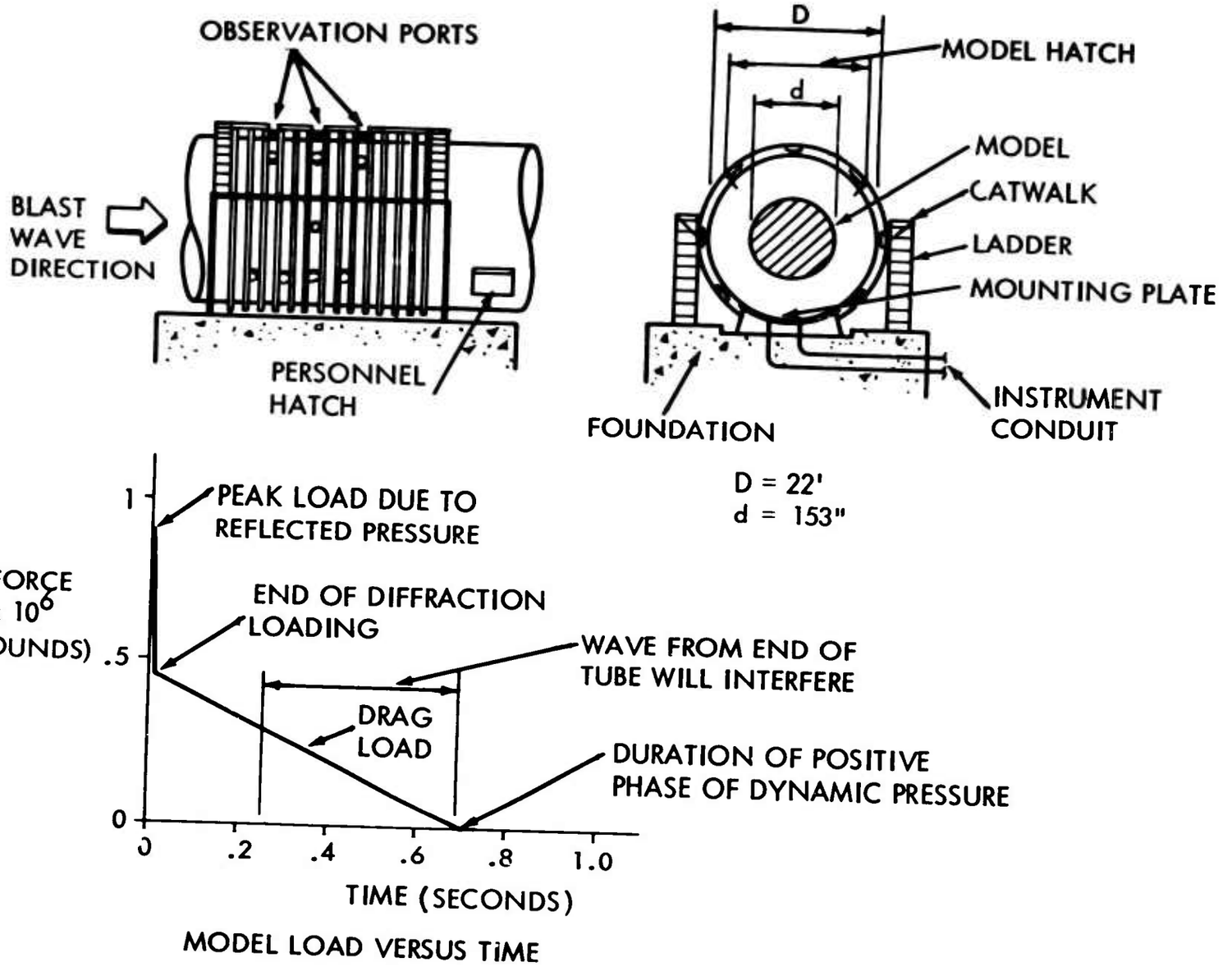


FIG. 13 TEST AREA NC . 3

THE EQUAL PRESSURE SHOCK TUBE

H. Reichenbach
Ernst-Mach-Institut der Fraunhofer-Gesellschaft
Freiburg/Br., Germany

When test objects are exposed to blast waves of long duration, numerous new problems arise. For experimental investigation of these problems one often uses blast wave simulators. Of particular interest are those simulators for which the duration of the pressure load on the test object can be adjusted independent of the generated peak pressure because the dynamic load not only depends on the peak pressure but also on the duration of the pressure pulse. Therefore, practical as well as scientific considerations require the development of simulators which could be used under various conditions.

To investigate especially the stability of slab-shaped test objects in our laboratory two blast wave simulators have been developed. We call these "shock pressure chamber" and "equal pressure shock tube," respectively. In the following I want to explain the principle of the equal pressure shock tube and to give some examples of its application.

Essentially the blast-wave simulator consists of a well known conventional diaphragm shock tube. In Figure 1 such a shock tube is shown schematically and the development of the wave fronts is represented in an x - t diagram. At the endplate of the expansion section the pressure profile is such as indicated in a simplified manner at the right side of the diagram. If the test object is placed at the location of the endplate, it is exposed to a pressure load with an infinitely steep wave front. The pressure load stays constant for a certain time which depends on the dimensions of the shock tube. But it is obvious that the various waves are reflected several times. At the location of the test object the pressure profile, as shown in Figure 1, is therefore repeated more or less periodically until the waves are died away by friction effects. After that a constant pressure is established throughout the whole length of the shock tube. This pressure is designated by P_e, the equalizing pressure.

A shock tube which works in the above described manner is by no means suitable as a shock wave simulator. Instead, we want to get a pressure-time profile in form of a step function with an infinitely steep pressure rise and a constant peak pressure of unlimited duration. This can be realized indeed in a good approximation by two modifications:

1) by observing the so-called equal pressure condition, after which the shock wave simulator was denominated

2) by inserting a mechanical device into the shock tube in order to damp the wave reflections.

The equal pressure condition is explained in the lower part of Figure 1. We postulate that the pressure after reflection, p_5, and the static equalizing pressure, p_e, are equal. What conclusions can be drawn from this?

The relations developed from ideal shock tube theory are given in Figure 2. The pressure ratio P_{51} of the reflected wave depends on the initial pressure ratio P_{41} only. The formula given here is that for the normal reflection of a shock wave with the shock strength P_{21}. If, initially, both sections of the shock tube are filled with the same gas of equal temperature, P_{21} depends on the pressure ratio p_4/p_1 in the implicit way given here.

Neglecting the energy exchange with the walls of the shock tube the energy equation states that the static equalizing pressure P_{e1} depends not only on the pressure ratio P_{41} but also on the volume ratio V_4/V_1 of the pressure section to the expansion section. For a shock tube with constant cross-section the ratio of the volumes can be replaced by the ratio of the length of the two sections, l_4/l_1.

From this it follows that the pressure after reflection P_{51} is determined only by P_{41} and therefore can be chosen at will. The condition of equal pressure can always be realized by an appropriate choice of the ratio l_4/l_1; therefore, for a given pressure p_5 a particular ratio l_4/l_1 is necessary.

When applying the above described procedure, the end-pressure p_5 at the test object can be kept constant for an unlimited time. The variation of pressure, however, caused by the repeatedly reflected waves is still present. Damping of these reflections will be the next task.

By inserting baffles into the pressure section an efficient attenuation takes place. The principle of this device is illustrated in Figure 3 where only one baffle is shown. When arriving at the location of the baffle, each wave is partly reflected and partly transmitted. It is obvious that several baffles, spaced along the tube, increase the number of reflections considerably. This means that the pressure is equalized very rapidly throughout the whole length of the shock tube. An example

is given in Figure 4 where two original registration curves of the pressure profiles taken at the endplate of the expansion section are represented. In both cases the condition of equal pressure was realized. One curve describes the case where no baffles are inserted into the tube; the other curve shows the results for an arrangement of five baffles which reduce the cross-section of the tube 30% to 50%, respectively. It can be seen that, by the insertion of the baffles, the almost periodic variation of pressure can be suppressed to a large extent. Furthermore, the pressure profile of the wave has nearly the ideal form of a step function. A plane test object located at the endplate of the simulator is exposed therefore to a quasi-static pressure load of unlimited duration.

If a pressure decay behind the shock front is desired, this can be realized by providing openings of variable cross-section in the walls of the expansion section. An example is given in Figure 5 where a closed tube is compared with a tube which is equipped with openings. The upper registration curve represents an ideal step function, whereas the lower curve shows an exponential decrease.

The prototype of such a shock tube, with a length of 5 m and a diameter of 15 cm, has been replaced now by a tube with a diameter of 1 m and a length of 30 m. Figure 6 shows the experimental set-up. The shock tube consists of several sections of 1 m and 2 m length, respectively. This construction makes it possible to set the diaphragm - mostly a deep drawing sheet - at any desired location of the shock tube, thus keeping the condition of equal pressure for various peak pressures. Figure 7 shows the working range of the blast wave simulator. The ordinates represent the length of the various sections. Since the admissible overpressure of the compression section is 25 atm. (about 360 psi) the maximum overpressure after reflection at the location of the test object is 12 atm. (about 170 psi), as computed from shock wave theory. To fulfill the condition of equal pressure this maximum pressure after reflection has to be related to a particular ratio of the length of the compression and the expansion section. Therefore, the line for a pressure at 12 atm. represents the limit of the working range of the simulator. A second limit is given by the condition that the blast wave has to travel about 10 times the diameter of the shock tube in order to develop a sufficiently steep shock front. As shown in the diagram a minimum length of 7.5 times the tube diameter has been chosen. The third limit is determined by the total length of the shock tube which at the present time is 28 m.

The working range then lies within the triangle which is marked by thick lines. From this one notes that the condition of equal pressure can be realized for a reflection overpressure ranging between 4 and 12 atm. (about 60-170 psi). Lower pressures require a greater total length of the shock tube; higher pressures are attainable only through a higher initial pressure in the compression section.

A few remarks about the current and planned experiments may be added. First of all, it may be said that the shock wave simulator has a broad

field of application. The equal-pressure shock tube can be used for the investigation of slab-shaped test objects exposed to a quasi-static wave load. As test objects slabs of various structure, doors, etc., can be used in full size or on a reduced scale.

Of course, other test objects can be investigated too. Several big valves, as installed in shelters, have been tested already.

Another problem to be investigated is the behavior of filters with coarse-grained sand as filter material which are going to be installed in German shelters. Such a filter is shown in Figure 8. At the bottom the test section of the shock tube has a rectangular opening where the filter to be investigated is attached.

To avoid the disturbance of the flow field a smooth transition has been made between the circular cross-section of the shock tube and the rectangular cross-section of the filter.

For the investigation of the effect of shock waves on various soil specimen a similar experimental set-up is in preparation (Fig. 9). For this purpose an iron case can be attached to the shock tube in the same way as it was described for the filter. The case is lifted to the rectangular opening at the bottom of the shock tube, thus providing an air-tight seal between the case and the shock tube.

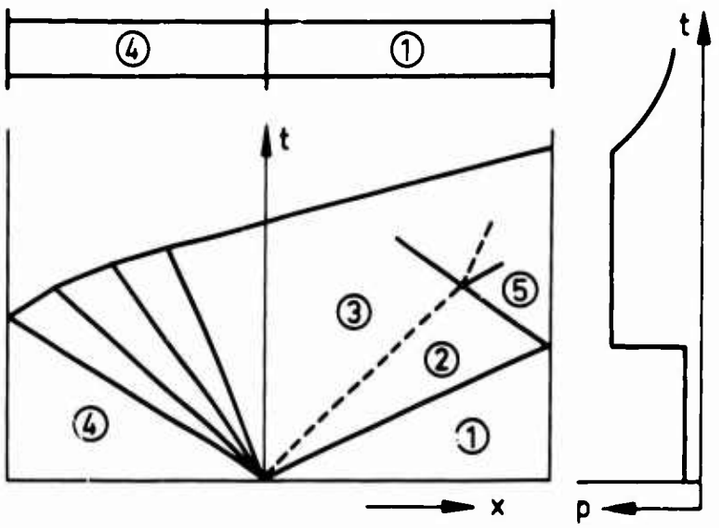
Furthermore an optical test section with a field of view of 80 cm x 60 cm (about 32 ft by 24 ft) can be attached to the shock tube as shown in Figure 10.

A short tube section of rectangular cross-section is inserted into the shock tube. This tube is provided with very sharp edges, thus cutting out a part of the incident shock wave which propagates into the test section where the observation windows are mounted parallel to the walls.

The scope of optical observations can be the same as in shock tubes of smaller diameter. The advantage of a big optical test section is that test objects of very different model scale can be investigated.

This information should give an idea about the diversity of the operating conditions of the equal-pressure shock tube and about the variety of its applications.

Wellendiagramm Wave diagram



Gleichdruckbedingung Equal-pressure condition

$$p_5 = p_e$$

p_e = statischer Ausgleichsdruck im Rohr
static pressure after equalization
in the tube

Figure 1

Gleichdruckbedingung Equal pressure condition

$$P_{51} = \frac{p_5}{p_1} = \frac{(3\gamma-1)P_{21} - (\gamma-1)}{(\gamma-1)P_{21} + (\gamma+1)} = f_1(P_{41})$$

$$\frac{p_1}{p_4} = \frac{1}{P_{21}}\left[1 - \frac{\gamma-1}{\gamma}(P_{21}-1)\sqrt{\frac{2\gamma}{(\gamma+1)P_{21}+(\gamma-1)}}\right]^{\frac{2\gamma}{\gamma-1}}$$

$$P_{e1} = \frac{p_e}{p_1} = \frac{1 + P_{41}\frac{v_4}{v_1}}{1 + \frac{v_4}{v_1}} = \frac{1 + P_{41}\cdot\frac{l_4}{l_1}}{1 + \frac{l_4}{l_1}} = f_2\left(P_{41}; \frac{l_4}{l_1}\right)$$

$$\boxed{P_{51} = f_1(P_{41}) \overset{!}{=} f_2\left(P_{41}\frac{l_4}{l_1}\right) = P_{e1}}$$

Figure 2

Wellendiagramm	wave diagram
eine Blende	one baffle

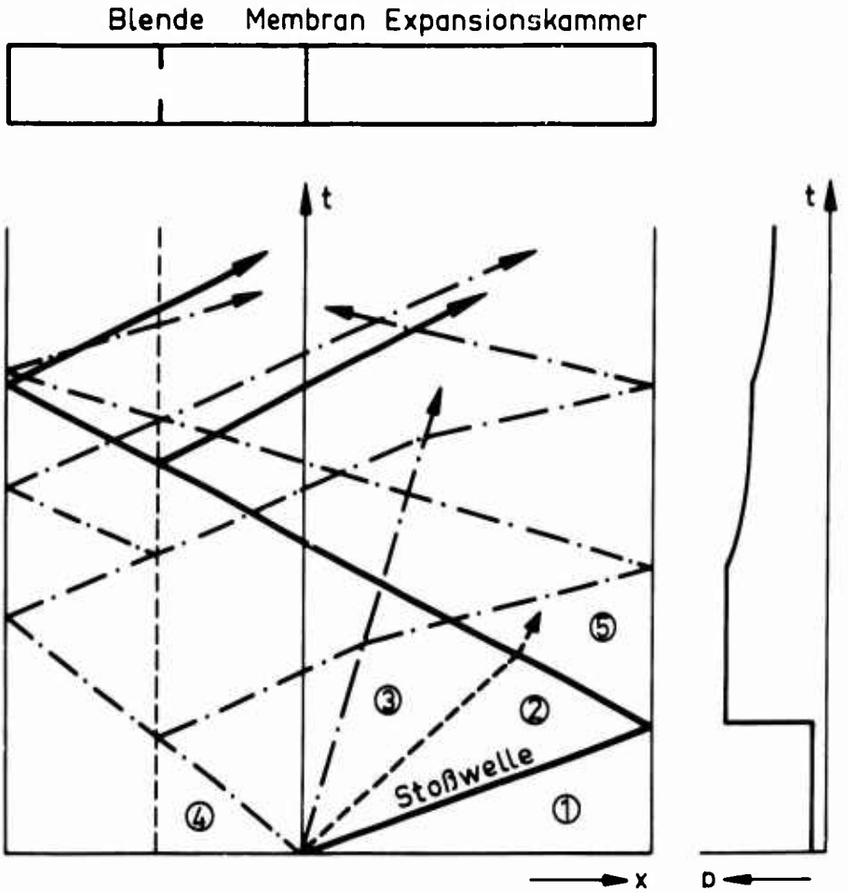


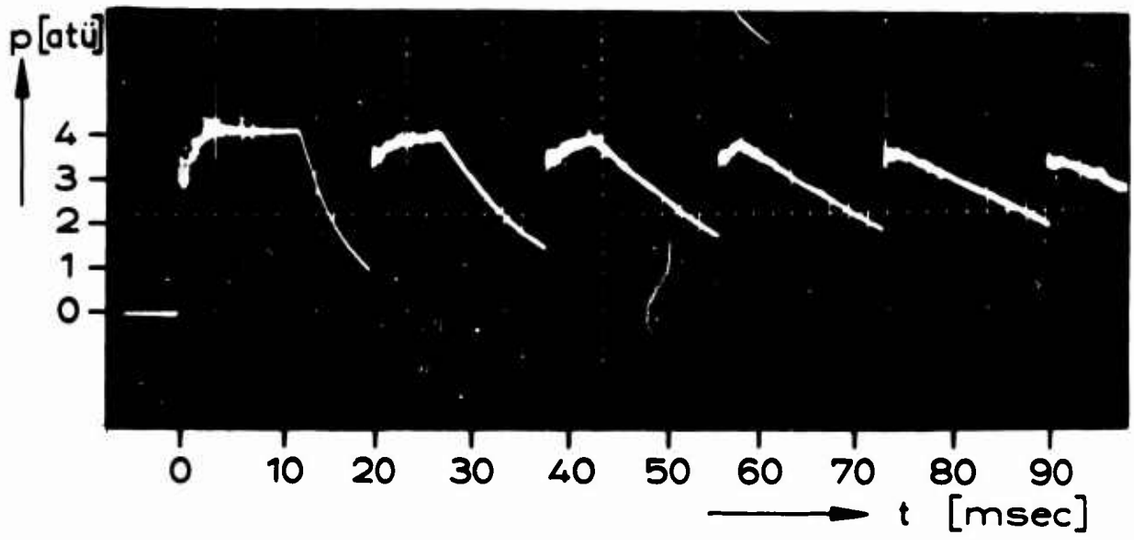
Figure 3

Gleichdruckstoßwellenrohr

Druck–Zeit-Verlauf am Ort des Testobjekts

Reflexionsdruck: 4,1 atü
Zeitablenkung: 10 msec/cm

a) ohne Blenden



b) mit 5 Blenden

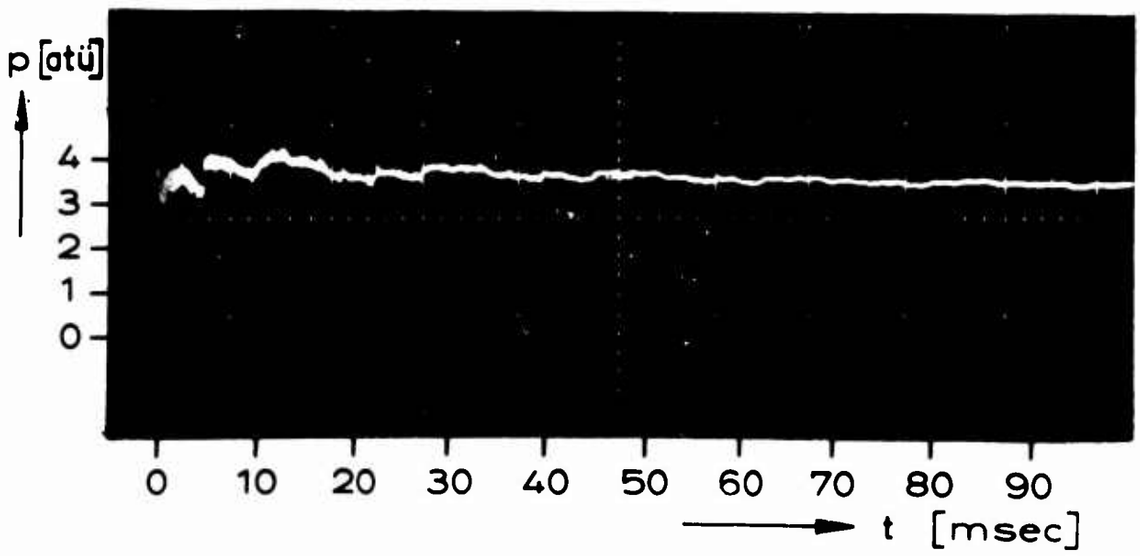


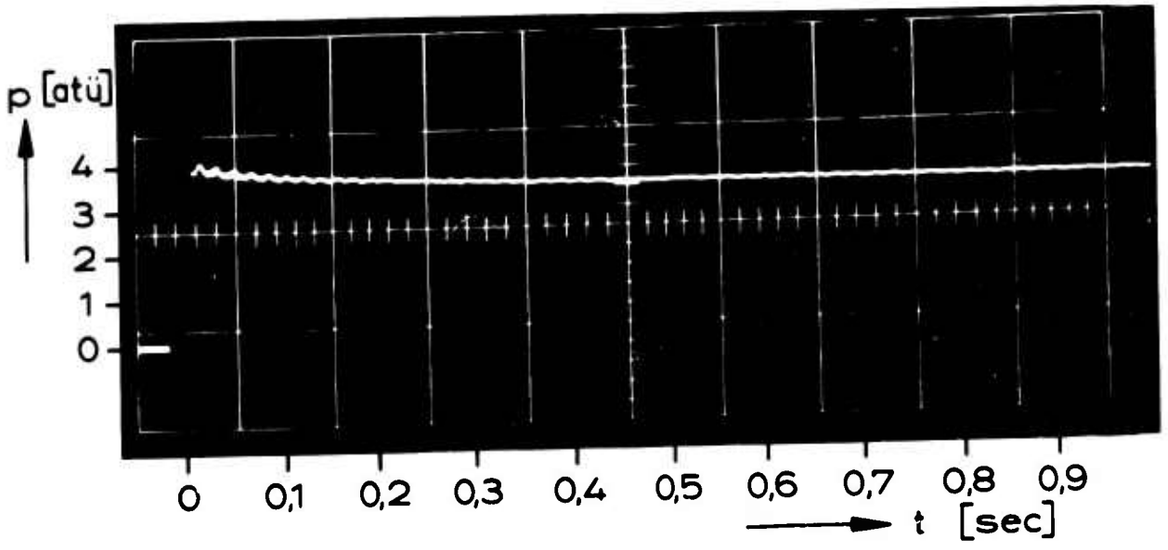
Figure 4

Gleichdruckstoßwellenrohr

Druck-Zeit-Verlauf am Ort des Testobjekts

Reflexionsdruck: 4,1 atü
Zeitablenkung: 100 msec/cm

a) Ausströmöffnung geschlossen



b) Ausströmöffnung offen

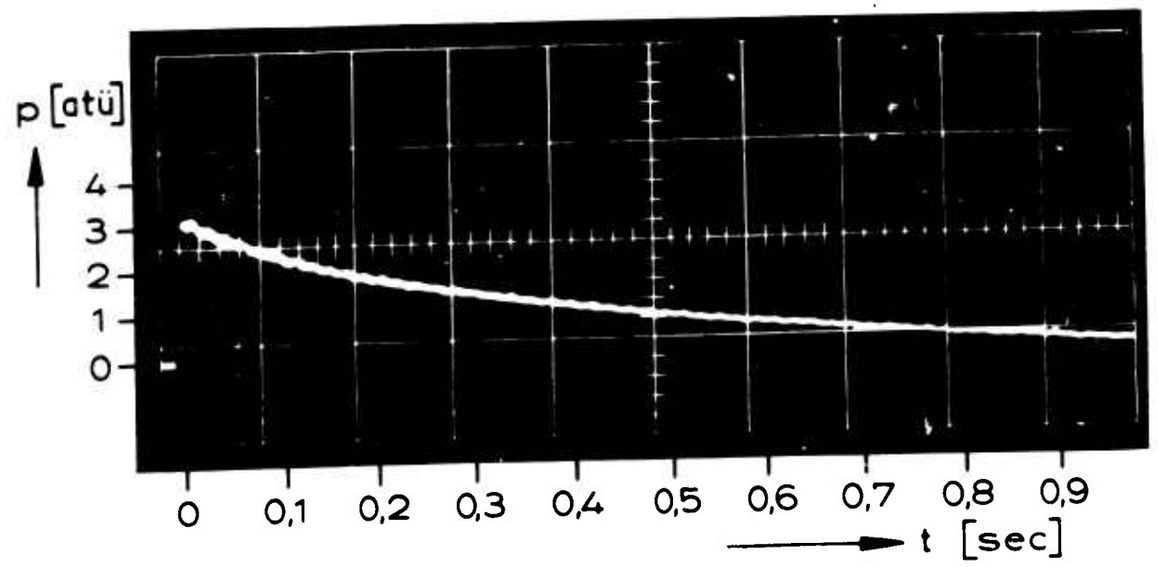


Figure 5

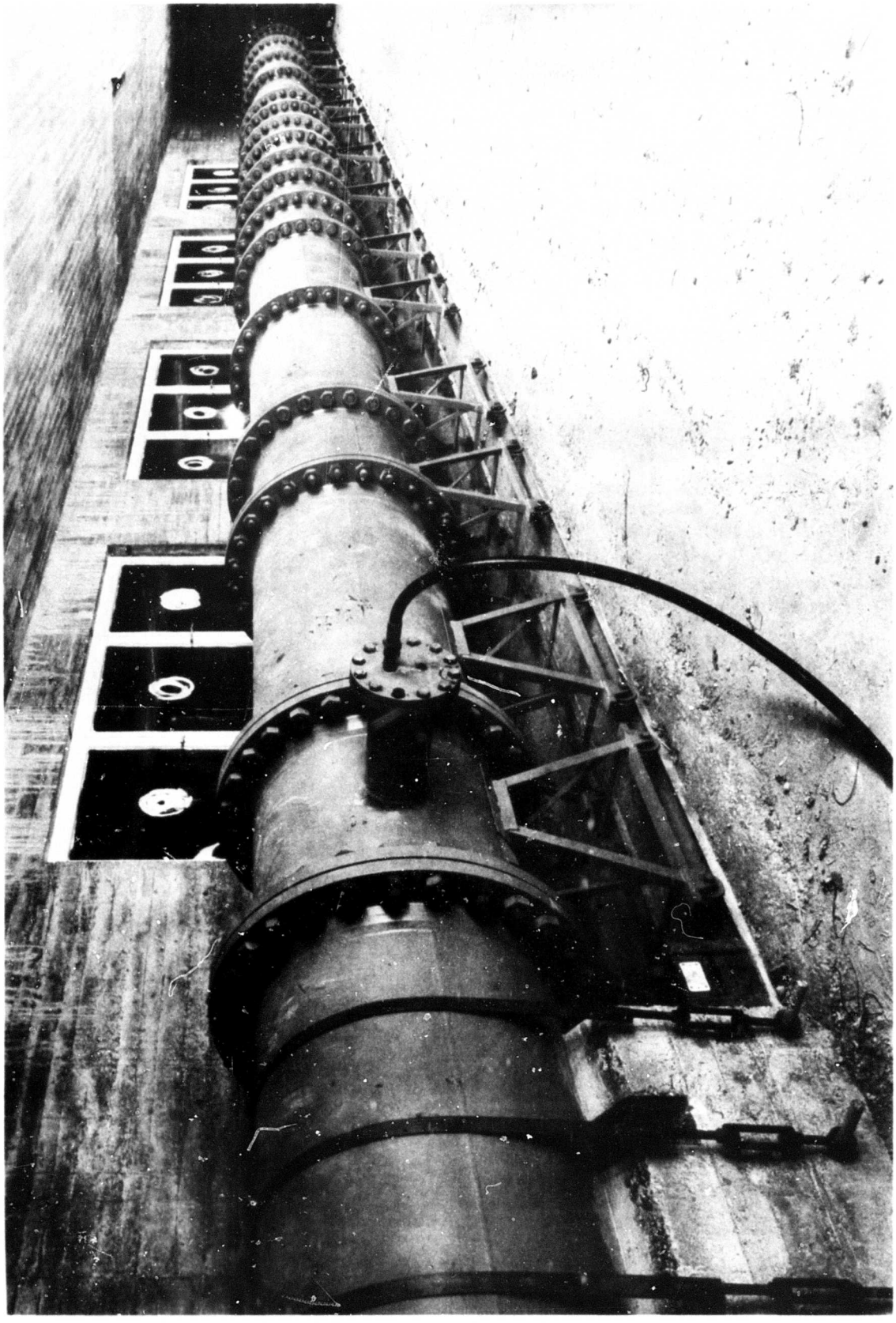
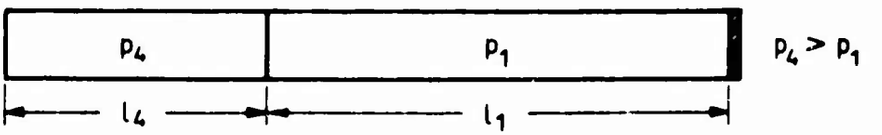


Figure 6

Arbeitsbereich des Gleichdruckstoßwellenrohres



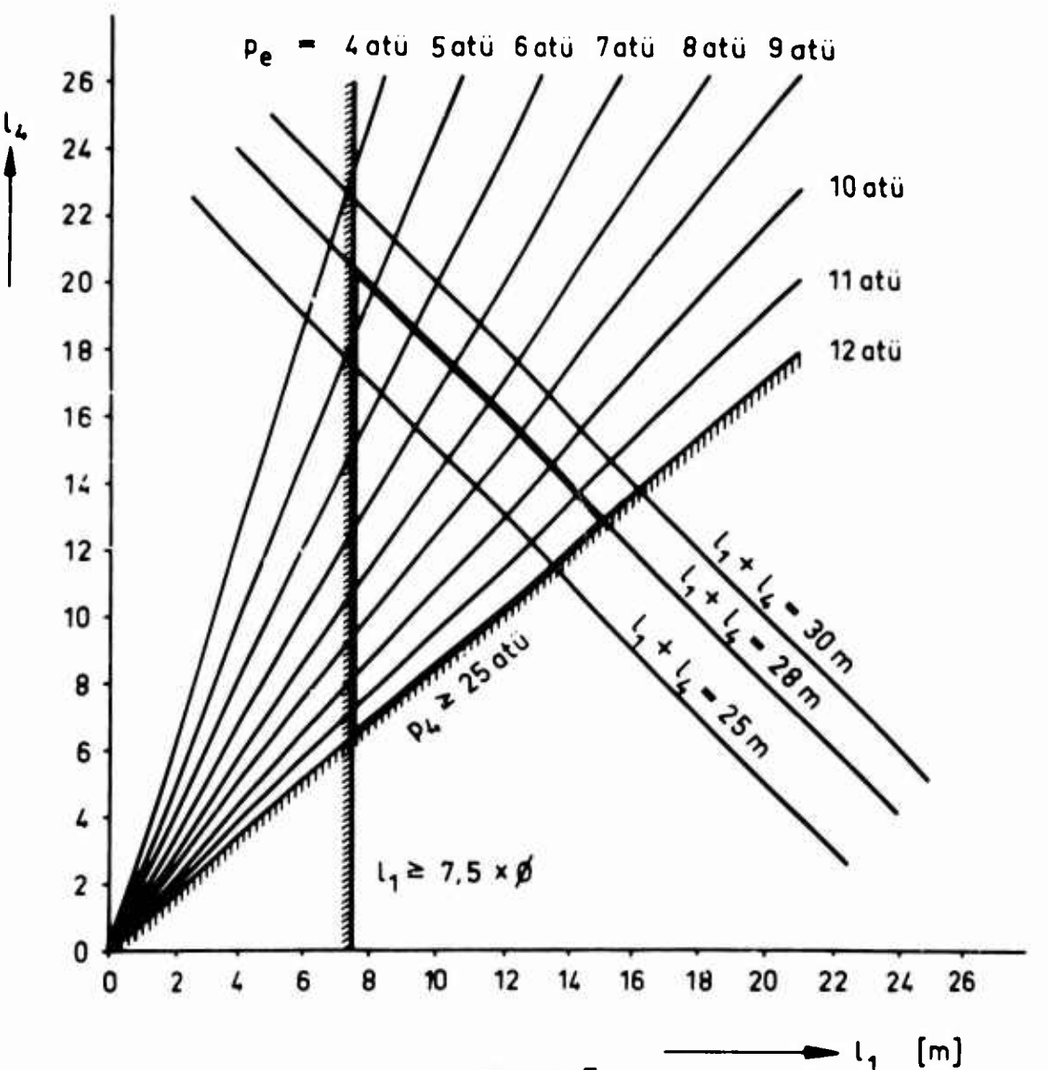


Figure 7

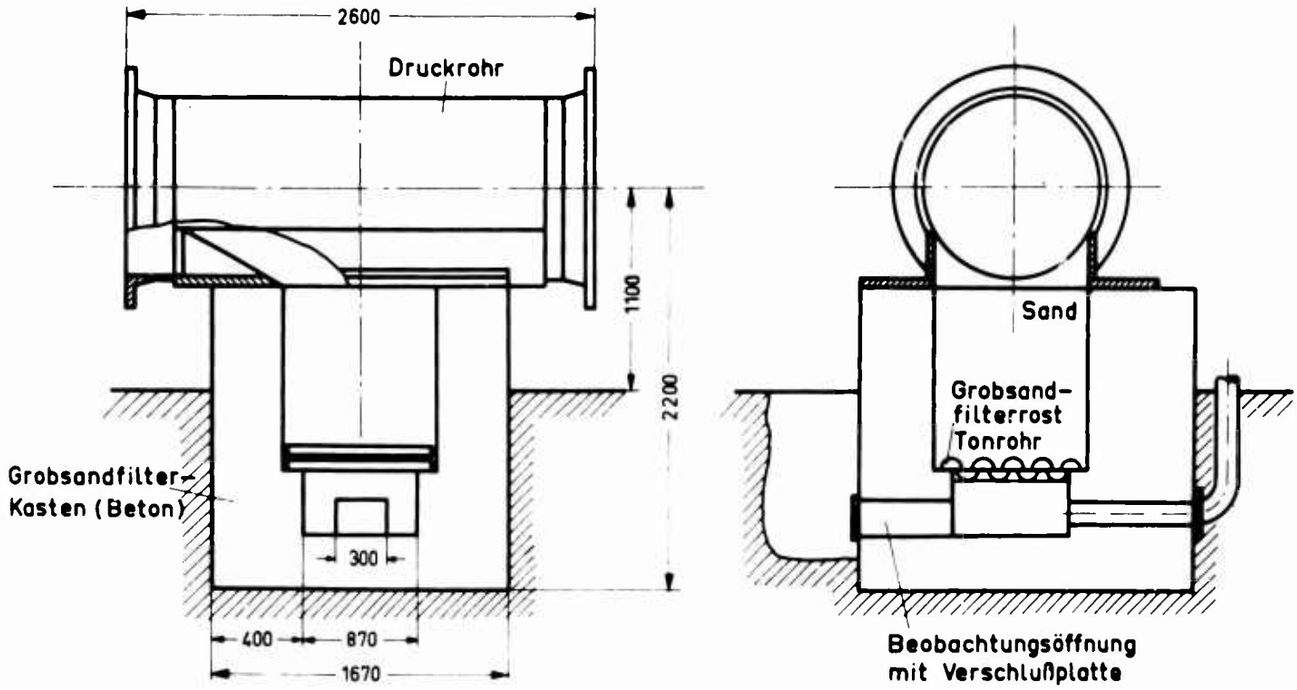


Figure 8

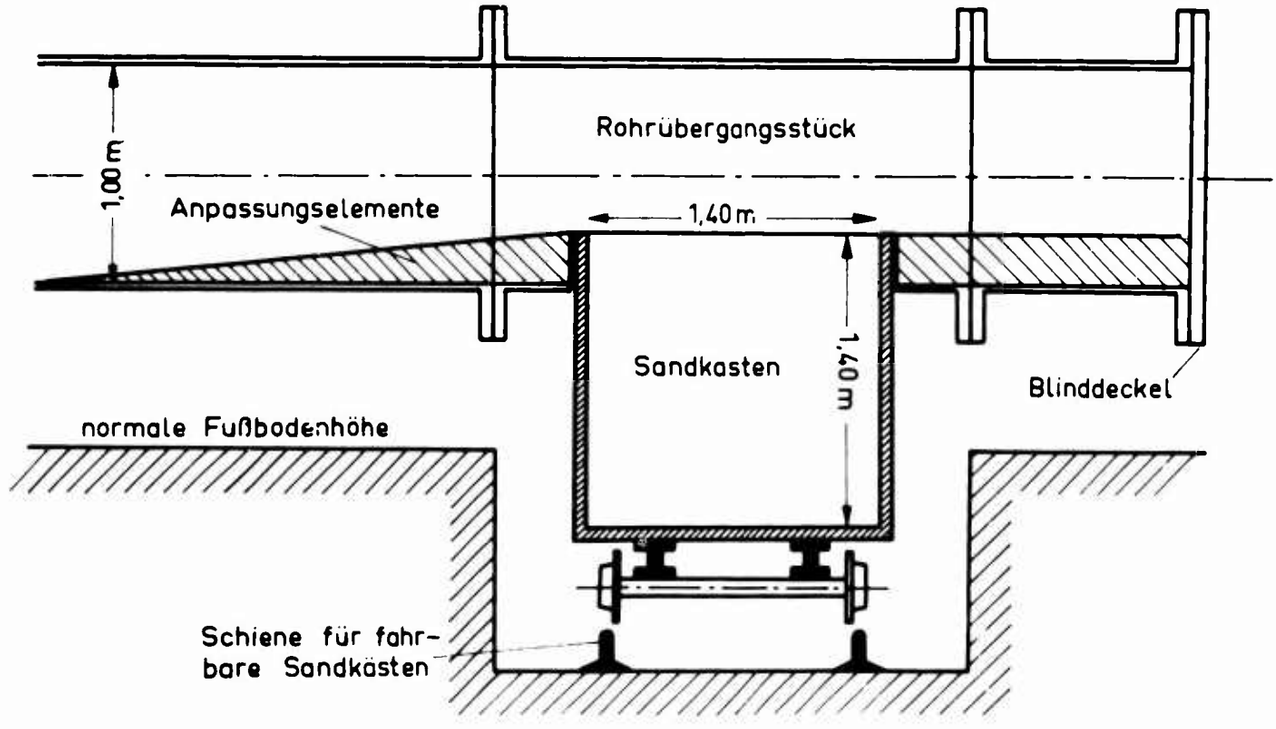


Figure 9

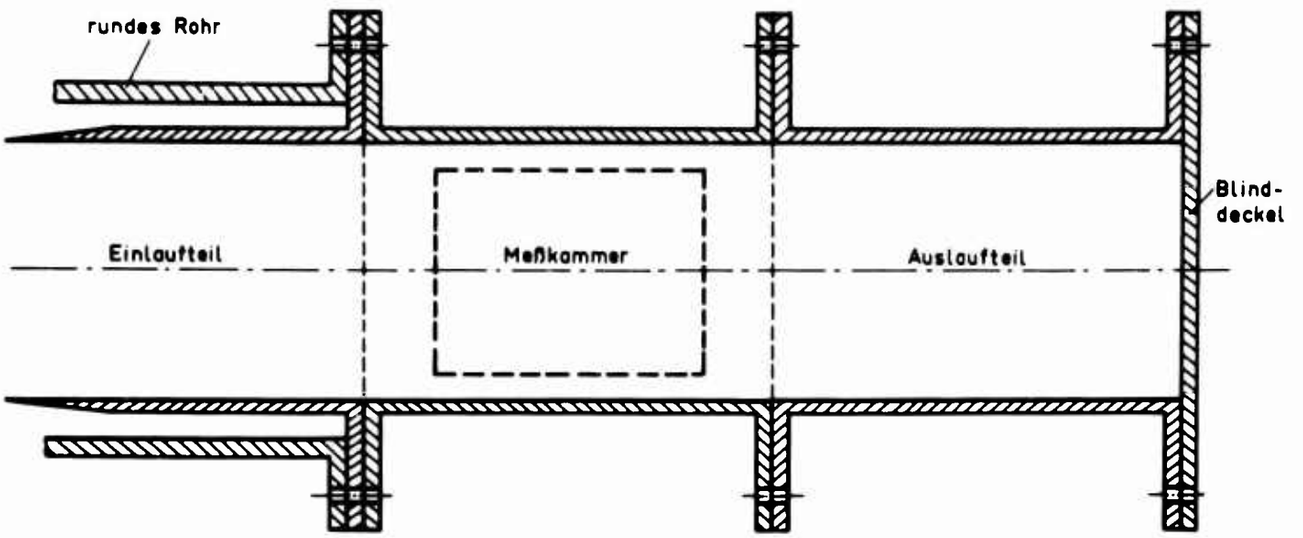

rundes Rohr
Einlaufteil
Meßkammer
Auslaufteil
Blind-
deckel

Figure 10a

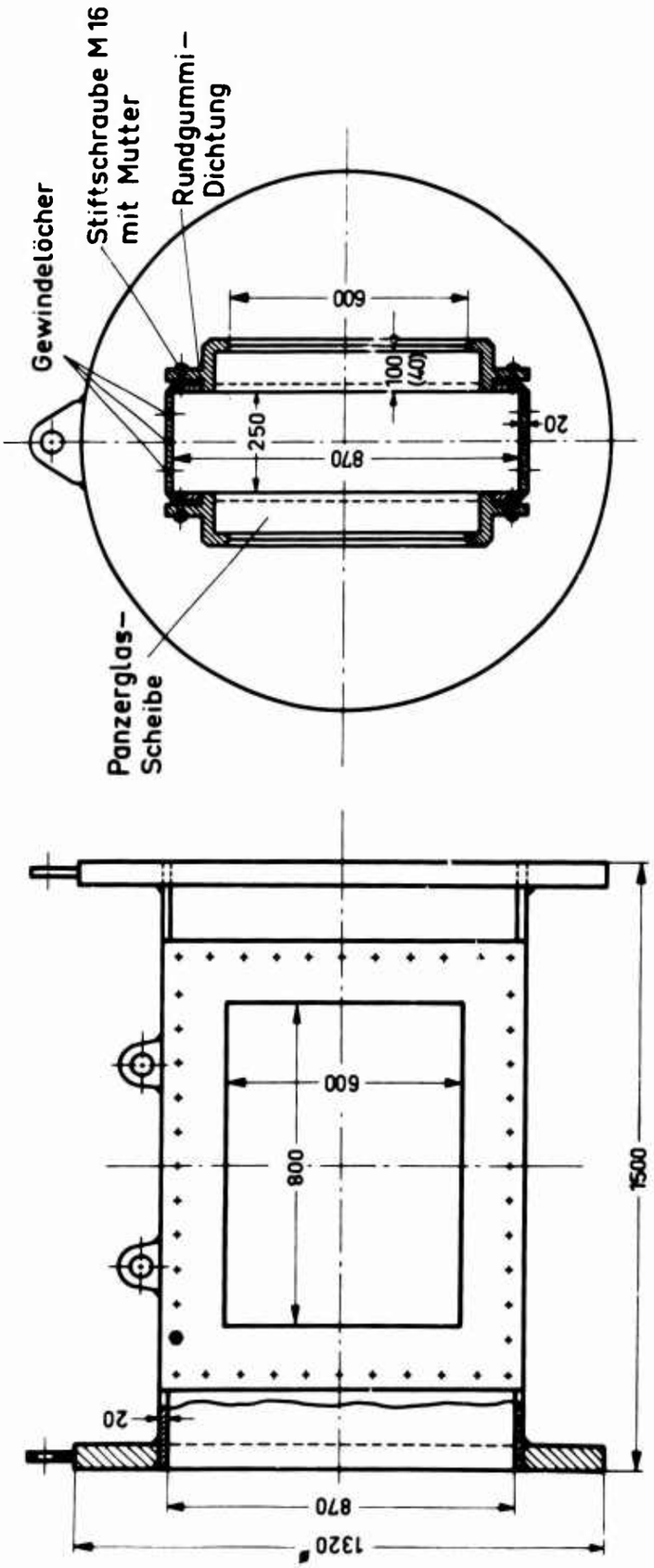

Gewindelöcher
Stiftschraube M 16
mit Mutter
Rundgummi-
Dichtung
600
100
(97)
20
250
870
Panzerglas-
Scheibe
600
800
1500
20
870
1320

Figure 10b

NOTE ON REFLECTED SHOCK CONDITIONS IN A SINGLE-PULSE TUBE*

H. B. Palmer, E. T. McHale+, and G. P. Starkey
Department of Fuel Technology, The Pennsylvania State University, University Park,

INTRODUCTION

The single-pulse (or "chemical") shock tube has become a rather commonly used tool for measuring the rates of chemical reactions that may be difficult to study by other methods. With the exception of comparative rate studies of the type performed by Tsang (1), it is necessary for the analysis of experimental data to have either a direct measure of the temperature-time history of the gas in the reflected shock, or else to have a means of calculating it accurately from measurements of other properties of the shock.

Because of the difficulty of measuring temperatures, the usual practice has been to assume that shock reflection is ideal. One-dimensional ideal relations are then used to calculate the reflected shock properties from the initial conditions plus the measured velocity of the incident shock. The pressure-time history is also measured and employed to determine the effective reaction time. When the pressure in the reflected shock is found to rise with time (as frequently happens) before quenching, it is possible to complete the corresponding temperature history if one assumes that the compression is isentropic (2).

The main uncertainty in this procedure, at least for purposes of chemical kinetics, has been the assumption of ideal reflection, and this has been the subject of extensive discussions as well as a number of experiments. We attempt a summary of these at a later point, after presenting our measurements and calculations. The data to be presented were taken during and after a study of the thermal decomposition of hydrazine (3) at temperatures between about 950°K and 1120°K and pressures between about 2 atm and 9 atm. The hydrazine was diluted about 100-fold with argon.

*Work supported by the Army Research Office-Durham
+Present address: Atlantic Research Corp., Alexandria, Va.

This particular kinetic study illustrates rather well the importance of understanding the behavior of reflected shocks, especially with respect to the non-ideality of temperature. In Reference (3), we have analyzed the probable decomposition mechanism by comparing our kinetic data with other shock tube results (4) obtained at somewhat higher temperatures. If the temperatures in either or both of these studies were in systematic error by, say, 30°K, the mechanistic arguments might have to be discarded. Therefore we have carried out measurements on reflected shocks, both in pure Ar and in dilute N_2H_4-Ar mixtures, in an effort to assess the accuracy of our reported temperatures. The work is similar to some reported several years ago by Skinner (5). The data consist primarily of velocities and pressure-time histories.

EXPERIMENTS, OBSERVATIONS, AND CALCULATIONS

The shock tube was of conventional single-pulse design (6), having a 6-foot driver and a 12-foot low-pressure section, both of 3 inch i.d. stainless steel. The dump tank had a volume of about 300 liters. Diaphragms were of Ethocel sheet. The endplate was 1/4-inch steel, pulled down hard against the end of the tube and sealed either with O-rings or with a bonded Al gasket.

Oscilloscope triggering and recording of arrival times of shocks at four stations along the tube were achieved by means of BD-25 piezoelectric transducers (Atlantic Research Corp.). The detailed pressure record of the reflected shock was provided by a Kistler PZ-6S piezoelectric transducer (later replaced with a Kistler 601A) that, together with the PT-6 amplifier-calibrator, had been calibrated at the factory and checked in the laboratory. Mounting positions for the transducer were available in the endplate and at positions 10.5 cm and 20.5 cm from the endplate. The data reported here were all obtained from the endplate and 10.5-cm positions. A few records from the 20.5-cm position were obtained merely to see if they were broadly consistent with the observations at the other two positions (they were). Sample records from these positions appear in Fig. 1. On these, smoothing of the noise and/or ringing permits measurement of pressures with an estimated uncertainty of ±0.5 psi.

Incident shock velocities were measurable with a precision of about ±0.5 per cent. Comparisons of pressure records with ideal reflection behavior were based upon velocities at the endplate, obtained by extrapolation. The incident shock typically attenuated at about 1 per cent per meter.

41 measurements were made of the pressure history at the 10.5-cm position for shocks in ca. 1:100 N_2H_4:Ar mixtures. These were obtained as part of the data in decomposition studies. The contact surface was tailored, or nearly so, in all of these runs. He-Ar mixtures (7) were used in the driver section. Initial pressures of the N_2H_4-Ar mixture ranged from about 125 torr to 425 torr; pressures and temperatures in the reflected shock ranged respectively from about 2.5 atm to 9 atm and from about 970°K to 1120°K

More recently, we have run 17 shocks in pure Ar using He as a driver. The initial pressure was ca. 175 torr and the bursting conditions were such as to give reflected shocks at about 4.5 atm pressure and 1180°K. These shocks were not tailored, at least in theory (7), but the latter portion of the pressure profile revealed no peculiarities. This corresponds to our previous experience with these weak shocks, which is that one must be very far from ideal tailoring conditions before dips or humps begin to appear in pressure records. In any event, interest in these shocks centered mainly upon the pressure step from incident shock to reflected shock and upon the rate of pressure increase close behind the step, so tailoring was not vital.

Examination of records from the 58 runs showed:

A. Incident shock conditions. To within the available accuracy of measurement (about ±0.5 psi), there was no indication of a pressure rise behind the incident shock. However, it was found in some exploratory runs to test the effect of transducer mounting that the recorded pressure profile was a good square wave (aside from noise) only when the transducer face was accurately flush with the tube wall. If slightly protruding, the result was a pressure step below the final value, followed by a rise toward the correct level. If recessed, the result was an overshoot and subsequent decay.

B. Reflected shock conditions.

1. Pressures. 49 records were obtained from the 10.5-cm position and 9 from the endplate. An obvious experiment, viz., to record both positions from the same shock, was not performed because of instrumental limitations.

No effect of transducer mounting of a type comparable to that in incident shocks was found. In order to make sure that the observed pressure rise was not a specious effect of the mounting, a special mounting was constructed in which the probe adapter was completely isolated in Teflon on the theory that, because of the very different mechanical properties of Teflon (relative to steel), the pressure records should then appear quite different (presumably square) if there were actually no rise in pressure in the reflected region. The Teflon mounting had no observable effect. Further confirmation of the reality of the rise in pressure was contained in a comparison of records from the endplate and from the lateral wall (Fig. 1). The average rate of rise in the two positions was the same.

Two special difficulties did arise in the endplate mounting. One was ringing, easily observed in Fig. 1. Fortunately, in reading photographs it was possible to average this out quite well. The other was an acoustic oscillation of the endplate that was eliminated by changing its gasketing from an O-ring to aluminum.

At the 10.5-cm position, the ratio of the reflected shock pressure at the top of the pressure step (P_5°) to that calculated for ideal reflection (P_5^{id}) was 1.02 ± 0.02 for 49 shocks. The stated uncertainty represents the average absolute deviation. Since we estimate the pressure measurements to be accurate to within about 1 per cent, and since the combination of

measurements and calculations may produce a comparable uncertainty in P_5^{id}, the average deviation in (P_5°/P_5^{id}) is reasonable. However, a few shocks gave unexpectedly large deviations (e.g. $P_5^\circ/P_5^{id} = 0.94$). We think that these represent real discrepancies in behavior, but they are not discernible either from a velocity record or from qualitative examination of the pressure record. Such anomalous shocks may be responsible for some of the scatter in kinetic data from single-pulse experiments.

The 9 shocks for which endplate pressures were obtained yielded $(P_5^\circ/P_5^{id}) = 0.99 \pm 0.01$. Thus the experimental difference determined between the properties at the endplate and those 10.5 cm away is just on the borderline of statistical significance. The difference is undoubtedly real, however. The rate of rise of pressure, measured in either position, averaged 6%/msec. Since the reflected shock in these experiments moved at about 4×10^4 cm/sec, approximately 0.25 msec were required to move out from the endplate to the 10.5-cm position. During this time, the pressure rose 1.5%, on the average. The pressure rise would be expected to be essentially uniform throughout the growing column of gas because the reflected shock moved at only about 2/3 of the velocity of sound in the gas behind it. Therefore if $(P_5^\circ/P_5^{id}) = 0.99$ at the endplate, it should have been 1.005, rather than 1.02, at the 10.5-cm position. This is about as close a check as one could expect. Actually, it probably means that the best ratios to select are more like $(P_5^\circ/P_5^{id}) = 0.995$ at the endplate and 1.01 at the 10.5-cm position.

2. Temperatures

Assuming that the reflected shock is one-dimensional even though it is not quite ideal, one can calculate the temperature at the front using the experimentally determined pressure. For the shocks in argon (or slightly impure argon) under consideration here ($T_5 \approx 1180°K$), the 0.5% deficiency in P_5° at the endplate corresponds to a temperature 3°K below ideal and the 1% excess P_5 at the 10.5-cm position gives a temperature 6°K above ideal. This change is slightly larger (2°K) than one calculates on the assumption that the change in pressure corresponds to an isentropic compression, which may support the idea that finite waves are responsible for the pressure rise. However, for purposes of making temperature corrections with the aid of the experimental pressure profile, the isentropic approximation appears to be adequate.

We have also tested the model suggested by Skinner (5), in which it is assumed that the experimentally determined velocity of the reflected shock represents the true one-dimensional change in gas properties, with a secondary compression as weak pressure waves traverse the gas in the reflected shock and bring it to rest. This is discussed in the next section.

3. Velocities

A number of rather rough measurements of reflected shock velocities have been made during this study. The measurements yielded an average velocity over a 27.5-cm interval starting at the endplate. All of the

results were several per cent below the ideal values, averaging 4% low. This is broadly consistent with the observations of others (8, 9). It is interesting to find that the discrepancy agrees adequately with the attenuation-parameter correlation presented by Greene and Toennies (10) although their plot* was for incident shocks of Mach No. = 5.5 while ours were about Mach 2.

For ideal temperatures in the vicinity of 1180°K, temperatures calculated from the observed velocities, assuming an ideal incident shock and one-dimensional but non-ideal reflection, gave results some 40°K below ideal values. Thus there is an apparent incompatibility between the velocities and the pressures. Skinner's model (outlined above) can reconcile the difference if the gas is brought to rest within a time of the order of 10 μsec after the front. That is, while our records from the endplate have too much ringing to permit this conclusion, the records from the 10.5-cm position are sufficiently free from noise and ringing to make it quite clear that the "thickness" of the pressure step does not exceed 10 to 20 μsec. Therefore if Skinner's model is to reconcile the apparent pressure step and the velocity, it cannot also account for the slow rise (ca. 6%/msec) in pressure behind the front. Actually, it seems that at or adjacent to the endplate, if there is any deviation from ideality at all, it almost has to be explained by something close to Skinner's model. Any residual velocity toward the endplate must become zero at the endplate itself, and the time required for this to occur must approach zero at the endplate.

Application of this model to reconcile the pressure step and reflected velocity goes as follows, for a shock of Mach No. = 2.15 in Ar:

a. The reflected shock velocity is taken to be 96% of ideal. This brings the temperature up to some 40°K below ideal and the pressure to about 96% of ideal.
b. Rapid stagnation of the residual flow is taken to be equivalent to isentropic compression, which brings the gas pressure up to 99.5% of ideal, taken as the observed ratio. The resultant final temperature is about 10°K below ideal. This compares to a temperature 3°K below ideal calculated previously by assuming the observed pressure step to represent entirely a shock compression, ignoring the velocity discrepancy.

It is incidentally our impression that Skinner intended his argument as a case for taking T_{rs} to be about 10°K below ideal (as in the calculation here), and not 30°K below, as has frequently been cited. The latter figure represented his estimate of the uncertainty in T_{rs}, in the neighborhood of T_{rs} = 1800°K.

4. Relationship of reflected shock properties to incident shock attenuation

Attenuation in the velocity of the incident shock is experimentally

*The numbers on the abscissa appear to be too large by a factor of 2.

associated with an increase in temperature (11) and pressure (12) behind the shock front. The behavior of the density does not yet appear to be well established. A number of theories have been put forth to explain and correlate attenuation phenomena by Hollyer, Mirels, Trimpi and Cohen, Spence and Woods, and others. We are not competent to discuss these (summary discussions may be found in refs. 10 and 13), but rather we simply intend to see whether the pressure rise in the reflected shock may be compatible with reasonable changes in the gas behind the incident shock. Specifically, we ask what changes in properties of the gas prior to stagnation are necessary in order to account for the change in stagnation pressure, using a one-dimensional model.

Previously an increase of 1.5% in the stagnation pressure was adopted as best representing the change between the endplate and the 10.5-cm position. This corresponds to 6%/msec. For an increase of 6% in P_5, the conservation equations require a 4% increase in P_2, for reflected shock temperatures around 1200°K. For our shocks, to discern a 4% change in P_2 would have required that we detect a change of about 0.3 to 0.4 psi in P_2 during the observation time (ca. 400 μsec) at the 10.5-cm position; unfortunately, the pickup noise rendered this impossible. The change in P_2 is of the order of that observed by Trimpi and Cohen (12).

From the one-dimensional equations it then follows that the temperature and density behind the incident shock should both rise at about 2%/msec, and one calculates that the incident shock Mach number M_s decreases at about 2%/msec, corresponding to an attenuation of about 2.8%/meter. In this same model the velocity of the reflected shock (relative to the laboratory) should increase at about 1.2%/msec. Incident-shock attenuation of up to 1.8%/meter was found, but the average was closer to 1.0%/meter. Thus the one-dimensional treatment yields results that are not quantitative, but neither are they altogether unreasonable.

One serious deficiency of the treatment is that it does not offer any insight into the increase with time of the pressure at a fixed point, e.g. at the endplate. That is, the treatment would say that there should be spatial gradients of pressure, temperature, and density in the reflected region that would not change significantly with time. The experimental measurements of pressure indicate that such gradients, at least in the pressure, must be slight, if they are indeed appreciable at all; furthermore, there is direct evidence that the properties at a fixed point do change with time.

CONCLUSIONS AND COMPARISONS WITH OTHER WORK

Shock tubes are almost biological in their variety, so one must be cautious in describing their behavior. We shall first summarize and state some conclusions regarding our own observations and then briefly examine some results obtained by others in the hope that some generalization may be possible.

We have studied shocks in Ar, driven by He or He-Ar mixtures, covering a range of incident shock Mach numbers from about 1.95 to 2.2, giving reflected shock temperatures from about 970°K to 1200°K. The tube was 3 inch i.d. steel with a 12-foot channel and a 1/4-inch steel endplate rigidly attached to the end. Initial pressures were typically about 175 torr. Incident shock attenuation was observed to range from 0 to 1.8%/meter over the last 1.5 m of travel. The reflected shock pressure at the front, P_5^o, was measured with calibrated Kistler transducers and found to average 99.2% ± 1% of ideal at the endplate and 102% ± 2% of ideal at a position 10.5 cm away. The pressure in the reflected shock, P_5, was found to increase with time at rates ranging from 0 to 13.3%/msec, averaging 6.2% ± 2.0%/msec. From the average rate of rise it was concluded that the best values of the ratios, (P_5^o/P_5^{id}), were 0.995 at the endplate and 1.01 at the 10.5-cm position. Temperatures calculated from these ratios on one-dimensional theory, assuming uniform properties in the incident shock, were respectively 3°K below and 6°K above the value calculated from the incident shock velocity at the endplate, assuming ideal reflection.

Measurements of reflected shock velocities, (averaged over a 27-cm interval) though crude, indicated clearly that velocities were below (averaging 4% below) the values for ideal reflection. Since on one-dimensional shock theory such velocity discrepancies were incompatible with the observed pressures, a model related to Skinner's (5) was examined and found to predict a temperature 10°K below ideal at the endplate for these shocks. The model which combines shock compression and a final, rapid, isentropic stagnation, predicts that the temperature discrepancy will be the larger, the hotter the shock or the more strongly attenuated the shock. The prediction may find some support in experience.

The slow rise in pressure in the reflected region was shown to be essentially uniform throughout the gas, though small gradients are not excluded. A temperature rise is assumed to accompany the pressure rise by what may approximate an isentropic relationship. However, a second possibility was explored in which the pressure rise is attributed to a pressure rise behind the incident shock, resulting from attenuation. In this treatment, a simple one-dimensional model of the attenuating incident shock was adopted in which attenuation is taken as an empirical fact and the gas properties at any point behind the front are assumed to be those initially attained when that element passed through the front. This model can account for about half of the observed (dP_5/dt), using the average attenuation of about 1%/meter. The temperature-pressure relationship given by this model is close to an isentropic one. We think that the model has some virtues in helping one to envision the reflected-shock region and also, possibly, the incident shock; but it is not quantitative and therefore is of limited usefulness.

On those points that concern chemical kinetic measurements, our conclusions concerning the shocks studied are:

(a) the Skinner-type model seems quite appealing as a way to reconcile

the reflected-shock pressures and velocities. It probably sets a lower limit on the temperature, while application of one-dimensional shock theory to the pressure alone may set an upper limit. Thus the temperature at the endplate is in all probability between 10° and 3°K below ideal, while that at the 10.5-cm position is about the ideal value or a few degrees above it.

(b) Without being unduly concerned about a theory that can account for the pressure rise in the reflected region, one can probably adopt an isentropic relation to calculate the temperature profile from the pressure profile.

In thinking about this problem, we have attempted to gather together all the pertinent experimental work of others. Not all of it seems reconcilable, particularly some involving quite strong shocks. However, we suspect that a combination of the Greene-Toennies attenuation-parameter correlation for reflected velocity (10) and the Skinner-type model presented here could go a long way toward unifying the various observations. An effort to summarize them is presented below.

Velocities

Strehlow and Cohen (8) observed reflected-shock velocities in Ar averaging 4% below ideal at the endplate and a few cm away. The incident shock Mach numbers were $2.75 < M_s < 3.60$ and the tube was 1.5 x 3 inches.

Toennies and Greene (14) found reflected velocities from 5% to 35% below ideal, and successfully correlated them with an attenuation parameter dependent upon tube dimensions and initial pressure.

Strehlow and Case (15) reported reflected velocities below theoretical.

Brabbs et al. (9), in a tube very similar (2.5 inch i.d.) to ours but in a slightly higher range of Mach numbers, measured reflected velocities that were several per cent below ideal for Ar. Acceleration was found.

Tschuikow-Roux and Marte (16) measured reflected velocities in Ar in a tube much like ours, under similar conditions. Values were not specifically reported, but from other information in their paper we estimate them to have been about 5% below ideal.

Densities

Gardiner and Kistiakowsky (17) used X-ray absorption by xenon and found reflected shock densities close to the ideal. The density increased with time.

Knight and Rink (18) found reflected shock densities in krypton, again using X-ray absorption, that agreed with ideal calculations to within their uncertainty of measurement (ca. ± 2%).

Strehlow and Case (15), by an interferometric method, found reflected densities in argon that agreed with ideal calculations at $M_s \approx 2$ but exceeded them at $M_s \approx 5$. The density increased with time. Accuracy of the density measurements was estimated to be ca. ± 3%.

Pressures

Skinner (5), using an experimental arrangement much like ours, found for $M_s \approx 2.75$ that the incident-shock pressure was within about 1% of ideal, while P_5° was slightly below ideal (1.3% ± 1.6%) at a position 3 inches from the endplate. Pressure rose with time.

Rudinger (19, 20) found pressure rising with time in the reflected region and attributed the rise to the effects of weak waves generated by the growing boundary layer behind the incident shock. The waves cross the reflected shock front and are brought to rest. The effect should be very like isentropic compression.

Brabbs, Zlatarich, and Belles (9), in the study mentioned above, measured reflected pressures P_5° as well as velocities. The values of P_5°, at a position 15 cm from the endplate, averaged 1%-2% below ideal for M_s between about 2.5 and 3.4. Pressure increased with time.

Tsuchiya and Kuratani (21), using a 10-cm i.d. tube with a 4.2-m channel at initial Ar pressures of 45 torr, reported no absolute values of P_5° but stated that pressure in the reflected region increased at 11% ± 3%/msec for $M_s \doteq 3.3$.

Trimpi and Cohen (12) found a gradient in the pressure behind incident shocks of $M_s \doteq 2$ in air initially at room conditions, amounting to an increase of about 3%-5%/msec. The shock channel was 2 x 1.5 inches and pressure was measured 8 feet from the diaphragm.

Holbeche and Spence (22) observed an increase of pressure with time behind reflected shocks of about $M_s = 6.5$ in nitrogen.

Lauver, Hall, and Belles (23) have reported reflected shock front pressures of approximately ideal magnitudes in Ar containing some CO_2, and find that at a fixed point, pressures increase with time.

Baganoff (24), using a newly devised pressure transducer, has shown that the pressure step in reflected shocks at the endplate is essentially ideal in shape (we are not sure about magnitude). Characteristics of his transducer at present limit useful observation times to less than about 20 μsec.

Essentially flat pressure-time profiles in the reflected region have been found by Tsang (25), using a single-pulse tube with a modified dump chamber arrangement, and by Napier et al. (26), who commented that the form of their pressure records was largely determined by the method of mounting

of the transducer.

Temperatures

Napier and Simonson (27) used sodium line reversal methods for determining temperatures of reflected shocks in 90% Ar-10% CH_4. Within the rather large uncertainty (±ca. 50°K), temperatures appeared to match the ideal values below about 1800°K, falling off markedly above that. Later, Napier et al. (26) explored C_2 band reversal and found agreement with temperatures from Na reversal. In a recent note, Kimber and Napier (28) have reported that reversal of Cr lines yields shock temperatures 30° to 80°K higher than C_2 reversal (and, presumably than Na) in the 1900°-2500°K range. It is not clear which measurement is to be regarded as the more accurate (presumably the one giving the higher result).

Johnson and Britton (29), using light absorption, compared rates of dissociation of Br_2 in Ar behind incident and reflected shocks in a 10 cm i.d. tube and concluded that, in the temperature range 1500°-1900°K, their reflected shock temperatures averaged 35° ± 5°K below ideal, roughly independent of distance from the endplate (over a 16-cm range). Their results also appear to imply near-ideal behavior at temperatures above about 2000°-2200°K, in direct contradiction to the results of Napier and Simonson. The smallest temperature discrepancy found by Johnson and Britton was at the observation point nearest the endplate. This suggests the possibility that the apparent rate of disappearance of Br_2 may have been affected by the opposing effect of a growing boundary layer, which might be less significant near the endplate. This gains some support in their finding of the largest discrepancies at the lowest temperatures where, because of the slow rate of dissociation, the countereffect of boundary layer growth would be most important. We do not mean to dismiss their results by these remarks, but it does seem probable that the temperature discrepancy is substantially less than their estimate.

Other kinetic evidence concerning temperatures in reflected shock waves is less direct, consisting mainly of those few cases for which shock tube data can be compared with data obtained by other methods. In two such cases, the decomposition of CH_4 (30) and of C_2H_2 (31), the indications are that the temperatures assigned to reflected shocks using ideal theory (modified in some cases to include isentropic compression behind the front) contain a possible error not exceeding about 20°-25°K at temperatures above 1600°K. Tsang (1) concluded from comparison of results in a single-pulse study of four compounds in the range, 750°-1300°K, that his reflected shock temperatures were 10°-25°K below ideal. His published pressure record shows what seems to be a weak rarefaction wave behind the reflected shock front, and we are inclined to agree with his remark that the unconventional position of his dump tank may, somehow, have caused a lowering of the reflected shock temperature. A second possibility may lie in the proximity of his sampling valve to his endplate (one quarter inch away). The effective reaction temperature of the sampled gas may have been appreciably affected by the cool endplate.

Holbeche and Spence (22), in the previously-mentioned study of nitrogen, measured temperatures by line reversal and found an almost incredibly high rate of increase behind the reflected front, amounting to around 100°K in 50 μsec. They found this to be compatible with attenuation theory and their measurements of attenuation of the incident shock.

Tsuchiya and Kuratani (21), in their previously-mentioned study, determined reflected shock temperature profiles by measuring the vibrational temperature of CO in Ar. They reported temperature discrepancies ($T_5^{id} - T_5^{exp}$) of 70° ± 30°K and 30° ± 30°K in the front at 1-cm and 5-cm positions for shocks at $T_5 \doteq 2500$°K. Because of slow relaxation of CO, shock front temperatures were determined by extrapolation. The rate of rise of temperature behind the front was found to be approximately in an isentropic relationship with the rise in pressure.

A similar pressure-temperature relationship was reported by Lauver et al. (23), who used infrared pyrometry on CO_2-containing Ar to measure temperatures. They reported good agreement between measured and ideally calculated values of T_5. Reasonable agreement was also reported by Watson (32) in a study in the range, 3000°-4500°K, utilizing emission from OH as a thermometer.

An often-considered thermometric device, viz., a technique for measuring the velocity of sound, seems to have been perfected by Carnevale, Carey, and Marshall (33), who reported excellent agreement with ideal calculations for reflected shocks in Ar over the range, 3000°-9000°K.

Final Remarks

Although variable in character and no doubt also in reliability, reports in the literature--plus our own results--seem broadly consistent, with a few exceptions. For argon shocks in typical tubes at initial pressures higher than about 50 torr, the following consensus seems to emerge:

(a) Attenuation of the incident shock produces a gradual increase in temperature and pressure (and, perhaps, density) behind the incident front.
(b) Reflected shock front temperatures at the endplate are only very slightly below ideal values; not more than 10°K at 1000°K, perhaps as much as 25°K at 1750°K and 50°K at 2500°K. The details can probably be correlated with an attenuation parameter.
(c) Reflected shock velocities are not good indicators of the reflected shock temperatures and are incompatible with measured pressures. They may be reconcilable in a simple model that assumes shock compression followed by rapid, isentropic stagnation of the residual flow.
(d) Pressure, density, and temperature all rise slowly behind the reflected shock. Pressure and temperature are adequately related by an isentropic compression law. Part of the slow rise may be attributed, on a one-dimensional basis, to changes in the incident

gas properties; but it is also necessary to imagine additional perturbations, probably of the type that Rudinger (20) has discussed.

ACKNOWLEDGMENT

The authors appreciate the support of this investigation by the Army Research Office (Durham).

REFERENCES

(1) W. Tsang, J. Chem. Phys. 41, 2487 (1964).

(2) H. B. Palmer, B. E. Knox, and E. T. McHale, AIAA Jour. 1, 1195 (1963).

(3) E. T. McHale, B. E. Knox, and H. B. Palmer, Tenth Symposium (Internat.) on Combustion, The Combustion Institute, Pittsburgh (1965), in press.

(4) K. Michel and H. Gg. Wagner, Tenth Symposium (Internat.) on Combustion, The Combustion Institute, Pittsburgh (1965), in press.

(5) G. B. Skinner, J. Chem. Phys. 31, 268 (1959).

(6) H. S. Glick, W. Squire, and A. Hertzberg, Fifth Symposium (Internat.) on Combustion, Reinhold, New York (1955), p. 393.

(7) H. B. Palmer and B. E. Knox, ARS Jour. 31, 826 (1961).

(8) R. A. Strehlow and A. Cohen, J. Chem. Phys. 30, 257 (1959).

(9) T. A. Brabbs, S. A. Zlatarich and F. E. Belles, J. Chem. Phys. 33, 307 (1960).

(10) E. F. Greene and J. P. Toennies, Chemical Reactions in Shock Waves, Edward Arnold, London (1964).

(11) A. G. Gaydon and I. R. Hurle, The Shock Tube in High-Temperature Chemical Physics, Chapman and Hall, London (1963).

(12) R. L. Trimpi and N. B. Cohen, N.A.C.A. Tech. Note 3375, March (1955).

(13) J. N. Bradley, Shock Waves in Chemistry and Physics, John Wiley, New York (1962).

(14) J. P. Toennies and E. F. Greene, J. Chem. Phys. 26, 655 (1957).

(15) R. A. Strehlow and C. T. Case, J. Chem. Phys. 35, 1506 (1961).

(16) E. Tschuikow-Roux and J. E. Marte, J. Chem. Phys. 42, 2049 (1965).

(17) W. C. Gardiner, Jr. and G. B. Kistiakowsky, J. Chem. Phys. 34, 1080 (1961).

(18) H. T. Knight and J. P. Rink, J. Chem. Phys. 35, 199 (1961).

(19) G. Rudinger, J. Chem. Phys. 35, 1507 (1961).

(20) G. Rudinger, Phys. Fluids 4, 1463 (1961).

(21) S. Tsuchiya and K. Kuratani, J. Chem. Phys. 42, 2986 (1965).

(22) T. A. Holbeche and D. A. Spence, Proc. Roy. Soc. A279, 111 (1964).

(23) M. R. Lauver, J. L. Hall, and F. E. Belles, this symposium, Paper C3.

(24) D. Baganoff, this symposium, Paper C5.

(25) W. Tsang, J. Chem. Phys. 40, 1498 (1964).

(26) D. H. Napier, M. Nettleton, J. R. Simonson and D. P. C. Thackeray, AIAA Jour. 2, 1136 (1964).

(27) D. H. Napier and J. R. Simonson, ARS Jour. 32, 1736 (1962).

(28) G. M. Kimber and D. H. Napier, Comb. Flame 9, 103 (1965).

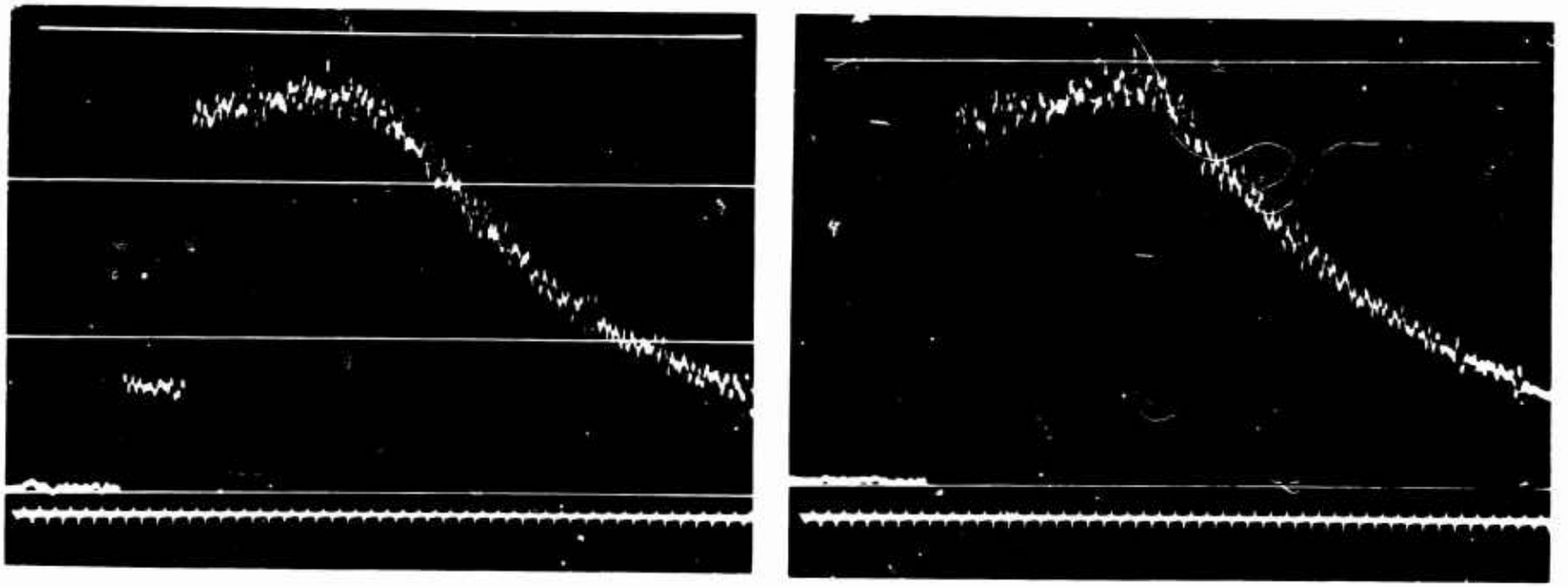
(29) C. D. Johnson and D. Britton, J. Chem. Phys. 38, 1455 (1963).

(30) H. B. Palmer and T. J. Hirt, J. Phys. Chem. 67, 709 (1963).

(31) H. B. Palmer and F. L. Dormish, J. Phys. Chem. 68, 1553 (1964).

(32) R. Watson, this symposium, Paper E3.

(33) E. H. Carnevale, C. Carey, and T. Marshall, this symposium, Paper E8.



a b

Fig. 1. (a) Pressure record from 10.5-cm position. Time markers occur at 100 μsec intervals.
(b) Pressure record from the endplate position, for a shock similar to that in (a).

THE EXPERIMENTAL STUDY OF THE INTERACTION OF A PROJECTILE WITH A PLANE SHOCK WAVE

J. E. Uppard, R. Burch, R. Allen
Atomic Weapons Research Establishment,
Foulness, England

INTRODUCTION

The work which is the subject of this paper concerns the problem of a body of supersonic speed when struck by a plane shock wave. The basic situation is shown in (Fig. 1).

This shows the plane shock moving from left to right and about to meet the projectile flying in the opposite direction. The Mach number of the projectile is

$M' = \frac{W}{C_o}$, and it has, because of its supersonic speed, a bow wave

moving with it.

The shock Mach number is given by

$$M = \frac{U}{C_o},$$

and the flow Mach number by

$$M_1 = \frac{V_1}{C_1}$$

The experiments to be described consisted of firing a projectile into the shock and photographing the shock and flow fields. A sphere was

chosen as the missile to obviate any problems of the model "yawing" in flight. To produce the shock wave use was made of the A.W.R.E. 8" x 2" shock tube, and the sphere, a $\frac{1}{4}$" dia. ball bearing, was fired into it. The gun used was an engineers "stud" or rivetting gun, the barrel is 6" long, smooth-bored, and projected the $\frac{1}{4}$" sphere at a velocity of 2,500 ft. sec. using 0.22 blank ammunition. The missile Mach number was therefore about 2.2.

EXPERIMENTAL ARRANGEMENTS

(Fig. 2) shows the schematic diagram of the first experimental arrangement. The shock tube compression chamber is 2'6" long, and the expansion chamber 7'6", and this has an observation section, fitted with 6" dia. glass windows, at the end. At the back of the compression chamber was another 2'6" length of tube fitted with a wooden block to act as a "catcher" for the spheres fired into the tube.

For most of the experiments a shock strength of 2.4 (20 p.s.i. overpressure) was used, with a shock velocity of 1,650 ft./sec. The shock tube diaphragm was ruptured by means of a small electric detonator. The firing sequence was as follows: The gun was fired mechanically, and the sphere, emerging from the end of the barrel, passed over a small piezo-electric transducer. The pressure from the bow wave caused a pulse from the transducer to operate the firing pack which fired the detonator and ruptured the diaphragm. Taking into account the relative velocities of the shock wave and the sphere, together with delays in the firing circuit, the gun had to be placed about 13ft. from the point of shock/missile impact at the observation section of the tube. The argon-jet, sub-microsecond spark source at the observation section was triggered by means of a piezo-electric transducer operated by the shock wave. The probability therefore of getting a picture of the impact depended upon the constancy of the shock wave and sphere velocities from shot to shot - literally a "hit or miss" method. The percentage of misses to hits was fairly high and became higher as the gun barrel became worn and the sphere velocity varied. However, a fairly good series of pictures of the penetration phase was obtained, one of which is shown in (Fig. 3).

These photographs will be discussed at greater length later on but the plane shock S, the newly forming bow wave B_1, the unaffected bow wave B, and the bridging shock BS are of immediate interest. The new missile Mach number is now given by

$M'_s = \frac{W}{C_1}$ assuming no change in actual sphere velocity, giving a value of about 2.5.

To overcome the difficulties of the hit and miss method and to obtain a continuous history of the missile shock penetration phase from a single shot a system was devised to compute the time of impact of the sphere and the shock by means of a voltage ramp technique. This, used in conjunction with a Cranz-Schardin Optical system, enabled a series of five shadowgraphs to be obtained separated by accurately known time-intervals of a few micro-seconds. The complete experimental arrangement is shown in (Fig. 4).

The full operating sequence is as follows:

The gun is fired and gives a pulse to the firing pack rupturing the shock tube diaphragm as before. The bow wave from the sphere, on reaching the piezo-electric transducer T_B placed at one end of the observation section, triggers a voltage ramp generator B. Similarly the shock wave triggers the voltage ramp generator A by means of the transducer T_A at the other end of the observation section. The voltage ramps A and B are adjusted so as to reach a value E_T in the time taken for the shock wave or the sphere to cross the observation section. The outputs from the two generators are summed by the operational adder unit C, which produces a voltage which is fed to the thyratron trigger unit, biased from firing by the voltage E_T.

The operation of the thyratron trigger unit provides a pulse which in turn provides accurately timed delay pulses to trigger the five element Cranz-Schardin spark light source. Small "search" coils were wound around the discharge condensers of this unit and pulses from these, together with a pulse from the ramp generator B, are fed to a spiral time base oscilloscope, so that all the time intervals are known after firing. The amount of additional electronic equipment required for the above computing circuit is small, and is fully met by the use of two Tektronix 551 scopes as voltage ramp generators and a Tektronix 'O' type operational pre-amplifier summing the ramps.

The Cranz-Schardin optical system is quite conventional. The light sources are five argon-jet gaps as shown in (Fig. 5). These are arranged in the form of a cross with a unit in the centre. The lens L makes the beam parallel through the observation section and this is reflected back by a mirror, not shown, to give an image of the five light beams on to the small lenses L_2 which focus the phenomena in the observation section on to the photographic plate. The piece of wood at the end of the tube is merely to prevent damage due to bad markmenship.

(Fig. 6) shows a sequence of 5 exposures separated by about $2\frac{1}{2}$ micro-seconds.

THEORETICAL CONSIDERATIONS

Whilst the above work was going on our attention was drawn via an excellent review paper by Professor Pack in the J. Fluid Mechanics (ref. 1) to some theoretical work by Dr. Smyrl which had been

previously published in the same journal (ref. 2). Smyrle referred to a paper by Ehlers and Shoemaker (ref. 3) who solved the problem of a weak shock wave meeting, at any angle of incidence, a flat plate moving subsonically or supersonically. In contrast Smyrl's solution is for a shock wave of arbitrary strength meeting thin aerofoil moving at supersonic velocity and implies a collision between two shocks of finite strength.

Treating the problem two-dimensionally he found the shock pattern was "steady" and is shown in (Fig. 7).

It is made up of LC, the new bow wave in the shock; ID a bridging shock; IG the part of the bow wave which has not yet entered the shock and IB the continuation of the plane shock onto the wedge. The points BCDE all lie on a "sonic-circle", (the path of the disturbance caused by the wedge entering the shock) which expands at velocity C_1 (the speed of sound behind the shock). O_1 is the place where the shock front and the wedge originally met and this moves in the direction of the shock with velocity V_1 (particle velocity), to the new position O after time t. This represents one end of a contact surface OI which devides the air entering regions (3) and (4) into two non-mixing regions. The air enters these regions from (0) across the bridging shock, path (0) (1) (3) and across the old bow wave (0) (2) (4) respectively.

The above situation is summarised in the following assumptions:

(1) the shock is deflected at I through a small angle,

(2) the bow wave is deflected at I into the position of the tangent ID, and a new bow wave is formed in position of tangent LC.

(3) a contact discontinuity, IO, divides the air behind the shock into two, non-mixing regions.

(4) outside the sonic-circle the flow consists only of uniform regions, (0), (1) etc. In particular the shock is straight except for the position AB which must bend so as to meet the wedge face normally.

The coordinates, given in terms of the time independent variables $x = \frac{X}{C_1 t}$, $y = \frac{Y}{C_1 t}$ are as shown.

From the old and the new bow wave angle it will be seen that in this case, as in the experimental case, the missile Mach number inside the shock is greater than outside, i.e. in the experimental case the missile Mach number went from 2.2 to 2.5. Assuming therefore no change in C_D, the ratio of the Mach number after entering the shock M'_s, to that before entering M_1, is given by

$$\frac{M'_s}{M'} = \frac{C_o}{C_1}\left(1 + \frac{V_1}{W}\right)$$

and a graph of this, against velocity for various shock pressures, is shown in (Fig. 8).

This shows that the Mach number for the missile inside the shock can be greater, less or equal to the Mach number before passing into the shock, and we are led to consider these conditions as summarised in (Fig. 9). This is a graph of shock strength, defined as the density ratio behind and in front of the shock, against M', the Mach number of the missile before entering the shock. The interesting tangent condition is confined to $M'_s > M'$; the curve (1) is the coincident tangent condition $M' = M'_s$; and the non-intersecting tangent condition is for $M' < M'_s$. There is a further condition, the single tangent condition, where the point I has fallen inside the sonic-circle, i.e. the bridging shock has disappeared, and here again $M'_s < M'$.

DISCUSSION OF EXPERIMENTAL RESULTS

(Fig. 10) shows a sequence of shots giving the history of the sphere travelling into the shock. The times after the initial impact between the shock and the sphere are shown. It will be seen that the pattern is not now steady as for the ideal 2-dimensional case. Qualitatively however all the features of the "ideal" solution are evidence - the new bow wave, the bridging shock, the unaffected old bow wave and a formation analogous to the "sonic-circle" shown as X, X'. This formation is of particular interest and is of course, basically different from the ideal case. The major physical difference is the collision of the shock wave with an intense bow wave shock of about 80 p.s.i. increasing rapidly to about 100 p.s.i. at the stagnation point on the sphere. The part of the circle X appears to expand over a limited region at about 2,000 ft./sec. from a centre which is somewhat ill-defined but appears to move towards the sphere with a velocity of about 230 ft./sec. This is in contrast to the ideal case where the centre of the sonic circle at the foot of the contact surface moves away from the leading edge with velocity V_1. It is of interest that in some of the shadowgraphs a faint curved line can be seen which makes an angle of 20^o with the vertical and this must be the trace of the contact discontinuity. The movement of the foot of this in the case of the sphere is very complex, involving the flow in the wake.

In spite of the physical differences between the two cases the qualitative resemblance is remarkable. (Fig. 11) shows the comparison between the ideal case and the sphere case for the same missile velocity and shock strength, the sphere having penetrated about 10 diameters into the shock. It is seen that the shock angles are very similar. It is hoped to continue these experimental studies in the more interesting region where the Mach number before entering the shock is about 14

and the shock overpressure about 80 p.s.i. i.e. in the single tangent region of (Fig. 9). It is of some interest that the curve (2) which is the boundary between the non-intersecting and single tangent conditions gives an almost exact value for the ratio of

$$\frac{M_s'}{M_1'} \text{ of } 0.8$$

REFERENCES

(1) Pack, D. C., The Reflexion and diffraction of Shock Waves. J. Fluid Mechs 18, 1964.

(2) Smyrl, J. L., The Impact of a Shock Wave on a Thin Two-Dimensional Aerofoil Moving at Supersonic Speed. J. Fluid Mechs., 5, (1963)

(3) Ehlers, F. E. and Shoemaker, E. M., The Impact of a Weak Shock Wave and a Flat Plate moving Subsonically and Supersonically. J. Aero/Space Sciences, 26, 75, (1959)

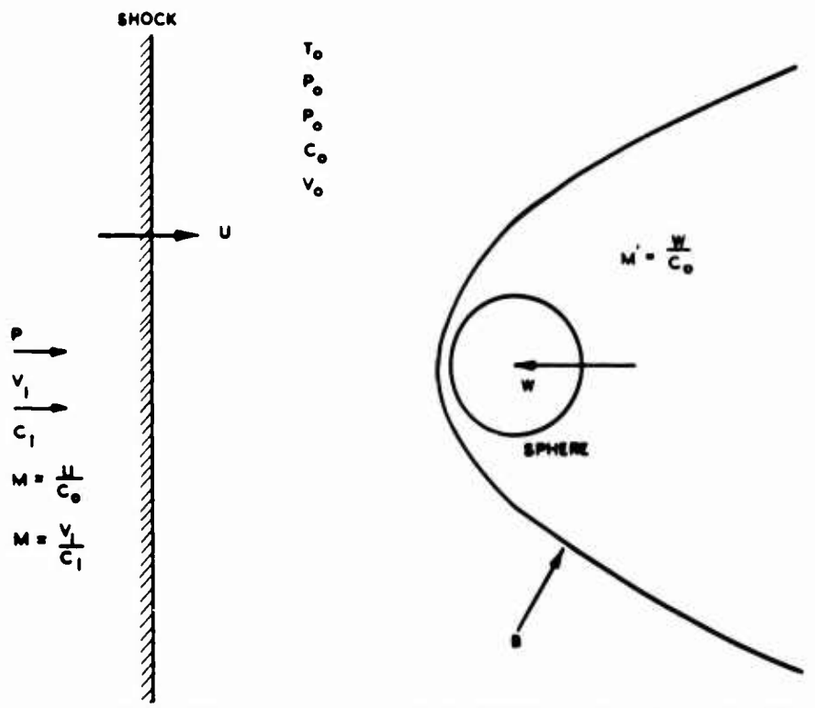


FIG. 1 SHOCK WAVE AND PROJECTILE BEFORE INTERACTION

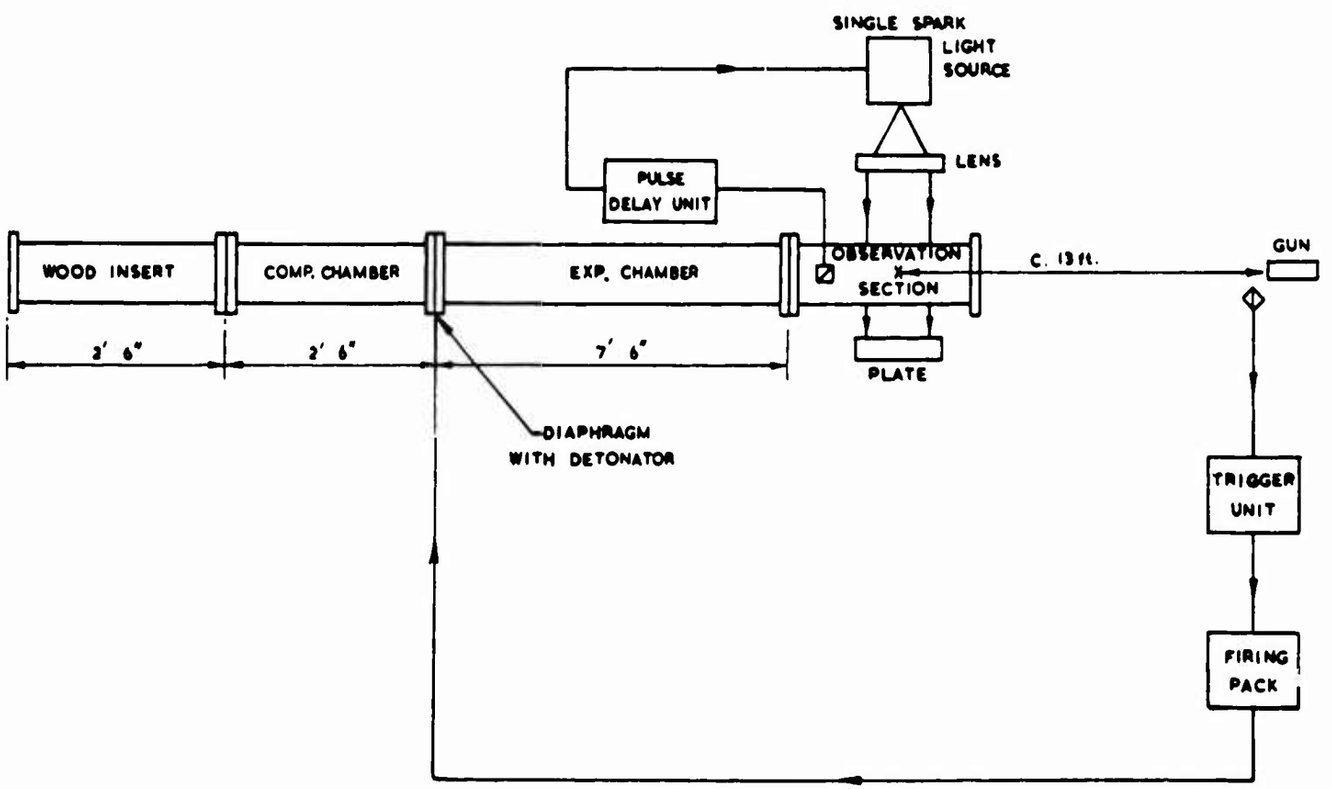


FIG. 2 FIRST EXPERIMENTAL ARRANGEMENT



FIG. 3 PROJECTILE AND SHOCK AFTER INTERACTION

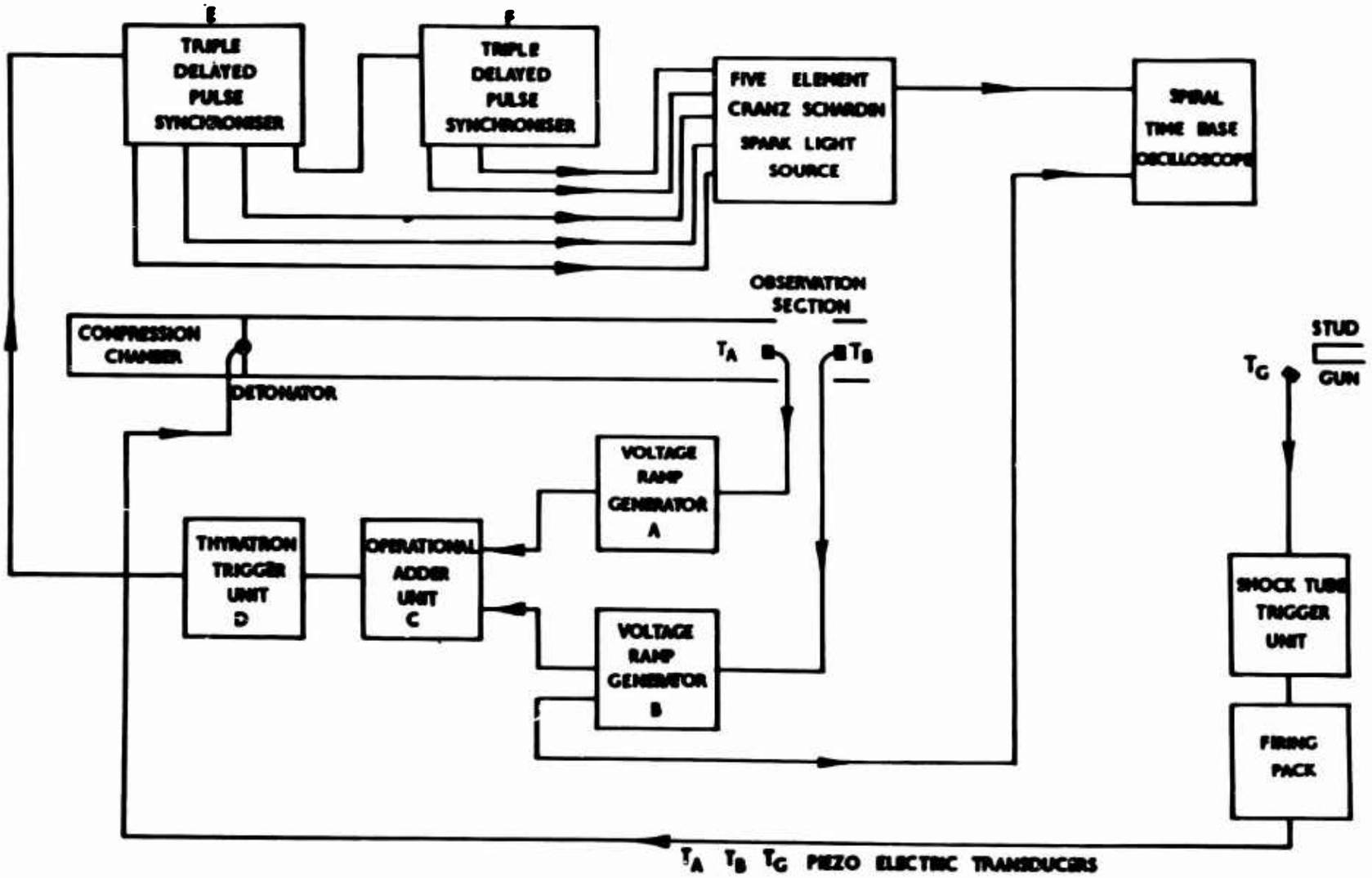


FIG. 4 SECOND EXPERIMENTAL ARRANGEMENT

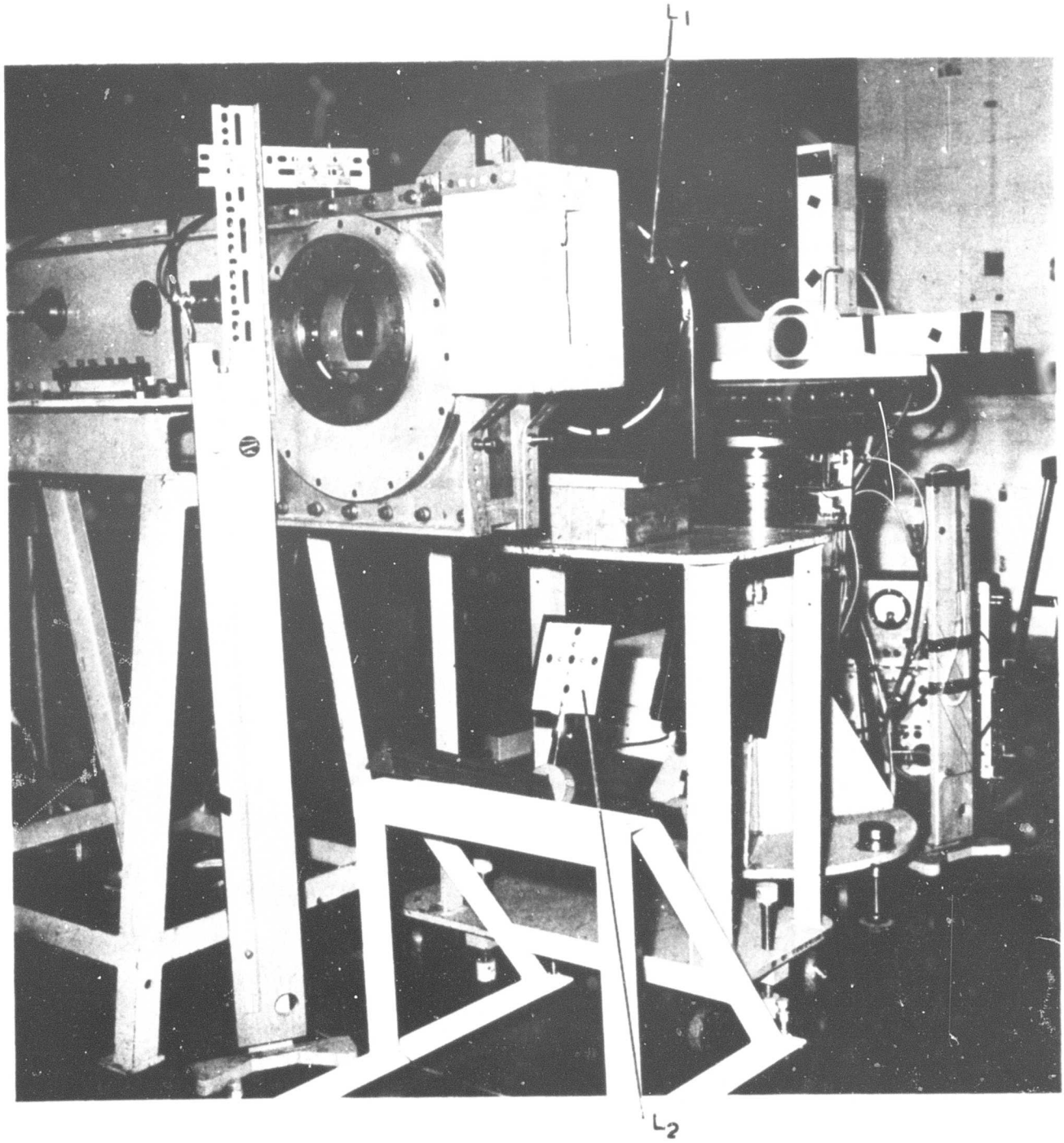


FIG. 5 CRANZ - SCHARDIN SYSTEM

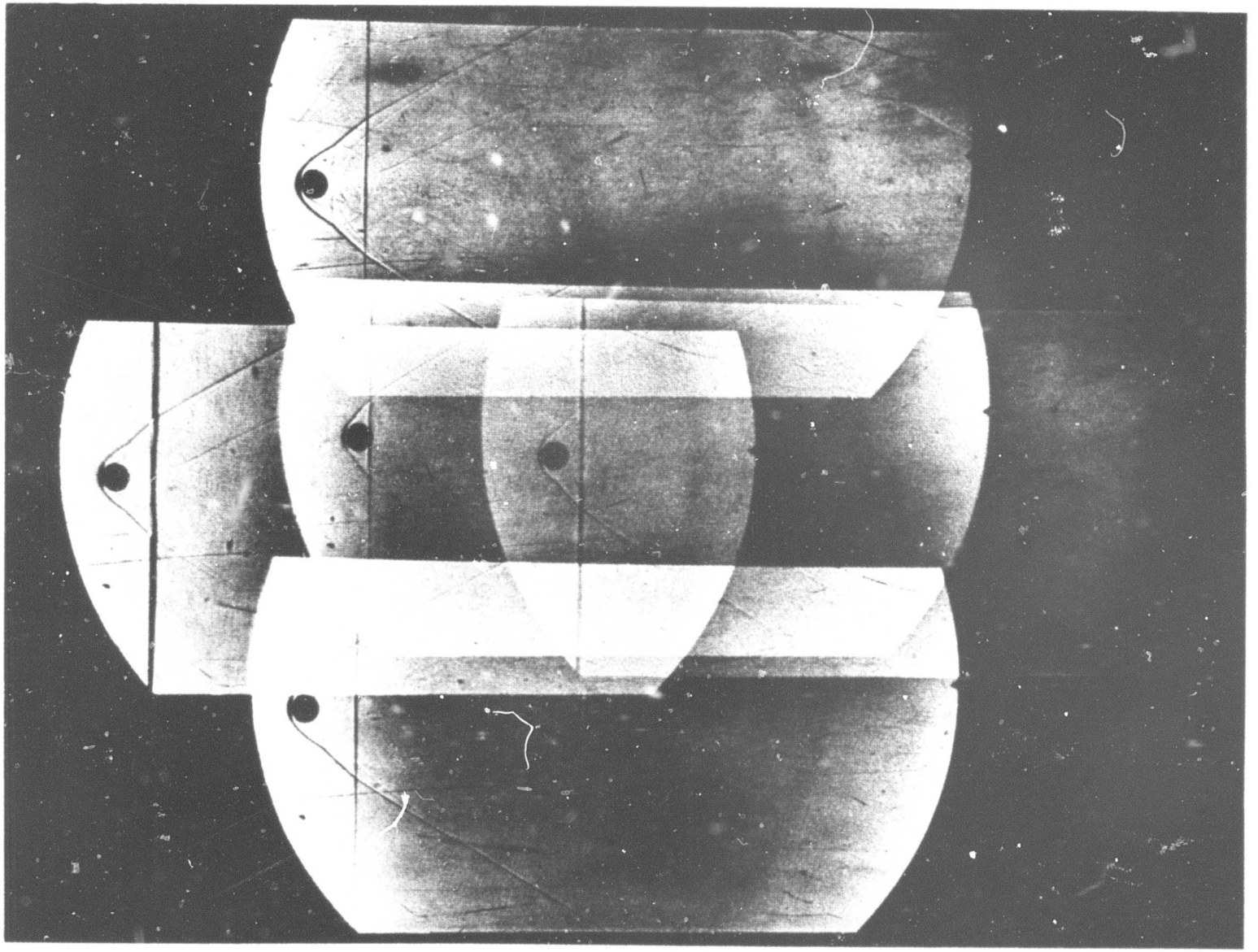


FIG. 6 FIVE EXPOSURE SHOT, CRANZ - SCHARDIN SYSTEM

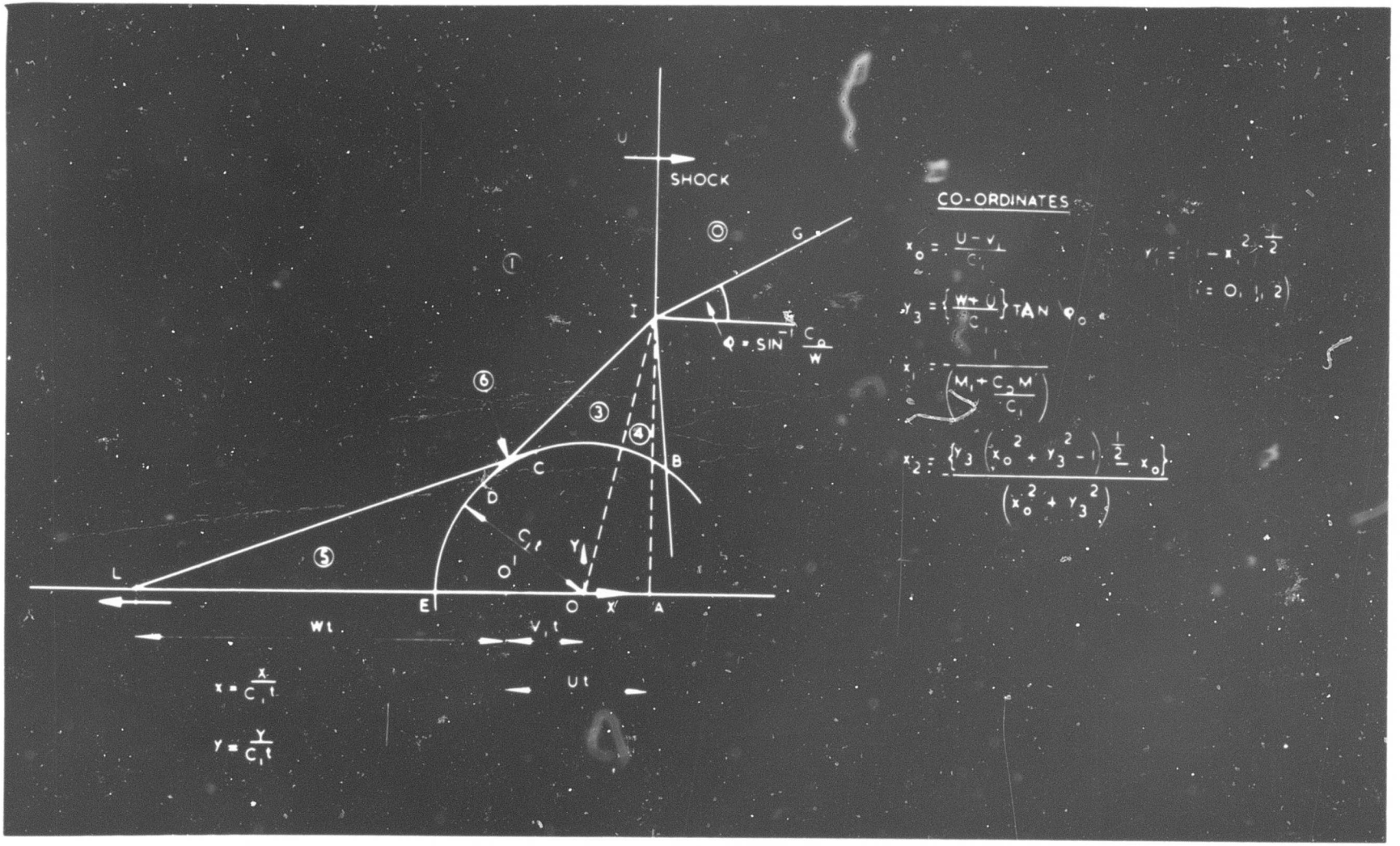


FIG. 7 'STEADY' PROJECTILE/SHOCK INTERACTION PATTERN

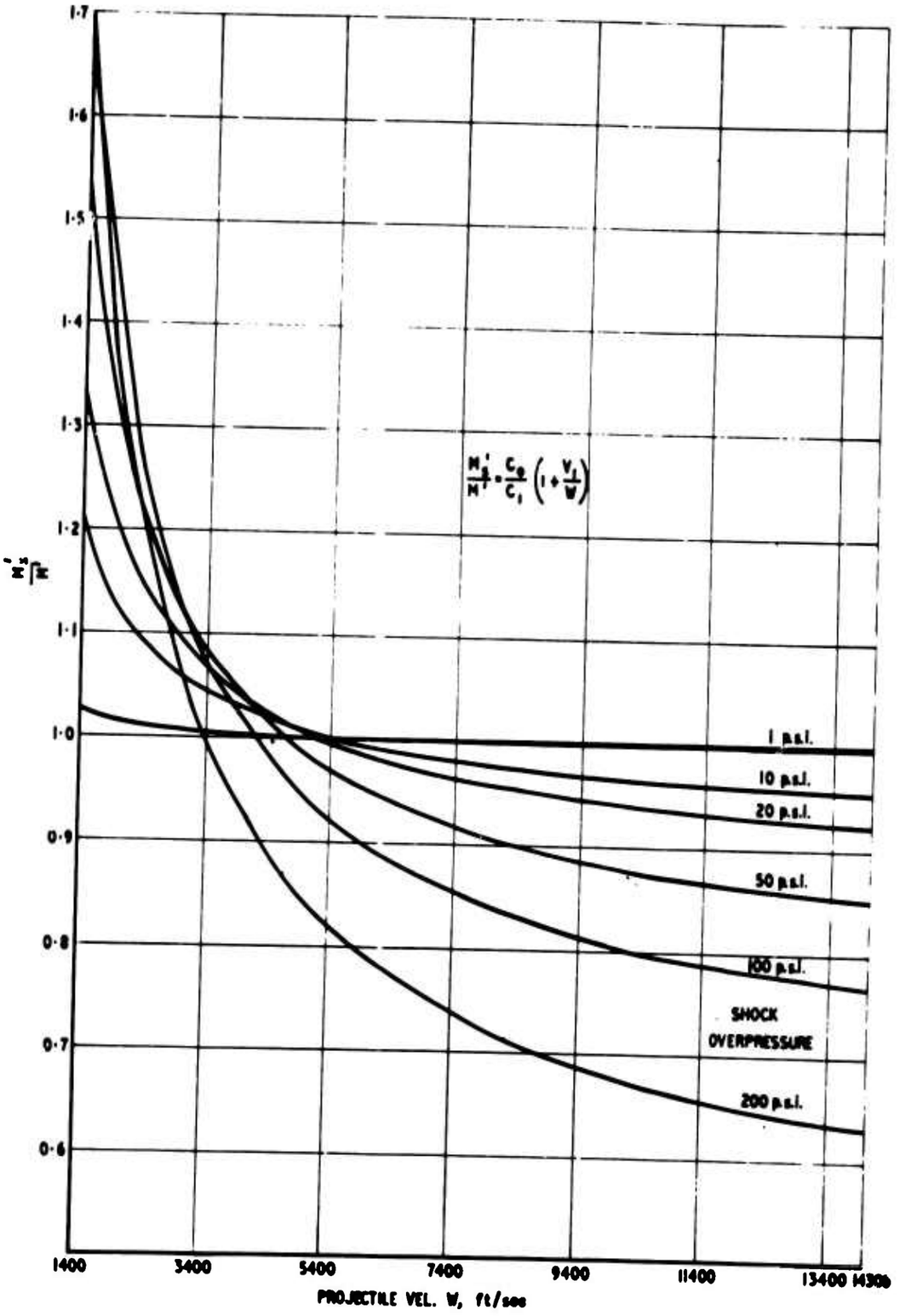


FIG. 8 MACH NUMBER RATIOS BEFORE AND AFTER SHOCK

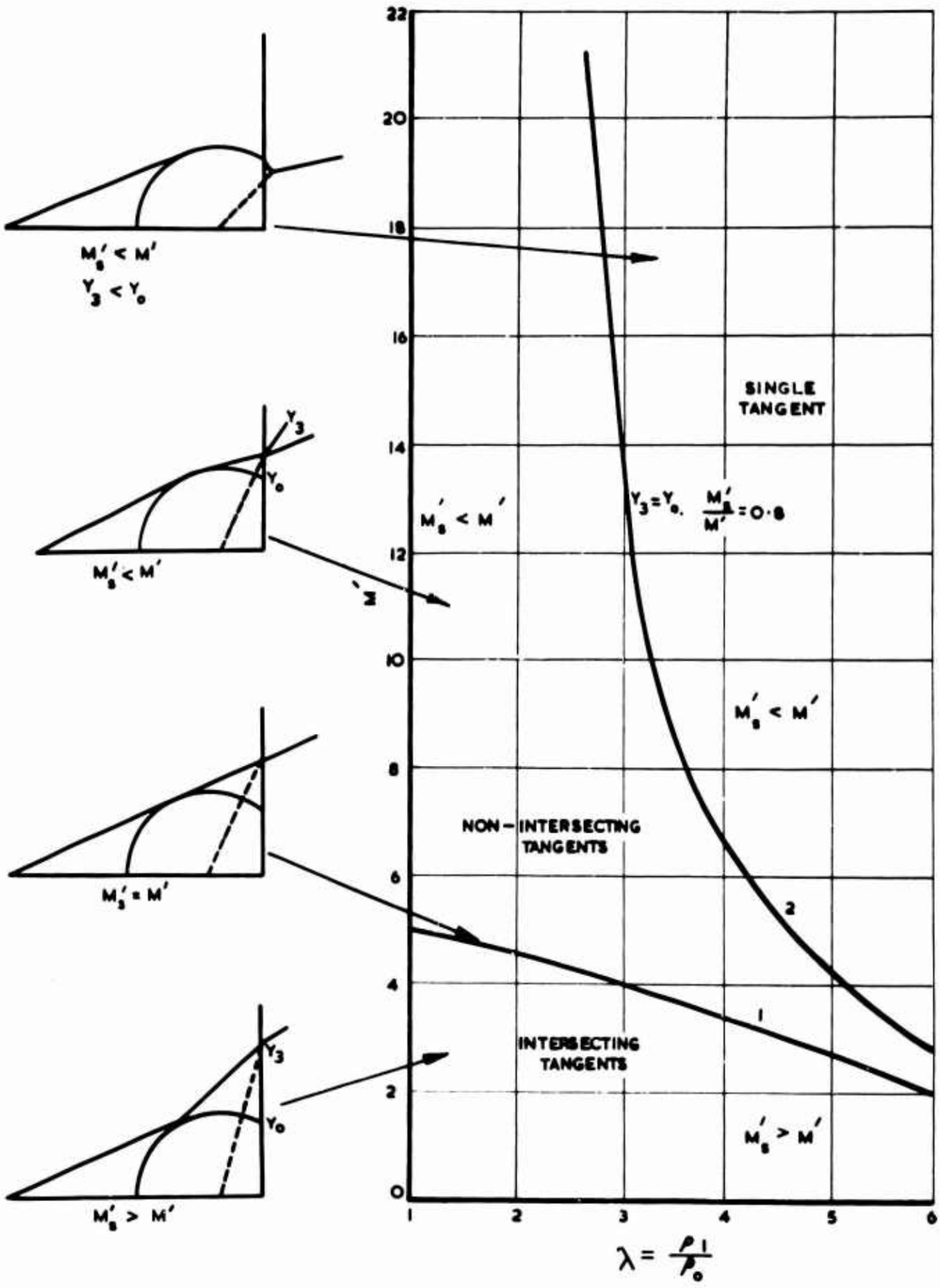


FIG. 9 CHANGE OF BOW WAVE SHAPE WITH CHANGE OF SHOCK STRENGTH AND MISSILE VELOCITY

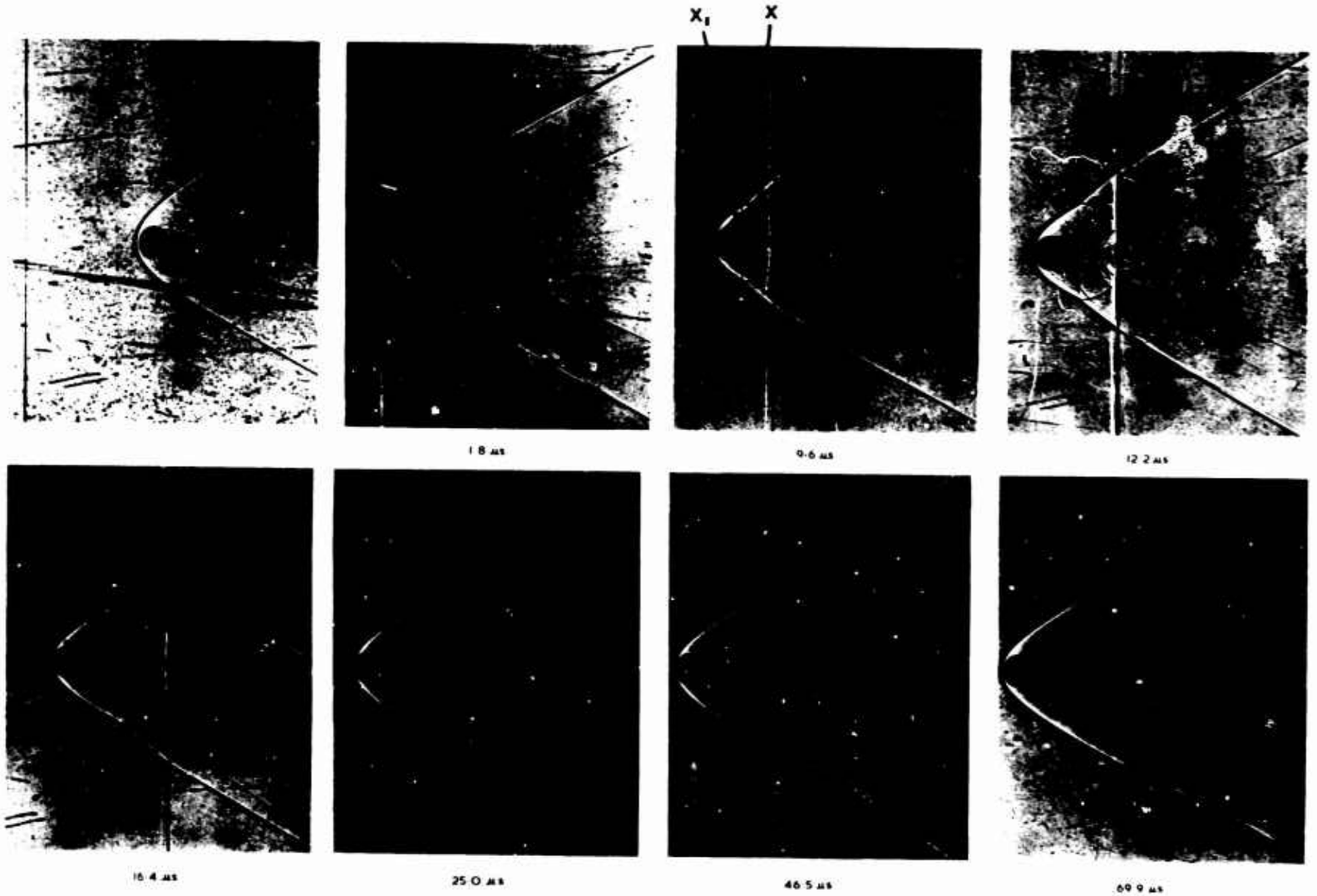
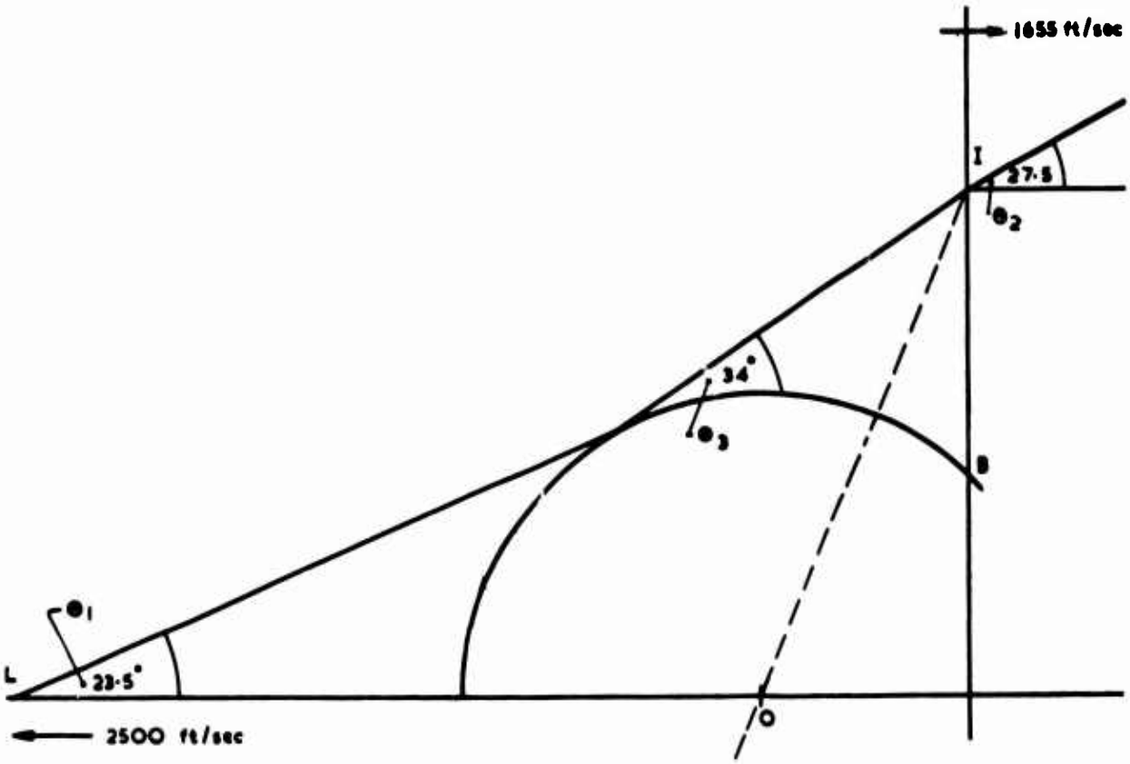
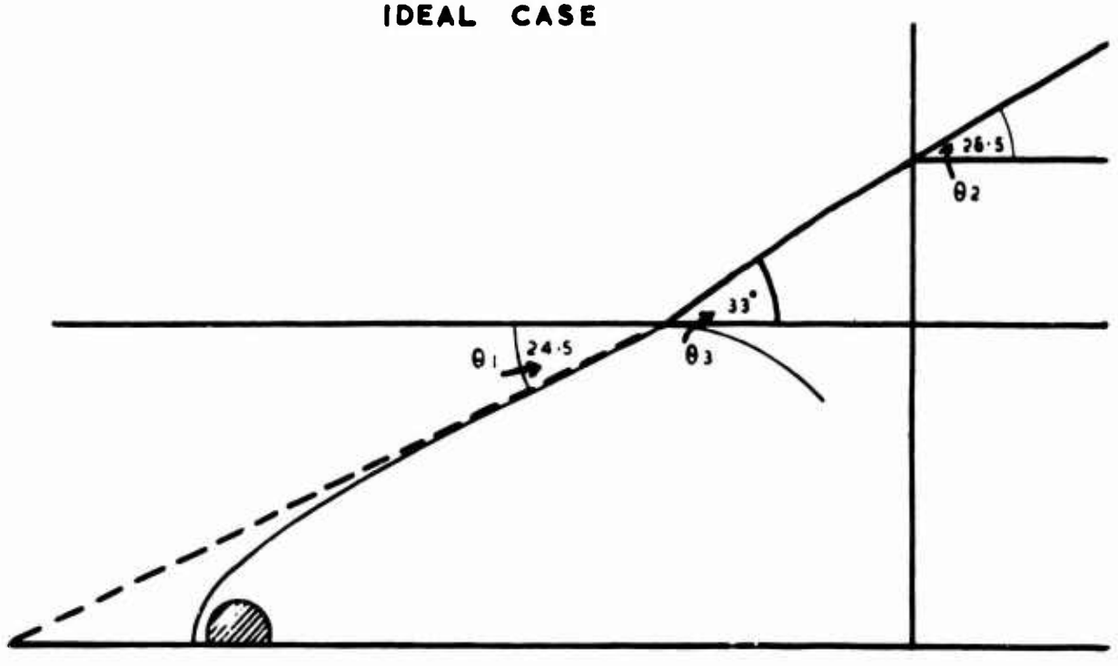


FIG. 10 MISSILE - SHOCK PENETRATION



IDEAL CASE



SPHERE

FIG. 11 COMPARISON BETWEEN IDEAL AND SPHERE CASES

DETERMINATION OF HOT GAS THERMAL CONDUCTIVITY BY SHOCK TUBE EXPERIMENTS.

G. Smeets
Deutsch- Französisches Forschungsinstitut
St. Louis, Haut Rhin, France

INTRODUCTION

There exist two groups of gas properties. One group comprises the thermodynamic properties, that is, the properties of the gas in equilibrium. They are described by the equation of state, e. g. in the form of the Mollier- diagram. They can be calculated to a good degree of accuracy by using the atomic and molecular constants, which are very well known from spectroscopy.

The other group of gas properties are the transport properties, comprising thermal conductivity, viscosity and diffusion. In calculating these properties one must know the collision cross sections of the different constituent gas particles. Since our knowledge of the cross sections at present is still rather poor, one has to make assumptions. The theoretical results differ to some extend due to different assumptions made.

For low temperatures the transport coefficients are nevertheless well known, as they can be determined experimentally. There exist for example several methods allowing to measure the coefficient of thermal conductivity. But since nearly all of these methods make use of a constant heat flux, they will no longer work for temperatures higher than 1500° to 2000° K, as there exist no container material, being able to stand the high temperatures. Therefore experimental data of thermal conductivity become poor as well, when the high temperature area is concerned.

In the present paper the coefficient of thermal conductivity in air is determined experimentally in the temperature region $1140^{\circ}K \leq T \leq 6075^{\circ}K$ by means of a shock tube.

The idea is outlined in Fig.1, which showes in a schematic way the closed end of a shock tube with the reflected shock moving to the right. The shock heated homogenious region after the reflected shock touches on the cold end plate of the tube. The temperature jump in the separation area disappears immediately, and some time after the shock reflection a temperature distribution as shown in Fig.1 will have been formed. The kind of temperature distribution and the extension of this temperature boundary layer δ does somehow depend on the thermal condutivity of the gas. In the present paper this dependence is investigated and a method is developped, which allowes to determine the coefficient of thermal conductivity from interferograms of the temperature boundary layer. Fig.2 schemtically showes the closed end of the shock tube with a differential interferometer mounted perpenticular to the tube axis.

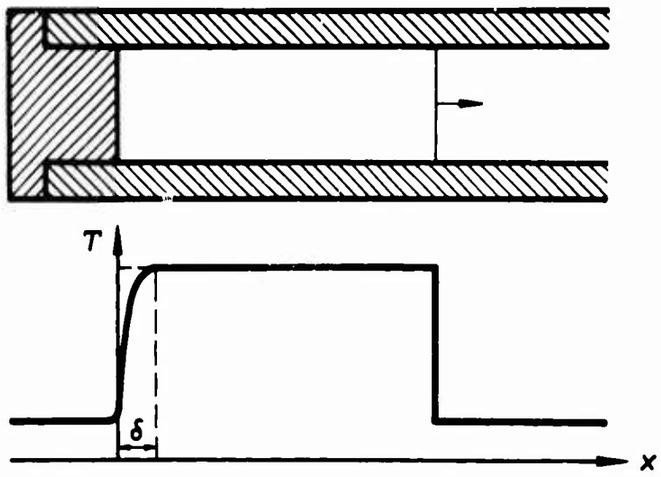


Fig.1 Temperature distribution (schematic) after shock reflection at the end plate.

THEORY OF THE TEMPERATURE BOUNDARY LAYER

The theory starts with the conservation equations. They are simplified, as the problem is one- dimensional. In addition one can assume the pressure to be constant in the region behind the reflected shock. This assumption does not hold in the first μ-second after shock reflection, because the abrupt cooling of the gas very close to the end plate surface gives rise to an expansion wave. Strong relaxation effects will be predominant in the very first moment as well, so that the theory cannot cover the first μ-second anyway. but some hundred μ-seconds after reflection, when the interferograms are taken, the assumption of constant pressure and gas being in local thermal equilibrium are pretty good.

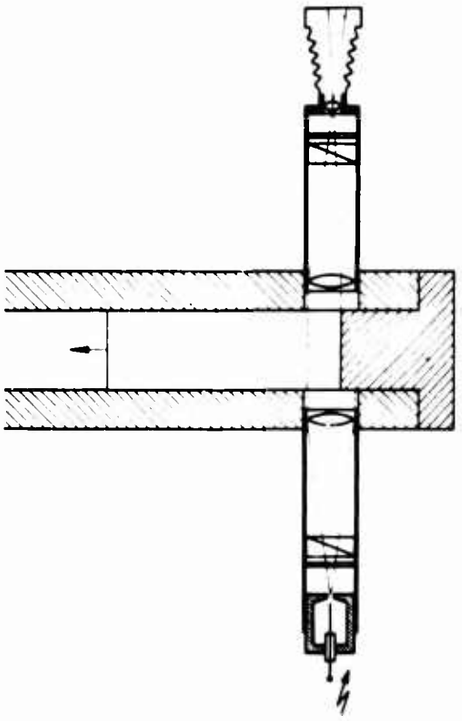


Fig.2 Arrangement for taking interferograms of the end plate temperature boundary layer.

Conservation of mass:

$$\frac{D\varrho}{Dt} + \varrho \frac{\partial u}{\partial x} = 0 \qquad (1)$$

Conservation of energy:

$$\varrho\ c_p \frac{DT}{Dt} = \frac{\partial}{\partial x}\left(k\frac{\partial T}{\partial x}\right) \qquad (2)$$

Equation of state:

$$p = Z\ \varrho\ R\ T \qquad (3)$$

The equation of state gives the relationship between the temperature T and the density ϱ at constant pressure p. The quantities c_p, Z and k are specific heat at constant pressure, compressibility factor and coefficient of thermal conductivity, all being functions of T and p.

One can reduce the above system of two partial differential equations to one ordinary differential equation by the following double transformation of coordinates:

$$x^+ = \int \varrho/\varrho_\infty\ dx, \quad \tau^+ = x^+/\sqrt{t} \qquad (4)$$

The resulting differential equation is:

$$T'' + r(T)T'^2 + s(T)\tau^+T' = 0 \qquad (5)$$

with r(T) and s(T) being the following functions of T:

$$r(T) = \frac{\partial}{\partial T}\ln\frac{k}{Z\ T}, \qquad s(T) = \frac{c_p\ p\ Z\ T}{2k\ R\ Z_\infty^2\ T_\infty^2} \qquad (6)$$

The boundary conditions are:

$$\begin{aligned} &\tau^+ \to \infty \quad \text{for} \quad T \to T_\infty \\ &\tau^+ = 0 \quad \text{for} \quad T = T_w \end{aligned} \qquad (7)$$

The subscript ∞ signifies the constant value outside the boundary layer, whereas w means the value at the wall.

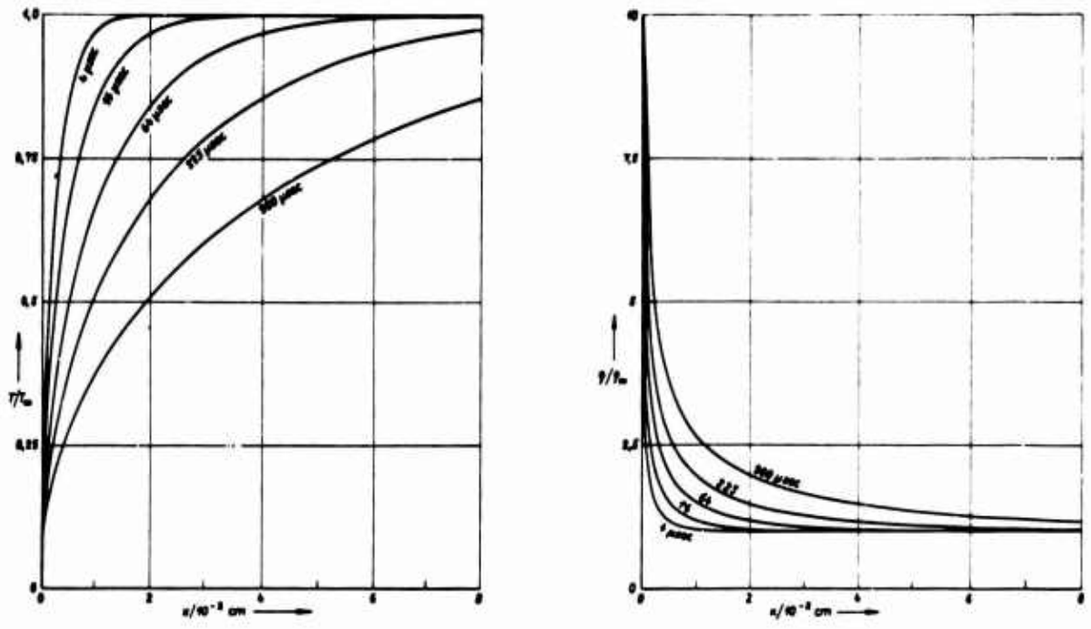


Fig.3 and 4 Temperature and density distributions in the end plate boundary layer for the ideal gas, when the thermal conductivity increases proportional to temperature.

Fig.3 and 4 show the temperature and density distributions for an ideal gas with the coefficient of thermal conductivity increasing proportional to temperature.

There is a very steep density gradient in the region close to the wall. The light rays being parallel to the wall when entering this region, are refracted because of the density gradient. They hit the wall and cannot form any picture of this region. Therefore on interferograms only the border of the boundary layer is visible.

At the border of the temperature boundary layer temperature is very close to its assymptotic value T_∞. The differential equation describing the temperature distribution can be linearized there:

$$T'' + s_\infty \tau^+ T' = 0 \qquad (8)$$

It has the solution:

$$\frac{T - C}{T_\infty - C} = \mathrm{erf}\left(\sqrt{s_\infty/2}\ \tau^+\right) \qquad (9)$$

The constant C can be calculated in approximation. It depends on the gas properties within the whole temperature re-

gion of the boundary layer. The constant

$$s_\infty = \frac{\varrho_\infty \, c_{p\infty}}{2 \, k_\infty}$$

only depends on the hot gas properties.

DETERMINATION OF THE THERMAL CONDUCTIVITY

The interfering light rays of a differential interferometer pass the test section very close to each other. When there is no density gradient, the field of view is filled with straight equidistant fringes.

A density gradient results in a fringe shift, which is proportional to the density gradient at the point concerned. Fig.5 showes how the temperature boundary layer is seen by a differential interferometer.

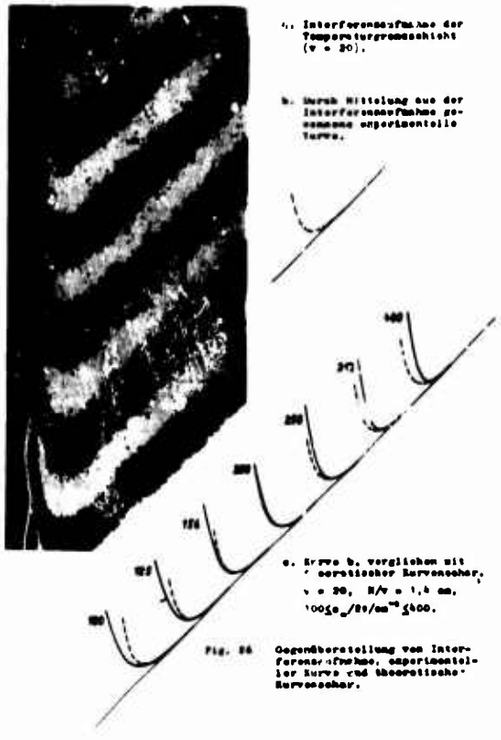


Fig.5
Interferogram and experimental curve compared with set of theoretical curves.

From this kind of interferograms the coefficient of thermal conductivity has been determined by the following indirect method of evaluation.

Equation (9) permits to calculate the temperature distribution for a certain hypothetic value of thermal conductivity. With the temperature distribution one calculates the density distribution and finally the fringe shift to be expected on the corresponding interferogram of the temperature boundary layer. Comparison with the experimentally taken interferogram cheques the correctness of the hypothetic value.

Fig.5 showes how evaluation is done in practice. As the fringes have no ideally smooth borders, the experimental curve (dotted) has been taken as an average of all the fringe borders in the interferogram. The comparison with a set of theoretical curves selects the one with the correctly assumed value of thermal conductivity k_∞.

It must be mentioned here, that the evaluation is somewhat complicated by the fact, that according to equation (9) the temperature distribution at the boundary layer border

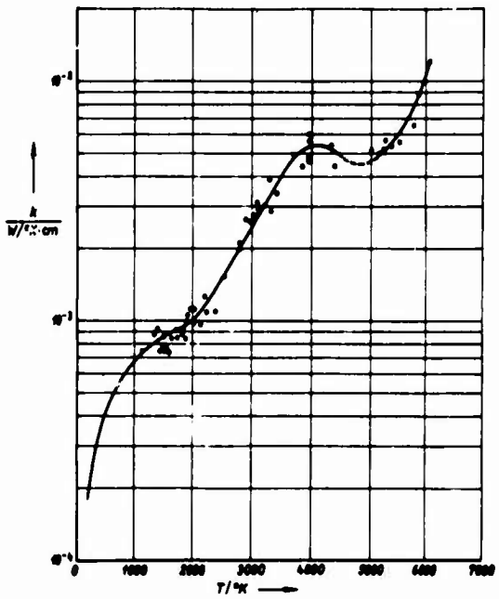


Fig.6 Temperature dependence of thermal conductivity in air for $\varrho=1/10\varrho_0$ (experimental).

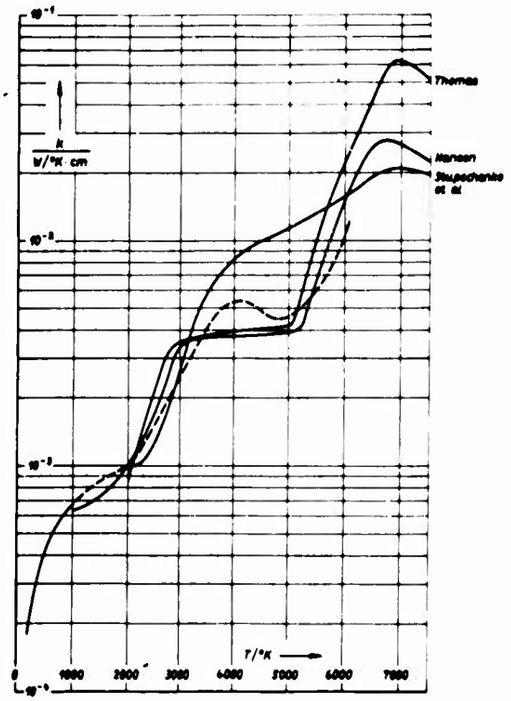


Fig.7 Thermal conductivity in air.
Experimental ($\varrho=1/10\varrho_0$).
Theoretical (p = 1atm).

though mainly depending on the hot gas thermal conductivity k_∞ does also depend on C. To calculate the constant C one must already know the thermal conductivity for the lower temperature region. So one has to evaluate a series of interferograms corresponding to ascending temperatures T_∞.

Fig.6 showes the coefficient of thermal conductivity in air, determined experimentally from about 50 interferograms. The possible error has been estimated to be inferior to 50%.

In Fig.7 the experimental curve is compared with 3 theoretical curves by Thomas, Hansen and Stupochenko. There is fairly good general agreement. The theoretical curves differ due to different assumptions concerning the collision cross sections of the gas particles.

The theoretical curves in Fig.7 have been taken from a paper presented by James A. Fay on the AGARD Hypersonics specialists' conference in Brussels (April 1962).

INTERACTION OF SHOCK WAVES WITH TAPER SECTIONS*

M. Dvir, J. Low, J. Stricker and S. Maniv
Microwave Division, Department of Physics
The Hebrew University
Jerusalem, Israel.

INTRODUCTION

The passage of a shock wave through ducts has been treated theoretically by many authors (Refs. 1–4). These theories can be divided into two types. The steady state theory matches parameters across an instantaneous area change. Given strong shock waves, an area change of 4 and an ideal gas with $\gamma = 1.4$, it predicts a ratio of the Mach Number upstreams (M_U) and downstreams (M_D) as

$$\frac{M_D}{M_U} = 1.15 .$$

The linear theory has recently been reviewed by Chester (Ref. 3). This theory leads to the following set of formulae

$$\frac{dA}{A} = \frac{2M_U}{(M_U^2 - 1)K(M_U)}\, dM$$

where $K(M_U)$ is a function of γ and M_U. For arbitrary large cross-section this can be written as $Af(M) \frac{\gamma}{K}$ constant. For $M_U \sim 8$ and for the above conditions this leads to $(M^2 - 1)A^K$ = constant with $K = 0.396$ and therefore

$$\frac{M_D}{M_U} = 1.31$$

*The research has been supported in part by the Airforce Office of Scientific Research, Mechanics Division, through the European Office of Aerospace Research (OAR).

The larger velocity predicted by the linear theory must eventually attenuate to the steady state value since far downstreams one should not be able to discriminate between these two theories.

Neither the linear nor the steady state theory take into account the various mechanisms of attenuation which presumably are caused by boundary layer and other higher order viscosity and heat transfer effects.

The impetus for our study of the shock speed behind taper sections came through an analysis of the time dependence of the electron density behind such a taper section. These results were very different from those found in a straight shock tube (Ref. 5), showed anomalous electron density and several sharp peaks indicating as if several shock waves were set up by the constriction. A literature search showed that while considerable research was carried out with the flow through nozzles behind the diaphragm, very little reported experimental information exists of a flow of an established shock wave through such a nozzle. An exception to this, however, are the recent measurements by Russel (Ref. 6). Our results indicate that the various theories do not account for a shock tube flow through such a constriction. The performance of small diameter shock tube deviates considerably from that predicted by a simple one dimensional shock tube theory.

EXPERIMENTAL TECHNIQUES, RESULTS AND INTERPRETATION

The experiments were designed so that the only perturbing influence on the shock wave would be the taper section. The pressure driven shock tube has been described previously (Ref. 7). It consists briefly of a high pressure chamber of 1" I.D., 60cm long, followed by different conical tapers, and a tube "a" of 0.5"I.D. and variable length, ending in a dump tank. The conical reaction was carefully machined, polished, and aligned. The velocity measurements (M_D) were made with spark plugs (Ref. 7), 12cm apart, and were measured consecutively at five different positions in the section "a". Upstreams of the taper section measurements (M_U) were made up to 80cm before the nozzle opening. It was established that the shock wave before entering the nozzle has a regular behaviour (shape) with hardly any, or only small attenuation. It should also be remarked that if the $\frac{1}{2}^{\circ}$ nozzle is placed right behind the diaphragm a nearly linear attenuation curve results. In all these experiments the driven gas was air, and the driver, either H_2 or He.

The transmitted shock speed was measured as a function of the following parameters.

1. Angle of the transition taper (90°, 60°, 30°, 15°, $1^{\circ}12'$ and $36'$).
2. Distance "a" from the exit of the taper section. Measurements were made from 9cm to 175cm downstreams. All measurements are referred to the average speed over a 12cm distance at the midpoint.

3. The initial low pressure p_1, at 0.1, 1, and 5 Torr.
4. The initial high pressure p_4.

Before commenting on our results we briefly note the main differences between our experiments and those of Russel.

(a) Our speed measurements were made over small distances, and hence sudden variation in the Mach No. could be easily detected, whereas Russel's measurements were averages over large distances.

(b) Russel used a small steel insert inside shock tube followed by a conical section. It has been our experience that such inserts (cookie cutter section) modify the flow pattern somewhat. Moreover, the boundary layer problem is obviously different in these two cases since in our cases the boundary layer of the shock wave interacts with the taper section.

(c) Finally our measurements were made over larger and smaller angles of conical sections and over a larger and higher Mach range.

We shall illustrate only a few of our results.

Nozzle angle 90°, p_1 : 5 and 1 Torr: This is shown in Figs. 1 and 2. The results indicate fluctuations in the Mach No. (M_D) with one or two pronounced minima, the position of which is a function of M_U and p_1.

Nozzle angle 15° and 1°12' . 5 Torr: Figs. 3 and 4 give the results for these taper angles. The results are qualitatively similar but do not show such strong fluctuations.

The striking features of all these Figures are the following:

1. The maximum of the ratio $\frac{M_D}{M_U}$ falls usually between the values calculated from the linear or the steady state theory but closer to the linear theory. At very low pressures the values may be somewhat larger than the prediction of the linear theory.

2. At large distances downstreams the final shock velocity is nearly the same for all taper sections in agreement with the prediction of the steady state theory. The absolute value of the Mach No. is somewhat lower; mainly because of general attenuation in the narrow shock tube. If M_D values are corrected for this attenuation $\left(\frac{\Delta M}{\Delta a} \sim -0.012 \ \frac{\text{Mach}}{\text{cm}}\right)$ the resultant values are close to the calculated values by the S.S. theory.

3. There are variations of shock velocity close to the exit of the nozzles. These maxima and minima are more pronounced for small values of p_1 and for tapers with large angles. The first peak usually occurs within 30-50cm from the exit of the nozzle. The appearance is similar to a spatial interference effect. For tapers with small angles these fluctuations are small and nearly washed out (Ref. 8).

A clue to these effects is obtained from the microwave attenuation measurements which were taken simultaneously with these measurements. Fig. 5, 6 and 7 show microwave attenuation curves at 1.8, 11.8cm for the sudden (90^{o}) constriction and for a very gradual taper (36^{1}). The last curve is similar to many microwave attenuation curves that are obtained for shock waves in which the testing time is not sufficient. However, for the 90^{o} constriction one clearly observes the evolution of two pronounced peaks, one of which attenuates rapidly at distances downstreams. The shock velocity measurement, because of the poorer resolution, cannot detect these subtle effects.

The simple one dimensional theories cannot explain these phenomena. Part of the shortcomings of all the present theories are that they do not take into account the interaction of the reflected and the rereflected waves with the shock wave,which may result in constructive or destructive interference. It also neglects the interaction of the boundary layers with the transition section, the effects of the finite time of diaphragm rupture, and finally the effects of turbulence which will effect the viscosity and the heat transfer. It is also clear from these results that the performance of small diameter shock tube cannot be approximated by a simple shock tube theory.

REFERENCES

(1) R. F. Chisnell. J. Fl. Mech. 2, 286 (1957).

(2) W. Chester. Quart. J. Mech. Appl. Math. 6, 440 (1953)

(3) W. Chester. Adv. in Appl. Mech. 6, 119 (1960)

(4) G. B. Whitham. J. Fl. Mech. 4, 337 (1958)

(5) M. Dvir and W. Low. Comptes Rendus de la VI^{e} Conference Internationale sur les Phénomènes d'Ionisation dans les Gas, Vol. IV, Paris 1963, p. 324

(6) D. A. Russel. Thesis. Ph.D., Cal. Inst. Techn. (1961)

(7) M. Dvir and W. Low. Phys. of Fluids 7, 570 (1964)

(8) R. A. Alpher and D. R. White. J. Fl. Mech. 3, 417 (1958), mentions that they have observed a rapid acceleration of the shock to a maximum velocity in a system in which the nozzle follows the diaphragm. They also mention that this is followed by a rapid deceleration. However, in their system a stable shock wave has not yet been formed as it passes through the nozzle.

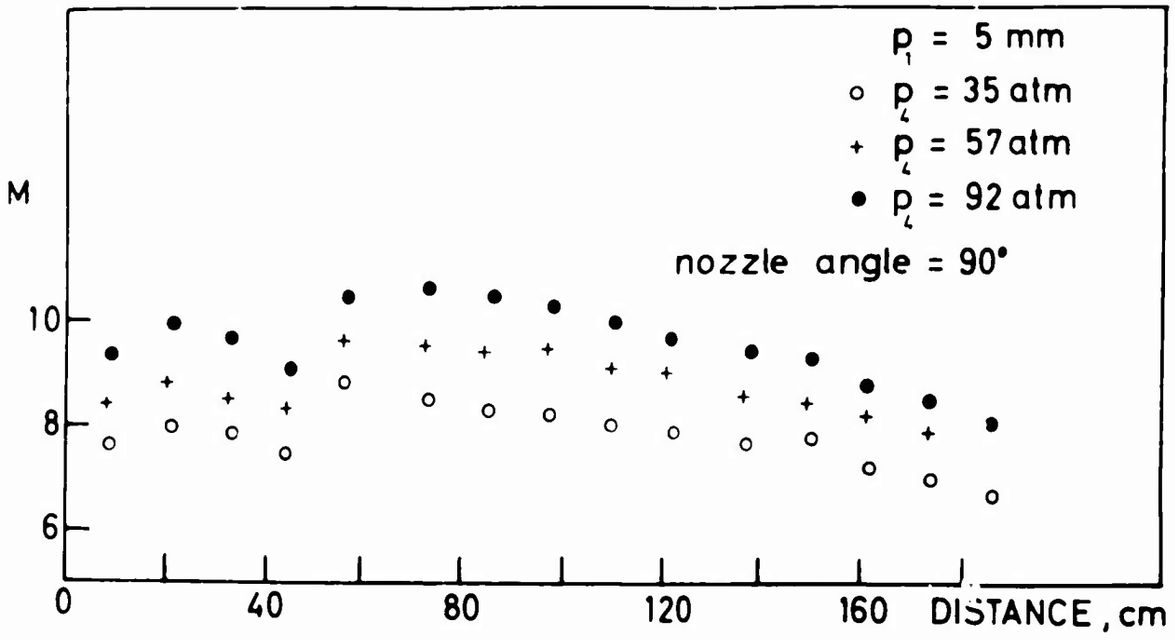


Figure 1

Mach No. as a function of distance from a 90° taper. p_1 = 5 Torr

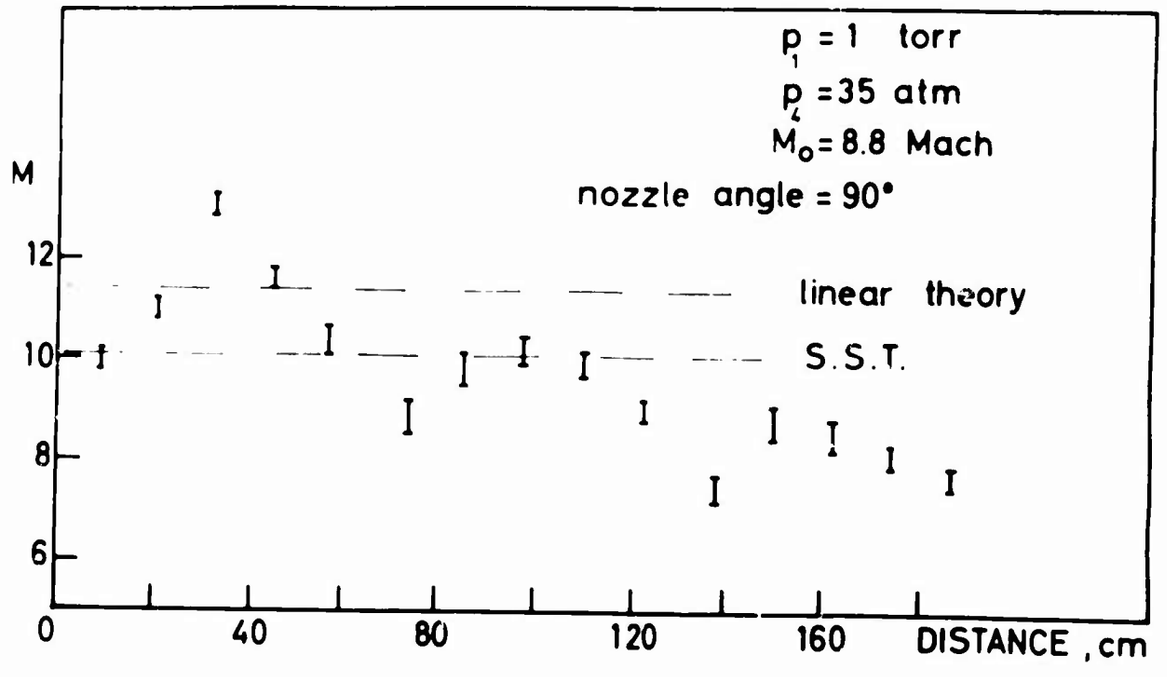


Figure 2

Mach No, as a function of distance from a 90° taper. p_1 = 1 Torr

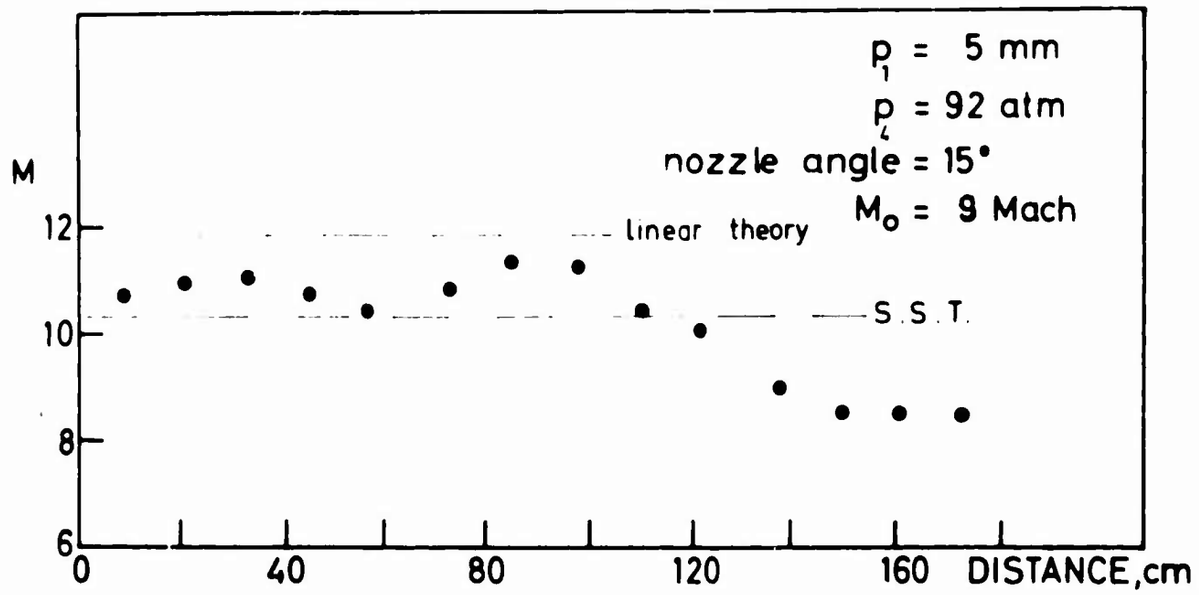


Figure 3

Mach No. as a function of distance from a 15^o taper. p_1 = 5 Torr

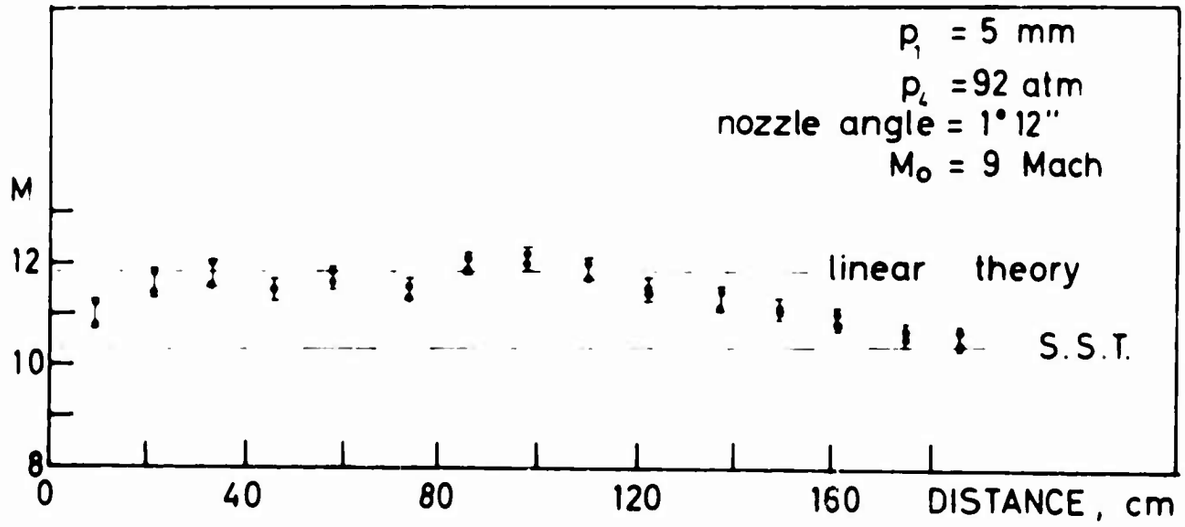


Figure 4

Mach No. as a function of distance from a $1^o12'$ taper. p_1 = 5 Torr.

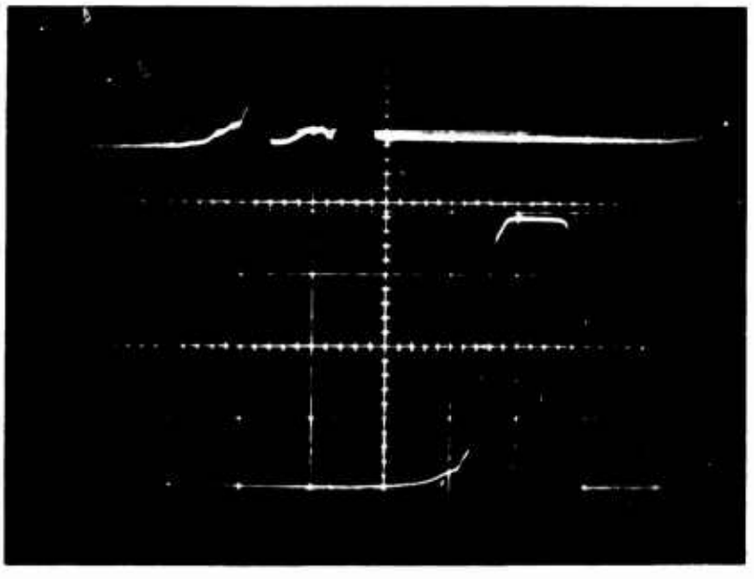


Figure 5

Microwave Attenuation at 1.8cm from the 90^{o} taper.

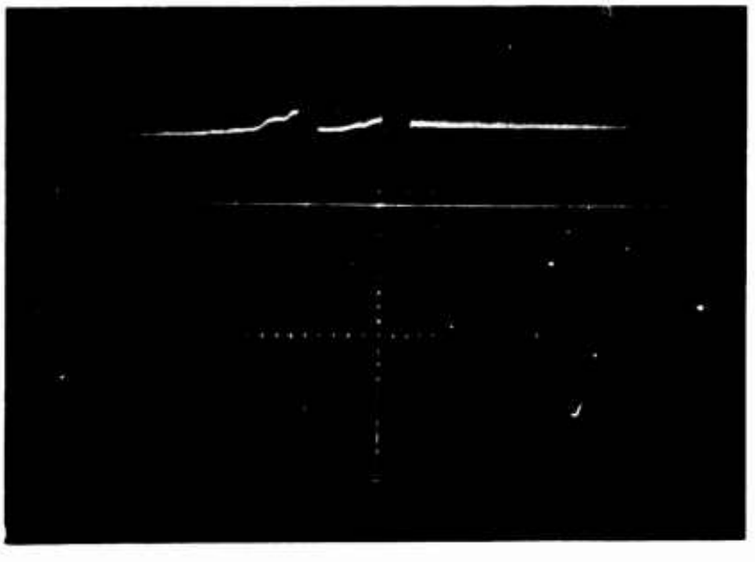


Figure 6

Microwave Attenuation at 11.8cm from the 90^{o} taper.
N.B. The emergence of two peaks.

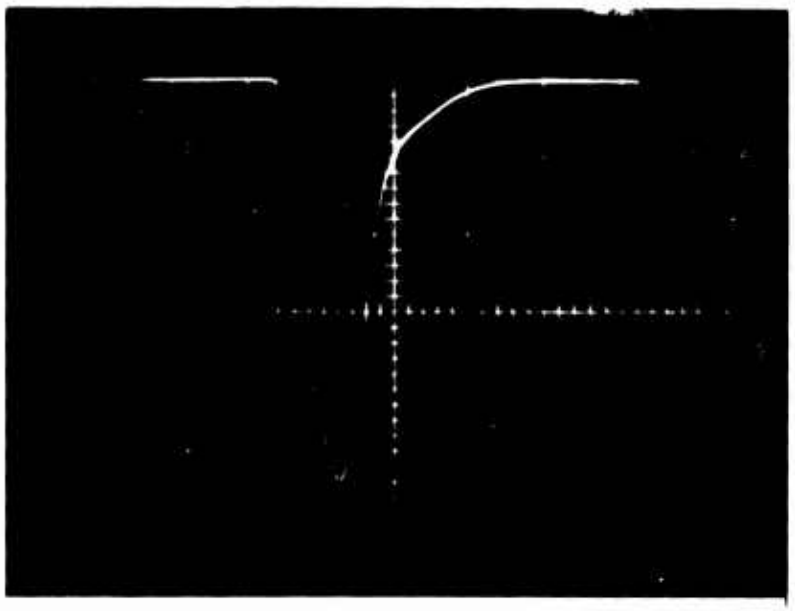


Figure 7

Microwave Attenuation at 11.8cm for a gradual 36' taper.

NF_2 DECOMPOSITION BEHIND SHOCK WAVES

A. P. Modica* and D. F. Hornig
Frick Chemical Laboratory
Princeton University, Princeton, N. J.

ABSTRACT

The decomposition of the NF_2 radical in excess argon was studied behind incident shock waves over a temperature range from 1400°K to 2000°K at total concentrations between 0.9×10^{-3} and 1.9×10^{-3} mole/liter. The NF_2 radicals produced from shocked N_2F_4 were characterized by absorption spectra in the 2600Å region, recorded with a Hilger medium quartz spectrograph. Kinetics were deduced from oscillogram histories of NF_2 absorption at 2600Å. The rate law for decomposition was first-order in both NF_2 and argon concentration, $d[NF_2]/dt = -k_{Ar}[Ar][NF_2]$, with

$$k_{Ar} = 1.62 \times 10^{10} T^{1/2} \exp(-47{,}838/RT) \text{ liter/mole-sec.}$$

The absorption-spectroscopy results are compared with shock tube/TOF mass spectrometer data obtained at higher temperatures.

INTRODUCTION

The tetrafluorohydrazine-difluoramino radical equilibrium was shown to exist by ultraviolet,[1] infrared[2] and mass spectrometric[3] observations. A kinetic study of this system was conducted in shock waves and second-order rate constants for the reaction, $N_2F_4 \xrightarrow{Ar} 2NF_2$, were determined. Recently, this reaction was used to investigate the high temperature kinetics of the NF_2 radical decomposition in a shock tube coupled to a time-of-flight mass spectrometer.[5] The mass spectrometer data revealed that at temperatures above 1900°K, the NF_2 radical decomposed by the reaction

R1 $\quad NF_2 + Ar \longrightarrow NF + F + Ar$

* Group Leader, Aerophysics Department, Avco, Wilmington, Mass.

and that at lower temperatures, the disproportionation reaction

R2 $NF_2 + NF_2 \longrightarrow NF_3 + NF$

may have occurred.

In the present shock tube work, the NF_2 radical decomposition was examined by heating N_2F_4-Ar gas mixtures to temperatures between 1400°K to 1900°K behind incident shock waves. The progress of the reaction was followed by monitoring the time rate of change of NF_2 in absorption at 2600Å. Experimental evidence supporting R1 as the decomposition mechanism and the rate constants for this reaction are reported.

EXPERIMENTAL TECHNIQUE

The NF_2 radicals were produced for kinetic study by dissociating N_2F_4 in a shock tube under pressure and temperature conditions, such that the formation of NF_2 was instantaneous. The NF_2 concentration was determined by light absorption at 2600Å. Gas mixtures containing N_2F_4 (Dupont, 99% purity) and argon (Matheson, 99% purity) in mole ratios of 1:103, 1:204, and 2:104 were studied.

Complete details of the experimental apparatus have been described previously (ref. 4). Shock waves were generated in a stainless steel shock tube, having a driver section 2-ft. in length of 2-in. i.d. and a driven section 8-ft. in length of 1 3/8-in. square-cross section. Cold driving with helium and plastic diaphragms (Kodapak film) in combinations of 3 mil and 5 mil thickness were used to obtain desired shock velocities. The driven section was provided with three observation stations, the first and third being light-screens to determine the shock velocity, the remaining one to monitor the NF_2 UV-absorption behind the shock front. A Beckman (Model 7260) time interval meter was used to measure the shock transit time between light screens.

The optical system for UV-absorption measurements consisted of a xenon-mercury arc lamp (Hanovia, type D-901B-1), a quartz lens, a pair of collimating slits (1 mm slit width), a Baird Atomic optical interference filter (2600Å peak wavelength), and a 1P28 photomultiplier detector. The output of the photomultiplier was displayed on a Tektronix 535A oscilloscope and recorded on 3000 speed Polaroid film. The time-delay-sweep of the scope, triggered by the pulse from the first light-screen, was employed to synchronize the oscilloscope trace with the arrival of the shock wave in the vicinity of the absorption station. A schematic diagram of the experimental set up is shown in Figure 1.

Temperature and density conditions behind the incident shock wave were calculated from the Rankine-Hugoniot equations, considering N_2F_4 completely dissociated to NF_2 immediately behind the shock front.[6] Dependence of the incident temperature and density ratio on shock velocity for the N_2F_4-Ar gas mixtures studied is presented in Figures 2 and 3. Because

of shock attenuation which amounted to a shock velocity decrease of 1.9% and 0.93% per 10 cm of tube length for the weakest and strongest shocks, the error in shock temperature was almost 10°K under conditions of interest.

UV-ABSORPTION OF THE NF_2 RADICAL

The UV-absorption spectrum of NF_2 taken with high dispersion instruments consists of a series of diffuse bands in the 2600Å region.[7,8] In this study similar spectra were also obtained from 5:100 N_2F_4-Ar gas mixtures shock heated to 800°K at 2 atm pressure (Fig. 4). Ultraviolet-absorption spectra were recorded on 103-F plates using a Hilger medium quartz spectrograph with a 50μ slit width. A xenon flash-lamp having a 200 microsecond flash was synchronized with the shock front and multiple exposures totaling 1 millisecond were taken.

For kinetic study the absorption at 2600Å was monitored with a photomultiplier. A typical absorption record is shown in Figure 5. The NF_2 concentration was obtained from the transmission equation

$$\frac{I_0}{I} = \exp(\epsilon L[NF_2]) = \frac{H}{H-h} \qquad (1)$$

where I_0 and I equal the intensity of the incident and transmitted light, ϵ equals the extinction coefficient (liter/mole-cm), L equals the optical path (3.5 cm), and $[NF_2]$ equals the concentration of species behind the shock. The quantity H is the deflection of the oscilloscope trace for 100% absorption produced by a light chopper, h is produced by the NF_2 radicals during the run. The absorption coefficient ϵ was determined from the initial rise in absorption at the shock front and varied slightly with temperature (± 10% from 240 liter/mole-cm) as seen in Figure 6.

KINETICS OF NF_2 DECOMPOSITION

According to reactions R1 and R2, the decomposition of NF_2 radicals may be either first-order or second-order in NF_2 concentration. In R1 if argon acts as a second-body, the rate law

$$-d[NF_2]/dt = k_{Ar}[Ar]\,[NF_2] \qquad (2)$$

may apply, yielding upon integration

$$-\ln(1-\alpha) = k_{Ar}[Ar]t \equiv k_{exp}\,\rho_{21}\,t_l \qquad (3)$$

for the fraction of NF_2 species (α) decomposed in time.[9] When the experimental data were plotted $\log(1-\alpha)$ against t_l, excellent straight line fits

were obtained (Fig. 7) which demonstrated the decomposition reaction to be first-order in NF_2 concentration. To check the kinetics for Ar, a log-log plot of the first-order rate constant (k_{exp}) and Ar concentration was examined for a given temperature (Fig. 8). The slope of the line (0.7, least squares value) indicated, within experimental scatter, the NF_2 decomposition was approximately first-order in argon concentration.

The results of the kinetic study are compiled in Tables 1, 2 and 3. Second-order rate constants for NF_2 decomposed by argon were determined over a temperature interval from 1400°K to 2000°K at total concentrations between 0.9×10^{-2} and 1.9×10^{-2} mole/liter. These rate constants are plotted against reciprocal temperature in Figure 9 and are least-squares fitted by the function.

$$k_{Ar} = 1.62 \times 10^{10} T^{1/2} \exp(-47{,}838/RT) \text{ liter/mole-sec}, \qquad (4)$$

using a simple collision theory expression. The apparent activation energy is observed to be lower than the (NF-F) dissociation energy,[10] E_o = 66.3 ± 12 kcal/mole, which may reflect participation of internal degrees of freedom in dissociation. The error in temperature due to attenuation (approximately 5°K for higher shock temperature and 10°K for those lower) changes the activation energy by 300 cal/mole or the rate constant by about 10%.

DISCUSSION

Classical collision theories[11] for bimolecular reactions derive a rate constant in the form

$$k = \frac{PAT^{1/2}}{n!} \left(\frac{E_o}{RT} \right)^n \exp(-E_o/RT) \qquad (5)$$

where E_o is the minimum dissociation energy, A is the collision number and P is the steric factor. The quantity n is determined by the number of degrees of freedom leading to reaction and is related to the apparent activation energy E_a and E_o by the formula

$$n/2 = \frac{E_a - E_o}{RT} . \qquad (6)$$

For polyatomic species, n/2 is generally considered as the number of effective "oscillators" in the molecule and is found to vary between 1 and 2 for triatomics.[12] Regarding NF_2 with E_o = 66.3 kcal/mole and $\bar{T}$ = 1700°K (average value of present temperature range), n/2 is 5.5 which seems high. However, with the lowest value of E_o (54.2 kcal/mole) a more reasonable value of 1.9 is obtained.

From the shock tube/TOF mass spectrometer data (ref. 5), the rate constant, 1.98×10^7 liter/mole-sec at 2550°K and 7.17×10^{-4} mole/liter may be evaluated and compared to 6.5×10^7 liter/mole-sec by equation (4) of this work. In view of the wide range in concentration between the two studies (around 20-fold) and the rather good agreement in results, second-order kinetics for the decomposition of NF_2 in excess argon are clearly evident.

ACKNOWLEDGMENT

The support of the Office of Naval Research [Contract No. Nonr 1858(26)] in this study is gratefully acknowledged. We express thanks to Mr. John E. LaGraff for assisting in the reduction of data.

REFERENCES

(1) F. A. Johnson and C. B. Colburn, J. Am. Chem. Soc. 83, 3043 (1961)

(2) M. D. Harmony, R. J. Myers, L. J. Schoen, D. R. Lide and D. F. Mann, J. Chem. Phys. 35, 1129 (1961); M. D. Harmony and R. J. Myers, ibid 37, 636 (1962)

(3) J. T. Herron and V. H. Diebler, J. Chem. Phys. 35, 747 (1961)

(4) A. P. Modica and D. F. Hornig, "Kinetics of the Thermal Dissociation of N_2F_4 in Shock Waves," Princeton University, Report Nr. 357-275 (October 1963)

(5) R. W. Diesen, J. Chem. Phys. 41, 3256 (1964)

(6) For the shock tube performance calculations, the N_2F_4 and NF_2 enthalpy tables of Dr. D. R. Ettinger, Rohm and Haas Company, Redstone Arsenal Division (private communications) were extrapolated from 1000°K to 2000°K by a power series, $(H_T-H_0) = AT + BT^2 + CT^3$ [W. Moore, "Physical Chemistry" (Prentice-Hall, Inc., 2nd ed.-1955), p. 44]. The N_2F_4 dissociation energy was taken to be 19.35 kcal/mole (ref. 4).

(7) P. L. Goodfriend and H. P. Woods, J. Mol. Spec. 13, 63 (1964)

(8) L. A. Kuznetsova, Yu.Ya. Kuzyakov and V. M. Tatevskii, Optics and Spectroscopy 16, 295 (1964)

(9) The density ratio ρ_{21} is introduced as a correction to the laboratory time scale, since the gas being observed is initially heated by the shock wave further upstream.

(10) The (NF-F) bond energy was calculated from the heat-of-formation of NF_2, NF and F given in the JANAF tables (ARPA, Washington, D. C., U.S.A.)

(11) See R. Fowler and E. A. Guggenheim, "Statistical Thermodynamics," Cambridge University Press, Cambridge (1956)

(12) A. P. Modica and J. E. LaGraff, "Thermal Decomposition of C_2F_4 Behind Shock Waves: II. Kinetics and Equilibria of the $CF_2 = CF + F$ Reaction," Avco RAD-TM-65-4 (22 Jan 1965)

TABLE 1

NF_2 Decomposition in Shocked 1:103 N_2F_4-Ar Gas Mixtures

Run #	U_s (mm/μsec)	T_2 (°K)	ρ_{21}	$C_s \times 10^2$ (tot. shocked gas concn. mole/liter)	†$[NF_2]_o \times 10^4$ (mole/liter)	k_{Ar} (liter/mole-sec)
1	1.16	1440	3.46	1.88	3.63	3.31×10^4
2	1.18	1480	3.49	1.90	3.66	5.21×10^4
3	1.18	1480	3.49	1.61	3.13	7.41×10^4
4	1.18	1480	3.49	0.949	1.84	5.75×10^4
5	1.19	1500	3.50	1.90	3.67	7.25×10^4
6	1.19	1500	3.50	0.952	1.85	1.07×10^5
7	1.19	1500	3.50	0.952	1.85	9.25×10^4
8	1.20	1520	3.51	1.62	3.15	6.74×10^4
9	1.24	1605	3.56	1.45	2.82	1.65×10^5
10	1.255	1630	3.58	1.46	2.84	1.62×10^5
11	1.27	1675	3.61	1.47	2.86	5.00×10^5
12	1.31	1770	3.64	1.19	2.30	1.37×10^6
13	1.32	1800	3.64	1.19	2.30	1.24×10^6
14	1.33	1815	3.64	1.19	2.30	1.82×10^6
15	1.39	1950	3.68	1.00	1.94	2.90×10^6
16	1.40	1975	3.69	1.00	1.95	4.73×10^6

†Subscript "o" denotes concentration behind shock front before decomposition.

TABLE 2

NF_2 Decomposition in Shocked 1:206 N_2F_4-Ar Gas Mixtures

Run #	U_s (mm/μsec)	T_2 (^oK)	ρ_{21}	$C_s \times 10^2$ (tot. shocked gas concn. mole/liter)	$[NF_2]_o \times 10^4$ (mole/liter)	k_{Ar} (liter/mole-sec)
1	1.17	1475	3.46	1.51	1.46	6.96×10^4
2	1.19	*1500	3.47	1.32	1.28	5.42×10^4
3	1.20	1540	3.47	1.51	1.46	9.80×10^4
4	1.25	1650	3.51	1.43	1.39	1.35×10^5
5	1.25	1650	3.51	1.14	1.11	3.01×10^5
6	1.26	1670	3.51	1.43	1.39	4.97×10^5
7	1.28	1700	3.53	1.15	1.12	6.97×10^5
8	1.28	1700	3.53	1.44	1.40	8.65×10^5
9	1.29	1725	3.54	1.15	1.12	5.44×10^5
10	1.31	1775	3.56	1.16	1.13	4.69×10^5
11	1.34	1850	3.58	1.17	1.13	2.07×10^6
12	1.35	1875	3.59	1.17	1.13	1.54×10^6

*Corrected for attenuation by noting shock velocity further upstream where observed species were heated.

TABLE 3

NF_2 Decomposition in Shocked 2:104 N_2F_4-Ar Gas Mixtures

Run #	U_s (mm/μsec)	T_2 (^oK)	ρ_{21}	$C_s \times 10^2$ (tot. shocked gas concn. mole/liter)	$[NF_2]_o \times 10^4$ (mole/liter)	k_{Ar} (liter/mole-sec)
1	1.21	*1490	3.71	1.21	4.56	4.26×10^4
2	1.21	*1490	3.71	1.20	4.56	4.26×10^4
3	1.25	1580	3.75	1.53	5.78	1.40×10^5
4	1.26	1600	3.75	1.53	5.78	1.66×10^5
5	1.26	1600	3.75	1.53	5.78	1.77×10^5
6	1.30	1700	3.78	1.23	4.65	4.65×10^5
7	1.32	1740	3.79	1.24	4.66	5.11×10^5
8	1.34	1790	3.80	1.24	4.67	5.08×10^5
9	1.345	1800	3.80	1.03	3.92	1.15×10^6
10	1.36	1840	3.81	1.04	3.92	1.25×10^6
11	1.36	1840	3.81	1.04	3.92	1.29×10^6

*Corrected for attenuation by noting shock velocity further upstream where observed species were heated.

$S's$	SLITS
P_1, P'_1	931A PHOTOMULTIPLIERS
P	IP28 PHOTOMULTIPLIER
L	PLANO CONVEX LENS
F	OPTICAL INTERFERENCE FILTER
R_1, R'_1	TUNGSTEN FILAMENT LAMPS
R	ULTRA-VIOLET LIGHT LAMP

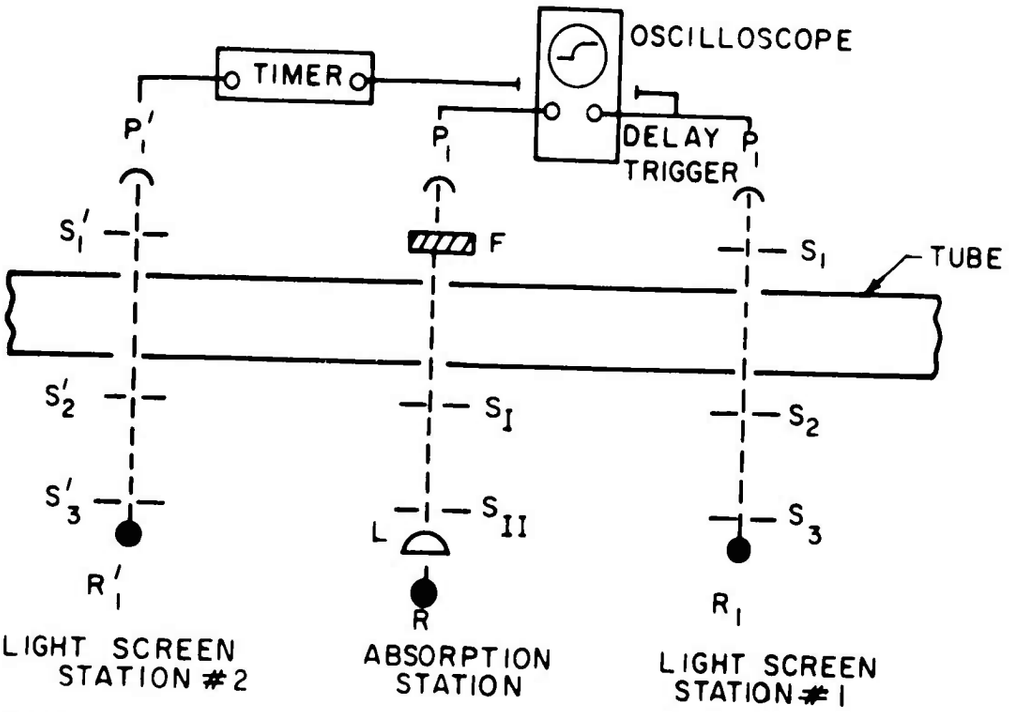


Fig. 1 Diagram of Light Screens and Absorption Station

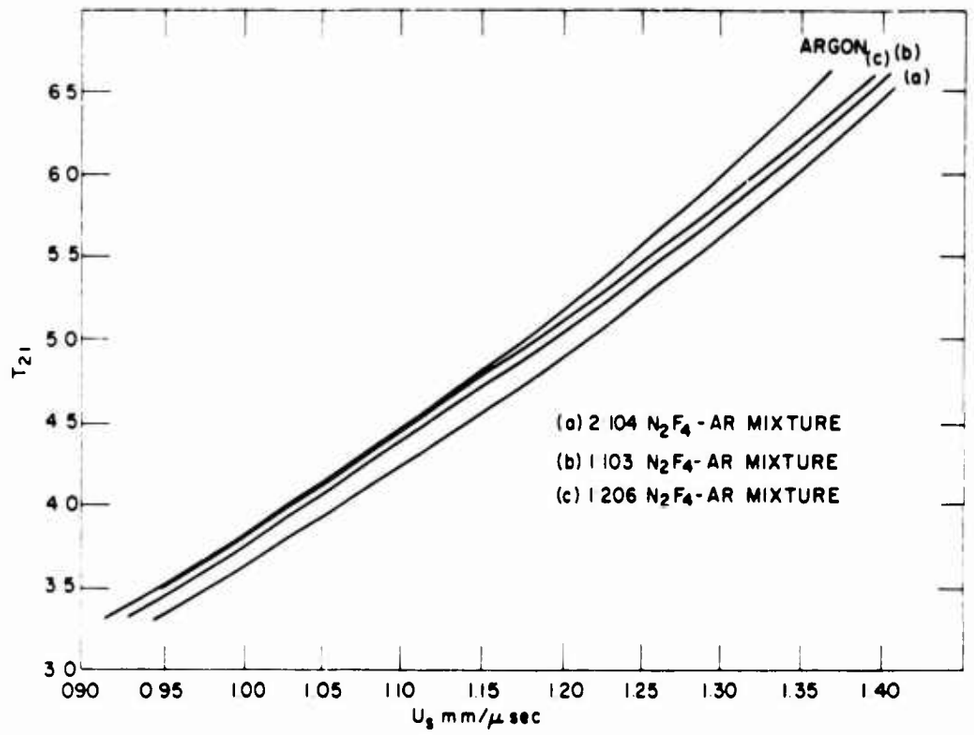


Fig. 2 Shock Tube Performance Data for N_2F_4 Completely Dissociated to NF_2 in Argon: Temperature Ratio Across Incident Shock versus Shock Velocity.

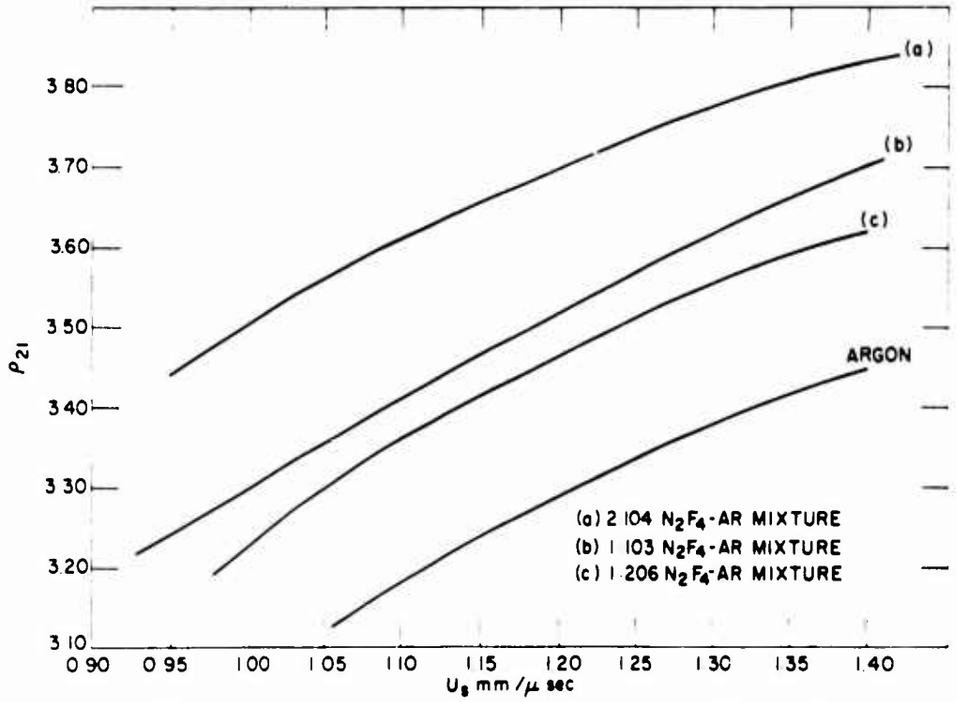


Fig. 3 Shock Tube Performance Data for N_2F_4 Completely Dissociated to NF_2 in Argon: Density Ratio Across Incident Shock versus Shock Velocity.

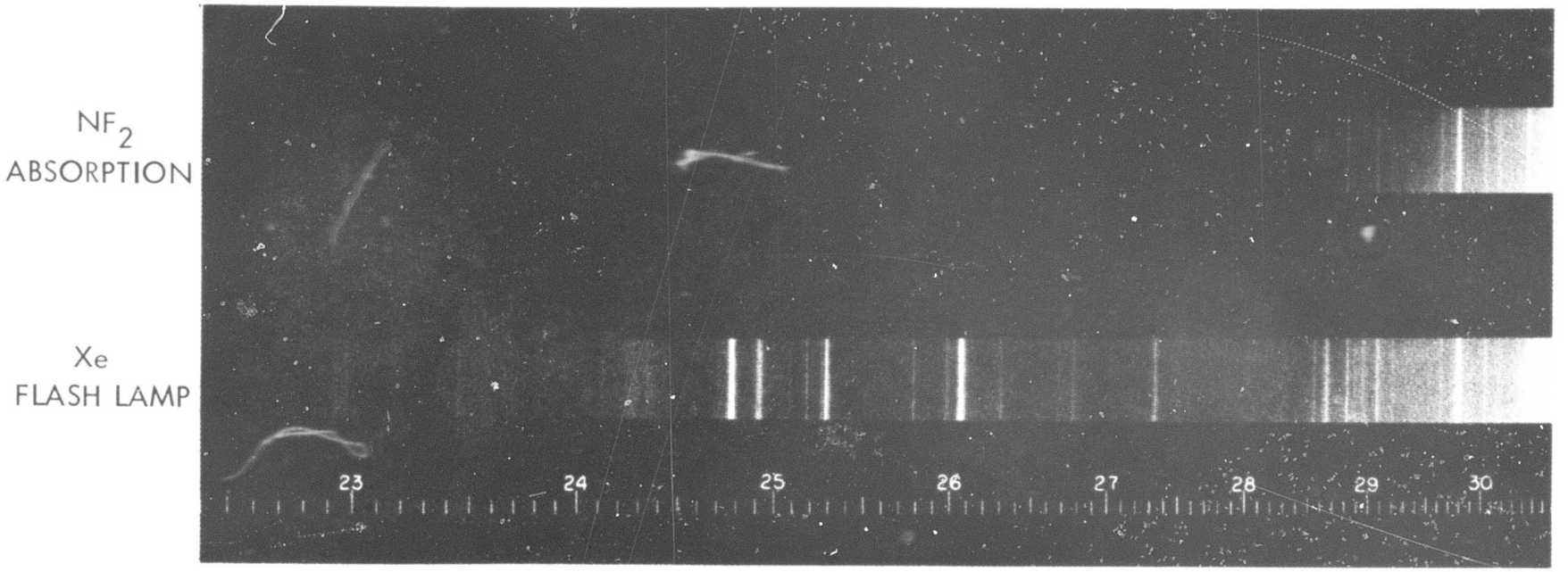


Fig. 4 Spectrogram of NF_2 Radical Absorption from Dissociated N_2F_4 Behind Shock Waves.

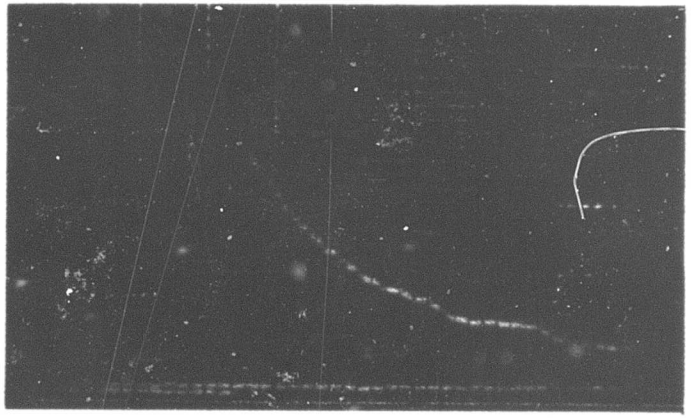


Fig. 5 Oscillogram of NF_2 UV-Absorption Behind Incident Shock Wave for a 2:104 N_2F_4-Ar Gas Mixture at 1800°K and 1.52 atm. Writing speed = 10 μsec/cm.

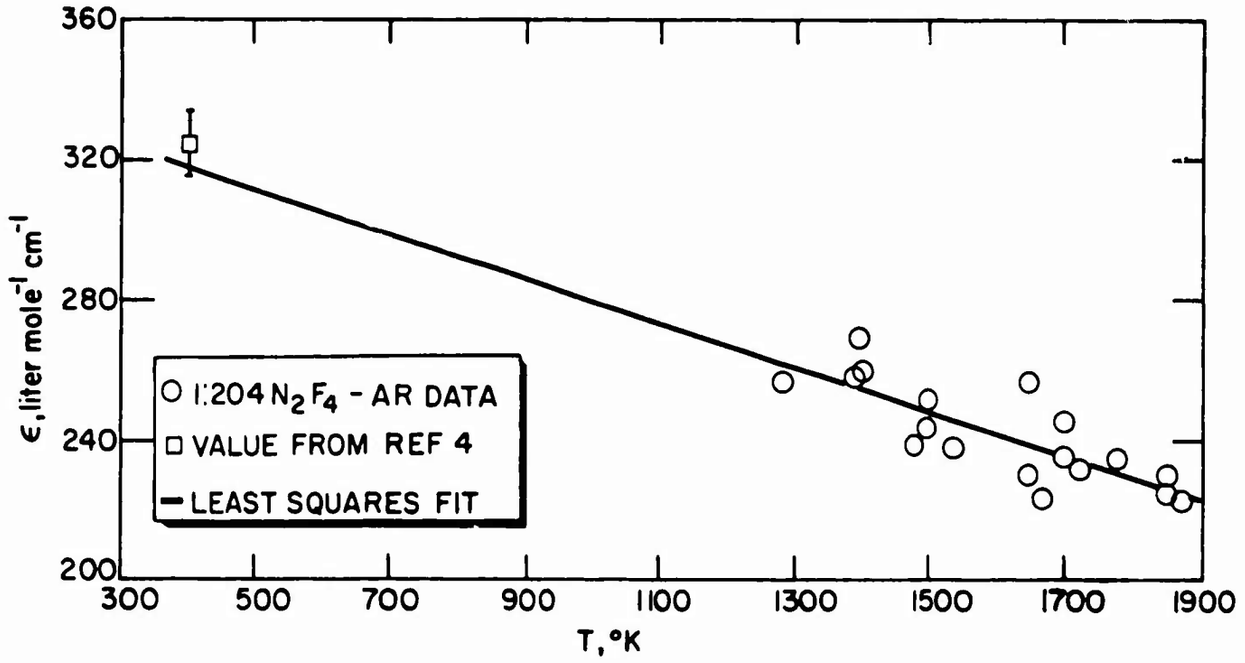


Fig. 6 Variation of the NF_2 Absorption Coefficient with Temperature

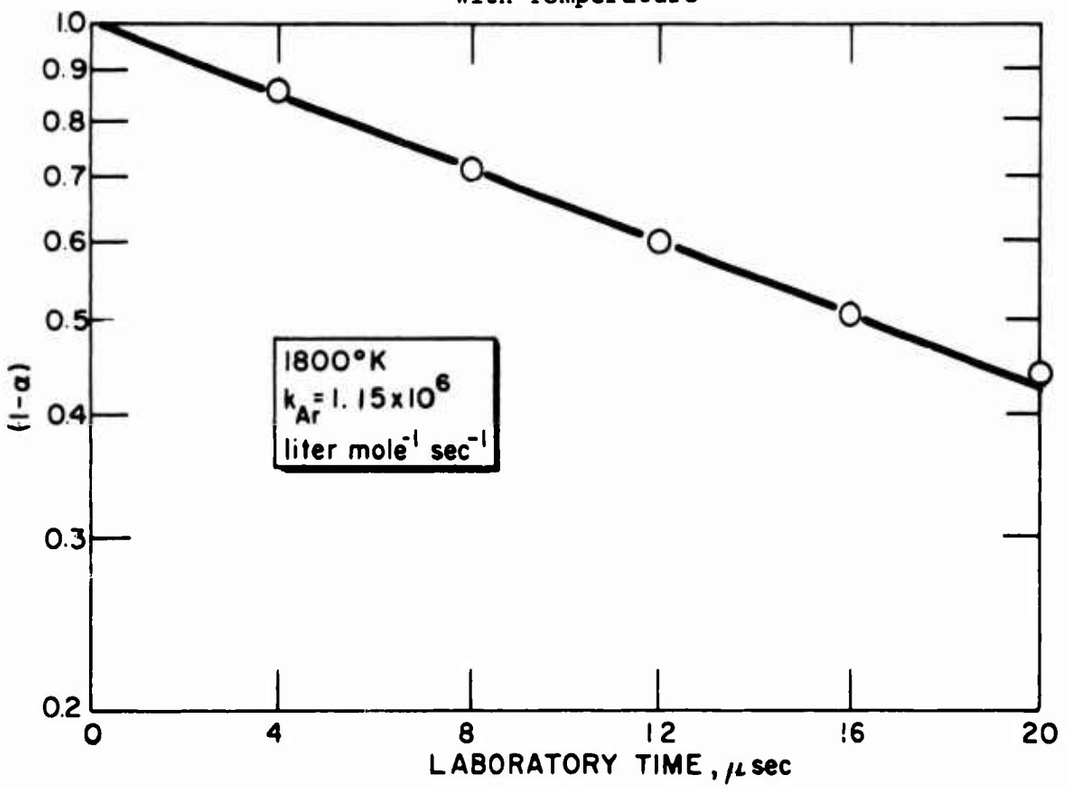


Fig. 7 Plot of log(1-α) versus Laboratory Time

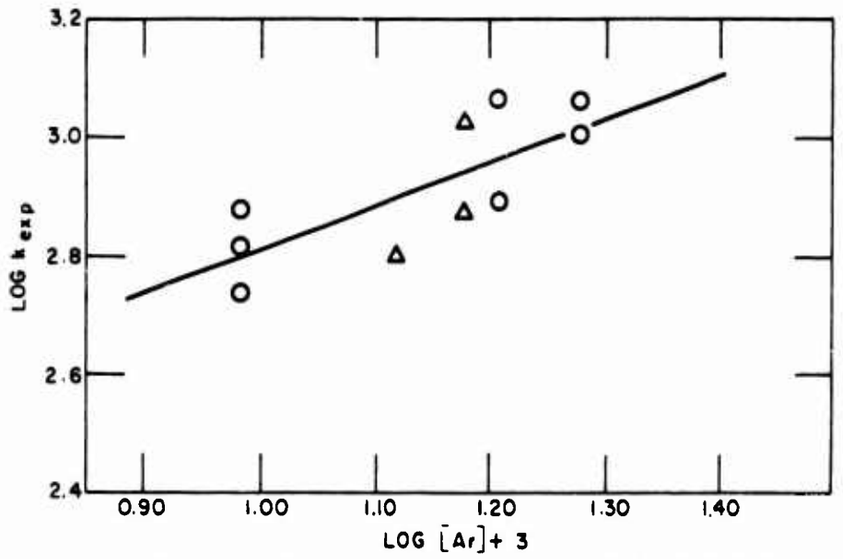


Fig. 8 Dependence of NF_2 First-Order Rate Constant on Ar Concentration. O, 1:103 N_2F_4-Ar Data and Δ, 1:206 N_2F_4-Ar Data Taken at, or Corrected to 1480°K with E_a = 47.838 kcal/mole.

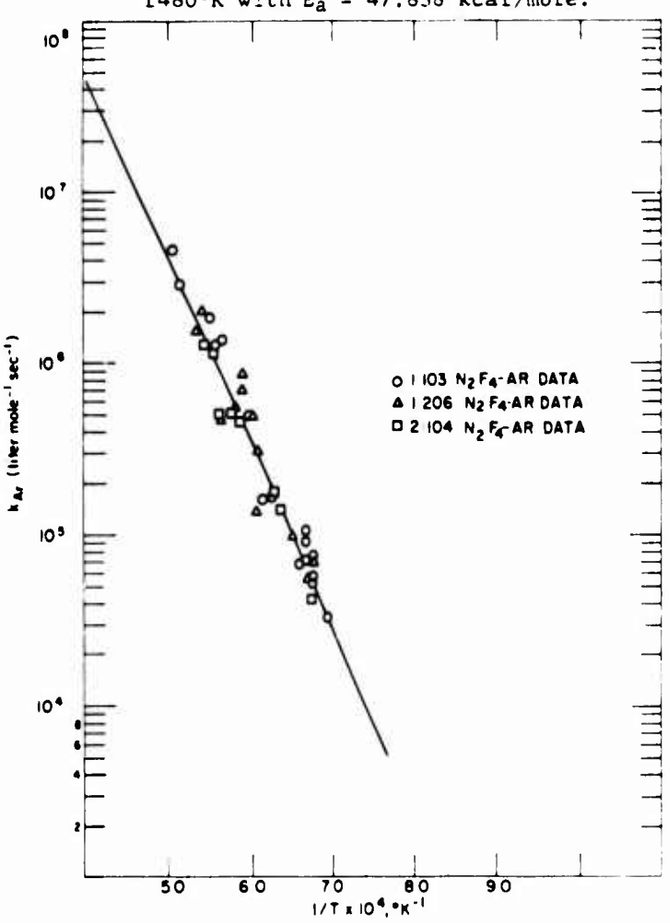


Fig. 9 Second-Order Rate Constant for NF_2 Decomposition In Argon Behind Incident Shock Waves.

USE OF A MICROWAVE INTERFEROMETER FOR MAPPING ELECTRON DENSITY VARIATION ACROSS THE FLOW FIELD IN A PRESSURE DRIVEN SHOCK TUBE

James C. Blackburn and Frank L. Tevelow
Harry Diamond Laboratories, Washington, D. C. 20438

INTRODUCTION

This paper describes a series of tests in which the electron density was measured with a microwave interferometer at various radial locations across the flow field of a 2 by 2 in. pressure-driven shock tube. Although the radial properties are assumed constant out to the boundary layer, unexplained results of Dvir and Low[1] suggested that this might not be true. Since our experimental apparatus could be readily adapted for such an investigation and since no experimental evidence as to the radial uniformity of the electron density was available, an investigation was started to determine the variation that might exist for our geometry and our test conditions.

The interferometer described here, with its small and accurately delineated sensing region, gives measurements of electron density resolved with respect to both time and radial location. The data were obtained by repeating an experiment with the nozzle ("cookie cutter") of the interferometer located at various radial positions in the flow field. In addition, an attempt was made to determine whether curvature of the shock front could be determined from the electron density data using the time intervals between the signal from a fixed ionization probe and the signal from the microwave probe for the nozzle located at the various radial positions. The results reported here were obtained at initial pressures of 1 mm and 10 mm Hg, using air as the test gas and helium as the driver gas.

The paper is divided into several parts. A brief background of the measurements and of the bridge circuit is presented first. This is followed by details of the construction of the microwave test section as it is used in the shock tube along with an analysis of the errors that it may introduce into the data. Finally, the experimental results are presented.

BACKGROUND

The theory of the dielectric slab measurements has been described previously in some detail.[2,3] Although various electromagnetic properties may be calculated from the measurements, only N_e (electron density) and ν (collision frequency) are calculated for this report from the complex transmission coefficient for the plasma slab in the waveguide. The theoretical assumptions (uniform plasma slab completely inclosed by waveguide) are closely approximated by the arrangement shown in figure 1. The knife-edged nozzle is aligned with the shock tube axis and cuts out a segment of the flow, which passes through gap L, approximately 1/6 wavelength wide. The quartz windows, which constrain the internal flow through the nozzle to original streamlines, are 1/2 wavelength thick and appear almost reflectionless at the test frequency. Any residual reflections are tuned out by transformers external to the test section.

THE BRIDGE CIRCUIT

The bridge circuit[5] used to determine τ^* is shown in figure 2. The detector used in the circuit is a magic tee that yields signals proportional to the vector sum and vector difference of the input signals when properly matched at all four ports.[4] These signals are measured by crystal detectors D_1 and D_2. The appendix gives more information about the circuitry of the bridge and presents equations for calculating the instantaneous values of $|\tau|$ and $\angle\tau$ from the instantaneous voltages at D_1 and D_2.

Transformers T_4 and T_5 (figure 2) must be precisely matched looking through the quartz windows into I_4 or I_3; otherwise a standing-wave pattern may exist across the gap in the nozzle.[3] In this case the signal "seen" by the plasma slab, which is considerably less than a wavelength wide, depends on the position of the slab relative to the standing-wave pattern. This matching is an especially critical part of these measurements since the window assemblies must be disconnected and displaced when the nozzle is moved.

An error analysis was made for this equipment and technique taking into acccunt the errors in the electronics, calibration procedure, and data reduction.[5] It was found that the signal levels at the crystal detectors could be evaluated within $\pm$ 3 percent, giving rise to a maximum error of less than $\pm$ 25 percent in the computed values of N_e and ν**.

*τ is the transmission coefficient defined in the appendix.

**For the range of data presented in this paper, the computed errors are much less than the indicated maximum since overall deviations, including variations due to shot dissimilarities, are about $\pm$ 15 percent.

Owing to the procedure of moving the nozzle, additional sources of experimental error were present in these tests and are evaluated in a later section of this paper.

MICROWAVE TEST SECTION

Figure 3 shows the test section housing, nozzle, and waveguide window assemblies as they appear when arranged for measurements at the center of the shock tube. In this picture the wedges have been removed so that the waveguide support may be seen clearly. The waveguide passes through closely machined slots in the housing, which position it accurately with respect to the shock tube flow. One length of the test section was made larger than the 2-in. dimension of the shock tube so that the wedges and waveguide were located in the expansion section of the shock tube.

Figure 4 shows the 0.5 and 0.9-in. nozzles together with the wedges. The 0.9-nozzle has the same leading-edge profile and type of knife edge as has the shorter nozzle, but an additional rectangular segment extends the knife edges farther upstream. Although use of the wedges presented additional experimental complications, they were necessary to maintain attached shock conditions for the entire test duration.(6)

Figures 5 and 6 show how the shock tube, test section, and expansion section were aligned in these experiments. A large dump tank was connected aft of the expansion section but is not shown here. The distance from the leading edge of the side wall of the supporting waveguide to the end of the test section was 1.00 in. D indicates the nozzle length, the distance from the sidewall of the waveguide to the leading edge of the nozzle. Figure 6 shows a top view of the arrangement of figure 5. It is seen that the sidewall of the test section toward which the nozzle was moved is aligned exactly with the wall of the shock tube. Q is the distance from the nozzle axis to the shock tube axis.

Figure 7 is a sketch of the microwave test section looking directly into the nozzle, with the nozzle offset from the center of the tube. W are the wedge segments, N the nozzle, F the mounting flanges for the window assemblies, M the microwave flange, O the O-rings which vacuum seal the assembly, and S one of the several spacer rings of different sizes, which may be placed under one or both of flanges F to properly position the waveguide, which supports the nozzle. Dashed line R shows the location of the 2-by 2-in. shock tube opening in relation to the 2-1/16-by 3-1/4-in. test section opening.

PROCEDURE IN MOVING NOZZLE

In moving the nozzle from one position to another, the following operations were performed. First, the shock tube was opened at junction K-K (figure 6), the alignment between the shock tube and test section being left intact. Next the nozzle, window assemblies, wedge segments, and spacing rings were removed. To reassemble, the proper spacers S were

put in place on the window assembly mounting flanges F, the nozzle was put in place, the waveguide tightened against it by the bolts, and the wedge segments clamped in place on the waveguide. The position of the waveguide, and consequently of the nozzle, was fixed by the close fit of the waveguide through the slots in the housing and by metal-to-metal contact between the mounting flanges and spacer rings.

ERROR ANALYSIS

An error analysis for similar measurements in which the nozzle remained in a fixed position at the center of the test section has already been mentioned. Several additional sources of experimental error may be introduced while moving and repositioning the nozzle. These are:

(1) misalignment of the nozzle relative to the flow,

(2) contamination entering the shock tube while the nozzle is being moved,

(3) changes in the microwave circuit resulting from disconnecting and moving the window assemblies.

To investigate possible errors resulting from misalignment of the nozzle with the flow, the nozzle was located at the center of the shock tube cross-section and was first rotated clockwise and then counterclockwise by hand against the machined tolerances.* Analysis of the data showed that no significant difference was produced in experiments performed with this forced maximum misalignment compared with measurements with the aligned nozzle.

It has been found that contamination introduced after opening the tube and while moving the nozzle produces spurious results in the next one or two shots[6]. The electron density in these shots was several times higher than the stable value reached several shots later. It was normal procedure, therefore, to fire several cleanup shots after moving the nozzle before data were used for comparison.

Considerable error can result from electrical mismatch at the nozzle, as mentioned earlier. Since moving the nozzle entails repositioning the waveguide window assemblies while the rest of the bridge circuitry remains fixed in position, changes were required in the waveguide line connecting the windows to the circuitry. Isolators I_3 and I_4 (figure 2) minimize the effects of such changes provided the waveguide between the windows and the isolators is left unchanged. Frequent checks, however, were made of the match at the nozzle. This was done by removing the assemblies consisting of the input waveguide assembly, I_4, S_2, and I_3 or the output assembly,

* All critical tolerances are about $\pm$ .001 in. The rotation angle was not measured but calculation shows that total rotation would not be greater than 0.05 deg.

I_4, and T_5 from the circuity, placing a termination at the free end of the isolator, and using a signal source and a slotted line clamped directly to the end of the quartz window to monitor the VSWR while tuning T_4 or T_5 for a minimum. The termination was then removed and the assembly replaced into the circuit intact.

The entire bridge was then checked by adjusting the phase and amplitude in the bridge arms to the proper levels, calibrating the crystal detector outputs, and measuring the dielectric constant of a closely fitting Teflon slug inserted into the nozzle. The results of this dielectric measurement have been found to repeat to within ±1 percent, if the equipment is adjusted properly.

EXPERIMENTAL RESULTS

In these tests, initial conditions were closely controlled in an attempt to duplicate both shock Mach number and shock velocity history. In addition, only data were used in which the average* shock Mach numbers for the individual shots agreed to within ± 3/4 percent.

The measurements made at M_s 9.5, P_i = 10 mm Hg with the 0.5-in. nozzle showed considerable variation in electron density across the flow field as presented in table I. When similar measurements were repeated with the 0.9-in. nozzle, the density measured across the flow field was essentially constant within an experimental error of ± 15 percent, if evaluated up to a time of 60 μsec - that region where the velocity profiles are known to be similar.[6] This is shown in figure 8. The collision frequency for these shots (also determined up to a time of 60 μsec) remained constant at 1 x 10^{11} cps within ± 10 percent for the 0.9-in. nozzle and ± 20 percent for the 0.5-in. nozzle.

Similar measurements were made at M_s 11.4 for an initial pressure of 1 mm Hg. Here again, all data for the 0.9-in. nozzle located at different positions agreed within limits of experimental error. However, differences between 0.9-in. and 0.5-in. nozzle data showed less variation at 1 mm than at 10 mm. At 1 mm, peak levels of electron density for both length nozzles and all locations were approximately the same (2.2 x 10^{12} electrons/cm^3) and the major difference was in the shape of the electron density-time response. The average collision frequency for the 0.9-in. nozzle was 2.40 x 10^{10} cps to within ± 15 percent.

* This value is the average M_s for the velocity measurements made over the 6-ft length preceding the test section.

Differences between data using the 0.5-in. and 0.9-in. nozzles, when the 0.5-in. nozzle was not located on center, appear to be the result of some flow disturbance due to the geometry used in the tests.

Previous tests have indicated[6] that the constriction of flow by the nozzle, the wall of the shock tube, and the wedges may give rise to a reflected shock structure that may exist as far upstream as the location of the nozzle entrance. This condition is enhanced as the nozzle is brought closer to one wall and is also likely to increase the upstream travel distance of the reflected shock. It is therefore assumed that the measurements with the 0.5-in. nozzle when located off center are exhibiting effects of these reflected shock waves, whereas the 0.9 in. nozzle is of sufficient length to be upstream of any influence of the reflected shock for all test positions.

Since the purpose of these tests was to check flow uniformity rather than wall or boundary layer effects, no attempt was made to get closer to the wall than 0.157 in.

To investigate whether shock front curvature or tilt could be detected, an ionization probe imbedded in the shock tube wall at a fixed position 4 in. upstream of the test section was used as a reference to measure the time interval between the shock front passing the probe and the plasma entering the waveguide. Since the ionization probe operated under fixed conditions, its output was independent of nozzle location. If the shock front were curved or tilted, the time interval between the probe signal and the plasma signal should vary as the nozzle is moved across the flow field. As seen in table II the maximum difference in time intervals is 0.9 μsec, which is within the error of the measurement ($\pm$ 0.9 μsec). This error consists of $\pm$ 0.8 μsec from reduction of the oscillograms and an additional $\pm$ 0.1 μsec from variability in the position of the shock front with respect to the ionization probe when the probe fires.[7] The shock front therefore was bowed or tilted less than 0.12 in. (the shock velocity being approximately 0.13 in./μsec) across the region of the measurements. Shadowgraphs of the shock front taken in connection with previous work showed it to be plane and perpendicular to the tube axis to within 0.03 in.

Evaluation of the time intervals between the ionization probe signal and the microwave signal cutoff in the contact region showed that their variations from shot-to-shot were maximally about 8 times the time variations measured to the shock front; table II shows these data.

SUMMARY

Measurements made with the 0.9-in. nozzle at M_s 11.4, 1 mm Hg and M_s 9.45, 10 mm Hg showed that the electron density was essentially constant across the flow field throughout the range of positions investigated. The measurements made with the 0.5-in. nozzle were probably influenced by reflected shocks and did not yield useable data.

The curvature of the shock front was found to be less than 0.12 in., which is within the precision to which these measurements can be evaluated.

ACKNOWLEDGMENTS

The authors thank F. J. Nelson and A. Meeks for operating the shock tube throughout these tests. Acknowledgment is made to H. D. Curchack for his many helpful suggestions and comments concerning both the paper and the experimental work. And finally, we thank Drs. F. J. Tischer and I. Pollin for their constructive comments in regard to this paper.

This work was performed under the sponsorship of the U. S. Army Materiel Command, Washington, D. C. AMCRD-R.

APPENDIX

Theory of Measurements

The theory of the measurements assumes a uniform rectangular block of plasma inclosed by waveguide with a $TE_{1,0}$ mode signal incident upon it, as shown in figure 9. A portion of the incident signal is transmitted and a portion reflected, with multiple internal reflections at the boundaries of media (1) and (2). A complex transmission coefficient τ is defined

$$\tau = E_t/E_i \tag{1}$$

where E_t and E_i are the complex incident and transmitted signals. With τ known from the microwave measurements, the complex propagation constant $\gamma = \alpha + j\beta$ may be computed from the following relation, which takes into account the multiple internal reflections[2,3]

$$1/\tau = 1/2\ [\gamma_\varepsilon/j\beta_g + j\beta_g/\gamma_\varepsilon]\ \sinh \gamma_\varepsilon L + \cosh \gamma_\varepsilon L \tag{2}$$

Here L is the width of the plasma sample and β_g is the phase velocity constant in air-filled waveguide.

With γ_ε known, the complex permittivity constant $\varepsilon_r = \varepsilon_r' - j\varepsilon_r''$ is calculated from

$$1 - \varepsilon_r' = (\lambda_0/\lambda_g)^2\ [1 + (\alpha_\varepsilon/\beta_g)^2 - (\beta_\varepsilon/\beta_g)^2] \tag{3}$$

$$\varepsilon_r'' = 2(\lambda_0/\lambda_g)^2 (\alpha_\varepsilon/\beta_g)(\beta_\varepsilon/\beta_g) \tag{4}$$

where λ_0 and λ_g are the free-space and guide wavelengths of the test signal, α_ε is the attenuation constant in plasma, and β_ε and β_g are the phase velocity constants in plasma and air-filled guide.

From ε_r, the plasma frequency ω_p, collision frequency ν, and electron density N_e, are obtained from

$$\omega_p = \omega[\ (1 - \varepsilon_r') + (\varepsilon_r'')^2/(1 - \varepsilon_r')\ ]^{1/2} \tag{5}$$

$$\nu = \omega\ \ \varepsilon_r''/1 - \varepsilon_r' \tag{6}$$

$$N_e = m\,\varepsilon_0 \omega_\rho^2\, e^{-2} \tag{7}$$

where ω is the radian frequency of the incident signal, m the electron mass, e the electron charge, and ε_0 free-space permittivity. A detailed presentation of the theory is found in references (2) and (3).

CIRCUITRY

The circuitry marked source and calibration in figure 2 supplies a signal of stable frequency to coupler C_1, which divides this signal into two equal parts, each part energizing one bridge arm. A precision calibrated attenuator A_2 is used to produce known changes in signal strength in order to calibrate the crystal detector outputs. The ionization probe, located in the shock tube upstream of the test section, initiates two actions. First, its signal, suitably delayed, is used to start the sweep of the dual-beam oscilloscope, which records the voltage from D_1 and D_2. Second, it triggers the pulse generator to provide pulses to Y_1, a modulating diode shunted across the waveguide. This modulator decreases the signal level to both crystal detectors by exactly 3 db during two short pulses immediately before and immediately after the passage of the plasma through the test section. These pulses of exactly 3-db height provide reference lengths for the calibration of the crystal outputs.

The phase and amplitude of the signal through arm 2, the test arm, is fixed by the adjustment of A_1 and A_2 and the mechanical dimensions of the circuit. The phase and amplitude of the signal in arm 1, the reference arm, is adjustable to the proper equal amplitude and 90-deg phase difference by A_3 and P_1. This produces equal signals in D_1 and D_2 in the steady-state (no plasma present) condition. The phase and amplitude of τ may be calculated from the following, where E_Σ and E_Δ are the voltages in the crystal detectors and E_i is the amplitude of the signal in the reference arm.(2)

$$|\tau| = \left[\frac{|E_\Sigma|^2 + |E_\Delta|^2 - 2|E_i|^2}{2|E_i|^2}\right]^{1/2} \tag{8}$$

$$\angle\tau = \sin^{-1}\frac{|E_\Sigma|^2 - |E_\Delta|^2}{4|\tau|\,|E_i|^2} + \beta_g L \tag{9}$$

Here β_g is the phase velocity constant in air-filled guide and L is the gap width.

REFERENCES

(1) Dvir, M. and Low, W., "Microwave Attenuation by Shock-Heated Air," Physics of Fluids, Vol. 7, No. 4, Apr 64.

(2) Tevelow, F. L., and Curchack, H. D., "Shock Tube Microwave Propagation Measurements Using the Dielectric Slab Approximation," HDL Report TR-962, 21 Aug 61.

(3) Tischer, F. J., "Measurement of the Wave Propagation Properties Of Plasma in the Microwave Region," Ohio State University Report 941-1, Aug 59.

(4) Montgomery, E. G., and Dicke, H. H., "Principles of Microwave Circuits," Radiation Laboratory Series, Vol 8, McGraw-Hill, 1948 (307).

(5) Blackburn, J. C., and Tevelow, F. L., "Circuitry and Operation of an X-Band Interferometer for Shock Tube Measurements using the Dielectric Slab Approximation," HDL Report TR-1275, 22 Apr 65.

(6) Tevelow, F. L., "Microwave Measurements of the Electromagnetic Properties of Shocked Air in the Range $8 \leq M_s \leq 12$ and $1 \leq p_i \leq 20$ mm," (to be issued as a Harry Diamond Laboratories Technical Report).

(7) Gieske, H., and Smith, J., "Use of Ionization Probes to Locate Shock Fronts," 5th Shock Tube Symposium, Naval Ordnance Laboratories, Silver Spring, Maryland (1965).

TABLE I. Electron Densities Measured with 0.5-in. Nozzle at 10 mm Hg, M_s-9.45

Distance from Nozzle Center to Shock Tube Wall* (in.)	Electron Density (electrons/cm^3) at time t(μsec)			Distance from Nozzle Sidewall to Shock Tube Wall (in.)
	25	50	75	
1.032	8.2×10^{11}	8.2×10^{11}	7.8×10^{11}	0.807
0.812	1.4×10^{12}	2.3×10^{12}	1.1×10^{12}	0.585
0.542	1.4×10^{12}	2.5×10^{12}	1.3×10^{12}	0.307
0.382	1.1×10^{12}	1.1×10^{12}	9.5×10^{11}	0.157

*The center of the test section was located 0.032 in. from the shock tube axis to align the walls toward which the nozzle was displaced. The report refers to these data as being on center.

TABLE II. Time Intervals used in Determining Curvature at 10 m m Hg, M_s-9.45

Distance from Nozzle Center to Shock Tube Wall (in.)	Interval between Probe and Plasma Signals (μsec)		Duration of Plasma Signal (μsec)		Number of Test Shots
	Average Value	Range of Values	Average Value	Range of Values	
1.032	34.2	33.5 - 35.0	94.5	91.0 - 98.5	4
.542	35.0	35.0 - 35.0	97.0	96.5 - 98.0	2
.382	34.5	34.0 - 35.0	95.5	94.0 - 97.5	2

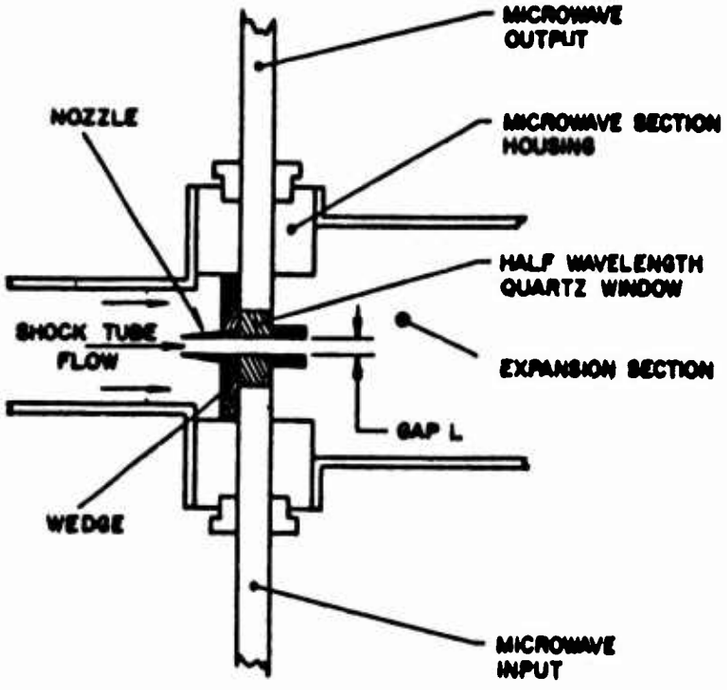


Figure 1. Sketch of the microwave test section.

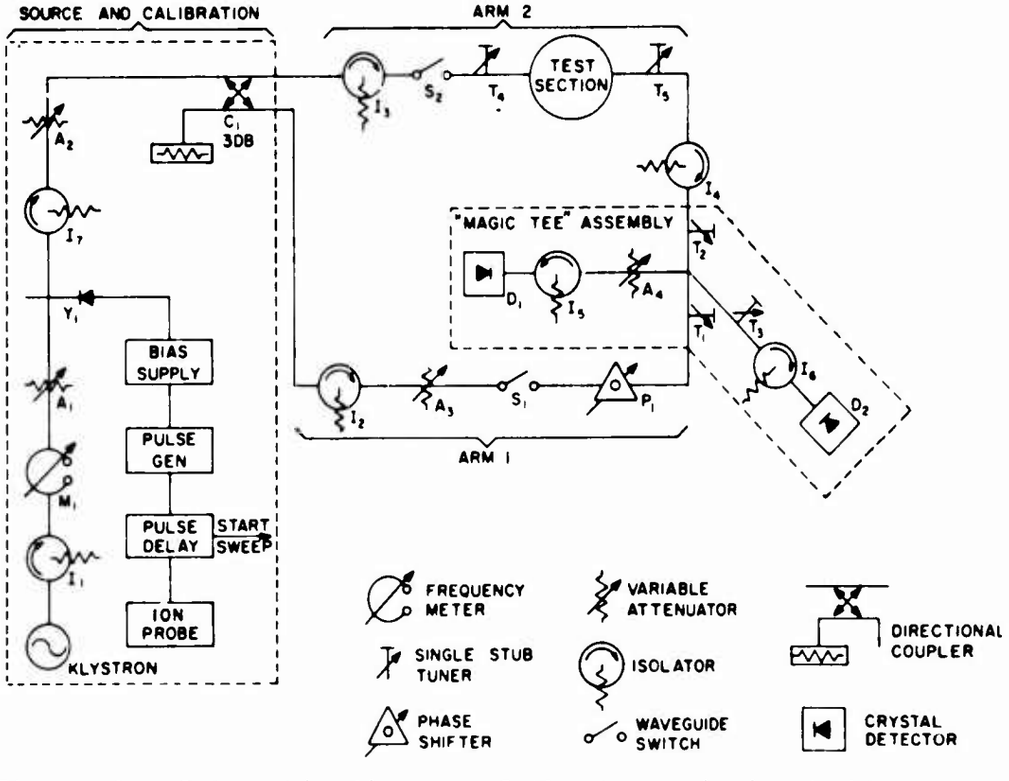


Figure 2. Schematic diagram of the transmission bridge.

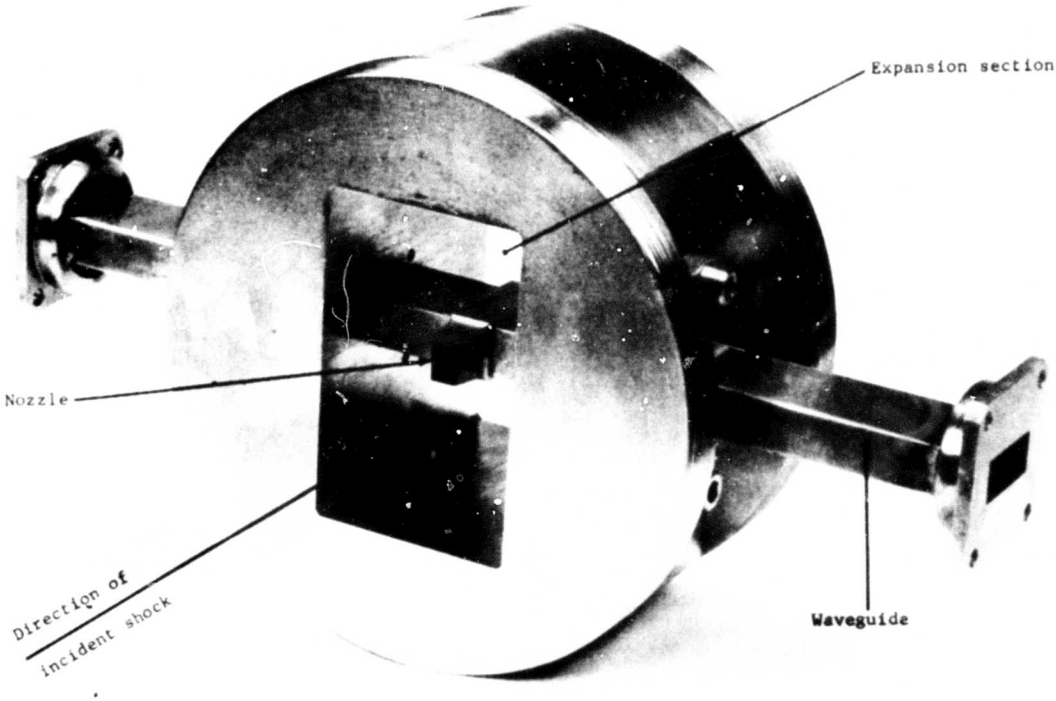


Figure 3. Microwave test section. (The wedges, normally located on either side of the nozzle, are left out for clarity.)

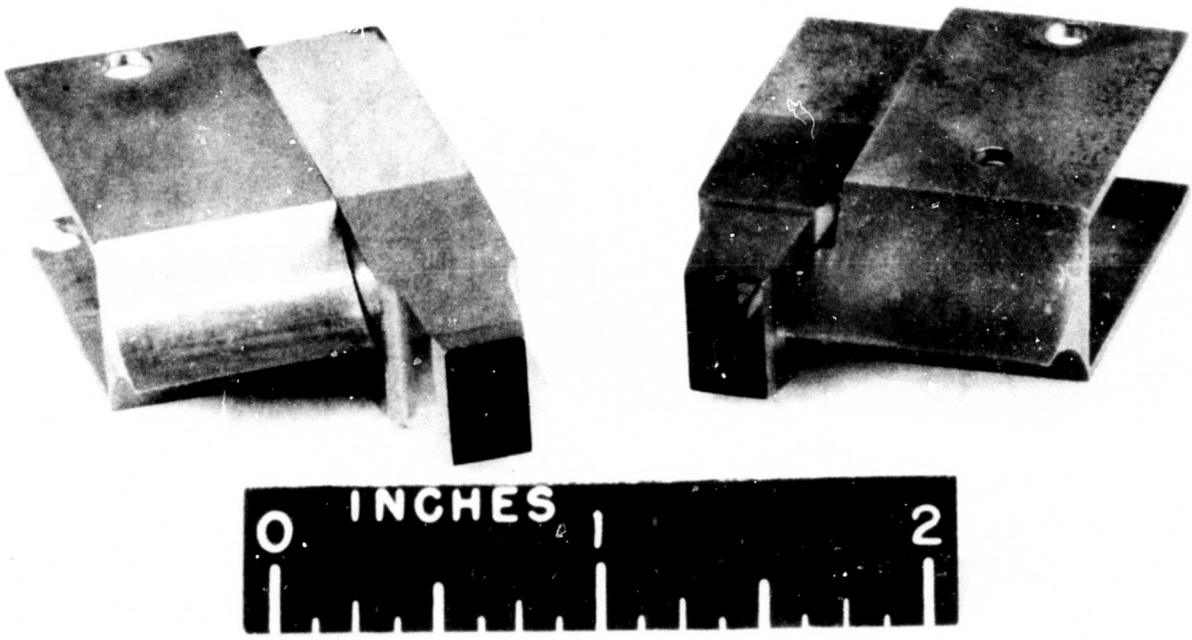


Figure 4. Photograph of the .5" and .9" nozzles, each with one associated wedge.

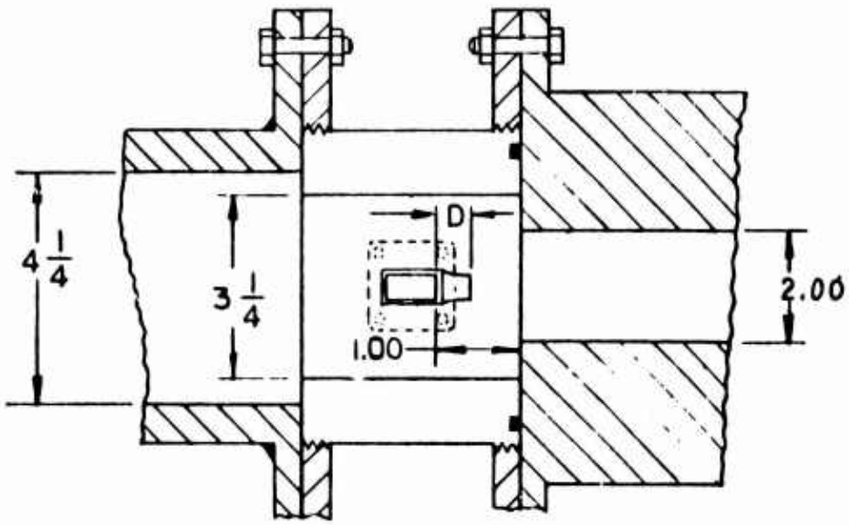


Figure 5. Side view of the test section relative to shock tube and expansion section.

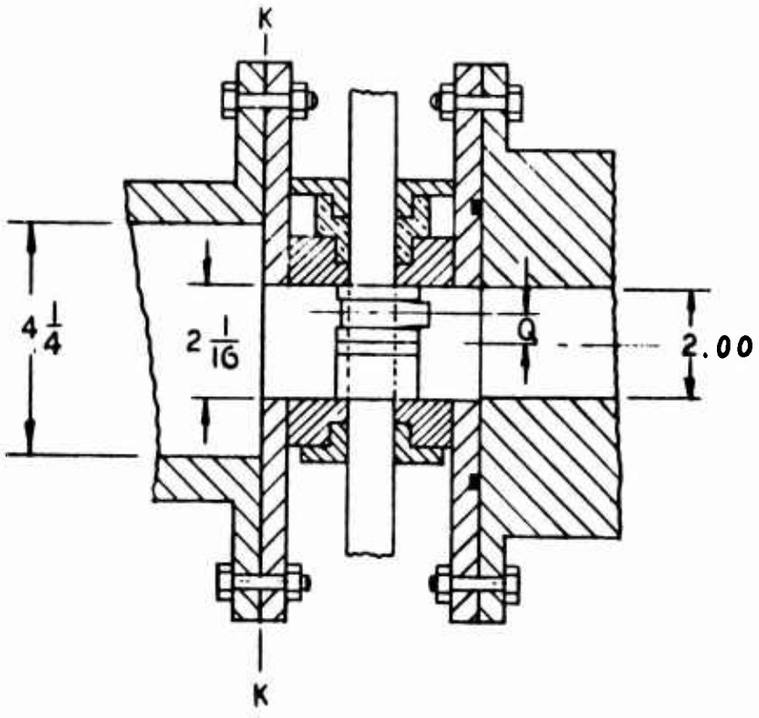


Figure 6. Top view of the test section relative to shock tube and expansion section.

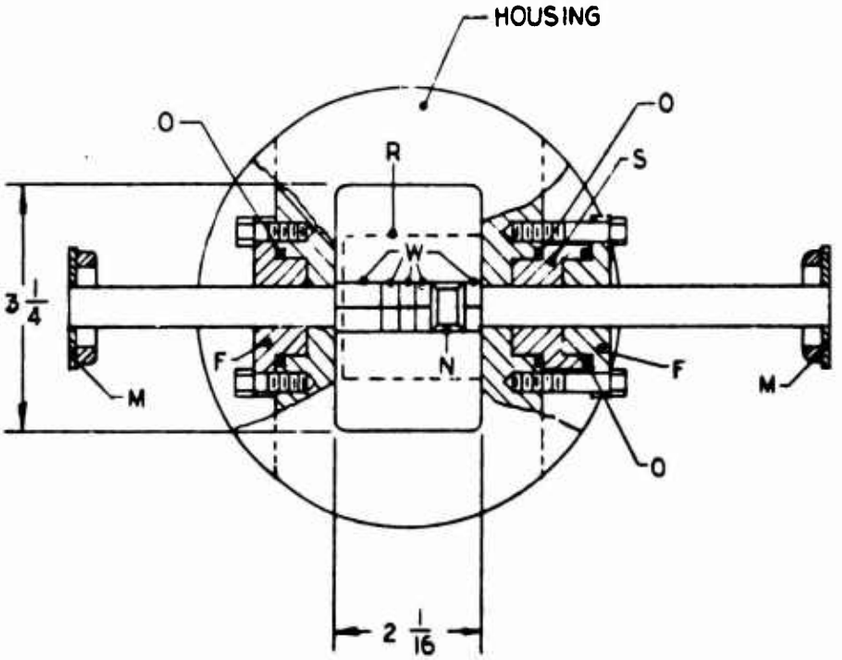


Figure 7. Cut-away drawing showing details of microwave test section assembly.

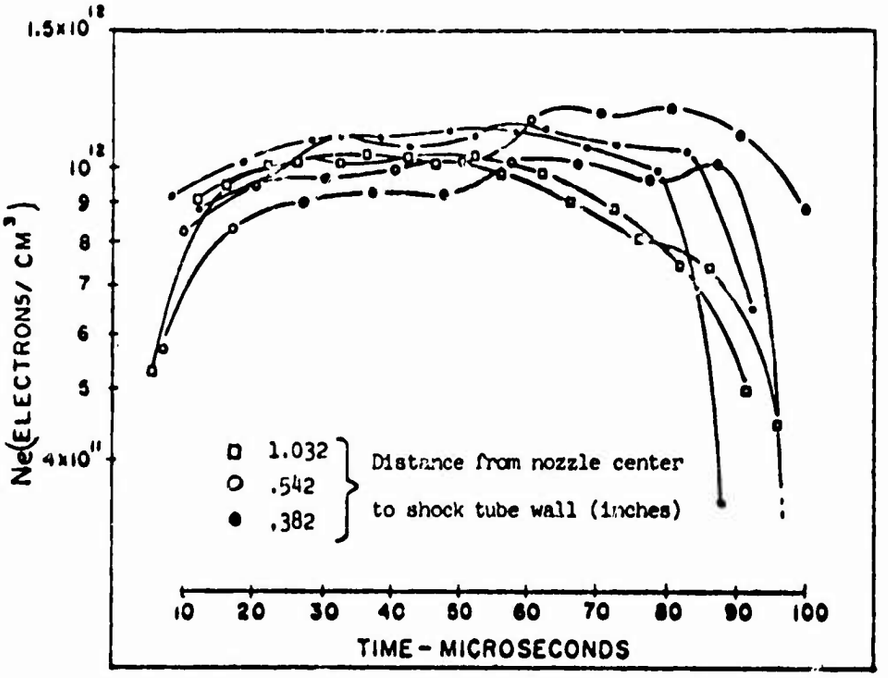


Figure 8. Plasma electron density as a function of time for three nozzle locations across the flow field. (.9" nozzle, M_s -9.45, P_i = 10 mm Hg).

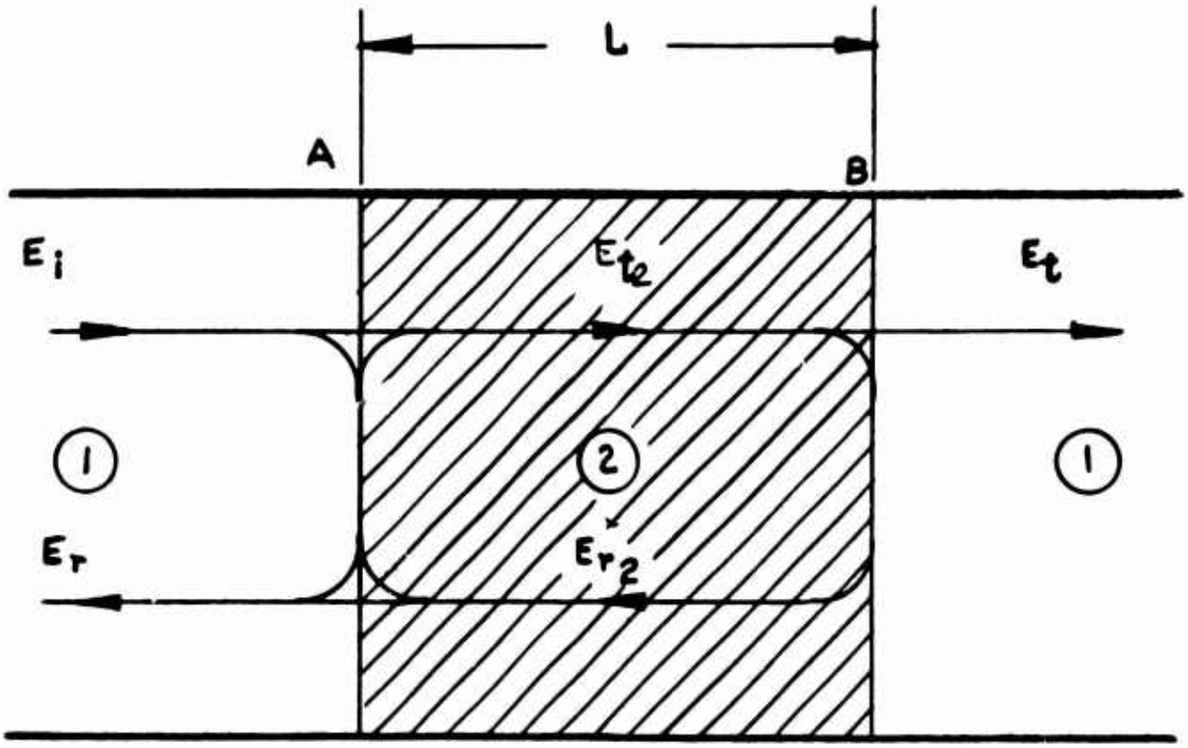


Figure 9. Plasma slab enclosed by waveguide.

MINIMIZATION OF ERRORS IN SHOCK TUBE INVESTIGATION OF BROMINE DISSOCIATION RATES IN PRESENCE OF NOBLE GASES

by Marvin Warshay
Lewis Research Center
National Aeronautics and Space Administration
Cleveland, Ohio

ABSTRACT

A shock tube with a glass driven section was employed to obtain reliable dissociation rates of bromine in dilute mixtures (1 percent) with various noble gases (Ar, Ne, and Kr) at temperatures of 1200° to 1900° K. Extensive theoretical treatments have recently been applied to dissociation and recombination of gases; however, evaluation of these theories and continued progress has been hampered by the lack of sufficiently precise experimental data. This investigation attempts to partly fill this need by using a carefully designed apparatus and a procedure that would produce reliable kinetic data. Using dilute bromine mixtures and successfully avoiding bromine-metal contact eliminated two serious problems that have plagued other investigators, namely, large temperature changes during dissociation and bromine-metal reactions. The driven section and gas mixture bottles were made of glass and were strengthened (as much as tenfold) by external fiber glass bonding; all valves, lines, and a novel shock-tube transition section were made of TFE fluorinated polymer. Bromine concentrations were measured by a light absorption technique in which highly stable power supplies and incandescent light sources (< 0.05 percent change/hr) were employed. The photomultiplier system developed for this work produced low fatigue rates (0.1 percent/msec), high signal-to-noise ratios (100), and rapid response (0.7 μsec).

INTRODUCTION

In the past decade the shock wave method has been used extensively in the field of chemical kinetics; it has been of particular value in the measurement of the rates of dissociation of diatomic molecules. These experimental results have heightened interest in the theory of dissociation and recombination (refs. 1,2,3,4, and 5). However, in spite of the large number of shock tube investigations that have been made in this area the experimental rate data are still not sufficiently reliable to adequately test present theoretical assumptions nor to provide a solid basis for future

theories. Palmer (ref. 6) stated the problem succinctly in saying that shock tube measurements of rate constants have been notoriously imprecise.

The results of past investigations of the dissociation of bromine in the presence of argon clearly fit this description. As can be seen in Figure 1, the agreement among the four different investigations (refs. 7, 8,9, and 10) is not good and the scatter of the data of several of the investigations is pronounced. For example, in spite of the fact that the fourth investigation (ref. 10) is a repeat of the third investigation (ref. 9), using the same equipment, there is a 50 percent discrepancy between the data.

Despite the previous inadequacies, the outlook for making reliable measurements of bromine dissociation rates is not bleak. Bromine in many respects is a convenient substance to work with. It dissociates at relatively low temperatures. It absorbs light strongly in the visible region providing a good means of following the course of reaction. Secondly from careful analysis of the past bromine shock tube experiments the major trouble areas could be uncovered. These areas, as it develops, are associated with bromine-metal contact, light absorption measurements, and cooling of the gas as dissociation proceeds.

In the present investigation of bromine dissociation, the problems that had plagued past investigations were tackled and largely overcome. An apparatus and a procedure were carefully designed to obtain reliable bromine dissociation rate data. A shock tube with a glass driven section was employed to measure dissociation rates of bromine in dilute mixtures (1 percent) in the presence of argon, neon, and krypton, at temperatures of 1200° to 1900° K.

EXPERIMENTAL CONSIDERATIONS

In the following discussion of experimental apparatus and procedures many points are treated only briefly because they are well understood and have been discussed at length in other papers (refs. 8,11, and 12). However, at the beginning of each subsection an effort is made to stress the pertinent aspects of the design and/or procedure.

Materials Considerations - Bromine Reactivity

Shock Tube

The significant feature of the shock tube design was the avoidance of all contact of bromine with metal surfaces. Since bromine reacts with all common metals, the actual concentration of bromine in a mixture would be in doubt if it were in contact with metal surfaces. Several experiments have confirmed this. Palmer and Hornig (ref. 8) reported an observable reaction when aluminum diaphragms were used with pure bromine. They did not use aluminum diaphragms with bromine mixtures. In the present study, preliminary experiments indicated that bromine has a strong affinity

for both copper and stainless steel. A rather surprising phenomenon was the fact that the walls of a stainless-steel shock tube have a chromatographiclike effect on the bromine in the 1 percent Br_2-99 percent Ar mixture. In these experiments it required about 20 minutes, after the mixture was injected into one end of the 12-foot stainless-steel driven section, for the bromine concentration of the mixture at the opposite end to stop increasing and to attain its ultimate value. (See Figure 2, which shows a typical response.)

Therefore, with metals completely ruled out and with TFE fluorinated polymer commercially unavailable in the size needed, the logical choice for driven section was glass. Palmer and Hornig (ref. 8), Davidson and Britton (ref. 7), and Britton (refs. 8 and 10) all used driven sections that were at least partly glass. With a glass driven section the previously mentioned chromatographiclike effect was not observed.

The main components of the shock tube used in this investigation were a 6-foot stainless-steel driver section and a 9-foot driven section made of borosilicate glass pipe, (Fig. 3). Both sections had an inner diameter of 4 inches. Placed between the two sections, on the low-pressure side of the diaphragm, was a 1-inch-long transition section made of TFE. The vacuum and gas sample lines were connected to this section rather than directly to the glass driven section. Cutting through the glass wall of the driven section would have weakened the walls and presented a sealing problem*.

The face of the transition section was cut to mate with the flange used to clamp the diaphragm into place. A 4-inch hole was cut into the center together with eight properly located bolt holes. Drilled and tapped radially in this piece were the inlets for vacuum and for the gas mixtures.

The entire gas mixture line and the initial portions of the vacuum lines leading from the shock tube consisted of TFE tubing, fittings, and valves. These TFE valves were used to prevent the bromine gas samples from coming into contact with the metal portion of the vacuum lines.

The glass wall of the driven section was strengthened; this was necessary in order to increase the pressure range over which the tube could be used. As was discovered separately by Britton (ref. 9) and by this investigator, glass can break when subjected to too severe a shock. Therefore, using a glass driven section over a reasonable range of pressures necessitates finding a way to strengthen the glass walls. This investigator's solution to the problem was to join materials to the outside of the glass, which added tensile strength to the glass walls. Three materials were joined to the outside of the glass at different places along the pipe. A steel tube covered the first $1\frac{1}{2}$ feet of driven section, being bonded to the glass with

*The transition piece is advantageous from other standpoints as well. it has room for several additional inlets that can easily be machined in the TFE. Furthermore, sealing is no problem. The TFE glass pipe O-ring type gaskets that were used form their own impression in the TFE transition piece.

epoxy cement. This cement was forced into the annulus through grease fittings in the metal tube. The next 12 inches of glass were strengthened by means of fiber glass tape wound in a crisscross fashion. The remaining length of driven section was strengthened by a 1/4-inch-thick polymethyl methacrylate tube that had been split lengthwise to allow it to fit over the conical end of the glass pipe. Several clamps kept the polymethyl methacrylate tightly pressed against the glass. Polymethyl methacrylate is convenient because it is transparent. Of the three methods, the fiber glass method is considered to impart the greatest strength to the glass due to its intimate contact. Fiber glass was also used to strengthen the glass mixture bottles. This will be discussed in the next section.

At the beginning of the driven section, connected to the metal tube, was a stainless steel flange. This flange was installed as a substitute for the conical end of glass pipe that had broken off during preliminary experiments†. The very small area of flange that was exposed to the gas mixture was covered with monochlorotrifluoroethylene polymer grease which is inert to bromine.

Instead of an end plate at the far end of the driven section, a thin Mylar diaphragm was used as a closure. Beyond this diaphragm was a pipe which led to the stack. By breaking through the end diaphragm, the shock itself provided the means to dispose of the shock tube contents.

The driver section was fitted with a solenoid-operated piercing mechanism which was used to pierce the mylar type D diaphragms. Multiple diaphragms were used to obtain the desired rupture strength. The pressure of the helium driver gas was raised to a pressure within 3 psig or less of the diaphragm bursting pressure, 80 psig in most experiments. In practically all cases, Mach number and temperature variation was produced by varying the initial driven gas pressures.

Gas Mixtures

In the preparation of the mixtures of bromine and noble gas in a gas-handling apparatus, bromine did not come into contact with any metals, only glass or TFE surfaces. The valves, fittings and tubing were TFE.

The 1-percent-bromine mixtures were prepared by the partial pressure method. A calibrated Wallace and Tiernan FA160 (0-220 mm) pressure gage was used to measure the bromine pressure. To keep bromine out of the gage and metal line, a buffer of the noble gas was used. The total gas mixture pressure was measured with a calibrated (0 - 100 psig) gage.

†Before this mishap, only polymethyl methacrylate was used to strengthen the glass; however, the polymethyl methacrylate tube only covered to within 2 inches of the conical end, and this area is where the glass broke during a preliminary experiment in which pressure bursting was used. The pressure was 140 psig.

The gas mixture bottles were large borosilicate glass boiling flasks whose walls were strengthened by bonding fiber glass gauze to them with epoxy cement. With the use of the measured tensile strength of a test specimen of the glass epoxy bond, it was calculated that the strengthened walls of the glass bottle would withstand pressures up to 800 psi. Gas bottle pressure was now limited by the TFE valve connected to the bottle, which was capable of withstanding 150 psig. This provided ample confidence to prepare samples at pressures of 80 psig. If properly applied to the glass portion of the shock tube, this method of glass strengthening could allow the shock tube, which has a glass driven section, to be used at far greater pressures than are presently being considered. Because the number of coatings determine the wall strength, practical considerations such as covering the conical end and still attaching the flange would govern ultimate strength.

Reagent grade Br_2 (99.5 percent minimum purity) was further purified by distillation before being used. The argon, neon, and krypton purities were 99.998, 99.96, and 99.994 percent, respectively. Before being used the two components of the mixtures were allowed to mix for 1 week.

Light Absorption Measurements - Determination of I_0

Keeping I_0, the incident light intensity, within narrow bounds was the single most important part of the measurements of the Br_2 concentration by the light absorption technique. Wray (ref. 13) has pointed out that the largest source of error in the use of absorption spectrometry for the present type of application is the measurement of I_0. Jacobs and Giedt (ref. 14), who used an expression for calculating the dissociation rate of Cl_2 involving the term log log (I_0/I), estimated that a maximum error of 30 to 40 percent in k_D could result from an error of only ±2 percent in I_0. The magnitude of the error in k_D that results from an error in I_0 depends on the particular expression used to calculate this rate constant as well as the initial bromine concentration. The error is lower for lower bromine concentrations.

The determination of I_0 hinges on both the apparatus and the procedures used. The critical features of apparatus are stable power supplies and light sources, a photomultiplier system that produces stable signals with high signal-to-noise ratios, and a good device to measure the I_0 signal. These features will now be described in the following paragraphs.

The incandescent light source (6.5 V, 2.75 A) powered by a highly regulated power supply gave extremely good stability, <0.05 percent change/hr for either the power supply voltage or the bulb current. The light beam was made parallel by placing the bulb at the focal point of a converging-diverging lens. This lens was mounted in a camera shutter, which served to regulate the exposure of the light beam to the shock tube and to the detection system. A fixed 1-mm slit was used where the beam entered the shock tube. The light emerging from the shock tube passed through an interference filter that fed monochromatic light into the 931A photomultiplier. The mea-

sured peak and band width used at the filter half peak were 4400Å and 80Å, respectively. The high voltage required to operate the photomultiplier was produced by a very stable power supply (<0.01 percent change/hr). The photomultiplier output was recorded by the lower beak of a dual beam oscilloscope. An oscilloscope camera was used to photograph the oscilloscope traces.

The ideal photomultiplier system would respond instantaneously to an input light signal and would produce a stable signal with no noise. Unfortunately, time response, minimization of phototube fatigue and high signal-to-noise ratios are goals which often require opposing actions. For example, to minimize fatigue and still maintain a high output would require a high load resistance in the circuit; however, good time response requires a low load resistor. To solve the apparent dilemmas associated with the use of the photomultiplier required not only a good compromise in designing the system, but also a proper procedure for its use. The photomultiplier system developed for this work produced low fatigue rates (0.01 percent signal change per msec) good rate response (0.7 μsec) and good signal to noise ratios (up to 100). The photomultiplier circuit diagram is shown in Figure 4.

With respect to procedure, it was important not to expose the photomultiplier indiscriminately to the light. The shutter blocking light from the phototube was controlled by a solenoid connected to a timing mechanism. (This timing mechanism also controlled the solenoid that operated the piercing mechanism.) Keeping the duration of each light exposure as low as possible was not the only thing that was necessary to minimize fatigue. It was learned that intervals between exposures that were too short resulted in erratic rates of decay of I_0. Therefore, the exposure duration was <0.1 second and the interval between exposures was on the order of 15 minutes. (The higher the anode current, the greater the required interval between exposures.) Measurements of I_0 were made both before and after each shock; the I_0 at the time of the shock was calculated by interpolation. This value deviated by no more than ±0.5 percent in most cases. The traces were measured on a time-motion analyzer.

Two additional light beams (at stations A and C) together with associated optical equipment, like that just described, were located 6 in. on either side of the beam (station B) that was used to measure Br_2 concentration. The signal from station A, which was 24 in. from the end of the shock tube, was used to trigger the oscilloscope. Photomultiplier signals from stations A and C were used to measure the shock velocity. With the aid of a cathetometer, all three beams were carefully alined perpendicular to the shock tube axis.

Temperature Drop During Dissociation

Br_2 Concentration

The dissociation of Br_2 is an endothermic reaction, consequently,

the gas mixture cools as dissociation proceeds. This leads to a change in all the parameters characterizing the gas in the reaction zone and must be taken into account to properly evaluate the rate constants. Palmer and Hornig (ref. 8) derived a factor, which they called F, to make this enthalpy correction (defined in the next section). However, for their 1 to 10 Br_2 - Ar mixture, their corrections varied nonlinearly with temperature between the extremes 50 and 690 percent ($1.50 \leq F \leq 7.90$). Though theoretically correct, the determination of F involves uncertainties that are a reflection of the uncertainties associated with the components that make up F, for example, temperature and extinction coefficient. Therefore, the most satisfactory solution is to minimize temperature drop thereby making its influence minor. By properly designing the experiment, gas mixtures containing only 1 percent Br_2 could be used. At these concentrations the enthalpy corrections were both small and varied little with temperature ($1.07 \leq F \leq 1.13$).

Calculations

The rate of dissociation of bromine is determined from the initial slope of the oscilloscope trace. The rate constants were calculated from the following expression

$$k_D = \frac{\left(\frac{dI_2}{d\tau}\right)\left(\frac{V_2}{V_1}\right)_F}{I_0(I_2/I_0)\epsilon_2 l[Br_2][M]} \tag{1}$$

where $[Br_2]$ and $[M]$ are the concentrations of bromine and the noble gas, respectively, I_0 and I_2 are the incident and transmitted light intensities, V_1 and V_2 are the particle velocities relative to the shock front, ϵ is the extinction coefficient, τ is the reaction time on the oscilloscope trace, l is the path length of the light in the gas, and F is the Palmer and Hornig enthalpy correction factor (ref. 8) due to dissociation. The subscripts 1 and 2 refer to the unshocked and shocked gases, respectively. Hiraoka and Hardwick (ref. 16) have written a convenient expression for the F correction factor

$$F = \frac{1}{1 - \frac{\dot{\rho}_2}{\rho_2}\frac{1}{\dot{f}} - \frac{d \ln(\epsilon_2 l)}{dT_2}\frac{\dot{T}_2}{\dot{f}}} \tag{2}$$

For the case of a very small fraction of Br_2 dissociated, they derived equations for the changes in density ρ and temperature T as the dissociation progresses, assuming the ideal gas law and using the conservation laws for mass, momentum, and energy.

$$\frac{\dot{\rho}_2}{\rho_2}\frac{1}{\dot{f}} = \frac{X_0(\Delta H - C_V T_2)}{C_p T_2 - (M/R)V_2^2 C_V} \tag{3}$$

$$\frac{\dot{T}_2}{\dot{f}} = \frac{\dot{\rho}_2}{\rho_2}\frac{1}{\dot{f}}\left(\frac{M}{R}V_2^2 - T_2\right) - X_0 T_2 \qquad (4)$$

where $\Delta H = D_0 - RT_2/2$. The dissociation energy at 0° K is D_0, f is the fraction of dissociation, and X_0 and M are the mole fraction of Br_2 and mean molecular weight, respectively, of the driven gas.

In these calculations the shock wave parameters were calculated with the standard one-dimensional relations (ref. 12).

RESULTS

Extinction Coefficients of Br_2

The static measurement of the room temperature extinction coefficient ϵ served to test the efficacy of the optical and electronic equipment that were to be used later in the shock wave measurements. The value of ϵ found for the $\log_{10}$ form of the Beer - Lambert law was 144.8±1.8 liter/(cm)(mole).

The measurements of ϵ were considerably less scattered than those made by other investigators (refs. 7, 8, and 9), who reported uncertainties as high as ±15 percent. Part of the reason for their poorer precision lies in the fact that these measurements were done directly in the shock tube, in some cases prior to the shocks, while those of the present investigation were carried out in a precision absorption cell connected to the gas handling apparatus. In the latter case, better control of the measured parameters that determine ϵ is achieved. Also, the bromine is never in contact with any metal surfaces.

The experimental determination of ϵ at elevated temperatures was conducted from shock tube experiments in the conventional manner, that is, from the initial absorption of light caused by the shock wave. These data are shown in Figure 5. The solid line was calculated from the theoretical expression of Sulzer and Wieland (ref. 15). The agreement is good. Furthermore, the scatter of the data is lower than that of most other investigations of this kind.

Measured Rate Constants

With the aid of equations (1) through (4), bromine dissociation rate constants were calculated for each of the three systems, Br_2-Ar, Br_2-Ne, and Br_2-Kr. These data are presented in Figure 6, in the traditional manner, $\log k_D$ against $\frac{1}{T}$. The least square lines representing the data were calculated by assuming the simple collisional form for k_D, that is $AT^{1/2} \exp(-E/RT)$. The data for each of the three systems exhibit definite linear trends over wide temperature ranges. Furthermore, the precision of

the data is significantly higher than that of most published data for bromine dissociation rates in the presence of argon. If figures 6(a) to (c) are compared with figure 1, the mean $\frac{|k_{obs} - k_{cal}|}{k_{obs}}$ values for the Br_2-Ar, Br_2-Ne, and Br_2-Kr systems are seen to be 12, 11, and 8 percent, respectively.

In separate experiments conducted with the light source turned off it was determined that emission from the shock heated gas could be ignored in the absorption experiments. Also, Britton (ref. 9) reported that below 1900° K bromine emission is negligible.

DISCUSSION

The improvement in the reliability of these results is attributed to the efforts made to uncover and improve weaknesses in past investigations. Major efforts were devoted to the avoidance of bromine-metal contact, to the maintenance of a stable incident light source I_0, and to the reduction of the enthalpy effect to a minor influence. Of the remaining sources of error, two that are difficult to eliminate completely are associated with the non-ideal shock-wave behavior and the measurement of initial slopes from oscilloscope traces.

While not the subject of this present paper, it is proper to make two brief statements regarding the relative influences of Ar, Ne, and Kr upon the Br_2 dissociation rate. A comparison of the least-square lines representing the data indicate that Br_2 dissociation is approximately 15 percent lower in Ne than in Ar. In the Kr system Br_2 dissociates at higher rates than it does the Ar system at high temperatures, while the reverse is true at low temperatures.

REFERENCES

(1) D. L. Bunker and N. Davidson, J. Am. Chem. Soc. 80, 5090 (1958).

(2) J. C. Light, J. Chem. Phys. 36, 1016 (1962).

(3) S. E. Nielsen and T. A. Bak, J. Chem. Phys. 41, 665 (1964).

(4) E. E. Nikitin and N. D. Sokolov, J. Chem. Phys. 31, 1371 (1959).

(5a) S. W. Benson and T. Fueno, J. Chem. Phys. 36, 1597 (1962).

(5b) S. W. Benson and G. C. Berend, J. Chem. Phys. 40, 1289 (1964).

(6) H. E. Palmer, Project Squid Tech. Report PSU-11-P, August (1964).

(7) D. Britton and N. Davidson, J. Chem. Phys. 25, 810 (1956).

(8) H. B. Palmer and D. F. Hornig, J. Chem. Phys. 26, 98 (1957).

(9) D. Britton, J. Phys. Chem. 64, 742 (1960).

(10) C. D. Johnson, and D. Britton, J. Chem. Phys. 38, 1455 (1963).

(11) D. Britton, N. Davidson, and G. Schott, Discussions Far. Soc. 17, 58 (1954)

(12) I. I. Glass, W. Martin, and G. N. Patterson, UTIA Report 2, November (1953).

(13) K. L. Wray, J. Chem. Phys. 37, 1254 (1962).

(14) T. A. Jacobs and R. R. Giedt, J. Chem. Phys. 39, 749 (1963).

(15) P. Sulzer and K. Wieland, Helv. Phys. Acta 25, 653 (1952).

(16) H. Hiraoka and R. Hardwick, J. Chem. Phys. 36, 1715 (1962).

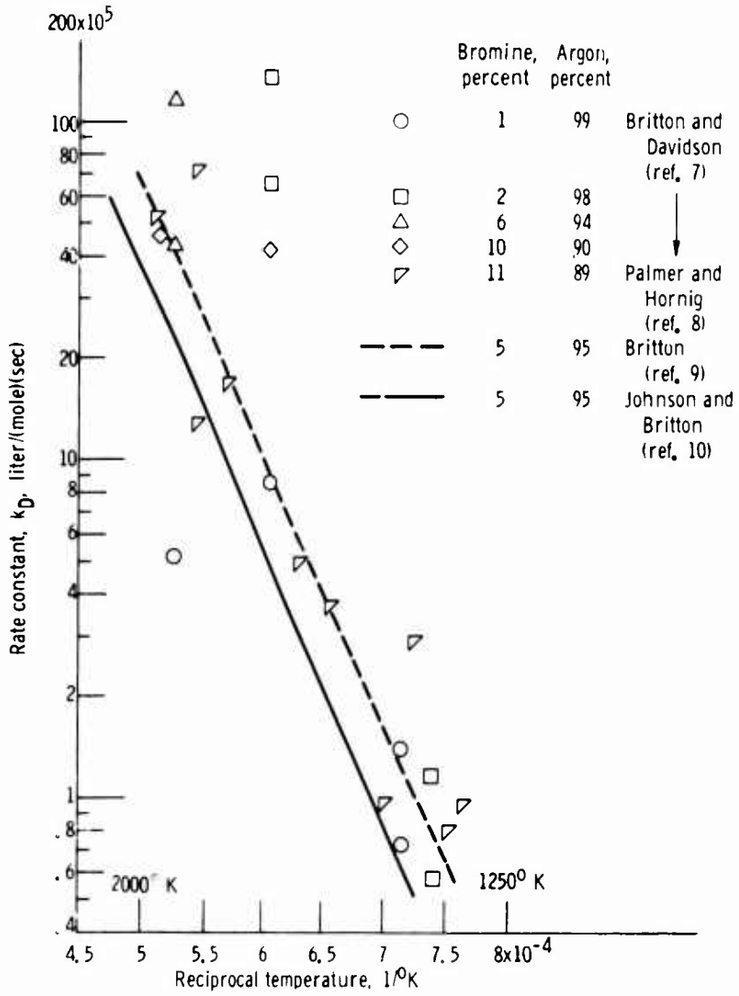


Figure 1. - Rate constants for dissociation of Br_2 in Br_2 - Ar mixtures. (Not all experimental data included for ref. 7.)

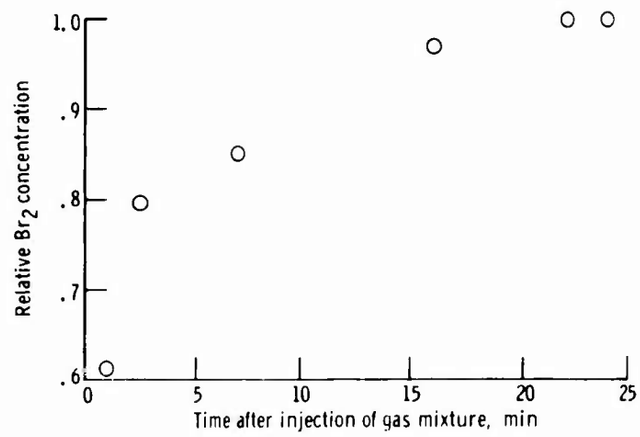


Figure 2. - Measured Br_2 concentrations of 1 percent Br_2 - 99 percent Ar mixtures in stainless-steel shock-tube driven section.

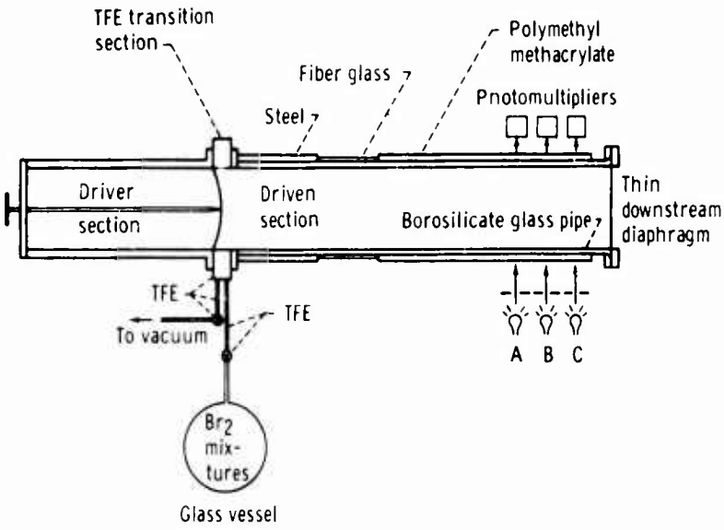


Figure 3. - Schematic of shock tube.

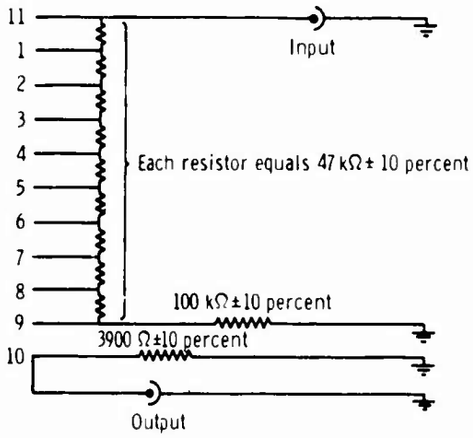


Figure 4. - 931A Photomultiplier circuit diagram.

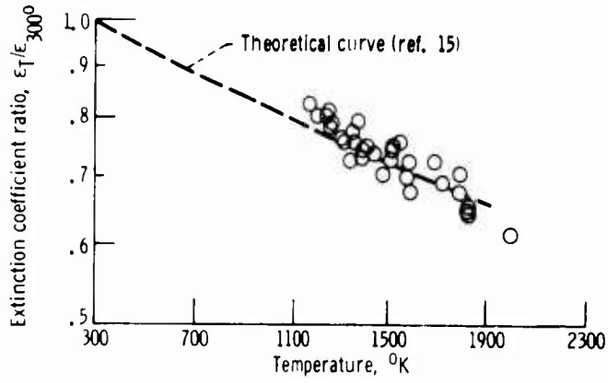
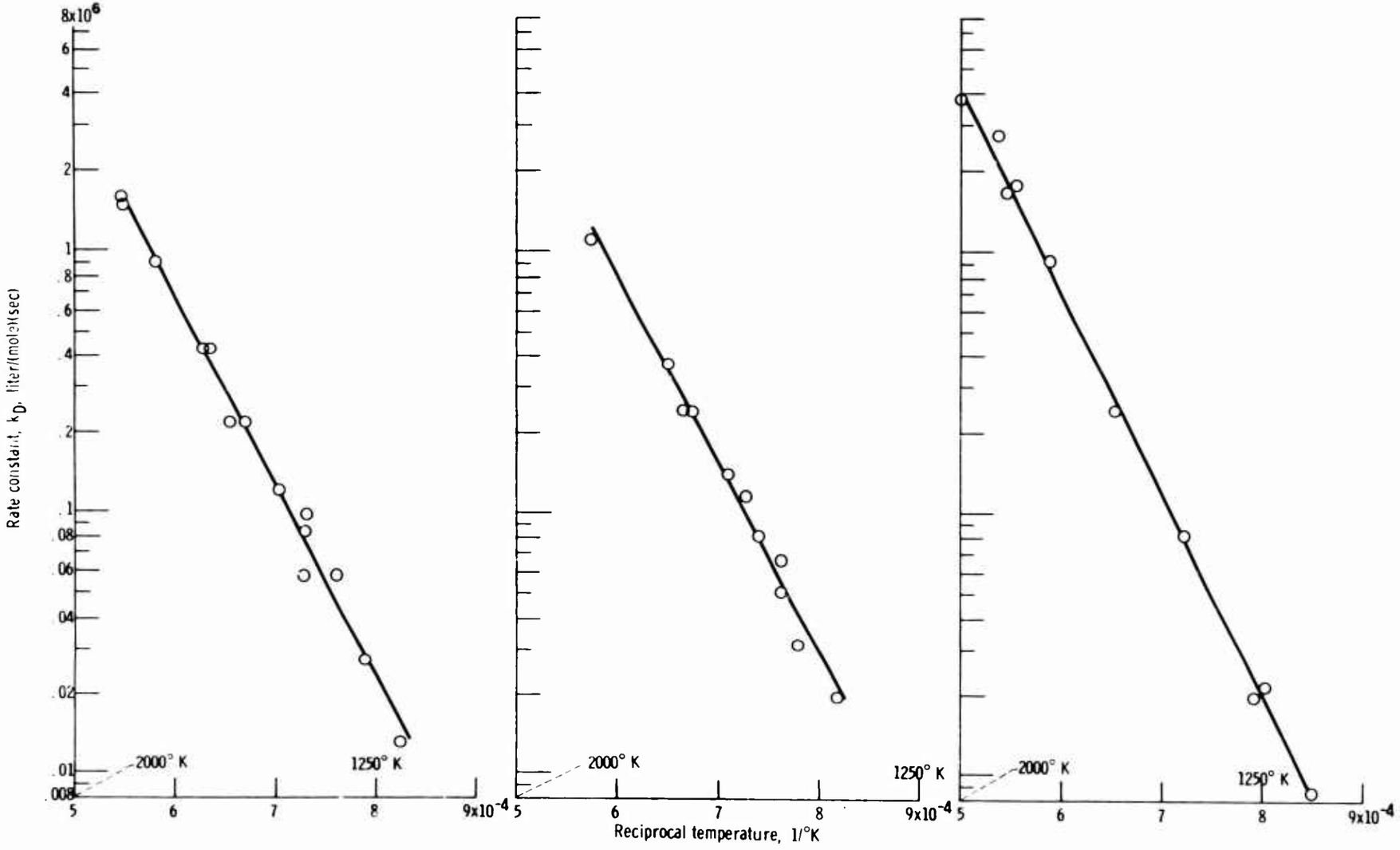


Figure 5. - Temperature dependence of Br_2 extinction coefficient at 4400 Å.



(a) 1 Percent Br_2 - 99 percent Ar.

(b) 1 Percent Br_2 - 99 percent Ne.

(c) 1 Percent Br_2 - 99 percent Kr.

Figure 6. - Rate constants for dissociation of Br_2.

BLANK PAGE

ANOMALOUS ELECTRON-DENSITY PROFILES IN SHOCK-HEATED AIR: EFFECTS OF Na and NaCℓ

M. S. Wecker
T. Baurer
R. Tomboulian

General Applied Science Laboratories, Inc.
Westbury, L.I., New York

INTRODUCTION

Observations of electron-density profiles in General Applied Science Laboratories' microwave-instrumented shock tube (MIST) had indicated the existence of discrepancies between the experimental data and profiles predicted by a computer program, based on generalized one-dimensional chemically reacting flow theory for pure air (Ref. 1). The appearance of sodium D-line emission behind both the incident and reflected shocks in the MIST had also been noted (Ref. 5).

Accordingly, the program described in Ref. 1 was expanded to include contamination of the air by NaCℓ in concentrations (initial mass fraction = $\alpha_o = 10^{-6} - 10^{-3}$) approximating the natural occurrence of salt in the air in coastal regions (Ref. 2). In order to demonstrate the effects of negative ions other than the electron, e.g. $C\ell^-$, the equivalent concentrations of Na in air were considered in a separate computation.

The calculations for pure air under typical shock conditions (u_s = 3 km/sec; p_i = 2 mm; T_i = 273°K; see Fig. I) had shown a gradual buildup of electron density behind the incident shock, as illustrated in curve A of Fig. II. When NaCℓ contamination was introduced, the calculated buildup of electron density was considerably faster, as shown in curve B of Fig. II. A comparison of Fig. II with the experimentally determined electron

densities shown in Fig. III indicates a much closer agreement between theoretical and experimental rates of electron buildup when salt contamination is included in the computation.

ANALYTICAL PROGRAMMING

The computer program used in this work was designed for maximum flexibility in its application to problems of one-dimensional flows. As presently written for the 7090 line of computers, it can simultaneously handle up to twenty species and fifty reactions in prescribed pressure or prescribed area flows with or without normal or oblique shock waves.

Among other important features are the following: optional relaxation of the vibrational energy of diatomic species, coupling of vibrational energy to dissociation rate, provision for elaborate vibrational relaxation models, flexibility in the treatment of electron energy, and statistical calculation of thermodynamic quantities from spectroscopic data.

One rate, either forward or reverse, is input for each reaction, and the equilibrium constant, which is then used to calculate the opposite rate, is calculated statistically from the partition functions of the relevant species. These partition functions are calculated using spectroscopically determined data for the energy levels of the species. Individual reaction rates may be modified at any time as new evidence becomes available.

RESULTS

Two models of the air chemistry (i.e., 7-species, 7-reactions and 9-species, 9-reactions) were utilized in the present work. These are summarized in Table I. In addition, a 3-species, 8-reactions model of Na-air interactions and a 6-species, 12-reactions model for NaCℓ-air, as summarized in Table II, were coupled to the pure air cases.

The results of electron density computations as a function of distance behind the incident shock front are shown in Fig. II. Examination of Fig. II reveals that no substantial difference in computed electron densities exists between the results of the

two air chemistry models (7 reactions vs. 9 reactions) either in the pure state (curve A) or in the slightly ($\alpha_o = 10^{-9}$) NaCℓ-contaminated state (curve B). Thus in these two instances, the effects upon electron density of reactions 8 and 9 of Table I are negligible.

However, a significant difference between the two air models was inferred in the case of slightly ($\alpha_o = 10^{-9}$) Na-contaminated air. Here, the 9-reactions air model turned out to be an absolute minimum requirement in describing the coupled Na-air chemistry and the generation of electrons therefrom, and curve C of Fig. II was plotted accordingly.

This conclusion may be demonstrated by reference to Figs. IV and V. These illustrate, for air slightly ($\alpha_o = 10^{-9}$) contaminated with NaCℓ and Na, respectively, the relative importance of all electron-producing reactions in Tables I and II as contributors to the computed net electron densities. In Fig. IV, where Cℓ is present, the prime electron producer very close behind the incident shock is the $Cℓ^-$ detachment reaction, and the O^- and O_2^- detachments are of negligible consequence. This is in agreement with curve B of Fig. II, which shows no particular difference in computed electron density as a result of adding the latter two reactions to the chemistry package when NaCℓ is the contaminant.

On the other hand, once Cℓ is eliminated from the reaction scheme, as in Fig. V, the O_2^- detachment becomes the predominant electron producer at short distances behind the incident shock. Therefore, for air slightly ($\alpha_o = 10^{-9}$) contaminated with Na, and in the absence of Cℓ-containing species, electron production within a few millimeters of the shock front is the result of the reaction: $Na + O_2 = Na^+ + O_2^-$, followed by: $O_2^- + M = O_2 + e^- + M$. This is in agreement with recent calculations reported in Ref. 4.

It should be noted further, in comparing Figs. IV and V, that in both instances the ionization of Na is relatively unimportant as a source of electrons, and that for these low levels of contamination the pure-air reaction: $N + O = NO^+ + e^-$ becomes predominant with respect to electron generation beyond approximately 6-8 mm behind the incident shock. That this distance would increase for higher levels of contamination becomes apparent from an examination of Fig. VI. Here we present the

variations of electron density over the full range ($\alpha_o = 10^{-6}$ - 10^{-3}) of atmospheric contamination by NaCℓ specified in Ref. 2. In actual experimental practice, additional contamination occurring upon surfaces might be expected to enhance considerably the amounts of NaCℓ present. This circumstance would arise, for instance, as a result of inadvertent handling of shock-tube materials, or the inclusion of sodium-containing components, e.g. greases or rubber gaskets, in the tube construction.

Figure VII is a representation of the variation of ion mole fractions for four species (Na^+, NO^+, $C\ell^-$, e^-) in a typical calculation ($\alpha_{o_{NaC\ell}} = 10^{-3}$; 7-species air). As might be expected, the Na^+ and $C\ell^-$ populations start approximately equal, very close behind the incident shock, but as $C\ell^-$ detachment sets in, this ion becomes less important. Meanwhile, the e^- and NO^+ variations converge as the pure-air chemistry begins to predominate. The Na^+ concentration appears to approach an equilibrium level. Finally, the continuing rise in electron concentration apparently causes an abrupt reversal of direction of the $C\ell^-$ detachment reaction. The latter tendency is probably aided further by the effect of decreasing temperature (cf. Fig. I) upon the equilibrium constant of the reaction.

CONCLUSIONS

Summarizing the results of this work, we find that:

1. In shock-heated pure air or slightly NaCℓ-contaminated air, the effects upon electron density of the O^- and O_2^- detachment reactions are negligible behind the incident shock.

2. In shock-heated slightly Na-contaminated air, the principal initial ionization appears to arise from the O_2^- detachment reaction.

3. In shock-heated slightly NaCℓ-contaminated air, the principal initial ionization appears to arise from the $C\ell^-$ detachment reaction.

4. For the lowest contaminant levels considered ($\alpha_o = 10^{-3}$) the pure air chemistry begins to predominate, with respect to the net production of electrons, several millimeters behind the incident shock.

5. The quantitative effects of the contaminants considered, with respect to net electron production behind the incident shock wave in air, appear to increase with increasing initial contaminant concentration.

ACKNOWLEDGMENTS

The authors would like to acknowledge the assistance of Mr. H. Hopf, who was called upon to make many modifications to the computer program used in this work. The program itself was the work of Dr. B. D. Gavril.

REFERENCES

(1) Gavril, B. D., Generalized One-Dimensional Chemically Reacting Flows with Molecular Vibrational Relaxation, GASL TR-426 (January 1964)

(2) Junge, C. E., Air Chemistry and Radioactivity, Academic Press, New York, p. 158 (1963)

(3a) Napolitano, L. G., et. al., Studies of the Electromagnetic Characteristics of Moving Ionized Gases, GASL TR-290 (May 1962)

(3b) Gavril, B. D., et. al., Studies of Electromagnetic Properties of Non-uniform Plasmas, GASL TR-316 (October 1962)

(4) Langan, W. T., Cresswell, J. D., and Browne, W. G., Effects of Ablation Products on Ionization in Hypersonic Wakes, AIAA Preprint No. 65-54 (January 1965)

(5) Tomboulian, R., Measurement of Electron-Density Profiles, Using a Microwave Technique; 5th Shock Tube Symposium, U. S. Naval Ordnance Laboratory, White Oak, Silver Spring, Maryland (April 1965).

TABLE I

PURE AIR CHEMISTRY

A. 7-Species, 7-Reaction Model	
Species	Reactions
1. O_2	1. $O_2 + M = 2O + M$
2. O	2. $N_2 + M = 2N + M$
3. N_2	3. $NO + M = N + O + M$
4. N	4. $O + N_2 = NO + N$
5. NO	5. $NO + O = N + O_2$
6. NO^+	6. $N_2 + O_2 = 2NO$
7. e^-	7. $N + O = NO^+ + e^-$
B. 9-Species, 9-Reaction Model - Above Plus:	
8. O^-	8. $O^- + M = O + e^- + M$
9. O_2^-	9. $O_2^- + M = O_2 + e^- + M$

TABLE II

CONTAMINANT CHEMISTRY

A. Sodium (3-Species, 8-Reactions)	
Species	**Reactions**
1. Na	1. $Na + M = Na^+ + e^- + M$
2. Na^+	*2. $Na + O = Na^+ + O^-$
3. NaO	*3. $Na + O_2 = Na^+ + O_2^-$
	4. $Na + NO^+ = Na^+ + NO$
	5. $NaO + M = Na + O + M$
	6. $Na + O_2 = NaO + O$
	7. $Na + NO = NaO + N$
	8. $Na + 2O = Na^+ + e^- + O_2$
B. Sodium Chloride (6-Species, 12-Reactions) - Above Plus:	
4. $NaCl$	9. $NaCl + M = Na + Cl + M$
5. Cl	10. $NaCl + M = Na^+ + Cl^- + M$
6. Cl^-	11. $Na + Cl = Na^+ + Cl^-$
	12. $Cl^- + M = Cl + e^- + M$

*N.B. - Reactions 2 and 3 are omitted in all calculations involving coupling with the 7-species, 7-reactions model of pure air chemistry; cf. Table I, Part A.

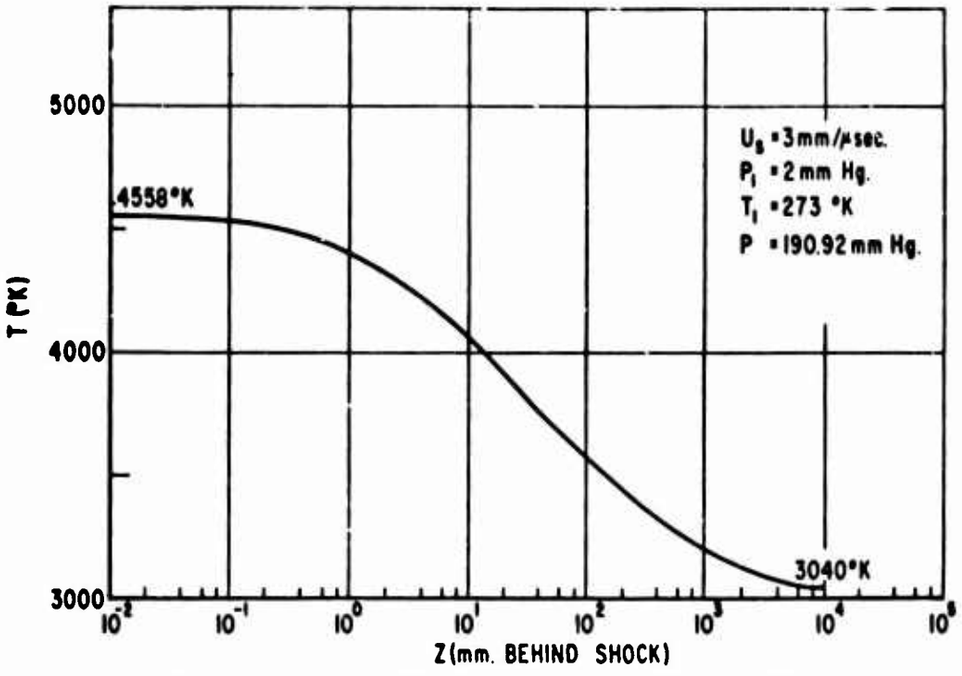


FIG. I TRANSLATIONAL TEMPERATURE PROFILE BEHIND NORMAL SHOCK IN AIR

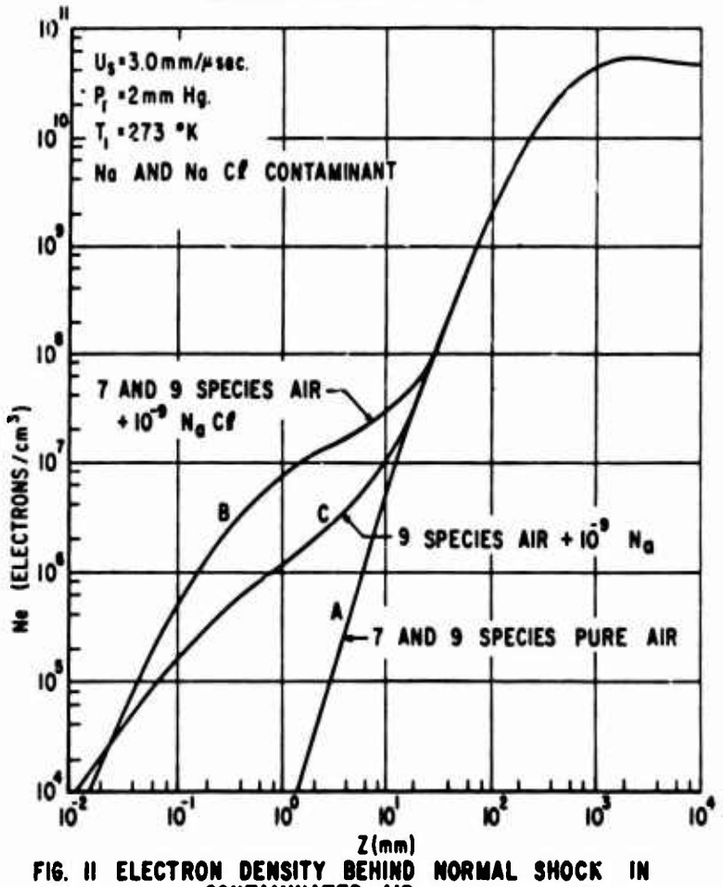


FIG. II ELECTRON DENSITY BEHIND NORMAL SHOCK IN CONTAMINATED AIR

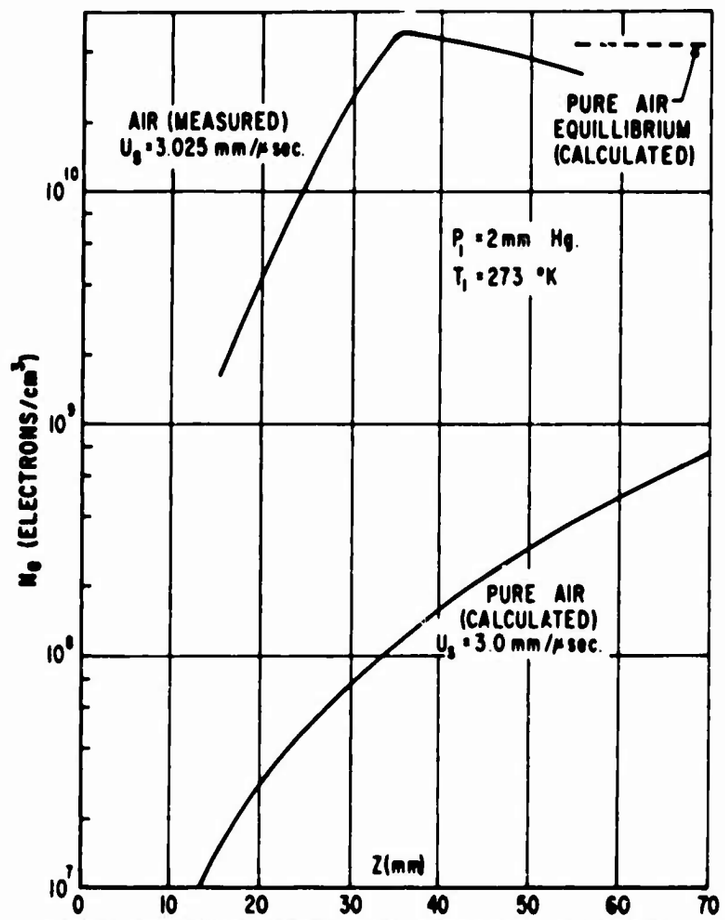


FIG. III ELECTRON DENSITY BEHIND NORMAL SHOCK IN AIR

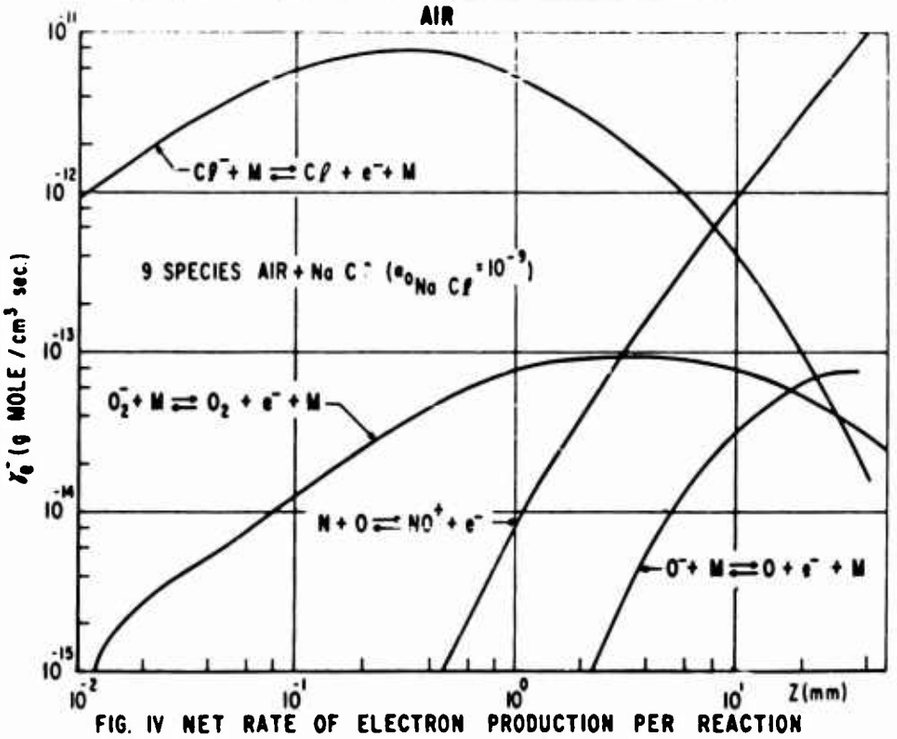


FIG. IV NET RATE OF ELECTRON PRODUCTION PER REACTION

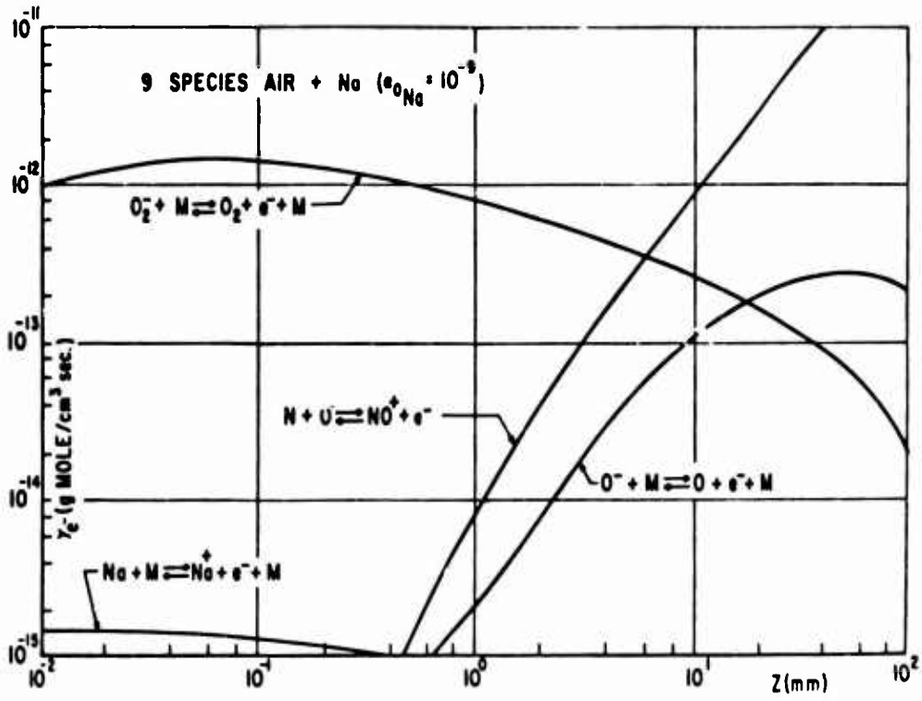


FIG. V NET RATE OF ELECTRON PRODUCTION PER REACTION

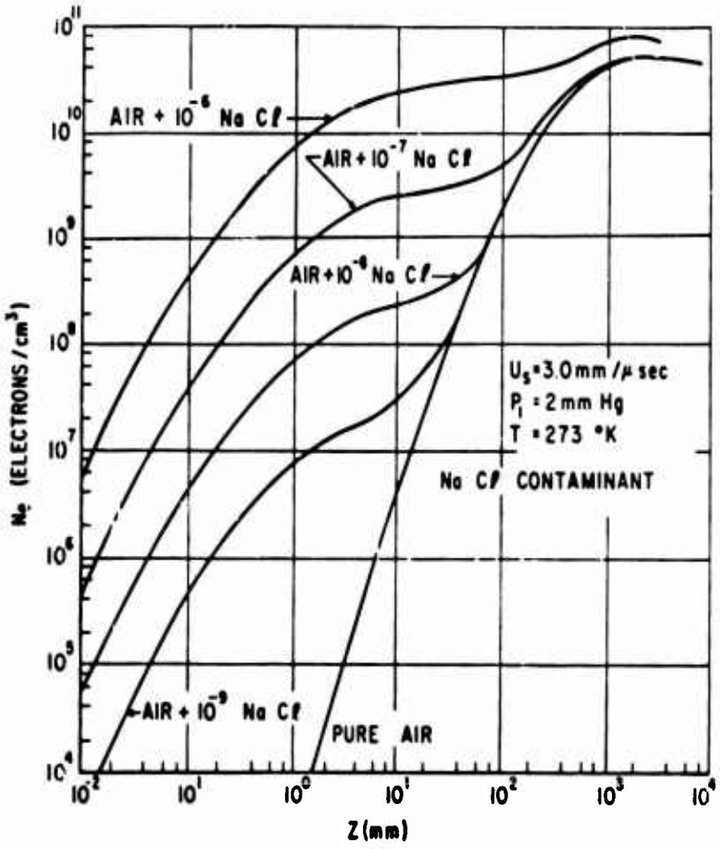


FIG. VI ELECTRON DENSITY BEHIND NORMAL SHOCK IN CONTAMINATED AIR

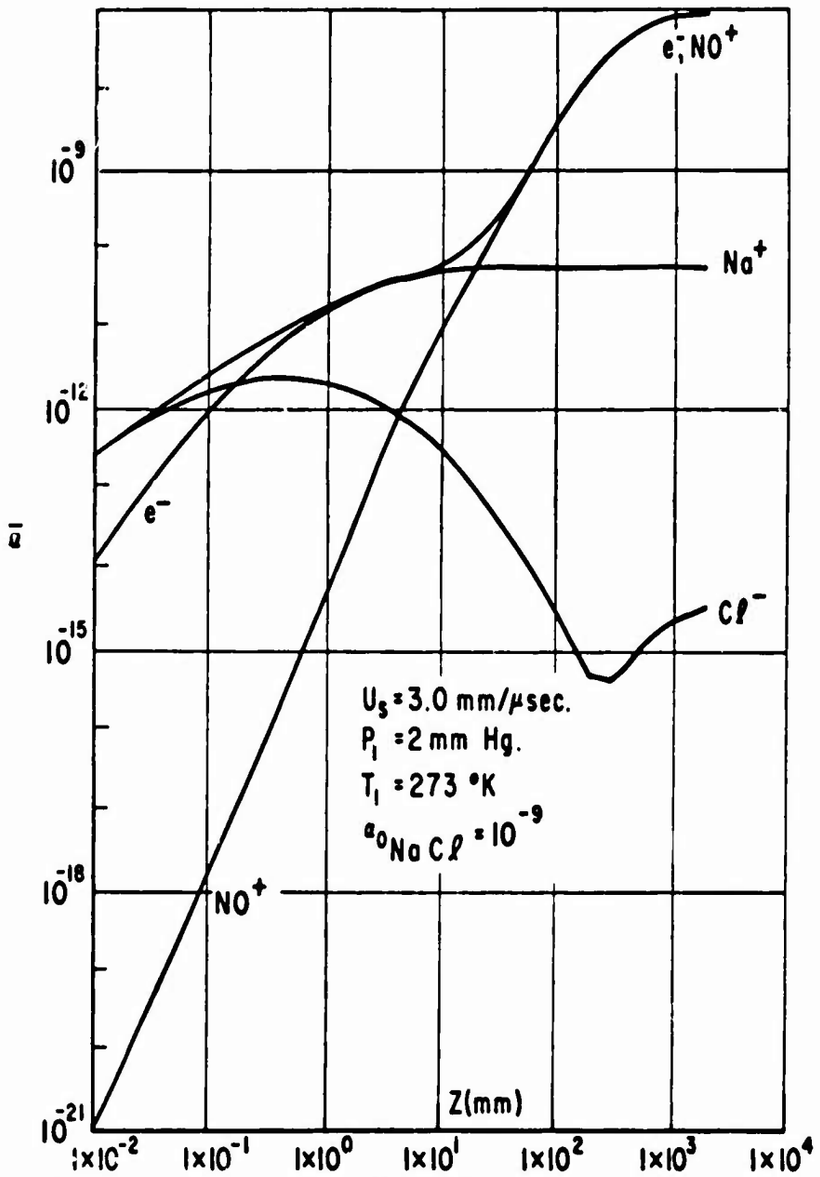


FIG. VII DISTRIBUTION OF ION MOLE FRACTIONS BEHIND NORMAL SHOCK IN CONTAMINATED AIR

BLANK PAGE

THE ASSOCIATION OF CN IN AN EXPANSION WAVE

S. H. Bauer and W. S. Watt*
Department of Chemistry, Cornell University
Ithaca, New York

ABSTRACT

The expansion wave generated by the simultaneous arrival of the "contact" surface and the reflected rarefaction wave was used for a direct kinetic study of a condensation process, the association of CN radicals generated by shocking C_2N_2/Ar mixtures to about 2000°K in the reflected shock region. During the quenching-expansion phase the concentration of CN radicals decreases due to the concurrent chemical association and the lowering in total density. The CN concentration was followed spectrophotometrically at 3883 A^o.

The results were reduced in three ways: (A) unidirectional association to C_2N_2 in the presence of a third body, (B) relaxation to the local equilibrium via a three body process, and (C) bimolecular reaction with C_2N_2 and C_mN_m polymers (formed during the heating process) to produce higher polymers. The data show that at the onset of quenching the removal of CN was sluggish. This is attributed to failure to attain equilibrium in the preparation of the sample. After $\approx$ 200 μsecs the data were best fitted by the third mechanism. This conclusion is in agreement with results obtained by another method and is supported by a reaction scheme which account for the formation and decay of CN in the presence of C_mN_m species. For a 2% initial concentration of C_2N_2, an average polymer number of $\approx$ 10 was indicated.

---

* Now at the Cornell Aeronautical Laboratory, Buffalo, New York

INTRODUCTION

Despite significant studies by several groups of workers the thermodynamics and kinetics of the decomposition of C_2N_2, and of the associated disappearance of CN radicals are not well established. In a shock tube study of C_2N_2 dissociation Tsang et al (1) have shown that CN is formed more slowly in the reflected shock than in the incident shock, although the activation energy found for the reflected shock region was less than that deduced for the incident shock conditions. This difference was attributed to the formation of low molecular weight polymers during exposure of the sample gas to the incident shock. More direct evidence for the existence of such species stems from the data of Berkowitz (2) who, while studying the formation of CN and C_2N_2 in the reaction of nitrogen with carbon in a Knudsen cell, observed in the mass spectrometer several low molecular weight C_xN_y (x and y $\neq$ 6) species which can only be presumed to have resulted from some polymerization process.

Paul and Dalby (3) followed the disappearance of CN radicals produced by photolysis of C_2N_2 and found that the loss of CN was given by the expression:

$$\frac{d\,CN}{dt} = k\,(CN)\,(C_2N_2).$$

This conclusion conflicts somewhat with the earlier experiments of White (4) who reported that CN radicals, produced in an electric discharge through C_2N_2, disappeared by a first order process, the rate of which was independent of the pressure. In contrast to the results of Paul and Dalby and of White, Basco et al (5) claim to have demonstrated that CN radicals formed by photolysis of C_2N_2, BrCN and ICN were removed by a second order process, presumed to be the ter-molecular recombination reaction. These authors point out, however, that their experimental results could be roughly fitted to a first order plot, which gave a rate constant that varied with the pressure of XCN in an inexplicable way.

In single pulse operation, a shock tube can be used to heat a sample of gas behind the reflected shock and then to cool it rapidly (6). Cooling is caused by an expansion wave which under selected conditions is generated when the "contact surface" and the reflected rarefaction wave interact simultaneously with the reflected shock. The rate of cooling can be as high as 10^6 degrees per second (7). This experimental procedure is suitable for studying the formation and decay of free radicals and/or other reactive intermediates which may be produced at temperatures attainable in the shock tube, provided that a fast response analytical technique can be employed. The following report appears to be the first in which the quenching-expansion wave has been used for a direct kinetic study of a condensation process. In this study we

undertook to produce CN radicals and low molecular weight $(CN)_m$ polymers by shocking mixtures of C_2N_2 in argon to about 2000°K in the reflected shock region; and then to follow the disappearance of the CN radicals during the expansion.

KINETIC RELATIONS

During the expansion the concentration of CN radicals decreases by (a) chemical reaction (association) and (b) lowering in density due to the large drop in pressure. Examination of the pressure-time records of many shocks has revealed that during the expansion the pressure at any time is given by:

$$p_6(t) = p_5 \exp(-t/\tau_p) \tag{1}$$

where p_5 is the pressure at $t = 0$, the onset of the expansion process, and τ_p is the characteristic time for the pressure decay. However, to a good approximation the expansion is adiabatic; hence

$$\rho_6(t) = \rho_5 \exp(-t/\tau_\rho) \tag{2}$$

where $\rho_6(t)$ and ρ_5 are the corresponding densities, and $\tau_\rho = \gamma \tau_p$; γ is the specific heat ratio. A parallel expression follows for the temperature, provided the reactants are present in low concentrations and the reaction is not excessively endo- or exothermic.

Let us examine an element of gas at a distance x from the end wall during the expansion regime; then the total change in concentration $(\frac{\partial c}{\partial t})$ plus a correction for the motion of the particles through this element, will give the chemical rate Γ,

$$\frac{\partial c}{\partial t} + \frac{\partial (cu)}{\partial x} = \Gamma \tag{3}$$

$$\frac{\partial c}{\partial t} + c\frac{\partial u}{\partial x} + u\frac{\partial c}{\partial x} = \Gamma \tag{4}$$

The density, however, is not affected by chemical reaction in a highly diluted system:

$$\frac{\partial \rho}{\partial t} + \frac{\partial (\rho u)}{\partial x} = \frac{\partial \rho}{\partial t} + \rho\frac{\partial u}{\partial x} + u\frac{\partial \rho}{\partial x} = 0$$

$$\frac{\partial u}{\partial x} = -\frac{1}{\rho}\left(\frac{\partial \rho}{\partial t} + u\frac{\partial \rho}{\partial x}\right) \tag{5}$$

Substituting Eq. 5 into Eq. 4

$$(6) \qquad \frac{\partial c}{\partial t} - \frac{c}{\rho}\left(\frac{\partial \rho}{\partial t} + u\frac{\partial \rho}{\partial x}\right) + u\frac{\partial c}{\partial x} = \Gamma$$

At the end wall $u = 0$ but $\frac{\partial u}{\partial x} \neq 0$. Consider the relative magnitudes of the terms inside the parenthesis in Eq. 6:

$$(7) \qquad (\partial\rho/\partial t)/u(\partial\rho/\partial x) = (\partial\rho/\partial t)/u(\partial\rho/a\partial t) = a/u$$

but $a >> u$ near the wall; hence Eq. 6 may be simplified to

$$(8) \qquad \frac{\partial c}{\partial t} - \frac{c}{\rho}\frac{\partial \rho}{\partial t} = \Gamma$$

There are several possible models for the chemical rate Γ. Consider first a non-reversible three body association reaction,

$$(A) \qquad 2\,CN + M \xrightarrow{k_3} C_2N_2 + M$$

Then Eq. 8 reduces to

$$(9) \qquad \frac{dc}{dt} - \frac{c}{\rho}\frac{d\rho}{dt} = -k_3 c^2 \cdot M$$

and finally, because of Eq. 2,

$$(10) \qquad \frac{dc}{dt} + \frac{c}{\tau_\rho} = -k_3 c^2 M$$

In the second model, consider a three body association reaction in which the system attain equilibrium under reflected shock conditions at the end of the dwell time. The expansion perturbs this state but not excessively, so that throughout the decay it remains close enough to equilibrium for a relaxation equation to apply.

$$(B) \qquad 2\,CN + M \underset{k_3}{\overset{k_{-3}}{\rightleftharpoons}} C_2N_2 + M$$

The net association rate is then linearly dependent on the magnitude of the departure from equilibrium (8) (9). Then

$$\frac{dc}{dt} + \frac{c}{\tau_\rho} = \frac{c_{eq} - c}{\tau_c} \tag{11}$$

where $\tau_c^{-1} = (4\, k_3\, c_{eq} + k_{-3})\,[M]$, and $[M]$ is the concentration of third body collision partners. Note that whereas both c_{eq} and c are functions of time, the functional relation for c_{eq} can be calculated from $\rho(t)$. However, far from equilibrium there is no such simplification.

The third plausible expression for Γ is based on the assumption that the rate of disappearance of CN is first order in CN and in polymer, $(CN)_m$ where $m \geq 2$;

$$CN + (CN)_m \xrightarrow[k_1]{} (CN)_{m+1} \tag{C}$$

Then for neglibible reversible rate

$$\frac{dc}{dt} + \frac{c}{\tau_\rho} = -k_1\, c \cdot (CN)_m \tag{12}$$

Since the specific reaction rate constants are temperature dependent and since the temperature is changing throughout the expansion process, these constants, as well as c_{eq} are time dependent. To integrate Eqs. 10, 11, and 12 specific functional dependencies have to be introduced.

The experimental data show that if the mechanism involves the direct recombination reaction, the CN concentration remains close to its equilibrium value only for a short time at the beginning of the expansion region but thereafter becomes much greater than the equilibrium value. Hence, model B and Eq. 11 need not be considered further.

For model A, integration of Eq. 10, assuming that k_3 has the form (A/T^3) as suggested by Tsang et al (1), gives

$$(c_o/c) \exp(-t/\tau_\rho) = 1 + 5\, \tau_\rho \cdot c_o \cdot k_3 \cdot M_o\, (1 - e^{-0.2t/\tau_\rho}) \tag{13}$$

Further, since $t/\tau_\rho \not< 1$, Eq. 13 can be simplified to

$$(14) \qquad (c_o/c) \exp(-t/\tau_\rho) = 1 + c_o \cdot M_o \cdot k_3^o \cdot t$$

where k_3^o, c_o and M_o are the rate constant for association, the concentration of CN and the concentration of third bodies, respectively, at $t = 0$, i.e., at the onset of expansion.

For model (C) write $(CN)_m = N_o \exp(-t/\tau_\rho)$ in Eq. 12; rearrange to

$$(15) \qquad -\frac{dc}{c} = \left[\frac{1}{\tau_\rho} + k_1 N_o \exp(-t/\tau_\rho) \right] dt$$

where N_o is the concentration of polymers at $t = 0$. If one assumes that over the relatively short temperature range involved k_1 is independent of the temperature, integration of Eq. 15 leads to

$$(16) \qquad \ln(c_o/c) - t/\tau_\rho = k_1 N_o \tau_\rho (1 - e^{-t/\tau_\rho})$$

However, a small activation energy is usually required for polymer growth; write, $k_1 = A \exp(-\Delta E/RT)$, and $T = T_o \exp(-t/\tau_T)$. Hence

$$(17) \qquad k_1/k_1^o = \exp\left[-\alpha \left[\exp(t/\tau_T) - 1 \right] \right]$$

where $\alpha \equiv \Delta E/RT_o$ and k_1^o is the rate constant at T_5, i.e. at $t = 0$. Since $\tau_T = \left(\frac{1}{\gamma-1}\right)\tau_\rho \approx 2.2$ msec, whereas t varies from 0 to 1.1 msec for all experiments reported below, $t/\tau_\rho \leq 0.5$; and one may approximate $[\exp(t/\tau_T) - 1]$ by t/τ_T. Then $k_1/k_1^o = \exp\left(\frac{-\alpha(\gamma-1)t}{\tau_\rho}\right)$;

On substituting this expression into Eq. 12 and integrating,

$$(18) \qquad \ln(c_o/c) - t/\tau_\rho = \frac{k_1^o N_o \tau_\rho}{(1 + \alpha(\gamma-1)} \left[1 - \exp(-[1 + \alpha(\gamma-1)]\, t/\tau_\rho) \right]$$

From Paul and Dalby's data extended to the range of our experiments we find α 0.5, while $\gamma = 1.67$ for these very dilute systems,

$$(19) \qquad \ln (c_o/c) - t/\tau_\rho = \frac{k_1^o N_o \tau_\rho}{1.25} (1 - \exp [-1.25t/\tau_\rho])$$

If the decay process is second order in CN and first order in Ar, Eq. 14 requires that a plot of $(c_o/c) \exp (-t/\tau_\rho)$ vs t give a straight line with slope $[c_o M_o k_3^o]$. If the decay is first order in CN and first order in $(CN)_m$, the indicated functions for a linear plot are $[\ln(c_o/c) - t/\tau_\rho]$ vs $\exp (-t/\tau_\rho)$ for k_1 independent of T, or $\exp (-1.25t/\tau_\rho)$ for k_1^o given by Eq. 17. The corresponding slopes are given by the coefficients of the right member in Eqs. 16 and 19.

EXPERIMENTAL

Cyanogen, obtained from the American Cyanamid Company, was degassed by freezing and pumping at -78° to remove any O_2 and N_2, and then distilled at - 25° to remove ClCN. Mass spectrometric analysis of samples thus treated showed no impurities. Linde argon, 99.99% was used without further treatment for the carrier gas. Samples of 2%, 1% and 0.5% C_2N_2 in argon were prepared in five and ten liter bulbs and allowed to mix overnight before use.

The shock tube and the technique of specific absorption spectroscopy were described in previous publications from these laboratories (1). Absorption at the (0, 0) band head of the $B, {}^2\Sigma^+ \rightarrow X, {}^2\Sigma^+$ transition of CN was used to measure the CN concentration. The analytical ray passed through the tube 7 mm. from the end wall. Experiments were carried out over the temperature range 1875° to 2325°, in the reflected shock region. Dwell times at these temperatures were ≈1100 μsec. Total reflected shock densities ranged from 11.4×10^{-3} moles/liter to 15.3×10^{-3} moles/liter.

RESULTS

Figure 1a shows the oscilloscope record of the signals from the photomultiplier monitoring the output (at 3883A°) of the spectroscopic flash lamp; the band pass of the monochromator was 0.75A°. The upper trace records the intensity of the light beam which passes through the shock tube, while the lower trace records the intensity of the reference light beam (bypasses the shock tube). These two traces were matched as closely as possible before filling the tube. Figure 1b is a recording of the output of these photomultipliers during the reflected shock and the subsequent cooling period. The ratio of intensities of the two signals is a measure of the CN concentration during its

formation and disappearance regimes. Figure 1c records the intensity of the light beam which passes through the tube and the pressure as monitored by a piezoelectric gauge situated in the same plane as the optical windows. This trace provides time correlation between the spectral absorption data and the gas dynamic processes.

Figure 2a shows a typical plot for 2% C_2N_2, of reduced absorption (in optical density units) and of the pressure trace. Shortly after the arrival of the reflected shock CN radicals were generated. The concentration of CN appears to be approaching an equilibrium level toward the end of the dwell period. Upon the arrival of the expansion wave, the CN concentration begins to fall and eventually reaches zero. Also shown on this graph are calculated concentrations of CN assuming (a) no reaction and (b) the reaction rate is sufficiently rapid to maintain equilibrium for the association $2\ CN \rightleftharpoons C_2N_2$, with no polymerization. One disturbing feature was that in the experiments performed with 1% (Fig. 2b) and 0.5% (Fig. 2c) of C_2N_2, the CN concentration did not begin its decline at the onset of expansion, but "overshot" by up to 150 microseconds before any decline became evident. This feature was not observed for the 2% C_2N_2 runs. Analysis of the data for the rate of formation of CN during the reflected shock regime confirmed the measurement of Tsang et al (1) that the activation energy for this process is between 60 and 70 kcal/mole. It thus appears that considerable quantities of higher polymeric species containing C and N are generated and that the concentration of CN radicals may be almost completely dependent on the thermal decomposition of the polymers. Further evidence that in the reflected shock region the CN radicals are not primarily produced by decomposition of C_2N_2 is shown by the fact that the amount of CN found is considerably less than would be formed if CN were in equilibrium with C_2N_2, assuming no polymerization had taken place. This disparity becomes greater as the initial C_2N_2 concentration is decreased from 2% to 1% and 0.5%. The overshoot is qualitatively accounted for in Fig. 3. Only at the higher concentration was the equilibrium level of CN nearly attained during the reflected shock dwell time (curve —x x—); it was not attained for the 1% and 0.5% C_2N_2 mixtures (curve —o o—). Fig. 4 are quantitative plots of the pressure, density and temperature for typical runs.

Fig. 5a and 5b show, respectively, the results of plotting reduced values for typical runs assuming mechanism A, Eq. 14, and assuming mechanism C, Eqs. 16 and 19. It is evident from these graphs that the rate of depletion of CN is sluggish at the beginning and only becomes appreciable after about 200 μsec. It is also clear that despite some scatter the data favor mechanism C, if one ascribes the scatter during the first $\approx$ 200 μsec to the overshoot phenomenon indicated in Fig. 3.

Table I is a summary of the experimental results obtained. In this reduction we used the effective absorption coefficient reported by Tsang (1), $\mu\ell = 3.77 \times 10^5$ liters/mole. It may be readily seen that t_{delay}, the time lapse between the sharp decline in pressure and the first decline in the (CN) concentration, is larger when $(C_2N_2)_{initial}$ is smaller; the ratio $(CN)^{(5)}_{found}$ to $(CN)^{(5)}_{no\ polymer}$ (at the end of the dwell period) also decreases in this direction. $k_1^o N_o$, where N_o is assumed to be $C_m N_m$, is seen to be essentially independent of temperature, Fig. 6. Paul and Dalby found that the rate constant for the reaction of CN with C_2N_2 was only slightly temperature dependent, changing by $\approx 10\%$ over the temperature interval 1900° - 2300°K. By analogy one may expect that k_1 would have a similar temperature dependence, i.e., over the temperature range studied k_1 remains essentially unchanged. From the value quoted in Table I, it follows that consequently N_o is also approximately independent of T_5, and that the degree of polymerization is greatest at the highest initial C_2N_2 concentration. If one accepts the value of k_1 from Paul and Dalby's data extrapolated to the temperature regime used in these experiments, he can deduce a value for N_o from these data. Since $(C_2N_2)_o$ is readily calculated on the assumption of no polymerization, it is then possible to estimate the degree of polymerization. This procedure indicates that at the lowest $(C_2N_2)_{initial}$ the average polymerization number is two; at the highest $(C_2N_2)_{initial}$, $N_o/(C_2N_2)_{o,\,no\ polymer} \approx 0.2$; i.e., that the average polymer species contains ten CN units.

MECHANISM

The following mechanism is proposed to explain the formation of polymeric C_mN_m and CN radicals behind the reflected shock and to account for the other observed features:

(I) $$C_2N_2 + Ar \overset{(i)}{\rightleftharpoons} 2\,CN + Ar$$

(II) $$CN + C_2N_2 \xrightarrow{(ii)} C_3N_3$$

$$C_3N_3 + C_2N_2 \xrightarrow{(iii)} C_5N_5$$

$$C_5N_5 + C_2N_2 \xrightarrow{(iv)} C_6N_6 + CN$$

(III) $$C_6N_6 \overset{(v)}{\rightleftharpoons} C_5N_5 + CN$$

$$C_5N_5 \overset{(vi)}{\rightleftharpoons} C_4N_4 + CN$$

In part (I) it is proposed that a small number of CN radicals are produced by dissociation of cyanogen at the incident shock temperature. Polymerization is initiated by the monomeric species. This reduces the net rate of production of CN, while propagation proceeds by the chain mechanism written in part (II). It is likely that initiation and propagation take place in both the incident and reflected shock regions. The consequence of (II) following (I) is that the concentration of CN is greatly reduced from that which would be expected if (I) were allowed to reach equilibrium, and reaction (III) suggest that the main production of CN in the reflected shock region is by thermal decomposition of the C_mN_m polymers; reversal of the reactions leads to the eventual disappearance of CN by association with the polymer fragments.

Although it is assumed that C_6N_6 has a somewhat higher stability than the lower species, this does not imply that higher polymeric species are not formed in small amounts by further condensation. C_6N_6 may well be cyanuric tricyanide, from which the species C_5N_5 is readily formed by loss of one CN group. If C_6N_6 indeed has the structure proposed, then C_5N_5 will retain a large measure of the stability inherent in the cyanuric ring structure. Classical structures may be written for the even-number polymers of CN, while the odd-number species have a free valence.

From the mechanism proposed, assuming steady state concentrations for C_3N_3 and C_5N_5 it can be shown that the production or loss of CN depends only on the species involved in reaction (v).

$$\frac{d\,CN}{dt} = 2\,k_{(v)}(C_6N_6) - 2\,k_{-(v)}(C_5N_5)(CN)$$

For $\frac{d\,CN}{dt}$ to become negative (when the expansion region arrives) C_6N_6 must have reached a steady-state or equilibrium level which may depend on whether higher polymers are being formed. Its temperature dependence is such that as the temperature falls $k_{-(v)}(C_5N_5)(CN) > k_{(v)}(C_6N_6)$. Clearly, C_6N_6 will be generated more slowly at low initial C_2N_2 concentrations and hence it will take longer to attain the steady state of C_6N_6. The delay observed in the decay of (CN) radicals in shocks containing low initial C_2N_2 concentrations is greater the lower $(C_2N_2)_{initial}$. If equilibrium were reached at all $(C_2N_2)_{initial}$ one would expect that the ratio $(CN)^{(5)}_{found}$ to $(CN)^{(5)}_{expected}$

if there were no polymerization, would be relatively insensitive to changes in $(C_2N_2)_{initial}$. However, it can be seen that this ratio decreases by a factor of 3 - 4 as $(C_2N_2)_{initial}$ is lowered by a factor of four, again indicating that the steady state or equilibrium concentration of C_6N_6 was not attained. For the higher concentrations, an average polymer number of 10 was deduced, assuming the value for k_1 [$= 7.3 \times 10^7 \exp\left(-\frac{2100}{RT}\right)$, liters/mole sec] reported by Paul and Dalby.

ACKNOWLEDGEMENTS

This work was supported by a grant from NASA (NsG-116-61), to whom grateful acknowledgement is made.

REFERENCES

(1) Tsang, W., Bauer, S. H., and Cowperthwaite, J. Chem. Phys., 36, 1768 (1962).

(2) Berkowitz, J., J. Chem. Phys., 36, 2533 (1962).

(3) Paul, D. E., and Dalby, F. N., J. Chem. Phys., 37, 592 (1962).

(4) White, J. U., J. Chem. Phys., 8, 79, 459 (1940).

(5) Basco, N., Nicholas, J. E., Norrish, R.A.W., and Vickers, W.H.J., Proc. Roy. Soc., (London) - 272A, 147 (1963).

(6) Glick, H. S., Squire, W., and Herzberg, A., Fifth International Symposium on Combustion, Reinhold Publishing Corp., New York., (1955).

(7) Lifshitz, A., Bauer, S. H., and Resler, E. L., Jr., J. Chem. Phys., 38, 2056 (1963).

(8) Eigen, M., and de Maeyer, L., Techniques Of Organic Chemistry, A. Weissberger Editor, Vol. VIII, part 2., page 901,916 (1963).

(9) Duff, R. E., Phys. Fluids, 1, 242 (1958).

TABLE 1

Run No.	mole % C_2N_2	T_5 (°K)	τ_ρ (m sec)	τ_{delay}	$CN^{(5)}_{found}$ (mole/ℓ)	$CN^{(5)}_{no\ poly}$ (mole/ℓ)	$k_1^o N_o$ (sec^{-1})	k_1^o(P+D) ℓ $mole^{-1}$ sec^{-1}	N_o (mole/ℓ)	C_2N_2 no poly (mole/ℓ)
					x 10^6	x 10^6	x 10^{-3}	x 10^{-7}	x 10^5	x 10^5
W01	2	1940	1.33	0	1.43	1.85	2.57	4.22	6.09	30.6
02	2	1920	1.34	0	0.84	1.57	2.85	4.20	6.79	31.0
04	2	1875	1.31	0	0.79	1.10	3.54	4.15	8.53	31.0
06	2	1960	1.36	0	1.49	2.22	3.27	4.25	7.69	30.6
07	2	1890	1.45	0	0.92	1.18	2.09	4.17	5.02	31.0
2W03	1	1990	1.29	140	0.80	1.62	1.97	4.29	4.59	13.1
04	1	1985	1.30	30	0.57	1.60	2.82	4.28	6.58	13.1
05	1	2090	1.35	0	0.95	3.62	4.18	4.40	9.52	12.8
3W01	.5	2105	1.30	100	0.49	2.74	1.82	4.42	4.12	6.3
02	.5	2030	1.44	100	0.61	2.48	2.58	4.33	6.96	6.2
03	.5	2215	1.24	75	1.09	5.33	3.70	4.53	8.17	5.9
05	.5	2325	1.35	115	1.91	9.85	3.40	4.63	7.34	5.7
C105	1	2090	1.33		1.88	3.63	1.96	4.40	4.46	13.2
106	1	1965	1.33		0.83	1.48	2.32	4.25	5.46	13.8
108	1	1945	1.33		0.56	1.40	1.55	4.23	3.67	14.6
110	1	2120	1.33		1.79	4.47	2.12	4.44	4.77	14.1
111	1	2050	1.33		1.23	2.78	2.57	4.35	5.91	13.7
113	1	2030	1.33		0.96	2.38	2.50	4.32	5.78	14.1
115	$.5_5$	2090	1.33		1.20	2.70	2.38	4.40	5.41	7.3
116	$.5_5$	2055	1.33		0.84	1.97	2.72	4.36	6.25	6.9
117	$.5_5$	2195	1.33		1.88	5.22	3.37	4.52	7.46	6.8
118	$.5_5$	2110	1.33		1.24	2.91	2.17	4.42	4.91	6.7
120	$.5_5$	2070	1.33		0.72	2.34	2.63	4.38	6.00	7.4
121	$.5_5$	2060	1.33		1.18	2.08	2.22	4.37	5.08	6.9
122	$.5_5$	2155	1.33		1.59	4.00	2.72	4.47	6.08	7.2
123	$.5_5$	2115	1.33		0.99	3.13	3.57	4.43	8.06	7.5
124	$.5_5$	2055	1.33		0.89	2.09	1.58	4.36	3.63	7.8

NOTES: Column 2 is the initial concentration
6 is the maximum level attained at T_5
7 is the calculated value for C_2N_2 = 2 CN, eq. at T_5, assuming no polymer format
11 is calculated concentration at T_- - amount dissociated is negligible

11 is calculated concentration at T_5 - amount dissociated is negligible.

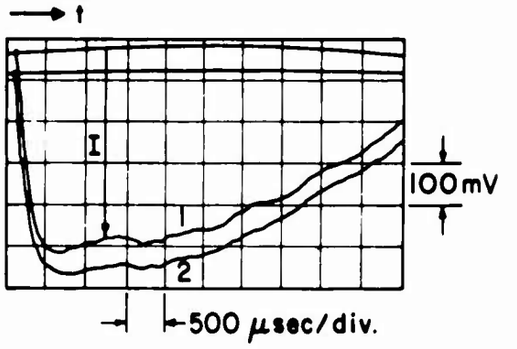


Fig. Ia
1 Through tube
2 Reference beam
Prior to Shock

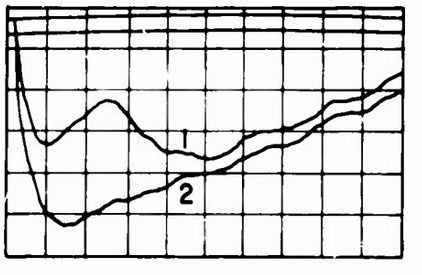


Fig. Ib
Under Shock Conditions

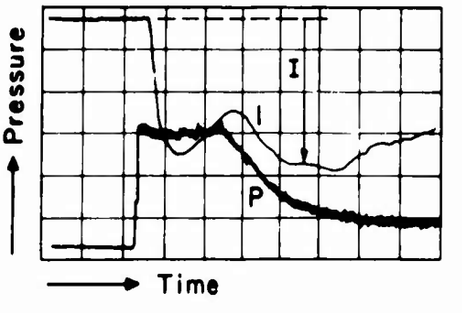
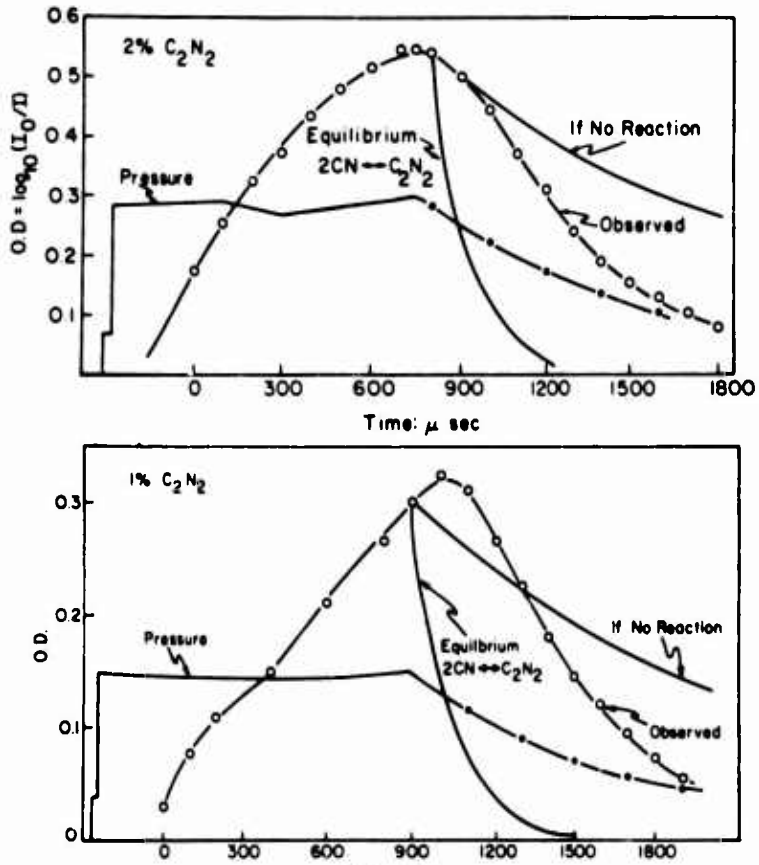


Fig. Ic
Simultaneous Absorption (I) and Pressure (P) Records

Figure 1. Typical oscillogram traces.
Trace 1 - analyzing beam, through the tube
2 - reference beam

(a) prior to shock: shows match condition
(b) under shock conditions
(c) simultaneous absorption and pressure records.



a.

b.

c.

Figure 2. Reduced absorption (optical density) and pressure traces as observed.
The calculated traces for (CN) assuming no reaction and maintainance of equilibrium with the expansion, are also given, for

(a) 2% initial C_2N_2

(b) 1% initial C_2N_2

(c) 0.5% initial C_2N_2

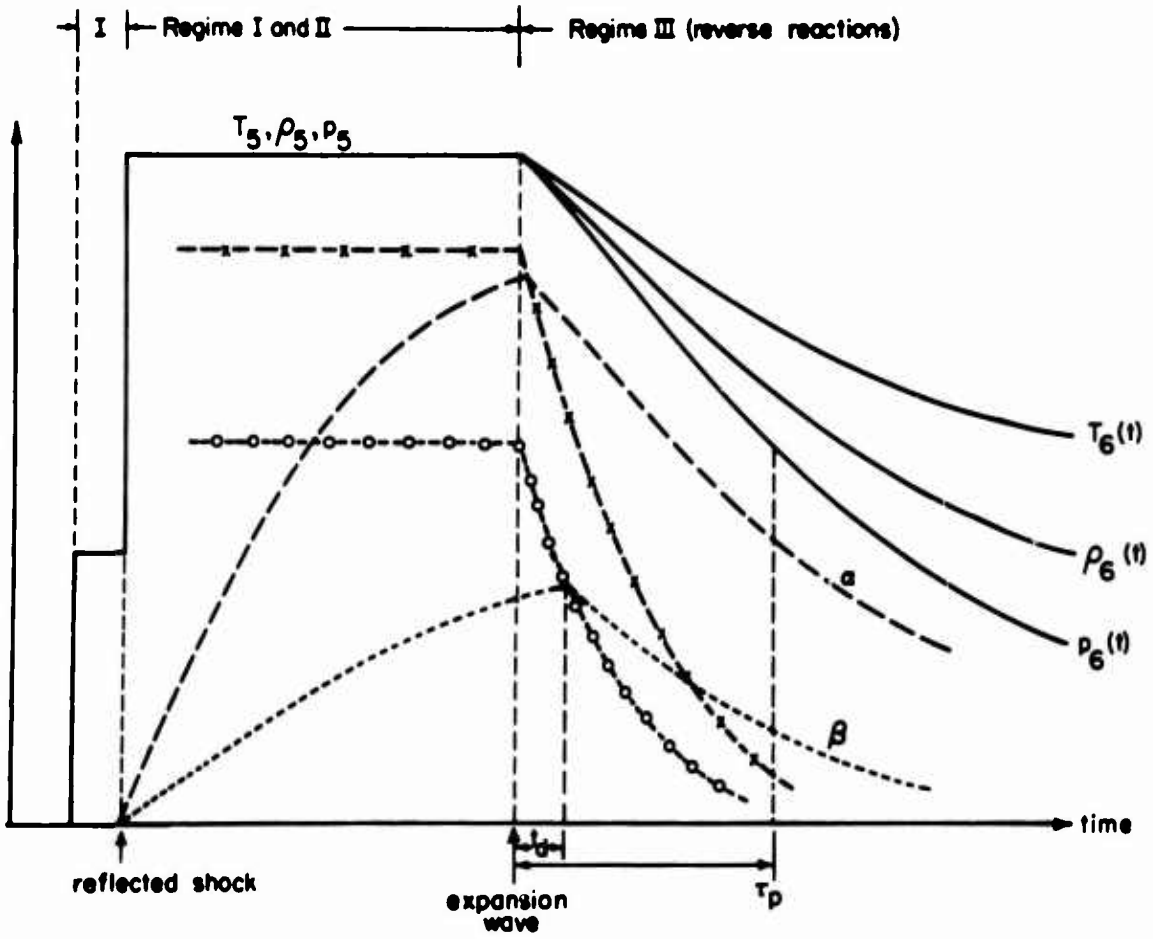


Figure 3. Schematic histogram which qualitatively accounts for the occurance of a delay (t_d) in the decline of CN, past the initiation of expansion.

—— x —— —— x —— shows the calculated equilibrium
-- o -- o -- o -- concentrations of CN for high and low initial C_2N_2, respectively

Curves α, β are the corresponding anticipated concentrations due to finite dissociation and association rates.

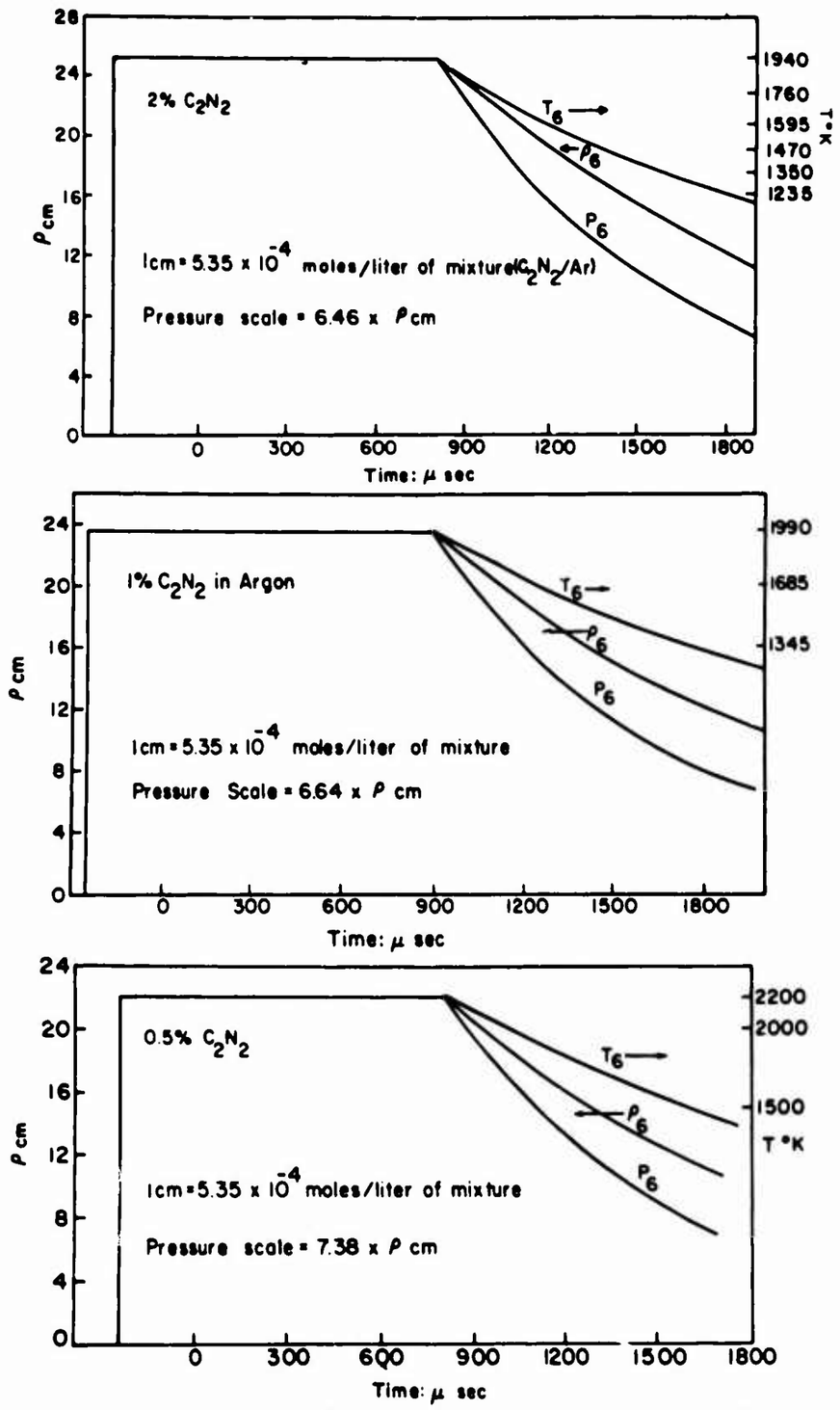
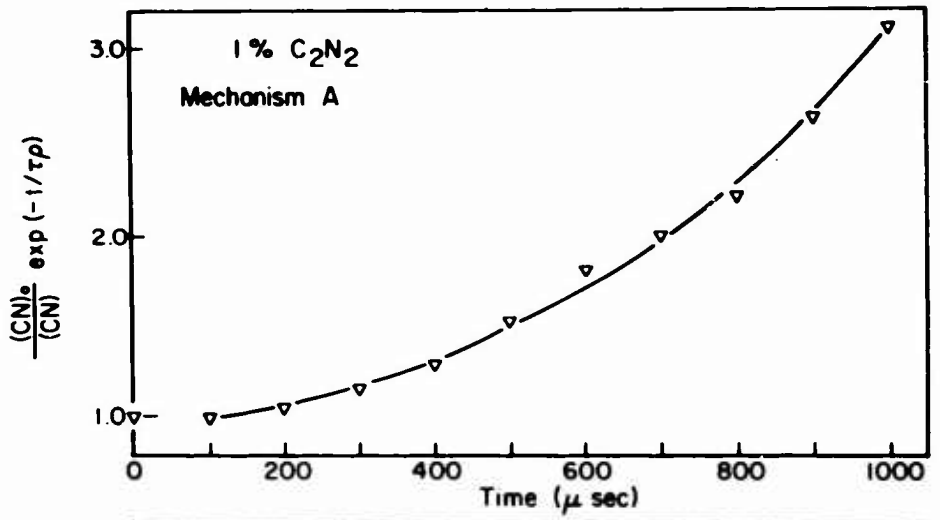
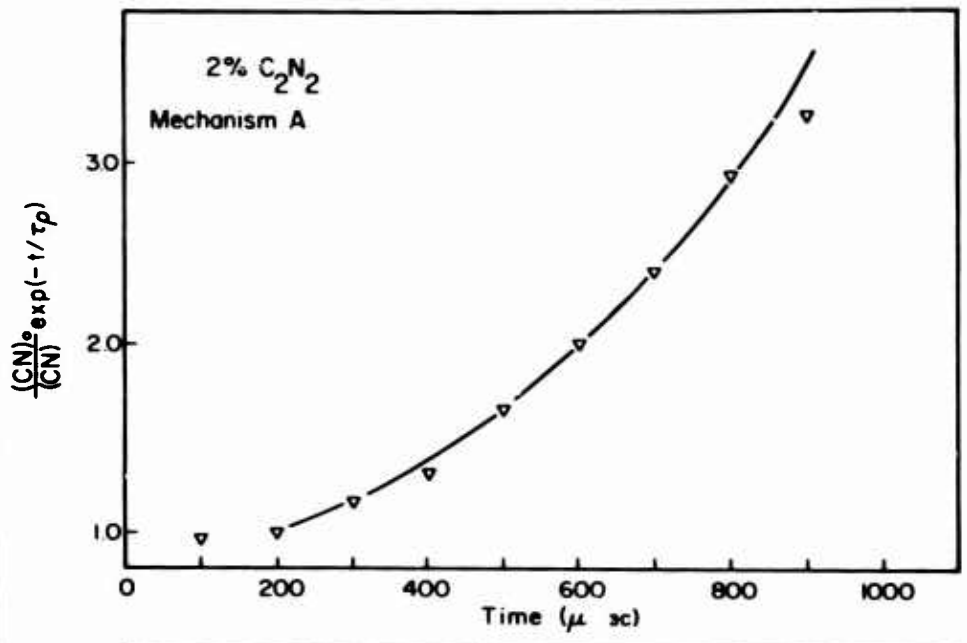
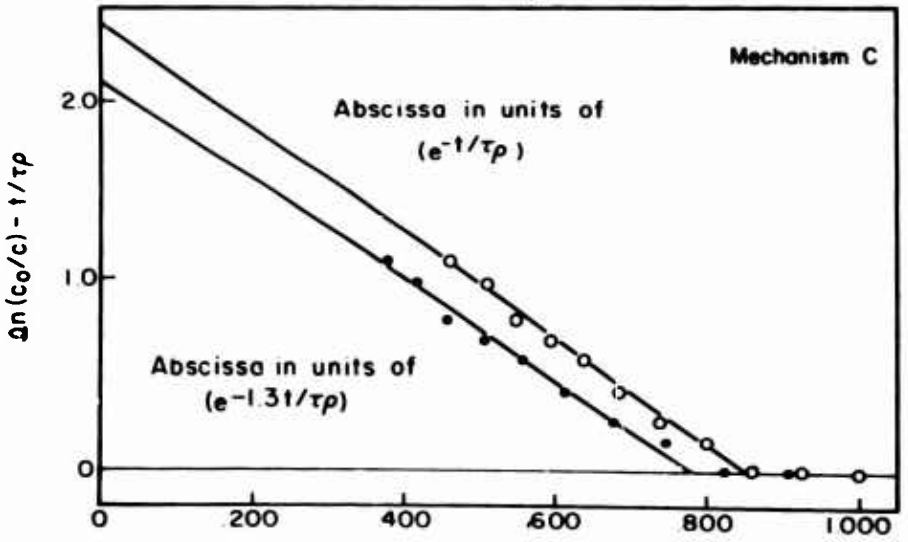


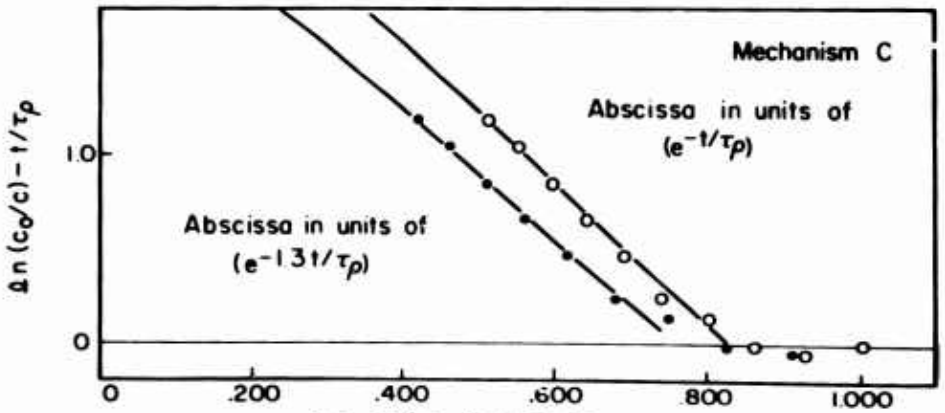
Figure 4. Quantitative relations for the temperature, density and pressure during the expansion regime, based on typical pressure traces
(a) 2% initial C_2N_2
(b) 1% initial C_2N_2
(c) 0.5 initial C_2N_2







(a) 2% initial C_2N_2



(b) 1% intial C_2N_2

Figure 5. Graphs of appropriate functions for proposed mechanisms. Departure from a linear relation excludes mechanism A (2% and 1% initial C_2N_2 shown). However, mechanism C is supported by the linearity of the graphs. The data are not sensitive to the assumed temperature dependence for k_1. Note the effect of t_{delay} on the first two points.

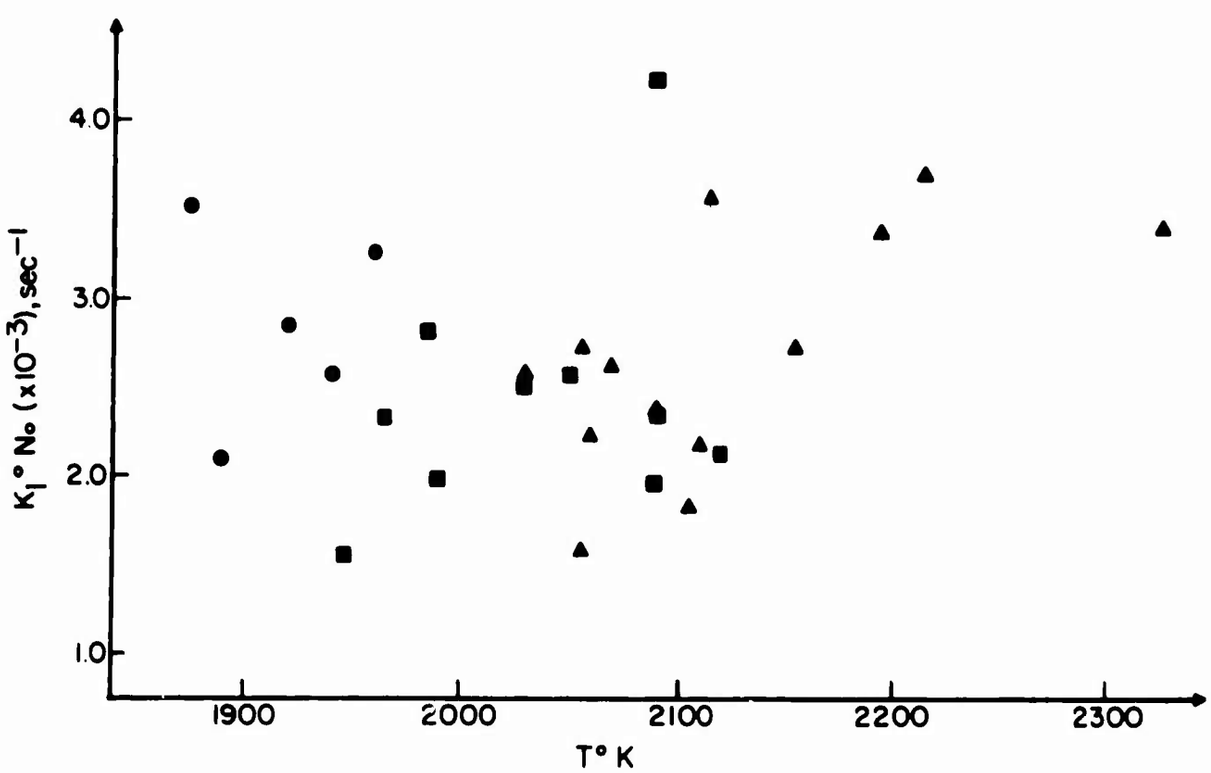


Figure 6. Plot of $k_1^o N_o$ vs the temperature to demonstrate the absence of a significant trend

circles - - - 2% C_2N_2

squares - - - 1% C_2N_2

triangles - - 0.5% C_2N_2

TWO WAVELENGTH LASER INTERFEROMETER FOR SHOCK TUBE AND PLASMA DIAGNOSTICS*

A. B. Larsen, W. B. Johnson, T. P. Sosnowski
Case Institute of Technology
Cleveland, Ohio

I. INTRODUCTION

A considerable number of plasma experiments can be performed to give quantitative information on physical phenomena if plasma electron densities in the 10^{10}-10^{12} electrons/cm^3 can be measured reliably. This is even more useful if a diagnostic technique having a time resolution of $\sim$ 1μsec. and good spatial resolution is available with the above sensitivity. It is the purpose of this work to describe such a method.

A number of diagnostic techniques are available for determining plasma parameters at low electron densities. The two most widely used employ electric probes (1) and microwaves.(2) Good results have been obtained with these methods but there is often a question as to whether the probe causes a perturbation of the plasma into which it is placed. Microwaves do not suffer from this criticism but have the difficulty of not providing good spatial resolution, this being limited to the wavelength of the probe signals. Care also must be taken when using both techniques in a strong magnetic field. Other techniques have been used but to a much limited extent. Ferguson and Schluter (3), for example, have used spectral line broadening methods to investigate plasmas having densities in the order of 10^{13} to 10^{14} electrons/cm^3. When it is desired to probe the non-equilibrium region of a shock wave, the best technique to use is microwaves since probe theory depends on the existence of thermal equilibrium. Microwaves again run into difficulty because the shock equilibration region may be less than the wavelength of the probe signal. All other techniques (4), such as interferometry and continuum light output, become useful only in the density range $\gtrsim 10^{15}$ electrons/cm^3.

The method described here is an extension of interferometry techniques to provide greater sensitivity and is analogous to microwave methods utilizing the shift in the resonant frequency of a cavity.(2)

*Supported by the National Aeronautics and Space Administration, The National Science Foundation, and Case Institute of Technology Research Fund.

Probing is accomplished at optical frequencies so that no difficulties are encountered with spatial resolution, the limitation here being only the diffraction limit within the laser cavity. Spatial resolutions of .010" are readily achievable in two dimensions. In the other dimension there is no problem if an axi-symmetric plasma is being probed. If the plasma is cylindrically symmetric the results may be inverted using the Abel inversion technique.(4) If no symmetry is apparent, then this method determines the total optical path length along the laser beam.

II. THEORETICAL ANALYSIS

A. Basic Method

When an electromagnetic wave traverses a plasma, an index of refraction is encountered which is given by

$$n_p = (1 - \omega_p^2/\omega^2)^{1/2}$$

$$\simeq 1 - \frac{1}{2}\omega_p^2/\omega^2 \qquad \omega^2 >> \omega_p^2 \qquad (1)$$

where $\omega_p^2 = \frac{4\pi n_e e^2}{m}$ and ω is the probe frequency. This index of refraction may be determined with good precision if the plasma medium is placed within the resonant cavity of an oscillating laser. If a medium with an index of refraction of unity ($n = 1$) is present within the cavity, then the resonant wavelength for the longitudinal modes is given by

$$\frac{m\lambda_1}{2} = L \qquad (2)$$

where L is the length of the cavity and where all transverse modes (6) are taken to be absent. Slight deviations from this occur since the laser media is not one which has $n = 1$. Anomalous dispersion effects occur which will be taken into account later. Assuming that a plasma of length, ℓ is placed within the cavity then the resonant condition becomes

$$\frac{m\lambda_2}{2} = L - \ell + n_p\ell$$

$$= L + (n_p - 1)\ell$$

$$= L - \frac{1}{2}\omega_p^2/\omega^2\ell. \qquad (3)$$

It would be impossible to measure the change in wavelength due to the introduction of the plasma but a convenient method exists if the shift in the resonant frequency is measured. This shift is found by subtracting (3) and (2). Thus

$$\frac{m}{2} d\lambda = \frac{m}{2} (\lambda_2 - \lambda_1) = - \frac{1}{2} \left(\frac{\omega_p^2}{\omega^2}\right) \ell$$

which when converted to the change in frequency becomes

$$d\nu = - \frac{\nu}{\lambda} d\lambda$$

$$= \frac{1}{4\pi} \frac{\omega_p^2}{\omega} \frac{\ell}{L} . \qquad (4)$$

Notice that the frequency shift is linearly dependent on the electron density and inversely proportional to the nominal laser operating frequency. This latter dependency will become important later when the effects of extraneous changes in the index of refraction must be corrected. The frequency shift for two laser wavelengths of neon, λ6328 and λ11523, are given in Table I.

	λ6328 ℓ/L		λ11523 ℓ/L	
n_e	1/2	1/10	1/2	1/10
10^{10}	.43 kc/s	.086 kc/s	.76 kc/s	.151 kc/s
10^{11}	4.3	.86	.7.6	1.51
10^{12}	43	8.6	76	15.1
10^{13}	430	86	760	151

Table I

Predicted Frequency Shift due to Plasma Effects

Figure 1 illustrates the general configuration of this experimental apparatus. The shift in the resonant frequency of one laser is measured by comparing its frequency against that of another unperturbed laser which is the local oscillator laser. The difference frequency is that quantity which is shown in Table I.

B. Spatial Resolution

The spatial resolution obtainable by the two beam laser interferometer can be deduced from the theory of cavity resonators.(6) For a cavity of length, L, limiting aperture, D, the spot size on the mirrors of a confocal cavity is given by

$$\omega_s = \left(\frac{\lambda L}{\pi}\right)^{1/2} \tag{5a}$$

and at the center

$$\omega_s' = \left(\frac{\lambda L}{2\pi}\right)^{1/2}. \tag{5b}$$

in the limit of large Fresnel numbers, ie. large values of $\phi = \frac{D^2}{L\lambda}$. For a cavity with L = 100 cm, operating on the Ne I, λ6328 line, ω_s - 0.015 in. An improvement on this may be effected by using a hemispherical cavity having one flat and one spherical mirror. In this case the spot size on the flat mirror becomes

$$\omega_s = \left(\frac{\lambda L}{\pi}\right)^{1/2} (\eta - 1)^{1/4} \tag{5c}$$

where $\eta = R_c/L$, R_c being the radius of curvature of the spherical mirror. The allowed value of η is determined by the diffraction loss due to the size of the laser tube at the opposite end of the tube. Thus the ultimate spot size is actually due to the focussed diffraction image of the end of the laser tube. A typical value for this parameter is 3mm. yielding a spot size of .003". Since the plasma tube to be probed will have a finite length the latter spot size is a lower limit. Typically a nominal value of .010" should be realized for the spatial resolution of this system.

C. Time Resolution

This method has a finite time resolution due to the fact that the frequency of the cavity cannot change discontinuously because of the necessity for establishing appropriate boundary conditions at the mirrors. Thus optical transit times are important with the length between mirrors L, being effectively increased due to the large number of multiple reflections within the cavity. Thus one would expect that the time resolution would be

$$\tau = \frac{L}{c} \frac{1}{1 - R} \tag{6}$$

where R is the mirror reflectivity. Equation (6) is in essential agreement with an approach in which the cavity Q is determined.(5) Typical mirror reflectivities are in the range from 99% to 99.9%. Yielding, for a one meter cavity, a time resolution of 0.3 to 3.0 microseconds. This should suffice for all but the most rapidly varying phenomena.

D. Two Wave Length Interferometry

When a gas is heated to the point where appreciable ionization occurs, there is an appreciable fraction of the gas atoms in excited states. These excited states have a different polarizability which changes the index of refraction of the gas. It is apparent that any change in the index of refraction will cause a frequency shift so that considerable errors could conceivably be made in any electron density determination.(7) using a technique which is dependent upon the index of refraction. The effects of any wavelength independent contribution to the index of refraction, such as that due to atomic or ionic polarizability, can be subtracted away by making measurements at two wavelengths. The laser method is particularly suited to the two wavelength technique since lasers can be made to operate simultaneously at more than one wavelength.(11) The schematic of how this would operate is shown in Figure 2. Two lasers operating simultaneously on the $\lambda 6328$ and $\lambda 11523$ lines of neon will be used. The output beams are brought together in the beam splitter which divides the combined beams into two channels. The visible light is excluded from being detected by the infra-red sensitive photomultiplier by a narrow pass-band filter thus producing an "infra-red channel". The "visible channel" is formed in the same way.

If the background medium has a change in the index of refraction, n_o, then equation (4) becomes modified such that

$$d\nu = + \frac{\nu}{2} \frac{\ell}{L} \frac{\omega_p^2}{\omega^2} - \nu \frac{\ell}{L} n_o \,. \qquad (7)$$

Determining the frequency shift at two laser frequencies, ν and ν', the relative shifts in frequencies can be computed to give

$$\frac{d\nu}{\nu} - \frac{d\nu'}{\nu'} = + \frac{1}{2} \frac{\ell}{L} \omega_p^2 \left(\frac{1}{\omega^2} - \frac{1}{\omega'^2}\right) \qquad (8)$$

which indicates how the effects of wavelength independent indices of refraction are to be eliminated.

E. Mode Pulling Effects

A possible source of error in relating the shift in frequency of the probe laser to the electron density is the fact that the position of

the laser operating frequency is intermediate to the resonant frequency of the cavity, ν_c, and the frequency, ν_ℓ, at the maximum of the gain curve of the laser medium. This deviation is strictly dependent upon the shape of the line and has been analyzed (8) for lines with Lorentz and Doppler profiles. This effect is known as mode, or frequency, pulling. The resulting oscillation frequency, ν_{osc}, is

$$\nu_{osc} = \frac{\nu_c \Delta\nu_\ell + \nu_\ell \Delta\nu_c}{\Delta\nu_\ell + \Delta\nu_c} \tag{9}$$

for the Lorentz shape where $\Delta\nu_c = \frac{1}{4\pi}\frac{c}{L}(1 - R)$ is the cavity bandwidth and $\Delta\nu_\ell$ is the gain bandwidth of the line. For a Doppler line profile, as is normally encountered, the result is more complex and is given by

$$\nu_{osc} = \nu_c + 0.56\, e^{-\left(\frac{\nu_\ell - \nu_{osc}}{\Delta\nu_D}\right)^2} \operatorname{Sin} 2\left(\frac{\nu_\ell - \nu_{osc}}{\Delta\nu_D}\right) \tag{10}$$

where $\Delta\nu_D = \nu_\ell\sqrt{\frac{2kT}{M}}$ is the Doppler width.

A convenient, and valid, approximation is that $\frac{\Delta\nu_c}{\Delta\nu_\ell} << 1$. For this case the Lorentz relation (9) reduces to

$$\nu_{osc} \simeq \nu_c + (\nu_\ell - \nu_c)\frac{\Delta\nu_c}{\Delta\nu_\ell} \tag{11}$$

whereas the Doppler expression (12) gives

$$\nu_{osc} \simeq \nu_c + 0.94\,(\nu_\ell - \nu_c)\frac{\Delta\nu_c}{\Delta\nu_\ell} \tag{12}$$

if the additional restriction is made that the oscillation occurs near the line center.

In the situation encountered in this experiment, the shift in frequency of one laser with respect to another is to be measured. It will be assumed that both lasers will initially be oscillating at the same frequency as determined by a null beat between the lasers and also that the gain curves of each laser are identical. The exact position of the frequency of oscillation on the gain curve need not be at any particular value, eg. at the peak (except for the Doppler profile). Thus, if equation (11) is considered, the two lasers operate at the frequencies

$$\nu'_{osc} = \nu'_c + (\nu_\ell - \nu'_c)\frac{\Delta\nu_c}{\Delta\nu_\ell}$$

$$\nu''_{osc} = \nu''_c + (\nu_\ell - \nu''_c)\frac{\Delta\nu_c}{\Delta\nu_\ell}$$

so that the shift in frequency is given by

$$\Delta\nu_{osc} = \nu''_{osc} - \nu'_{osc} = (\nu''_c - \nu'_c)(1 - \gamma)$$

$$= \Delta\nu_c\,(1 - \gamma)$$

where $\gamma = \frac{\Delta\nu_c}{\Delta\nu_\ell} \simeq 10^{-4}$. This then shows tha the actual observed frequency is proportional to the shift in the cavity frequency with the proportionality constant being very close to unity. Thus under these assumptions any effects due to mode pulling are negligible.

For actual situations care must be taken that the assumptions are satisfied. For the He-Ne laser the gain profile is not Lorentzian but has a Doppler shape so that it is necessary to operate close to the line center due to the extreme non-linearity as indicated in equation (12). Another important effect to consider is the consequence of holes being burned in the gain curve at the oscillation frequency.(8) It is extremely difficult to make a quantitative estimate of this phenomena although Lamb (9) has given a theoretical expression for the gain curve in the presence of strong radiation fields. Another difficulty that needs to be avoided is the isotopic effect on the shape of the gain curve. For the case of neon the important natural isotopes are Ne^{20} and Ne^{22}, each of which contributes to the total gain curve for natural neon. The isotopic energy level shift causes the individual gain profiles to be shifted, resulting in an assymmetric shape for the total gain curve. This can obviously be eliminated through the use of separated isotopes. A very graphic demonstration of the hole burning and the isotopic effect is to be found in the work of Szoke and Javan.(10)

III. EXPERIMENTAL DETAILS

A. General Discussion

As is apparent from the preceding section, the experiment consists of determining the change in the optical path length within a laser cavity by measuring its change in frequency. This is accomplished as is seen in Figure 1 by comparing the variable frequency laser with a constant frequency local oscillator laser. In principle, this is straight-

forward until one calculates the change in actual cavity length needed to produce a shift of 5 kc/s at λ6328. This turns out to be 0.1 Ang from which it is concluded that extreme stability of the system must be maintained. In addition it is to be expected that air turbulence, acoustic vibrations, and similar disturbances would cause unstable operations. The former was found to be very important whereas the latter has not been a particular nuisance.

B. Optical Detection System

All frequency measurements to date have been made with a very simple set-up. Since photoelectric effect is light intensity dependent, a photomultiplier is an ideal square law detector. Thus when light from the two lasers is brought together, there is a signal at the photomultiplier output which has a component at a frequency equal to the difference in frequency of the two lasers. Ordinary photomultipliers sensitive to light at λ6328 and λ11523 have been used and from which an adequate signal has been obtained to drive a fast oscilloscope. Except for some work in which surplus spectrum analyzer was used, all measurements have been made with the photomultiplier set-up. To obtain the beat frequency, reasonably good superposition of the laser beams must be had. This is done visually by allowing the beam to traverse about a ten foot path with the condition being that the two spots from each laser be superimposed at both the beam splitter and the distant surface.

The two optical channels sensitive to the infra-red and visible lines are produced by the use of narrow and pass-band filters (10 Ang). In many cases the infra-red light may be excluded from the detection by the spectral response of the photomultiplier. It is felt that in many cases the luminosity of the event being studied would cause considerable noise in the photomultipliers. It is for this reason that filters are used on both channels. It is obviously necessary for the infra-red channel to be blocked in the visible region.

C. Methods for Laser Stabilization

Initial experiments designed to show the feasibility of this technique were performed on massive iron tables specially adapted for optical work. No special techniques were employed to isolate this table from building vibrations. These experiments and all subsequent ones were conducted in an ordinary laboratory area on the second floor of a five story building. Beat frequencies were obtained although stability of the beat frequency was good only to about 500 kc/s for short periods of time (~5 seconds).

To improve the overall stability changes in the system were made:

a) Introduction of vibratory isolation
b) Minimization of air turbulence effects
c) Close coupling of the two laser cavities.

To provide good vibratory isolation the iron table was uniformly supported by a stack of rough plywood sheets which were in turn isolated from the floor by automobile inner tubes. It has been found that four of these tubes will easily support a complete platform weighing about one ton. Such an arrangement was found to isolate the table quite adequately such that no drastic changes in a laboratory environment needed to be made. For example, mechanical vacuum pumps are left in operation and reasonable results can be obtained during the daytime although best results are still obtained at night.

Air turbulence was minimized by placing small glass tubes between the ends of the laser tubes and the Brewster windows. These just about eliminate this problem although perhaps evacuated tubes would be somewhat better. A good test of the efficacy of these tubes is indicated by the observation of single dust particles, illuminated by the internal laser beam, which are suspended motionless within the tubes. This problem is very critical since air turbulence caused by convective currents produced by the hot laser tubes is sufficient to cause severe frequency instability.

To minimize the effects of thermal expansion effects and mechanical vibrations, a close coupled laser system was constructed and is illustrated in Figure 4. This employs the hemispherical cavity arrangement in which the flat mirror is common to both lasers. The spherical mirrors on the opposite ends of the cavities are both held in a single heavy mirror mount. In this case any change in the physical length of the system will change the frequency of each laser by an identical amount. The actual oscillation frequency of each laser moves to a different position on the gain curve which is a disadvantage in the case of a Doppler broadened line (Sect. II-E) and which will be corrected for in future work. Figure 5 is a close-up picture of the close-coupled laser system in operation.

D. Experimental Results

After the above changes were made the system produced excellent stability. In fact at the present time one is somewhat at the mercy of system to come into a null beat region since no effective and reproducible method has been included to shift the difference frequency. Changes are usually made by: (1) Waiting a sufficient length of time for the beat frequency to drift to lower (~50-100 kc/s) values, (2) torquing the steel table and (3) jumping on the floor. None of these methods are very satisfactory. Our best stability to date on these two, freely operating lasers is a total drift of about 5 kc/s on a beat frequency of 100 kc/s over a period of several minutes. An example of the signals obtained from

the photomultipliers is seen in Figure 6 as obtained from the λ6328 radiation. A hybrid laser, operating at λ6328 and λ11523 has been constructed. However, simultaneous observations on both the infra-red and visible channels have not been made although little difficulty is to be expected.

IV CONCLUSIONS AND FUTURE PLANS

Major emphasis to date has been placed on improvement of the overall laser system stability. As is seen from Table I, this stability is now sufficient to allow electron density determinations to be made in the 10^{11}-10^{12} range. To put this technique on as absolute a scale as possible a test chamber will be placed within the laser cavity. This chamber will be filled with helium of know index of refraction. This index of refraction will be varied by changing the pressure although problems will be encountered here since a change of pressure of 1 mm. causes a frequency shift of 1mc/s. This will then allow an absolute calibration to be made of this method.

To minimize the difficulties due to non-linear mode pulling for Doppler gain profiles (Sect. II-E), a frequency stabilization system is being designed to hold the laser at the peak of the gain curve. Sensing of the frequency shift of the local oscillator laser will be made which will control the position of the common flat mirror. In this way both lasers will be stabilized to the line center in the absence of any perturbation. The other laser, however, is free to shift its frequency due to any change in its internal optical path length.

A variety of experiments are planned for use with this diagnostic device. Shock tube diagnostics is primary and will be accomplished as in Figure 7 and 8. Figure 7 shows the close coupled cavity configuration which affords the advantage of good stability. It, however, would measure a differential change in the electron density between the positions of the two beams. This has some disadvantage due to possible sensitivity problems. If this is found troublesome the configuration in Figure 8 will be used which will produce an integral determination of the electron density. In this case sufficient stability might be achieved for the times encountered in shock tube diagnostics. Initial experiments will be to determine the rate of approach to thermal equilibrium within a shock front. Other experiments to be performed are a check of Langmuir probes and microwave breakdown and afterglow studies.

V ACKNOWLEDGEMENTS

This experiment could not have been performed without the excellent technical assistance available on the Case campus. Particularly the excellent skills of our glassblowers, Mr. I. Szilogyi and Mr. E. Parrillo have come to be indispensable to our work.

REFERENCES

(1) E. O. Johnson and L. M. Malter, Phys. Rev. 30, 58 (1950).

(2) M. Heald and C. B. Wharton, Microwave Plasma Diagnostics (McGraw-Hill Book Co., Inc., New York, 1965).

(3) E. F. Ferguson and H. Schluter, Annal. Phys. 22, 341-372 (1963).

(4) H. R. Griem, Plasma Spectroscopy (McGraw-Hill Book Co., Inc., New York, 1964).

(5) G. Birnbaum, Optical Masers (Academic Press, Inc., New York, 1965).

(6) G. D. Boyd and H. Kogelnik, Bell System Tech. J. 41, 1347 (1962).

(7) J. B. Gerardo and J. T. Verdeyen, Proc. IEEE 52, 690, 1964.

(8) W. R. Bennett, Jr., Phys. Rev. 126, 580 (1962).

(9) W. E. Lamb, Proceedings of the Third Quantum Electronics Conference, Paris, 1963.

(10) A. Szoke and A. Javan, Phys. Rev. Lett. 10, 521 (1963).

(11) J. D. Rigden and A. D. White, Proc. IEEE 51, 943-5 (1963).

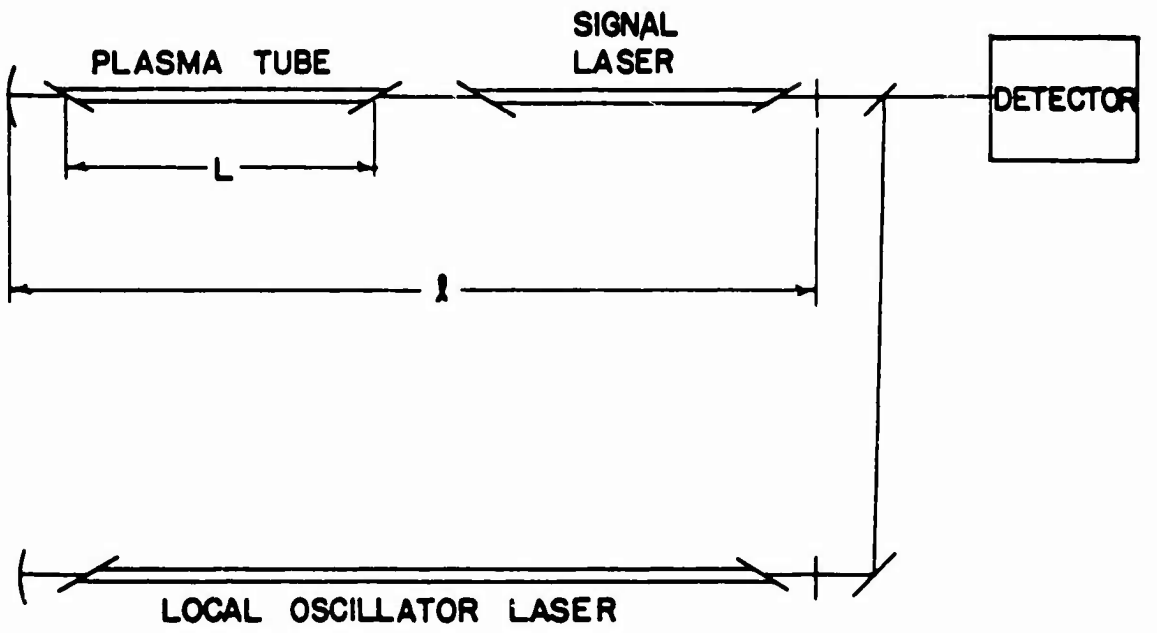


Figure 1 General Configuration of Laser Interferometer for Plasma and Shock Tube Diagnostics.

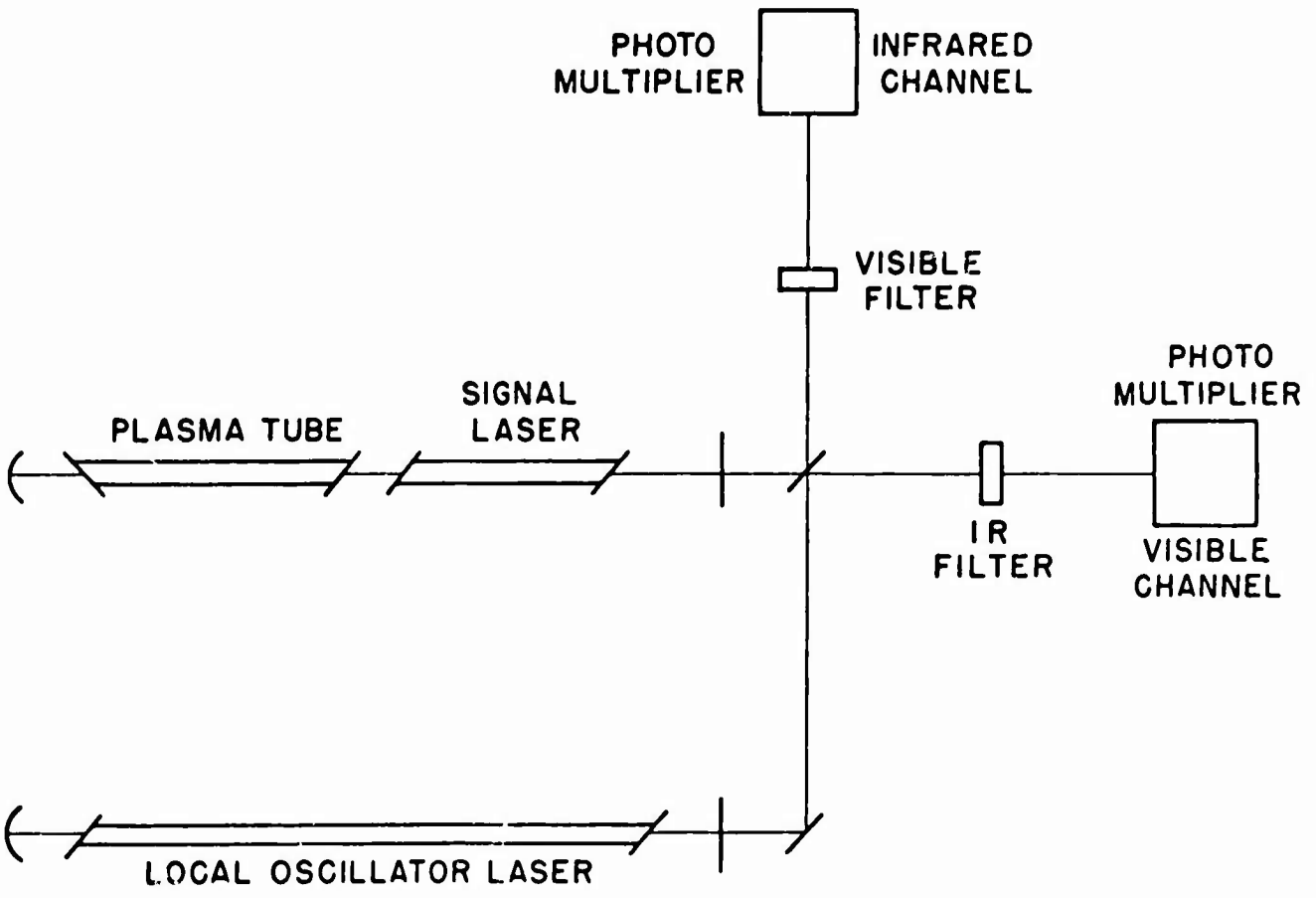


Figure 2 Dual Wavelength Laser Interferometer.

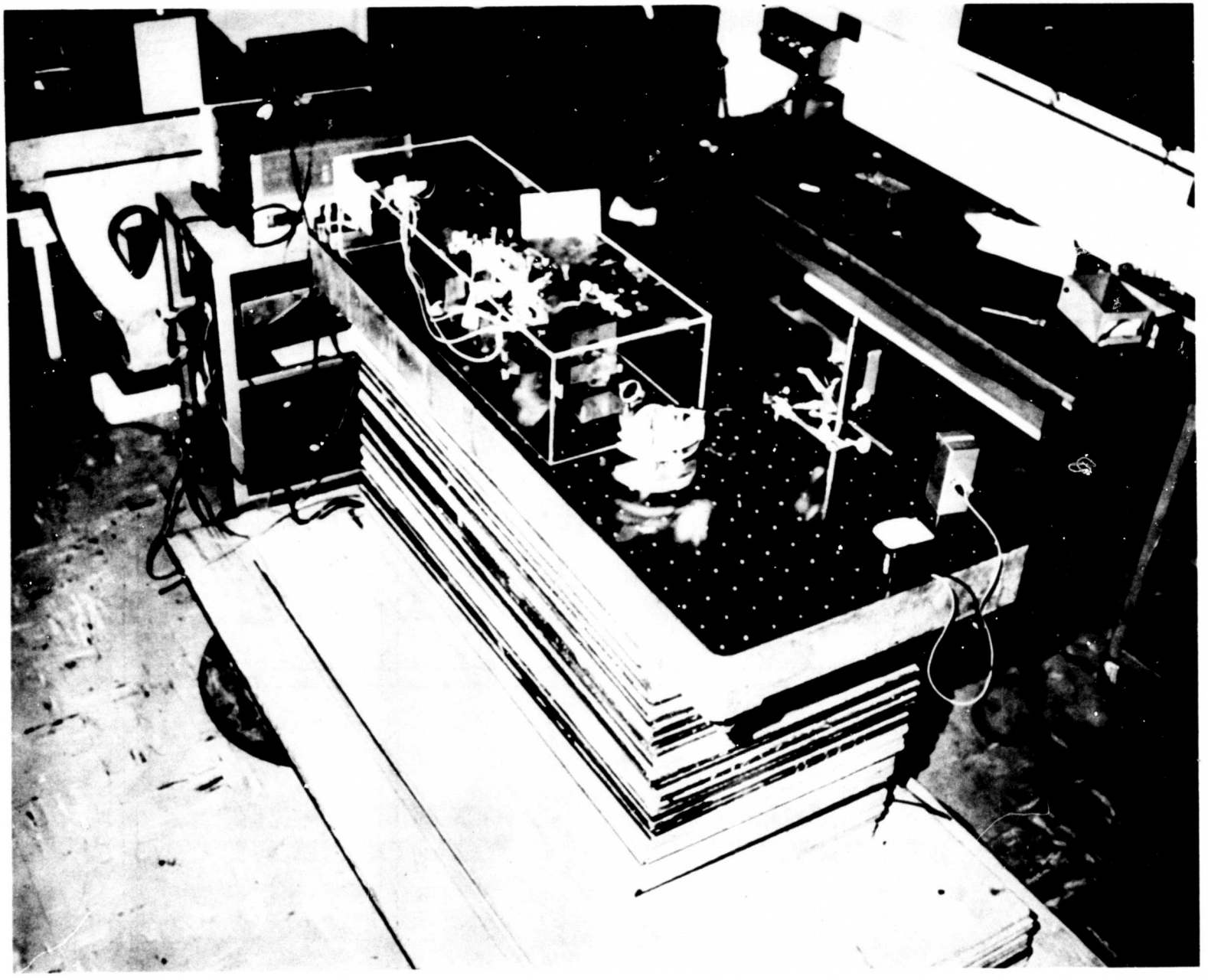


Figure 3 Overall View of Laser Interferometer Showing Methods of Shock Isolation.

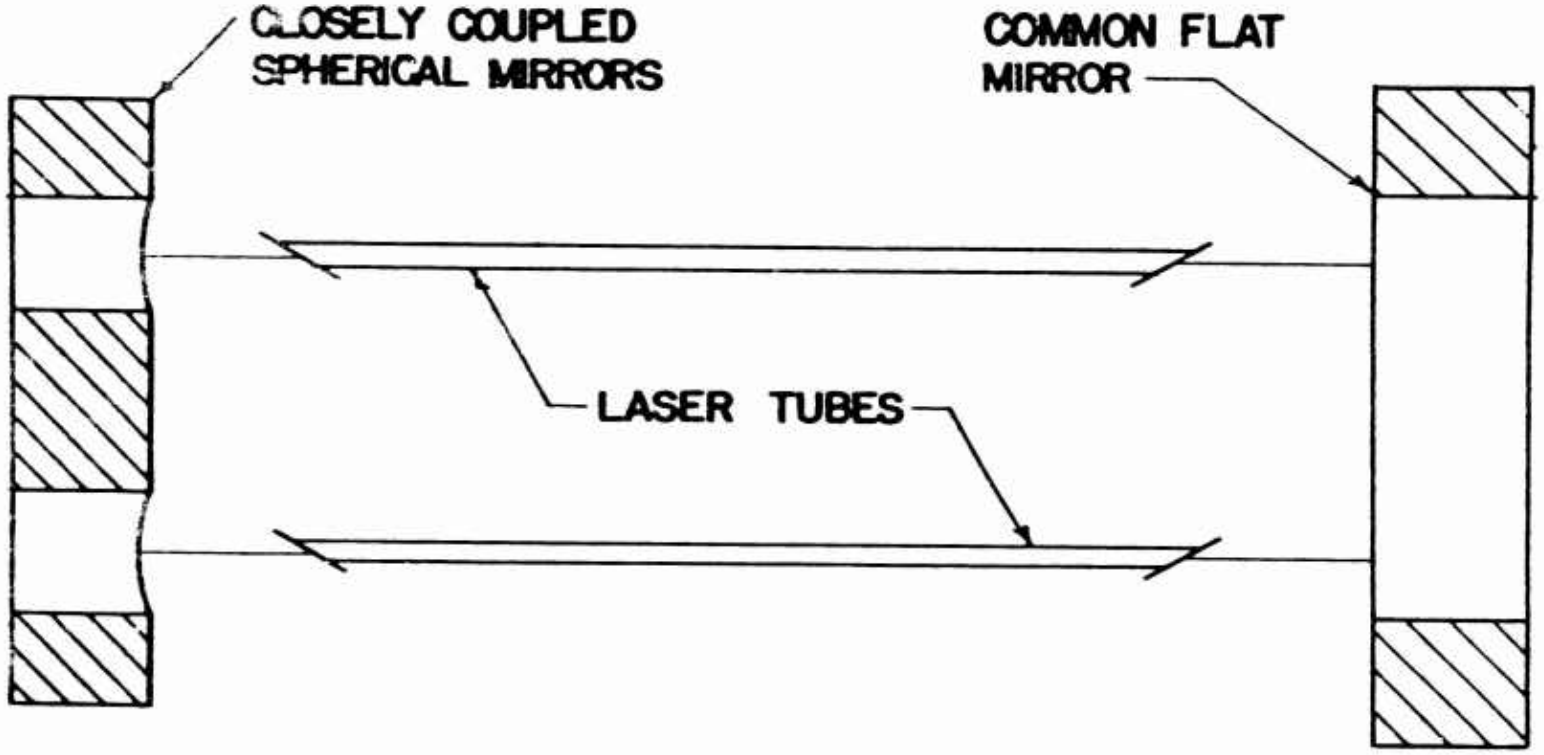


Figure 4 Close Coupled Dual Laser Cavities.

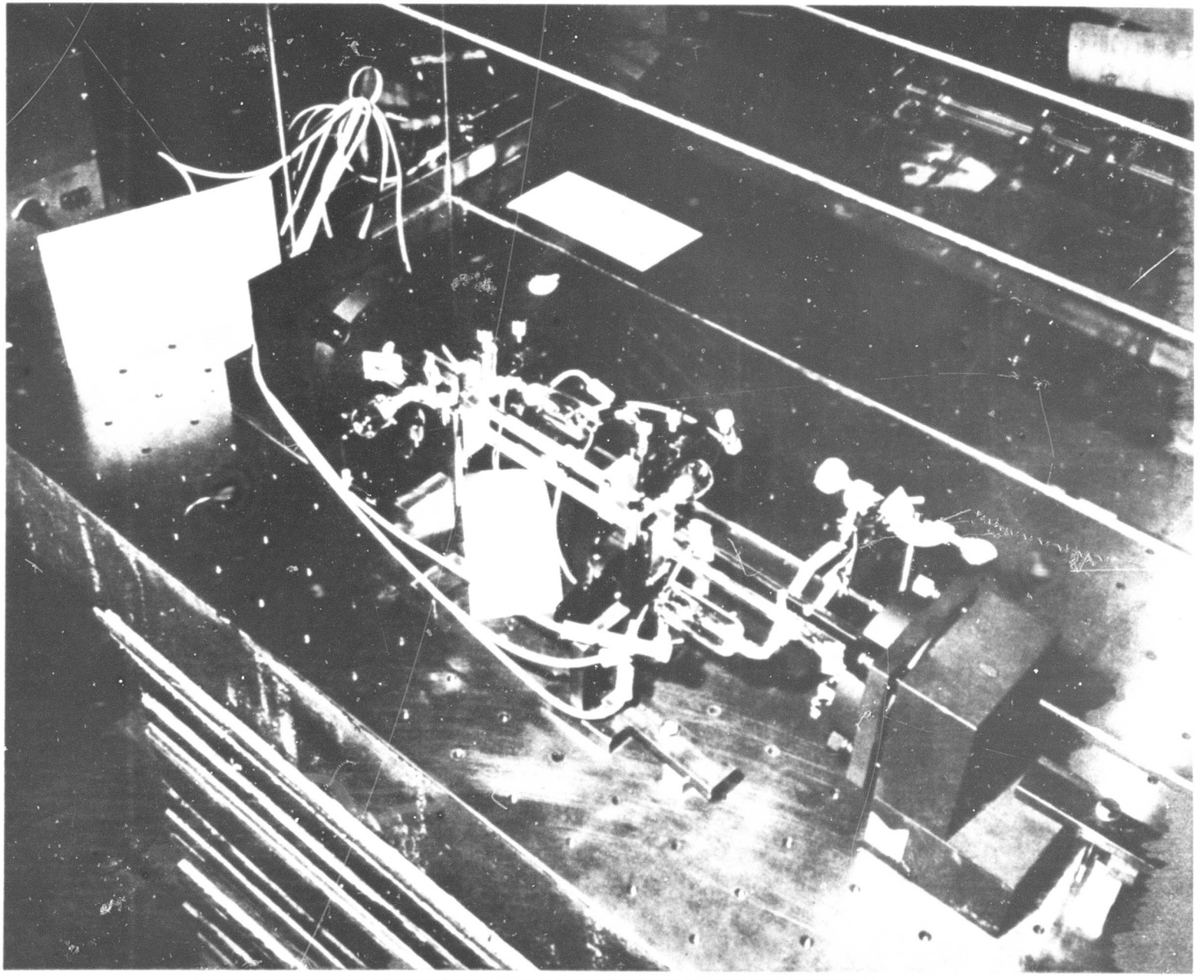


Figure 5 Closeup Picture of Operating Dual Laser Cavity.

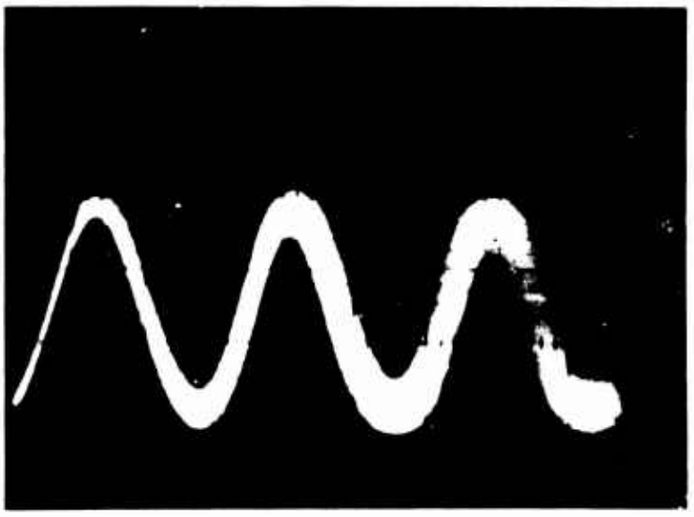


Figure 6 Oscilloscope Trace of 100 Kc/s Beat Frequency. Observation Time: Three Minutes.

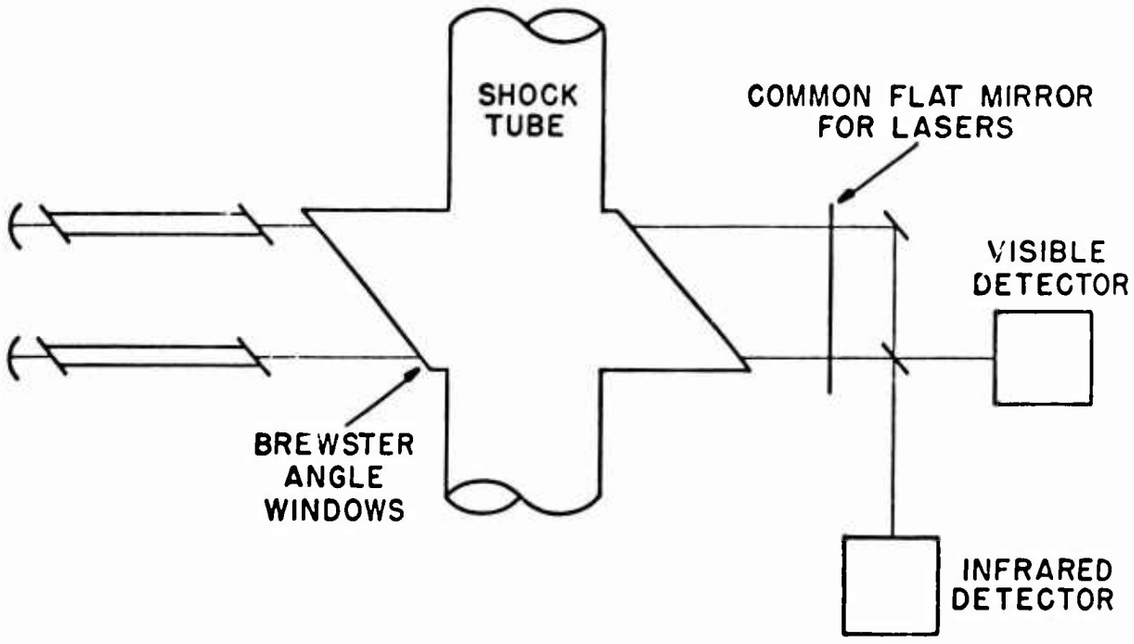


Figure 7 Schematic Diagram of a Method for Determination of Electron Densities in a Shock Tube.

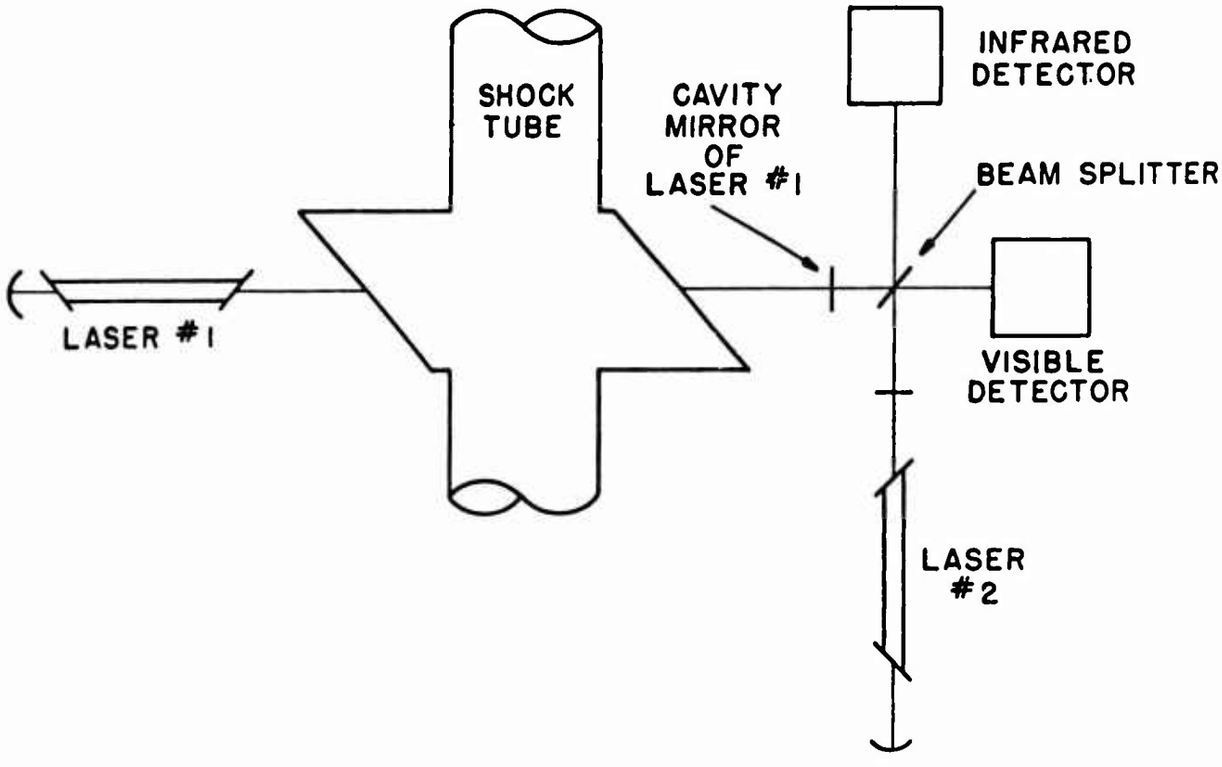


Figure 8 Alternate Method for Determination of Shock Tube Electron Densities.

BLANK PAGE

RADIATION MEASUREMENT TECHNIQUES

W. A. Menard and G. M. Thomas
Jet Propulsion Laboratory
Pasadena, California

ABSTRACT

This paper describes quantitative radiation measurement techniques developed for use with an electric arc-driven shock tube. Shock-layer radiance in the 0.3 to 2.7 μ region was measured using a carbon-coated thin film gage. The method of calibrating the gage and of relating the gage response to the source radiance are described. Spectral reflectance measurements for multi-layer carbon films are presented. The effects of shock wave attenuation and radiation from sources outside the shock layer are shown to be important in certain thermochemical regimes. Shock standoff distance measurement techniques are described. Prism and grating monochromators have been adapted to the shock tube and used in photometric studies of oscillator strengths, relaxation times, and nonequilibrium and equilibrium radiation intensities in the 2000 A to 10,000 A region, with resolution as high as 1 Å. Typical calibration spectrograms obtained from a pyrometric carbon arc are presented showing the rotational line structure of the CN violet band system. Photometric intensity measurements of these bands are also presented. In the ultraviolet stray light presents a problem with grating instruments. Techniques to eliminate the stray light such as using filters, flourescent coatings and solar blind detectors are discussed.

INTRODUCTION

The purpose of this paper is to present the laboratory techniques developed at the Jet Propulsion Laboratory for studying the gaseous radiation produced in a hypervelocity shock tube. These techniques have been used in a recent investigation of the radiation from planetary atmospheres (ref. 1). To make measurements in a high performance shock tube, such as the JPL electrically driven facility (ref. 2), an important requirement of the instrumentation is fast response time. To meet this requirement all

radiation instruments to be described here were designed for response times of the order of 1 μ sec or less.

In the first section a gage for measuring stagnation point radiance in the spectral region from .3 μ to 2.7 μ and the method by which it is calibrated are described. The gage is a platinum film coated with a thin layer of carbon. In order to isolate the gage from the hot gas and measure radiation alone the gage is mounted behind a window in the shock tube model. The gage measures heat transfer and, in order to obtain the gas intensity, a measurement of shock standoff distance is required. Techniques for measuring shock standoff distance are presented.

In the second section methods are presented for measuring the spectrum of shock heated gases in the region from 2000 A to 10,000 A. Prism and grating monochromators equipped with sensitive photomultipliers are described. Calibration techniques and data reduction procedures are discussed. The carbon arc as a calibration source is discussed and the plasma CN radiance was measured. Some of the problems involved in eliminating stray light for measurements in the ultraviolet spectral region are discussed.

TOTAL RADIATION

Total Radiation Gage

A gage has been developed for measuring the total equilibrium radiation to the stagnation point of a shock tube model. This gage has been described in detail previously (ref. 3) so only a general description will be given here. The gage consists of a thin film platinum resistance thermometer coated with a thin film of carbon. The gage is mounted behind a pyrex window in a flat-faced cylinder model shown schematically in Figure 1. Radiant energy from the shock layer strikes the carbon covering of the resistance gage and the energy is transformed into heat. The resistance gage then responds to the temperature rise of its backing material.

Two requirements of the highly absorbing carbon film are (1) that its absorptance does not vary with wavelength over the wavelength region of interest, and (2) that it be thin enough to allow rapid diffusion of heat to the sensing element in order not to seriously affect the gage response time. An evaporated carbon film of uniform thickness less than 1 μ was prepared and mounted over a platinum sputtered sample. The sample was tested for spectral reflectance in the wavelength region from .2 to 2.7 μ. The measurements in the form of absorptance are presented in Figure 2. For comparison the absorptance of an uncoated opaque platinum film is also presented. In the ultraviolet and visible regions of the spectrum the carbon absorptance is nearly constant at 0.80, but in the infrared the absorptance varies ± 20%. If the bulk of the radiation being measured lies below 0.6 μ, such as in the case of planetary atmospheres (ref. 1), there is little error in assuming the absorptance to be constant from .2 to 2.7 μ. The wavelength coverage in practice, however, has been determined by the trans-

mission of the window. For the case of a pyrex window the wavelength range of the gage is from about .3 to 2.7 μ. The response time of the gage has been shown to be on the order of 2 μ sec (ref. 3).

A photograph of the gage is shown in Figure 3. The gage element was prepared by sputtering a thin film of platinum (0.035 x 0.75 in.) upon a quartz backing material, and heat treating to bond the two materials at the interface. The approximate thickness of the platinum for a typical 200 Ω gage was calculated to be .01 μ from the following equation

$$T = \frac{\rho}{R}\frac{\ell}{W} \tag{1}$$

where ρ is the resistivity of the platinum, R is the resistance, ℓ is the length of the gage, and W is the width.

The carbon coating was prepared by first evaporating carbon onto a microscope slide and then floating it off the slide in a weak solution of potassium hydroxide and distilled water. The film was then gently lifted from the surface by bringing the gage up from below. After drying, the carbon film was found to form a good mechanical bond and have good thermal contact with the platinum film.

The electrical circuit for the gage is shown in Figure 4. Power is supplied to the circuit by a 45-v battery. The current limiting resistors, R, are chosen large in comparison to the gage resistance, R_g, in order to maintain a constant current in the gage circuit. The gage output-voltage leads are connected to a Tektronix Type D differential preamplifier in order to eliminate circuit noise. The output of the amplifier is displayed on an oscilloscope.

To make the gage measurement quantitative, the gage response must be related to the radiance of the source. The geometry of the problem is illustrated in Figure 5 for the case of a plane parallel layer. The gage is isolated from the gas by a window. For a transparent and isotropic radiating gas volume the radiant flux (watts) reaching a differential element dA_i of the detector surface is given by

$$dq_i dA_i = \tau\, G_\lambda d\lambda dV \left(\frac{dA_i \cos\theta}{S_i^2} \right) \tag{2}$$

where $G_\lambda d_\lambda$ is the rate of energy emitted from the volume element dV per unit solid angle in the wavelength interval λ to $\lambda + d\lambda$, τ is the spectral transmission of a window located between the volume element and the detector surface, and the quantity in parenthesis is the solid angle. The heat transfer to the area dA_i from the entire volume seen by the elemental area is thus

$$q_i = \tau \frac{G}{4\pi} f_i(y) \tag{3}$$

where

$$f_i(y) = \int \frac{dV \cos \theta}{S_i^2}$$

$G = 4\pi \int G_\lambda d\lambda$ is the gas intensity per unit path length $(\frac{\text{watts}}{\text{cm}^3})$.

Assuming that the heat flow remains one-dimensional for each differential element of the gage surface the solution of the one-dimensional heat conduction equation may be applied to each element to relate the heat transfer to the temperature rise of the gage element:

$$\Delta T_i = \frac{2}{\beta} \sqrt{t} \; q_i H \tag{4}$$

where H is the absorptance of the gage, $\beta = \sqrt{\pi \rho c k}$ is a thermal material property of the quartz backing material, and t is the time. The voltage change of the element is related to ΔT_i as follows:

$$\Delta E_i = I_o \alpha \frac{R_o}{\ell} \Delta T_i \Delta y_i \tag{5}$$

where I_o is the current flowing through the gage, R_o/ℓ is the gage resistance per unit length, Δy_i the element length, and α is the temperature coefficient of resistance of the gage material.

The total voltage change for all elements of the gage is then given by

$$\Delta E = \sum_i \Delta E_i \tag{6}$$

Combining Equations (3) through (6) the following expression is obtained:

$$G = \frac{\Delta E}{\sqrt{t}} \left(\frac{\ell \pi}{\tau} H E_o \Phi \int_o^{y_o} f_i(y) dy \right) \tag{7}$$

where $\Phi = \alpha/\beta$ and $E_o = I_o R_o$.

The window transmission τ is obtained from simple photometric measurements and the absorptance measurements have been described previously. The values of ℓ and E_o are obtained in a straightforward manner. The term accounting for the geometry, $\int f_i(y)dy$, is obtained by numerical integration and is found (ref. 3) to result in the distribution illustrated in Figure 6. The quantity Φ is determined in the following way: The gage response for a constant amplitude heat pulse, Q, is given by

$$\frac{\Delta E}{\sqrt{t}} = \Phi\, 2QE_o \tag{8}$$

Thus the lumped constant Φ is obtained most simply by joule heating the gage with a constant amplitude current pulse and observing the gage response. For a constant heating current the joule heat is given by

$$Q = \frac{I_o^2 R_o}{A_g} \tag{9}$$

where I_o is the current and A_g is the gage area. Combining Equations (8) and (9) we obtain with $E_o = I_o R_o$:

$$\Phi = \frac{\Delta E/\sqrt{t}\; A_g}{2 I_o^3 R_o^2} \tag{10}$$

Equation (10) shows that large errors can occur if the current pulse amplitude is not maintained constant to a high degree of accuracy. A circuit has been developed at the JPL which limits the current droop to about $\pm \frac{1}{2}\%$ of I_o. The measurement of R_o may be done accurately using standard techniques. The measurement of gage area is possibly the largest source of error for this technique. The sputtered platinum film area is measured most accurately for films of large dimensions. An oscillogram of the current pulse and the parabolic gage response predicted by Equation (10) is shown in Figure 7. The time history of the gage voltage is measured from the oscillogram and plotted as shown in Figure 8. The slope of the straight line in Figure 8 determines $\Delta E/\sqrt{t}$ in Equation (10). The current pulse I_o is measured from the oscillogram and Equation (10) may be solved for the constant Φ. For gages ranging in resistance from 100 to 400 ohms we have obtained Φ values from 0.007 to 0.008 $cm^2/w\sqrt{sec}$. This data compares favorably with values quoted in the literature (ref. 4) for much lower resistance gages.

The total radiation gage has been used to measure stagnation point heating and shock layer radiance on a flat faced cylinder model (ref. 1), in an arc heated shock tube. The gage was mounted in the model as illustrated in Figure 1. A photograph of the model is presented in Figure 9. The model was supported by a sting along the shock tube centerline facing the oncoming shock wave. In a few μ sec after the incident shock passed the model, a bow shock was formed and a steady constant thickness layer of gas behind the bow shock was viewed by the gage. The test time was terminated by the arrival of the contact surface. A typical trace of the gage response is presented in Figure 10. The slight bump on the trace indicates arrival of the incident shock. The formation of the bow shock requires approximately 4 μ sec, after which a parabolic response of the gage begins. Also shown on the oscillogram is the output of a photomultiplier viewing the test gas ahead of the bow shock. The smoothness of the gage response is indicative of the high signal to noise ratio of the gage and circuitry.

The gage sensitivity has not been a limiting factor in our experiments. For the lowest as well as the highest heating rates applied to the gage the signal to noise ratio remained large and the response remained parabolic. The only limit encountered at low heating rates was the inability to amplify the signal on the oscilloscope so that accurate measurements of ΔE could be made.

Shock Standoff Distance

To evaluate the geometrical view factor for the gage the shock standoff distance, δ, is needed. The standoff distance was measured using an STL image converter camera and a rapid shutter technique.

A photograph from the image converter camera is shown in Figure 11a. The camera views the gas through the wall of a one foot length glass test section. The model is the $1\frac{1}{4}$ inch flat faced cylinder and the test condition was a shock velocity of 28,000 ft/sec in a .25 mm Hg mixture of 9% CO_2 - 90% N_2 - 1% A. The camera has insufficient resolution for measuring the standoff distance accurately and it was necessary to enlarge the photograph for more accurate measurements. By this technique the uncertainty in the δ measurement was about 25%.

In Figure 12 a more accurate photographic technique is illustrated. An electromechanical shutter of the type designed by Camm (ref. 5) was used to obtain photographs of the standoff distance through a slit and window in the shock tube sidewall. The shutter has an open and close time of approximately 30 μ sec.

The shutter consists of a thin rectangular slide of micarta with a slit at the center, which rides in V-grooves milled into Teflon guides. The slit, about 50 μ wide, is formed by cementing thin shim-stock over a hole in the micarta. Before firing, the shutter rests against the end of an 0.040-in. D nichrome wire which is peened flat to give good surface contact with the

shutter. The Teflon guides are fastened to a metal base containing a 50 μ fixed slit. A 14.5 μf capacitor charged to 7.5 kv and in series with an electrode spark gap is connected across the ends of the nichrome wire. In operation, a high voltage trigger pulse is sent to the trigger electrode of the spark gap and breaks down the gap, discharging the capacitor through the resistance of the nichrome wire. The wire is heated to a high temperature in a few μ sec and undergoes thermal expansion, imparting an impulse movement to the shutter. The motion of the moving shutter is stopped by momentum exchange when it collides with a second slide located nearby and the resulting motion of the second slide is, in turn, stopped by an inelastic collision with a stop covered with soft damping material.

The optical system for photographing the shock layer contains a lens which focuses objects at the shock tube centerline on the film plane with 1 to 1 magnification. The slits are arranged with their longest dimension in the direction of the shock tube axis, with the shutter slit moving transverse to the shock tube. The shutter is triggered approximately 100 μ sec prior to arrival of the incident shock by a photomultiplier upstream of the measuring station. After an inherent fixed delay of 80 μ sec, the shutter opens and closes, exposing the film to the luminosity of the shock layer in front of the model. A photograph of the shock layer in front of flat faced cylinder model is shown in Figure 11b. The gas was 9% CO_2 - 90% N_2 - 1% A, and the shock speed was 26,500 ft/sec. The standoff distance could be measured to within 0.1 mm or an accuracy of 1% for this model. The results were within 6% of Vinokur's prediction (ref. 6) in this case.

Contribution from Sources Outside the Shock Layer

The gage measures all radiation lying in its field of view. Therefore, the contribution of sources outside the shock layer must be considered in interpreting the measurement. These sources include the test slug gas lying between the model and the contact surface as well as the hot driver gas upstream of the contact surface.

The ratio of the heat transfer to the gage from the stagnation region, q_3, to the heat transfer from the test slug gas, q_2, is given approximately by

$$\frac{q_3}{q_2} = \frac{G_3\,\delta}{G_2 L(t)} \tag{11}$$

where δ is the standoff distance, $L(t)$ is the distance from the model face to the contact surface, G_2 and G_3 are the gas intensities per unit path length of the test slug and shock layer gas, respectively. The total heat transfer q_i to the gage is the sum of the two:

$$q_i = q_2 + q_3 \tag{12}$$

The measured heat transfer q_1, therefore, exceeds the desired heat transfer q_3 by the ratio:

$$\frac{q_1}{q_3} = 1 + \frac{G_2\, L(t)}{G_3\, \delta} \tag{13}$$

The length L(t) may be approximated by the equation:

$$L(t) = U_s\, t_{max} \left(1 - \frac{t}{t_{max}}\right) \tag{14}$$

where U_s is the shock velocity, t_{max} is the total test time and t is time after the arrival of the shock at the model nose. Equation (13) and (14) show that this source of error decreases linearly with time and will depend also on the ratio of the intensities G_2 and G_3. To evaluate this effect, independent intensity measurements (such as the spectral measurements to be described later) or a theoretical prediction of the intensity as a function of the gas and its thermochemical state must be available.

The results of this calculation are presented in Figure 13 for a planetary gas mixture consisting of 30% CO_2 and 70% N_2. The intensities were obtained from the predictions of Ref. 7. The ratio q_1/q_3 given by Equation (13) is plotted as a function of shock speed for test times of 10 and 20 μs. At about 28,000 ft/sec the correction is negligible. We have not made measurements at 23,000 ft/sec, however, the effect should be observed as a decrease in measured intensity with time in the oscillogram records.

The driver gas contribution to the signal is more difficult to predict since this radiation is due to impurities near the contact surface in an arc-driven shock tube. If this radiation is assumed confined to a constant thickness slug moving at constant velocity, the gage would sense a constant heating rate after the slug enters its field of view and the effect could not be separated from the shock layer contribution. However, this source should be seen on the oscillogram prior to the arrival of the incident shock at the model face. This effect has been observed as a slight rise in the gage signal for lower shock velocities but has not been observed at incident shock velocities above about 20,000 ft/sec. It was concluded that the error due to these sources should be measured for each experimental condition and are not negligible for some thermochemical regimes depending upon the test gas.

Another effect which has been investigated is the contribution of the nonequilibrium shock front radiation to the measurement. This requires the experimental measurement of the nonequilibrium radiation relaxation distance and quantitative nonequilibrium intensity measurements. For

simulated planetary atmospheres (CO_2 - N_2 mixtures), the nonequilibrium intensities have been found (ref. 1) to exceed that in the earth's atmosphere by as much as a factor of 10 at the same flight velocity. The nonequilibrium contribution to the measurement will be correspondingly greater in this case. The relaxation distances are also about a factor of 3 greater than for air and will represent a larger fraction of the standoff distance on a given model. For the 1.25 in. dia. flat faced cylinder model used in our studies the relaxation distance is less than 1% of the standoff distance and the nonequilibrium contribution was estimated to be negligible. The nonequilibrium contribution depends largely on the size of the model. For example, the shock layer of a small hemispherical 5 mm nose radius ballistic range model would have a nonequilibrium relaxation distance nearly equal to the standoff distance for a flight velocity of 20,000 ft/sec and free-stream pressure less than about 15 mm Hg.

Shock wave attenuation is another effect which has been considered in interpreting our stagnation point measurements. For a 40 foot length driven tube on the 6-in. arc-heated shock tube, the attenuation is about 2,000 ft/sec over the length of the tube for shock velocities in the range from 20,000 to 30,000 ft/sec. This velocity increment will theoretically cause large gradients in the thermodynamic state of the test gas. For this reason the radiation from the gas behind the bow shock has been monitored photometrically. The results indicate that an approximately constant temperature is maintained in the shock layer on a large number of runs when the test gas is air and for shock velocities above 25,000 ft/sec. However, on other runs the assumption of a constant temperature in the shock layer is clearly untenable from the measurements. An increase of the radiation by a factor of two during the test time is not uncommon. These "bad runs" appear to occur at random, but the reason for this random performance of the shock tube has not been explained. The measured shock attenuation on these runs is about the same as for "good runs" where the temperature remains constant. This phenomena requires further study, however, it is clear that the test gas at the nose of the model needs to be monitored on each run in order to avoid large errors in the measurement.

SPECTRAL RADIATION

In addition to total radiation measurements spectral measurements have been made for identification of radiating species and determination of electronic oscillator strengths. Spectral measurements have also been used for studying nonequilibrium and equilibrium radiation in planetary atmospheres (ref. 1). The excitation and relaxation processes of various species produced behind shock waves have also been studied spectrally. From the spectrum of shock heated gas the dominant radiative species are identified. From intensity measurements of the vibrational transitions of molecular bands it has been possible to determine electronic oscillator strengths (ref. 1). A typical spectrum of the radiation from a planetary gas mixture is shown in Figure 14. The dominant radiator is seen to be the violet band system ($B^2\Sigma \rightarrow X^2\Sigma$) of the CN molecule.

Spectral measurements such as shown in Figure 14 are obtained from monochromators equipped with multiplier phototubes. The monochromator disperses the radiant energy from the shock tube into a spectrum. The dispersing element may be either a prism or a diffraction grating. The choice of whether to use a prism or a grating depends upon the application. Due to transmission losses through a prism it is often desirable to use a grating when observing sources of low intensity or working in the ultraviolet. The grating has, in general, a considerable advantage in resolving power. Gratings also produce a linear dispersion of the spectrum at the focal plane of the monochromator, while the dispersion of a prism varies with wavelength, becoming poorer with increasing wavelength. Overlapping of the various order is a disadvantage of the grating monochromator. Stray light interference from the grating can also cause serious problems in the ultraviolet region as discussed later.

Experimental Apparatus

Three Perkin-Elmer Model 98 quartz prism monochromators have been used for low resolution (50 Å - 400 Å band pass) work in the spectral region from 4000 Å to 10,000 Å. For resolution of about 30 Å in the 3000 Å to 5000 Å region a Bausch and Lomb ½ meter grating monochromator has been used. To obtain higher resolution and to extend the wavelength coverage down to about 2000 Å a Jarrell-Ash f/6.3 spectrograph has been modified. This spectrograph has been fitted with adjustable exit slits along the focal plane which allows the band pass to vary from 100 Å to about 1 Å. Six photomultipliers mounted behind the exit slits allow six channels of spectral data to be obtained from one shock tube run. In Figure 15 a photograph of the exit compartment of the monochromator is presented. To obtain good response time requires a low RC time constant in the photomultiplier circuitry. For this reason and because of the limited space in the exit compartment, the circuitry was miniaturized and packaged in the tube holders.

Figure 16 shows a schematic of the optical arrangement of the various monochromators with respect to the shock tube. The prism instruments are arranged to view the radiation from a single shock tube port. Radiant energy leaving the shock tube slit is collected by a quartz lens which sends a collimated beam to the pyrex beam splitter. The light is split into three beams and focused on the monochromator entrance slits by lenses. The grating instruments are arranged such that radiation from the shock tube slit is focused by a single suprasil lens directly onto the monochromator entrance slit. Suprasil is used to obtain transmission down to 2000 A.

The time response of the optical system used for obtaining photometric measurements is given by

$$t = \frac{X}{U_s} \tag{15}$$

where X is the width of the monochromator field of view within the shock tube and U_s is the shock velocity. By using small slit widths and appropriate magnification of the optical system response times of 10^{-7} sec are obtainable.

An RCA 7102 photomultiplier detector is used in one of the prism monochromators to cover the spectral region from 10,000 Å to 6500 Å. In the grating instruments and remaining prism instruments RCA 1P28 detectors are used in the spectral region from 6500 Å to 2700 Å. The 1P28 photomultiplier circuit is shown in Figure 17. Large divider resistors are used across the dynodes and the supply voltage is varied from 900 to 1200 volts to allow flexibility in gain. The photomultiplier output is amplified by a Type L plug-in preamplifier, and the signal is recorded by means of a Tektronix Type 555 oscilloscope and Polaroid film camera. To obtain sufficient rise time the effective capacitance of the circuitry is lowered by means of an emitter follower. The emitter follower shown in Figure 17 provides a net electrical time constant better than .2 μ sec.

Calibration Techniques

Wavelength calibration is accomplished by the identification of lines from a known light source. For this purpose we have used mercury, sodium, thallium, and cadmium lamps. The dispersion is measured by taking a spectrogram of a common light source and measuring the separation distance between the known lines. The reciprocal linear dispersion is the ratio of the wavelength separation of two close spectral lines to their actual separation distance in the dispersed spectrum. The order I dispersion of the Jarrell-Ash spectrograph is shown in Figure 18. Spectrograms were obtained with a Polaroid camera at the exit plane of the instrument using a Hg light source. The reciprocal linear dispersion is seen to be about 10 Å/mm at 3000 Å and about 9 Å/mm at 5000 Å.

The monochromators are aligned by adjusting the optics so that all entrance slits are completely filled by the light beam, and are focused at the centerline of the shock tube. The entrance slits are adjusted to focus at the shock tube centerline by using a light source at the monochromator exit slit.

The entire optical system, including the shock tube window and slit, are calibrated as one unit using a standard lamp located at the shock tube centerline. The calibration accuracy is limited by the statistical noise of the photomultiplier. To improve the signal-to-noise ratio, an ac calibration was made using a high speed light chopper. Two standard sources have been used; a tungsten ribbon filament lamp and a pyrometric carbon arc. The spectral intensity of the tungsten lamp was certified by Eppley Laboratories (ref. 6) by means of absolute calibration techniques developed by the National Bureau of Standards. In the ultraviolet, down to 2700 Å, a carbon arc has been used. Figure 19 presents the intensity distribution for the two calibration sources. Two tungsten lamp curves are shown. One lamp was

calibrated at 35 amperes to be used in the visible and near ultraviolet portions of the spectrum, and the other was calibrated at 30 amperes to be used in the infrared. The true filament temperatures of the lamps are indicated on the figure. The carbon arc radiance is seen to be much higher than the tungsten lamp over the entire spectrum. With the exception of the C_2 and CN molecular bands the arc radiance is a smooth function with wavelength. The carbon arc source is discussed further in Section III-D.

Data Reduction

By calibrating the entire optical system as a unit, it is possible to ratio the calibration and experiment photomultiplier outputs so that the transmission of all optics and photomultiplier response cancel out in the data reduction, thus eliminating several sources of error. To accomplish this the monochromator entrance slit is focused at the shock tube centerline, as shown in the top schematic of Figure 20. To calibrate the source is placed at the centerline. The spectral radiant flux (watt/μ) entering the monochromator from the calibration source is then

$$F_c = \tau N_\lambda A_i \frac{A_s}{\left(a + \frac{L}{2}\right)^2} \tag{16}$$

where τ is the fractional transmission of the optics, N_λ is the spectral intensity of the source in watt/cm^2 μ ster, A_i is the image of the monochromator slit and remaining quantity is the solid angle.

The gas volume seen by the monochromator is bounded by the shock tube walls and the field of view subtended by the slits A_i and A_s as shown in Figure 20. Only radiators contained within the field of view will contribute to the energy entering the monochromator slit.

To calculate the radiant flux from the gas the volume is divided into two regions. A coordinate system is established at the cross-over point of the field of view rays. For the particular geometry here the cross-over point lies a distance e between the shock tube axis and the wall. In the general case e can have different values for the x-z and y-z planes, as shown

x-z plane:
$$e = \frac{\left(\frac{L}{2} + a\right)\left(\frac{s'}{s}\right) m}{b + \left(\frac{s'}{s}\right) m} \tag{17}$$

y-z plane:
$$e = \frac{\left(\frac{L}{2} + a\right)\left(\frac{s'}{s}\right)n}{d + \left(\frac{s'}{s}\right)n} \tag{18}$$

where $2m$ = height of monochromator slit

$2n$ = width of monochromator slit

$2b$ = height of shock tube slit

$2d$ = width of shock tube slit

Only for the special cases where

$$\left.\begin{aligned} m &= ib \\ n &= id \end{aligned}\right\} \quad i = \text{any real number}$$

will e be the same in both planes. The dimensions of the slits were, thus, chosen so that there was a common cross-over point in both planes.

Assuming the radiation is isotropic the radiant flux entering the monochromator from Region-1 is

$$F_1 = \tau \int G_\lambda \Omega(z) dV = 4\tau G_\lambda A_s \frac{b''d''}{\left(\frac{L}{2} + e\right)^2} \int_0^{\frac{L}{2} + e} \frac{z^2 dz}{(c + z)^2} \tag{19}$$

and from Region-2

$$F_2 = 4\tau G_\lambda A_s \frac{b'd'}{\left(\frac{L}{2} - e\right)^2} \int_0^{\frac{L}{2} - e} \frac{z^2 dz}{(c - z)^2} \tag{20}$$

G_λ is the specific intensity of the gas in watts/cm^3 μ ster, dV is a slab of gas having a volume $4xy\,dz$, and $\Omega(z)$ is the solid angle as a function of z.

Integrating Equations (19) and (20), and combining with Equation (16) the ratio of the gas radiant flux to the calibration radiant flux is obtained

$$\frac{F_g}{F_c} = K \frac{I_\lambda}{N_\lambda} \tag{21}$$

Where $$F_g = F_1 + F_2$$

$$K = \frac{\frac{bd}{c^2}\left(a + \frac{L}{2}\right)^2}{mn\left(\frac{s'}{s}\right)^2}\left[L + \frac{c^2}{a} - \frac{c^2}{L + a} + 2c(\ln|a| - \ln|L + a|)\right]$$

and where $4mn\left(\frac{s'}{s}\right)^2$ was substituted for A_i. It should be noted that K is only a function of the geometry and will remain constant as long as the optical arrangement of the experiment is unchanged.

Let E be the photomultiplier output for radiant flux F entering the monochromator at wavelength λ. Then for a linear photomultiplier $E \sim F$ and

$$\frac{E_g}{E_c} = \frac{F_g}{F_c} \tag{22}$$

Substituting into Equation (21) yields the data reduction equation in terms of the calibration constant C.

$$G_\lambda = \frac{C}{K} E_g, \qquad C = \frac{N_\lambda}{E_c} \tag{23}$$

Typical data obtained from the monochromators is shown in Figure 21. The nonequilibrium overshoot of species behind the shock wave is seen to occur in a fraction of a μ sec. The radiation then decays to an equilibrium level, and the flux to the monochromator remains constant until termination of the test by arrival of the driver gas. Typical measurements which have been made from these oscillograms are relaxation times, and the intensity of the nonequilibrium and equilibrium radiation.

Carbon Arc Calibration Source

A well controlled carbon arc burning high purity graphite rods is a reliable radiation standard (ref. 9). Null and Lozier made a thorough study of the arc temperature, operating procedures, and intensity distribution across the crater of various grade spectroscopic rods (ref. 10). They found that when operating just under the overload current the crater of the positive electrode radiates nearly as a 3800°K blackbody. Hankins has developed an arc lamp (ref. 11) which meets all the requirements outlined by

Null and Lozier. This type of lamp has been used at this laboratory to calibrate the monochromators.

The positive electrode is formed by a $\frac{1}{4}$ inch diameter Grade SPK graphite rod and the negative electrode is formed by a 1/8 inch diameter Grade AGKS graphite rod. The electrodes are positioned at a 127° included angle and are continuously fed by two adjustable speed motors. When calibrating, only the central portion of the positive crater was focused on the monochromator entrance slit, thus insuring a uniform source intensity. The only spectral regions where the calibration source does not radiate as a blackbody is in the vicinity of the CN and C_2 molecular bands (see Figure 19). These bands originate in the arc plasma which has a temperature of about 7000°K (ref. 12) and dominates over the solid carbon crater radiation. Spectrograms of the CN bands obtained with the Jarrell-Ash spectrograph are shown in Figure 22. The plasma was viewed from the front, i.e., normal to the anode crater. The weak background luminosity seen on the spectrograms is radiation from the crater. The top spectrogram was obtained in order I using Polaroid 3000 speed film, a slit width of 10 μ and an exposure time of 1/400 sec. The bottom spectrogram was obtained from order II using the same film but a slit width of 5 μ and an exposure time of 1/10 sec. The band head vibrational transitions are identified along with their respective wavelengths. Much of the rotational line structure is seen in the spectrograms, particularly in order II.

In most spectrometric work where the carbon arc is used as a standard radiation source, the spectral regions containing the molecular bands are avoided. If the intensity distribution of these bands is known, however, the distribution may be integrated and used as a standard for low and moderate resolution work. Several experimenters have investigated the plasma radiation. Johnson (ref. 13) has studied the spectral intensity of the arc below 2500 Å in some detail. The integrated CN band intensity has been estimated by Euler (ref. 14) and Null and Lozier (ref. 10) to be 16 w/cm^{2}ster and 6 w/cm^{2}ster respectively. Measurements by the authors with the Jarrell-Ash monochromator, described above, indicate an intensity contribution of 13.6 w/cm^{2}ster from the CN bands. The band intensity was obtained by measuring an over-all "efficiency factor" for the monochromator and then using the efficiency factor to calculate the band intensity.

It was assumed that $E \sim R\tau N_\lambda \epsilon$, where E is the photomultiplier output voltage, R is the photomultiplier response, τ is the transmission of any filters in the optical system, N_λ is the spectral intensity of the source (crater surface + plasma), and ϵ is the efficiency. For any two wavelengths the ratio of efficiency factors is

$$\frac{\epsilon_2}{\epsilon_1} = \frac{E_2}{E_1} \left(\frac{R_1}{R_2} \frac{N_{\lambda_1}}{N_{\lambda_2}} \frac{\tau_1}{\tau_2} \right) \tag{24}$$

By holding the monochromator slit sizes and the photomultiplier supply voltage constant, measurements of E were made from 2800 Å to 5400 Å. In portions of the spectrum it was necessary to introduce appropriate filters into the optical path to prevent photomultiplier saturation and to eliminate overlapping of order II. The spectral transmission, τ, of the filters was independently measured. The photomultiplier response was obtained from the manufacturer and the spectral intensity, N_λ, was calculated from Planck's equation for wavelengths on both sides of the CN bands. A plot of the data in the form $\frac{E}{R\tau N_\lambda}$ is presented in Figure 23. The data has a maximum at 5000 Å; the blaze wavelength of the grating. A smooth curve was fitted to the data from which a normalized efficiency was obtained as follows

$$\frac{e_\lambda}{e_o} = \left(\frac{R\tau N_\lambda}{E}\right)_o \left(\frac{E}{R\tau N_\lambda}\right)_\lambda \qquad (25)$$

The subscript zero refers to conditions at λ = 3300 Å. Knowing the instrument efficiency it was then possible to calculate the CN intensity from further photomultiplier measurements as follows

$$N_\lambda = \frac{(V_\lambda/V_o)\, N_{\lambda_o}}{(e_\lambda/e_o)(R_\lambda/R_o)(\tau_\lambda/\tau_o)} \qquad (26)$$

The results of these measurements are shown graphically in Figure 24 and numerically in Table 1. A resolution of 5 Å was used in order to separate the major vibrational lines. The collective contribution of the rotational lines in the R-branches of the three bands forms a gradual falling off in intensity from the band heads. The blackbody curve plotted through the data is illustrative of the crater contribution to the total radiation from the arc in this region of the spectrum. It also shows good agreement with the data on both sides of the CN bands which, of course, is a necessary condition from the calculations. Around 4000 Å the data falls below the blackbody curve but still within the estimated $\pm$ 15% accuracy assigned to the measurements. The total CN intensity of 13.6 w/cm^{2}ster quoted above was obtained by integrating the band area above the blackbody curve.

Stray Light Problems in the Ultraviolet

Stray light is a severe problem when working in the ultraviolet. Our experience has been that at wavelengths shorter than 2700 Å, visible stray light interferes significantly with the ultraviolet signal. By limiting the light from the monochromator entrance slit to a narrow beam falling on the grating surface and by trapping the central image and undesired protions of the spectrum, the stray light was found to originate at the grating. Stray light of this nature comes from imperfections in the grating and occurs even in the most carefully prepared gratings.

A common approach for reducing the stray light intensity in the near ultraviolet has been to use a pre-dispersing prism or grating. This may be accomplished by crossing two spectroscopes; the second one being the monochromator. The stray light is effectively reduced by this method, but at the sacrifice of useful signal intensity due to losses from the additional optics and path length. Another method is to use a filter that cuts out radiation of wavelength greater than 3000 Å. Unfortunately, filters possessing this quality do not have adequate transmission down to 2000 Å.

Still another method is to coat the window of the photomultiplier tube with sodium salicylate ($NaC_7H_5O_3$). Sodium salicylate is often used in ultraviolet work because of its high and relatively constant quantum yield characteristics (refs. 15-19). In the usual application a thin layer (2-4 mg/cm^2) is applied to the photomultiplier tube window (which does not transmit UV radiation). As incident ultraviolet radiation passes through the coating, molecules are excited, and visible fluorescence is observed. The visible fluorescence is then transmitted through the photomultiplier window to the detector. Knowing the quantum efficiency of the sodium salicylate it is possible to calibrate the coated photomultiplier tube. Stray light of long wavelength does not cause fluorescence but is transmitted through thin coatings and acts directly on the photomultiplier. A thick coat should attenuate, by scattering, the specular transmission of stray light more than it does the fluorescent light, and so improve the stray light characteristics of the system (ref. 13).

Coatings of various thicknesses were prepared by spraying a solution of sodium salicylate and methyl alcohol onto microscope slides with an artist air brush. The slides were placed in front of the photomultiplier with the coated surface facing the incident radiation. The photomultiplier signal was recorded for λ between 2000 Å and 3000 Å. It was found that only with the thickest coating (7 mg/cm^2) was there a noticeable reduction in stray light. The reduction was not sufficient for our purposes, however, and thicker layers are not feasible because they become flaky and nonuniform. In principle, the technique appears useful, but a better coating procedure than used in these experiments is needed.

Dunkelman (ref. 20) has studied the spectral response of a large number of detectors. He shows cesium telluride to be an exceptional UV detector

for its quantum efficiency is high in the ultraviolet and very low in the visible. Solar blind detectors with cesium telluride cathodes have the necessary spectral response characteristics and are commercially available. An EMR 541F-05M photomultiplier equipped with a sapphire window has been obtained. Its quantum efficiency curve is nearly flat at 7% from 1800 Å to 2700 Å then drops off rapidly to .01% at 3600 Å. Adaption of the EMR to the monochromator is still in the preliminary stages but appears to be a promising method of solving the stray light problem.

SUMMARY

Techniques for measuring spectral and total radiation in a hypervelocity shock tube have been developed. A carbon coated thin film gage with μ sec time response has been used to measure total stagnation point radiation. The spectral absorptance of the carbon coating was shown to vary not more than $\pm$ 20% from .2 to 2.7 μ. A high signal to noise ratio for the gage was obtained, allowing the gage to be used over a wide range of heating rates. When used to study stagnation point radiation it was pointed out that heating contributed from sources outside the bow shock can become important, depending upon the thermochemistry of the gas. A heat pulse technique was used for calibrating the total radiation gage. Shock stand-off distances, needed to reduce total radiation data, have been measured by two independent methods.

By using commercially available monochromators and spectrographs, it has been shown how they can be adapted to the shock tube to make spectral radiation measurements. Spectral coverage from 2000 Å to 10,000 Å can be obtained by using various combinations of detectors and dispersing elements. Quantitative interpretation of the data was made possible by calibrating the entire optical system with standard light sources. The response time of the optical system was defined. The electrical response time was reduced by the addition of an emitter follower to the photomultiplier circuit. The data reduction procedure was outlined and the monochromatic gas intensity was shown to be directly proportional to the photomultiplier output signal. The carbon arc calibration source was studied and new measurements of the plasma CN radiance were obtained. The integrated CN radiation was found to contribute 13.6 watts/cm^{2}ster to the intensity of the carbon arc. Stray light problems were encountered between 2000 Å and 2700 Å. The stray light was found to originate at the grating face and to be of visible wavelength. Methods of eliminating the stray light were discussed.

REFERENCES

(1) Thomas, G. M. and Menard, W. A., "Experimental Measurements of Nonequilibrium and Equilibrium Radiation from Planetary Atmospheres", Paper presented at the AIAA Entry Technology Conference, October, 1964, AIAA Publ. CP-9.

(2) Collins, D. J., Livingston, F. R., Babineaux, T. L., and Morgan, N. R., "Hypervelocity Shock Tube", TR No. 32-620, Jet Propulsion Laboratory, June, 1964.

(3) Thomas, G. M. and Menard, W. A., "Total Radiation Heat Transfer Gage for Hypervelocity Shock Tube Experiments", TR No. 32-636, Jet Propulsion Laboratory, August, 1964.

(4) Hewitt, E. W., "Description of the Aeromechanics Laboratory Heat Transfer Gage Calibration Unit", Space Technology Laboratories, STL/TN-60-0000-19200, November, 1960.

(5) Camm, J. C., "High Speed Spectrograph Shutter", Rev. Sci. Instr., 31, 1960, p. 278.

(6) Vinokur, M., "Inviscid Hypersonic Flow Around Blunt Bodies", Tech. Note LMSD-48454, Lockheed Missiles and Space Company, Palo Alto, California, March, 1959.

(7) Spiegel, J. [illegible] and Wolf, F., private communication, Jet Propulsion Laboratory, February, 1964.

(8) Scholar, W., "Two Standards of Spectral Radiance", private communication, March, 1963.

(9) MacPherson, H. G., "The Carbon Arc as a Radiation Standard", Temperature, Its Measurement and Control in Science and Industry, 1, Reinhold Publ. Corp., New York, 1941, p. 1141.

(10) Null, M. R. and Lozier, W. W., "The Carbon Arc as a Radiation Standard", Temperature, Its Measurement and Control in Science and Industry, 3, Reinhold Publ. Corp., New York, 1962, p. 551.

(11) Hankins, M. A., "The Pyrometric Molarc Radiation Standard at 3800°K", paper presented at the Second Annual Conference of the Temperature Measurements Society in Los Angeles, California, July, 1962.

(12) Lochte-Holtgreven, W., "Production and Measurement of High Temperatures", Reports on Progress in Physics, XXI, The Physical Society, Great Britain, 1958, p. 312.

(13) Johnson, F. S., "Spectral Radiance of the Carbon Arc from 1900 to 2500 Angstroms", J. of the Opt. Soc. of Amer., 46, Feb., 1956, p. 101.

(14) Euler, J., Ann. Physik (6), 11, 1953, p. 203.

(15) Johnson, F. S., Watanabe, K., and Tousey, R., "Fluorescent Sensitized Photomultipliers for Heterochromatic Photometry in the Ultraviolet", J. of the Opt. Soc. of Amer., 41, Oct., 1951, p. 702.

(16) Watanabe, K. and Inn, E. C. Y., "Intensity Measurements in the Vacuum Ultraviolet", J. of the Optical Soc. of Amer., 43, Jan., 1953, p. 32.

(17) Hammann, J. F., "Untersuchungen uber die Quantenausbeute von Leuchtstoffen unter Berucksichtigung ihrer Anwendung bei Strahlungsmessungen im UV", Z. Angew. Phys., 10, 1958, p. 187.

(18) Allison, R., Burns, J., and Tuzzolino, A. J., "Absolute Fluorescent Quantum Efficiency of Sodium Salicylate", J. of the Opt. Soc. of Amer., 54, June, 1964, p. 747.

(19) Kristianpollar, N., "Absolute Quantum Yield of Sodium Salicylate", J. of the Opt. Soc. of Amer., 54, Oct., 1964, p. 1285.

(20) Dunkelman, L., "Ultraviolet Photodetectors", J. Quant. Spectrosc. Radiat. Transfer, 2, p. 533.

ACKNOWLEDGEMENTS

The authors wish to thank the following personnel at the Jet Propulsion Laboratory for their contribution to this work: R. L. Hill for the development of the electrical circuits; C. L. Tuttle for mechanical and optical instrumentation; and D. R. Etheridge for construction of the thin film gages. The authors would also like to thank K. Betchner for typing the paper.

This paper presents the results of one phase of research carried out at the Jet Propulsion Laboratory, California Institute of Technology, under Contract No. NAS 7-100, sponsored by the National Aeronautics and Space Administration.

Table 1

Spectral intensity of the carbon arc, including contributions from the incadescent anode and the arc plasma, in watts/cm^2 μ s'er.

λ $\mathring{A}$	Spectral Intensity	λ $\mathring{A}$	Spectral Intensity	λ $\mathring{A}$	Spectral Intensity
4411	138	3883	1520	3581	1035
4383	136	3881	1980	3578	579
4356	130	3878	1560	3576	335
4329	127	3875	880	3573	199
4301	125	3871	2010	3570	147
4274	123	3865	1290	3567	159
4247	122	3862	1490	3565	178
4233	120	3857	1530	3562	197
4218	145	3854	1640	3559	210
4216	231	3851	1780	3554	226
4213	231	3848	1650	3551	217
4205	153	3846	1240	3549	202
4198	301	3843	1050	3546	193
4192	174	3841	976	3543	191
4180	244	3838	979	3538	172
4175	175	3835	897	3532	136
4169	234	3829	876	3518	95.2
4166	234	3823	828	3504	67.1
4164	199	3818	775	3491	54.9
4158	246	3813	724	3477	45.7
4153	246	3807	644	3463	42.9
4147	165	3793	508	3449	40.1
4137	164	3779	394	3422	37.5
4123	153	3766	312	3395	35.9
4109	133	3752	216	3367	34.8
4082	110	3724	110	3339	33.4
4054	94.4	3697	77.0	3311	32.8
4027	83.1	3670	66.5	3284	31.2
3999	79.3	3642	64.5	3256	30.2
3972	80.1	3615	68.6	3229	29.0
3945	78.1	3601	93.1	3200	27.8
3916	77.1	3596	103	3174	26.6
3903	77.6	3590	287	3146	25.2
3889	90.9	3587	561	3118	23.8
3886	365	3584	879		

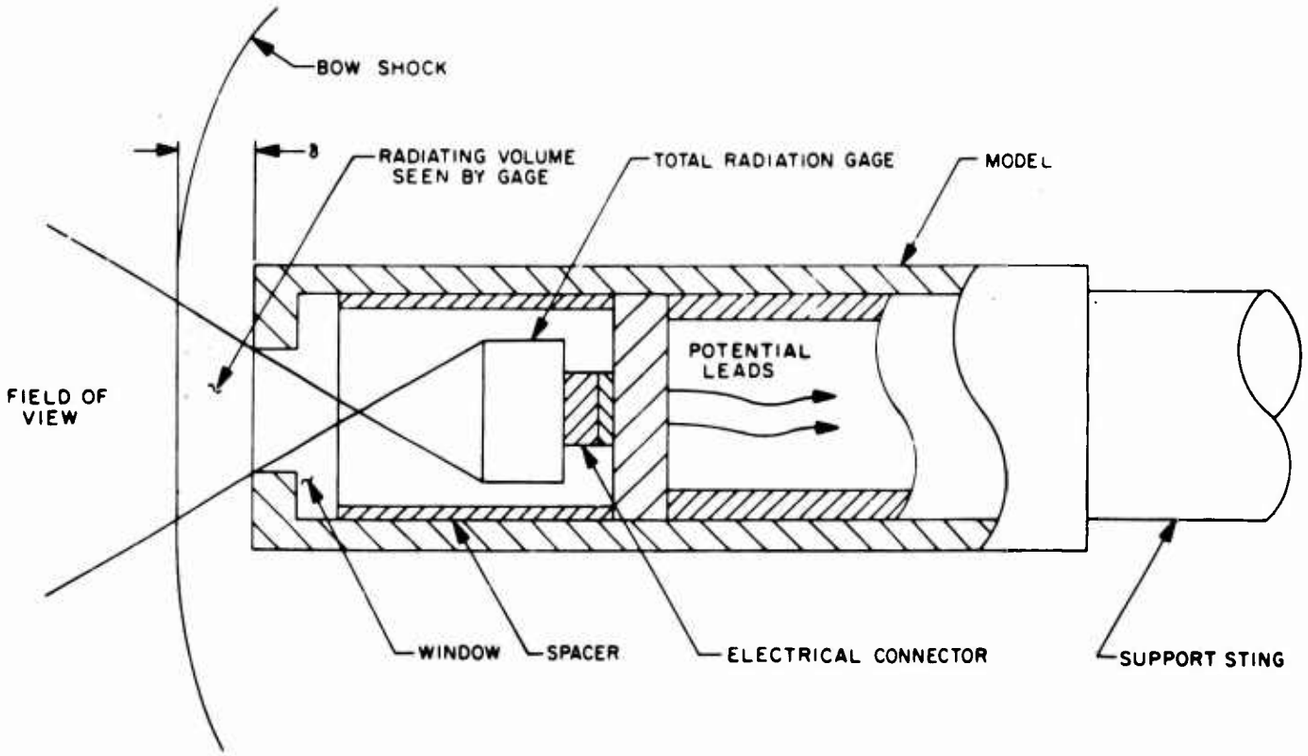


Figure 1 Schematic of total radiation gage and model

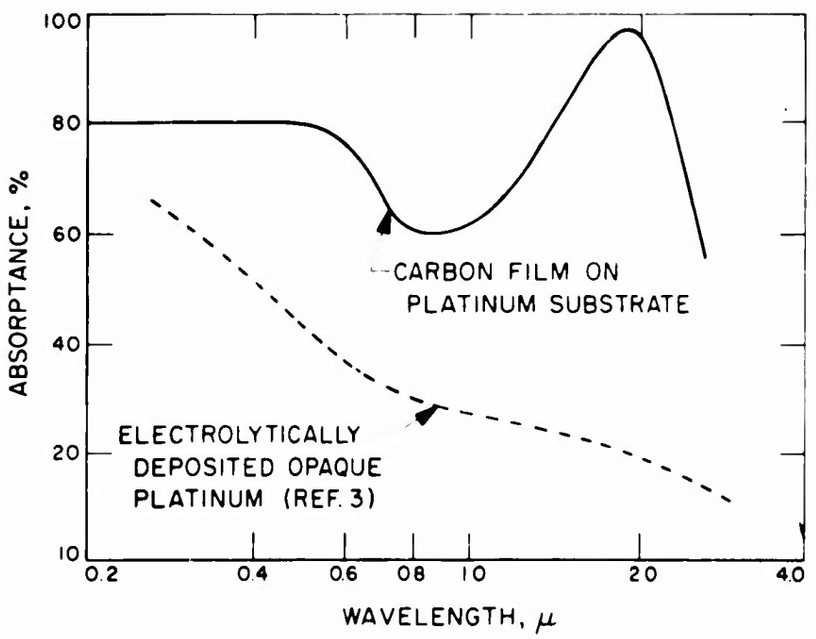


Figure 2 Spectral absorptance of carbon coated total radiation gage

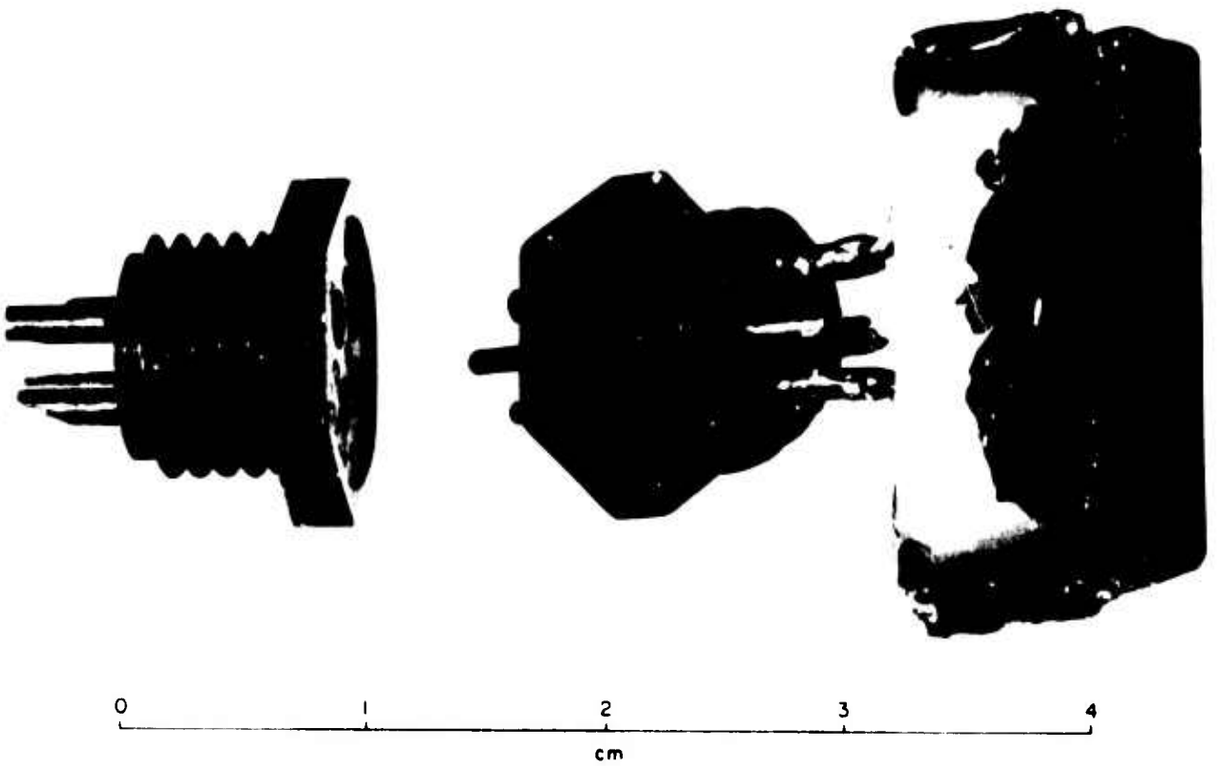


Figure 3 Total radiation gage

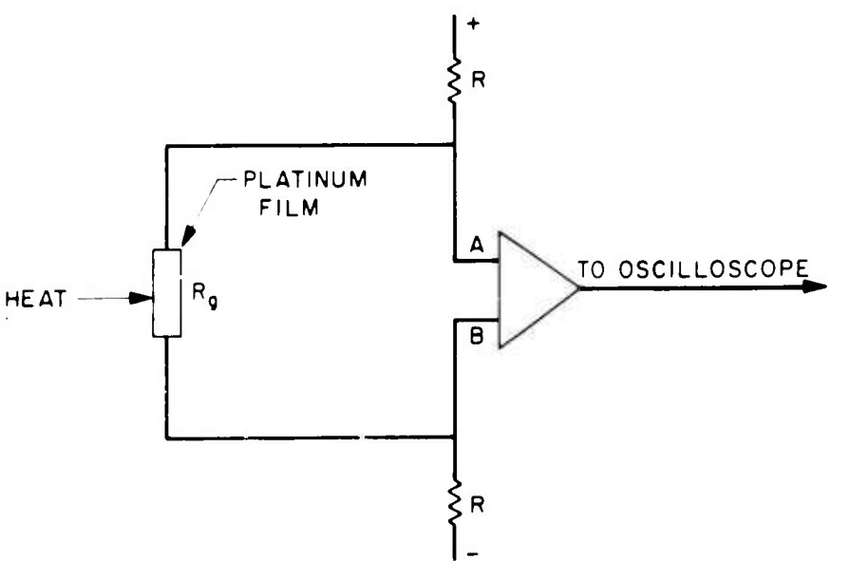


Figure 4 Schematic of total radiation gage circuit

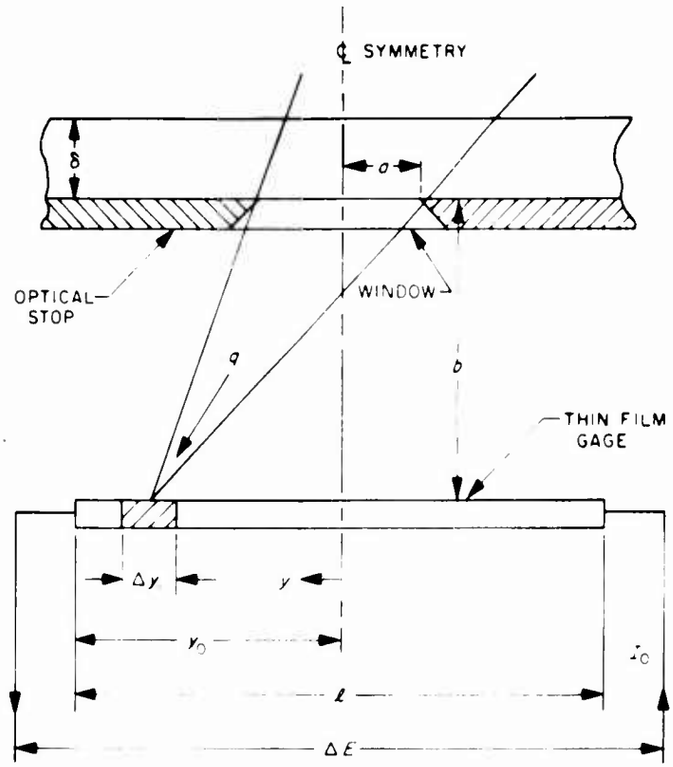


Figure 5. Theoretical model for relating the gage response to the heat transfer distribution along the gage surface.

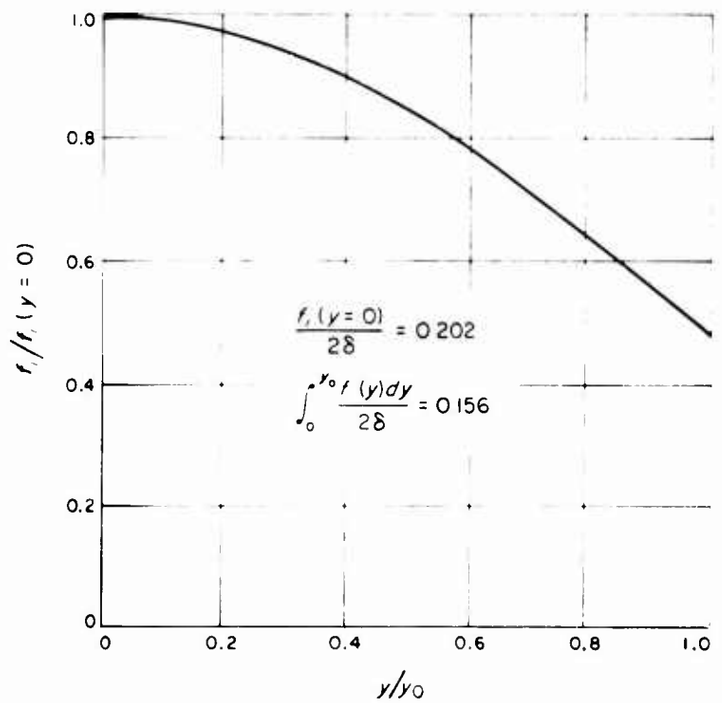


Figure 6. View factor for the experimental geometry: a = 0.795 cm; b = 2.11 cm; and y_o = 0.953 cm.

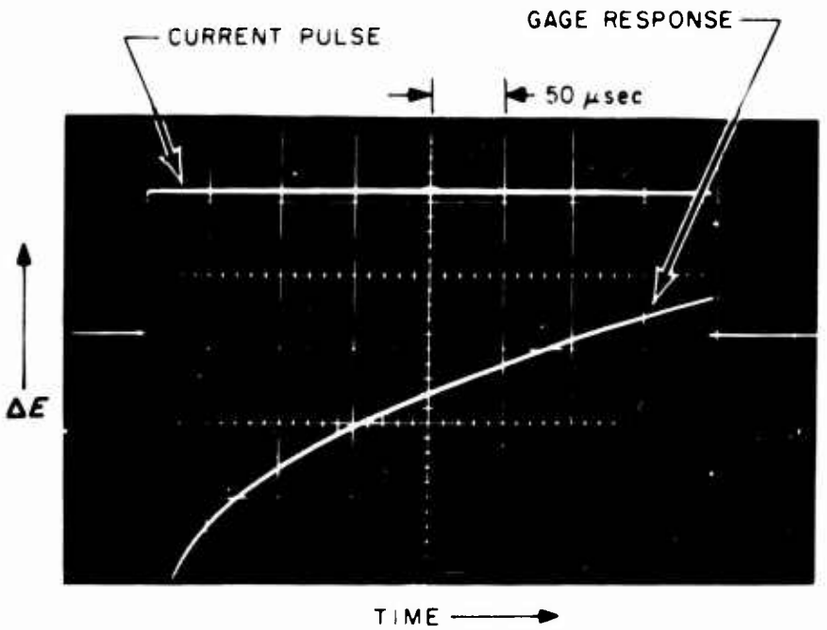


Figure 7 Oscillogram showing radiation gage response to a constant amplitude heat pulse

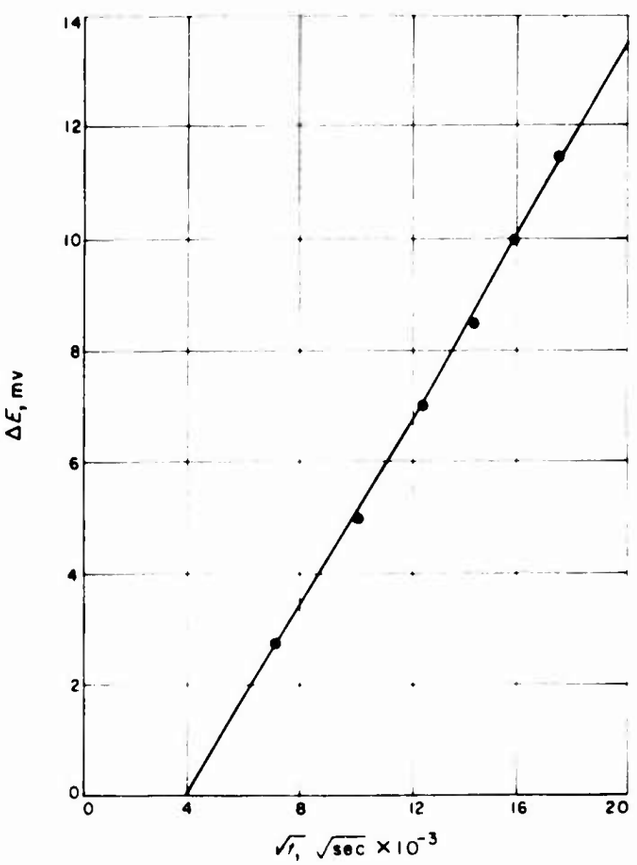


Figure 8 Typical gage calibration results

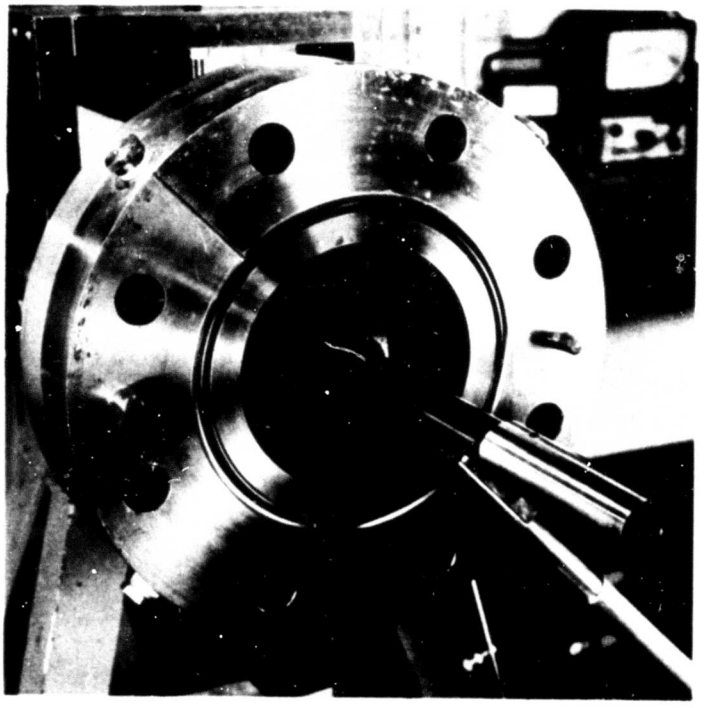


Figure 9 Photograph of shock tube model used for stagnation point radiative heat transfer measurements

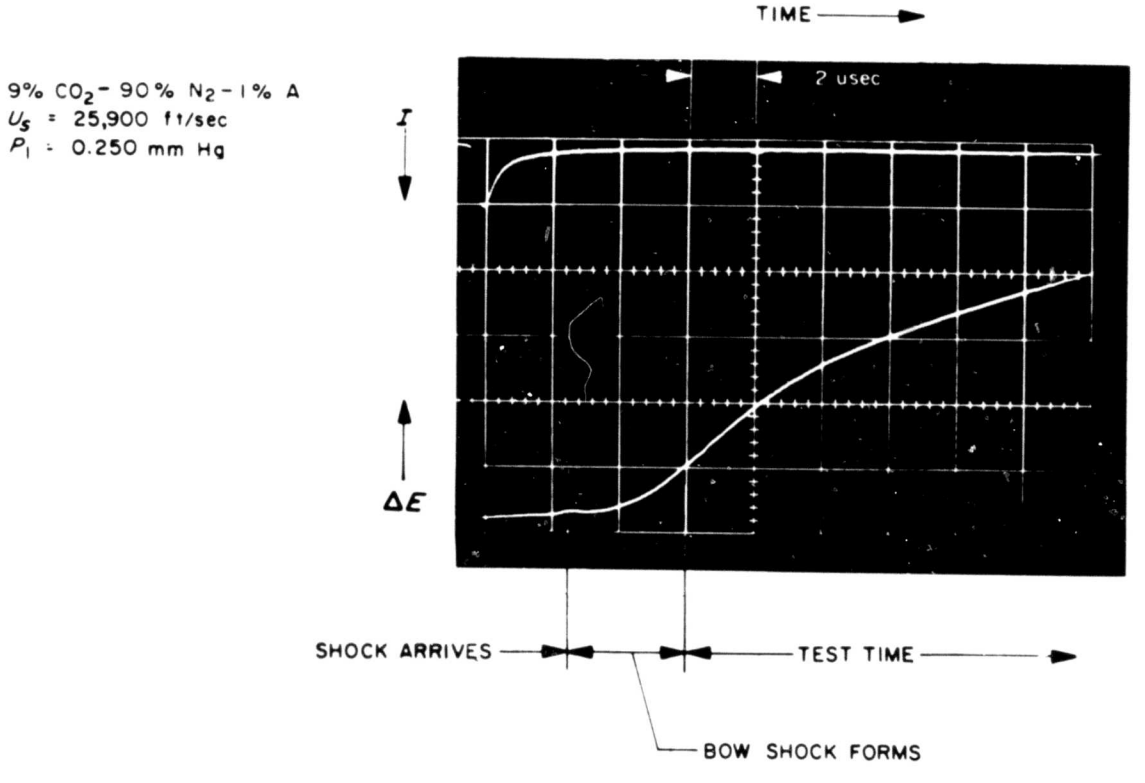


Figure 10 Oscilloscope trace showing response of the stagnation point total radiation gage

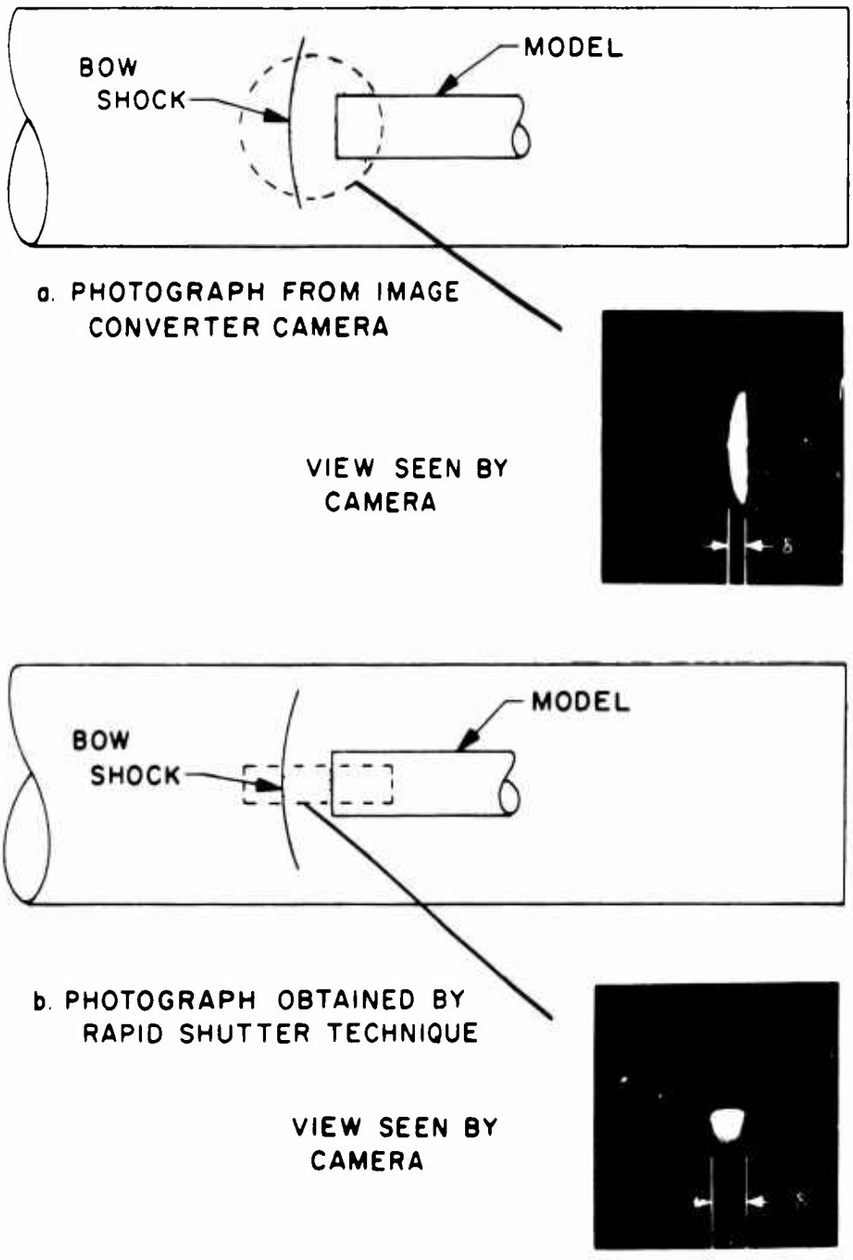
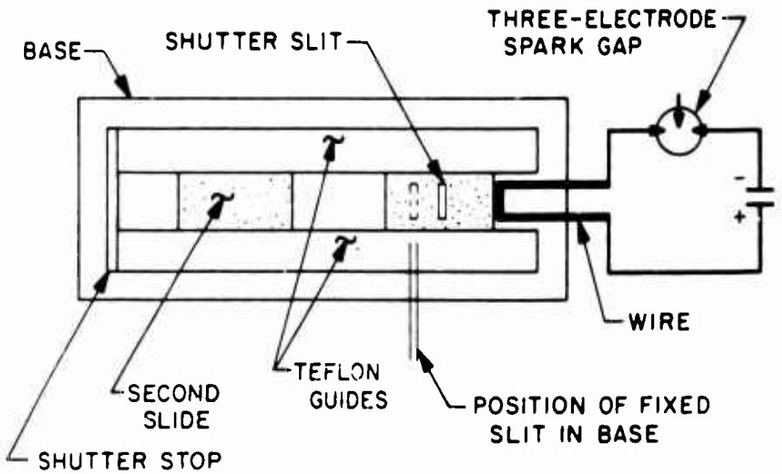
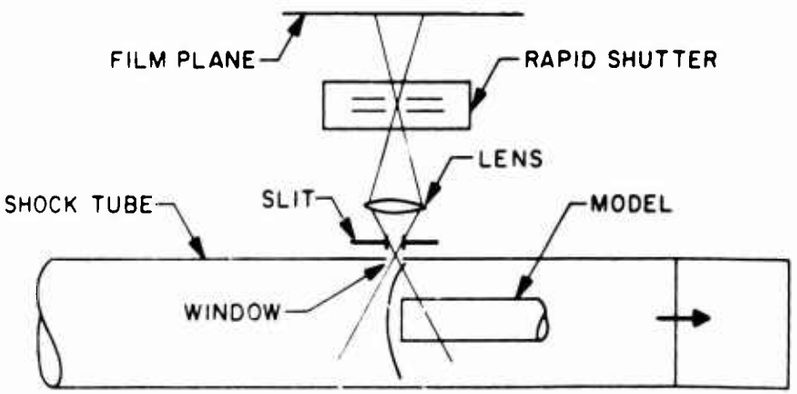


Figure 11 Shock standoff measurements on a $1\frac{1}{4}$" flat-faced cylinder model. Top photograph was taken with an image converter camera. Bottom photograph was obtained using the rapid shutter. Photographs do not have the same magnification.



(a) SCHEMATIC OF RAPID SHUTTER



(b) RAPID-SHUTTER OPTICAL ARRANGEMENT

Figure 12 The rapid shutter. Top: Schematic of rapid shutter mechanism. Bottom: Schematic showing how standoff distance measurements are made in the shock tube.

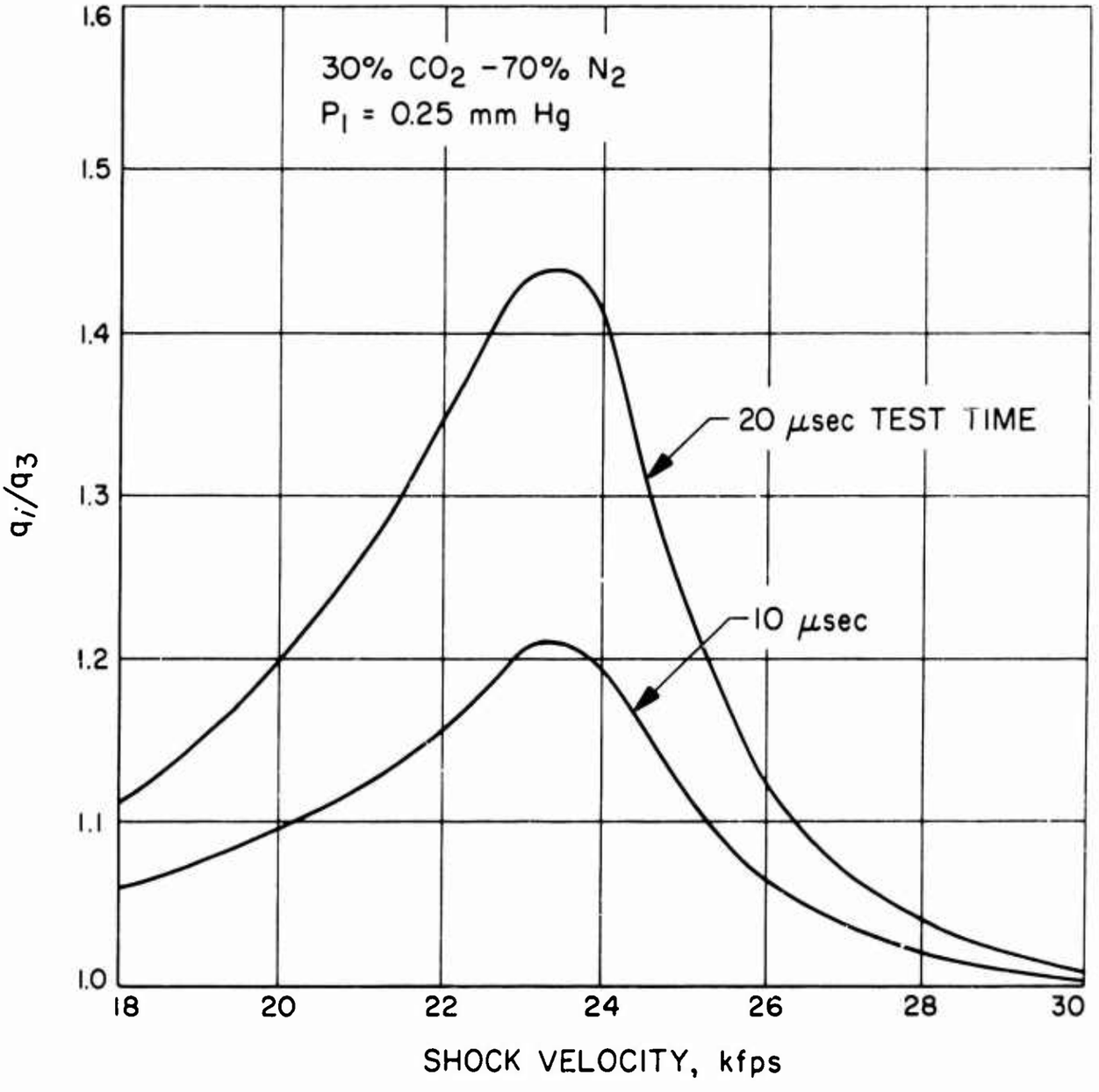


Figure 13. Effect of test gas radiation on the total gage measurement.

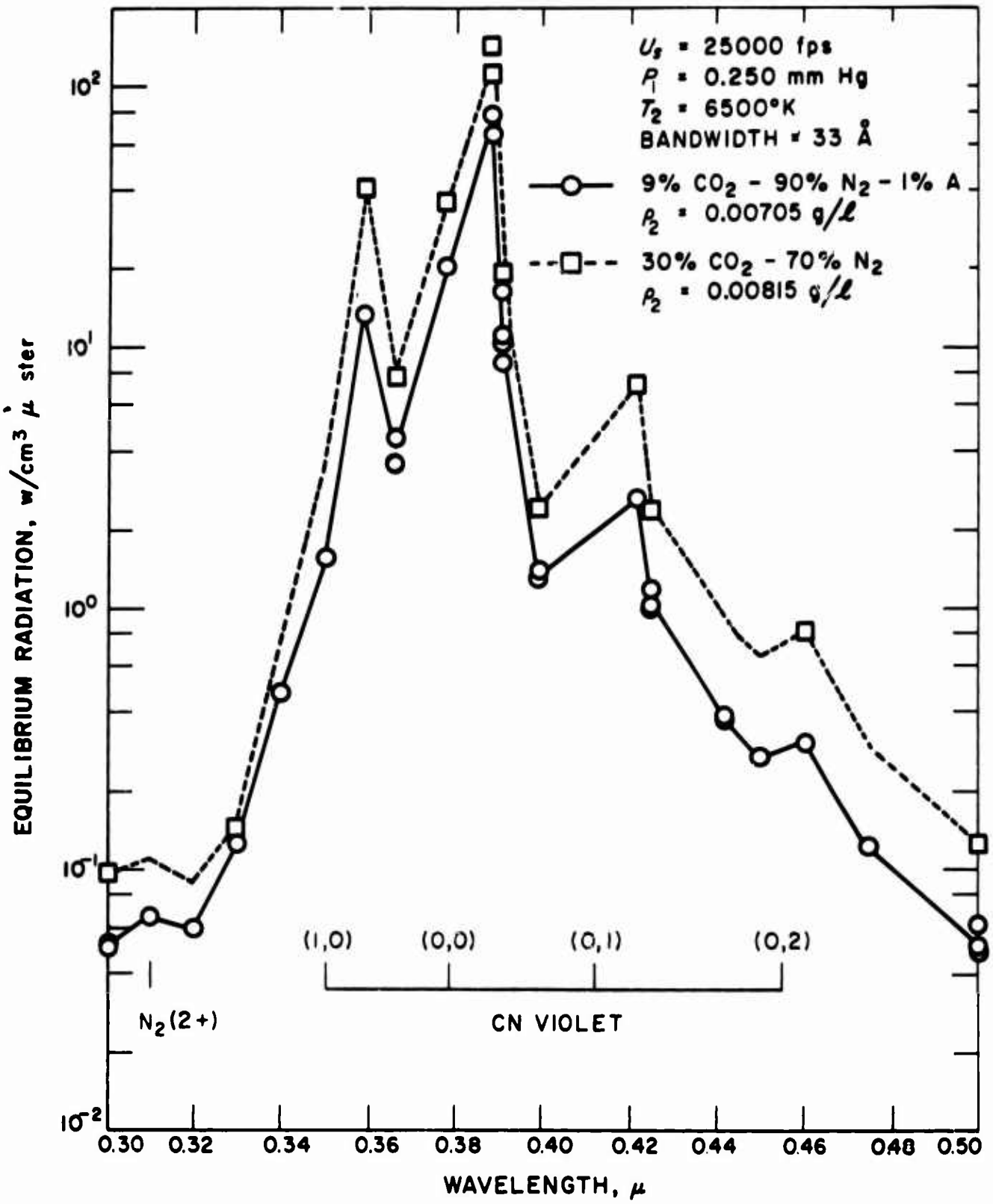


Figure 14 Typical spectral radiation results. Taken from Ref. 1

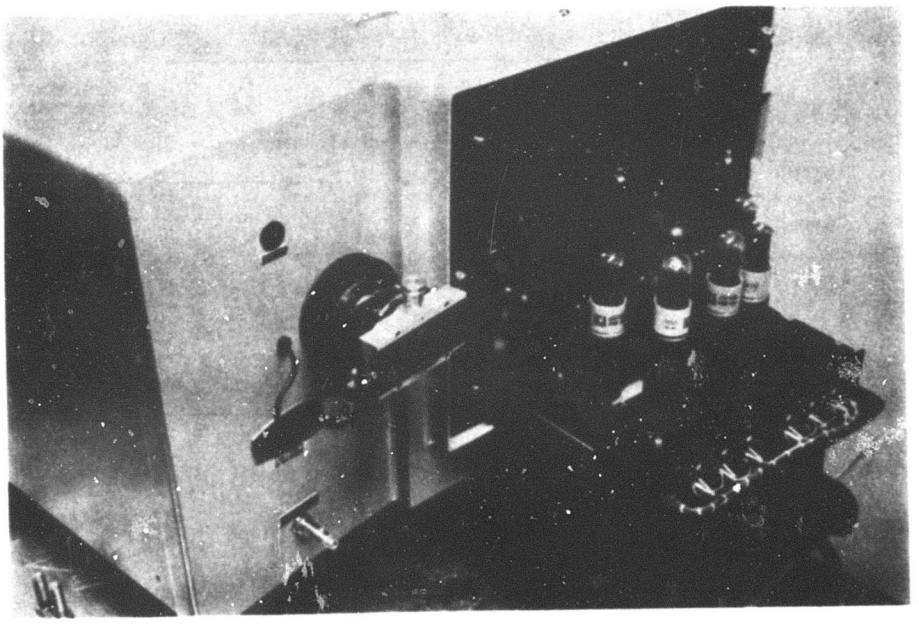


Figure 15 Exit compartment of modified Jarrell-Ash monochromator

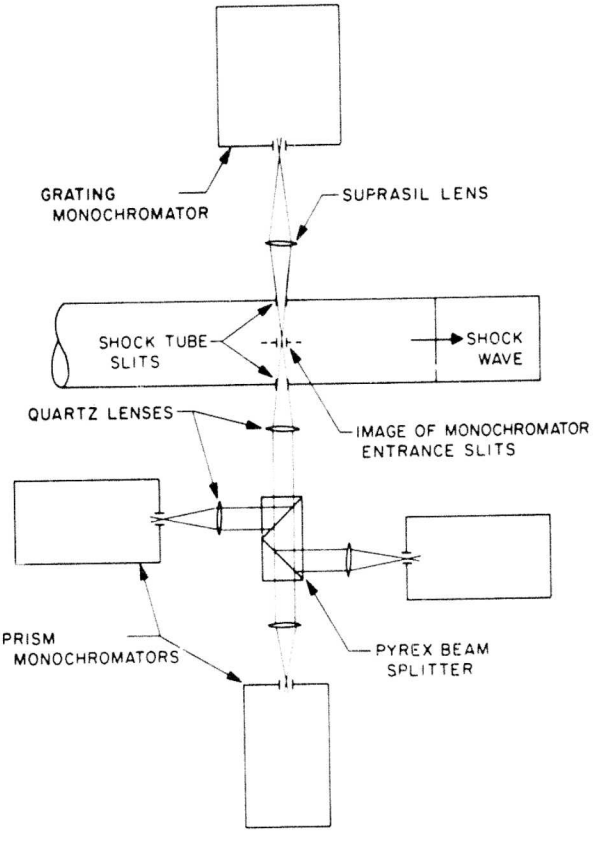


Figure 16 Optical arrangement of the prism and grating monochromators with the shock tube

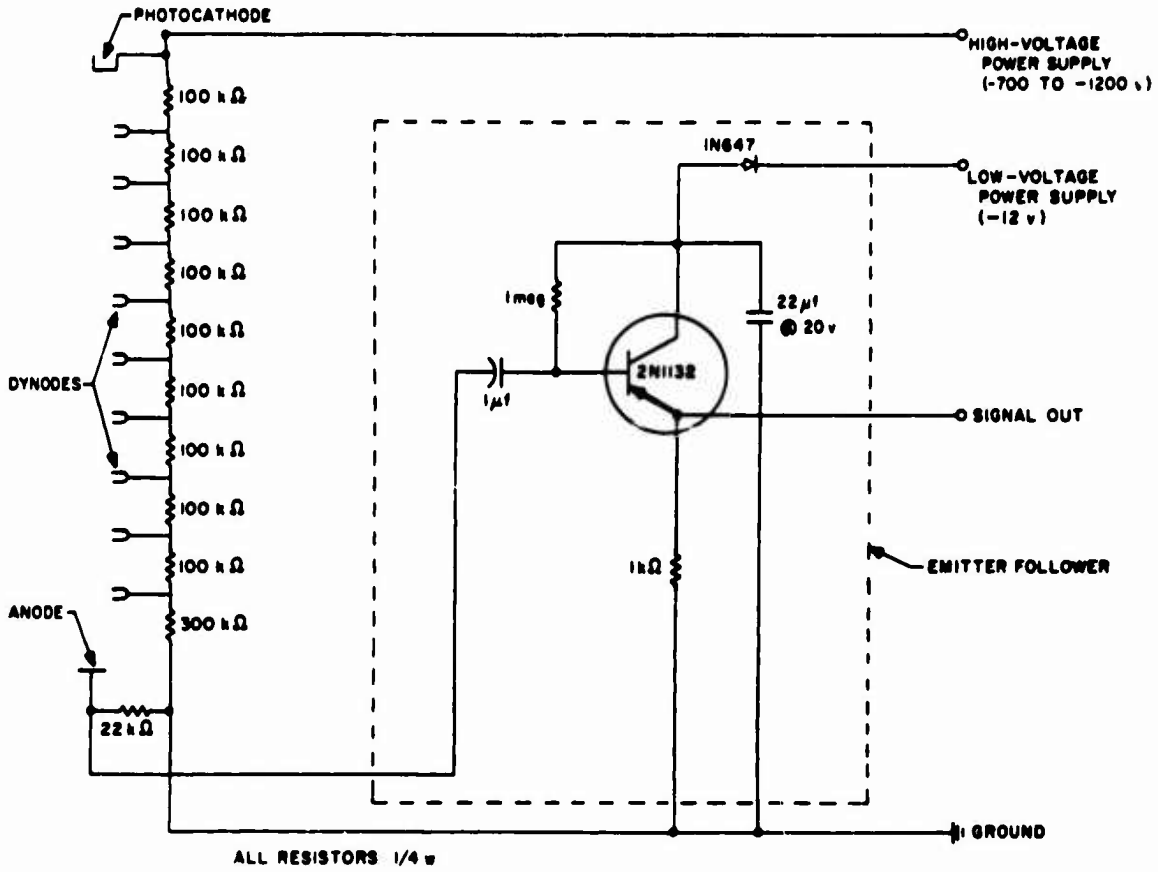


Figure 17 Multiplier phototube circuitry

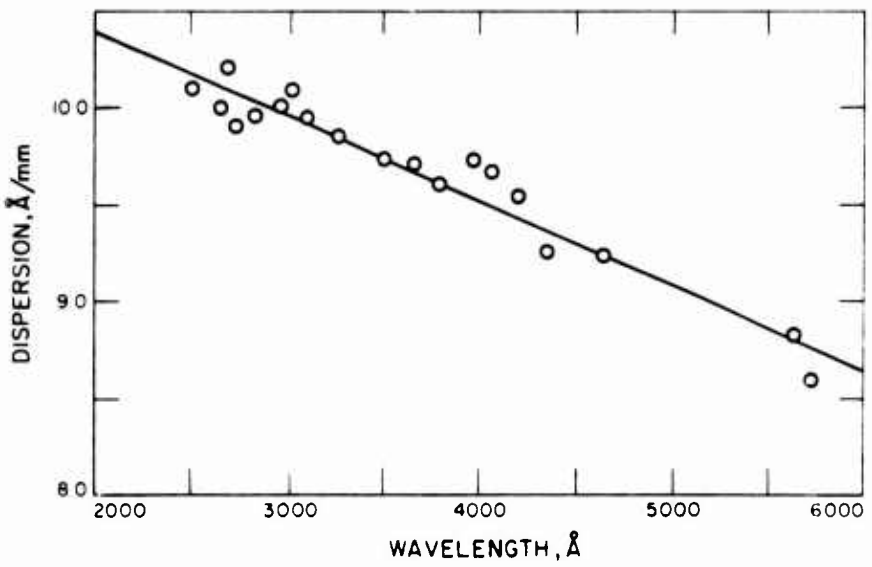


Figure 18 Reciprocal linear dispersion in order I of the Jarrell-Ash grating spectrograph.

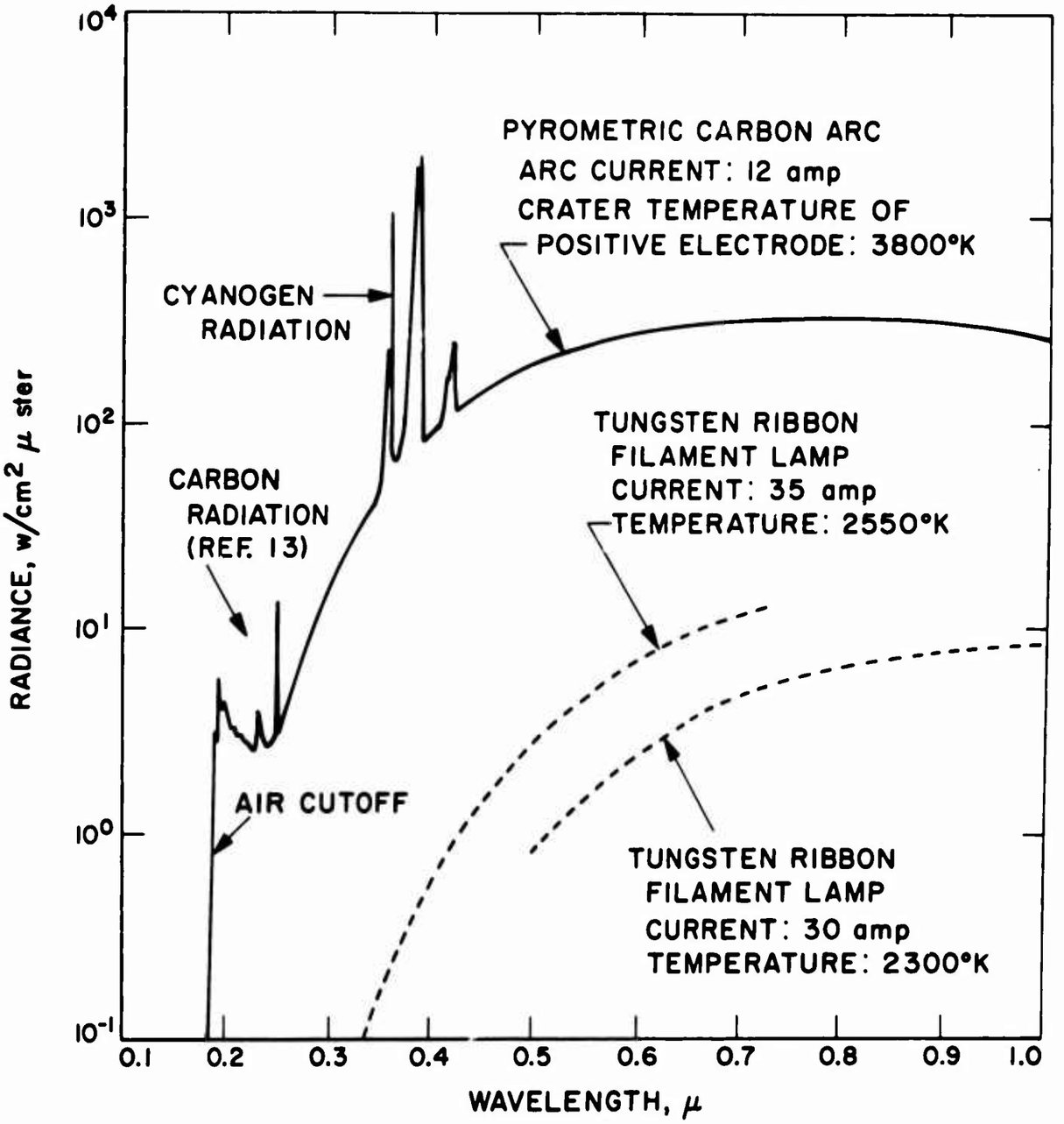


Figure 19 Spectral radiance of typical carbon arc and tungsten lamp calibration sources

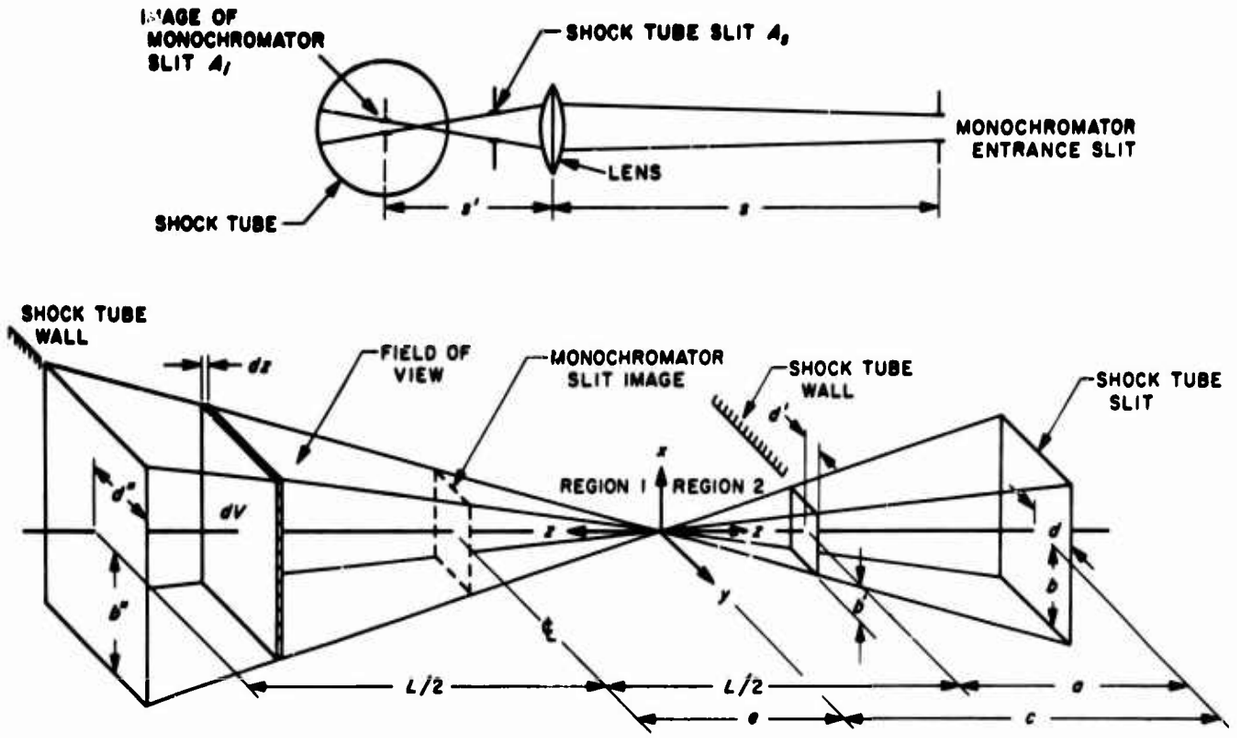


Figure 20 Field of view and gas volume geometry for data reduction of monochromator measurements. Top: Two dimensional field of view. Bottom: Gas volume geometry.

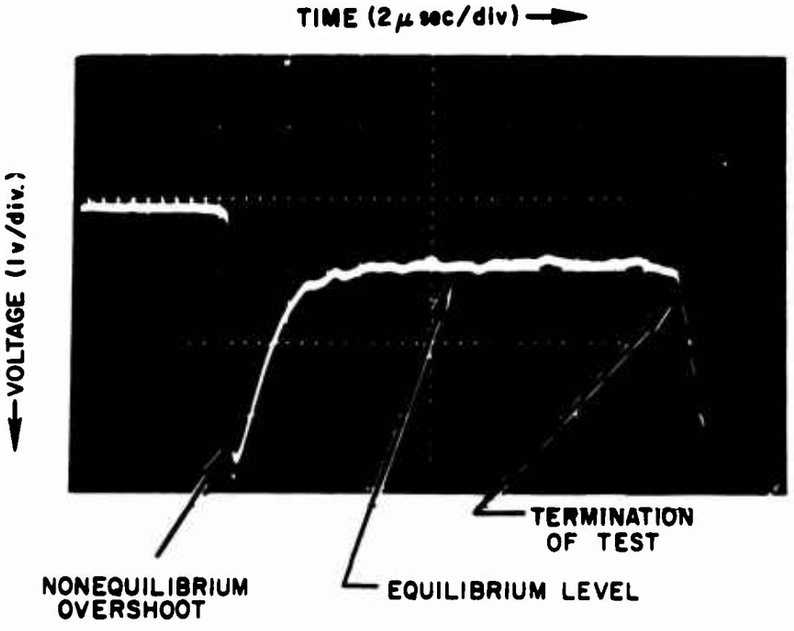


Figure 21 Typical spectral radiation data. The data was obtained at $\lambda = 5165$ Å from a mixture of carbon dioxide, nitrogen and argon. Shock speed was 25,600 fps and initial pressure was .25 mm Hg.

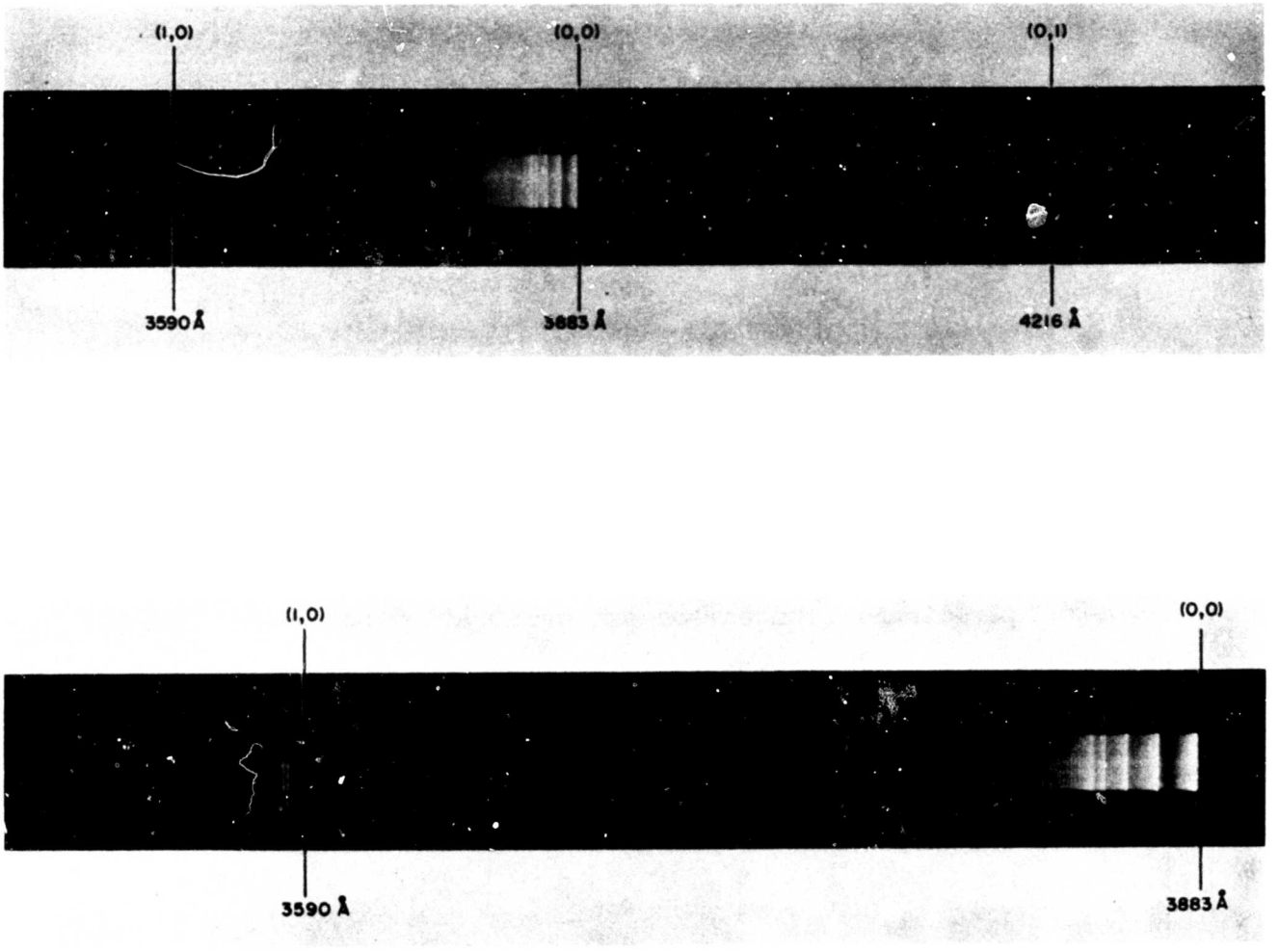


Figure 22 Spectrograms of CN bands from the plasma of a carbon arc. The top spectrogram was obtained in order I and the bottom was obtained in order II.

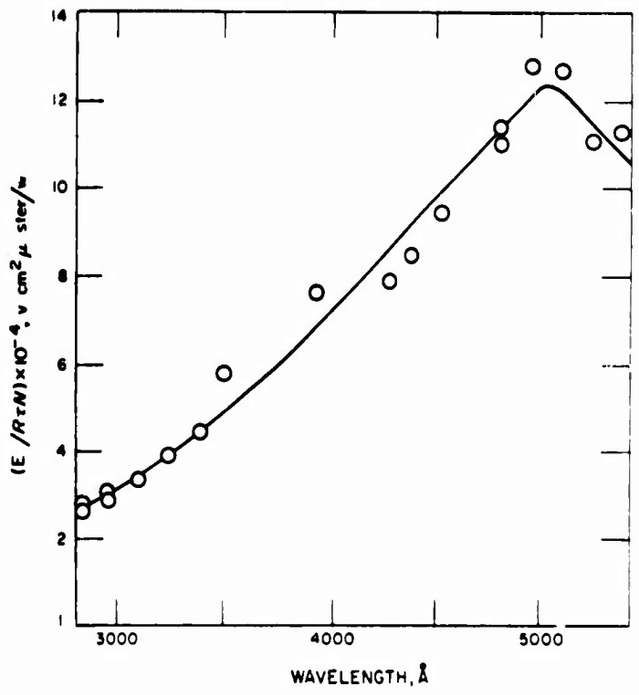


Figure 23 Efficiency of monochromator used in determination of CN radiance from carbon arc calibration source.

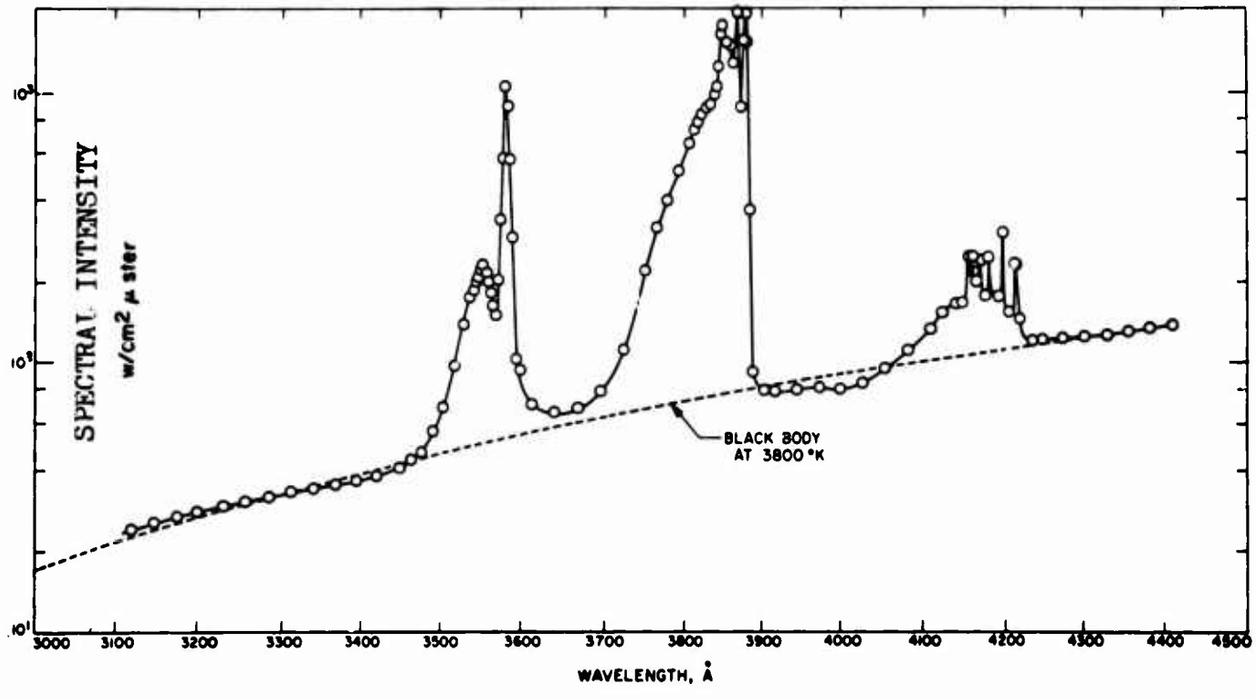


Figure 24 CN radiation from carbon arc

OPTIMIZATION OF SHOCK TUBE WAVE SPEED TRANSDUCER LOCATIONS BY A MONTE CARLO TECHNIQUE

A. A. Taylor* and R. Watson**
Engineering Center
Arizona State University
Tempe, Arizona

Abstract--Optimum spacing of wave speed transducers in a shock tube has been obtained by a computing machine routine using a Monte Carlo technique. The calculations assume random errors in the signals from the velocity pickups within a spread of digital counter timing errors over 100 otherwise identical cases. Least-squares fits to the simulated velocities were made and the number of intercepts falling within different tolerances at the shock tube end plate were counted. A comparison of the resulting velocity intercepts to the true velocity (using typical experimental velocity profiles) was then made in terms of a fraction of the 100 cases for a given tolerance (e.g., $\pm\frac{1}{2}\%$) around the true velocity. Results are interpreted in terms of an optimum spacing and number of transducers for an assumed velocity profile with shock Mach numbers up to $M_S = 10$. The results presented are for an instrumented test section length of $10\frac{1}{2}$ feet, but the method may be applied to other shock tubes and other velocity ranges.

I. INTRODUCTION

Although the measurement of shock wave velocities is generally a relatively straightforward procedure, in cases where severe variations in velocity occur along the test section, a linear extrapolation of velocities determined from a few observation stations can lead to significant errors in the calculated gas properties; this is particularly true if the time resolution of the measuring system is of the order of plus-or-minus one

---

*Captain, USAF, Present Address: Los Angeles Contract Management District, AFSC, Los Angeles, California.

**Present Address: Heliodyne Corporation, Los Angeles, California.

microsecond. The present study describes a procedure to determine the optimum location for wave speed instrumentation and provides a measure of the statistical confidence for velocity measurements in individual shock tube experiments.

References 1 and 2 report on velocity profile measurements in shock tubes, but the experiments were concerned only with the variation of shock speed along the tube for various driver/driven pressure ratios and gas combinations. No attempt was made to predict the accuracy of the velocity measurements nor was any criteria for placement of the wave speed instrumentation given.

The calculations for the present study are based on a typical measurement system using thin-film gages and digital counters. The accuracy of measurement of shock wave velocities with a digital counting system depends principally upon the maximum counting rate used. Other factors of importance are, of course, the spacing and number of gages used. The calculations presented here account for the effects of these factors on the accuracy of measured velocities as compared with true (assumed) velocities, and the results may be interpreted as design information for shock tube wave speed instrumentation systems.

II. DESCRIPTION OF TYPICAL WAVE SPEED INSTRUMENT SYSTEM

The measurement system considered in this study is typical of a large number of shock tube installations. These systems utilize the signals generated by the resistance change in thin-film gages (3) as the shock front passes, to actuate digital counters. The average shock velocity is then computed from the time interval required for the shock wave to traverse the distance between gages. A series of gages and counters is often used to estimate the variation in wave speed along the shock tube. A variation of this approach utilizes a series of counters operated from a master oscillator (4).

The use of a master oscillator results in a reduction in the over-all counting error compared with a system using separate oscillators for each set of gages, and such a system was assumed for this study. The reduction in over-all counting error occurs because the timing error in the $(n+1)$-counter tends to be offset by the error in the nth-counter since the total error from the initiation of the first count until the termination of the last count is limited to plus-or-minus a single count when a master oscillator is used. If each counter bank had a separate oscillator, the total counting error in a single experiment could be as high as plus-or-minus n counts for n counting intervals.

It is apparent however, that for any measurement system, an analysis of velocity measurements based on maximum possible deviations from the true velocity (e.g., by use of maximum timing errors, etc.) has little practical significance because of the statistical improbability of the occurrence of

this maximum deviation in actual experiments. The timing errors actually assume random values of the plus-or-minus one count, and the probability of the extreme error limits occurring in an individual experiment is small.

III. COMPUTER MODEL

In order to determine the most probable timing errors in shock tube experiments, a computer model of the shock wave velocity profile was constructed to allow calculation of a large number of simulated experiments with random errors being assumed in the velocity measuring apparatus. Identical (true) velocity profiles were assumed for each of the sets of simulated experiments, and various simulated velocity measurements were obtained each being the result of the occurrence of a series of random timing errors throughout the system. The most probable excursions of measured profiles for a given true velocity profile were then calculated.

By a comparison of the variances of the results of otherwise identical series, it was determined that a series of 100 tests was sufficient to establish valid results.

A. Introduction of Error

Since finite distances between pickup locations are used, the measured velocity is actually a mean velocity $\bar{V}$ rather than an instantaneous velocity, i.e.,

$$\bar{V} = \frac{\int_{x_1}^{x_2} V dx}{x_2 - x_1} = \frac{\Delta x}{t} \qquad (1)$$

where $\bar{V}$ is the true mean velocity between the two transducers located Δx apart if t is the actual time interval required for the shock wave to traverse the distance between the transducer locations.

However, an uncertainty exists in the mean velocity $\bar{V}$ due to uncertainties in the time interval t. This velocity uncertainty $\Delta\bar{V}$ is given by

$$\Delta\bar{V} = \frac{\bar{V}^2}{\Delta x} \Delta t \qquad (2)$$

where Δt is the error in the true time interval caused by the inherent inaccuracy in the counting units which display only integral units of time (single counts). Since the signals from the wave speed transducers are not synchronized with the oscillator wave form, the timing errors would be different for each of a series of shock tube experiments even if the velocity profile were the same for all runs; the timing errors would be random fractions of the maximum possible error of plus-or-minus a single

count. The velocity error $\Delta\bar{V}$ is superimposed on the true $\bar{V}$ and may be additive or subtractive, depending on the direction of the timing error. The velocity as given by the measurement system is then $V = \bar{V} + \Delta\bar{V}$ and is assumed to be the wave speed midway between the thin-film gages.

A sketch illustrating the possible introduction of error in the measured velocity (for a single experiment) at the end plate of a shock tube compared to the true velocity is shown in Fig. 1.

B. Simulation of Velocity Measurement

The origin for the assumed, or true, velocity profile was taken at the end plate of the test section, i.e., as would be required for reflected shock wave tests. For the great portion of the Mach number range covered in these calculations, the experimental velocity profiles in shock tubes appear to be linear functions of velocity near the end plate (1,2,5). Proceeding towards the diaphragm from the end plate, higher order components of the velocity profile become important.

Assuming the velocity to be a polynomial function of the distance from the end plate, an assumed true profile may be constructed. Within each measurement interval along the shock tube length, a velocity error defined by equation (2) can be imposed as a result of the random timing error. From the values of $V = \bar{V} + \Delta\bar{V}$ at the midpoint of the measurement interval, a least squares analysis for curve fitting may be used to determine a simulated measured velocity intercept (modified from the true velocity by the random timing errors) at the end plate. If the assumed true profile is held constant while repeated sets of random errors are introduced and the resultant error-modified velocity intercepts calculated, the fraction of the population of intercepts falling within specified limits about the true intercept can then be determined. This intercept fraction is shown in the shaded area of Fig. 2. Thus, for individual shock tube experiments, the probability of an experimentally determined intercept being within a specified tolerance from the true velocity intercept is the fraction of the population of calculated intercepts that lie within the tolerance width. An equivalent confidence limit may be associated with the prescribed tolerance limits, i.e., a certain percentage of all velocity measurements will fall within the tolerance band around the true velocity.

C. Computation Procedure

Input information to the computer program consisted of (a) a set of transducer locations, and (b) polynomial coefficients appropriate to the assumed velocity profile (5,6). Available experimental velocity profiles were analyzed by the Abbreviated Doolittle method (7) to determine the polynomial coefficients required to represent these profiles. The results indicated that over a distance of about twenty feet before the end plate is reached, simple linear or quadratic models were not adequate for all cases. Accordingly, cubic and quartic profiles were also considered in the present calculations. Thus, the true velocities were determined

from a general expression of the form $V = V_o + ax + bx^2 + cx^3 + dx^4$, the coefficients being taken as variable parameters according to the representative data of Ref's. 5 and 6. While higher order profiles may be more severe than those ordinarily experienced with a cold helium driver gas up to $M_S = 10$, the inclusion of cubic and quartic profiles assured coverage of a wide range of shock tube operating conditions.

For each set of input data, a random velocity intercept was calculated for each of five true velocities corresponding to $M_S = 2, 4, 6, 8$ and 10 at the end plate. For the transducer interval Δx nearest the diaphragm, the true mean velocity $\bar{V}$ was calculated. A random number stimulus was provided to calculate a random timing error Δt. The corresponding velocity error $\Delta\bar{V}$ was added to the true mean velocity $\bar{V}$ to yield the resultant velocity measurement, $V = \bar{V} + \Delta\bar{V}$.

For the succeeding interval, a new random timing error was generated. At this point, however, a check was performed to determine if the total timing error for both intervals summed to less than one count which is the maximum over-all timing error that can result in a system using a master oscillator. If the total Δt was greater than one count, the random number process was recycled until the Δt was within the correct range; as discussed previously, the maximum error in the total Δt can be only plus-or-minus one count when using a system with a master oscillator.

The calculation of random velocity errors proceeded in this fashion until values were obtained for all intervals subject to the restriction that the total timing error was always less than one count. With these values, a regression analysis was performed to determine the experimental intercept on the end plate.

The process was repeated 100 times and the mean, the variance, and the fraction of intercepts within specified tolerances of the true velocity were obtained for the given combination of transducer locations and velocity polynomial coefficients. A large number of variations in the transducer locations and spacing were made and the computation procedure repeated for each set to give the fraction of the intercepts associated with each configuration.

IV. EFFECTS OF MECHANICAL PLACEMENT OF TRANSDUCERS ON VELOCITY ACCURACY

The previous sections have been concerned with random errors due only to timing uncertainties. Errors in uncertainties of the actual or effective gage location affect the spacing Δx and hence can also contribute to a velocity error. Sources of uncertainties in Δx are caused by (a) initial placement of the transducer mounts (measurement tolerances), (b) width of any unknown unhomogeneities in the thin-film material (deposition uncertainty), and (c) thermal expansion of the shock tube.

The velocity error caused by a location uncertainty is

$$\frac{\Delta \bar{V}}{\bar{V}} = \frac{\Delta L}{\Delta x} \qquad (3)$$

where ΔL is the uncertainty in location of a gage and it is seen that this effect is independent of the shock wave speed. Assuming measurement tolerances of $\pm$ .001 inches on four dimensions required to locate a set of transducers (one each for the transducer mount and its hole location in two adjacent shock tube sections), a conservative over-all spacing error is $\pm$ .004 inches. For a spacing of one foot between the transducers, $\Delta \bar{V}/\bar{V}$ is less than 0.04%; for a spacing of two feet, $\Delta \bar{V}/\bar{V}$ is less than 0.02%.

Unhomogeneities in the films and uncertainties in the location of the film on the transducer base can contribute to an uncertainty in the initiation of the timing signal. A conservative estimate for this error may be obtained by considering the width of the unhomogeneous region to be the total width of the film. If ΔL is $\sim$0.20 inches, then for a Δx of one foot $\Delta \bar{V}/\bar{V}$ is $\sim$0.2%. The effects of unhomogeneities alone are probably much less severe than the preceding calculation indicates since thermal diffusion times for thin platinum films are typcially much less than a microsecond (8) and counter triggering should occur when the shock wave passes the leading edges of the film regardless of unhomogeneities.

Uncertainties in transducer location due to thermal expansion may be estimated from the thermal coefficient of expansion of the shock tube material. For an aluminum shock tube with a change in ambient temperature of 60°F, $\Delta \bar{V}/\bar{V}$ is only about 0.08%.

In comparison to these errors, the velocity error introduced by a timing uncertainty of $\pm$ 1 microsecond for a transducer spacing of 2 feet is about 0.5% at M_S = 10. Thus the effects of mechanical placement of the transducers are generally unimportant compared with possible timing errors.

V. RESULTS AND CONCLUSIONS

Based upon the magnitudes of timing and mechanical placement errors, it is apparent that for high Mach numbers, the dominant error is caused by the timing uncertainty when 1 microsecond counters are used. At low Mach numbers, the errors due to timing and mechanical uncertainties are about equal but both errors are small and do not affect the accuracy of velocity measurement appreciably. The results presented here are therefore based only on errors due to timing uncertainties. The calculations were restricted to cases with transducer locations limited to a $10\frac{1}{2}$ feet long section preceding the end plate; interpretations of the results were made in terms of the fraction of velocity measurements that would lie within a specified

tolerance at the end plate.

The majority of calculations were performed for master oscillator frequencies of 1.0 and 1.2 megacycles. A gain of from 3 to 10% in the intercept fraction can be achieved by using the 1.2 megacycle oscillator (0.833 microsecond least count). The results of a series of calculations indicated that 6 measurement intervals (7 transducers) spaced about 21 inches apart (the last transducer being in the end plate) gave the greatest percentage of measured velocities falling within specified tolerances of the true velocity. Table I summarizes the results.

If a 10 megacycle oscillator is used with a 0.1 microsecond least count system, results (not presented in detail here) indicate that the velocity uncertainties due to timing errors are less than those due to mechanical placement errors for the 6-interval spacing of Table I. No attempt was made to optimize spacing for a system with 0.1 microsecond counters.

Variations in the intercept fraction for different measurement intervals become more pronounced as the order of the velocity polynomial is increased. For both cubic and quartic models, the intercept fraction for each tolerance band initially increased with the number of measurement intervals, then reached a peak and finally diminished. Increasing the number of intervals restricts the freedom of the curve fitted to the experimental points so that less error in curve extrapolation results. However, increasing the number of measurement intervals in a fixed distance of the test section decreases the spacing between transducers which in turn increases the velocity error (as per equation 2). The optimum number of intervals and their spacing thus lies between these two extremes.

If it is desired to measure shock wave velocities at an observation point before the end plate is reached (as in incident shock wave studies), then the transducer spacing should be distributed about the observation point since the variance achieved at the midsection of the instrumented portion is less than at the end points. For example, the variance at the midpoint of the 6-interval configuration of Table I is about one-half that at the end plate.

In all cases, it is important to note that with any transducer spacing, a general degradation in confidence in the velocity prediction occurs if the order of the velocity polynomial is increased. To apply the techniques of the present study to a particular shock tube installation, the experimental velocity profiles should be analyzed to prevent overestimation of the order of the model which severely penalizes the expected confidence. A lesser number of transducers (and counting units) will suffice if the velocity profiles are not severe.

REFERENCES

(1) J. J. Jones, Experimental Investigation of Attenuation of Strong Shock Waves in a Shock Tube with Hydrogen and Helium as Driver Gases, NACA TN 4072 (1957).

(2) D. R. White, Jour. Fluid Mechanics 4, 585 (1958).

(3) R. J. Vidal, Model Instrumentation Techniques for Heat Transfer and Force Measurements in a Hypersonic Shock Tunnel, Cornell Aeronautical Laboratory Report No. AD-917-A-1, Buffalo, New York, (1956).

(4) W. H. Wurster and R. J. Hiemenz, Cornell Aeronautical Laboratory, Buffalo, New York, (private communication, 1963).

(5) T. A. Jacobs, Aerospace Corporation, El Segundo, California, (private communication of experimental data, 1964).

(6) J. L. Copper, Douglas Aircraft Company, El Segundo, California, (private communication of experimental data, 1964).

(7) B. Ostle, Statistics in Research, Iowa State University Press, Ames, Iowa, 1963, Second Edition.

(8) B. D. Henshall and D. L. Schultz, Some Notes on the Use of Resistance Thermometers for the Measurement of Heat Transfer Rates in Shock Tubes, (Aeronautical Research Council, London, England, C.P. 408, 1959).

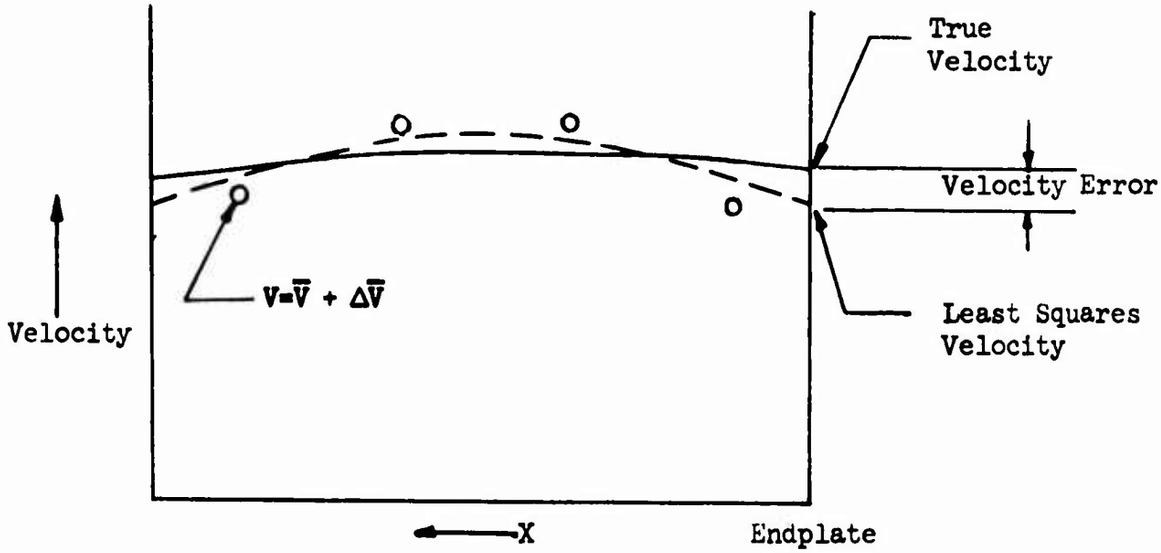


Fig. 1. Illustration of Velocity Measurement Error At The Endplate Due to Random Timing Errors

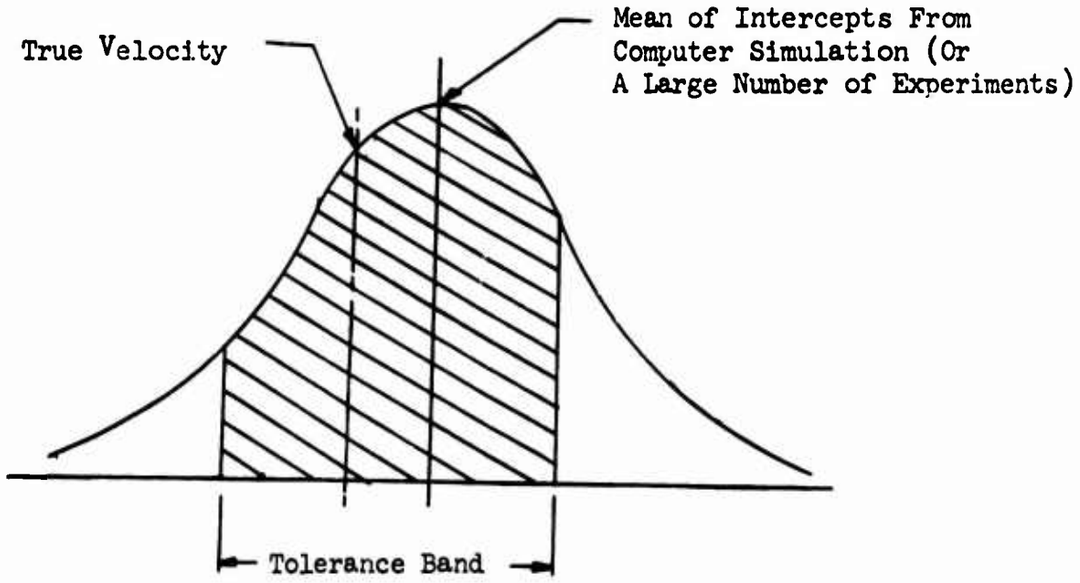


Fig. 2. Typical Velocity Intercept Population Showing Relations Between True Velocity Intercept, Velocity Tolerances, And Mean Velocity Intercept As Would Be Determined By A Large Number of Shock Tube Experiments

BLANK PAGE

A MULTIPLEXED SPARK SOURCE SCHLIEREN SYSTEM FOR SEQUENTIAL OBSERVATION OF HIGH SPEED SHOCK WAVE PHENOMENA

W. M. Robinson*, R. Watson**, and J. G. Dean***
Engineering Center
Arizona State University
Tempe, Arizona

I. INTRODUCTION

A multiple spark, modified schlieren system that yields a sequenced series of photographic observations of high speed shock wave phenomena in a shock tube has been constructed and its operation is described in this paper. Optical multiplexing of the light output from four short duration (~0.5 microsecond) spark light sources spaced radially about a pyramidal mirror permits independent silhouette records of a shock wave to be taken at electronically preset intervals from 6 to 200 microseconds apart. The multiplexing of the light beam allows effectively high framing rates to be obtained without requiring a high speed drum camera or Kerr cell, and all records are taken on a single 4 x 5 inch Polaroid film.

This system permits a series of observations to be made of the development of shock wave phenomena in a localized region of the shock tube. Utilization of a "defocused" optical system reduces the problem of background illumination due to incandescence in the hot test gas.

A schematic diagram of the optical system is presented along with experimental records of the interaction of an incident shock wave with a model in the shock tube test section.

---

*Present Address: California Institute of Technology, Pasadena, California.
**Present Address: Heliodyne Corporation, Los Angeles, California.
***1st Lt. USAF, Present Address: Headquarters, Space Systems Division, Los Angeles, California.

II. OPTIC - PHOTOGRAPHIC SYSTEM

A. The Optical System

The optical system incorporates a multiplexed principle and uses the same optical path for a series of separate channels through the test section area (see Fig. 1). Four separate high intensity light sources S_1 at right angles to one another are focused individually onto the surfaces of a four-sided pyramidal mirror PM_1, and each light source is then adjusted to completely fill a single concave mirror M_1. From the mirror M_1, the optical path for all four sources is through the test section windows W, onto another concave mirror M_2. The images of the four sources are then separated by the surfaces of a second pyramidal mirror PM_2 at the focal length of M_2. Thus the light from the sources is collimated through the test section with the images of all four sources focused at PM_2. Immediately in front of PM_2, four round apertures A, the same diameter as the image of the sources are positioned to remove light rays that are refracted by density gradients in the test section; the apertures thus serve as circular knife edges as in a conventional schlieren system.

Achromatic lenses L are placed so as to form a real image of the virtual image of the test section formed by mirror M_2. A film pack holder containing 4 x 5 inch Polaroid film is positioned at the focal plane of the system. The lenses L are positioned so as to reduce the image sizes to accommodate all four pictures on the same film sheet. The system thus allows four independent schlieren pictures to be taken in sequence as rapidly as the four individual light sources can be flashed. The same area in the test section is illuminated each time and reference points in the test section may be compared with the relative positions of flow phenomena taking place in the area of observation.

Luminescence from the hot gas behind the shock wave is emitted in all directions, but only the radiation essentially parallel to the optical path of the collimated light in the photographic system is focused onto the film because the limiting apertures (A) reduce the solid angle for the hot gas emission. This "defocusing" effectively decreases the intensity of the hot test gas relative to the intensity of the light sources and thus relieves to some degree the high intensity requirement of the sources. Also, the essentially collimated light from the sources is adjusted to just cover the area of the test section windows. In this manner the ratio of the flux of illuminating light from the spark sources to the flux of light radiated behind the shock wave is kept to a maximum.

Except for the achromat lenses L, the entire optics system is composed of first surface mirrors so that the system produces no chromatic aberrations. The off-axis light source position (with respect to the normal to the flow field in the test section) tends to cause astigmatic and comatic aberrations in the source image. However, these effects are minimized by keeping the deflection angles θ_1 and θ_2 (see Fig. 1) as small as physically possible, depending on placement of the optical components.

B. The Light Sources

The optical system requires very short pulses of high intensity light to avoid blurring of the shock wave image on the photograph. Four spark gap light sources were constructed, the design being patterned after that reported by Kovasznay in Ref. 1. Six tubular capacitors (0.02 microfarads, 5000 VDC, non-inductive Glassmike ASG-203-5M supplied by Condenser Products Co.) are located concentrically about the main electrodes to minimize circuit inductance, the spark being initiated by the application of a high voltage pulse to an adjustable trigger electrode which extends into the gap between the main electrodes.

The trigger electrode adjustment, the electrical connections, and the lenses for focusing the spark gap onto the first pyramidal mirror are all self-contained in a compact Plexiglas container, allowing ease of adjustment in aligning the optical system as well as serving to insulate the high potentials from accidental contact or arcing to instrumentation fixtures. With reasonable care (e.g., a low frequency of flashing), the capacitors of each light source could be used for a few hundred flashes with very reproducible results. The effective duration of the sources was about 0.5 microsecond (measured at half peak intensity) and triggering of the individual light sources was achieved by signals from conventional thin film gages utilizing appropriate delays for the desired timing sequence. A pulse generator for each spark source was constructed with a delay capability in each channel of from 6 to 200 microseconds after the time the initial signal from the thin film transducer is received.

III. EXPERIMENTAL RESULTS

A sample of the photographs obtained from this system is presented in Fig. 2. The last three frames were obtained in a shock tube test following the one in which the first three were taken. The individual time delays were adjusted to allow an approximately equal time interval between the sequenced photographs.

REFERENCE

(1) L. S. G. Kovasznay, Rev. Sci. Instr. 20, 696 (1949).

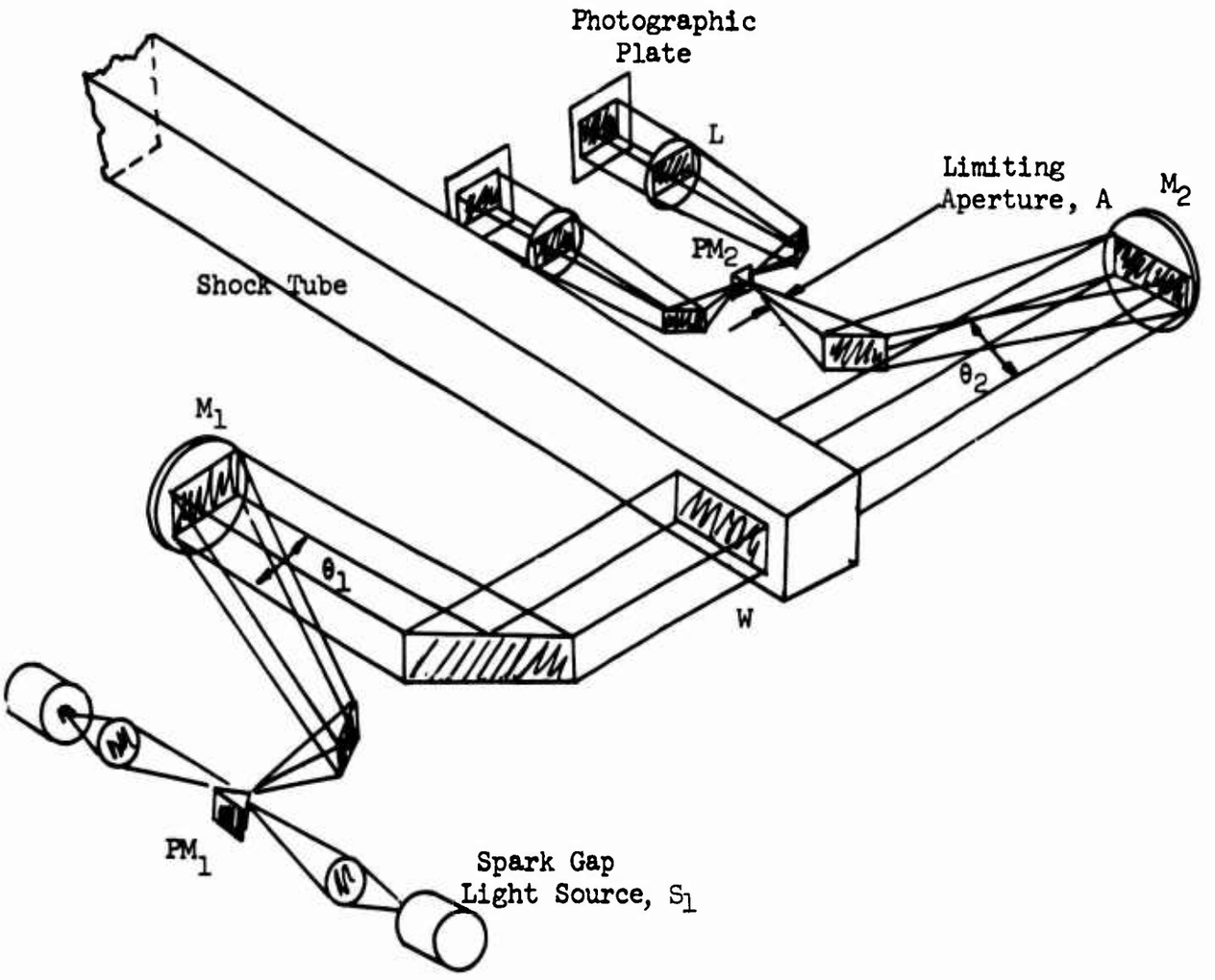


Fig. 1. Schematic of Two Channels of Modified Schlieren System



Fig. 2. Schlieren Pictures Showing the Flow Phenomena About a Seven-Sixteenths Inch Diameter Sphere for M_s = 2.11. The Sequencing is 10 Microseconds Between Each Photograph.

DATA DISPLAY AND RECORDING APPARATUS FOR MASS SPECTROMETRIC STUDY OF CHEMICAL REACTIONS IN SHOCK WAVES IN GASES

S. C. Barton, M. A. Di Valentin, J. E. Dove
Department of Chemistry
University of Toronto
Toronto 5, Ontario, Canada

INTRODUCTION

The shock tube offers many advantages for the study of chemical reactions in gases at high temperatures. However a serious difficulty has been the lack of a universal detector of high sensitivity which would be capable of following very rapid changes in concentration of chemical species. The use of the time-of-flight mass spectrometer, whose application to the study of fast gas reactions was pioneered in the laboratory of G. B. Kistiakowsky (1,2), is an extremely promising development in this direction.

The principle of the time-of-flight mass spectrometer has been described elsewhere (3,4). Recent commercial models can produce complete mass spectra at repetition frequencies of 10 to 100 kc/s. The mass range which can be covered depends on the frequency used; at the highest frequency, a spectrum up to about mass number 60 or higher can be produced every 10 microseconds. These spectra are normally displayed on a cathode ray oscilloscope.

In applications to the study of reactions in shock waves (2,5,11), gas is usually sampled continuously from the reflected shock through an orifice directly into the ion source of the mass spectrometer. When the gas is heated by the shock wave, any resulting changes in chemical composition of the sampled gas will be shown as corresponding changes in the mass spectrum. In a typical experiment, some twenty-five or thirty mass spectra might need to be recorded separately in a time of 300 microseconds. Each mass spectrum could possibly contain as many as several dozen mass peaks, some of them very closely spaced in time. Since the height of each

peak needs to be measured accurately, the data recording problem is formidable. Several previous approaches to this problem will be reviewed briefly.

Recording on to Moving Film

This method (1,6) photographs the mass spectra from the oscilloscope tube face on to moving film in a rotating drum camera. Workers have had serious difficulty with inadequate light intensity and with image blurring due to glow persistence of the cathode ray tube phosphor. Nevertheless, with suitable equipment a large number of mass spectra can be successfully recorded in a time-resolved sequence. A disadvantage is that specialized equipment is needed. In addition to the rotating drum camera, an expensive oscilloscope with very large accelerating potential is needed for best results. At the higher repetition frequencies, the difficulties mentioned above are accentuated. Additional problems are encountered with the dead time of the oscilloscope time base, which may need modification to allow sufficiently rapid triggering. Also, to obtain sufficient spacing on the film between spectra at the highest frequencies, a rotating mirror camera is likely to be needed. This will probably result in a restricted working time and may cause synchronization problems.

Z-axis Modulation

This method (7) enables oscilloscope display of the time variation of the amplitude of the mass peak at one single mass number, using a relatively slow sweep of the time base. This trace can be photographed on to stationary film using standard equipment and techniques. Additional masses can be observed by adding an extra oscilloscope and modulation unit for each mass. A major disadvantage is that for systems containing a large number of mass spectral peaks, much of the data is necessarily lost. Unless very many experiments are made, to cover all conceivable mass peaks under all experimental conditions, unsuspected effects may be missed in any reaction. Moreover experience has shown (11) that on arrival of the shock wave, mass spectrum peak shapes may be changed and the peaks may even be shifted slightly along the base line. These effects could cause serious errors in interpretation, especially because their occurrence is not readily discerned on the z-axis modulation records.

A modification of this method feeds the whole mass spectrum signal to modulate the z-axis, at the same time using a fast repetitive horizontal time base sweep and a relatively slow vertical single sweep (8,9). Mass spectrum peaks are recorded as bright dots on the horizontal lines, while the vertical dimension becomes a time axis. This method would be useful to survey the processes occurring in a reaction, but quantitative work requiring measurement of spectrum peak heights is probably not feasible.

The method described below eliminates the difficulties mentioned above. Moreover, apart from some fairly straightforward counting circuitry which

would need to be built, it uses standard wideband oscilloscopes and power supplies which will be available in most laboratories. The system is based on one developed at Harvard (10,11) but has important advantages of its own and differs very considerably from the earlier system, so that a separate description appears desirable.

SUMMARY OF PRESENT METHOD

Our equipment uses a shock tube linked to a Bendix type 12 mass spectrometer operating at 10 to 100 kc/s, whose output is displayed on Tektronix 543B oscilloscopes with 1A2 twin channel plug-ins. This type of oscilloscope has a 6 x 10 cm screen and 33 mc bandwidth and has been found very suitable. Data are photographed using standard oscilloscope cameras and Polaroid film.

Two sets of signals from the mass spectrometer are used, (a) trigger pulses occurring once every cycle of the spectrometer (henceforward referred to as "spectrometer pulses") and (b) the mass spectrum itself.

The mass spectrometer runs continuously but data are only recorded for a few hundred microseconds following arrival of the shock wave. The mass spectrum signal is fed simultaneously into all the vertical inputs of the display oscilloscopes. A signal from the shock wave starts the sequence of events. The first oscilloscope then displays in succession a predetermined number of mass spectra, each one displaced vertically above the previous one. The action is then switched to the second oscilloscope, and so on down the line. Records obtained in this way are shown in Figure 1. The waveforms needed to perform these functions are produced by electronic circuitry described below.

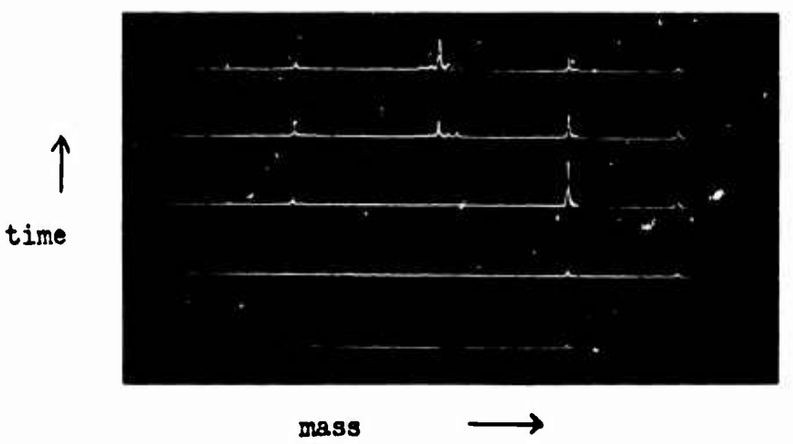


Figure 1. Reaction profile, showing arrival of shock and subsequent reaction resulting in decrease of mass-peaks 15, 43, 58 but increase in the product peaks 28, 29, 30.

Refinements to this system include a z-axis brightening amplifier which considerably improves the records, and a timing display which shows not only the movement of the shock wave but also each triggering of the oscilloscopes. In this way, the chemical reaction time scale can be defined with considerable accuracy.

DESCRIPTION OF APPARATUS

Initial Triggering

The sequence is started by a pulse from a shock tube velocity gauge, suitably delayed. We use the "B" time base of a Tektronix 535A oscilloscope as a precisely adjustable variable delay. (A simple modification enables this time base to be used independently, without affecting use of the rest of the oscilloscope for a normal display).

Counting Registers

The function of these units is to count and gate the spectrometer pulses. This is done using transistorized computer circuits described in reference (12). These are designed to operate reliably at counting rates up to 150 kc/s, so that the present system is well within their capacity. The terminology used in the description below is taken from reference (13).

Two counting registers are used, as shown schematically in Figure 2. Each register consists of a number of binary circuits arranged in modified T connection. The binaries are identical with PSC 9 of reference (12) except that in most cases only two of the diode inputs have been built, one on each side.

The number of binaries in the upper register in Figure 2 is made equal to the largest number of mass spectra that might need to be displayed on a single oscilloscope. The number of binaries in the lower register is equal to the maximum number of oscilloscopes that might be used. The maximum total number of mass spectra that can be recorded is thus equal to the product of the number of binaries in the upper register times the number in the lower register. The number recorded can of course be less than this and is easily selected by a switch.

The sequence begins with all the binaries in the "1" state, i.e. with X outputs at -6 volts. (To make certain that the binaries settle into this state when first turned on, a "set" control is provided.) Spectrometer pulses are fed continuously as serial shift pulses into the diode gates of the upper register. The $\bar{X}$ output of one of the upper register binaries is selected by S1 to be fed as a serial shift pulse into the diode gates of the lower register.

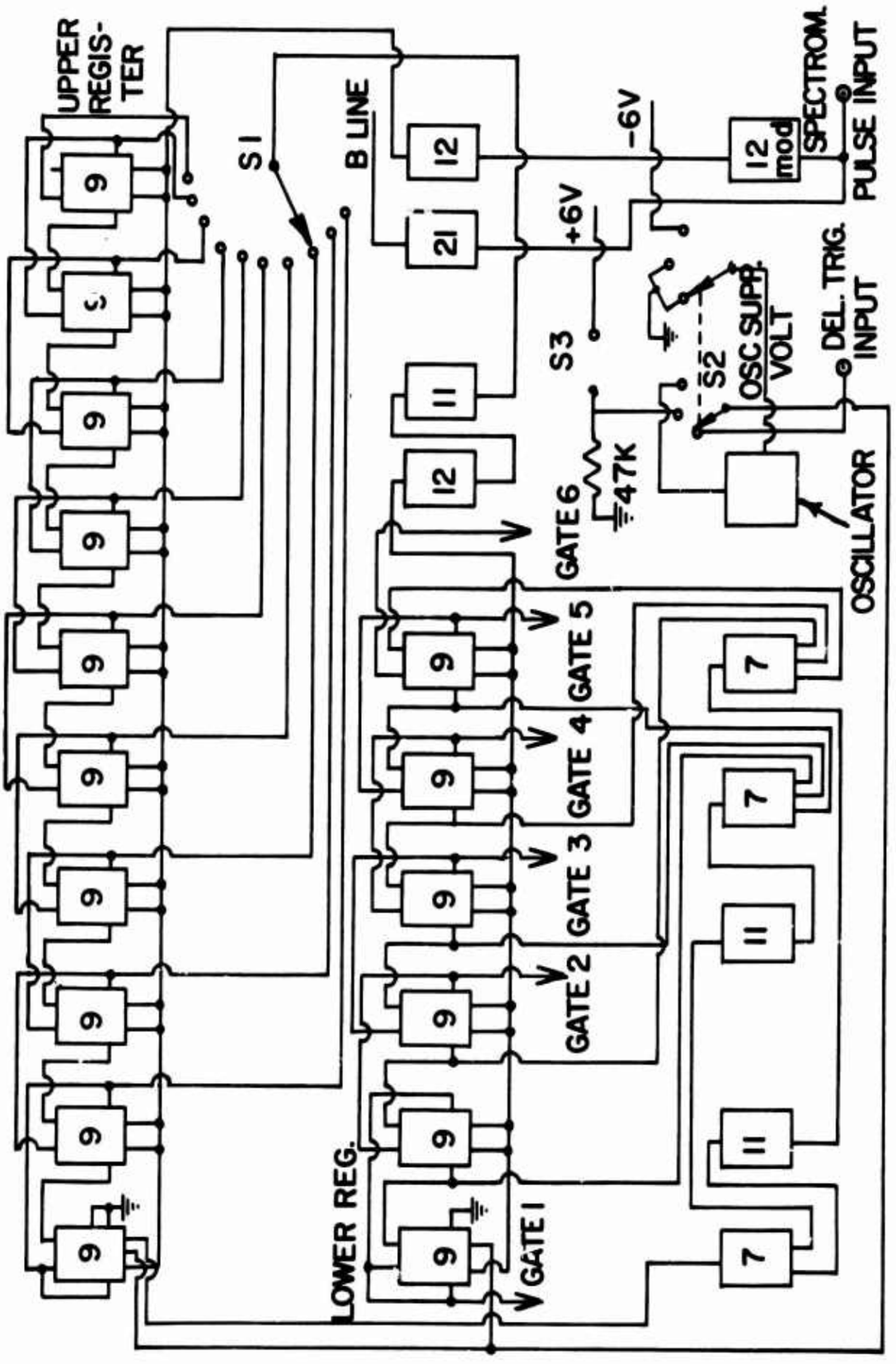


FIG. 2. COUNTING REGISTER

Full details of operations of these shift registers will be found in reference (12). Only a brief account will be given here. Suppose that at the start of operations switch S1 is in position 3. This implies that 3 spectra are to be displayed on each oscilloscope.

The registers will remain indefinitely with their binaries in the "1" state until arrival of the trigger pulse from a shock velocity gauge. This shock wave pulse is fed as a shift pulse into the first binary of each register, thus shifting these two binaries to the "0" state. The first binary in the lower register remains in this state for a period while the upper register is counting. However the first binary of the upper register is turned back to the "1" state on arrival of the next spectrometer pulse. Because of the way in which the outputs and gates are interconnected, the second upper binary is simultaneously changed to the "0" state. After an interval a second spectrometer pulse arrives. This does not affect the first upper binary, but the second upper binary is turned to "1" and the third to "0". Similarly, a third spectrometer pulse changes the third binary to "1" and the fourth to "0".

The important result of this is that on the third spectrometer pulse after arrival of the shock wave pulse (and not before), the $\overline{X}$ output of the third upper binary has changed from -6 volts to 0 volts, i.e. has produced a positive-going step. This step is taken off at the switch, amplified and inverted twice and then fed as a serial shift pulse to the lower register. The first binary of the lower register is thereby returned to the "1" state; the second binary of this register simultaneously changes to "0". The X output of the first lower binary has now produced a positive-going square wave which lasted from the arrival of the initial trigger pulse until after three spectrometer pulses had been counted.

It is now necessary to restart the counting operation of the upper register. This is done by combining the $\overline{X}$ outputs of the lower binaries by means of "or" gates and inverters (PSC 7 and PSC 11 of reference (12) and feeding them back as shift pulses to the first upper binary. Thus each time a lower binary changes, a pulse is fed through to start the upper register counting again.

The X output of the first lower binary is called "Gate 1" and can now be used to gate the first group of three spectrometer pulses, so that they can be fed to trigger the oscilloscope no. 1. The second lower binary serves the same purpose for oscilloscope no. 2, and so on.

Each time the counting register system is triggered, it runs through the complete sequence and produces a gating waveform for each oscilloscope once only. It then remains inactive until externally triggered again.

Gating of Oscilloscope Trigger Pulses

In order to gate the spectrometer pulses to use them to trigger an oscilloscope, they are combined with a gating waveform from a lower register binary (see Figures 2 and 4). Combination occurs in a gate circuit which is a modification of PSC 8 of reference (12), as shown in Figures 4 and 10. The output, after inversion in a circuit PSC 7, is fed to the external trigger input of the relevant oscilloscope.

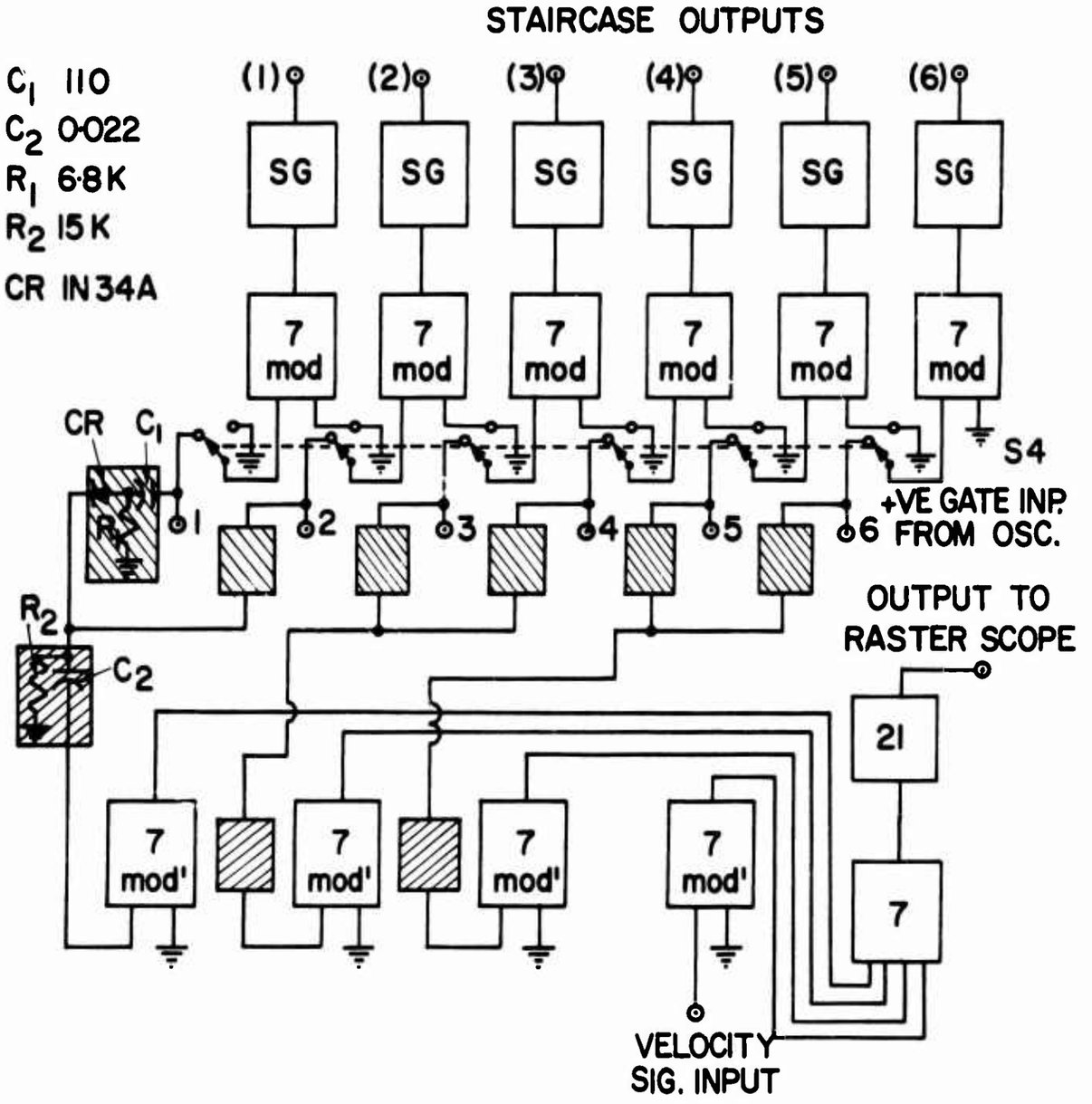
Staircase Generator

This circuit produces a waveform consisting of a succession of voltage steps, which are then fed into one channel of the oscilloscope preamplifier and added to the vertical signal. The steps are so arranged that they deflect the oscilloscope beam vertically upwards between each sweep. The amount of deflection is adjusted at the oscilloscope. The circuit, shown in Figures 3 and 12, uses the positive-going square wave produced by the oscilloscope time base, which is available on the oscilloscope front panel. This square wave is differentiated, and the pulse which comes from its trailing edge is converted into a step change in voltage.

Z-axis Brightening Amplifier

A problem with this type of oscilloscope display is that it consists of very narrow pulses (e.g. 20 nsec) on a relatively slow time base sweep (typically 0.5 or 1.0 usec per cm). If the cathode ray tube beam intensity is turned up high enough for the taller pulses to be clearly visible, then the base line becomes heavily over-exposed, and small peaks may be lost. This effect restricts the available dynamic range. The records can be considerably improved by amplifying part of the mass spectrum signal and applying it as a negative voltage to the c.r.t. cathode (8,9). This selectively brightens the large mass peaks and enables the base line intensity to be greatly reduced. The method is shown schematically in Figure 5. Note that a delay must be inserted into the system to compensate for that caused by the delay line in the oscilloscope vertical amplifier. We have found that a coil of ordinary coaxial cable is a convenient, cheap and easily adjusted delay. It must of course be fed from a low enough impedance to enable it to be properly terminated without too great losses. Where several oscilloscope cathodes are fed from one amplifier, care is needed to measure and adjust for the individual oscilloscope delays. If necessary, the lengths of cable between final amplifier and c.r.t. cathodes can be varied to compensate.

The considerable improvement that can be made in this way is illustrated in Figure 6.



STAIRCASE GENERATOR; GATES FOR ADDING OSCILLOSCOPE TRIGGER PULSES AND SHOCK VELOCITY SIGNALS

FIG. 3.

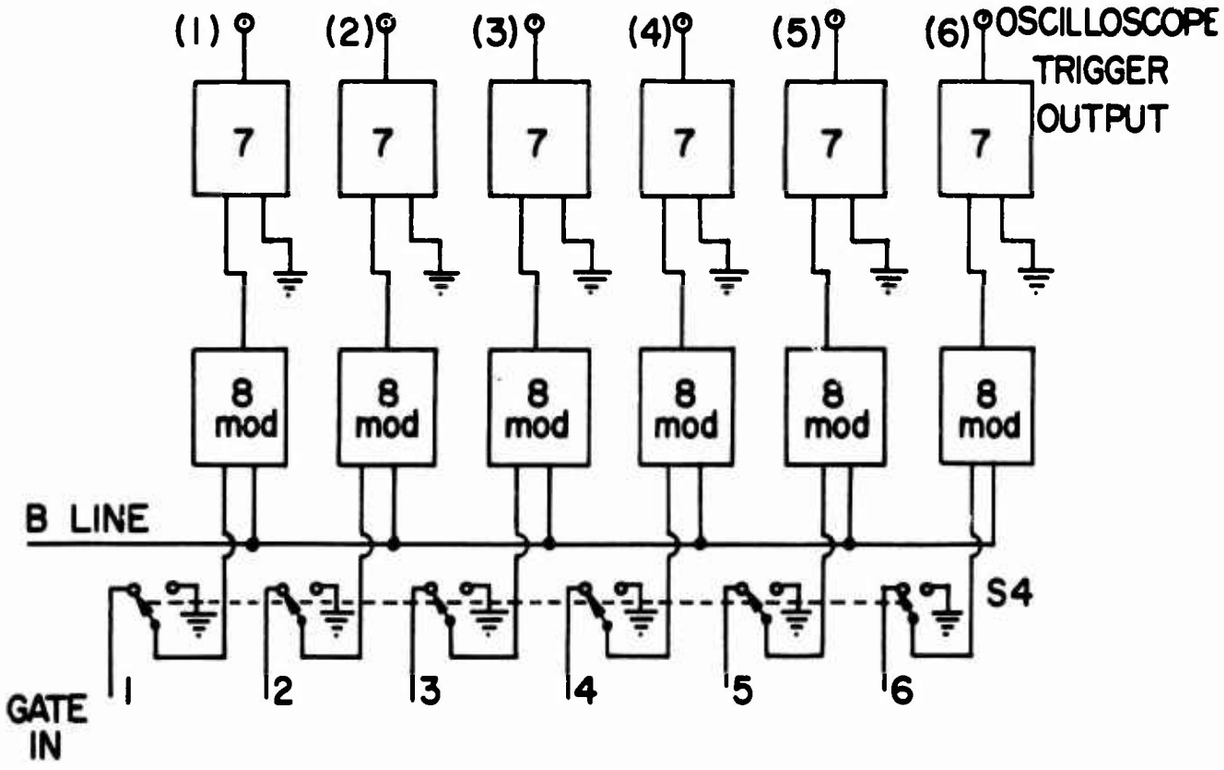
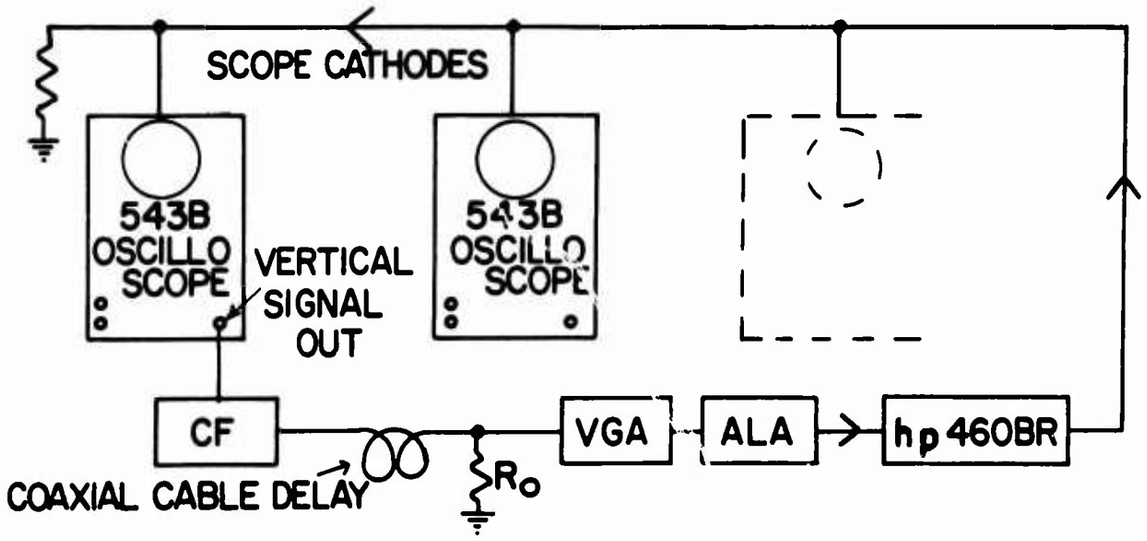


FIG. 4. GATING OF OSCILLOSCOPE TRIGGER PULSES



CF = cathode follower; VGA = variable gain amplifier;
ALA = adjustable limiting amplifier;
hp 460BR = Hewlett-Packard type 460BR wideband amplifier

FIG. 5. Z-AXIS PULSE BRIGHTENING SYSTEM.

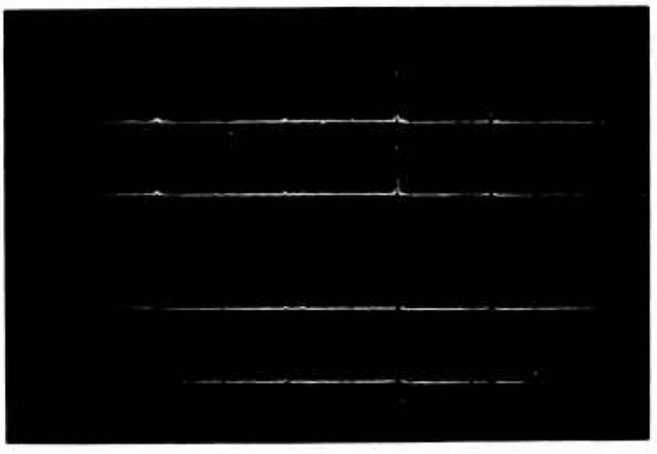


Figure 6. Comparison of mass spectral traces, with and without z-axis brightening.

Display of Oscilloscope Trigger and Shock Velocity Signals

The signals from the shock tube velocity gauges are added together, combined with signals which indicate the triggering time of the oscilloscopes and recorded from a c.r.t. raster display. The raster is produced by a Radionics TWM-2A timing generator* and Tektronix 535A oscilloscope. The system, which is shown schematically in Figure 4, enables the time of triggering of the oscilloscopes (and hence of the mass spectrometer) to be measured accurately, relative to the motion of the shock wave. It thus allows the reaction time coordinate to be established with precision, as well as measuring the shock wave velocity (compare Figure 7).

Additional Details and Construction Problems

A small astable multivibrator, adapted from reference (14), and operating at about 2 c/s is incorporated. This is found very useful for triggering the registers repetitively during adjustment and focusing of the oscilloscopes. A higher frequency trigger is not advisable, as it might not give sufficient time for all the voltages (especially those on the staircase generator) to decay between scans. The system has a manual trigger for one shot tests. In addition, switch S4 enables the spectrum to be displayed repetitively without vertical deflection, for ordinary visual observation.

The precautions mentioned in reference (12), especially on page 7-6 there, should be very carefully observed during the construction. The use

*Radionics Inc., 76 Cambridge Street, Burlington, Mass.

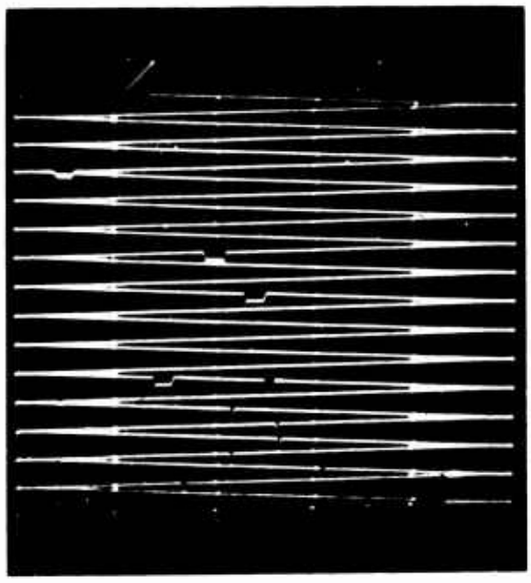


Figure 7. Raster oscilloscope trace showing 10 microsecond time markers (dots), velocity gauge signals (square pulses) and signals indicating the time of each triggering of the display oscilloscopes (sharp pulses).

of heavy power and ground leads is especially advisable. Otherwise, stray signals from the counting circuits can cause interference with the mass spectrum signals. The staircase generators need to be decoupled with particular care, since their outputs are fed directly to the oscilloscope inputs.

Non-standard circuits used by us are shown in Figures 8 to 12. The remaining circuits are taken from reference (12), and are indicated in Figures 2 to 4 by their "PSC" numbers in that reference.

PERFORMANCE

This system gives very good results and has now been in trouble-free operation for one year. It is very easy to operate. Only one switch has to be turned to alter the number of mass spectra to be displayed. Setting up is very simple when the internal oscillator is used.

Occasionally the first oscilloscope is found to have recorded one spectrum more or less than the selected number. This occurs because of a near-coincidence between the initial trigger and a spectrometer pulse. We have not found that this creates any particular difficulty when it happens, especially since it cannot occur with any oscilloscope except the first.

One limitation of any system which requires frequent re-triggering of an oscilloscope lies in the dead time of the oscilloscope time base. A finite time must elapse between the end of one sweep and the beginning of the next, in order for voltages to decay sufficiently. Our present oscilloscopes require a minimum of about 5 microseconds between sweeps at the fastest sweep speeds. At 100 kc/s, this means that at most one-half of the time duration of a mass spectrum can be displayed. This proportion could be increased somewhat by modifying the time base circuit, with however a risk of some loss in sweep linearity. In practice this inability to display for more than half the time has not been a serious limitation for our experiments. However we wish to point out that a fairly small modification of the present system would enable the whole of each mass spectrum to be recorded on every sweep. A small rearrangement of the connections in the two counting registers is required. The output of upper register binary no. 1 would then be used to trigger oscilloscope no. 1, upper no. 2 would trigger oscilloscope no. 2 and so on. As an illustration, suppose that 4 oscilloscopes were used. The first oscilloscope would then display the 1st, 5th, 9th, etc. spectra, the second oscilloscope would display the 2nd, 6th, 10th, etc., and so on. The number of binaries in operation in the lower register would then be determined by the number of spectra to be displayed per oscilloscope, rather than by the number of oscilloscopes, as at present. The present oscilloscope trigger gate circuits would not be needed. One possible difficulty is variation in turn-on time from one binary to another, but this could probably be overcome by matching of transistors if it proved a problem.

ACKNOWLEDGMENTS

This work has been generously supported by the National Research Council of Canada, by Imperial Oil Limited and by the Advisory Committee on Scientific Research of the University of Toronto. S. C. B. thanks the National Research Council for a Studentship and M. D. V. thanks the Government of the Province of Ontario for a Graduate Fellowship. We also wish to express our indebtedness to Drs. J. V. Michael and D. McL. Moulton for helpful discussions and for freely making available to us details of their own work on this problem.

REFERENCES

(1) Kistiakowsky, G. B., Kydd, P. H., J. Amer. Chem. Soc. 79, 4825 (1957)

(2) Bradley, J. N., Kistiakowsky, G. B., J. Chem. Physics 35, 256, 264 (1961)

(3) Wiley, W. C., McLaren, I. H., Rev. Sci. Instr. 26, 1150 (1955)

(4) Harrington, D. B. in (Waldron, J. D., ed.) Advances in Mass Spectrometry, 249, Pergamon Press, London (1959)

(5) Diesen, R. W., Felmlee, W. J., J. Chem. Physics 39, 2115 (1963)

(6) Meyer, R. T., Rev. Sci. Instr. 35, 1064 (1964)

(7) Damoth, D. C., ASTM meeting on Mass Spectrometry, Atlantic City, New Jersey (1960)

(8) Kendall, B. R. F., J. Sci. Instr. 39, 267 (1962)

(9) Lincoln, K. A., Rev. Sci. Instr. 35, 1688 (1964)

(10) Moulton, D. McL., Michael, J. V., Rev. Sci. Instr. 36, 226 (1965)

(11) Dove, J. E., Moulton, D. McL., Proc. Roy. Soc. (London) A283, 216 (1965)

(12) NAVWEPS 16-1-519-2, Handbook Preferred Circuits Navy Aeronautical Electronic Equipment, Volume II, Semiconductor Device Circuits, National Bureau of Standards, Washington, D. C. (1962)

(13) Phister, M., Logical Design of Digital Computers, Wiley, New York (1958)

(14) Schwartz, S., ed., Selected Semiconductor Circuits Handbook, Wiley, New York (1961), p. 6-48

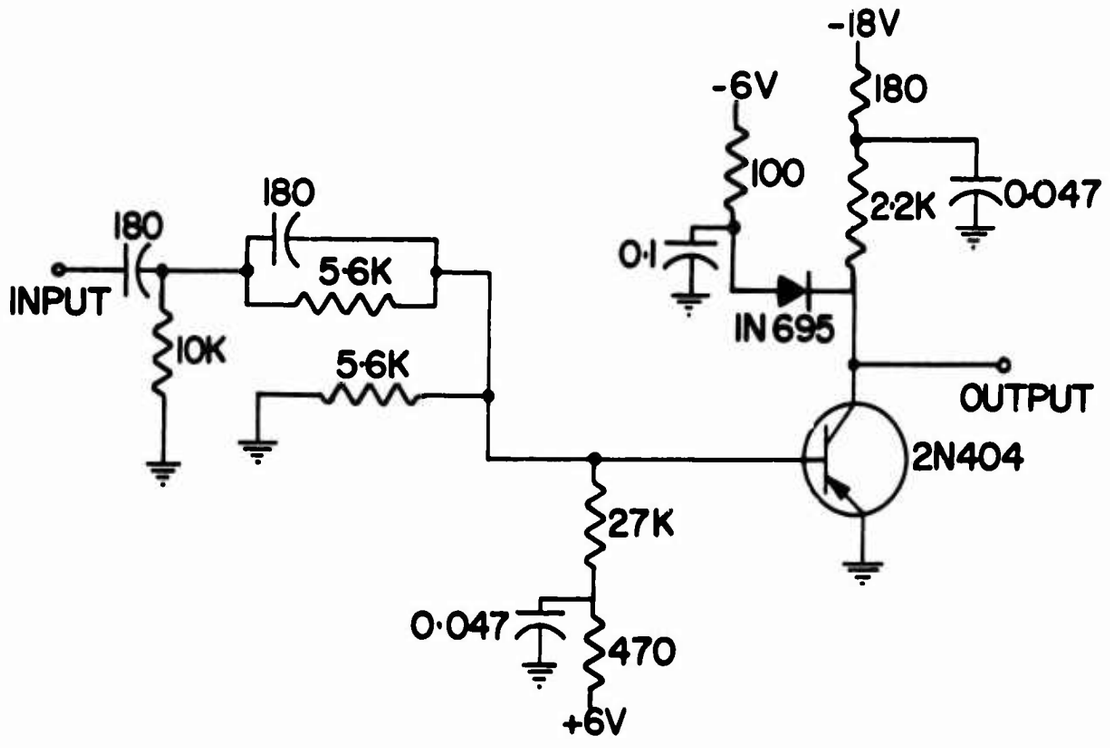


FIG. 8. PSC 7 (mod)

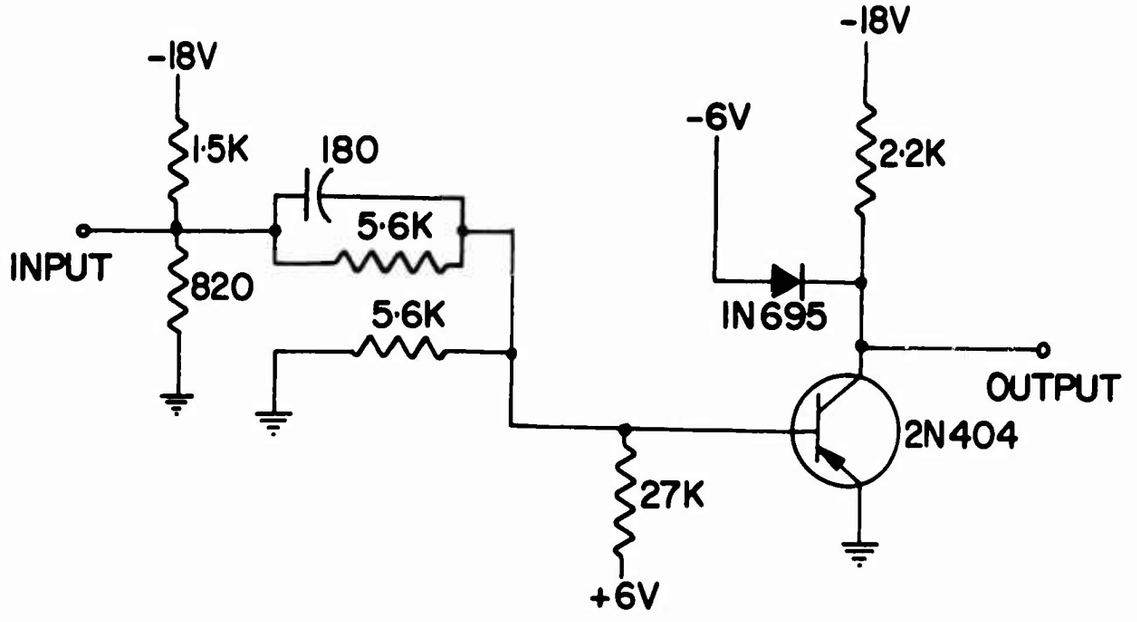


FIG. 9. PSC 7 (mod')

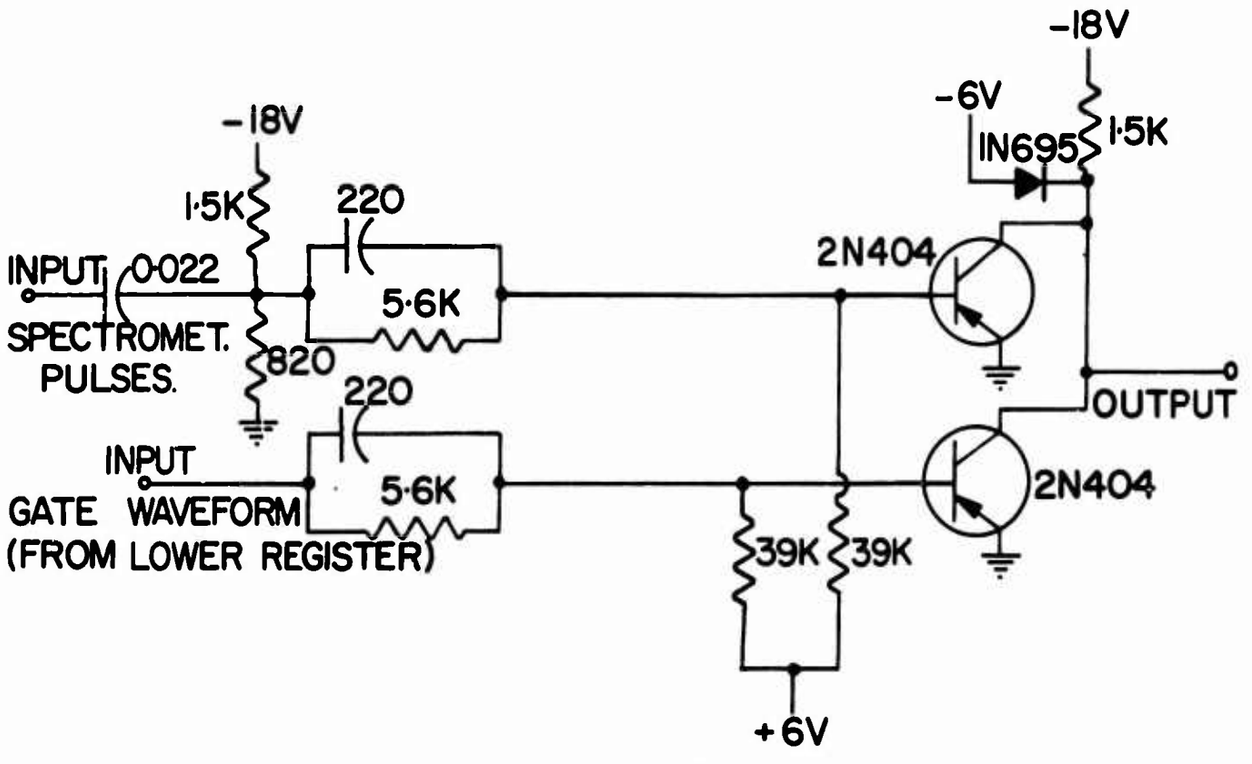


FIG. 10. PSC 8 (mod) "AND" GATE

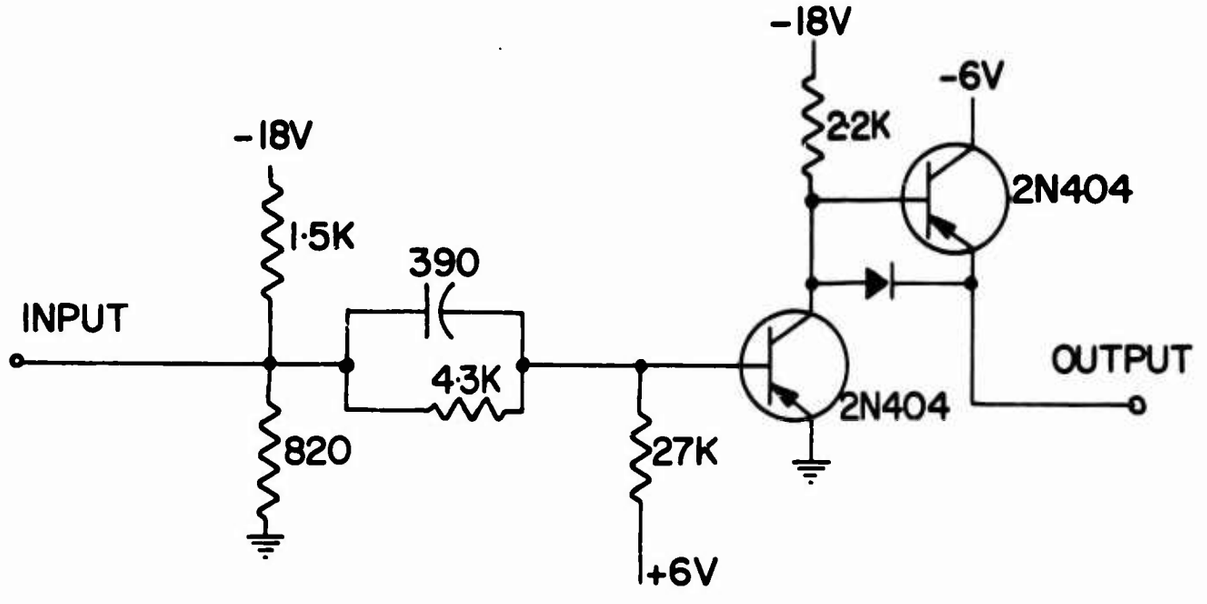


FIG. 11. PSC12(mod) PULSE POWER AMPLIFIER

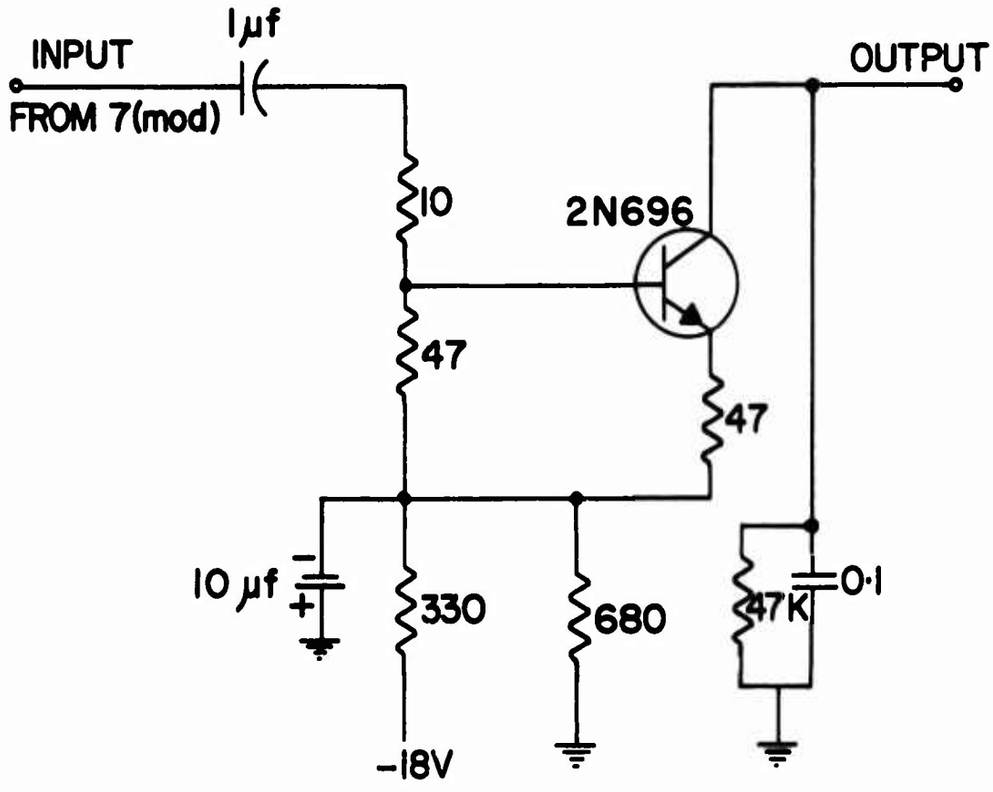


FIG. 12. STAIRCASE GENERATOR

SOLID PROPELLANT AS A SHOCK TUBE DRIVER

J. F. Melichar
Ballistic Research Laboratories
Aberdeen Proving Ground, Maryland

A high-energy driver gas source is needed to drive high Mach number shock waves into atmospheric air. The most common method uses the detonation or combustion of gases to provide the high-energy gases. The criterion of producing high internal energy gas is also met by solid propellants. This paper discusses an investigation of the usefulness of solid propellant as a shock tube driver.

Upon ignition a solid propellant evolves gas at a rate controlled by its surface temperature and pressure, composition and geometric configuration. The chemical transformation of the propellant from solid to gaseous state is an exothermic controlled process producing a stable homogenous gas. The thermodynamic state of that gas is dependent on the ratio of the propellant charge weight to the chamber volume.

The propellant was burned in the shock tube compression chamber. The gaseous combustion products increased the chamber pressure until the diaphragm ruptured forming a shock and rarefaction wave system. As the shock wave was driven down the tube the rarefaction wave traveled over any unexpended propellant, reducing its surface pressure and, consequently, the amount of gas evolving. The result was a discrete slug of hot high-pressure gas driving the shock wave.

One set of criteria for selecting a driver propellant was that the combustion products have a high internal energy, a large ratio of heats (k), and be capable of burning stably at pressures from 1,000 to 30,000 psi. A second requirement was that the propellant burn rapidly enough to reduce energy losses due to heat transfer. In establishing rapid burning it was hoped demands on diaphragms might also be reduced. The requirement for a large value of (k) was eliminated since it is approximately constant for the combustion products of all the propellants considered. M9 mortar propellant, in a thin flake, was determined to most nearly meet the remainder of the requirements.

The computed thermodynamic properties (1) of the M9 propellant were used to predict the driven shock wave strengths. The calculations showed a useful range of chamber pressures from 500 to 10,000 psi. As 10,000 psi was approached the driven shock strength did not increase relative to the chamber pressure. The decreased efficiency reduced the previously structurally attractive driver pressure to driven shock strength ratio.

An experiment was carried out in a 2 inch inside diameter shock tube with a compression and expansion chamber length of 9 and 21 tube diameters respectively. The structural strength of the tube limited the maximum experimental chamber pressure to 5,000 psi. This chamber pressure range was calculated to be able to drive shock waves with shock Mach numbers between 3 and 6 into atmospheric air.

The propellant was placed in the compression chamber in a plastic bag. A vented type electrical squib was placed into the charge, and connected through a firing circuit to a thyratron discharge of a short 300 volt pulse. The squib, upon closing of the circuit, ignited the propellant immediately surrounding it. The combustion products from the burning propellant expanded igniting the remaining propellant.

Unscored copper and aluminum diaphragms were used in the experimental program. The diaphragms were selected to burst below the maximum pressure that could be attained if the propellant were completely burned in a closed chamber. The diaphragms were bolted between flanges, with annular gripping rings on their faces.

The compression chamber pressure was monitored by a Kistler quartz piezo-electric transducer. The "side-on" and reflected driven shock wave pressures were monitored by BRL tourmaline piezo-electric bar gages. The gage outputs were fed to oscilloscopes through 100 kc Kistler charge amplifiers. A time-of-arrival system was used to determine the shock wave velocity.

RESULTS

The experimental shock strengths were near predicted values, as illustrated by Figure 1. The predicted curve is slightly higher than that experimentally derived. The lower curve is for a cold helium driver and provides a comparison to a common driver gas.

Figure 2 exhibits several monitored shock wave profiles, while in Figure 3 two compression chamber pressure-time histories are illustrated.

DISCUSSION OF RESULTS

The compression chamber pressure-time histories indicate a smooth compression occurred prior to diaphragm removal. This gradual increase produced a stable homogeneous driver gas resulting in the driven shock wave having a smooth classical step profile. The small amount of noise monitored on the shock wave profiles was attributed to a combination of structural noise transmitted to the gages, gage characteristics, and mixing of the driver and driven gages.

The propellant burned slowly up to 500 psi, then the burning accelerated to a more rapid rate. With the increase of mass evolution of gas, the pressure similarly increased more rapidly. Beginning at about 1,300 psi the rate of pressure increase exceeded 1,000 psi per millisecond. This rate, though rapid, was not fast enough to eliminate the need for a diaphragm.

As the chamber pressures and the rate of chamber filling increased, the diaphragms began to burst above their static strengths. The ability of the diaphragm to respond was being exceeded by the increase of the chamber pressure. With higher operating pressures, and correspondingly higher burning rates, the overshoot of the diaphragm's static bursting strength became increasingly greater.

In the experiment described a 0.007 inch thick propellant flake was used. The thickness limited the burning rate, since the surface area per unit volume was fixed. In subsequent experiments, in another 2" diameter shock tube, a 0.003 inch thick flake increased the burning rate two fold. The effect on the bursting of the diaphragm was more pronounced. For chamber pressures of 4,000 to 4,400 psi the final rate of pressure increase was 1,900 psi per millisecond, and the diaphragm thickness appeared to exert very little control on the driven shock strength. For example, 0.042, 0.048 and 0.064 inch thick copper diaphragms all released driven shock strengths within a 5% band.

The value of the effective diaphragm strengthening is two-fold. It allows the use of a lighter diaphragm, reducing opening times and thus formation distances. Secondly in the high pressure regions, where the effect is most pronounced, it allows the use of thin diaphragms rather than milled plates to separate the compression and expansion chambers.

The relationship of the M9 driver chamber pressure to the driven shock wave Mach number is presented in Figure 1. The predictions were calculated from thermodynamic properties of the gaseous combustion products extrapolated from the data calculated by Baer and Bryson (1) for loading densities above 0.05 grams per cc. The computer program used by them has since been updated, and has been rerun to include loading densities below 0.05 grams per cc. Preliminary results (2) indicate the previous data, including the extrapolations, had values of internal energy, pressure and temperature, for a given loading density, in the range of 3 to 4 percent high.

The variation of driven shock parameters from predicted, approximately 1.5% in shock Mach number between 4.5 and 5.7, cannot be completely attributed to the small error in the thermodynamic properties. The prediction used the real gas properties in the anisentropic, ideal model, driver equation (3). White (4) has illustrated the existance of higher than predicted shock strengths for large diaphragm pressure ratios based on an isentropic formation-from-compression model. In the formation-from-compression model the shock forms in seven to ten diameters, but then accelerates. The distance and magnitude of the acceleration is determined by the gases involved, their thermodynamic properties, the diaphragm pressure ratio, and the diaphragm opening-time.

White's opening-time model indicated the shock waves driven by the lower diaphragm pressure ratios probably approached their maximum strength in 21 tube diameters; but, as the shock strengths and the diaphragm pressure ratios increased, the shock waves should still have been accelerating at the end of the shock tube. In relation to the predicted strength, the accelerating shock waves would not have reached their predicted strength at the point of measurement. In that the predicted error is slight, it is concluded the prediction technique is adequate, though not exact.

The wave system in the shock tube is represented in the wave diagram of Figure 4. The contact surface and shock wave did not separate rapidly for the test shock strengths; for example, for a shock Mach number of 5.67 at the end of the shock tube they are but 50 microseconds apart. The short separation distance is responsible for the short testing-time, as the rarefaction system from the diaphragm rupture, in relation to the testing-time, was an order of magnitude in time from reaching the end plate. The reflected incident shock wave interacted with the contact surface reflecting a rarefaction wave which propagated to the end plate to terminate the test period.

During the short test period no effects of the reflected shock-wall boundary layer interaction were visible. The thinness of the boundary layer due to the high density and the short testing-time were responsible for the lack of an observable effect. Had the tube been used open-ended, the contact surface-reflected wave interaction would have been eliminated producing a wave with a flat-top duration of approximately one millisecond.

The strength of the waves resulting from the reflected shock-contact surface interaction were calculated based on existing analytical methods (3),(5). The technique predicted the resulting wave system, i.e., a transmitted shock and a reflected rarefaction wave, but could not accurately predict the strength of the waves. The contact surface and wave interactions were not limited to the one interaction, but continued after the testing period was over with a diminished effect on the pressure signature.

The rarefaction wave from the reflected shock-contact surface interaction in conjunction with the measured testing-time provided a method for determining the position of the contact surface. The algebraic relationship for the position can be written (Equation 1) by considering the wave speeds, the distances and the time increments involved (6):

$$1 - C = \frac{(W_{21} + U_{21})\, a_1\, t_t\, W_{11}\, A_{51}}{(A_{51} + W_{21})\,(W_{11} - U_{21})X} \qquad (1)$$

C is defined as a function of the shock strength and distance (x) from the diaphragm and is presented in Figure 5, (t_t) as the flat top duration presented in Figure 6, (a_1) as the sound speed ahead of the driven shock wave, W_{11} as the ratio of the shock wave velocity (u_s) to a_1, W_{21} as the ratio of the reflected wave speed to a_1, U_{21} as the ratio of the particle velocity behind the shock wave (u_2) to a_1, and A_{51} as the ratio of the reflected sound speed to a_1. The shock parameters were calculated using real gas tables and represent the case of a real gas. The location of the contact surface (x_{cs}) with respect to the diaphragm at any time (t) would be given by Equation 2.

$$x_{cs} = U_2\, t + (U_s - U_2)\, tC \qquad (2)$$

C has been evaluated for the experimental 21 diameter case and should not vary significantly for several diameters. The position $(X_{cs})e$ of the contact surface relative to the diaphragm, when the shock wave strikes the reflecting end plate, is given algebraically by Equation 3.

$$(X_{cs})e = X\left[C + (1-c)\,\frac{U_2}{U_s}\right] \qquad (3)$$

CONCLUDING REMARKS

It was determined that M9 propellant is a suitable driver for a conventional shock tube. The propellant burns smoothly and rapidly producing high energy gaseous combustion products. The pressure-time profiles of the driven shock waves were found to be acceptable, with only a slightly less ideal wave form than that produced by a cold helium driver.

REFERENCES

(1) Baer, P.G., Bryson, K.P., Tables of Computed Thermodynamic Properties of Military Gun Propellants, BRL M 1023, Aberdeen Proving Ground, Maryland, August 1957.

(2) Private communications with R. Geene of the Interior Ballistics Laboratory, Ballistic Research Laboratories, Aberdeen Proving Ground, Maryland.

(3) Glass, I.I., Hall, J.G., Handbook of Supersonic Aerodynamics, Sec.18, Shock Tubes, NAVORD Report 1488 (Vol. 6), 1959.

(4) White, D.R., Influence of Diaphragm Opening Times on Shock Tube Flows, So. of Fluid Mechanics, Vol. 4, p 585, 1958.

(5) McKee, R.M., An experimental Study of the Interaction of a Plane Shock Wave with a Contact Surface, UTIA TN No. 1, University of Toronto, Toronto, Ontario, Canada, Sept. 1954.

(6) Melichar, J.F., Solid Propellant as a Shock Tube Driver, BRL report to be published, Ballistic Research Laboratories, Aberdeen Proving Ground, Maryland.

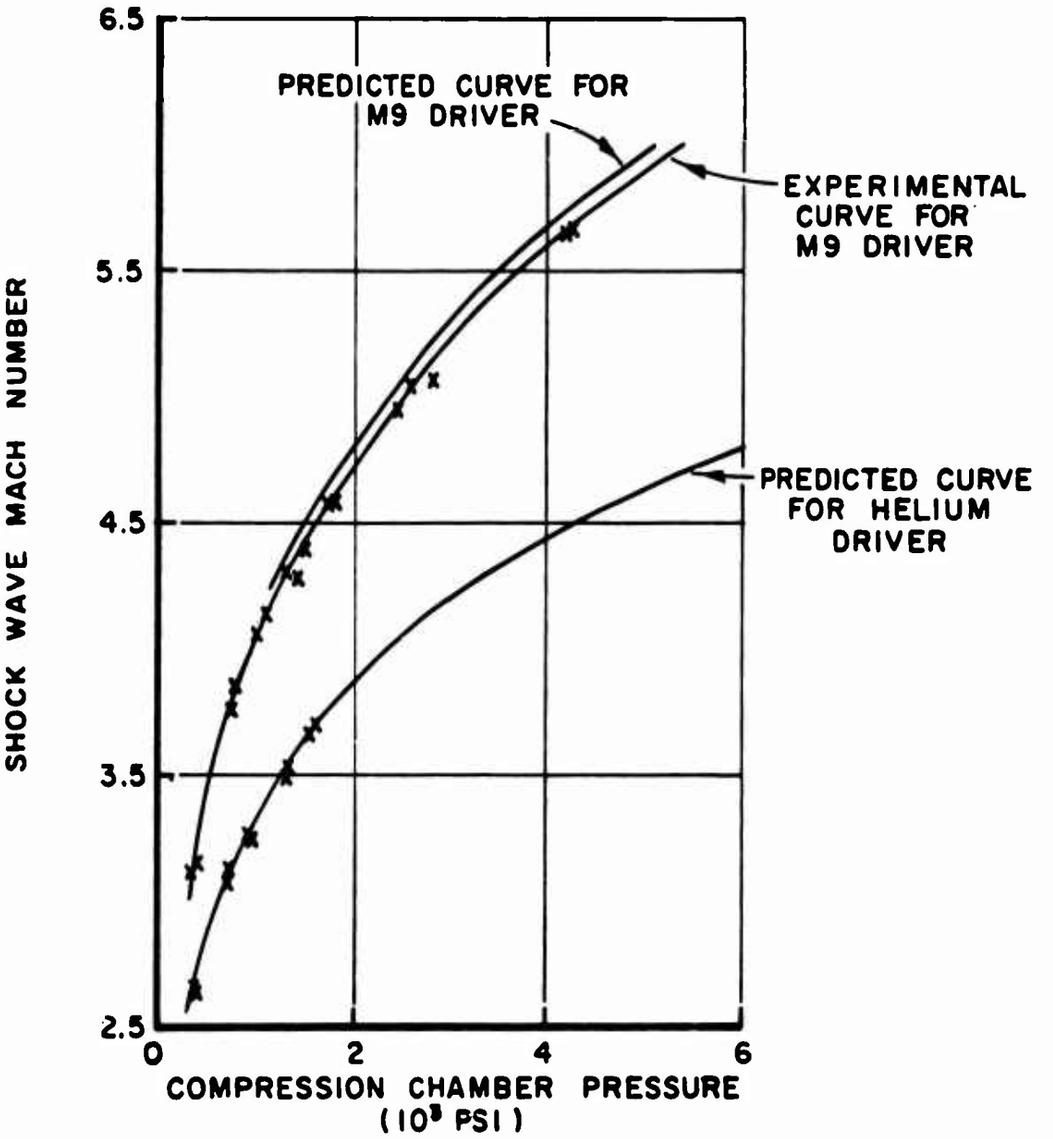
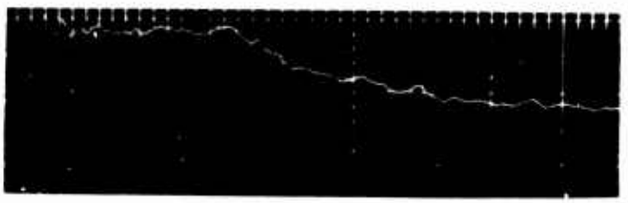


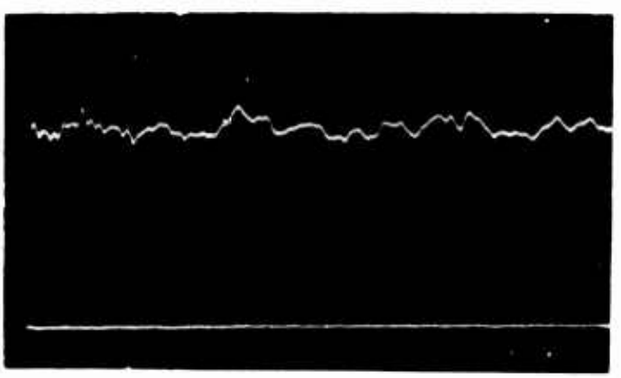
FIGURE 1
DRIVER PRESSURE vs SHOCK WAVE
MACH NUMBER



REFLECTED SHOCK-
PRESSURE SIGNATURE,
1425 PSI, 50 μSEC / DIV



REFLECTED SHOCK-
PRESSURE SIGNATURE,
4160 PSI, 50 μSEC / DIV



"SIDE-ON" SHOCK-
PRESSURE SIGNATURE,
465 PSI, 20 μSEC / DIV

FIGURE 2

"SIDE-ON" AND REFLECTED SHOCK WAVE PROFILES

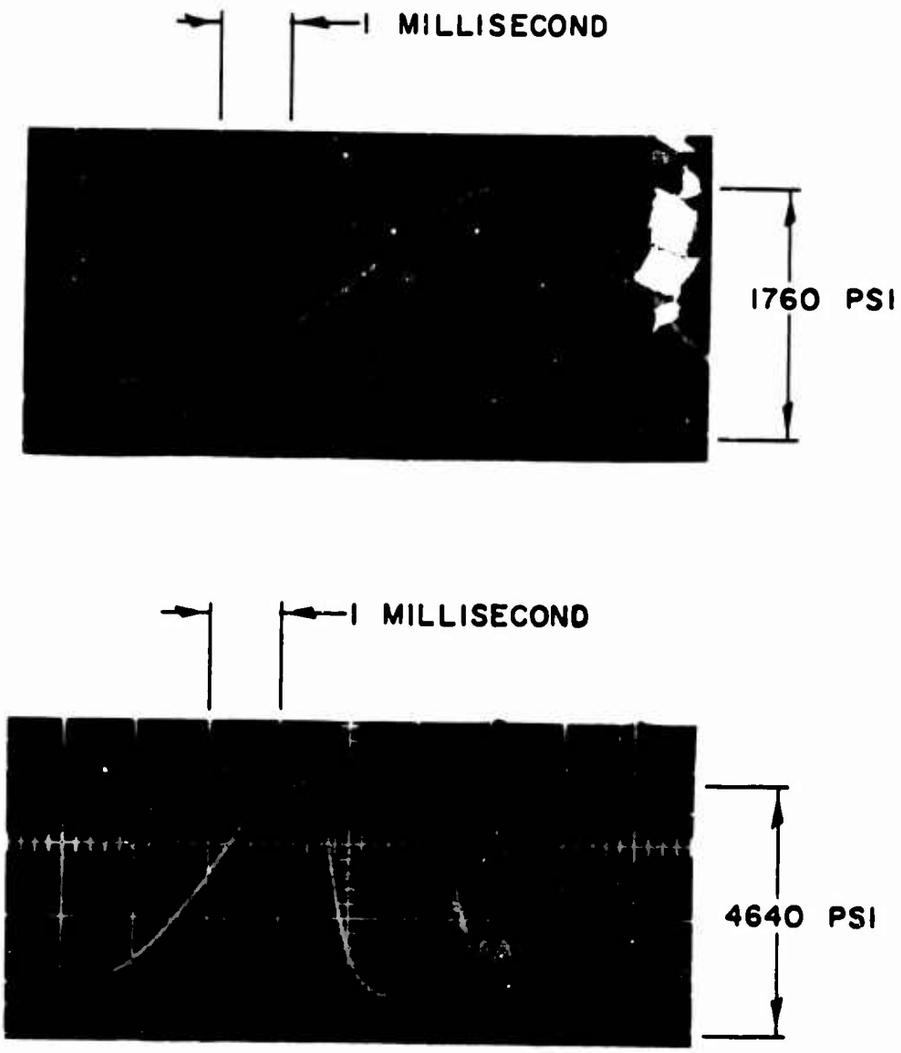


FIGURE 3

COMPRESSION CHAMBER PRESSURE-TIME HISTORIES

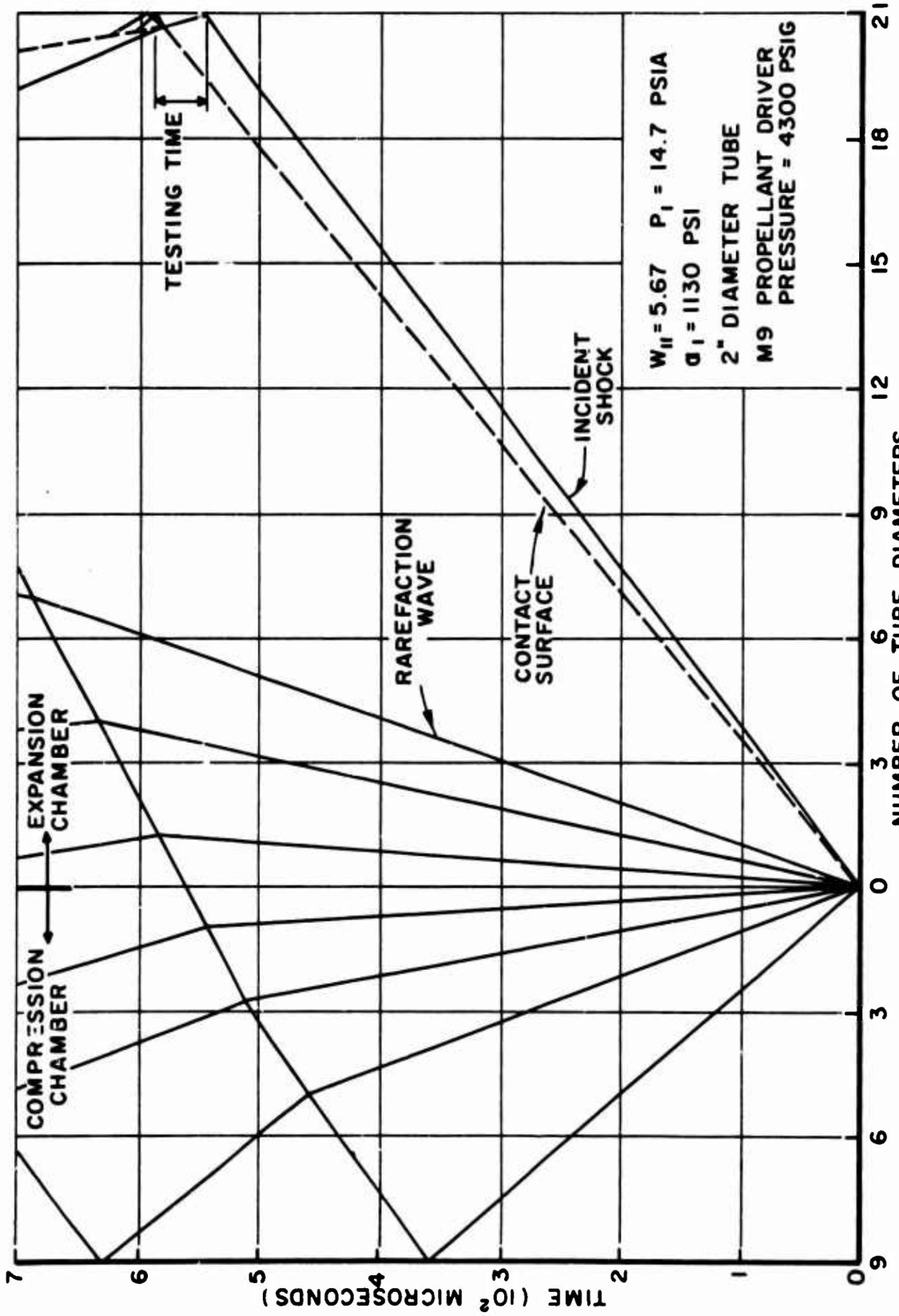


FIGURE 4
WAVE DIAGRAM

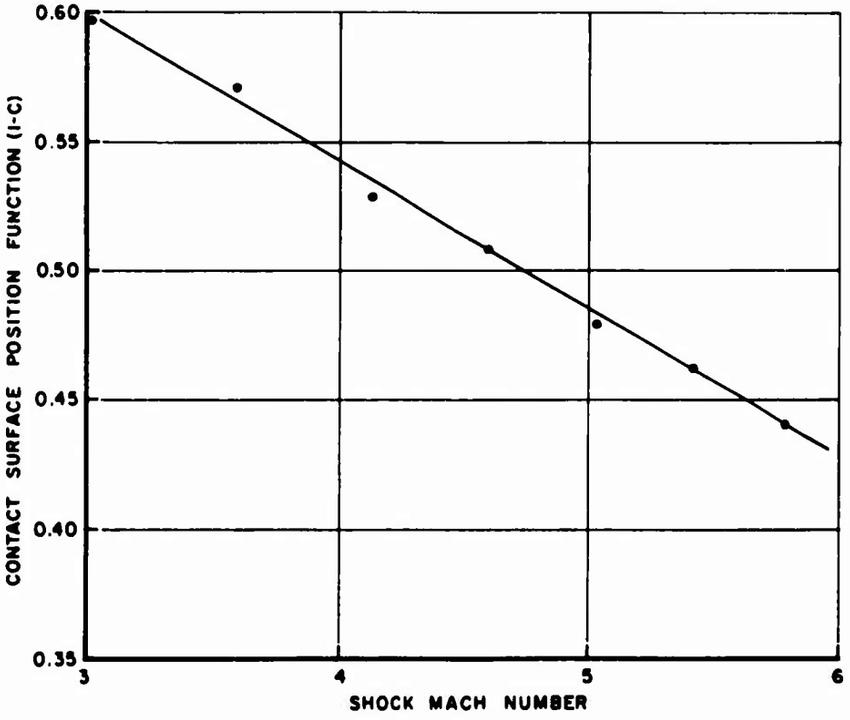


FIGURE 5
CONTACT SURFACE POSITION FUNCTION (1-C)
AS A FUNCTION OF SHOCK MACH NUMBER

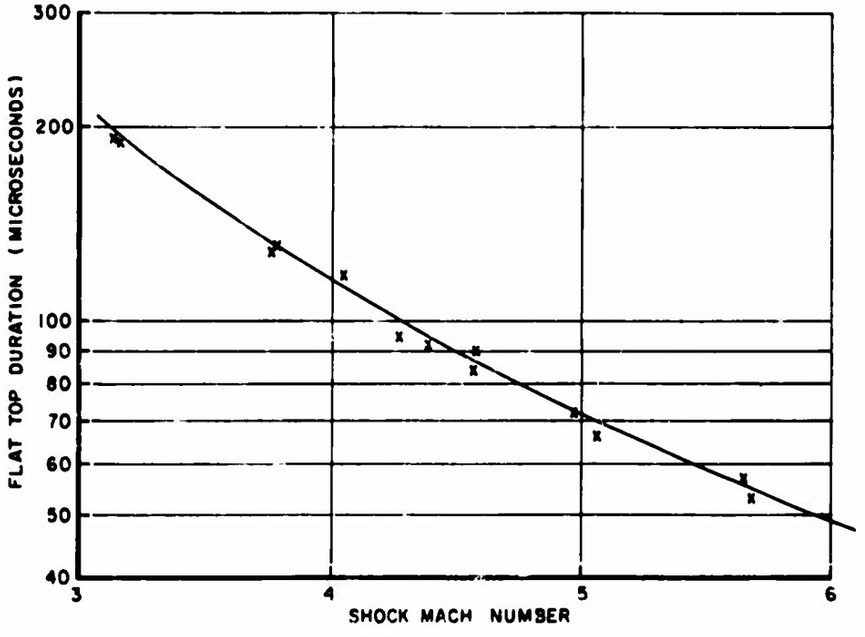


FIGURE 6
DURATION vs SHOCK STRENGTH

BLANK PAGE

A THEORETICAL ANALYSIS OF THE DRIVER-RESERVOIR METHOD OF DRIVING HYPERSONIC SHOCK TUNNELS

Robert F. Flagg
Institute for Aerospace Studies University of Toronto
Toronto, Canada

INTRODUCTION

One limitation to the duration of the steady state reservoir condition of a tailored hypersonic shock tunnel is the arrival of the head of the rarefaction wave which has been reflected from the upstream end of the driver as in Figure 1. This reflected wave, which results from the bursting of the diaphragm, cannot be eliminated directly but can be controlled to advantage. For example, the quasi-steady test time may be increased simply by lengthening the driver to a value such that the reflected rarefaction wave does not arrive at the downstream reflecting surface until after a given period of time. The driver length cannot be extended indefinitely since the limit to the test time may then be determined by the arrival of the tail of the rarefaction wave. The optimum test time for a given geometry occurs when both the head and the tail of the rarefaction arrive simultaneously at the reflecting surface. This point is discussed in detail by Holder and Schultz in reference 1. Further gains in test time can only be obtained by lengthening the overall length of the entire tube while preserving the driver to driven length proportion. This raises the practical problem of space and cost since relatively long sections are required if tunnel test time is to be increased significantly.

Another technique for increasing the tunnel test time is the so-called driver-reservoir technique suggested by Henshall, Teng, and Wood (ref. 2). They demonstrated experimentally that this method can significantly increase the shock tunnel running time. However, the physical model used to explain the results is in error. They suggested that since the closed end of a shock tube reflects a disturbance of the same sense as the incident disturbance, (shocks reflect as shocks and rarefactions reflect as rarefactions) and that an open end reflects a disturbance of the opposite sense (shocks reflect as rarefactions and rarefactions reflect as shocks) that there would exist a partially opened-partially closed configuration that would produce a Mach wave i.e., a vanishingly small disturbance for a given set of initial conditions, analogous to the steady transonic tunnel case. However, it will be

shown subsequently that, in general, a very complex flow containing both steady and unsteady flow regimes is generated and for a unique nozzle area ratio a flow system is possible which contains no downstream running disturbances. Hence the running time of a hypersonic shock tunnel may be increased without recourse to extension of the length of the facility.

SOME BASIC CONSIDERATIONS

The essence of the driver reservoir problem is the interaction of rarefaction wave with a perforated plate separating a constant area duct and a large volume. In ref. 3 the equivalence between a perforated plate or wire grid of a given open to closed area ratio and a nozzle of the same ratio was established. In ref. 4 it was shown from chambered shock tube theory that for cross-section area ratios greater than about 6, the results of an area change are essentially those obtained from an infinite area ratio. Hence, the reservoir can be assumed to be infinite in diameter with little loss in generality. The prototype and the flow system to be analyzed are shown schematically in Fig. 2.

A partial analogy exists between the driver-reservoir case and the case of colliding unsteady expansions. Recall that the solution to the problem of two colliding rarefaction waves can be obtained either by using the method of characteristics in the (x,t)-plane wherein all of the details including the interaction region are laboriously calculated or by applying the simpler (p,u)-plane analysis to predict what final disturbances will emerge from the collision. The latter approach is considerably less involved and yields all of the required information for the resulting quasi-steady states. However, no details of the interaction region can be obtained in this manner. For the (p,u)-plane analysis the appropriate equations are applied to solve the problem "in the large". A discussion of such interaction problems is given in Refs. 5 and 6.

A similar approach can be used in the driver-reservoir flow problem. That is, a solution can be obtained either by analyzing the complex interaction region using the laborious method of characteristics in the (x,t)-plane or by moving away from the interaction region and with the aid of a simpler (p,u)-plane analysis and the appropriate steady and unsteady flow equations, obtaining an analytic algebraic solution for the disturbances that finally emerge from the interaction region.

The type of analysis in effect neglects the effects of secondary interactions of characteristic lines. As shown by Bird (ref. 7) this assumption is valid as long as the wave strengths are not extreme. The neglect of secondary characteristic interactions implies that a definite wave pattern bounding quasi-steady regions finally emerges from the interactions. It will be shown later that the experimental data agrees well with the simplified theoretical approach hence the neglect of secondary disturbances appears to be a reasonable assumption.

EXPANSION PROCESSES

When the diaphragm separating the driver and driven sections opens, the gas in the driver (the term "driver" will be restricted to the region between the diaphragm and the perforated plate) undergoes an unsteady expansion to a new state (3u) Fig. 1, which is fixed by the initial conditions in both driver and driven sections. The gas flowing through the nozzle or perforated plate ultimately undergoes a steady expansion to a condition (3s), which is fixed by the area ratio and is governed by the steady flow relations. Since the physical properties of these two expansions are very different, some "patching" of these two processes is necessary in terms of additional unsteady waves to satisfy the boundary conditions imposed by each flow. It is essentially these "patching" solutions which provide the basis for theory of the driver-reservoir technique.

An isentropic expansion of a perfect gas may be either steady or unsteady. The unsteady isentropic expansion of the driver gas is such that the pressure distribution in the driver (Fig. 1) will be changing with time. For the backward (left) facing rarefaction wave $\overleftarrow{R}$, a quantity P defined by (ref. 5)

$$P = \frac{2}{\gamma - 1} a + u \tag{1}$$

is constant across the unsteady expansion and provides the relation between thermal and directed motion. The pressure ratio across an unsteady expansion where the gas is initially at rest may be written as

$$\frac{p_{3u}}{p_4} = \left[1 - \frac{(\gamma_4 - 1)}{2} \frac{u_{3u}}{a_4} \right]^{\frac{2\gamma_4}{\gamma_4 - 1}} \tag{2}$$

The steady isentropic expansion of the reservoir gas through the nozzle produces a pressure distribution which after the initial starting transient is invariant with time. The steady flow energy equation provides the counterpart of Eq. 1, and is expressed by

$$C_p T_o = C_p T + \frac{u^2}{2} \quad . \tag{3}$$

The pressure ratio across an isentropic steady expansion, where the gas is initially at rest, follows from Eq. 3, and

$$\frac{p_{3s}}{p_4} = \left[1 - \frac{(\gamma_4 - 1)}{2} \left(\frac{u_{3s}}{a_4} \right)^2 \right]^{\frac{\gamma_4}{\gamma_4 - 1}} \tag{4}$$

Note that Eqs. (2) and (4) are not in general equal and that a given initial state expanded to a given velocity by both methods will not yield the same temperature or pressure. The properties of the two expansion flows are shown clearly in the (p,u)-plane on Fig. 3.

From Fig. 3 it is seen that there is only one point other than the initial state where the two expansions will produce the same end state. This unique state is found by equating Eqs. (2) and (4) giving

$$\left(1 - \frac{(\gamma_4-1)}{2}\frac{u_{3u}}{a_4}\right)^2 = 1 - \frac{\gamma_4-1}{2}\left(\frac{u_{3s}}{a_4}\right)^2 \qquad (5)$$

Solving for u yields:

$$\frac{u_3}{a_4} = \frac{4}{\gamma_4+1} \quad \text{or} \quad M_3 = \frac{4}{3-\gamma_4} \qquad (6)$$

It is worth noting that a detailed analysis of the conditions at this point (the "cross-over" point) and their compatability with the tailoring constraint is done in Appendix A. The results show that very stringent requirements are placed on the initial conditions if both tailoring and cross-over conditions are to be satisfied simultaneously. (The problem is trivial if only the cross over condition is specified (i.e. nontailored operation) since the shock tube initial conditions may be readily adjusted to yield this value. However it is assumed throughout this paper that tailored operation is implied.) Appendix A demonstrates that the conventional shock-tunnel driving methods i.e. hydrogen drivers, helium drivers and combustion drivers will not satisfy both of these requirements simultaneously. In fact for air as the driven gas only a driver gas having a specific heat ratio of 1.18 will satisfy this requirement for perfect gases.

Additional disturbances, shocks or expansions or combinations of the two, will be necessary to "patch" the steady and unsteady flow regimes, for the general case.

POSSIBLE WAVE SYSTEMS

The problem of determining the wave systems which will patch the two expansion flows for a tailored condition reduces to the following. A point (A) (the so-called right state of ref. 5) as in Fig. 3, is specified on the unsteady expansion curve corresponding to the tailored condition. A nozzle area ratio is chosen for the steady expansion curve, hence a point (B) (the so-called left state of ref. 5) is specified on the steady expansion curve. These two points must now be connected by some additional unsteady disturbances, such as left or right running shocks, left or right running rarefactions, Mach waves or combinations of these.

There are many combinations that can be hypothesized from these disturbances. However, most of them are "unstable", that is, they consist of overtaking waves which would have to originate (at infinity) prior to the interaction hence violate the initial collision conditions (at t = 0) of the problem. Several "stable" transitions do exist. Stable transitions are those in which no change in the character of the patching wave system occurs with time, that is the waves are receding from the interaction. It should be noted that

any right running wave arising from the above wave system will ultimately overtake the incident shock if the tube is sufficiently long. However, it will be assumed that the tube is short enough in that the incident shock reflects from the end of the tube before any overtaking occurs. It will be shown later that only cases that contain no right running waves are of interest hence this point is of little interest.

An additional restriction must be imposed on some wave systems, since the strength of the left (upstream) running wave must be such that it either stands still in the laboratory coordinates or is swept downstream to the right. The restriction to be satisfied is

$$M_{F_E} \geq M_s'$$

where, M_{F_E} is the flow Mach number evaluated at the nozzle exit and M_s' is the shock Mach number of the upstream running shock based on a shock velocity taken with respect to the velocity and sound speed of the gas just upstream of the shock. Shocks of greater strength would propagate upstream into the nozzle and break down the flow, hence are "unstable".

The patching waves which emerge from the interaction region are the result of the collision of rarefaction waves and compression waves which are generated when the initial left running rarefaction first interacts with a decreasing area ratio (the exit (right Fig. 2) side of the nozzle) and the transmitted rarefaction wave interacts with an increasing area ratio (the entrance(left) side of the nozzle). A second interaction occurs when the disturbance generated at the entrance side of the nozzle, moves downstream through the exit of the nozzle. The detailed nature of the interactions can only be obtained by using the method of characteristics. The final emergent wave system is the product of several basic shock (compression wave) and rarefaction wave interactions.

In references 8 and 9 these basic interactions are discussed. It is shown (ref. 8) that for real gases the overtaking of a rarefaction wave by a shock (compression wave) always results in a reflected shock and a transmitted rarefaction wave if the overtaking shock is weak, and a transmitted shock if the overtaking shock is strong. In ref. 9 it is shown that in the case of the overtaking of a shock wave by a rarefaction wave both reflected shock waves and rarefaction waves are possible. If the overtaking rarefaction is weak then the transmitted wave is a shock wave; if it is strong then transmitted rarefaction wave results.

Since at the nozzle both of these cases can exist, it can readily be shown that 9 stable configurations are possible (counting the 5 limiting cases which have transmitted or reflected mach waves), as shown in Table 1.

Which of the nine stable systems occurs in a given situation depends on two parameters; the ratio of the tailored shock Mach number to cross over shock Mach number (M_{S_T}/M_{S_X}), and the ratio of the actual nozzle area ratio to an ideal nozzle area ratio (δ/δ_{IDEAL}), that is, there will be three distinct cases which depend on whether the tailored condition occurs at a lower, identical to, or higher velocity than the cross over velocity and for

each of these three cases there will be different subcases produced depending on whether the nozzle area ratio is larger, identical to, or smaller than the ideal value.

Case 1 $M_{S_T}/M_{S_X} < 1$

For this case the tailored conditions occurs at a lower velocity or shock Mach number than does the cross-over condition. (Methods of finding the tailored and cross-over conditions are given in ref. 10 and Appendix A respectively.)

This is the case usually found in practice and is representative of the more common modes of operation, He/Air, H_2/Air and Combustion gases/Air. The possible wave systems are indicated on the (p,u)-plane of Fig. 4, and are tabulated in Table 1. For no nozzle i.e. $\delta = 1$ the matching is accomplished by a single left running rarefaction wave and right running shock wave (wave system 3). This right running shock will ultimately reach the shock tunnel reservoir region and increase the reservoir pressure signaling the end of the steady running conditions. As the nozzle size is decreased the strength of both the left running rarefaction and right running shock are decreased. When $\delta = \delta_S^{\rightarrow}$ a single right running shock is sufficient to join the two flow regimes (wave system 6). A further decrease in nozzle area ratio gives rise to left and right running shocks (wave system 9) the right running shock decreasing in strength as the left one increases in strength. As δ approaches δ_{IDEAL} the right running shock become progressively smaller and vanishes in the limit and the matching is accomplished by a single left (upstream) running shock (wave system 8). It is important to note that in this limit there are no right running disturbances other than Mach waves are being produced in the flow (except for the original incident shock). Hence, no waves are available which could alter the steadiness of the shock tunnel reservoir. The initial rarefaction wave has been replaced by a steady expansion, a single left running shock and Mach waves. If the nozzle area ratio decreases further, non-ideal operation again occurs in that matching is accomplished by a left running shock wave and a right running rarefaction wave (wave system 7). The right running rarefaction will ultimately propagate into the reservoir region and decrease the reservoir pressure and signal the end of the steady reservoir conditions. The static pressure profiles produced along the tube for the several types of waves systems, are included in Fig. 4.

Case 2 $M_{S_T}/M_{S_X} = 1$

This case is not usually found in practice but is included for completeness. It corresponds to the case where the tailored condition and the cross over condition occur at the same state. It is the simplest of the three cases to analyse and is closest to the explanation put forward in ref. 2. The possible wave diagrams are shown in Fig. 3 and tabulated in Table 1. For $\delta = 1$, matching is accomplished through a left running rarefaction and a right running shock (wave system 3). As in the previous case the right running shock will propagate into the reservoir region and end the steady tunnel reservoir time. As δ is decreased both the shock and the expansion

weaken till in the limit as δ approaches δ_{IDEAL} both vanish simultaneously (wave system 5), leaving no disturbances in the flow. The steady and unsteady expansions are now matched together without that aid of any additional disturbances. This is the ideal situation for the $M_{S_T} = M_{S_X}$ case. If δ is further decreased, the roles of the shock and rarefaction are interchanged, the shock propagating upstream and the rarefaction propagating downstream into the reservoir region, and eventually lowering the reservoir pressure (wave system 7). The static pressure profiles along the tube for this case are included in Fig. 5.

Case 3 $M_{S_T}/M_{S_X} > 1$

This case is not generally attained in practice but is included since it may be of further interest in tailored chemical shock tubes where exotic gases or mixtures of gases are being investigated. The possible wave systems are indicated in Fig. 6 and are tabulated in Table 1. For no nozzle, $\delta = 1$, the matching is accomplished by a single left running rarefaction and a right running shock (wave system 3), a situation which will ultimately produce an increase in pressure in the shock tunnel reservoir region. As δ is decreased the strength of the left running shock decreases until as δ approaches δ_{IDEAL}, which is also equal to δ_X for this case, matching is accomplished by a single upstream running rarefaction wave (wave system 2). The initial starting rarefaction has been replaced by a steady expansion, a left running rarefaction wave, and Mach waves. This is to be contrasted to the $M_{S_T}/M_{S_X} < 1$ case where the matching in the ideal case was accomplished through the steady expansion and a left running shock. As δ is decreased further from δ_{IDEAL}, a pair of right and left running rarefaction waves is sufficient to patch together the two flows (wave system 1). As δ is decreased further, the left running rarefaction wave decreases in strength until in the limit as δ approaches $\delta_{\vec{R}}$ a single right running rarefaction wave is sufficient to join the flows (wave system 4). This character is symmetric to the $M_{S_T}/M_{S_X} < 1$ case where a single right running shock could patch the two flows but for δ greater than δ_{IDEAL} rather than δ less than δ_{IDEAL}. If δ is further decreased, matching is obtained by the addition of a left running shock (wave system 7). The pressure profiles for the above cases are also shown on Fig. 6.

In summary, it is found in general, that it takes two additional unsteady disturbances to match the steady flow of the reservoir gas with the unsteady flow of the driver gas. Further, there are special cases where only one disturbance is required, and what is very important is that it is possible to choose the nozzle area ratio to make this disturbance a left (upstream) running disturbance. This disturbance will be either a shock wave or a rarefaction wave depending on the ratio M_{S_T}/M_{S_X} and in the limit as this ratio approaches unity (i.e. the cross-over point) matching is accomplished automatically.

For all cases if the nozzle area ratio is made larger than the ideal value, right running shocks will propagate into the reservoir region and increase the reservoir pressure. Conversely, if the nozzle area ratio is made smaller than the ideal area ratio a rarefaction wave propagates into the reservoir region decreasing the reservoir pressure. This fact was observed in the experimental work of ref. 2 and substantiates the present analysis.

It should be noted that the mass flow could have been used instead of the pressure in a "(m,u)-plane" analysis. However the features of the expansion flows in this plane are similar to the behavior of them in the (p,u)-plane. Hence, to imply that the two flows can be patched if the mass flows are matched is not sufficient since equal mass flows does not imply equal pressures or velocities except, as has been shown above, at the cross-over point.

IDEAL NOZZLE AREA RATIOS

In the previous section it was shown that a wave system containing no right running disturbances of any kind can be obtained by expanding the gas in the reservoir through a steady expansion to a certain specific value, which is governed by the area ratio δ of the nozzle which is placed between the driver and reservoir regions.

It was specifically shown that for the cases $M_{S_T}/M_{S_X} = 1$ and $M_{S_T}/M_{S_X} > 1$ the ideal area ratio is the cross over area ratio. For these two cases a simple exact result for the ideal nozzle area ratio can be obtained.

From steady isentropic flow theory, the nozzle area ratio is related to the flow Mach number by

$$\delta = M_{3s}\left[\frac{2}{\gamma_4+1}\left(1+\frac{\gamma_4-1}{2}M_{3s}^2\right)\right]^{-\frac{1}{2}\left(\frac{\gamma_4+1}{\gamma_4-1}\right)} \tag{7}$$

Substituting into this relation the value of the flow Mach number at the cross-over point gives for the ideal nozzle area ratio:

$$\delta_{IDEAL} = \frac{4}{3-\gamma_4}\left[\frac{2(\gamma_4+1)}{(3-\gamma_4)^2}\right]^{-\frac{1}{2}\left(\frac{\gamma_4+1}{\gamma_4-1}\right)} \quad \text{For } \frac{M_{S_T}}{M_{S_{X_o}}} \geq 1 \tag{8}$$

Note the interesting result that δ is a function of the driver gas ratio of specific heats only and is independent of all the other parameters. Values of δ are plotted in Fig. 7 and tabulated in Table 2 for the range of driver gas ratios of specific heat of interest.

For $M_{S_T}/M_{S_X}<1$ the introduction of the upstream running matching shock complicates the system to the extent that no simple result for δ has been obtained to date. This is unfortunate since it is the case of immediate interest. The ideal area ratio can be calculated as follows. For a given γ_1,γ_4 and tailored shock Mach number, the corresponding diaphragm speed of sound ratio can be found from a simultaneous solution of four equations, as shown in Ref. 10. The area ratio δ may be found by using these four parameters as inputs to a system of equations which includes Eq. A-1 (Appendix A) evaluated at the tailored shock Mach number

$$\frac{u_{3u}}{a_4} = \frac{2}{a_{41}(\gamma_1+1)}\left(M_{S_T} - \frac{1}{M_{S_T}}\right), \tag{9}$$

Equation 2 evaluated at the tailored velocity

$$\frac{p_{3u}}{p_4} = \left(1 - \frac{\gamma_4-1}{2}\frac{u_{3u}}{a_4}\right)^{\frac{2\gamma_4}{\gamma_4-1}} \tag{10}$$

the general shock velocity-pressure ratio relation written for the left running matching shock

$$\frac{u_{3s} - u_{3u}}{a_4}\left(\frac{a_4}{a_3}\right) = \left[\frac{2}{\gamma_4(\gamma_4-1)}\right]^{\frac{1}{2}} \frac{\frac{p_{3u}}{p_4}\frac{p_4}{p_{3s}} - 1}{\left[1+\frac{\gamma_4+1}{\gamma_4-1}\frac{p_{3u}}{p_4}\frac{p_4}{p_{3s}}\right]^{\frac{1}{2}}} \tag{11}$$

the pressure ratio across the steady expansion as given by Eq. (4) above, the speed of sound ratio across the steady expansion given by

$$\frac{a_3}{a_4} = \left[1 - \frac{\gamma_4-1}{2}\left(\frac{u_{3s}}{a_4}\right)^2\right]^{\frac{1}{2}} \tag{12}$$

and an area-ratio-velocity relation for steady isentropic flow which may be expressed by,

$$\delta = \left(\frac{\gamma_4+1}{2}\right)^{\frac{\gamma_4+1}{2(\gamma_4-1)}} \frac{u_{3s}}{a_4}\left[1 - \frac{\gamma_4+1}{2}\left(\frac{u_{3s}}{a_4}\right)^2\right]^{\frac{1}{\gamma_4-1}} \tag{13}$$

The procedure for finding δ consists of solving Eq. (9) for u_{3u}/a_4, substituting into Eq. (10) to obtain p_{3u}/p_4, then solving simultaneously Eqs. (11) and (4) for u_{3s}/a_4 using the auxiliary equation Eq. (12) for the speed of sound ratio. Finally u_{3s}/a_4 is inserted into Eq. (13) to yield δ .

This system of equations was solved numerically on the IBM 7090 using the above procedure. The results are presented in Fig. 8 and tabulated in Table 3.

From Fig. 8 it is noted that the ideal nozzle area ratio, δ_{IDEAL}, for the case $M_{ST} < M_{S_{XO}}$ is somewhat greater than δ_x depending on the tailored shock Mach number. The lowest shock Mach number shown here is 2.0, since at lower values the analysis begins to break down. For example $M_{S_T} = 1$ implies a zero velocity of the unsteady expanded gas or no flow in the nozzle. As seen in Fig. 8, for increasing values of tailored Mach number the value of δ_{IDEAL}

rapidly approaches δ_X from above. As a practical matter, as a first trial value to use in an experimental situation the value of δ_X would usually suffice, the nozzle being enlarged as the results of the experiment dictate.

In this respect, it should be noted that the experimental value for hydrogen driving air ($\delta_{IDEAL} = 1/3$), as determined in ref. 2, agrees very well with the exact value from this theory $\delta_{IDEAL} = 0.382$ and $\delta_X = 0.378$, considering that real gas effects, viscous effects, attenuation and secondary interactions are neglected.

Although the above has been derived for the tailored condition it is possible to operate "off-tailored" and still use the driver reservoir to extend the steady state shock tunnel reservoir time. In general, over-tailored operation ($M_S > M_{ST}$) requires a nozzle smaller than the ideal ($\delta < \delta_{IDEAL}$, see Fig. 4) and for "under-tailored" operation ($M_S < M_{ST}$) requires an area ratio larger than ideal. It may be seen from Fig. 8 that the value of δ_{IDEAL} changes very little, especially at the higher values of M_{ST}, consequently, the ideal nozzle area ratio will usually suffice even for the "off-tailored" conditions. This effect was verified in ref. 2 where it is noted that within the accuracy of the experiment, δ_{IDEAL} was satisfactory for a wide range of over and under-tailored conditions.

DRIVER-RESERVOIR TEST TIME LIMITS

Within the limits of the analysis it was shown that the driver-reservoir removes two of the test time limitations from shock tunnels, that of the arrival of the reflected head and tail of the rarefaction at the shock tunnel nozzle. However, test time limitations due to waves arriving at the nozzle do not vanish entirely since the unsteady matching disturbances which are being generated and propagated along the duct must be dealt with but later in time. New interfaces and contact regions are being generated but since they are produced by nearly isentropic compression waves or at worst weak shocks their effect can usually be disregarded.

For the case where $M_{S_T} = M_{S_X}$ and $\delta = \delta_{IDEAL}$, the limitation to the test time now is the arrival of a shock wave at the nozzle as can be seen from Fig. 9a (relevant wave systems shown in Table 1 are drawn symbolically for completeness since a detailed calculation by the method of characteristics has not been done). This wave is the end result of the incident shock being reflected first from the shock tube downstream end then travelling upstream to the reservoir nozzle and then again travelling downstream to the shock tunnel nozzle.

The resulting running time can be many times the original tailored test time for usual shock tube geometries. It must be noted that new test time limitations can now be imposed which are now more stringent than this, as by mass flow, radiative or convective heat loss considerations, for example.

For the case where $M_{S_T}/M_{S_{XO}} < 1$ and $\delta = \delta_{IDEAL}$, the matching between steady and unsteady expansion is made by a left running shock. Therefore, the

limitation to the test time is now the arrival at the shock tunnel reservoir region of the right-running rarefaction wave, which is generated by the collision of the original reflected shock and the upstream running patching shock as indicated in Fig. 9b. That this disturbance must be an expansion for all physically possible ratios of specific heat was shown in ref. 11. The expansion which limits the test time in this case was observed in ref. 2. However, they incorrectly ascribed this to the original expansion being "delayed" at the reservoir. From a comparison of Fig. 11a and 12b it can be seen that the test time for this case will be greater than the original (no driver-reservoir) test time but will generally be less than that produced by the $M_{S_T}/M_{S_{XO}} = 1$ case because the limiting disturbance is generated closer to the shock tunnel nozzle reservoir region. There is also an additional interface or interface region which is generated by the patching shock (see Table 1) which is not significant since it is found that the mismatch shock is relatively weak. However, if the nozzle and diaphragm stations are made coincident, then this second interface can in principle, at least, be made coincident with the original interface and adjustment of the tailoring Mach number to a somewhat higher value will obscure this effect.

For $M_{S_T}/M_{S_{XO}}>1$ and $\delta = \delta_{IDEAL}$ the situation is similar in character to the $M_{S_T}/M_{S_{XO}} \leq 1$ case except that shocks are replaced by expansions and visa versa. The end of the steady test time is signalled by the arrival of a shock or compression wave which is the result of the interaction of the reflected normal shock and upstream running patching rarefaction wave. This type of collision was analyzed in ref. 7, and it is shown that the disturbance must be a shock or compression wave for all physically possible specific heat ratios. The wave diagram for this case is shown in Fig. 9.

CONCLUSIONS

It has been shown that a complex flow containing both steady and unsteady flow regimes is produced by using the driver-reservoir technique to extend hypersonic shock tunnel running times. It is shown that by assuming the existence of a patching wave system that separate quasi-steady states a solution can be obtained "in the large" by using a (p,u)-plane type of analysis. The results show that in general two additional disturbances separated by a contact surface are necessary to satisfy the boundary conditions imposed by the two different expansions. It is also shown that the actual flow pattern resulting from a given set of initial conditions is uniquely determined by the parameters $M_{S_T}/M_{S_{XO}}$ and δ/δ_{IDEAL}, where M_{S_T} is the tailored shock Mach number, M_{S_X} is the cross-over shock Mach number, δ is the given nozzle area ratio and δ_{IDEAL} is the nozzle area ratio which produces no downstream running waves. For a few special cases the flows can be joined with a single disturbance and for three unique cases corresponding to $M_{S_T}<M_{S_X}$, $M_{S_T} = M_{S_X}$, and $M_{S_T}>M_{S_X}$ an upstream running shock, a Mach wave, and an upstream running expansion respectively are produced. Since no downstream running disturbances (other than Mach waves) are contained in the flow, the shock-tunnel reservoir region will remain undisturbed for a longer period of time. In effect, the driver-reservoir when used ideally will replace the initial

unsteady expansion by a steady expansion, an upstream running disturbance, and Mach waves, hence limitations due to both the reflected head and the tail of the original expansion are eliminated.

The ideal nozzle area ratio, which will produce this optimum condition (δ_{IDEAL}) is calculated for a wide range of conditions and compared with the available data. The agreement is very good considering that ideal, perfect gas flow is assumed throughout, and that secondary interactions of characteristics are neglected, and it lends support to the validity of these assumptions.

It is worth noting that a (p,u)-plane type of analysis is ideally suited for this type of problem, once it is assumed that quasi-steady states must exist after the interaction. However, it lacks the detail that a characteristics diagram in the (x,t)-plane provides. Consequently, it would be of value to do a characteristics solution in the (x,t)-plane for a few cases in order to establish precisely how the final wave system is generated. A comparison of the (p,u)-plane analysis (where secondary interactions were neglected) with a more exact analysis in ref. 7, shows good agreement as long as the wave strengths are not too large, which is generally the case in the present analysis.

The effect of driver length was not considered in the present problem. However, it can be seen that it is desirable to generate the final states in the neighbourhood of the driver reservoir.

In conclusion, it can be stated that the present analysis is representative of the physical conditions and can be used with confidence to predict values of the ideal nozzle area ratio in order to extend the running times of a hypersonic shock tunnel.

REFERENCES

(1) Holder, D.N. and Schultz, D.L., On the Flow in a Reflected Shock Tunnel, A.R.C. 22152-Hyd. 130, (August, 1960) Also Progress in Astronautics and Aeronautics, Vol. 7, Hypersonic Flow Research, Academic Press, New York (1962).

(2) Henshall, B.D., Teng, R.N. and Wood, A.D., A Driver-Sphere Technique for Increasing the Steady State Test Time of a Hypersonic Shock Tunnel, Proceedings of the Second Symposium on Hypersonic Technique, University of Denver, (20-21 March 1962), also Avco RAD-TM-62-16 (April 1962).

(3) Benton, E.R., and Knapton, D.A., Supersonic Drag of Porous Wire Screens, A.R.S. Journal, Vol. 32, No. 10 (Oct. 1962).

(4) Seigal, A.E., The Influence of Chamber Diameter on the Muzzle Velocity of a Gun with an Infinite Length Chamber. NOL Navord Report 2691,(1954).

(5) Glass, I.I. and Hall, J.G., Handbook of Supersonic Aerodynamics, Section 18, Shock Tubes, NAVORD 1488, Vol. 6, p. 1959.

(6) Oppenheim, A.K., Urtiew, P.A. and Laderman, A.J., Vector Polar Method for the Evaluation of Wave Interaction Processes., Archiwum Budowy Maszyn, Vol. 11, No. 3, 1964.

(7) Bird, G.A., Extreme Temperatures in Shock-Wave Interactions with Rarefaction Waves, J. Fluid Mech, Vol. 13, p. 282 (1963).

(8) Bremner, G.F., Dukowicz, J, and Glass, I.I., On the One Dimensional Overtaking of a Rarefaction Wave by a Shock Waves, ARS Journal Vol. 31, No. 10, (1959) also UTIA Technical Note No. 33, Institute of Aerophysics, University of Toronto (1960).

(9) Glass, I.I., Heuckroth, L.E. and Molder, E., One Dimensional Overtaking of a Shock Wave by a Rarefaction Wave, ARS Journal, Vol. 31, No. 10, (Oct. 1961) also UTIAS Tech. Note No. 30 (1959).

(10) Flagg, R.F., Detailed Analysis of Shock Tube Tailored Conditions, Avco RAD-TM-63-64 (Sept. 1963).

(11) Bull, G.V., Fowell, L.R. and Henshaw, D.H., The Interaction of Two Similarly-Facing Shock Waves, UTIA Report No. 23, Insititute of Aerosphysics, University of Toronto (1952).

ACKNOWLEDGEMENTS

I wish to express my thanks to Dr. G. N. Patterson for the opportunity to continue this work at the Institute for Aerospace Studies. I wish also to express my appreciation to the AVCO Research and Advanced Development Division of Wilmington, Massachusetts for permission to release that part of the work which was conducted during my affiliation with them. I am also indebted to Mr. H. Weisblatt under whose supervision this research was initiated at AVCO-RAD and to Dr. I.I. Glass whose continued interest and guidance is gratefully acknowledged.

The work was supported by the Defence Research Board of Canada and by the U.S. Airforce under contract number ARL-AF-33(615)-2766.

NOTATION

A	area
a	speed of sound
C_p	specific heat at constant pressure
f	"tailoring constant"
g	"cross-over constant"
m	molecular weight
M	Mach wave
M_f	flow Mach number
M_S	shock Mach number
M_{S_T}	tailored shock Mach number
M_{S_X}	cross-over shock Mach number
p	pressure
P	defined by Eq. 1
$\overleftarrow{R}$	left (upstream) running unsteady expansion
$\overrightarrow{R}$	right (downstream) running unsteady expansion
$\mathcal{R}$	universal gas constant
$\overleftarrow{S}$	left (upstream) running shock
$\overrightarrow{S}$	right (downstream) running shock
S_i	incident shock
T	temperature
t	time
u	velocity
ρ	density
γ	specific heat ratio
δ	ratio of nozzle minimum area to tube cross section area (A^*/A_1)
δ_{IDEAL}	area ratio which produces no right (downstream) running disturbances (except a Mach wave)
$\delta_{\overrightarrow{R}}$	area ratio which produces a single right (downstream) running unsteady expansion
$\delta_{\overrightarrow{S}}$	area ratio which produces a single right (downstream)running shock
$(\ )^*$	conditions at nozzle minimum area
$(\ )_1$	driven section initial conditions
$(\ )_2$	conditions behind a moving normal shock
$(\ )_{3u}$	conditions in unsteady expanded driver
$(\ )_{3s}$	conditions in steady expanded river
$(\ )_4$	driver initial conditions
$(\ )_5$	conditions behind reflected normal shock
$(\ )_o$	stagnation conditions
$(\ )_s$	conditions at shock front
$(\ )_x$	cross-over conditions
$(\ )_{ij}$	$(\ )_i/(\ )_j$

TABLE 1

WAVE SYSTEMS FOR DRIVER-RESERVOIR FLOWS

System No.		Stability	Occurance
1	$\overleftarrow{R}$ C $\vec{R}$	Stable Provided $M_{F_E} \geq 1$	$M_{S_T} > M_{S_x}$, $\delta_{IDEAL} > \delta > \delta_{\vec{R}}$
2	$\overleftarrow{R}$ C M	Stable Provided $M_{F_E} \geq 1$	$M_{S_T} > M_{S_x}$, $\delta = \delta_{IDEAL}$
3	$\overleftarrow{R}$ C $\vec{S}$	Stable Provided $M_{F_E} \geq 1$	$M_{S_T} > M_{S_x}$, $\delta > \delta_{IDEAL}$; $M_{S_T} < M_{S_x}$, $\delta > \delta_{\vec{S}} > \delta_{IDEAL}$
4	M C $\vec{R}$	Stable	$M_{S_T} > M_{S_x}$, $\delta = \delta_{\vec{R}}$
5	M C M	Stable	$M_{S_T} = M_{S_x}$, $\delta = \delta_{IDEAL} = \delta_x$
6	M C $\vec{S}$	Stable	$M_{S_T} < M_{S_x}$, $\delta = \delta_{\vec{S}}$
7	$\overleftarrow{S}$ C $\vec{R}$	Stable Provided $M_{F_E} \geq M_S'$	$M_{S_T} < M_{S_{xo}}$, $\delta < \delta_{IDEAL}$; $M_{S_T} = M_{S_x}$, $\delta < \delta_{IDEAL}$; $M_{S_T} > M_{S_x}$, $\delta < \delta_{\vec{R}} < \delta_{IDEAL}$
8	$\overleftarrow{S}$ C M	Stable Provided $M_{F_E} \geq M_S'$	$M_{S_T} < M_{S_x}$, $\delta = \delta_{IDEAL}$
9	$\overleftarrow{S}$ C $\vec{S}$	Stable Provided $M_{F_E} \geq M_S'$	$M_{S_T} < M_{S_x}$, $\delta_{\vec{S}} > \delta > \delta_{IDEAL}$

TABLE 2

CROSS-OVER AREA RATIO VERSUS DRIVER GAS SPECIFIC HEAT RATIO

γ_3	δ_x
1.05	.438
1.10	.430
1.15	.421
1.20	.413
1.25	.404
1.30	.396
1.35	.388
1.40	.379
1.45	.370
1.50	.362
1.55	.354
1.60	.345
1.67	.333

TABLE 3

IDEAL NOZZLE AREA RATIO FOR $M_{S_T} < M_{S_x}$

γ_4	γ_1	M_{S_T}	δ_{IDEAL}	γ_4	γ_1	M_{S_T}	δ_{IDEAL}
1.1	1.1	2.0	.439	1.5	1.1	10	.362
	1.2		.441		1.2		.362
	1.3		.442		1.3		.364
	1.4		.444		1.4		.365
	1.5		.445		1.5		.367
	1.67		.446		1.67		.371
1.2	1.1	2.0	.426	1.5	1.2	∞	.362
	1.2		.428		1.3		.363
	1.3		.430		1.4		.365
	1.4		.432		1.5		.367
	1.5		.433		1.67		.370
	1.67		.435				
1.3	1.1	2.0	.413	1.67	1.1	2.0	.366
	1.2		.415		1.2		.368
	1.3		.418		1.3		.371
	1.4		.419		1.4		.373
	1.5		.421		1.5		.374
	1.67		.423		1.67		.376
1.4	1.1	2.0	.401	1.67	1.1	5.0	.334
	1.2		.403		1.2		.337
	1.3		.405		1.3		.340
	1.4		.407		1.4		.343
	1.5		.408		1.5		.346
	1.67		.410		1.67		.350
1.4	1.1	5.0	.379	1.67	1.1	10	.333
	1.67		.388		1.2		.334
1.5	1.1	2.0	.388		1.3		.337
	1.2		.390		1.4		.340
	1.3		.392		1.5		.343
	1.4		.394		1.67		.347
	1.5		.396	1.68	1.2	∞	.334
	1.67		.398		1.3		.336
1.5	1.1	5.0	.362		1.4		.339
	1.2		.363		1.5		.342
	1.3		.365		1.67		.346
	1.4		.368				
	1.5		.370				
	1.67		.374				

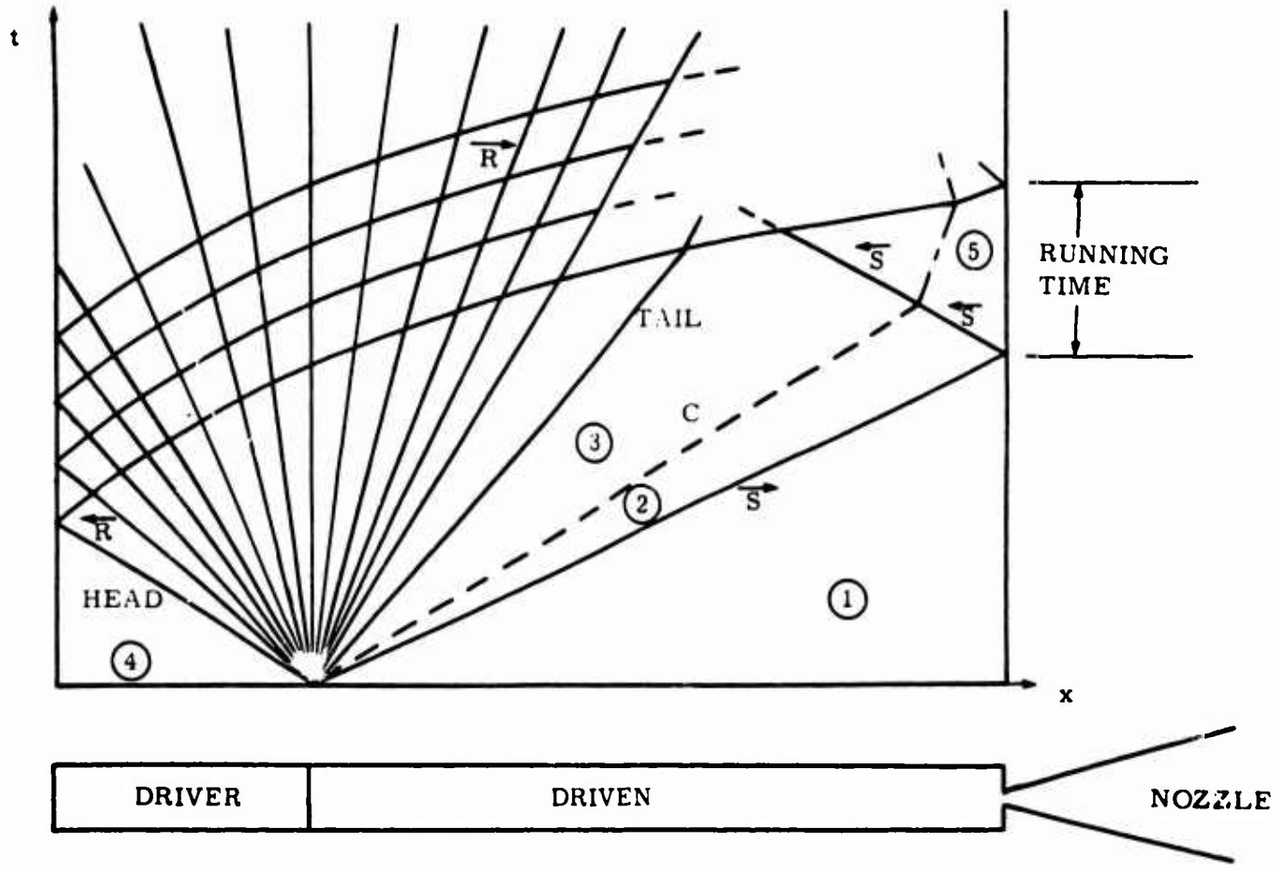


FIGURE 1 CONVENTIONAL SHOCK TUNNEL x-t DIAGRAM

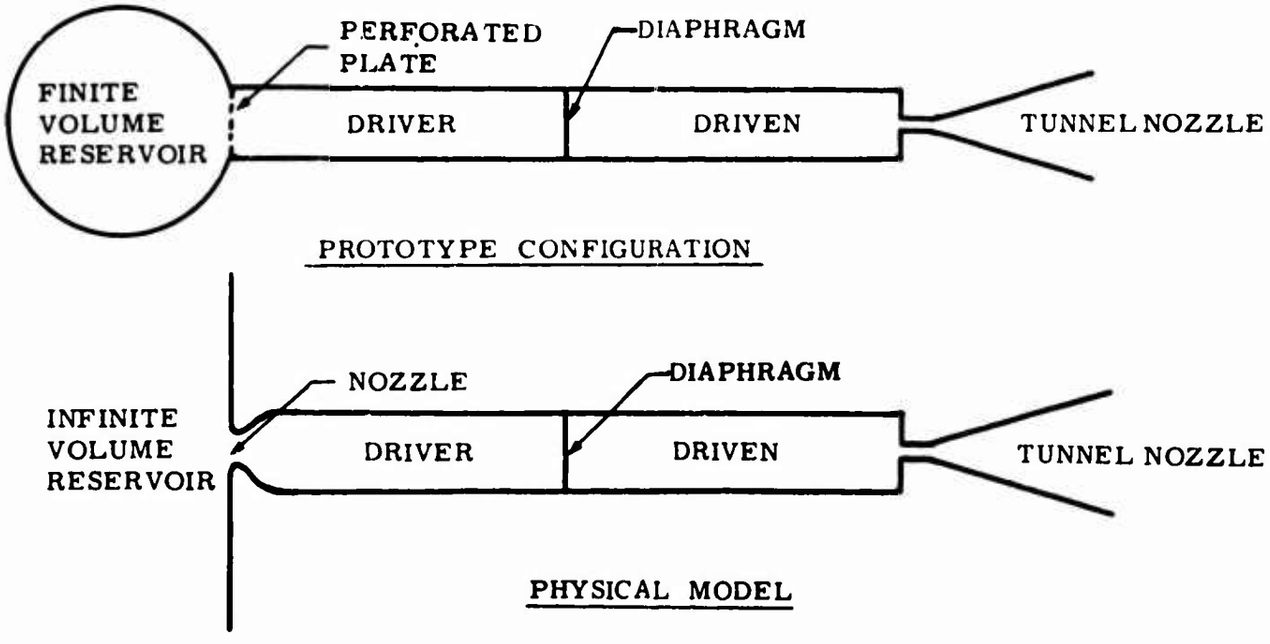


FIGURE 2 PROTOTYPE AND PHYSICAL MODEL OF DRIVER RESERVOIR

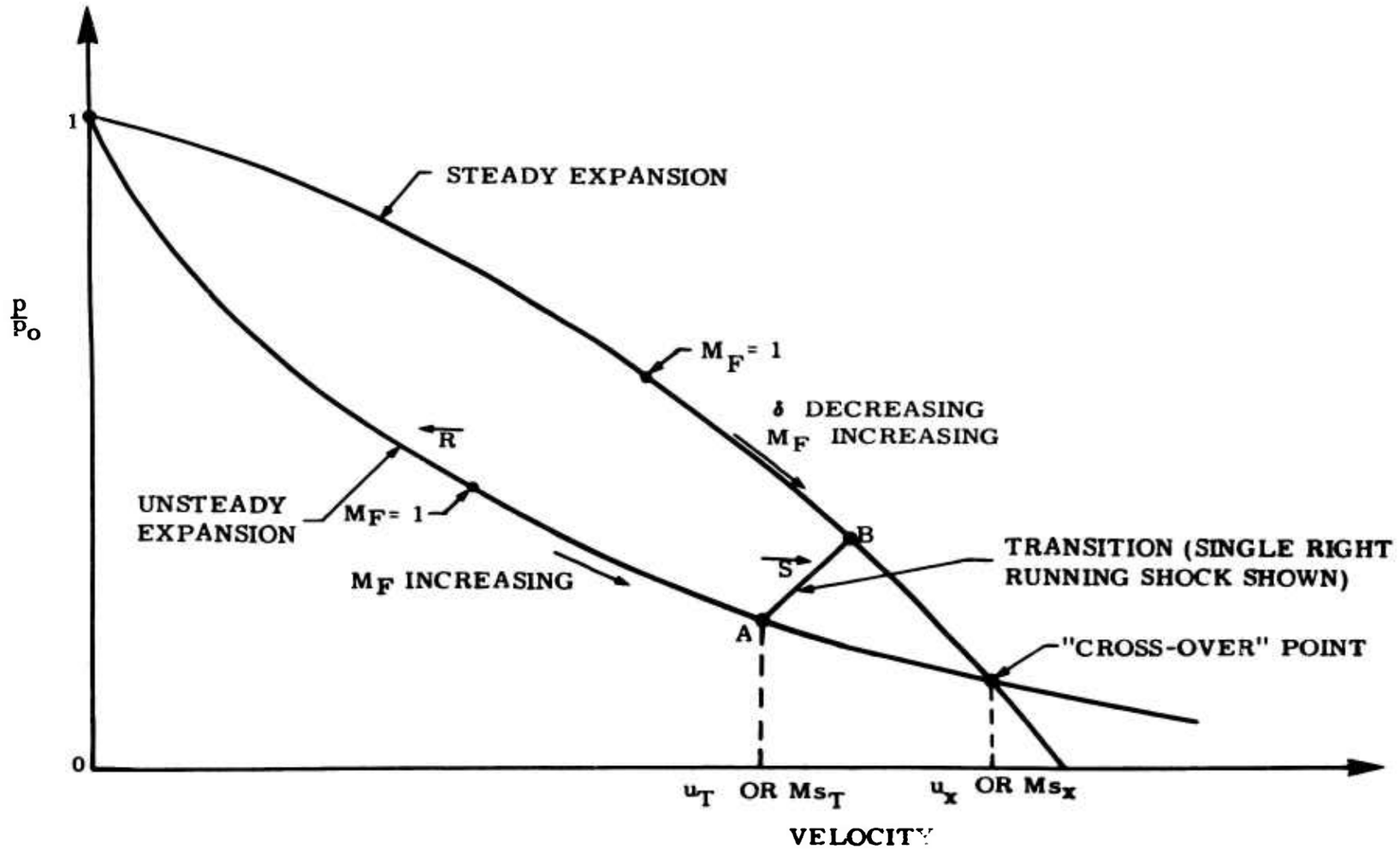


FIGURE 3 CHARACTERISTICS OF STEADY AND UNSTEADY EXPANSIONS ON THE (p, u) -PLANE

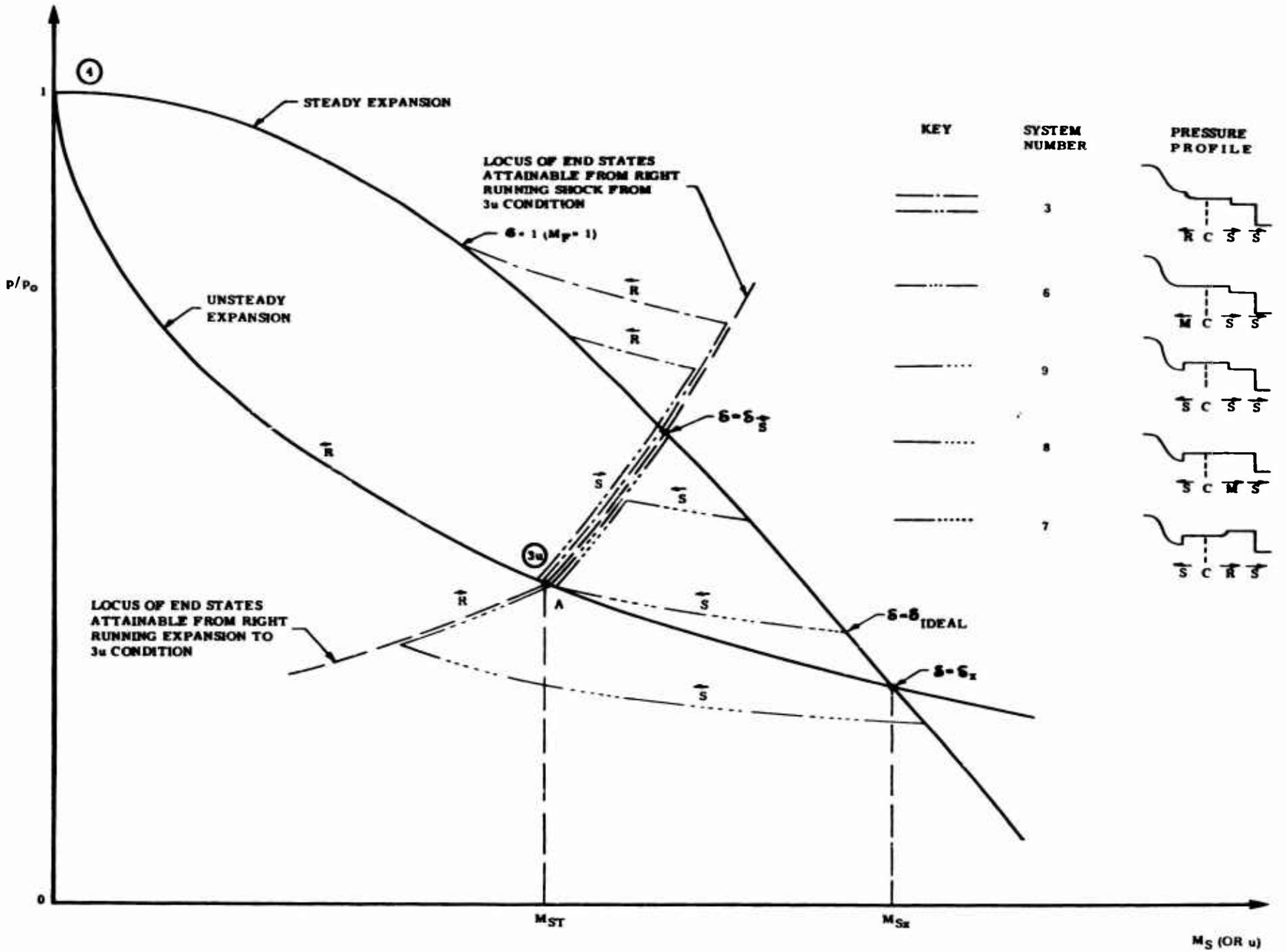


FIGURE 4 PRESSURE - VELOCITY PLANE TRACES OF WAVE SYSTEMS FOR $M_S/M_{Sx} < 1$

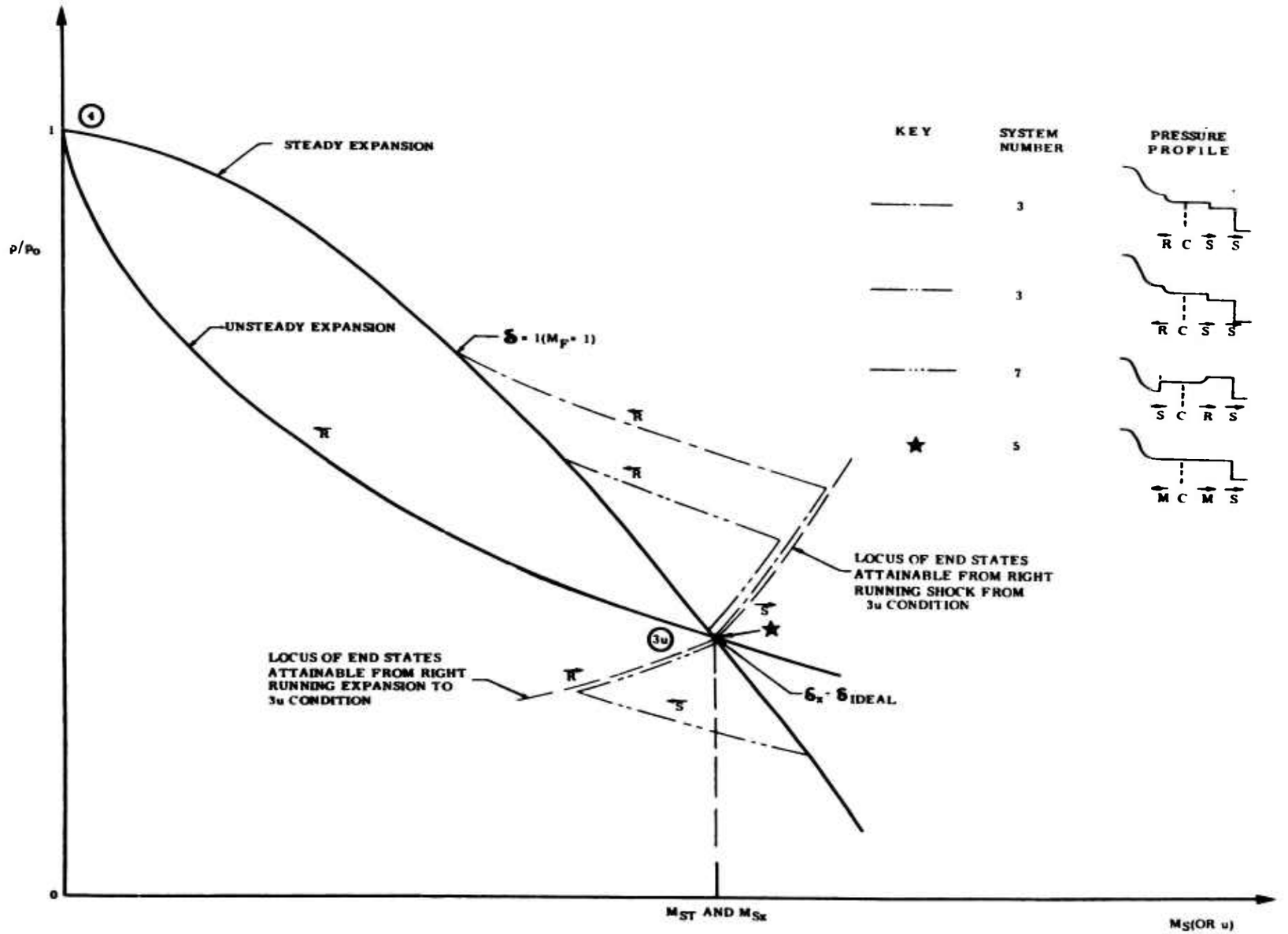


FIGURE 5 PRESSURE - VELOCITY PLANE TRACES OF WAVE SYSTEMS FOR $M_{ST}/M_{Sx} = 1$

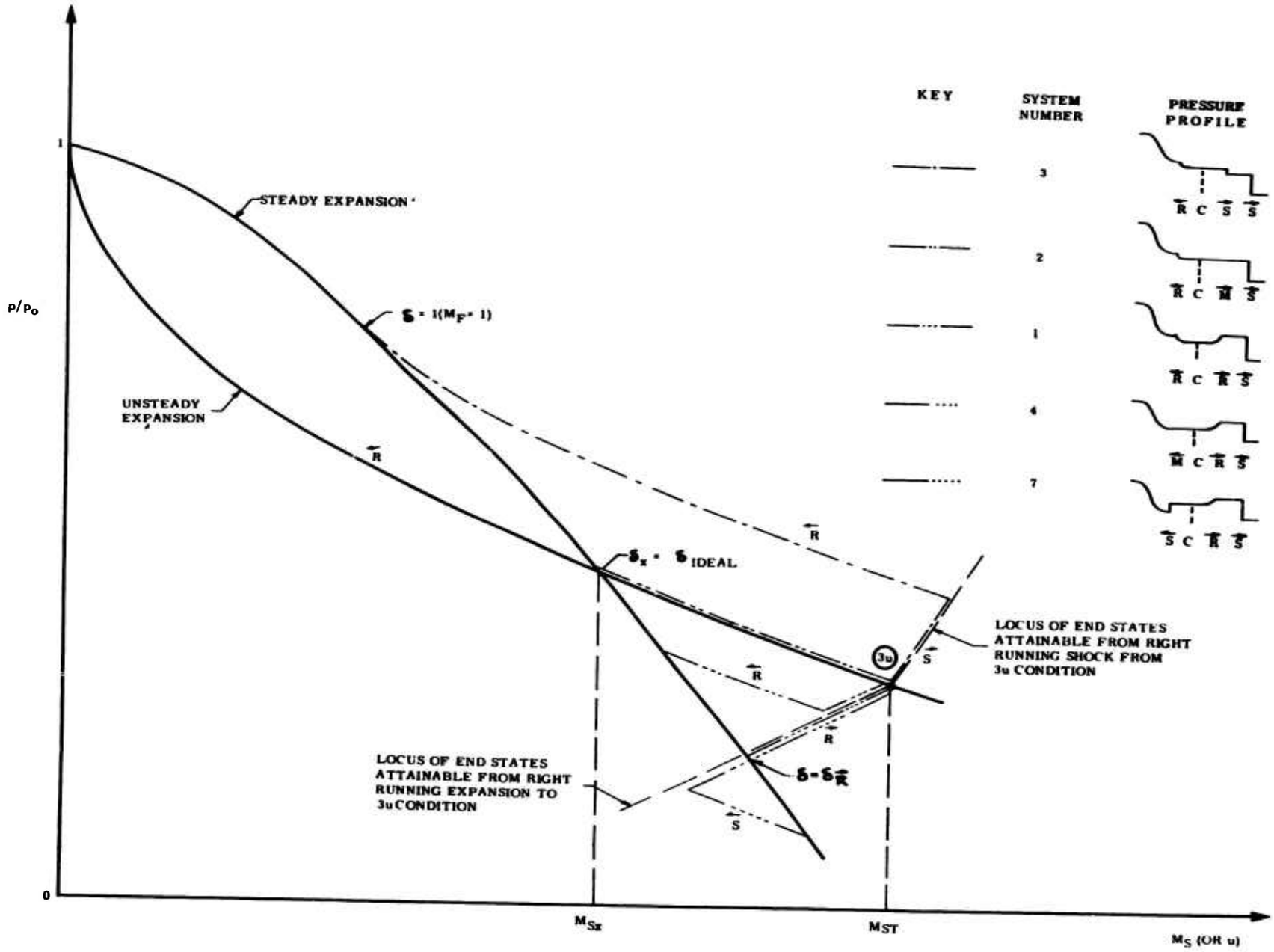


FIGURE 6 PRESSURE - VELOCITY PLANE TRACES OF WAVE SYSTEMS FOR $M_{ST}/M_{Sx}>1$

FIGURE 7

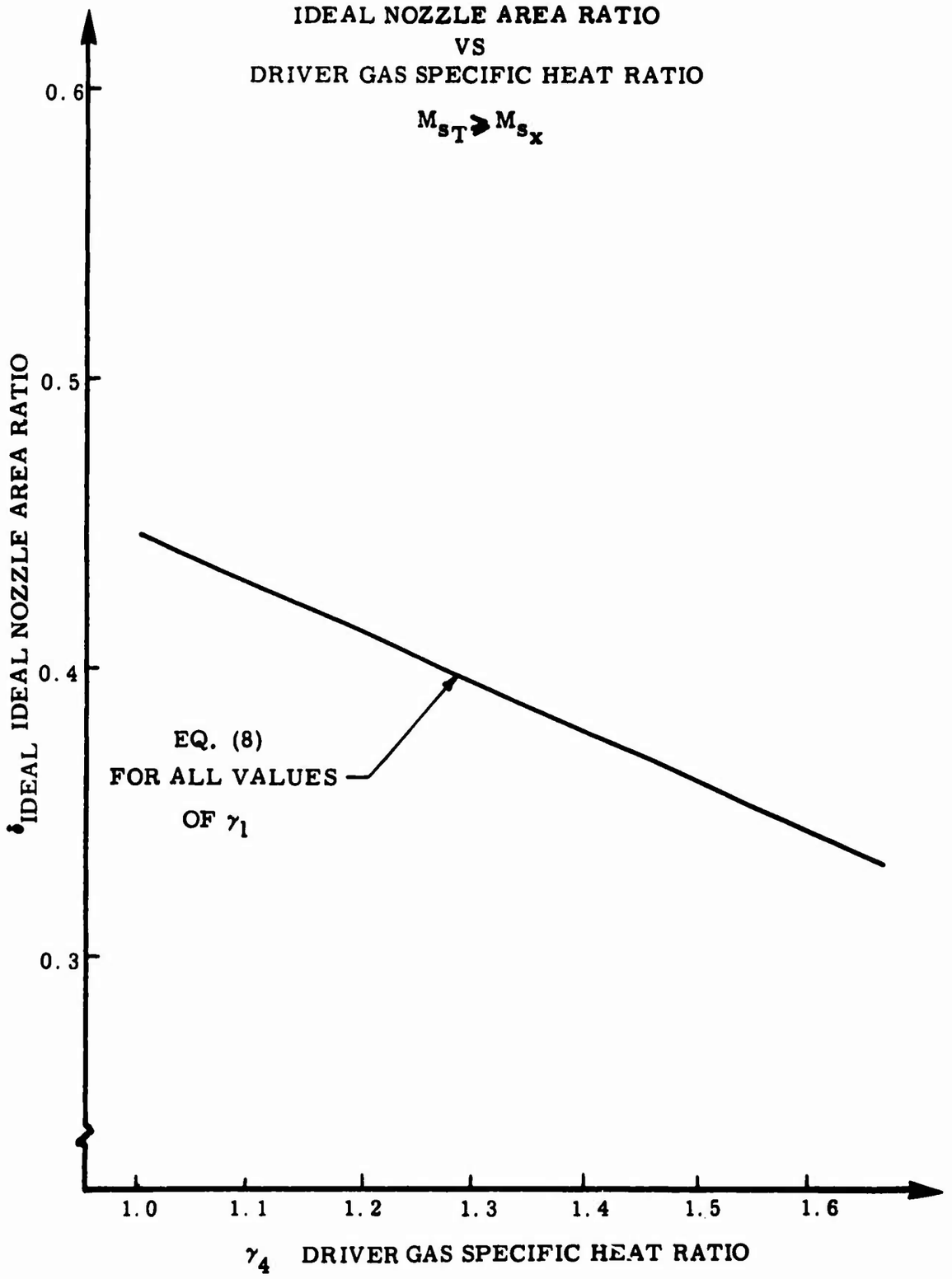
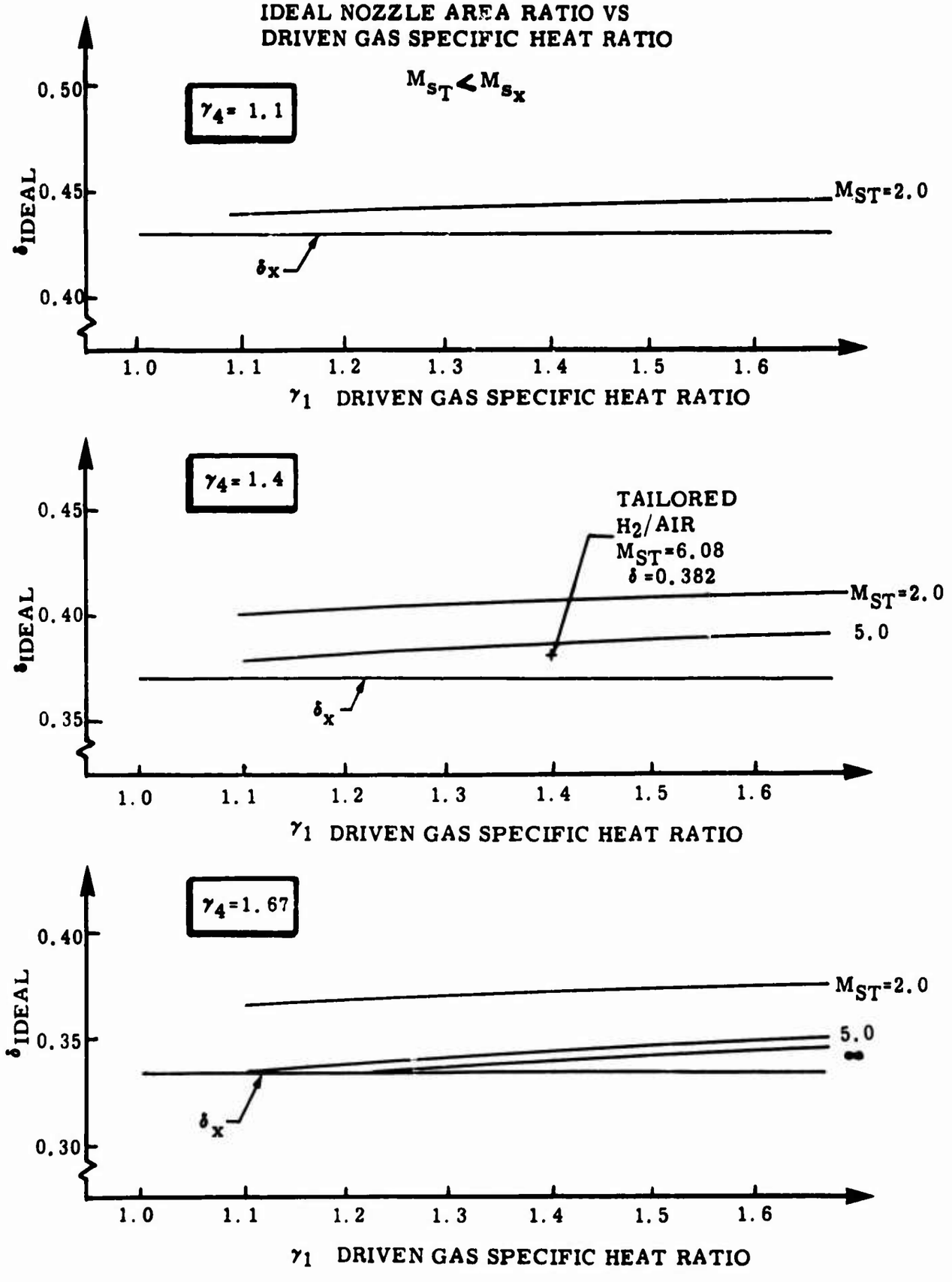

IDEAL NOZZLE AREA RATIO
VS
DRIVER GAS SPECIFIC HEAT RATIO
$M_{s_T} \geq M_{s_x}$
0.6
0.5
0.4
0.3
ϵ_{IDEAL} IDEAL NOZZLE AREA RATIO
EQ. (8)
FOR ALL VALUES
OF γ_1
1.0
1.1
1.2
1.3
1.4
1.5
1.6
γ_4 DRIVER GAS SPECIFIC HEAT RATIO

FIGURE 8
IDEAL NOZZLE AREA RATIO VS
DRIVEN GAS SPECIFIC HEAT RATIO



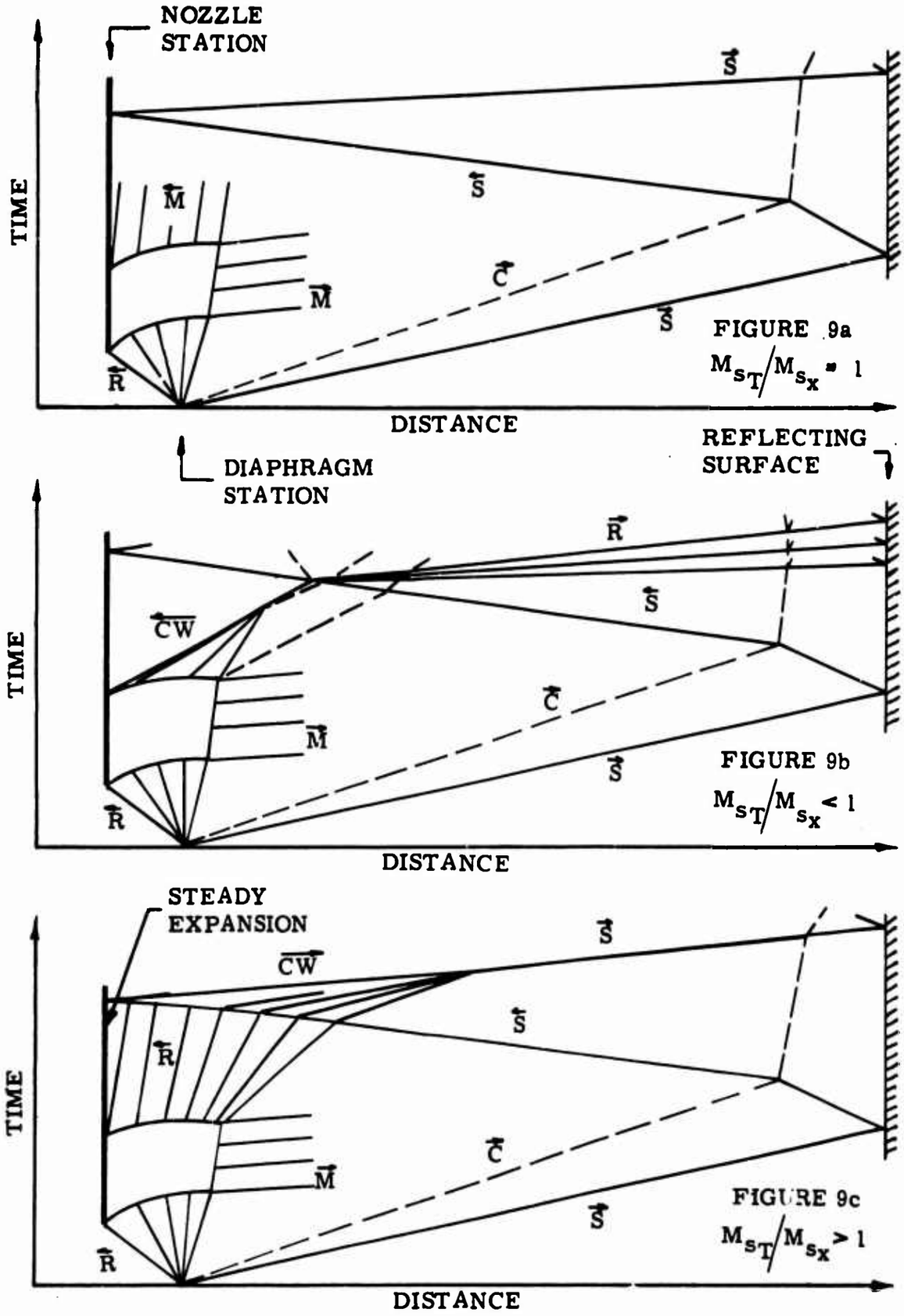


FIGURE 9 WAVE DIAGRAMS FOR LIMITING DRIVER-RESERVOIR FLOWS

APPENDIX A - ANALYSIS OF THE CROSS-OVER POINT

It is worthwhile to see if the point denoted as the "cross-over" point is of practical interest, for if it is , the problem of using the driver-reservoir technique is considerable simplified. The velocity u_3 in general, is related to the shock Mach number by:

$$u_3 = a_1 \frac{2}{\gamma_1+1}\left(M_s - \frac{1}{M_s}\right) \tag{A-1}$$

Using M_{s_x} to denote the shock Mach number for the cross-over condition and equating Eqs. (6) and (A-1) results in

$$M_{s_x}^2 - 2\frac{\gamma_1+1}{\gamma_4+1}\, a_{41}\, M_{s_x} - 1 = 0 \tag{A-2}$$

The positive root provides a physical solution given by:

$$M_{s_x} = \frac{\gamma_1+1}{\gamma_4+1}\, a_{41} + \left[\left(\frac{\gamma_1+1}{\gamma_4+1}\right)^2 a_{41} + 1\right]^{\frac{1}{2}} \tag{A-3}$$

or for the case where $a_{41} \gg 1$ (generally $M_s \gg 1$) this can be approximated by:

$$\frac{M_{s_x}}{a_{41}} \approx 2\frac{\gamma_1+1}{\gamma_4+1} = g \tag{A-4}$$

where, g, the "cross-over constant" is defined by this equation. Equations (A-3) and (A-4) are plotted in Fig. A-1 for several specific heat ratios of interest and Eq. (A-4) is plotted in Fig. A-2 for the complete range of specific ratios of physical interest. If the shock tube is to be operated at the cross-over point a restriction is placed on the values of M_s that may be used for a given speed of sound ratio across the diaphragm.

If this constraint were the only one placed on the shock Mach number there would be no problem with using the driver reservoir as the initial conditions could be readily adjusted to yield this shock Mach number. However, in addition to the above, the shock tunnel is required to be tailored, hence, there is an additional constraint placed on the shock Mach number. Reference 10 presents the exact tailored shock Mach numbers for a wide variety of driver and driven gases and diaphragm speed of sound ratios. An exact analytic solution has not been obtained. However, for the assumption of a large shock Mach number, i.e., $M_s \gg 1$, a simple approximate expression for the tailored shock Mach number is given by (ref. 10),

$$M_{s_T} \approx a_{41}\left[\frac{(\gamma_1+1)^2(\gamma_4-1) - \left[2\gamma_4\,(\gamma_1-1)(\gamma_4+1)(\gamma_1+1)^3\right]^{\frac{1}{2}}}{(\gamma_4-1)^2(\gamma_1+1) - 2\,\gamma_4\,(\gamma_1-1)\,(\gamma_4+1)}\right] \tag{A-5}$$

Equating Eqs. (A-4) and (A-3), the approximate equations for the cross over and tailored shock Mach numbers yields,

$$2[(\gamma_4-1)^2(\gamma_1+1)-2\ {}_4(\gamma_1-1)(\gamma_4+1)]= (\gamma_4+1)\left\{(\gamma_1+1)(\gamma_4-1)-\left[2\gamma_4(\gamma_1-1)(\gamma_4+1)(\gamma_1+1)\right]^{\frac{1}{2}}\right\} \tag{A-6}$$

Hence there are only certain combinations of specific heat ratios that will satisfy both the cross over and tailoring requirements, simultaneously. For the special case of $\gamma_1 = \gamma_4$ Eq. (A-6) reduces to

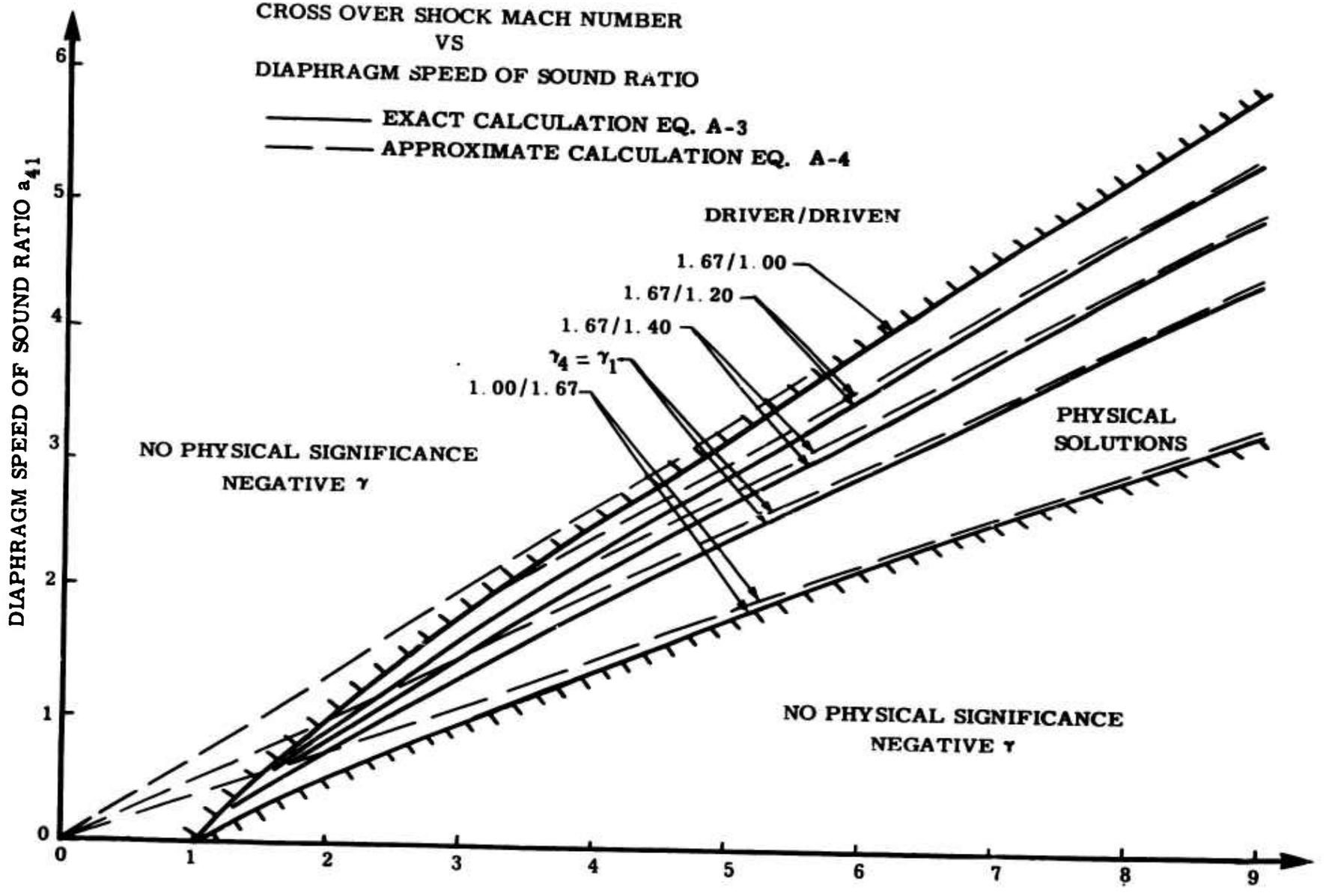
$$\gamma = \frac{9}{7}$$

Equation (A-6) is plotted in Fig. A-3. Note that this figure can be used to immediately determine which catagory (i.e. $M_{S_T} \gtrless M_{S_X}$) a given set of initial conditions falls into if M_S can be assumed large. It should be noted that the driver and reservoir gases are assumed initially at the same temperature and pressure. M_{S_T} and M_{S_X} can be matched if different initial temperatures and pressures exist in the driver and the reservoir. However, this mode of operation does not appear to be a practical one since it introduces the problem of heating driver gas and cooling the reservoir gas and adding a second diaphragm. To prevent mixing different gases or alternatively, mixtures of gases could in principle produce the same end pressures. However, an interface separating the different gases of different emperatures would give rise to an additional tailoring constraint. In general the conditions across this second interface could not be arbitrarily presented and hence would not be tailored simultaneously with the first interface.

Included in Fig. A-3 are the points corresponding to Helium/Air, Hydrogen/Air and Combustion/Air modes of operation. One notes that none of these combinations corresponds to the situation where the tailored shock Mach number and the cross-over shock Mach number are identical. Hence, some additional disturbances must be generated in these cases to match the two flow regimes.

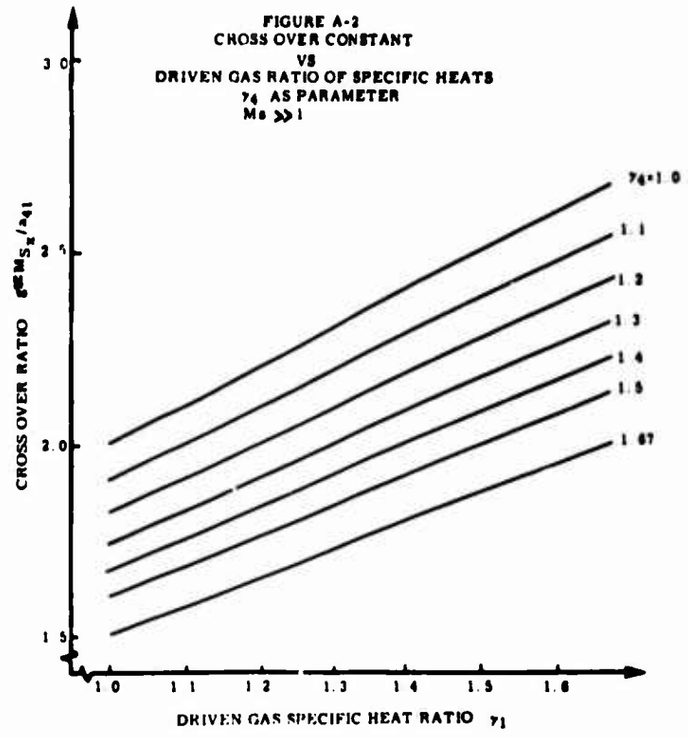
FIGURE A 1

CROSS OVER SHOCK MACH NUMBER
VS
DIAPHRAGM SPEED OF SOUND RATIO



M_{S_X} CROSS-OVER SHOCK MACH NUMBER

FIGURE A-2
CROSS OVER CONSTANT
VS
DRIVEN GAS RATIO OF SPECIFIC HEATS
γ_4 AS PARAMETER
$M_S \gg 1$



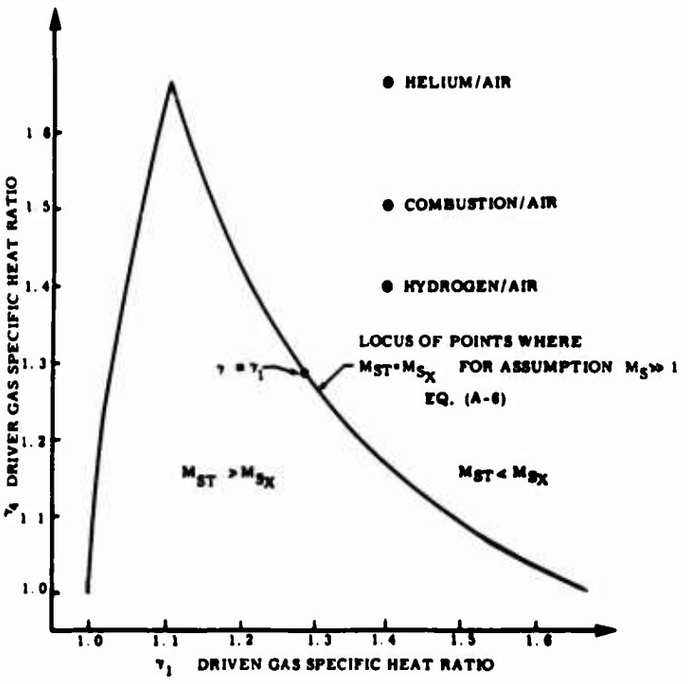


FIGURE A-3
RATIO OF SPECIFIC HEAT COMBINATIONS
THAT YIELD $M_{ST} = M_{S_X}$ FOR $M_S \gg 1$

BLANK PAGE

COMBUSTION STUDIES IN THE UTIAS HYPERSONIC SHOCK TUNNEL DRIVER

R. P. Mason* and N. M. Reddy*
Institute for Aerospace Studies, University of Toronto
Toronto, Canada

ABSTRACT

The relative advantages and disadvantages of heated, electrically heated and combustion drivers are discussed. It is pointed out that for many applications, particularly when simplicity and low cost are at a premium, the combustion driver offers many advantages. Many workers, however, have found that this method is limited by its lack of repeatability, unless special precautions are taken. The work done at UTIAS in a 2-in.x 2in. shock tube using a crimped aluminum wire confirmed that even great care could not prevent occasional combustion problems, especially detonations. However, a method employing tungsten wire has been proven to give smooth and repeatable combustion even with 60% helium dilution in a stoichiometric hydrogen-oxygen mixture. The method requires no special care and is simple, cheap and reliable. In conjunction with a program of diaphragm calibration, the method has been employed to give extremely repeatable tailored interface operation. Tailoring Mach numbers from 6 to 9.5 have been achieved by using both constant volume and constant volume-constant pressure driving techniques.

INTRODUCTION

A hypersonic shock tunnel requires a driver which is capable of both high pressures and temperatures, the reason for the latter being that tailored operation at high shock Mach numbers is usually required

For example, room temperature helium tailors at shock Mach numbers of 3.3, whereas if heated in some fashion to 700°K the tailored Mach number is about 5.5 (ref. 1). Various methods of heating the driver gas have been employed, namely,

---

* Research Fellow

(a) Heating the driver gas in the tube by means of a heated jacket (ref. 1), known as the heated driver.

(b) Electrically heated driver (ref. 2)

(c) Combustion heating by burning stoichiometric mixture of oxygen and hydrogen with helium dilution.

The disadvantages of the heated driver are many, including the technical problems of pumping, storing and transferring gases at high pressures, sealing of hot driver gases at high pressures up to 30,000 psi without the use of organic seals of any kind, and the uncertain distribution of temperature within the driver gas. However, even when these are solved, the basic limitation of temperatures due to strength considerations makes the method unsuitable for tailored operation of a shock tunnel at large enthalpies.

Another promising technique is the electrically heated driver. Theoretically, constant volume combustion of stoichiometric oxygen and hydrogen mixtures diluted with 70% helium will produce a tailored shock Mach number of 11 (ref. 2). However attenuation and heat losses to the driver wall reduce the values that can be obtained in practice to about 7 or 8. The disadvantages of this are: a) The initial pressure governs the final driver temperature and indirectly controls the radiative losses to the driver wall, and hence the final temperature and pressure that can be obtained. b) Erosion of driver liner material contaminates the test flow.

There are many advantages offered by combustion-drivers, namely that there are no high pressure and temperature problems, the method is simple, cheap and no contamination of test gas if a heated tungsten wire is used to ignite the mixture. Also, the operation of a hypersonic shock tunnel at tailored shock Mach numbers up to 10.0 comes within the capability of a research institution with limited funds. The occasional occurance of detonation in the comoustion driven technique which has influenced many research workers to abandon this method, could be avoided entirely by using the heated wire technique (this method was initiated by Hendershot, see Ref. 3) and observing some special precautions. Thus, the main aim of this note is to describe these aspects of the problem.

IGNITION SYSTEMS FOR COMBUSTION DRIVERS

The success of combustion drivers mainly depends on the way in which combustion is initiated. Point ignition was used in almost all the early methods so that detonation was frequently experienced. The possibility of point ignition is completely eliminated in the heated wire technique by heating the wire throughout its length just enough to initiate burning of the combustible mixture. The wire contamination problem, which frequently accompanied the early methods, is entirely avoided by retaining the wire after combustion. The various ignition methods employed and their relative advantages and disadvantages are outlined in Table I.

It can be seen from Table I that the method employing a heated tungsten wire such as used at UTIAS has many advantages, whereas no disadvantages have been found to date. The wire is a General Electric tungsten wire of 0.010 in. diameter and an energy of 280 joules is discharged from a 50 μF capacitors into the 7 ft. length, causing it to glow bright (cherry) red.

CONTAINED COMBUSTION STUDIES IN THE 2-in. x 2-in. SHOCK TUBE DRIVER

Although considerable care was taken at all times, occasionally erratic combustion and detonation were being encountered with the crimped aluminum wire used at one time in the 2-in.x 2-in. driver. Figure 1 shows a pressure history of erratic combustion with helium dilution as high as 80 per cent.

However, a later series of tests using the heated wire technique immediately brought about an improvement, such that relatively smooth and repeatable combustion was obtained even with 65 per cent helium dilution, as shown in Fig. 2. It is interesting to note that there are two successive runs on Fig. 2, which were so similar that the two traces are almost completely superimposed. An added advantage was that the wire can be reused, as many as five times, without encountering combustion problems. The pressure rises obtained at different initial pressures and dilutions are plotted in Fig. 3, and compared with the analysis of ref. 4. The time to reach peak pressure is also plotted in Fig. 4. In both cases the results are similar to those reported in ref. 5.

APPLICATION OF THE COMBUSTION DRIVER TO THE OPERATION OF SHOCK TUNNEL

Having obtained repeatable combustion, the first criterion for repeatable operation of shock tunnel had been met, the second being the repeatability of bursting strength of diaphragms. The latter is not exceptionally stringent if tailoring is required in the range of shock Mach numbers up to $M_s = 7.0$, when constant volume combustion is utilized. However, if partial constant pressure combustion (ref. 6) is used to achieve tailoring shock Mach numbers up to 10, then the accuracy of diaphragm bursting strength is more important.

Detailed calibration of diaphragm strength both in a static calibration rig and in the 2-in.x 2-in. shock tube was done. The diaphragms used are stainless steel of thickness varying from 0.019 to 0.047 inches. They are cut with a tolerance of 0.0005 in. by means of a milling cutter (see ref. 7). Samples of the diaphragms are tested by bursting in a Hydraulic Test Rig described in ref. 8. Both in the shock tube and in the test rig the standard deviations of bursting pressure averaged about ± 10 per cent. The bursting pressures of diaphragms of 0.029 in. thickness are given in Fig. 5. The lengths of the vertical bars indicate the experimental scatter in bursting strength.

INVESTIGATION OF TAILORING CONDITIONS

Detonation-free, repeatable combustion is necessary for successful operation of a hypersonic shock tunnel, especially, if tailored interface operation is desired. After having obtained smooth, repeatable combustion using a heated tungsten wire, this method was utilized to obtain a range of tailoring shock Mach numbers. Constant volume combustion with different helium dilutions is employed to obtain tailoring shock Mach numbers in air. The tailoring shock Mach number is that which gives a reflected Mach wave when the reflected shock refracts at the contact surface and gives a reflected pressure history which remains constant during the tunnel running time. This condition is achieved by varying channel pressure for a given combination of initial charging pressure and helium dilution. Some typical tailored pressure histories as well as combustion pressure histories are shown in Fig. 6.

Tailoring shock Mach numbers attainable from constant volume burning is limited by the attenuation of the incident shock wave in the channel. However, it has been shown in refs. 6 and 9 that by using partial constant pressure burning tailoring shock Mach numbers could be extended up to $M_s = 10$. This principle was used in the 2-in. x 2-in. shock tube to extend the range of tailored shock Mach numbers. During these runs helium dilution was tried at 70 per cent, and "over-pressure" combustion ratios varied from 1.27 to 1.67. (This ratio is defined as the ratio of pressure rise in contained combustion to the pressure rise at the instant of diaphragm rupture.) Tailored shock Mach numbers were extended up to 9.45. Typical reflected pressure histories are shown in Fig. 7. The first three (a to c) pressure traces in Fig. 7 are considered tailored. The slight rise in the reflected pressure histories is probably due to the arrival of the tail of the rarefaction wave from the diaphragm station. The fourth trace (d) is slightly over-tailored, since the reflected pressure history increases with time. Further details are given in ref. 10.

CONCLUSIONS

Provided that simple precautions are taken regarding cleanliness of the high-voltage contact points and wire tightness, it has been demonstrated that very repeatable and smooth combustion can be achieved using the heated tungsten wire technique. The same technique was used to obtain tailoring shock Mach numbers up to $M_s = 9.45$. Under these operating conditions repeatable detonation-free combustion, and repeatable diaphragm bursting strength are the deciding factors. The combustion method has the advantage of simplicity and low cost, which is well within the capabilities of small research institutions.

ACKNOWLEDGEMENTS

We should like to thank Dr. G.N. Patterson for providing us with the opportunity to do this research at UTIAS.

This research was supervised by Dr. I.I. Glass and we wish to express our appreciation for his valuable discussions, suggestions and guidance.

This work was supported under contract by the U.S. Air Force AFOSR-365-65, and NASA NsG 633 and the Canadian Defence Research Board and National Research Council.

REFERENCES

(1) Bird, K.D., Martin, J.F., and Bell, T.J., Recent Developments in the Use of the Hypersonic Shock Tunnel as a Research and Development Facility. Third Hypervelocity Techniques Symposium. pp. 7 - 51 Denver (March 1964).

(2) Flagg, R.F., Advances in Shock Tunnel Driving Techniques. Third Hypervelocity Techniques Symposium, pp. 89-116, Denver (March 1964).

(3) Hendershot, K.C., Development of a Combustion Driven Shock Tunnel. Proceedings of Hypervelocity Techniques Symposium, Institute of Aerospace Sciences (1960).

(4) Benoit, A., Thermodynamic and Composition Data for Constant-Volume Combustion of Stoichiometric Mixtures of Hydrogen-Oxygen Diluted with Helium or Hydrogen, UTIAS T.N. 85 (Nov. 1964).

(5) Nagamatsu, H.T., Martin, E.O., Combustion Investigation in the Hypersonic Shock Tunnel Driver Section, J. Appl. Phys. Vol. 30, No. 7, pp. 1018 - 1021 (July 1959).

(6) Weisblatt, H., Flagg, R.F., Experimental Technique for Tailored Operation of a Combustion Driven Shock Tunnel. Proceedings of 4th Shock Tube Symposium. Aberdeen Proving Ground (April 1961).

(7) Drewry, J.E., Walenta, Z.A., Determination of Diaphragm Opening Times and Use of Diaphragm Particle Traps in a Hypersonic Shock Tube. UTIAS T.N. 90 (see also the paper by above authors in this volume).

(8) Boyer, A.G., Design, Instrumentation, and Performance of the UTIAS 4-in.x 7-in. Hypersonic Shock Tube. UTIAS Report No. 99 (to be issued).

(9) Flagg, R.F., Detailed Analysis of Shock Tube Tailored Conditions. AVCO-RAD-TN-63-64 (Sept. 63).

(10) Chan, Y.Y., Mason, R.P., Reddy, N.M., Instrumentation and Calibration of UTIAS 11" x 15" Hypersonic Shock Tunnel, UTIAS Technical Note No. 91 (1965),

(11) Wittliff, C.E., Wilson, M.R., Shock Tube Driver Techniques and Attenuation Measurements, CAL Report AD-1052-A-4 (Aug. 1957).

(12) "Private communication", Naval Ordnance Laboratories, Maryland.

TABLE I

Method	Advantages	Disadvantages
(a) crimped wire (ref. 11 and 8)	1) Theoretically good, gives multi-point ignition	1) Difficulty in handling wire without breakage 2) High accuracy required in crimping 3) Energy used to explode wire must be exact. 4) Wire breaks into pieces and is carried down the tube as projectiles. Any failure in the first three requirements assists detonation.
(b) exploding wire (ref 3)	1) Line ignition	1) Energy used is very critical 2) Wire vaporizes and contaminates the tube. 3) Particles can act as projectiles.
(c) aluminum foil (ref. 12)	1) Multi-point ignition	1) Difficulties in manufacture and handling. 2) Foil breaks causing contamination
(d) multiple spark systems (ref. 5)	1) Multi-point ignition 2) No contamination	1) Spark plugs must be checked and maintained frequently 2) Large number of plug holes required in driver which causes problems in driver design. 3) Failure of single plug causes hazards. 4) Not all workers have had success with this method. It appears to be a function of tube geometry.

TABLE I (con'd)

Method	Advantages	Disadvantages
(e) Heated Tungsten Wire (ref. 3)	1) Wire stays in place, hence no contamination 2) Even and line ignition 3) Low energy requirement 4) Easy handling, wire is tough 5) Energy requirement is not too critical. 6) Wire can be used many times	

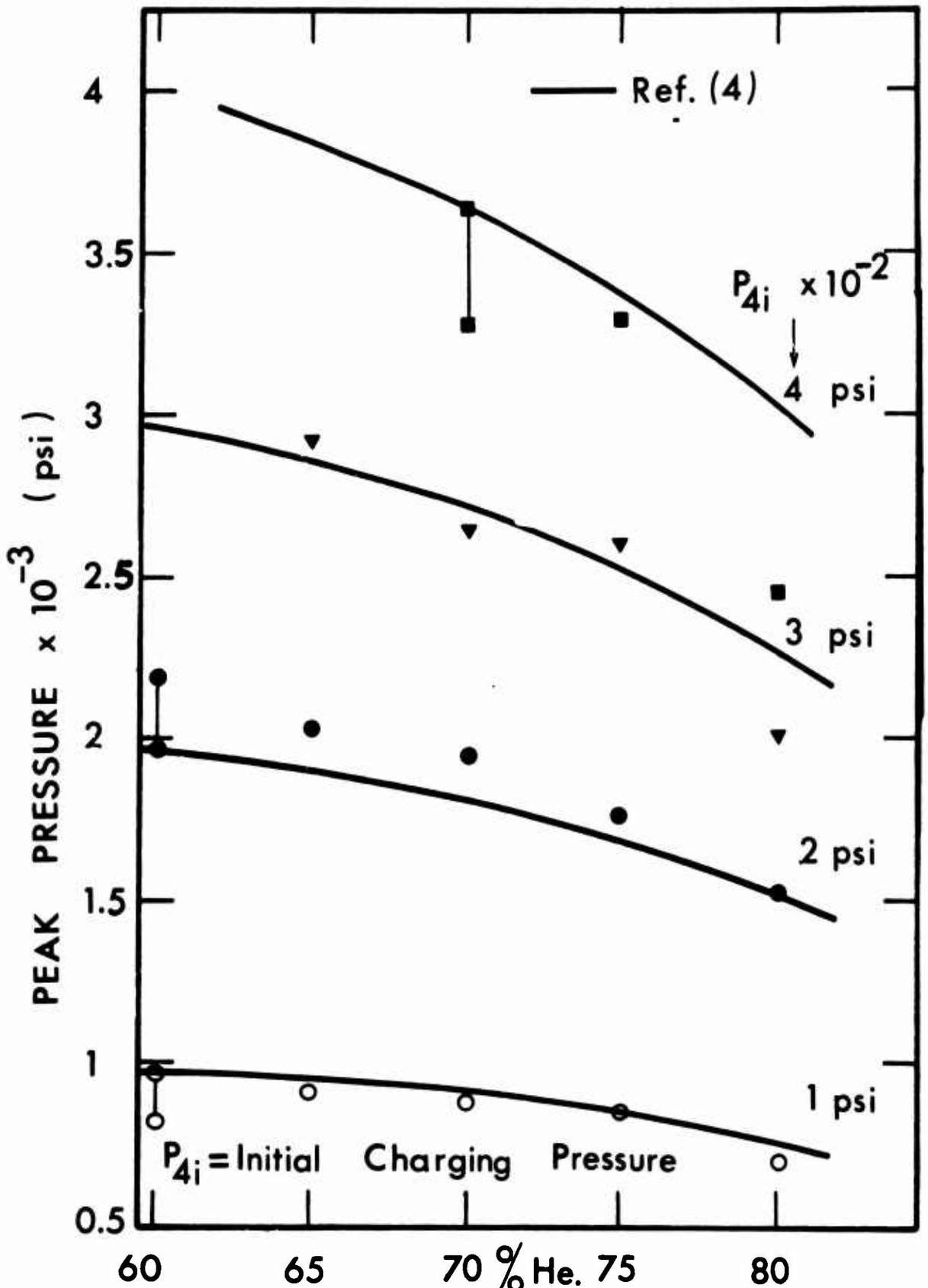


FIG. 3 PEAK PRESSURE VERSUS HELIUM DILUTION (Constant Volume Combustion)

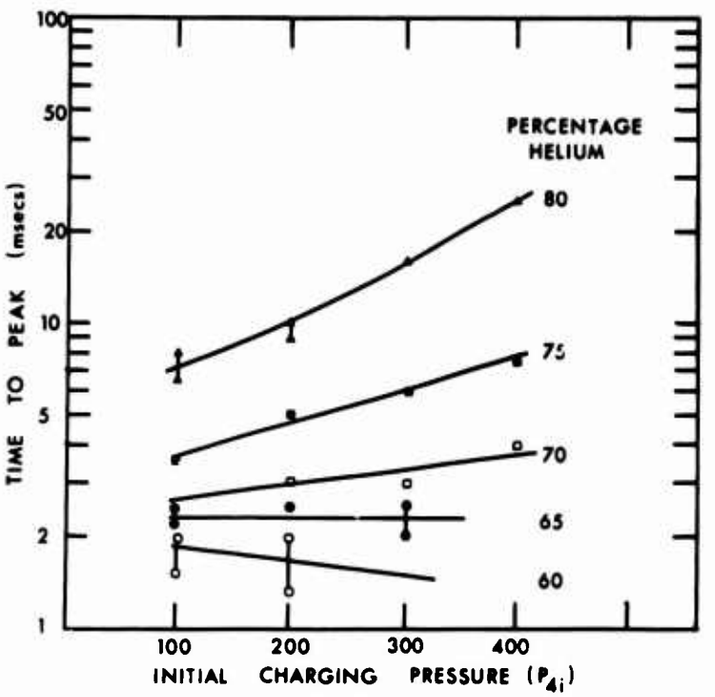


FIG. 4 TIME TO PEAK VERSUS INITIAL CHARGING PRESSURE (P_{4i})

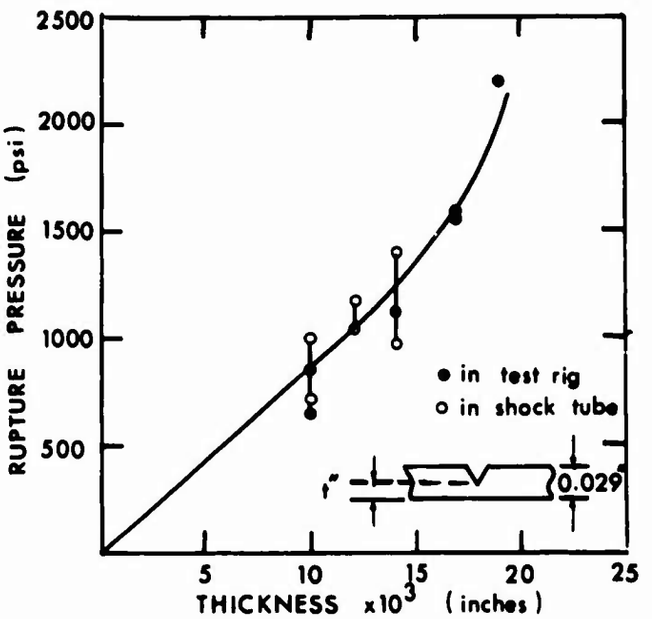
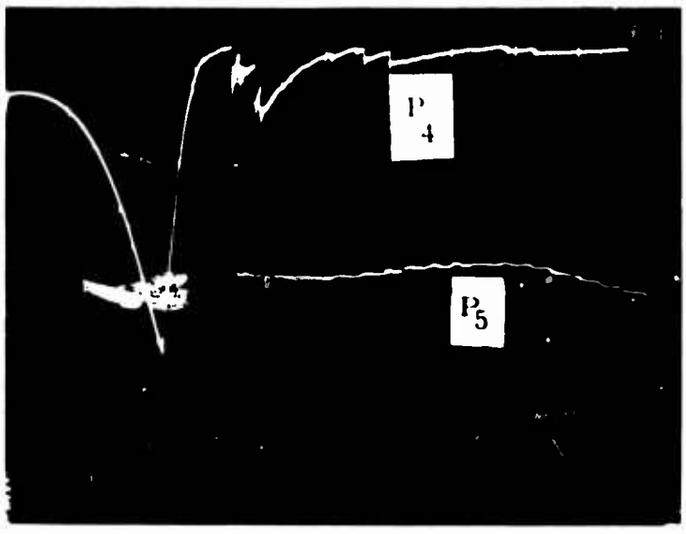
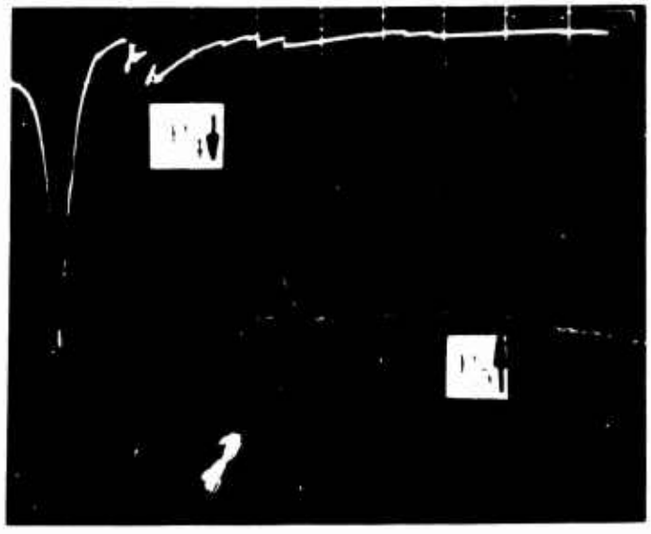


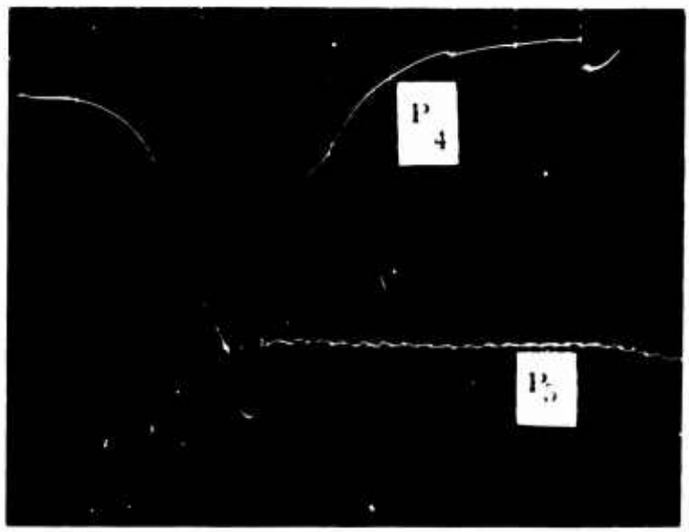
FIG. 5 VARIATION OF DIAPHRAGM RUPTURE PRESSURE WITH THICKNESS



a) 80% Helium; M_s=6.12
Horiz: 1div=200μsec.
Vert : 1div=330 psi.
(both traces)

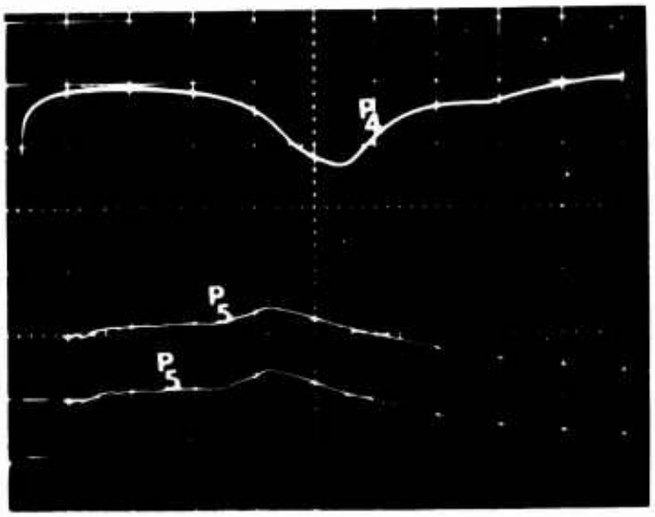


b) 75% Helium; M_s=6.64
Horiz: 1div=200μsec.
Vert : 1div=330 psi.
(both traces)

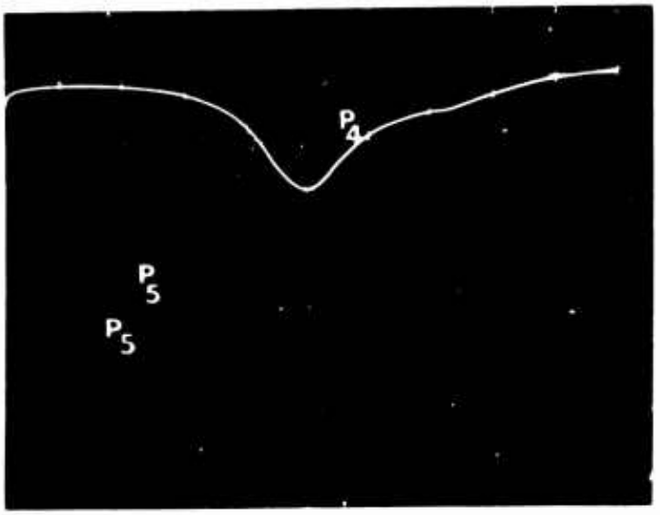


c) 70% Helium; M_s=7.42
Horiz: 1div=200μsec.
Vert : 1div=330 psi.
(both traces)

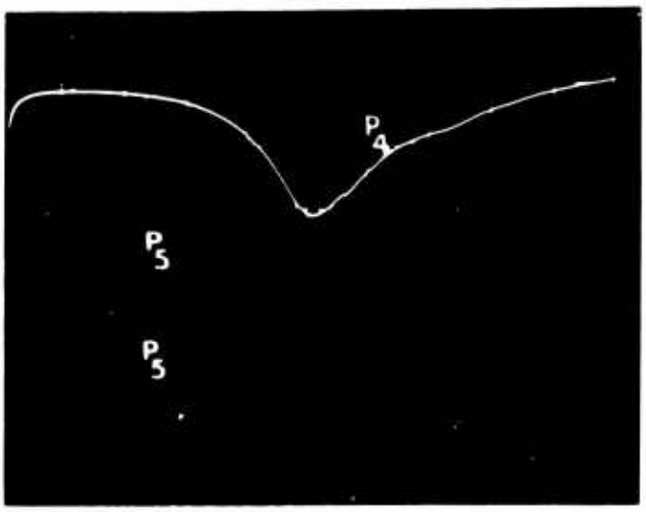
FIG. 6 REFLECTED PRESSURE (TAILORED) HISTORIES AT DIFFERENT HELIUM DILUTIONS (Constant Volume Combustion)



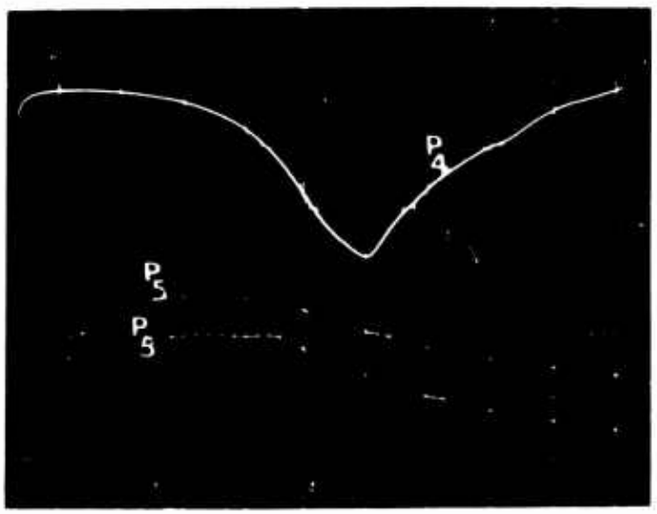
a) M_s=8.18; Overpressure Ratio=1.27
Horiz. Scale: 1div=0.5 msec.
Middle Trace: 1div=200 psi.
Lower Trace: 1div=240 psi.



b) M_s=8.74; Overpressure Ratio=1.42
Horiz. Scale: 1div=0.5 msec.
Middle Trace: 1div=480 psi.
Lower Trace: 1div=100 psi.



c) M_s=9.45; Overpressure Ratio=1.50
Horiz. Scale: 1div=0.5 msec.
Middle Trace: 1div=200 psi.
Lower Trace: 1div=240 psi.



d) M_s=9.85; Overpressure Ratio=1.67
Horiz. Scale: 1div=0.5 msec.
Middle Trace: 1div=400 psi.
Lower Trace: 1div=480 psi.

FIG. 7 **REFLECTED PRESSURE HISTORIES WITH DIFFERENT "OVER-PRESSURE COMBUSTION RATIOS" (CONSTANT VOLUME-CONSTANT PRESSURE COMBUSTION)**
Helium Dilution: 70%
Test Gas : Oxygen

BLANK PAGE

AN MHD AUGMENTED DRIVER SHOCK TUBE

R. Leon Leonard and Peter H. Rose
Avco-Everett Research Laboratory
Everett, Massachusetts

ABSTRACT

A j x B accelerator has been placed just downstream of the driver diaphragm in an electric arc driven shock tube to augment the velocity of the driver gas and permit shock front velocities in excess of the limit now imposed by radiation losses within the arc driver. The driver gas is helium seeded with potassium. The j x B accelerator has a spatially decreasing B field of 40 kilogauss peak magnitude which permits constant current density and constant gas temperature along the channel. Total currents up to 400,000 amps are possible using a 120 kilojoule capacitor bank as an energy source. With an energy input of 67,000 joules to the arc driver and 43,000 joules to the accelerator, the system yields a front velocity of 12 mm/μs; putting that 110,000 joules into the driver alone yields 9 mm/μs. The duration of test gas with the accelerator operating is the same as with the shock tube alone, between 5 and 10 μs. Shock velocities up to 22 mm/μs are predicted for the shock tube accelerator combination at the maximum available power level. The advantage of this technique is its production of a clean, homogeneous test gas with properties established by the Rankine-Hugoniot relations.

AN MHD AUGMENTED DRIVER SHOCK TUBE

R. Leon Leonard and Peter H. Rose
Avco-Everett Research Laboratory
Everett, Massachusetts

INTRODUCTION

High enthalpy technology encompasses many fields, and the availability of laboratory tools for creating dissociated and ionized gases has promoted much of the interest in this area. The shock tube has been unique in this technology because of its ability to produce a gas sample of well defined properties in a simple one-step process. However, many problems such as the simulation of the flow occurring during superorbital entry, the simulation of strong blast waves from nuclear explosions, and the creation of a flow in which radiation is the dominant transport mechanism, are presently outside the limits of shock tube technology.

The electric arc driven shock tube[1] has made inroads in all of the above mentioned problems, extending shock tube simulation into the superorbital entry regime,[2] simulating blast conditions within a few hundred feet of the blast origin,[3] and reaching the limit of radiation as a transport mechanism.[4] Although the electric arc driven shock tube pushed further toward the above objectives than previously possible, a higher energy facility is needed to generate a flow completely dominated by radiation.

Attempts to extend the operating limit of the electric arc driven shock tube to achieve higher shock velocities by adding more electrical energy to the arc driver have not been successful. The limitation appears to be on the energy which can be stored in the shock tube driver. This is limited due to radiative losses occurring in the stagnant driver gas while the driver diaphragm is opening. It was shown in Ref. 1 that the practical upper limit to the temperature of helium as a driver gas due to this effect is about 20,000°K, and for an initial driven tube pressure of 0.1 mm Hg, this produces a shock velocity of at most 14 mm/μs.

This radiation limitation cannot be easily circumvented, so that

attainment of higher enthalpies demands use of a new technique. One technique which has been applied with reasonable success to the problem of energy addition to a flow has been the use of a pulsed j x B accelerator in the shock tube (Refs. 5 and 6). In those experiments, a j x B accelerator placed far downstream of the driver diaphragm in a combustion driven shock tube added kinetic energy to the shocked gas - Argon - which had been sufficiently ionized by the incident shock to have an electrical conductivity above 1000 mho/m. Maximum velocities of the accelerated gas of above 12 km/sec were observed (Ref. 6), but the technique was plagued by both an excessive drop in shock velocity at the exit to the accelerator and uncertainty as to the thermodynamic state of the test gas after it had been accelerated.

In order to maintain the inherent simplicity of the gas dynamic shock tube and thus avoid the question of determining the thermodynamic state of the test gas, as well as circumventing any possible test gas contamination due to seed materials or electrode ablation in an accelerator, the magnetohydrodynamically augmented driver shock tube (M. A. D. Shock Tube) was conceived. In this device, the Lorentz force from a j x B accelerator is applied to the driver gas rather than the driven gas, consequently increasing the driver gas piston velocity so that a stronger shock is propagated. In this manner, the advantages which the accelerator offers of significantly increasing gas flow enthalpies at moderate static temperature, and pulsed operation at power levels of hundreds of megawatts where losses are low, can be achieved without undesirable effects on the test gas.

THEORY

In a conventional gasdynamic shock tube with a diaphragm separating the high and low pressure sections, the wave pattern in the x-t plane can be duplicated (neglecting viscous effects) by placing a piston at the diaphragm station and moving it downstream at the flow velocity of the shocked gas. In the MHD Augmented Driver Shock Tube, the shock tube starts exactly as in the conventional tube, but the Lorentz force applied in the accelerator section increases the velocity of the driver gas "piston," and the compression waves generated by the gas piston catch up with and steepen the shock front downstream of the accelerator. Figure 1 shows a simplified x-t diagram for this process in which it is assumed that the pressure and and temperature of the gas at the accelerator exit are the same as for Region 2, the shocked gas. The waves generated in the accelerator are shown as a discontinuous increase in shock front velocity at the accelerator exit. If the accelerator is at the diaphragm station, the flow inside will be steady and sonic at the accelerator entrance until the rearward traveling rarefaction reflected from the end of the driver enters the accelerator channel. This wave will upset the test gas and limit test time regardless of what the accelerator does subsequently. The arrival of this rarefaction then establishes the necessary operating duration for the accelerator at approximately 100 μs for the geometry and sound speeds used in the experiments described later. If the accelerator operates for this duration then, rarefaction wave limitations on shock tube test time will be no

different than for the shock tube operating without the accelerator.

To ascertain next the performance we could expect from the accelerator, we considered the accelerator an idealized "black box" with a given velocity ratio and pressure ratio across it, and inlet conditions corresponding to the diaphragm station.

The pressure ratio across the shock tube may then be written

$$\frac{P_4}{P_1} = \frac{P_4}{P_5}\,\frac{P_5}{P_6}\,\frac{P_6}{P_3}\,\frac{P_3}{P_2}\,\frac{P_2}{P_1} \tag{1}$$

where, as shown in Fig. 2, Region 4 is the stagnant driver condition, Region 5 is the condition at the accelerator entrance, assumed to be a sonic condition reached by a centered rarefaction wave, Region 6 is the condition at the accelerator exit, Region 3 is the condition behind the contact interface which is at lower pressure and higher velocity than the accelerator exit due to the second rarefaction wave also assumed centered, Region 2 is the condition in front of the contact interface in the shocked gas, and Region 1 is the stagnant driven tube condition.

As can be seen in Fig. 2, to proceed in this manner, it was necessary to separate the flow into steady and unsteady segments, or, in another sense, to assume that the accelerator occupies an infinitesmal length of the shock tube at the diaphragm section at which the area changes from driver to driven tube diameter. Further, it was necessary to assume that both the rarefactions from Region 4 to 5 and Region 6 to 3 are centered at the diaphragm station.

For the rarefaction fans, one can write the Riemann invariant as

$$\frac{2}{\gamma - 1}\, a_i + u_i = \frac{2}{\gamma - 1}\, a_j + u_j \tag{2}$$

where in going from region 4 to 5, $i = 4$, $j = 5$, $u_4 = 0$ and $u_5 = a_5$ so that

$$a_5 = \frac{2}{\gamma + 1}\, a_4 \tag{3}$$

To make the problem tractable, we assume constant specific heat ratio, and that the gases involved are perfect. Since the rarefaction fan is isentropic, we may say

$$\frac{P_i}{P_j} = \left(\frac{a_i}{a_j}\right)^{\frac{2\gamma}{\gamma - 1}} \tag{4}$$

and

$$\frac{P_4}{P_5} = \left(\frac{\gamma_4+1}{2}\right)^{\frac{2\gamma_4}{\gamma_4-1}} \tag{5}$$

Across the accelerator, we assume a constant temperature $T_5 = T_6$, and hence $a_5 = a_6$. The velocity ratio across the machine is governed by the input power,

$$W_{IN} = (1/2)\,\rho_5\, u_5\, A_5\, (u_6^2 - u_5^2) \tag{6}$$

and the density change is governed by the continuity equation,

$$\rho_5\, u_5\, A_5 = \rho_6\, u_6\, A_6$$

These may be combined and coupled with the perfect gas law to give

$$\frac{p_5}{p_6} = \left(\frac{A_6}{A_5}\right)\sqrt{\frac{2W}{\rho_5\, A_5\, u_5^3} + 1} \tag{7}$$

and

$$\frac{u_6}{u_5} = \sqrt{\frac{2W}{\rho_5\, A_5\, u_5^3} + 1} \tag{8}$$

where the effect of the input energy is determined by comparison to the flow energy at the inlet to the accelerator.

For the next rarefaction fan, i = 6 and j = 3 in the Riemann invariant, but $a_6 = a_5 = u_5$, so that we get

$$\frac{2}{\gamma_4-1}\, a_5 + u_6 = \frac{2}{\gamma_4-1}\, a_3 + u_3 \tag{9}$$

To obtain the pressure ratio, we need to solve for a_3/a_5 and this may be done in terms of known quantities by solving Eq. (9) for a_3/a_5 and using Eqs. (3) and (8) to get

$$\frac{a_3}{a_5} = 1 + \frac{\gamma-1}{2}\sqrt{\frac{2W}{\rho_5\, A_5\, u_5^3} + 1} - \frac{\gamma^2-1}{4}\,\frac{u_3}{a_4} \tag{10}$$

Velocity remains the same across the contact interface so that u_3 may be related directly to the shock front velocity. For a strong shock ($M_s > 10$), this relation is (Ref. 7)

$$u_3 = u_2 = \frac{2a_1}{\gamma_1+1} M_s \tag{11}$$

From Eq. (4) then, using Eq. (10) and Eq. (11) we get

$$\frac{P_6}{P_3} = \left[1 + \frac{\gamma-1}{2} \sqrt{\frac{2W}{\rho_5 A_5 U_5^3} + 1} - \frac{\gamma^2-1}{2(\gamma_1+1)} \frac{a_1}{a_4} M_s \right]^{\frac{2\gamma}{1-\gamma}} \tag{12}$$

Since pressure also remains constant across the contact interface,

$$\frac{P_3}{P_2} = 1 \tag{13}$$

and the pressure ratio across the shock front is well known (Ref. 7) as

$$\frac{P_2}{P_1} = \frac{2\gamma_1 M_s^2}{\gamma_1 + 1} \tag{14}$$

where again we have assumed a strong shock.

These relations for pressure, Eqs. (5), (7), (12), (13) and (14) may be combined in Eq. (1) to obtain the characteristic pressure-shock velocity relation

$$\frac{P_4}{P_1} = \left[\frac{2}{\gamma+1} + \frac{\gamma-1}{\gamma+1} \sqrt{\frac{2W}{\rho_5 A_5 u_5^3} + 1} - \frac{\gamma-1}{\gamma_1+1} \frac{a_1}{a_4} M_s \right]^{\frac{2\gamma}{1-\gamma}} \frac{A_6}{A_5} \left(\frac{2\gamma_1 M_s^2}{\gamma_1 + 1} \right) \sqrt{\frac{2W}{\rho_5 A_5 u_5^3} + 1} \tag{15}$$

This shock velocity-pressure ratio relation is shown in Fig. 3 for various values of $\frac{2W}{\rho_5 A_5 u_5^3}$. For $\frac{2W}{\rho_5 A_5 u_5^3} = 13$ and an operating duration of 100 μs, the total energy required is 100 kilojoules. The "black box" accelerator has an area ratio across it of 4, and has inlet conditions predicted by the initial pressure of and energy input to the driver. The improvement indicated with the accelerator over the shock tube alone is impressive, even if the initial pressure in the shock tube is limited to 100 μ Hg by boundary layer considerations.

The "black box" technique also permitted first order determination of effects on accelerator performance of such things as increasing static temperature through the accelerator, changing the area ratio through the accelerator, and changing the energy distribution between the shock tube driver and the accelerator.

One interesting result of these crude optimumization studies was that there is very little effect on shock tube performance when the temperature increases in the accelerator by as much as a factor of two. This is due to two things. First, radiative losses and energy invested in ionization are neglected in the black box calculation, and these effects may be significant. Second, for the same total energy input to the accelerator, an increase in temperature indicates a decrease in velocity increment. This is not an overly detremental effect in a shock tube because an isentropic rarefaction downstream of the accelerator will recover much of the thermal energy by converting it to kinetic energy. This characteristic differentiates the proposed accelerator from most of the other proposed devices where achievement of kinetic energy in the accelerator is at a premium.

Having obtained these results for the effect of the accelerator on shock tube performance, it then was necessary to see if an accelerator with characteristics such as those assumed in the "black box" analysis could be built. To perform this task, use was made of an analysis of one-dimensional MHD channel flow developed by Louis, Lothrop and Brogan (Ref. 8).

Although this analysis was developed rather specifically to predict the performance of large MHD generators, its basic form was suitable for application to the analysis of an accelerator. The program was modified for this use by including a black body radiation heat loss term since radiation losses were principally responsible for the limitations on the conventional electric arc driver shock tube, and by assuming the working fluid to be a perfect gas, which is the case for helium at temperatures below 10,000°K.[9] This second assumption immediately demanded that the gas be seeded because deviations from perfect helium are synonymous with ionization and high electrical conductivity.

Using this analysis, the accelerator inlet conditions, variation of

area, variation of magnetic field, and variation of electric field are given; and the analysis yields the variations along the channel of pressure, temperature, Mach number, and the overall heat transfer and power in.

Our solution used as inlet conditions values appropriate to the measured shock velocity and electric conductivity, an area ratio through the accelerator of 4, a maximum magnetic field strength of 40,000 gauss, and continuous electrodes at a single electrode potential.

The magnetic field strength was varied to keep the loading factor, E/uB, approximately constant. Since E [illegible], D and u increased approximately as D^2, this required that B vary approximately as D^{-3}.

Since no optimization for the channel to our particular requirements existed it was necessary in order to apply this analysis that an accelerator design be specified, and this analysis be applied to determine how well that design met our requirements of a particular velocity ratio achieved at constant static temperature in the accelerator. After obtaining results, the accelerator geometry and magnetic field distribution were altered until the requirements were satisfied.

The results of the analysis for the accelerator which was finally constructed are shown in Fig. 4. The first 5 cm at the inlet to the machine is a matching region because the maximum B field was established at 40,000 gauss. For the electrode potential suitable for the remainder of the accelerator (2800 volts) the velocity was not yet high enough to keep the loading small. The temperature increased slightly through the accelerator in this computation, but the extent of temperature increase is dependent upon the electrode potential, and at lower potential the temperature will decrease.

Because the loading and temperature are nearly constant, the current density is also nearly constant at a value of 800 A/cm^2. This current density is typical for the range of energy levels for which the analysis was carried out; and although it is quite high, it is not beyond the capability of copper electrodes; nor is it high enough to produce nonequilibrium effects in the electron temperature, principally because the gas pressure is quite high (40 atmospheres at the inlet).

Since continuous electrodes short out any Hall field, presenting a possible energy loss mechanism, it is important that the Hall coefficient remain small. This is the case since at the accelerator inlet where the magnetic field is high the pressure is also high so that the Hall coefficient is low. At the exit to the accelerator, where the pressure is low, the magnetic field is also low, and the Hall coefficient remains low. For all of the conditions at which analyses were made, the Hall coefficient stayed below 0.5.

By varying the magnetic field strength and electric field strength in the accelerator analysis, various exit conditions and total power levels

would result, and these may be displayed as the voltage-current characteristics for the accelerator. For the accelerator configuration actually constructed, these characteristics are shown in Fig. 5. The B field strength was changed by varying the current to the magnetic field coil, so that the field distribution remained constant, but the field magnitude changed. Bo is the maximum field for the magnet, corresponding to 40, 000 gauss peak field from 10, 000 amps in the field coil. To determine the operating point for the accelerator it was necessary to plot also the characteristics of the power supply for the accelerator. These characteristics will be discussed in the description of the apparatus.

For each operating point actually calculated for the accelerator, the accelerator exit flow velocity, static pressure and temperature were obtained. The flow velocity and temperature enable one to calculate the Riemann invarient for a centered rarefaction wave. From Eq. (2), with the i state the exit state and the j state behind the contact interface, we have

$$\frac{2}{\gamma-1} a_e + u_e = \frac{2}{\gamma-1} a_3 + u_3$$

and from Eq. (4),

$$\frac{P_e}{P_3} = \left(\frac{a_e}{a_3}\right)^{\frac{2\gamma}{\gamma-1}}$$

Across the shock front, Eq. (11) and Eq. (14) give the velocity and pressure which should equal P_3 and u_3. Specifying the initial pressure, we obtain this relationship from which shock Mach number may be obtained:

$$\frac{P_e}{P_1} = \frac{2\gamma_1 M_s^2}{\gamma_1+1} \left[1 + \frac{\gamma-1}{2} M_e - \frac{\gamma-1}{\gamma_1+1} \frac{a_i}{a_e} M_s\right]^{\frac{2\gamma}{1-\gamma}} \qquad (15)$$

In the above analysis, the shocked gas is assumed perfect, an assumption not valid for strong shocks. To take account of this, use was made of calculations of properties of air across normal shocks[10, 11] and the shock velocity was obtained by a simple iteration which used as an initial pressure $P_1 = 100\ \mu$ Hg. It is this information that is shown in Fig. 5 - the resultant shock velocity downstream of the accelerator for $P_1 = 100\ \mu$ Hg and for real air.

APPARATUS

Experiments have been performed in an electric arc driven shock tube of the type described by Camm and Rose.[1] The shock tube has a six inch diameter driven tube 30 feet long and terminated with a large dump tank. The driver is three inches in diameter, and is separated

from the driven tube by a stainless steel diaphragm .06 inches thick. The transition from the three inch driver to the six inch driven tube is made in the accelerator section which is located just downstream of the driver diaphragm. The arc is discharged axially in the driver along a 2 mil tungsten wire with energy from a 585 μ farad, 20 kv capacitor bank. The arc discharge is triggered using a high energy spark gap similar to the Lovotron switch described in Ref. 1.

For typical operation, the driven tube is evacuated to about 1 μ Hg pressure and then filled with room air to 100 μ Hg. The leak rate of the driven tube is less than 1 μ Hg/minute.

To improve its electrical conductivity (see RESULTS), the driver gas is seeded by spraying 6 ml of a saturated solution of potassium hydroxide in methyl alcohol into the driver before it is closed with the diaphragm. The section is then closed and evacuated to a few millimeters mercury for about 30 minutes to remove the alcohol and leave the potassium hydroxide evenly distributed on the driver walls. The driver is then filled with helium to 50 psig and the tube is ready for a run.

The accelerator channel is of circular cross section, about 5 feet long, and is made of filament wound fiberglass. The electrodes extend for 80 cm along the channel, subtending an arc of 80° from the center line. This angular segment is the optimum predicted by Fishman[12] for a circular section. The first 20 cm of electrode is in a constant three inch diameter section, and the remaining 60 cm is in the conically diverging section between the three inch and six inch diameters.

Current is delivered to the electrodes by 20 coaxial busses on each the anode and cathode, and the electrodes are segmented into 20 pieces, one for each buss. These busses are connected together at the power source so that the electrodes are continuous with regard to the shorting of hall potentials, but current is prevented from flowing axially along the electrodes within the channel. This is done to minimize the normal magnetic field which would be induced by such current flow.

The power source for the electrodes is a lumped parameter transmission line capacitor bank that delivers a square wave pulse of 100 or 200 μs duration depending on the inductors used. The characteristic impedance of the line was determined experimentally by discharging the bank through a noninductive load, and this was used to plot the V-I characteristic of the bank in Fig. 5 for each of the two operating durations. The bank has an energy storage capacity of 120 kilojoules and it is switched using four ignitrons which are triggered from the u x B potential in the channel.

Design and construction of the magnetic field coil for this experiment was made difficult because of the severe spatial variation of field strength necessitated by the requirement of constant loading factor, E/uB. Although it was difficult, a coil was constructed with a field distribution within 5%

of that shown in Fig. 4. This coil, shown in Fig. 6, is an air core copper coil, made in two halves and wound from 6 inch wide copper strip, .050 inches thick. It is powered from a 3 megawatt battery bank at a current of 10,000 amps for an operating duration of one second. The energy stored in the magnetic field is about 300,000 joules.

For a typical run, the charge voltages on the capacitor banks for the driver and accelerator are noted, as well as the initial pressures in both the driver and driven tubes.

The potential between electrodes is monitored using voltage dividers and displayed on an oscilloscope as shown in Fig. 7. The initial step increase in voltage is the u x B potential induced on the electrodes and corresponds to a flow velocity of 5000 m/sec. The second step occurs when current starts to flow between the electrodes.

The current is monitored using the intergrated output of a Rogowski coil as shown in Fig. 7. Using this technique, it is possible to monitor the current to each of the 20 electrode segments individually, giving a coarse indication of current density, but for the initial experiments, only the total current was monitored.

It can be seen from the current trace that the capacitor bank is not "matched" to the accelerator, resulting in current reversal for the second half cycle, between 200 and 400 μs after current is initiated. This occurs after the experiment is over; it does not affect the shock tube operation as can be seen in Fig. 1, and it can be corrected by changing the parameters in the transmission line.

The shock velocity was measured using two independent techniques. The outputs of nine equally spaced thin film heat transfer gauges located on the walls along the length of the shock tube were differentiated and displayed on a raster-modified oscilloscope to obtain the shock velocity and its variation along the tube. As a check on this, two photomultipliers were set 60 inches apart some four feet downstream of the accelerator looking across the shock tube. The output of these photomultipliers was monitored directly, and the shock front passage observed to obtain a front velocity. These two techniques agreed well for all of the runs made.

At the test section 30 feet downstream of the accelerator, another photomultiplier looked perpendicular to the flow similarly to those used to measure front velocity. Output from this PM is shown in Fig. 8.

In addition to these measurements the magnet current when the shock tube fires is monitored, and this current never varied detectably during the duration of the experiment.

RESULTS

One dimensional shock tube theory predicts a temperature of helium

behind the contact interface in an electric arc driven shock tube of about 8000°K. For pure helium, this temperature is insufficient to give a conductivity of the order of 100 mho/meter; the amount generally considered to be sufficient for operation of a successful MHD device in the Faraday mode. Since performance of the arc driven shock tube is partially explained by assuming contamination of the helium driver by ablation products from the walls of the shock tube driver, experiments were undertaken to determine whether these ablation products might also act as a seed material to increase the driver gas electrical conductivity.

The first experiments were made in a 1-1/2 inch diameter tube downstream of the driver diaphragm in an electric arc driven shock tube with a driver diameter of 1-1/2 inch and a driven tube diameter of six inches. The conductivity was measured for helium with no seed material deliberately added using a high frequency bridge technique.[13] The results are shown in Fig. 9. Since the bridge technique is very sensitive to boundary layers, these results should be considered as a lower limit on conductivity. The wide scatter in the data, typical for the measuring device used, is due to variations in shock tube cleanliness which strongly affects the boundary layer conductivity. It can be seen that the measured conductivity was as high as 300-400 mho/m, quite adequate for accelerator operation.

Attempts were made to design an accelerator using this driver, but the area ratio of 16 required for the accelerator to go between the driver and driven tube was too great. Accelerator designs with this area change either choked near the inlet, or the loading factor, E/uB, went below one near the exit resulting in energy extraction from the flow. This could be avoided by reducing the area ratio, but an isentropic expansion downstream of the accelerator degraded the static pressure so severely that the shock tube could not be operated at high enough initial pressure to avoid large boundary layer effects. Although experience gained on this accelerator will probably make it possible to design a larger area ratio accelerator in the future, the larger three inch diameter driver was used for this experiment.

Initial measurements of conductivity just downstream of the three inch diameter driver diaphragm gave results shown in Fig. 10. It is seen that for unseeded helium, the conductivity in this device was at least a factor of 30 below that for the 1-1/2 inch driver. No completely acceptable explanation for this has been offered, but the situation clearly required the addition of a seed material with lower ionization potential than the driver ablation products. Both potassium hydroxide and cesium chloride were tried, using the injection technique described earlier, with the results shown in Fig. 10. The failure of the CsCl to produce higher conductivities in spite of the lower ionization potential for cesium is due to the large electron attachment characteristic of chlorine. Better conductivities could probably have been realized with cesium hydroxide, but the expense and handling difficulties present with CsOH plus the acceptable results obtained for KOH led us to select the latter as seed material.

Before power was applied to the accelerator, a number of runs were

made with only the applied B field, and with the electrodes open circuited in both the axial and transverse directions so that the accelerator was operated as a flowmeter. Typical data for these runs is shown in Fig. 11. Three bits of information could be obtained from these tests. First, the shock velocity could be determined from the time between the appearance of voltage on sequential electrode pairs. Second, neglecting the effects of a circular channel, assuming one dimensional flow, and assuming an infinite measuring impedance, the flow velocity could be determined by

$$u = \frac{V}{hB}$$

where V is the open circuit voltage, h is the distance between electrodes equal to the channel diameter, and B is the magnetic field strength. Third, since the magnetic field is constant for the duration of the experiment, the duration of steady flow and the variation of flow velocity with time can be determined from the voltage variations with time.

Figure 12 shows the x-t diagram for the shock tube (using the accelerator channel only as a flowmeter, with no power applied) for one run as constructed from the flowmeter data. In this figure, the voltage data such as shown in Fig. 11 is converted to velocity, and the short lines are path lines of the flow, with the particle velocity indicated by the slope of the lines. The rarefaction fan was then drawn by connecting points of constant velocity. Steepening of the shock front can be observed, and by extrapolating the data back to the diaphragm station an effective time of opening for the diaphragm can be identified. This time corresponds roughly to the time at which light is first observed by a photomultiplier looking from the dump tank at the downstream face of the diaphragm.

From this diagram one can also get an idea of the steadiness of the flow into the accelerator during its operation. Steady flow would be indicated if all of the path lines were parallel, and consequently no rarefaction waves were present. This is seen clearly not to be the case, with the flow at the accelerator inlet for this run varying between about 4000 and 2800 m/sec over the 100 μs operating duration. This assumes that one waits until the accelerator channel is full before starting current. It would be desireable to have as high an inlet velocity to the accelerator as possible, but attempts to operate the accelerator from the time flow appeared at the first electrode yielded very poor results. Much more satisfactory operation was obtained by turning on the accelerator after the channel was full. It is only this latter acceleration data that will be reported here. Research is continuing to determine whether a partially full channel may give best performance.

The accelerator has been operated under power at two levels of total energy input, 45,000 joules and 59,000 joules for power levels of approximately 180 MW and 290 MW respectively. For all the runs made, data has been taken of electrode potential, total current, shock front velocity and shock tube test time.

The electrode potential and current are shown in Figs. 13 and 14 for the 43,000 joule runs. The theory plotted is obtained from Fig. 5 by taking the appropriate capacitor bank charge voltage characteristic (V=6KV), and for accelerator characteristics corresponding to various B/B_o, noting the predicted voltage and current. The quantity B/B_o is the fraction of design B field (40 kgauss peak), and is obtained experimentally by measuring the current delivered to the B field coil and comparing that to the design current of 10,000 amps.

The predicted electrode potential and current do not vary greatly and the data shows this same insensitivity to variations in magnetic field, as well as the proper magnitude of both potential and current. The error bars noted on the values recorded for electrode potential are variations in the time history of potential, rather than a spatial variation. This variation is probably due to unsteadiness in the flow as discussed earlier.

The shock front velocity observed downstream of the accelerator is plotted in Fig. 15 against the total relative Lorentz force, $I\ B/B_o$. The present equipment has been operated only up to a value of $I\ B/B_o$ of 100 kA out of a total capability of about 300 kA, and although the data is below the theoretical velocity increase for the accelerator, the data indicates an increased efficiency at greater force levels. One feature of the data that was observed was a distinct increase in the shock front attenuation along the length of the tube as higher and higher velocities were attained. This can be seen from the increasing length of error bars whose extremes were the velocities far upstream and far downstream in the driven tube.

As is mentioned in Ref. 3, runs made in electric shock tubes frequently have no test time due to turbulence at the contact interface as a result of the driver diaphragm opening. This occurs on about 1/3 to 1/2 of the runs and is also the case with the MHD augmented driver shock tube. Considerable speculation existed early in the program on whether the acceleration of the driver gas would aggravate this turbulent instability. An oscillogram of a photomultiplier output is shown in Fig. 8. This run, made at slightly greater than 10 mm/μs shock velocity shows the characteristic radiation overshoot at the shock front followed by 7 μs of homogeneous test gas, and then the contact interface. Test times and frequency of bad runs are about the same for MHD augmented driver shock tube as for conventional electric arc-driven shock tubes.

CONCLUSIONS

Preliminary results obtained with the MHD augmented driver shock tube indicate that it will be a feasible technique for attaining higher shock velocities than possible with the electric arc driven shock tube. The test time of the shock tube is not adversely affected by the acceleration mechanism, and the gross characteristics of the accelerator operation are understood.

Future work with this accelerator device will include the development

of higher resolution diagnostics so that a better comparison between the experimental operation and the theoretical model can be made. Also, attempts will be made to find the optimum starting procedure for the accelerator so that maximum velocity increase and minimum disturbance due to rarefaction waves will result. Finally, higher energy level operation will be attempted so that higher shock velocities will be obtained. Precursor effects due to radiative heating and test slug cooling to the shock tube walls are areas of interest which have not been attainable with previously available shock tubes, and these effects should provide much interesting information.

REFERENCES

(1) Camm, J. C. and Rose, P. H., "Electric Shock Tube for High Velocity Simulation," Phys. of Fluids 6:663-678 (May 1963); also Avco-Everett Research Laboratory Report 136, July 1962.

(2) Rose, P. H. and Stankevics, J. O., "Stagnation Point Heat Transfer Measurements in Partially Ionized Air," AIAA J, 1:2752-63, December 1963; also Avco-Everett Research Laboratory Report 143, April 1963.

(3) Taylor, G. I., "The Formation of a Blast Wave by a Very Intense Explosion. II. The Atomic Explosion of 1945," Proc. Roy. Soc., London, Series A 201, 175-186, 1950.

(4) Johannsen, N. H. and Hoshizaki, H., "Effect of Radiation on Flow Properties Behind Strong Shock Waves in Air," AIAA J. 1, 713, March 1963.

(5) Hogan, W. T., "An Experimental Investigation of a Magneto-gasdynamic Accelerator, MIT, Dept. of Mechanical Engineering, Magneto-gasdynamic Laboratory Report No. 62-1, January 1962; also Mather, N. W. and Sutton, G. W., ed., Third Symp. Engr. Aspects of Magnetohydrodynamics, Gordon and Breach, 1964.

(6) Leonard, R. L. and Fay, J. A., "Experiments on a Quasi-Steady j x B Accelerator," AIAA J 3:115-121, January 1965.

(7) Resler, E. L., Lin, S. C. and Kantrowitz, A. R., "The Production of High Temperature Gases in Shock Tubes, J. of App. Physics, 23:1390-1399, December 1952.

(8) Louis, J. F., Lothrop, J. and Brogan, T. R., "Studies of Fluid Mechanics Using a Large Combustion Driven MHD Generator," Phys. of Fluids, 7:362-374, March 1964; also Avco-Everett Research Laboratory Report 145, March 1963.

(9) Lick, W. J. and Emmons, H. W., "Thermodynamic Properties of Helium to 50, 000°K," Harvard University Press, 1962.

(10) Feldman, S., "Hypersonic Gas Dynamic Charts for Equilibrium Air," Avco-Everett Research Laboratory Report 40, January 1957.

(11) Laird, J. D. and Heron, K., "Shock Tube Gasdynamic Charts, Part 1: Equilibrium Argon Free Air from 3000 to 40, 000°K," Avco Research and Advanced Development Division, TM 64-12, April 1964.

(12) Fishman, F., "Steady MHD Flow Through a Channel of Circular Section," Avco-Everett Research Laboratory Report 97, December 1960.

(13) Koritz, H. E. and Keck, J. C., "A Technique for Measuring the Electrical Conductivity of Wakes of Projectiles at Hypersonic Speeds," Rev. Sci. Instr. 35:201-208, February 1964; also Avco-Everett Research Laboratory Report 167, September 1963.

M.H.D. AUGMENTED SHOCK TUBE

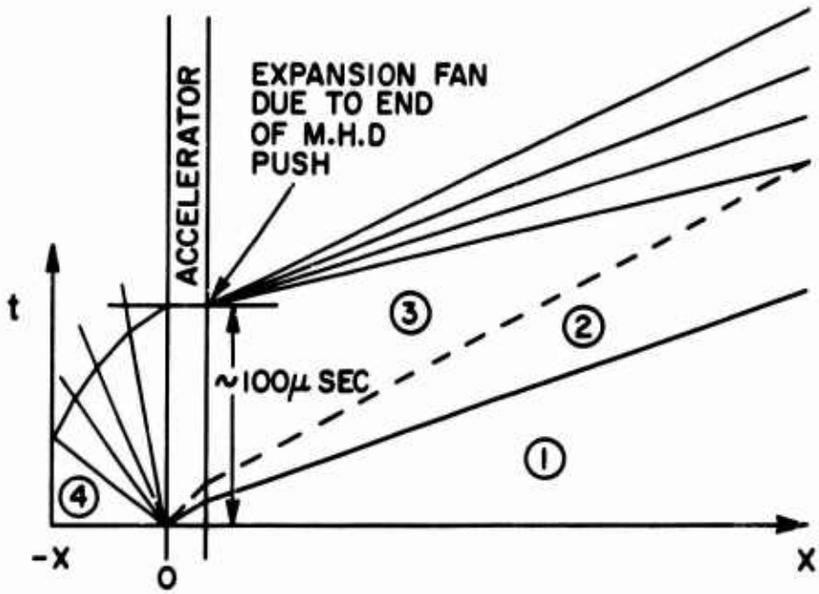


Fig. 1 The distance time (x-t) diagram for the MHD augmented shock tube. The case shown is that for which the accelerator exit is "matched" to the initial shock tube pressure; that is, no upstream facing rarefaction wave sits at the accelerator exit.

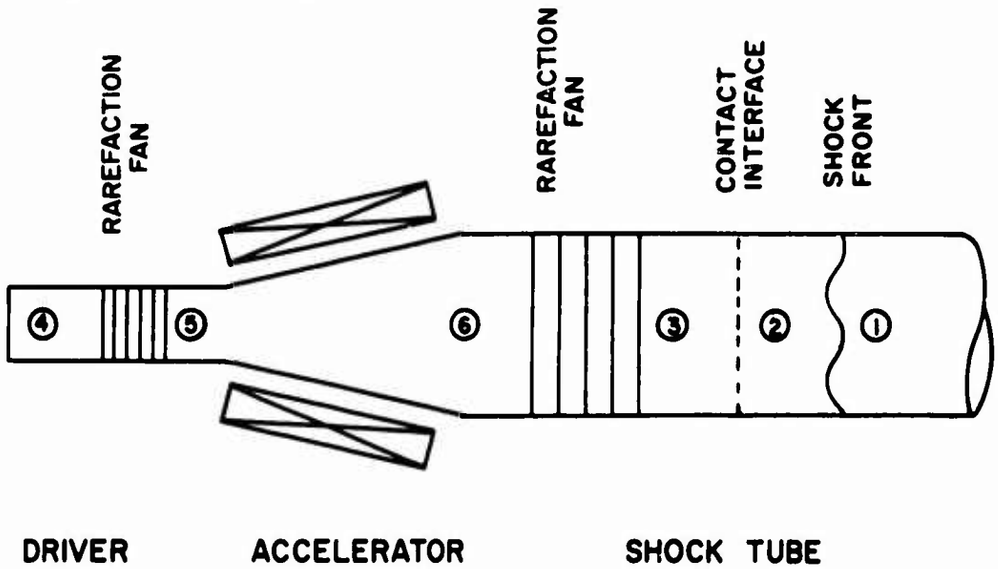


Fig. 2 Shock tube wave location with the MHD accelerator operating. The upstream rarefaction expands the flow to sonic conditions from which it is accelerated supersonically. The strength of the second rarefaction is determined by the initial pressure in the shock tube.

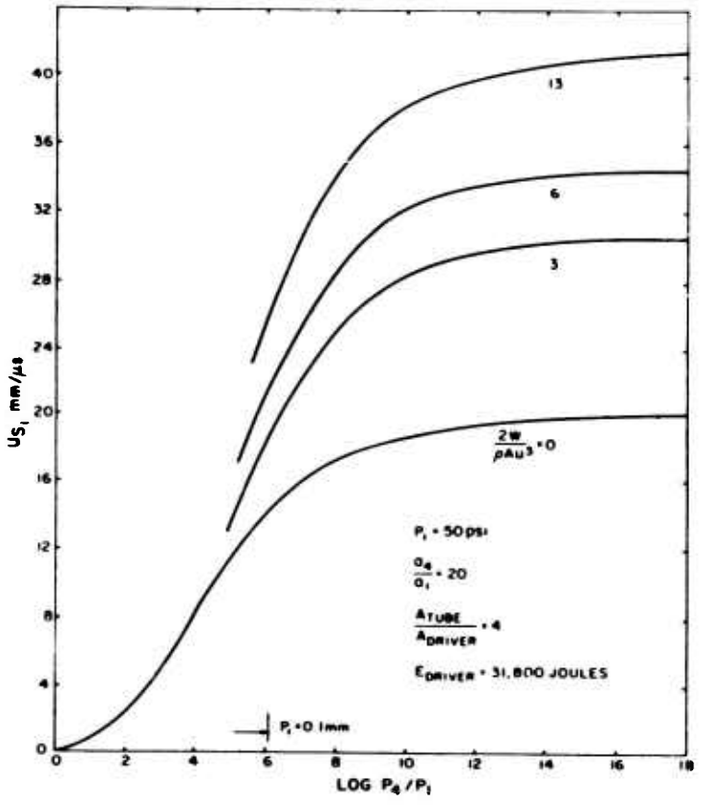


Fig 3 Shock velocity vs driver to driver tube pressure ratio for the accelerator of Fig. 2. A dimensionless energy input $W \rho Au^3 = 1$ corresponds in this experiment to an energy input of 100,000 joules and an operating duration of 100μs.

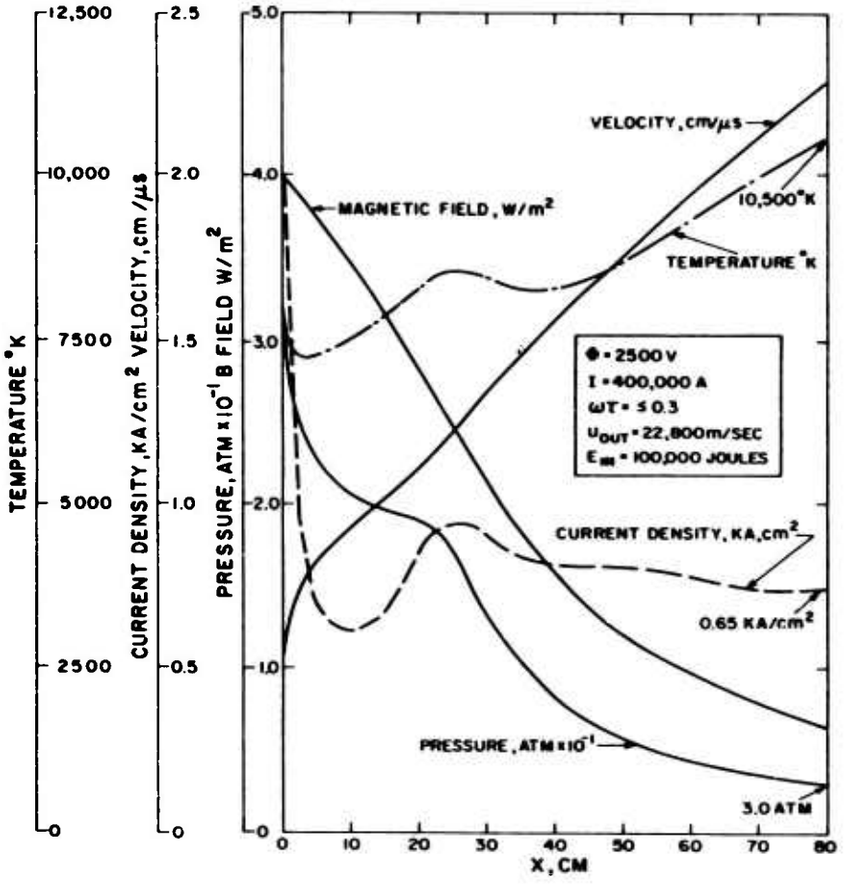


Fig. 4 Distribution of properties and fields through the accelerator channel at the design condition using the analysis developed by Louis, et al (Ref. 8). The channel is a constant 3" in diameter for the first 20 cm and then diverges conically for the last 60 cm to a diameter of 6".

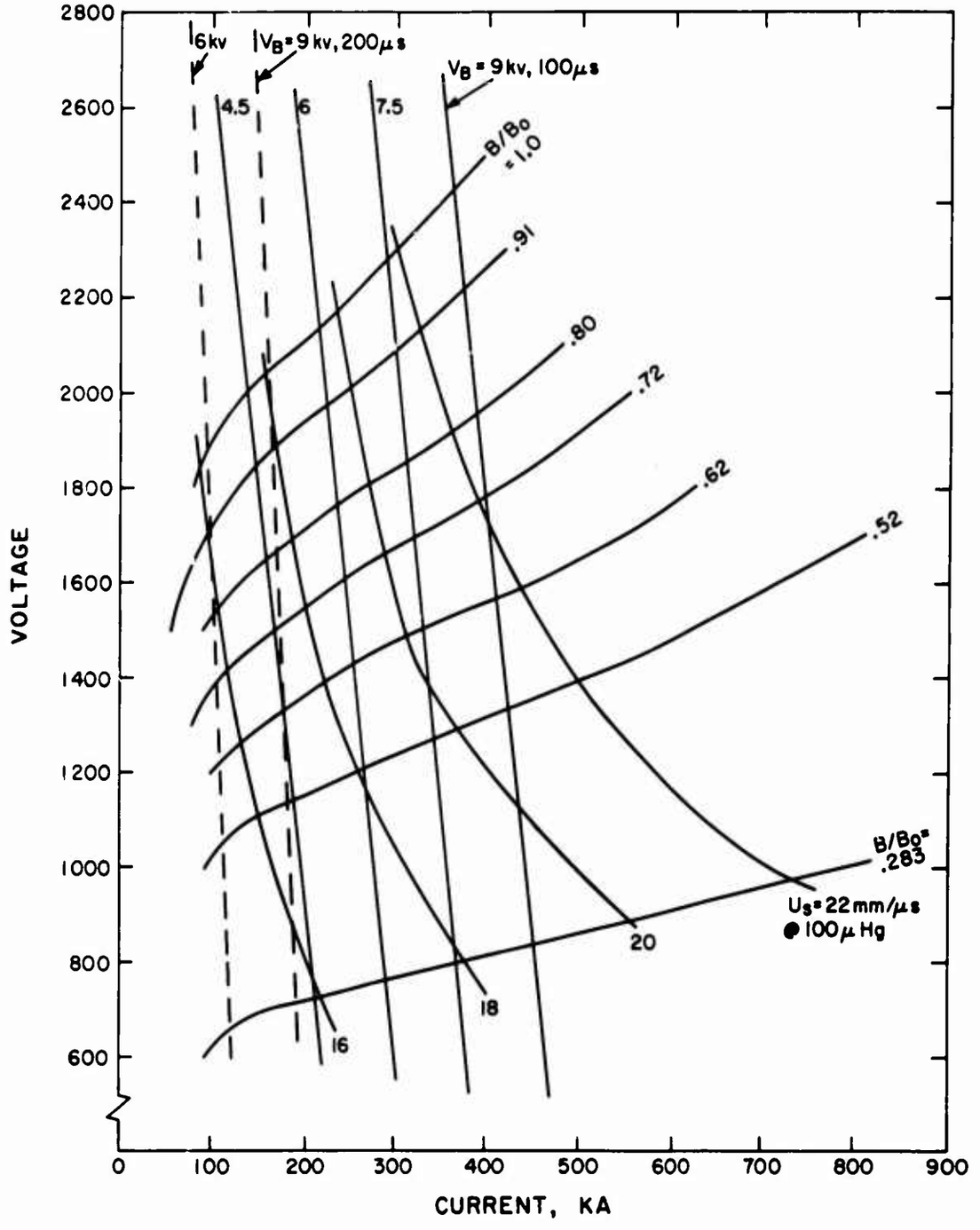


Fig. 5 Voltage current characteristics for the accelerator at various magnetic field strengths (B/B_o = 1.0 corresponds to 40 KG peak field and 10,000 amps field coil current) and for the transmission line-capacitor bank power supply (V_B is the capacitor bank voltage; the time is the duration of square pulse). The intersection of appropriate curves determines the operating point for the accelerator.

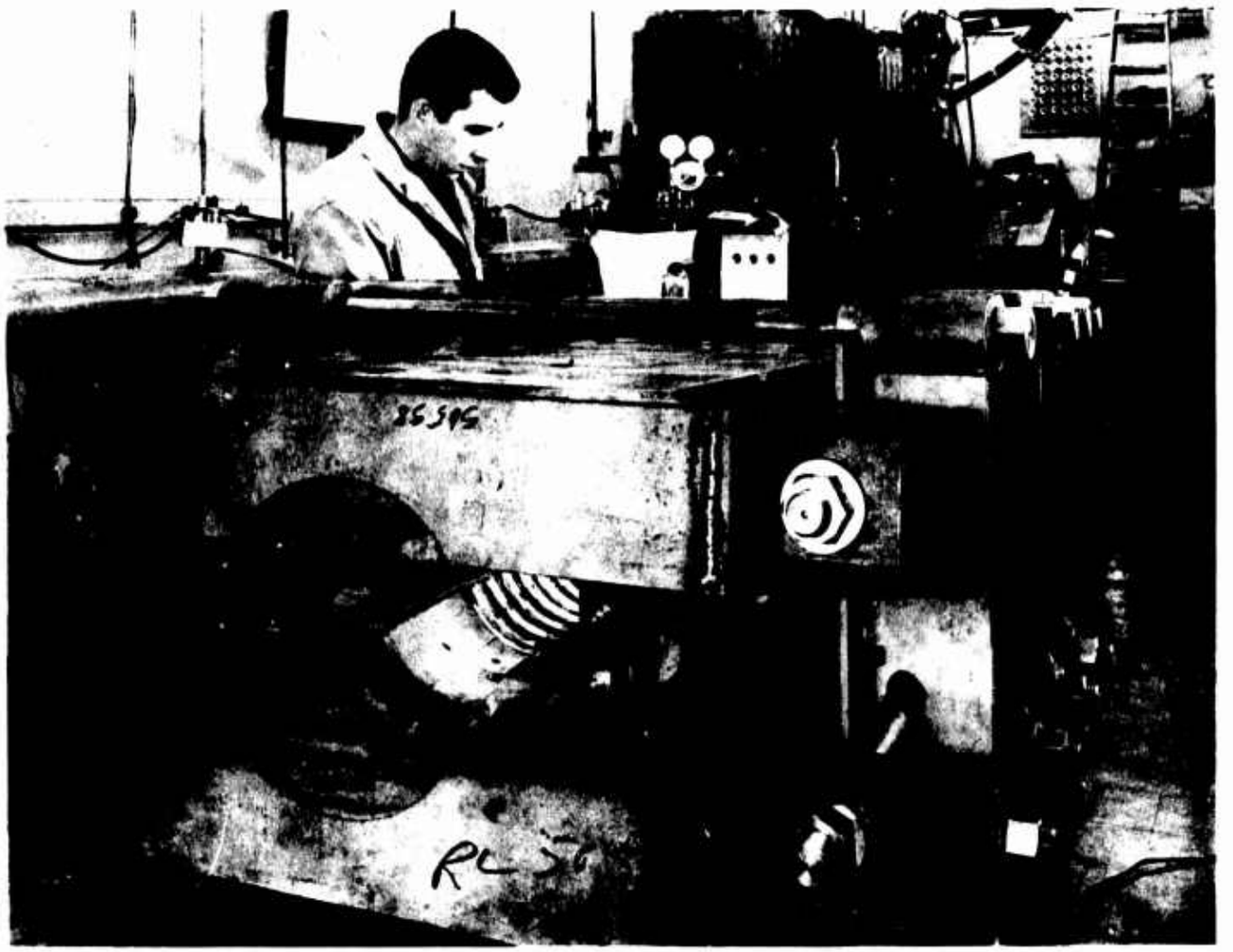


Fig. 6 The 40 KG peak field magnet for use on the accelerator. The coil is uncooled and designed for a 1 second operating duration.

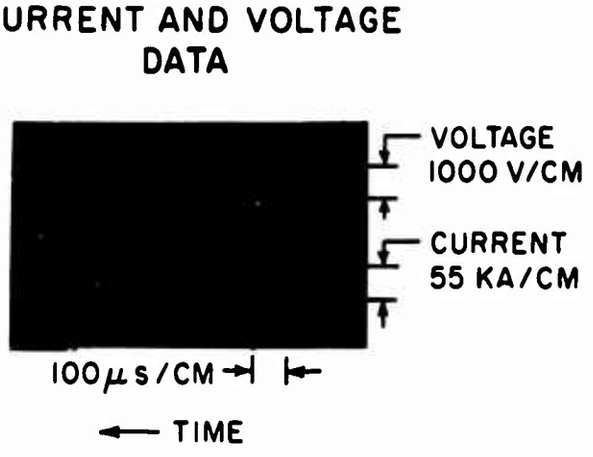


Fig. 7 Total current and electrode potential for the accelerator operating at a capacitor bank voltage of 6 KV and a magnetic field $B/B_o = 0.70$.

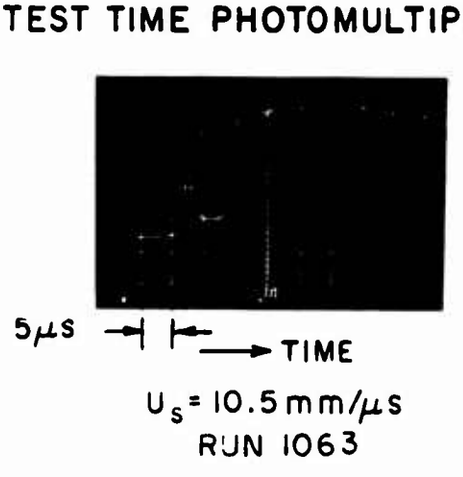


Fig. 8 Visible light intensity vs time at the shock tube test section for an accelerator run. The initial peak is radiation overshoot at the shock front, followed by a region of relatively low radiation from the homogeneous test gas, and finally the high intensity radiation from the seeded driver gas. The test time of $\simeq 7\mu s$ is comparable to that for electric shock tubes operating at this velocity.

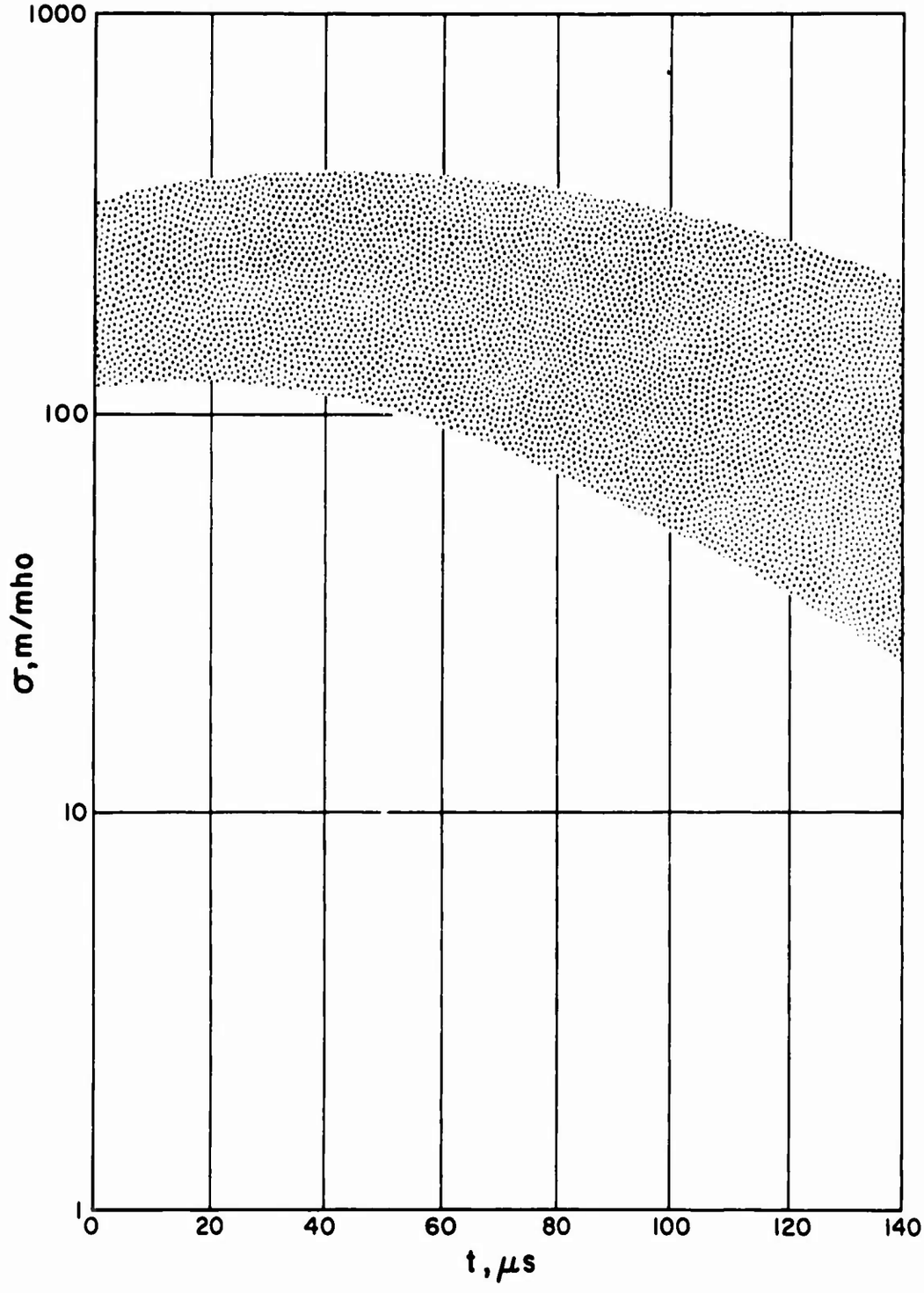


Fig. 9 Electrical conductivity of unseeded helium measured just downstream of the 1-1/2 inch driver before the gas has expanded to the 6" shock tube diameter. The data scattered uniformly over the range shown for a large number of runs.

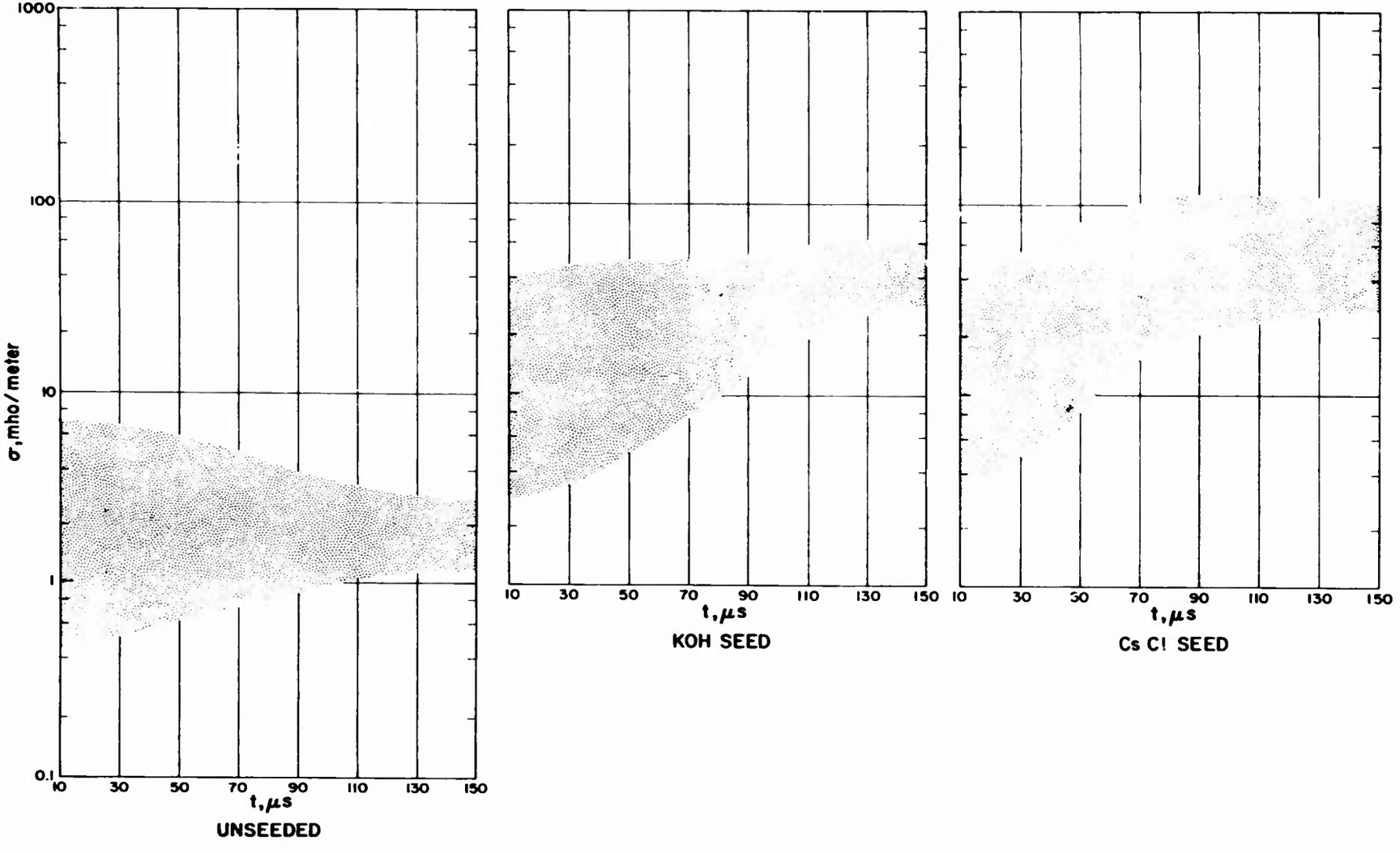


Fig. 10 Electrical conductivity of seeded and unseeded helium for a 3" diameter driver. The measurements were made just downstream of the driver diaphragm before the gas had expanded to the 6" diameter shock tube. The data scattered uniformly over the range shown for a large number of runs.

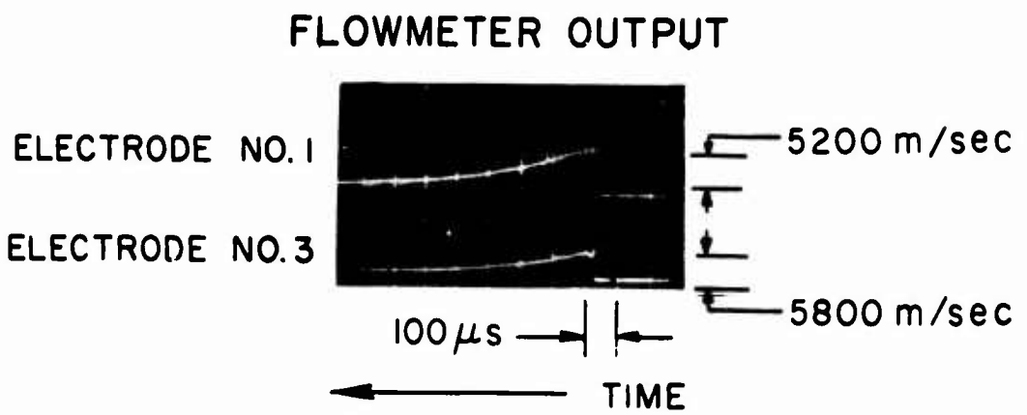


Fig. 11 Induced electrode potential for the accelerator channel used as a flowmeter with no externally applied electric field. The potential can be related to the flow velocity of the gas.

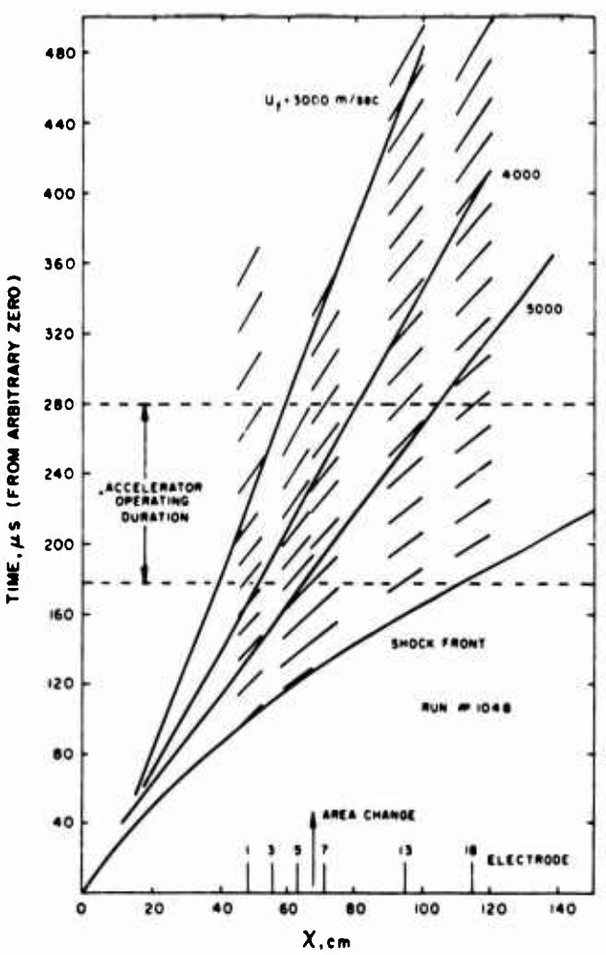


Fig. 12 Experimentally obtained x-t diagram for the electric shock tube without the accelerator operating. The path line slopes are determined from the measured electrode potential and the rarefaction waves are the locus of points of the same velocity.

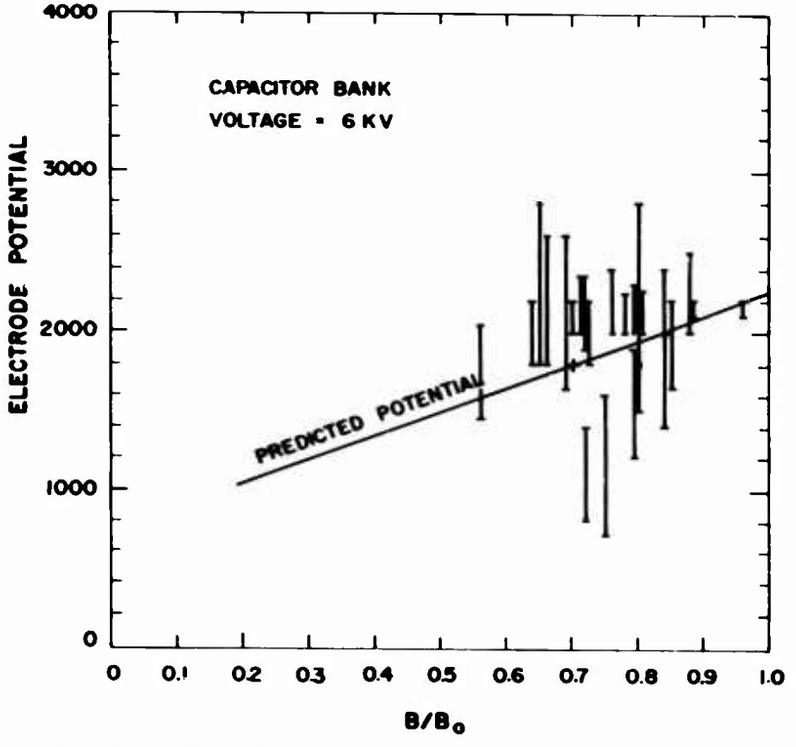


Fig. 13 Electrode potential vs relative magnetic field strength for the accelerator with an input energy of 43,000 joules in 200 μs. (B/B_0 = 1.0 corresponds to a peak field of 40 KG and 10,000 amps magnetic field coil current.) The error bars indicate time variations of potential during the 200 μs run.

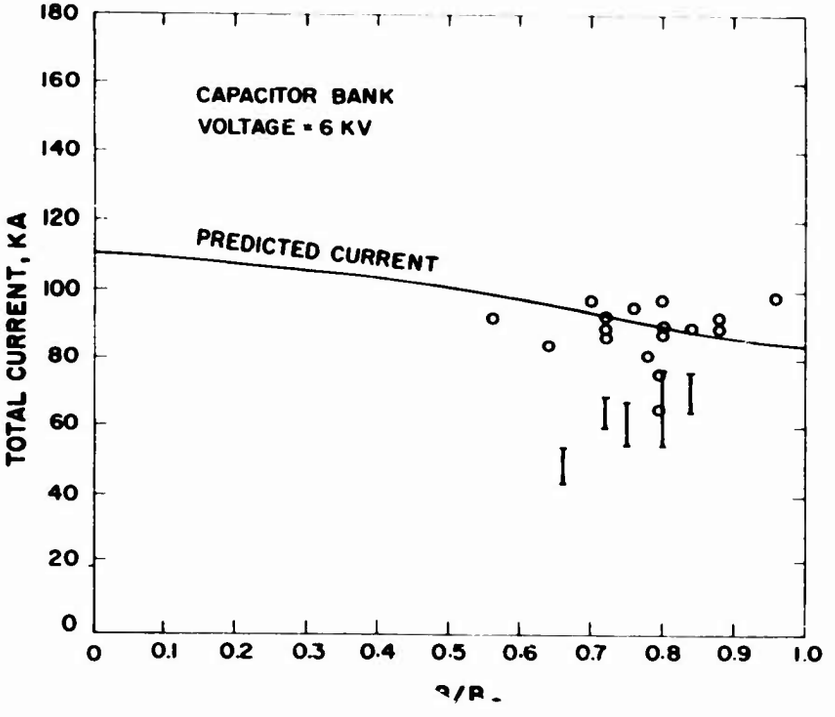


Fig. 14 Total current through the accelerator vs relative magnetic field strength for an input energy of 43,000 joules in 200 μs. (B/B_0 = 1.0 corresponds to a peak field of 40 KG and 10,000 amps magnetic field coil current.)

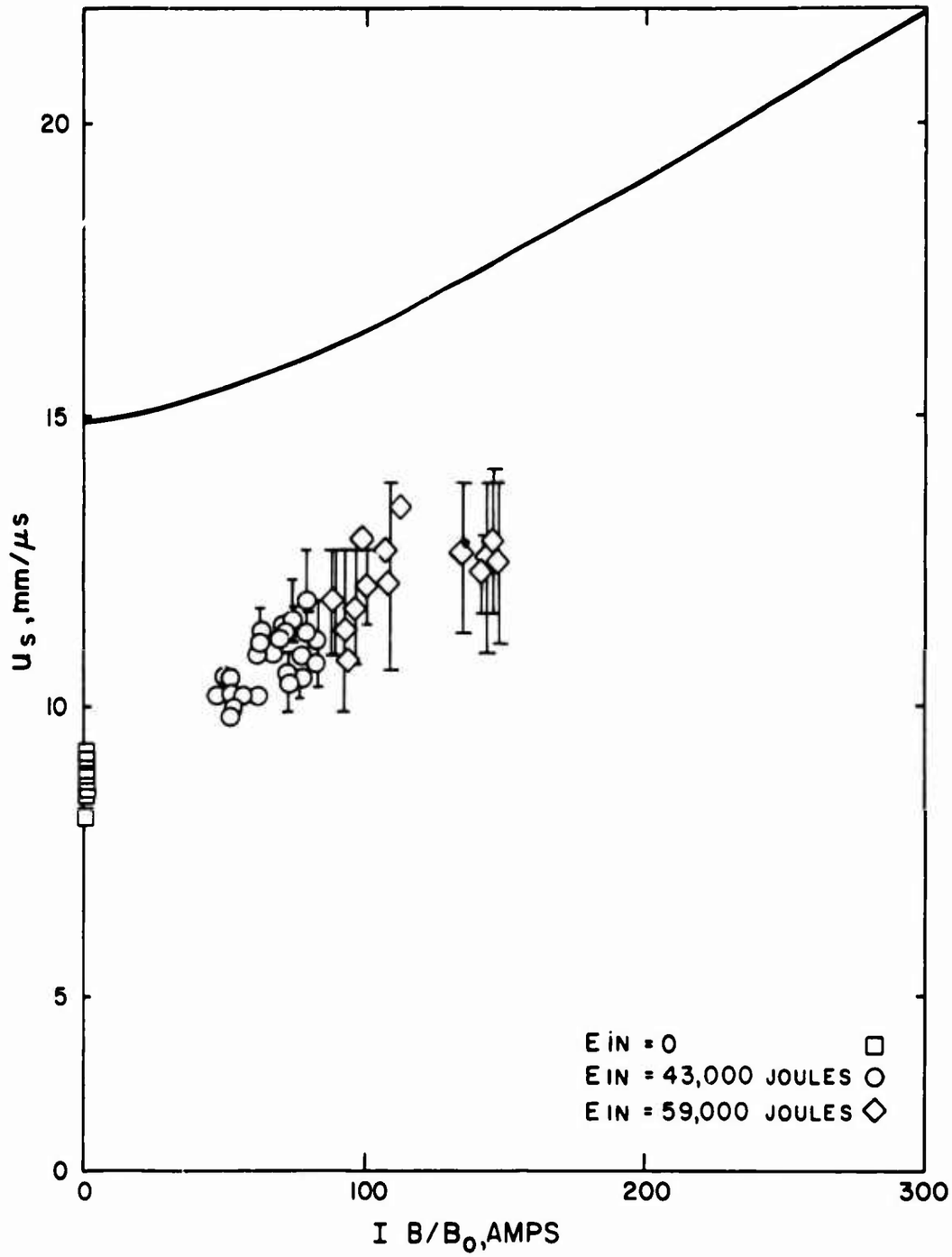


Fig. 15 Shock front velocity vs the relative integrated Lorentz force, $I \cdot B/B_0$, total current through the accelerator times the relative magnetic field. The error bars on velocity indicate the velocity variation over the length of the shock tube; the highest velocity occurring just downstream of the accelerator.

A Piston Problem

T. S. Lee
Department of Electrical Engineering
University of Minnesota
Minneapolis, Minnesota

Abstract: The following new one-dimensional problem is considered: A shock-led recompression layer is induced next to an interface-type discontinuity if the latter moves against a fully-developed centered rarefaction wave from the rear in such a way that its distance from a certain virtual vacuum edge is proportional to the w power of time after inception. The present study treats the detailed character of this layer by conclusively establishing an exact similarity solution for any constant-γ medium undergoing a $w > 1$ drive. Main features are 1) that flow similarity exists only when viewed from the virtual vacuum edge, 2) that layer entropy is uniform, and 3) that any flows sharing common w and γ have identical profiles and shock strength (the last being measured by the explicit constant shock Mach number $M = [(\gamma + 1)w - 2]/(\gamma - 1)$, which is linear in w). A profile calculation using $\gamma = 7/5$ and $w = 5$ is included for demonstration. Applications to shock tube and other experimental flows are investigated.

A Piston Problem

T. S. Lee
Department of Electrical Engineering
University of Minnesota
Minneapolis, Minnesota

INTRODUCTION

It is well knownfrom conventional shock tube experience that production of strong shocks is contingent upon a high initial ratio of pressures in the driving and working gases. Typically, a weak initial thermodynamic state is desirable for the driven section. It is also known, however, that practical difficulties accompanying any sustained maintainence of this condition preclude the attainment of high strength shock waves in a conventional tube. In this paper, a special scheme is proposed to obtain a weak ambient gas in a transient manner and to generate shock waves of arbitrary constant strength. It will be shown that an exact similarity solution of the flow can be used to give a proper analytical description.

PHYSICAL SCHEME

If a piston were abruptly removed from the end of a semi-infinite column of uniform gas originally in constant motion, a fully-developed centered rarefaction wave would be created between a vacuum boundary and a sonic front. Suppose that, instead of allowing the gas to expand freely, the piston is to move in such a way that its instantaneous distance from the otherwise present vacuum-gas boundary shall be a power-law function of time after inception. We then postulate that a shock-led recompression layer exists in front of the piston. The following sections will show this layer to be isentropic and the leading shock to be uniform.

TRANSFORMATION

The governing equations of plane isentropic flows with constant adiabatic exponent γ may be written as

$$\frac{1}{2}(\gamma-1)a\frac{\partial u}{\partial x} + u\frac{\partial a}{\partial x} + \frac{\partial a}{\partial t} = 0$$
$$\frac{2}{\gamma-1}a\frac{\partial a}{\partial x} + u\frac{\partial u}{\partial x} + \frac{\partial u}{\partial t} = 0 \quad , \tag{1}$$

where u and a are local mass and sound velocities respectively. We introduce

$$a/a_o(\hat{X}) \equiv A(y)M; \qquad \hat{u}/a_o(\hat{X}) \equiv U(y)M$$

with

$$y \equiv \hat{x}/\hat{X}, \qquad \hat{x} \equiv x - x_v, \qquad \hat{X} \equiv X - x_v$$
$$V \equiv dX/dt, \qquad \hat{V} \equiv d\hat{X}/dt, \qquad V_v \equiv dx_v/dt$$
$$\hat{u} \equiv u - V_v$$
$$k \equiv \hat{V}/[V - u_o(\hat{X})] = [1 - (\hat{u}_o/\hat{V})]^{-1}$$
$$N \equiv -d\ell n(\hat{V} - \hat{u}_o)/d\ell n\hat{X}$$
$$M \equiv (\hat{V} - \hat{u}_o)/a_o \ .$$

If a linear $x_v(t)$ is selected to describe the motion of the indicated virtual vacuum boundary and if a front of the shock type exists along $x = X(t)$, then we may interpret $\hat{x}$, $\hat{u}$, $\hat{X}$, $\hat{V}$ as fluid position and velocity, and front position and velocity respectively, all measured with respect to the moving virtual vacuum boundary. In addition, if "o" designates the state immediately ahead of the front, then M is the usual shock Mach number, N is a shock acceleration parameter, and k is an environmental unsteadiness parameter.

Equation (1) becomes upon substitution

$$(U - ky)A' + 2^{-1}(\gamma - 1)AU' = kNA$$
$$2(\gamma - 1)^{-1}AA' + (U - ky)U' = kNU \quad , \tag{2}$$

which must be coupled with the equivalent Hugoniet conditions at the front $y = 1$

$$A(1) = (\gamma + 1)^{-1}\left\{[2\gamma - (\gamma - 1)M^{-2}][\gamma - 1 + 2M^{-2}]\right\}^{1/2}$$
$$U(1) = k - 1 + 2(\gamma + 1)^{-1}(1 - M^{-2}) \ , \tag{3}$$

It is seen that a similarity solution is possible if k, N, and M are simultaneously constant.

RAREFACTION ENVIRONMENT

We first treat the noted centered rarefaction wave. Let an over-head bar accompany all quantities connected with this flow. If $\bar{u}_o$ and $\bar{a}_o$ characterize the original undisturbed flow and if $x = 0$ coincides with the fluid boundary at inception $t = 0$, the following system

$$\bar{M} = 1,\ \bar{N} = 0,\ \bar{k} = (\gamma+1)/(\gamma-1),\ x_v = \left[\bar{u}_o - 2(\gamma-1)^{-1}\,\bar{a}_o\right] t$$

$$\bar{X} = (\bar{u}_o + \bar{a}_o)t,\ \bar{\bar{X}} = (\gamma+1)(\gamma-1)^{-1}\,\bar{a}_o t$$

results with flow profiles given by the $(d\hat{x}/dt)_{\bar{y}} = \hat{u}$ + a singular solution of equation (2):

$$\left.\begin{aligned} \bar{A}(\bar{y}) &= \bar{y} \\ \bar{U}(\bar{y}) &= 2(\gamma-1)^{-1}\,\bar{y} \end{aligned}\right\} \quad \text{for } (0 \leqslant \bar{y} \leqslant 1) \qquad (4)$$

Figure 1 gives a phenomenological sketch.

RECOMPRESSION LAYER

With the above rarefaction wave serving as an environment, let us assume the recompression shock trajectory to be

$$X(t) = \Omega\, t^w \quad , \qquad (5)$$

where Ω and w are constants. In particular, let it be restricted that $\Omega > 0$ and $w > 1$. Seen from the rarefaction front, it has the normalized position

$$\bar{y}_s \equiv \hat{X} / \bar{\bar{X}} = \frac{(\gamma-1)\Omega}{(\gamma+1)\bar{a}_o}\, t^{w-1} \quad .$$

The environment influences the recompression layer through the quantities

$$a_o(\hat{X}) = \bar{a}_o \bar{A}(\bar{y}_s) = \bar{a}_o \bar{y}_s$$

and

$$\hat{u}_o(\hat{X}) = \bar{a}_o \bar{U}(\bar{y}_s) = 2(\gamma-1)^{-1}\,\bar{a}_o \bar{y}_s \ .$$

Calculation shows that

$$k = \left[1 - 2(\gamma+1)^{-1}\, w^{-1}\right]^{-1},$$

$$N = w^{-1} - 1 \ ,$$

and

$$M = (\gamma-1)^{-1}\ \left[\ (\gamma+1)w - 2\ \right]$$

are now all constants. Hence the existence of a similarity solution is established.

Equation (2) may be integrated to yield the flow profiles between the shock wave and the piston, the latter having a location y_p determined by the condition that the piston and the adjacent gas share common motion, i.e., $U(y_p) - ky_p = 0$. Respectively, Figures 2 and 3 give typical $\hat{x}$ - t plane and x - t plane sketches.

It should be noted that, besides γ, w alone determines the flow details. In other words, any family of piston paths sharing common w and γ lead to identical shock strength and flow profiles, irrespective of the value of Ω .

Having arisen from a uniform flow, the rarefaction is isentropic. Now that the recompression is also isentropic, the shock strength must be uniform as expected. This is explained by the fact that, as the shock pushes into the rarefaction wave, the effect of kinematic acceleration is exactly balanced out by the effect of increasing acoustic velocity experienced during propagation in the environment.

In Figure 2 the shock eventually intercepts the rarefaction front at A, whose location is given by

$$\left(\left[\left(\frac{\gamma+1}{\gamma-1} \right) \frac{\bar{a}_0}{\Omega^{1/w}} \right]^{w/(w-1)} ; \left[\left(\frac{\gamma+1}{\gamma-1} \right) \frac{\bar{a}_0}{\Omega} \right]^{1/(w-1)} \right).$$

From A, a rear-facing Riemann characteristic extends to the piston at B. Then OAB constitutes the area of interest. While OAC is well described by the present treatment, ABC needs special attention. Notice that affairs after the shock has reached the uniform flow cannot influence this region. Thus, the flow field therein would remain unchanged were we to alter the physical assemption by allowing the shock after A to continue moving into a continuation of the same singular rarefaction wave rather than meet a uniform flow. Analytically, this should involve extending the range of validity of equation (4) beyond $\bar{y} = 1$. Whatever needed extension is contingent upon the position of B, which must in general be found by the conventional method of characteristics. A horizontal line through B meets the extension of y = 1 at D. Connecting $\overline{OD}$ and comparing its inclination with that of $\overline{OA}$ would then determine the uppermost $\bar{y}$ value needed for the flow calculation for ABC.

Referring to Figure 3, we may define a turning-point characteristic as a curve on which all similarity characteristics, including the shock and the piston, change directions of propagation. It may be shown that this characteristic is straight and is given by $x/t = (1 - w^{-1})V_v$.

GEOMETRIC SIMILARITY

The similarity characteristics in Figures 2 and 3 are respectively $\hat{x} = y\Omega t^w$ and $x = V_v t + y\Omega t^w$. We conclude that, with the exception of the

$\bar{u}_o = 2(\gamma - 1)^{-1} \bar{a}_o$ case, geometric similarity does not exist in the x - t plane, whereas it exists in the $\hat{x}$-t plane.

TEST PROFILE CALCULATION

In principle, profile details follow equation (2) for any pair of given $w > 1$ and $\gamma > 1$ values. The procedure of integration is numerical in general. Suffice it to note that the solution is exact for all dynamical properties including piston and shock motions.

For demonstration, we select a diatomic gas ($\gamma = 7/5$) and a driving power of $w = 5$. The associated quantities are then

$$k = 6/5, \qquad N = -4/5, \qquad M = 25$$

$$U(1) = 1.032, \qquad A(1) = 0.4428, \qquad y_p = 0.976 \ .$$

Figure 4 plots A and U, both shown to decrease gradually with y.

DISCUSSIONS

The analogy in the two-dimensional steady flow of the one-dimensional centered rarefaction wave is the Prandtl-Meyer expansion. There is the natural temptation to regard the analogy with the one-dimensional recompression complete by identifying the piston path with some corresponding wall shape (see Figs. 5 and 6). However, this analogy is only qualitative in general. It is only when the upstream flow is hypersonic that a quantitative basis is also valid. This observation agrees with Greifinger and Cole's suggestion (ref. 1) that the lateral expansion of a steady hypersonic jet bounded by vacuum can have an analogy with an equivalent unsteady expansion in one dimension. The overall concept underlying the noted analogy is of course in keeping with the hypersonic similitude of Tsien and Hayes (ref. 2).

The recompression layer is usually thin. A potential difficulty lies with those two-dimensional steady flow problems, where, depending on the values of Ω, local Reynolds number, etc., the thicknesses of the conventional boundary layers (e.g., viscous, thermal, etc.) or the shock thickness may become comparable in magnitude to that of the recompression layer. There, a collective consideration of several physical effects would appear unavoidable. Possible approaches to this broader problem shall not be scrutinized here.

Near any predicted vacuum-gas boundary, the conventional continuum concept breaks down in favor of a free molecule concept (ref. 3). However, the basic continuum model does not necessarily become invalidated, because principal features of the main fluid body are still being correctly preserved and exception need be made only for a narrow zone of non-continuum transition. For the class of problems considered in this paper, there is good ground for optimism. By the recompression layer theory, a real vacuum-gas boundary need exist only for the initial instant. Subsequent forcing actually eliminates any need for considering the said transition zone.

In this paper, a new flow model has been developed and presented. Since the results are characterized by predictions of uniform shock strength and Ω independence, experimental implications are immediate. For instance, a definite scheme is now available, in principle, to generate a shock wave of any desired uniform strength (notice that M(w) is linear and monotonic in w) by appropriately driving a piston or an interface in a conventional one-dimensional shock tube or by specifying a particular model wall shape in a hypersonic wind tunnel flow.

A useful corollary can be established for a triple-front interaction mechanism. We shall now illustrate this concept only for the steady hypersonic flow system, showing it to be a versatile approach to the study of shock interaction. Consider in Figure 7 that the Mach rarefaction front reaches the oblique wedge shock at T. According to the recompression layer theory, for any given w, thus for any given M, there exists an Ω such that the recompression shock may intercept the Mach front also at T. In other words, some recompression shock can emerge with known strength from a region of rarefaction simply to encounter immediately the wedge shock which is also of known strength. Ensuing from this triple interaction, subsequent flow details in the immediate neighborhood of T such as the outer shock deflection angle can follow the treatment of the well-known simple shock-overtaking theories (ref. 4). Since the strength of the wedge shock can be moderately adjusted by changing the wedge angle and the strength of the accompanying recompression shock can be vastly adjusted by changing w, the corresponding experimental flexibility should be significant.

REFERENCES

(1) Greifinger, C. and Cole, J., RAND Rep. 2008, (1960)

(2) For example, see Hayes, W. D. and Probstein, R. F., Hypersonic Flow Theory, Acad. Press, (1959)

(3) von Neumann, J., John von Neumann Collected Works, Vol. VI, 348 Pergamon Press, (1963).

(4) For example, see Courant and Friedrichs, Supersonic Flow and Shock Waves, Interscience, (1948).

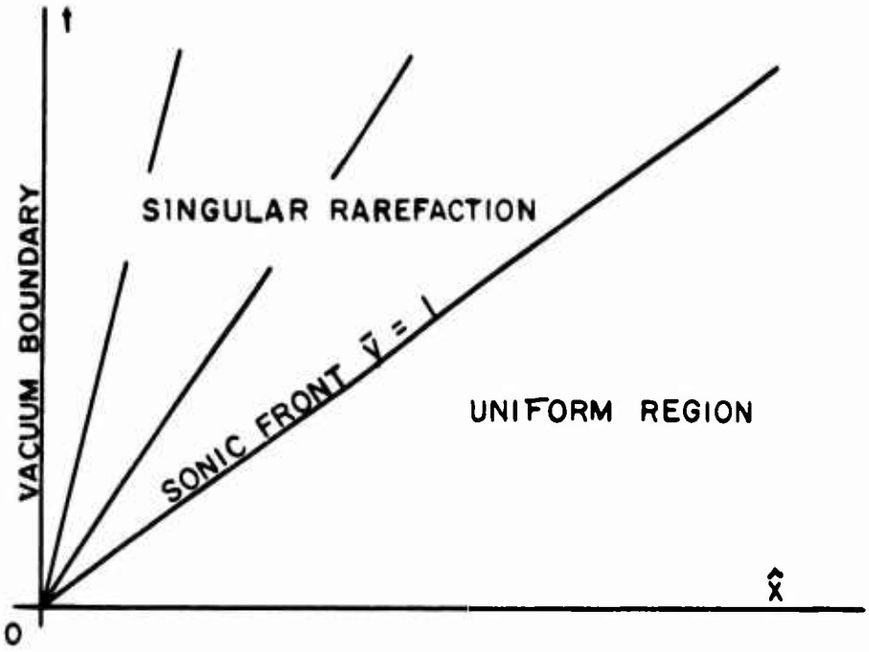


Fig. 1 $\hat{x}$-t Representation of a Fully Developed Centered Expansion

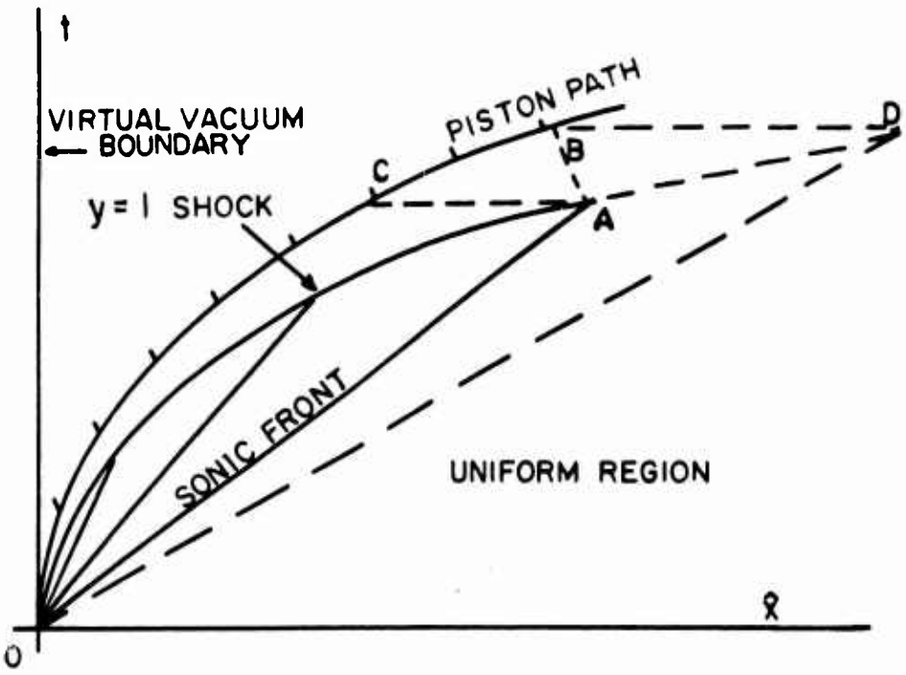


Fig. 2 $\hat{x}$-t Representation of a General Piston-Driven Recompression Layer

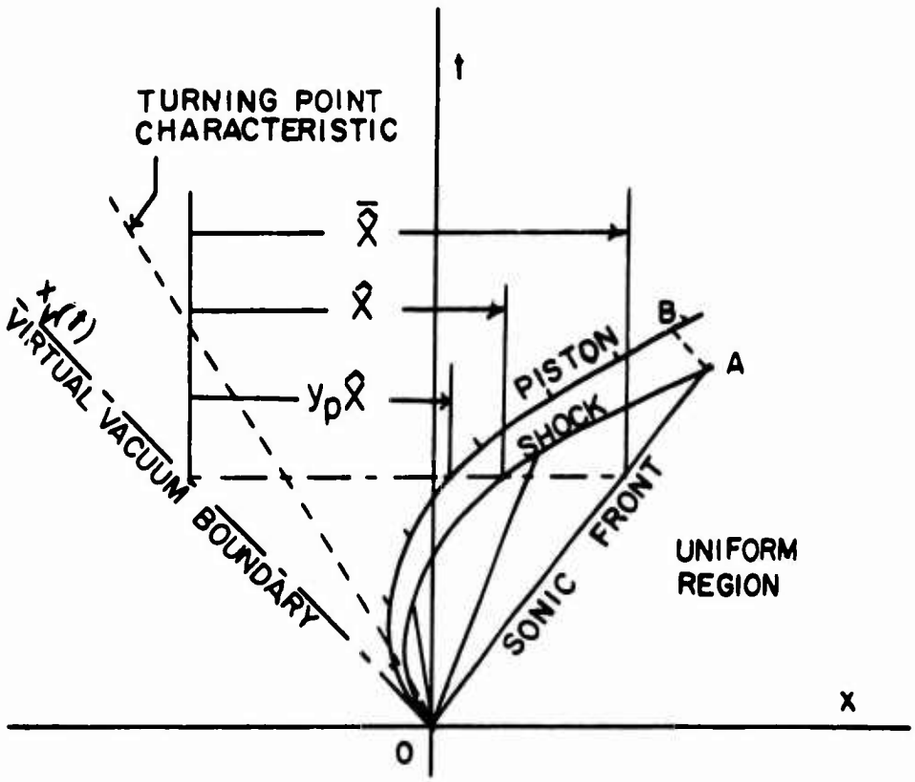


Fig. 3 Physical Plane Representation for a General Power-Law Piston-Driven Recompression Layer

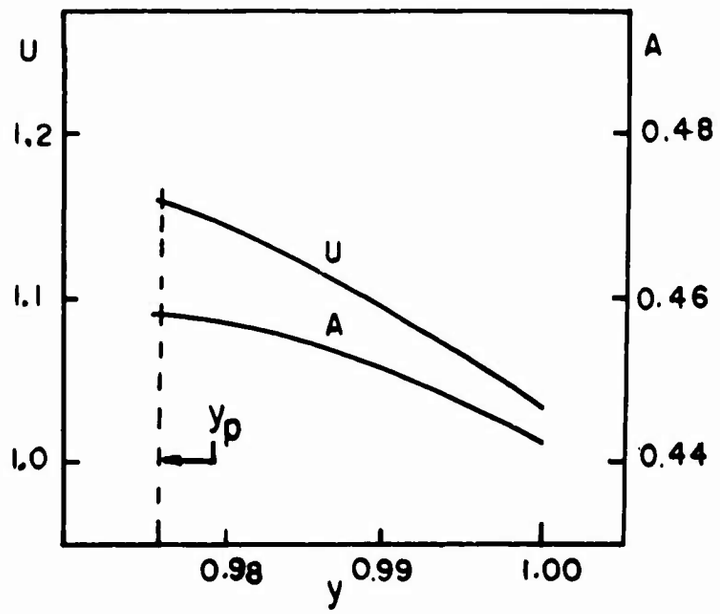


Fig. 4 U and A Distributions for a $\gamma = 7/5$ and $w = 5$ Recompression Layer

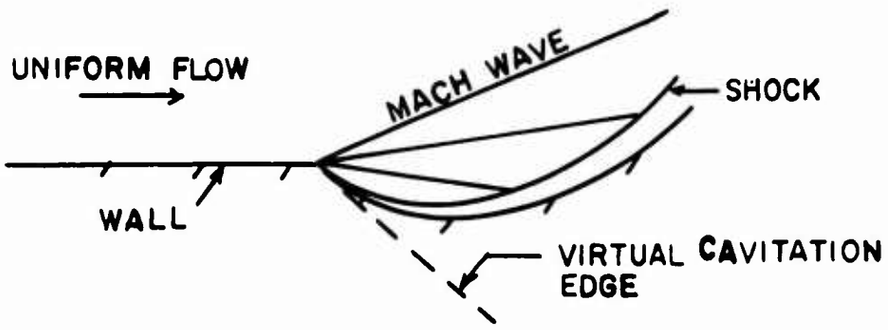


Fig. 5 A Steady-Flow Analogy for the Piston Recompression Layer

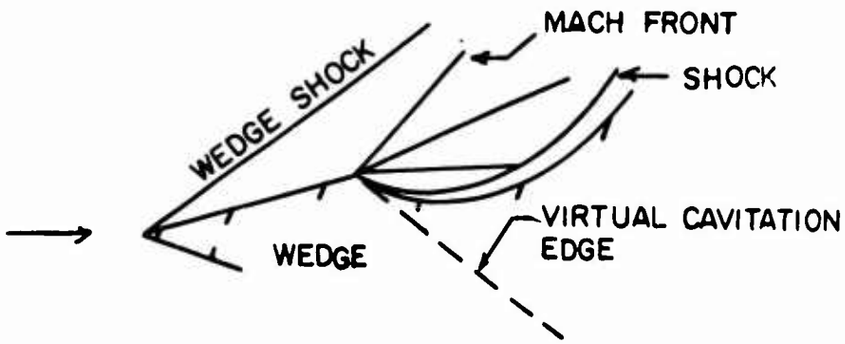


Fig. 6 General Steady-Flow Analogy for the Piston-Driven Recompression Layer (Wedge-Corner Flow)

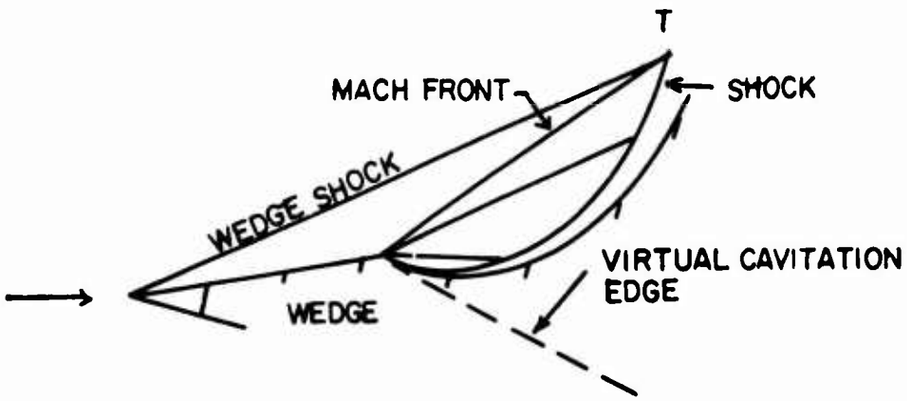


Fig. 7 Triple-Front Interaction in the wedge Corner Flow

NOTE ON A LOW PRESSURE SHOCK TUBE WITH AREA CHANGE NEAR THE DIAPHRAGM

Christian A. Kot
IIT Research Institute
Chicago, Illinois

INTRODUCTION

Shock tubes with area changes or nozzles near the diaphragm area have been used to achieve very high pressures and/or Mach numbers at the test section (ref. 1 and 2). Here we are interested in using a shock tube with area change to produce low overpressure shocks in a test section of large cross-section (4 ft to 8 ft). The driver or compression chamber in this case has a smaller cross-section. The motivation for such a shock tube design is to find an economic means of testing large components for their structural integrity and performance under blast conditions.

This paper presents a gas dynamic analysis of the shock tube with area change and compares its performance and operation with a conventional shock tube.

ANALYSIS OF SHOCK TUBE WITH AREA CHANGE

The shock tube to be investigated has a large diameter test-section and compression chamber which is of smaller cross-section. The diaphragm is located at the transition, and the transition section is very short in comparison with either the test or compression section. The solution and wave configuration for a given initial ambient (test section) pressure and compression chamber pressure is unique if we assume that frictional effects are negligible and that the gas is a perfect gas. However, the wave configuration is not known a priori and thus the problem has to be solved by trial and error. The matching of pressures and velocities in the various states, separated by contact surfaces and shocks, yields the solution. The possible wave configurations are shown in Figure 1. This figure also gives the notation for the various flow regions which will be used throughout this paper. The states shown indicate steady state behavior and are applicable to times when all transients which follow breaking of the diaphragm have been damped out.

For very weak shocks the flow in the entire shock tube is subsonic (Fig. 1a). As the shock strength in state 1 is increased the flow from the driver chamber into the test section cannot adjust continuously and the velocity in state 3 becomes sonic. Another shock wave appears first as a stationary shock in the transition section (Fig. 1b) and finally for still higher shock Mach numbers the secondary shock appears in the large diameter section where it is swept to the right by the fast supersonic flow in state 3' (Fig. 1c). As the shock Mach number is further increased the strength of the secondary shock is reduced until it becomes a shock of zero strength, i.e., a Mach wave. For still higher shock Mach numbers it becomes necessary that the flow leaving the area transition be further expanded and accelerated; thus the secondary wave becomes an upstream-facing non-steady expansion wave (Fig. 1d).

Notation and Assumptions

The symbols to be repeatedly used throughout this paper are listed below:

A = area

c = sound velocity

D = diameter

L = unit length, compression chamber length

M = Mach number

p = absolute pressure

R = gas constant

t = time

T = absolute temperature

u = particle velocity

U = shock velocity

W = U/c_o

x = distance

X = x/L dimensionless distance

β = $\frac{\gamma-1}{2\gamma}$

γ = ratio of specific heats

μ = $\frac{\gamma+1}{\gamma-1}$

ρ = density

τ = tc_o/L dimensionless time

σ = A_1/A_4 area ratio

φ_i = u_i/c_o

χ_i = c_i/c_o

ξ_{ij} = p_i/p_j

Δ = difference or change in any quantity

Subscripts:

i = 0, 1, 2... designates the corresponding state

* = designates sonic conditions

s = primary shock

ss = secondary shock

The shock tube to be considered is an air to air shock tube. Only cold flow conditions will be considered. Since interest is restricted to moderate pressures we assume the air to be a perfect gas with a constant ratio of specific heats of $\gamma = 1.4$. Ideal flow theory neglecting viscous effects and dissipation (except across shocks) will be used throughout the calculations.

The initial conditions are ambient room conditions thus

$$p_o = 14.7 \text{ psia}; \quad c_o = c_4 = 1,117 \text{ fps}; \quad T_o = T_4 = 520^\circ \text{ R}$$

Initial Pressures and Wave Configurations

Let us assume that the area ratio is $\sigma = 4$. For any desired shock pressure ratio ξ_{10} it is necessary to compute the compression chamber pressure p_4 and the wave pattern resulting in the shock tube. Since the latter is not known a priori a configuration must be assumed and checked by the existence of a solution. It should be noted that except for the subsonic case (very weak shocks) state 3 must be sonic.

We will illustrate the computational procedure using a shock strength $\xi_{10} = 2$ or a shock overpressure of 14.7 psi. We assume that

a secondary shock is moving in the large diameter section. Thus state 2 coincides with state 2'. The solution is best carried out by assuming values of the compression chamber pressure ratio ξ_{40}.

States 3 and 4 are related by the characteristic relationship

$$\frac{\gamma-1}{2} u_3 + c_3 = \frac{\gamma-1}{2} u_4 + c_4 \tag{1}$$

Since $c_4 = c_o$; $u_4 = 0$ and $u_3 = c_3$ equation (1) simplifies to

$$\varphi_3 = \chi_3 = \frac{2}{\gamma+1} \cdot \tag{2}$$

The pressure is obtained from the isentropic relationship

$$\xi_{34} = \frac{p_3}{p_4} = \left(\frac{c_3}{c_4}\right)^{\frac{2\gamma}{\gamma-1}} \tag{3}$$

From state 3 to 3' a steady isentropic expansion takes place; thus these states are related by the energy and continuity equation in the form

$$\frac{\gamma-1}{2} u_3^2 + c_3^2 = \frac{\gamma-1}{2} u_{3'}^2 + c_{3'}^2 \tag{4}$$

$$u_3 c_3^{\frac{2}{\gamma-1}} = \sigma u_{3'} c_{3'}^{\frac{2}{\gamma-1}} \tag{5}$$

These equations can be combined to give the relationship (ref. 3)

$$M_3 \left(1 + \frac{\gamma-1}{2} M_3^2\right)^{-\frac{\gamma+1}{2(\gamma-1)}} = \sigma M_{3'} \left(1 + \frac{\gamma-1}{2} M_{3'}^2\right)^{-\frac{\gamma+1}{2(\gamma-1)}} \tag{6}$$

Since $M_3 = 1$ we get

$$\sigma = \frac{A_{3'}}{A_3} = \frac{A_{3'}}{A_*} = \frac{1}{M_{3'}} \left(1 + \frac{\gamma-1}{2} M_{3'}^2\right)^{\frac{\gamma+1}{2(\gamma-1)}} \left(\frac{\gamma+1}{2}\right)^{-\frac{\gamma-1}{2(\gamma-1)}} = 4 \tag{7}$$

Equation (7) permits the computation of $M_{3'}$, and $c_{3'}$ can be obtained from equation (5). The pressure $p_{3'}$ is then calculated from isentropic relations.

Next the change of conditions across the secondary shock have to be computed, i.e., $\xi_{23'}$ has to be obtained. This is best accomplished by assuming that $\xi_{10} = \xi_{20} = 2$. The strength of the secondary shock is then immediately computed from

$$\xi_{23'} = \frac{\xi_{20}}{\xi_{3'0}} \quad . \tag{8}$$

Obviously only one value of $\xi_{23'}$, and thus ξ_{40}, will yield a change in particle velocity across the secondary shock which matches the velocity in state 2. We can write

$$\frac{\Delta u_+}{c_-} = \frac{(\mu-1)(\xi-1)}{\sqrt{(\mu+1)(1+\mu\xi)}} \tag{9}$$

where Δu_+ is the change in particle velocity relative to the particle of gas in the state ahead of the shock wave and c_- is the sound velocity ahead of the shock. Formula (9) yields both, the velocity $u_1 = u_2$, and the change in velocity across the secondary shock. The velocity in state 2 is then also computed from

$$\frac{u_2}{c_o} = \frac{u_{3'}}{c_o} + \frac{\Delta u_{23'}}{c_{3'}} \frac{c_{3'}}{c_o} \tag{10}$$

and when the values obtained from equations (9) and (10) are in agreement a solution point is found. To ascertain if this solution is physically valid, i.e., if the assumed wave configuration was correct, the absolute velocity of the secondary shock has to be computed. If it is found that the secondary shock moves downstream then a valid solution is obtained. An upstream moving secondary shock indicates an unstable and physically unreal situation since the shock would move into the transition section and thus the wave pattern is different from the assumed configuration.

The calculations are easily performed using shock tables and isentropic flow tables (ref. 3). Table I shows the numerical values for a particular computation of the shock tube problem ($\sigma = 4$, $\xi_{10} = 2$). A series of ξ_{40} values is assumed and the computations are performed according to the above outline. The solution value of ξ_{40} is found by interpolation or graphically. Values of the required compression chamber pressures for different shock strengths ξ_{10} can be found in an analogous manner or by a slight variation of the procedure. Thus, for weaker shocks when the secondary shock is stationary in the transition section it is first necessary to locate the position of the shock. This is accomplished by assuming the position and checking its correctness by the velocity resulting in state 2. Once the proper position is established the pressure in the compression chamber is obtained by matching the pressure in state 2. The

results of such computations for a fixed area ratio of 4 are presented in Figures 2 and 3. The first of these gives the compression chamber pressure ratio as a function of the primary shock pressure ratio. Figure 3 presents the shock velocity, the particle velocity, and the absolute velocity of the secondary shock as a function of shock strength.

Shock Tube Performance

To evaluate the usefulness of the shock tube with area change it is necessary to establish test time durations which can be achieved in the shock tube. From Figure 2 we see that for shock strength in excess of $\xi_{10} = 2$ the required compression chamber pressure becomes quite high, at the same time the velocity of the secondary shock increases considerably (Fig. 3). We will thus arbitrarily limit our considerations to shock strengths of 2 or less. Since a test section for large components (4 to 8 feet) would most likely be located at the shock tube end, testing would take place in the reflected pressure state. The reflected shock strength is $\xi_{51} = 1.87$ for an incident shock of strength $\xi_{10} = 2$, i.e., the pressure behind the reflected shock is about 55 psia.

Figure 4 presents a wave diagram for the shock tube. It can be shown that the optimum test durations in the incident region (state 1) can be obtained by placing the test section at X_c. For optimum durations in the reflected region (state 5) and the shortest shock tube length, the test section must be located at X_r. The dimensionless time in which the first reflected expansion wave reaches the transition section is (ref. 5)

$$\tau_a = \frac{t_a c_o}{L} = \left|\xi_{34}\right|^{-\frac{\beta\mu}{2}} \tag{11}$$

Since the transition section is assumed to be very short we neglect the time required to traverse it. In time τ_a the secondary shock travels a distance

$$X_{ssa} = \tau_a W_{ss} \tag{12}$$

The distance X_b at which the secondary shock is overtaken by the first reflected wave is

$$X_b = \left|\varphi_{3'} + \chi_{3'}\right| \Delta\tau_b = X_{ssa} + W_{ss}\Delta\tau_b \tag{13}$$

where

$$\Delta\tau_b = \frac{X_{ssa}}{\varphi_{3'} + \chi_{3'} - W_{ss}} \tag{14}$$

The time of this interaction is simply

$$\tau_b = \tau_a + \Delta\tau_b \tag{15}$$

In this time the contact surface has travelled a distance X_{pb} given by

$$X_{pb} = \varphi_2 \tau_b \,. \tag{16}$$

The point at which the reflected rarefaction wave overtakes the contact surface X_c (which is also the point of intersection with the reflected shock wave for optimum conditions) is obtained from

$$X_c = X_b + \left(\varphi_2 + \chi_2\right) \Delta\tau_c = X_{pb} + \varphi_2 \Delta\tau_c \tag{17}$$

where

$$\Delta\tau_c = \frac{X_{pb} - X_b}{\chi_2} \,. \tag{18}$$

The time for this intersection is simply given by

$$\tau_c = \tau_b + \Delta\tau_c \,. \tag{19}$$

Further the optimum testing time in state 1 is computed as

$$\Delta\tau_{1m} = \tau_c - \frac{X_c}{W_s} \tag{20}$$

The location of the test section for optimum testing time in the reflected region is given by

$$X_r = \frac{\tau_c - X_c/W_r}{1/W_s - 1/W_r} \,. \tag{21}$$

Finally the testing time available in the reflected state at location X_r is

$$\Delta\tau_{5m} = \left(X_r - X_c\right)\left(\frac{1}{\chi_5 + \varphi_5} - \frac{1}{W_r}\right) \tag{22}$$

Table II shows representative results computed with the aid of equations (11) through (22), for a chock tube with an area ratio $\sigma = 4$ and a strength

of the primary shock equal to $\xi_{10} = 2$. Also shown are results for the same shock strength but for a conventional shock tube. These were obtained with the aid of equations and graphs in reference 5.

Table II

Shock Tube Performance Parameters
$\xi_{10} = 2.0$

Dimensionless Parameters	Conventional $\sigma = 1$	Area Change $\sigma = 4$
τ_a	1.44	1.73
X_a	- 0.60	0
τ_c	2.87	2.71
X_c	1.50	1.42
$\Delta\tau_{1m}$	1.67	1.67
τ_r	1.83	1.72
X_r	2.49	2.34
$\Delta\tau_{5m}$	1.73	1.73

DISCUSSION AND CONCLUSIONS

A comparison of the values in Table II indicates that the dimensionless performance parameters at low overpressures (shock strength of 2 or less) are virtually identical for an air to air shock tube having an area change of 4 and for its conventional counterpart. However, the shock tube with an abrupt area change offers definite advantages in case of large test sections, say 6 feet in diameter. To obtain clean shock waves the test section must be about 8 diameters downstream of the diaphragm station which for a 6 foot diameter tube is 48 feet. If testing is done in the reflected state we find with the aid of Table II that the lengths of the compression chambers are 19 feet and 21 feet for the conventional and area change shock tube respectively. This gives compression chamber aspect ratios of approximately 3 and 7 for the two cases. The first of these numbers for the conventional shock tube is rather low and it may therefore be necessary to increase the length of the chamber and thus also the length of the tube. It is also interesting to note, that the ratio of the

weights of wall material per linear foot of compression chamber is about 0.75, the chamber for the shock tube with an area change weighing less ($\xi_{10} = 2$; $\sigma = 4$). This is particularly significant if we consider that the compression chamber pressure for the shock tube with an area change exceeds the pressure for the conventional design by a factor of 3. The above weight ratio is easily established if we remember that the weight is proportional to the product of diameter D and wall thickness m while the hoop stress s is simply

$$s = \frac{pD}{2m}$$

It is probably safe to say that fabrication costs for the smaller diameter compression chamber will be lower than for the larger chamber required in the conventional tube. For equal length of compression chamber we find that the mass of air required in the case of area change is 0.75 of the mass of air for the conventional tube. Also the horsepower for isothermal compression (equal inlet pressure and velocity) is proportional to $\ln(p_2/p_1)$ where p_2 is the delivery pressure and p_1 the pressure at the intake. Thus, the costs of pressurizing of the compression chambers in the two cases should not be radically different.

The smaller diameter of the compression chamber and thus the diaphragm offers definite advantages in handling and operations of the shock tube with the area change. Further, it is a well known fact that to produce weak shocks in a shock tube problems arise with the piercing and tearing of the diaphragm particularly for large diameters. Here again, the smaller diameter of the diaphragm for the shock tube with an area change should be an advantage. Further, the higher compression chamber pressure of this arrangement should aid in the production of clean shocks of low strength.

In conclusion we can thus state that the performance of the shock tube with an area change is comparable with the low over-pressure performance of a conventional shock tube and that in case of large diameter test sections it offers the advantages of lower initial costs and ease of operation.

ACKNOWLEDGMENT

This work was sponsored by the Department of the Army, Office of the Chief of Engineers under contract DA-49-129-ENG-526.

REFERENCES

(1) Russell, D. A., "A Study of Area Change near the Diaphragm of a Shock Tube," GAL California Institute of Technology, Hypersonic Research Program Memorandum No. 57 (July 20, 1960)

(2) Hall, J. G., "Shock Tubes" Part II, UTIA Review No. 12 (May 1958)

(3) Ames Research Staff, "Equations, Tables, and Charts for Compressible Flow" NACA Report 1135 (1953)

(4) Rudinger, G., Wave Diagrams for Nonsteady Flow in Ducts, D. Van Nostrand Company, Inc., New York (1955)

(5) Glass, I. I., "Shock Tubes" Part I, UTIA Review No. 12 (May 1958)

Table I

Table of Parameters for Shock Tube Problem

$\sigma = 4$; $\xi_{10} = \xi_{20} = 2.0$

$c_3/c_4 = \chi_3 = \varphi_3 = 0.833$; $\xi_{34} = 0.278$

$M_{3'} = 2.94$; $M_{3'*} = 1.95$

$\varphi_{3'} = 1.63$; $\chi_{3'} = 0.553$; $\xi_{3'3} = 0.0570$

$\varphi_1 = \varphi_2 = 0.523$; $\chi_1 = 1.109$; $W_s = 1.362$

ξ_{40}	ξ_{30}	$\xi_{3'0}$	$\xi_{23'}$	$\frac{\Delta u_{23'}}{c_{3'}}$	φ_2
16	4.45	.254	7.88	-1.871	.594
15	4.17	.238	8.40	-1.950	.550
14	3.89	.222	9.01	-2.040	.500
13	3.62	.206	9.70	-2.136	.450
12	3.34	.190	10.52	-2.247	.384
14.52	4.01	.229	8.74	-2.001	.523

NOTE: Last row gives solution

$\frac{\Delta U_{ss}}{c_{3'}} = -2.763$; $\frac{c_2}{c_{3'}} = 1.552$

$W_{ss} = 0.100$; $\chi_2 = 0.859$; $\varphi_2 = 0.523$

Compression Chamber Pressure $p_4 = 212$ psia

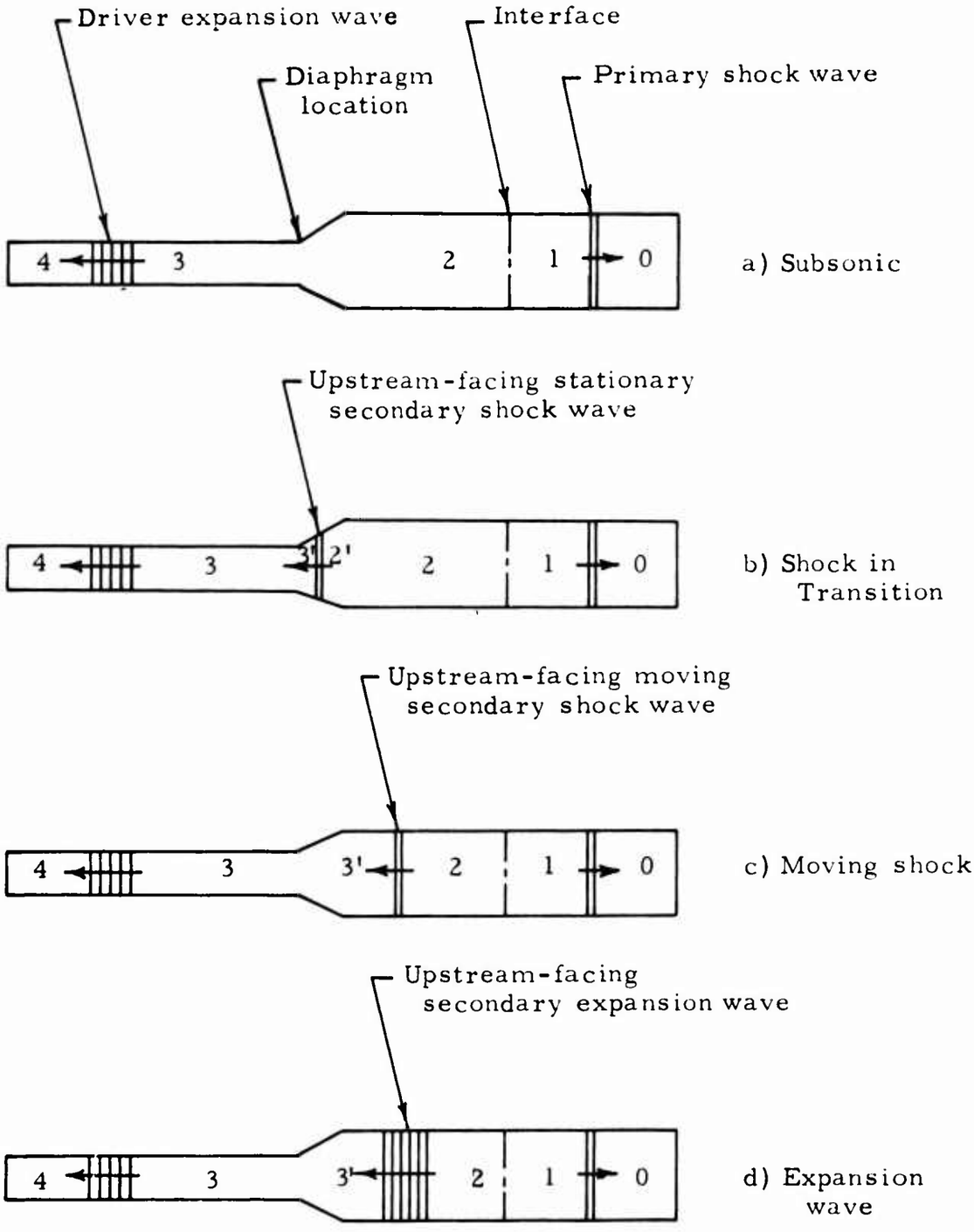


Fig. 1 Schematic Shock Tube Configurations

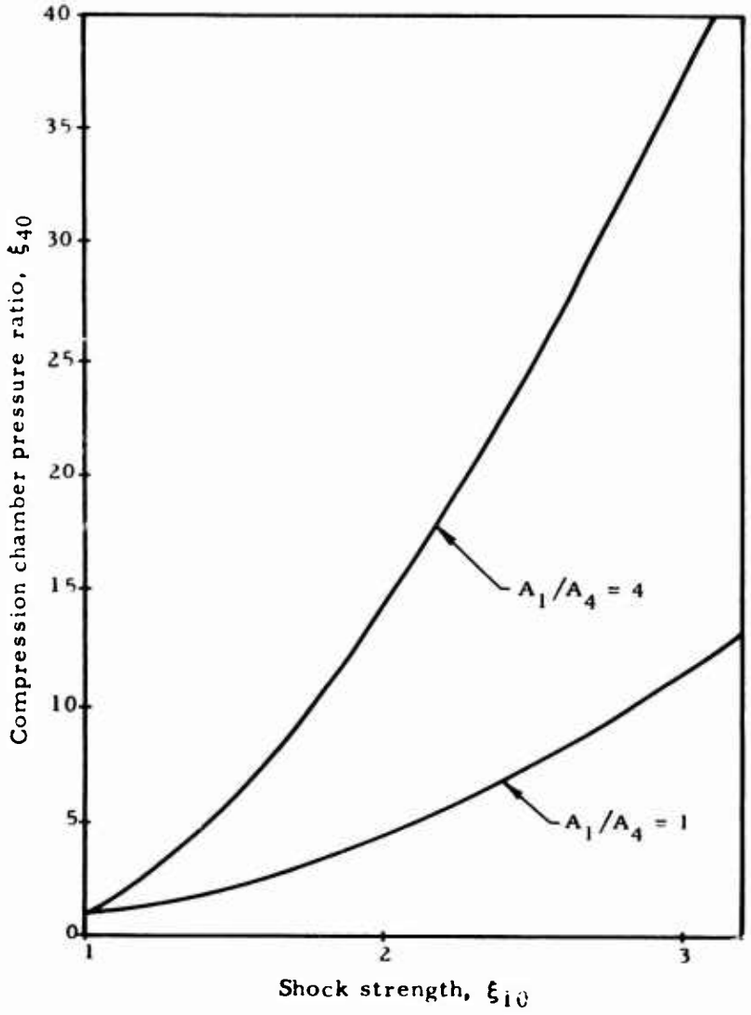


Fig. 2 Variation of Compression Chamber Pressure Ratio as a Function Shock Strength for Different Area Ratios: Air/Air Shock Tube

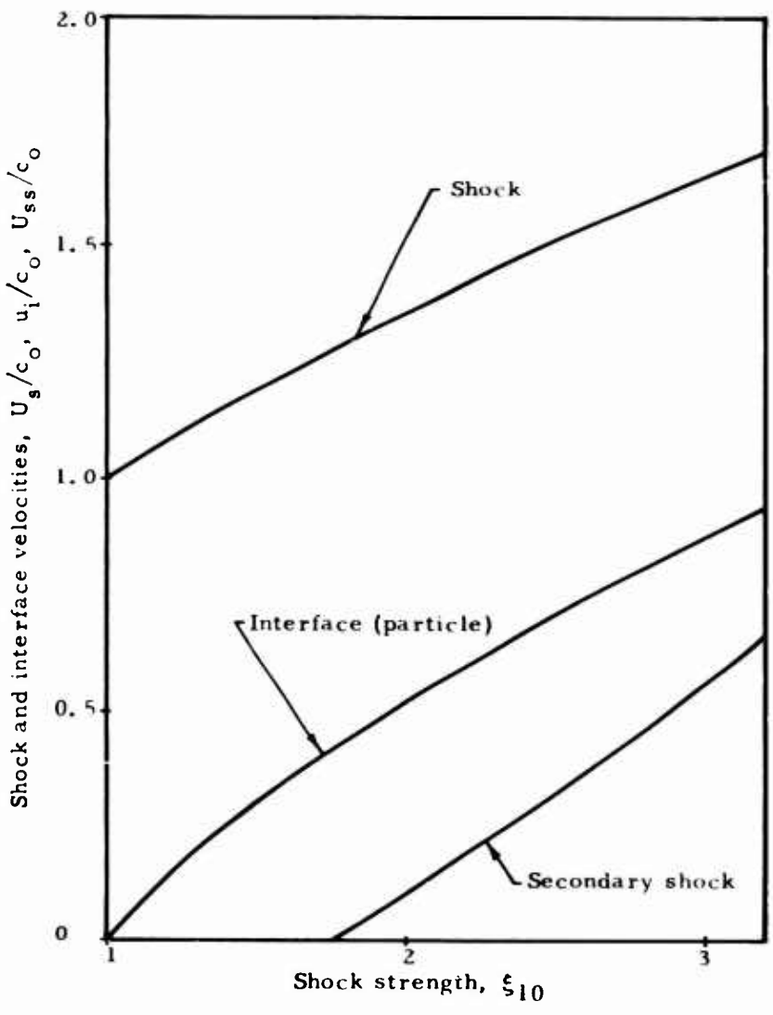


Fig. 3 Variation of Shock, Interface (Particle), and Secondary Shock Velocity with Shock Strength, Area Ratio $A_1/A_4 = 4$: Air/Air Shock Tube

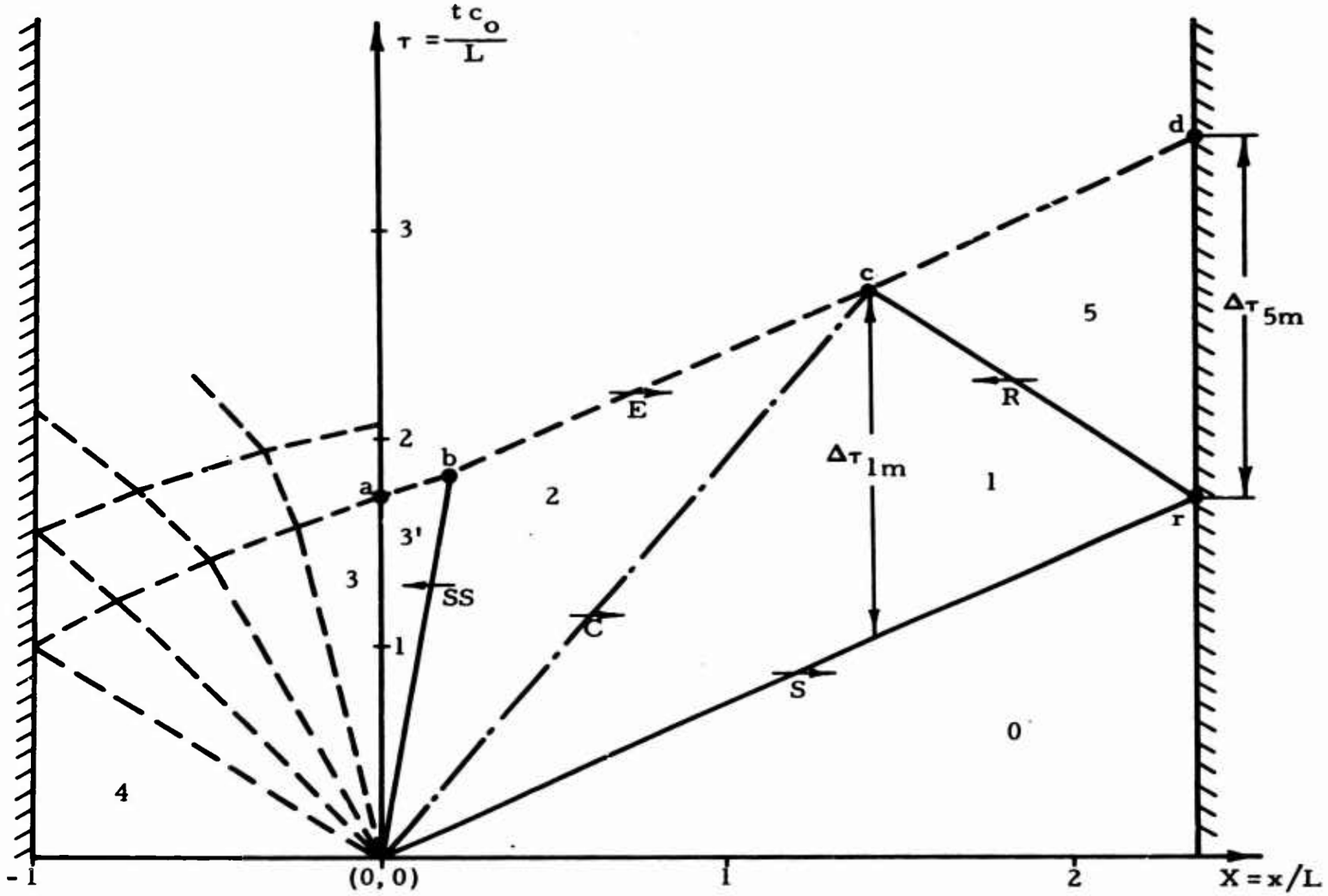


Fig. 4 Wave Diagram for a Shock Tube with Area Change $\sigma = 4$, $\xi_{10} = 2$

A 1 MJ ARC DISCHARGE SHOCK TUBE AS A CHEMICAL KINETICS RESEARCH FACILITY

L. L. Presley and G. E. Falkenthal
Ames Research Center, NASA
Moffett Field, California

and

J. T. Naff
MHD Research Incorporated
Newport Beach, California

INTRODUCTION

A shock tube driven by an arc discharge has recently been placed in operation at Ames Research Center for use in gas physics and chemical kinetics research. Consistent with this use it was designed to produce shock wave velocities as high as 12 km/sec and for initial test gas pressures as low as 10μ of Hg. The shock tube has comparatively large physical dimensions, the most significant being the 6-inch internal diameter of the driver, the largest diameter arc heated driver known to the authors. The pertinent physical features of the shock tube are described, particularly those related to the performance objectives. The primary features of the energy storage and delivery portion of the shock tube system and the problems encountered in placing the capacitor bank in operation are discussed. A few preliminary test results obtained in checking the operation of the shock tube are also presented.

DESCRIPTION OF FACILITY

Shock Tube

In the design of this facility, the following three requirements were considered: (1) high shock wave velocities, of the order of 12 km/sec (mm/μsec) or greater for simulating planetary entry conditions; (2) low driven gas pressures for stretching the nonequilibrium reaction zone to a

resolvable length; (3) adequate testing time at these low driven gas pressures for studying the reactions of interest.

In the following sections, the pertinent features of the shock tube will be discussed in light of meeting the performance objectives. The discussion will proceed from the driver to the driven tube, much the same as the operational chain of events. The over-all arrangement of the shock tube is shown in figure 1 where the components to be discussed are noted.

Driver

The first requirement clearly dictated the necessity for an arc heated driver gas of low molecular weight, as demonstrated in the pioneering work of references (1) and (2). Figure 2 is a detailed drawing of the driver. The comparatively large driver diameter, a nominal 6-inch inside diameter, was selected in compromise to the following considerations:

(1) The circuit for discharging the energy stored in a capacitor bank into an arc heated driver is usually an RLC series circuit. For such a circuit the discharge can be either oscillatory, critically damped, or overdamped. For this driver, it was desired that the discharge be at least critically damped, i.e., nonoscillatory. This criterion stipulates the RC time constant of the circuit. On this basis, and since the resistance of the arc was assumed to be inversely proportional to the area of the arc chamber, calculations were made which indicated that a driver diameter as large as 6 inches would assure a nonoscillatory discharge.

(2) It was believed that the ratio of driven tube to driver area should be small (for arc discharge shock tubes, the usual practice is for the area ratio, $A_{\text{driven tube}}/A_{\text{driver}}$, to be greater than 1.0). Since the amount of energy required to produce a given shock wave increases with area ratio, the choice of a small area ratio (e.g., 4.0) would make for much more efficient use of the capacitor bank energy. (For example, normalizing the energy required, Q, to an area ratio of 1, would give $Q = 2$ for an area ratio of 4, and $Q = 10$ for an area ratio of 20.) It was also believed that a smaller area ratio would permit a transition from the driver to driven tube that would minimize the disturbance of the interface and thereby increase the testing time.

(3) It was known for reasons described in the next section that the driven tube diameter would have to be about 12 inches.

Because of the above considerations, the driver diameter was made as large as possible, nominally 6 inches.

The length of an arc heated driver of this type must be as short as possible so that the mass of gas can be heated to the maximum gas temperature (sound speed) attainable with a given amount of energy. It should be

recalled that the performance of this type of shock tube is controlled by the speed of sound ratio across the diaphragm; thus to increase the shock speed for a fixed amount of energy stored in the capacitor bank and fixed driven tube pressure, the initial driver pressure is decreased. However, a minimum length is stipulated by the criterion that the rarefaction wave, generated by the diaphragm opening and reflected from the rear of the driver, does not catch up with the test gas. The required driver length is therefore inversely proportional to shock wave velocity. With this in mind, provision was made for varying the internal length of the driver up to 2 feet.

Figure 3 is a photograph of the driver. The collector rings and electrical cables, to be described later, are seen at the end of the driver. The teflon liner, which prevents the arc from striking the walls of the driver, consists of two 1/8-inch sheets, rolled and pressed into the driver chamber. The rear electrode is fully insulated from the driver walls by the various materials shown in figure 2, while the front electrode is also the diaphragm retaining ring and is in front of the teflon liner shown in figure 3. The seams of the teflon sheets are staggered 180° to provide adequate electrical insulation. The driver is fabricated with a modified 18-8 stainless steel having a very low permeability.

Diaphragm and Transition Section

The shock wave stabilizing section and the diverging section connect the 6-inch diameter of the driver to the 12-inch diameter of the driven tube. The diaphragm at the upstream end of the shock wave stabilizing section is held in place by the diaphragm retaining ring (front electrode) and can be installed without the driver being coupled to the diaphragm section; this allows the driven tube to be evacuated while the driver is being prepared for firing.

Flat diaphragms scored, as shown in figure 4, are used. They are scored to various depths to control their bursting pressure. The scoring is accomplished with an end mill which cuts a 90° included angle groove. The diaphragms, which are fabricated of an 18-8 stainless steel, rupture into a square section, shown in figure 5. The recesses for the diaphragm petals to fold into upon rupturing are clearly seen in figure 5. The square cross section was chosen, as opposed to a circular cross section, to minimize the risk of losing petals. The square portion of the diaphragm section transforms smoothly into the 6-inch-diameter circular configuration of the driven tube's shock wave stabilizing section.

The purpose of the shock wave stabilizing section was to allow the shock wave to become at least partially formed before entering the diverging section. The equivalent conical diffusion angle of the diverging section defined as

$$\alpha \equiv \tan^{-1} \frac{\text{(Maximum diameter) - (Minimum diameter)}}{\text{Length of section}}$$

was held at 12° to minimize shock wave perturbation of the interface. The entrance and exit portions of the diverging section were faired with a radius of curvature equal to the local diameter. The diffusion angle and shape of the entrance and exit fairing were believed to be particularly important because the strength and curvature of the oblique shock waves that stand at the exit, as well as the possibility of having a normal shock wave at the focal point of the oblique shock waves, are increased with large diffusion angles and sharp corners.

Driven Tube

The second and third design requirements, defined earlier, are concerned mainly with the driven tube. An over-all view of the driven tube was given in figure 1 and a photograph is presented in figure 6.

The second requirement stipulates material, internal finish, and vacuum pumping for the driven tube. Consistent with good vacuum practice, type 304 stainless steel tubing was used and this was honed to an interior finish of at least RMS 16. Vacuum pumping capacity adequate to obtain an ultimate pressure at least two orders of magnitude lower than the lowest anticipated initial driven tube pressure was incorporated (ultimate vacuum of 10^{-5} mm of Hg is obtainable in the driven tube).

The third requirement sets the size of the driven tube. The behavior of the interface between the driven and driver gas is not ideal in any shock tube, but this behavior is particularly non-ideal at the low gas densities required for chemical kinetics research. At these conditions, the interface is far from being a planar surface, behaving, in fact, similarly to the leaky piston which travels at a velocity greater than its ideal velocity and thereby decreases the length of the useful slug of gas between the shock wave and the interface. The result is a decrease of testing time. The useful testing time is increased by increasing the driven tube length until the interface and the shock wave are travelling at the same velocity. Then the slug of test gas becomes a fixed length, and no further increase in testing time is realized with increased length. This phenomenon governs the practical length of this type of shock tube. Testing time is also increased by increasing the diameter of the driven tube and it will change in proportion to the square of the diameter.

The 12-inch diameter was chosen because it appeared that it would provide a testing time adequate for the needs of the research. (A minimum testing time of 10 μsec was necessary.) The over-all length of 32-1/2 feet from the diaphragm to the center of the test section was selected since it was long enough to give nearly maximum testing time, yet not long enough to be physically cumbersome.

Electrical Components

On the basis of parametric calculations of the energy input into the driver that is required to produce shock waves with a velocity of 12 km/sec an energy storage of 1×10^6 J in the capacitor bank was selected. A survey of experimental information on the voltage necessary to produce an arc of a given length indicated that approximately 7.5 kV/ft were needed. In order to provide an adequate operating margin for a 2-foot driver length, a voltage of 20 kV was selected for the capacitor bank.

Capacitor Bank

The 1 MJ bank contains a total of 208 capacitors, each rated for 20 kV and having a nominal capacitance of 24 μF. The bank is divided into four segments so that the energy input into the driver can be varied in units of 250,000 J at full rated voltage or at any intermediate value by varying the charge voltage. Within each segment there are 4 rows of 13 capacitors and each row of 13 is bused together in parallel. A schematic diagram of one row is shown in figure 7. Thirteen coaxial cables connect each high voltage bus to the collector ring on the driver. Each capacitor has an expulsion type fuse between its high voltage terminal and the common high voltage bus. It is necessary to bus the capacitors together in groups of 13 to insure that there is, immediately available, sufficient energy to actuate a fuse (approximately 10 to 15 kJ) before the rest of the bank can discharge into a faulty capacitor. A photograph of the physical arrangement of the bank showing fuses and charging resistors (tubes at the bottom of photograph) is given in figure 8. The vertical partitions shown between the fuses are necessary to prevent the plasma flare from an exploding fuse from shorting out the adjacent fuse.

Several problems have been encountered in the initial operation of the capacitor bank. Failures of capacitors have occurred in situations wherein it was necessary that a fuse isolate the faulty capacitor in order to prevent the energy in the rest of the bank from being discharged into that faulty capacitor. However, on two occasions, the fuses have failed to function properly. The cause of the first fuse failure appeared to be a plasma leak from the fuse case which shorted the high voltage bus and the ground bushing of the capacitor. The cause of the second fuse failure has not been determined.

The capacitors used in this bank are not rated for voltage reversal. They are rated for, what is comparatively speaking, a short life; in this case 500 hours of electrification. They are designed to operate at a high static dielectric stress of 2500 V/mil, based on dielectric pad thickness. Since for the most part similar capacitors with a high static dielectric stress have not been used extensively throughout the country, the only safeguard for insuring that problems are not encountered is to submit the capacitors to a thorough testing program before installation. Accordingly the following testing program is being initiated for the capacitors of this bank:

(1) All capacitors are submitted to the following tests at the factory: (a) high voltage dielectric test at 150-percent rated voltage (30,000 V) for 1 minute. (It has been determined that one source of capacitor failure was the dielectric damage resulting from a fabrication error.); (b) discharge tests for a total of 10 shots on each capacitor at 60,000 A peak current, 65-percent reversal, and 24 kc discharge frequency. (The capacitors are rated for 25,000 A, nonoscillatory peak current discharge.)

(2) Upon receipt of the capacitors at the site, the following tests are performed to detect transportation damage: (a) high voltage dielectric test at 125-percent rated voltage (25,000 V) for 1 minute; (b) discharge test for a total of 10 shots on each capacitor at 25,000 A, critically damped.

After the capacitors are installed in the racks, the entire bank will be charged to rated voltage and discharged a sufficient number of times to prove that the capacitor bank is fully operational. During these tests, the capacitors will be bused together only through their charging resistors.

Collector Rings

The energy from each of the four segments of the capacitor bank is fed to the rear electrode of the driver through a coaxial collector ring. One of the four coaxial collector rings is shown in figure 9. The outer ring is the ground terminal and the inner ring is the high voltage collector. The inner and outer rings are separated by a micarta insulator. Each collector ring is separately removable from the driver and is attached to a grounded plate when its particular segment of the capacitor bank is not in use.

Arc Initiator

The arc is initiated with an exploding wire, similar in arrangement to that described in reference (2). In the prefire condition, the wire is held away from the rear electrode by a nylon rod. Upon firing, a solenoid releases the spring-loaded rod and the wire is drawn back until an arc is established between the wire and the rear electrode. A simple yoke of the same wire, 0.010-inch-diameter aluminum, provides the support at the front electrode.

Current Viewing Shunt

In order to determine the electrical efficiency of the driver, it is necessary to know the current in the arc discharge. The series shunt for making these measurements (fig. 2) is an integral part of the driver and measures the total current in the discharge at one time as opposed to the usual technique of measuring the current in a few cables. The current is determined from the voltage drop across the shunt which is measured through separate leads attached at each end of the shunt. The shunt is fabricated of 1/8-inch-thick type 330 stainless steel. Resistance of the

shunt was measured with a compensated Kelvin bridge. The error in shunt signal due to the inductance of the shunt and leads has been calculated to be no more than 1 percent of the total signal. Thus, the current in the arc can be measured to good accuracy.

Safety Features

The entire capacitor bank and driver are housed in a protective room. The inside of the room is lined with 1/8-inch steel sheet, and the outside is covered with 1-1/2 inches of plywood. This has proved adequate for stopping shrapnel from the explosion resulting from a capacitor failure wherein 600,000 J was discharged into a faulty capacitor. The protective room is vacated and locked before either the driver or the capacitor bank is charged. Before the capacitor bank can be charged, a series interlock chain encompassing protective room door locks, driver charging valves, driven tube charging and evacuation valves, and driver arming must indicate that it is safe to proceed. After the bank has been charged, the protective room door locks cannot be opened unless the bank voltage is less than 20 V. A motor driven bank grounding switch is situated so as to be clearly visible to all personnel entering the protective room and to indicate that the bank is grounded.

PRELIMINARY PERFORMANCE

Some performance data have been obtained in the process of checking the operation of the shock tube. These data are solely concerned with the shock tube itself and do not represent research data. All of the testing has been with air as the driven gas.

To assess the performance of a shock tube of this type, it is important to know the electrical efficiency of the discharge process. The energy actually dissipated in the discharge process is:

$$W = \int_0^\infty E(t)I(t)dt$$

and the electrical efficiency is then defined as

$$\eta_E = \frac{2W}{CE_0^2}$$

where C is bank capacitance, E_0 is bank voltage, and I is discharge current. The time dependent voltage and current are obtained from oscilloscope records as shown in figure 10. The electrical efficiencies obtained in this manner are between 70 and 80 percent which are lower than the 90- to 95-percent values of reference (2). The reason for these low values has not been determined.

The primary measure of the efficiency of an arc discharge shock tube is defined by its ability to produce a certain shock wave velocity from the energy discharged into the driver. The ideal energy density required to produce a shock wave of a given velocity is shown in figure 11. These curves were calculated from those of reference (2) and are plotted for a constant initial pressure of 10^{-4} atmosphere of air in the driven tube, and for various initial pressures in the driver. Also plotted in this figure are several experimental points that have been obtained in the preliminary tests. The experimental points have been obtained with the internal length of the driver set at 12 inches which gives a volume of 5105 cm^3. The low energy densities are due to limiting the capacitor bank voltage to 10 kV until the testing program discussed earlier had been completed and that only 156 capacitors (3750 μF) were available. Extrapolation of the performance obtained with energy densities ranging from 26 to 37 J/cm^3 to the value of 195 J/cm^3 obtainable with a full megajoule of energy in the capacitor bank and allowing for a decrease in efficiency with increasing energy density, indicates that shock wave velocities in excess of 12 km/sec should be obtained. Defining the over-all efficiency as the ideal energy density required to produce the measured shock velocity divided by the actual energy density gives:

$$\eta = \frac{(W/V)_{ideal}}{(W/V)_{actual}}$$

This efficiency takes into account all possible losses such as arc losses, radiation from the driver gas, and non-ideal shock tube performance. It can be seen from figure 11 that over-all efficiencies as high as 60 percent have been obtained. This figure compares well with the 50-percent efficiency that is usually obtained with this type of shock tube.

The shock wave velocities have been measured by observing the radiation behind the shock wave with photomultipliers and by ionization gages, located at two accurately known stations. The photomultipliers had an S-5 spectral response. In order to obtain meaningful data the radiation was collimated by two 0.0015-inch slits, 1 foot apart.

Typical outputs of the photomultipliers at two different initial driven tube pressures are shown in figure 12. The initial spike in both traces is taken to be the nonequilibrium radiation from behind the shock wave. The shock wave was assumed to have arrived when the signal was 5 percent of its maximum value behind the first peak. (Note, the signal shown on the oscilloscope traces is inverted.) The jagged signal immediately following the first maximum is interpreted as the driver gas radiation. The low level of the driver gas radiation is as would be expected from the low energy densities of the testing to date. The testing time appears to be about 30 μsec which is greater than half the 30 μsec value that is calculated to be attainable from the leaky piston model. Since these values are greater than those

in reference (3) (a 6-inch-diameter driven tube) the choice of a 12-inch-diameter driven tube and the care in designing the diverging section are well justified.

A typical output of an ionization gage is also shown in figure 12. The signal rise from these gages is much more sharply defined. The shock velocities presented in figure 11 are based on the ionization gage signal.

The pressures in the driver have been measured with a Kistler Model 601 Transducer. A small 1/8-inch hole was drilled through the liner and a 1/32-inch sheet of teflon was placed at the bottom of the hole. The face of the transducer was backed up against the 1/32-inch sheet. A typical output trace is shown in figure 13. This output has been filtered with a 50 kc filter, but there is still a significant amount of ringing. However, a rough estimate of the pressure can be made and this checks fairly well with anticipated results. The time history of driver pressure is evident.

CONCLUDING REMARKS

From the preliminary results that have been obtained, the following remarks can be made:

Preliminary evaluation indicates the achievement of fairly high over-all efficiencies. Extrapolation from the performance obtained with energy densities of less than 37 J/cm^3 to the value of 195 J/cm^3 obtainable with a full megajoule of energy in the capacitor bank indicates the shock wave velocities in excess of 12 km/sec should be obtained.

A testing time of about 30 μsec has been obtained which confirms the choice of a large diameter driven tube.

Problems have been encountered with capacitor and fuse failures. A testing program has been initiated to prove that the capacitor bank is operational.

REFERENCES

(1) Warren, W. R., Rodgers, D. A., and Harris, C. J., The Development of an Electrically Heated Shock Driven Test Facility. 2nd Symp. on Hypervelocity Techniques, Univ. of Denver, Denver, Colorado, March 1962.

(2) Camm, J., Escape Velocity Shock Tube With Arc Heated Driver. 2nd Symp. on Hypervelocity Techniques, Univ. of Denver, Denver, Colorado, March 1962.

(3) Camm, J. C., and Rose, P. H., Electric Shock Tube for High Velocity Simulation, Res. Rep. 136, Avco-Everett Res. Lab., July 1962.

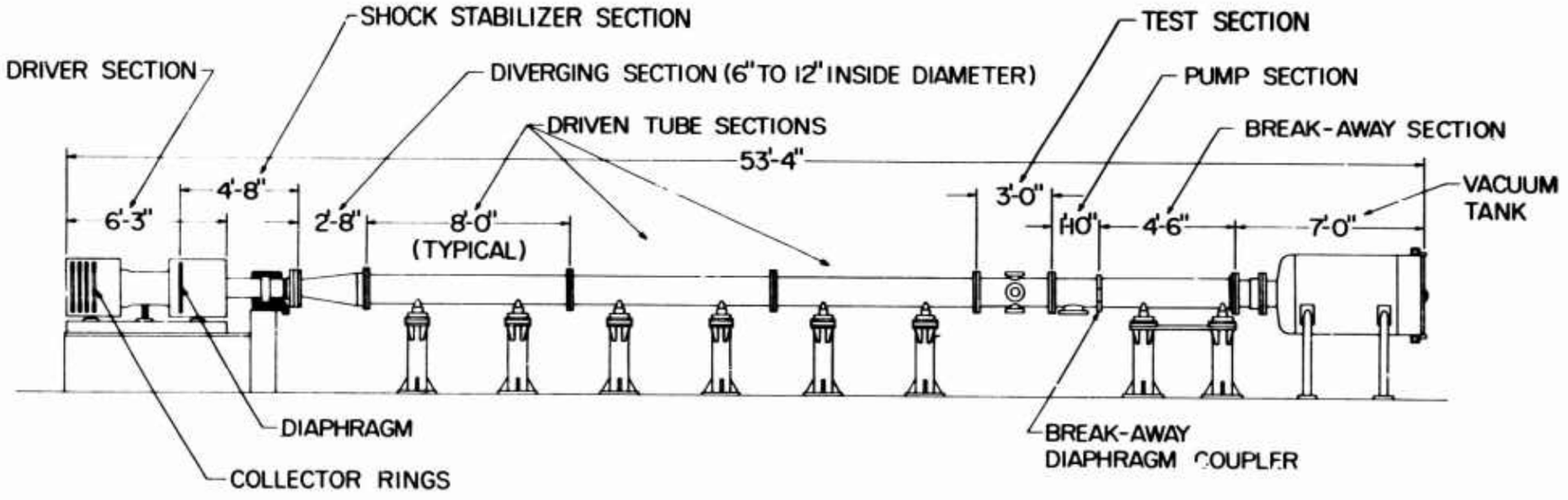


Fig. 1.- Sketch of arc discharge shock tube.

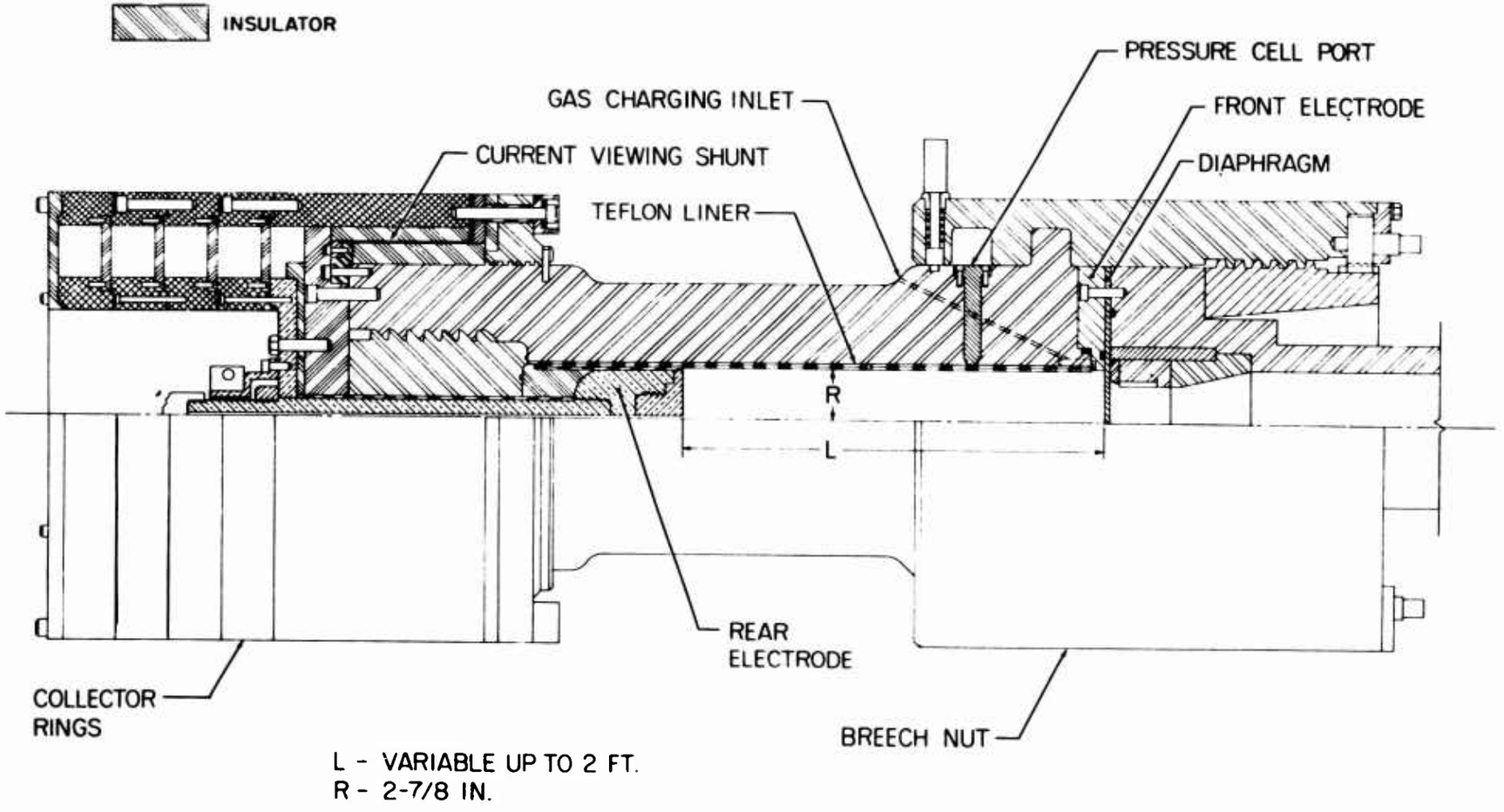


Fig. 2.- Details of arc discharge driver.

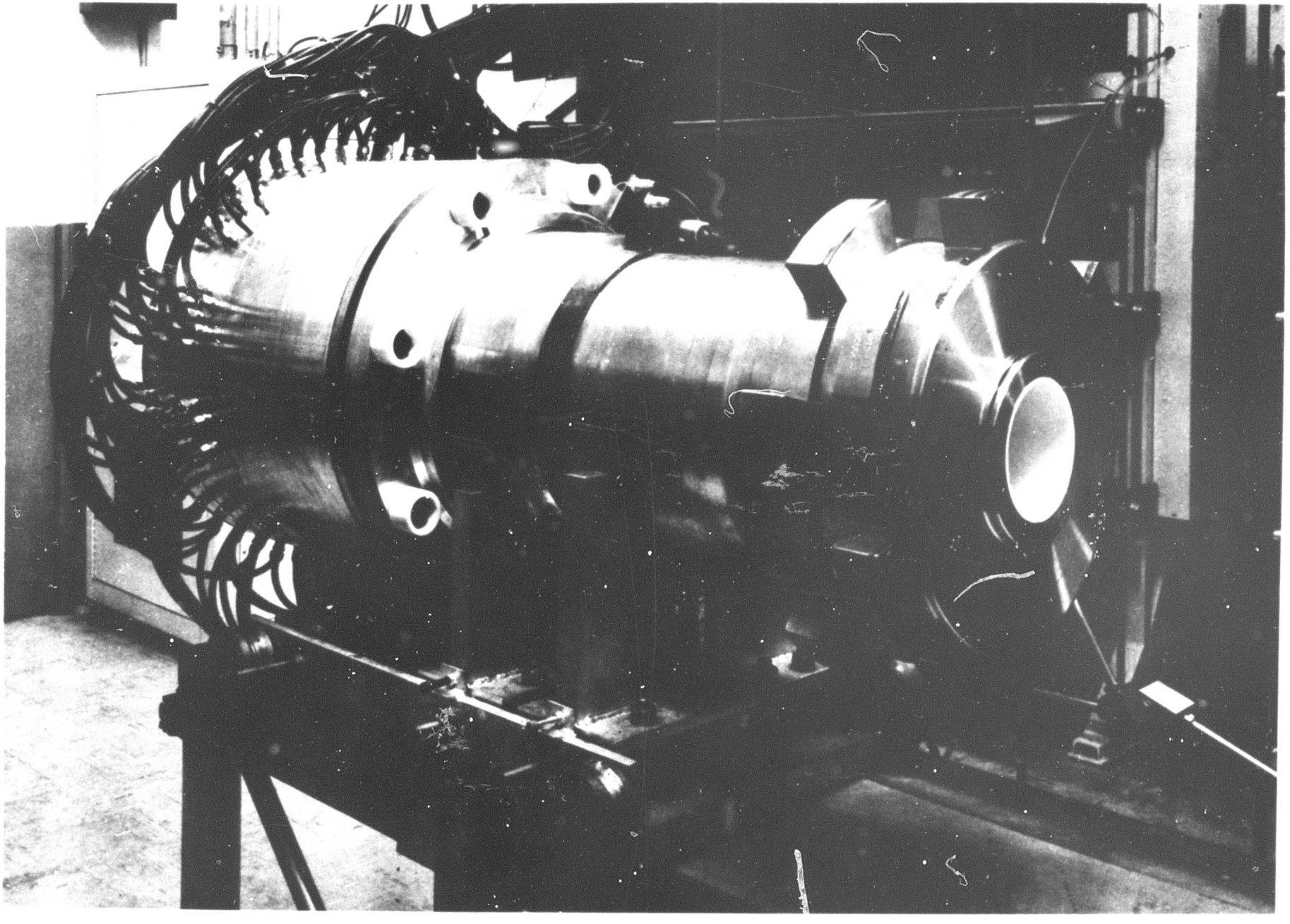


Fig. 3.- Arc discharge driver.

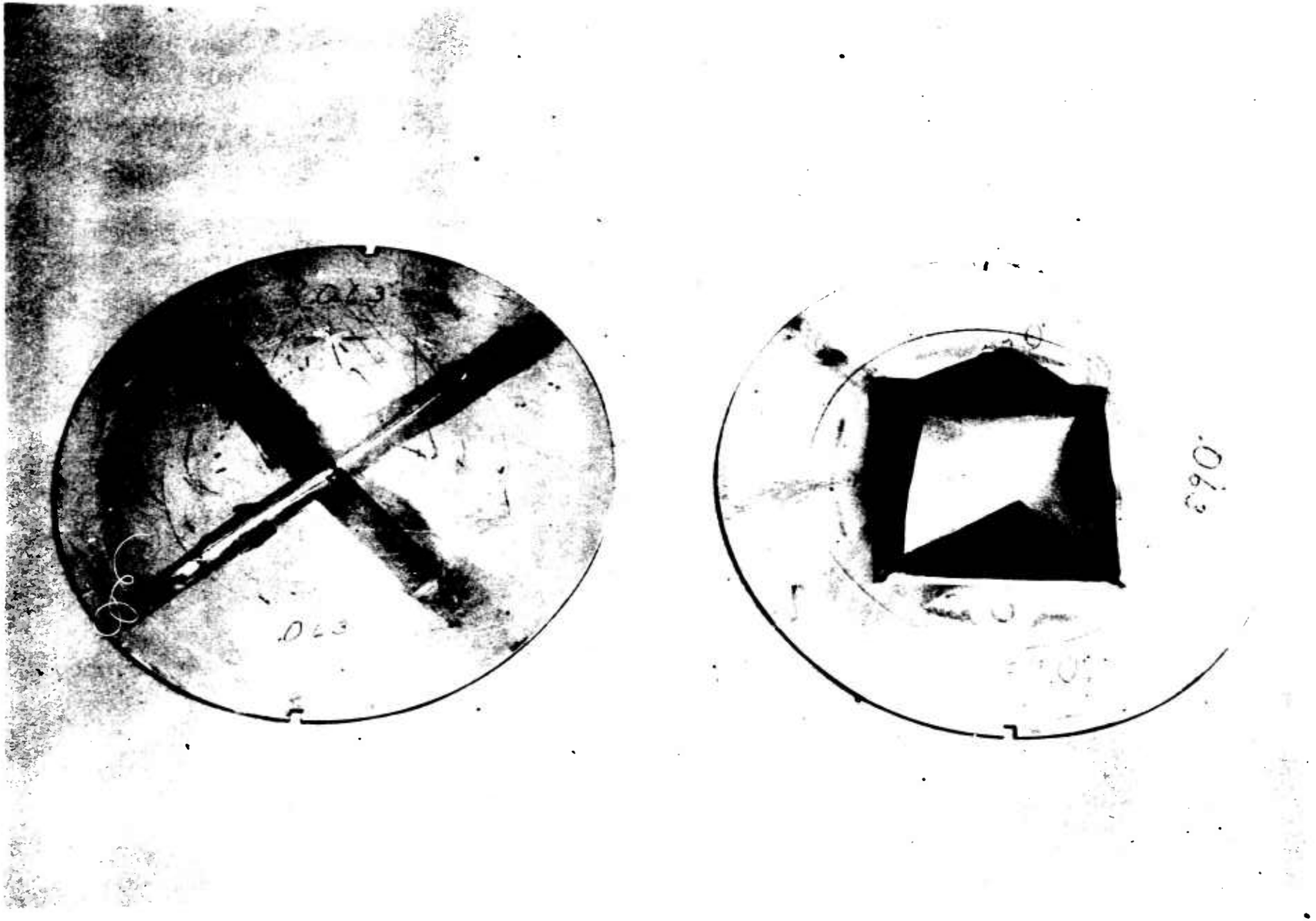


Fig. 4.- Scribing and petaling pattern of diaphragms.

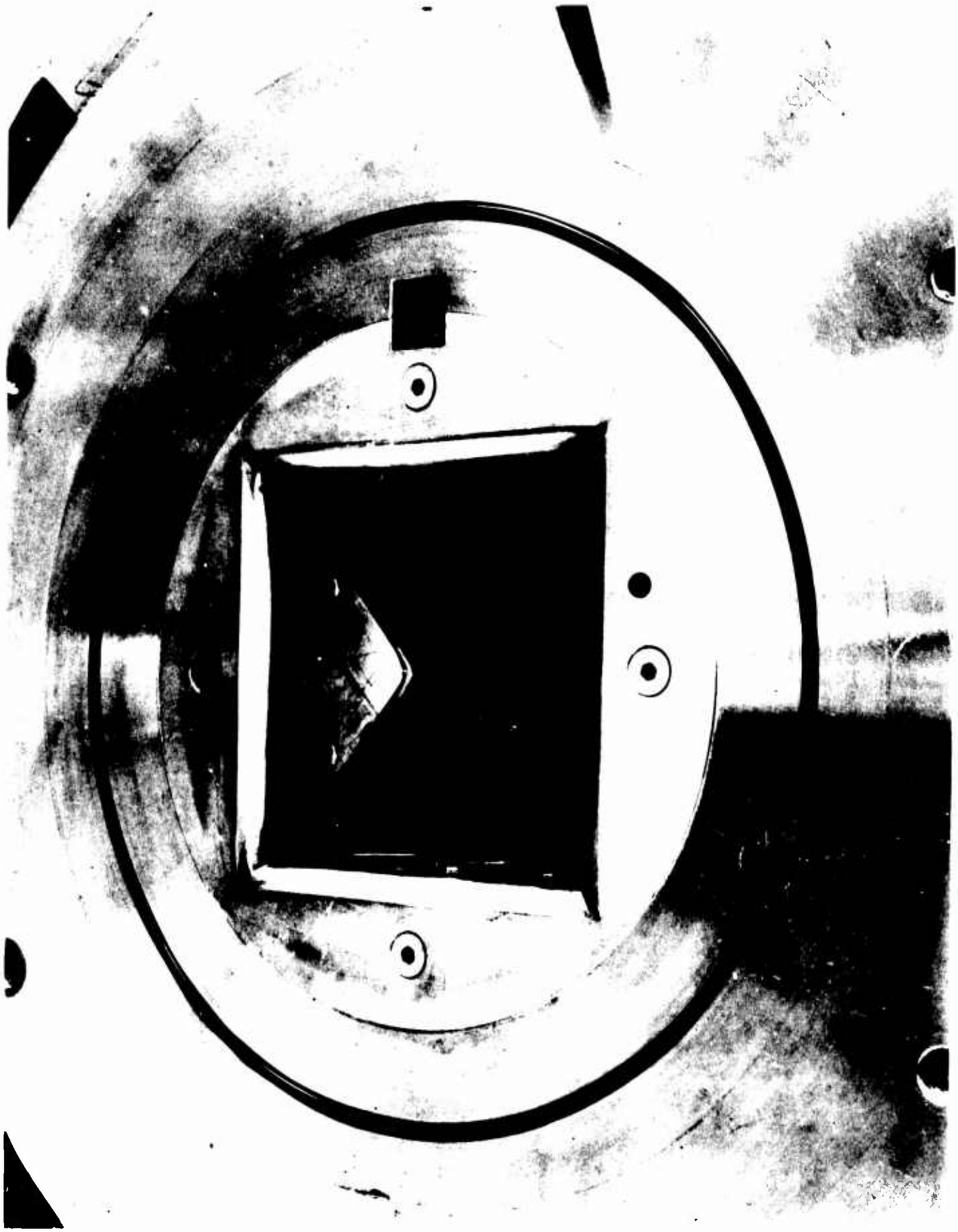


Fig. 5.- Diaphragm holder.



Fig. 6.- Over-all view of driven tube.

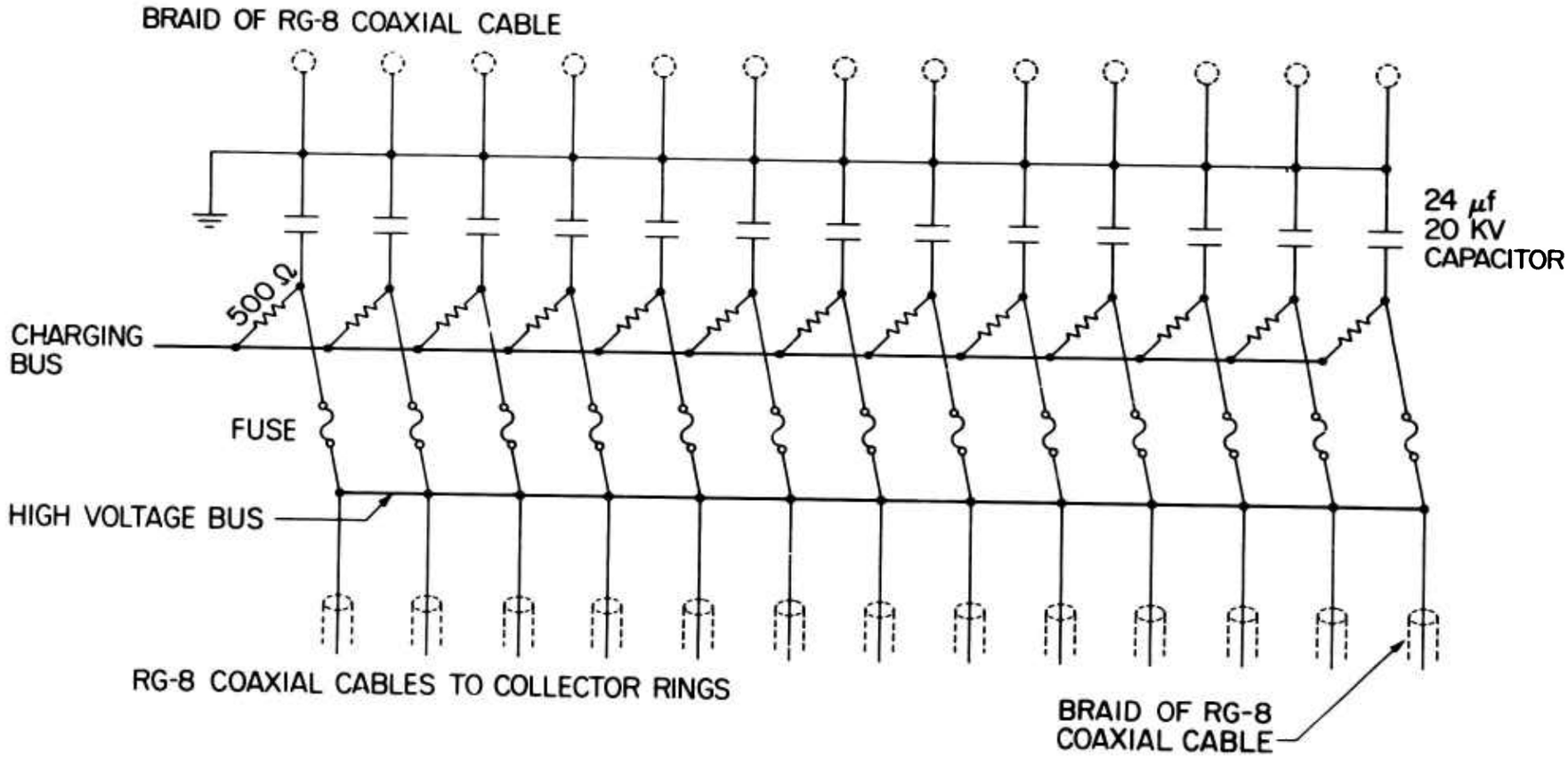


Fig. 7.- Schematic diagram of one row of capacitor bank.

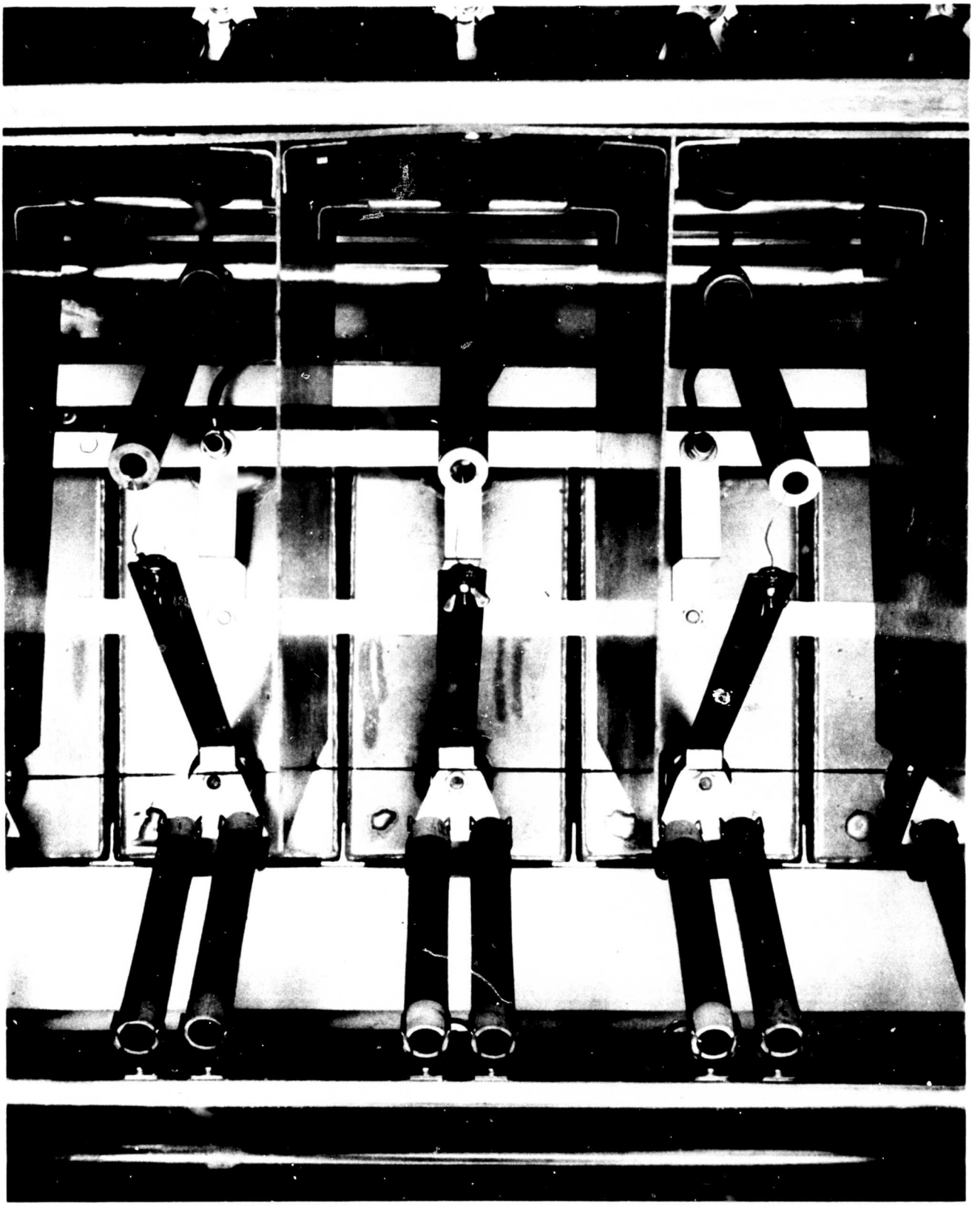
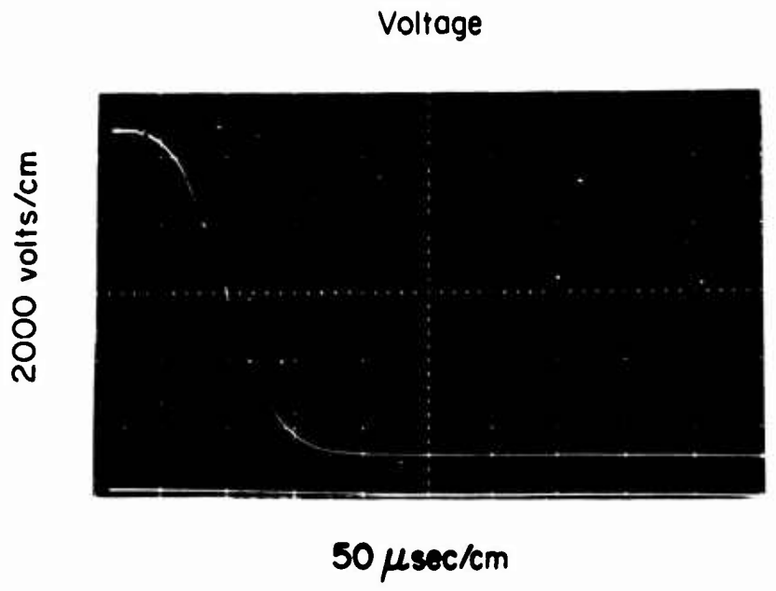


Fig. 8.- View of capacitors, fuses, charging resistors, and related buswork.



Fig. 9.- Details of collector ring.



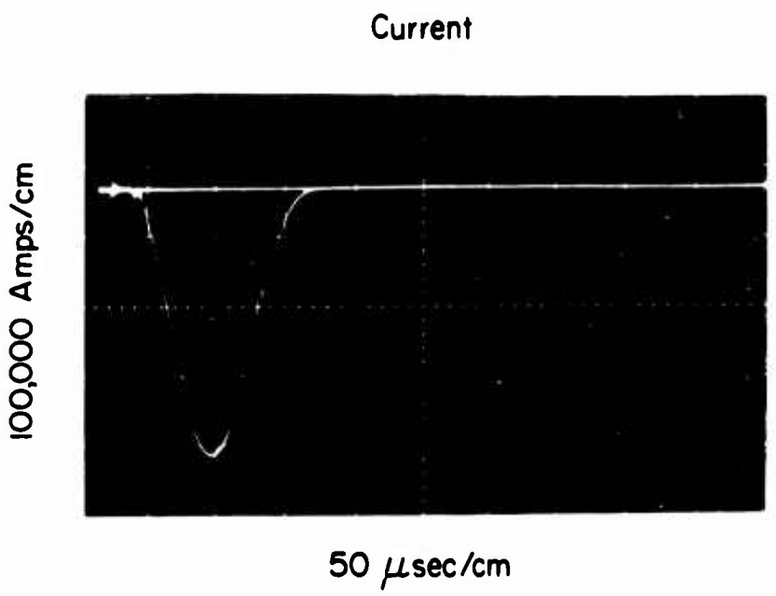


Fig. 10.- Voltage and current wave forms. Nominal voltage of 10 kv.

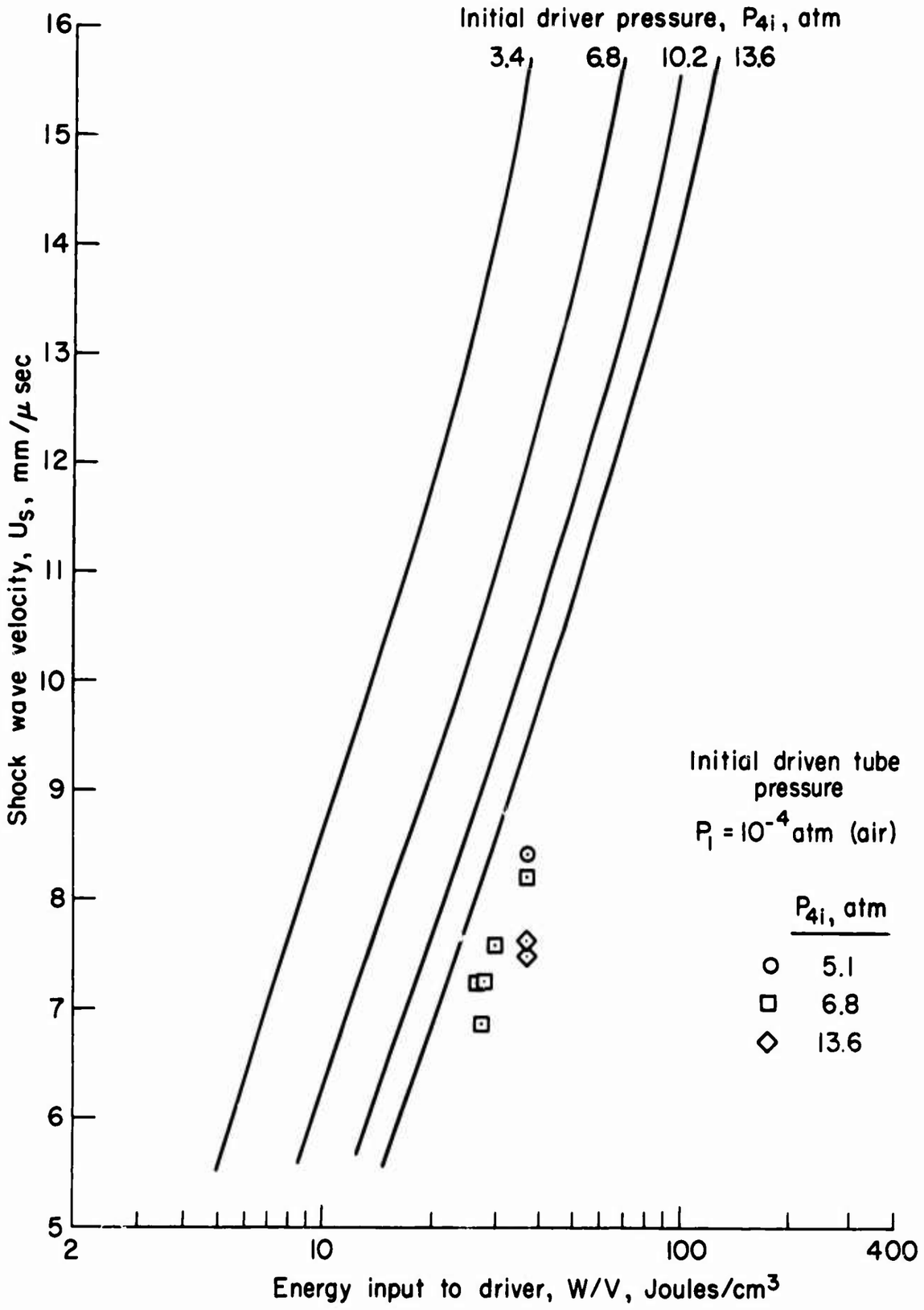


Fig. 11.- Theoretical and actual shock wave velocities as a function of energy input to driver and initial driven charging pressure.



50 μsec/cm

(a) Photomultiplier output at an initial driven tube pressure of 10^{-4} atm and a shock velocity of 8.1 km/sec.



50 μsec/cm

(b) Photomultiplier output at an initial driven tube pressure of 3×10^{-4} atm and a shock velocity of approximately 7 km/sec.



20 μsec/cm

(c) Ionization gage output at an initial pressure of 10^{-4} atm and a shock velocity of 7.1 km/sec.

Fig. 12.- Oscilloscope traces for shock velocity measurements.

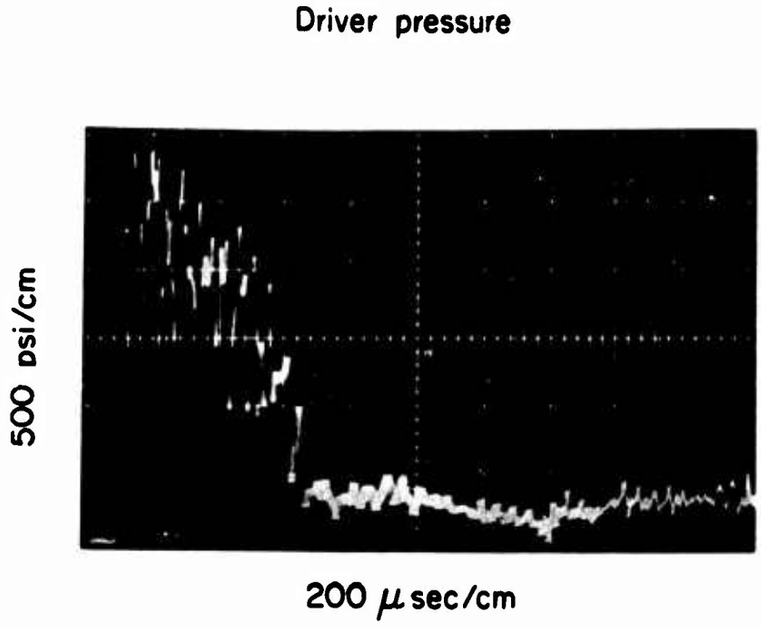


Figure 13.- Oscilloscope record of transducer output measuring driver pressure. Initial driver charging pressure is 13.6 atm. Ideal maximum pressure based on 100 percent efficiency is 226 atm. Output has been filtered with a 50 kc filter (500 psi/cm = 34 atm/cm).

REAL FLOW EFFECTS ON SHOCK ATTENUATION IN SHOCK-TUBE FLOWS

C. S. Kim and C. C. Chang
Catholic University of America.
Washington, D. C.

and

C. Park *
NASA, Ames Research Center
Moffett Field, California

The real flow effects, i.e., the effect of boundary layer growth, radiation, imperfect diaphragm rupture and contact-surface mixing, convective heat transfer, and crossed electric and magnetic fields, on shock-wave velocity attenuation in a constant-area shock-tube is evaluated. The gas is assumed to be an ideal reacting gas of Lighthill's type in chemical equilibrium, and the characteristic equations for the modified Riemann's variables for unsteady flow are derived. Assuming that the above-mentioned real flow effects are small in comparison with the ideal gas flow properties, a small-perturbation analysis is applied to the characteristic equations to derive the deviations from ideal conditions due to the real flow effects. By making a minimum number of assumptions, it is shown that (i) imperfect diaphragm rupture causes an initial lag in shock velocity, (ii) heat transfer from hot gas to cold gas through contact-surface mixing causes an overshoot in shock velocity, (iii) attenuation of shock speed due to radiation from the hot gas becomes an important effect at high density and is independent of tube diameter. In addition, (iv) the strengths of crossed electrical and magnetic fields needed to compensate for the attenuating effect of boundary layer growth and radiation to maintain a constant shock speed are calculated. The numerical calculations are carried out for the radiation and wall heat transfer effect for a range of operating conditions and some typical values are computed for the rest of the effects.

List of Symbols

A cross sectional area of shock tube

a variable similar to sound speed, defined by equation (8d)

---

* National Academy of Sciences Research Associate

B	magnetic flux density
C	gas combination parameter, defined by equation (21a)
C_i	see Appendix I for definition
C_f	surface friction coefficient
C_p	frozen specific heat at constant pressure
C_v	frozen specific heat at constant volume
D	perimeter of shock tube
D_i	see Appendix I for definition
E	electric field intensity
e	energy added per unit volume
F	see equation (23b)
f	body force per unit volume excluding $j \times B$ force
G_i	see Appendix I for definition
H	total enthalpy
H_i	see Appendix I for definition
h_r	energy of formation of chemical species present
j	electric current density
k	Boltzmann constant
L	length of hot gas column
m	exponent of attenuation rate or boundary layer growth
n	constant appearing in equilibrium species concentration, see equation (1b)
p	pressure
$P_{\pm}$	modified Riemann's variable, defined by equation (10)
Q_u, Q_a $Q_s, Q_{\pm}$	see equations (14) to (17) and Appendix I
q_w	heat loss through tube wall by conduction

R	gas constant
r	reflection parameter, see equation (23a)
S	modified entropy, defined by equation (8a)
T	temperature
T_r	characteristic temperature of reaction
t	time
t_c	crictical time for contact-surface mixing, see equation (36c)
U	velocity of shock wave
u	particle velocity
x	distance along shock-tube, from diaphragm position
y	distance normal to shock-tube axis, from wall
z	distance from contact surface, $z=ut-x$
α	species concentration
β	molecular thermal conductivity
δ	boundary layer thickness
δ_{ij}	generalized boundary layer thickness parameter, $\int_0^\delta \left(1 - \frac{\rho^i u^j}{\bar{\rho}^i \bar{u}^j}\right) dy$
$\epsilon_\pm, \epsilon_s$	perturbation due to over-all real-gas effects defined by equations (5) to (9)
κ	eddy thermal conductivity
ρ	density
ρ_r	characteristic density of reaction
$\Lambda(x)$	see equation (23c)
σ	electric conductivity
$\Omega_\pm, \Omega_s$	line integral of $\epsilon_\pm$, ϵ_s along a characteristic curve defined by equation (20)
τ	diaphragm opening time

ω_+, ω_s perturbation due to boundary-layer growth, defined by equations (8b, ω_u, ω_f 8c and 11a)

Prescript delta (Δ) deviation from ideal condition

Superscript bar ($\bar{}$) condition in central core of the shock-tube flow

Subscripts

1 initial condition in low pressure channel

2 condition in driven gas

3 condition in driver gas

4 initial condition in high pressure chamber

+ positive characteristics

- negative characteristics

s referred to energy conservation law or entropy increase

u referred to momentum conservation law

ρ referred to mass conservation law

I,J,K, H,M,N, H',M',N' points along typical characteristic curves as shown in Figure (2)

$\overline{IJ}$, etc line integration from point I to J, see equation (20)

INTRODUCTION

Although the problem of shock-wave velocity attenuation in a shock-tube flow has been solved theoretically by various authors[1-10], the only mechanisms causing attenuation treated so far have been boundary layer growth and effects resulting from imperfect diaphragm rupture. In an earlier work of the present authors[2], however, the effect of crossed electrical and magnetic fields was also considered. The most recent development in dealing with the boundary layer effect is to regard the boundary layer as an area-reducing mechanism. The diaphragm rupturing process has been analyzed mainly with the emphasis on the pressure and density disturbances[7-9]. All these theories resort, to a varying degree, to a judicious intuition and simplification, but nevertheless have shown a fair degree of agreement with experimental results for medium-high shock strengths[1,3,5,6,10], up to shock Mach number of 15 say. At higher shock strengths, the experimental results have shown a considerable departure from the prediction of these theories[8].

These departures of the experimental shock wave strengths from the predictions of the existing theories at high shock strengths may be due to considerable energy transfer by processes which have not been considered in the existing theories. These processes are radiative and conductive heat transfer to the tube wall, entropy increase due to imperfect diaphragm rupture, contact-surface heat transfer through conduction or turbulent mixing, and real-gas effects, i.e. dissociation or ionization, that may affect the boundary layer characteristics. These effects are termed here as "real flow" effects. At high shock strengths the boundary-layer cannot be regarded as merely a mechanism for area reduction because the energy transfer can be as important as the mass defect. The partial opening of the diaphragm may cause separated flow and turbulence, leading to a loss of energy, i.e. an increase in temperature in exchange for a lowered shock speed. Likewise, the energy transfer through the contact surface may have more effect on shock attenuation than the previously considered production and reflection of waves by hydrodynamical instabilities at the contact surface[7].

In the present paper, the earlier work of the present authors is extended to include the above mentioned effects, focusing on the energy transfer effects mentioned above. Riemann's characteristic equations are derived including real-gas effects, radiative and conductive heat transfer to tube wall, the crossed electromagnetic effect and possible body force. By this means, a unified approach is made in analyzing the various real flow effects from a common basis so that each may be assessed in importance relative to the others.

EQUATIONS OF MOTION

The equations of motion for the unsteady flow through a duct of constant cross section, in the presence of the wall boundary layer and uniform crossed electric and magnetic fields, are derived under the following assumptions.

(1) The deviation of mean flow properties from an ideal, uniform condition of a perfect gas due to viscosity, crossed electromagnetic fields and radiation is small.

(2) Both the driver and the driven gas are ideal reacting gases and are in equilibrium; that is, they satisfy the following conditions

(Equation of State) $$p = \rho RT(1 + \alpha) \tag{1a}$$

(Condition of equilibrium) $$\frac{\alpha^2}{1-\alpha} = \frac{\rho_r}{\rho}\left(\frac{T}{T_r}\right)^n \exp\left(-\frac{T_r}{T}\right) \tag{1b}$$

(Equation of energy) $$H = C_p T + h_r \alpha + \frac{u^2}{2} \tag{1c}$$

The C_p in equation (1c) is the frozen specific heat at constant pressure, i.e. the portion of specific heat due to collisional energy transport alone. The above gas model reduces to that of the ideal dissociating diatomic gas of Lighthill[11] for $n = 0$ and $C_p = (4 + \alpha)R$, and to that of ideal ionizing monatomic gas of Bray[12] for $n = 1.5$ and $C_p = 2.5(1 + \alpha)R$. The change in C_p due to the change in the species concentration α is small, and so C_p is assumed to be constant for each gas throughout.

The physical picture of the flow field is shown in figures (1a) and (1b). The duct has a perimeter D and cross-sectional area A. The boundary layer developed near the wall is sufficiently thin compared with the diameter of the tube that $2\delta/D \ll 1$. Through the wall, the heat q_w is transmitted per unit area per unit time by conduction. The energy e is added per unit volume. The electric and magnetic fields are applied perpendicularly to the flow in a crossed configuration and are uniform within the free stream core. Thus the velocity, temperature, electric and magnetic fields are assumed to vary only in the boundary layer. The equations of motion for this flow condition are[2,13,14]

(mass)
$$\frac{\partial}{\partial t}\int \rho\, dA + \frac{\partial}{\partial x}\int \rho u\, dA = 0 \tag{2a}$$

(momentum)
$$\frac{\partial}{\partial t}\int \rho u\, dA + \frac{\partial}{\partial x}\int \rho u^2\, dA + A\frac{\partial p}{\partial x} + C_f \frac{\bar{\rho}}{2}\bar{u}^2 D + \int f\, dA - \int jB\, dA = 0 \tag{2b}$$

(energy)
$$\frac{\partial}{\partial t}\int \rho(H - RT)dA + \frac{\partial}{\partial x}\int \rho H u\, dx - \int \frac{j^2}{\sigma}\, dA + Dq_w + \int e\, dA = 0 \tag{2c}$$

The integrations appearing in the above equations are facilitated by introducing the generalized boundary layer thickness

$$\delta_{ij} = \int_0^{\delta}\left(1 - \frac{\rho^i u^j}{\bar{\rho}^i \bar{u}^j}\right) dy \tag{3}$$

which allows one to write:

$$\int \rho^i u^j\, dA = \bar{\rho}^i \bar{u}^j (A - D\delta_{ij}) \,. \tag{4}$$

In particular δ_{11} and δ_{12} are the boundary layer displacement and momentum thicknesses, respectively.

Using equation (4), equations (2a) to (2c) reduce to

$$\frac{D\bar{\rho}}{Dt} + \frac{\partial \bar{u}}{\partial x} = \epsilon_\rho \equiv \bar{\rho}\bar{u}\,\frac{D}{A}\,\omega_\rho \tag{5}$$

$$\frac{D\bar{u}}{Dt} + \frac{\partial \rho}{\partial x} = \epsilon_u \equiv \bar{u}^2\,\frac{D}{A}\,\omega_u + \frac{\sigma B}{\bar{\rho}}\,(E - \bar{u}B) + \frac{f}{\bar{\rho}} \tag{6}$$

$$\frac{1}{C_p}\,\frac{D\bar{S}}{Dt} = \frac{\epsilon_s}{C_p} \equiv \frac{1}{2}\,\frac{R}{C_p - R} - \frac{D}{A}\,\frac{\bar{u}^2}{\bar{a}^2}\,\omega_s + \frac{R}{C_p - R}\,\frac{1}{\bar{\rho}\bar{u}^2}\left[\sigma(E - \bar{u}B)(E - 2\bar{u}B) - \frac{D}{A}\,q_w + e\right] \tag{7}$$

where

$$\frac{dS}{C_p - R} \equiv \frac{dp}{p} - \frac{C_p}{C_p - R}\,\frac{d\rho}{\rho} + \frac{R}{C_p - R}\,\frac{h_r}{RT(1 + \alpha)}\,d\alpha \tag{8a}$$

$$\omega_\rho \equiv -\frac{C_f}{2} + \frac{1}{\bar{u}}\,\frac{\partial}{\partial t}\,(\delta_{11} - \delta_{10}) + \frac{\partial}{\partial x}\,(\delta_{12} - \delta_{11}) \tag{8b}$$

$$\begin{aligned}\omega_s \equiv\ & C_f + \frac{\partial \delta_{13}}{\partial x} + \left(\frac{1}{\bar{u}}\,\frac{\partial}{\partial t} - \frac{\partial}{\partial x}\right)\delta_{12} \\ & - \left\{\frac{2}{\bar{u}}\,\frac{\partial}{\partial t} + \left[\left(\frac{C_p}{R} - 1\right)\frac{\bar{a}^2}{\bar{u}^2} - 1\right]\frac{\partial}{\partial x}\right\}\delta_{11} \\ & - \frac{1}{\bar{u}^2}\left[2\left(\frac{C_p}{R} - 1\right)\frac{\bar{a}^2}{\bar{u}^2} - 1\right]\frac{\partial \delta_{10}}{\partial t} \\ & + 2\left(\frac{C_p}{R} - 1\right)\frac{\bar{a}^2}{\bar{u}^2}\,\frac{\partial \delta_{01}}{\partial x}\end{aligned} \tag{8c}$$

The ω_ρ, ω_u, ω_s and ϵ_ρ, ϵ_u, ϵ_s can be interpreted respectively as the perturbation factors due to boundary-layer alone and due to the over-all perturbations of the mass, momentum and energy conservation equations. The variable S is the entropy modified to include the dissociation cr ionization effect and a is defined as

$$a = \sqrt{\frac{C_p}{C_p - R}\frac{p}{\rho}} \tag{8d}$$

which reduces to sonic speed for a perfect gas.

Forming the characteristic equations for Riemann's variables, there results

$$\frac{d_{\pm}P_{\pm}}{dt} = \epsilon_{\pm} \equiv \frac{\bar{a}\bar{u}}{2}\frac{D}{A}\omega_{\pm} + \frac{\sigma}{2\bar{\rho}}(E - \bar{u}B)\left\{\frac{R}{C_p - R}\cdot\frac{\bar{a}}{\bar{u}^2}(E - 2\bar{u}B) \pm B\right\}$$

$$- \frac{1}{2}\frac{R}{C_p - R}\frac{\bar{a}}{\bar{\rho}\bar{u}^2}\left(\frac{D}{A}q_w - e\right) \pm \frac{1}{2}\frac{f}{\bar{\rho}} \tag{9}$$

where $P_{\pm}$ is the modified Riemann's variable defined as

$$dP_{\pm} = \frac{C_p - R}{R}d\bar{a} \pm \frac{d\bar{u}}{2} - \frac{\bar{a}}{2C_p}\left(\frac{C_p}{R} - 1\right)d\bar{S} \tag{10}$$

and

$$\omega_{\pm} = \omega_\rho \pm \frac{u}{a}\omega_u \pm \frac{1}{2}\frac{R}{C_p - R}\frac{\bar{u}^2}{\bar{a}^2}\omega_s \tag{11a}$$

$$\frac{d_{\pm}}{dt} = \frac{\partial}{\partial t} \pm (\bar{u} \pm \bar{a})\frac{\partial}{\partial x} \tag{11b}$$

The $\omega_{\pm}$ and $\epsilon_{\pm}$ can again be interpreted as the perturbation factors due to boundary layer alone and due to over-all effect, respectively, for the positive or negative characteristics.

Since the RHS's of equations (7) and (9) are zero for an ideal shock-tube flow without real flow effects, the nonzero values of the dependent variables on LHS represent deviations from the ideal flow. Denoting a deviation from the ideal shock-tube flow by a prescript Δ, equations (7) and (9) can be written as

$$\frac{D}{Dt}(\Delta\bar{S}) = \epsilon_s \tag{12}$$

$$\frac{d_{\pm}}{dt}(\Delta\bar{P}_{\pm}) = \epsilon_{\pm} \tag{13}$$

where ϵ_s and $\epsilon_\pm$ are defined by equations (7) and (9). Equations (12) and (13) are forms of the equations of motion relating the deviation from the ideal gas shock-tube flow to the real flow effects.

Across the shock wave (denoted by the letter U in Figure 2 and in the following analysis), the Rankine-Hugoniot relations for ideal reacting gas hold even though electric and magnetic fields are assumed to be present. This is because in the present treatment, the fields are taken to be zero in front of the shock and uniform behind it, and no secondary electric current is allowed to flow. The electro-magnetic field effects thus appear as a body force only in the hot gas, and so, for the determination of the properties immediately behind the shock, the presence of the fields can be disregarded. The situation is thus entirely different from an ordinary MHD shock wave where no external electric field exists and the induced electric current controls the shock structure. Thus the deviation of properties from the ideal gas flow behind the shock can be written, for small deviations, as

$$\Delta\bar{u}_{2U} = Q_u \Delta U \tag{14}$$

$$\Delta\bar{a}_{2U} = Q_a \Delta U \tag{15}$$

$$\Delta \frac{\bar{S}_{2U}}{C_{V2}} = \frac{Q_s}{U} \Delta U \tag{16}$$

$$\Delta\bar{P}_\pm = Q_\pm \Delta U \equiv \left\{ \frac{Q_a R}{C_p - R} - \frac{1}{2} \frac{(C_p - R)^2}{C_p R} \frac{Q_a \bar{a}_{2u}}{U} \pm \frac{Q_u}{2} \right\} \Delta U \tag{17}$$

where the numerical subscript 2 refers to the hot driven gas region, i.e. region 2 in the x-t diagram of Figure 2. The functional forms of Q_a, Q_u and Q_s for the driven gas under consideration are given in Appendix I.

Across the contact surface, the condition $\bar{u}_2 = \bar{u}_3$ gives the relation

$$\Delta P_{+3u} - \Delta P_{-3u} = \Delta P_{+2u} - \Delta P_{-2u} \tag{18}$$

If the pressure is allowed to differ by Δf, i.e. $p_3 = p_2 + \Delta f$, there results

$$2\left(\frac{C_p}{C_p - R}\right)_3 \lambda_{a3} \frac{\Delta\bar{a}_{3u}}{\bar{a}_3} - \lambda_{s3} \frac{\Delta\bar{S}_{3u}}{C_{V3}} = 2\left(\frac{C_p}{C_p - R}\right)_2 \lambda_{a2} \frac{\Delta\bar{a}_{2u}}{\bar{a}_2} - \lambda_{s2} \frac{\Delta\bar{S}_{2u}}{C_{V2}} + \left(\frac{C_p}{R} - 1\right)\Delta f \tag{19}$$

where λ_a and λ_s are factors accounting for the dissociation or ionization effect defined in Appendix I. These factors reduce to unity for a perfect gas. Along the head of the centered rarefaction wave and at the origin $x = 0$ and $t = 0$, all deviations are zero.

Now $\Delta\bar{P}_{\pm}$ and $\Delta\bar{S}$ can be obtained formally by integrating equations (12) and (13) along the relevant characteristics. Since the deviation from the ideal flow is small, the products of deviations can be neglected and so the integrating paths can be taken as the characteristics of the ideal flow.

Denoting the line integrals of $\epsilon_{\pm}$ or ϵ_s with respect to time from a point A to a point B along the relevant characteristics by $\Omega_{\pm\overline{AB}}$, $\Omega_{s\overline{AB}}$ etc.,

$$\Omega_{\pm\overline{AB}} = \int_A^B \epsilon_{\pm}dt, \qquad \Omega_{s\overline{AB}} = \int_A^B \epsilon_s dt \tag{20}$$

For example $\Omega_{\pm\overline{IM}}$ represents the line integral of the over-all perturbation effect along the positive characteristic from point I to point M, Figure 2. Physically, ϵ's represent the time rate of change of the characteristic wave quantity P's due to real flow effects, and the line integral Ω's denote the net change in P's gained within the time interval specified by the subscripts $\overline{AB}$. Using these notations, one can show, from equations (14) to (20), that

$$(1 + C)Q_+\Delta U(x_H) - (1 - C)Q_-\Delta U(x_N) - (1 + C)\Omega_{+\overline{MH}} - (1 - C)\Omega_{-\overline{NM}} - 2\Omega_{+\overline{IM}} = 0 \tag{21}$$

where C is the gas combination parameter defined as

$$C \equiv \left(\frac{C_{p_2} - R}{C_{p_1} - R}\right)^2 \frac{\bar{a}_2}{\bar{a}_1} \tag{21a}$$

The parameter C is very small, $C \ll 1$, when an unheated heavy gas is used as the driver and is of the order of unity when a heated light gas is used for the driver. Also, there follows

$$\Delta\bar{u}_{3M} = Q_+\Delta U(x_H) - Q_-\Delta U(x_N) - \Omega_{+\overline{MH}} - \Omega_{-\overline{NM}} \tag{22a}$$

$$2\left(\frac{C_p}{C_p - R}\right)_3 \lambda_{a3}\frac{\Delta\bar{a}_{3M}}{\bar{a}_3} = \frac{C_{p_2}R}{(C_p - R)_2^2} \cdot \frac{\lambda_{a2}}{\bar{a}_2}\left\{Q_+\Delta U(x_H) + Q_-\Delta U(x_N) + \Omega_{-\overline{NM}} - \Omega_{+\overline{MH}}\right\} - \lambda_{s2}\frac{\Omega_{s2\overline{OM}}}{C_{V_2}} + \lambda_{s3}\frac{\Omega_{s2\overline{OM}}}{C_{V_3}} + \left(\frac{C_p}{R} - 1\right)\Delta f \tag{22b}$$

$$\Delta\bar{S}_{3M} = \Omega_{s3\overline{OM}} \tag{22c}$$

Equation (21) determines the conditions behind the shock wave through equations (14) to (17), and equations (22a) to (22c) determine the conditions behind the contact surface.

Since the points I, J, K, M, and N of Figure 2 are all uniquely determined once the point H is given, equation (21) can be written further as

$$\Delta U(x) - F\Delta U(rx) = \Lambda(x) \tag{23}$$

where

$$r \equiv \frac{x_N}{x_H} = \frac{\bar{a}_2 - (U - \bar{u}_2)}{\bar{a}_2 + (U - \bar{u}_2)} < 1 \tag{23a}$$

$$F \equiv \frac{1 - C}{1 + C}\frac{Q_-}{Q_+}, \qquad (|F| < 1) \tag{23b}$$

$$\Lambda(x) \equiv \Lambda(x_H) \equiv \frac{(1 + C)\Omega_+\overline{ML} + (1 - C)\Omega_-\overline{NM} + 2\Omega_+\overline{BM}}{(1 + C)Q_+} \tag{23c}$$

Since equation (23) is a recursion formula of the type

$$\Delta U(r^n x) = F\Delta U(r^{n+1}x) + \Lambda(r^m x)$$

it can be written, with the aid of the condition

$$\lim_{n\to\infty} F^n \Delta U(r^m x) = 0$$

as

$$\Delta U = \sum_{n=0}^{\infty} F^n \Lambda(r^m x) \tag{24}$$

Equation (24) is a general expression for the shock velocity attenuation in the shock-tube flow, subject to the approximations of the linearized theory. Equation (24) should be valid when the resulting shock attenuation ΔU is small compared with the perfect gas shock velocity U, less than 10 percent say, so that the square of the neglected perturbations are negligible, e.g. $0.1 \times 0.1 = 0.01$. The series form of the final shock attenuation formula, equation (24), can be interpreted physically as the reflection of the expansion and compression waves at the shock and the contact surfaces. That is, the first term on the RHS of equation (24) represents the direct effect of a perturbation by the real flow effects, and the second term represents the residual effect of the perturbation before the first reflection, and so forth. The constant F in equation (24) is in general smaller than unity and approaches zero or even becomes negative as shock velocity increases (see equation (23b)), and so the wave reflection becomes negligible at high shock strengths.

The corresponding expression for the contact-surface acceleration $\Delta\bar{u}_{3M}$ is obtained from equation (22a) with the aid of the relation (24) as

$$\Delta\bar{u}_{2M} = F(Q_+ - Q_-)\sum_{n=0}^{\infty} F^n\Lambda(r^m x_N) - \Omega_{-\overline{NM}} \tag{24a}$$

This last formula applies at the point M in Figure 2, which is earlier in time than the point H for which equation (24) is derived. Unless there is a singularity at $x = 0$, $t = 0$, the infinite series in equation (24a) is small in comparison with the second term in equation (24a) and becomes negligibly small at high shock strengths.

In order to calculate the change in shock wave velocity and contact-surface velocity due to the real flow effects, one must first evaluate the time integral Ω's by performing the actual integration, equation (20), then substitute the result into equations (24) or (24a). In the following sections, this process has been taken to evaluate the effect of each real flow effect.

INDIVIDUAL EFFECTS

Boundary-Layer Growth Alone, Similar Profiles

When the prevailing real flow effect is boundary-layer growth alone, the line integral Ω's in equations (24) and (24a) can be calculated by performing the integration of ϵ's (see equations 8b, 8c, and 11a) provided the local velocity profiles are known. If the boundary-layer profiles are similar within each driver and driven gas, which implies among other things that there is no leakage of gas through the contact surface, such that the boundary layer thickness grows with distance from the shock surface by a power m, then there follows

$$\Lambda(r^m x) = r^m\Lambda(x) \tag{25a}$$

and so the series in equation (24) converges and the resulting shock-wave velocity is given by

$$\Delta U(x) = \frac{\Lambda(x)}{1 - r^m F} \tag{25b}$$

Then the contact-surface velocity is described by (see equation (24a))

$$\Delta\bar{U}_M = \frac{F}{1 - r^m F}\,\frac{Q_+ - Q_-}{Q_+}\cdot\frac{(1 + C)\Omega_{+\overline{M'H}} + (1 - C)\Omega_{-\overline{N'M'}} + 2\Omega_{+\overline{I'M'}}}{1 + C} - \Omega_{-\overline{NM}} \tag{26}$$

However, $\Omega_{\pm\overline{IM}}$ (and hence $\Omega_{\pm\overline{I'M'}}$) is quite complicated and is not suitable for analytical integration. Mirels and Mullen, and Spence and Woods neglect this term in comparison with $\Omega_{+\overline{ML}}$ and $\Omega_{-\overline{NM}}$ in equations (23c) and (26); that is, they neglect the effect of boundary-layer growth in driver gas. This is justified, in the light of present analysis, when the density of the driver gas is much higher than that of the driven gas so that the boundary layer thickness in the driver gas is much thinner than in the driven gas. It can be shown using the present results that the shock wave always decelerates and contact-surface accelerates due to the boundary-layer growth. By using the condition that the hot gas temperature is much higher than the wall temperature, one can show, from the formulae given in Appendix II, that

$$\Omega_{+\overline{ML}} < 0, \quad \Omega_{-\overline{NM}} < 0 \tag{27}$$

From equations (26) and (27) it is seen that the contact surface is always accelerated by the growth of boundary layer. The shock wave is attenuated (see equations (23c) and (25)), when the sum of two integrals, $\Omega_{+\overline{ML}}$ and $\Omega_{-\overline{NM}}$, is greater in magnitude than $2\Omega_{+\overline{IM}}$, in proportion to

$$\frac{\Delta U}{U} \propto \delta_M \frac{D}{A} \tag{28}$$

where δ_M is the boundary layer thickness at the contact surface.

The analysis of Spence and Woods,[3] and Mirels and Mullen[4] are both a special case of the present formulation; that is, the case where $\omega_u = \omega_s = 0$, other real flow effects being absent. By using the relationship between C_f, q_w and δ_{ij}'s, one can show that ω_u and ω_s are indeed small for a normal perfect gas boundary layer flow such as Blasius'. Mirels and Mullen show that the effects of driver gas boundary-layer growth or wave reflection from shock and contact surfaces are small. In the present formulation, this statement is equivalent to neglecting $\Omega_{+\overline{IM}}$ as mentioned earlier and assuming $F \simeq 0$, which can be shown to be approximately valid for high shock strengths. Thus the present analysis agrees with that of Mirels and Mullen on this point. However, it is doubtful whether one can legitimately neglect ω_u and ω_s at high shock strengths where the real gas effect, i.e. vibrational excitation, dissociation, etc., becomes important in the determination of boundary-layer characteristics within the hot gas. When these real-gas effects are considered, the boundary-layer displacement thickness can be very small and even negative, and so ω_ρ would not be particularly greater than ω_u or ω_s. No effort has been made in the present paper, however, to numerically calculate the magnitude of attenuation rates for the real-gas, because the boundary-layer solutions for the real-gas in a shock tube are not well known. Thus, for the comparison of the magnitudes of each real flow effect, the results of Mirels and Mullen[4] are used (see Figs. 7a and 7b).

Radiation Alone, Optically Thin Gas

When radiation loss is the only real flow effect present, and when the gas is optically thin, the line integrals $\Omega_{+\overline{MH}}$ and $\Omega_{-\overline{NM}}$ become

proportional to time, or distance x. Equations (25a) or (25b) are satisfied for this case with m = 1 and so the series in equations (24) and (24a) converges and the resulting shock speed attenuation and contact surface acceleration are, neglecting the terms of the order

$$\left(\frac{\bar{a}_2}{\bar{u}_2}\right)^2$$

$$\frac{\Delta U}{U} = \frac{1 - r}{1 - rF} \frac{R}{2(C_{p_2} - R)} \cdot \frac{\bar{a}_2}{UQ_+} \left(\frac{\bar{\rho}_2}{\rho_1} - 1\right) \frac{eL}{\bar{\rho}_2 \bar{u}_2^3} \tag{29a}$$

$$\frac{\Delta u_M}{u_M} = \frac{-1}{1 - rF} \frac{R}{2(C_{p_2} - R)} \left[r + (1 - r) \frac{\rho_1}{\rho_2} + \frac{\bar{a}_2}{U}\right] \left[(1 + rF^2) \frac{U}{u_2 - a_2} - rF\right] \frac{eL}{Q_+ \bar{\rho}_2 \bar{u}_2^3} \tag{29b}$$

where e in this case is the emissivity per unit volume assigned with the negative sign and L is the length of the hot gas column. Thus for high shock strengths the shock wave is attenuated and contact-surface is accelerated linearly with column length, or time. The difference between the two, that is, the sum of the absolute values of equations (29a) and (29b), is approximately equal to the fractional test time loss. As is seen from equations (29a) and (29b), the shock speed attenuation and contact-surface acceleration are not affected directly by the driver gas property to the approximation of $(\bar{a}_2/\bar{u}_2)^2 = 0$. The shock attenuation and the contact-surface acceleration are calculated by equations (29a) and (29b) under the following assumptions:

(1) $T_o = 300^o$ K,

(2) driven gas is air,

(3) emissivity e is taken as the mean value of those given by Kivel and Bailey[15], Nardon et al[16], and Meyrott et al[17] in their radiation data.

(4) hot gas conditions are determined from Feldman's[18] charts. The results are written in the form

$$\frac{\Delta U}{U_i} = - \text{ a constant} \times L(\text{meters})$$

$$\frac{\Delta u}{u_i} = \text{a constant} \times L(\text{meters})$$

where U_i and u_i are the shock wave and contact-surface velocities of a radiationless gas and ΔU and Δu are the perturbation from U_i and u_i due to the radiation. The constant in the last two equations are functions of

U and p_1 and are plotted in Figure 3. Figure 3 shows that for $L \geq 0.1$ meter, radiation causes a significant deceleration of shock wave and acceleration of contact surface for approximately $p_1 \geq 0.1$ mm Hg and $U \geq 5$ mm/μsec. At a very high initial pressure and shock velocity, $p_1 \geq 10$ mm Hg and $U \geq 8$ mm/μsec say, $\Delta U/U_i$ and $\Delta u/u_i$ become large even for a small L, i.e. -0.045 and 0.09 for this case for $L = 0.01$ meter. When the calculated $\Delta U/U_i$ and $\Delta u/u_i$ exceed the linear limit, 0.1 say, as is the case in the present example for $L \geq 0.11$ meter, the present theory breaks down because the characteristic integrating path would be significantly different from those of ideal gas flow and so the square of the perturbation terms neglected in the basic equations (12) and (13) would not be small.

Assuming that the radiation is caused solely from two-body free-bound transitions of electrons, the attenuation rate becomes proportional, at high shock strengths, to

$$\frac{\Delta U}{U} \quad \propto \quad \frac{L}{u^3} T_2^{3/2} \exp\left(-\frac{T_r}{T_2}\right) \tag{30}$$

where T_r is the characteristic temperature of the ionization, which can be taken as 162,000° K for air (mean value of oxygen and nitrogen). Since T_2 increases as the flow density increases in an ionizing gas, the radiation loss becomes an important shock attenuating mechanism at high densities, as seen from Figure 3. It is independent of the tube diameter to the accuracy of the assumption of optically thin gas.

Imperfect Diaphragm Rupture

The rupturing of diaphragm takes place during a finite length of time. During the very early period of shock-tube flow, therefore, the diaphragm is only partly open and so the pressure downstream of diaphragm is lower than the pressure upstream. The effect of this pressure inequality on shock and contact-surface velocities can be formulated by introducing a body force assumed as acting on the cold gas to retard it. Since the thickness of the pressure transition region (see Fig. 4) is very small compared with the total length of driver gas, the transition thickness can be assumed to be infinitesimally small. The exact distribution of this fictitious body force is immaterial in the calculation of shock attenuation because this force must be integrated and the resulting integral always represents the total pressure drop across the contact-surface regardless of the actual shape of pressure change. Thus the body force is written as

$$f = -\Delta f I(z - z_A) J(t) \tag{31}$$

where $I(z - z_A)$ is the unit impulse function located at $z = z_A$ and $J(t)$ is a function (unknown at this stage) having the property

$$J(0) = 1$$

$$J(t) < 1 \quad \text{for} \quad t > 0$$

and

$$J(\infty) = 0$$

Then Δf represents the effective pressure difference across the contact-surface in the limit of $t \to 0$. The shock attenuation due to the force described by equation (31) can be obtained if the function $J(t)$ is specified. For example, if

$$J(t) = \exp(-t/\tau), \qquad z_A = -0$$

then there results

$$\frac{\Delta U}{U_i} = \frac{\Delta u}{u_i} = -\frac{1}{1+C} \cdot \frac{1}{\bar{u}_3 + \bar{a}_3} \cdot \frac{\Delta f}{\bar{\rho}_3 Q_+} \cdot \frac{1}{1 - F \exp\left(-\frac{t}{\tau}\right)} \frac{1}{U} \tag{32}$$

where τ can be regarded as a characteristic diaphragm opening time. The model thus results in a finite residual attenuation of shock strength at $t = \infty$. The testing time is not altered. This result is different from that of White[8] which predicts an increase in shock velocity within the transient period and zero attenuation at $t = \infty$. The basic difference between the two methods may be that White implicitly assumes an isentropic process within the pressure step during the diaphragm rupture while the present method is based on the nonisentropic process; that is, White[8] regards the partial opening of the diaphragm as an aerodynamic throat through which an isentropic expansion is achieved; the present method regards any gain of kinetic energy through this expansion as being completely lost by a nonisentropic process, such as separated flow motion around the corner of the partially opened diaphragm. It is also to be noted that White visualizes the pressure step as being located in the hot gas region whereas in the present method it is assumed to be in the cold gas.

If z_A is located at $+0$, i.e. in the hot gas region, the present method is still unaltered except that the multiplicative coefficient in equation (32) is slightly altered. The magnitude of deceleration determined by equation (32) is of the order

$$\frac{\Delta U}{U} \simeq \left(\frac{\bar{a}_3}{\bar{u}_3}\right)^2 \frac{\Delta f}{p_3}$$

Since the maximum value of $\Delta f/p_3$ is limited to 1, the attenuation rate given by equation (32) cannot be greater than reciprocal of the square of the driver gas Mach number. For a high shock strength, this parameter is small and so the attenuation effect due to the pressure step is accordingly small.

Contact Surface Heat Transfer

The heat transfer from the hot gas to the cold gas through the contact-surface can be formulated from the equation of heat conduction

$$\rho C_p \frac{\partial T}{\partial t} = \frac{\partial}{\partial z}\left(\kappa \frac{\partial T}{\partial z}\right) \tag{33}$$

The result of presence of this heat transfer is to add heat to the flow at any local point by the amount

$$e = \frac{\partial}{\partial z}\left(\kappa \frac{\partial T}{\partial z}\right) \tag{34}$$

the sign of the RHS in equation (34) being negative in the hot gas region and positive in the cold gas region. If a strong turbulent motion is initiated at the rupture of the diaphragm, the effective thermal conductivity κ in the above equations is that of turbulent mixing, i.e. eddy conductivity. Since the exact value of this eddy conductivity is not known, a linear, constant coefficient approximation is made here to obtain an approximate solution to the problem, i.e. with the assumption

$$\frac{\partial \kappa}{\partial z} = 0, \qquad \frac{\kappa}{\rho C_p} = \text{const.} \tag{35}$$

The resulting differential equation can be solved by considering that a plane heat source of strength $(U^2/2C_p)$ is located at the shock wave surface, superimposed on a plane doublet of strength $[\kappa/\rho(U - \bar{u}_2)](U/C_p)^2$ at that plane[19]. The solution of this problem is drawn schematically in Figure 5a. When equation (34) is substituted in equations (9), (23c), and (24), there results for $\bar{u}_2 \gg \bar{a}_2$

$$\left(\frac{\Delta U}{U}\right) \doteq \frac{1}{1 + C} \frac{\bar{a}_3}{\bar{\rho}_3 \bar{u}_3{}^3 U} \frac{R}{C_{p_2} - R} \cdot \frac{1}{Q_+}\left[1 + \left(\frac{C_{p_3} - R}{C_{p_2} - R}\right)^{3/2}\left(\frac{\bar{\rho}_3}{\bar{\rho}_2}\right)^{3/2}\left(C \frac{\bar{a}_2}{\bar{u}_2} - 1\right)\right] \times$$

$$\sum_{n=0}^{\infty} F^n \left(\kappa \frac{\partial T}{\partial z}\right)_{\substack{z=0 \\ t=r^n t_H}} \tag{36a}$$

$$\left(\frac{\Delta u}{u}\right) \doteq \frac{1}{2} \cdot \frac{R}{C_{p_2} - R} \cdot \frac{\bar{a}_2}{\bar{\rho}_2 \bar{u}_2^3} \cdot \frac{1}{\bar{u}_2 - \bar{a}_2} \cdot \left(\kappa \frac{\partial T}{\partial z}\right)_{\substack{z=0 \\ t=t_M}}$$

$$+ \frac{F}{1 + C} \cdot \frac{Q_+ - Q_-}{Q_+} \cdot \frac{R}{C_{p_3} - R} \cdot \frac{\bar{a}_3}{\bar{\rho}_3 \bar{u}_2^3} \left[1\right.$$

$$\left. + \left(\frac{C_{p_3} - R}{C_{p_2} - R}\right)^{3/2} \left(\frac{\bar{\rho}_3}{\bar{\rho}_2}\right)^{3/2} \left(C \frac{\bar{a}_2}{\bar{u}_2} - 1\right)\right] \sum_{n=0}^{\infty} F^n \left(\kappa \frac{\partial T}{\partial t}\right)_{\substack{z=0 \\ t=r^n t_M}} \qquad (36b)$$

Thus both the shock wave attenuation and contact surface acceleration are determined explicitly only by the temperature gradient at the contact surface. The shock attenuation rate is dependent mainly on the driver gas properties $\bar{a}_3$ and $\bar{\rho}_3$ while contact-surface acceleration is only weakly dependent on the driver gas property.

At large t, the situation approaches that of a heat conduction from a semi-infinite hot solid to a semi-infinite cold solid. A characteristic width can be defined in this regime such that most of the temperature change occurs within this width. This width is called here the 'natural mixing width'. According to the theory of heat transfer[19], this natural mixing width is proportional to $t^{1/2}$ and the temperature gradient at the interface varies with $t^{-1/2}$, leading to an infinite heat transfer at $t \to +0$. Since the length of hot gas column L is growing proportionally with time, it happens that at small t, the natural mixing half-width can be greater than the column length. For this regime of small t, the temperature profile does not follow that of the two semi-infinite solids, and so the heat transfer equation has to be solved to determine $(\partial T/\partial z)_o$. Thus the series in equations (36a) and (36b) converge because of the relation $F < 1$ (see eq. (23b)).

The solution of the heat transfer equation (34) with the assumption of equation (35) is obtained and are plotted in Figure 5b. The density is fixed for Figure 5b and the conductivity κ is varied from 50 times the laminar thermal conductivity to 5000 times the thermal conductivity β, where β is taken from Yos's data.[20] The profiles are all similar with respect to the characteristic time

$$t_c = \frac{\kappa}{\rho C_p} \cdot \frac{4}{(U - u)^2} \qquad (36c)$$

for a fixed $U - \bar{u}_2$. The similar profile is weakly affected by $U - \bar{u}_2$, but since $U - \bar{u}_2$ is almost constant over the range $4 < U < 9$ mm/μsec, the profile shown in Figure 5b can be regarded as common to all shock velocity U for a high shock strength. As seen from Figure 5b, the heat transfer rate peaks approximately at $t = 0.4t_c$. The corresponding shock attenuation

and contact-surface acceleration rate are shown in Figure 5c, for the case $\bar{\rho}_2 = \bar{\rho}_3$, $\bar{a}_2 = \bar{a}_3$, and $F = 0.649$. As seen from Figure 5c, the shock velocity peaks at around $t = 1.2t_c$ for $F = 0.649$. For other F values, the peak occurs at slightly different locations but are within the range $0.4t_c < t < 1.5t_c$. The absolute magnitude of the attenuation rate at the peak point is proportional to

$$\frac{\Delta U}{U} \propto \frac{\sqrt{\kappa}}{\bar{\rho}_3} \frac{\bar{a}_3}{\bar{u}_3} \tag{37}$$

For a rough calculation, therefore, one can extrapolate the results of Figures 5b and 5c with the relation equation (37) and making use of the fact that the peak occurs at around $t = t_c$. When $\bar{\rho}_3 > \bar{\rho}_2$ and $\bar{a}_3 < \bar{a}_2$ that is, when an unheated heavy gas is used as the driver, the quantity within the large parenthesis in equations (36a) and (36b) becomes negative. In this case the shock speed is attenuated, i.e. $\Delta U < 0$, and also the contact-surface acceleration remains small. The absolute magnitude of shock attenuation is small; however, because the factor $\bar{a}_3/\bar{\rho}_3$ in equation (37) is small. This is because when an unheated heavy gas is used as the driver, the mass and the heat capacity of the driver gas is so large that the heat transfer from the hot driven gas through the contact surface is insufficient to cause any effect on the driver gas but cools the driven gas to cause a deceleration of shock speed. When a heated light gas is used, the quantity within the parenthesis becomes positive and so the shock and contact surface are both accelerated, to a large amount because of large $\bar{a}_3/\bar{\rho}_3$ in this case. This is because when a heated light gas is used as the driver gas, the mass and heat capacity of the driver gas is comparable with those of the driven gas and so the heat transfer through contact-surface causes a sufficient expansion of the driver gas to overcome the contraction of the test slug. Thus the effect of heat conduction through the contact surface is to increase the shock speed at high shock strengths, as illustrated in the example shown in Figure 5c.

The magnitude of the eddy conductivity κ is unknown here, but is thought to be a function of tube diameter as well as thermodynamic properties, because the turbulence eddy size is determined by the tube diameter. A study in this subject is desirable. It is to be noted here that the loss of test time, calculated by $\Delta U/U - \Delta\bar{u}/\bar{u}$ in this case merely represents the shortening of the hot gas column. The temperature distribution within the hot gas becomes nonuniform because of the heat transfer through the contact surface and so the portion of the hot gas having a uniform temperature may be extremely small. In particular if the natural mixing half-width is greater than the hot gas column length L, there will be theoretically no uniform region within the hot gas.

Heat Conduction to Tube Wall

A closed form expression for the effect of heat conduction to the shock-tube wall from the hot gas can be obtained if the conductive heat transfer rate q_w varies with a fixed power of distance or equivalently if

the thermal boundary layer thickness varies with a fixed power of distance, i.e.

$$\delta_T \quad \propto \quad z^m \tag{38}$$

Thus the cases of completely laminar boundary layer and turbulent boundary layer flow can be formulated. For an arbitrary power $m < 1$, equations (24) and (24a) become, neglecting the heat conduction to/from cold gas, from/to the wall,

$$\frac{\Delta U}{U} = -\frac{1}{1-m}\frac{1}{1-r^{mF}}\cdot\frac{1}{Q_+}\frac{R}{C_{p_2}-R}\cdot\frac{q_M}{\bar{\rho}_2\bar{u}_2^2 U}\cdot\frac{D}{A} \tag{38a}$$

$$\frac{\Delta\bar{u}}{\bar{u}} = \frac{1}{2}\cdot\frac{R}{C_{p_2}-R}\cdot\frac{1}{U-u_2+a_2}\cdot\frac{\bar{a}_1}{\bar{\rho}_2\bar{u}_2^2}\cdot\frac{D}{A}\cdot\frac{q_M}{1-m}$$

$$-F\frac{Q_+ - Q_-}{Q_+}\frac{1}{m}\frac{1}{1-r^{mF}}\frac{R}{C_{p_2}-R}\cdot\frac{q_M}{\bar{\rho}_2\bar{u}_2^2 U}\cdot\frac{D}{A} \tag{38b}$$

The numerical calculations for the above formulae are carried out under the following assumptions.

(1) The Nusselt number is taken from a Blasius-type laminar boundary layer.

(2) Tube diameter is 10 cm

(3) The flow properties are obtained from Feldman's charts[18]. The results are shown in Figure 6. Equations (38a) and (38b) yield the law of proportionality

$$\frac{\Delta U}{U} \propto \frac{\Delta\bar{u}}{\bar{u}} \propto \frac{Nu}{D}\frac{L^{1-m}}{\sqrt{\rho U}} \tag{39}$$

The shock attenuation and contact-surface acceleration rates for the cases other than calculated can be obtained using the above proportionality relation. As seen from Figure 6, the effect of heat conduction to tube wall is important at low density range.

Crossed Electric and Magnetic Fields

When crossed electric and magnetic fields are applied in the hot gas so that the resulting $j \times B$ force acts to accelerate the flow, the shock velocity can be accelerated arbitrarily by controlling the field intensities. If $E = 2uB$, the entropy is unchanged (see eq. (7)) and so the electric energy is most efficiently consumed in increasing the kinetic energy of the flow. This is similar to the condition of maximum acceleration in a steady one-dimensional magnetogasdynamic channel flow[14].

$$\frac{E}{uB} = \frac{1}{2}\frac{C_p - R}{R}\frac{C_p + R}{C_p - R}$$

In the following, the shock attenuation rates due to 4 different field distributions are given.

(i) E = constant, B = constant.

$$\Delta U = \frac{1 - \bar{u}_2/U}{1 + C} \cdot \frac{\sigma}{2\bar{\rho}_2} \cdot \frac{E - \bar{u}_2 B}{Q_+} \cdot \frac{x}{1 - rF}\left\{\frac{R}{C_{p_2} - R} \cdot \frac{E - 2\bar{u}B}{\bar{u}_2^2}\left[(1 + C) + (1 - C)r\right]\right.$$

$$\left. + \frac{B}{\bar{a}_2}\left[(1 + C) - (1 - C)r\right]\right\} \qquad (40)$$

In particular, if $E = 2\bar{u}B$,

$$\Delta U \doteqdot \frac{jBL}{2\bar{\rho}_2\bar{a}_2 Q_+} \qquad (40)$$

(ii)

$$E = 2\bar{u}B, \quad E = E_o t^{-\frac{1-m}{2}}, \quad B = B_o t^{-\frac{1-m}{2}}$$

$$\Delta U = \frac{\sigma\bar{u}_2}{2\bar{\rho}_2} \cdot \frac{1}{1 + C} \cdot \frac{1}{Q_+} \cdot \frac{B_o t^m}{1 - r^m F}\left[\frac{1}{4} \cdot \frac{C_2^2}{C_1} - \frac{1}{2} \cdot \frac{E_o}{\bar{u}_2 B_o} + \frac{1}{4}\frac{C_2}{C_1}\right.$$

$$\left. - 2\frac{\bar{a}_2}{\bar{u}_2} \cdot \frac{R}{C_{p_2} - R}(G_1 + G_2) + G_1 - G_2\right] \qquad (39)$$

when C_1, C_2, G_1 and G_2 are the parameters defined as in Appendix I.

(iii) $E = 2\bar{u}B, \quad E = E_o x^{-\frac{1-m}{2}}, \quad B = B_o x^{-\frac{1-m}{2}}$

$$U = \frac{\sigma\bar{u}_2}{2\bar{\rho}_2} \cdot \frac{1}{1 + C} \cdot \frac{1}{Q_+} \cdot \frac{B_o x^m}{1 - r^m F}\left[\frac{1}{4}\frac{D_2^2}{D_1} - \frac{1}{2} \cdot \frac{E_o}{\bar{u}_2 B_o} + \frac{1}{4} \cdot \frac{C_2}{C_1}\right.$$

$$\left. - 2\frac{\bar{a}_2}{\bar{u}_2} \cdot \frac{R}{C_{p_2} - R}(H_1 + H_2) + H_1 - H_2\right] \qquad (40)$$

(iv) condition leading to $U = c_1 x + c_2 x^m$

When

$$E(x) = E_1(x) + E_2(x)$$

$$B(x) = B_1(x) + B_2(x)$$

and E_1, E_2, B_1 and B_2 are the solutions of the following nonlinear simultaneous equations,

$$E_1 - 2\bar{u}_2 B_1 + E_2 - 2\bar{u}_2 B_2 = 0$$

$$(E_2 - \bar{u}_2 B_2)B_1 + (E_1 - \bar{u}_2 B_1)B_2 = 0$$

$$(E_2 - \bar{u}_2 B_2)B_2 = E_3 B_3 = \text{const.}$$

$$(E_1 - \bar{u}_2 B_1)B_1 = \bar{u}_2 B_0^2 x^{m-1}$$

$$\Delta U = \frac{1 - \bar{u}_2/U}{1 + C} \cdot \frac{\sigma}{2\bar{\rho}_2} \cdot \frac{E_3 B_3}{Q_4} \frac{x}{1 - \gamma F} \cdot \frac{1}{\bar{a}_2} [(1+C) - (1-C)\gamma] + \Delta U \quad \text{of equation (40)} \tag{41}$$

$$= C_1 x + C_1 x^m \tag{41a}$$

A typical example is given for the case equation (38a) as follows. Given conditions:

p_o = 10 mm Hg

T_o = 300° K

U = 8 mm/μsec

B = 1000 gauss

hot gas condition = determined from Feldman's charts[18]

Result:

$$\frac{\Delta U}{U} = 0.75\ jL \quad \begin{matrix} \text{where L is in meters} \\ \text{j is in kiloamperes/cm}^2 \end{matrix} \tag{42}$$

When the magnetic field is removed, the effect of applying the electric field is merely to add energy to the flow by the amount equal to Joule heating, σE^2. Under this condition, the direction of the E field is immaterial and so a configuration such as multi-ring electrodes will result in the same shock attenuation rates. The problem is exactly the same as if the radiation power emission e is replaced by the Joule heating σE^2, the sign being reversed. The formulae for shock and contact-surface speed are equations (29a) and (29b) with e replaced by σE^2. An effort is currently being made at the Catholic University of America to experimentally measure the shock wave speed under this condition. As seen from the above-mentioned example, equation (42), the required electrical current to cause a significant change in shock speed is not too excessively large, and is indeed in the range attainable in a laboratory without much difficulty.

COMBINED EFFECTS, ZERO ATTENUATION CONDITION

In a real shock tube flow, all the effects described above occur simultaneously. As a result of the small-perturbation type analysis, the problem is strictly linear and hence all the real flow effects are directly additive to the accuracy intended in the present paper.

The relative magnitudes of each real flow effects are compared in Figures 7a and 7b for two typical operating conditions. As seen from these Figures, the relative magnitude of the real flow effects diff greatly by the change in initial pressure. Generally speaking, the boundary-layer growth and tube wall heat transfer are important at low density operation, initial channel pressure below 1 mm Hg say, as expected from a low Reynolds number. The radiation is a controlling parameter for $p_1 > 10$ mm Hg at high shock strengths. The effect of imperfect diaphragm rupture is always negligible. The contact-surface mixing effect is dependent mainly on the eddy conductivity and the driver gas condition.

The effect of imperfect diaphragm opening is to suppress the initial shock velocity. After the characteristic diaphragm opening time, τ, is elapsed, the imperfect diaphragm opening leaves the after effect of slightly lowered shock velocity. This is because of the entropy increase in passing through the partially opened diaphragm (see the section on imperfect diaphragm rupture). The contact-surface mixing effect is most widely varying and depends on the gas combination and eddy conductivity, and increases the shock velocity in a high-shock-strength flow. The peak shock acceleration occurs at around the critical mixing time, i.e. the time when the hot gas column length is roughly the same as the natural mixing half-width of the contact surface mixing. Thus, when the driver gas density is high, there will be no recognizable shock speed overshoot; when the driver gas density is low and the gas is heated, there will be an overshoot in shock speed at around the critical mixing time. This critical mixing time is greater as the eddy conductivity becomes larger and the driver density smaller. The heat transfer from the shock tube wall has an effect similar to the boundary layer growth effect, and causes a decrease to the shock velocity according to the same power law as that for boundary-layer growth. The effect of radiation is to reduce the shock speed linearly with time. The ratio of the boundary-layer growth and radiation effects is proportional approximately to

$$\frac{\Delta U \text{ by radiation}}{\Delta U \text{ by boundary-layer growth}} \alpha\, D \sqrt{\rho L}\, e^{-\frac{T_r}{T_2}}$$

where T_r is the characteristic temperature of ionization (see eq. (30)). Thus, the radiation effect dominates when the size is large and density is high.

It is interesting to notice that for all real flow effects considered, the contact-surface acceleration is greater in absolute magnitude than the shock wave attenuation, by 20 to 100 percent. Thus, in the absence of complete information, one could estimate the contact-surface acceleration rate

from a known shock wave attenuation rate by adding somewhat around 50 percent. Conversely, the reduction of test time in the hot gas is approximately 40 percent due to the shock wave attenuation and 60 percent to the contact-surface acceleration. This nominal test time is based on the total length of the hot gas column, but the length of the uniform region within the test gas will be only a fraction of this length.

By applying the crossed electric and magnetic fields, the shock velocity can be maintained constant for the types of attenuation given by equation (41a); that is, for the boundary layer and radiation effects. The necessary field strengths are determined from equating the attenuation with acceleration, i.e.

[Eq. (28) + Eq. (29)] = Eq. (41), when both boundary layer growth and radiation are to be compensated (45a)

= Eq. (38) or (38a), for radiation alone, or (45b)

= Eq. (39) or (40), for boundary layer growth alone (45c)

A typical example of a compensating condition is obtained as follows:
Given conditions:

p_o = 10 mm Hg

T_o = 300° K

U = 8 mm/μsec

B = 1000 gauss

hot gas condition = determined from Feldman's charts[18]

emissivity e = mean value of the data given by Kivel and Bailey[15] Nardone et al[16] and Meyerott et al[17]

Result:

j = 187 amp/cm^2

It is worth noting that the chemical species concentration does not explicitly affect the attenuation of shock velocity. It may, however, affect the variation of properties within the test gas because the species concentration determines conditions along the contact surface.

CONCLUSIONS

From the present study, the following conclusions are drawn:

(i) imperfect diaphragm rupture suppresses the shock velocity by a negligibly small fraction.

(ii) heat transfer from hot gas to cold gas through turbulent mixing at the contact surface causes an overshoot in shock speed at high shock strengths, the absolute magnitude of this overshoot being proportional to $\sqrt{\kappa}\ \bar{a}_3/\bar{\rho}_3$. The peak occurs near the time when the hot gas column length is approximately equal to the natural mixing half-width.

(iii) the boundary-layer growth attenuates shock velocity in proportion to boundary-layer thickness at the contact surface and present estimates of this effect roughly agree with those calculated by Mirels and Mullen, and Spence and Woods.

(iv) the radiation heat loss from the hot gas causes an attenuation of shock velocity that is linear with time, and radiation becomes an important shock attenuating mechanism at high density.

(v) on the average, the acceleration of the contact surface is approximately 1.5 times greater than the shock attenuation; approximately 40 percent of testing-time loss is due to shock attenuation and 60 percent is due to the contact-surface acceleration.

(vi) the strengths of crossed electrical and magnetic fields necessary to compensate for the attenuating effect on shock velocity of radiation and the boundary-layer growth is shown to be in the attainable range.

APPENDIX I

DEFINITION OF PARAMETERS

$$C_1 = \frac{R}{C_{p_2} - R} \cdot \frac{\bar{a}_2}{\bar{u}_2} (G_1 + G_2)$$

$$C_2 = \left(\frac{3R}{C_{p_2} - R} \cdot \frac{\bar{a}_2}{\bar{u}_2} - 1\right) G_1 + \left(\frac{3R}{C_{p_2} - R} \cdot \frac{\bar{a}_2}{\bar{u}_2} + 1\right) G_2$$

$$D_1 = \frac{R}{C_{p_2} - R} \cdot \frac{\bar{a}_2}{\bar{u}_2} (H_1 + H_2)$$

$$D_2 = \left(\frac{3R}{C_{p_2} - R} \cdot \frac{\bar{a}_2}{\bar{u}_2} - 1\right) H_1 + \left(\frac{3R}{C_{T_2} - R} \cdot \frac{\bar{a}_2}{\bar{u}_2} + 1\right) H_2$$

$$G_1 = (1 + C)\left[1 - \left(\frac{t_M}{t_H}\right)^m\right]$$

$$G_2 = (1 - C)\left[\left(\frac{t_M}{t_H}\right)^m - \left(\frac{t_N}{t_H}\right)^m\right]$$

$$H_1 = \frac{1 + C}{\bar{u}_2 + \bar{a}_2}\left[1 - \left(\frac{x_M}{x_H}\right)^m\right]$$

$$H_2 = \frac{1 - C}{\bar{u}_2 - \bar{a}_2}\left[\left(\frac{x_M}{x_H}\right)^m - \left(\frac{x_N}{x_H}\right)^m\right]$$

$$\frac{t_M}{t_H} = \frac{\bar{u}_2 + \bar{a}_2 - U}{\bar{a}_2}$$

$$\frac{t_N}{t_H} = \frac{\bar{u}_2 + \bar{a}_2 - U}{\bar{a}_2 - \bar{u}_2 + U}$$

$$\frac{x_N}{x_H} = \frac{\bar{a}_2 + \bar{u}_2 - U}{\bar{a}_2 - \bar{u}_2 + U}$$

$$\frac{x_M}{x_H} = \frac{\bar{u}_2(\bar{a}_2 + \bar{u}_2 - U)}{\bar{a}_2 U}$$

$$Q_u = \frac{R}{W}\begin{vmatrix} 1 + \alpha_2 + B_1B_3 & \bar{u}_2 - B_1\dfrac{R\bar{T}_2}{U - \bar{u}_2} \\ \left(1 + \dfrac{h_r}{C_{p_2}T_2}B_1B_3\right)\dfrac{C_{p_1}}{F} & 2\bar{u}_2 - B_1\dfrac{R\bar{T}_2}{U - \bar{u}_2} \end{vmatrix}$$

$$Q_a = \frac{1}{W}\begin{vmatrix} U - \bar{u}_2 & U - 2\bar{u}_2 \\ U & U - \bar{u}_2 + \dfrac{B_1}{U - u_2}\left(h_r + \dfrac{C_{p_2}\bar{T}_2}{1 + \alpha_2 + B_1B_3}\right) \end{vmatrix}$$

$$Q_s = \frac{U}{W}\begin{vmatrix} U - \bar{u}_2 & U - 2\bar{u}_2 + \dfrac{R\bar{T}_2}{U - \bar{u}_2}\left[B_1 - \dfrac{1 + \alpha_2 + B_1B_3}{1 + B_2B_3}\left(\dfrac{R}{C_{p_2} - R} + B_2\right)\right] \\ U & U - \bar{u}_2 + \dfrac{B_1h_r}{U - \bar{u}_2} - \dfrac{C_{p_2}\bar{T}_2}{U - \bar{u}_2}\cdot\dfrac{1 + h_rB_1B_3/(C_{p_2}\bar{T}_2)}{1 + B_2B_3}\left(\dfrac{R}{C_{p_2} - R} + B_2\right) \end{vmatrix}$$

$$W = \begin{vmatrix} (1 + \alpha_2 + B_1B_3)R & U - 2\bar{u}_2 + \dfrac{B_1R\bar{T}_2}{U - \bar{u}_2} \\ \left(1 + \dfrac{h_r}{C_{p_2}\bar{T}_2}B_1B_3\right)C_{p_2} & U - \bar{u}_2 + \dfrac{B_1h_r}{U - \bar{u}_2} \end{vmatrix}$$

$$B_1 = \alpha_2\frac{1 - \alpha_2}{2 - \alpha_2}$$

$$B_2 = \left(1 + \frac{R}{C_{p_2} - R}\cdot\frac{h_r}{R\bar{T}_2}\right)\frac{B_1}{1 + \alpha_2}$$

$$B_3 = n + \frac{T_r}{\bar{T}_2}$$

$$\lambda_a = 1 + \frac{\alpha(1 - \alpha)\left[(r - 1)\left(n + \dfrac{T_r}{T}\right) - 1\right](C_{p_2} - R)}{\left[\alpha(1 - \alpha) + (2 - \alpha)(1 + \alpha)\dfrac{T}{T_r} + \left(n\dfrac{T}{T_r} + 1\right)(1 - \alpha)\alpha\right]C_{p_2}}$$

$$\lambda_s = 1 - \frac{\alpha(1 - \alpha)}{(1 - \alpha)\alpha + (2 - \alpha)(1 + \alpha)\dfrac{T}{T_r} + \left(n\dfrac{T}{T_r} + 1\right)(1 - \alpha)\alpha}$$

APPENDIX II

LINE INTEGRALS Ω FOR SIMILAR BOUNDARY-LAYER

$$\Omega_{+\overline{MH}} = \frac{\delta_M}{2} \cdot \frac{D}{A} \cdot \frac{\bar{a}_2\bar{u}_2}{\bar{u}_2 + \bar{a}_2 - U} \left[\frac{U}{\bar{a}_2} \left(\frac{1}{2} \frac{R}{C_{p_2} - R} \cdot \frac{\bar{u}_2}{\bar{a}_2} - 1 \right) \frac{\delta_{10}}{\delta} \right.$$

$$+ \frac{1}{2} \left(\frac{R}{C_{p_2} - R} \cdot \frac{\bar{u}_2^2}{\bar{a}_2^2} - 1 \right) \frac{\delta_{11}}{\delta_M} + \frac{1}{2} \cdot \frac{R}{C_{p_2} - R} \cdot \frac{\bar{u}_2^2}{\bar{a}_2^2} \left(\frac{U}{\bar{u}_2} - 1 \right) \frac{\delta_{12}}{\delta}$$

$$\left. - \frac{1}{2} \frac{R}{C_{p_2} - R} \cdot \frac{\bar{u}_2^2}{\bar{a}_2^2} \frac{\delta_{13}}{\delta} - \frac{\delta_{01}}{\delta} \right]$$

$$\Omega_{-\overline{NM}} = \frac{\delta_M}{2} \cdot \frac{D}{A} \cdot \frac{\bar{a}_2\bar{u}_2}{U - \bar{u}_2 + \bar{a}_2} \left[\frac{U}{\bar{a}_2} \left(\frac{1}{2} \frac{R}{C_{p_2} - R} \cdot \frac{\bar{u}_2}{\bar{a}_2} + 1 \right) \frac{\delta_{10}}{\delta} \right.$$

$$+ \frac{1}{2} \left(\frac{R}{C_{p_2} - R} \frac{\bar{u}_2^2}{\bar{a}_2^2} - 1 \right) \frac{\delta_{11}}{\delta} + \frac{1}{2} \cdot \frac{R}{C_{p_2} - R} \cdot \frac{\bar{u}_2^2}{\bar{a}_2^2} \left(\frac{U}{\bar{u}_2} - 1 \right) \frac{\delta_{12}}{\delta}$$

$$\left. - \frac{1}{2} \frac{R}{C_{p_2} - R} \cdot \frac{\bar{u}_2^2}{\bar{a}_2^2} \cdot \frac{\delta_{13}}{\delta} - \frac{\delta_{01}}{\delta} \right]$$

$$\Omega_{+\overline{KM}} = \frac{\bar{a}_4}{2} (\delta_M - \delta_K) \frac{D}{A} \left[\frac{\bar{a}_0}{\bar{u}_2} \cdot \frac{\bar{a}_3}{\bar{u}_2} \left(\frac{1}{2} \frac{R}{C_{p_3} - R} \cdot \frac{\bar{u}_3}{\bar{a}_3} - 1 \right) \frac{\delta_{10}}{\delta} \right.$$

$$- \frac{1}{2} \left(\frac{R}{C_{p_3} - R} \cdot \frac{\bar{u}_3^2}{\bar{a}_3^2} - 1 \right) \frac{\bar{a}_2}{\bar{a}_4} \frac{\delta_{11}}{\delta} + \frac{1}{2} \frac{R}{C_{p_3} - R} \left(\frac{a_2}{u_3} + \frac{a_2}{a_4} \right) \frac{\bar{u}_3^2}{\bar{a}_3^2} \frac{\delta_{12}}{\delta}$$

$$\left. + \frac{1}{2} \frac{R}{C_{p_3} - R} \cdot \frac{\bar{u}_3^2}{\bar{a}_3^2} \cdot \frac{a_2}{a_4} \frac{\delta_{13}}{\delta} + \frac{a_2}{a_4} \delta_{01} \right]$$

$$\Omega_{+\overline{IK}} = \frac{a_4}{2} \cdot \frac{C_{p_4} - R}{2C_{p_4} - 3R} \frac{\delta_J D}{A} \int_0^{\delta K/\delta J} \frac{2C_{p_3} - 3R}{2C_{p_3} - R} \left[A_1 \frac{a_4}{a} + A_2 + A_3 \frac{a}{a_4} + A_4 \left(\frac{a}{a_4}\right)^2 \right] \Big/ \left[1 - \frac{2C_{p_3} - 3R}{2C_{p_3} - R} \frac{a}{a_4} \right] d\left(\frac{\delta}{\delta_J}\right)$$

$$A_1 = 2 \frac{\delta_{10}}{\delta} - \frac{4R}{C_{p_2} - R} \frac{\delta_{11}}{\delta} + 2 \frac{2C_{p_3} - R}{R} \cdot \frac{\delta_{12}}{\delta} + 4 \frac{C_{p_3} - R}{R} \frac{\delta_{13}}{\delta}$$

$$A_2 = -2 \left[3 \frac{\delta_{10}}{\delta} - 6 \frac{C_{p_3} - R}{R} \frac{\delta_{11}}{\delta} + 2 \frac{C_{p_3} - R}{R} \left(2 + \frac{C_{p_3}}{C_{p_3} - R} \right) \frac{\delta_{12}}{\delta} + 6 \frac{C_{p_3} - R}{R} \frac{\delta_{13}}{\delta} \right]$$

$$A_3 = 2 \frac{\delta_{01}}{\delta} + 4 \frac{\delta_{10}}{\delta} - \frac{C_{p_3} - R}{R} \left(13 - \frac{C_{p_3}}{C_{p_3} - R} \right) \frac{\delta_{11}}{\delta} + 2 \frac{C_{p_3} - R}{R} \left(5 + \frac{C_{p_3}}{C_{p_3} - R} \right) \frac{\delta_{12}}{\delta} + 12 \frac{R}{C_{p_3} - R} \frac{\delta_{13}}{\delta}$$

$$A_4 = -\frac{1}{8} + \frac{C_{p_3} - R}{R} \left(5 - \frac{C_{p_3}}{C_{p_3} - R} \right) \frac{\delta_{11}}{\delta} - 4 \frac{C_{p_3} - R}{R} \frac{\delta_{13}}{\delta}$$

$$\frac{\delta}{\delta_J} = \left[\frac{z'}{a_4 t} \left(\frac{1}{2} \frac{2C_{p_3} - R}{C_{p_3} - R} - \frac{1}{2} \frac{R}{C_{p_3} - R} \frac{z'}{a_4 t} \right)^{-\frac{2C_{p_3} - R}{2R}} \right]^m$$

$$\frac{a}{a_4} = 1 - \frac{R}{2C_{p_2} - R} \cdot \frac{z'}{a_4 t}$$

$$\frac{\delta K}{\delta M} = \left[\frac{\bar{u}_3 - \bar{a}_3 + a_4}{2(\bar{a}_3 + \bar{a}_4)} \right]^m$$

$$\frac{\delta_M}{\delta_Q} = \left(\frac{\bar{u}_2}{\bar{a}_2} + 1 - \frac{U}{\bar{a}_2} \right)^m$$

$$z' = a_4 t - x$$

REFERENCES

(1) Trimpi, R. L. and Cohen, N. B., "A nonlinear theory for predicting the effects of unsteady laminar, turbulent, or transitional boundary layers on the attenuation of shock waves in a shock tube with experimental comparison," NASA TR-85, 1961.

(2) Kim, C. S. and Park, C., "Theoretical studies on shock attenuation and its electro-magnetic compensation in shock tube flows," Proc. of third international symposium on rockets and astronautics, Tokyo, 1961, 171-188, 1962.

(3) Spence, D. A. and Woods, B. A., "A review of theoretical treatments of shock-tube attenuation," Jour. of Fluid Mech. 19 (2) 161-174, June 1964.

(4) Mirels, H. and Mullen, J. F., "Small perturbation theory for shock tube attenuation and nonuniformity," Physics of Fluid 7 (8) 1208-1218, August 1964.

(5) Bernstein, L., "Notes on some experimental and theoretical results for the boundary layer development aft of the shock in a shock tube," British ARC 22,753, 1961.

(6) Livingston, F. R., "Experimentally measured effects of the wall boundary layer on shock tube performance," Jet Propulsion Laboratory TR No. 32-714, 1965.

(7) Markstein, G. H., "Flow disturbances induced near a slightly wavy contact surface, or flame front, traversed by a shock wave," Journal of Aeronautical Sciences 24 (3) 238-239, March 1957.

(8) White, D. R., "Influence of diaphragm opening time on shock-tube flows," Journal of Fluid Mechanics 4 (6) 585-599, November 1958.

(9) Kireev, V. R., "On motion of a shock wave during noninstantaneous opening of a diaphragm in shock tube," Izvestiya AN SSSR Otm, Mekhanika i Mashinostroyeniye, Nr. 6, 17-24, 144-146, 1962.

(10) Holbeche, T. A. and Spence, D. A., "A theoretical and experimental investigation of temperature variation behind attenuating shock waves," Proc. of the Royal Society, Series A, 277 (1376) 111-128, May 1964.

(11) Lighthill, M. J., "Dynamics of dissociating gas Part I Equilibrium Flow," Journal of Fluid Mechanics 2 (1) 1-32, January 1957.

(12) Bray, K. N. C. and Wilson, J. A., "A preliminary study of ionic recombination of argon in wind tunnel nozzle," University of Southampton Aeronautics and Astronautics Rep. No. 134, February 1960.

(13) Rosziszewski, J., "Influence of shock-wave attenuation by boundary-layer growth on contact-surface motion in a shock-tube," Journal of Aerospace Sciences 26 (6) 388-389, August 1959.

(14) Resler, E. L., Jr. and Sears, W. R., "The prospects for magneto-aerodynamics," Journal of the Aeronautical Sciences 25 (4) 235-245, April 1958.

(15) Kivel, B. and Bailey, K., "Tables of radiation from high temperature air," Avco Res. Rep. 21, December 1957.

(16) Nardone, M. C., Breene, R. G., Zeldin, S. S., and Riethof, T. R., "Radiance of species in high temperature air," G. E. Missile and Space Division R63SD3, June 1963.

(17) Meyrott, R. E., Sokoloff, J., and Nicholls, R. W., "Absorption coefficients of air," Geophysical Research Paper No. 58, GRD-TN-60-277, July 1960.

(18) Feldman, S., "Hypersonic gas dynamic charts for equilibrium air," Avco Everett Research Report 40, January 1957.

(19) Carslaw, H. S. and Jaeger, J. C., "Conduction of heat in solids," Chapter 10, Oxford University Press, 1947.

(20) Yos, J. M., "Transport properties of nitrogen, hydrogen, oxygen and air to 30,000° K," Avco Rep. RAD TM 63-7, 1963.

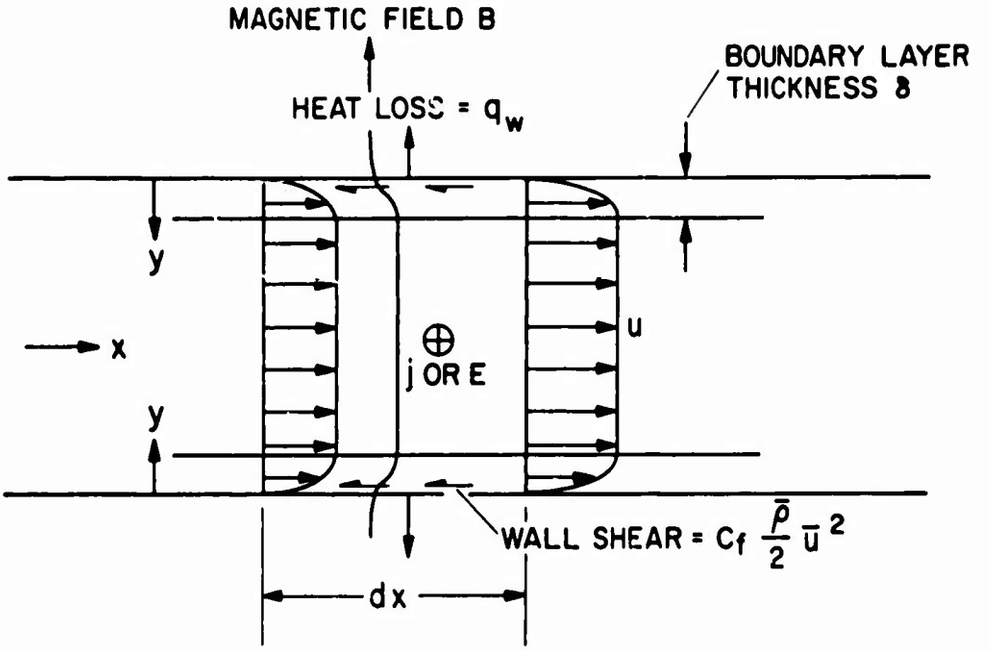


Figure 1(a).- Flow profile.

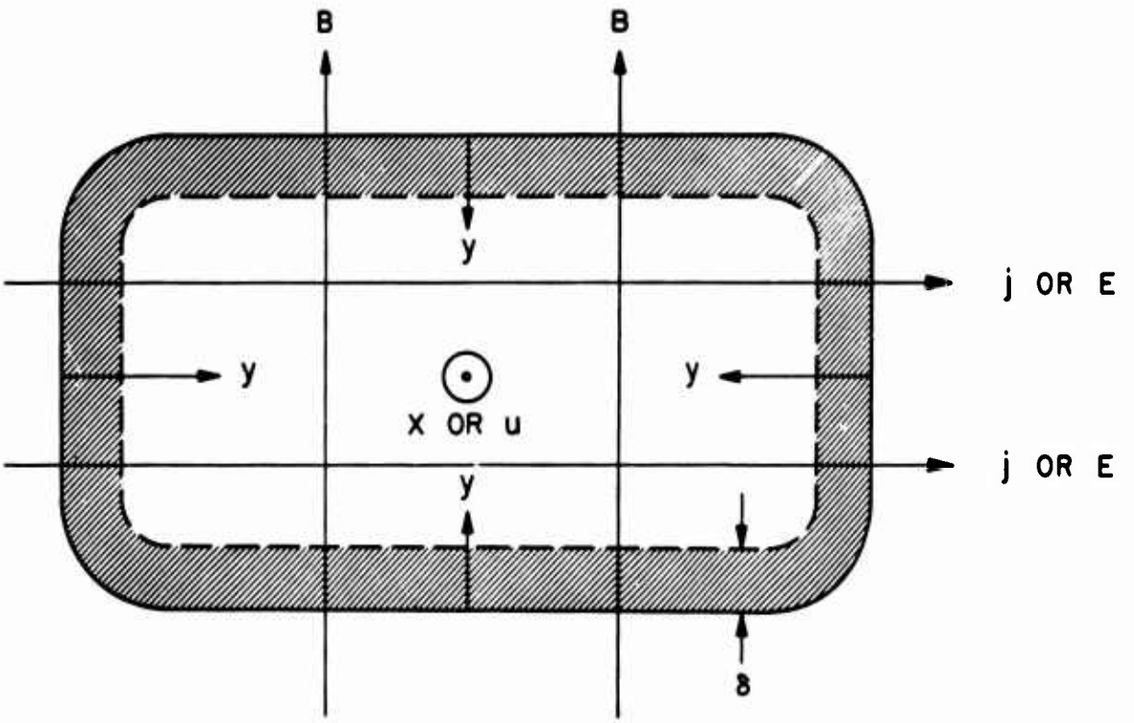


Figure 1(b).- Flow cross section.

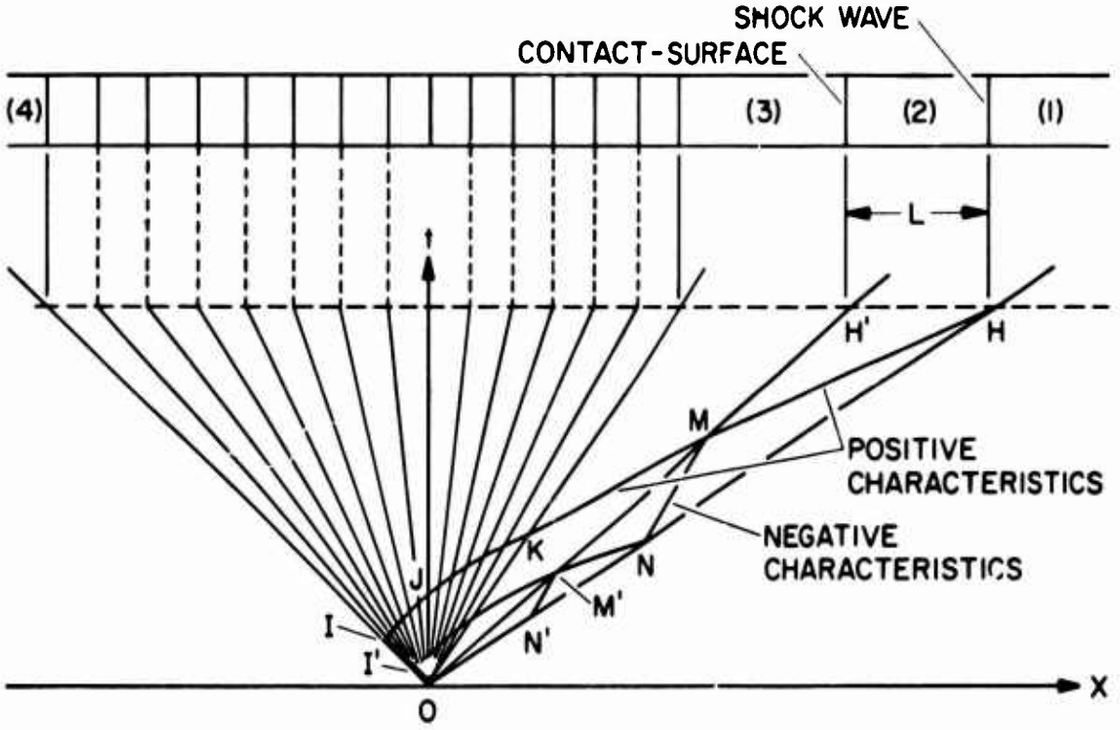


Figure 2.- Typical x-t diagram of a shock tube flow.

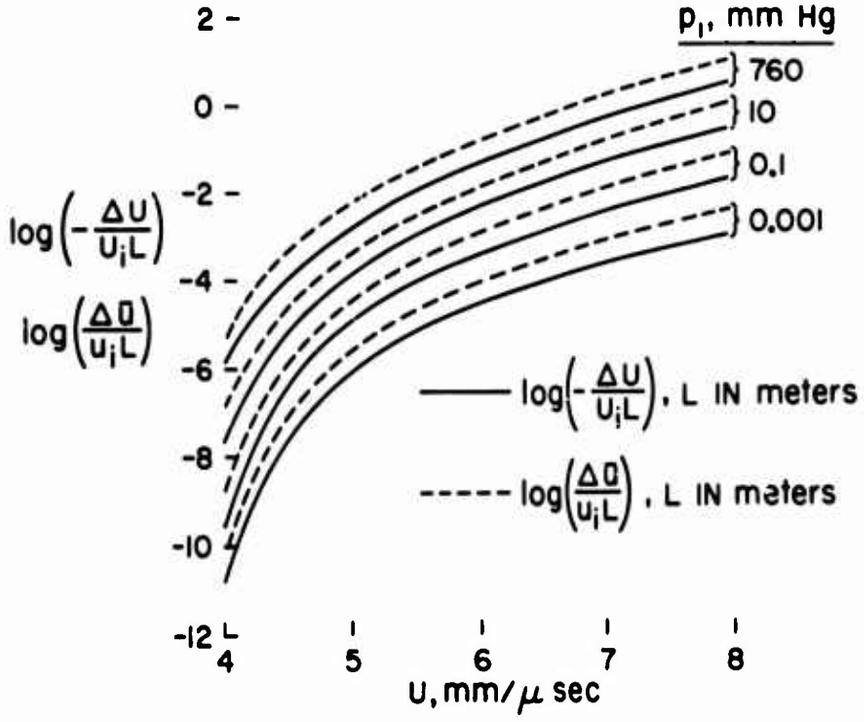


Figure 3.- Attenuation of shock wave and acceleration of contact surface due to radiation.

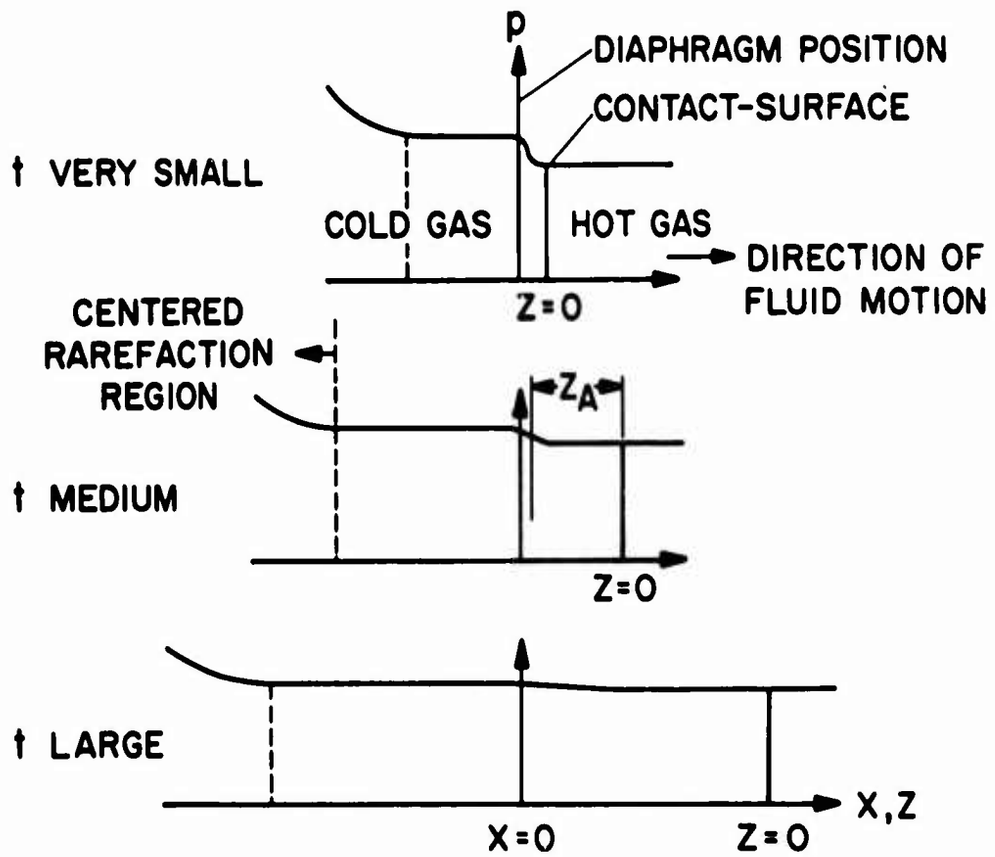


Figure 4.- Pressure drop across the contact surface due to imperfect rupture of diaphragm during initial transient period.

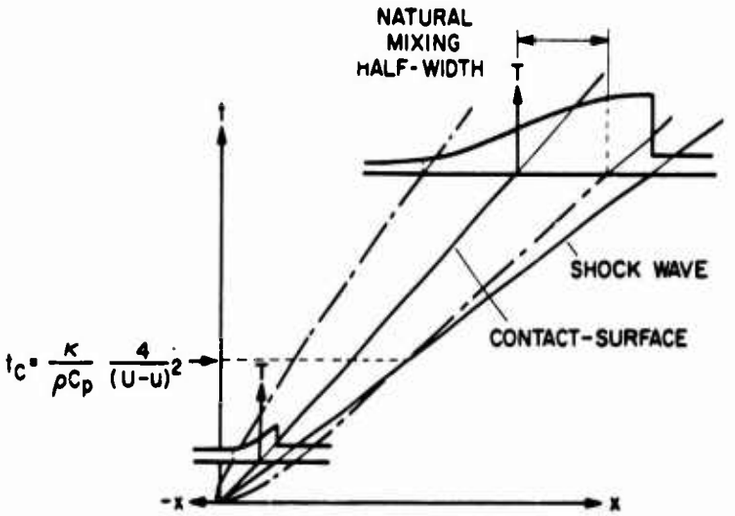


Figure 5(a).- Schematic diagram showing the variation of temperature in contact-surface mixing region.

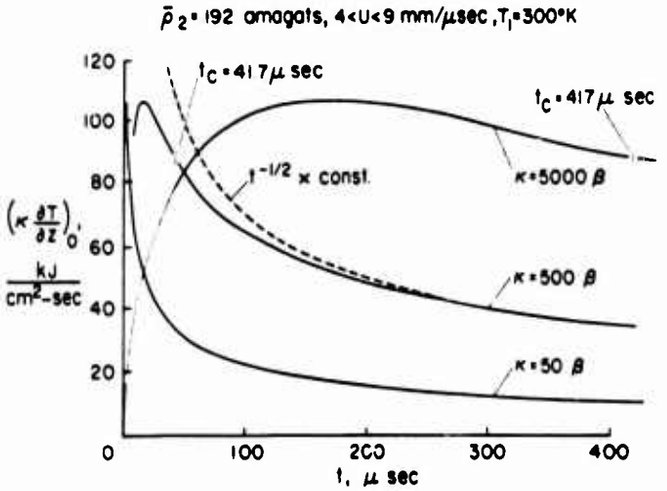


Figure 5(b).- Heat transfer rate through contact surface for different eddy conductivity at fixed density.

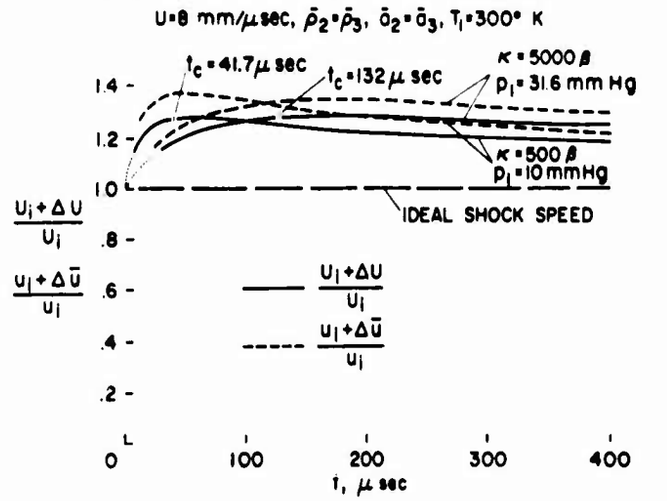


Figure 5(c).- Variation of shock wave velocity due to heat conduction through contact surface.

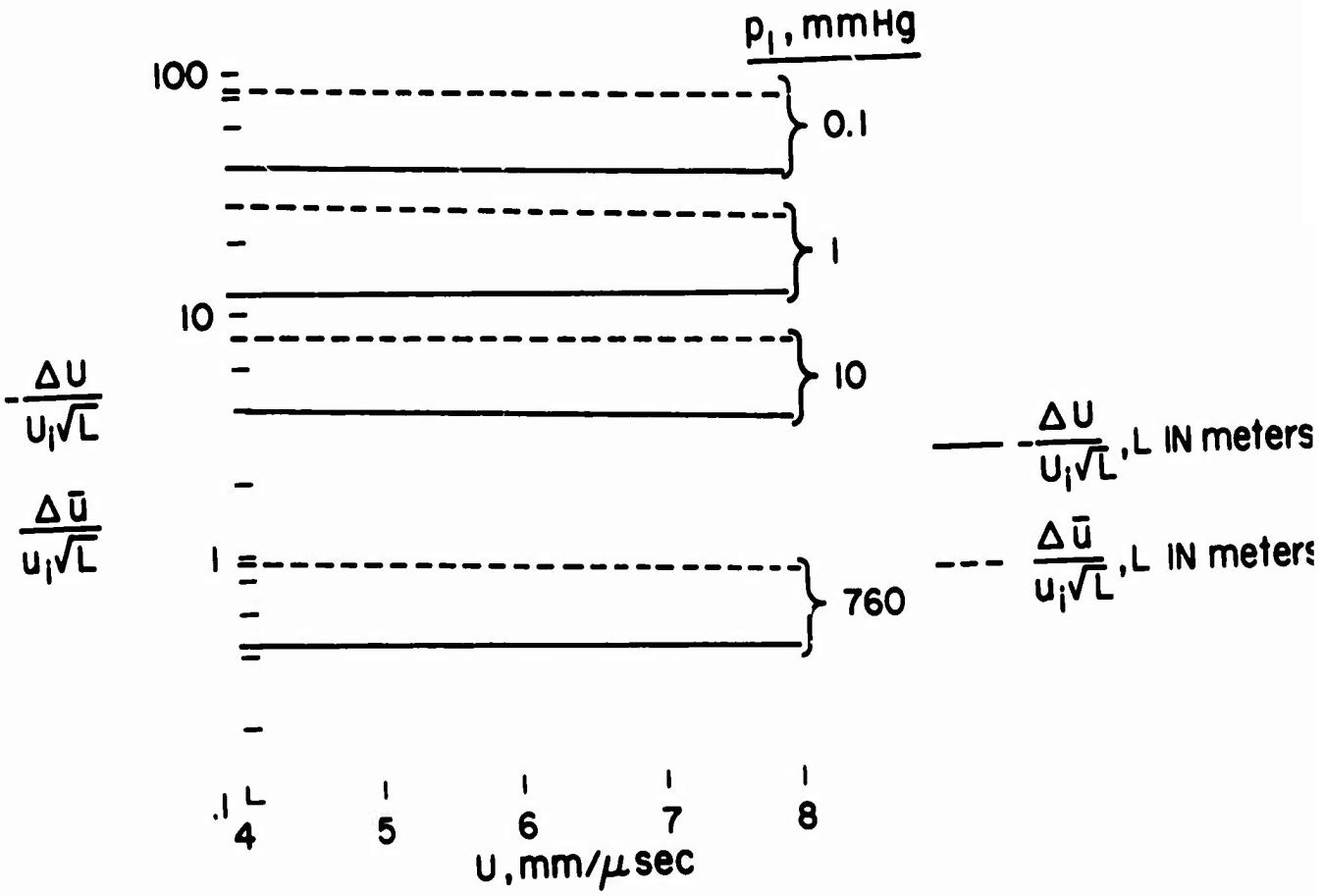


Figure 6.- Shock wave attenuation and contact-surface acceleration due to laminar heat transfer to wall for shocktube of 10 cm dia., $T_1 = 300^\circ$ K.

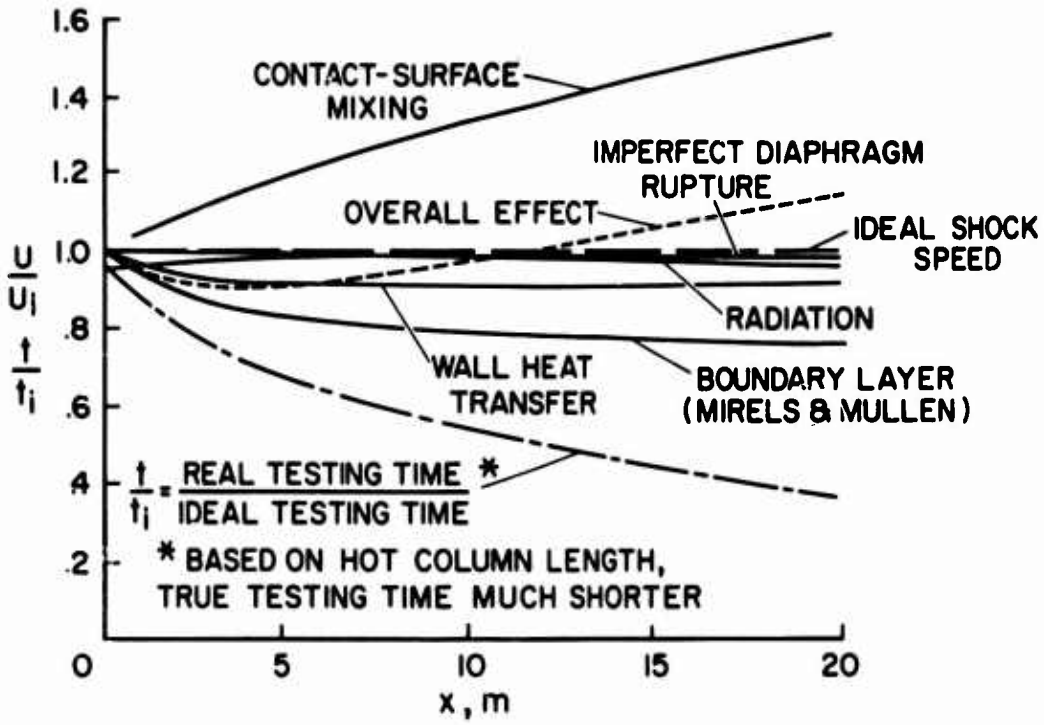


Figure 7(a).- Comparison of relative magnitude of individual real flow effect; p_1 = 1 mm Hg, T_1 = [illegible] K, U = 8mm/μsec, κ = 500 β, τ = 200 μsec, Δf = p_3, laminar boundary layer.

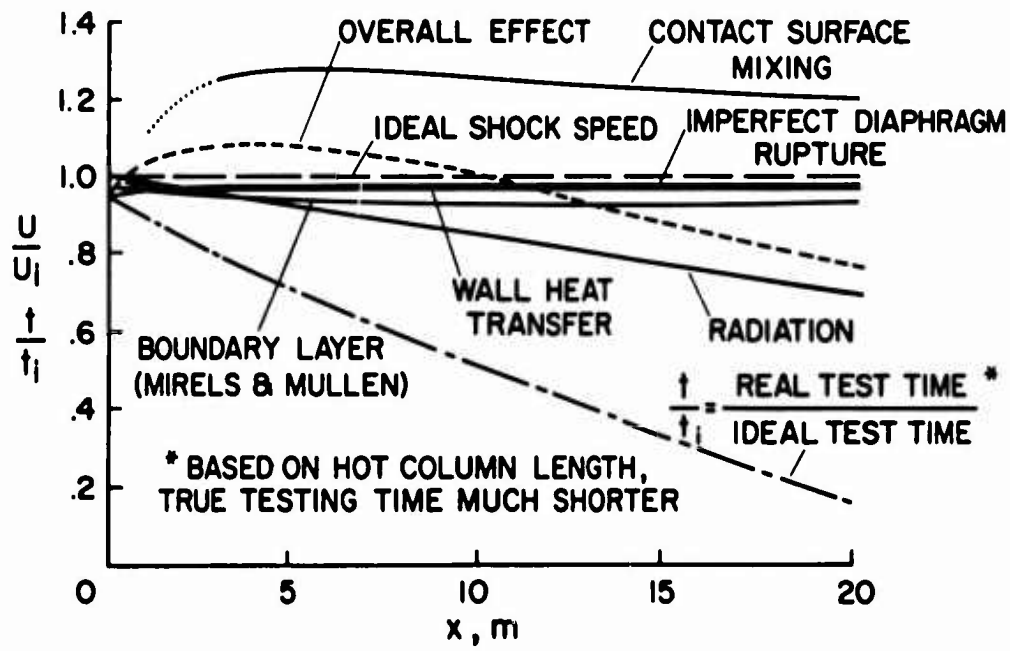


Figure 7(b).- Comparison of relative magnitude of individual real flow effect; p_1 = 10 mm Hg, T_1 = 300° K, U = 8 mm/μsec, κ = 500 β, τ = 200 μsec, Δf = p_3, laminar boundary layer.

BLANK PAGE

RAREFACTION DISCHARGE LAYER AS A TOOL FOR OBTAINING HIGH SPEED GAS FLOW

Jan Rosciszewski
General Dynamics/Convair
San Diego, California

INTRODUCTION

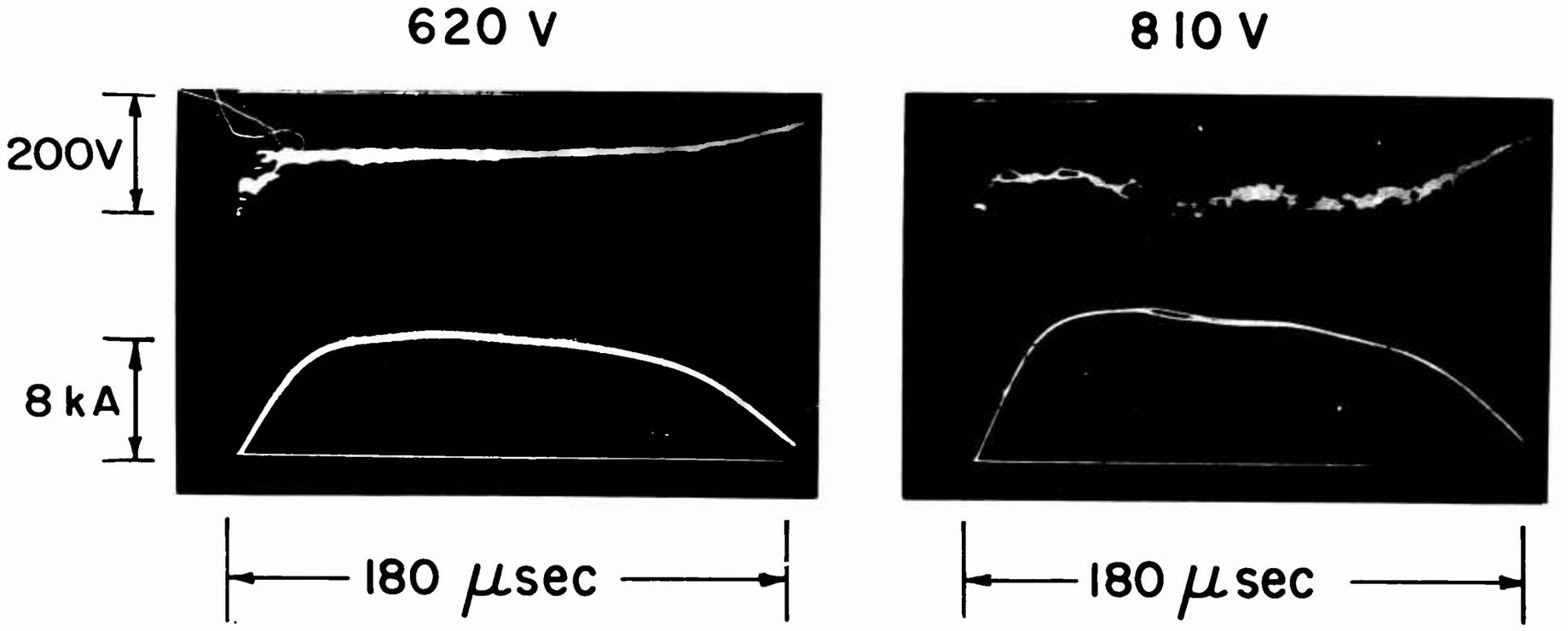
In Reference (1) a simplified model is given of a rarefaction (deflagration type) of ionizing layer by feeding a discharge layer with a non-ionized gas. Such a discharge layer has been obtained experimentally in a pulsed gas coaxial gun, and it remains stationary after the time interval of the order of 150 μsec (Ref. 2). The time variation of voltage and current is presented in Figure 1 indicating uniform distribution over a relatively long period of time. The ion probe, velocity measurements also indicate a constant velocity over a similar period of time (Ref. 2).

The velocity is of the order of 10^4 m/sec and, because of its uniform distribution in time, it can be utilized for high speed aerodynamic research.

The stationary discharge layer reminds one of a deflagration process in classical gas dynamics where the density decreases and the velocity increases as an element of gas crosses the layer. These types of current layers are different from the current layers of magnetic piston type in electromagnetically driven shock tubes.

In the latter case, the current layer is of the compression character with an increasing density of gas element entering the layer. Also the non-ionized gas in the rarefaction discharge layer enters it from the side of the high magnetic field, but in the magnetic piston type of discharge layer it enters from the side of the zero magnetic field (Figs. 2a, 2b).

In the case of electromagnetically driven shock tubes, the testing time is extremely short and, as was shown experimentally by R. Lovberg using magnetic field probes and schlieren systems, gas density concentration and magnetic field lines are closely coupled (Ref. 3). Some authors even claim that the "magnetic piston" moves ahead of the shock (Ref. 4). Therefore, magnetic field lines are trapped in the flow.

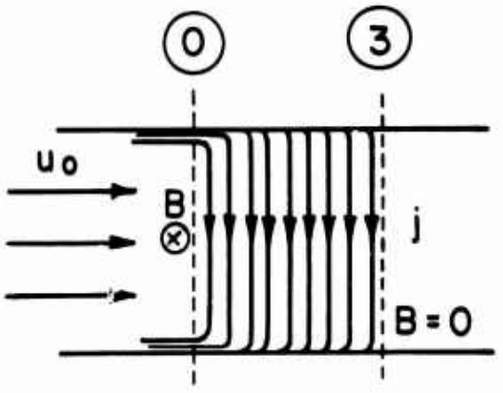


BARRELS : 3" LONG , 3" O.D. , 1.5" I.D.

GAS : NITROGEN

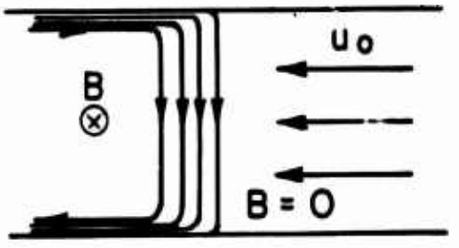
FIG. 1 : TYPICAL VOLTAGE AND CURRENT WAVEFORMS. (REF. 2)

There are two possible systems utilizing the quasi-stationary rarefaction type of discharge layer; one is a "plasma gun" with a vacuum system (Fig. 3), and another is a classical shock tube with the discharge in a diaphragm section. The wave diagram for the last case is shown in Fig. 4.



(a)

Fig. 2a. Rarefaction (deflagration type) of the current layer.



(b)

Fig. 2b. Magnetic piston type of the current layer.

BASIC RELATIONS FOR A STATIONARY DISCHARGE LAYER

The conservation of mass reads

$$m = \rho_0 u_0 = \rho_3 u_3 \tag{1}$$

where ρ is the mass density ($\rho = nM$), u the velocity, and subscripts zero and 3 denote the state upstream and downstream of the current sheet, respectively.

Neglecting viscous forces (rarefaction discharge layer is fairly thick) and assuming that electrons, ions, and neutrals have the same velocity,* conservation of momentum for one-dimensional flow can be written in the form

$$m\frac{du}{dx} + \frac{dp_n}{dx} + \frac{dp_e}{dx} = jB = -\frac{1}{2\mu}\frac{dB^2}{dx} \tag{2}$$

where j is the current density ($j = \frac{-1}{\mu}\frac{dB}{dx}$), B is the magnetic field, $p_n p_e$ denotes neutrals and electron pressure respectively, and μ is the magnetic permeability.

*Ions and neutrals have approximately the same velocity because of the large collision cross section, electrons and ions because of the space charge field.

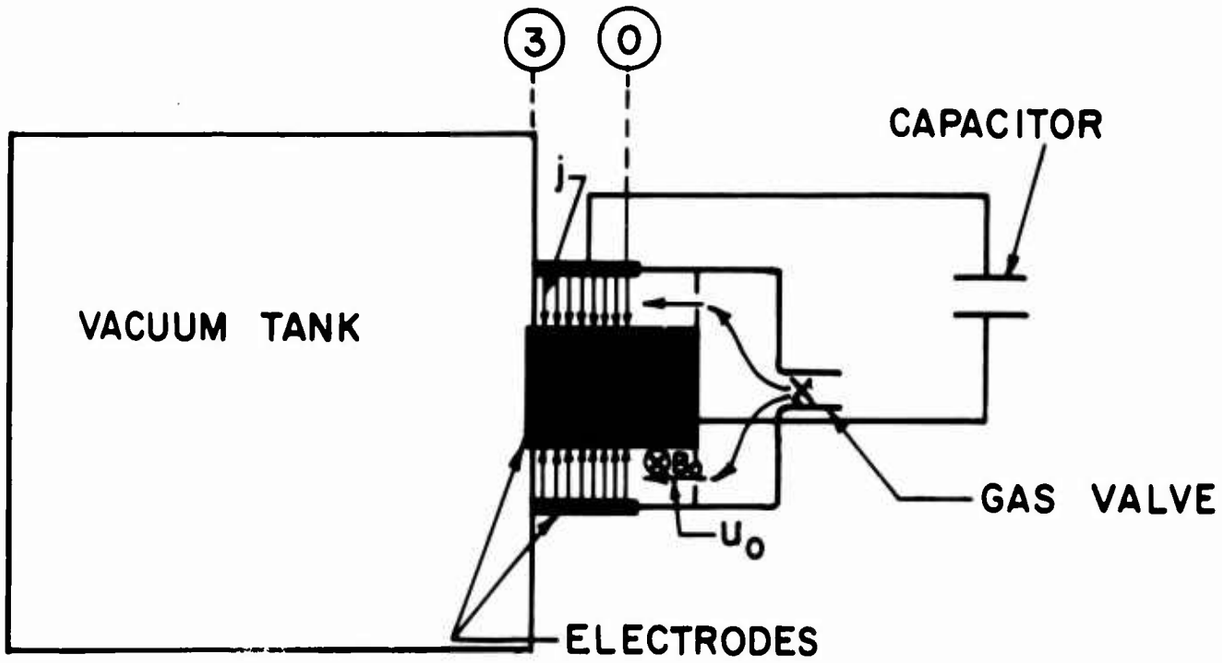


Fig. 3. Plasma accelerator with quasi-stationary rarefaction discharge layer.

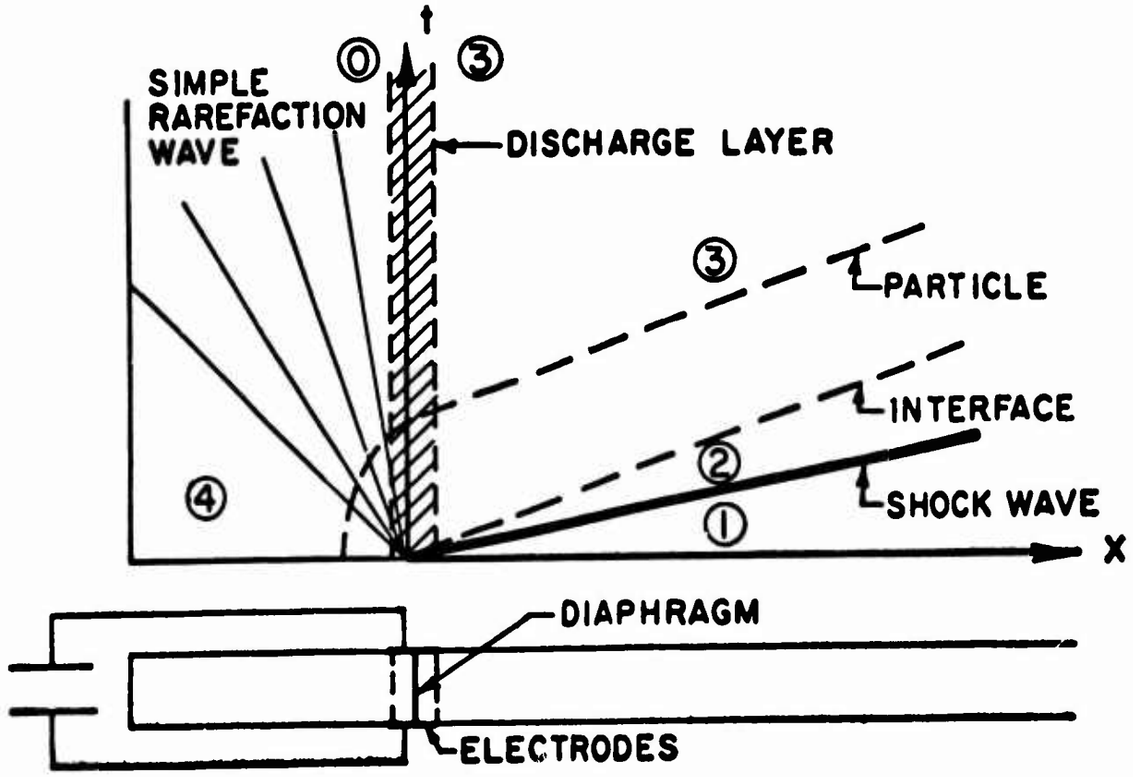


Fig. 4. Wave diagram for a shock tube with quasi-stationary discharge layer in the diaphragm section.

Integrating this expression, one gets

$$mu + p_n + p_e + \frac{B^2}{2\mu} = mu_0 + p_{n_0} + \frac{B_0^2}{2\mu} \tag{3}$$

This expression becomes exact when applied to the end section of the discharge layer $u = u_3$, $B = 0$, etc.

Taking into account that ($n = \frac{m}{uM}$)

$$p_e = k n_e T_e = k\alpha n T_e = k\alpha \frac{m}{uM} T_e$$

and

$$p_n = k(1-\alpha)\frac{m}{uM} T_n \tag{4}$$

where M is the molecular mass and $\alpha = \frac{n_e}{n}$ the degree of ionization, k the Boltzmann constant.

Substituting expressions (4) into (3) and solving with respect to u, one gets

$$\bar{u} \equiv \frac{u}{u_0} = \frac{b + \sqrt{b^2 - 4c}}{2} \tag{5}$$

where

$$b = \frac{1}{\gamma M_0^2} + \frac{1}{2K}(1 - \bar{B}^2) + 1$$

$$c = \frac{k}{u_0^2 M}\left[\alpha T_e + (1-\alpha) T_n\right]$$

$M_0 = \frac{u_0}{A_0}$ is the Mach number at the entrance to the current sheet,

$$K = \frac{\mu n_0 M u_0^2}{B_0^2}, \quad \bar{B} \equiv \frac{B}{B_0}$$

Taking into account the fact that at the downstream side of the current sheet (subscript 3) $B_3 = 0$ and that electron temperature is limited because

of radiation (usually electron temperature cannot be higher than 1/3 of ionization potential in ev), one obtains for typical numerical values $b^2 >> 4c$ and therefore ($\frac{I}{2K} >> 1$)

$$u_3 \cong \frac{B_0^2}{2\mu n_0 M u_0} \tag{6}$$

At the same time, the pressure ratio across the current sheet is ($T_e >> T$),

$$\frac{p_3}{p_0} = \frac{n_e T_e}{n_0 T_0} = \frac{n \alpha T_e}{n_0 T_0} = \frac{u_0 \alpha T_e}{u_3 T_0} \tag{7}$$

In the case of the system utilizing a vacuum tank, assuming fully ionized gas ($\alpha = 1$), taking p_3 equal to the reservoir pressure, and assuming radiation limited electron temperature ($T_e \simeq 1/3\ V_i$ ev where V_i is the ionization energy in ev), from Equation (7) one can calculate the velocity u_3, and from Equation (6) the magnetic field B_0 which in turn will give the total current.

SHOCK TUBE WITH THE STATIONARY CURRENT SHEET

For a strong shock wave, the following expressions are valid:

$$\frac{p_2}{p_1} = \frac{2\gamma}{\gamma+1} M_s^2, \qquad \frac{u_2}{a_1} = \frac{2}{\gamma+1} M_s \tag{8}$$

where $\gamma = \frac{c_p}{c_v}$, M_s, the shock Mach number, and subscript (1) denotes the state of the gas ahead of the shock (Fig. 1).

From these relations, it follows that

$$M_s = \frac{\gamma+1}{2} \frac{u_2}{a_1} \tag{9}$$

$$\frac{p_2}{p_0} = \frac{2\gamma}{\gamma+1} \frac{p_1}{p_0} M_s^2 = \frac{\gamma(\gamma+1)}{2} \left(\frac{u_2}{a_1}\right)^2 \frac{p_1}{p_0} \tag{10}$$

From Equations (7) and (10), it follows that ($p_3 = p_2$)

$$\frac{u_2}{a_1} = \left[\frac{2}{\gamma(\gamma+1)} \frac{u_0}{a_1} \alpha \frac{T_e}{T_0} \frac{p_0}{p_1}\right]^{-1/3} \tag{11}$$

The shock Mach number is

$$M_s = \left[\frac{(\gamma+1)^2}{4\gamma}\frac{u_0}{a_1}\frac{T_e}{T_1}\frac{p_0}{p_1}\alpha\right]^{1/3} \tag{12}$$

Assuming that the gas becomes fully ionized, $\alpha = 1$.

Because of the radiation, the electron temperature has an upper limit and the approximate relation between the electron temperature and the ionization potential is

$$T_e \cong \frac{V_i}{3} \quad (ev)$$

From this, it follows that the driver gas must be of high V_i and helium will be very good (V_i = 24.58 ev, $T_e \cong 90{,}000^\circ K$). Also, the driven gas should be of low a_1 (a heavy gas like argon).

From Equations (6) and (12) the magnetic field B_0 or total current $I = \frac{B_0}{\mu}$ can be calculated (for a plane case)

$$I = (2\mu n_0 M u_0 u_2)^{1/2} = (2\mu n_0 M u_0)^{1/2}\left[\frac{2}{\gamma(\gamma+1)}\frac{u_0}{a_1}\alpha\frac{T_e}{T_0}\frac{p_0}{p_1}\right]^{1/6}\cdot a_1^{1/2}$$

This expression for I enables us to design a proper capacitor bank. In fact, this expression is not complete because α_2 is not known. The proper evaluation of α_2 could be only obtained by consideration of the ionization phenomena in the current layer. However, I is proportional to $\alpha_2^{1/3}$ and the assumption of $\alpha_2 = 1$ should be fairly good.

Assuming that the discharge layer is located in the diaphragm section, we have

$$u_0 = a_0 = \frac{2}{\gamma+1}a_4 \tag{13}$$

where a_4 is the speed of sound in the driver before the diaphragm breaks.

Also

$$\frac{T_0}{T_4} = \left(\frac{2}{\gamma+1}\right)^2, \quad \frac{p_0}{p_4} = \left(\frac{2}{\gamma+1}\right)^{\frac{2\gamma}{\gamma+1}} \tag{14}$$

Therefore, one gets

$$M_s = \left[\left(\frac{2}{\gamma+1} \right)^{\frac{\gamma-1}{\gamma+1}} \frac{1}{\gamma} \frac{a_4}{a_1} \frac{p_4}{p_1} \frac{T_e}{T_4} \right]^{1/3} \tag{15}$$

Example:

$$\frac{T_e}{T_4} = 10^2, \quad \frac{a_4}{a_1} = 4, \quad \gamma = 5/3$$

initial diaphragm pressure ratio $p_4/p_1 = 10^3$. From Equation (15) it follows that $M_s \cong 60$. The shock Mach number in a shock tube without electric acceleration is limited and for strong waves ($p_4/p_1 \gg 1$), it depends on the initial speed of the sound ratio[5]

$$M_s = \frac{\gamma_1+1}{\gamma_4-1} \frac{a_4}{a_1}$$

Therefore, for the same as before, $\frac{a_4}{a_1}$, and $\gamma_4 = \gamma_1 = 5/3$ one gets

$$M_s = 16$$

so that discharge in the diaphragm section increases the shock Mach number by almost four times.

CONCLUSIONS

1. A stationary type of discharge layer in the diaphragm section increases significantly the shock Mach number as compared to the classical shock tube.

2. The proposed shock tube with electric discharge in the diaphragm section offers advantages over magnetic piston driven shock tubes where the flow time is extremely short and the gas flow is highly non-uniform with a trapped in magnetic field. In the present device, there is no magnetic field between the shock wave and the discharge layer, and the test time would be much higher (of the same order of magnitude as in an ordinary shock tube).

3. The light driver gas, with a high ionization potential like helium, and a heavy driven gas appear to be best for obtaining highest shock Mach numbers.

ACKNOWLEDGMENT

The author expresses his gratitude to Dr. T. Gooding, Dr. A. V. Larson, and their associates for experimental illustrations. The work has been supported by the Air Force Office of Scientific Research under Contract No. AF 49(638)-1357 and -1556.

REFERENCES

1. J. Rosciszewski, "Energy Partition in the Current Layer," AIAA Journal, Vol. 3, No. 2, 1965.

2. T. J. Gooding, B. R. Hayworth, A. V. Larson, and D. E. T. F. Ashby, "Development of a Coaxial Plasma Gun for Space Propulsion," GDA-DBE 64-052-2, General Dynamics/Astronautics, Nov. 1964.

3. R. Lovberg, private communication.

4. G. C. Vlases, "Experiments in a Cylindrical Magnetic Shock Tube," Journal of Fluid Mechanics, 16, pp. 82-96, 1963.

5. H. Liepmann and A. Roshko, Elements of Gas Dynamics, J. Wiley, New York, p. 389, 1957.

BLANK PAGE

ANALOGUE NETWORKS FOR HIGH HEAT-TRANSFER RATE MEASUREMENTS IN SHOCK TUBES AND SHOCK TUNNELS

Z. A. Walenta*
Institute for Aerospace Studies, University of Toronto
Toronto, Canada

ABSTRACT

Analogue networks for calculating automatically the rate of heat transfer between the model and the flowing gas have been used for several years. Such networks are accurate provided the thermal properties of the model are constant. If they are not constant, using a simple analogue network will introduce serious errors. Assuming that thermal diffusivity is constant and a linear variation of thermal conductivity with surface temperature, a simple relation between the ideal and actual surface temperature rise has been derived. Using this relation as a basis, an automatic correction circuit for use with analogue networks has been designed and built. A series of experimental tests have been performed during which two analogue networks, with and without the correction circuit, were connected to the same thin-film gage mounted on pyrex 7740 glass along the stagnation line of a circular cylinder. For surface temperature increments in the gage from 40°C to 75°C the analogue network without correction gave heat-transfer rates 10 to 20 per cent below the expected values. Application of the correction circuit in the same range of temperatures reduced the average discrepancy between the heat-transfer rates expected and measured to about 3.5 per cent.

INTRODUCTION

All objects flying at hypervelocities in the Earth's atmosphere, as well as in atmospheres of other planets, are subjected to very intense aerodynamic heating, which in some cases may even lead to their destruction. This creates many problems for the engineers designing spacecrafts and rockets and for the scientists, investigating the aerodynamic heating itself.

* Research Fellow, on leave from the Polish Academy of Sciences, Warsaw, Poland.

The facilities most often used to investigate aerodynamic heating are shock tubes and shock tunnels. They are the only facilities capable of producing stagnation enthalpies characteristic of vehicles reentering the Earth's atmosphere. However, the testing times available in shock tubes and shock tunnels are very short and require special kinds of measuring devices.

Out of all the devices that are used for heat transfer measurements in shock tubes and shock tunnels, perhaps the most widely accepted is the thin-film gauge. These gauges have extremely fast response and are very sensitive. Unfortunately they measure essentially the surface temperature of the model as a function of time. In order to obtain a heat-transfer rate from such a history, a very troublesome numerical integration must be performed. To overcome this difficulty, special analogue networks (ref. 2 and 3) have been designed and used successfully for several years. However, if the heat-transfer rates are very large, the gauge temperature rise may be high enough to cause a variation of the thermal properties of the gauge. In such a situation the simple analogy no longer holds and unless large errors can be tolerated, a numerical integration is again necessary.

To avoid this, the use of a very simple correction circuit, placed between the thin-film gauge and the analogue network is recommended. Such a circuit has been built at UTIAS and experiments indicate that it works very well within the temperature range of the experiments. These were performed at shock Mach numbers $2.8 < M_s < 6.9$ in air, at initial pressures 0.7 mm Hg $< p_1 <$ 60 mm Hg and gave rise to gauge surface temperature changes $3.5^{\circ}C < \theta < 75^{\circ}C$, for stagnation temperatures $980^{\circ}K < T_s < 3500^{\circ}K$. The heat transfer rates encountered varied between $40 < \dot{q} < 1230$ watts per sq. cm.

IDEAL ANALOGUE NETWORK

Principle of the Analogy

As it was mentioned in the Introduction, thin-film heat-transfer gauges do not measure the heat-transfer rate directly. These gauges consist essentially of a piece of "backing material" like pyrex, quartz, or even ordinary glass, on the surface of which an extremely thin (less than one micron) metallic layer is deposited (ref. 1). This layer works as a resistance thermometer measuring, because of its thinness, the actual temperature of the surface of the backing material. To obtain the rate of heat transfer into the gauge the heat conduction equation inside the backing material must be solved. Fortunately, for the times involved in shock tubes and shock tunnels, the depth of penetration of heat into the backing material is small. Therefore, even for gauges made out of relatively thin pieces of glass and having curved surfaces, the problem may be considered one-dimensional and the material semi-infinite (Fig. 1). The heat conduction equation in the gauge is then

$$\frac{\partial \theta}{\partial t} = \frac{K}{\rho c} \frac{\partial^2 \theta}{\partial x^2} \qquad (1)$$

and since the gauge surface temperature is known (measured) the initial and boundary conditions are

$$\begin{aligned} &\theta(x,t) = 0 && \text{for } t = 0 \;;\; x > 0 \\ &\theta(x,t) = \theta_w(t) && \text{for } t \geq 0 \;;\; x = 0 \\ &\lim_{x \to +\infty} \theta(x,t) = 0 \end{aligned} \tag{2}$$

The heat flux through the unit area of the plane x = 0, which is sought in this problem, is

$$\dot{q}(t) = -K\left[\frac{\partial \theta(x,t)}{\partial x}\right]_{x=0} \tag{3}$$

The electrical conduction equation in a one-dimensional conductor having continuous distribution of resistance and capacitance is (ref. 3),

$$\frac{\partial u}{\partial t'} = \frac{1}{RC}\,\frac{\partial^2 u}{\partial x'^2} \tag{4}$$

Take the initial and boundary conditions corresponding to a semi-infinite conductor, charged at the end

$$\begin{aligned} &u(x',t') = 0 && \text{for } t' = 0 \;;\; x' > 0 \\ &u(x',t') = u_g(t') && \text{for } t' \geq 0 \;;\; x' = 0 \\ &\lim_{x' \to +\infty} u(x',t') = 0 \end{aligned} \tag{5}$$

The electric current through the x' = 0 cross-section of the conductor is

$$i(t') = -\frac{1}{R}\left[\frac{\partial u(x',t')}{\partial x'}\right]_{x'=0} \tag{6}$$

If the functions $\theta_w(t)$ and $u_g(t')$ fulfill the condition

$$\frac{\theta_w}{T_0} = \frac{u_g}{U_0} = f \tag{7}$$

then it will be shown that there is a complete analogy between equations (1) - (3) and (4) - (6).

Introducing the non-dimensional variables

$$\zeta = \frac{\theta}{T_0}, \quad \zeta' = \frac{u}{U_0}$$

$$\eta = \frac{t}{t_0}, \quad \eta' = \frac{t'}{x_0'^2 \bar{R} \bar{C}}$$

$$\xi = \sqrt{\frac{\rho c}{K}} \frac{x}{\sqrt{t_0}}, \quad \xi' = \frac{x'}{x_0'} \tag{8}$$

$$Q = \frac{\sqrt{t_0}}{\sqrt{K \rho c}} \frac{\dot{q}}{T_0}, \quad Q' = \frac{x_0' \bar{R}}{U_0} i$$

permits reducing both equations (1) - (3) and (4) - (6) to one set of equations (by dropping the primes) of the same form

$$\frac{\partial \zeta}{\partial \eta} = \frac{\partial^2 \zeta}{\partial \xi^2} \tag{9}$$

$$\zeta(\xi, \eta) = 0 \qquad \text{for} \quad \eta = 0 \; ; \; \xi > 0$$

$$\zeta(\xi, \eta) = f(\eta) \qquad \text{for} \quad \eta \geq 0 \; ; \; \xi = 0 \tag{10}$$

$$\lim_{\xi \to +\infty} \zeta(\xi, \eta) = 0$$

$$Q = - \left[\frac{\partial \zeta(\xi, \eta)}{\partial \xi} \right]_{\xi = 0} \tag{11}$$

Assuming (ref. 3)

$$t_0 = x_0'^2 \bar{R} \cdot \bar{C}$$

one obtains from equation (8)

$$t' = t$$

$$\dot{q}(t) = \frac{T_0}{U_0}\sqrt{\frac{\bar{R}}{\bar{c}}\kappa\rho c}\quad \dot{i}(t) \tag{12}$$

The last relation permits the conversion of the current history obtained from the analogue network into an actual heat-transfer rate history.

Response of an Ideal Analogue Network to Idealized Inputs

Applying the Laplace transformation to equations (9) - (11) one obtains (see ref. 7 for derivation)

$$Q = \frac{1}{\sqrt{\pi}}\left[\frac{f(+0)}{\sqrt{\eta}} + \int_0^{\eta}\frac{f'(\lambda)}{\sqrt{\eta-\lambda}}\,d\lambda\right] \tag{13}$$

where $$f'(\eta) = \frac{df}{d\eta}$$

Consider three cases of the "input function" f which are important for shock tube applications

(a) "step function" input

$$f(\eta) = A = \text{constant} \tag{14}$$

(b) input proportional to the square root of time

$$f(\eta) = B\sqrt{\eta} \tag{15}$$

(c) input proportional to time

$$f(\eta) = D\,\eta \tag{16}$$

Case (a) is realized in shock-tube flows immediately after a shock wave passes the gauge mounted in the tube wall - as long as the boundary layer is laminar (ref. 5). Case (b) corresponds to the stagnation point heat transfer in a shock tube. Conditions close to case (c) may be observed during formation of turbulent spots on shock tube walls (ref. 6).

From equation (13) it follows immediately in case (a)

$$Q = \frac{A}{\sqrt{\pi\eta}} \tag{17}$$

in case (b)

$$Q = \frac{\sqrt{\pi}}{2} B = \text{constant} \tag{18}$$

in case (c)

$$Q = \frac{2}{\sqrt{\pi}} D \sqrt{\eta} \tag{19}$$

These are output functions from an ideal analogue network, given in non-dimensional form. In order to convert to dimensional variables, equation (8) must be used.

REAL ANALOGUE NETWORK

Principle of Operation of a Real Analogue Network

It is difficult to build an analogue network with resistance and capacitance continuously distributed and it is also impossible to build a network which is infinitely long. In a real case (ref. 3), an analogue network always consists of a finite number of lumped R C-sections (Fig. 2). For such a lumped network there is

and $$\sqrt{\frac{\bar{R}}{\bar{C}}} = \sqrt{\frac{R}{C}} = \frac{R}{\sqrt{RC}}$$

$\frac{1}{2} R\, i(t) = \Delta u(t)$ - voltage drop across the first resistor

and equation (12) reduces to

$$\dot{q}(t) = \frac{2 T_o}{U_o} \sqrt{\frac{K \rho c}{RC}}\, \Delta u(t) \tag{20}$$

The analogue network is connected to a thin-film gauge where the following relation applies (ref. 1)

$$\frac{u_g}{U_{g_o}\, \theta_w} = \frac{R_g - R_{g_o}}{R_{g_o}\, \theta_w} = \beta \tag{21}$$

which is valid if the electric current in the gauge and coefficient β are both constant.

There is usually some amplification $\mathcal{K}$ between the gauge and analogue, consequently

$$\frac{T_o}{U_o} = \frac{\theta_w}{\mathcal{K} u_g} = \frac{1}{\mathcal{K} \beta U_{g_o}} \tag{22}$$

and equation (20) reduces finally to

$$\dot{q}(t) = \frac{2}{\mathcal{H}\beta}\sqrt{\frac{K\rho c}{RC}}\,\frac{\Delta u(t)}{U_{q_0}} = E\,\Delta u(t) \tag{23}$$

Hence the heat-transfer rate is directly proportional to the voltage across the first resistor of the analogue network. Since a lumped network only approximates a continuous distribution of resistance and capacitance, the values obtained from a real analogue network are not quite exact. However, in cases of interest the error can be readily estimated (ref. 3 and subsequent discussion in the next two subsections).

Error Due to Finite Size of the Lumped Elements

According to the results obtained by Meyer (ref. 3) the ratio of a lumped network output to that of an ideal analogue is:

in case (a)

$$\Lambda = 2\sqrt{\pi\eta}\; e^{-2\eta}\, I_0(2\eta) \tag{24}$$

in case (b)

$$\Lambda = \operatorname{erf}\left(2\sqrt{\eta}\right) \tag{25}$$

in case (c)

$$\Lambda = \sqrt{\pi\eta}\; e^{-2\eta}\left\{I_0(2\eta) + I_1(2\eta)\right\} \tag{26}$$

where, according to the previous definition

$$\eta = \frac{t}{RC} \tag{27}$$

The values of $\Lambda = \Lambda(\eta)$ in all three cases are given in Fig. 5.

According to Meyer's later results (ref. 4) the accuracy of the analogue network, at the beginning of its operation, can be greatly improved by evaluating the heat-transfer rate $\dot{q}(t)$ from the analogue output delayed by RC/8, i.e. by replacing the equation (23) with

$$\dot{q}(t) = \frac{2}{\mathcal{H}\beta}\sqrt{\frac{K\rho c}{RC}}\,\frac{1}{U_q}\,\Delta u\left(t + \frac{RC}{8}\right) = E\,\Delta u\left(t + \frac{RC}{8}\right) \tag{23a}$$

When equation(23a) is used, the ratio of the lumped network to the ideal analogue output is:

in case (a)

$$\Lambda^* = 2\sqrt{\pi\eta}\; e^{-2\left(\eta+\frac{1}{8}\right)}\; I_0\left[2\left(\eta+\frac{1}{8}\right)\right] \tag{24a}$$

in case (b)

$$\Lambda^* = \operatorname{erf}\left(2\sqrt{\eta+\frac{1}{8}}\right) \tag{25a}$$

and in case (c)

$$\Lambda^* = \sqrt{\pi}\,\frac{\left(\eta+\frac{1}{8}\right)}{\sqrt{\eta}}\; e^{-2\left(\eta+\frac{1}{8}\right)}\left\{I_0\left[2\left(\eta+\frac{1}{8}\right)\right] + I_1\left[2\left(\eta+\frac{1}{8}\right)\right]\right\} \tag{26a}$$

The curves of $\Lambda^* = \Lambda^*(\eta)$ in all three cases are also given in Fig. 5. It is readily seen from Fig. 5, that the analogue will provide accurate results for $t > \frac{1}{2}$ RC and should be used in this manner in practice.

Error Due to Finite Length of the Network

Evaluation of the error due to finite length of the lumped network is rather complex. It is usually assumed, that the error is the same as if the network was finite, but continuous (ref. 3).

The error due to finite length of the network depends on the conditions at its end. For the network shown in Fig. 3, in case (a) ("step function" input) Meyer (ref. 3) obtained the ratio of the finite to infinite analogue output

$$\delta = \sqrt{\pi\tau}\left(1 + 2\sum_{n=1}^{\infty} e^{-n^2\pi^2\tau}\right) \tag{28}$$

where

$$\tau = \frac{t}{L^2 R C} = \frac{\eta}{L^2} \tag{29}$$

$$L = \frac{l}{x_0'}$$ nondimensional length of the network.

(For x_0' equal to the length of a single segment of the network, L is identical with the number of segments and $\tau = 1/L^2(t/RC)$.

For the network shown in Fig. 4, it was found (see ref. 16 for complete derivation)

in case (a)

$$\left(1 - e^{-\frac{1}{\tau}}\right)\operatorname{erf}\left(\frac{1}{\sqrt{\tau}}\right) \leq \delta \leq \left(1 - e^{-\frac{1}{\tau}}\right) \tag{30}$$

in case (b)

$$\left[1-e^{-\frac{1}{\tau}}+\frac{\sqrt{\pi}}{2\sqrt{\tau}}\ \mathrm{erfc}\left(\frac{1}{\sqrt{\tau}}\right)\right]\mathrm{erf}\left(\frac{1}{\sqrt{\tau}}\right)\leq\delta\leq\mathrm{erf}\left(\frac{1}{\sqrt{\tau}}\right) \qquad (31)$$

in case (c)

$$\delta\geq\left[1+\frac{2}{\sqrt{\pi\tau}}\ e^{-\frac{1}{\tau}}-\left(1+\frac{2}{\tau}\right)\mathrm{erfc}\left(\frac{1}{\sqrt{\tau}}\right)\right]\left[1-e^{-\frac{1}{\tau}}+\sqrt{\frac{\pi}{\tau}}\,\mathrm{erfc}\left(\frac{1}{\sqrt{\tau}}\right)\right] \qquad (32)$$

$$\delta\leq\left[1-e^{-\frac{1}{\tau}}+\sqrt{\frac{\pi}{\tau}}\,\mathrm{erfc}\left(\frac{1}{\sqrt{\tau}}\right)\right]$$

Figure 6 gives a comparison of the values obtained from the equations (28) and (30) - (32). It is seen that a value of $\tau = 0.2$ will cause an error of 1.5% in Meyer's case and 1% in the present case.

Figure 5 permits the calculation of the desired value of RC and knowing the total flow time Fig. 6 will provide a value of L.

HEAT TRANSFER GAUGE WITH TEMPERATURE DEPENDENT PROPERTIES

Variation of the Properties of the Gauge Backing Material

In the present section, unlike the preceding section on "Ideal Analogue Network", the gauge surface temperature will be obtained in the case when the heat-transfer rate to the gauge is given. This problem requires solving the heat conduction equation with initial and boundary conditions

$$\begin{aligned}
&\theta(x,t)=0 && \text{for}\quad t=0\ ;\ x>0\\
&\frac{\partial\theta(x,t)}{\partial x}=-\frac{\dot{q}(t)}{K} && \text{for}\quad t>0\ ;\ x=0\\
&\lim_{x\to+\infty}\theta(x,t)=0
\end{aligned} \qquad (33)$$

In the case of an ideal gauge with constant properties the heat conduction equation is of the form given by equation (1). The gauge surface temperature (which is proportional to the gauge output) is then expressed as (ref. 7)

$$\left[\theta_w(t)\right]_{ideal}=\frac{1}{\sqrt{\pi K\rho c}}\int_0^t\frac{\dot{q}(v)}{\sqrt{t-v}}\,dv=\frac{1}{K}\sqrt{\frac{\alpha}{\pi}}\int_0^t\frac{\dot{q}(v)}{\sqrt{t-v}}\,dv \qquad (34)$$

or, in nondimensional form

$$\left[f(\eta)\right]_{ideal} = \frac{1}{\sqrt{\pi}} \int_0^{\eta} \frac{Q(\lambda)}{\sqrt{\eta - \lambda}}\, d\lambda \tag{34a}$$

It is evident from the above relation that for $Q(\eta)$ defined by equations (17); (18) and (19) the function $\left[f(\eta)\right]_{ideal}$ is given by equations (14), (15) and (16) respectively.

If the heat-transfer rate is high and time long enough, the gauge temperature may become so high, that its influence on the gauge properties must be taken into account (ref. 9). Under these circumstances equation (1) is no longer valid and must be replaced by the following nonlinear equation

$$\rho c(\theta) \frac{\partial \theta}{\partial t} = \frac{\partial}{\partial x}\left[K(\theta) \frac{\partial \theta}{\partial x}\right] \tag{35}$$

This equation may be reduced to the form

$$\frac{\partial q}{\partial t} = \alpha \frac{\partial^2 q}{\partial x^2} \tag{36}$$

by means of transformation

$$q = \int_0^{\theta} K(\theta')\, d\theta' \tag{37}$$

The conditions given by equation (33) become

$$\begin{aligned} &q(x,t) = 0 \qquad \text{for} \quad t=0 \;;\; x>0 \\ &\frac{\partial q}{\partial x} = -\dot{q}(t) \qquad \text{for} \quad t \geq 0 \;;\; x=0 \\ &\lim_{x \to +\infty} q = 0 \end{aligned} \tag{33a}$$

Hartunian and Varwig (ref. 9) proved that for gauge backing materials like pyrex, quartz or soda glass, the thermal diffusivity α may be considered constant if the surface temperature rise does not exceed 150°K. (The error in the surface temperature, calculated with this assumption is negligible.) Equation (36) is then linear and for the gauge surface there is

$$q_w = \int_0^{\theta_w} K(\theta')\, d\theta' = \sqrt{\frac{\alpha}{\pi}} \int_0^{t} \frac{\dot{q}(t)}{\sqrt{t-v}}\, dv \tag{38}$$

Comparing the above with equation (34) one obtains

$$\frac{1}{K_0} \int_0^{\theta_w} K(\theta')\, d\theta' = \left[\theta_w(t)\right]_{ideal} \tag{39}$$

where k_o is identical with the constant k from equation (34) and equals the value of k from equation (38) for $\theta = 0$.

In order to make use of equation (39) the dependence of k on temperature must be known. Hartunian and Varwig (ref. 9) assumed the form

$$K = K_o \left(1 + a \log_{10} \frac{T_o + \theta}{T_o}\right) \tag{40}$$

and obtained a very complicated result. For the sake of simplicity it will be assumed here that

$$K = K_o \left(1 + b\,\theta\right) \tag{41}$$

It is evident from Fig. 7, that equation (41) is at least as good as equation (40). A substitution of the equation (41) in equation (39) gives

$$\theta_w + \tfrac{1}{2} b\,\theta_w^2 = \left[\theta_w\right]_{ideal} \tag{42}$$

This expression relates the surface temperature of a real gauge to an ideal one (with constant properties) when both are subjected to the same flow conditions. It will constitute the basis for all subsequent considerations.

It is important to note that the nonlinear term when added to the actual gauge temperature permits a calculation of the ideal surface temperature with constant properties. Consequently, it is now possible to use the simple analogue network to obtain the correct heat transfer rate when variable gauge properties exist.

Variation of the Properties of a Thin Film

The temperature coefficient of resistance of the gauge

$$\beta = \frac{1}{R_{g_o}} \frac{dR_g}{d\theta} \tag{43}$$

generally is not constant (as it was assumed in the subsection on "Principle of Operation of a Real Analogue Network") but depends on temperature. If the temperature changes are small, this dependence may be neglected and equation (21) is valid. For larger changes however, it is no longer true and equation (43) must be used. The change in the gauge resistance with temperature is then given by

$$\frac{R_g - R_{g_o}}{R_{g_o}} = \int_0^{\theta_w} \beta(\theta)\, d\theta \tag{44}$$

According to ref. 10, β may be expressed as

$$\beta = \beta_o \left(1 - \gamma\theta\right) \tag{45}$$

from where

$$\frac{R_g - R_{g0}}{R_{g0}} = \beta_0 \int_0^{\theta_w} (1 - \gamma\theta)\, d\theta = \beta_0 \left(\theta_w - \frac{\gamma}{2}\theta_w^2\right) \quad (44a)$$

or, in the case of a constant gauge supply current

$$\frac{u_g}{U_{g0}} = \beta_0 \left(\theta_w - \frac{\gamma}{2}\theta_w^2\right) \quad (44b)$$

Reversing this relation one obtains

$$\theta_w = \frac{1}{\gamma} - \sqrt{\frac{1}{\gamma^2} - \frac{2u_g}{\beta_0 \gamma U_{g0}}} = \frac{1}{\beta_0}\frac{u_g}{U_{g0}} + \frac{\gamma}{2\beta_0^2}\left(\frac{u_g}{U_{g0}}\right)^2 + \ldots \quad (46)$$

For a thin film platinum gauge $\beta_0 \sim 2.5 \times 10^{-3}$ 1/°K and $\gamma \sim 4.7 \times 10^{-4}$ 1/°K (ref. 10). For θ_w less than 150°K contribution of the third and subsequent terms of the series in equation (46) is negligible (less than 0.25%) and it is then justified to take

$$\theta_w = \frac{1}{\beta_0}\frac{u_g}{U_{g0}} + \frac{\gamma}{2\beta_0^2}\left(\frac{u_g}{U_{g0}}\right)^2 \quad (46a)$$

For an ideal gauge with constant properties it was noted before that (compare equation (21))

$$(\theta_w)_{ideal} = \frac{1}{\beta_0}\frac{u_{g\,ideal}}{U_{g0}} \quad (47)$$

A substitution of equations (46a) and (47) into equation (42) gives

$$\frac{u_{g\,ideal}}{U_{g0}} = \frac{u_g}{U_{g0}} + \frac{1}{2\beta_0}(b+\gamma)\left(\frac{u_g}{U_{g0}}\right)^2 + \frac{b\gamma}{2\beta_0^2}\left(\frac{u_g}{U_{g0}}\right)^3 + \frac{b\gamma^2}{8\beta_0^3}\left(\frac{u_g}{U_{g0}}\right)^4 \quad (48)$$

For pyrex, quartz or glass $b \leq 6 \times 10^{-3}$ 1/°K, so that for temperature rises up to 150°K the contribution of the last two terms of equation (48) is less than 2% and within the accuracy of the present considerations these terms may be neglected. Finally

$$u_{g\,ideal} = u_g + \varepsilon' u_g^2 \quad (49)$$

where

$$\varepsilon' = \frac{b+\gamma}{2\beta_0 U_{g0}} \quad (50)$$

The above may also be expressed in nondimensional form

$$f_{ideal} = f\,\psi(f) \quad (51)$$

where

$$\psi(f) = 1 + \varepsilon f$$

$$\varepsilon = \frac{b + \gamma}{2\beta_0 \frac{v_0}{D_0}} \tag{52}$$

It should be pointed out that the remarks made at the end of the previous section apply equally well here, with the additional fact that the non-linearity in gauge resistance has also been taken into account.

ERRORS ARISING WHEN ANALOGUE NETWORK IS CONNECTED TO A GAUGE WITH VARIABLE PROPERTIES

In the present section we will investigate what happens when an ordinary analogue network is connected to a gauge with properties depending on temperature. For convenience of calculations the equations in nondimensional form will be used. Three cases, corresponding to those considered in the subsection on page 5 will be treated. As mentioned in the section on "Variation of the Properties of the Gauge Backing Material", the inputs to the gauge in these cases are given by equations (17)-(19) and the outputs from an ideal gauge $[f(\eta)]_{ideal}$ by equations (14)-(16). The outputs from a real gauge $f(\eta)$ can then be found from equation (19). Substituting these outputs into equation (13) the analogue outputs can be calculated and then finally compared with the assumed input to the gauge.

For convenience equation (13) will be used in the form

$$Q = \frac{1}{\sqrt{\pi}} \left[\frac{f(+0)}{\sqrt{\eta}} + \int_0^{f(\eta)} \frac{dw}{\sqrt{\eta - \lambda(w)}} \right] \tag{53}$$

obtained by substitution

$$w = f(\lambda) \tag{54}$$

Case When the Heat-Transfer Rate is Inversely Proportional to the Square Root of Time

The input to the gauge is given by equation (17)

$$Q_{input} = \frac{A}{\sqrt{\pi \eta}}$$

The output from an ideal gauge is found from equation (14)

$$f_{ideal} = A = \text{constant}$$

From equation (51) it follows that

$$f\,\psi(f) = A \tag{55}$$

or, in reversed form

$$f = \chi(A) = \text{constant} \tag{56}$$

Substituting the above in equation (53) one obtains the output from the analogue

$$Q_{output} = \frac{f}{\sqrt{\pi \eta}}$$

Finally, the ratio of gauge input to analogue output is given by

$$\mathcal{H} = \frac{Q_{input}}{Q_{output}} = \frac{A}{f} = \psi \tag{57}$$

Case When the Heat-Transfer Rate is a Step Function

The input to the gauge is now given by equation (18)

$$Q_{input} = \frac{\sqrt{\pi}}{2} B = \text{constant}$$

and the output from an ideal gauge is given by (15)

$$f_{ideal} = B\sqrt{\eta}$$

From the above, equation (51) and equation (52)

$$\eta = \frac{1}{B^2} f^2 (1 + \varepsilon f)^2 \tag{58}$$

Substituting this in equation (53) one obtains

$$Q_{output} = \frac{B}{\pi} \int_0^f \frac{dw}{\sqrt{f^2(1+\varepsilon f)^2 - w^2(1+\varepsilon w)^2}} \tag{59}$$

and the ratio of the gauge input to analogue output is

$$\mathcal{H} = \frac{Q_{input}}{Q_{output}} = \frac{\pi}{2}\left[\int_0^f \frac{dw}{\sqrt{f^2(1+\varepsilon f)^2 - w^2(1+\varepsilon w)^2}}\right]^{-1} \tag{60}$$

This equation can be rearranged after some labour to give the following form (see ref. 16 for complete derivation)

$$\mathcal{H} = \frac{\pi}{4} \frac{2\psi - 1}{F\left(X, \frac{\pi}{4}\right)} \tag{61}$$

where

$$X = \arcsin\left[\frac{2\sqrt{2\psi(\psi-1)}}{2\psi - 1}\right]$$

for

$$\psi \leq \frac{\sqrt{2}+1}{2}$$

and

$$\varkappa = \frac{\pi}{\sqrt{2}} \frac{\sqrt{\psi(\psi-1)}}{F(Y,Z)}$$

where

$$Y = \arcsin\left[\frac{2\psi-1}{2\sqrt{2\psi(\psi-1)}}\right] \qquad (62)$$

$$Z = \arcsin\left[\frac{2\sqrt{\psi(\psi-1)}}{2\psi-1}\right]$$

for

$$\psi \geqslant \frac{\sqrt{2}+1}{2}$$

Case When the Heat-Transfer Rate is Proportional to the Square Root of Time

In this case the input to the gauge is given by equation (19)

$$Q_{input} = \frac{2}{\sqrt{\pi}} D\sqrt{\eta}$$

The output from an ideal gauge is expressed by equation (16)

$$f_{ideal} = D\eta$$

From the above, and equations (51) and (52)

$$\eta = \frac{1}{D} f(1+\varepsilon f) \qquad (63)$$

Upon substitution into equations (53) and (19)

$$Q_{output} = \sqrt{\frac{D}{\pi}} \int_0^f \frac{dw}{\sqrt{f(1+\varepsilon f) - w(1+\varepsilon w)}} \qquad (64)$$

$$Q_{input} = 2\sqrt{\frac{D}{\pi}} \sqrt{f(1+\varepsilon f)} \qquad (65)$$

and

$$\varkappa = \frac{Q_{input}}{Q_{output}} = 2\sqrt{f(1+\varepsilon f)} \left[\int_0^f \frac{dw}{\sqrt{f(1+\varepsilon f) - w(1+\varepsilon w)}}\right]^{-1} \qquad (66)$$

After integration and some additional manipulations the final form is obtained as

$$\varkappa = \frac{2\sqrt{\psi(\psi-1)}}{\frac{\pi}{2} - \arcsin\left(\frac{1}{2\psi-1}\right)} \qquad (67)$$

Correction of Errors

The values $\varkappa$, as given by equations (57), (61)-(62) and (67) may be used as correction factors for heat transfer measurements performed with a real gauge of variable properties and an analogue network. The diagrams of

$\mathcal{H}$ as a function of ψ according to these equations are given in Fig. 8. The fact, that ψ instead of f was chosen as an independent variable makes these curves valid for arbitrary gauge backing materials, and is very convenient in actual applications. However, for each gauge it is necessary to find by some method of calibration the actual dependence of ψ on f according to equation (52) (i.e., to find the actual value of ε). The correction $\mathcal{H}$ is then found from Fig. 8.

The method of correction indicated above, is simple in application, but is not very accurate. The curves in Fig. 8 are not close to each other, so if the conditions of an experiment do not correspond exactly to one of these three cases, errors may arise. (See for example Fig. 20 where the parabolic surface temperature starts after a step jump, whereas ideally the step should be absent.)

The previous considerations however offer a method of an automatic correction, more general, more accurate and even simpler in application than using the correction factor $\mathcal{H}$ The automatic correction is obtained by placing a circuit between the gauge and analogue network which can calculate u_{gideal} from u_g, according to equation (49).

AUTOMATIC CORRECTION OF ERRORS ARISING FROM VARIABLE GAUGE PROPERTIES

Electronic Circuitry

A correction circuit following the previous section has been designed and built at UTIAS. A block diagram of the whole unit, consisting of a low noise preamplifier, correction circuit and analogue network is given in Fig. 9. A detailed circuit diagram appears in Fig. 10.

The unit has been designed for shock tube applications. It can handle input signals up to 0.2V. It has a response time of about 2 μ secs and a maximum working time of approximately 1 msec. Within these limits any electrical inaccuracies of the amplifier and correction circuit as well as the errors due to the finite length and finite size of the lumped elements of the analogue network are less than 3.5 per cent.

The analogue itself consists of 39 sections. The time constant (RC) of a single section equals 3.94 μ sec. (R = 9.95 kΩ , C = 396pF).

The unit can be used for measurements with and without the correction circuit. When used without correction, the amplification factor $\mathcal{K}$ (defined as the ratio of the signal at the analogue input to the output signal from the gauge) is approximately equal 32. The correction circuit permits adjusting the value ε' (as defined by equation (50)) in the range from zero to 6.5 V^{-1}, sufficient for any gauge.

Two outputs from the unit with independent adjustment of the amplitude of the output signal are provided. Output 1 is essentially used to register the undisturbed signal from the gauge. It may also be used to register the

corrected signal u_{gideal}, the signal by-passing correction circuit, or the correcting signal itself. (Registering the last two signals is necessary for calibration of the unit.) Output 2 serves to register the signal from the analogue network, i.e., the actually desired heat-transfer rate.

Calibration of the Apparatus for Heat Transfer Measurements

The calibration of the previously described apparatus starts with measuring the gauge properties - constants β_o, γ , b . Measuring β_o and γ is best accomplished using the method described by Bogdan (ref. 10). Gauge resistance R_g is measured at various temperatures and then suitable values β_o and γ are assumed so that equation (44a) fits best the experimentals points.

The constant b is determined using the current-pulse technique (ref. 15). Relatively strong current pulses of the step-function type are fed to the gauge, connected in one arm of the Wheatstone bridge (Fig. 12). The increase of the gauge resistance due to Joule heating throws the bridge out of balance and produces a signal, which is fed to the analogue network. The output from the analogue is given by

$$K = \left[\frac{1}{4\ell^2\bar{d}^2}\mathcal{H}^2 R C R_1^2 \mathcal{N}'^2 U_{so}\, \Phi^2\left(\frac{t}{\bar{t}}\right)\right] \frac{R_{go}^4}{(R_1+R_{go})^8}\,\frac{\bar{\beta}^2}{\rho c}\,\frac{1}{(\Delta u)^2} \qquad (68)$$

For derivation of equation (68), see ref. 16.

If for all the calibrating pulses U_{so} is maintained constant and Δu is measured at the same $(t/\bar{t})$, the quantity in the square bracket can be considered constant. The remaining quantities depend only on temperature. Consequently from equation (68)

$$\frac{K(\theta)}{K_o} = \left[\frac{R_{go}(\theta)}{R_{go}(0)}\right]^4 \left[\frac{R_1+R_{go}(0)}{R_1+R_{go}(\theta)}\right]^8 \left[\frac{\bar{\beta}(\theta)}{\bar{\beta}_o}\right]^2 \frac{\rho c(0)}{\rho c(\theta)} \left[\frac{\Delta u(0)}{\Delta u(\theta)}\right]^2 \qquad (69)$$

In order to change its temperature without affecting anything else the gauge is placed inside a test tube, immersed in a hot oil bath (as described in ref. 9). It was found that this provided conditions which were sufficiently stable for the present experiments.

Having Δu measured for several different temperatures, and R_{go} and $\bar{\beta}$ for those temperatures from previous measurements and $\rho c(\theta)/\rho c(0)$ found from some other method, the values of $k(\theta)/k_o$ are determined. The quantity b is then chosen in such a way, that equation (41) fits best the obtained results.

Having found β_o, γ , b and assuming U_{go} the value ε' is calculated from equation (50). After application of a sine wave with known amplitude u_{calib} at the input to the unit, the attenuator of the squared signal is

adjusted so that the ratio of amplitudes of the correcting signal and the signal by-passing the correction circuit, measured at output 1 is equal to $\varepsilon \, u_{calib.}$ The final step of the calibration is the determination of the constant E of the equation 23 . This is accomplished directly in the shock tube at low shock Mach numbers, using the results of ref. 12 . That is, for a given shock Mach number M_s and initial conditions $\dot{q}$ is known from this theory. Consequently, since Δu has been measured E is determined. This procedure is simple and is justified on the basis of the accumulated results in support of the theory.

EXPERIMENTAL RESULTS AND DISCUSSION

In order to check the usefulness and accuracy of the automatic correction a series of experiments were performed in the UTIAS 4 in. x 7 in. Hypersonic Shock Tube. Thin-film platinum gauges, mounted on Pyrex 7740 glass were placed at the stagnation line of a circular cylinder 13 mm dia. with the axis perpendicular to the flow. The films were approximately 14 mm long and 0.4 mm wide. Their resistance ranged from about 50 to 100 ohms. The voltage across all the gauges was maintained at a level of 0.5V.

The gauges were calibrated using the technique described in the previous section. However, the assumption

$$\alpha \equiv \frac{K}{\rho c} = \text{constant}$$

was used once more to simplify the measurement of b. This assumption eliminated the necessity of measuring (ρc) since it gave

$$\frac{K}{K_0} = \sqrt{\frac{K \rho c}{K_0 \rho_0 c_0}}$$

Beside this the change in coefficient β with temperature was not taken into account, since in the range of temperatures used for calibration (up to 125°C) this change was so small, that it was difficult to detect.

The final calibration was performed in the shock tube. It consisted of 1 to 4 "cold runs" (with a cold driver gas) taken before each test run. As the calibration constant E (equation 23), an average of the values obtained from all the runs was taken.

During the test runs the same gauge was connected to two analogue networks: one with and one without correction. Two sets of test runs were taken:

1. "Cold runs", during which the gauge surface temperature rise was less or equal to 10°C (in one case it was about 12.5°C). During these runs, as well as during all the calibration runs, single mylar diaphragms 0.005 in. thick were used. The driver gas was helium, or a mixture of helium and air at a pressure of about 45 psia. The driven gas was air. Its pressure varied from 10 mm Hg (for calibration runs) to about 0.7 mm Hg.

2. "Hot runs", generated by a combustion driver (75% argon and 25% stoichiometric mixture of hydrogen and oxygen). During these runs the driven gas was

also air, at initial pressures from 10 to 60 mm Hg. The gauge surface temperature rises varied from about 40°C for lower shock Mach numbers to about 75°C for higher shock Mach numbers.

During all the runs the traces of corrected and uncorrected heat-transfer rate and also gauge surface temperature were recorded. The values from the traces were measured with a travelling microscope at the point where the corrected heat transfer stabilized for the first time after the shock arrival (i.e. at the point, where the trace became parallel to the time axis for the first time). This occurred during the cold runs between 50 and 250 μsecs after the shock arrival and during the combustion runs between 60 and 140 μsecs after the shock arrival.

Figure 14 of the present paper shows the test model with the gauge mounted on it. Figure 15 illustrates the entire experimental set up, consisting of the gauge, two analogue networks and a Tektronix Type 555 Dual Beam Oscilloscope with Type M Plug-In Units.

Figure 16 shows the setup for the gauge calibration, consisting of an oil bath, Wheatstone bridge, analogue network and oscilloscope. Figure 17 shows a typical trace obtained during a calibration with the current-pulse technique. Figure 18 gives the dependence of $\sqrt{k\rho c}$ on temperature for Pyrex 7740 glass as measured with this technique.

A typical trace obtained during a cold run and a combustion run in the shock tube are shown in Figs. 19 and 20, respectively. Finally Fig. 21 gives the ratios of the heat-transfer rates measured and calculated from the Fay and Riddell theory plotted as a function of shock Mach number. In this figure, the circles correspond to "cold runs" without correction; triangles to "hot runs" without correction; squares to "hot runs" with correction.

From the last figure it is evident, that while no correction for the variation of the gauge properties is needed for temperature rises of the order of 10°C or less, such a correction is essential for temperature rises above 40°C. It is also evident, that the proposed method of an automatic correction works very well, reducing the mean deviation of the experimental points from the Fay and Riddell theory to only about 3.5%. The remaining discrepancy is probably due to the assumption that α and β are constant.

It should be noted here, that the overall accuracy of the measurements is of the order of $\pm$ 5%, which agrees quite well with the scatter of the experimental data.

It is also worth pointing out, that the heat-transfer rate measured from the trace without correction, as shown in Fig. 20, decreases with time, which is erroneous for this type of flow. However, the corrected heat transfer trace does not indicate this peculiarity, as expected. These two traces clearly demonstrate the validity of the correcting circuit.

CONCLUSIONS

1. The use of ordinary analogue networks with thin-film, heat-transfer gauges mounted on pyrex may lead to serious errors in measuring heat-transfer rates if the temperature rise of the gauge is of the order of 40°C or more. Analytical corrections of these errors are reasonably easy only in a few very special cases (such as those treated in the section "Errors Arising When Analogue Network is Connected to a Gauge With Variable Properties"). A correction of that type which is applicable to any general heat-transfer function has not been found. However, although such a correction would have been of interest, it is of little value in practice when an automatic correction circuit is available.

2. It has been demonstrated that by putting a relatively simple automatic correction circuit between the gauge and the analogue network, it is possible to compensate for the influence of the variation of the gauge properties with temperature. This compensation is quite general and unlike the analytical corrections does not depend on the variation of heat transfer with time.

It has been verified experimentally that this compensation works very well at temperature rises up to 75°C. It is expected, however, that it will work satisfactorily at temperature rises up to 150°C or more as long as the thermal diffusivity does not change appreciably.

NOTATION

A	constant defined in equation (14)
a	constant defined in equation (40)
B	constant defined in equation (15)
b	constant defined in equation (41)
$\underline{C}$	capacitance of a single capacitor of the analogue network
$\bar{C}$	capacitance per unit length of the analogue network
c	specific heat of the gauge backing material
D	constant defined in equation (16)
$\underline{d}$	width of the thin film
$\bar{d}$	average width of the thin film
E	constant defined in equation (23)
$F(Y,Z)$	elliptic integral of the first kind
f	non-dimensional gauge surface temperature or input voltage to the analogue (equation 7)
g	function defined in equation (37)
g_w	function defined in equation (38)
$I_n(\eta)$	modified Bessel Function of the first kind
i	electric current
i_g	electric current through the thin film
$\mathcal{K}$	amplification factor (equation 22)
k	thermal conductivity of the gauge backing material
k_o	thermal conductivity of the gauge backing material at the initial temperature
L	non-dimensional length of the analogue network; number of sections

ℓ	length of the thin film
l	length of the analogue network
Q	non-dimensional heat-transfer rate, or electric current (equation 8)
$\dot{q}$	heat-transfer rate through the gauge surface (1 watt/cm^2 ≡ 0.88 BTU/sq.ft./sec)
$\underline{R}$	resistance of a single resistor of the analogue network
R	resistance per unit length of the analogue network
R_1	resistance connected in series with the gauge
R_g	resistance of the thin film
R_{go}	initial resistance of the thin film
ΔR_g	change in the resistance of the thin film
$\underline{r}_{go}$	initial resistance per unit length of the thin film
r_{go}	mean value of the initial resistance per unit length of the thin film
T_o	reference temperature
T_s	stagnation temperature
t	time, equation (1)
t'	time, equation (4)
t_o	reference time, equation (8)
U_g	voltage across the gauge
U_{go}	initial voltage across the gauge
U_o	reference voltage
U_s	voltage of the gauge power supply
ΔU_s	change in the voltage of the gauge power supply
u	voltage
u_g	voltage rise across the gauge
Δu	voltage across the first resistor of the analogue network
v,w	dummy variables
X	function defined in equation (61)
x	space coordinate, equation (1)
x'	space coordinate, equation (4)
x'_o	reference length, equation (8)
Y	function defined in equation (62)
y	distance along the thin film
Z	function defined in equation (62)
α	thermal diffusivity, $k/\rho c$
β	temperature coefficient of resistance of the thin film
β_o	temperature coefficient of resistance of the thin film at the intial temperature
γ	constant defined in equation (45)
δ	ratio of the finite to infinite network output
ε	constant defined in equation (52)
ε'	constant defined in equation (50)
ζ	nondimensional temperature, or voltage (equation 8)
τ	nondimensional time (equation 8)
ϑ	temperature measured from its initial level ("temperature rise")
ϑ_w	gauge surface temperature rise
$\varkappa$	ratio of nondimensional gauge input to nondimensional analogue output
Λ	ratio of the lumped network output to an ideal analogue output (equations 24 - 26)
Λ^*	ratio of the lumped network output to an ideal analogue output after correction introduced in Ref. 4 (equations 2.4a - 2.6a)

λ dummy variable
ξ, nondimensional space coordinate (equation 8)
ρ_c density of the gauge backing material
χ function defined in equation (29)
ψ function defined in equation (56)
gauge surface temperature function (equation 52)

Subscripts

ideal corresponds to an ideal gauge with constant properties
input corresponds to an input to the gauge
output corresponds to an output from the analogue

REFERENCES

(1) Hall, J.G. and Hertzberg, A., Recent Advances in Transient Surface Temperature Thermometry. Jet Propulsion, Vol. 28, No. 11 (Nov., 1958).

(2) Skinner, G.T., Analogue Network to Convert Surface Temperature to Heat Flux. Cornell Aeronautical Laboratory Report No. CAL-100, (Feb. 1960).

(3) Meyer, R.F., A Heat-Flux Meter for Use with Thin Film Surface Thermometers, National Research Council of Canada, Aeronautical Report LR-279, (April 1960).

(4) Meyer, R.F., Further Comments on Analogue Networks to Obtain Heat Flux From Surface Temperature Measurements, National Research Council of Canada, Aeronautical Report LR-375 (March, 1963).

(5) Hartunian, R.A., Russo, A.L., and Marrone, P.V., Boundary Layer Transition and Heat Transfer in Shock Tubes. Cornell Aeronautical Laboratory Report No. AD-1118-A-3, (Dec. 1959).

(6) Thompson, W.P., An Experimental Study of Turbulent Spots and Wall Roughness Effects in Shock Tube Boundary Layer Transition. Lehigh University Institute of Research Technical Report No. 16, (15 June, 1963).

(7) Carslaw, H.S., and Jaeger, J.C., Conduction of Heat in Solds. Oxford University Press (1959).

(8) Smirnov, V.I., Kurs Vvsshei Matematiki, Vol. IV. Gosudarstvennoe Izdatelstvo Tekhniko-Teoreticeskoi Literatury (1959).

(9) Hartunian, R.A., and Varwig, R.L., On Thin-Film Heat-Transfer Measurements in Shock Tubes and Shock Tunnels. The Physics of Fluids Vol. 5, No. 2, pp. 169-174, (Feb. 1962).

(10) Bogdan, L., Thermal and Electrical Properties of Thin-Film Resistance Gages Used for Heat Transfer Measurements. AIAA Journal Vol. 1, No. 9, (Sept. 1963) pp. 2172-2173.

(11) Seely, S., Electron-Tube Circuits, McGraw-Hill Book Company, Inc., New York, Toronto, London, (1950).

(12) Fay, J.A., and Riddell, F.R., Theory of Stagnation Point Heat Transfer in Dissociated Air. Journal of the Aeronautical Sciences, Vol. 25, No. 2, pp. 73-85 (Feb. 1958).

(13) Sabol, A.P., Measurements in a Shock Tube of Heat-Transfer Rates at the Stagnation Point of a 1.0-Inch-Diameter Sphere for Real Gas Temperatures up to 7900°R. NACA TN 4354 (1958).

(14) Skinner, G.T., A New Method of Calibrating Thin Film Gauge Backing Materials. Cornell Aeronautical Laboratory Report No. CAL-105, (June 1962).

(15) Taylor, B.W., Development of a Thin Film Heat-Transfer Gauge for Shock-Tube Flows. UTIA Technical Note No. 27, (June 1959).

(16) Walenta, Z.A., Analogue Networks for High Heat-Transfer Rate Measurements. UTIAS Technical Note No. 84 (Nov. 1964).

ACKNOWLEDGEMENTS

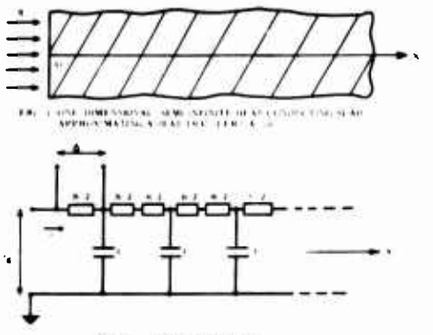
I should like to thank Dr. G.N. Patterson for providing me with the opportunity to do this research at UTIAS.

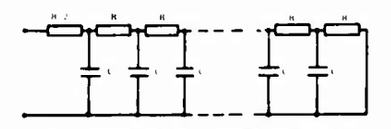
The research was supervised by Dr. I.I. Glass and I wish to express my appreciation for his valuable discussions, suggestions, and guidance.

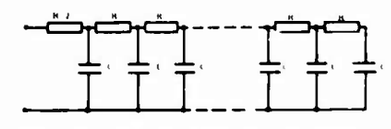
Many of my colleagues in the laboratory who are too numerous to mention by name were of considerable assistance to me in providing suggestions, critical comments, and help in conducting the experiments.

I wish to express my gratitude to the Polish Academy of Sciences and Prof. W. Fiszdon fo. granting me a leave of absence, which made this research possible. The discussions held originally with Dr. W.J. Prosnak on heat-transfer analogues were most helpful.

The research was supported by the U.S. Air Force Office of Scientific Research Grant No. AFOSR-365-65.







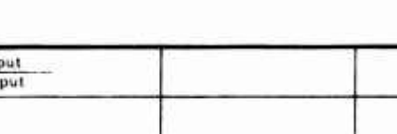


FIG. 5 TIME DEPENDENCE OF LUMPED NETWORK OUTPUT (ACCORDING TO REFS. 3 and 4)

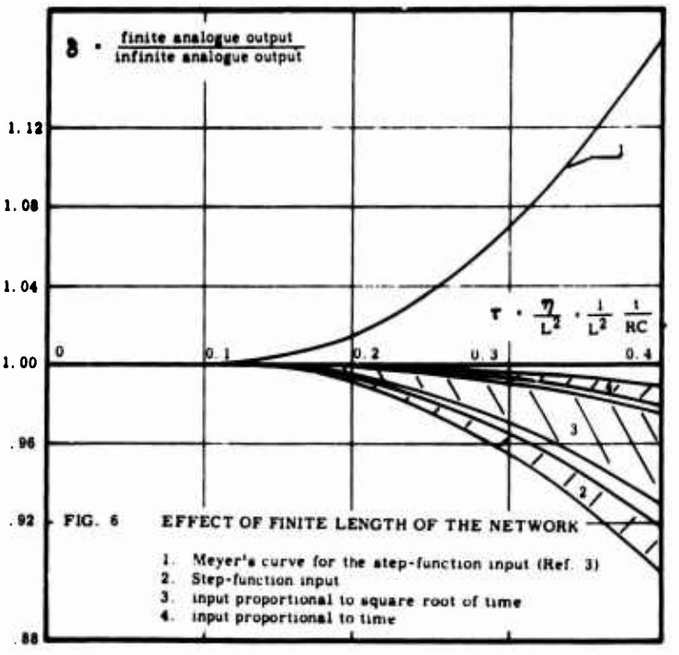


FIG. 6 EFFECT OF FINITE LENGTH OF THE NETWORK

1. Meyer's curve for the step-function input (Ref. 3)
2. Step-function input
3. input proportional to square root of time
4. input proportional to time

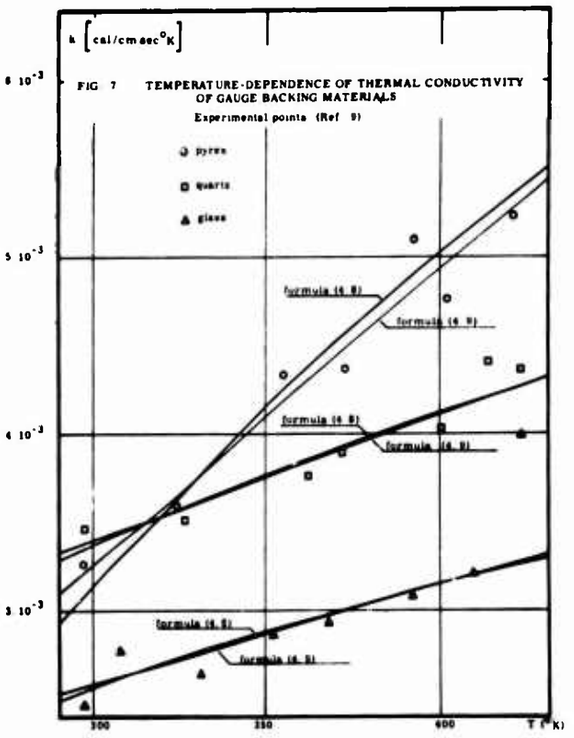


FIG 7 TEMPERATURE-DEPENDENCE OF THERMAL CONDUCTIVITY OF GAUGE BACKING MATERIALS

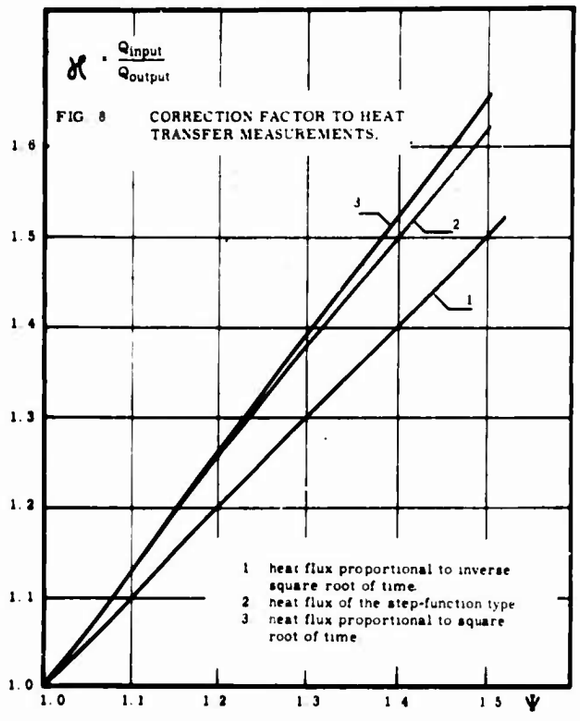


FIG. 8 CORRECTION FACTOR TO HEAT TRANSFER MEASUREMENTS.

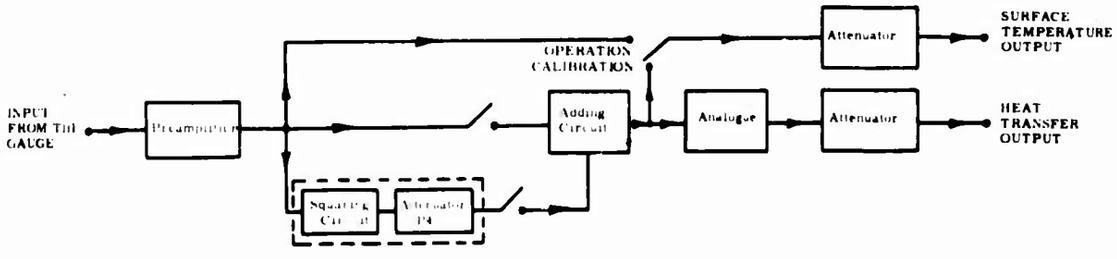


FIG. 9 BLOCK-DIAGRAM OF THE UNIT FOR HEAT TRANSFER MEASUREMENTS

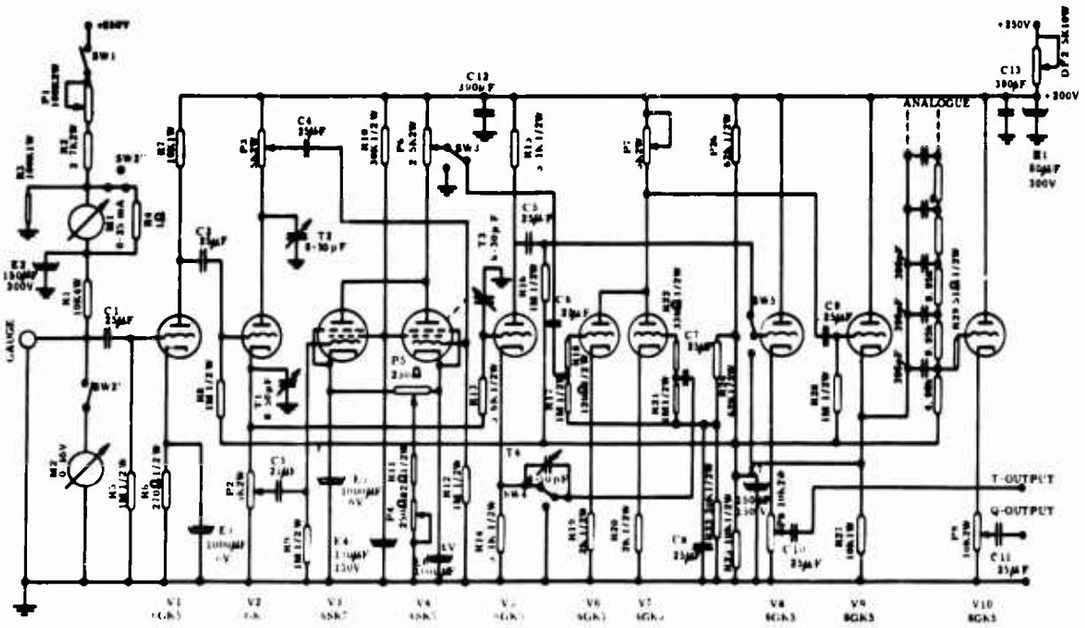


FIG 10 CIRCUIT DIAGRAM OF COMPLETE UNIT FOR HEAT TRANSFER MEASUREMENTS

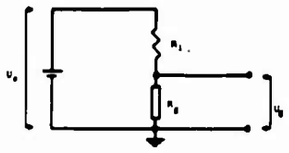


FIG 11 CIRCUIT DIAGRAM (SCHEMATIC) OF THE GAUGE CONNECTION

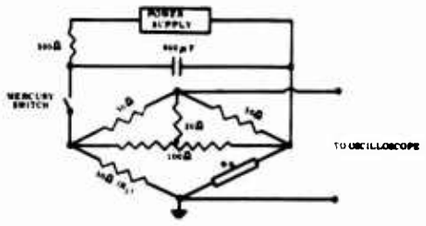


FIG 12 GAUGE CALIBRATION BRIDGE (REF 18)

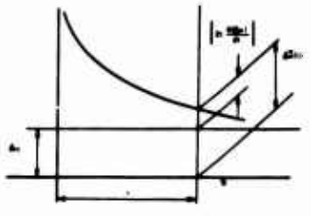


FIG 13 CALIBRATION TRACE FOR A STEP FUNCTION CURRENT PULSE IN CASE OF AN UNBALANCED BRIDGE

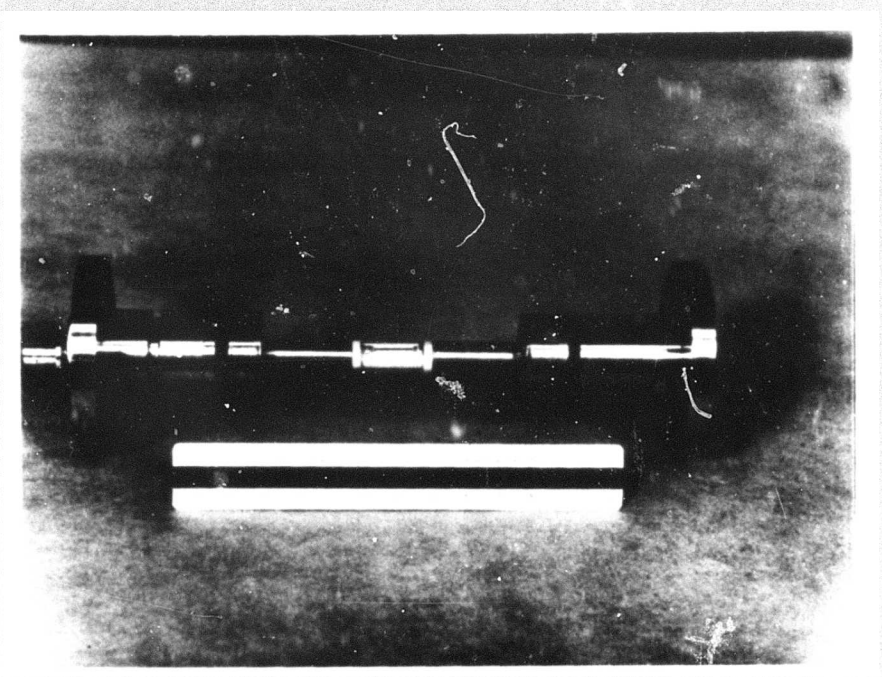


FIG. 14 MODEL FOR STAGNATION POINT HEAT-TRANSFER MEASUREMENTS ON A CIRCULAR CYLINDER WITH MOUNTED THIN-FILM GAUGE

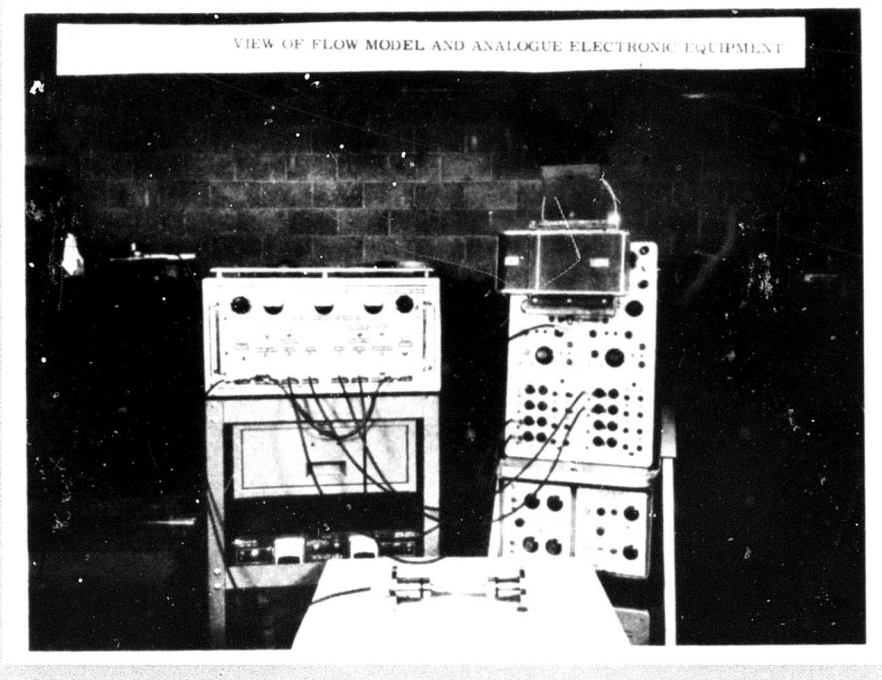


FIG. 15 EXPERIMENTAL SETUP FOR HEAT TRANSFER MEASUREMENTS IN A SHOCK TUBE

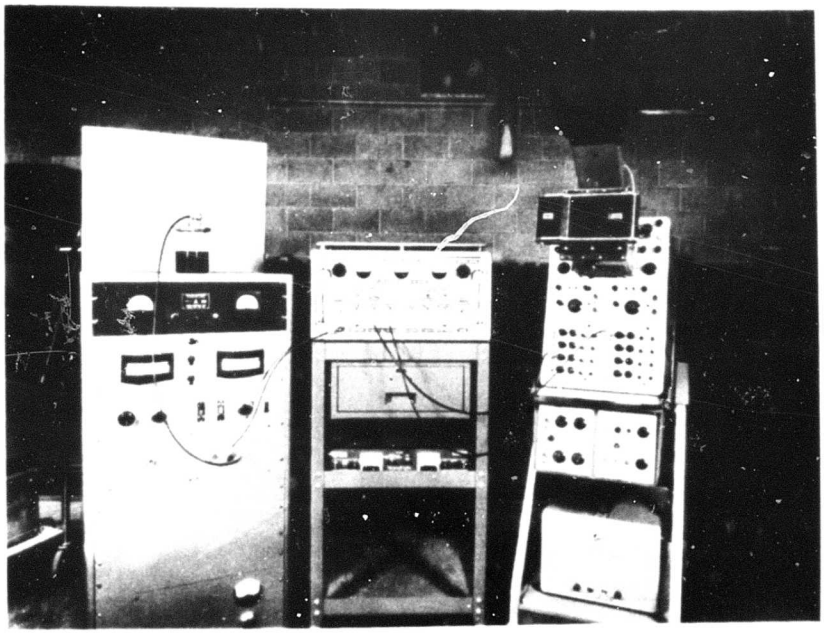


FIG. 16 SETUP FOR THIN FILM-GAUGE CALIBRATION USING CURRENT-PULSE TECHNIQUE

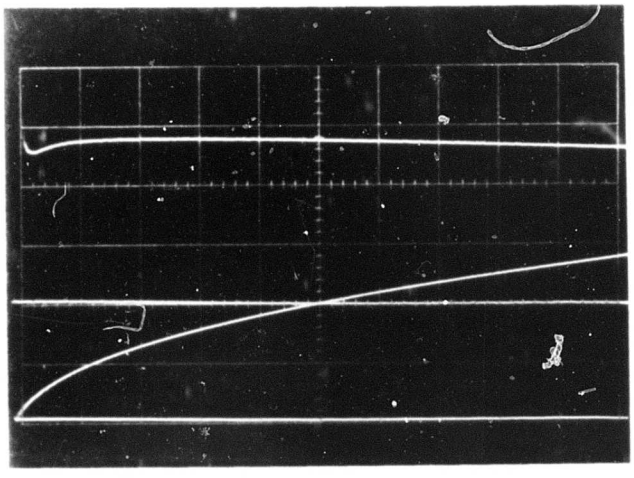


FIG. 17 TYPICAL OSCILLOGRAM OBTAINED DURING GAUGE CALIBRATION WITH CURRENT-PULSE TECHNIQUE

Sweep Time 50 μ sec/div

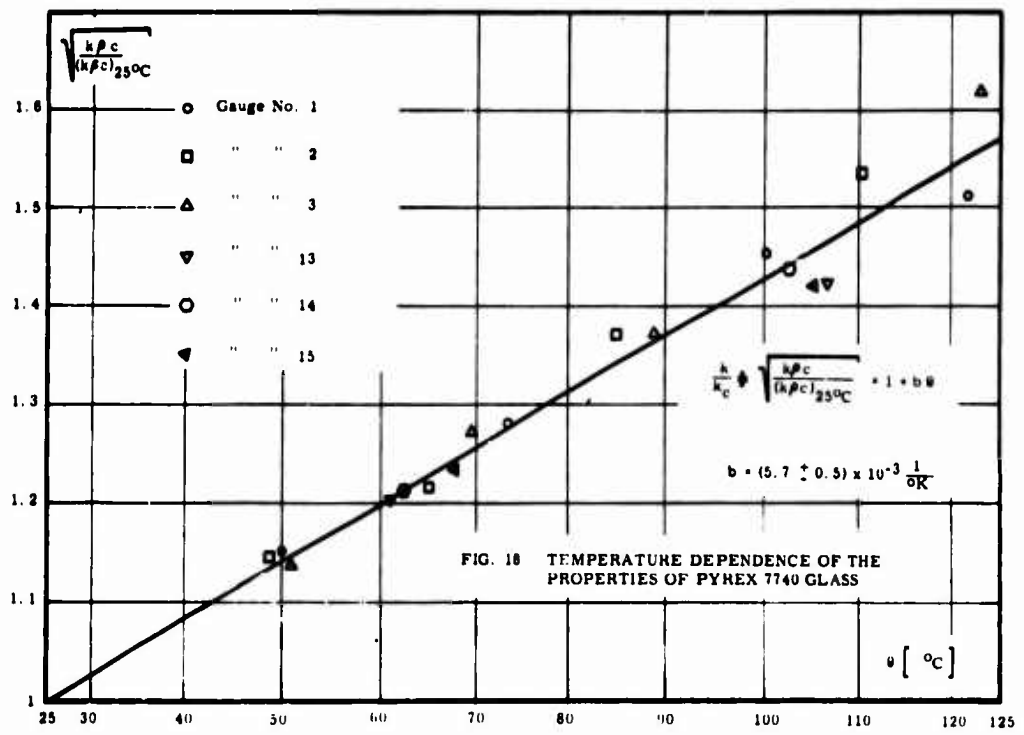


FIG. 18 TEMPERATURE DEPENDENCE OF THE PROPERTIES OF PYREX 7740 GLASS

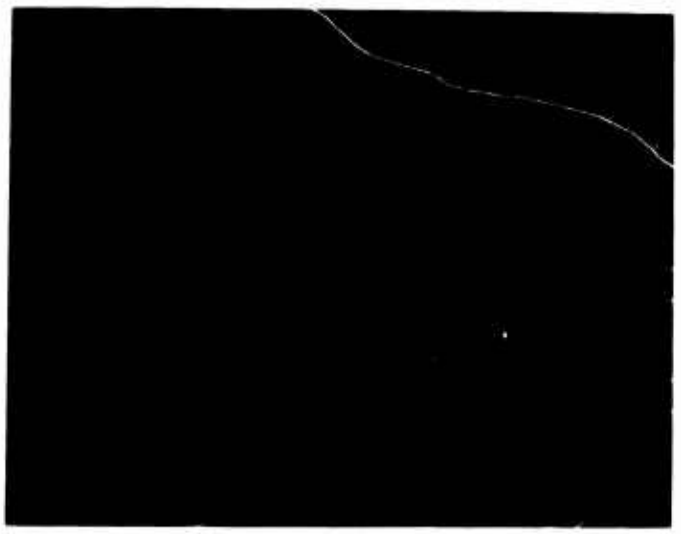


FIG. 19 TYPICAL OSCILLOGRAM OBTAINED DURING CALIBRATION RUN IN THE SHOCK TUBE

Sweep Time	200 μ sec/div
Temperature Scale	10.8°K/div
Heat Transfer Scale	84 W/cm^2/div

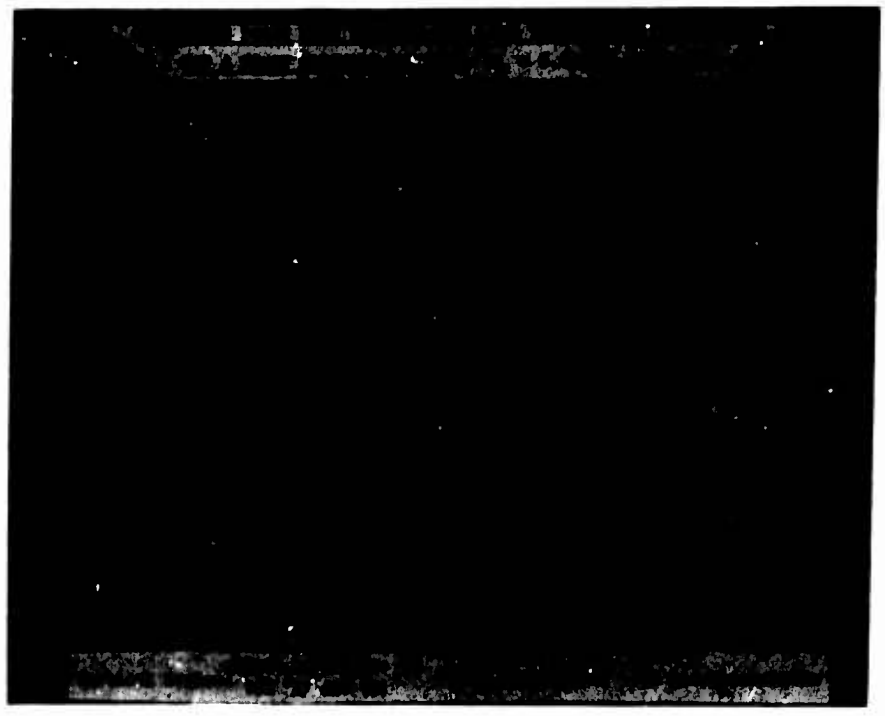


FIG. 2 TYPICAL OSCILLOGRAM OBTAINED DURING TEST RUN IN THE SHOCK TUBE

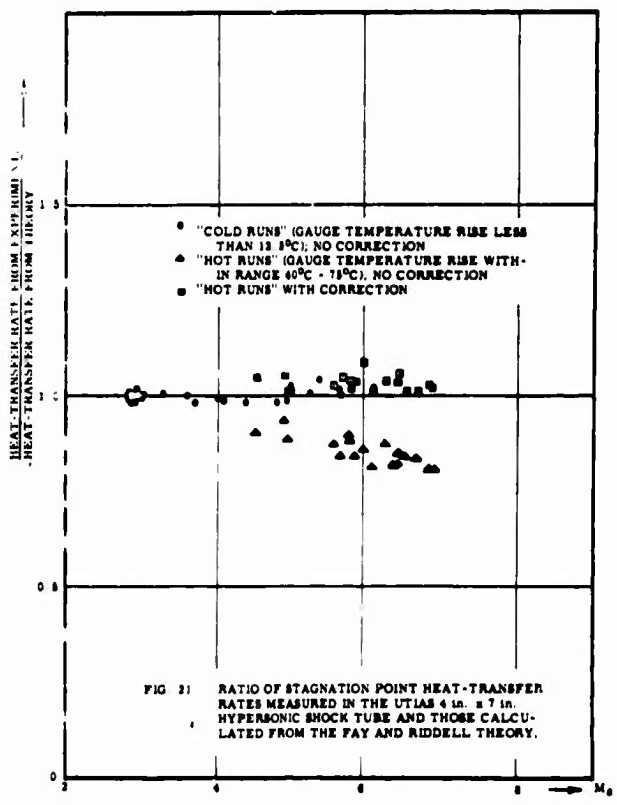


FIG. 21 RATIO OF STAGNATION POINT HEAT-TRANSFER RATES MEASURED IN THE UTIAS 4 in. x 7 in. HYPERSONIC SHOCK TUBE AND THOSE CALCULATED FROM THE FAY AND RIDDELL THEORY.

BLANK PAGE

CONTACT-SURFACE TAILORING IN REAL SHOCK TUBES

by Theodore A. Brabbs and Frank E. Belles
Lewis Research Center
National Aeronautics and Space Administration
Cleveland, Ohio

ABSTRACT

The equilibrium pressure after interaction of a reflected shock with the contact surface can be confused with the tailored state, unless quantitative pressure measurements are made. Such measurements were used to find the true tailored conditions for CO_2 + Ar and CO_2 + Ar + He mixtures, and for N_2 driven by He. Calculated conditions in excellent agreement with these resulted when the real performance of the tube, instead of the ideal performance, was employed in the usual tailoring formula. This suggests a rapid systematic way to produce the tailored state, and shows that it will not be the same in all tubes. However, a small pressure excursion due to contact-surface interaction still remains even when perfect tailoring is achieved.

INTRODUCTION

In recent years considerable use has been made of the reflected shock wave in studying high temperature gas dynamic phenomena. Because it provides stationary test gas, increased testing time, higher gas enthalpy and density, and lends itself to chemical sampling, the reflected-shock technique has found wide usage in chemical shock tubes and shock tunnels. However, both applications require a detailed understanding and close control of the state of the gas behind the reflected shock wave. Because interaction between the reflected shock wave and the contact surface causes a pressure and temperature distrubance to be reflected back into the test zone, it is desirable to eliminate this interaction. This is usually accomplished by using the tailored-interface mode of operation.

In the tailored-interface mode, initial conditions in the driver (diaphragm pressure ratio, gas composition, and in some tubes, temperature) are adjusted so that the reflected shock wave, on encountering the contact surface, produces the same pressure and the same particle velocity on both sides of it. These requirements, when expressed in terms of the usual relations among shock strength and gas properties, lead to the tailoring formula

$$\frac{\alpha_4 + P_{25}}{\alpha_2 + P_{25}} = \frac{m_2(\gamma_2 - 1)T_{34}}{m_4(\gamma_4 - 1)T_{21}} \tag{1}$$

However, when this equation is used the calculations are usually made by assuming the shock tube behaves ideally; that is, the Mach number is related to the initial pressure ratio P_{41} by the ideal shock tube performance equations. Because most shock tubes do not behave ideally, the initial test conditions calculated from equation (1) are only approximate, and achievement of tailoring can be established only by observing the experimental pressure record. The experimental procedure usually employed is to calculate the initial tailoring conditions and to use these test conditions to obtain an experimental pressure record. If tailoring has not been achieved, which is the usual case, the initial pressure ratio (P_{41}) is adjusted somewhat and another pressure record is obtained. Because it is difficult to judge how much the pressure ratio must be changed by looking at the pressure record, the procedure usually requires several test runs. This procedure can be very time consuming and a simpler and more direct method for tailoring is desirable.

Ideally the tailored oscillogram is expected to show the reflected-shock pressure as a flat-topped plateau, and in principle there should be only one incident-shock Mach number that would yield such a record for a given driver-driven gas combination. In practice, however, records having the qualitative appearance described are obtained over a small range of incident Mach numbers close to the tailoring conditions. This is because the interaction is weak and has little effect on the pressure history. If, however, the shock tube is operated outside this range, the reflected shock wave will experience multiple reflections between the contact surface interface and the end of the tube. The result of these multiple shock reflections is the formation of a quasi-uniform region known as the "equilibrium" state (ref. 1). This equilibrium state like the tailored state is characterized by a flat-topped pressure history as shown in figure 1.

Figure 1 shows a typical nontailored pressure-time history. The arrival of the reflected disturbance from the contact surface can be seen by the abrupt change in the pressure. The flat region after the interaction is the equilibrium state. Thus a flat-topped pressure record is not always sufficient proof that tailoring has been achieved. Experimental results to be presented later show that confusion can exist between these two states and that a better criterion for tailoring is required.

At Mach numbers greater than the tailored one, the equilibrium pressure (p_e) is greater than the reflected shock pressure (p_5). Below the tailored Mach number, $p_e < p_5$. When tailoring has been achieved there is no interaction and $p_e = p_5$. Therefore, the criterion for tailoring chosen for this work was that the pressure after interaction be equal to the initial reflected shock pressure; that is, $P_{e5} = 1$. A plot of P_{e5} against M_s will yield the experimental tailored Mach number which can be compared with the calculated one.

The aims of the present work then were (1) to determine the tailored Mach number for several driver-driven gas combinations from the criterion $P_{e5} = 1$ and to compare it with the value calculated by means of equation (1), and (2) tc develop a straightforward and rapid means of arriving at the tailored conditions without resorting to trial-and-error methods.

SYMBOLS

A_{ij} a_i/a_j

a sound speed

M_s incident shock Mach number

m molecular weight

P_{ij} p_i/p_j

p pressure

T temperature

T_{ij} T_i/T_j

U_{ij} u_i/a_j

u particle velocity

α $\frac{\gamma + 1}{\gamma - 1}$

β $\frac{\gamma - 1}{2\gamma}$

γ C_p/C_V ratio of specific heats

Subscripts:

e equilibrium region after interaction

1 undisturbed test gas

2 region behind incident shock wave

3 region behind contact surface

4 undisturbed driver gas

5 region behind reflected shock wave

APPARATUS

The shock tube was of the single-pulse type and was similar to that described by Glick, Squire, and Hertzberg (ref. 2). It was made up of sections of 6.35-centimeter inside-diameter stainless-steel tubing; the driven section was 3.2 meters long and the driver 1.88 meters. The dump tank volume was about 5600 liters. The basic instrumentation consisted of three miniature piezoelectric pressure transducers located 11.4, 29.2, and 47 centimeters from the end of the shock tube. These operated the start-stop circuits of two microsecond time-interval meters so that the velocity could be measured over two intervals for each run. A fourth pickup located 11.4 centimeters from the end of the tube was a calibrated SLM (Kistler Inst. Corp., type 601) pressure transducer. Its output, recorded on an oscilloscope, gave the pressure-time history in the reaction zone behind the reflected shock wave. The reflecting surface of the shock tube could be moved to within 0.63 centimeter of the SLM pressure transducer by inserting close fitting plugs into the tube.

In order to eliminate contamination of the helium driver gas by residual air, the driver section was evacuated to 1 torr or less and then purged with helium before filling.

The test section was always evacuated to about 4×10^{-3} torr and flushed with test gas before filling. This section was isolated from the pump by a cold trap cooled in liquid nitrogen and had a leak rate of 1 to 2×10^{-3} torr per minute.

The driven gases were nitrogen and various mixtures of argon, helium, and carbon dioxide. The mixtures were prepared by the method of partial pressures. The procedure was described in a previous paper (ref. 3).

RESULTS AND DISCUSSION

In each experiment the following data were obtained: initial temperature and pressures of driver and driven gas, incident shock velocities (over two intervals), and an oscilloscope record containing the pressure-time history. The shock velocities over the two intervals were generally found to be the same within the resolution of the measurement; therefore, attenuation was neglected. The pressure transducer was dynamically calibrated by plotting the measured p_5 against the calculated p_5. Figure 2 is the calibration plot for the test gases used.

Pressure Histories

A survey of the literature showed that some of the typical pressure records reported were extremely difficult or impossible to interpret for the first 300 to 500 microseconds after passage of the reflected shock wave. This was due mainly to three things:

(1) Acceleration response of the transducer

(2) Excessive ringing of the transducer due to the mounting

(3) Effect exerted on the pressure record by the interaction of the reflected shock wave and the boundary layer

This inability to determine the initial reflected shock pressure with any certainty lead us to question whether the flat-topped equilibrium state was not being confused with the tailored state. In order to illustrate the problem as it might arise from the third cause just listed, two reflected-pressure records were obtained in nitrogen at the same incident Mach number. Nitrogen was selected as the test gas because it is subject to strong bifurcation of the reflected shock near the wall, as described by Mark (ref. 4). Center (ref. 5) showed that the bifurcation becomes more pronounced as the shock recedes from the end wall. Thus, a pressure record obtained close to the end wall may clearly resolve p_5, while one obtained farther away will have p_5 obscured by the effects of shock bifurcation.

The results of these tests are shown in figure 3. In figure 3(a), obtained at 0.63 centimeter from the end wall, the arrival of a strong disturbance from the contact surface at about 500 microseconds shows clearly that tailoring did not occur. But in the record of figure 3(b), which was obtained at 11.4 centimeters from the end wall, the interaction blends with the disturbance in the boundary layer that results from the more pronounced bifurcation. The record thus indicates a smoothly rounded pressure front followed by a plateau.

If the shock bifurcation were assumed to be responsible for all the curvature in a trace such as figure 3(b), then it would be quite possible to conclude that the flat portion signals the achievement of tailoring. In making this mistake, errors in pressure and temperature would arise amounting, in this particular case, to about 40 percent in the pressure and 180° K in the temperature. This is much too large an error for most experiments.

Thus, this experiment has shown that a greater degree of confidence can be achieved in tailoring by locating and mounting the pressure transducer so that the reflected shock pressure (p_5) can be measured and compared with theory. If this is impossible, then the equilibrium pressure should be measured and compared with the calculated p_5 since at the tailored conditions these two should be equal.

Tailoring

The first experiments were conducted with 7 percent CO_2 + 93 percent Ar driven by helium. Figure 1 shows a typical pressure-time history. The arrival of the reflected disturbance from the contact surface can be seen by the abrupt change in the pressure. The flat region after the interaction is the equilibrium state. The value of p_{e5} was determined by

using the ratio of the distances measured on the oscilloscope trace for $p_1 - p_5$ and $p_1 - p_e$ where p_1 was the initial pressure. This method has a small error since the initial pressure p_1 should be added to each measurement. However, this error is always less than 0.3 percent in p_{e5}, which is less than other sources of error in the determination. In figure 4 p_{e5} is shown plotted against the incident Mach number, which is also typical of the data for the other driver-driven gas combinations. Plotted also is the tailored Mach number calculated by equation (1) when ideal performance is assumed. This lack of agreement between experiment and theory is usual for most tailored experiments and is probably due to the nonideal behavior of most shock tubes.

A performance curve (P_{41} against M_s) for this gas combination is shown in figure 5. The ideal-performance curve is obtained for a real gas by using the relation

$$\left(\frac{P_{21}}{P_{41}}\right)^{\beta_4} = 1 - \frac{U_{21}A_{14}(\gamma_4 - 1)}{2} \tag{2}$$

which for a monatomic driver gas is

$$\left(\frac{P_{21}}{P_{41}}\right)^{0.2} = 1 - \frac{U_{21}A_{14}}{3} \tag{3}$$

where P_{21} and U_{21} are real gas shock properties. The experimental data is above the ideal curve, which is typical for most shock tubes. This behavior can be caused by a number of things such as diaphragm opening or shock attenuation. In any event, this higher than ideal P_{41} can effect the tailoring conditions because the temperature ratio T_{34} (eq. (1)) is calculated from the adiabatic expansion of the driver gas. And since the real p_4 is higher than ideal, the temperature T_3 will be lower than previously calculated. This would tend to lower the tailored Mach number calculated by means of equation (1), which is what was observed experimentally. Therefore, the tailoring calculations were performed by using the actual performance of the shock tube. The result of this calculation is shown in figure 4 and is clearly in close agreement with the experiment.

The Mach number at which tailoring occurs was calculated by using equation (1) and variable γ shock properties for the series of gas combinations studied. The results of these calculations are shown in table I along with the experimentally-observed tailored Mach number. For 7 percent CO_2 + 93 percent Ar and nitrogen tailoring calculations were also made for constant γ shock properties; these two examples showed

that the simpler constant γ calculation was as good as the variable γ calculation in the Mach number range of these experiments. It can be seen that all tailoring calculations fail when the ideal performance of the shock tube is used in the calculation. However, if the actual performance is used, the agreement with experiment is excellent.

The actual performance curves for all gas mixtures used were found to be about parallel to the ideal curves. This makes it possible to obtain the actual performance curve for a given driver-driven gas combination after just one test run. With the actual performance of the shock tube so obtained the tailored Mach number can be calculated, and the second experimental run should be extremely close to being tailored. If it should happen that the first P_{41} were somewhat in error, the second run should correct this and the third test should be tailored.

Contact Surface

Figure 6 is a pressure history for the tailored conditions predicted by the present method. The pressures p_5 and p_e are equal as required but the rise and fall of the pressure (hump) is out of character with the ideas of tailoring. This hump probably results from the mixing of the cold driver and hot driven gases in the contact zone. Evidence that the hump is associated with the contact surface can be provided by comparing experimental arrival times (time from passage of the reflected shock wave to return of the reflected disturbance from the contact surface) with calculated values.

Figure 7 shows a typical time-distance diagram of the kind used to calculate arrival times. Several of these were constructed, for various values of incident shock Mach number in the 7 percent CO_2 + 93 percent Ar mixture. Each diagram included both the trajectory followed by the contact surface in an ideal shock tube and the more realistic trajectory calculated by the analysis of Mirels (ref. 6) for a turbulent boundary layer. In the latter case, it was assumed that the gas mixture could be treated as pure argon for purposes of the calculation.

In order to calculate arrival times from these diagrams, the reflected disturbance from the contact surface was assumed to travel at the speed of sound in the undissociated and stationary gas behind the reflected shock wave. The results are plotted against M_s in figure 8. The contact surface trajectory calculated by the method of Mirels depends somewhat on initial pressure; two curves are therefore shown that correspond to the upper and lower extremes of initial pressure used in the present work.

The experimental arrival times were obtained by assuming that any abrupt change in the slope of the reflected shock pressure history indicated the arrival of the reflected disturbance from the contact surface. In tailored records, a small dip in pressure invariably occurred just before the hump and this was taken as the arrival of the disturbance (see fig. 6). At Mach numbers above the tailored value, the disturbance appeared as a sharp rise in the pressure, as in figure 1. In order to

extend the data below the tailored Mach number for helium driver gas, and to avoid reflected rarefaction waves whose arrival time is hard to read, some tests were made with an argon-helium driver. This driver mixture gave an easily read trace with a sharp pressure rise as in figure 1.

Figure 8 shows very good agreement between experimental arrival times and those expected on the basis of Mirels' contact surface trajectory. The arrival times calculated for an ideal contact surface were far outside the scatter of our data. The agreement between calculation and experiment suggests that a pressure hump is unavoidable even under tailored conditions, and as mentioned earlier, this interaction is probably due to the existence of a contact zone rather than a contact discontinuity. It is interesting to note that this zone evidently follows the trajectory predicted by Mirels, even though his analysis treats it as a discontinuity.

CONCLUDING REMARKS

Experiments showed that a flat-topped pressure record does not necessarily prove that tailoring had been achieved. This was because the equilibrium state, which also has a flat-topped pressure history, can be confused with the tailored state if the pressure transducer does not follow the initial reflected pressure history. However, with the criterion $p_e = p_5$ no such confusion can exist, since p_5 can be calculated and p_e measured.

An improved method for calculating the tailoring conditions has been presented. It requires the substitution of the actual shock tube performance (P_{41} against M_s) in the tailoring equations. Tailored pressure records can be achieved in two or three systematic experiments. Since no two shock tubes necessarily have the same performance curves, it follows from this work that the reflected conditions corresponding to tailored operation will be different in each tube, even though the driver-driven gas combination is the same.

Even at the tailored conditions a small hump was observed in the pressure record. This was shown to be associated with the contact surface. Measured arrival times (time from passage of the reflected shock wave to arrival of the reflected disturbance from the contact surface) in the Mach number range of 3.1 to 4.4 showed good agreement with those calculated by Mirels' analysis of the testing time between the shock wave and the contact surface.

REFERENCES

(1) Hertzberg, A.; Smith, W. E.; Glick, H. S.; and Squire, W.: Modifications of the Shock Tube for the Generation of Hypersonic Flow. Rep. AD-789-A-2 (AEDC TN 55-15), Cornell Aeronautical Lab., Mar. 1955.

(2) Glick, H. S.; Squire, W.; and Hertzberg, A.: A New Shock Tube Technique for the Study of High Temperature Gas Phase Reactions. Fifth Symposium (International) on Combustion, Fifth, Univ. of Pittsburgh, 1954, Reinhold Pub. Corp., 1955, pp. 393-402.

this the value of $\frac{du_e}{ds}$ is also largest near the shock and, consequently, the nonsimilar effect of the boundary layer will be most pronounced for small values of s. Hence, it is important for the evaluation of shock tube test time that the most accurate solution of the present governing equations, which include the nonsimilar terms, be available for small vaues of s. With this in mind, solution of the governing equations is sought in series forms in the following manner.

There are three variables u_e, ρ_e, and h_e, and two equations, Equations (1) and (2), for the inviscid region. Hence, ρ_e and h_e can be expressed in terms of u_e. The solution for u_e is first postulated in the series form

$$\frac{u_e}{u_{e0}} = 1 + \epsilon K_1 + \epsilon^2 K_2 + \epsilon^3 K_3 + O(\epsilon^4) \tag{18}$$

where ϵ is defined, with Equation (15) in mind, by

$$\epsilon = \frac{4(2s\ell)^{1/2}}{(\rho_e \mu_e)_0 d} \tag{19}$$

The K_n are a set of unknown constants. The corresponding series for ρ_e/ρ_{e0} and h_e/h_{e0} are then readily obtained from Equations (1), (2), and (18) in terms of K_n. Now, the solution of the inviscid flow will become complete as soon as K_n, defining u_e/u_{e0}, are determined. K_n will be determined later with the use of the boundary layer solutions to be obtained in the following.

The solutions for f and H are sought in the following series forms

$$f(\epsilon, \eta) = f_0(\eta) + \epsilon f_1(\eta) + \epsilon^2 f_2(\eta) + \epsilon^3 f_3(\eta) + O(\epsilon^4) \tag{20}$$

$$H(\epsilon, \eta) = H_0(\eta) + \epsilon H_1(\eta) + \epsilon^2 H_2(\eta) + \epsilon^3 H_3(\eta) + O(\epsilon^4) \tag{21}$$

The substitution of Equations (18), (20), and (21) into Equations (9) through (12), and the subsequent collection of terms with equal powers of ϵ yield, with aid of Equations (1) and (2), the following set of perturbed equations and boundary conditions. Only, the first three sets are shown here for brevity.

Zeroth-order set

$$\begin{aligned} &f_0''' + f_0 f_0'' = 0 \\ &\frac{1}{P_r} H_0'' + f_0 H_0' = -2\left(\frac{P_r - 1}{P_r}\right)\left(\frac{\gamma - 1}{\gamma + 1}\right)\frac{u_{e0}}{u_w}\left[f_0' f_0''\right]' \end{aligned} \tag{22}$$

boundary conditions:

$$\begin{aligned} &f_0'(\infty) = 1 && H_0(\infty) = 1 \\ &f_0(0) = 0 && H_0(0) = 1 \\ &f_0'(0) = u_w/u_{e0} \end{aligned} \tag{23}$$

First-order set

$$\begin{aligned} &f_1''' + f_0 f_1'' + 2 f_1 f_0'' - f_0' f_1' = -K_1(1 + E)\left[H_0 - f_0'^2\right] \\ &\frac{1}{P_r} H_1'' + f_0 H_1' - f_0' H_1 = -2 f_1 H_0' - 2\left(\frac{P_r - 1}{P_r}\right)\left(\frac{\gamma - 1}{\gamma + 1}\right)\frac{u_{e0}}{u_w}\left[(f_1' f_0'' + f_0' f_1'')' + 2K_1(f_0' f_0'')'\right] \end{aligned} \tag{24}$$

boundary conditions:

$$f_1'(\infty) = 0 \qquad H_1(\infty) = 0$$

$$f_1(0) = 0 \qquad H_1(0) = 0 \tag{25}$$

$$f_1'(0) = -K_1 f_0'(0)$$

Second-order set

$$f_2''' + f_0 f_2'' + 3f_2 f_0'' - 2f_2' f_0' = -2f_1 f_1'' + f_1'^2 - (2K_2 - K_1^2)K_1(1 + E)\left[H_0 - f_0'^2\right] - K_1(1+E)H_1 + 2K_1 E\left[K_1 f_0'^2 + f_0' f_1' - K_1(1+E)\left(H_0 - \left(\frac{\gamma-1}{\gamma+1}\right)\frac{u_{e0}}{u_w} f_0'^2\right)\right] + 2K_1 f_0' f_1' \tag{26}$$

$$\frac{H_2''}{P_r} + f_0 H_2' - 2f_0' H_2 = -3f_2 H_0' - 2f_1 H_1' + f_1' H_1 - 2\left(\frac{P_r - 1}{P_r}\right)\left(\frac{\gamma-1}{\gamma+1}\right)\frac{u_{e0}}{u_w}\left\{\left[f_0' f_2'' + f_0'' f_2' + f_1'' f_1'\right]' + 2K_1\left[f_1' f_0'' + f_0' f_1''\right]' + (2K_2 + K_1^2)\left[f_0' f_0''\right]'\right\}$$

boundary conditions:

$$f_2'(\infty) = 0 \qquad H_2(\infty) = 0$$

$$f_2(0) = 0 \qquad H_2(0) = 0 \tag{27}$$

$$f_2'(0) = -f'(0)\left[K_2 - K_1^2\right]$$

where

$$E = \frac{u_{e0}^2}{2h_{e0}} = \frac{\gamma-1}{2} M_{e0}^2 \tag{28}$$

Now, the boundary layer solution can be completed by integrating the various order perturbed equations as soon as K_n are known.

The unknown set of constants, K_n, is now determined by employing the yet unused Equation (15) which couples the inviscid and boundary layer flow regimes. The series (18) for u_e/u_{e0}, the corresponding series (11) for ρ_e/ρ_{e0} and the series, Equations (20) and (21) for f and H, are first substituted into Equation (15). When the terms with equal powers of ϵ are collected, the following equations defining K_n result

$$K_1 = \frac{1}{M_{e0}^2 - 1} G_0$$

$$K_2 = \frac{1}{M_{e0}^2 - 1} \left[G_1 - \frac{3}{2} K_1 (K_1 + G_0) - \frac{(\gamma - 2)}{2!} (K_1 + G_0)^2 \right] \tag{29}$$

$$K_3 = \frac{1}{M_{e0}^2 - 1} \left\{ G_2 - K_1 \left[K_2 + G_1 - K_1 (K_1 + G_0) \right] - 2K_2 (K_1 + G_0) \right.$$

$$- (\gamma - 2) \left[K_2 + G_1 - K_1 (K_1 + G_0) \right] (K_1 + G_0)$$

$$\left. + \frac{(\gamma - 2)(\gamma - 3)}{3!} (K_1 + G_0)^3 \right\}$$

where

$$G_0 = \int_0^\infty \left\{ f_0' - (1 + E) H_0 + E f_0'^2 \right\} d\eta$$

$$G_1 = \int_0^\infty \left\{ f_1' - (1+E)H_1 + 2E \left[K_1 f_0'^2 + f_0' f_1' - K_1 \left| (1+E)H_0 - E f_0'^2 \right| \right] \right\} d\eta$$

$$G_2 = \int_0^\infty \left\{ f_2' - (1+E)H_2 + 2E \left[f_0' f_2' + f_1'^2 + (K_2 + K_1^2) f_0'^2 + 2K_1 f_0' f_1' - (K_2 + K_1^2/2) \left[(1+E)H_0 - E f_0'^2 \right] - K_1 \left((1+E)H_1 - 2E \left[K_1 f_0'^2 + f_0' f_1' - K_1 \left| (1+E)H_0 - E f_0'^2 \right| \right] \right) \right] \right\} d\eta \quad (30)$$

The zeroth order perturbed equations, Equations (22), through the third order equations, not shown here for brevity, for the boundary layer are integrated numerically by the use of a digital computer for various combinations of the parameters M_s, γ, and Pr. The parameters appearing in the perturbed equations, such as u_w/u_{e0} and μ_{e0}, depend on the values of γ and M_s through Equations (17). Typical results are shown on Figures 2 and 3. The various values of the perturbed functions which will be needed for the subsequent analysis are tabulated in Table 1.

The series for u_e/u_{e0}, Equation (18), and the corresponding series for ρ_e/ρ_{e0} and h_e/h_{e0}, obtainable from Equation (1) and (2), now describe all the flow properties of the inviscid flow since K_n are given by Equations (29). The series for f and H given by Equations (20) and (21) describe the major boundary layer properties, such as surface heat transfer, with the aid of

Table 1. Therefore, the solution of the governing equation is now completed on the ϵ - η plane.

In order to apply the present solution to a physical shock tube problem, the streamwise variable ϵ must be related to the physical distance x. The variable ϵ will be related to x in the subsequent section.

IV. CORRELATION OF ϵ AND X

The variable ϵ defined by Equation (19) is related to the physical distance x through Equation (4b). An explicit expression for ϵ in terms of the physical distance will be derived here.

Equations (4b) and (19) give:

$$\epsilon = \frac{4(2\ell)^{1/2}}{\rho_{e0} u_{e0}^{d}} \left[\int_{o}^{x} \rho_e u_e \mu_e dx \right]^{1/2} \tag{31}$$

Equation (31) is first squared and differentiated with respect to x. Various series for the inviscid flow, such as Equation (18), Equation (16), are then substituted into the equation for the variables ρ_e, u_e, and μ_e. After some manipulation, there results the first order differential equation,

$$2\epsilon \frac{d\epsilon}{d\zeta} = 1 + \epsilon\Gamma_1 + \epsilon^2\Gamma_2 + \epsilon^3\Gamma_3 + O(\epsilon^4) \tag{32}$$

where

$$\zeta = \frac{32\ell}{R_{ed}} \left(\frac{x}{d}\right) \tag{33}$$

and

$$\begin{aligned} \Gamma_1 &= -G_0 - 2EK_1 \\ \Gamma_2 &= -G_1 + 2EK_1G_0 - 2E\left(K_2 + \frac{K_1^2}{2}\right) \\ \Gamma_3 &= -G_2 + 2EK_1G_1 + 2E\left(K_2 + \frac{K_1^2}{2}\right) - 2E(K_3 + K_1K_2) \end{aligned} \tag{34}$$

Equation (32)* is readily soluble by substituting the series

$$\epsilon = \sum_{n=0}^{\infty} a_n \zeta^{n/2} \tag{35}$$

into the equation and determining the coefficients. This results in the following solution

$$\epsilon = \zeta^{1/2} + \frac{\Gamma_1}{3}\zeta + \left(\frac{\Gamma_1^2}{18} + \frac{\Gamma_2}{2}\right)\zeta^{3/2} + \left(\frac{2}{15}\Gamma_2\Gamma_1 + \frac{\Gamma_3}{5} - \frac{\Gamma_1}{15}\left(\frac{\Gamma_1^2}{18} + \frac{\Gamma_2}{2}\right)\right)\zeta^2 + O(\zeta^{5/2})$$

Typical results of Equation (36) for $\gamma = 5/3$ and $Pr = 0.72$ are shown on Figure 4.

*Note that if Equation (32) is truncated for terms of $O(\epsilon^4)$, which is the case taken here, the equation is in the form of the Abel equation of the second kind.

V. HEAT TRANSFER

The heat transfer to a unit area of wall per unit time, at a given distance from the shock, is

$$q_w = \frac{\mu_w}{Pr} \left\{ h_{te0} (H_y)_w - u_w (u_y)_w \right\}$$

The local heat transfer, hence, becomes

$$q_w \left[\frac{Pr \frac{\rho_{e0}}{\rho_w} \epsilon}{4\mu_w h_{te0}} \right] = \left(1 + \epsilon K_1 + \epsilon^2 K_2 + \epsilon^3 K_3 + O(\epsilon^4)\right) \left\{ H_0' + \epsilon H_0' + \epsilon^2 H_2' \right.$$

$$\left. + \epsilon^3 \quad O(\epsilon^4) - 2\left(\frac{\gamma - 1}{\gamma + 1}\right) \left(f_0''' + \epsilon(f_1''' + K_1 f_0''') \right.\right.$$

$$\left. + \epsilon^2 (f_2''' + K_1 f_1''' + K_2 f_0''') + \epsilon^3 (f_3''' + K_1 f_2''' + K_2 f_1''' \right.$$

$$\left.\left. + K_3 f_0''') + O(\epsilon^4) \right) \right\}_w \qquad (37)$$

Typical results for $\gamma = 5/3$ and $Pr = 0.72$ are shown on Figure 5. If the variation of inviscid stream is neglected, as was done in Ref. 9, the value of the nondimensional heat transfer, for a given M_s, will be that corresponding to $\zeta^{1/2} = 0$ for all ζ. The results of Figure 5 shows, therefore, that the heat transfer is increased for given x, as the pressure is increased due to the entrainment of mass by the boundary layer.

VI. SHOCK TUBE TEST TIME

According to ideal shock tube theory without boundary layers, the test section, the distance between shock and contact surface, increases linearly with time following the diaphragm eruption. The test section, however, for a given time after the diaphragm eruption, is reduced in practice as portions of the shocked gas are continuously being entrained into the boundary layer along x. After a sufficient length of time following the diaphragm eruption, a condition is reached wherein all the gas crossing the shock becomes entrained into the boundary layer by the time the gas reaches the contact surface. No further increase of test section with time is then possible beyond this point, and this determines the maximum obtainable test time.

In the present section, the rate of mass entrainment by the boundary layer will first be determined, along x by the use of the analysis performed hitherto. The results will be compared with those obtained in Ref. 6. The maximum obtainable test section will then be determined for various shock Mach numbers.

(Mass Entrainment by Boundary Layer)

The quantity $\bar{\delta}$ is the ratio of the mass flow entrained into the boundary layer at any location downstream of the shock to that mass flow which has entered through the shock. It is defined as

$$\bar{\delta} = 1 - \frac{\rho_e u_e}{\rho_{e0} u_{e0}} = \sum_{n=0}^{\infty} \epsilon^{n+1} G_n \qquad (38)$$

with the aid of the series for ρ_e/ρ_{e0} and u_e/u_{e0}. Since ϵ is related to ζ from Equation (36), the above equation gives $\bar{\delta}$ as the function of ζ. Note that the maximum test section is reached when $\bar{\delta} = 1$.

Both numerical results, from the present analysis, Equation (38) shown as circles, using the first four terms of the series, and from Ref. 6, are plotted in Figures 6 and 7 for various shock Mach numbers. It is seen that the approximate results of Ref. 6 agree with the present solutions very well for high shock Mach numbers. The figure shows, however, that the present results give much larger values of $\bar{\delta}$, for given $\zeta^{1/2}$, than those predicted in Ref. 6 when the Mach number is low. The discrepancy between the results of the two analyses, in fact, increases rapidly as the Mach number decreases below about 2. Therefore, at the low Mach numbers, the present solution predicts much smaller test sections, and hence, much smaller test times, than those predicted previously.*

Because the present solutions of the governing equations are obtained in series form, in terms of ζ, it is only for a few cases which the solutions can describe the flow completely across the maximum test section that is for $\bar{\delta} = 1$. In the following, a method of enhancing the applicability of the present solution will be discussed.

*Concurrently, but independently, Ref. 10 developed an incompressible Momentum Integral solution. It is not discussed here because it is restricted to high M_s and incompressible flow whereas our model treats real shock tube flows.

(Extension of Solution to Large ζ)

As it was mentioned in the beginning of Section II, the rate of mass entrainment is maximum near the shock where ζ is small. This may be ascertained from Figure 6 by recognizing that $\frac{1}{\bar{\delta}}\frac{d\bar{\delta}}{d\zeta}$ which is proportional to the rate of mass entrainment divided by entrainment, decreases with increasing ζ.

Previous experiences with boundary layers have shown that local similarity assumptions are adequate if boundary conditions are provided a priori, along the inviscid stream and the wall, as in conventional boundary layers. In the present case, however, the inviscid stream is continuously being depleted resulting in a continuous change of boundary conditions which is strongly dependent upon what has occurred upstream. Hence, the local similarity is destroyed by the mass entrainment effect incurring deviations of the boundary conditions from the correct ones, especially so for small M_s. Since in the present problem, the similarity of the boundary layer is destroyed by this mass entrainment process, it is important that an exact solution be available for small values of ζ. For large values of ζ, on the other hand, an approximate solution based on some modifications of local similarity principle should be functionally adequate. Therefore, with the present solution which takes care of the most critical region (region of small ζ), as the basis, the following approximate extension of the theory is developed for large values of ζ.

In a similar boundary layer, one finds

$$\bar{\delta} = \zeta^{1/2} G_c \tag{39}$$

where G_c is a constant. However, in the nonsimilar boundary layer treated here, with the aid of Equations (36) and (38), it is found that

$$\bar{\delta} = G_0\zeta^{1/2} + \left(G_1 + \frac{\Gamma_1}{3} G_0\right)\zeta + \left[G_2 + \frac{2}{3}\Gamma_1 G_1 + \left(\frac{\Gamma_1^2}{18} + \frac{\Gamma_2}{2}\right) G_0\right] \zeta^{3/2} + O(\zeta^2) \tag{40}$$

which suggests the following form.

$$\bar{\delta} = \zeta^{1/2} G(\zeta) \tag{41}$$

By analyzing the various terms of Equation (40) it may be shown that, within the region of convergence of Equation (38), $G(\zeta)$ is represented very well as an exponential function, such as

$$G(\zeta) = C_2 e^{C_1 \zeta^{1/2}} \tag{42}$$

By taking the various terms of Equation (40), the best values for C_2 and C_1 may be determined. Values of C_2 and C_1 are shown on Figure 8.

The numerical results obtained in the present analysis, Equations (38) and (41) are shown as Figures 6 and 7. It is interesting to note from these figures the simple function $G(\zeta) = C_2 e^{C_1 \zeta^{1/2}}$ chosen enables the approximate solution, Equation (41), to predict the exact solution accurately for all ζ

within the regions of the convergence of the exact solution*, and Mach numbers. The extension to larger ζ will incur some slight error and can be analyzed once an exact solution is available for the whole range of ζ.

Also shown on Figure 6 are two data points indicated by triangles. These results were taken from Ref. 6 in the form of asymptotic data.

(Maximum Test Time)

For a given shock Mach number, the test time, at a given period of time after the diaphragm eruption, is proportional to the distance between the shock and the contact surface. The maximum test time, τ_M, is hence proportional to ζ_M where ζ_M denotes that value corresponding to $\overline{\delta} = 1$. The various values of ζ_M computed from the present theory and from the analysis of Ref. 6, and also the available experimental data are shown in Figure 6.

Although the present analysis yields an improvement, a vast improvement for decreasing shock Mach number, over that of Ref. 6, it still shows a variance with the experimental data. The present analysis treated the entrainment effect of the boundary layer more accurately than Ref. 6 did. It, however, still did not take into account other nonideal effects such as the mixing at the interface and the real diaphragm opening process (see Ref. 3). Also, the shock speed was treated as being uniform. The collective effect of all these quantities might provide for the remaining deriviation between the present analysis and experimental data.

*The extension to large ζ is taken in the spirit of being somewhat like analytic continuation.

In order to elucidate the difference between the results of the present analysis and those of Ref. 6, the ratio of the maximum test times obtained from the respective analyses is plotted in Figure 9. The mounting disagreement at the lower shock Mach numbers is evident.

VII. CONCLUSION

The effect of the shock-induced laminar boundary layer on the length of flow between the shock and contact surface has been investigated. The inviscid flow-boundary layer problem associated with shock tube flows has been studied. The study was made by first analyzing the most critical region by an exact method, and then extending the result to the rest of the flow region with an approximate method. The study showed that the reductions in shock tube test time are considerably greater than those predicted by previous theories when the shock Mach number is low.

The comparison of the present results with the available experimental data showed that other nonideal effects in addition to the boundary layer effect considered herein, must be also included.

ACKNOWLEDGMENT

The authors thank Dr. F. Meyers for programming the exact solutions of the perturbation equations.

REFERENCES

1. Anderson, G. F., "Shock-Tube Testing Time," J. Aerospace Sci, 26, 3, 184 (1959).
2. Brocher, E. F., "Hot Flow Length and Testing Time in Real Shock Tube Flow," Phys. Fluids 7, 347, (1964).
3. Camm, J. C. and Rose, P. N., "Electric Shock Tube for High Velocity Simulation," Avco-Everett Research Report 136, Avco Corp., Everett, Mass., (July 1962).
4. Duff, R. E., "Shock-Tube Performance at Low Initial Pressure," Phys. Fluids 2 (2), 207-216 (1959).
5. Hooker, W. J., "Testing Time and Contact Zone Phenomena in Shock Tube Flows," Phys. Fluids 4, 1451 (1961).
6. Mirels, H., "Test Time in Low Pressure Shock Tubes," Phys. Fluids 6, 1201 (1963)
7. Mirels, H. "Shock Tube Test Time Limitation Due to Turbulent Wall Boundary Layer," TDR-169(3230-12)TR-3, Aerospace Corporation, El Segundo, California, (1963).
8. Roshko, A. "On Flow Duration in Low-Pressure Shock Tubes," Phys. Fluids 3, 835 (1960).
9. Mirels, H. "Laminar Boundary Layer Behind a Strong Shock Moving into Air," NASA TN D-291, (1961)
10. Mirels, H. and King, W. S., "Incompressible Momentum Integral Boundary Layer Solution Relating to Shock Tube Test Time," Aerospace Corporation Report No. TDR-469(5240-10)-3, (1964).

Table I

$\gamma = 5/3, \quad Pr = 0.72$

	M_s				M_s		
	1.067	1.34	1.6	1.73	3.0	4.0	∞
u_w/u_{e0}	1.1000	1.5000	1.8417	2.000	3.0000	3.3684	4.0000
M_{e0}^2	0.8824	0.6000	0.4712	0.4286	0.2727	0.2405	0.2000
G_0	0.133620	0.552804	0.830290	0.943860	1.53395	1.71521	1.99708
G_1	1.20497	1.33217	1.48243	1.55589	2.02334	2.19044	2.46842
G_2	-2.51512	0.0967892	0.859271	1.16261	2.91181	3.53996	4.62412
G_3	38.7098	4.76710	4.18457	4.36163	7.26043	8.72176	11.5510
K_1	-1.13577	-1.38201	-1.570100	-1.65175	-2.10919	-2.25837	-2.49635
K_2	2.84726	0.680470	0.319040	0.200371	-0.355547	-0.526214	-0.800545
K_3	-46.3532	-5.35314	-4.06237	-3.93937	-4.62025	-5.08954	-5.99706
K_4	841.827	21.8404	8.96542	-0.189738	-0.189738	-1.98194	-5.03553
f_0''	-0.0822861	-0.457778	-0.831227	-1.01906	-2.39732	-2.97996	-4.06222
H_0'	-0.00648676	-0.0398770	-0.0759351	-0.0946012	-0.236381	-0.297623	-0.412395
f_1''	-1.52240	-2.53081	-3.73929	-4.40792	-10.2461	-13.1061	-18.9049
H_1'	-0.112823	-0.168427	-0.229368	-0.261999	-0.535798	-0.666974	-0.930672
f_2''	2.95979	-2.79659	-6.65896	-8.85621	-30.9638	-43.3092	-70.5515
H_2'	0.318233	-0.00984224	-0.1510316	-0.225862	-0.945679	-1.34152	-2.21087
f_3''	-82.5631	-17.4331	-27.4456	-35.2390	-134.742	-198.449	-350.854
H_3'	-6.59894	-1.14986	-1.49391	-1.82275	-6.16549	-8.93536	-15.5210

this the value of $\frac{du_e}{ds}$ is also largest near the shock and, consequently, the nonsimilar effect of the boundary layer will be most pronounced for small values of s. Hence, it is important for the evaluation of shock tube test time that the most accurate solution of the present governing equations, which include the nonsimilar terms, be available for small vaues of s. With this in mind, solution of the governing equations is sought in series forms in the following manner.

There are three variables u_e, ρ_e, and h_e, and two equations, Equations (1) and (2), for the inviscid region. Hence, ρ_e and h_e can be expressed in terms of u_e. The solution for u_e is first postulated in the series form

$$\frac{u_e}{u_{e0}} = 1 + \epsilon K_1 + \epsilon^2 K_2 + \epsilon^3 K_3 + O(\epsilon^4) \tag{18}$$

where ϵ is defined, with Equation (15) in mind, by

$$\epsilon = \frac{4(2s\ell)^{1/2}}{(\rho_e \mu_e)_0 d} \tag{19}$$

The K_n are a set of unknown constants. The corresponding series for ρ_e/ρ_{e0} and h_e/h_{e0} are then readily obtained from Equations (1), (2), and (18) in terms of K_n. Now, the solution of the inviscid flow will become complete as soon as K_n, defining u_e/u_{e0}, are determined. K_n will be determined later with the use of the boundary layer solutions to be obtained in the following.

The solutions for f and H are sought in the following series forms

$$f(\epsilon, \eta) = f_0(\eta) + \epsilon f_1(\eta) + \epsilon^2 f_2(\eta) + \epsilon^3 f_3(\eta) + O(\epsilon^4) \tag{20}$$

$$H(\epsilon, \eta) = H_0(\eta) + \epsilon H_1(\eta) + \epsilon^2 H_2(\eta) + \epsilon^3 H_3(\eta) + O(\epsilon^4) \tag{21}$$

The substitution of Equations (18), (20), and (21) into Equations (9) through (12), and the subsequent collection of terms with equal powers of ϵ yield, with aid of Equations (1) and (2), the following set of perturbed equations and boundary conditions. Only, the first three sets are shown here for brevity.

Zeroth-order set

$$\begin{aligned} &f_0''' + f_0 f_0'' = 0 \\ &\frac{1}{P_r} H_0'' + f_0 H_0' = -2\left(\frac{P_r - 1}{P_r}\right)\left(\frac{\gamma - 1}{\gamma + 1}\right)\frac{u_{e0}}{u_w}\left[f_0' f_0''\right]' \end{aligned} \tag{22}$$

boundary conditions:

$$\begin{aligned} &f_0'(\infty) = 1 \qquad && H_0(\infty) = 1 \\ &f_0(0) = 0 \qquad && H_0(0) = 1 \\ &f_0'(0) = u_w/u_{e0} \end{aligned} \tag{23}$$

First-order set

$$\begin{aligned} &f_1''' + f_0 f_1'' + 2 f_1 f_0'' - f_0' f_1' = -K_1(1 + E)\left[H_0 - f_0'^2\right] \\ &\frac{1}{P_r} H_1'' + f_0 H_1' - f_0' H_1 = -2 f_1 H_0' - 2\left(\frac{P_r - 1}{P_r}\right)\left(\frac{\gamma - 1}{\gamma + 1}\right)\frac{u_{e0}}{u_w}\left[(f_1' f_0'' + f_0' f_1'')' + 2K_1(f_0' f_0'')'\right] \end{aligned} \tag{24}$$

boundary conditions:

$$f_1'(\infty) = 0 \qquad H_1(\infty) = 0$$

$$f_1(0) = 0 \qquad H_1(0) = 0 \tag{25}$$

$$f_1'(0) = -K_1 f_0'(0)$$

Second-order set

$$f_2''' + f_0 f_2'' + 3f_2 f_0'' - 2f_2' f_0' = -2f_1 f_1'' + f_1'^2 - (2K_2 - K_1^2)K_1(1 + E)\left[H_0 - f_0'^2\right] - K_1(1+E)H_1 + 2K_1 E\left[K_1 f_0'^2 + f_0' f_1'\right.$$
$$\left. - K_1(1+E)\left(H_0 - \left(\frac{\gamma - 1}{\gamma + 1}\right)\frac{u_{e0}}{u_w} f_0'^2\right)\right] + 2K_1 f_0' f_1' \tag{26}$$

$$\frac{H_2''}{P_r} + f_0 H_2' - 2f_0' H_2 = -3f_2 H_0' - 2f_1 H_1' + f_1' H_1$$
$$- 2\left(\frac{P_r - 1}{P_r}\right)\left(\frac{\gamma - 1}{\gamma + 1}\right)\frac{u_{e0}}{u_w}\left\{\left[f_0' f_2'' + f_0'' f_2' + f_1'' f_1'\right]'\right.$$
$$\left. + 2K_1\left[f_1' f_0'' + f_0' f_1''\right]' + (2K_2 + K_1^2)\left[f_0' f_0''\right]'\right\}$$

boundary conditions:

$$f_2'(\infty) = 0 \qquad H_2(\infty) = 0$$

$$f_2(0) = 0 \qquad H_2(0) = 0 \tag{27}$$

$$f_2'(0) = -f'(0)\left[K_2 - K_1^2\right]$$

where

$$E = \frac{u_{e0}^2}{2h_{e0}} = \frac{\gamma - 1}{2} M_{e0}^2 \tag{28}$$

Now, the boundary layer solution can be completed by integrating the various order perturbed equations as soon as K_n are known.

The unknown set of constants, K_n, is now determined by employing the yet unused Equation (15) which couples the inviscid and boundary layer flow regimes. The series (18) for u_e/u_{e0}, the corresponding series (11) for ρ_e/ρ_{e0} and the series, Equations (20) and (21) for f and H, are first substituted into Equation (15). When the terms with equal powers of ϵ are collected, the following equations defining K_n result

$$K_1 = \frac{1}{M_{e0}^2 - 1} G_0$$

$$K_2 = \frac{1}{M_{e0}^2 - 1} \left[G_1 - \frac{3}{2} K_1 (K_1 + G_0) - \frac{(\gamma - 2)}{2!} (K_1 + G_0)^2 \right] \qquad (29)$$

$$K_3 = \frac{1}{M_{e0}^2 - 1} \left\{ G_2 - K_1 \left[K_2 + G_1 - K_1 (K_1 + G_0) \right] - 2K_2 (K_1 + G_0) \right.$$

$$- (\gamma - 2) \left[K_2 + G_1 - K_1 (K_1 + G_0) \right] (K_1 + G_0)$$

$$\left. + \frac{(\gamma - 2)(\gamma - 3)}{3!} (K_1 + G_0)^3 \right\}$$

where

$$G_0 = \int_0^\infty \left\{ f_0' - (1 + E) H_0 + E f_0'^2 \right\} d\eta$$

$$G_1 = \int_0^\infty \left\{ f_1' - (1+E)H_1 + 2E \left[K_1 f_0'^2 + f_0' f_1' - K_1 \left| (1+E)H_0 - E f_0'^2 \right| \right] \right\} d\eta$$

$$G_2 = \int_0^\infty \left\{ f_2' - (1+E)H_2 + 2E \left[f_0' f_2' + f_1'^2/2 + (K_2 + K_1^2) f_0'^2 + 2K_1 f_0' f_1' - (K_2 + K_1^2/2) \left[(1+E)H_0 - E f_0'^2 \right] - K_1 \left((1+E)H_1 - 2E \left[K_1 f_0'^2 + f_0' f_1' - K_1 \left| (1+E)H_0 - E f_0'^2 \right| \right] \right) \right] \right\} d\eta \quad (30)$$

The zeroth order perturbed equations, Equations (22), through the third order equations, not shown here for brevity, for the boundary layer are integrated numerically by the use of a digital computer for various combinations of the parameters M_s, γ, and Pr. The parameters appearing in the perturbed equations, such as u_w/u_{e0} and μ_{e0}, depend on the values of γ and M_s through Equations (17). Typical results are shown on Figures 2 and 3. The various values of the perturbed functions which will be needed for the subsequent analysis are tabulated in Table 1.

The series for u_e/u_{e0}, Equation (18), and the corresponding series for ρ_e/ρ_{e0} and h_e/h_{e0}, obtainable from Equation (1) and (2), now describe all the flow properties of the inviscid flow since K_n are given by Equations (29). The series for f and H given by Equations (20) and (21) describe the major boundary layer properties, such as surface heat transfer, with the aid of

Table 1. Therefore, the solution of the governing equation is now completed on the ϵ - η plane.

In order to apply the present solution to a physical shock tube problem, the streamwise variable ϵ must be related to the physical distance x. The variable ϵ will be related to x in the subsequent section.

IV. CORRELATION OF ϵ AND X

The variable ϵ defined by Equation (19) is related to the physical distance x through Equation (4b). An explicit expression for ϵ in terms of the physical distance will be derived here.

Equations (4b) and (19) give:

$$\epsilon = \frac{4(2\ell)^{1/2}}{\rho_{e0}u_{e0}^{d}} \left[\int_{o}^{x} \rho_e u_e \mu_e dx \right]^{1/2} \tag{31}$$

Equation (31) is first squared and differentiated with respect to x. Various series for the inviscid flow, such as Equation (18), Equation (16), are then substituted into the equation for the variables ρ_e, u_e, and μ_e. After some manipulation, there results the first order differential equation,

$$2\epsilon \frac{d\epsilon}{d\zeta} = 1 + \epsilon\Gamma_1 + \epsilon^2\Gamma_2 + \epsilon^3\Gamma_3 + O(\epsilon^4) \tag{32}$$

where

$$\zeta = \frac{32l}{R_{ed}} \left(\frac{x}{d}\right) \tag{33}$$

and

$$\begin{aligned} \Gamma_1 &= -G_0 - 2EK_1 \\ \Gamma_2 &= -G_1 + 2EK_1G_0 - 2E\left(K_2 + \frac{K_1^2}{2}\right) \\ \Gamma_3 &= -G_2 + 2EK_1G_1 + 2E\left(K_2 + \frac{K_1^2}{2}\right) - 2E(K_3 + K_1K_2) \end{aligned} \tag{34}$$

Equation (32)* is readily soluble by substituting the series

$$\epsilon = \sum_{n=0}^{\infty} a_n \zeta^{n/2} \tag{35}$$

into the equation and determining the coefficients. This results in the following solution

$$\epsilon = \zeta^{1/2} + \frac{\Gamma_1}{3}\zeta + \left(\frac{\Gamma_1^2}{18} + \frac{\Gamma_2}{2}\right)\zeta^{3/2} + \left(\frac{2}{15}\Gamma_2\Gamma_1 + \frac{\Gamma_3}{5} - \frac{\Gamma_1}{15}\left(\frac{\Gamma_1^2}{18} + \frac{\Gamma_2}{2}\right)\right)\zeta^2 + O(\zeta^{5/2})$$

Typical results of Equation (36) for $\gamma = 5/3$ and $Pr = 0.72$ are shown on Figure 4.

*Note that if Equation (32) is truncated for terms of $O(\epsilon^4)$, which is the case taken here, the equation is in the form of the Abel equation of the second kind.

V. HEAT TRANSFER

The heat transfer to a unit area of wall per unit time, at a given distance from the shock, is

$$q_w = \frac{\mu_w}{Pr} \left\{ h_{te0} (H_y)_w - u_w (u_y)_w \right\}$$

The local heat transfer, hence, becomes

$$q_w \left[\frac{Pr \frac{\rho_{e0}}{\rho_w} \epsilon}{4\mu_w h_{te0}} \right] = \left(1 + \epsilon K_1 + \epsilon^2 K_2 + \epsilon^3 K_3 + O(\epsilon^4) \right) \left\{ H_0' + \epsilon H_0' + \epsilon^2 H_2' + \epsilon^3 H_3' + O(\epsilon^4) - 2\left(\frac{\gamma - 1}{\gamma + 1} \right) \left(f_0'' + \epsilon(f_1'' + K_1 f_0'') + \epsilon^2 (f_2'' + K_1 f_1'' + K_2 f_0'') + \epsilon^3 (f_3'' + K_1 f_2'' + K_2 f_1'' + K_3 f_0'') + O(\epsilon^4) \right) \right\}_w \tag{37}$$

Typical results for $\gamma = 5/3$ and $Pr = 0.72$ are shown on Figure 5. If the variation of inviscid stream is neglected, as was done in Ref. 9, the value of the nondimensional heat transfer, for a given M_s, will be that corresponding to $\zeta^{1/2} = 0$ for all ζ. The results of Figure 5 shows, therefore, that the heat transfer is increased for given x, as the pressure is increased due to the entrainment of mass by the boundary layer.

VI. SHOCK TUBE TEST TIME

According to ideal shock tube theory without boundary layers, the test section, the distance between shock and contact surface, increases linearly with time following the diaphragm eruption. The test section, however, for a given time after the diaphragm eruption, is reduced in practice as portions of the shocked gas are continuously being entrained into the boundary layer along x. After a sufficient length of time following the diaphragm eruption, a condition is reached wherein all the gas crossing the shock becomes entrained into the boundary layer by the time the gas reaches the contact surface. No further increase of test section with time is then possible beyond this point, and this determines the maximum obtainable test time.

In the present section, the rate of mass entrainment by the boundary layer will first be determined, along x by the use of the analysis performed hitherto. The results will be compared with those obtained in Ref. 6. The maximum obtainable test section will then be determined for various shock Mach numbers.

(Mass Entrainment by Boundary Layer)

The quantity $\bar{\delta}$ is the ratio of the mass flow entrained into the boundary layer at any location downstream of the shock to that mass flow which has entered through the shock. It is defined as

$$\bar{\delta} = 1 - \frac{\rho_e u_e}{\rho_{e0} u_{e0}} = \sum_{n=0}^{\infty} \epsilon^{n+1} G_n \qquad (38)$$

with the aid of the series for ρ_e/ρ_{e0} and u_e/u_{e0}. Since ϵ is related to ζ from Equation (36), the above equation gives $\overline{\delta}$ as the function of ζ. Note that the maximum test section is reached when $\overline{\delta} = 1$.

Both numerical results, from the present analysis, Equation (38) shown as circles, using the first four terms of the series, and from Ref. 6, are plotted in Figures 6 and 7 for various shock Mach numbers. It is seen that the approximate results of Ref. 6 agree with the present solutions very well for high shock Mach numbers. The figure shows, however, that the present results give much larger values of $\overline{\delta}$, for given $\zeta^{1/2}$, than those predicted in Ref. 6 when the Mach number is low. The discrepancy between the results of the two analyses, in fact, increases rapidly as the Mach number decreases below about 2. Therefore, at the low Mach numbers, the present solution predicts much smaller test sections, and hence, much smaller test times, than those predicted previously.*

Because the present solutions of the governing equations are obtained in series form, in terms of ζ, it is only for a few cases which the solutions can describe the flow completely across the maximum test section that is for $\overline{\delta} = 1$. In the following, a method of enhancing the applicability of the present solution will be discussed.

*Concurrently, but independently, Ref. 10 developed an incompressible Momentum Integral solution. It is not discussed here because it is restricted to high M_s and incompressible flow whereas our model treats real shock tube flows.

(Extension of Solution to Large ζ)

As it was mentioned in the beginning of Section II, the rate of mass entrainment is maximum near the shock where ζ is small. This may be ascertained from Figure 6 by recognizing that $\frac{1}{\bar{\delta}}\frac{d\bar{\delta}}{d\zeta}$ which is proportional to the rate of mass entrainment divided by entrainment, decreases with increasing ζ.

Previous experiences with boundary layers have shown that local similarity assumptions are adequate if boundary conditions are provided a priori, along the inviscid stream and the wall, as in conventional boundary layers. In the present case, however, the inviscid stream is continuously being depleted resulting in a continuous change of boundary conditions which is strongly dependent upon what has occurred upstream. Hence, the local similarity is destroyed by the mass entrainment effect incurring deviations of the boundary conditions from the correct ones, especially so for small M_s. Since in the present problem, the similarity of the boundary layer is destroyed by this mass entrainment process, it is important that an exact solution be available for small values of ζ. For large values of ζ, on the other hand, an approximate solution based on some modifications of local similarity principle should be functionally adequate. Therefore, with the present solution which takes care of the most critical region (region of small ζ), as the basis, the following approximate extension of the theory is developed for large values of ζ.

In a similar boundary layer, one finds

$$\bar{\delta} = \zeta^{1/2} G_c \tag{39}$$

where G_c is a constant. However, in the nonsimilar boundary layer treated here, with the aid of Equations (36) and (38), it is found that

$$\bar{\delta} = G_0\zeta^{1/2} + \left(G_1 + \frac{\Gamma_1}{3} G_0\right)\zeta + \left[G_2 + \frac{2}{3}\Gamma_1 G_1 + \left(\frac{\Gamma_1^2}{18} + \frac{\Gamma_2}{2}\right) G_0\right] \zeta^{3/2} + O(\zeta^2) \tag{40}$$

which suggests the following form.

$$\bar{\delta} = \zeta^{1/2} G(\zeta) \tag{41}$$

By analyzing the various terms of Equation (40) it may be shown that, within the region of convergence of Equation (38), $G(\zeta)$ is represented very well as an exponential function, such as

$$G(\zeta) = C_2 e^{C_1 \zeta^{1/2}} \tag{42}$$

By taking the various terms of Equation (40), the best values for C_2 and C_1 may be determined. Values of C_2 and C_1 are shown on Figure 8.

The numerical results obtained in the present analysis, Equations (38) and (41) are shown as Figures 6 and 7. It is interesting to note from these figures the simple function $G(\zeta) = C_2 e^{C_1 \zeta^{1/2}}$ chosen enables the approximate solution, Equation (41), to predict the exact solution accurately for all ζ

within the regions of the convergence of the exact solution*, and Mach numbers. The extension to larger ζ will incur some slight error and can be analyzed once an exact solution is available for the whole range of ζ.

Also shown on Figure 6 are two data points indicated by triangles. These results were taken from Ref. 6 in the form of asymptotic data.

(Maximum Test Time)

For a given shock Mach number, the test time, at a given period of time after the diaphragm eruption, is proportional to the distance between the shock and the contact surface. The maximum test time, τ_M, is hence proportional to ζ_M where ζ_M denotes that value corresponding to $\bar{\delta} = 1$. The various values of ζ_M computed from the present theory and from the analysis of Ref. 6, and also the available experimental data are shown in Figure 6.

Although the present analysis yields an improvement, a vast improvement for decreasing shock Mach number, over that of Ref. 6, it still shows a variance with the experimental data. The present analysis treated the entrainment effect of the boundary layer more accurately than Ref. 6 did. It, however, still did not take into account other nonideal effects such as the mixing at the interface and the real diaphragm opening process (see Ref. 3). Also, the shock speed was treated as being uniform. The collective effect of all these quantities might provide for the remaining deriviation between the present analysis and experimental data.

*The extension to large ζ is taken in the spirit of being somewhat like analytic continuation.

In order to elucidate the difference between the results of the present analysis and those of Ref. 6, the ratio of the maximum test times obtained from the respective analyses is plotted in Figure 9. The mounting disagreement at the lower shock Mach numbers is evident.

VII. CONCLUSION

The effect of the shock-induced laminar boundary layer on the length of flow between the shock and contact surface has been investigated. The inviscid flow-boundary layer problem associated with shock tube flows has been studied. The study was made by first analyzing the most critical region by an exact method, and then extending the result to the rest of the flow region with an approximate method. The study showed that the reductions in shock tube test time are considerably greater than those predicted by previous theories when the shock Mach number is low.

The comparison of the present results with the available experimental data showed that other nonideal effects in addition to the boundary layer effect considered herein, must be also included.

ACKNOWLEDGMENT

The authors thank Dr. F. Meyers for programming the exact solutions of the perturbation equations.

REFERENCES

1. Anderson, G. F., "Shock-Tube Testing Time," J. Aerospace Sci, 26, 3, 184 (1959).
2. Brocher, E. F., "Hot Flow Length and Testing Time in Real Shock Tube Flow," Phys. Fluids 7, 347, (1964).
3. Camm, J. C. and Rose, P. N., "Electric Shock Tube for High Velocity Simulation," Avco-Everett Research Report 136, Avco Corp., Everett, Mass., (July 1962).
4. Duff, R. E., "Shock-Tube Performance at Low Initial Pressure," Phys. Fluids 2 (2), 207-216 (1959).
5. Hooker, W. J., "Testing Time and Contact Zone Phenomena in Shock Tube Flows," Phys. Fluids 4, 1451 (1961).
6. Mirels, H., "Test Time in Low Pressure Shock Tubes," Phys. Fluids 6, 1201 (1963)
7. Mirels, H. "Shock Tube Test Time Limitation Due to Turbulent Wall Boundary Layer," TDR-169(3230-12)TR-3, Aerospace Corporation, El Segundo, California, (1963).
8. Roshko, A. "On Flow Duration in Low-Pressure Shock Tubes," Phys. Fluids 3, 835 (1960).
9. Mirels, H. "Laminar Boundary Layer Behind a Strong Shock Moving into Air," NASA TN D-291, (1961)
10. Mirels, H. and King, W. S., "Incompressible Momentum Integral Boundary Layer Solution Relating to Shock Tube Test Time," Aerospace Corporation Report No. TDR-469(5240-10)-3, (1964).

Table I

$\gamma = 5/3, \quad Pr = 0.72$

	M_s				M_s		
	1.067	1.34	1.6	1.73	3.0	4.0	∞
u_w/u_{e0}	1.1000	1.5000	1.8417	2.000	3.0000	3.3684	4.0000
M^2_{e0}	0.8824	0.6000	0.4712	0.4286	0.2727	0.2405	0.2000
G_0	0.133620	0.552804	0.830290	0.943860	1.53395	1.71521	1.99708
G_1	1.20497	1.33217	1.48243	1.55589	2.02334	2.19044	2.46842
G_2	-2.51512	0.0967892	0.859271	1.16261	2.91181	3.53996	4.62412
G_3	38.7098	4.76710	4.18457	4.36163	7.26043	8.72176	11.5510
K_1	-1.13577	-1.38201	-1.570100	-1.65175	-2.10919	-2.25837	-2.49635
K_2	2.84726	0.680470	0.319040	0.200371	-0.355547	-0.526214	-0.800545
K_3	-46.3532	-5.35314	-4.06237	-3.93937	-4.62025	-5.08954	-5.99706
K_4	841.827	21.8404	8.96542	-0.189738	-0.189738	-1.98194	-5.03553
F_0''	-0.0822861	-0.457778	-0.831227	-1.01906	-2.39732	-2.97996	-4.06222
H_0'	-0.00648676	-0.0398770	-0.0759351	-0.0946012	-0.236381	-0.297623	-0.412395
F_1''	-1.52240	-2.53081	-3.73929	-4.40792	-10.2461	-13.1061	-18.3044
H_1'	-0.112823	-0.168427	-0.229368	-0.261999	-0.535798	-0.666974	-0.930672
F_2''	2.95979	-2.79659	-6.65896	-8.85621	-30.9635	-43.3092	-70.5515
H_2'	0.318233	-0.00984224	-0.1510316	-0.225862	-0.945679	-1.34152	-2.21087
F_3''	-82.5631	-17.4331	-27.4456	-35.2390	-134.742	-198.449	-350.854
H_3'	-6.59894	-1.14986	-1.49391	-1.82275	-6.16549	-8.93536	-15.5210

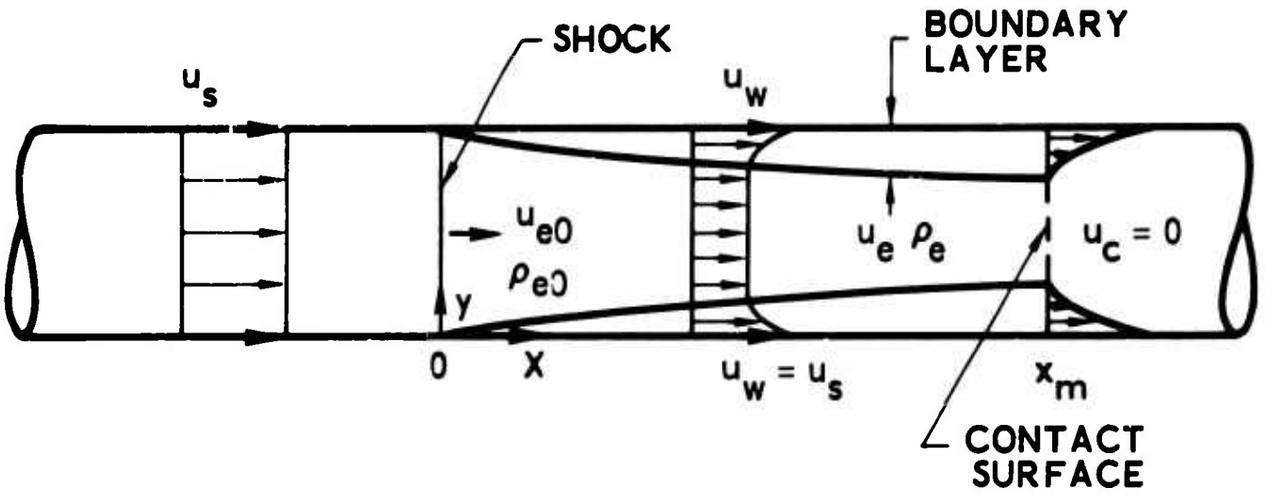


Figure 1. Shock-Fixed Coordinate System, Maximum Separation Distance Shown

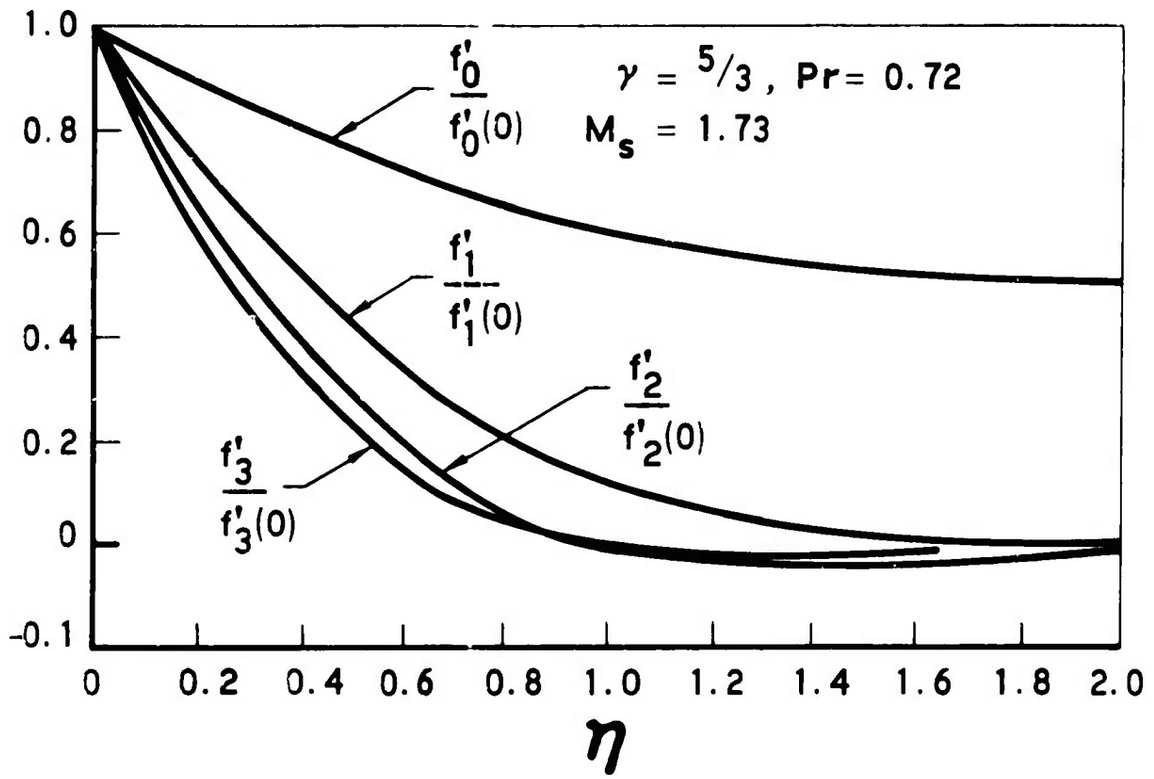


Figure 2. Velocity Profile Perturbations

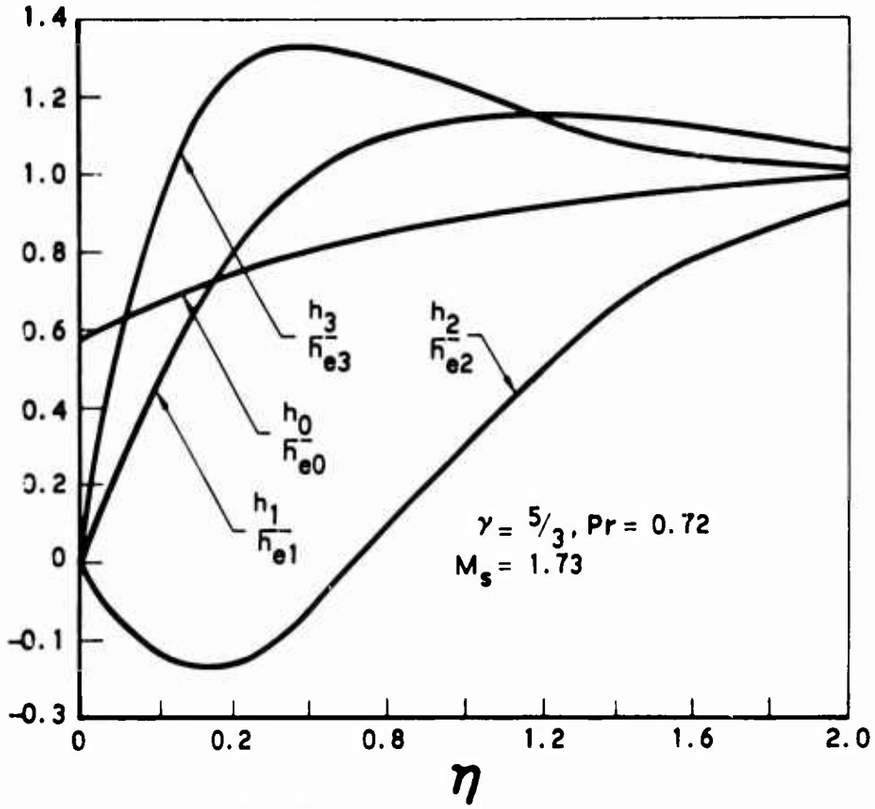


Figure 3. Static Enthalpy Perturbations

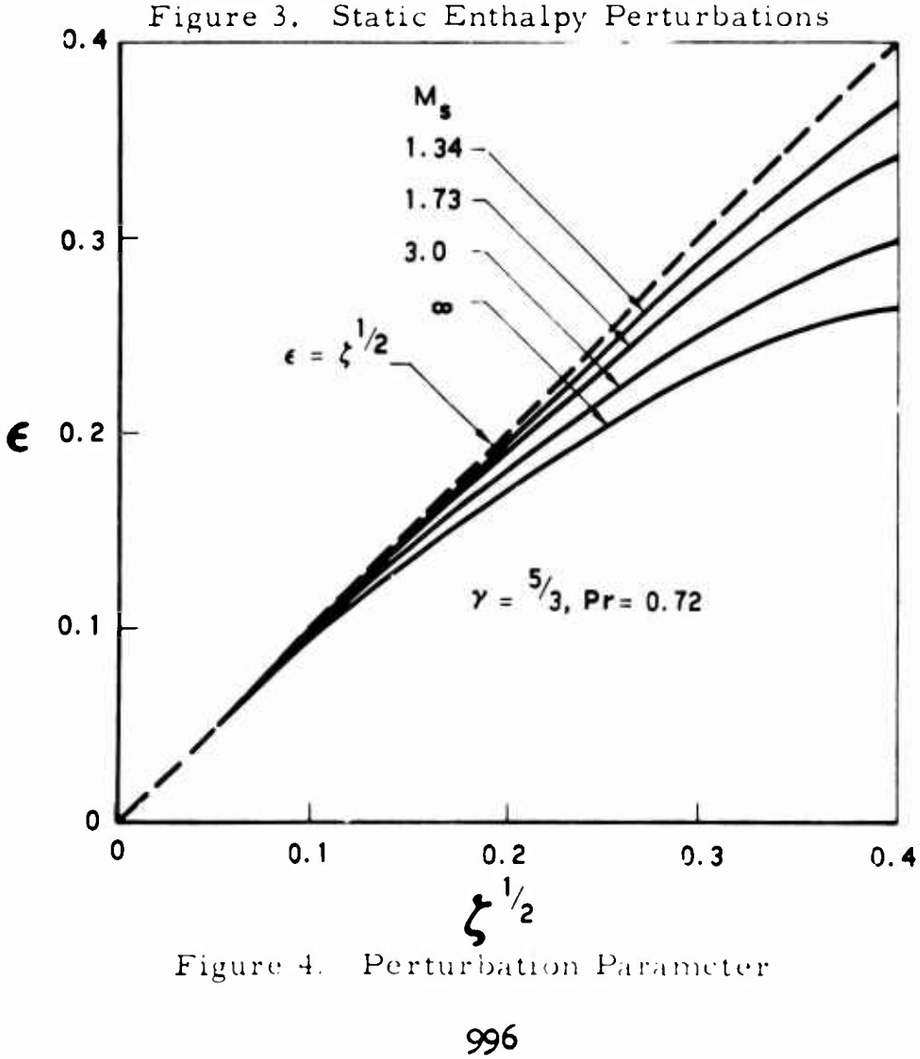


Figure 4. Perturbation Parameter

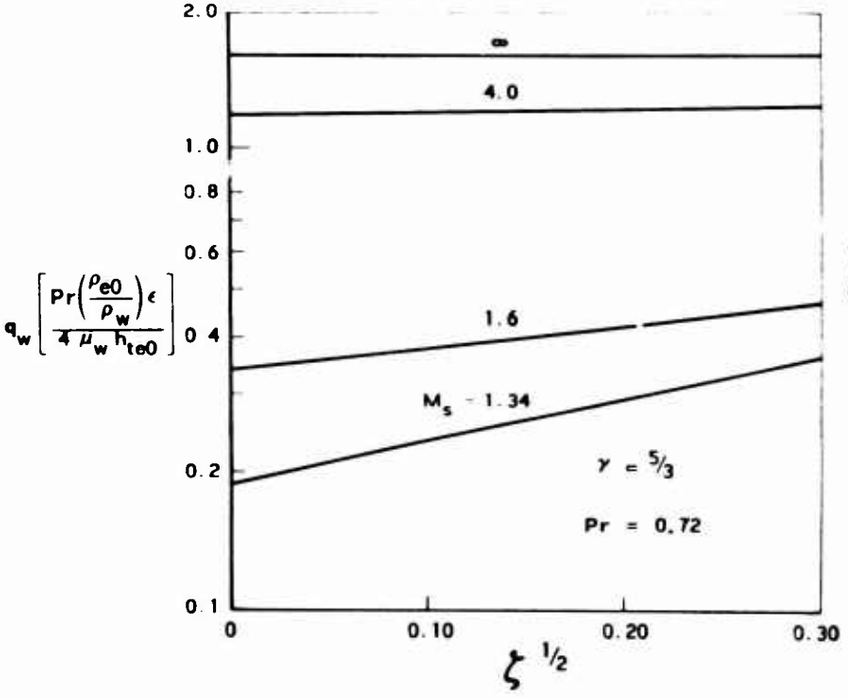


Figure 5. Local Heat Transfer

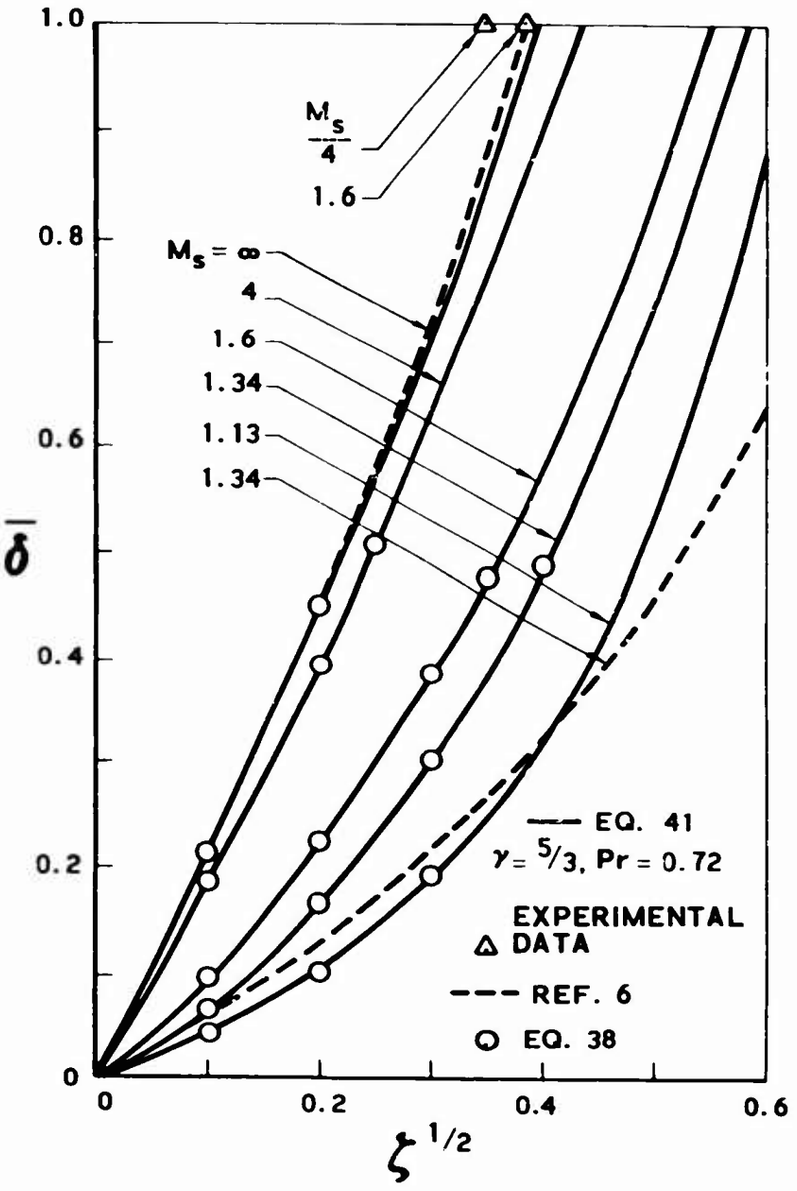


Figure 6. Mass Flow Entrainment and Experimental Data

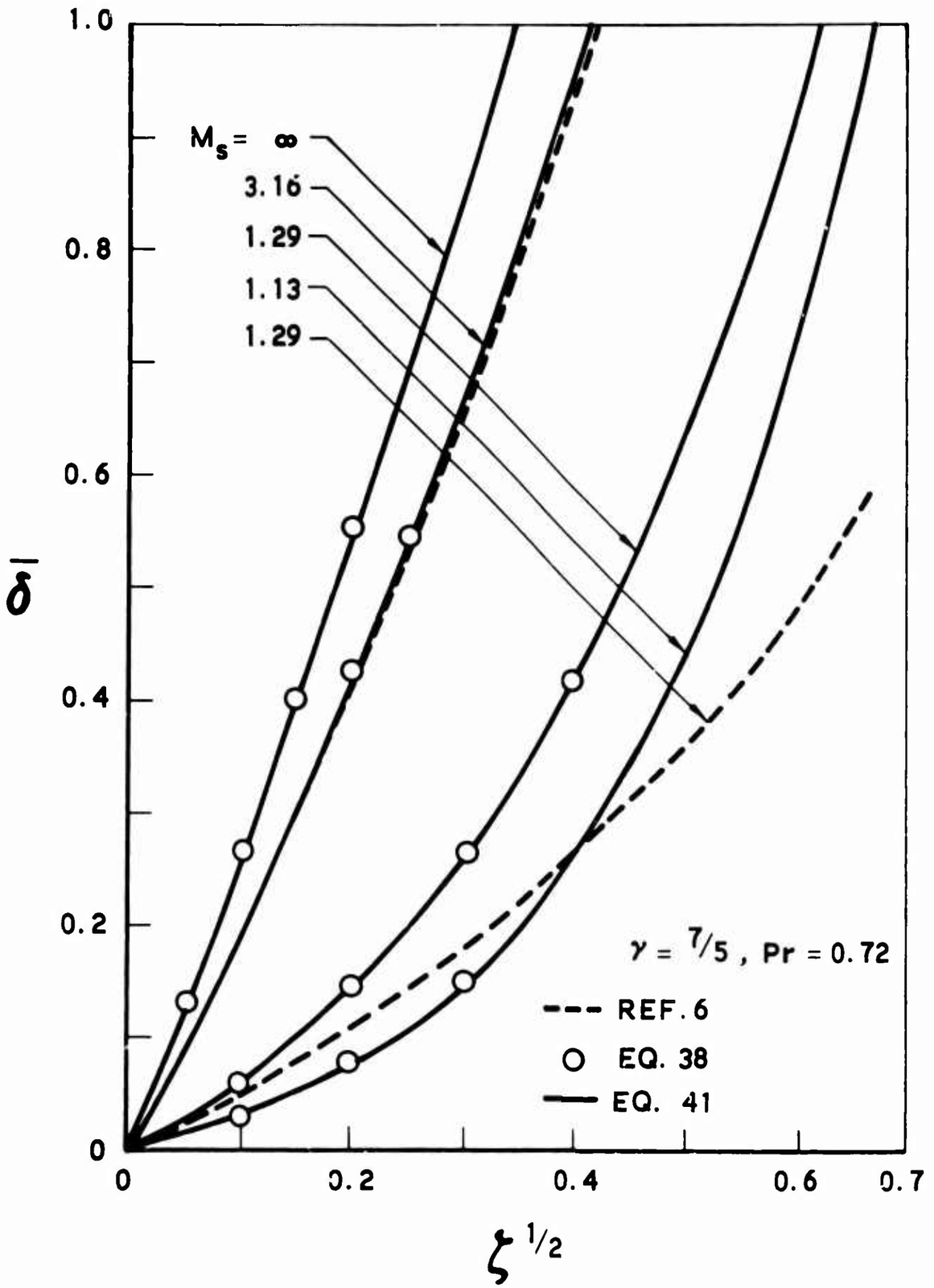


Figure 7. Mass Flow Entrainment

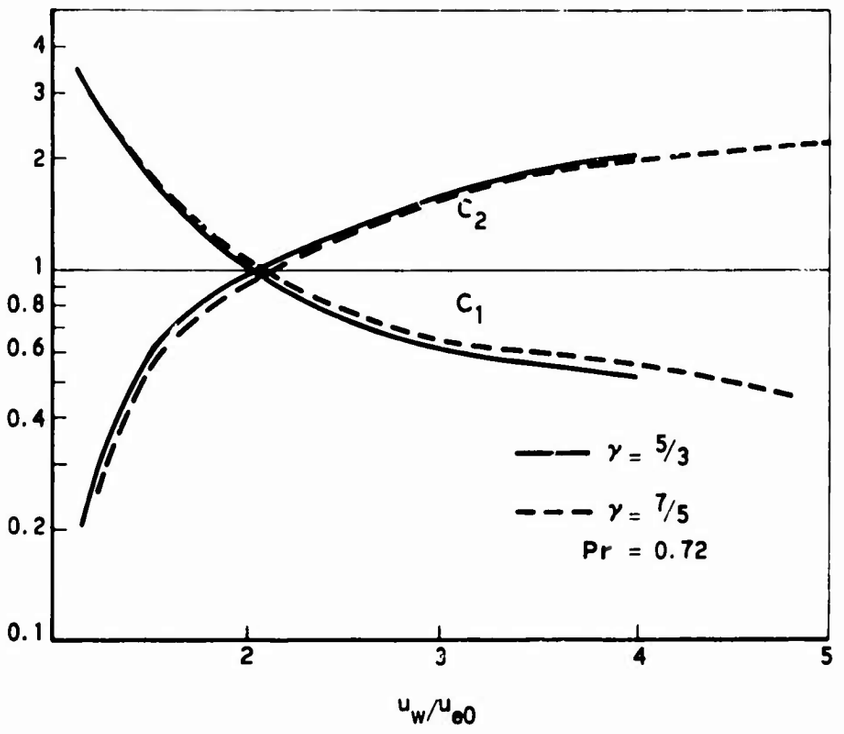


Figure 8. Coefficients of Equation (42)

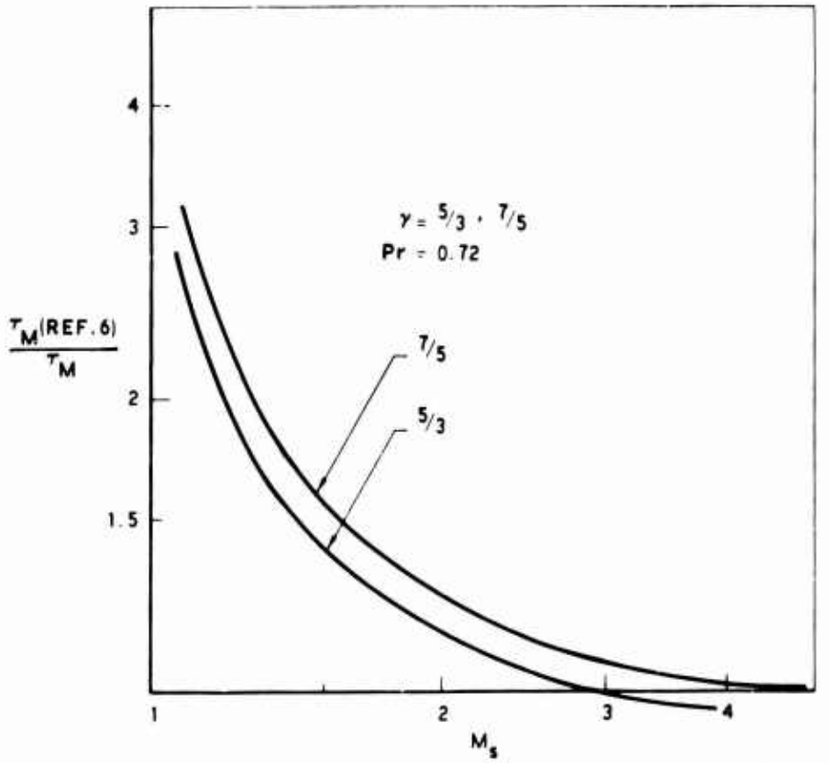


Figure 9. Maximum Test Time Compared to Ref. 6

BLANK PAGE

STRESS JUMP ANALYSIS METHODS FOR SHOCK WAVES

Norman Davids
Pennsylvania State University
University Park, Pa.

and

Meir Ben-Amoz
General Electric Co.
Valley Forge, Pa.

INTRODUCTION AND STATEMENT OF PROBLEM

The stress jump method replaces the problem of continuous interaction between a uniform shock and an overtaking rarefaction wave by a series of discrete interactions between two(possibly infinitesimal)shocks. This is achieved by replacing the actual equation of state by one made up of a series of polygonal lines. The effect is to reduce the simple wave region behind the shock to several constant-state regions separated by weak shocks across which one may apply either the mechanical shock conditions or equivalently the characteristics relations. It is always possible to cross from one constant-state region to a neighboring one through a weak shock by proper approximation in the equation of state. The advantage is that the entire process of interaction may be reduced to a series of interactions between two shocks of different strength. This is one of the most elementary processes of interaction, see (3) p.166. In the case of moderate shocks, the interaction gives rise to a reflected and transmitted shock with a constant state between them. If, however, strong shocks are considered with appreciable entropy changes behind the curved shock, the elementary interaction gives rise as in the previous case, to a reflected and transmitted shock as well as a contact discontinuity between them. Across the discontinuity, the pressure and particle velocity are continuous but density and entropy are discontinuous. One may still apply the shock conditions to the computation of flow parameters by adding a third shock relation, expressing energy conservation, to the two mechanical shock relations.

By using an analysis which is discrete to begin with, as done in this paper, one is led more easily and efficiently to the implementation of

the method to obtain results through either computer use or graphical procedures. The usual difficulties associated with numerical stability or artificial viscosity do not arise with this method. Another advantage of such a procedure is that it lends itself, unlike some other methods, to a transition to elastoplastic wave propagation theory when shock strength has sufficiently decayed to invalidate hydrodynamic theory. Some problems of this type were treated by Kumar and Davids in (1). The types of pulses considered here are a rectangular pulse and a finite initial pressure jump followed by a gradual unloading of arbitrary shape. In addition, we treat the case of a semi-infinite solid to which thermal energy from some external source is suddenly added. The instantaneous temperature gradient resulting from the sudden addition of energy gives rise to initial 'constraining' pressures from which the solid is subsequently relaxed. It is found that a shock is initiated within the solid, progressing a considerable distance without attenuation.

Chou (2) has treated a problem in hypervelocity impact by analytical and field procedures. Fowles (5) worked out an expression for plane shock decay for a certain equation of state.

2. BASIC THEORY

If the pressures applied to a solid far exceed the yield strength, compressibility effects predominate. The material response can then be analyzed, at least during the early phase of pressure attenuation, on the basis of a compressible inviscid fluid model. By using the Murnaghan equation of state

$$p = A\cdot\left[(\rho/\rho_0)^{\gamma} - 1\right] \tag{2.1}$$

which is widely accepted for solids, the characteristics relations equivalent to the one-dimensional equations of mass and momentum conservation are:

$$(2/\gamma - 1)\cdot\bar{c} + \bar{v} = 2r \quad \text{along } dx/dt = c+v \tag{2.2}$$

$$(2/\gamma - 1)\cdot\bar{c} - \bar{v} = -2s \quad \text{along } dx/dt = c-v \tag{2.3}$$

where $\bar{c}=c/c_0$, $\bar{v}=v/c_0$ are dimensionless sound velocity and particle velocity, c_0 being the zero pressure sound velocity and r,s are the Riemann invariants.

Wherever the flow is continuous, relations (2.2), (2.3) are valid. But at shock fronts they must be replaced by the mechanical shock relations

$$\rho_0(v_0 - U) = \rho_1(v_1 - U) = m \tag{2.4}$$

$$p_0 + \rho_0 v_0(v_0 - U) = p_1 + \rho_1 v_1(v_1 - U) \tag{2.5}$$

U being the shock velocity and subscripts o,1 refer, respectively, to the states ahead and behind the shock. The third shock relation, expressing energy conservation, becomes redundant in isentropic flow and serves merely to compute energy conversion into heat after the problem has been solved.

3. DISCONTINUOUS THEORY FOR PROBLEM

In most analyses one proceeds from a mathematical analysis to a numerical method to a computer code. In some problems it is possible-in fact, advantageous- to bypass the intermediate steps and build the code directly on the statement of the basic physical principles for the problem. Since the stress-jump method is already formulated in finite form, it lends itself to direct coding. The advantage is that the method becomes, within wide limits, independent of any particular equation of state or pulse shape, and thus is an approach to a more general solution. The medium is at present assumed to be semi-infinite. Later, reflections from free boundaries will be included.

We start by dividing the medium into elements of fixed density levels, as shown in Fig.1a. In moderate shock theory for solids, unlike the analysis of plastic waves, we consider density changes as primary. If these discrete density levels have the values $\rho_0, \rho_1, \ldots \rho_n$ then a set of points are determined in the medium, given by

$$x_j = x(\rho_j) \qquad j= 1,\ldots m \tag{3.1}$$

These levels or contours move through the medium as a function of time. The aim of the method is to keep track of these points. In effect, this method interchanges the role of density level and distance by making the former as independent variable. The corresponding pressure levels are determined from the point by point equation of state

$$p_j = f(\rho_j) \qquad j= 1,\ldots n \tag{3.2}$$

If a shock is moving into the j-th state(the state ahead) it becomes converted into the (j+1)-th state (the state behind). The shock speed relative to the medium ahead is given by

$$c = \left[(p_{j+1}- p_j)\rho_{j+1}/ (\rho_{j+1}- \rho_j)\rho_j\right]^{\frac{1}{2}} \tag{3.3}$$

i.e., c is the velocity of the shock as seen by an observer moving with the velocity v_j in the state ahead. (This expression applies for either a finite or infinitesimal jump). If the j-th element is at rest, then c is the true or absolute shock speed. In the latter case, however, for $p_{j+1} \to p_j$ and $\rho_{j+1} \to \rho_j$ this reduces to $c= (dp/d\rho)^{\frac{1}{2}}$, the relative local speed of sound.

A. Momentum Balance

If the shock advances into state j with this velocity, it is displaced during the time interval dt, a distance

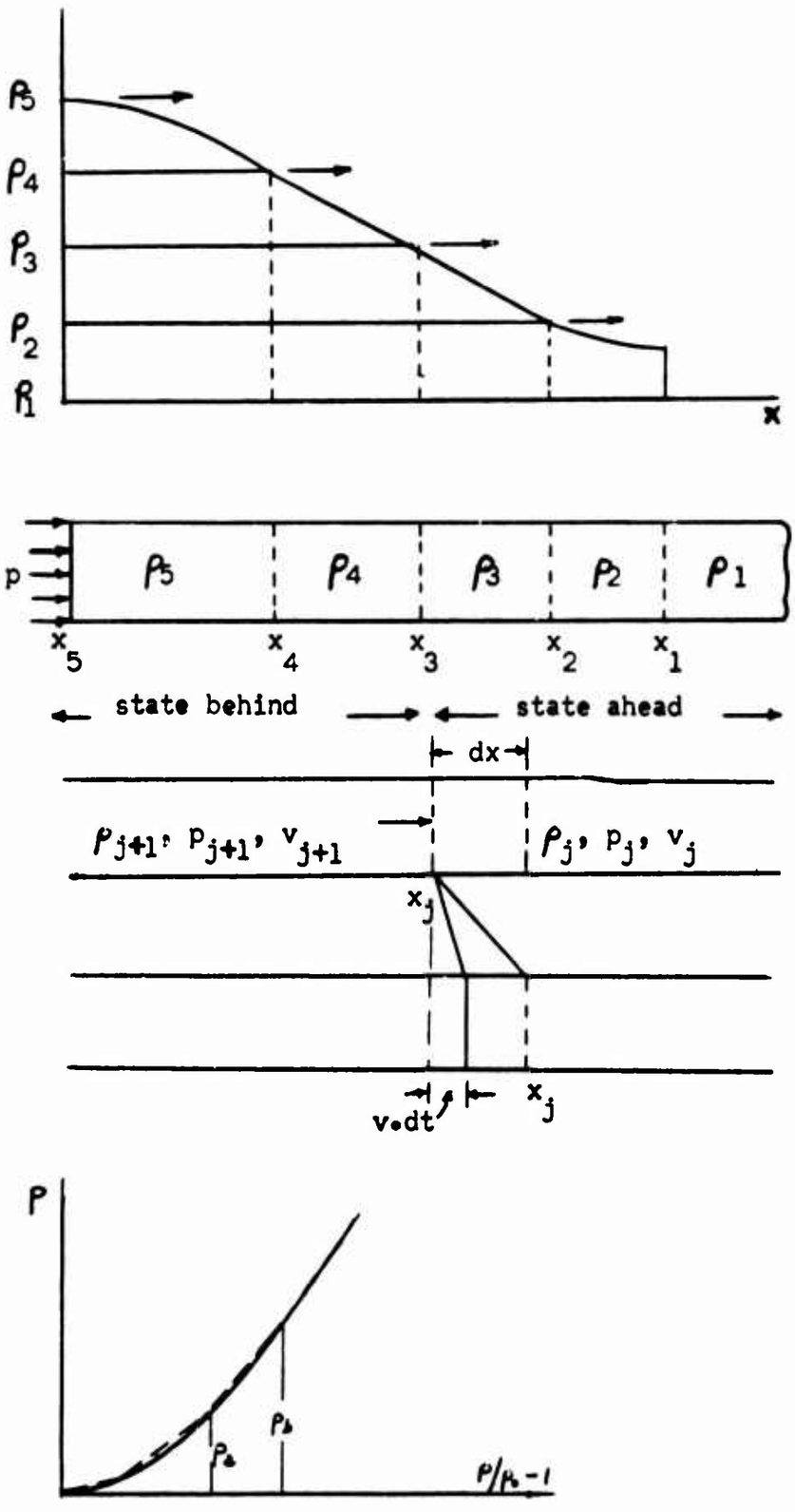


Fig. 1 Basic Geometry For Shock Propagation

$$dx = c \cdot dt \tag{3.4}$$

as shown in Fig.1c. Hence, the amount of material which has been converted from state j to state j+1 is

$$dm_j = \rho_j \cdot dx \cdot A = \rho_j \cdot cA \cdot dt \tag{3.5}$$

The velocity of this material has been changed from v_j to v_{j+1}, hence the momentum change, equated to the net impulse is

$$(v_{j+1} - v_j)dm = (p_{j+1} - p_j)Adt \tag{3.6}$$

solving for the velocity gradient $dv = v_{j+1} - v_j$ we have

$$dv = (p_{j+1} - p_j)Adt/dm \tag{3.7}$$

$$v_{j+1} = v_j + dv \tag{3.8}$$

These constitute the first of the Rankine-Hugoniot conditions in the form incorporated into the method.

B. Mass Balance(continuity relation)

From (3.5) the mass dm as seen from behind the shock is given by

$$\rho_{j+1}(c + v_j - v_{j+1})Adt = \rho_j \cdot cAdt \tag{3.9}$$

Of course, since c'=c this relation is redundant if we already have used the shock speed relation (3.3). We have thus two alternative ways of computing c. It has been convenient to alternate between them. Actually, this same procedure could be used without essential change for plastic wave propagation. The shock problem requires one additional feature arising from the fact that higher density levels would overtake the lower levels, resulting in a distribution which would not be single-valued. To prevent this, the method must allow the (j+1)th state to be skipped, and so on, so that a single jump from the ground state to the full compression is attained at once. In this logic a computer would automatically 'discover' that a shock exists directly from the physical principles. Results showing pressure attenuation vs. depth are shown in Fig.2.

By way of comment, we note that (3.6) is formally a finite difference relation. However, in actual practice this is not the method of finite differences whose central idea is the replacement of derivatives by finite expressions. The numerical analysis by finite differences requires a study as to which of the many types of difference procedures give stable and accurate results. It is at this point that artificial viscosity usually enters the problem. In the present approach, statements obtained directly from physical relations are exact when applied to the finite elements which have been introduced into the problem.

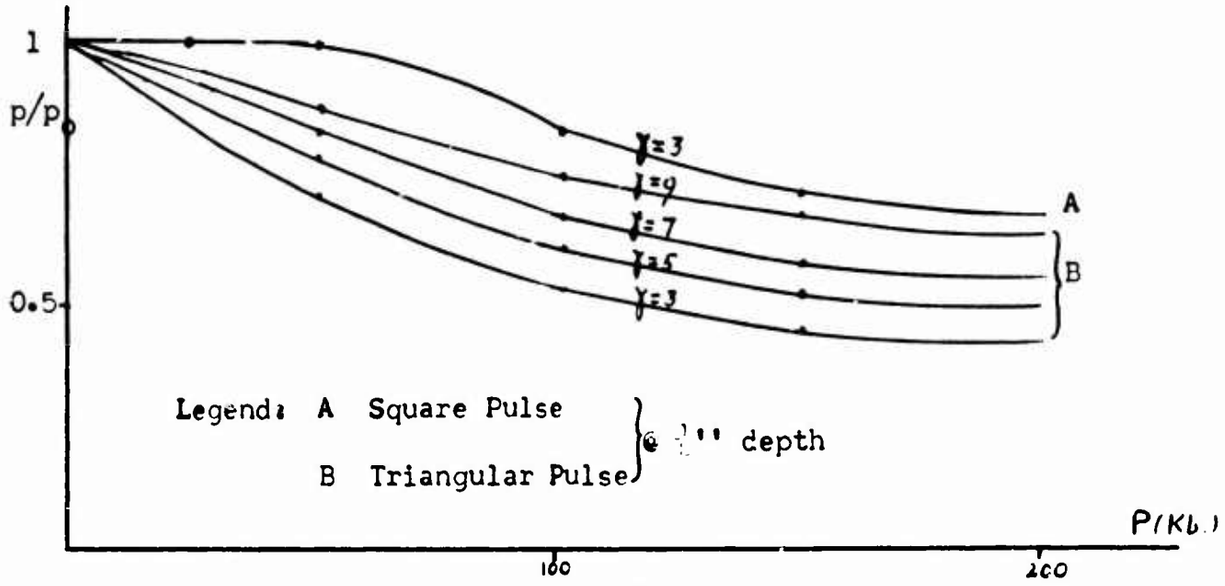


Fig.2 - Shock Attenuation for ¼ μs. Pulse.

4. ALTERNATE TREATMENT OF SHOCK ATTENUATION

Consider again the case of a rectangular pulse. Suppose that the actual equation of state is replaced by a series of chords as in Fig.1d. The effect of this approximation is that all pressure levels between p_a and p_b, for example, have a common (local) sound velocity given by the slope of the chord. We can now treat the interaction problem as follows. Referring to Fig.3, the unloading phase is replaced by a series of step unloadings. To each pressure reduction there will correspond a constant sound velocity measured by the slope of the corresponding chord in Fig.1d. By selecting sufficiently small pressure decreases, it is clear that all pressure levels within a given step are propagated with the same velocity. This means that the complete process of unloading can be represented by a sequence of weak unloading shocks, each separating adjacent constant state regions. It is known (ref.3) that the Riemann invariant through a weak shock remains constant, which means that relation (2.3) is valid. Since the state ahead and the sound velocity behind the shock are given, relation (2.3) determines the particle velocity behind the shock. The shock velocity is then computed from the relation

$$U = \tfrac{1}{2}\left[(c_1 + v_1)+(c_2 + v_2)\right] \qquad (4.1)$$

which is the average sum of sound and particle velocities on both sides of the shock. The interaction process can now be analysed on the basis of a single elementary interaction. It is known(ref.3) that if a shock is overtaken by another shock the interaction results in a reflected shock, a transmitted shock and a contact discontinuity between them (Fig.4). Across the contact discontinuity both pressure and particle velocity are continuous but density and entropy are discontinuous. If, however, the flow is assumed to be isen-

tropic the contact discontinuity disappears and the two shocks can be determined from the mechanical shock relations alone. If shock B (Fig 4) is much

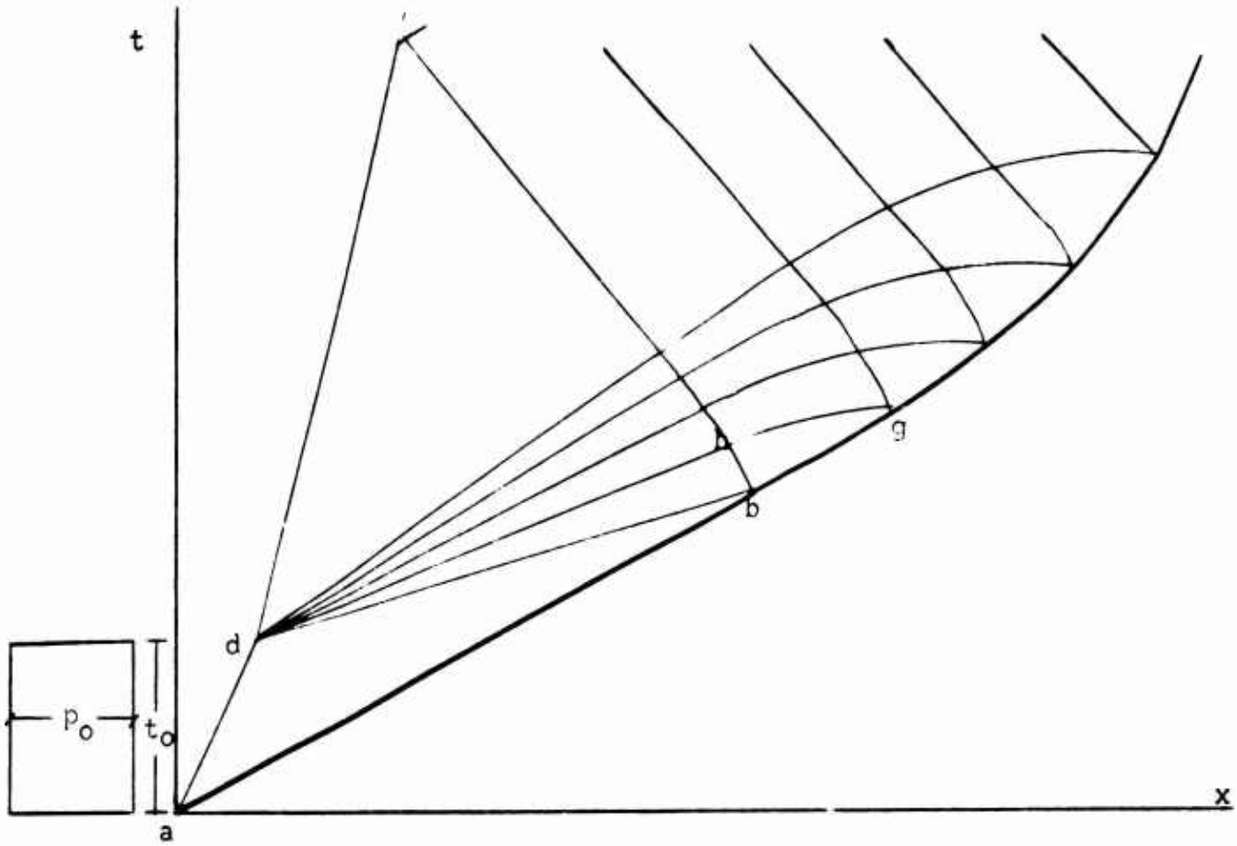
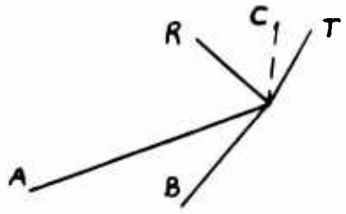


Fig. 3 - Characteristics Regions for a Rectangular Pulse.

weaker than shock A, the reflected shock R is also weak and relation (2.2) can be used. The advantage of such an approach becomes apparent when shock A and consequently the transmitted shock T are strong which invalidates the assumption of isentropic flow. One can then apply relation (2.2) across shock R and use the three Rankine-Hugoniot relations across shock T. This is equivalent to the assumption that entropy changes are confined to the region bounded by shock T and the line C. In the case of a rectangular pulse, (Fig 3) the interaction between b-d and a-b results in shock b-h (reflected) and b-g



T-transmitted shock
R-reflected shock
C-contact discontinuity

Fig. 4 - Interaction Between Two Shocks

(transmitted). The state within b-d-h is completely determined from relation (2.2). The state within b-g-h and the shock velocity along b-g can be computed from (2.1) and the two shock relations. Considering an arbitrary segment y-z along the curved shock opposite the simple wave region γ^*-γ^* such computations lead to the simple relation

$$(2/\gamma-1)\cdot\tilde{c}_{yz} + \left[1/\gamma\,(1 - \tilde{c}_{yz}^{-2/\gamma-1})(\tilde{c}_{yz}^{2\gamma/\gamma-1} - 1)\right]^{\frac{1}{2}} =$$

$$(2/\gamma - 1)(2\cdot\tilde{c}^{*}_{yz} - \tilde{c}_{A}) + \left[1/\gamma(1 - \tilde{c}_{A}^{-2/\gamma-1})(\tilde{c}_{A}^{2\gamma/\gamma-1} - 1)\right]^{\frac{1}{2}} \tag{4.2}$$

from which the sound velocity behind the shock can be determined. The pressure can then be computed from the relation

$$p/\rho_o c_o^2 = 1/\gamma\,(\tilde{c}^{2\gamma/\gamma-1} - 1) \tag{4.3}$$

In (4.2), $\tilde{c}_{yz}$ is the sound velocity behind the shock segment y-z and $\tilde{c}^{*}_{yz}$ is the sound velocity in the simple wave region opposite y-z. $\tilde{c}_A$ is the maximum sound velocity behind the uniform shock.

The analysis of a triangular pulse is completely similar. The shock attenuation vs. depth is shown in Figs. 5a,5b for a rectangular pulse and in Fig.6 for a triangular pulse.

5. THE SEMI-INFINITE SOLID SUBJECTED TO SUDDEN ENERGY ADDITION

Suppose that energy from some extraneous source is suddenly added to a solid resulting in an instantaneous temperature gradient over some depth. We assume that the temperature gradient is maintained indefinitely thereafter which is justified if temperature relaxation times associated with heat conduction are much longer than the times involved in shock attenuation. The formulation of this problem is again based on the one-dimensional equations of mass and momentum conservation, except that the Murnaghan equation of state (2.1) is modified to account for the entropy increase resulting from the addition of energy. Instead of (2.1) we take as an equation of state

$$p = A\cdot\left[(\rho/\rho_o)^{\gamma} - 1\right] + \rho\cdot c_s^2(s-s_r) \tag{5.1}$$

where the second term provides the necessary correction and is a function of the entropy increase over some reference entropy s_r. This function can be determined experimentally, since from (5.1) the sound velocity is

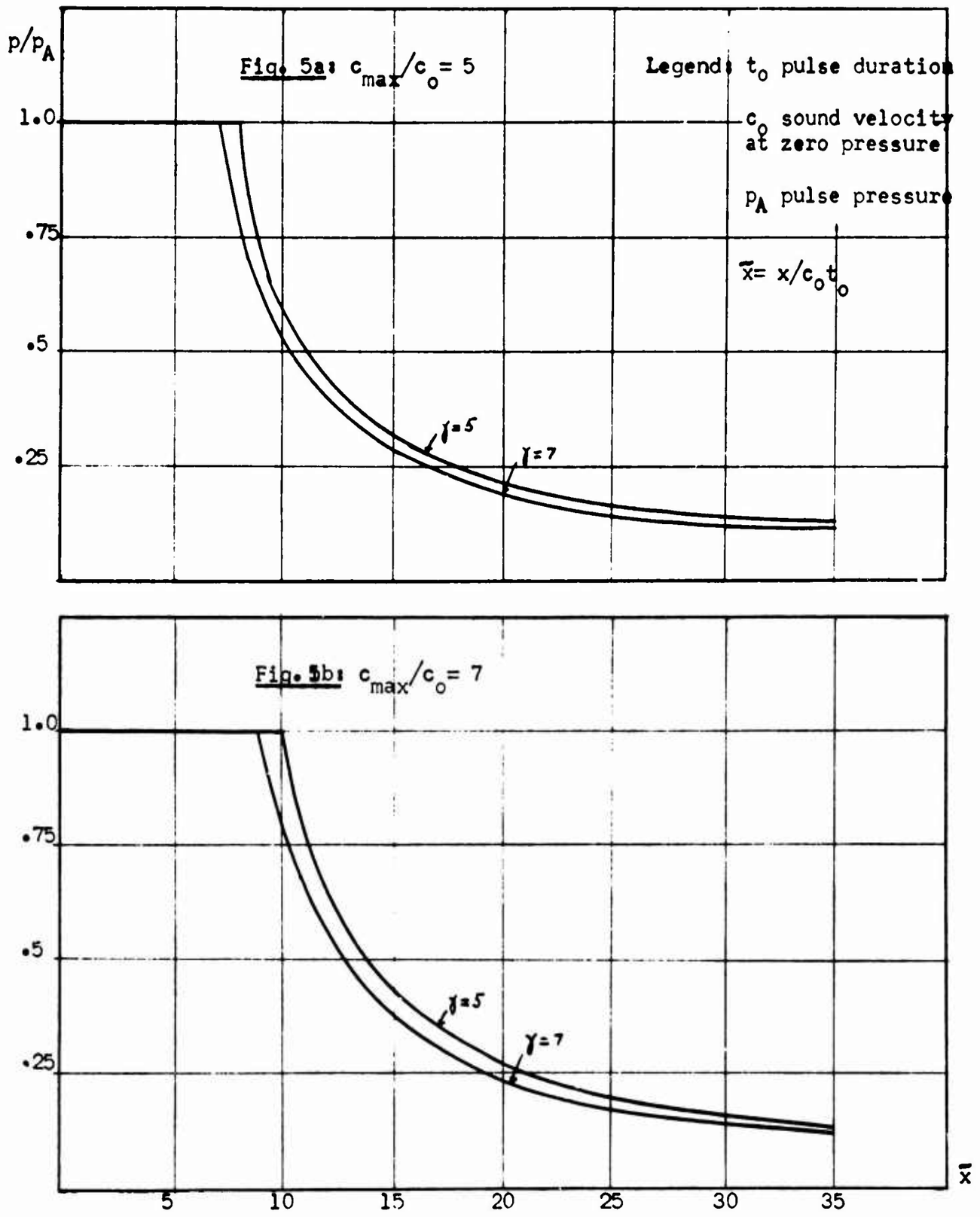


Fig.5- Shock Pressure Attenuation vs. Penetration Depth(Rectangular Pulse)

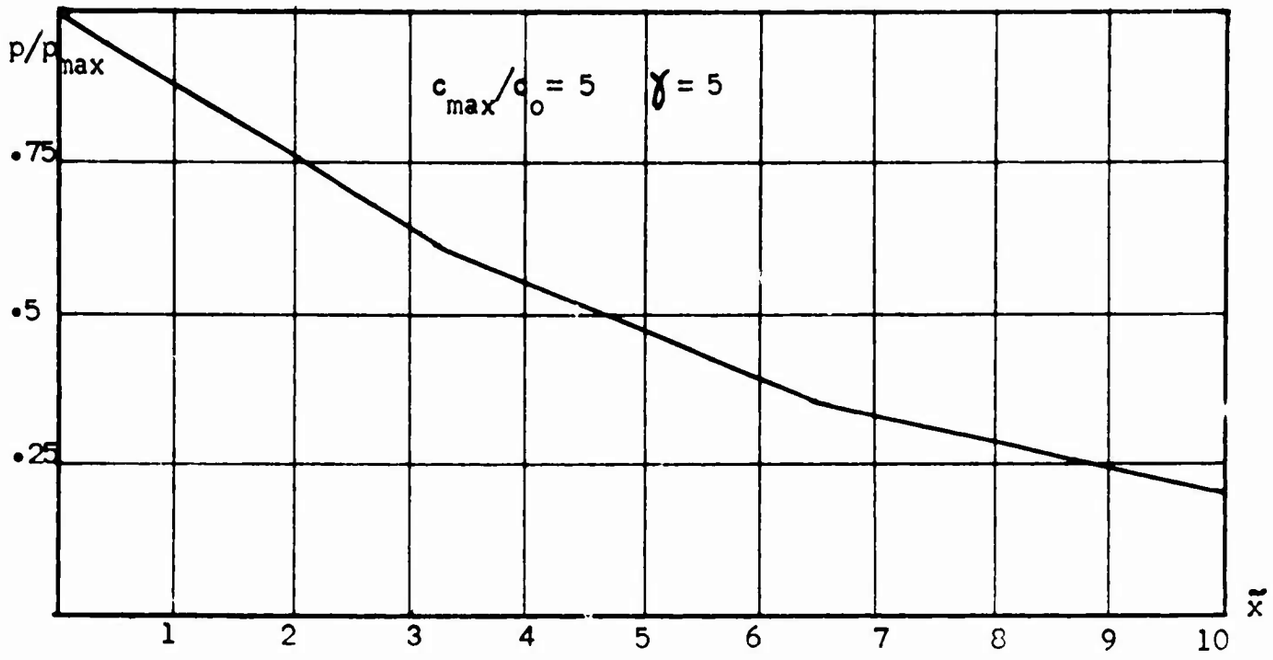


Fig. 6 - Shock Pressure Attenuation vs. Penetration Depth(triangular Pulse)

$$\bar{c}^2 = (\rho/\rho_o)^{-1} + \bar{c}_s^2 \qquad (5.2)$$

where $\bar{c}_s = c_s/c_o$

If the sound speeds are measured at various entropy(or temperature) levels and at room temperature, the value of c_s can be computed from (5.2).

Using the modified equation of state, the characteristics relations corresponding to the mass and momentum conservation equations are

$$(2/\gamma-1)\left[\bar{c} + \bar{c}_s \log(\bar{c}-\bar{c}_s/\bar{c}+\bar{c}_s)^{\frac{1}{2}}\right] + \bar{v} = 2r \quad \text{along } dx/dt = c+v \qquad (5.3)$$

$$(2/\gamma-1)\left[\bar{c} + \bar{c}_s \log(\bar{c}-\bar{c}_s/\bar{c}+\bar{c}_s)^{\frac{1}{2}}\right] - \bar{v} = -2s \quad \text{along } dx/dt = c-v \qquad (5.4)$$

The formulation of initial conditions is based on the assumption that the initial heating takes place through an isovolumetric process in which case (5.1) gives the initial 'constraining' pressure distribution

$$p = \rho_o c_s^2 \qquad (5.5)$$

Another initial condition is $\bar{v}=0$ since the solid is initially at rest.

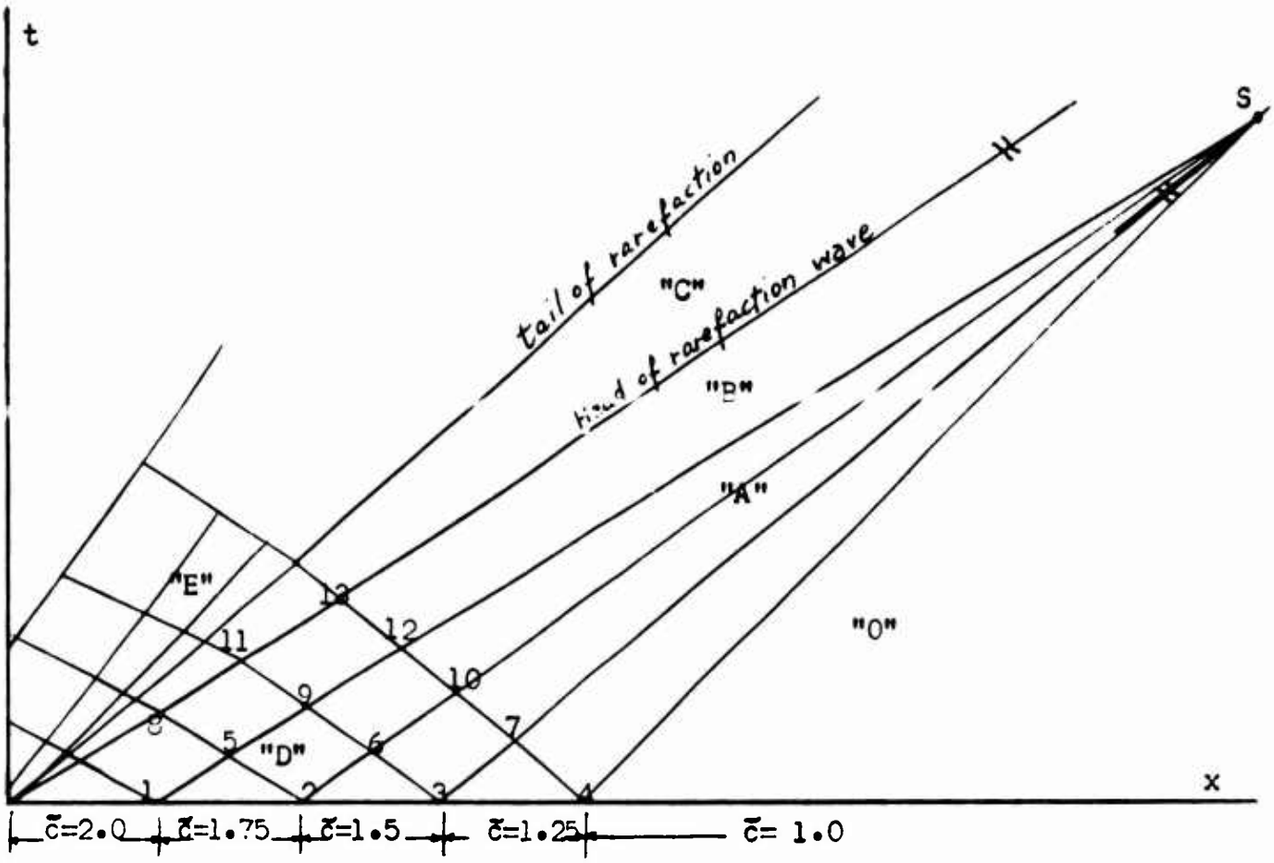


Fig.7- Characteristics Regions for Instantaneous Energy Addition.

If the function c_s is given, relations (5.3), (5.4) together with the initial conditions are sufficient to construct the complete solution. However, since no experimental data is available at present, it is necessary to ignore the logarithmic terms in the characteristics relations. We feel that such an approximation would not alter our conclusions which are based on equations (2.2) and (2.3). Fig. 7 shows the characteristics regions associated with this problem. As initial pressures we assume a distribution corresponding to the shown sound variation. Such a distribution would tend in the limit to a continuous distribution as the number of intervals increases indefinitely.

Using the previous procedure, the solution is constructed starting from stations o-4 along which the initial data is given. In region D, forward and backward facing weak shocks emanating from two neighboring stations interact. From station "o" a rarefaction wave is started which is soon distorted by the backward facing shocks emanating from the line t=0. If the solution is continued beyond the line 4-13 it is found that all forward shocks converge at point S. The region "A" is then a simple compression wave centered at S, where a shock is initiated. The shock velocity is given by the average sum of sound and particle velocities in regions "o" and "B". At the same time, the rarefaction wave emerges, due to interaction in region "E", confined to

region "C". The head of this wave is found to be moving at nearly the shock velocity, which means that interaction with the shock will begin only after a considerable length of time. For practical purposes, it can be concluded that shock attenuation does not occur at all.

REFERENCES

1. Kumar,S. and Davids, N.,"Elastic-Plastic Analysis of Scabbing in Materials" Jour. Franklin Inst. 265, No.5, May 1958, pp. 371-383.
2. Chou,P. Sidhu, H. and Zajac, L. "The Strong Plane Shock Produced by Hypervelocity Impact and Late Stage Equivalence" DIT Report 125-6, Drexel Institute of Technology, Oct.1964.
3. Courant,R. and Friedrichs, K. "Supersonic Flow and Shock Waves", Interscience,N.Y.1948.
4. Davids,N. and Mehta, P. "Computer Analysis Methods for Stress Waves and Spherical Cavities", Final Technical Report, Pa.State Univ.,Nov.30.1964.
5. Fowles, G.R., "Attenuation of the Shock Wave Produced in a Solid by a Flying Plate", J.Appl.Phys. 31-4, April 1960, pp.655-661.

LAMINAR BOUNDARY LAYER BEHIND A VERY STRONG SHOCK MOVING INTO NITROGEN

Nelson H. Kemp* and Tzu-Chung Moh
Massachusetts Institute of Technology
Cambridge, Massachusetts

ABSTRACT

The laminar wall boundary layer behind a very strong shock advancing into nitrogen has been considered. Numerical results have been obtained for shock speeds from 4 to 12 mm/μsec, extending considerably the range of available results, which had been limited to less than 6.5 mm/μsec. Not only is nitrogen dissociation included, but also ionization at the upper end of the speed range. Initial pressures of 1, 0.1 and 0.01 torr were used, and both chemically frozen and equilibrium cases were included. The nitrogen thermodynamic and transport properties were taken from Fay and Kemp (5) with slight modification of the viscosity, and so make use of the binary diffusion approximation to simplify the calculations. Results for displacement thickness, heat transfer and shear stress are presented and compared with previous lower-speed air calculations and correlation formulas (3). Some deviations are found. The primary application of these results is the determination of test time in high speed arc-driven shock tubes (2).

I. INTRODUCTION

As shock tubes are operated at higher and higher shock speeds, the problem of test time comes more and more to the fore. In arc-driven shock tubes, which are now in wide-spread use for making heat transfer and radiation measurements at shock speeds up to 12 mm/μsec, test time is measured in only a few tens of microseconds. It is essential to monitor each run to verify the existence of sufficient time for taking the data. One of the chief considerations in the design and operation of such facilities is obtaining the requisite length of homogenous test gas samples.

---

*Present Address: Avco-Everett Research Laboratory

Modern theories for predicting test gas lengths (1, 2) rely heavily on calculations of the boundary layer on the shock tube wall behind the incident shock. The most extensive existing calculations of this boundary layer at high speeds are those of Mirels (3) and Hartunian and Marrone (4). Mirels has results for air in thermochemical equilibrium behind shocks moving up to 4.8 mm/μsec. He took Lewis number unity, i.e., diffusivity of heat and mass equal, and Prandtl numbers of 0.72 and 1.0. Hartunian and Marrone did calculations in equilibrium oxygen up to 6.5 mm/μsec. They also took the Prandtl number to be 0.72, but allowed the Lewis number to take on the (constant) values 1.4 and 2.0 as well as 1.0.

The purpose of the present work is to extend the range of available shock tube boundary layer calculations up to shock speeds of 12 mm/μsec thereby including both dissociation and ionization, and providing information with which test time estimates can be made for high speed arc-driven shock tubes. The main difficulty in making such calculations is specification of the transport properties in the gas mixture which results from the chemical processes in the high energy boundary layer. However, a set of properties for dissociating and ionizing nitrogen has already been developed for use in a stagnation-point heat transfer investigation (5), and in order to utilize this information, the present study considers nitrogen. The two limiting cases of frozen and equilibrium thermochemical states in the boundary layer are considered, with variable Lewis and Prandtl numbers, and use is made of the binary diffusion approximation (5). Equilibrium is assumed behind the incident shock wave. Thus, in addition to being the first available calculations beyond 6.5 mm/μsec, these are the first to include ionization, and to give numerical results for frozen as well as equilibrium boundary layers.

In addition to the usual boundary layer parameters of shear stress and heat transfer, the displacement thickness is important for determining test time. Mirels (3) has given correlation formulas for these three quantities based on his calculations of boundary layers with Lewis number unity for air in thermochemical equilibrium at shock speeds up to 4.8 mm/μsec. Hartunian and Marrone (4) extended the heat transfer correlation to Lewis numbers different from unity, based on their equilibrium oxygen results, but found the effect extremely small. The present calculations for nitrogen are compared with Mirels' correlation formulas from 4 to 12 mm/μsec and some deviations are found.

The next section of the paper presents the analysis of the high speed shock tube boundary layer in nitrogen, while the third sections presents the results.

II. ANALYSIS

The analysis will follow closely that of the stagnation-point boundary layer in Fay and Kemp (5) with the changes necessitated by the differing geometry and a slight change in the viscosity of the gas mixture. The same notation as in that paper will be used, except the subscript e will denote

the (constant) properties at the edge of the boundary layer, which are those behind the incident shock. The x, y coordinate system denotes distance parallel and normal to the wall in a reference frame fixed to the incident shock, with the origin at the intersection of the shock and the wall, and x measured from the shock toward the driver. In this system, the wall is moving in the positive x direction with the shock speed U_s, while the external flow is moving in the same direction with the smaller speed u_e. The ratio $U_s/u_e = U$ is equal to the shock density ratio, and is the new parameter which distinguishes this from the usual flat-plate boundary layer. Instead of the velocity in the boundary layer going from u_e at the edge to 0 at the wall, it goes from u_e to $U_s > u_e$, i. e., is accelerated rather than slowed to a stop.

Boundary Layer Equations

The equations describing the boundary layer in a chemically-reacting gas are well known. In the two-dimensional, zero-pressure gradient case the momentum and over-all mass conservation equations are:

$$\rho \frac{Du}{Dt} = \frac{\partial}{\partial y}\left(\mu \frac{\partial u}{\partial y}\right), \tag{2.1}$$

$$\frac{\partial}{\partial x}(\rho u) + \frac{\partial}{\partial y}(\rho v) = 0. \tag{2.2}$$

For each chemical species a mass conservation condition states

$$\frac{\partial}{\partial x}\left[\rho c_i (u+U_i)\right] + \frac{\partial}{\partial y}\left[\rho c_i (v+V_i)\right] = w_i ;$$

upon using (2. 2) and the boundary layer simplifications, this becomes

$$\rho \frac{Dc_i}{Dt} + \frac{\partial}{\partial y}(\rho c_i V_i) = w_i . \tag{2.3}$$

Finally the energy equation can be written

$$\rho \frac{Dh}{Dt} = \frac{\partial}{\partial y}(-q) + \mu \left(\frac{\partial u}{\partial y}\right)^2, \tag{2.4}$$

where h is the enthalpy of the mixture, defined by

$$h \equiv \sum c_i h_i , \tag{2.5}$$

and q is the component of the energy flux vector normal to the surface given by

$$-q = k\,\partial T/\partial y - \sum \rho c_i V_i h_i \,. \tag{2.6}$$

The energy flux has two parts. The first is the Fourier heat conduction with k the frozen thermal conductivity, i.e., the conductivity the mixture would possess if no chemical change occurred when a temperature gradient was impressed on it. The second part is the energy flux due to the enthalpy carried by diffusion.

Since the fluid properties will be specified in terms of temperature, the energy equation is transformed by using the definitions of component specific heats, c_{pi}, and frozen mixture specific heat, c_p:

$$c_{pi} \equiv \left(\partial h_i/\partial T\right)_p \,, \quad c_p \equiv \sum c_i c_{pi} \,. \tag{2.7}$$

By using (2.7) in the derivative of (2.5) to replace the left side, and (2.6) in the right side, (2.4) can be written

$$\rho c_p \frac{DT}{Dt} + \rho \sum h_i \frac{Dc_i}{Dt} = \frac{\partial}{\partial y}\left(k \frac{\partial T}{\partial y} - \sum \rho c_i V_i h_i\right) + \mu\left(\partial u/\partial y\right)^2 . \tag{2.8}$$

For the equilibrium case, the c_i are determined by T (and the constant boundary layer pressure p)* together with the mass action law, so (2.8) is the convenient form of the energy equation.

When the boundary layer gas is considered frozen chemically, so that $w_i = 0$, the c_i are determined by the species mass conservation relations (2.3). They can be used to eliminate the Dc_i/Dt term in (2.8), yielding

$$\rho c_p \frac{DT}{Dt} = \frac{\partial}{\partial y}\left(k \frac{\partial T}{\partial y}\right) - \sum \rho c_i V_i c_{pi} \frac{\partial T}{\partial y} + \mu\left(\frac{\partial u}{\partial y}\right)^2 . \tag{2.9}$$

This is the form of the energy equation appropriate to the frozen case.

The boundary conditions for the equations include a given wall temperature, a fully catalytic wall, and the wall tangential velocity equal to the shock speed:

---

*We assume that the diatomic gas consists of a single atomic component. When this theory is applied to a mixture such as air, this implies that the ratio of oxygen to nitrogen is invariant through the boundary layer.

$$y=0:\ u=U_s,\ v=0,\ T=T_w,\ c_M=1,\ c_i=0\ (i\neq M); \tag{2.10a}$$

$$y\to\infty:\ u\to u_e,\quad T\to T_e,\ c_i\to c_{ie}. \tag{2.10b}$$

Thermodynamic Properties

We are dealing with a mixture of diatomic molecules, atoms, singly ionized atomic ions, and electrons, denoted by subscripts M, A, I, and E, respectively. Taking each component to be a perfect gas we have

$$p_i = n_i \mathcal{K} T\ ,\quad h_i = \int_0^T c_{pi}\,dT + h_i^\circ\ , \tag{2.11}$$

where h_i° is the chemical enthalpy at zero degrees. For reaction variables we introduce the fraction of molecules dissociated β and the fraction of atoms ionized α. The number densities are then related to the number density of undissociated molecules n_o by

$$n_M = n_o(1-\beta),\quad n_A = 2n_o\beta(1-\alpha),\quad n_I = n_E = 2n_o\alpha\beta. \tag{2.12}$$

The corresponding mass fractions are

$$c_M = 1-\beta,\quad c_A = \beta(1-\alpha),\quad c_I = \beta\alpha,\quad c_E = \beta\alpha\, m_E/m_A. \tag{2.13}$$

The specific heats are all $5\mathcal{K}/2$ per particle except for the molecule which is taken to have a fully-excited rotational contribution of $2\mathcal{K}/2$ and a vibrational contribution of $\mathcal{K}\phi$ where

$$\phi \equiv (T_v/T)^2 \exp(T_v/T)\left[\exp(T_v/T)-1\right]^{-2}.$$

Therefore the specific heats per unit mass are

$$c_{pM} = \left(\frac{7}{2}+\phi\right)\frac{\mathcal{K}}{m_M}\ ,\quad c_{pA} = c_{pI} = \frac{5\mathcal{K}}{2m_A}\ ,\quad c_{pE} = \frac{5\mathcal{K}}{2m_E}\ . \tag{2.14}$$

The enthalpies follow by integration, with h_D° the dissociation energy per unit mass of atoms and h_I° the ionization energy per unit mass of ions:

$$h_M = c_{pA}T(0.7+0.2\Psi),\quad h_A = c_{pA}T + h_D^\circ,\quad h_E = c_{pE}T,$$

$$\Psi \equiv T^{-1}\int_0^T \phi\,dT = (T_v/T)\left[\exp(T_v/T)-1\right]^{-1},\quad h_I = c_{pA}T + h_D^\circ + h_I^\circ. \tag{2.15}$$

The properties of the mixtures now are found by summation to be

$$p = n\mathcal{K}T = \rho Z T \mathcal{K}/m_M,\quad Z \equiv n/n_o = 1+\beta(1+2\alpha), \tag{2.16a}$$

$$c_p \equiv \sum c_i c_{pi} = c_{pA}[(1-\beta)(0.7+0.2\Phi)+\beta(1+\alpha)], \qquad (2.16b)$$

$$h \equiv \sum c_i h_i = (1-\beta)h_M + \beta(1+\alpha)c_{pA}T + \beta(h_D^\circ + \alpha h_I^\circ). \qquad (2.16c)$$

When the gas mixture is in thermochemical equilibrium, the fractions dissociated and ionized are determined by the equilibrium constants for the reactions

$$A_2 \rightleftarrows 2A, \qquad A \rightleftarrows A^+ + E^-.$$

These expressions can be written in terms of α and β as

$$\frac{\beta^2(1-\alpha)^2}{1-\beta}\,\frac{C_1(T/T_e)^{-1/2}}{1+\beta(1+2\alpha)} = e^{-T_D/T}, \qquad (2.17a)$$

$$\frac{\beta\alpha^2}{1-\alpha}\,\frac{C_2(T/T_e)^{-5/2}}{1+\beta(1+2\alpha)} = e^{-T_I/T}, \qquad (2.17b)$$

$$C_1 \equiv \frac{4p}{K}T_e^{-1/2}\left(\frac{h_P}{\pi m_A K}\right)^{3/2}\frac{Q_v Q_r}{T^2}\,\frac{Q_{elM}}{(Q_{elA})^2}, \qquad (2.18a)$$

$$C_2 \equiv \frac{2p}{K}T_e^{-5/2}\left(\frac{h_P^2}{2\pi m_E K}\right)^{3/2}\frac{Q_{elA}}{Q_{elI}Q_{elE}}, \qquad (2.18b)$$

where h_P is Planck's constant, T_D and T_I are related to the dissociation and ionization energy respectively, Q_v and Q_r are the vibrational and rotational partition functions of the molecule, and the Q_{el} are the various electronic partition functions. Since p is the constant boundary layer temperature p_e and the internal partition functions depend only on temperature, Eqs. (2.17) and (2.18) give α and β as functions of T alone.

Transport Properties

Our basic approach is to consider the flux of energy to be composed of two parts: the diffusion of translational, rotational and vibrational energy due to a temperature gradient, and the flux of dissociation and ionization energy due to concentration gradients, treating each part independently. This is in contrast to the method often employed in equilibrium boundary layer calculations which makes use of an "equilibrium" thermal conductivity, combining both of the above parts into one coefficient. The present approach is necessary for the study of nonequilibrium (including

frozen) boundary layers. It is still useful in the limiting case of equilibrium, though there it trades the specification of the thermal conductivity due to reaction for the specification of the equilibrium mass fraction of each species.

The thermal conductivity of the mixture of molecules, atoms, ions and electrons will be found by the following simple approach. First, the contribution of the ions to the thermal conductivity is smaller than that of the electrons by the square root of the mass ratio and will be neglected. Secondly, the thermal conductivity of the mixture will be assumed to be the sum of that for the electrons, as determined by Spitzer (6) for a singly ionized plasma, and the thermal conductivity of an atom-molecule mixture, as calculated by Yun, Weissman and Mason (7) for N_2-N mixtures.* The former is shown in Fig. 1 and was approximated by

$$k_E = AT^{2.16}, \tag{2.19}$$

where A was determined by the electron density at the edge of the boundary layer.** The atom-molecule thermal conductivity may be suitable approximated by

$$k_{MA} = k_A (0.72 + 1.28\beta)/(1+\beta),$$

$$k_A = 8.4 \times 10^{-7} T^{0.81} \quad \text{cal/sec-cm-}^\circ\text{K},$$

which gives the correct value for pure N_2($\beta = 0$) at 300°K. The mixture thermal conductivity becomes

$$k = k_{MA} + k_E . \tag{2.20}$$

Turning to the mixture viscosity, we first ignore the ionic contribution because of their large coulomb cross section, and the electronic contribution because of their small mass. The viscosity is taken to be that of an atom-molecule mixture with the same relative proportions found in the gas, times the mole fraction of atoms and molecules. The data of Reference (7) indicate that μ_{MA} and μ_A have the same temperature dependence above 2200°K, so their ratio may be written

$$\frac{\mu_{MA}}{\mu_A} = \frac{0.82 + 1.18\beta}{1+\beta} .$$

---

*A more exact calculation using the mixture rule of Fay (8) showed this approximation to be accurate for α greater than a few percent.

**The temperature dependence of k_E is somewhat less than $T^{2.5}$ because of the logarithmic term in the coulomb cross section.

Obtaining the mole fraction of atoms and molecules from (2.12), we then have for $T > 2200^{\circ}K$,

$$\frac{\mu}{\mu_A} = \frac{0.82+1.18\beta}{1+\beta} \quad \frac{1+\beta-2\alpha\beta}{1+\beta+2\alpha\beta} .$$

We take μ_A to have the same temperature dependence as k_A, leading to an expression for the Prandtl number σ:

$$\sigma \equiv \frac{c_p \mu}{k} = \frac{2}{3} \frac{0.82+1.18\beta}{1+\beta} \frac{1+\beta-2\alpha\beta}{1+\beta+2\alpha\beta} \frac{c_p k_A}{c_{p_A} k} , \qquad (2.21)$$

where we have put 2/3 for the Prandtl number of an atomic gas. Below $2200^{\circ}K$ the temperature dependence is different and we can use the Sutherland formula

$$\frac{\mu}{\mu_{300}} = \left(\frac{T}{300}\right)^{3/2} \frac{438}{T+138} , \qquad (2.22)$$

where T is in $^{\circ}K$ and $\mu_{300} = 0.179 \times 10^{-3}$ g/cm-sec. It is only in the use of (2.22) rather than (2.21) for μ below $2200^{\circ}K$ that the thermodynamic and transport properties used in this work differ from those of (5). It was felt important to have accurate viscosity in the present work, where shear and displacement thickness are of equal importance with heat transfer, as contrasted with (5), where only heat transfer was of interest.

We now consider the diffusion of species. This enters the problem in the species mass conservation equation (2.3), the energy equations (2.8) and (2.9), and the energy flux (2.6). (The latter is the same as the term on the right side of (2.8).) It is these terms which complicate the numerical solution of the problem, because of the involved nature of multicomponent diffusion fluxes. Also, for every additional species considered a separate mass conservation equation must be solved, unless the gas is in equilibrium.

The only simple case for diffusion is binary diffusion, where only two components are considered, and one species equation needs to be solved. The large majority of dissociated boundary layer studies made consider binary diffusion, regarding the gas to be made up of atoms and molecules. In our case, we have in addition ions and electrons, which represent at least one more species, since one assumes the ions and electrons so tightly bound by coulomb forces that they must diffuse together as a pair. This would appear to require consideration of ternary diffusion.

However, Fay and Kemp (5) showed that a useful and accurate approximation can be made for nitrogen (and probably other diatomic gases) which reduces the diffusion to the simplest case of only two species, the so-called binary diffusion model. This idea is based on the fact that the collision cross section between the N atom and the N^+ ion, the charge-exchange cross section, is probably close to an order of magnitude larger

than the kinetic cross section for $N\text{-}N_2$, or, presumably, $N_2\text{-}N^+$ collisions. This makes the relative motion of N and N^+ difficult and would tend to make their diffusion velocities nearly equal. The binary diffusion model takes the diffusion velocity of the atoms to be the same as that of the ion-electron pairs, so that for determination of the particle flux we have a binary mixture of molecules, M, and atom-ion-electron particles, which we shall denote by R.

Under this assumption, calculations of equilibrium stagnation point heat transfer were made in (5) which compared very well with those not using the binary diffusion model. A further and more detailed check was made by comparing equilibrium thermal conductivities, which contain both k and a diffusion term, and again the agreement shown in (5) was very good. So the binary diffusion model seems to give accurate results, at least for nitrogen.

When the model is applied to the diffusion terms in the energy equations (2.8) and (2.9), we make use of the zero net mass diffusion condition $\Sigma \rho c_i V_i = 0$ and find

$$\sum \rho c_i V_i h_i = \rho c_R V_R (h_R - h_M), \tag{2.23a}$$

$$\sum \rho c_i V_i c_{pi} = \rho c_R V_R (c_{pR} - c_{pM}). \tag{2.23b}$$

Here the quantities referring to the atom-ion-electron particle are found from (2.13), (2.14) and (2.15) as

$$c_R = \beta, \quad c_{pR} = (c_A c_{pA} + c_I c_{pI} + c_E c_{pE})/c_R = c_{pA}(1+\alpha),$$

$$h_R = (c_A h_A + c_I h_I + c_E h_E)/c_R = c_{pA}(1+\alpha)T + h_D^\circ + \alpha h_I^\circ. \tag{2.24}$$

The diffusional mass flux of atom-ion-electron particles is worked out in (5) be relating the partial pressure gradients to the rate of loss of momentum by collisions of atoms and ions with molecules. The result is Eq. (3.19) of (5):

$$-\rho c_R \underline{V}_R = \frac{c_R m_M}{kT} \frac{n_M + n_A + n_I}{n_A + n_I} \mathcal{D} \nabla (p_A + p_I + p_E), \tag{2.25}$$

where $\mathcal{D}$ is the binary diffusion coefficient for atoms diffusing through molecules, which is taken the same as that for ions diffusing through molecules. A suitable nondimensional representation of $\mathcal{D}$ is found by dividing by the thermal diffusivity, $k/\rho c_p$, of a pure atomic gas at the same heavy particle density and temperature as the mixture. This gives a Lewis number L of

$$L \equiv (n_M + n_A + n_I) \mathcal{D} m_A c_{pA}/k_A. \tag{2.26}$$

The final form of the diffusive mass flux is then

$$-\rho c_R \underline{V}_R = \frac{2L}{Z} \frac{k_A}{c_{pA}} \left[(1+\alpha)\nabla\beta + \beta(1-\beta)\nabla\alpha \right], \qquad (2.27)$$

where the pressure ratios p_i/p have been replaced by the expressions for n_i/n found from (2.12) and $2/Z$ is the ratio of the average mass of a particle ρ/n to the atomic mass. A value of L can be obtained from the work of (7), and was found to be 0.6 for $10^3 < T^\circ K < 10^4$.

We now consider the implications of the bindary diffusion model for a frozen boundary layer. The atoms and ion-electron pairs diffuse together, and there are no sources of these particles in a frozen flow. Therefore, α, which depends entirely on the ratio of ion and atom densities, cannot change, but remains fixed at its external value α_e. A more formal proof of this can be constructed by writing the frozen species mass conservation relation (2.3) for atoms and for ions, putting the same diffusion velocity for both. These two equations can be combined to show that the convective derivative of α following an atom-ion-electron particle is a constant, and since all particles come from the edge of the boundary layer where $\alpha = \alpha_e$, then α remains at that value.

We have now specified all the necessary thermodynamic and transport properties necessary to solve the boundary layer equations, and expressed all the diffusion terms in suitable form. The remaining summation term, on the left side of the equilibrium energy equation (2.8), is a purely thermodynamic term which represents the reaction contribution to the convection of enthalpy (or reaction specific heat times temperature convection). Using (2.13), (2.14), (2.15) and (2.24) it becomes

$$\sum h_i \frac{Dc_i}{Dt} = (h_R - h_M)\frac{D\beta}{Dt} + (c_{pA}T + h_I^\circ)\beta\frac{D\alpha}{Dt} . \qquad (2.28)$$

Transformation of Equations

The partial differential equations in two-variables x, y which determine the boundary layer with no pressure gradient can be transformed to ordinary differential equations in the equilibrium and frozen cases under consideration here. One introduces the similarity variable

$$\eta \equiv \sqrt{\frac{c_{pe}u_e}{2\rho_e k_e x}} \int_0^y \rho\, dy , \qquad (2.29)$$

and the normalized dependent variables

$$u/u_e = df(\eta)/d\eta , \quad T/T_e = \Theta(\eta), \quad \beta/\beta_e = s(\eta) . \qquad (2.30)$$

A solution exists where θ, f and s are functions of η only, if we take both wall and external conditions to be constants independent of x. (This exact reduction to ordinary differential equations is not possible for a case with finite reaction rates in the flat-plate geometry).

The transformation proceeds by eliminating v from the convective derivate operator using the mass conservation equation (2.2). Then the momentum equation (2.1) becomes

$$\frac{d}{d\eta}\left(\frac{k\rho/c_p}{k_e\rho_e/c_{pe}}\sigma\frac{d^2f}{d\eta^2}\right)+f\frac{d^2f}{d\eta^2}=0. \tag{2.31}$$

The equilibrium energy equation is transformed after use of (2.28) and (2.23a) combined with the y component of (2.27). We also make use of the fact that, for equilibrium, α and β are functions of T only. Equation (2.8) then transforms to

$$\frac{d}{d\eta}\left\{\frac{k\rho}{k_e\rho_e}\frac{d\theta}{d\eta}\left[1+\frac{k_A}{k}\frac{2L}{Z}\frac{h_R-h_M}{c_{pA}T_e}\left\{(1+\alpha)\frac{d\beta}{d\theta}+\beta(1-\beta)\frac{d\alpha}{d\theta}\right\}\right]\right\} \tag{2.32}$$

$$+f\frac{d\theta}{d\eta}\left[\frac{c_p}{c_{pe}}+\frac{h_R-h_M}{c_{pe}T_e}\frac{d\beta}{d\theta}+\frac{c_{pA}T_e\theta+h_I^\circ}{c_{pe}T_e}\beta\frac{d\alpha}{d\theta}\right]+\frac{u_e^2}{c_{pe}T_e}\frac{k\rho/c_p}{k_e\rho_e/c_{pe}}\sigma\left(\frac{d^2f}{d\eta^2}\right)^2=0.$$

For the equilibrium case, (2.31) and (2.32) are to be solved for f and θ with α and β given as functions of θ by (2.17) and (2.18). The frozen energy equation proceeds from (2.9) with (2.27) used in (2.23b) for the summation term, leading to

$$\frac{d}{d\eta}\left(\frac{k\rho}{k_e\rho_e}\frac{d\theta}{d\eta}\right)+\frac{u_e^2}{c_{pe}T_e}\frac{k\rho/c_p}{k_e\rho_e/c_{pe}}\sigma\left(\frac{d^2f}{d\eta^2}\right)^2 \tag{2.33}$$

$$+\frac{d\theta}{d\eta}\left[\frac{c_p}{c_{pe}}f+\frac{k_A\rho}{k_e\rho_e}(1+\alpha_e)\frac{2L}{Z}\frac{c_{pR}-c_{pM}}{c_{pA}}\beta_e\frac{ds}{d\eta}\right]=0.$$

The transformation of the species mass equation is done for the atom-ion-electron particles, with (2.27) for the diffusional mass flux, and frozen flow, $w_i = 0$. The result is

$$\frac{d}{d\eta}\left[\frac{k_A\rho}{k_e\rho_e}(1+\alpha_e)\frac{2L}{Z}\frac{c_{pe}}{c_{pA}}\frac{ds}{d\eta}\right]+f\frac{ds}{d\eta}=0. \tag{2.34}$$

In the frozen case, (2.31), (2.33) and (2.34) are to be solved for f, θ, and s, with $\alpha = \alpha_e$.

The boundary conditions are found from (2.10) to be

$$\eta=0: \; df/d\eta = u_s/u_e \equiv u, \; f=0, \; \theta=\theta_w, \; s=0;$$

$$\eta\to\infty: \; df/d\eta \to 1, \; \theta\to 1, \; s\to 1. \tag{2.35}$$

For the equilibrium case, the boundary conditions on s are not needed.

The variables η and f defined above differ from the conventional variables used by Mirels (3) and Hartunian and Marrone (4), among others. They were originally introduced in (5), where heating was of primary interest, and are most appropriate to that case. They differ from Mirels variables η_M and f_M by

$$\eta = \sqrt{\frac{\rho_e \mu_w}{\rho_e \mu_e}}\,\eta_M, \qquad f = \sqrt{\frac{\rho_e \mu_w}{\rho_e \mu_e}}\, f_M, \tag{2.36}$$

which must be kept in mind when comparing the present results with those of (3) and (4), as well as other previous studies.

III. RESULTS

Calculations

The physical constants of nitrogen were used for all calculations. These include a dissociation energy of 9.756 electron volts per molecule and an ionization energy of 14.48 electron volts per atom, leading to

$$T_D \equiv h_D^\circ/(K/m_M) = 113{,}200\,^\circ K, \qquad T_I \equiv h_I^\circ/(K/m_A) = 168{,}100\,^\circ K,$$

$$h_D^\circ/c_{pA} = 0.2T_D = 22{,}640\,^\circ K, \qquad h_I^\circ/c_{pA} = 0.4T_I = 67{,}200\,^\circ K. \tag{3.1}$$

The rotational and vibrational characteristic temperatures are

$$T_r = 2.90\,^\circ K, \qquad T_v = 3400\,^\circ K,$$

so the rotational partition function may be approximated by its asymptotic value $Q_r = T/2T_r$. The vibrational partition function is $Q_v = [1-\exp(-T_v/T)]^{-1}$ while for the electronic partition functions we take

$$Q_{elM} = 1, \qquad Q_{elA} = 4, \qquad Q_{elI} = 9, \qquad Q_{elE} = 2.$$

The quantities C_1 and C_2 of (2.18) become

$$C_1 = \frac{0.260 \times 10^{-10} p_e T_e^{-1/2}}{(\theta/\theta_v)\left[1 - \exp(-\theta_v/\theta)\right]}, \qquad C_2 = 1.33\, \rho_e T_e^{-5/2},$$

where p_e is in dynes/cm^2 and T_e in $^\circ$K. In all cases the wall temperature was taken as 300°K.

The input for the calculations are the values of U_s, T_e, p_e and u_e. These were determined by solving the equilibrium shock wave jump conditions at given values of U_s and initial pressure p_1. This was accomplished by means of an existing digital computer program at the Avco-Everett Research Laboratory. A range of shock speed from 4 to 12 mm/μsec was covered for initial pressures of 1.0, 0.1 and 0.01 torr. The values of the resulting external quantities are shown in Table I. From (2.18), then, α_e and β_e can be found. The equation of state (2.16a) then yields a value of ρ_e which can be combined with α_e to give the external electron density n_{Ee}. The value of the constant A in the expression (2.19) for k_E can then be found from Fig. 1 using T_e and n_{Ee}. The solution of the appropriate equations can then proceed. As is usual, we are faced with two-point boundary value problems, which we chose to solve by guessing extra boundary conditions at the wall and correcting the guesses in a linear fashion based on the errors obtained as $\eta \to \infty$. The form of the equations used for the machine integration is exactly analogous to the form used for the stagnation-point boundary layer, which is given in the Appendix to the Avco-Everett version of (5).

The results of interest are the shear stress, heat transfer rate and displacement thickness. The shear stress τ_w is given by $(\mu \partial u/\partial y)_w$ and in order to compare with the work of Mirels (3) we write

$$\frac{\tau_w}{\mu_w u_e}\sqrt{\frac{2x\mu_w}{u_e \rho_w}} = \left(\frac{d^2 f_m}{d\eta_m^2}\right)_w = \sqrt{\frac{\rho_e \mu_e \rho_w \mu_w}{\rho_e \mu_e}}\left(\frac{d^2 f}{d\eta^2}\right)_w . \tag{3.2}$$

The heat transfer rate is given by (2.6) and in the transformed version is the quantity in curly brackets in the first term of (2.32), except for some cancelled constants. If we restore these, and again use Mirels' form we find, for equilibrium,

$$\frac{-q_w}{h_e}\sqrt{\frac{2\rho_w c_{pw} x}{u_e \rho_w k_w}} = \left(\frac{d}{d\eta_m}\frac{h}{h_e}\right)_w \tag{3.3}$$

$$= \frac{c_{pe} T_e}{h_e}\sqrt{\frac{\rho_w k_w \rho_w c_{pw}}{k_e \rho_e c_{pe}}}\left(\frac{d\theta}{d\eta}\right)_w \left[1 + \frac{k_A}{k}\frac{2L}{Z}\frac{h_R - h_M}{c_{pA} T_e}\left\{(1+\alpha)\frac{d\beta}{d\theta} + \beta(1-\beta)\frac{d\alpha}{d\theta}\right\}\right]_w .$$

In the frozen case, α is a constant and β a function of η directly so the corresponding relation is

$$\frac{-q_w}{h_e}\sqrt{\frac{2\sigma_w c_{pw} x}{u_e \rho_w \mu_w}} = \frac{c_{pe} T_e}{h_e}\sqrt{\frac{\sigma_w k_w \rho_w c_{pw}}{k_e \rho_e c_{pe}}}\left[\frac{d\theta}{d\eta} + \frac{k_A}{k}\frac{2L}{Z}\frac{h_K - h_M}{c_{pA} T_e}(1+\alpha_e)\beta_e \frac{ds}{d\eta}\right]_w . \tag{3.4}$$

The displacement thickness, of importance for finding the test time, is defined to be

$$\delta^* \equiv \int_0^\infty \left(1 - \frac{\rho u}{\rho_e u_e}\right) dy = \sqrt{\frac{2 x k_e}{u_e \rho_e c_{pe}}} \int_0^\infty \left(\frac{\rho_e}{\rho} - \frac{df}{d\eta}\right) d\eta . \tag{3.5}$$

Mirels writes this as

$$\delta^* \sqrt{\frac{u_e \mu_w}{2 x \rho_w}}\frac{\rho_e}{\rho_w} = \sqrt{\frac{\rho_e \mu_e}{\sigma_e \rho_w \mu_w}} \int_0^\infty \left[\left(\frac{\rho_e}{\rho} - 1\right) + \left(1 - \frac{df}{d\eta}\right)\right] d\eta . \tag{3.6}$$

We can now compare our results with the calculations and correlation formulas of (3). Figures 2, 3, and 4 show such a comparison for shear, heat transfer, and displacement thickness in the equilibrium case. The pluses (+) are Mirels' exact calculations for air with Prandtl number 0.72 and Lewis number unity, at initial pressures of 0.01 and 0.001 atmospheres. The filled symbols are the present exact calculations for nitrogen at initial pressures of 1.0, 0.1, and 0.01 torr. In the small region of overlap, from 4 to 5 mm μsec, Mirels' results drop off, while the present results continue the trend begun by Mirels points below 4 mm μsec, and begin falling off around 9 mm μsec. This difference in behavior is probably attributable to the difference between air and nitrogen. For air, the value of the shock speed ratio U has a local peak around 4 mm μsec, corresponding to oxygen dissociation, while for nitrogen the first peak is around 9 mm μsec, corresponding to nitrogen dissociation. The boundary layer parameter curves seem to follow this trend very closely. Only the points at 10.5 and 12 mm μsec contain degrees of ionization greater than 1%, the maximum being 20% at the lowest pressure. No particularly outstanding effect of ionization is discernable.

Based on his calculations, Mirels derived correlation formulas for the three boundary layer parameters, in terms of velocity ratio U, Prandtl number σ, energy ratio u_e^2/h_e and $\rho\mu$ ratio ($\rho_e\mu_e/\rho_w\mu_w$). They are given in Eqs. (19)-(22) of (3) as:

The exponent on the $\rho\mu$ ratio is changed from 0.29 to conform with Mirels' suggestion for strong shocks. In the present case of variable σ, the wall value is used in the correlations for convenience. Use of σ_e might make some changes at the highest speeds, where σ_e goes as low as 0.26.

$$\frac{-\tau_w}{\mu_w u_e (U-1)}\sqrt{\frac{2x\mu_w}{u_e \rho_w}} = 0.489\sqrt{1+1.665U}\left(\frac{\rho_e \mu_e}{\rho_w \mu_w}\right)^{0.265},$$

$$\frac{-q_w}{h_e}\sqrt{\frac{2x\sigma_w c_{pw}}{u_e \rho_w k_w}} = 0.489\sqrt{1+1.665U}\left(\frac{\rho_e \mu_e}{\rho_w \mu_w}\right)^{0.265} \sigma_w^{(0.48+0.022U)} \times \left[1 - \frac{h_w}{h_e} + \frac{(U-1)^2 u_e^2}{2h_e}\sigma_w^{(0.39-0.023U)}\right],$$

$$-\delta^*\sqrt{\frac{u_e \rho_w}{2x\mu_w}}\frac{\rho_e}{\rho_w} = \left(\frac{\rho_e \mu_e}{\rho_w \mu_w}\right)^{0.37}\left\{\frac{1.134(U-1)}{\sqrt{1+1.022U}} - \frac{1.569(U-1)^2}{\sqrt{1+0.993U}}\frac{u_e^2/2h_e}{\sigma_w^{0.045(U-1)}} + \frac{1.134\,\sigma_w^{-(0.47+0.029U)}}{\sqrt{1+1.022U}}\left[1 - \frac{h_w}{h_e} + \frac{(U-1)^2 u_e^2}{2h_e}\sigma_w^{(0.34-0.023U)}\right]\right\}.$$

These relations are also plotted on Figs. 2, 3, and 4, using the values of the parameters appropriate to the exact calculations. For Mirels' cases, the crosses (X) show the points, while those for the present calculations are given by the open symbols.

The agreement is quite good, in most cases being within 10%. At the higher speeds, there are a few cases which go to 15% or 20% error. (Note the suppressed zeroes on the ordinates of Figs. 2, 3, 4.) So to within this accuracy, Mirels' correlation formulas can be used to predict boundary layer parameters in equilibrium nitrogen at speeds up to 12 mm μsec. Since Hartunian and Marrone (4) found they also work for oxygen up to 6.5 mm μsec, it is likely they will serve for air at higher speeds, although this should be checked.

The present calculations showed only a maximum of about 7% difference between results for frozen and equilibrium boundary layers, indicating that the correlation formulas are still probably satisfactory for frozen cases. It is expected that values for non-equilibrium boundary layers would lie between the equilibrium and frozen values.

ACKNOWLEDGEMENT

This work is part of a thesis presented by Tzu-Chung Moh to the Massachusetts Institute of Technology in May 1964, as part of the requirements for the degree of Master of Science in the Department of Mechanical Engineering.

LIST OF SYMBOLS

A	Constant in the electron thermal conductivity expression, (2.19)
C_1, C_2	Functions in the equilibrium constants for dissociation and ionization, (2.18)
c_{pi}	Specific heat at constant pressure per unit mass of species i
c_p	Frozen specific heat at constant pressure per unit mass of mixture, (2.7)
c_i	Mass fraction of species i
$\mathscr{D}$	Binary diffusion coefficient for atoms diffusing through molecules
D/Dt	Convective derivate operator following the mass-average velocity, $u\partial/\partial x + v\partial/\partial y$
f	$\int_o^\eta (df/d\eta)\, d\eta$, nondimensional stream function
f_M	Mirels stream function, (2.36)
h_i	Enthalpy per unit mass of species i
h_i^o	Chemical enthalpy per unit mass of species i at 0^oK
h	Enthalpy per unit mass of mixture, (2.5)
h_D^o	Dissociation energy per unit mass of atoms
h_I^o	Ionization energy per unit mass of ions
k_i	Thermal conductivity of species i
k	Frozen thermal conductivity of mixture
L	Lewis number, (2.26)
m_i	Particle mass of species i
n_i	Number density of species i
n	Number density of mixture
n_o	Number density of original undissociated molecules
p_i	Partial pressure of species i
p	Pressure of mixture
Q	Partition function
q	Energy flux in y direction
s	Normalized fraction dissociated, β/β_e
T	Absolute temperature
T_D, T_I	Dissociation and ionization energy temperatures, (2.17)
T_r, T_v	Characteristic temperatures for rotation and vibration
U_s	Incident shock speed
U	Normalized wall velocity, U_s/u_e

$\underline{V}_i(U_i, V_i)$	Diffusion velocity of species i
u, v	Components of mass average velocity
w_i	Mass rate of formation of species i
x, y	Distances along and normal to the wall, origin at the foot of the incident shock wave, x positive towards the driver
Z	Compressibility factor, (2.16a)
α	Fraction of atoms ionized
β	Fraction of molecules dissociated
δ^*	Displacement thickness, (3.5)
η	Similarity variable, (2.29)
η_M	Mirels similarity variable, (2.36)
Θ	Normalized temperature, T/T_e
κ	Boltzmann's constant
μ_i	Viscosity of species i
μ	Viscosity of mixture
ρ	Mass density of mixture
σ	Prandtl number, $c_p\mu/k$
ϕ	Vibrational contribution to molecular specific heat, (2.14)
ψ	Vibrational contribution to molecular enthalpy, (2.15)

Subscripts

A	Atom
D	Dissociation
E	Electron
e	Conditions at the edge of the boundary layer
el	Electronic partition function
I	Ion or Ionization
M	Molecule or Mirels
R	Atom-ion-electron particle in binary diffusion model

REFERENCES

(1) Rosko, A., Phys. Fluids, 3, 835 (1960)

(2) Mirels, H., Phys. Fluids, 6, 1201 (1963)

(3) Mirels, H., Laminar Boundary Layer Behind a Strong Shock Moving Into Air, NASA Technical Note D-291, February 1961

(4) Hartunian, R.A. and Marrone, P.V., Heat Transfer from Dissociated Gases in a Shock Tube, Cornell Aeronautical Laboratory Report No. AD-1118-A-7, November, 1959

(5) Fay, J.A. and Kemp, N.H., AIAA Journal, 1, 2741 (1963). Also, Avco-Everett Research Laboratory Research Report 143, April 1963

(6) Spitzer, L., Physics of Fully Ionized Gases, Interscience, New York (1956)

(7) Yun, K-S, Weissman, S., and Mason, E.A., Phys. Fluids, 5, 672 (1962)

(8) Fay, J.A., Hypersonic Heat Transfer in the Air Laminar Boundary Layer, in The High Temperature Aspects of Hypersonic Flow, p. 583, ed. by W. Nelson, Pergamon Press, Oxford (1964)

TABLE I Conditions Behind the Incident Shock

p_1 (torr)	U_s (mm/μsec)	u_e (mm/μsec)	T_e ^{0}K	$p_e \times 10^{-6}$ (dynes/cm^2)	h_e (mm/μsec)^2
1.0	4	0.488	5130	0.214	8.04
	5	0.435	5830	0.334	12.44
	7	0.446	6850	0.687	24.0
	9	0.512	8040	1.138	39.8
	10.5	0.645	10450	1.548	53.7
	12	0.755	12650	2.02	69.9
0.1	4	0.421	4750	0.214	8.04
	5	0.399	5300	0.340	12.44
	7	0.406	6100	0.694	24.0
	9	0.465	7160	1.140	39.8
	10.5	0.603	9630	1.548	53.7
	12	0.684	11250	2.03	69.9
0.01	4	0.388	4290	0.214	8.04
	5	0.368	4850	0.347	12.44
	7	0.370	5500	0.700	24.0
	9	0.426	6430	1.153	39.8
	10.5	0.560	8850	1.560	53.7
	12	0.621	10050	2.08	69.9

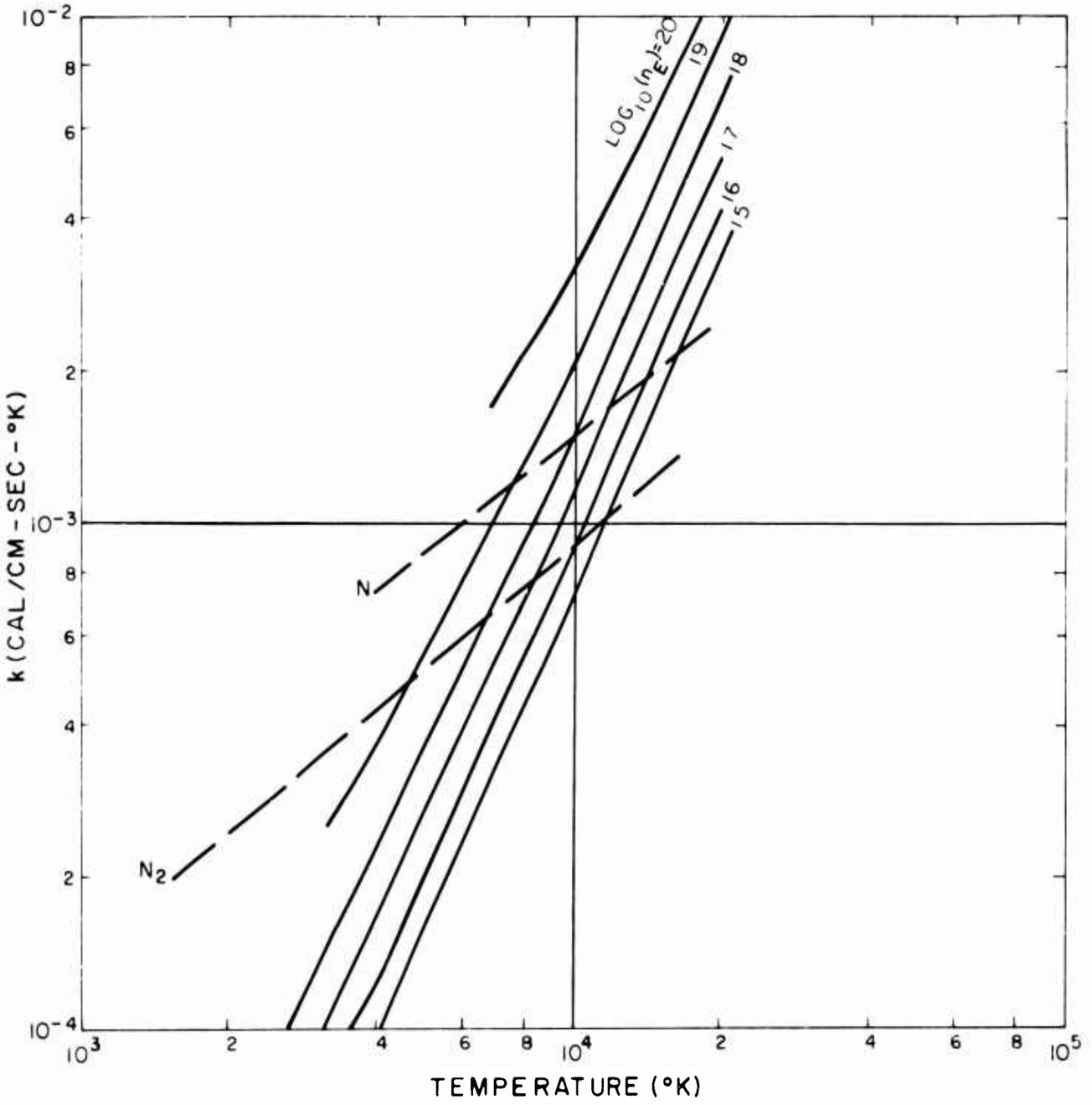


Fig. 1 The frozen thermal conductivity of a singly ionized gas as a function of gas temperature and electron number density in particles per cubic centimeter. The thermal conductivity of N and N_2 from (7) is shown for comparison

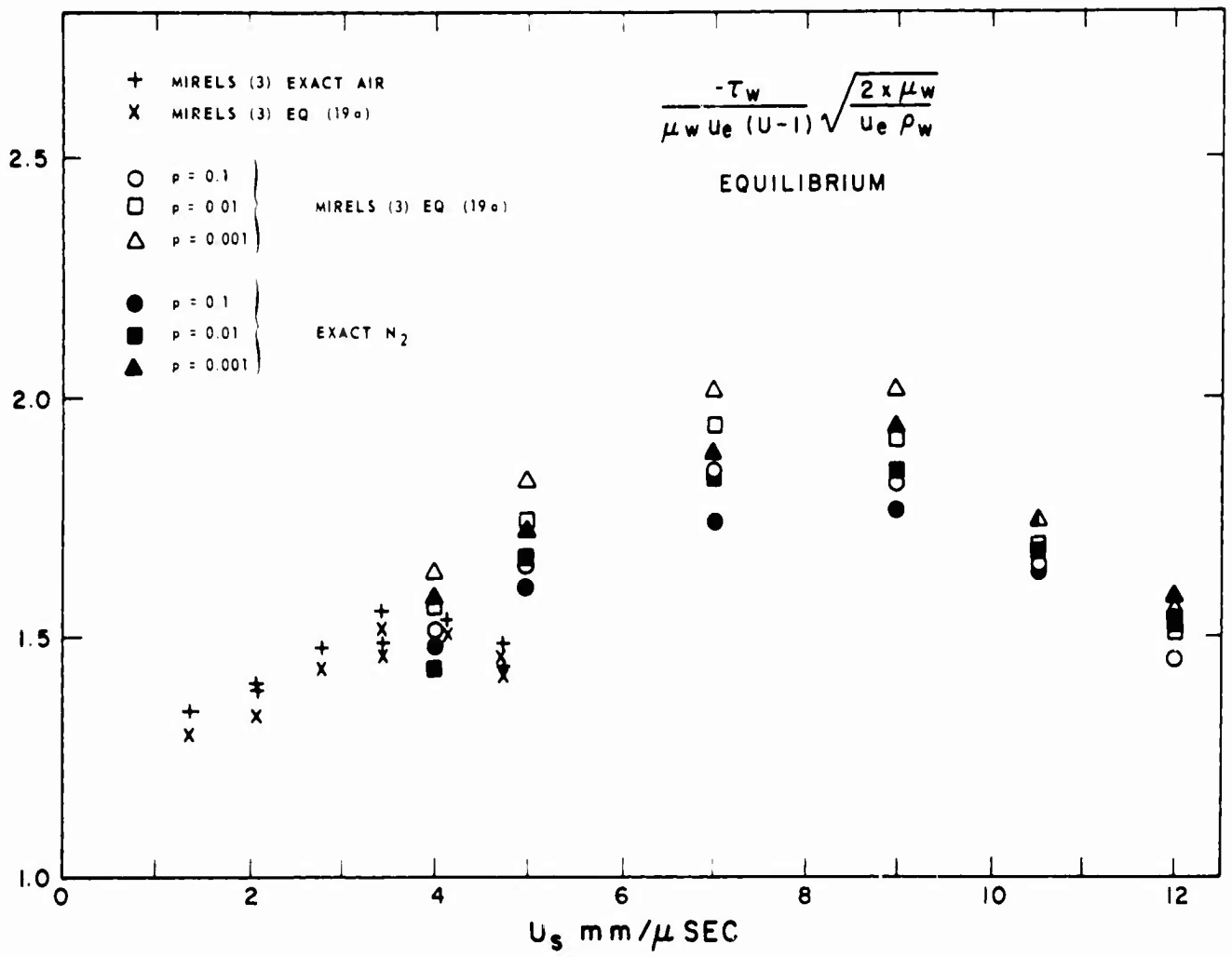


Fig. 2 Shear stress parameter. Comparison of exact calculations and Mirels' correlation formulas for equilibrium air up to 4.8 mm/μsec and equilibrium nitrogen up to 12 mm/μsec

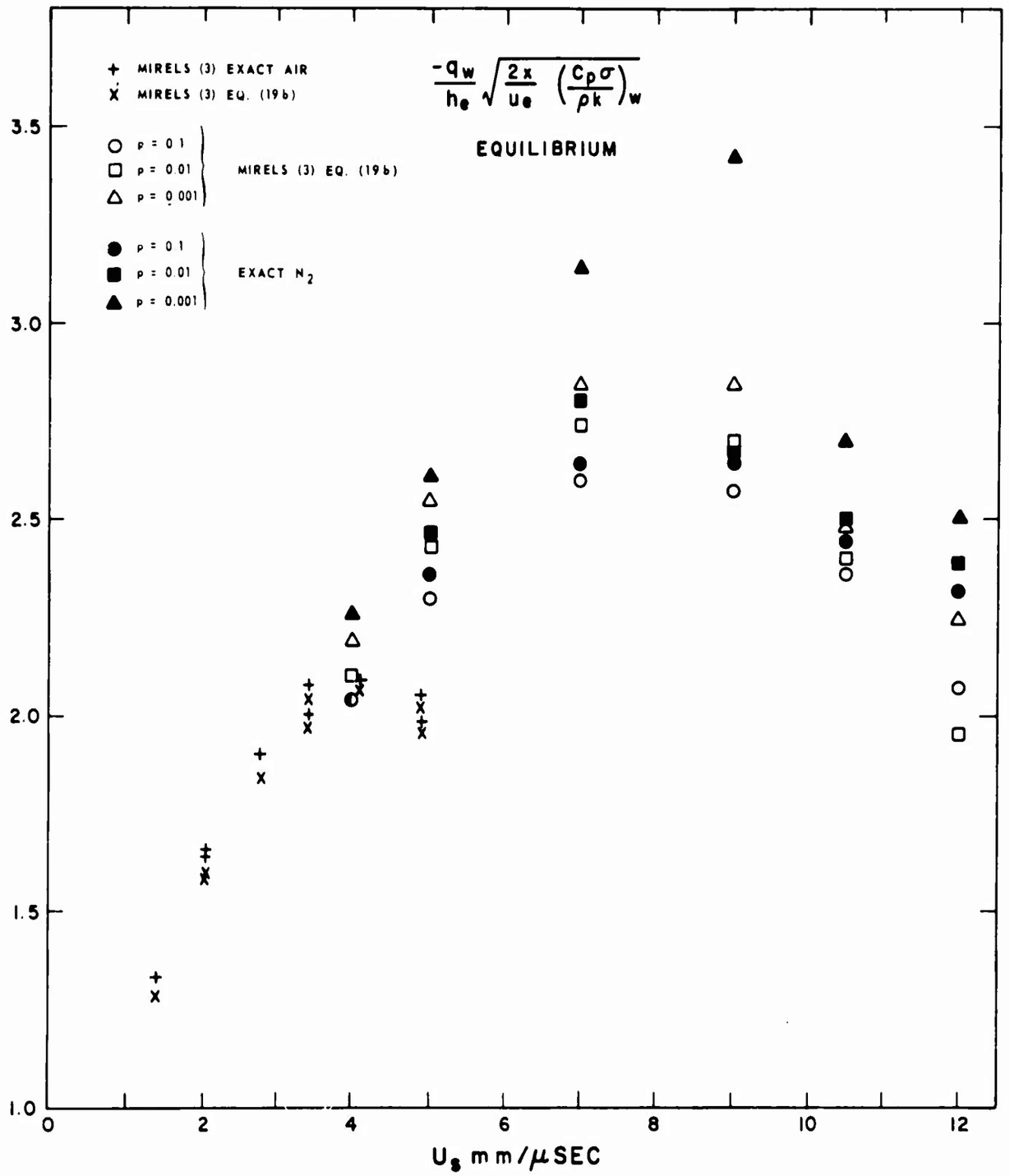


Fig. 3 Heat transfer rate parameter. Comparison of exact calculations and Mirels' correlation formula for equilibrium air up to 4.8 mm/μsec and equilibrium nitrogen up to 12 mm/μsec

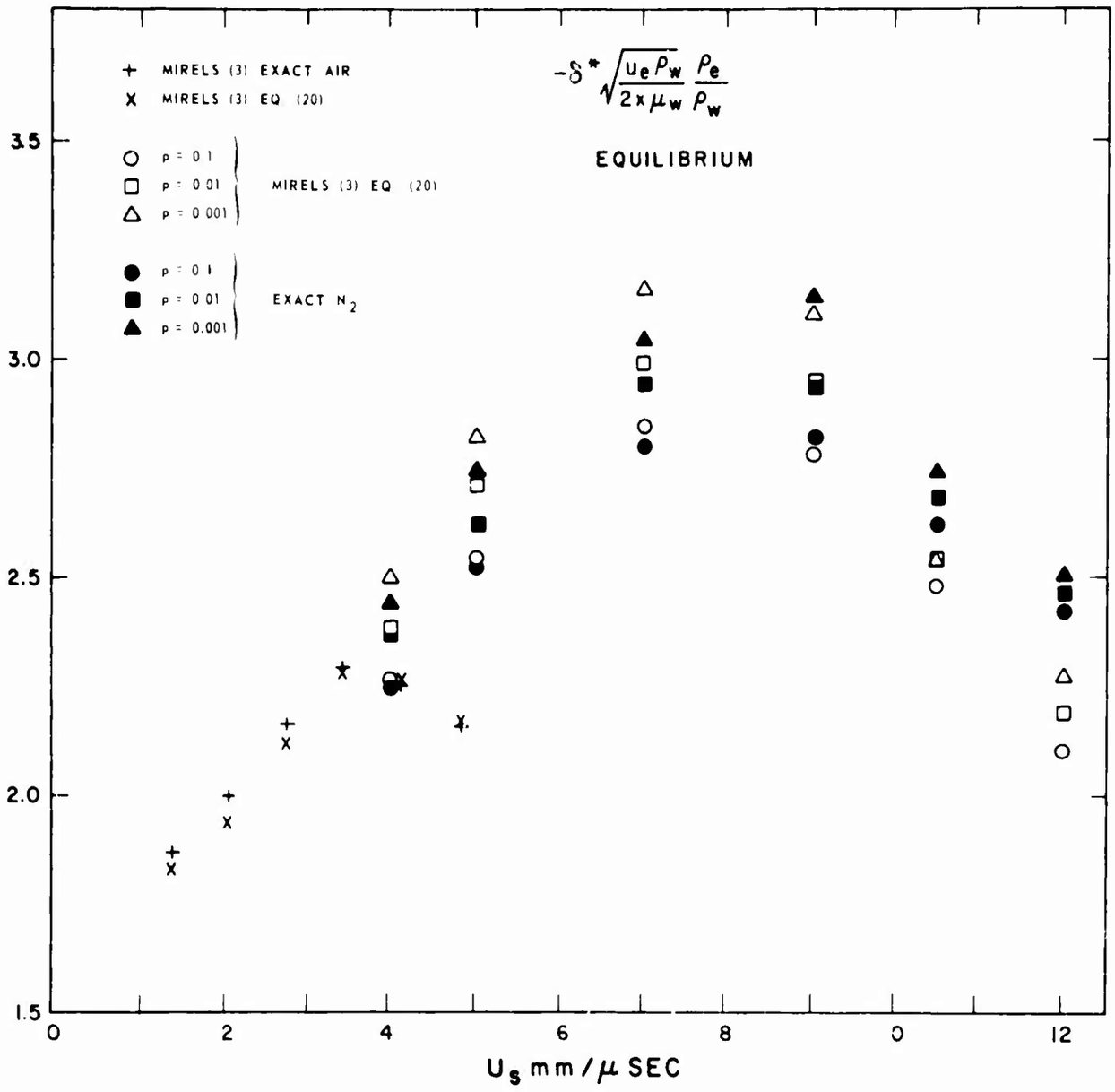


Fig. 4 Displacement thickness parameter. Comparison of exact calculations and Mirels correlation formulas for equilibrium air up to 4.8 mm/μsec and equiiibrium nitrogen up to 12 mm/μsec

ELECTRIC ARC-DRIVEN SHOCK TUBE DIAMETER, LENGTH AND ENERGY REQUIREMENTS FOR THE STUDY OF GAS RADIATION PHENOMENA

F. R. Livingston
Jet Propulsion Laboratory
Pasadena, California

INTRODUCTION

The shock speed and test time performance of electric arc-driven shock tubes is not well understood at the present time. In the present paper, correlation of experimental data on the basis of ideal shock tube theory and wall-boundary-layer theory reveals empirical rules to aid the electric arc-driven shock tube designer. The results of this work show that for gas radiation studies the required dimensions of the shock tube increase with increasing shock speed and decreasing initial test gas pressure, but not in a manner expected from consideration of the wall-boundary layer theory alone.

AVAILABLE TEST TIME IN ELECTRIC ARC-DRIVEN SHOCK TUBES

A good method to estimate shock tube test duration at planetary entry speeds has not yet been obtained. One reason for this state of affairs is that an adequate method of predicting contact surface mixing has not yet been presented. In the present paper an attempt will be made to correlate experimental data with results of boundary layer theory in order to formulate rules which describe the observed test time data.

Boundary Layer Calculations

Since the work of Mirels (ref. 1 and 2) does not extend to shock velocities of interest for gas radiation studies at superorbital planetary entry speeds, an extension of the numerical work was done to compute the length of the test slug of gas at higher speeds.

Laminar-Wall Boundary Layer

In the case of the laminar-wall boundary layer, the ratio of the

density-viscosity product across the boundary layer, $C_{e,o}$, was computed for test conditions of interest and this in turn was used to compute the boundary layer displacement thickness parameter, β_1, from the following relationship of reference (1):

$$\beta_1 = C_{e,o}^{0.37}\,(1.59)\left[1+\frac{1.796+0.802W}{W-1}\right]$$

where:

$$C_{e,o} = \rho_e u_e/\rho_w u_w$$

$$W = \rho_2/\rho_1$$

Mirels' used the Sutherland viscosity when computing the values of β_o, and when correlating the numerical results. In this paper both the Sutherland viscosity and the Yos viscosity (ref. 3) are used in the computations. Results of these computations are plotted in Figure 1 where the separation distance for air is illustrated both for the ideal gas and equilibrium air. Shocked gas properties of both Ziemer (ref. 4) and Lewis and Burgess (ref. 5) are used together with the viscosity of reference (3) to calculate the equilibrium real gas separation distance at an initial pressure of 0.1 cm Hg, and at an initial density of 10^{-4} the standard value.

Turbulent-Wall Boundary Layer

In calculating the boundary layer displacement thickness parameter, β_1, and the separation distance parameter, $\left(\frac{P_{st}}{P_\infty}\right)^{\frac{1}{4}} \frac{\ell_m}{d^{5/4}}$, for the turbulent-wall boundary layer, the method described by Mirels in Appendix A of reference (2) was applied. Again in these numerical computations the viscosity of Yos was used. Results of these computations are shown in Figure 2 for the non-uniform freestream condition (β_1) at an initial air pressure of 10^{-1} cm Hg. In order to extend the calculations to 15×10^5 cm/sec use was made of Ziemer's shock charts where it may be seen that the results are somewhat different than when using the shock properties of Lewis. Since viscosity data was not computed by Yos at pressures less than 1 atm, we could not compute the separation distance for lower initial pressures than those shown here.

When reference is made to the turbulent theory in this paper, it normally means the turbulent-wall boundary layer theory of Mirels, using the viscosity of Yos, and the shock properties of Lewis and Burgess.

Comparison of Theoretical Test Time with Experimental Results

Test time data from several existing electric arc-driven shock tubes

have been examined and compared to the theoretical results. In this comparison, test time from individual shock tubes are examined separately, then generalizations are made regarding these data.

Ohio State University Shock Tube

The Ohio State University electric arc-driven shock tube has both a driven and driver tube diameter of 1/3 ft. Test time data for this shock tube have been published in references (6) and (7). Experimental measurements of test duration at an initial pressure of 1 mm Hg using Schlieren and microwave techniques are shown in Figure 3 with the calculated laminar and turbulent non-uniform freestream results. At shock Mach numbers less than 16, the data tend to follow the trend of the laminar theory with data scatter up to the theoretical laminar boundary layer prediction. At increasing shock Mach numbers, the test time data indicates less agreement with the laminar theory. Additional test time data obtained in 1 mm Hg of air by optical methods at a driven tube length of 28 feet is shown in Figure 4 for the shock Mach numbers greater than 16. These data scatter uniformly between the laminar and turbulent theoretical prediction with the laminar curve providing an upper bound to the measured test time, and the turbulent curve providing a lower bound to the experimental data. At a distance of 15 feet from the diaphragm with 1 mm Hg of air as the driven gas, measured test time as seen in Figure 5 also scatters between the laminar and turbulent curves.

At an intial air pressure of 0.2 mm Hg, the observed test time data obtained from photomultiplier records in the 15-ft. configuration is predicted quite well by the laminar theory at shock Mach numbers less than 32 as may be seen in Figure 6. At shock Mach numbers greater than 32, the experimental test time is shorter than would be predicted by the extrapolated turbulent theory using the shock charts of Lewis, however, the observed test time does agree with the turbulent theory when using the shock properties of Ziemer to compute test time.

In Figure 7 is shown the test duration at an initial pressure of 0.060 mm Hg in the O.S.U. shock tube. The test time is measured at a station 15 feet from the diaphragm. Here occurs the unusual circumstance where the observed test time is longer than that predicted by the laminar or the turbulent theory. Also at this test condition the turbulent theory indicates longer test time than the laminar theory. It may be that the extended experimental test time is caused by nonequilibrium flow behind the shock wave. The time to reach radiation equilibrium ($\tau_{0.1}$) is shown in the figure to illustrate that at shock Mach numbers less than 20, the test gas is not equilibrated, and in addition a sizeable portion of the observed test slug is not in equilibrium at the faster shock Mach numbers.

General Electric Company Space Science Laboratory 2-Inch D Shock Tube

The performance of the General Electric Company 2-inch D by 11.3 ft. long shock tube was reported by Warren in reference (8). The driver

diameter of the shock tube is 1.75 inches. A limited amount of test time data was presented in the report. Three runs at a shock Mach number near 24 in 1.0 mm Hg of air indicated a flow time from 10 to 15 μsec in the shock tube. The calculated test time for these test conditions is 10.7 μsec for a laminar-wall boundary layer and 6.1 μsec for a turbulent wall boundary layer. The observed test time agrees with the laminar theory.

General Electric Company Space Science Laboratory 6-In. D Shock Tube

A considerable quantity of test time data for the 6-inch D shock tube has been reported in reference (9). This shock tube has a driver diameter of 3 inches. Test times at a station 29.5 feet from the diaphragm at initial air pressures of from 0.10 to 7.0 mm Hg and a shock velocities of from 15,000 to 35,000 ft/sec are shown in Figures 8a through 8d. In Figure 8a, measured test times for pressures of from 1 to 7 mm Hg are illustrated. The majority of the data are for pressure of 1.0 mm Hg. These test time data are scattered symmetrically about the turbulent boundary layer test time predicted curve. Of the 28 data points at a pressure of 1 mm Hg, 15 fall above the turbulent theory curve and 13 fall below. The measured test time does not exceed that predicted for a laminar wall-boundary layer. Similar results are shown for an initial air pressure of 0.5 mm Hg in Figure 8b. Again the data are scattered about the turbulent theory with no measured test time exceeding the laminar theory. Of the 26 data points obtained at 0.5 mm Hg pressure, 14 are above the turbulent theory curve, 11 points are below while 1 measured test time agrees with the turbulent theory.

Figure 8 illustrates the close agreement between measured data and the turbulent theory at an initial air pressure of 0.250 mm Hg. Twelve runs have test times longer than the turbulent theory, 12 shorter and 1 test time is in agreement with theory. In Figure 8, there are only 5 data points at 0.100 mm Hg. The laminar theory and turbulent theory predict almost the identical test time at this condition. The data scatters about the theoretical results, with 2 runs having test durations longer than either theoretical result. This was also seen in Figure 7 where experimental test time was more than twice as long as the theoretical predication.

Avco-Everett Research Laboratory 6-Inch D Shock Tube "B"

Test time results from the Avco-Everett 6-inch D shock tube "B" are typical of both this shock tube, the Avco-Everett 6-inch D shock tube "A", the JPL 6-inch D shock tube, and possibly the Avco-RAD 6.5-inch D shock tube. The driver diameter of all these shock tubes is about 1-3/8 inches, which represents a 20:1 driven to driver tube area ratio. Figure 9 from reference (10) illustrates the test duration obtained at a station 30 feet from the diaphragm in 0.250 mm Hg initial pressure of air. Except where a 30-inch long $1\frac{1}{2}$ inch diameter section was used downstream of the diaphragm, the turbulent theory curve represents an upper bound to the experimental data. With the additional section downstream of the diaphragm, test time duration does approach that for a laminar wall-boundary-layer. The experi-

mental data can best be described as having a mean level of 70 percent that of the turbulent theory.

Jet Propulsion Laboratory 6-Inch D Shock Tube

Since the basic design of this shock tube is very similar to that of the Avco-Everett shock tubes, "A" and "B", the test time performance is very similar also. Test times have been shown in reference (11). In this shock tube test time is measured at several stations along the tube. Results of 5 runs at an initial air pressure of 0.250 mm Hg is shown in Figure 10. Even though the test time measured 28 feet from the diaphragm is close to that predicted by the turbulent theory, the growth of test time with distance is that expected with a laminar boundary layer. It appears as if some distance is required to damp out initial disturbances occurring at the diaphragm and the expansion section before the test slug becomes well defined and grows as predicted by the laminar theory.

Test Time Rules

Comparison of the experimental test times of the several existing electric arc-driven shock tubes with laminar and turbulent wall-boundary layer theories have revealed rules which describe (1) the upper and/or lower limits of experimental test times, and/or (2) mean values of these test times. Parameters found to be of fundamental importance to test time duration are initial driven tube pressure, shock speed, driven tube diameter and length and driven to driver tube cross-sectional area ratio. Mirel's turbulent wall-boundary layer theory as modified by using the air viscosity of Yos describes: (1) an upper limit on test times measured in large (20:1) driven to driver tube area ratio shock tubes, (2) a mean value of test time for moderate (4:1) area ratio shock tubes and (3) a lower bound on test times in small (1:1) area ratio shock tubes. Also, test times computed from the laminar wall-boundary layer theory describe an upper limit to measured data in small and moderate area ratio shock tubes in initial pressures in excess of 0.200 mm Hg. In the small area ratio shock tube an initial air pressures less than 0.100 mm Hg (where computed turbulent test time is longer than laminar test time) the measured test times are longer than the theoretical equilibrium gas values.

A simple rule which quite adequately describes the test time performance of the electric arc-driven shock tubes is the following: In 1:1 driven to driver area ratio shock tubes the mean of the measured test time will be 1.4 times longer than expected from the turbulent theory. In 4:1 area ratio shock tubes the mean test time will equal that predicted by turbulent theory; and in 20:1 area ratio shock tubes the mean of measured results will be 0.7 that calculated by the turbulent-wall boundary layer theory. In this paper, the symbol "k" is used to designate the ratio of expected test time to that predicted by the turbulent wall boundary layer theory.

REQUIREMENTS FOR ARC-HEATED SHOCK TUBE DRIVERS

Energy requirements of arc-heated shock tube drivers are known when the

necessary energy density of the helium driver gas is known in addition to the diameter and length of the driver. The driver gas energy density requirements for arc-heated shock tubes have been obtained by correlation of data from seven existing electric shock tubes. The driver length required for a given shock tube is shown to be a function of the initial density ratio across the diaphragm and the driven to driver tube area ratio factor "g" - ref. (12), (13), (15), and (16).

Energy Requirements

In order to correlate experimental data from shock tubes of several driver to driven tube area ratios, correlation parameters are deduced from shock tube theory. The basic shock tube equation for a tube with arbitrary driver, diaphragm and driven tube cross-sectional areas is:

$$\frac{p'_4}{p_1} = \frac{p_2}{p_1} \left[1 - \frac{\gamma_4 - 1}{2} \frac{u_s (1 - \rho_1/\rho_2)}{a_4} \right]^{-\beta} \tag{2}$$

where:

$$p'_4 = g\, p_4$$

$$a'_4 = g^{\beta - 1} a_4$$

$$\beta = \frac{2\gamma_4}{\gamma_4 - 1}$$

$$g = \left[\frac{1 + \frac{\gamma_4 - 1}{2} M_3'}{1 + \frac{\gamma_4 - 1}{2} M_4'} \right]^2 \left[\frac{1 + \frac{\gamma_4 - 1}{2} M_4'^2}{1 + \frac{\gamma_4 - 1}{2} M_3'^2} \right]^{\frac{3}{2}}$$

Rearranging the basic shock tube equation in order to define the shock velocity, u_s, implicity gives:

$$u_s = \left[1 - \left(g \frac{p_4}{p_1} \frac{p_1}{p_2} \right)^{-\beta - 1} \right] \left[\frac{2}{\gamma_4 - 1} \frac{g^{\beta - 1} a_4}{(1 - \rho_1/\rho_2)} \right] \tag{3}$$

Also for an electric shock tube where the driver gas is heated by an arc discharge at constant volume the ideal final pressure, p_4, and final speed of sound, a_4, may be derived from basic thermodynamics:

$$p_4 = \frac{R}{C_v} \frac{Q}{V_4} \tag{4}$$

$$a_4 = \left(\frac{\gamma_4 R}{C_v \rho_4} \quad \frac{Q}{V_4} \right)^{\frac{1}{2}} \tag{5}$$

therefore, ideally, p_4, is approximately independent of the initial conditions in the driver tube, and is only a function of the gas properties and the energy density. Substituting these values for p_4 and a_4 into the foregoing equation results in:

$$u_s = \left[1 - \left(\frac{g}{p_1} \frac{Q}{V_4} \frac{R}{C_v} \frac{p_1}{p_2} \right)^{\beta - 1} \right] \frac{2}{\gamma_4 - 1} \frac{g^{\beta - 1}}{(1 - \rho_1/\rho_2)} \left(\frac{Q}{V_4} \right)^{\frac{1}{2}} \left(\frac{\gamma_4 R}{C_v \rho_4} \right)^{\frac{1}{2}} \tag{6}$$

Since variations in p_1/p_2, and $(1 - \rho_1/\rho_2)$ and are small at constant shock speed, and ρ_4 does not vary appreciably in experimental data, the parameters p_1/g and $g^{\beta - 1} \left(\frac{Q}{V_4}\right)^{\frac{1}{2}}$ show consistent agreement between data from widely varied shock tubes and hence are here presented as the correlation parameters. When experimental data are reduced on the basis of these parameters the effect of driven to driver tube area ratio on measured data is effectively accounted for.

Shock speed data from seven electric arc-driven shock tubes have been plotted in the attached Figure 11. Except for data from the JPL shock tube, these data were obtained from published reports as indicated. The shock tube driven tube diameters on these shock tubes vary from $1\frac{1}{2}$ inches to 6 inches. The driven to driver tube area ratio varies from 1:1 to over 20:1. It is surprising to find such good correlation based simply on the calculated "g" factor and measured energy density. Lines of constant energy density parameter $g^{1/5} (Q/V_4)^{\frac{1}{2}}$ have been drawn on the figure to represent the best fairing of the experimental data.

In order to use the figure in design problems, first determine the "g" factor from ideal gas flow equations or charts for the given shock tube, then calculate the required p_1/g, and read from the figure the required $g^{1/5} (Q/V_4)^{\frac{1}{2}}$ at the design shock speed, u_s. Convert the parameter to energy density (joules/cm^3) through the appropriate arithmetical steps to obtain the desired information.

Driver Length Requirement

From the work of Camm and Rose of reference (15), the relationship between driven to driver tube length for a shock tube with area change at the diaphragm is given as follows:

$$\frac{x_i}{x_4} = \frac{x_i}{x_4}\bigg|_{\frac{u_3}{a'_4}} - \frac{u_3}{a'_4}\left(1 - \frac{a'_4}{a_4}\right)\left(\frac{\gamma+1}{2}\right)^{\frac{\gamma+1}{2(\gamma-1)}} \tag{7}$$

A relationship for x_i/x_4 for a constant area shock tube can be obtained from Hall (ref. 16).

$$\frac{x_i}{x_4}\bigg|_{\frac{u_3}{a'_4}} = 2\frac{u_3}{a'_4}\left(1 - \frac{\gamma-1}{2}\frac{u_3}{a'_4}\right)^{-\frac{\gamma+1}{2(\gamma-1)}} \tag{8}$$

Combining the two foregoing equations results in an expression for driven the driver length as a function of the ratio of the contact surface velocity to the effective driver speed of sound.

$$\frac{x_i}{x_4} = \frac{u_3}{a'_4}\left[2\left(1 - \frac{\gamma-1}{2}\frac{u_3}{a'_4}\right)^{-\frac{\gamma+1}{2(\gamma-1)}} - \left(1 - \frac{a'_4}{a_4}\right)\left(\frac{\gamma+1}{2}\right)^{\frac{\gamma+1}{2(\gamma-1)}}\right] \tag{9}$$

With the knowledge of the ratio u_3/a'_4 it is now possible to calculate the driven to driver tube length ratio. A method to avoid having to know the explicit value of the driver gas speed of sound is found by considering the basic shock tube equation and by using the asymtotic shock speed conditions where:

$$\frac{u_3}{a'_4} = \frac{u_s}{a'_4} \tag{10}$$

and $p_3 \simeq \rho_1 u_3^2$. (11)

Also the driver pressure can be expressed as a function of the driver density and speed of sound as follows:

$$p_4 = a_4^2 \frac{\rho_4}{\nu_4} \tag{12}$$

Therefore, equation (?) becomes

$$g\frac{a_4^2}{\rho_1 u_3^2}\frac{\rho_4}{\nu_4} = \left(1 - \frac{\nu_4 - 1}{2}\frac{u_3}{a'_4}\right)^{-3} \tag{13}$$

Rearranging terms and letting $\gamma_4 = 5/3$ results in:

$$\frac{\rho_1}{g^{3/5}\rho_4} = 3/5 \left(\frac{a'_4}{u_3}\right) \left(1 - \frac{1}{3}\frac{u_3}{a'_4}\right)^5 \qquad (14)$$

If equations (9) and (14) are solved for x_i/x_4 as a function of the initial density ratio across the diaphragm, $\rho_1/g^{3/5}\rho_4$, the curve shown in Figure 12 results. Therefore, for a given initial density ratio across the diaphragm, and given driven to driver area ratio, the required driven to driver tube length can be obtained without explicit knowledge of the driver gas speed of sound.

TEST TIME REQUIRED FOR GAS RADIATION STUDIES

For the measurement of non-equilibrium and equilibrium radiation behind the incident shock wave in a shock tube, it is necessary that sufficient test time exist for the test gas to achieve thermo-chemical equilibrium. Also the radiation relaxation time cannot be less than 5 times the response time of the optical instruments in order to make meaningful measurements of non-equilibrium radiation.

The radiation relaxation time of air (in laboratory coordinates) has been measured by Allen, Camm and Rose (ref. 17) at shock speeds from 5×10^5 cm/sec to 10×10^5 cm/sec. The curve faired through the measured data points can be best expressed as follows:

$$\tau_{0.1}\, p_1 = 10^{2.3}\, u_s^{-6.15}$$

where:

$\tau_{0.1}$ = time for radiation to have fallen to 10% of the equilibrium level - μ sec.

p_1 = initial pressure ahead of the shock - atm.

u_s = shock velocity - cm/sec $\times 10^{-5}$

Radiation relaxation time for planetary atmospheric gases other than air measured in the Jet Propulsion Laboratory Electric Arc-Driven Shock Tube by Thomas and Menard (ref. 18) are shown in Figure 13 with above mentioned air data. The relaxation time for a 9% carbon dioxide - 90% nitrogen - 1% argon mixture has a radiation relaxation time roughly twice that of air.

APPLICATION OF RESULTS

In order to apply the results of this study to the design of an electric arc-driven shock tube, it is necessary to (1) choose a test time criterion, (2) select a shock velocity range of interest, and (3) define the initial pressure requirements. It is possible to minimize the shock tube dimensions and energy requirements for one set of the above criteria of test time, shock velocity and initial pressure in the driven tube. For example, in this section the radiation relaxation time is chosen to be 1 μ sec, the total test time is selected to be 10 μ sec, and the minimum shock tube dimensions are found for shock velocities ranging from 7×10^5 to 15×10^5 cm/sec. Driven to driver tube area ratios of 1, 4, and 20 are studied.

If the radiation relaxation time of 1 μ sec in air is chosen as a test time criterion, then the initial air pressure in the driven tube must vary with shock velocity as shown in Figure 14. At a shock speed of 7.0×10^5 cm/sec the initial air pressure is 1.26×10^{-3} atm, at a shock speed of 10.0×10^5 cm/sec the initial air pressure must be 1.40×10^{-4} atm, etc.

For the several driven to driver area ratios, the "g" factor has been obtained and is given in Table I where the example calculations are shown. These sample calculations are self explanatory and will not be completely described here, however, it should be noted that the length to diameter ratio of the driven tube is taken to be 60 in all cases so as to be in the range of the experimental configurations described in previous sections.

The variations of driven tube diameters with shock velocity required for shock tubes of the several area ratios is illustrated in Figure 15. Here it may be seen that the area-ratio 20 shock tube diameter will be a factor of 1.74 larger than the area-ratio 1.0 shock tube diameter. The area-ratio 4 shock tube diameter is a factor of 1.32 larger than the area ratio 1.0 shock tube diameter. Since the driven tube length is a factor of 60 times the diameter, the ratios of the lengths of the shock tubes with different driven to driver tube area ratios are in the same proportion as seen in Figure 16.

Driver tube diameter as a function of shock velocity is shown in Figure 17 for the several area ratios. Here it may be seen that the advantage of the large driven to driver tube area-ratio shock tube is the reduced diameter of the driver for a given test condition; however, the price in other dimensions for this advantage is extreme. Even the driver length of 20:1 driven to driver area ratio shock tube is more than 2.5 times longer than the 1:1 area ratio shock tube as seen in Figure 18.

Energy requirements for the family of shock tubes with various area ratios are shown as Figure 19. Energy required in the capacitor bank varies from about 5×10^3 joules at a shock speed of 7×10^5 cm/sec to

about 120 x 10^3 joules at a shock velocity of 15 x 10^5 cm/sec. The family of shock tubes with an area ratio of 1.0 required about 10 to 20 percent less energy than the shock tubes with greater driven to driver tube area ratio.

Thus it is shown that a 1:1 driver to driven tube area ratio shock tube of modest dimensions and energy requirements can be designed to study gas radiation in shock heated air. The Jet Propulsion Laboratory is now designing a 0.5-foot diameter driver for an existing 0.5-foot diameter driven tube in order to extend gas radiation studies from the present shock speed limit of 10 x 10^5 cm/sec to a new limit of 13 x 10^5 cm/sec based upon the conculsions reached in the present paper.

This paper presents the results of one phase of research carried out at the Jet Propulsion Laboratory, California Institute of Technology, under Contract No. NAS7-100, sponsored by the National Aeronautics and Space Administration

NOMENCLATURE

Symbol	
A	cross-sectional area (ft^2)
a	speed of sound (cm/sec)
C	specific heat (cm/sec $2/^\circ K$) ratio of density-viscosity product across boundary layer
d	diameter (ft)
g	driven to driver tube area-ratio factor
k	test time rule parameter
l	length of shock heated test gas
p	pressure (atm) (dynes/cm^2)
Q	driver system electrical energy (joules)
R	helium gas constant (2.077×10^7 $cm/sec^2/^\circ K$)
u	velocity (cm/sec)
V	volume (cm^3) (ft^3)
W	density ratio across shock, ρ_2/ρ_1
x	shock tube length (ft)
β	boundary layer displacement thickness parameter
γ	isentropic expansion coefficient
ρ	density (gm/cm^3)
τ	test time (sec)

Subscripts	
0	standard temperature and pressure conditions
1	condition ahead of shock wave
2	condition behind shock wave
3	condition behind contact surface
4	driver condition at flow initiation
e,o	condition immediately behind shock wave
i	condition at overtaking expansion wave
m	maximum
st	standard temperature and pressure conditions
s	stagnation condition behind shock wave
w	condition at wall

Superscript	
	reference condition in area ratio shock tube also, condition immediately upstream and downstream of diaphragm station

REFERENCES

(1) Mirels, H., "Test Time in Low Pressure Shock Tubes", The Physics of Fluids, Vol. 6, No. 9, pp. 1201-1214, Sept. 1963.

(2) Mirels, H., "Shock Tube Test Time Limitation Due to Turbulent-Wall Boundary Layers", AIAA Journal, Vol. 2, No. 1, pp. 84-93, Jan. 1964.

(3) Yos, J. M., "Transport Properties of Nitrogen, Hydrogen, Oxygen and Air to 30,000°K", AVCO Corporation, RAD-TM-63-7, 22 March 1963.

(4) Ziemer, R. W., "Extended Hypervelocity Gas Dynamic Charts for Equilibrium Air", STL/TR-60-000-09093, Space Technology Laboratories, Inc., April, 1960.

(5) Lewis, C. H., and E. G. Burgess, III, "Charts of Normal Shock Wave Properties in Imperfect Air", AEDC-TDR-64-43 (AD 433958), Mar. 1964.

(6) Graber, B. C., and R. M. Nerem, "Test Duration Measurements in an Arc-Driven Hypervelocity Shock Tube", Report 1573-2, The Ohio State University Research Foundation, October 15, 1963.

(7) Nerem, R. M., "Measurements of Aerodynamic and Radiative Heating at Super-orbital Velocities", Report 1598-1, The Ohio State University Research Foundation, January 15, 1964.

(8) Warren, W. R., D. A. Rogers and C. J. Harris. "The Development of an Electrically Heated Shock Driven Test Facility", 2nd Symposium on Hypervelocity Techniques, 20-21 March, 1962.

(9) Gruszczynski, J. S., and W. R. Warren, "Hypervelocity Heat Transfer Studies in Simulated Planetary Atmospheres", Final Report, JPL Purchase Order 950297, General Electric Space Sciences Laboratory, Mar. 1964.

(10) Camm, J. C., and P. H. Rose, "Electric Arc-Driven Shock Tube", The Physics of Fluids, Vol. 6, No. 5, May, 1963.

(11) Collins, D. J., F. R. Livingston, T. L. Babineaux, N. R. Morgan, "Hypervelocity Shock Tube", TR No. 32-620, Jet Propulsion Laboratory, June 15, 1964.

(12) Russell, D. A., "A Study of Area Change Near the Diaphragm of a Shock Tube", Guggenheim Aero. Lab., California Institute of Technology, June 15, 1960.

(13) Camm, J. C., "Escape-Velocity Shock Tube with Arc-Heated Driver", 2nd Symposium on Hypervelocity Techniques, 20-21 March 1962.

(14) Gruszczynski, J. S., W. R. Warren and N. S. Diaconis, "Laboratory Simulation of Hypervelocity Heat Transfer Problem During Planetary Entry", Report R64SD 73, General Electric Space Sciences Laboratory, Nov. 1964.

(15) Rose, P. H., and J. C. Camm, "Electric Shock Tube for High Velocity Simulation", Report 136, AVCO-Everett Research Laboratory, July, 1962.

(16) Hall, J. H., "Shock Tubes, Part II: Production of Strong Shock Waves; Shock Tube Applications, Design and Instrumentation", Institute of Aerophysics, University of Toronto, p. 168, May, 1958.

(17) Allen, R. A., P. H. Rose and J. C. Camm, "Nonequilibrium and Equilibrium Radiation at Super-Satellite Re-Entry Velocities", RR-156, AVCO-Everett Research Laboratory, Sept. 1962.

(18) Thomas, G. M., and W. A. Menard, "Experimental Measurements of Nonequilibrium and Equilibrium Radiation from Planetary Atmospheres", Publication CP-9, AIAA Entry Technology Conference, October 12-14, 1964.

TABLE I

CALCULATIONS FOR FAMILY OF SHOCK TUBES WITH 1μ SEC
AIR RADIATION RELAXATION TIME AND 10μ SEC TOTAL TEST TIME

$\tau = 10^{-5}$ sec

$\tau_{0.1} = 10^{-6}$ sec

		u_s (cm/sec)								
		7×10^5			10×10^5			15×10^5		
		A_1/A_4			A_1/A_4			A_1/A_4		
		1	4	20	1	4	20	1	4	20
(1)	g (ref.12)	1	0.409	0.175	1	0.409	0.175	1	0.409	0.175
(2)	$g^{3/5}$	1	0.585	0.351	1	0.585	0.351	1	0.585	0.351
(3)	$g^{1/5}$	1	0.836	0.706	1	0.836	0.706	1	0.836	0.706
(4)	p_1 (Figure 14) atm	1.26×10^{-3}	→	→	1.40×10^{-4}	→	→	1.16×10^{-5}	→	→
(5)	p_1/g ((4) ÷ (1)) atm	1.26×10^{-3}	3.15×10^{-3}	7.2×10^{-3}	1.40×10^{-4}	3.42×10^{-4}	8.0×10^{-4}	1.16×10^{-5}	2.84×10^{-5}	6.63×10^{-5}
(6)	$g^{1/5}\,(Q/V_4)^{\frac{1}{2}}$ (Figure 11) $(j/cc)^{\frac{1}{2}}$	6.24	6.86	7.80	7.37	8.0	8.95	9.57	9.93	11.08
(7)	Q/V_4 ((6) ÷ (3))^2 j/cc	39.0	67.4	122	54.4	91.4	161	91.5	140	246
(8)	$(p_{st}/p_1)^{\frac{1}{4}}\, \ell_m/d_1^{5/4}$ (Figure 2) $ft^{-\frac{1}{4}}$	9.5	9.5	9.5	9.45	9.45	9.45	9.45	9.45	9.45
(9)	k (Test Time Rules)	1.4	1	0.7	1.4	1	0.7	1.4	1	0.7
(10)	$k\ell_m$ ($k\tau\, u_s$) ft	0.23	0.23	0.23	0.328	0.328	0.328	0.492	0.492	0.492
(11)	$d_1^{5/4}$ ((10) ÷ (8) (4)$^{\frac{1}{4}}$ (9)) $ft^{5/4}$	0.0906	0.1282	0.1810	0.2255	0.319	0.451	0.566	0.801	1.138
(12)	d_1 ((10)$^{4/5}$) ft	0.1465	0.1935	0.255	0.304	0.401	0.529	0.635	0.8395	1.109
(13)	x_1 ((12) x 60) ft	8.8	11.62	15.3	18.22	24.1	31.7	38.1	50.2	66.5
(14)	ρ_1 gm/cm^3	0.15×10^{-5}	→	→	0.169×10^{-6}	→	→	0.140×10^{-7}	→	→
(15)	ρ_4 (P_{4_i} = 250 psia) gm/cm^3	0.283×10^{-2}	→	→	→	→	→	→	→	→
(16)	$\rho_1/\rho_4\, g^{3/5}$ ((14) ÷ (15) (2))	0.537×10^{-3}	0.919×10^{-3}	1.532×10^{-3}	0.596×10^{-4}	1.02×10^{-4}	1.70×10^{-4}	0.495×10^{-5}	0.847×10^{-5}	1.41×10^{-5}
(17)	x_1/x_4 (Figure 12)	37.5	30.0	24.4	94	75	60.5	264	210	170
(18)	x_4 ((13) ÷ (17)) ft	0.234	0.388	0.706	0.194	0.322	0.524	0.144	0.239	0.391
(19)	d_4 ((12) ÷ $(A_1/A_4)^{\frac{1}{2}}$) ft	0.1465	0.0968	0.057	0.304	0.200	0.118	0.635	0.419	0.248
(20)	V_4 ($\frac{\pi}{4}$ (19)^2 (18)) ft^3	3.98×10^{-3}	2.86×10^{-3}	1.61×10^{-3}	1.41×10^{-2}	1.017×10^{-2}	0.576×10^{-2}	.0456	.0329	.01885
(21)	Q ((7) (20) 2.783×10^4 cm^3/ft^3) j	4260	5370	9460	2.14×10^4	2.59×10^4	2.58×10^4	1.165×10^5	1.28×10^5	1.29×10^5

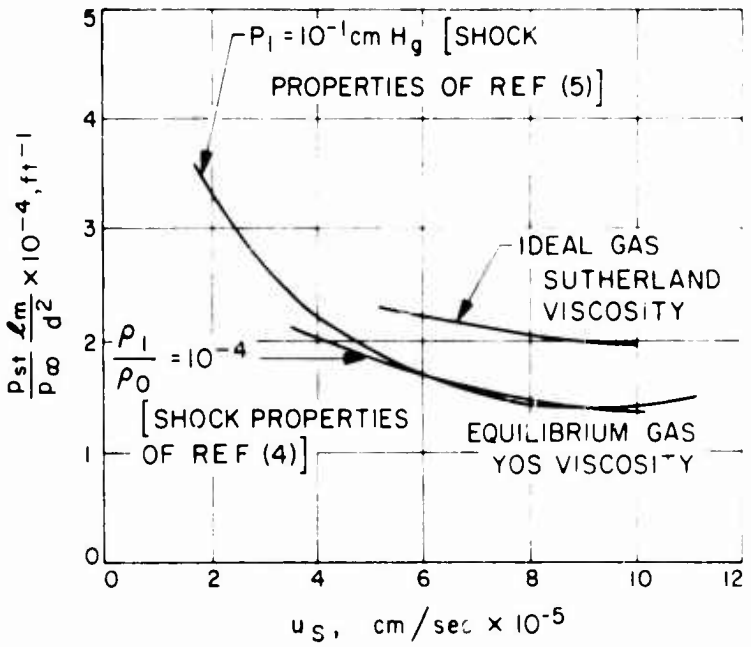


Fig. 1 Laminar-Wall Boundary Layer Separation Distance for Air.

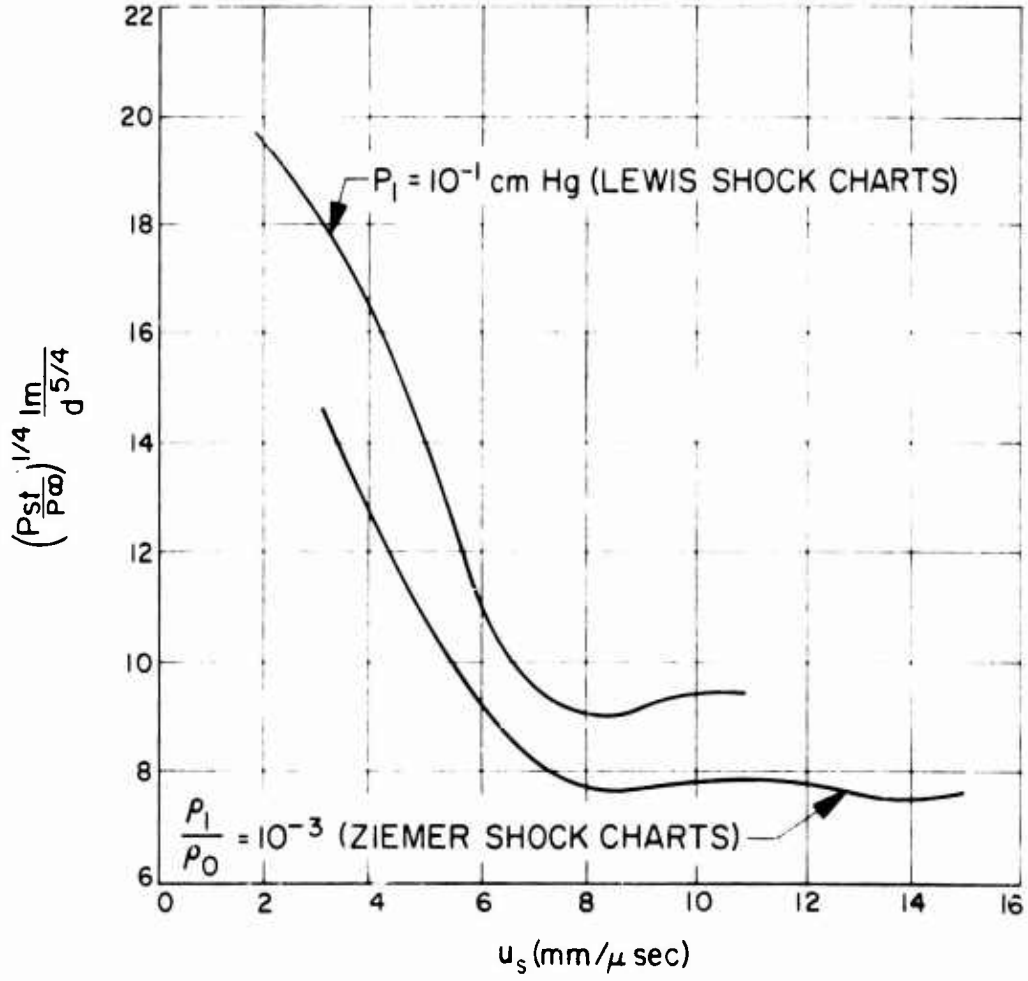


Fig. 2 Turbulent-Wall Boundary Layer Separation Distance for Air.

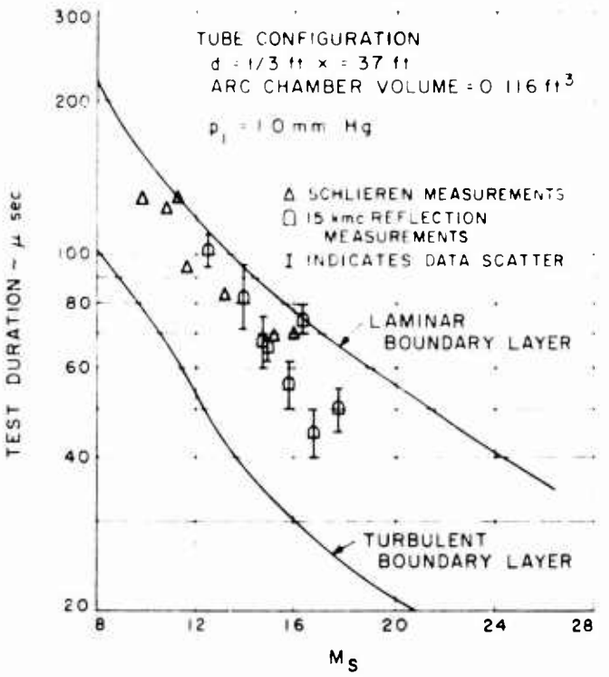


Fig. 3 Experimental measurements of Test duration using Schlieren and Microwave Techniques. Ohio State University Shock Tube.

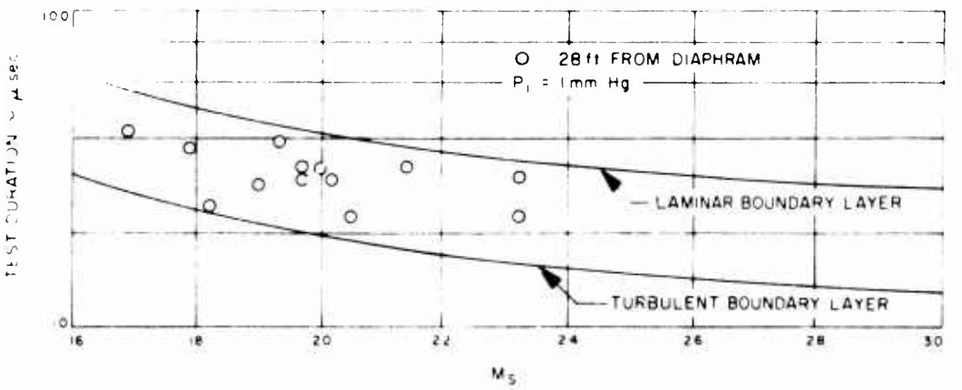


Fig. 4 Ohio State University Arc-Driven Shock Tube Test Duration Measurements.

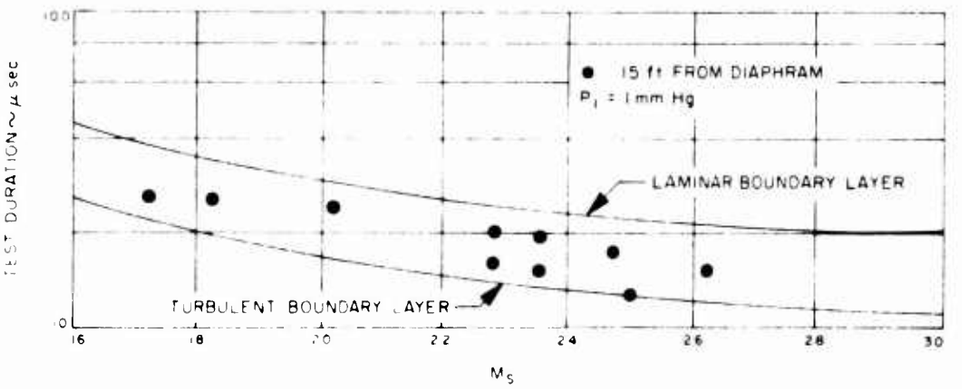


Fig. 5 Ohio State University Arc-Driven Shock Tube Test Duration Measurements.

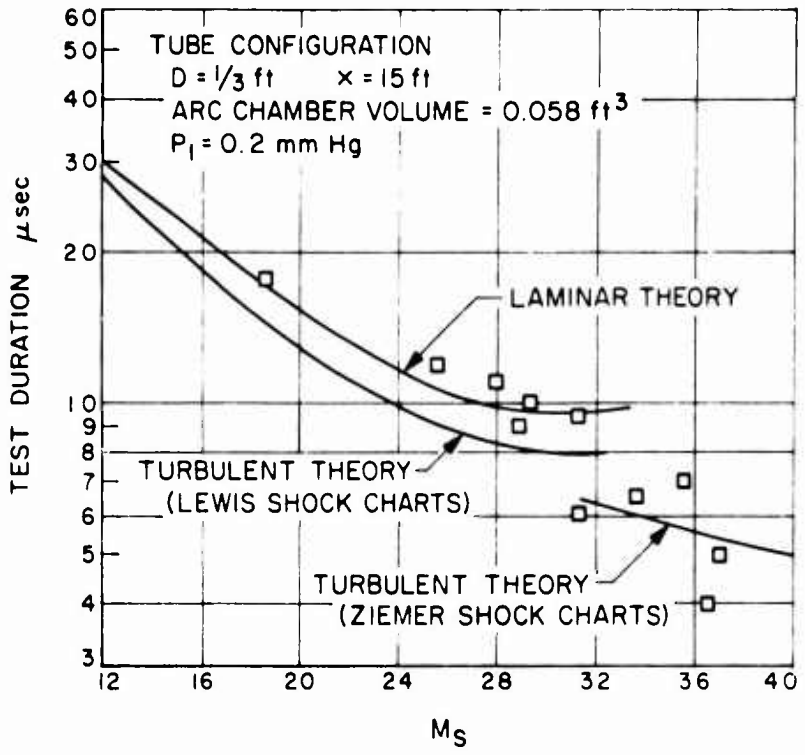


Fig. 6 Ohio State University Arc-Driven Shock Tube Test Duration Measurements.

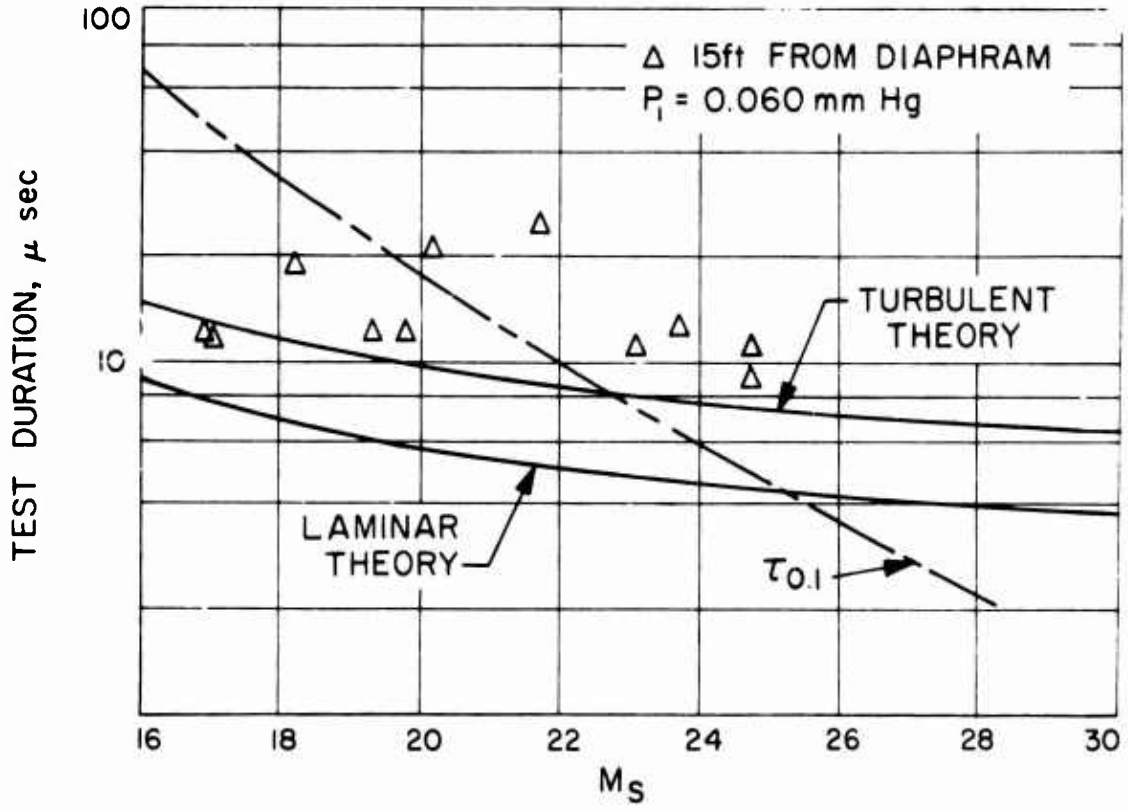


Fig. 7 Ohio State University Arc-Driven Shock Tube Test Duration Measurements.

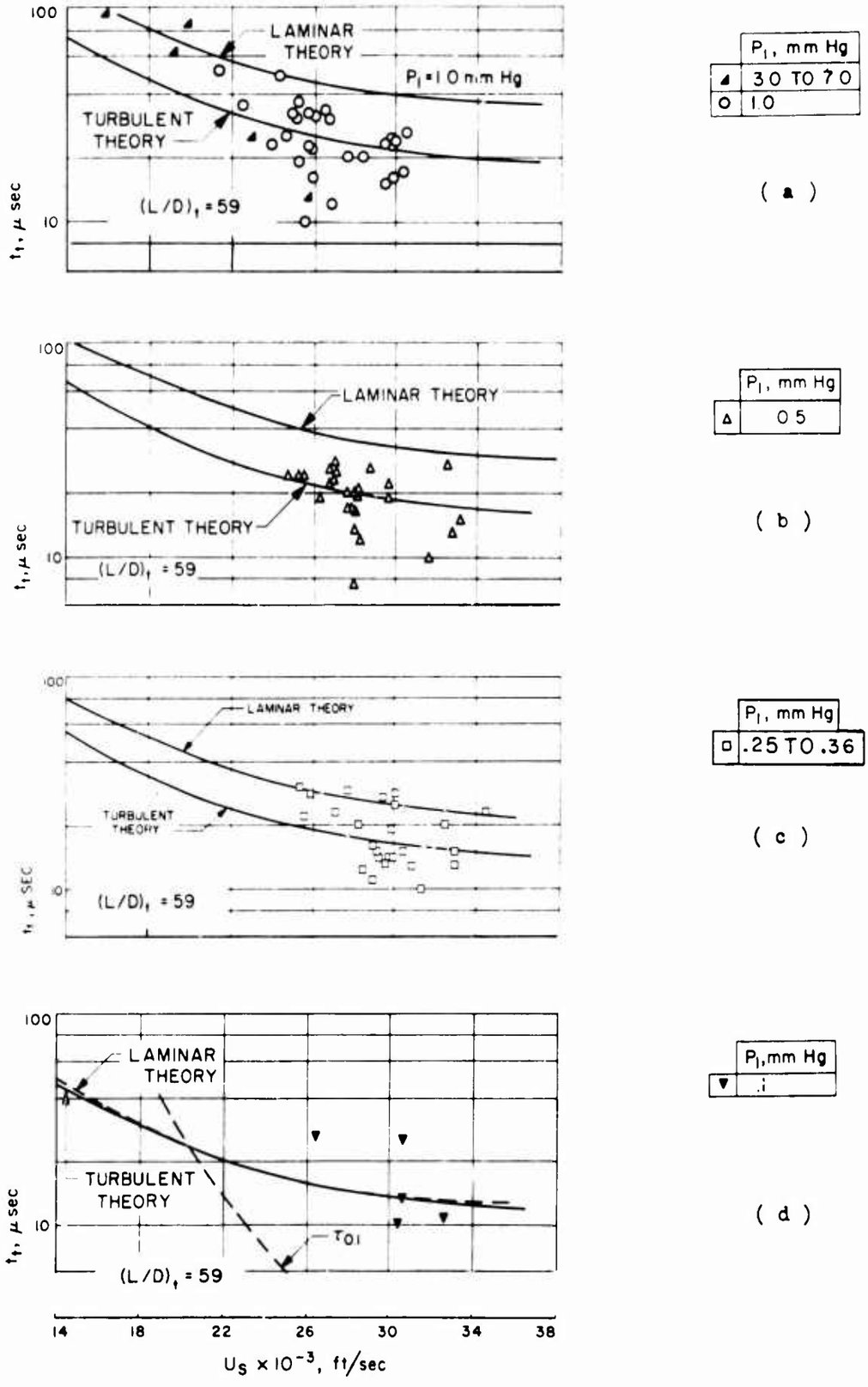


Fig. 8 General Electric Space Sciences Laboratory Electric 6-Inch Diameter Arc-Driven Shock Tube Test Duration Measurements.

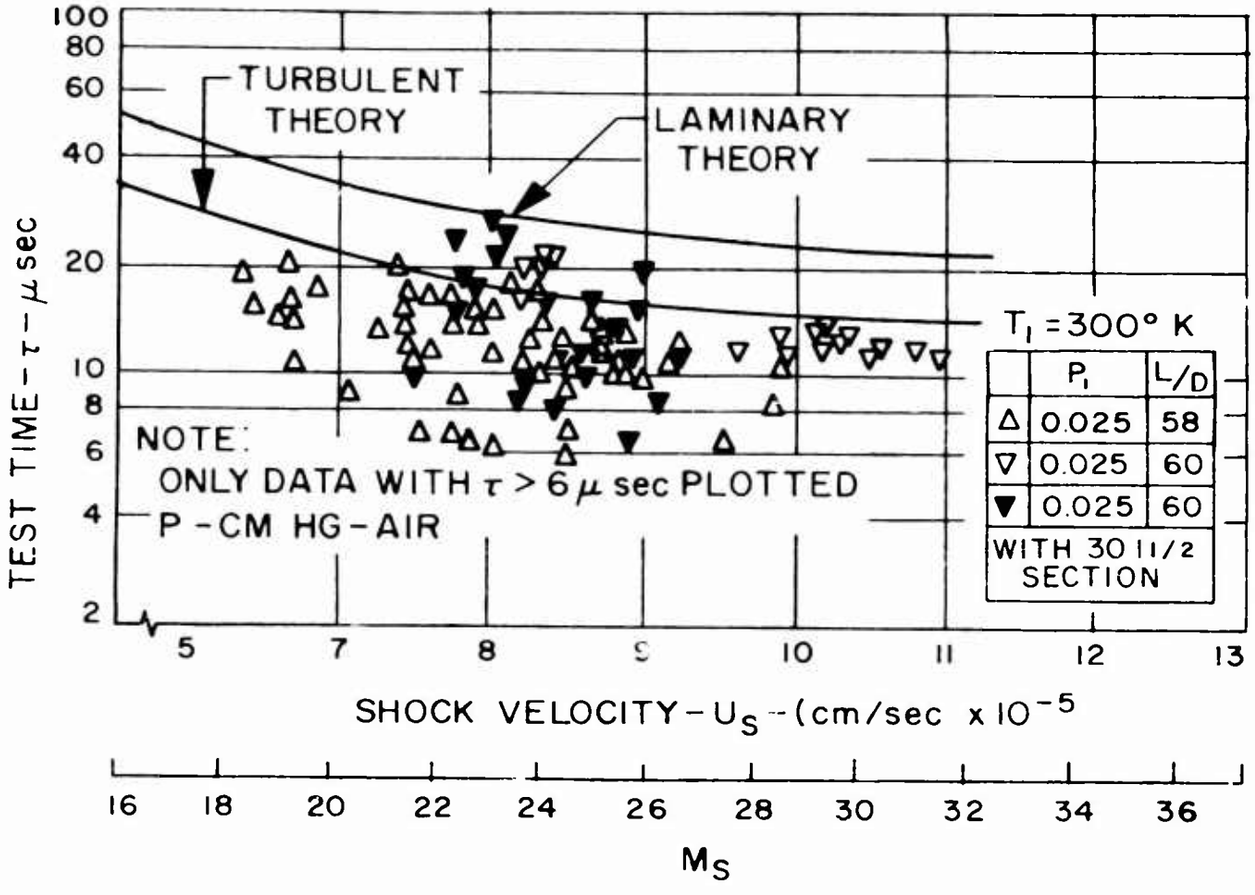


Fig. 9 Avco-Everett Research Laboratory 6-Inch Diameter Electric Arc-Driven Shock Tube 'B' Test Duration Measurements.

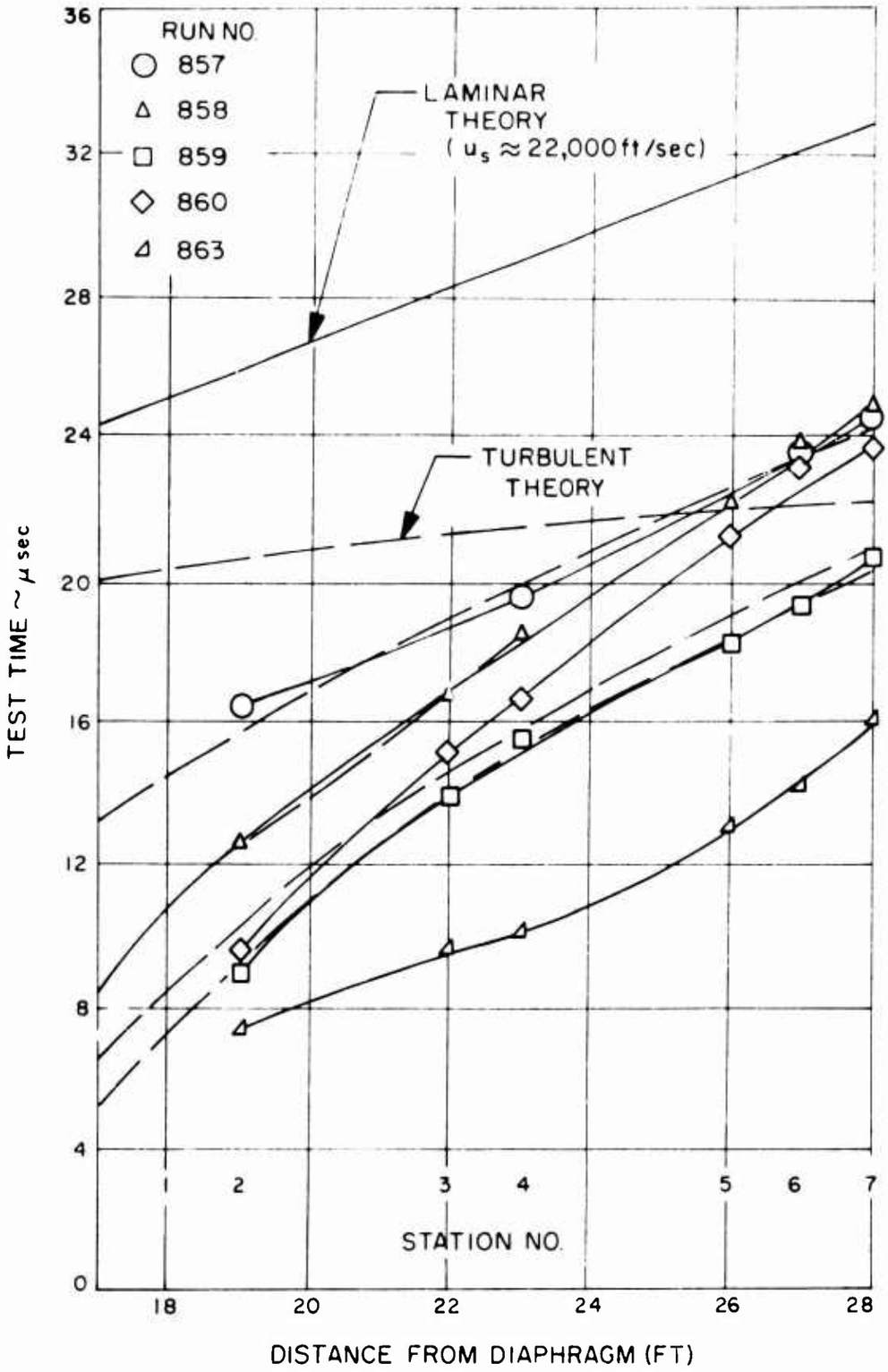


Fig. 10 Variation of Test Time with Distance from the Diaphragm for an Initial Pressure of 0.25 mm Hg.
JPL Electric Arc-Driven Shock Tube.

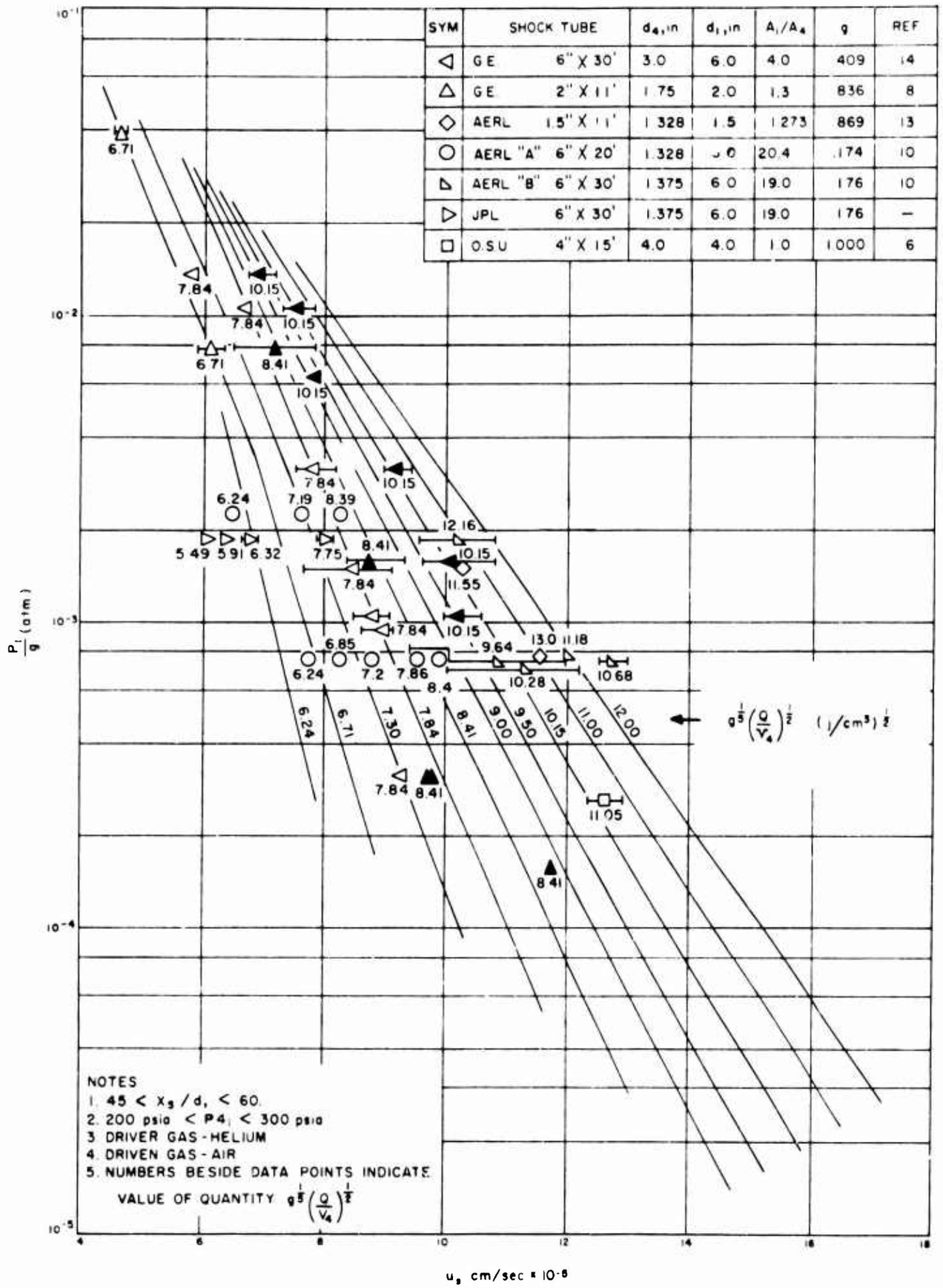


Fig. 11 Electric Arc-Driven Shock Tube Energy Density Requirements.

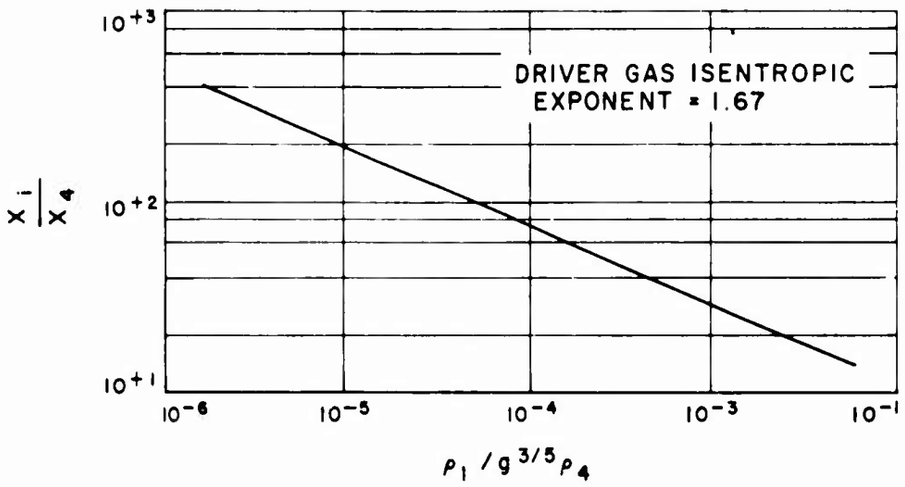


Fig. 12 Variation of Driven to Driver Tube Lengths with Diaphragm Density Ratio.

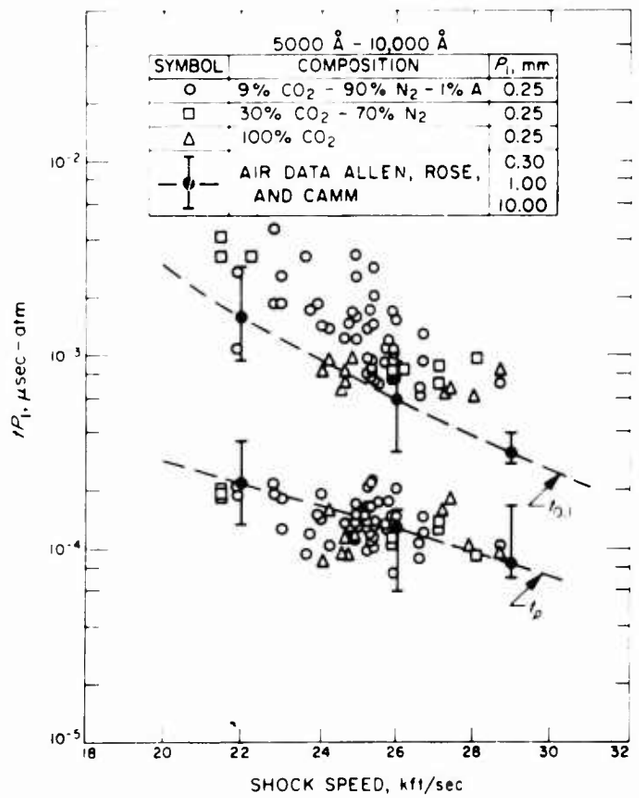


Fig. 13. Measurements of time to peak and time to reach an intensity 10% above the equilibrium radiation level in the wavelength region 3000 to 5000Å compared with air data for three CO_2-N_2 mixtures

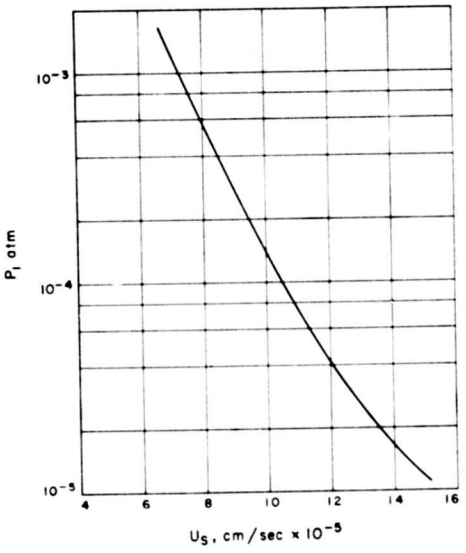


Fig. 14 Initial Air Pressure Required for Radiation Relaxation Time of 1 μsec.

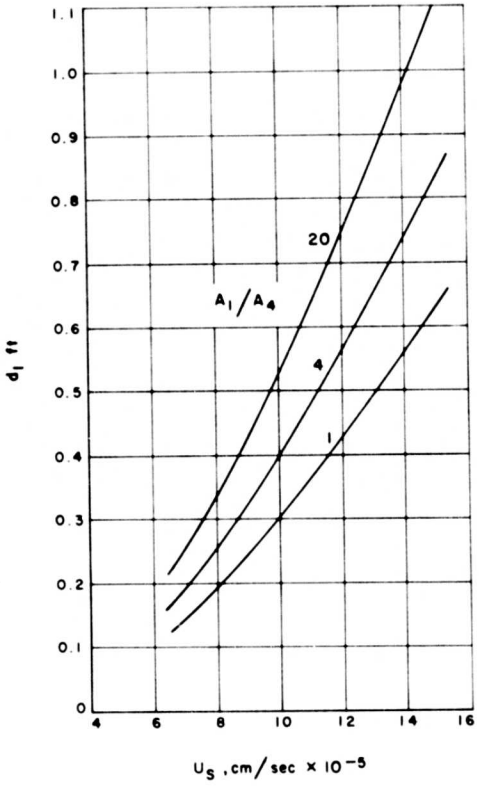


Fig. 15
Variation of Driven Tube Diameter

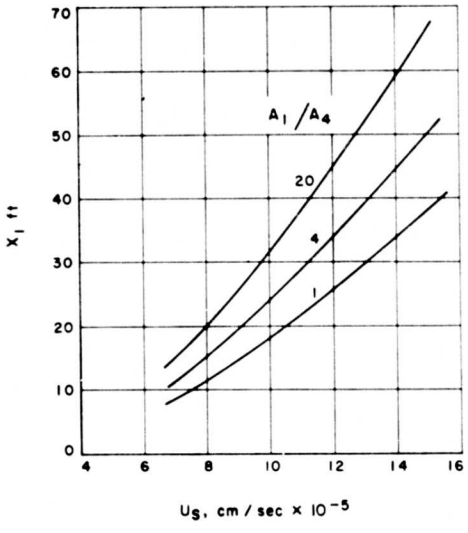


Fig. 16
Variation of Driven Tube Length

with

Shock Velocity for Radiation Relaxation Time of 1 μsec and Test Time of 10 μsec.

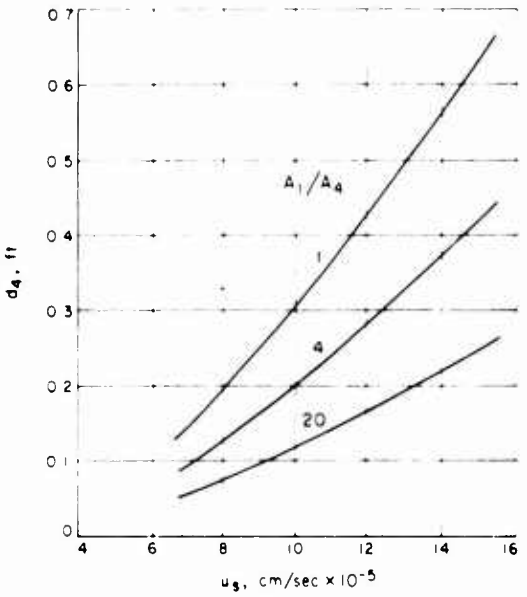


Fig. 17
Variation of Driver Tube Diameter
with Shock Velocity.

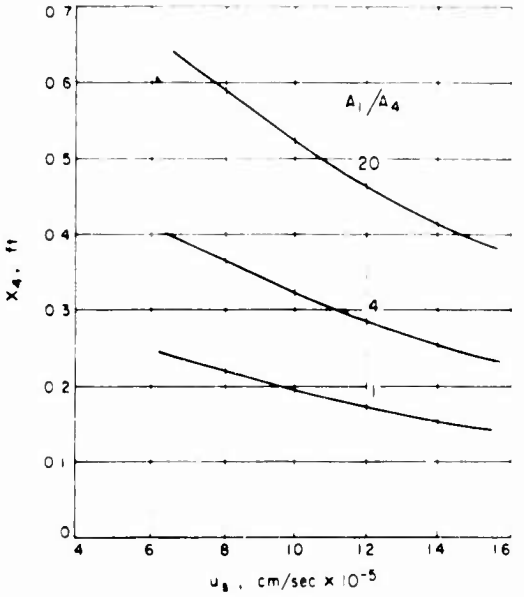


Fig. 18
Variation of Driver Length
with Shock Velocity

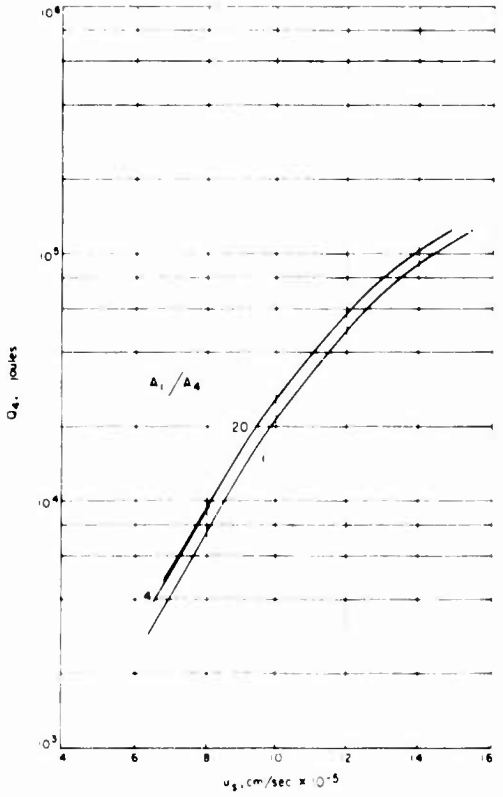


Fig. 19 Variation of Driver Energy Required with Shock Velocity for Air with Radiation Relaxation Time of 1 μsec and Test Time of 10 μsec.

BLANK PAGE

DIMENSIONAL ANALYSIS AND KINETIC THEORY OF SHOCKS

L. H. Holway, Jr.
Raytheon Research Division
Waltham, Massachusetts

INTRODUCTION

Although the methods of dimensional analysis have been useful in many classical problems of fluid dynamics, relatively little application has been made of these methods in problems involving kinetic theory. In this paper, the dimensional analysis methods which are appropriate to the Boltzmann equation are applied to a one-dimensional shock wave in a monatomic gas which behaves either as rigid spheres or as inverse-power molecules.

The results show that certain properties of the shock thickness as a function of Mach number, particularly in the limit $M \to \infty$, are determined by dimensional requirements. Although the same results can be obtained by other methods, such as the Chapman-Enskog (ref. 1) or Mott-Smith methods (ref. 2), dimensional analysis has the advantage of showing that these properties are independent of any particular approximation procedure. The present method also makes clear a fundamental difference between the inverse-power law and more complicated molecular force laws. In particular, for the more realistic force laws, it is no longer possible to plot X/λ (the shock thickness normalized by the mean free path in front of the shock) uniquely as a function of Mach number, instead a different curve is obtained for each different upstream temperature.

DIMENSIONAL ARGUMENTS

Let us consider a monatomic gas consisting either of rigid sphere molecules with diameter σ or of molecules which interact according to the power law, $F = \kappa/r^s$. The properties of a shock wave in such a gas are completely specified by the six parameters n_a, u_a, T_a, k, m, and either σ or κ. Here n_a, u_a and T_a are the number density, flow velocity and temperature in the equilibrium region upstream of the shock, k is

Boltzmann's constant and m is the mass of the molecule.*

The dimensions of n_a are (L^{-3}); of u_a, (LT^{-1}); of T_a, (degs); of k, $(ML^2T^{-2}deg^{-1})$; of m (M); of σ (L); of κ, $(ML^{s+1}T^{-2})$. Only two independent nondimensional numbers can be formed from the six parameters. We choose these to be the Mach number $(M^2 = 3u_a^2/5kT_a)$ and a nondimensional number ϵ, where, for rigid spheres,

$$\epsilon = n_a^{1/3}\sigma \quad , \tag{1}$$

and, for inverse-power molecules,

$$\epsilon = n_a^{1/3}(\kappa/kT_a)^{1/s-1} \quad . \tag{2}$$

If X is any length which is determined by the original six parameters, the nondimensional quantity $Xn_a^{1/3}$ must depend only on M and ϵ. Thus we may write

$$Xn_a^{1/3} = F(M, \epsilon) \quad . \tag{3}$$

In particular X may be taken to be the shock thickness, defined in the usual way by the maximum density gradient.

PHYSICAL ARGUMENTS

The parameter ϵ is equal to the ratio of the molecular diameter to the average distance between molecules. The Boltzmann equation, which includes only binary collisions and ignores multiple collisions, is valid only in the limit as $\epsilon \to o$. For this limiting condition, it is appropriate to expand the function $F(M, \epsilon)$ in a power series in ϵ, keeping only the lowest order term. In this way, we obtain

$$Xn_a^{1/3} = \epsilon^{\ell} g(M) \quad . \tag{4}$$

One way of determining the power of ℓ which appears in equation (4) is to argue that the shock thickness must scale as n_a^{-1}. It follows that $\ell = -2$, so that, for rigid spheres, equation (4) becomes

$$X = g(M)/n_a\sigma^2 \quad , \tag{5}$$

---

* For convenience in our notation, we consider that the exponent s is fixed.

while, for inverse power molecules, we obtain

$$X = g(M)(kT_a/\kappa)^{2/s-1}/n_a \quad . \tag{6}$$

According to equation (6), the shock thickness for inverse power molecules can only be determined when T_a and u_a are specified separately. In contrast, the shock thickness for rigid sphere molecules depends only upon the ratio $M^2 = 3u_a^2/5kT_a$.

Let us now consider two different limiting processes by which the Mach number can approach infinity. Define Limit Process 1 as a process in which u_a is fixed while the temperature $T_a \to o$, so that $M \to \infty$. This means that the random thermal velocity of the supersonic particles upstream of the shock approaches zero. Physically it is apparent that, once $kT_a \ll mu_a^2$, the shock structure cannot be affected by decreasing T_a still further, so that the shock thickness must approach a constant as $M \to \infty$. Thus, for equation (6), we have

$$\lim_{\substack{M \to \infty \\ u_a \text{ constant}}} T_a^{2/s-1}\, g(M) = \text{constant} \quad , \tag{7}$$

or

$$\lim_{M \to \infty} g(M) = c_s M^{4/s-1} \quad , \tag{8}$$

where c_s is a constant which, of course, depends upon s.

Next we define Limit Process 2 in which the upstream temperature T_a is held fixed, while the Mach number approaches infinity. This is the limiting process which is most often of physical interest. It follows from equations (6) and (8) that the shock thickness is given by

$$\lim_{\substack{M \to \infty \\ T_a \text{ constant}}} X = \left(\frac{c_s}{n_a}\right)\left(\frac{kT_a}{\kappa}\right)^{2/s-1} M^{4/s-1} \quad , \tag{9}$$

so that, in Limit Process 2, the shock thickness is proportional to $M^{4/s-1}$ as $M \to \infty$.

The physical arguments given in this section afford the simplest route to the desired results. However, the same results can be obtained by mathematical arguments if we note that the nondimensional Boltzmann equation becomes

$$u\frac{\partial f}{\partial x} = \epsilon^2 \int (f'f_1' - ff_1)\, g\sigma(\Omega, g)\, d\Omega\, d\vec{v}_1 \quad ,$$

where the dimensional distribution function is f^*, and $f^* = n_a u_a^{-3} f$ where f is nondimensional; similarly $u^* = u_a u$, $x^* = n_a^{-1/3} x$, $\sigma^*(\Omega, g) = \epsilon^2 n_a^{-2/3} \sigma(\Omega, g)$ and $\vec{v}_1^* = u_a \vec{v}_1$. The nondimensional boundary condition at $x = -\infty$ is $f = (5M^2/6\pi)^{3/2} \exp -5M^2(\vec{v} - \hat{i}_x)^2/6$, which depends only on Mach number. Thus, for fixed M, the maximum gradient of the nondimensional density must be proportional to ϵ^2, and the shock thickness therefore proportional to ϵ^{-2}.

THE MEAN FREE PATH

Conventionally, calculations of shock thicknesses are normalized by dividing the shock thickness by the mean free path in the equilibrium region upstream of the shock. The properties of a gas of inverse power molecules in equilibrium are completely specified by the six parameters n_a, u_a, T_a, k, m and κ. Therefore, the dimensional arguments used for shock thickness can be applied equally well to the mean free path which must have the functional form given by equation (6). However, if the mean free path is required to be independent of the local flow velocity of the gas,* the function of Mach number appearing in equation (6) must be taken as a constant. Therefore, the mean free path has the form**

$$\lambda_a = \text{constant} \times (kT_a/\kappa)^{2/s-1}/n_a \quad . \tag{10}$$

From equations (6) and (10), the normalized shock thickness is

$$X/\lambda_a = \text{constant} \times g(M) \quad , \tag{11}$$

---

* A definition of mean free path which does depend upon Mach number has been suggested by C. Muckenfuss, Phys. Fluids 5, 165 (1962). However, for most purposes, it seems preferable to define the mean free path as the average distance a particle moves between collisions relative to a coordinate system moving with the local speed of the fluid. Otherwise the mean free path cannot be used in the usual way for estimating the departure of a gas from continuum behavior.

** The dependence of mean free path on temperature given by equation (10) has usually been obtained by arguing that only those collisions in which the angular deflection exceeds some given small angle should be counted in defining a mean free path. The dimensional arguments show that no other form is possible if the mean free path is to be inversely proportional to n_a.

and it follows from equation (8) that

$$\lim_{M \to \infty} X/\lambda_a = \text{constant} \times M^{4/s-1} . \qquad (12)$$

According to equation (11), the normalized shock thickness depends only upon Mach number so that its behavior as $M \to \infty$ is independent of the particular limiting process under consideration. It is important to realize that the normalized shock thickness may depend upon both T_a and u_a for intermolecular potentials which are more complicated than the inverse-power law. For example, it is meaningless to plot X/λ_a versus Mach number for either a Lennard-Jones or a Sutherland molecular model unless the upstream temperature T_a is specified.

An alternative method for normalization is to divide the shock thickness by the mean free path in the center of the shock (ref. 3). For large Mach numbers, it can be shown that the temperature, either in the center of the shock or downstream of the shock, is equal to mu_a^2/k multiplied by a number of the order of unity. It follows from equations (9) and (10) that the shock thickness normalized by the mean free path in the center of the shock approaches a constant as $M \to \infty$. This normalization is useful for comparing the results of calculations for different force laws.

DISCUSSION

The dimensional arguments show that it is a special property of rigid spheres and inverse-power molecules that the normalized shock thickness X/λ_a is a function of Mach number alone; therefore, in experimental measurements on a real gas, it is important that both Mach number and upstream temperature be reported as part of the experimental results for each measurement of shock thickness. This fact becomes apparent in any theoretical calculation of shock thickness for a realistic molecular model and can, for example, be seen in Mott-Smith's calculation of shock thickness for a Sutherland law of force (ref. 2).

Since the asymptotic dependence of shock thickness upon Mach number given by equation (9) is determined by dimensional considerations, it follows that the asymptotic dependence of different approximations to the Boltzmann equation can differ only in the numerical value of the constant c_s which appears in equation (9). This casts a certain amount of light upon the question of why the Navier-Stokes equations are able to give reasonable estimates of the shock thickness at large Mach numbers.

From a kinetic theory viewpoint, the Navier-Stokes theory is internally inconsistent for Mach numbers greater than about four, since it implies that the density of particles is negative over certain regions of phase space (ref. 4). However, for dimensional reasons, any approximation procedure for which a solution exists at large Mach numbers must satisfy the asymptotic form given by equation (9), and inspection of the Navier-Stokes and

other approximation schemes suggests that this form is valid for Mach numbers greater than five. Since X(M) is a smooth function and the Navier-Stokes solution is accurate for Mach number less than, say, two, it should not be surprising that c_s as evaluated by the Navier-Stokes theory is within 50 percent of the correct value.

REFERENCES

(1) Chapman, S. and Cowling, T. G., The Mathematical Theory of Nonuniform Gases, Cambridge (1960).

(2) Mott-Smith, H. M., Phys. Rev. 82, 885 (1951).

(3) Ziering, S. and Ek, F., Phys. Fluids 4, 765 (1961).

(4) Sherman, F. S. and Talbot, L., in Rarefied Gas Dynamics (F. M. Deviennes, ed.), Pergamon Press (1960).

PERFORMANCE PREDICTIONS FOR THE

WISCONSIN HIGH ENTHALPY SHOCK TUBE

H.N. Powell,* W. G. Steenken, R. K. Suri,** and C.W. Fisher****
University of Wisconsin
Madison, Wisconsin

INTRODUCTION

There is a continuing interest in methods for increasing the shock tube's capacity for producing high enthalpy gas states. Let attention be confined to the "classic" form of the shock tube in contrast to devices which employ electromagnetic or detonation driven shocks. Except for the buffer gas modification (Ref. 1,2), current approaches are devoted to increasing the acoustic velocity of the driver gas. The principal ones are: heating by conduction and the more direct arc or combustion heating methods. A recent "state of the art" survey (largely in a shock tunnel context) is given by the papers of the Third Hypervelocity Techniques Symposium; those of references (3), (4) and (5) are particularly relevant to high enthalpy technique.

The present paper is concerned with the practical realization of another approach which has been previously described, in principle, by one of the authors (Ref. 6): by expanding the pre-shock test gas to $M \cong 2$ in a direction against the shock, substantial increases in the total enthalpy of the test gas in shock coordinates result. The gains, relative to a conventional tube using the same driver state, are realized in sizable increases in either shock temperature or density. However, the experimental approach outlined in reference (6) is somewhat impractical. A practical design which utilizes the essential aerodynamic principal requires the resolution of several somewhat conflicting demands. Their resolution, as embodied in the rather sizable Wisconsin High Enthalpy Shock Tube (WHEST), has generated several unconventional features as described in this paper. Experimental evaluation of these features is discussed. Overall performance predictions based on them are made and compared with the predictions of reference (6). Much of

*Professor of Mechanical Engineering
**Research Assistants; present address of R. K. Suri is U. of Roorkee, India

the material is drawn from the Ph.D. thesis of R. K. Suri (Ref. 7). The ultimate application of the apparatus is for the measurement of the transport properties of gases at high temperatures.***

The following nomenclature will be used. Major flow states are assigned numbers as shown in Figure 1, with modifications of these states denoted by primes. When needed, lower case lettere will be added to denote physical stations along the tube, Roman numerals distinguish basically different apparatus designs in comparative performance evaluations.

GENERAL DIMENSIONS:

The first and the key requirement is to produce a highly uniform, steady, $M \simeq 2$ flow in the shock duct before arrival of the shock. As shown in the Figure 1 t - x diagram, this can be accomplished, in principle, in the flow field 3 behind a contact surface following a weak ($M \simeq 2$) 5 - 4 shock. For the present let it be assumed that such a flow is achieved. Detailed analytical treatments of the complicated interactions produced by the transit of the strong shock through the partially stagnated gas at the end of the tube are given in reference (7). Using a preliminary $M_3 = 2$ value, for a case comparable to that shown in Figure 1 it is shown that after the strong shock enters the 3' field, the high enthalpy field 8 is free from reflected disturbances which originate in this region to the right. The interaction region length is 1.60 m.

A duct length of 3.60 m is used in addition to the interaction region length. This length, the continuity equation and the density ratios for strong shocks give the essentially constant 8 field thickness, $\Delta x \simeq 0.9$ and 0.6 m for $\gamma_1 = 5/3$ and 7/5 gases, respectively. Roughly, 1/2 to 2/3 of these thicknesses should be usable, disturbance-free 8 field states.

Next it is noted that, because of the steady flow character of much of the 3 field, frictional effects will be intermediate between those in a steady constant area flow and in an unsteady expansion to the same velocity in the same duct, i. e., an unusually low L/D is needed. Rough estimation of boundary layer growth and considerations connected with the final use of the apparatus led to the choice of 9.20 x 11.7 cm for duct dimensions. Thus, with a hydraulic diameter, D = 10.9 cm, L = 4 m, there results an L/D = 33 which is only slightly greater than the corresponding steady flow choking limit value, 31. Behind the shock and the 3' field, however, the boundary layer growth is still unsteady. No significant changes in the 5 - 4 shock velocity are detected over the length of the tube.

The low pressure (L.P.) and high pressure (H.P.) driver chambers were made sufficiently long, 4.82 and 3.50 m, respectively, to provide

***This work was sponsored, in part, by the National Science Foundation

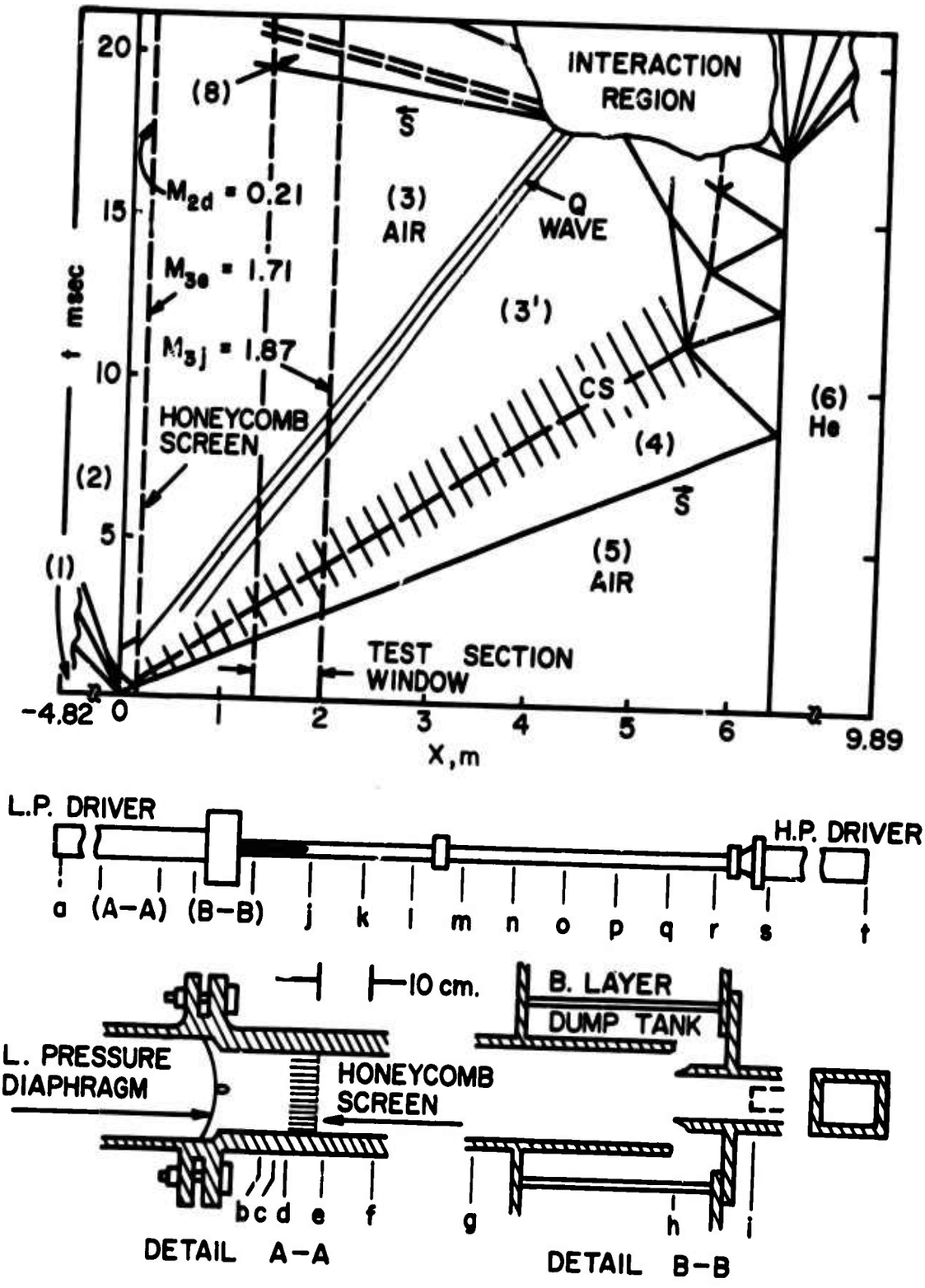


FIGURE 1: WAVE DIAGRAM OF WHEST

adequate undisturbed driving times. These lengths and an additional length of 1.19 m to be described below gives the WHEST apparatus an overall length of 14.71 m, or 48 ft. 4 in.

In view of the foregoing, it is also concluded that utilization of this design with reasonable safety factors is not possible in a small apparatus.

THE HONEYCOMB-SCREEN:

It will be appreciated that the success of the technique is dependent on the propagation of the strong 3 - 8 shock into a "clean" 3 field. The demands of flow uniformity are therefore substantially more severe than in the expanding driver gas of a conventional tube. A direct result of a finite diaphragm rupture time are transverse pressure disturbances which are carried with and spread laterally in the expanding gas. The shock duct diameter is too large to assure effective equilibration of these disturbances, i. e., in 18 msec only about 35 acoustic wave transits of the duct are available for the equilibration of what are initially very strong effects. It was therefore concluded that in order to obtain a 3 field of the desired size and uniformity, it is necessary to suppress the transverse disturbances at the source. It was this conclusion which led to one of WHEST's major innovations, the production of the supersonic 3 field with a honeycomb supported screen.

As an alternative to the nozzle, a high solidity fine mesh screen was resistance welded to a 3 in thick layer of 1/4 in cell size honeycomb, both of stainless steel. The technique of producing supersonic flows with single unsupported screens was previously investigated by Gould (Ref. 8). However, the pronounced system of shock diamonds in his duct flows reveals the presence of substantial transverse monemtum components. With a honeycomb cell L/D = 12, such transverse components are eliminated as well as those introduced by the diaphragm rupture. By locating the screen on the downstream face of the honeycomb, both the honeycomb induced turbulence and that generated by the ruptured diaphragm are "erased." Furthermore, by providing closely spaced local support, much finer mesh screens (and a correspondingly more rapid turbulence decay) can be used for the same pressure loading.

A single parameter correlation of several investigators' subsonic and supersonic screen flow data (including that of the present authors') has been given elsewhere (Ref. 9). $M \simeq 2$ is the maximum attainable Mach number. For the present application the honeycomb screen with a solidity 0.633 and a mesh number, m = 60 in $^{-1}$, is used and its relation to the low pressure diaphragn is shown in the detail A-A of Figure 1. The pertinent performance data are: $M_{2d} = 0.21$, $M_{3e} = 1.71$, $P_{2d}/P_{3e} = 10.0$, $P_{02d}/P_{03e} = 2.10$.

If the maximum high pressure driver pressure, P_6, is fixed by a safe design limit, the maximum P_6/P_1 is determined by the minimum P_1 permitted by Reynolds number limitations on the honeycomb screen. It has been ascertained experimentally (Ref. 9) that this minimum P_1 is 18 cm Hg. This corresponds to a screen Reynolds number of $9.5 \times 10^2 = (1/m - d)\rho^*a^*/\mu^*$ in which m in^{-1} is the mesh number, d in, the wire diameter, and the asterisk quantities are defined for sonic flow conditions. A transition regime for $Re < 9.5 \times 10^2$ is consistent with Cornell's (Ref. 10) curves from incompressible data. Thus, the honeycomb screen is an effective substitute for a converging-diverging nozzle for exit $M < 2$ and when significant total pressure losses are acceptable. The advantages become clear in the next section.

UNIFORMITY OF FIELD 3 FLOWS:

A question arises on the intensity and decay rate of the screen induced turbulence. Following Batchelor (Ref. 11) the range of Reynolds numbers [defined in the present nomenclature as $(1/m\ \rho_3 u_3/\mu_3) \simeq Re$ (screen) as previously defined] places the decay in the "initial period" as is also usual in wind tunnels. For this initial period and low Mach number, i. e., incompressible flows, Batchelor's formula is,

$$\left(\frac{u}{v}\right)^2 = \frac{b}{C_p}(xm - x_0m) \qquad (1)$$

in which:

u = downstream velocity

v = r.m.s. fluctuating velocity

x = downstream distance

m = mesh number

$C_p = \Delta P/(1/2\rho u^2)_{upstream}$ screen static pressure coefficient

b = 101)
) constants evaluated for present conditions
x_0m = 10)

This formula cannot be applied directly because of the large compressibility effects which are manifest in a static pressure coefficient involving a subsonic to supersonic transition. For example, equation (1) predicts an increasing turbulence intensity with increasing reversibility of the transition to a supersonic flow.

However, the sense of Batchelor's formula can be preserved if (u/v) and C_p are redefined with respect to a fictitious downstream subsonic state, 3"e, on the same Fanno line and with the same entropy as the actual supersonic 3e state. By attributing all of the observed entropy increase to viscous mechanisms of turbulence generation, i. e., neglecting the contributions of the shocks located in the screen inter-

stices, this procedure yields an estimate of the maximum turbulence intensity as a function of x. By introducing the appropriate ratios to refer u to the actual supersonic, u_{3e} velocity, the redefined pressure coefficient for use in equation (1) is:

$$C_{p''} = \frac{P_{2d} - P_{3''e}}{\frac{1}{2}(\rho u^2)_{2d}} \left(\frac{u_{3''e}}{u_{3e}}\right)^2 = \frac{1 - (P_{3''e}/P_{2d})}{\frac{\gamma}{2} M_{2d}^2} \left(\frac{M_{3''e}}{M_{3e}}\right)^2 \left(\frac{T_{3''e}}{T_{3e}}\right) \quad (2)$$

It is seen that for either subsonic or supersonic downstream flows, if the transition is made more reversible the entropies change as $S_{3e} = S_{3''e} \rightarrow S_{2d}$ so that $P_{3''e}/P_{2d} \rightarrow 1$, and $(v/u)_{3c} \rightarrow 0$, as is reasonable. For subsonic downstream flows the formula is identical with Batchelor's.

A turbulence decay length of x = 1.0 m or xm = 2.36×10^3 mesh sizes is provided before the flow enters the test section at x_h = 1.19 m. With the previously given honeycomb-screen performance data and $M_{3''e} = 0.50$ there results $C_{p''} = 2.42$, and the maximum $(v/u)_{3e} = 3.2 \times 10^{-3}$.

The relationship of the turbulence decay duct (stations e to h) to the test section entrance is shown in the detail sketches of Figure 1. The shock duct boundary layer starts with the knife edge entrance at station h and is still thin in the test section. The turbulence decay duct is slightly divergent (0.5° half angle) to conpensate duct friction and to slightly increase M_{3e}.

Extensive tests have shown the 3 field flow states to be independent of P_1/P_5. The 3 field is separated from the 3' field by a Q wave which, ideally, steepens to an "adjustment shock" if $P_1/P_5 < 80$; or forms the head of an "adjustment rarefaction" if $P_1/P_5 > 80$; if $P_1/P_5 = 80$, the 3 and 3' fields should become identical.

In reality, the residues of both adjustment processes are present at $P_1/P_5 = 80$ as shown in the t vs. P_1/P_5 diagram of Figure 2. A pressure dip of 10 to 15% is observed between the two lines shown and is presumed to stem from some equilibration process in or before the honeycomb screen. The optimum P_1/P_5 is seen to be in the range 50 to 60.

Figure 3 presents a P - t oscilloscope trace from a transducer at station j for $P_1/P_5 = 58.7$. After t = 9 msec, the flow is seen to be free of extraneous pressure disturbances with a gentle rise of 5% to the arrival of the terminal compression at t = 18 msec. The latter is produced by choking of the flow discharging into the boundary layer dump tank.

The Q wave shown in Figure 1 corresponds to the lower edge of the shaded "test condition" region of Figure 2. The pressure disturbances preceding it in the 3' field are seen to impinge on the strong shock

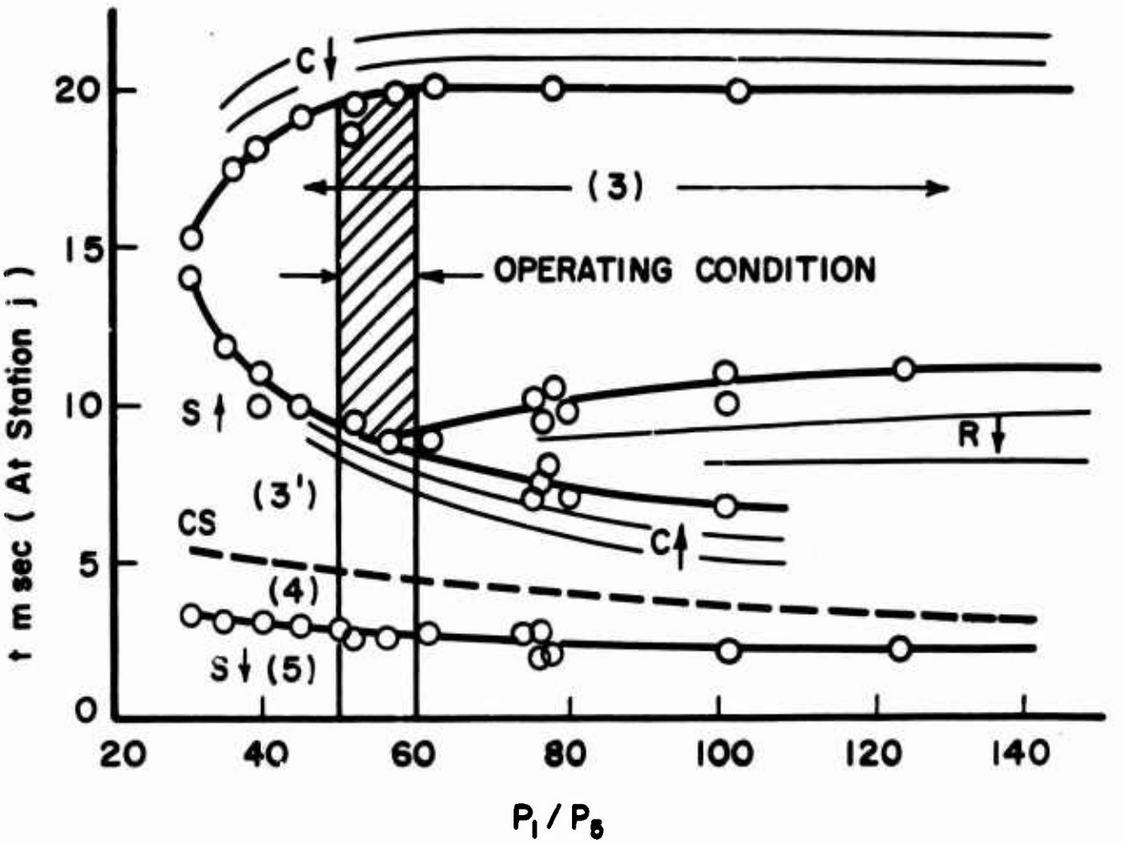


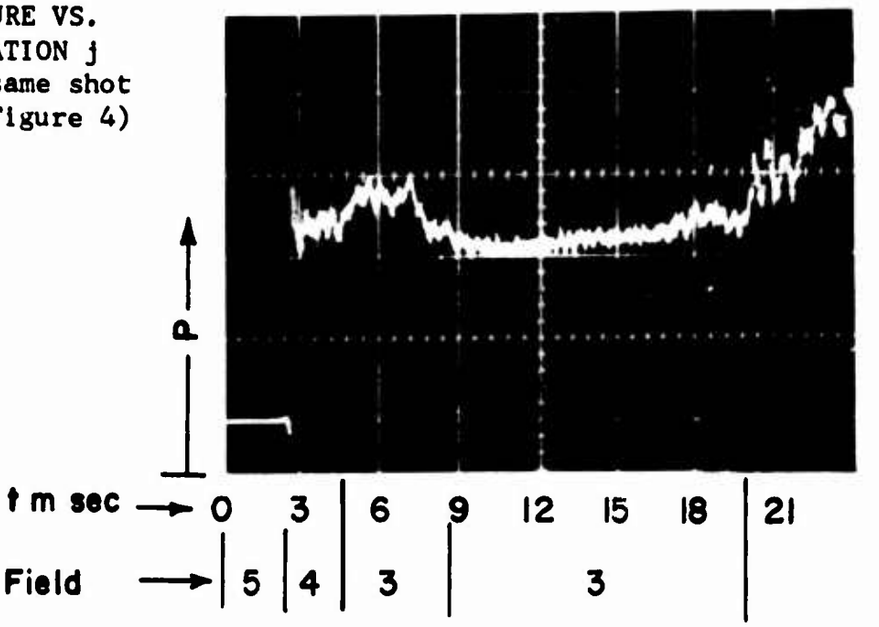
FIGURE 2: BOUNDARIES OF UNITORM TEST FIELD 3 AS A FUNCTION OF P_1/P_5

while it is still stabilizing and traversing the interaction region.

Figure 3 shows a submicrosecond schlieren photograph of the flow just to the left of station j at t = 17 msec. 1 mil "Scotch tape" strips on the floor and ceiling of the tube produce the four pronounced Mach waves. The photograph is of interest because of the absence of extraneous disturbances. It is representative of those taken in either the 3 or 3' fields after the zone of turbulence. The latter is shown in Figure 1 as shading around the 4 - 3' contact surface; its thickness has been determined from a sequence of schlieren photographs at different times through the window to the left of station j.

While the analysis of Mirels (Ref. 12) is not strictly applicable for $M < 5$ shocks, it does indicate that in the range of pressures near the screen Reynolds number limit P_1 = 18 cm Hg, P_3 = 1.44 cm Hg, significant boundary layer loss of 4 gas past the 4 - 3' contact surface will occur. As the resulting pressure and other disturbances are confined to the 4 and 3' fields, the effect is of no concern. In the 3 field itself, by regarding the boundary layer growth as generated by an impulsively started infinite flat plate in a gas of static temperature, T_3,

FIGURE 3: PRESSURE VS. TIME TRACE AT STATION j (obtained during same shot as photograph in Figure 4)



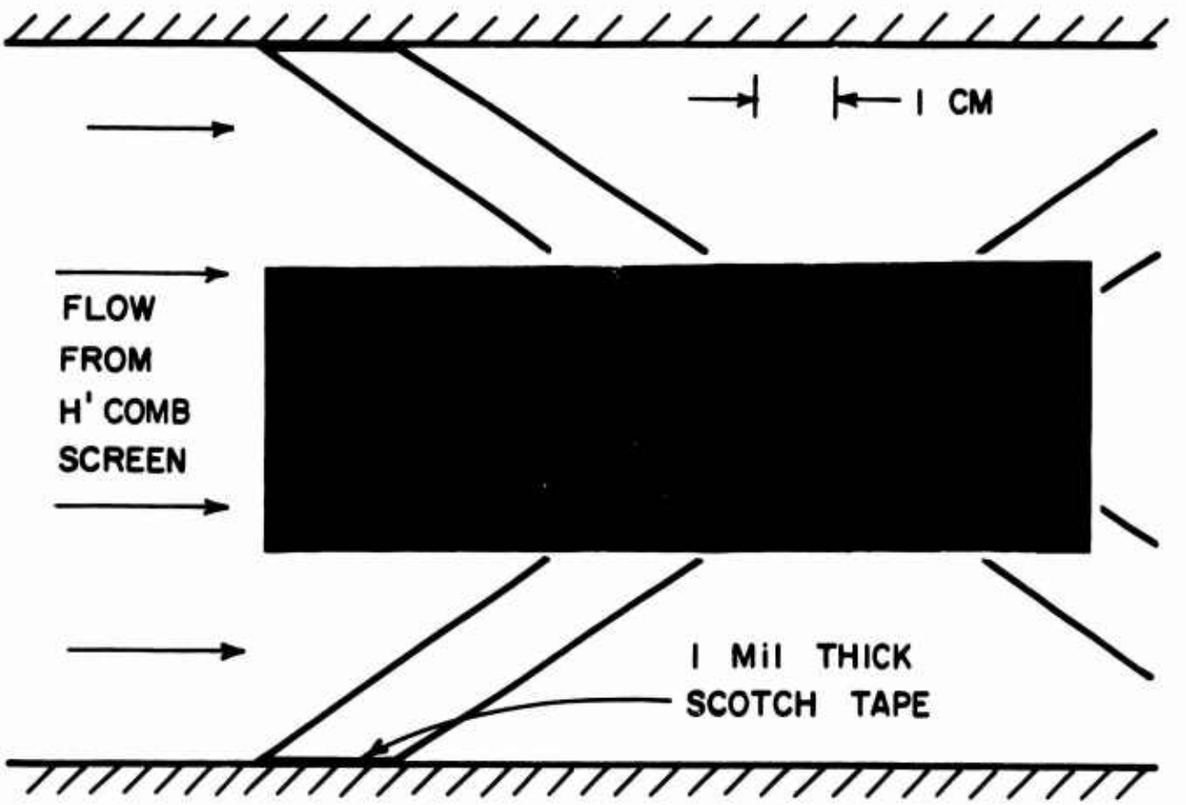


FIGURE 4: SUB-MICROSECOND SCHLIEREN PHOTOGRAPH OF FIELD 3 AT 17 msec

Illingworth's analysis (Ref. 13) gives an estimated maximum boundary layer thickness of 1.2 cm at 20 msec and P_3 = 1.44 cm Hg. The hydraulic diameter is 10.9 cm so that the minimum fraction of flow area uninfluenced by the walls is between 61% and 100% at station h. Systematic tests have not yet been conducted at the low pressure limit, but present evidence indicates that it represents a valid operating conditions.

It is therefore concluded that, except for a weak residue of screen induced turbulence, the honeycomb screen successfully fulfills its purpose of producing in the limited time available an extensive and disturbance-free supersonic flow field.

PREDICTED OVERALL PERFORMANCE CHARACTERISTICS:

From the now well defined 3 field flow state, overall performance predictions can be made. For the sake of simplicity, an ideal gas, constant C_p analysis will be used. The product, C_pT, formed on this basis is a fairly accurate measure of the static post-shock enthalpy of real gases. Two acoustic velocity ratios are used. a_6/a_5 = 3.15 and 6.06 pertain to the use of air at 300 K as the state 1 gas and He as the driver gas at 300 K and 1110 K (1540 F), respectively, the latter temperature being a reasonable metallurgical limit for stainless steel. The effects of an area ratio change (Ref. 2), A_6'/A_5 = 2.1 are included so that the above given values are the equivalent acoustic velocity ratios required of a uniform area tube.

Figure 5 shows the interaction of three designs in the pressure velocity plane for the same overall pressure ratio, P_6/P_1 = 426. Roman numerals designate the three basic designs: the conventional design (I), the reference (6) design (II), and the WHEST design (III). Since the static temperature produced by a strong shock is approximately proportional to the square of the relative velocity of the post-shock gas to the pre-shock gas, the reason for the increased T_8 values of designs II and III is clear: $[|u_8/a_1| + |u_3/a_1|]^2$ (II or III) is substantially greater than $[u_8/a_1]^2$ (I). Thus, given any arbitrary driver gas state, 6, and driver gas state, 1, it is possible to increase the shock temperature, T_8, by pre-expanding the state 1 gas in a direction counter to the shock motion.

Figure 5 also shows that since the various 3 states are indistinguishable on the scale of the graph, the frictional effects, etc., which cause these variations have a negligible influence on the desired 8 state. The The effect of an area change A_6'/A_5 = 2.1 in permitting the driver pressure to be reduced from P_6 to P_6' is also shown in dotted lines.

The T_8/T_1 vs. P_6/P_1 performance curves of design III are almost identical with those given in reference (6) for design II, showing minimal increases in T_8/T_1 for low P_6/P_1 ratios.

The overall design III performance curves are compared with those of

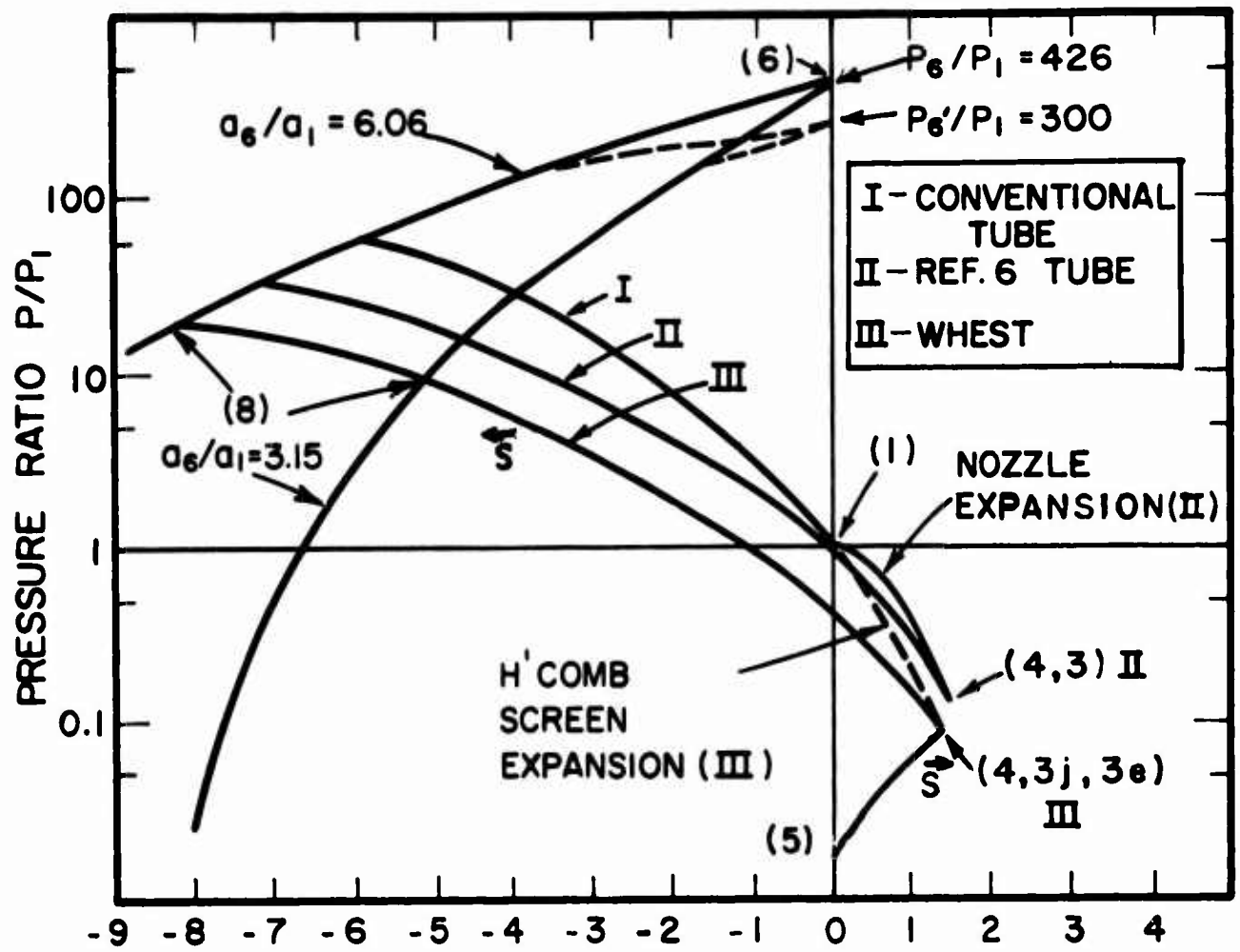


FIGURE 5: INTERACTIONS OF THREE DESIGNS IN THE PRESSURE-VELOCITY PLANE

design I in Figure 6. In view of the importance of density in chemical kinetic mechanisms and the central role of the Reynolds number and its density dependence for many test purposes T_8/T_1 is plotted against the the function, $\rho_8 RT_1/P_6 m_1 = (P_8/P_6)(T_1/T_8)$, in which m_1 is the molecular weight of the 1 gas. Thus, the range of accessible T_8's as a function of ρ_8 for any P_6 is given, or alternatively, the change in P_6 which is needed to compensate a change in ρ_8 is also readily determined. P_6/P_1 ratios in factors of 10 are shown by appropriate symbols along the curves. The Figure 6 curves are also virtually identical with the corresponding Figure 4 of reference (6) but is included here for the same of completeness in relation to the performance of the WHEST apparatus. It is seen (Fig. 6) that for an unheated He driver, sizable gain factors for T_8/T_1 in the design III relative to I result. On the common P_6/P_1 basis the gain factors range from 3.2 at low P_6/P_1 values to 2.82 at $P_6/P_1 = 10^3$ and 1.6 at 10^5. On the common $\rho_8 RT_1/P_6 m_1$ basis the gain factor is essentially

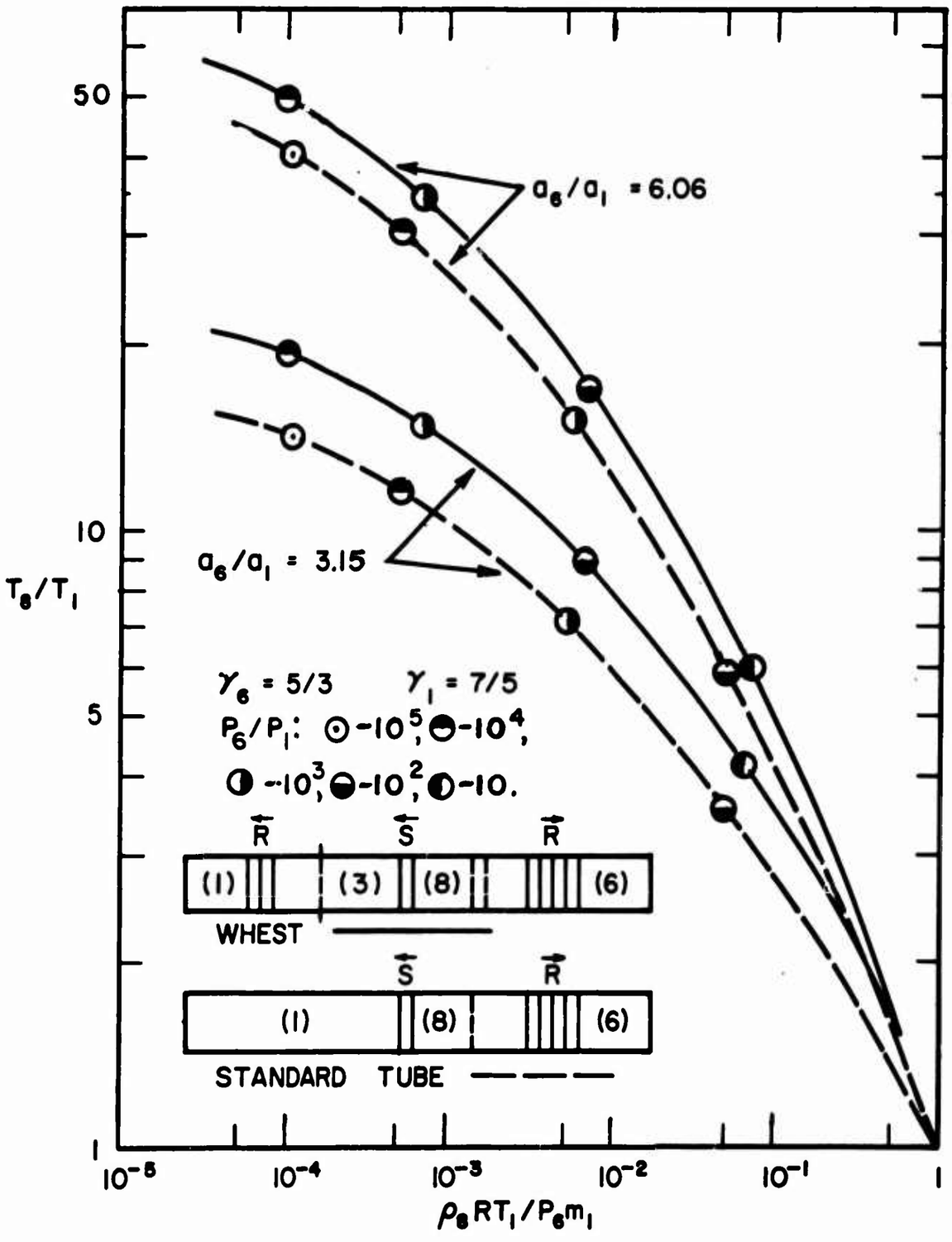


FIGURE 6: PERFORMANCE OF WHEST AND STANDARD TUBE IN SHOCK TEMPERATURE-DENSITY PLANE

constant at 1.31. For the heated He driver the common P_6/P_1 basis gives gain factors of 3.0 down to 2.2 at $P_6/P_1 = 10^3$ and 1.5 at 10^5. On the common $\rho_8 RT_1/P_6 m_1$ basis, the gain factor is essentially constant at 1.22. It is interesting to note that whereas heating the driver gas causes the relative gain of designs III to I to decrease, the absolute temperature gain increases. At $\rho_8 RT_1/P_6 m_1 = 10^{-3}$ with $T_1 = 300$ K, the unheated driver gain is 4140 - 3160 = 980K and the heated driver gain is 9510 - 7800 = 1710 K.

On the other hand, if the "profit" is taken in terms of density with a common T8, the gain factors increase slowly with T_8/T_1 to 10 at $T_8/T_1 = 15$ for the unheated driver and from a typical value of 1.6 to 4 at $T_8/T_1 = 45$ for the heated driver. As the curves flatten with increasing P_6/P_1 values, the density gain factors become infinite. These gains may also be viewed as the factor by which P_6 (I) would have to be increased to yield the same T_8 and ρ_8 as given by P_6 (III).

However, the WHEST design is subject to an additional limitation on P_6/P_1 due to the Reynolds number requirement, $P_1 > 18$ cm Hg. on the honeycomb screen. Thus, if structural limitations require that $P_6' \sim 5000$ psia, P_6 7100 psia and $P_6/P_1 \sim 2 \times 10^3$. While this ratio might seem low, Figure 6 shows that with a heated driver it is equivalent, shock temperature-wise, to a ratio of about 1.2×10^5 in a standard tube. Present WHEST equipment is limited to a 3000 psia room temperature driver, which will be replaced with one with heating capabilities (to 1540 F) and at a pressure not yet determined.

Ideal test durations of the 8 field vary from 0.59 msec at $T_8/T_1 = 10$ to 0.20 msec at 35. These are 127% and 90%, respectively, of the ideal test durations of a standard tube giving the same T_8's and of the same overall duct length, 5.20 m; however, the higher ρ_8's of the III design would favor lessened boundary layer effects and a closer approximation to the ideal test duration.

CONCLUSIONS:

It is concluded that WHEST is a feasible realization of the gas dynamic principle outlined in reference 6. Its significance is that it markedly extends the shock temperature and density domain of the simple compressed He driver, with its inherent advantages of uniformity, long observation times, safety and cost. In the case of a heated driver, the gains are most welcome in view of the structural problems and safety hazards of containing hot gases at high pressures. The basic principle involved is equally compatible with H_2, combustion, and buffered gas systems with commensurate gains.

REFERENCES

(1) **Henshall, B. D., The Use of Multiple Diaphragms** in Shock Tubes, ARC Tech. Rept. 19-062, CP No. 291 (1956)

(2) Russo, A. L. and Hertzberg, A., Modifications of the Basic Shock Tube to Improve Its Performance, Report No. AD-1052-A-7, Aug. (1958)

(3) Bird, K. D., Martin J. F. and Bell, T. J., Proc. Third Hypervelocity Techniques Symposium, Denver, March, 1964. (Denver Research Institute and Arnold Engineering Dev. Center, ARO, Inc.) p. 7 - 50

(4) Flagg, R. F., Ibid (3), p. 89 - 115

(5) Kaegi, E. M. and Muntz, E. P., Ibid (3), (available as a separate paper)

(6) Powell, H. N., ARS Jour (30), No. 10, 980 - 983 (1960)

(7) Suri, R. K., "Some Performance Aspects of the Wisconsin High Enthalpy Shock Tube" (Ph. D. Thesis Dissertation) U. of Wisconsin, Feb., 1965

(8) Gould, L. I. NACA RM E51F25 (1951) (declassified)

(9) Powell, H. N., Suri, R. K., Steenken, W. G. and Fisher, C. W., AIAA Jour. (tech. note to be published May or June, 1965)

(10) Cornell, W. G., Trans. ASME, 80, 791 - 799 (1958)

(11) Batchelor, G. K., Theory of Homogeneous Turbulence, Cambridge U. Press, 133 - 139 (1953)

(12) Mirels, H., Phys. Fluids, 6, (9), 1201 (1963)

(13) Illingworth, C. R., Proc. Camb. Phil. Soc. 46, pt. 4, 603 - 613 (1950)

BLANK PAGE

AIR BLAST SIMULATOR

G. Weigel
Ernst-Mach-Institute
Weil/Rhein, West.Germany

Shock-tubes of large diameter are highly expensive, they need a considerable space and are difficult in handling. On the other hand it is desiderable for air-blast test-installations to be able to set test objects as larges as possible. Then one may test samples of natural size. I'm here thinking of blast valves for shelters, entrance-doors and so on. Also in testing models of structures it is convenient to construct the model in a scale as large as possible or to confirm the course of the model-laws by measurements on the same structu·e in various model-scales. For certain objects the model-scale is limited by the material used as for example with samples of reinforced concrete, where it is almost impossible to go under a proportion of 1 : 5 without changing the caracteristic properties of the material.

No doubt the equal pressure shock tube discussed by my collegue Dr. Reichenbach beeing able to simulate infinitely long pressure impulses whereas the variation of the decay of pressure is rather difficult due to the great volumina and the consequent large quantities of air. Besides, for generating shock waves of a peak pressure of several atmospheres very high filling pressure in the compression chamber of a shock tube is needed.

Professor Schardin has proposed an installation for simulating air blasts based on an other principle which has many advantages in handling. Though it isn't able to produce a real shock wave - that is to say an infinitely steep rise of pressure - it is possible nevertheless to get a very short rise time - 1 - 2 ms - and the duration of the pressure impulse and the shape of decay are easily variable in wide limits.

We call this simulator "Shock pressure chamber". The principle is as follows: The test object is mounted in the inner partition wall of two volumina which are filled with air under the same overpressure. As the sample is submitted to the same pressure on both sides, no deformation appears as the result of one-sided load.

If the overpressure in one of the volumina is brought down of a sudden, a one-sided load to the sample coming from the overpressure which remains in the other volume is applied. The rise time of this load is determined by the time of emptying the first named volume.

If the sample is not destroyed the one-sided load is maintained for any desired time so one gets the ideal case of quasistatic load. Now it is possible to empty the loading volume more or less quickly, beginning at any time, and thus one can get any desired form of loading impulses with steep rise and more or less gradual decrease of pressure.

A very fast decrease of pressure can be achieved by means of diaphragms releasing a large opening very quickly when bursting. In the same way the de-loading of the loading volume is possible by diaphragms.

The actual performance of the simulator installed at our test-field will be demonstrated by the following picture, FIG. 1, showing a cross-section of the pressure-chamber, slightly simplified.

On a round table with a central opening of 1 meter in diameter is set a ring with a diaphragm of steel or cellulose acetade stretched in. Above this the specimen holder is mounted with an rectangular opening corresponding to the test-object that has been fixed outside of the chamber and fitted with the necessary transducers, for example strain-gages. The sketch shows a plate of reinforced concrete as specimen.

Over the whole is arranged a hemisphere with four circular openings closed by diaphragms. At the present stage one of the openings is closed by a plate with glands to introduce the cables for the transducers.

After setting the hemisphere on the table it is clutched by means of a multiple wedge lock which closes by turning the hemisphere after setting. The hemisphere forms the larger one of the volumina (I) mentioned before, the smaller one (II) is given by the space between the test-object and the lower diaphragm. Each of the two volumina contains corresponding trans-

ducers. The load acting on the test object begins the moment when the lower diaphragm is bursting. The decay of the load is initiated by bursting of one or more of the upper diaphragms by means of small charges fired at any desired time.

The simulator is laid out for a maximum overpressure of 25 atü (356 psi). The whole installation is mounted in a hall of corrugated iron the first section of which can be removed so as to have the simulator standing in open air.

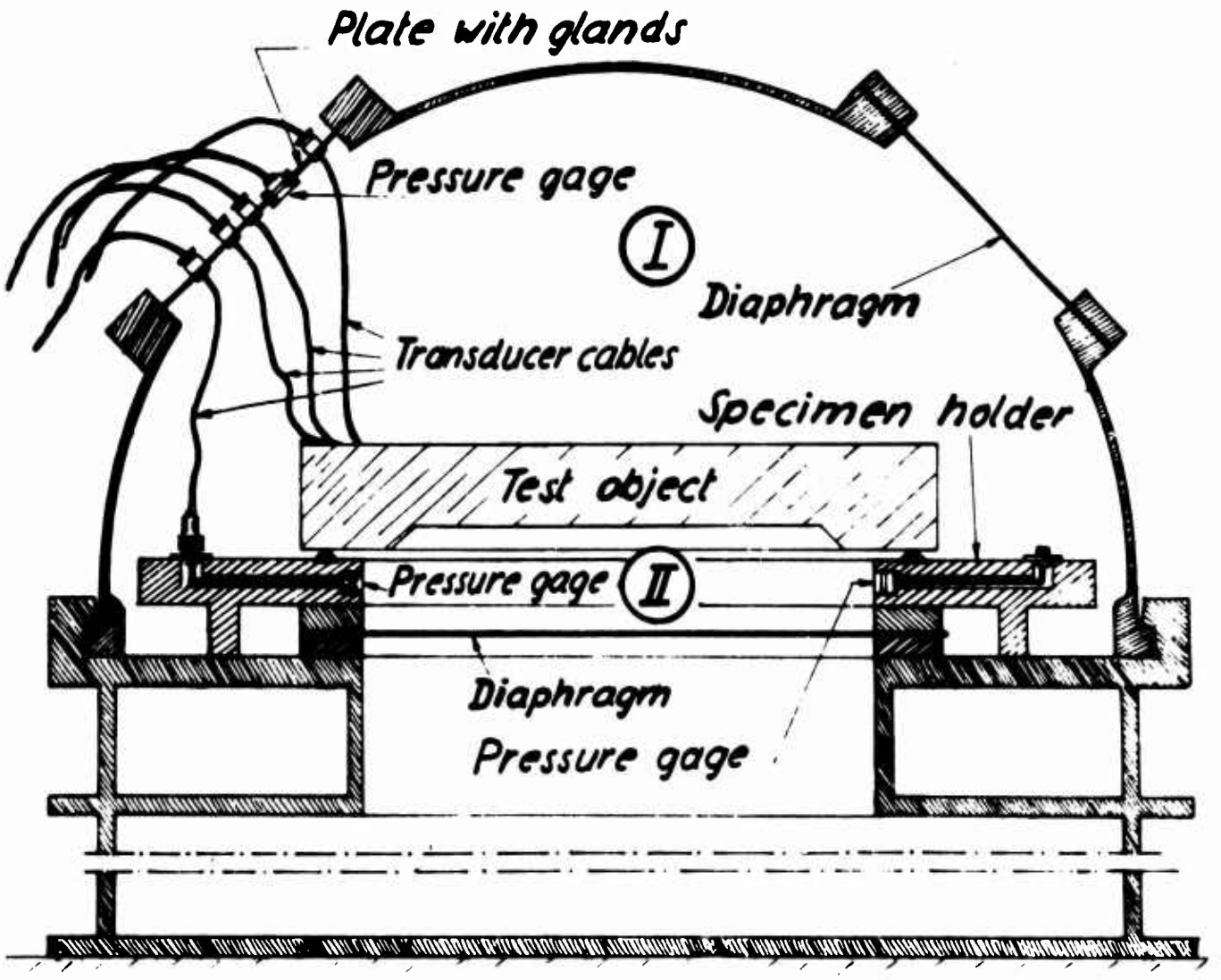

Plate with glands
Pressure gage
I
Diaphragm
Transducer cables
Specimen holder
Test object
Pressure gage
II
Diaphragm
Pressure gage

FIG. 1

A TECHNIQUE FOR STUDYING THE SHOCK-ON-SHOCK PROBLEM

E. A. Brown, Jr. and G. J. Mullaney
Boeing Scientific Research Laboratories
Seattle, Washington

INTRODUCTION

This paper reports on a technique developed to study the head-on interaction of a plane shock wave and a supersonic cone-cylinder body. The two-dimensional problem was studied analytically by Smyrl (ref. 1) and Miles (ref. 2), and this work was substantiated in part by the measurements of Merritt and Aronson (ref. 3). An analysis of the axisymmetric case (head-on interaction with a cone) was carried out for slender bodies by Blankenship (ref. 4); however, no experimental confirmation of these calculations has been reported to date. As a result it was decided to conduct a series of tests using a gun launched cone-cylinder model interacting with a plane shock wave generated by a conventional shock tube.

EXPERIMENTAL TECHNIQUE

The gun launched model technique was chosen as the simplest method of establishing aerodynamically clean supersonic flow over the body suitable for detailed optical observations. This method had the additional advantages of an unsupported model so that the studies could be extended into the base and wake flow regions as well as making the generation of the plane shock wave a straight forward matter with a conventional shock tube.

A .300 caliber smooth bore powder gun was used to launch the projectiles. They lodged in a mild steel bullet trap at the end of the shock tube driver after penetrating nearly 1/2 inch of the metal. An aerodynamically stable, unsaboted cone-cylinder projectile was used as shown in Figure 1. The aerodynamic stability was obtained by fabricating the conical section from a machinable tungsten alloy and the

cylindrical section from a high-impact strength polycarbonate resin, the two parts were threaded together. Both 10° and 20° cones were fired weighing 85 and 45 grains, respectively. They were inserted through the gun's action into the barrel to a station about 1 inch ahead of the chambered position of the Weatherby .300 magnum cartridge. The cartridges were loaded with 50 grains of #4227 powder to fire the 20° cone projectiles and 80 grains of #4350 powder for the 10° cone projectiles. For the tests reported herein the 20° cones were fired at 4000 fps and the 10° cones at 3700 fps. Higher velocities resulted in considerable distortion of the projectile in the vicinity of the cone-cylinder junction for the powder and loads used.

Figure 2 shows a schematic of the test set-up with the gun mounted on the left in the shock tube dump tank. Cold helium at 150 psia was used to drive a Mach number 4 shock into 100 mm Hg of air in the test section. A two frame shadowgraph system was used to obtain photographs of the interaction. Shuttering was accomplished by using two submicrosecond 15 KV air sparks as light sources. The trick was, of course, to get the projectile and the shock to interact within the view of the 3 inch I.D. window and obtain the photographs at the appropriate time. The sequence developed was first to fire the gun mechanically. After the projectile was launched, its velocity was measured by the use of two light screens noted as L_1 and L_2. The measured velocity was used to compute a suitable delay after which the shock tube diaphragm was fired. The computed delay was found to be necessary in order to account for the ± 5% variation in the projectile velocity.

A brief description of the computer system is as follows. When the projectile interrupted the first light screen L_1 a flip-flop was set which in turn applied a step function to the input of an integrator. The output of the integrator was then a ramp function of time. When the second light screen L_2 was interrupted by the projectile a second flip-flop was set which in turn reset the first flip-flop. When the first flip-flop was reset the output of the integrator was held at a constant level. This D.C. level was then inversely proportional to the projectile velocity. The integrator output was run through an inverter so that the proper polarity was available for control of the time delay generator. The second light screen signal, L_2, started the voltage controlled time delay generator. The control voltage was supplied by the integrator-inverter portion of the circuit. The output of the time delay generator was then used to trigger the diaphragm rupturing system. The diaphragm itself was a scribed 7075-T6 aluminum sheet 10 mils thick and was used with the required driver pressure preset. A 200 joule capacitor bank was discharged into the center of the diaphragm to initiate its opening. Figure 3 is a photograph showing the diaphragm holder assembly with the electrode on the left, and a typical burst diaphragm on the right. With suitable care, this technique resulted in shock transit times repeatable

to better than ± 1%. Another light screen (L_3) was arranged off axis at the viewing window in order to sense the arrival of the projectile and initiate the picture sequence. T_1, T_2, and T_3 denote measured times used to determine the projectile velocity and the shock velocity. P_1, P_2, and P_3 denote pressure transducers. The timing system performance is acceptable, but would benefit from further refinements. Typical system performance was as follows. In ten experiments, two will have the desired interaction on the body, four will have the shock wave and the projectile in the same pictures, and the rest, with the blast wave either early or late, will only be of value for wake studies.

RESULTS

Figures 4 and 5 show shadowgraph sequences of the interaction for 20° and 10° cone-cylinder bodies respectively. The plane shock wave was traveling from right to left and the projectile from left to right. The shadowgraph sensitivity was adjusted so that the bow shock on the projectile before interaction was just visible. As a result the base flow, wake and trailing shock were generally not visible in this region. The increased density after the interaction made this part of the flow field readily detectable. In Figure 4, the somewhat lower velocity and smaller cone angle increased the extent of the region between the bow shock and body wherein the interaction occurred. Part of the reflection process details at the body surface were obscured by the relatively wide shadow cast by the plane shock.

The major features which resulted from the interaction were, however, apparent in these photographs. The distortion of the bow shock was apparent for both the 10° and 20° cones and was seen to persist well after the shock passed over the body. The most prominent features inside the interaction region bounded by the plane shock and bow shock were the several contact interfaces generated. The details associated with the development of the new base flow-wake region were striking. A more complete analysis of the interaction process will be presented in a later paper.

CONCLUSIONS

1) The feasibility of collecting optical data on the shock-on-shock problem using a simple gun - shock tube combination has been demonstrated.

2) The 0.1% repeatability required for the timing was difficult, but, nevertheless, managable by the technique outlined above.

REFERENCES

(1) Smyrl, J. L., "The Impact of a Shock Wave on a Thin Two-Dimensional Aerofoil Moving at Supersonic Speed", J. Fluid Mech. 15, 223 (1963).

(2) Miles, J. W., "A Note on Shock-Shock Diffraction", Aerospace Corporation, El Segundo, California, Report No. TDR-269(4230-30)-5, (May 13, 1964).

(3) Merritt, D. L. and Aronson, P. M., "Study of Blast-Bow Wave Interactions in a Wind Tunnel", AIAA Paper 65-5 (1965).

(4) Blankenship, V., "Shock-Shock Interaction on a Slender Cone", Aerospace Corporation, San Bernardino, California, Report No. TDR-469(35810-11)-1 (Sept. 1964).

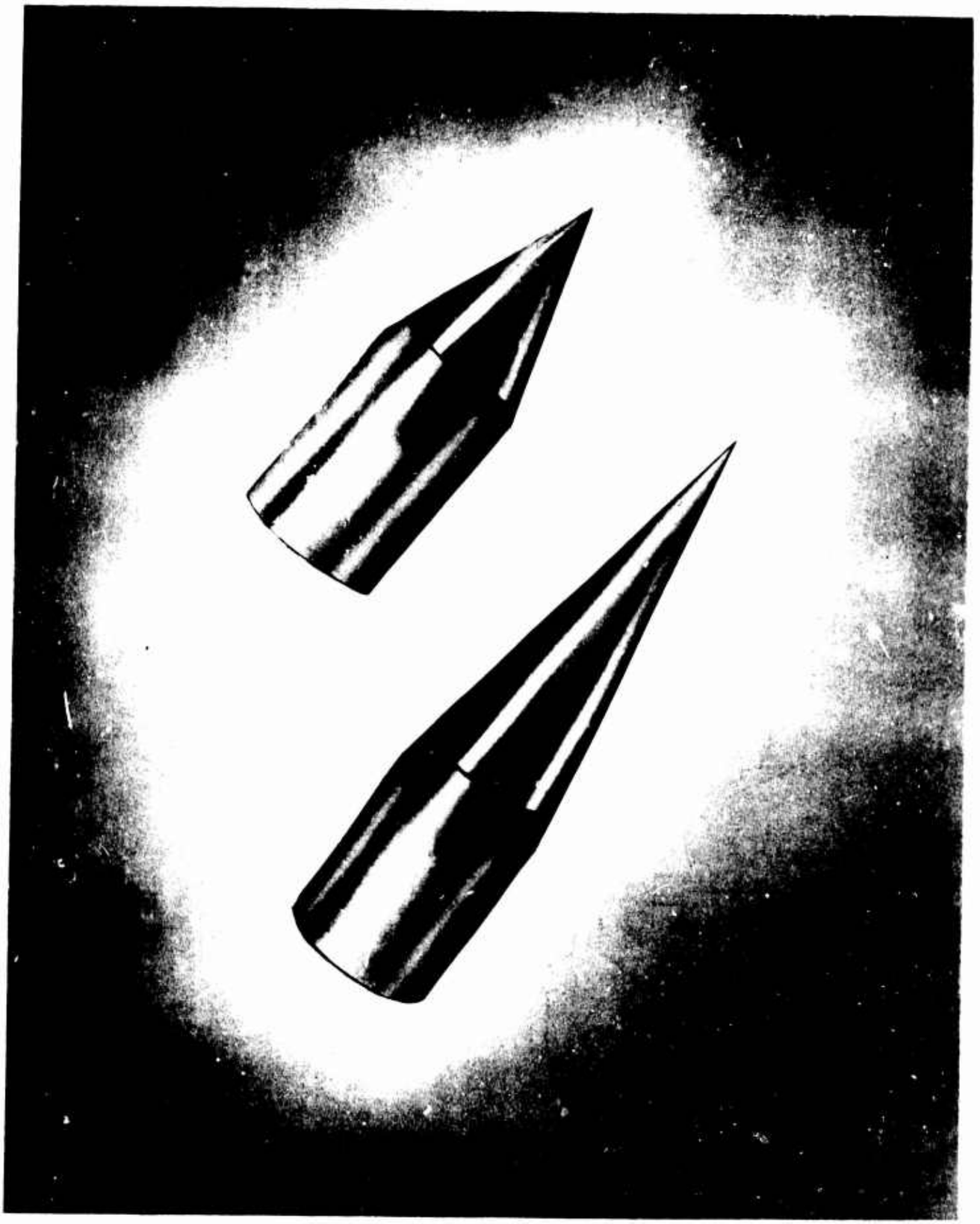


Fig. 1 Photograph of 10° and 20° cone-cylinder projectiles.

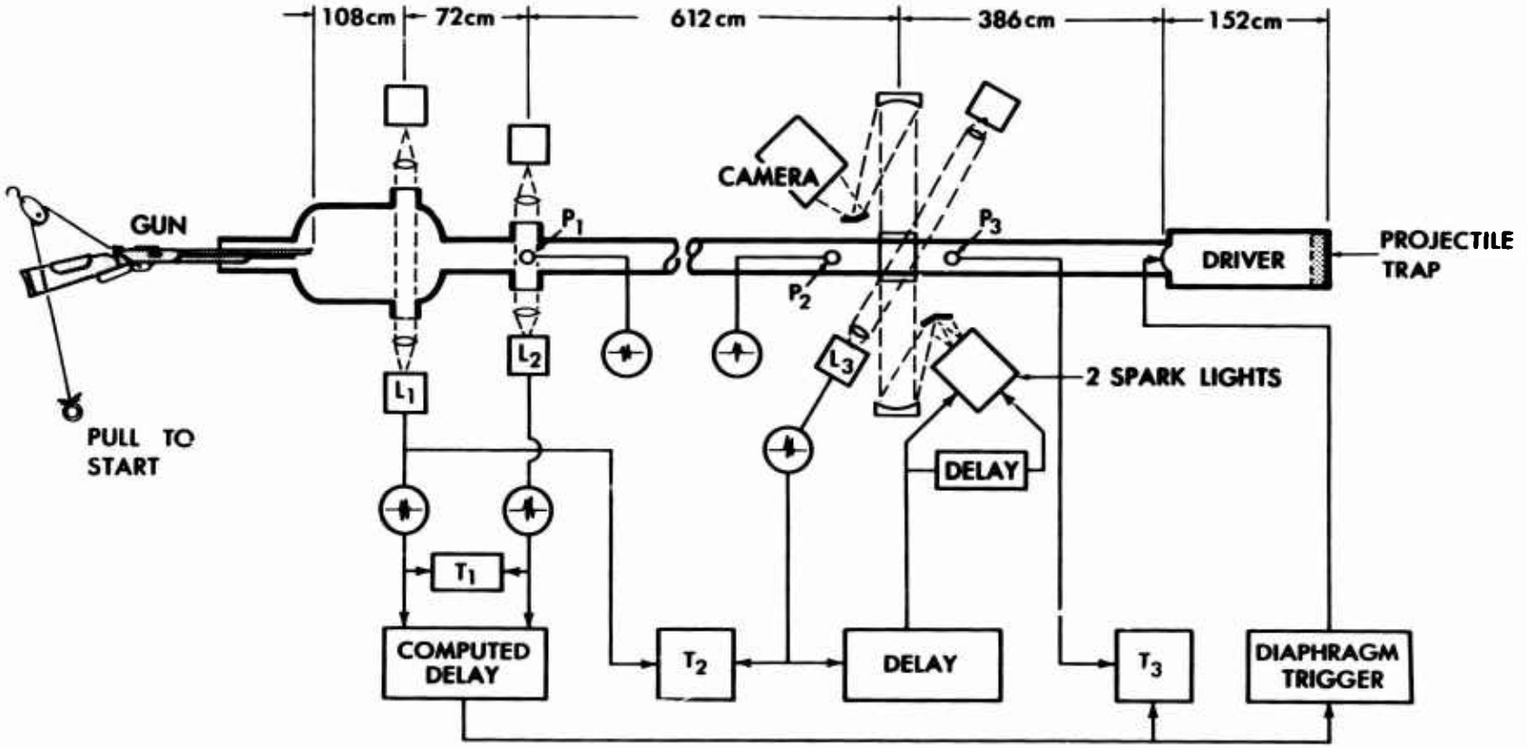


Fig. 2 Schematic of test setup.

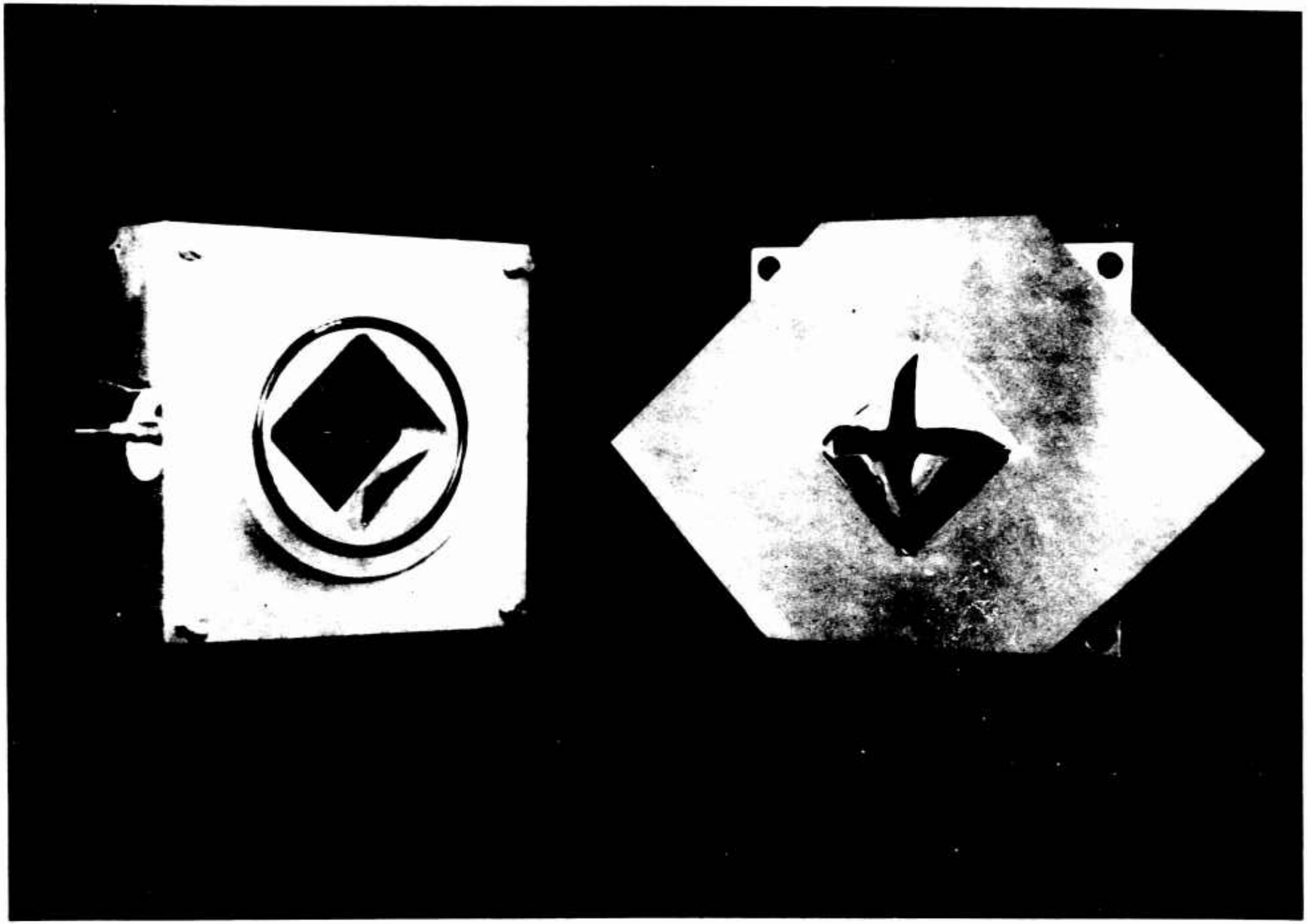


Fig. 3 Electrode, diaphragm and holder assembly.

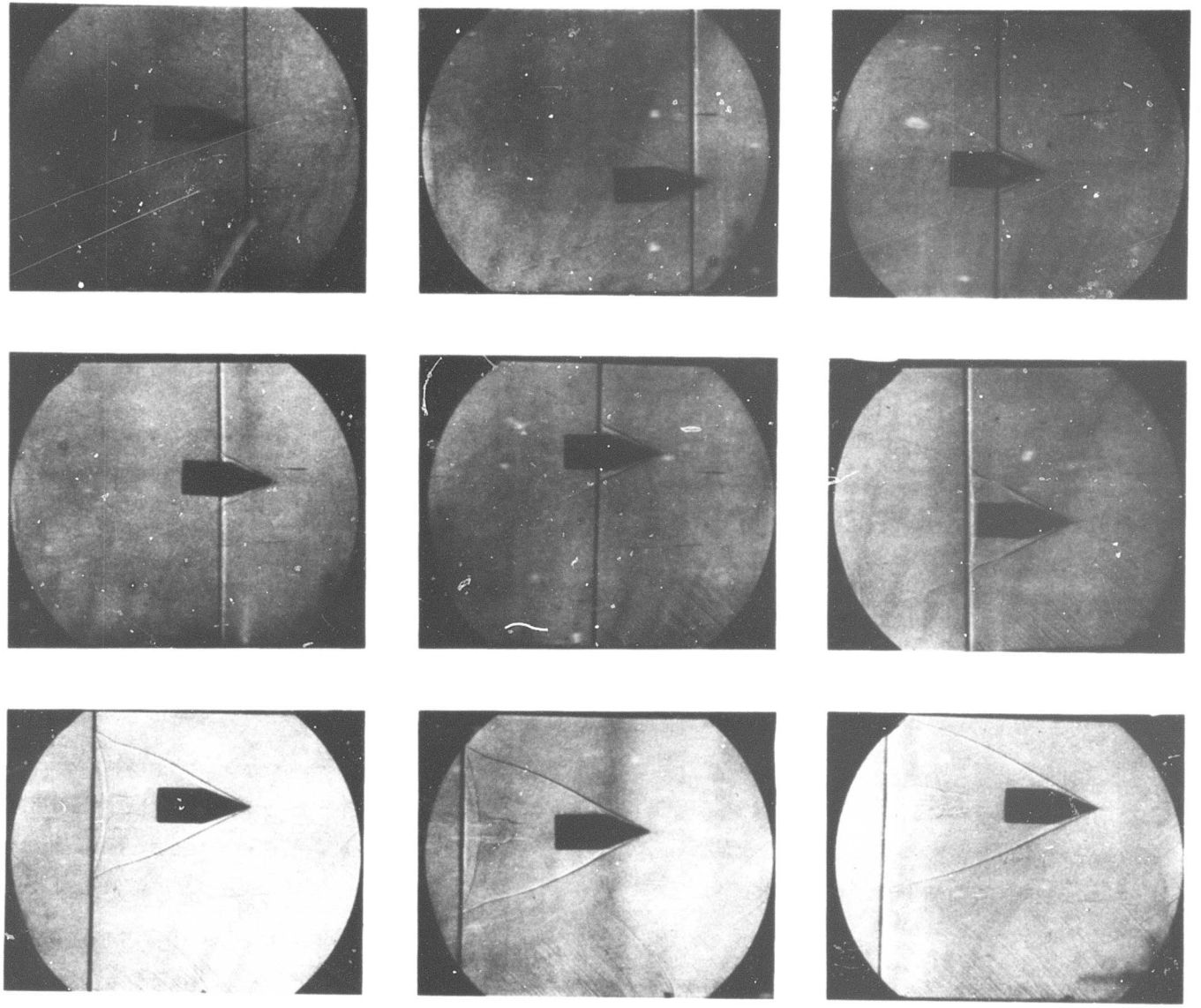


Fig. 4 Shadowgraph sequence showing head-on interaction of a plane shock and 20° cone-cylinder body.

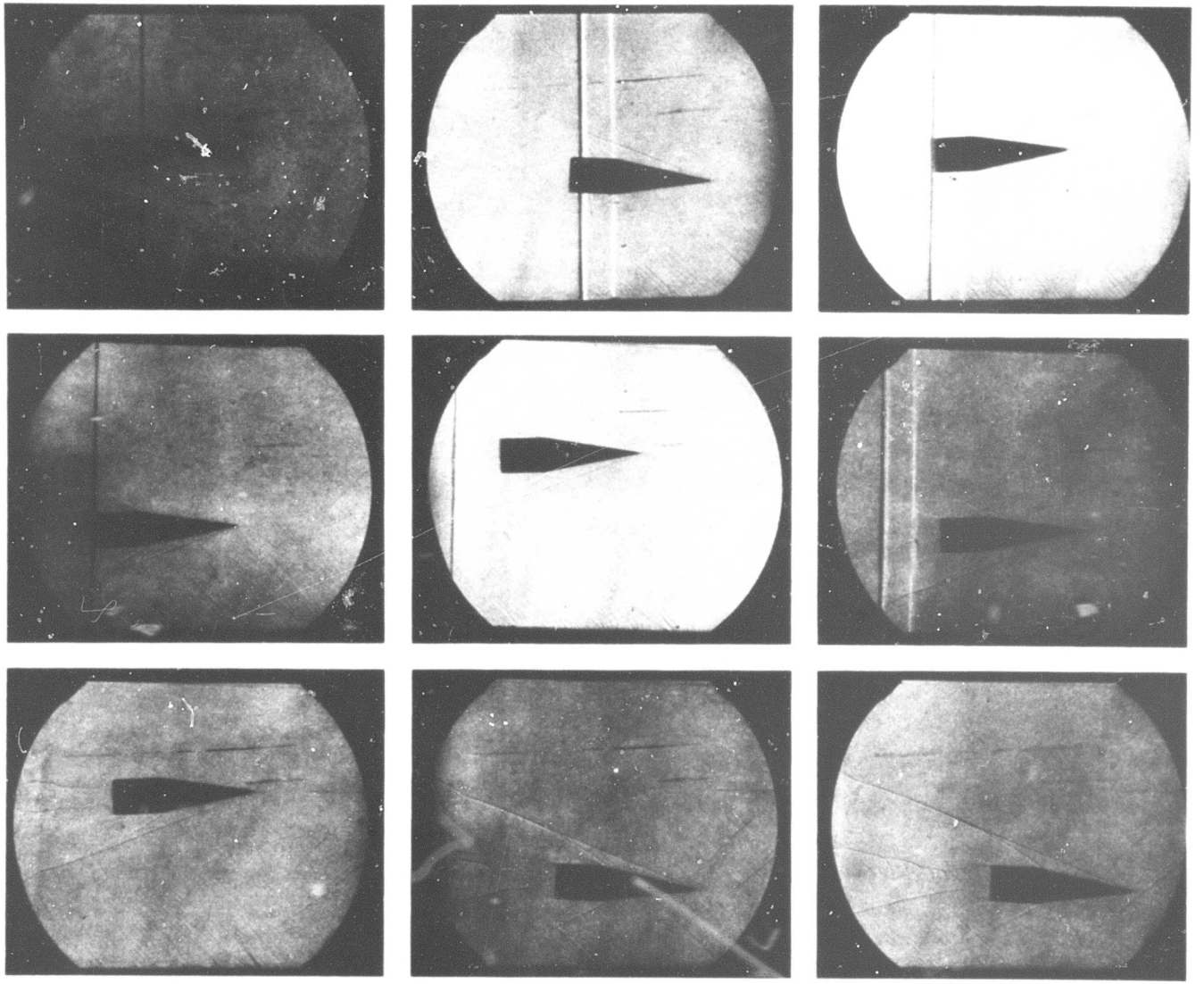


Fig. 5 Shadowgraph sequence showing head-on interaction of a plane shock and 10° cone-cylinder body.

BLANK PAGE

A SEVEN FOOT DIAMETER SHOCK TUBE FOR TRANSONIC AND SUPERSONIC AERODYNAMIC TESTING*

R. L. Varwig and L. Rosenman
Aerospace Corporation
El Segundo, California

ABSTRACT

A shock tube in which transonic and supersonic flows are produced with testing time adequate for aerodynamic measurements is described. The instrumentation includes pressure transducers and force balances that have been developed for use with hypersonic shock tunnels.

Measurements made to determine test time, flow uniformity, and flow establishment time are discussed. In general, steady, uniform flow at Mach numbers between 0.7 and 1.0 is obtained between the shock wave and the interface. Mach numbers from 1 to 2 are obtained upstream of the interface. Aerodynamic force coefficients measured for a sphere in both flow regimes agree within experimental precision with results obtained in steady flow wind tunnels.

INTRODUCTION

Hypersonic shock tunnels have been developed over the past ten years to provide flow conditions in the 10 to 20 Mach number range. Since the shock tube is the gas source for these tunnels, the steady flow duration is short, on the order of milliseconds. Along with shock tunnels the sensitive high speed instrumentation systems essential for measuring short duration aerodynamic phenomena have been developed. These systems include force balances capable of measuring forces as low as 1/4 lb, pressure transducers sensitive to 0.001 psi, and thin film resistance gages for measuring heat transfer.

*This research was performed under Air Force Contract AF-04(695)-469.

The purpose of this study is to examine the feasibility of using a shock tube for aerodynamic tests in the subsonic, transonic, and low supersonic range. By making the shock tube components sufficiently large, testing times equivalent to those of the hypersonic shock tunnel can be obtained. Therefore, the instrumentation systems developed for shock tunnels could be employed in the proposed low speed shock tube. Geiger, Mautz, and Hollyer (Ref. 1) described this type of shock tube as an "intermittent wind tunnel." Their shock tube had a constant 2 x 7 in. rectangular cross section. The maximum testing time was about 400 μsec at a flow Mach number of 2.6. This short testing time and the small tube dimensions limited the model size.

The present approach calls for a large diameter shock tube. Primarily large force balance models (on the order of 1 ft) will be investigated in such a facility. Hence testing times long enough to permit establishment of steady flow over such models must be obtained. With long testing times required, the walls must be remote enough that signals returning from them do not interfere with the testing time. Also the possibility of choking, as discussed in Ref. 1, is minimized by the large diameter of the driven section.

Due to the difficulties inherent in constructing large diameter pressure vessels and in the rupture of large diameter diaphragms, it was decided to construct a much reduced diameter high pressure vessel for the driver for the shock tube. It was expected from the work of Resler, Lin, and Kantrowitz (Ref. 2) that area ratio could be exchanged for pressure ratio.

In a recent study, Russell (Ref. 3) examined the effect of area change at the diaphragm on shock tube performance. The applicability of this work in predicting the performance, i.e., shock Mach number and testing time, for the facility described is determined. Flow uniformity transverse to the flow direction as well as flow steadiness (axial flow uniformity) is examined in both the region behind the shock (region 2) and upstream of the interface (region 3). A limited investigation of the time to establish steady flow about simple models is made. Final proof of the utility of the system for aerodynamic force measurements is obtained by inserting a force balance model, the aerodynamic parameters of which are well known. The force and moment data measured in the shock tube are compared with these known parameters. This also permits an evaluation of the application of force balances, used normally in shock tunnels, in the shock tube.

THEORY

In the study by Russell (Ref. 3) a shock tube is examined in which a small throat area A* exists between the driver and driven section. In his study Russell assumes that the area change may be treated as an isentropic nozzle. The calculation of the ensuing shock tube flows requires a matching of the pressure and velocity at each side of the interface. The flow between the shock and interface (region 2) is completely determined by the shock. Upstream of the interface the flow is fixed by the nozzle geometry. Hence,

some wave phenomena must take place between the nozzle flow and the interface to accomplish this matching. Russell considers two flow models. In the first model an upstream facing expansion wave or shock wave is used to match conditions between the shock wave and the driver region [Figs. 1(a) and (b)]. In this model an upstream facing rarefaction wave is needed at shock Mach numbers greater than about 3. With decreasing Mach number an upstream facing shock wave is needed. For the lowest shock Mach numbers [Fig. 1(c)] a stationary normal shock provides the matching. The diaphragm pressure ratio required at a given area ratio A^*/A_1 to produce various shock speeds can be determined. In Fig. 2 are plotted the diaphragm pressure ratio p_4/p_1 vs M_s for $A_1/A^* = 9$, 36, and 196 as determined for each of the above flow configurations. Russell experimentally verified that the above model was applicable in the range for $M_s > 3$ and in the range covered by the unsteady normal shock experimental agreement was less satisfactory. Consequently, he introduced a second model in which the flow matching was accomplished by an upstream facing "Fanno compression" region. Using this model he recomputed the required diaphragm pressure ratio, and this time the agreement with experiment was better.

The flow conditions in region 2 are fixed when the shock Mach number M_s is determined. Hence the duration of these flow conditions can be calculated directly from the difference in the shock velocity and flow velocity in region 2 once the shock tube geometry is fixed. In region 3 the testing time is determined by the time interval between the passage of the interface and any one of: (a) the secondary shock or rarefaction wave, (b) the reflected rarefaction wave, or (c) the shock wave reflected from the downstream end of the tube. From Figs. 3, 4, and 5 it is seen that for the configuration and shock Mach numbers considered here the secondary upstream facing shock wave terminates the testing time in region 3. The curves also indicate that ample test time is theoretically available for shock tunnel instrumentation systems.

SIMULATION

From Fig. 2 for a shock tube of $A_1/A^* = 196$, the flow simulation capability can be determined. By fixing the maximum driver pressure p_4 the driven section pressure p_1 for a variety of M_s values can be determined. Hence the flow Mach number M_2 and corresponding Reynolds numbers can be determined.

From Ref. 3, the flow Mach number M_3 in region 3 can also be predicted as a function of M_s. This dependence is exhibited in the curves of Fig. 6 for the unsteady normal shock and the Fanno Compression models. Ideal shock tube predictions of M_3 are also included for comparison. For given values of M_s, M_3 is determined and also the associated value of the Reynolds number per foot. In Table 1 values of the Mach numbers M_s, M_2 and M_3 and the Reynolds numbers per foot in regions 2 and 3 are tabulated as function of driver pressures from 100 to 5000 psi. From this Table it is seen that simulation of Reynolds number to nearly 10^7 at Mach numbers

over 2 can be obtained with the highest driver pressures proposed for the shock tube, and at transonic Mach numbers Reynolds numbers of 5×10^6 can be achieved.

The data in Table 1 are summarized in Fig. 7 which presents Reynolds number and Mach number ranges for the proposed shock tube operating conditions.

p_1 (atm)	p_4 (atm)	p_4/p_1	M_s	M_2	Re_2/ft (ft^{-1})	M_3	Re_3/ft (ft^{-1})
0.66×10^{-3}	4.8	7360	2.10	1.0	0.11×10^5	1.93	1.19×10^5
2.63×10^{-3}	19.4	7360	2.10	1.0	0.45×10^5	1.93	4.77×10^5
0.42×10^{-1}	312	7360	2.10	1.0	7.2×10^5	1.93	76×10^5
1.65×10^{-3}	4.8	2936	1.84	0.86	0.21×10^5	1.35	1.10×10^5
6.6×10^{-3}	19.4	2936	1.84	0.86	0.84×10^5	1.35	4.4×10^5
0.105	312	2936	1.84	0.86	13.5×10^5	1.35	70.4×10^5
3.3×10^{-3}	4.8	1468	1.64	0.72	0.31×10^5	1.00	1.06×10^5
1.3×10^{-2}	19.4	1468	1.64	0.72	1.24×10^5	1.00	4.25×10^5
0.21	312	1468	1.64	0.72	19.8×10^5	1.00	67.9×10^5

Table 1. Theoretical Estimates for Flow Conditions in Regions 2 and 3 for Various Driver Pressures

DESCRIPTION OF THE FACILITY

The facility is shown schematically in Fig. 8. The driven section of the shock tube consists of a vacuum tank 7 ft in diameter and 35 ft long. Schlieren windows are installed in this section. The windows are nearly flush with the inner surface of the driven section. In order to provide easy access to models being tested, the end of the driven section and model support sting are mounted on a rolling truck. The sting support and the truck are isolated from the shock tube end section by shock mounts and a double-walled pressurized bellows at the point where the support enters the tank. At the diaphragm end of the driven section a 45 deg half angle truncated cone acts as a transition between the driver and driven sections. The driver is fabricated of steel that is heat treated to 160 to 180 kpsi and has a working pressure of 5000 psi. A 300 cfm Stokes vacuum pump supplemented with a centrifugal booster is employed to evacuate the driven section to the appropriate initial pressures. Pressures as low as 30 μHg can be obtained although working pressures are normally on the order of millimeters. The

high pressure gas reservoir consists of five standard 1 - 1/2 ft^3 gas bottles. The maximum driver pressure available is slightly over 1000 psig. To conserve gas most of the testing was performed at driver pressures between 200 and 300 psi. In this range easily available diaphragms of mylar film are employed. Reynolds numbers obtained at these driver pressures are indicated by the shaded area of Fig. 7. Aluminum and stainless steel diaphragms have also been used for higher driver pressures.

Plans for regular high pressure operation to 5000 psi are being implemented with a high pressure pumping and storage capacity system.

MEASUREMENTS

To demonstrate the usefulness of the facility as a large diameter intermittant wind tunnel, the flow conditions produced in regions 2 and 3 are discussed. Test results to date on performance, transverse and axial flow uniformity, steady flow establishment time around bodies, and the aerodynamic force coefficients measured in the two regions are presented.

Performance

The performance for shock tubes with area changes at the diaphragm has been discussed in Ref. 3. Within the experimental error (largely due to difficulties of determining the bursting pressure of the diaphragm) the shock Mach number obtained for various driver pressure ratios was very much as predicted. The shock Mach number was measured by pressure gages installed in the wall fore and aft of the window in the region of the shock tube serving as the test area. The measured shock Mach number for various p_4/p_1 is in Fig. 2. The comparison is reasonably good.

The flow conditions in region 2 are fixed by the shock Mach number. Hence the flow Mach number is easily predicted. The gas upstream of the interface may pass through some type of pressure wave to match the pressure and velocity at the interface with driver gas conditions in the conical expansion section. Hence its entropy may not be isentropically related to the initial driver gas. However, the pitot and static pressures can be measured in region 3, and the gas properties can then be determined. The Rayleigh pitot formula is applied for this computation. Values of M_3 so obtained are entered in Fig. 6. As can be seen the Fanno Compression model, as concluded by Russell, comes closer to predicting the experimental results than does the unsteady normal shock model.

Transverse Flow Uniformity

From Schlieren photographs (Fig. 9), a single normal shock is seen to be formed. It is suspected that the apparent thickness is due to curvature of the shock since from Schlieren photographs the reflected shock from models located on the axis of the shock tube seemed to originate from the trailing edge of the incident shock. With the use of an impact tube rake in the shock tube, the time of arrival of the shock wave, resolved to within

10 μsec, was found at many points across the tube. These measurements defined the pitot pressure profile. The survey was limited to a core region 42 in. wide since that was the extent of the rake available. From the measurements it was determined that the shock front was concave downstream, as suspected, with the middle section about 1 in. behind the edge. Across the 7 ft of the test section, the lag is about 2-1/2 in. The magnitude of the pitot pressure in region 2 varied no more than ±6 percent across the 42 in. spanned by the rake measurements.

The arrival of the interface at each pitot gage across the 42 in. rake seemed to correlate well, indicating an essentially plane interface. The pitot pressure measured in region 3 varied no more than ± 7 percent across the impact tube rake, indicating a reasonably uniform flow profile.

Axial Flow Uniformity (Test Time)

From measurements of static pressure in the wall behind the shock, the steadiness of the pressure can be observed. Typical records of the pressure are shown in Fig. 10. Static pressure is continuous across the interface as indicated in the figure; however, the pitot pressure depends also on the density and therefore can indicate the arrival of the interface. Pitot pressures measured by gage elements of an impact tube rake are also exhibited in Fig. 10. From records such as these, the duration of uniform flow in region 2 is obtained. In Figs. 3, 4, and 5 the measured values of the test duration in region 2 have been added to show the comparison with predicted values. Uniform flows of 4, 6, and 11 msec for flows of $M_2 = 0.99$, 0.8, and 0.6 are obtained.

The test duration in region 3 is indicated in Fig. 11. Here for flow Mach number M_3 of 2.2, uniform flow is obtained for 4 msec, adequate for the instrumentation system available, which is seen in the section on force balance measurements. Driver conditions M_s, M_2, and M_3 and the uniform flow duration are summarized in Table 2. The Reynolds numbers associated with the flows are also listed. These may be compared with the theoretical estimates in Table 1.

Flow Establishment Around Models

A Schlieren system was used to observe the time to establish steady flow over an object in the transonic and supersonic regimes, (i.e., flow establishment time). Two models were employed: a 6 in. diameter sphere and a 3 in. diameter cylinder mounted normal to the flow. A series of tests in which the Schlieren observation is made at different intervals permitted the observation of the incident shock, the shock reflected from the body, the formation of the characteristic imbedded shocks for transonic flow conditions, and the arrival of the interface. Since the flow behind the interface is supersonic for all the test conditions experienced here, it was also possible to observe the formation of the bow shock in this flow, its duration, and the standoff distance. A typical series of observations is shown in Fig. 9. For this sequence of Schlieren photographs, the

p_1 (atm)	p_4 (atm)	p_4/p_1	M_s	M_2	Δt^* Reg. 2 (msec)	Re_2/ft (ft^{-1})	M_3	Re_3/ft (ft^{-1})	Δt^* Reg. 3 (msec)
6.6×10^{-3}	19.4	2950	1.80	0.86	6.3	0.842×10^5	1.45	4.39×10^5	4.0
2.6×10^{-3}	19.4	7370	2.05	0.99	4.0	0.450×10^5	2.0	4.77×10^5	4.4

*Indicates Test Times in Regions 2 and 3.

Table 2. Flow Conditions and Test Times Obtained in the Low Speed Shock Tube

conditions are p_1 = 5 mm, p_4 = 270 psig, and M_s = 1.79 with M_2 = 0.83 and M_3 = 1.4. In region 2, shock waves formed and became steady in about 3 msec, indicating that steady flow is established. This left about 3 msec for testing. In region 3 again about 3 msec is required for the bow wave to form with about 3 msec of testing time after that. It should be pointed out that the time intervals established from these observations cannot be generally applied to all bodies. A more general study (experimental and theoretical) of flow formation times is needed; the present observations were made primarily to show that for these spheres there was sufficient time for flow to become established so that meaningful force measurements could be attempted.

The turbulent character of the Schlieren photographs is due to a turbulent boundary layer along the shock tube wall in the cool, dense gas of region 3, which is expected (Ref. 4). It does not mean that the flow in the central part of the tube is turbulent.

Force Measurements

A principal purpose of the facility is to make aerodynamic force measurements on models in the low speed range using the acceleration compensated force balance developed for the Aerospace hypersonic shock tunnel. To check the shock tube for feasibility of this type of measurement, a 6 in. sphere was mounted on the force balance. A pressure gage was mounted at the stagnation point to record total pressure behind the normal shock. The data along with the static pressure measured at the wall were used in the Rayleigh formula to determine the flow Mach number in the two flow regions. The results of this test for M_s = 2.17 are shown in Fig. 11. The two flow regions are clearly evident in the force traces and the pitot gage record. From the pitot and static pressure records the flow Mach number is 1.13 in region 2 and 2.24 in region 3. Drag coefficients of 1.0 in region 2 and 0.96 in region 3 are obtained. These values are entered on the plot of drag coefficient vs Mach number in Fig. 12.

From this figure it is seen that the agreement is good.

CONCLUDING REMARKS

The shock tube described has proved to be a suitable device for aerodynamic tests in the transonic and supersonic flow regimes. Test times on the order of milliseconds are available. The high speed instrumentation previously developed for shock tunnels can be applied to make measurements of pressure, forces, and heat transfer.

REFERENCES

(1) Geiger, S. W., Mautz, C. N. and Hollyer, R. N., Jr., The Shock Tube as an Instrument for the Investigation of Transonic and Supersonic Flow Patterns, Engr. Res. Inst., Univ. of Mich., Ann Arbor, Project M720-4 (June 1949).

(2) Resler, E. L., Lin, S. C. and Kantrowitz, A., J. Appl. Phys. 23, 1390 (1952).

(3) Russell, D. M., A Study of Area Change Near the Diaphragm of a Shock Tube, Project Memo No. 57, Guggenheim Aeronautical Lab., Calif. Inst. of Tech., Pasadena (July 1960).

(4) Glick, H. S., Hertzberg, A. and Smith, W. E., Flow Phenomena in Starting a Hypersonic Shock Tunnel, AD-789-A-3, Cornell Aeronautical Lab., Cornell Univ., Buffalo (March 1955).

(5) Charters, A. C. and Thomas, R. N., J. Aero. Sci. 12, 468-476 (October 1945).

(6) Heinrich, H. G., Hess, S. R. and Stumbris, G., Drag Coefficients of Several Bodies of Revolution at Transonic and Supersonic Velocity, ASD-TDR-63-663, AF Flight Dynamics Lab., RTD-AFSC, WPAFB (September 1964).

(7) Morrison, R. B., Design Data for Aeronautics and Astronautics, John Wiley and Sons, Inc., New York (1962).

660r

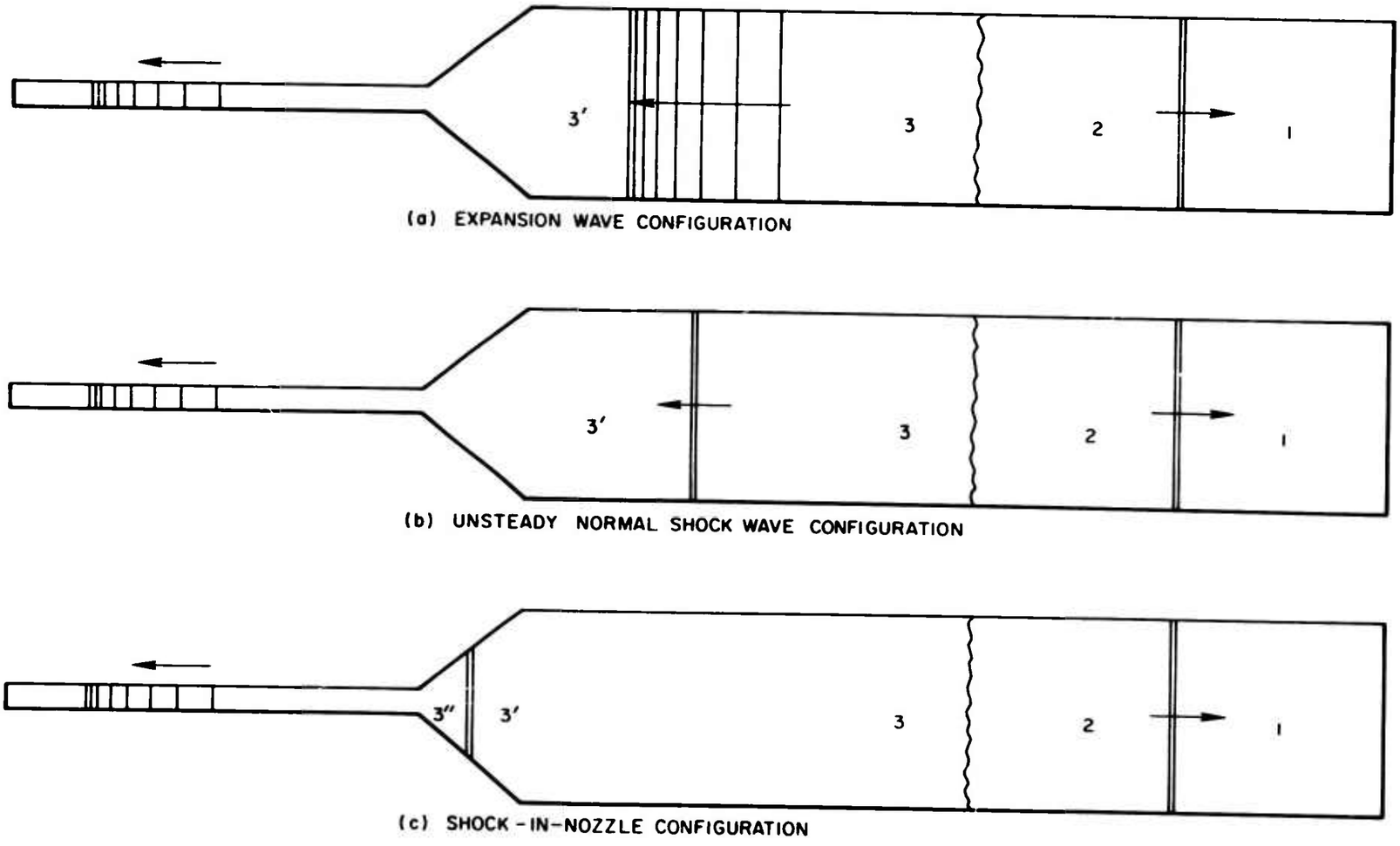


Fig. 1. Shock Tube Flow Model

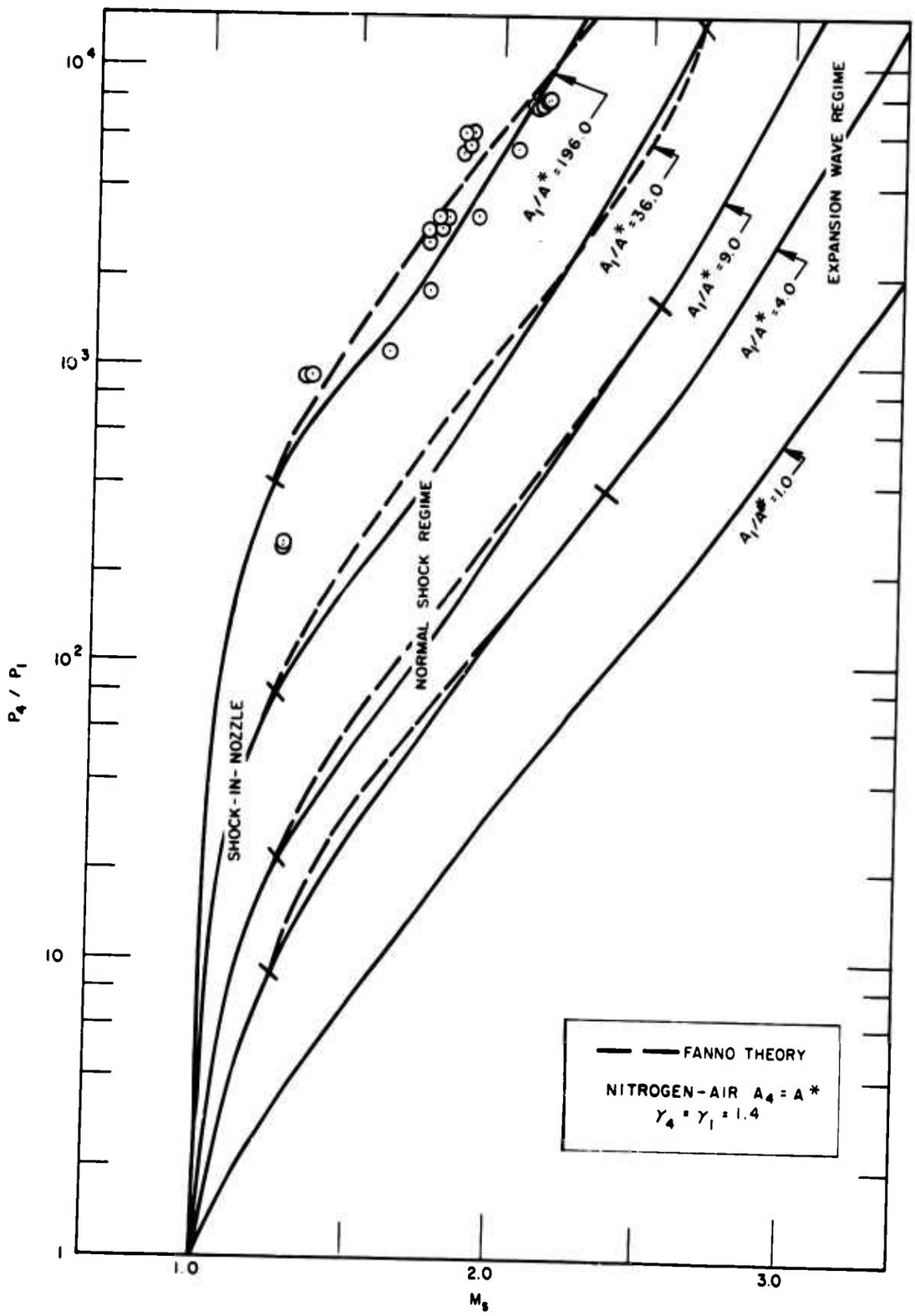


Fig. 2. Diaphragm Pressure Ratio p_4/p_1 as a Function of M_s

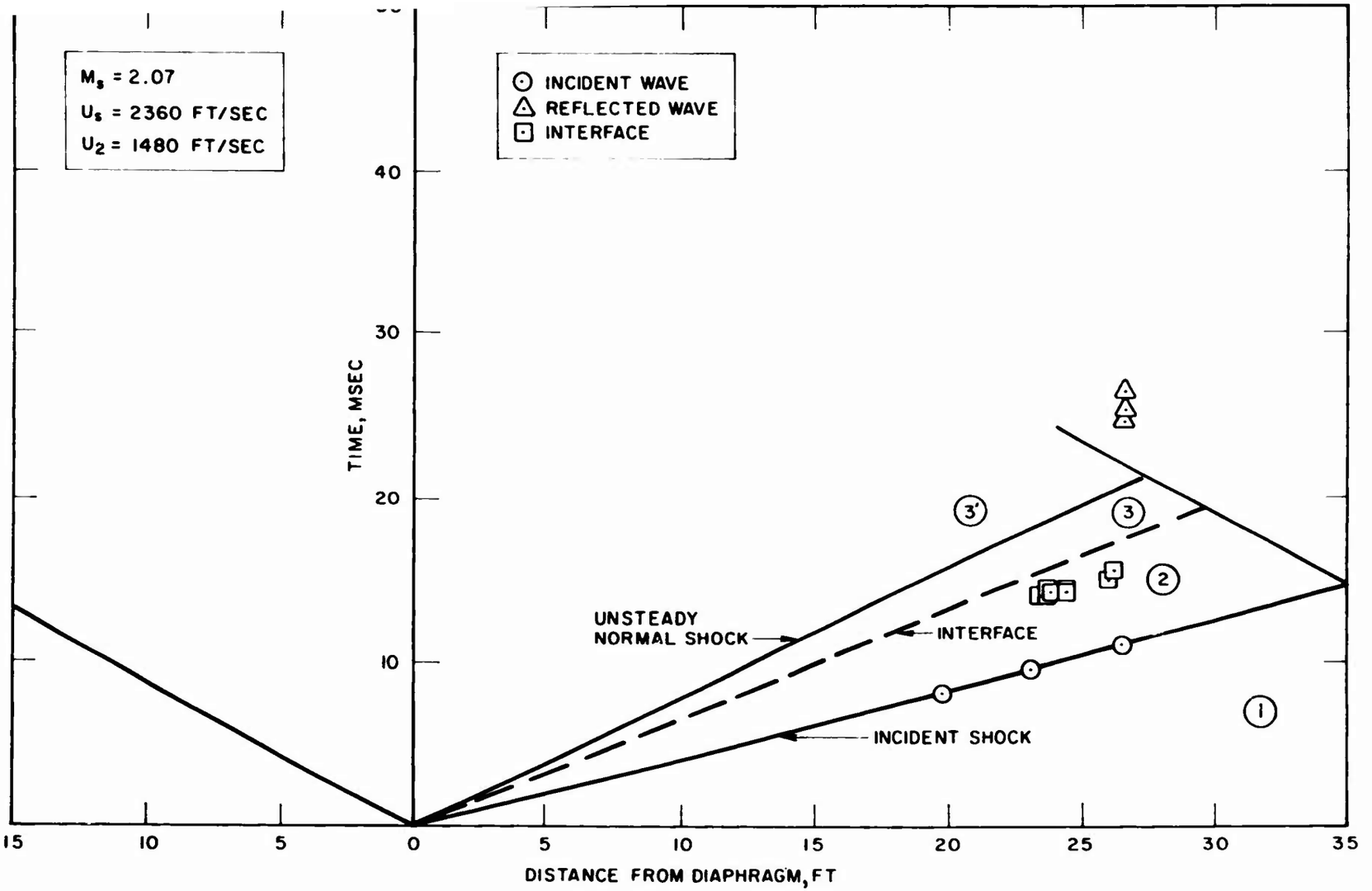


Fig. 3. Experimentally Determined Arrival of Shock, Interface, and Reflected Shock at the Test Area Compared with Predicted Values

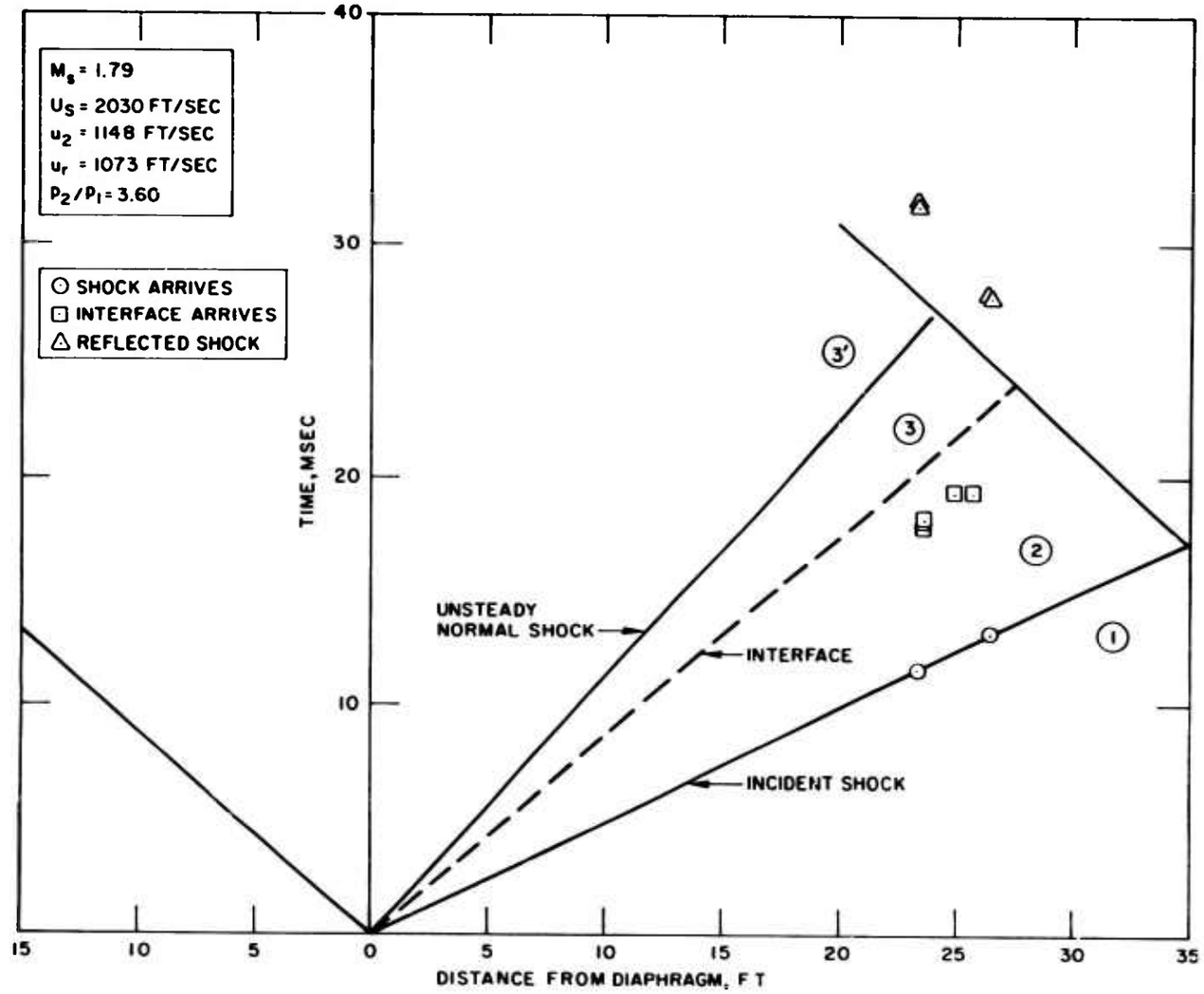


Fig. 4. Measured Arrival Time of Shock, Interface, and Reflected Shock for $M_s = 1.79$ Compared with Predicted Values

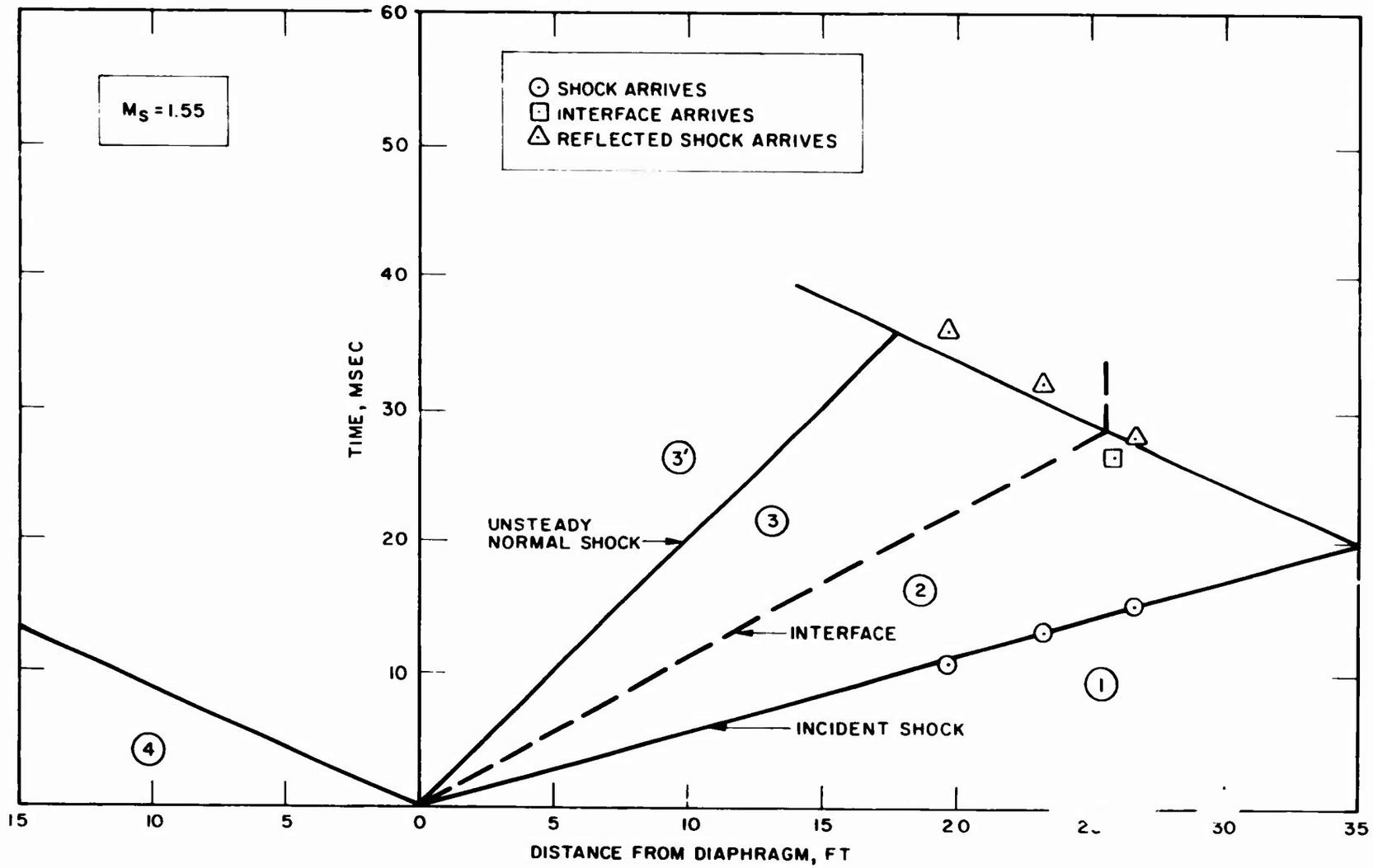


Fig. 5. Measurement of Arrival Time of Shock, Interface, and Reflected Shock for $M_s = 1.55$ Compared with Predicted Values

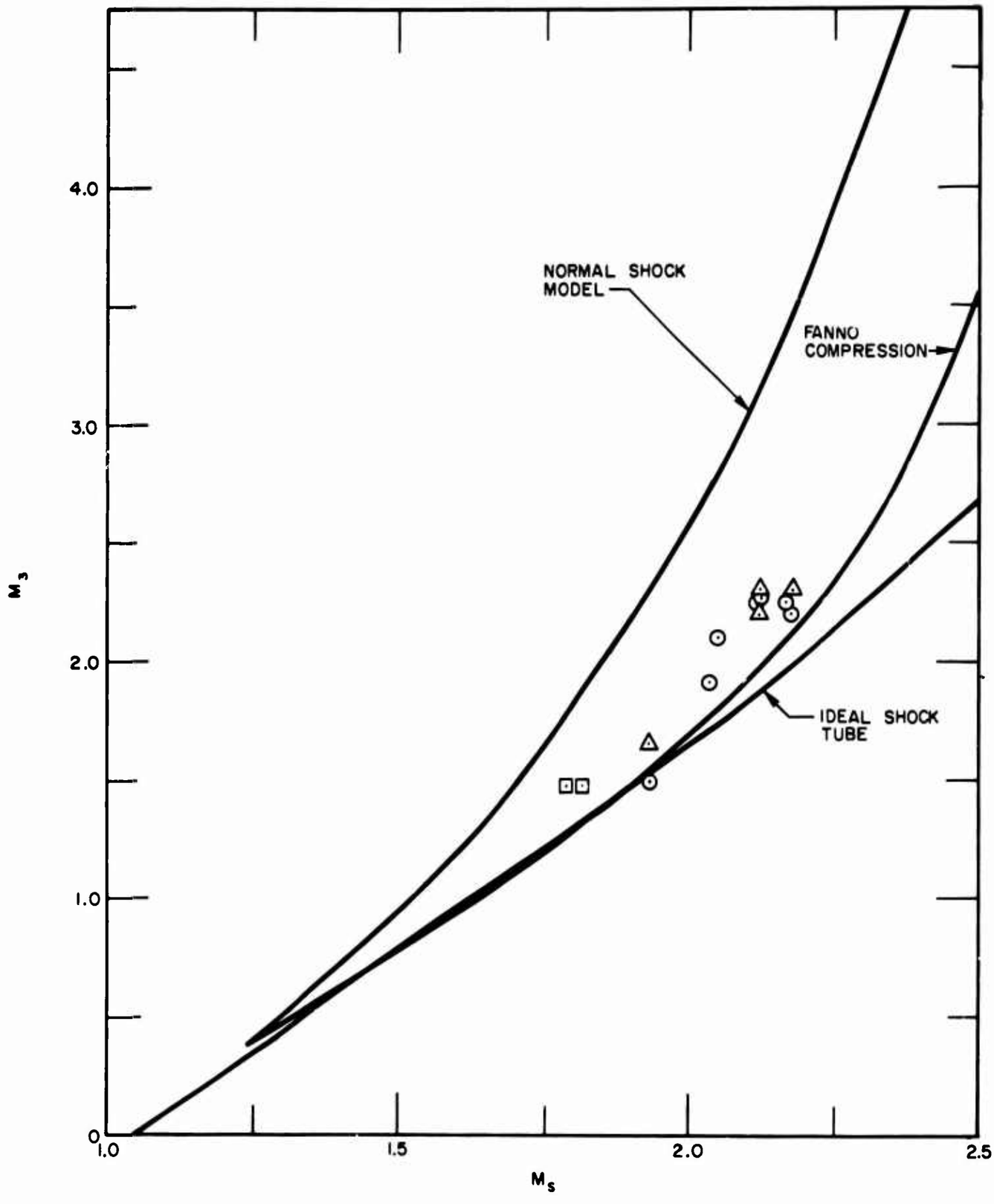


Fig. 6. Flow Mach Number M_3 as a Function of M_s

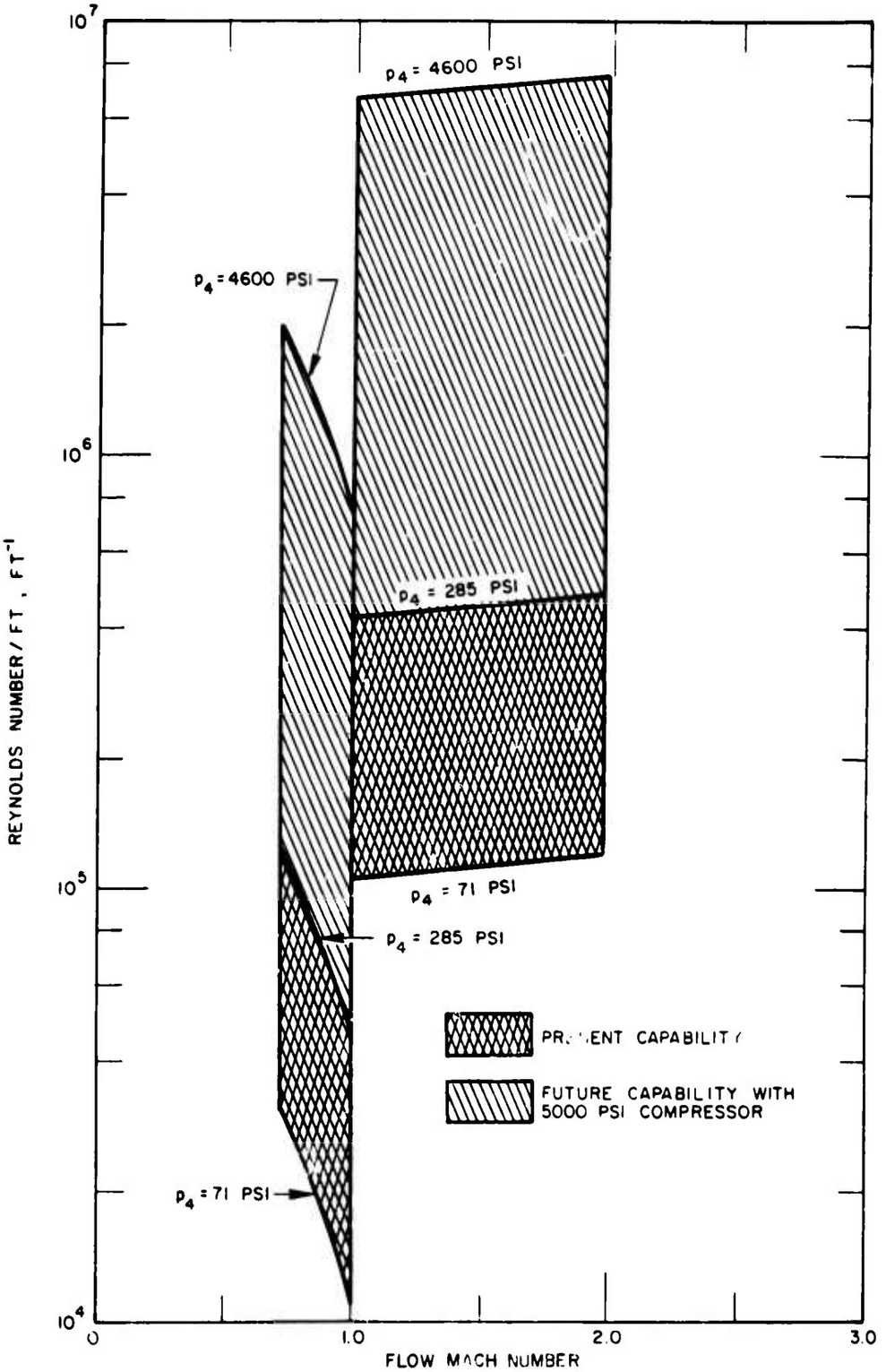


Fig. 7. Theoretical Test Envelope for the Aerospace Low Speed Shock Tube

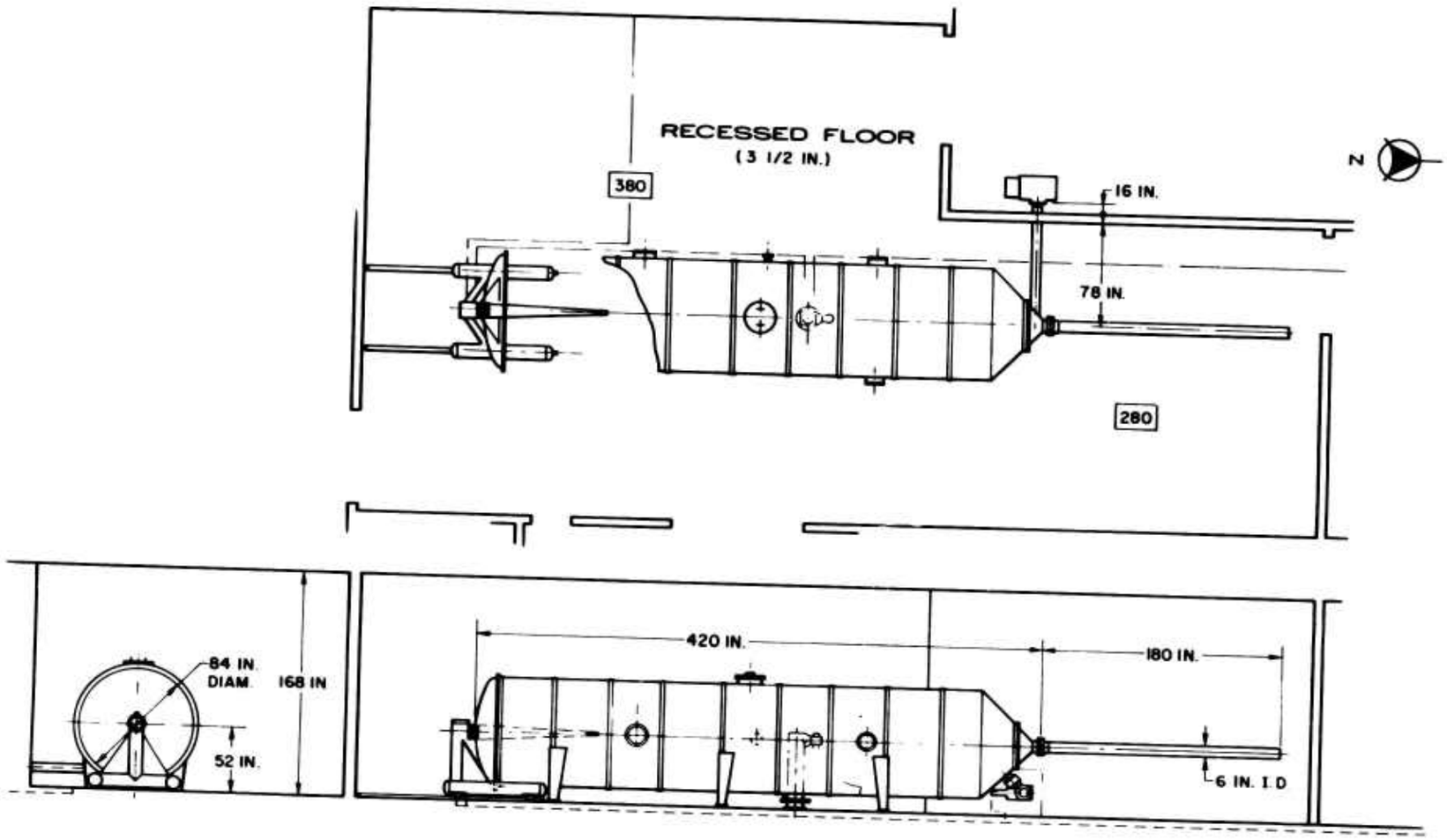


Fig. 8. Shock Tube Configuration for Producing Transonic and Supersonic Flows



Fig. 9. Time Sequence Schlieren Observations Showing Arrival of the Shock, Formation of Locally Supersonic Waves in Near Sonic Flow, Interface Arrival, and Supersonic Flow Bow Wave

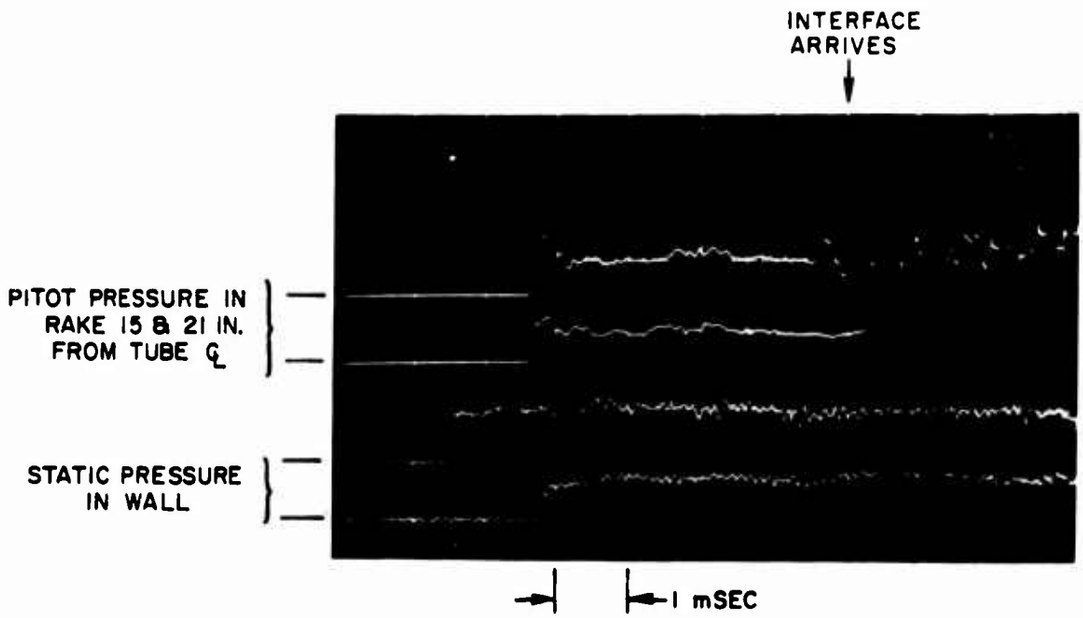
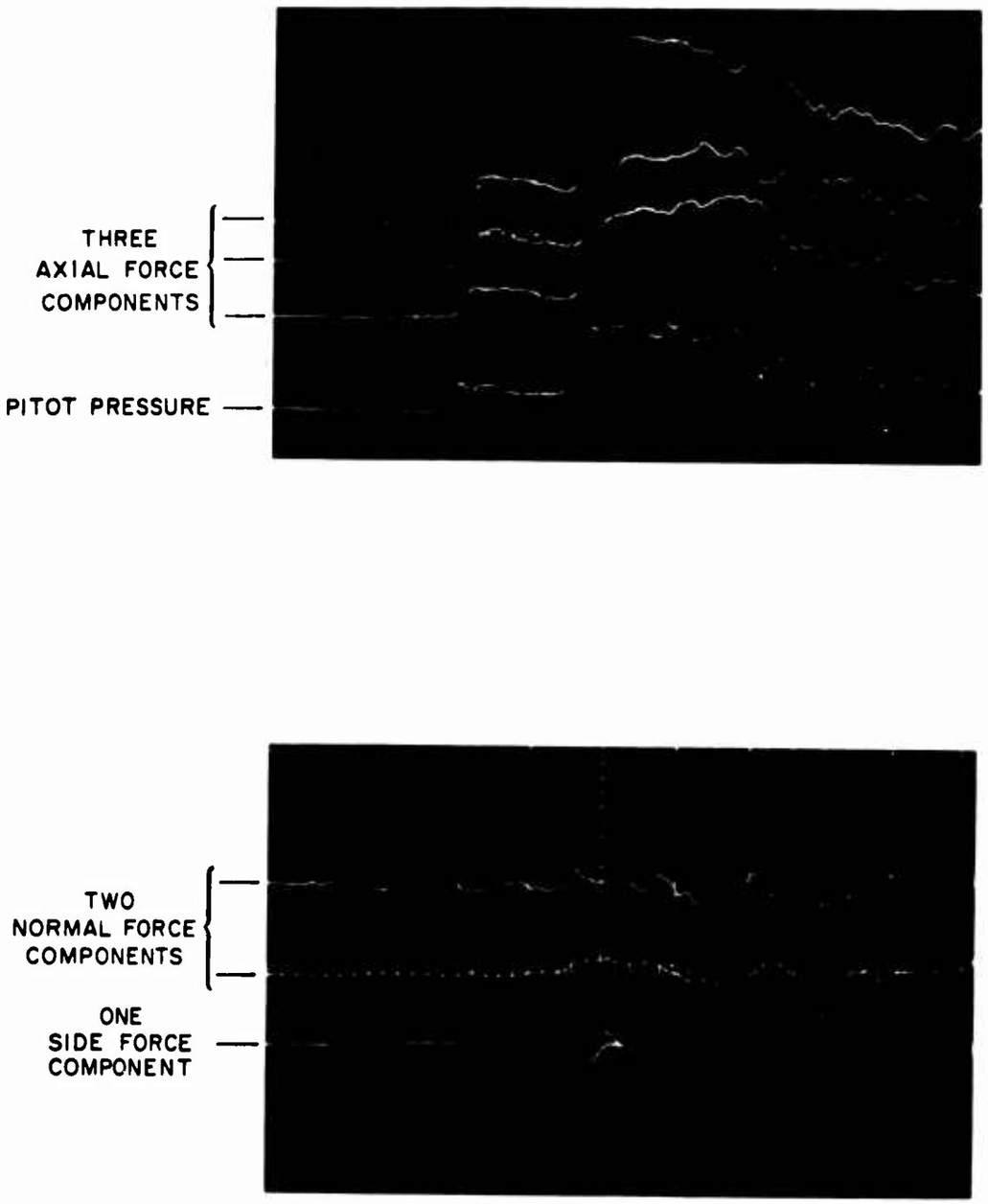


Fig. 10. Static Pressure Measured in the Shock Tube Wall and Total Pressure Measured in Region 2



DATA: $M_s = 2.17$

$M_2 = 1.1$ $C_{D2} = 1.0$

$M_3 = 2.2$ $C_{D3} = 0.96$

BALANCE ANGLE = 0 DEG

Fig. 11. Six-Component Force Balance Measurements on a Sphere in the Shock Tube

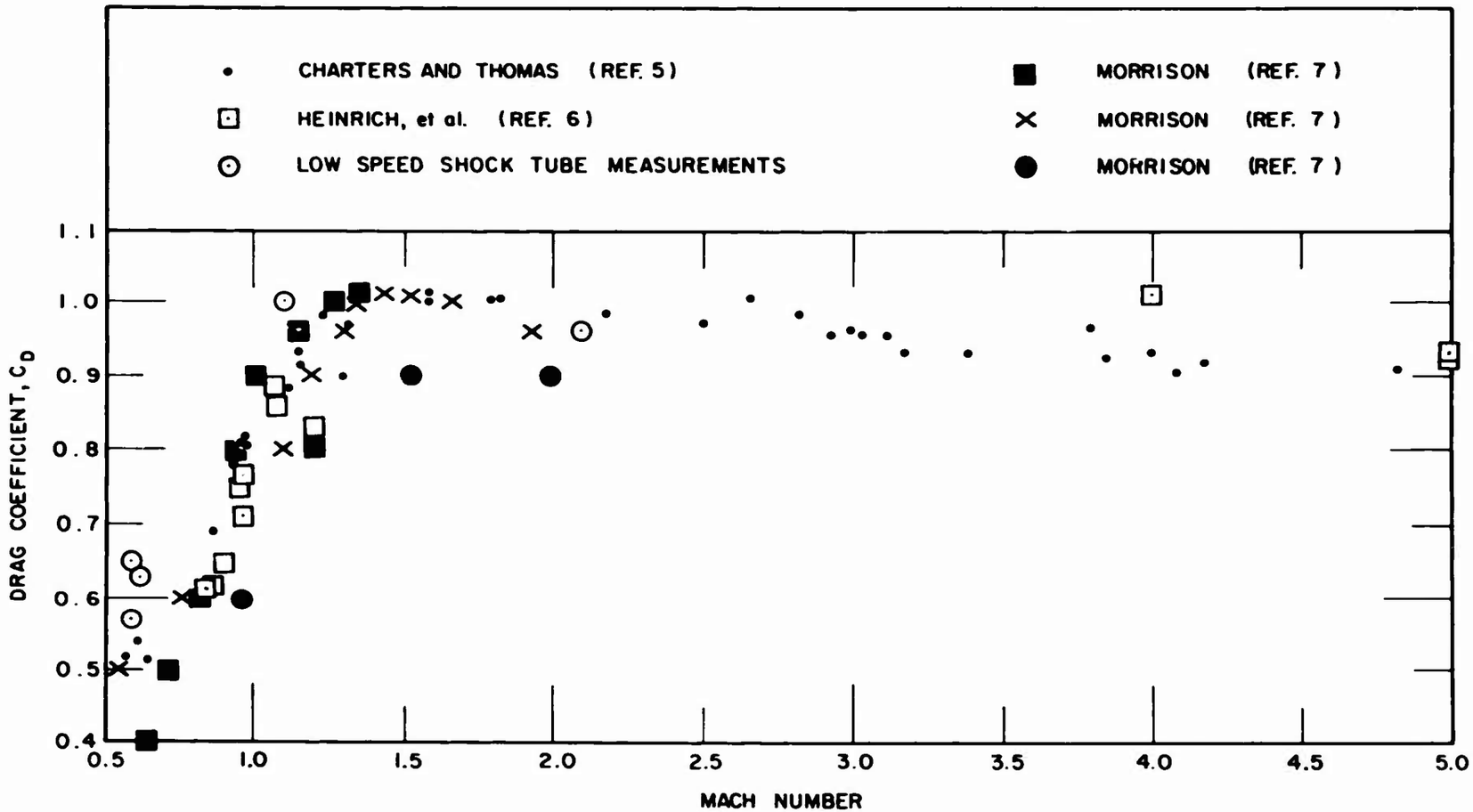


Fig. 12. Low Speed Shock Tube Sphere Drag Measurements Compared to Those from Wind Tunnels and Ranges

THE GASEOUS-DETONATION DRIVER AND ITS APPLICATION TO SHOCK TUBE SIMULATION TECHNIQUES

M. J. Balcerzak and M. R. Johnson
MRD Division, General American Transportation Corporation
Niles, Illinois

ABSTRACT

The operational characteristics of gaseous-detonation drivers are discussed. The advantages of using gaseous-detonation shock tube drivers for simulating explosive blast effects and hypervelocity flows are explained. Shock tubes employing detonation drivers can have large-diameter test sections capable of accepting large models and providing large cross-sections of flow, free from boundary layer effects. Detonation drivers can be used open-ended eliminating the need for massive recoils systems. Also lower driving pressures are required than with static high-pressure-gas drivers. This allows a reduction in the thickness of the shock tube wall.

Three applications of gaseous-detonation drivers are described. The first application presents a technique for simulating blast effects generated by nuclear and conventional explosions. Overpressures of thousands of psi and durations to one-half peak pressure of tens of milliseconds are practical. The second application describes a technique for simulating blast loading in supersonic flow, the shock-on-flow problem. In this application the gaseous-detonation driver is connected to a conventional high-pressure shock tube to produce the high-velocity preload flows and the subsequent blast wave on the model. The third application is a technique for obtaining high-enthalpy short-duration hypersonic gas flows.

BACKGROUND

The propagation of detonation waves through explosive gas mixtures has been investigated for many years. The literature on the subject is extensive and readily available, so that it will not be cited here. The objective of this paper is not to discuss the phenomenology of detonation waves, but rather to discuss the application of detonation wave phenomena to shock tube drivers.

The generation of high-strength shock waves with a gaseous-detonation driver was studied theoretically by Bird (ref. 1) and experimentally by Waldron (ref. 2). They studied the application of gaseous-detonation drive to the production of high-strength shock waves which had regions of steady flow in the test gas immediately behind the shock front. They concluded that shock waves generated by a gaseous-detonation wave attenuate both with length of shock propagation and with time, because of the mechanism by which detonation waves propagate, and were unacceptable for use in aerodynamic testing facilities.

It has been found, however, that if the nature of the decay of the flow properties behind a detonation front is understood and utilized, detonation drive can be successfully applied to many shock tube applications. Three of the applications are described in the sections which follow.

THE DETONATION-DRIVEN SHOCK TUBE

A detonation-driven shock tube is illustrated in Figure 1. It consists of a detonation chamber containing a detonable gas mixture and an expansion chamber containing the test gas. These two chambers are separated by a frangible diaphragm.

When a detonable gas mixture is ignited at the end of the detonation chamber, a detonation wave will form and move at high velocity towards the other end of the chamber. The gas mixture in the chamber should be chosen so that the detonation wave will rapidly attain the stable Chapman-Jouquet condition. The Chapman-Jouquet condition states that the gases behind a detonation wave travel relative to the detonation wave front at a speed just equal to their own local sonic velocity. On reaching the end of the detonation chamber, the detonation wave bursts the diaphragm and causes the formation of a shock wave in the test gas. The properties of the shock wave are a function of the properties of the detonable gas mixture and the initial gas pressures in the detonation and expansion chambers.

The wave shape or duration of the detonation wave can be determined from a corollary of the Chapman-Jouquet condition. The corollary states that the head of the rarefaction wave which follows the detonation wave will keep up with the detonation wave front (ref. 3). Thus, there is an immediate pressure decay behind the detonation wave front. The rarefaction wave may be assumed to be a centered wave emanating from the ignition point of the detonation wave. (Note: This is an approximation since a short, but finite, length is required for the detonation wave and its concomitant rarefaction wave to reach stable conditions. However, it has been found experimentally, that if mixtures are used which have short predetonation distances, the approximation of a centered rarefaction wave emanating from the ignition point in the detonation chamber is acceptable.)

It is important to note that the rates of pressure and flow-velocity decay behind the wave front can be controlled since they will decrease with increasing propagational length of the detonation wave.

There are advantages of using a shock tube with a gaseous-detonation wave drive rather than a conventional constant volume combustion drive. These advantages are especially important when high-overpressure shock waves are required in large diameter tubes. The first advantage is that the end of the detonation chamber where the detonable gas mixture is ignited does not have to remain closed after the initiation of the detonation wave. Only a light diaphragm is required to contain the detonable gas mixture. The diaphragm will break open immediately after ignition and allow the gases at the tail of the rarefaction wave to exhaust into the atmosphere without affecting the properties behind the detonation wave front (ref. 4). This eliminates the recoil force on the tube caused by the unbalanced gas pressures.

A second advantage is that the maximum pressure of the detonation wave will be much less than the pressure of a driver gas initially at rest. Thus, a thinner tube wall thickness may be used. The reduced driver-gas pressure is due to the high velocity associated with the gas flow immediately behind the detonation front. The expansion of the driver gas into the expansion chamber begins from a moving flow of gas. Thus, a smaller pressure drop is required to gain the required flow velocity behind the shock front in the test gas than if the expansion takes place from a stationary gas.

A third advantage is that there is no fundamental limit to the establishment of plane detonation waves in large-diameter tubes. Because of this detonation drivers are particularly applicable to large-diameter shock tubes. The desirability of a large-diameter tube in test work is clear. Large-diameter test sections are capable of accepting large-diameter models and providing a large cross-section of flow which is free from boundary layer effects. This extends the flow duration at the test section since interference of the boundary layer with the flow around the model is delayed.

ANALYSIS OF FLOW USING DETONATION DRIVERS

There are two major aspects to the analysis of flow in a detonation-driven shock tube. The first is the analysis of the properties of the gas flow behind the detonation front. The second is the analysis of the interaction of the flow behind the detonation front with the test gas.

DETONATION WAVE ANALYSIS

The properties of the gas behind the detonation front may be determined from the conservation equations of mass, momentum, and energy across the detonation. A factor which complicates this analysis is the interrelation of the energy released by the exothermic chemical reaction across the detonation front and the other properties of the flow. It is therefore necessary to include a thermochemical analysis with the conservation equations.

The determination of the properties behind the detonation waves may be obtained using an approximate analysis of a one-dimensional plane detonation wave according to Taylor (ref. 3) or the computation method used by Huff, Gordon and Morrell (ref. 5).

In Taylor's analysis, it is assumed that the detonation products of combustion behave as an ideal gas mixture. Starting with the conservation equations across the detonation front, expressions are obtained for the detonation wave front velocity, the particle velocity behind the detonation front, and the initial pressure of the detonable gas mixture required to achieve a given final pressure. Figures 2, 3, and 4 show the properties of propane-oxygen-air detonation waves.

ANALYSIS OF FLOW INTERACTION

The wave system in a detonation-driven shock tube may be analyzed by the method of characteristics. The method of characteristics is described in classical texts dealing with compressible flow, such as the texts by Shapiro (ref. 6) or Courant and Friedrichs (ref. 7). Therefore, neither the derivation nor construction details of the method will be repeated here.

A typical characteristic diagram showing the interaction of the detonation wave with the test gas is shown in Figure 5. The time parameter has been nondimensionalized as at/L where "a" is the acoustic velocity immediately behind the detonation front, and "L" is the detonation chamber length. Horizontal lines on the diagram represent the variation of gas properties as a function of position in the tube at time at/L. Similarly, a vertical line represents the time variation of the gas properties at a particular location.

SIMULATION OF BLAST WAVES

The detonation shock tube shown in Figure 1 can be used to produce simulated blast waves in a test gas.

The blast effects which must be considered in the simulation problem are the shock front velocity, the shock overpressure and its time variation behind the shock front, the dynamic pressure and its time variation behind the shock front, and the temperature variation with time behind the shock front. Peak overpressure and peak dynamic pressure occur immediately behind the shock front in a blast wave from a point-source explosion, but maximum temperature may or may not occur at the shock front.

Blast overpressures may be easily simulated to within 5 percent of desired conditions from the peak overpressure to one-half of the peak. Temperature-time simulation is most difficult to obtain. The flow behind a shock front in high overpressure regions is hotter than at the shock front because it is convected from regions of higher shock pressure with correspondingly higher shock temperatures, and because of the absorption of the radiant energy diffusing out from the center of the fireball. This effect causes the simulation of the dynamic pressure history to differ slightly more than the overpressure history from the ideal profile.

Typical predicted results for the simulation of 1000-, 900-, and 800-psi blast waves are shown in Figures 6, 7, and 8. By comparing the calculated pressure-time curves with point-source blast predictions (e.g., Brode's

data (ref. 8)) the length of detonation tube required to simulate a given nuclear blast wave can be determined. For a 1-MT nuclear explosion, the detonation chamber length would be 233, 225, 196 feet, respectively, for the 1000-, 900-, and 800-psi waves.

Although it is impossible to obtain a closed-form analytical solution for the entire flow field, it is possible to determine analytically the maximum properties of the shock wave in the test gas as a function of the detonation wave properties. The maximum shock properties in the test gas occur immediately after the diaphragm is ruptured by the detonation wave. The maximum shock properties then decay with increasing length of propagation. Figure 9 gives the peak pressures for a detonation wave whose specific heat ratio of the gases immediately behind the detonation front is 1.2. The results for a static high-pressure gas driver are also shown. The lower detonation pressure required to achieve a shock strength in air is evident.

SUPERPOSITION OF BLAST WAVES ON SUPERSONIC FLOWS

The superposition of a blast wave on a supersonic flow can be achieved by coupling a detonation driver to a conventional shock tube. This concept, designated as the double-compression-chamber detonation shock tube, has the advantage of closely duplicating the flow conditions when a reentry vehicle encounters a high altitude explosion.

The shock tube arrangement is shown in Figure 10. The first chamber contains a detonable gas, the intermediate chamber contains the test gas, and the expansion chamber contains an accelerating gas and the test section. Frangible diaphragms separate the chambers.

The sequence of operation is given as follows: The diaphragm between the expansion chamber and the intermediate compression chamber is ruptured and a shock wave is produced which propagates into the expansion chamber and establishes flow (i.e., a preload) over the test vehicle. At some preselected time (this may be before, after, or at the same time as the second diaphragm ruptures) the detonation wave is initiated and it begins to travel through the detonable gas mixture. It strikes the first diaphragm ruptures it, and generates a shock wave in the intermediate compression chamber. This shock wave propagates through the intermediate chamber to the expansion chamber and eventually to the test section. By properly selecting the respective lengths and initial pressures of all three sections, the first shock wave establishes an initial pre-load on the test vehicle while the second shock wave produces a discontinuous rise in overpressure and dynamic pressure which simulates the blast loading.

Simulation is desired for the rapid engulfment of the test vehicle by the shock wave, the overpressure and dynamic pressure behind the shock wave, the rapid decay of the pressures with time, and the preload pressure conditions. The Mach and Reynolds numbers of the flows both ahead and behind the shock front, and the stagnation pressure associated with both the preload and the flow behind the shock front are also important.

Complex calculational procedures are required to analyze the flow fields. A typical characteristic diagram is shown in Figure 11.

Because of the extensive calculations required to analyze the structure of the decaying flow fields, a study was made of the flow and shock properties neglecting the decay of flow properties behind the detonation front. This made possible the examination of a much broader range of conditions than was possible with the more detailed characteristic analyses. A comparison of the results with the characteristic analyses showed close agreement.

Figures 12 and 13 show the simulation conditions that can be attained using the double-compression-chamber detonation shock tube. Simulation conditions using helium, hydrogen, and argon as intermediate driver gases are shown.

A point lying on one of the grids specifies 5 items of information:

1. The initial pressure of both the detonable gas mixture and the intermediate-driver gas pressure. These two pressures are assumed to be equal and are referred to as the "Initial Pressure in the Driving Sections (atm)".

2. The Mach number of the flow which would engulf the model prior to the superposition of a shock wave on the flow. This is referred to as the "Preload Mach Number". The lines of constant preload Mach number are vertical.

3. The peak dynamic pressure of the flow immediately behind the shock front (representing the blast wave) which is superimposed on the flow. This dynamic pressure is given as the ordinate on the figures and is labeled "Dynamic Pressure".

4. The velocity relative to the stationary RV model in the shock tube with which the shock front superimposed on the supersonic flow would engulf the model. This parameter is labeled "Engulfment Velocity" and is given as the abscissa on the figures.

5. The overpressure immediately behind the shock front which is superimposed on the flow. This is given by the curves labeled 50 psi, 100 psi, 200 psi, etc.

As a typical example, consider the point labeled "A" on Figure 12. This point indicates that if an initial pressure of 10 atmospheres is used for a detonable gas mixture of hydrogen and oxygen with an intermediate driver gas of helium, the following test conditions will result:

A Mach number of 2.5 for the preload flow,

A peak dynamic pressure in the flow immediately behind the shock front of about 100 psi,

An overpressure between 200 and 400 psi accompanying the peak dynamic pressure,

An engulfment velocity of the shock wave over the model of about 16,000 ft/sec.

It is evident from Figure 13 that a heavier gas, i.e., argon, produces high dynamic pressures but low engulfment velocities. On the other hand, hydrogen tends to yield higher engulfment velocities, but does not produce very high dynamic pressures.

The material presented in Figures 12 and 13 shows some of the overall capabilities of the double-compression-chamber detonation shock tube. It says nothing about the shock-wave time-histories. This information must be obtained from a characteristic analysis.

Pressure-time profiles were obtained at various values of x/L in the expansion chamber by drawing vertical lines on the characteristic diagram and noting the values of the flow properties at the intersections of the vertical line and the characteristics. The region of interest lies between the vertical lines which go through the points of intersection of the second shock wave and the tail of the rarefaction wave, and the contact surface behind the first shock wave. (See Figure 11.) Typical pressure-time data are shown in Figure 14. By judiciously choosing the detonation-chamber and intermediate-chamber lengths, and by correctly positioning the test section in the expansion chamber, the resultant wave shape in real time will closely simulate the desired shock-on-flow conditions.

HIGH-ENTHALPY SHORT-DURATION HYPERSONIC GAS FLOWS

A detonation-driven expansion tube (ref. 9) is shown schematically in Figure 15. The expansion tube is similar to a shock tunnel except that the steady-flow varying-area-nozzle expansion of the shock tunnel is replaced by a nonsteady constant-area expansion (ref. 10). The shock tube is divided into three sections by two diaphragms. The driver section contains a detonable gas mixture; the middle section is filled with test gas; and the expansion section is filled with low pressure gas.

The sequence of operation is described as follows: The detonable gas mixture is ignited and quickly develops into a detonation wave which propagates through the detonable gas. The detonation wave ruptures the diaphragm between the detonation section and the intermediate driver section. A shock wave is then produced in the test gas. The shock wave then propagates through the low-pressure diaphragm. This produces a new shock wave which propagates into the accelerating light gas while an upstream expansion wave moves into the test gas. This expansion wave is convected downstream since

the flow behind the shock wave in the test gas is supersonic. The test region lies between the contact surface and the trailing edge of the expansion fan.

One of the major problems of using shock tunnels is the contamination of the test gas by the driver gas. This has been attributed to mixing of the gases caused by the boundary layer growth behind the shock front and instabilities across the contact surface between the gases.

If the size of the test gas section were to be increased in diameter and length, one would expect that the problem would not be as serious. Increasing the diameter of the tube would reduce the significance of the boundary layer. Increasing the length of the test gas section would increase the volume of the test gas between the contact surface and the expansion wave. This would delay contamination of the driver gas from reaching the test gas as it flows through the expansion fan.

An increase in the length and diameter of the test-gas section requires a corresponding increase in the size of the driver section. Enlarging the driver section would be particularly difficult if an electric arc were used to heat the driver gas. This would require the distribution of the arc energy over a much larger volume. With detonation drive, however, it is quite feasible to work with long driver and test sections.

In order to illustrate the typical performance characteristics of the detonation-driven expansion tube, a specific example was chosen and analyzed in detail by the method of characteristics. Trimpi's (ref. 10) data was also used. The example chosen is that of an expansion tube providing a one millisecond test period of Mach 20 flow at a pressure-altitude of 150,000 feet. The lengths of the detonation drive section, test gas section, and expansion section which are required to give the desired flow are shown in Figure 16. The initial pressures of the detonable gas and the test gas (air) are also shown on the figure.

It should be mentioned at this point that the 460 foot distance from the beginning of the expansion section to the test section does not depend on the type of driver used. It would be the same with any type of driver.

The major disadvantage of the detonation drive is that there is no region of steady flow behind the detonation front. Therefore, the question regarding the use of a detonation drive is: What is the attenuation of the flow properties during the test period when using detonation drive?

The above question may be answered by an analysis of the flow. Figure 17 shows the characteristic diagram for the expansion tube for the conditions given in Figure 16. The diagram shows the rarefaction behind the detonation front in the detonation-driver section, the expansion fan between the detonation section and the test-gas section, the decay of shock front with propagation distance in the test-gas section, and the expansion fan into the expansion section. The test time at the test section is the time between the

arrival of the contact surface, which separates the shocked accelerating gas in the expansion section from the expanded test gas, and the arrival of the expansion wave.

The result of the analysis shows that the decrease in flow velocity during the test period is about 100 ft/sec, which is a small percentage of the total flow velocity. Thus, there is a negligible decrease in flow velocity during the test period when using detonation drive. The change in flow velocity could be made even smaller by using a longer detonation section.

REFERENCES

(1) Bird, G. A., "A Note on Combustion Driven Shock Tubes", RAE TN Aero-2511. Farnborough, Hants, England, Royal Aircraft Establishment, May (1957)

(2) Waldron, H. F., "An Experimental Investigation of the Flow Properties Behind Strong Shock Waves in Nitrogen", UTIA Report 50, Institute of Aerophysics, University of Toronto, March (1958)

(3) Taylor, J., Detonation in Condensed Explosives, Oxford at the Clarendon Press, (1952)

(4) Landau, L. D. and Lifshitz, E. M., Fluid Mechanics, Pergamon Press, Addison-Wesley Publishing Co., Inc., Reading, Massachusetts, (1959)

(5) Huff, V. N., Gordon, S., and Morrell, V. E., "General Method and Thermodynamic Tables for Computation of Equilibrium Composition and Temperature of Chemical Reactions", NACA Report 1037, (1951)

(6) Shapiro, A. H., The Dynamics and Thermodynamics of Compressible Fluid Flow, The Ronald Press Co., New York (1953)

(7) Courant, R. and Friedrichs, K. O., Supersonic Flow and Shock Waves, Interscience Publishers, Inc., New York (1948)

(8) Brode, H. L., "A Review of Nuclear Explosion Phenomena Pertinent to Protective Construction", R-425-PR, The Rand Corporation, California, May (1964)

(9) Johnson, M. R. and Balcerzak, M. J., "A Detonation Tube Drive for Producing Hypersonic Flows in a Shock Tube", Proceedings Third Hypervelocity Techniques Symposium, University of Denver, March (1964) pp. 116-134

(10) Trimpi, R. L., "A Preliminary Theoretical Study of the Expansion Tube, A New Device for Producing High-Enthalpy Short-Duration Hypersonic Gas Flows", NASA Technical Report R-133, (1962)

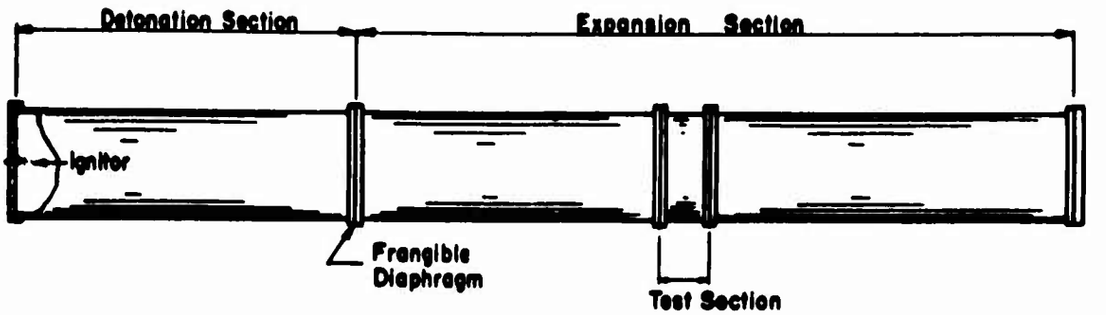


Figure 1 SCHEMATIC DIAGRAM OF DETONATION SHOCK TUBE

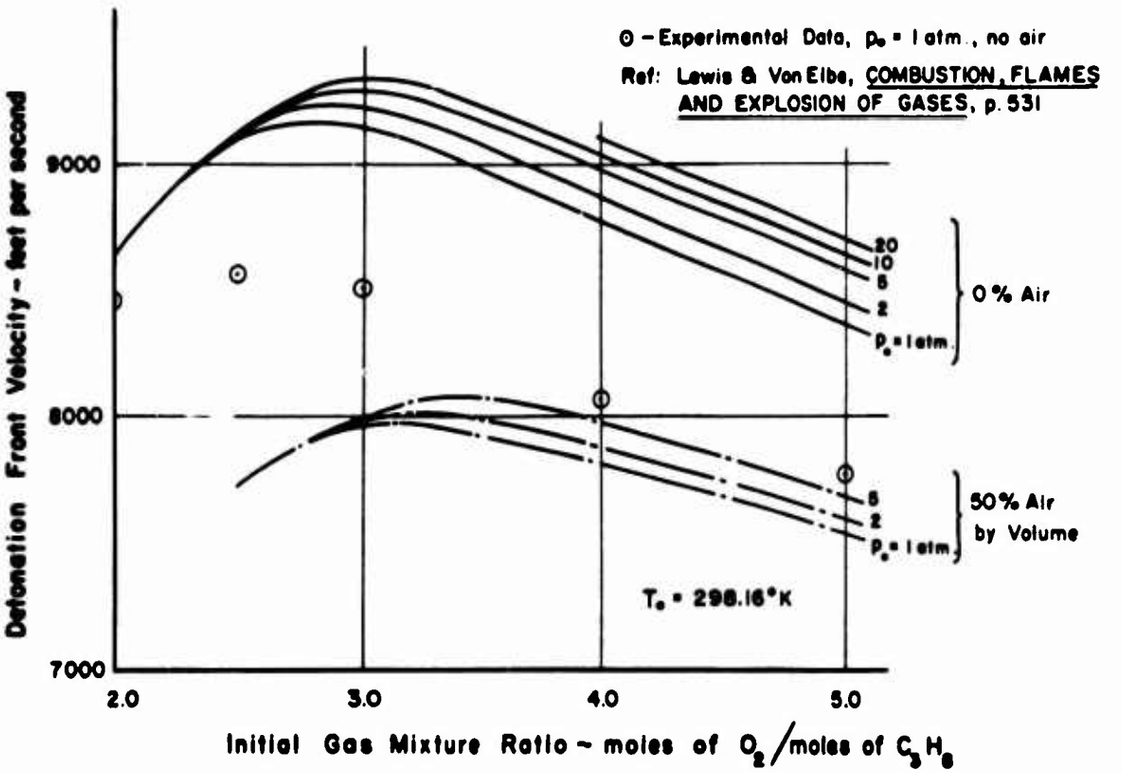


Figure 2 DETONATION FRONT VELOCITY VS GAS MIXTURE RATIO FOR OXYGEN & PROPANE MIXTURES.
COMPARISON OF CALCULATED VALUES WITH EXPERIMENTAL DATA.

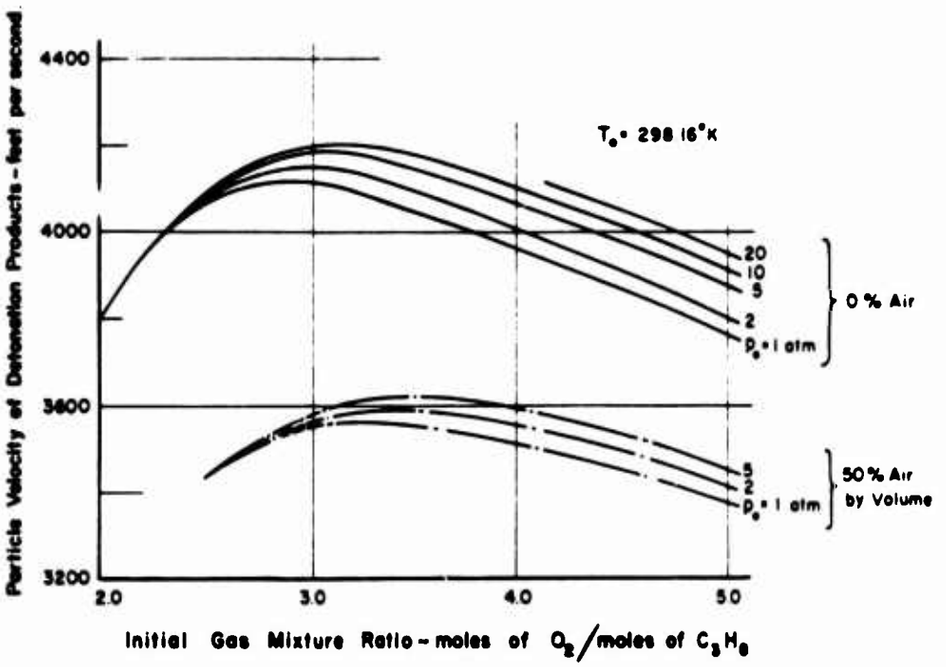


Figure 3 PARTICLE VELOCITY BEHIND DETONATION WAVE VS GAS MIXTURE RATIO

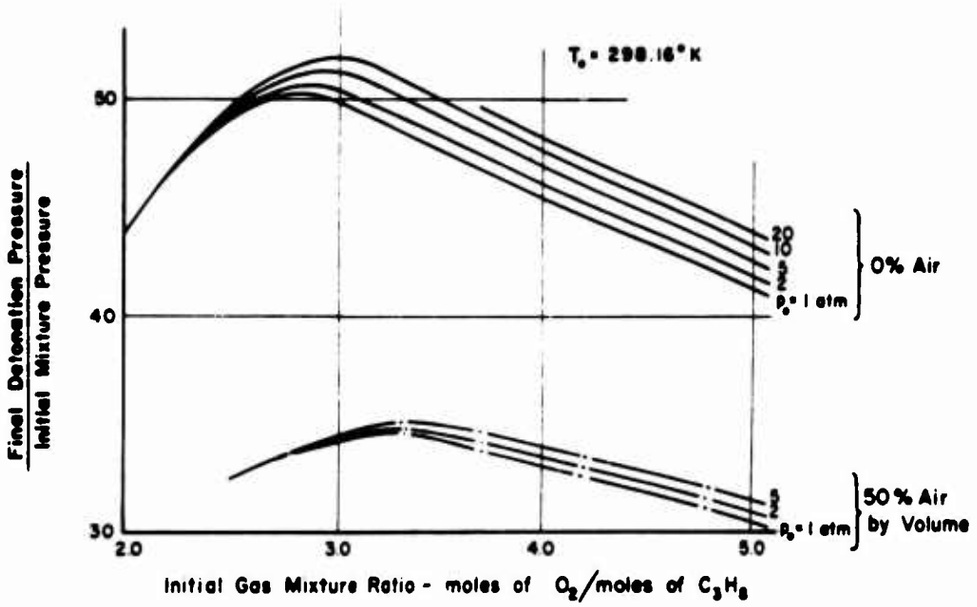
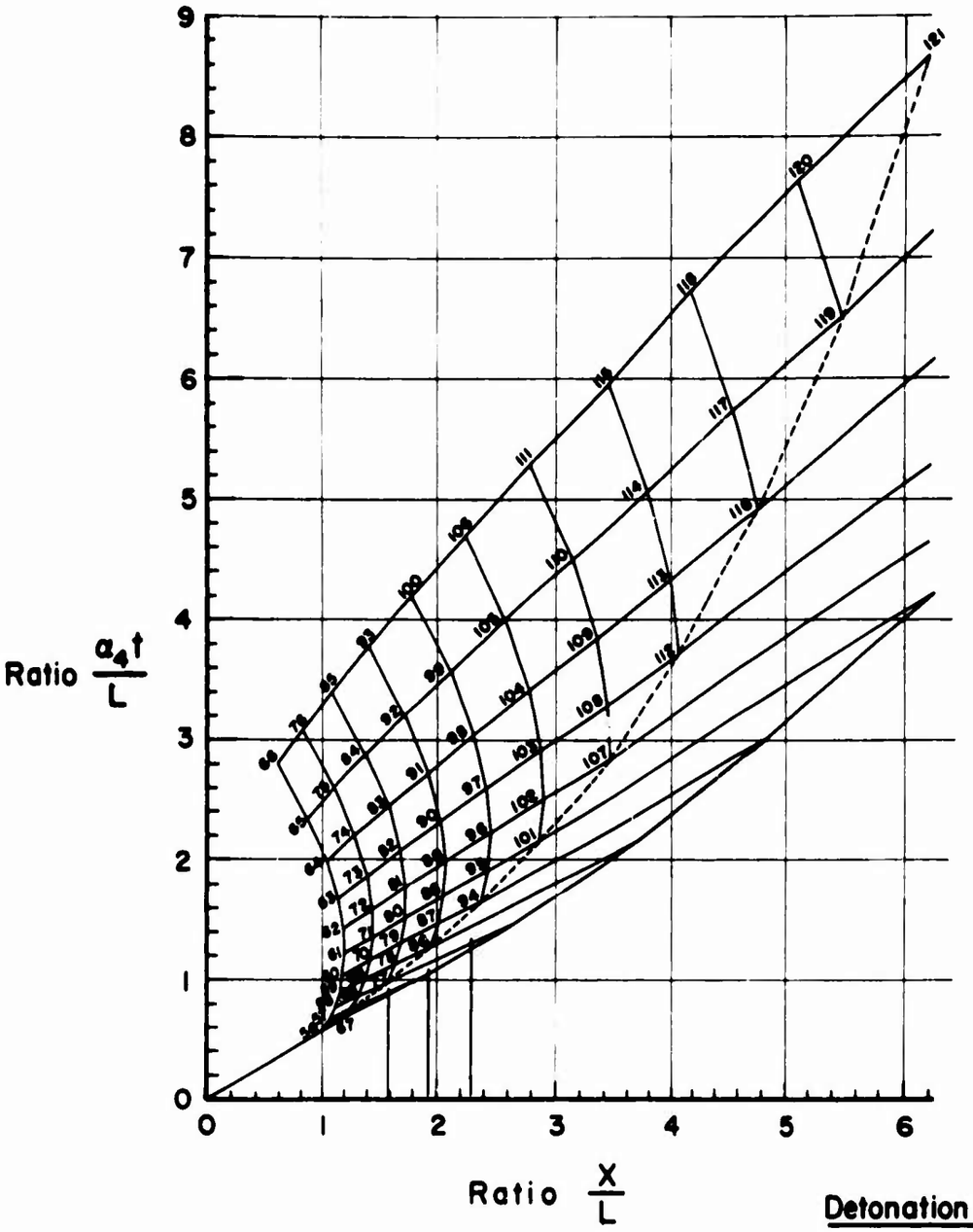


Figure 4 PEAK DETONATING PRESSURE VS GAS MIXTURE RATIO FOR OXYGEN AND PROPANE MIXTURES



GAS MIXTURE–METHANE & OXYGEN

$\frac{O_2}{CH_4} = 2.0$; $p_o = 7.0$ Atm.

Detonation Data

$p_4 = 3{,}584$ psi
$u_4 = 3{,}990$ fps
$a_4 = 4{,}780$ fps
$\gamma_4 = 1.2009$

Figure 5 TYPICAL CHARACTERISTIC DIAGRAM

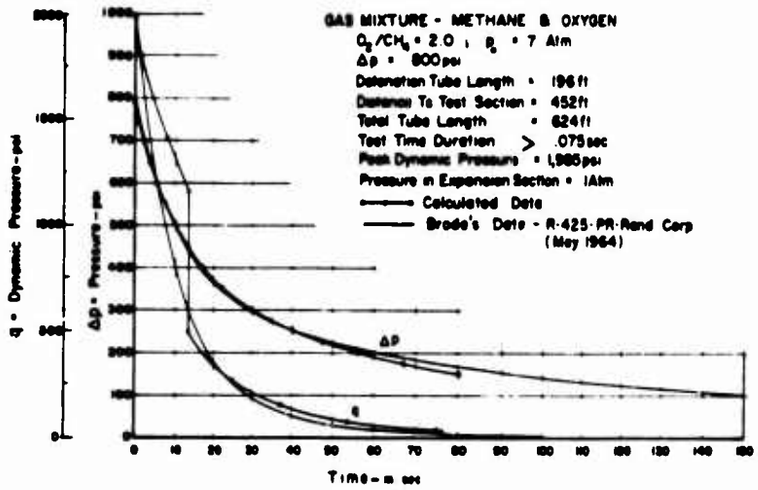


Figure 6 PRESSURE vs TIME HISTORY-COMPARISON OF THEORETICAL SHOCK TUBE DATA & BLAST DATA

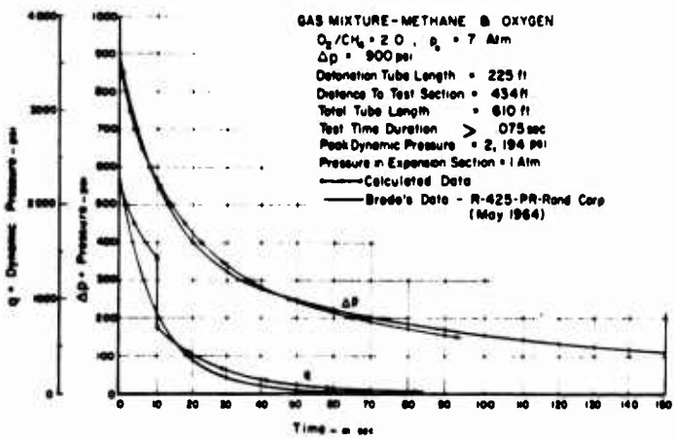


Figure 7 PRESSURE vs TIME HISTORY-COMPARISON OF THEORETICAL SHOCK TUBE DATA & BLAST DATA

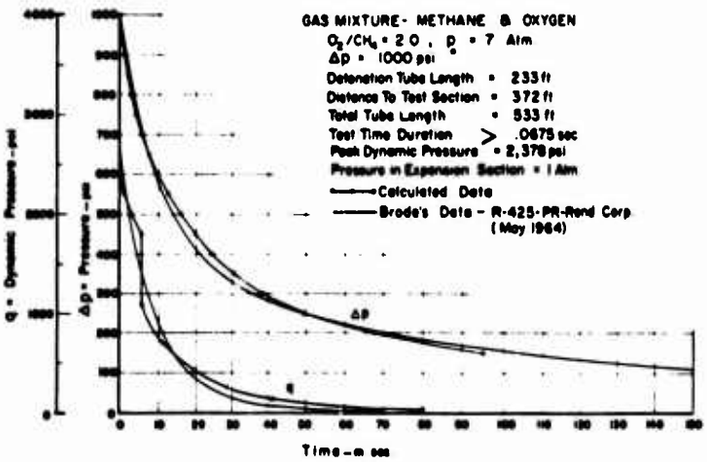


Figure 8 PRESSURE vs TIME HISTORY-COMPARISON OF THEORETICAL SHOCK TUBE DATA & BLAST DATA

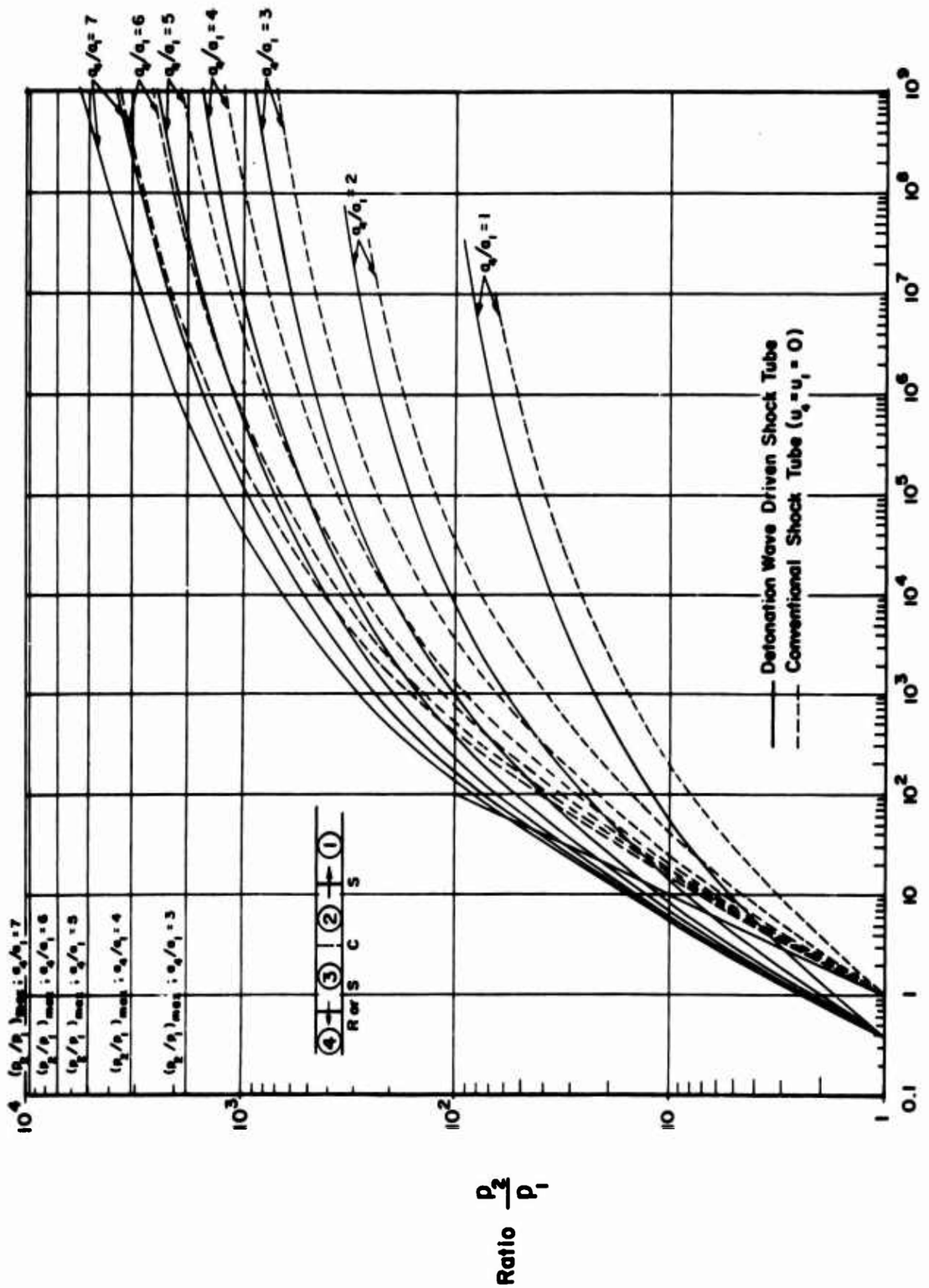


Figure 9 SHOCK STRENGTH vs. DETONATION PARAMETERS ($\gamma_4 = 1.2$)

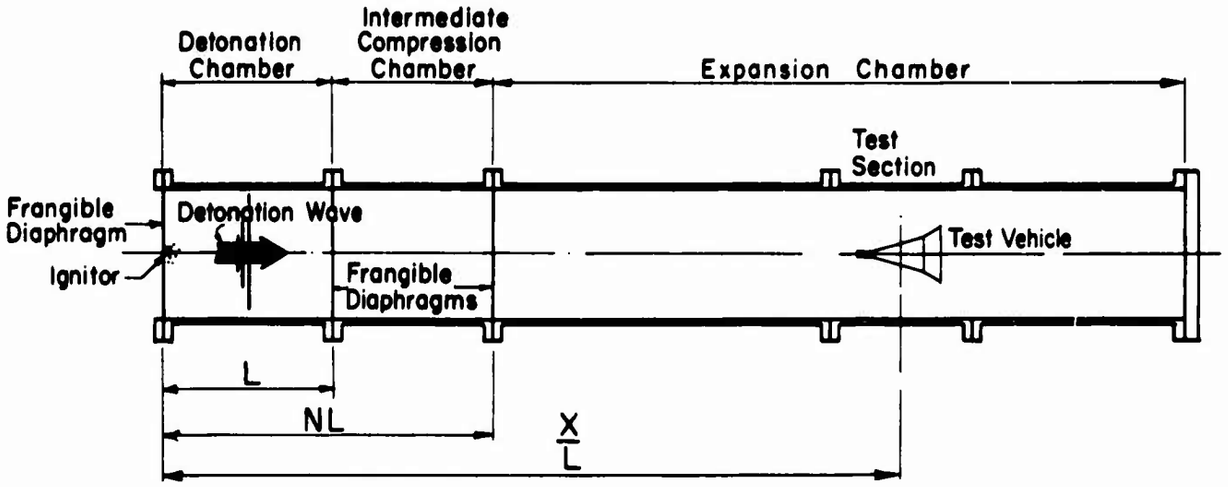


Figure 10 DOUBLE COMPRESSION CHAMBER DETONATION SHOCK TUBE

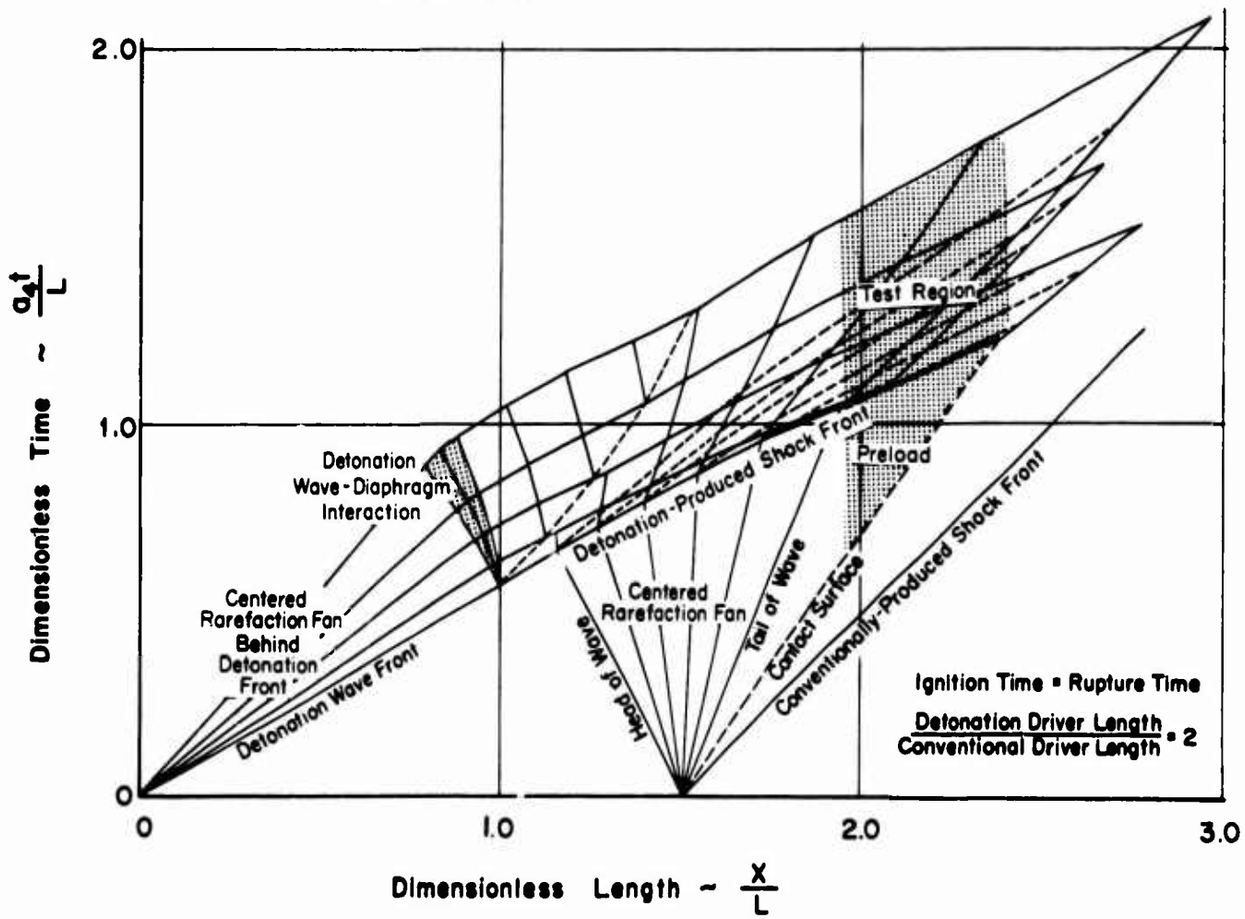


Figure 11 REPRESENTATIVE CHARACTERISTIC DIAGRAM FOR A DOUBLE-COMPRESSION-CHAMBER-DETONATION-SHOCK-TUBE CONCEPT

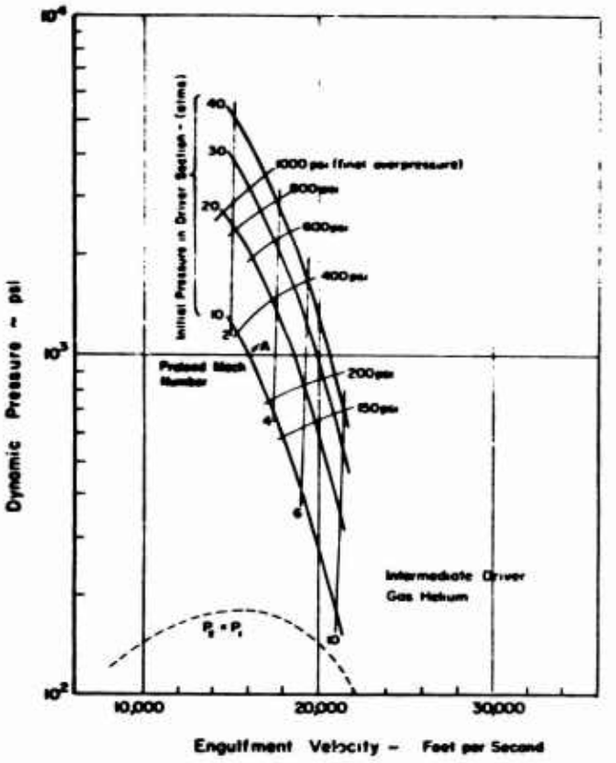


Figure 12 DYNAMIC PRESSURE & ENGULFMENT VELOCITY SIMULATION FOR A DOUBLE-COMPRESSION-CHAMBER-DETONATION-SHOCK-TUBE INTERMEDIATE DRIVER GAS HELIUM DETONATION DRIVER GAS HYDROGEN-OXYGEN (4:1 Ratio)

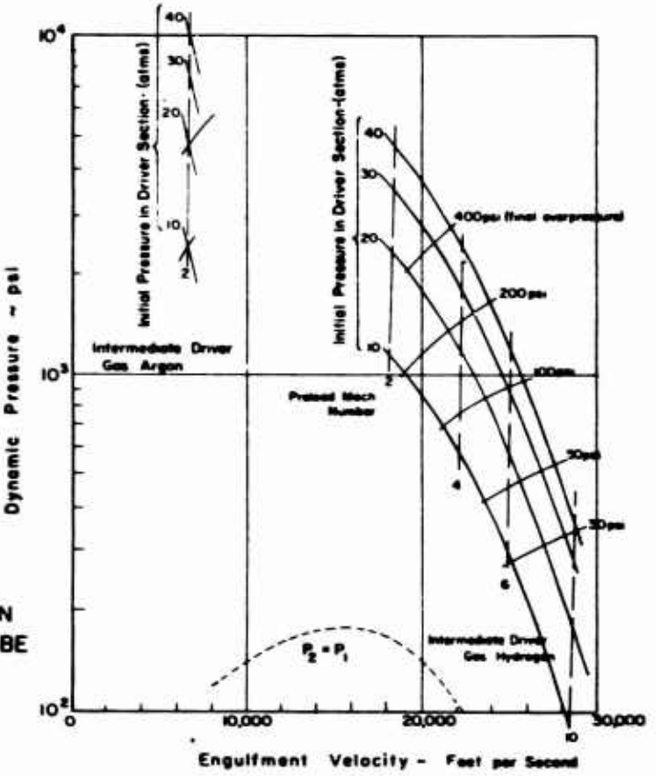


Figure 13 DYNAMIC PRESSURE & ENGULFMENT VELOCITY SIMULATION FOR A DOUBLE-COMPRESSION-CHAMBER-DETONATION-SHOCK-TUBE INTERMEDIATE DRIVER GAS HYDROGEN OR ARGON DETONATION DRIVER GAS HYDROGEN-OXYGEN (4:1 Ratio)

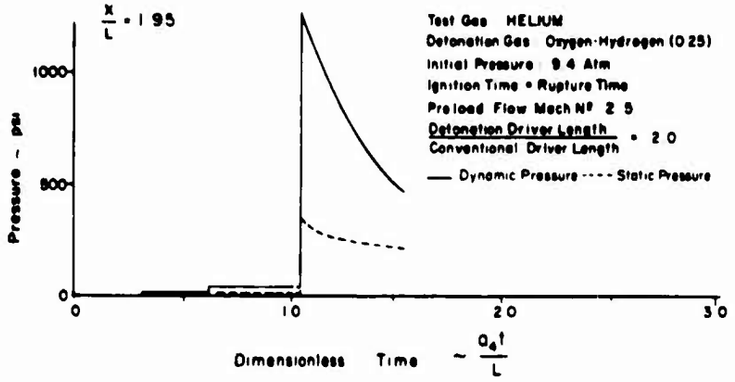


Figure 14 STATIC & DYNAMIC PRESSURE vs DIMENSIONLESS TIME FOR A DOUBLE-COMPRESSION-CHAMBER-DETONATION-SHOCK-TUBE

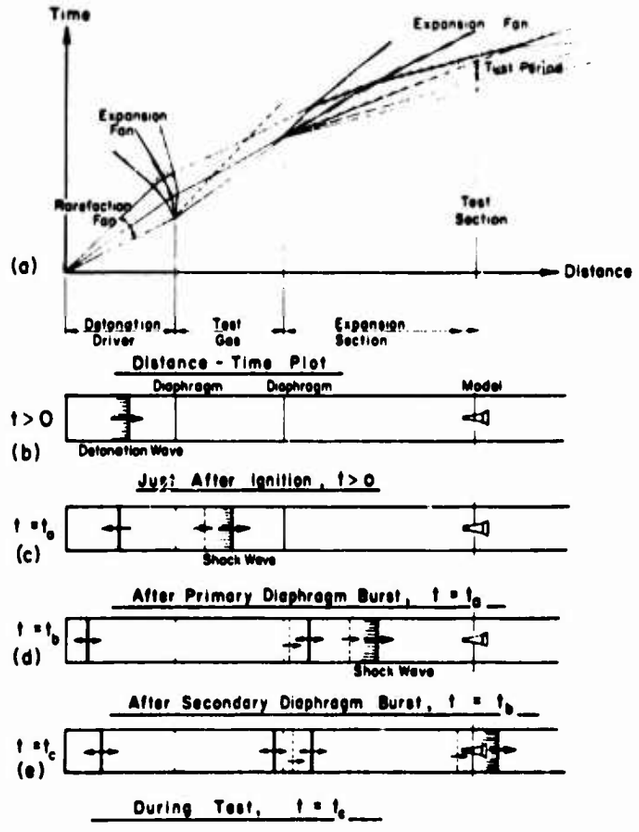
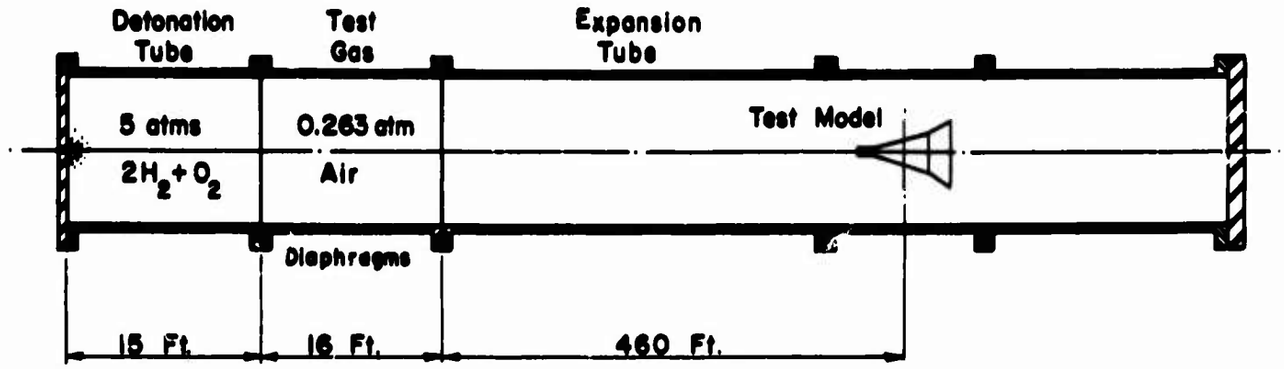


Figure 15 - SCHEMATIC ILLUSTRATION OF DETONATION-DRIVE-EXPANSION SHOCK TUBE CYCLE



Flow Properties

Mach 20

1 msec. Test Time

p = .0014 atm

a = 1180 ft/sec

Figure 16 DETONATION DRIVEN EXPANSION TUBE

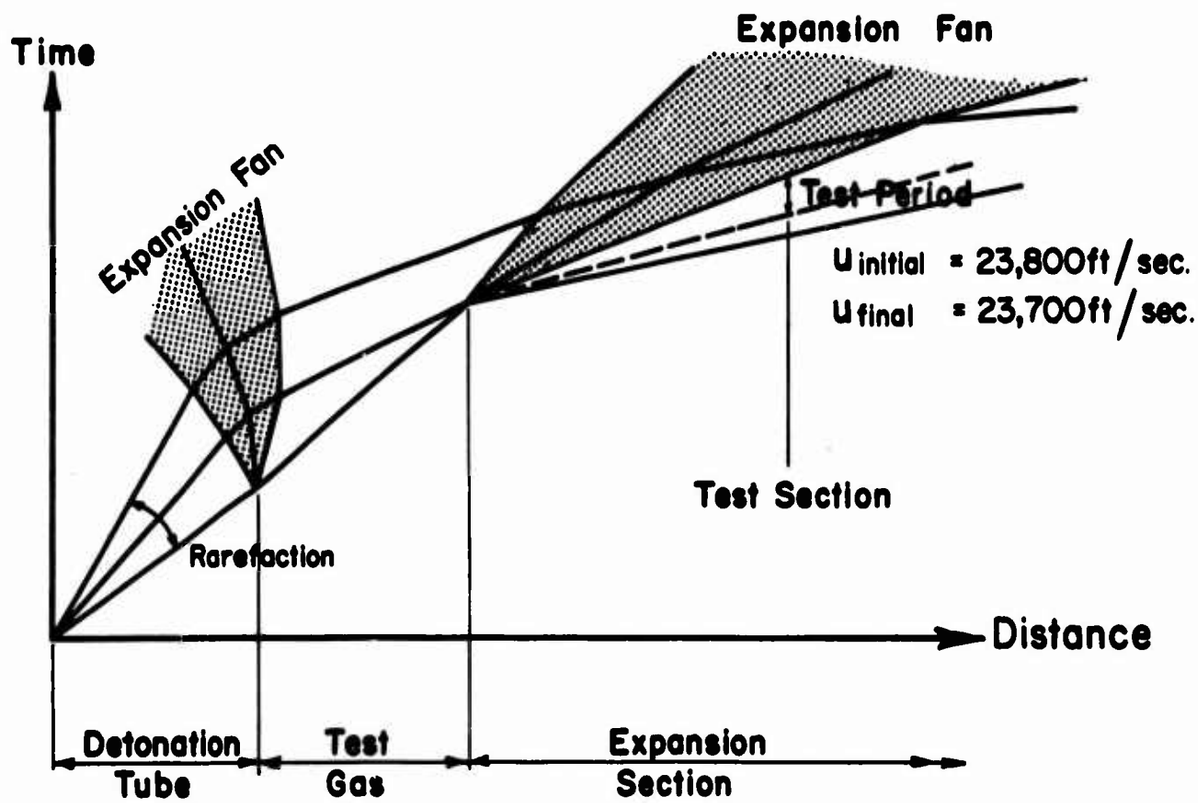


Figure 17 CHARACTERISTIC DIAGRAM

MODIFICATIONS TO A COMBUSTION DRIVEN SHOCK TUBE FOR USE IN A COUNTERFLOW FACILITY

L. C. Shrout
R. A. Schober
J. W. Leary
The Boeing Company
Seattle, Washington

ABSTRACT

Combined operation of a light gas gun and shock tunnel provides an attractive means of obtaining velocities in the 50,000 ft/sec regime. A facility of this type requires certain modifications to the shock tube wind tunnel system. These include precise timing control, methods of enthalpy variation over a wide range to provide necessary velocity simulation and means of alleviating nozzle damage due to projectile impact.

This paper discusses the adaptation of a 3-inch combustion driven shock tube tunnel for use in a counterflow system. A unique method of timing which utilizes an arc discharge technique is presented. Enthalpy variation by diluting the combustion gases with argon and helium and details of the projectile impact region in the nozzle are described.

INTRODUCTION

Counterflow facilities, utilizing the relative velocities obtained by firing a projectile from a light gas gun upstream into a shock tunnel, have been shown by NASA-Ames and AEDC to be a feasible technique of producing flight simulation at velocities in the 20,000 to 50,000 ft/sec regime. The Boeing Company Gas Dynamics Laboratory has modified a combustion driven shock tube and light gas gun into a counterflow configuration (Figure 1). This facility is presently undergoing calibration.

A 3-inch constant area combustion driven shock tube is used to supply air to a Mach 6.5 contoured nozzle. The tailored interface technique is employed to obtain flow velocities of 8,000 to 18,000 ft/sec for durations up to 4 milliseconds. Projectiles are launched upstream into the shock

tunnel by a 1/4-inch bore accelerated reservoir light gas gun. These projectiles may be launched at velocities ranging from 10,000 to 30,000 ft/sec. The superposition of the projectile and shock tunnel flow velocities provides velocity simulation of 18,000 to 48,000 ft/sec. The predicted enthalpy-altitude simulation regime of this facility is shown in Figure 2.

Three primary problems were encountered in the modification of the shock tube portion of the counterflow facility. The first of these was the development of a timing technique which assures projectile arrival in the test section during the period of useful shock tunnel flow. The second problem was the development of a method of varying the shock tube reservoir enthalpy to provide flow velocities other than that available using the standard helium diluted combustion driven mixture. Also, a means of protecting the shock tube tunnel nozzle area from projectile damage was developed.

TIMING MODIFICATIONS

To assure arrival of the projectile in the test section during the period of useful shock tunnel flow, the firing of both the gun and shock tunnel must be controlled within a close tolerance. A tolerance of ± 1 millisecond in flow establishment was selected. The time history requirements of both facilities are shown in Figure 3.

Past experience with combustion driven shock tubes showed that relying on simple scribed diaphragms for repeatable burst pressures and times to burst from ignition is not sufficient to provide the ± 1 millisecond firing tolerance. The double diaphragm arc discharge and explosive driven punch diaphragm rupturing techniques were considered as methods of maintaining firing time tolerance for the shock tunnel. The punch technique was discarded because of the performance penalties associated with the area reduction caused by the punch at the driver diaphragm station.

The double diaphragm arrangement shown in Figure 4 is similar to that used by many experimenters with the main exception being the arc discharge technique is utilized to overpressure the pilot diaphragm. The arc source is shown in the circuit diagram (Figure 5). A 5000-volt DC power supply is used to charge three 171 microfarad capacitors rated at 6000 volts, which in turn are discharged by ignitions through three electrodes (Figure 4) located in the diaphragm spacer. The diaphragm spacer is initially precharged with argon. Pressures are variable from 14.7 psi to 5000 psi. The electrodes are coaxial with the negative electrodes in the center. The negative electrodes are .125-inch diameter copper rods spun with interference fits into tapered lexan insulators. These insulators are pressed into a mating tapered hole in the diaphragm spacer to provide a pressure seal. The diaphragm spacer is the positive electrode.

A graphite pencil line is drawn across the insulators before each run for triggering the arc across the .187-inch gap. The three 171 microfarad capacitors are charged to 4500 volts with the negative side grounded at the

charger and then isolated prior to discharge. They are isolated to prevent ground loops while keeping the ignition firing circuit at ground potential. Discharge is accomplished by triggering the ignitrons with a thyratron capacitor discharge firing circuit (Figure 5). The ignitrons are used because of their repeatable short switching time which is on the order of 2 microseconds. A resistor capacitor time delay generator is used to trigger the ignitron firing circuit. This delay time is adjustable from 10 to 100 milliseconds and repeatable within ± .5 milliseconds.

Tests have been made using a dummy plug containing a pressure transducer in place of the main diaphragm. The results of these tests are shown in Figure 6. Pressure increases obtained with this technique have ranged from 500 psi for initial cavity pressures of 14.7 psi to 1950 psi for initial pressures of 5000 psi.

Typical arc discharge cavity records are shown in Figure 7. Initial argon precharge pressure for this case was 5000 psi. Transducer outputs display considerable ringing as a result of the sharp pressure pulse encountered when the arc discharges. The pressure differential is interpreted as the average transducer output, which in this case is 1950 psi. The arc discharge history shown had a delay of 60 milliseconds. Complete discharge occurs within 2 milliseconds. This discharge is repeatable within ± .1 milliseconds.

The effect of the double diaphragm arc discharge system on the flow has been a smoother reflected shock pressure history and more repeatable conditions from run to run. These effects are attributed to more complete combustion and, hence, less burning at the interface. Reflected shock pressure histories (Figure 8) show the difference in the smoothness of the reflected shock region with and without the double diaphragm arc discharge device. A comparison of the driver to driven tube pressure ratios versus shock Mach number scatter with and without the system is shown in Figure 9.

Early in the development of the double diaphragm arc discharge system there was concern about the possibility of a precursor shock from the pilot diaphragm: Driven tube pressure histories (Figure 10) do not indicate that the incident shock structure has been changed.

Timing data obtained from various shock tunnel tests were evaluated to determine the repeatability of shock tunnel flow establishment times when the double diaphragm arc discharge system is used. These data were obtained over a wide range of driver conditions, i.e., diaphragm characteristics, driver pressures, and double diaphragm precharge pressures. The results indicate repeatability of ± 1 millisecond.

ENTHALPY VARIATION

Variation of velocity simulation in the counterflow facility is achieved by varying the projectile velocity and the shock tunnel flow velocity. Variation of shock tunnel flow velocities implies variation of reservoir enthalpy. Since the tailored interface mode of operation is employed, only one reservoir enthalpy can be realized for a given set of driver gas parameters. Driver gas parameters are varied by using mixtures of inert diluted gases in the combustion driver.

In the counterflow mode of operation, the shock tunnel flow velocities will be varied from 8000 ft/sec to 18,000 ft/sec. Most of the shock tunnel calibration has been done with 50% He, 25% A, and stoichiometric O_2, H_2. This mixture tailors at a Mach number of 5.2 which provides reservoir conditions corresponding to flow velocities of 8000 ft/sec. The high end of the velocity spectrum will be obtained by using a 75% He, 25% stoichiometric O_2, H_2 mixture. This mixture has not been used extensively for the tailored interface mode of operation, however, preliminary results indicate tailoring is achieved near Ms = 11. This provides reservoir conditions corresponding to flow velocities of 18,000 ft/sec. Intermediate flow velocities will be obtained by varying the He, A dilutant proportions. A plot of the altitude enthalpy simulation components provided by the shock tunnel portion of the counterflow facility is shown in Figure 11.

PROTECTION FROM PROJECTILE DAMAGE

The third problem encountered when operating in the counterflow mode is that of damage in the nozzle throat area and the shock tube as a result of projectile impact. The design shown in Figure 12 which utilizes a replaceable nozzle throat extension, nozzle throat and projectile stopper was arrived at based on results of impact tests performed in the light gas gun. A 4340 alloy steel ramp, inclined 5° from the horizontal, was used as a target to simulate the nozzle throat region. One-quarter-inch diameter steel spheres were fired at this ramp at velocities of 20,000 ft/sec. The results of one of these shots is shown in Figure 13. The damage as a result of impact was superficial and it is felt that damage of this type can be repaired with a filler material. The nozzle throat extension section will be repaired after each shot and will be changed when damage reaches a level necessitating replacement.

In order to stop projectiles or spall material from damaging the shock tube walls, a projectile stopper has been incorporated in the design (Figure 12). This projectile stopper is located in the reflected shock region of the shock tube and is a symmetrical plate which does not influence nozzle flow characteristics. It is expected that the brunt of the impact damage occurring as a result of counterflow operation will be sustained by the projectile stopper, which is easily replaced.

SUMMARY

A 3-inch combustion driven shock tube tunnel has been modified for use in a counterflow facility. Timing tolerances of ± 1 millisecond repeatability for establishing flow in the test section have been achieved by using an arc discharge double diaphragm rupture technique. The velocity component provided by the shock tube tunnel is varied by using various dilutant mixtures of argon and helium in the combustion driver. Projectile impact damage to the nozzle throat area and shock tube is handled by using a replaceable throat section and a projectile stopper in the tube.

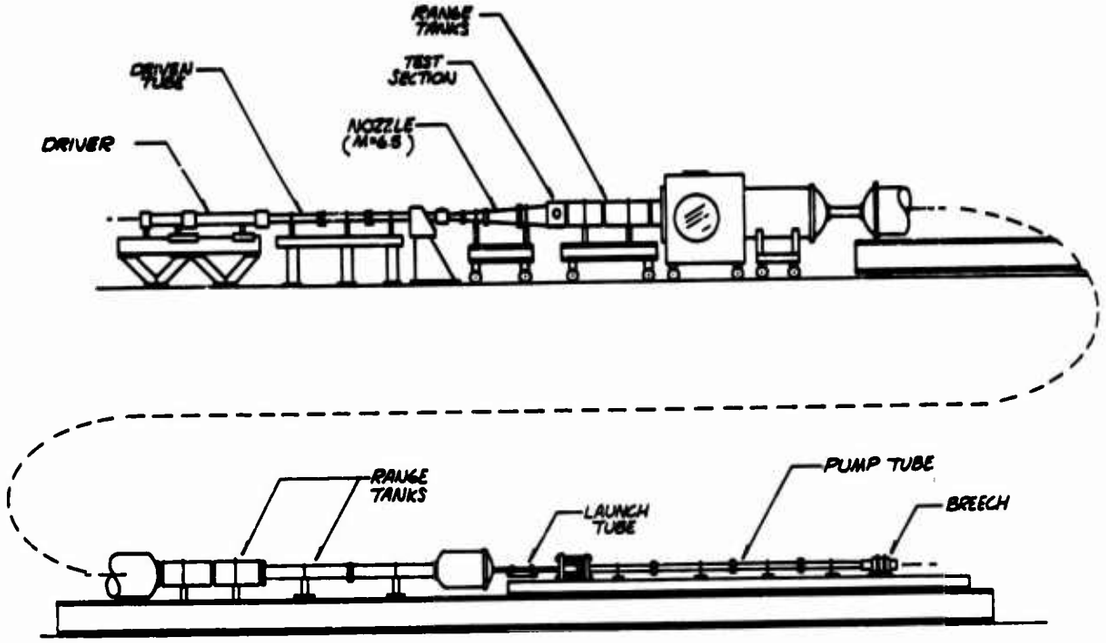


FIGURE 1 BOEING PILOT COUNTERFLOW FACILITY

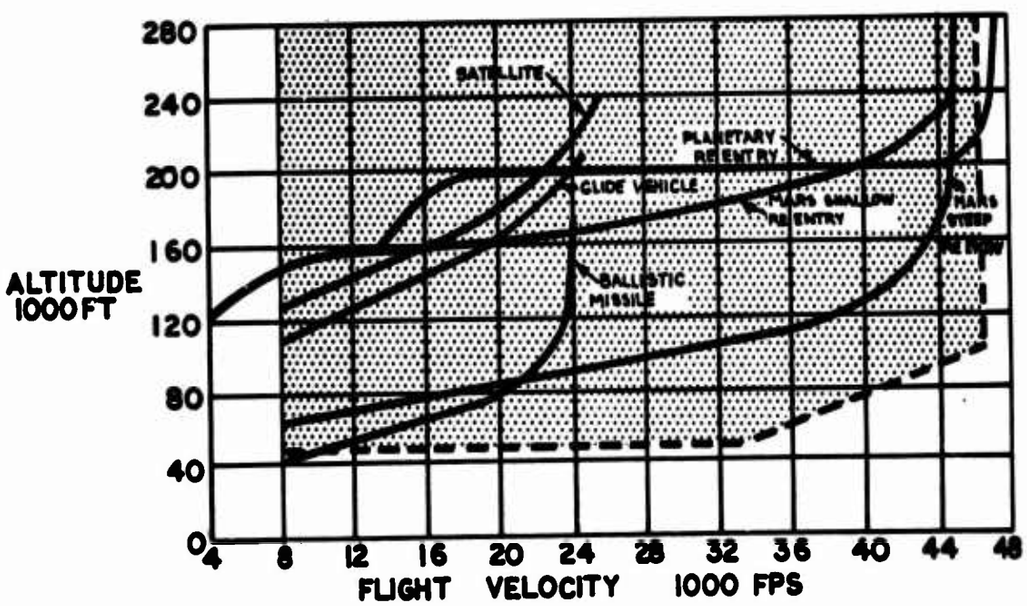


FIGURE 2 COUNTER FLOW FACILITY PREDICTED PERFORMANCE

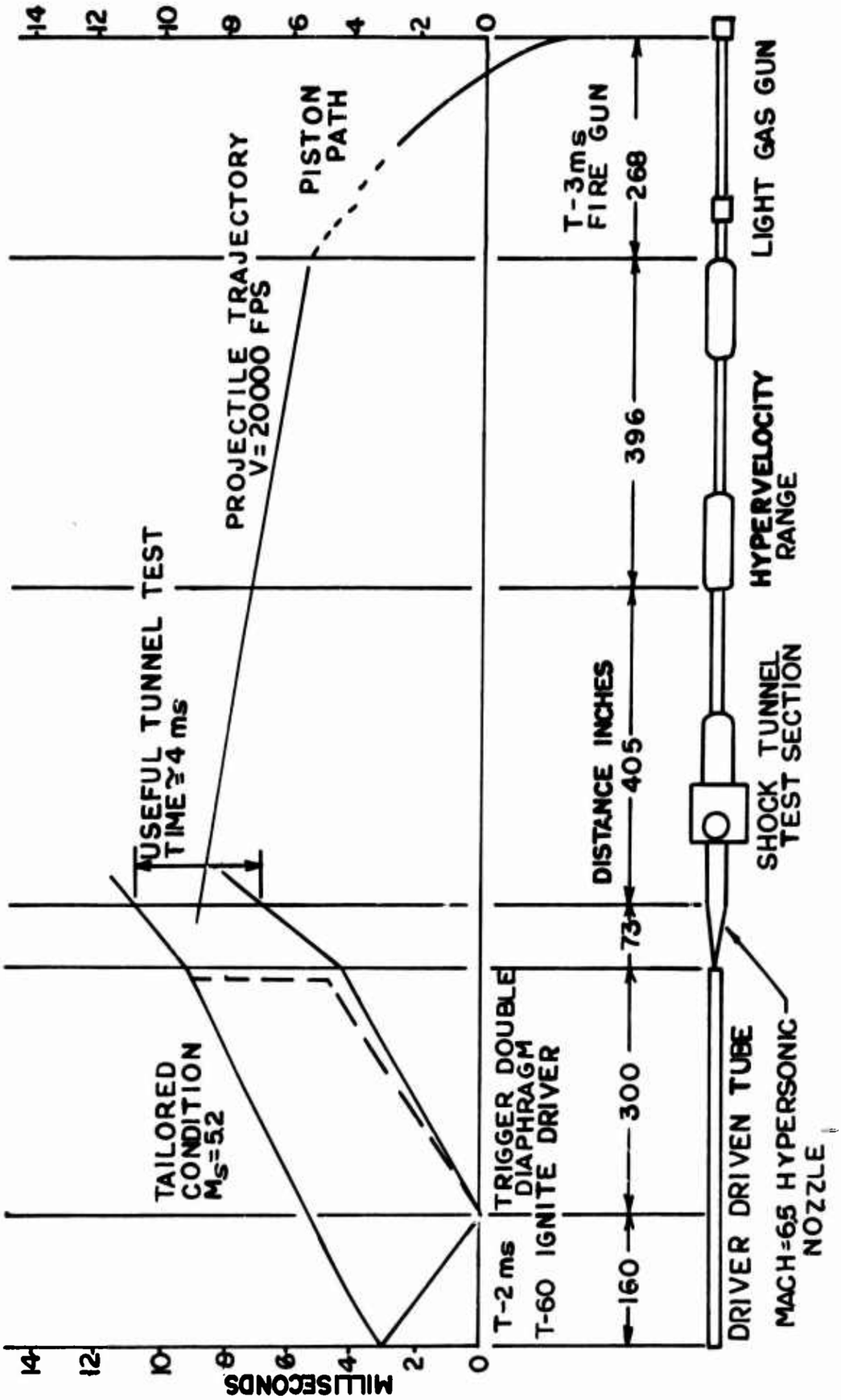
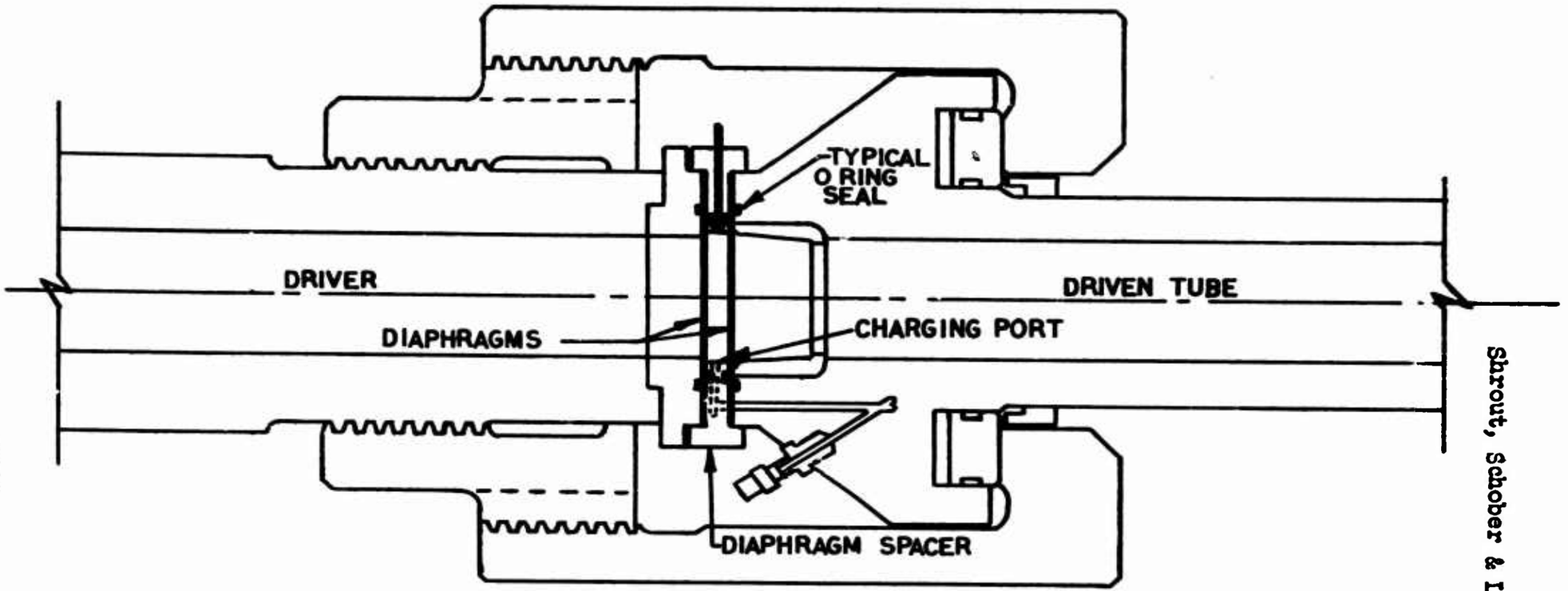


FIGURE 3-TIME HISTORY



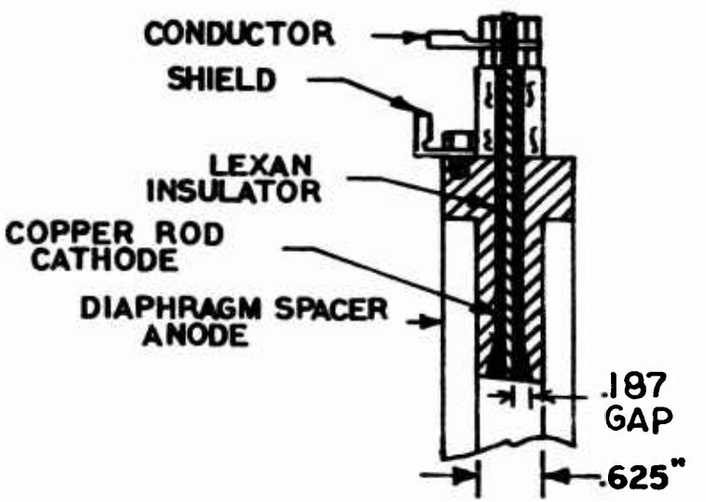


FIGURE 4- DOUBLE DIAPHRAGM ARRANGEMENT

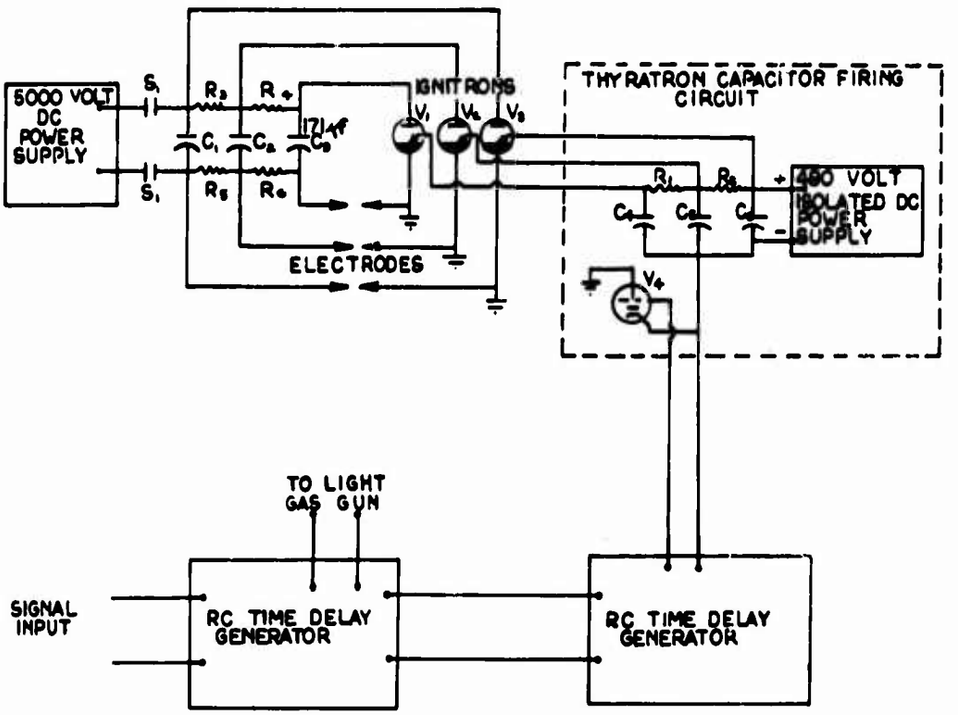


FIGURE 5-ARC SOURCE CIRCUITRY

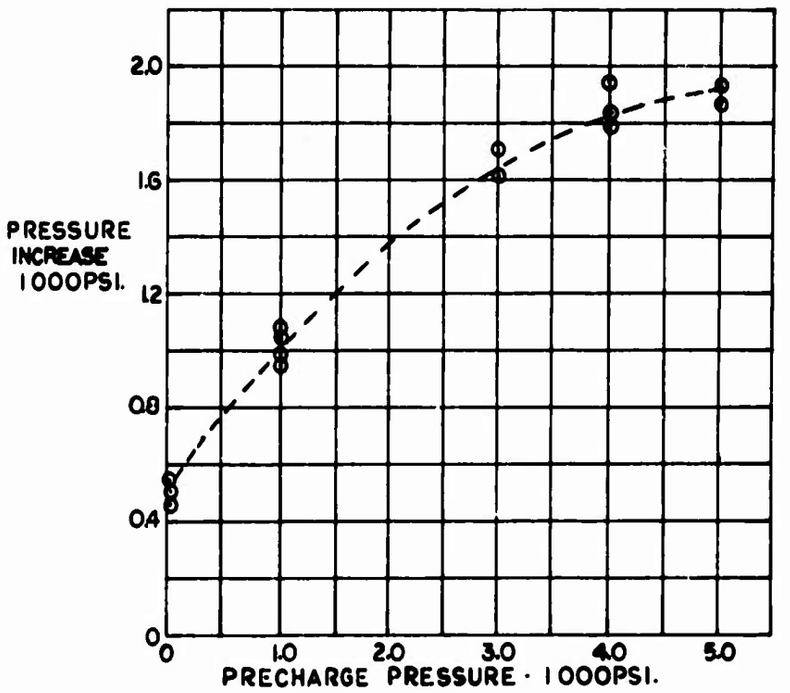
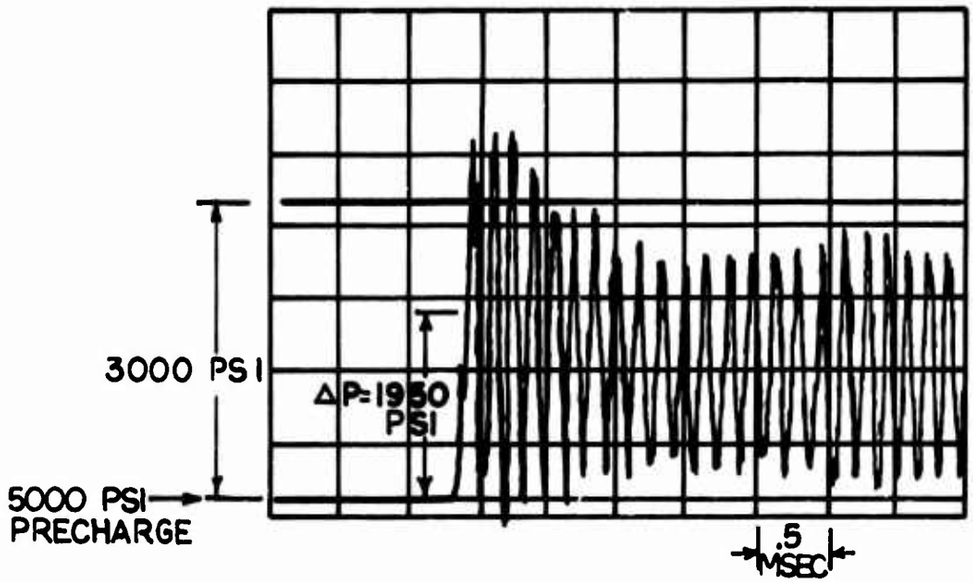
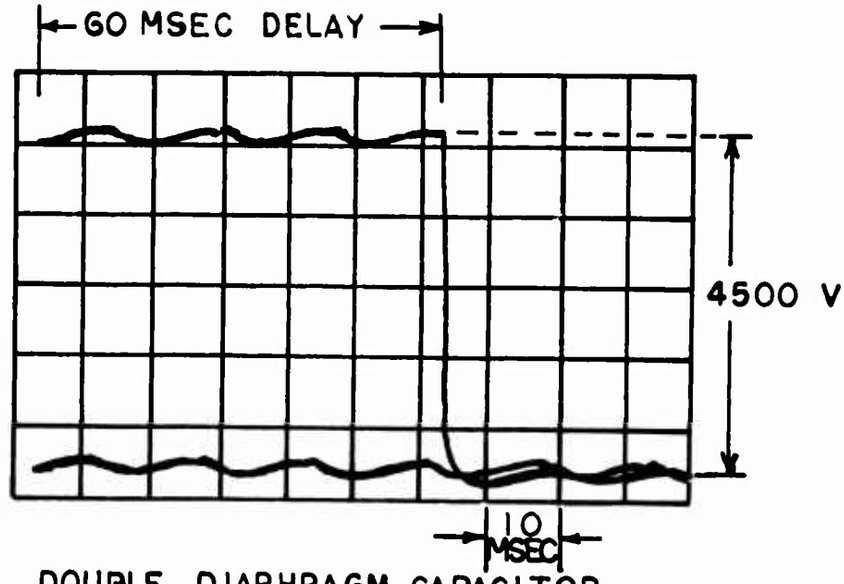


FIGURE 6 DOUBLE DIAPHRAGM PRESSURE RISE



DOUBLE DIAPHRAGM
PRESSURE HISTORY



DOUBLE DIAPHRAGM CAPACITOR
VOLTAGE HISTORY

FIGURE 7-ARC DISCHARGE CAVITY RECORDS

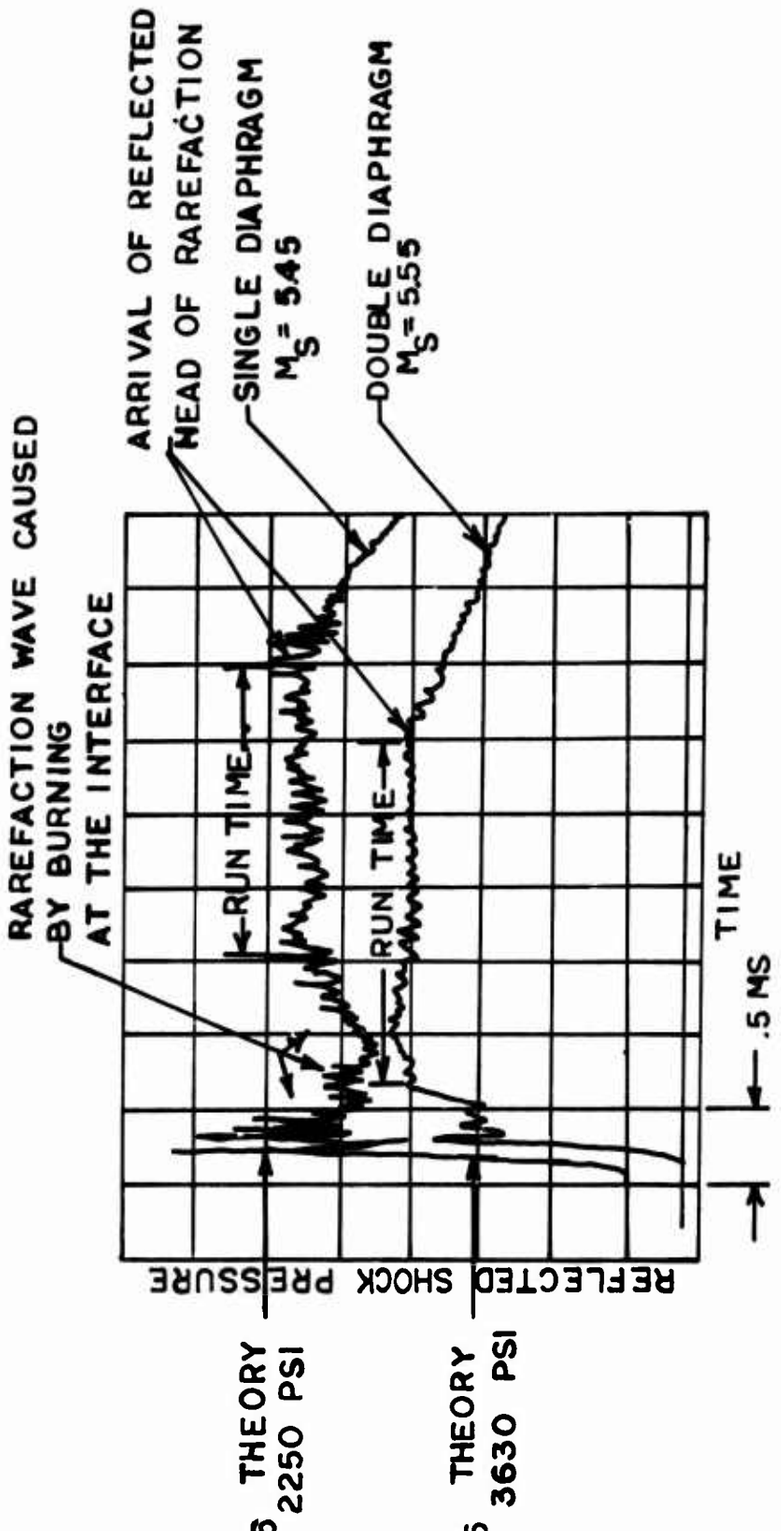
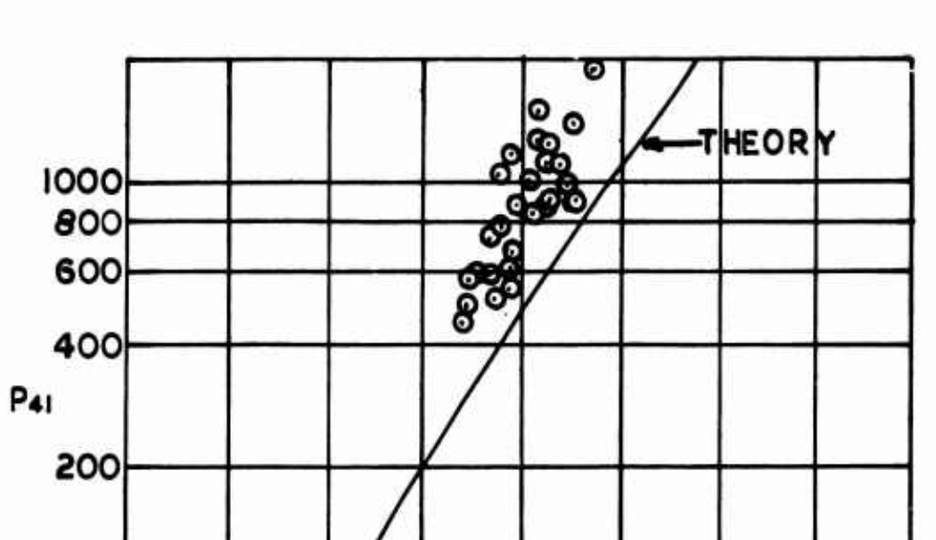
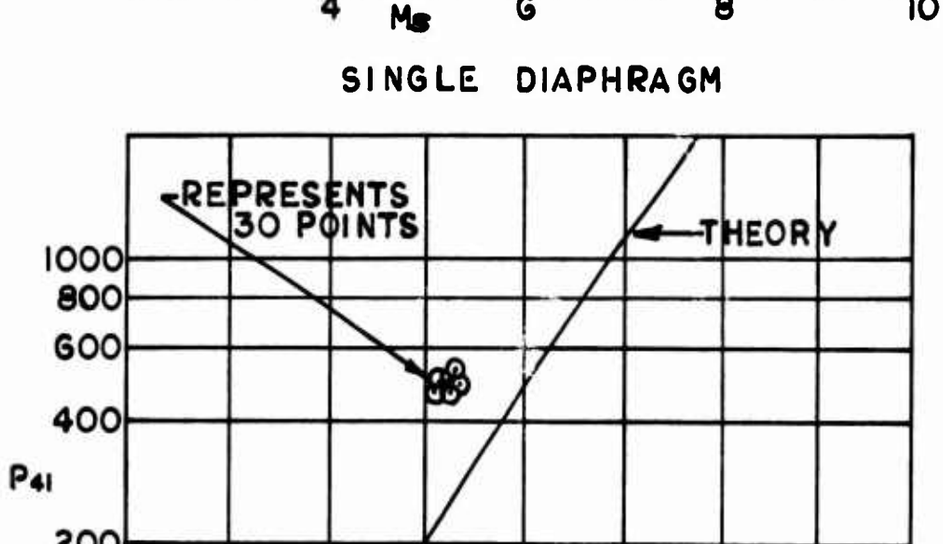


FIGURE 8 REFLECTED SHOCK PRESSURE HISTORY (100" DRIVER)

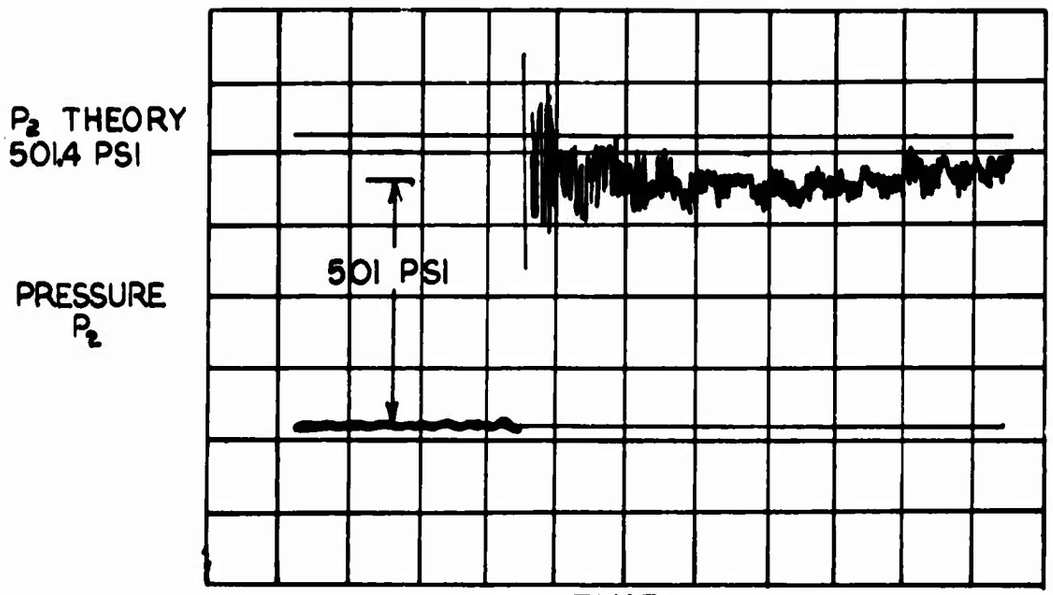


SINGLE DIAPHRAGM

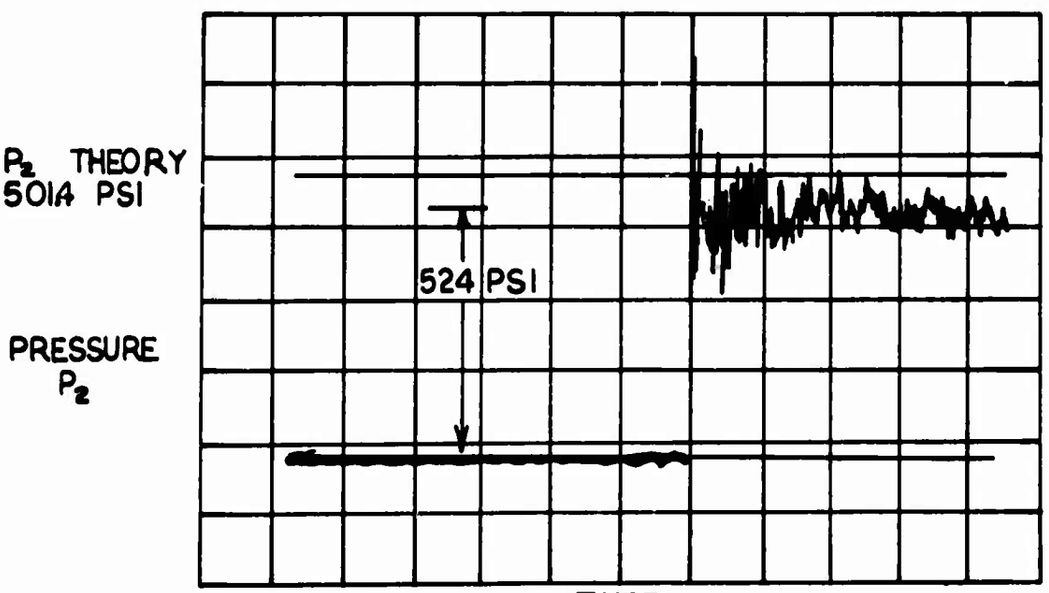


DOUBLE DIAPHRAGM

FIGURE 9 SHOCK MACH NUMBER REPEATABILITY



VERTICAL CALIB 150 PSI/DIV
HORIZONTAL CALIB 100 μSEC/DIV
STATION 3 M_i = 5.45



VERTICAL CALIB 154 PSI/DIV
HORIZONTAL CALIB 100 μSEC/DIV
STATION 5 M_i = 5.45

FIG 10-DRIVEN TUBE PRESSURE HISTORIES

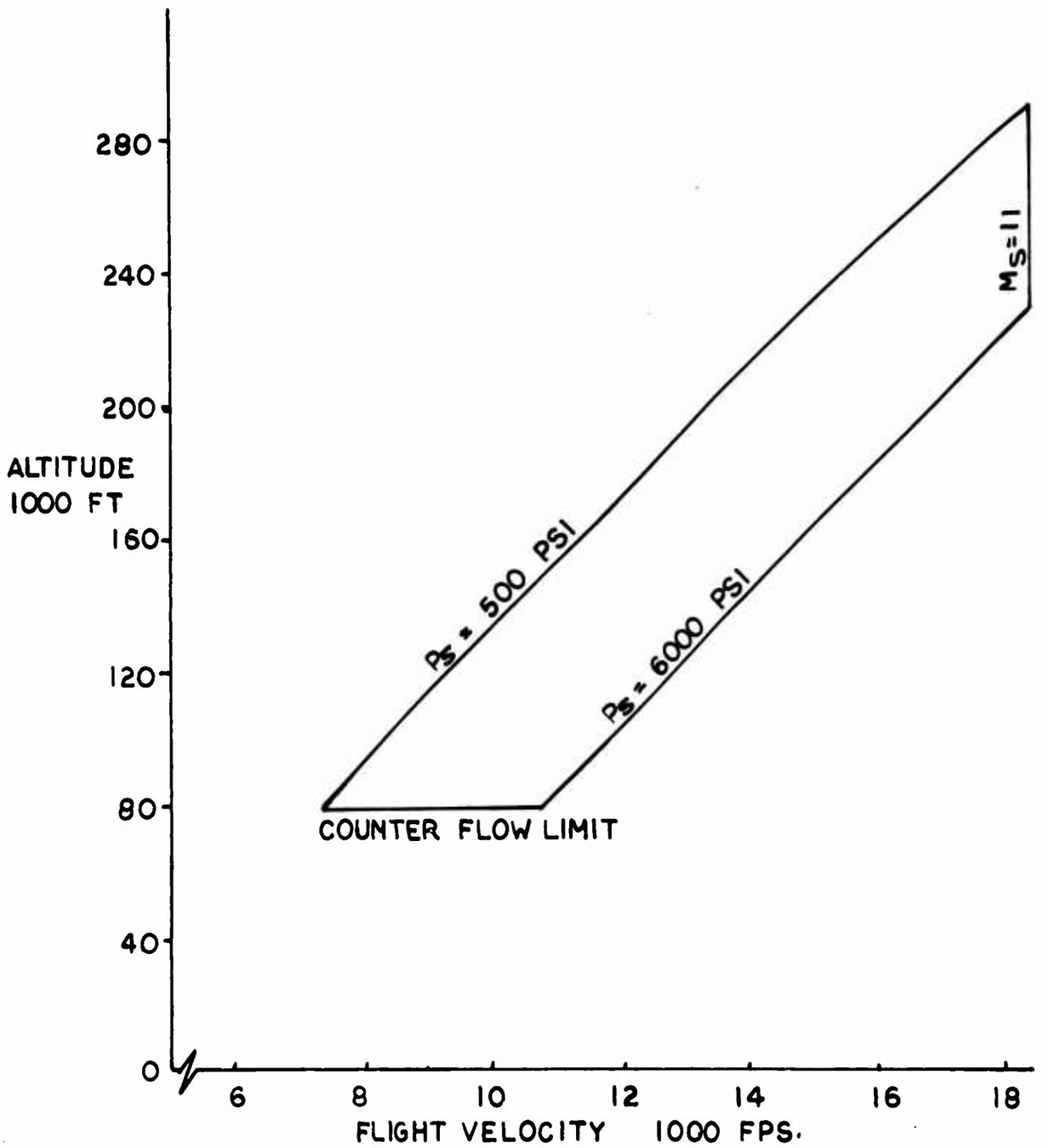


FIGURE 11 STAGNATION POINT ENTHALPY AND PRESSURE SIMULATION ENVELOPE FOR THE MACH 6.5 NOZZLE

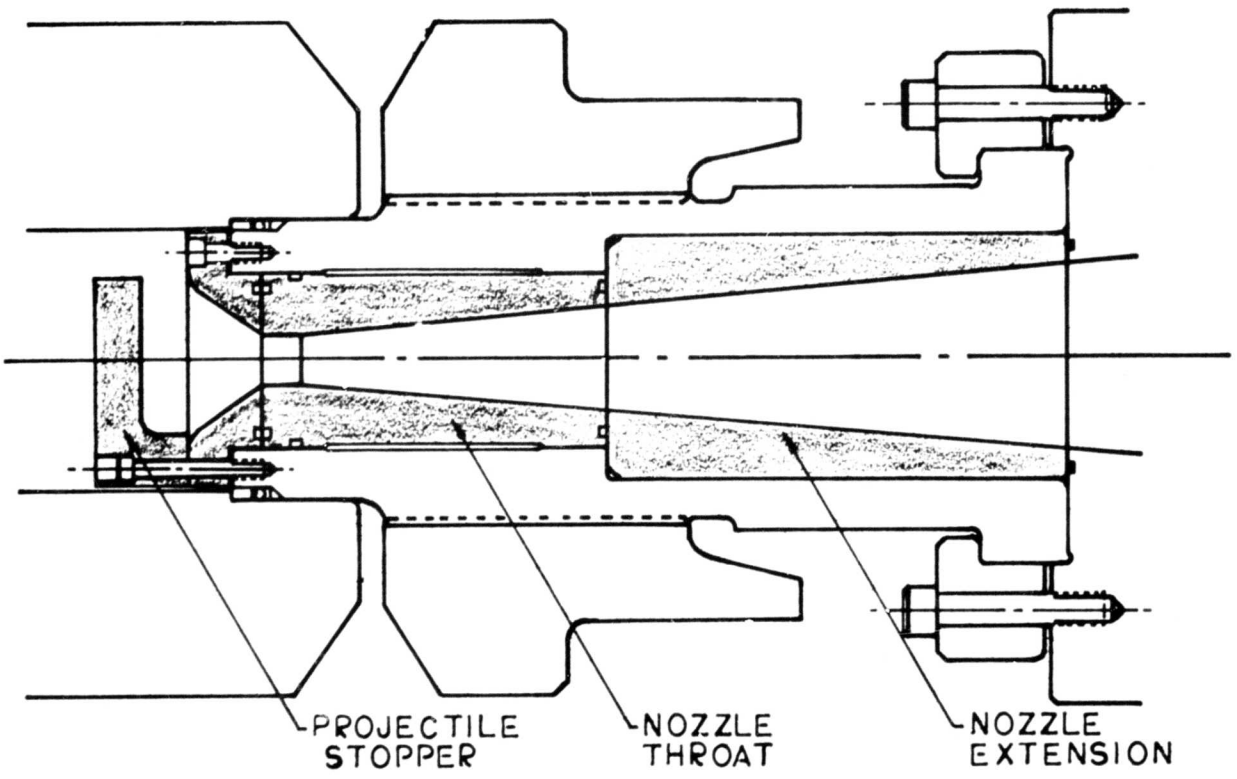
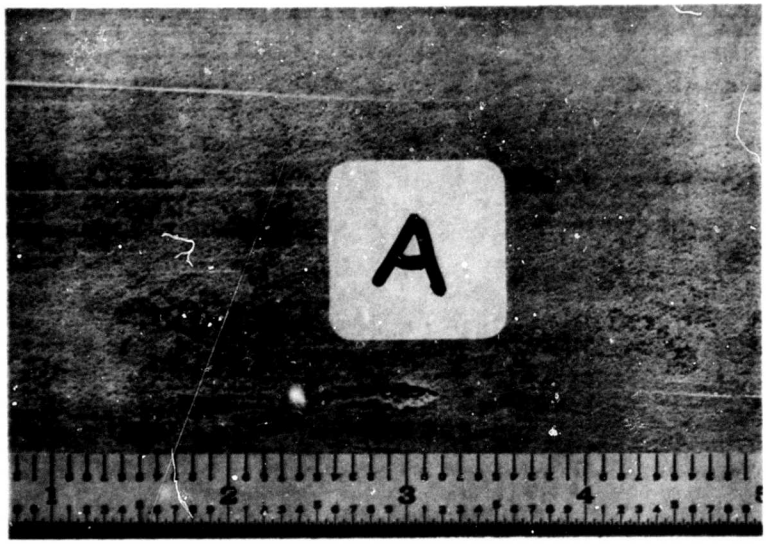


FIG 12 NOZZLE THROAT AREA



PROJECTILE
1/4" DIA.
STEEL
SPHERE
VEL: 20080
FPS

FIG 13 SIMULATED NOZZLE WALL IMPACT

BLANK PAGE

AERODYNAMIC BREAKUP OF LIQUID DROPS
I. THEORETICAL

W. H. Andersen* and H. E. Wolfe
Aerojet-General Corporation
Downey, California

INTRODUCTION

Experimental studies have shown (Ref. 1 - 7) that a liquid drop subjected to an air flow becomes increasingly flattened and then exhibits one of two general breakup behaviors. If the flow is equal to or slightly above a critical velocity required to break the drop under other specified conditions, then the drop is blown out in a concave manner into the form of a hollow bag attached to a roughly circular rim. This bag subsequently bursts and produces a shower of fine droplets, and the rim, which contains a large fraction of the total liquid mass, breaks up into larger droplets. This type of breakup is known as bag breakup. If the air velocity greatly exceeds the critical breakup velocity, then the drop deforms in a manner opposite to that of bag breakup, and forms a convex surface to the air flow. The edges of the saucer shape are drawn out into a thin sheet and then into thin filaments which break to form droplets. This is known as stripping breakup. The type of breakup is influenced by properties of the drop. The reason for the dual-mechanism breakup behavior of liquid drops has not previously been explained, and past studies have been concerned mainly with the (critical) conditions required for breakup from a pure stability (non-rate) point of view. The rate of bag breakup of drops was treated by Hinze (Ref. 8) who derived limiting expressions using the linearized hydrodynamic equations; and by Gordon (Ref. 9) who utilized Newton's second law in a simplified manner. However, experimental rate data have not been available to test their expressions. The droplet size produced by the stripping breakup of drops was treated theoretically by Mayer (Ref. 10) who considered air flow to induce liquid waves which either grow and strip-off to form droplets, or decay, depending on certain properties of the air-flow and of the drop. An experimental determination of the droplet sizes produced by the breakup of drops has not previously been available to test the Mayer theory.

---

*Presently employed at Shock Hydrodynamics, Inc., Sherman Oaks, California.

This paper (I) discusses the mechanism of the aerodynamic breakup of liquid drops and gives a simple model to compute the breakup time and the resultant average droplet size produced as a function of the properties of the air flow and the drop. The companion paper (II) describes an experimental determination of the aerodynamic breakup properties of drops and compares the results with the available theories.

MECHANISM AND TIME OF BREAKUP

Air flow acting on a liquid drop produces a non-uniform pressure that deforms (flattens) the drop, and subsequently breaks it up into smaller droplets by one of the two mechanisms cited above if the flow velocity is sufficiently great. The reason drops undergo two different breakup mechanisms may be seen as follows. The total drag force exerted on the drop is composed of two components, viz, the pressure drag due to the pressure distribution over the surface of the drop, and the friction drag due to viscous shear at the surface. It is postulated here that these two individual stresses are responsible for the two (extreme) breakup behaviors of liquid drops, and in particular that the pressure drag produces bag breakup, while the friction drag produces stripping breakup. During the initial flattening of the drop by the airflow the curvature of the front (edges) of the laterally deforming liquid increases. This increases the effective surface tension pressure resisting deformation and breakup at the edges of the flattened drop. Consequently, at flow velocities near critical, bag-type breakup occurs. At higher velocities the frictional stress, which is always greater then the pressure stress, is sufficient to erode the edges of the drop and stripping breakup occurs. Further discussion of this general breakup behavior will be given later.

During the breakup of a drop, liquid is either sheared away from the sides of the drop (stripping breakup), or the middle of the drop is sheared away from the sides (bag breakup). In either case, this shearing produces a stretching of the liquid to form a film which developes instabilities and subsequently breaks to form droplets. The breaking of the film is a very fast process, and it is the rate of formation of this film by shear which controls the breakup time of the drop. The rate of shear of a liquid is given in molecular terms by (Ref. 11):

$$d\,V/dr = L\,k_s/L_1 \qquad (1)$$

V is the liquid flow velocity in shearing direction, r is the radial distance, L_1 is the distance between the shear planes, L is the average jump distance of a molecular unit undergoing flow, and

$$k_s = 2\,k_r \sinh \frac{L}{2\,N\,k\,T} P_{xy} \quad \text{sec}^{-1} \qquad (2a)$$

k is the Boltzmann constant, T is the absolute temperature, P_{xy} is the shear stress, N is the average number of molecular bonds per unit area in the shear plane, and k_r is the thermal specific rate constant for the controlling molecular process involved in the flow:

$$k_r = K \frac{kT}{h} \exp\ (-\Delta F^*/kT) \quad \text{sec}^{-1} \tag{2b}$$

K is the transmission coefficient, h is Planck's constant, and ΔF^* is the Gibbs standard free energy of activation. High shear stresses cannot be built up in low viscous liquids and hence sinh X = X in Eq. (2a). Therefore,

$$\frac{dV}{dr} = \frac{L^2\ k_r}{L_1\ N\ kT} P_{xy} \tag{3}$$

Rate of shear should be controlled by molecular self-diffusion since a molecular flow is involved in the formation of the film from the bulk liquid. Then the coefficient of P_{xy} in Eq. (3) is equal to $1/\eta$, where η is the coeficient of viscosity of the liquid (Ref. 11). Hence:

$$dV/dr = P_{xy}/\eta \tag{4}$$

Equation (4) may be applied to the bag breakup of liquid drops as follows. Consider a cylindrical tube of liquid of length d and radius R to be shearing from the middle of a drop under the influence of an average viscous pressure head P_h. At any point whose distance from the axis of the tube is r, the shear stress is related to the pressure head by $\pi r^2 P_h = 2\pi r d P_{xy}$, or $P_{xy} = P_h\ r/2d$. Substituting in Eq. (4) and integrating under conditions V = 0 when r = R (assuming d V/dr is negative) gives $V = P_h (R^2 - r^2/4d\eta)$. Maximum velocity occurs at r = 0. Hence, $P_h = 4d\eta V/R^2$. The pressure head differs from the stagnation pressure P produced by the gas flow on drop by the kinetic energy of the liquid flow. Thus, (Ref. 12):

$$P_h = P - \rho_l v^2/2 \tag{5}$$

ρ_l is the density of the liquid. Substitution gives:

$$P = (\rho_l\ v^2/2) + (4d\eta V/R^2) \tag{6}$$

To obtain the proper order of magnitude for the breakup time, assume R and d are the radius and diameter of the original drop (the radius of the tube being sheared from the drop will actually be less than R due to the pressure distribution). Integrating Eq. (6) for the time rate of displacement of the shearing liquid and assuming breakup to occur when the sheared fluid length is 2 d gives the breakup time t:

$$t = d/\left[(A^2 + BP)^{0.5} - A\right] \tag{7a}$$

$$A = 16\eta/d\rho_l\ ;\ B = 2/\rho_l \tag{7b}$$

The pressure expression is:

$$P = (1/2)\rho_a\ U^2\ C_D - k\sigma/d \tag{8}$$

U is the relative velocity between the air stream and the drop, ρ_a is the

density of the air stream, C_D is the drag coefficient (later shown to be about unity), σ is the surface tension of the drop and k is a constant (later shown to be about 2) related to the drop curvature during breakup which determines the effective surface tension pressure retarding the breakup.

Equation (7a) simplifies for certain conditions. For liquids and/or flow conditions for which viscous and surface tension forces are negligible. Eq. (7a) becomes:

$$t = (d/U)\,(\rho_l/\rho_a)^{1/2} \qquad (9a)$$

This expression is similar to that of Gordon and also Hinze for similar conditions, differing only in the value of the numerical constant preceeding the function. For very viscous liquids and negligible surface tension, Eq. (7a) becomes:

$$t = 32\eta/\rho_a U^2 \qquad (9b)$$

This expression is identical to that of Gordon, and differs from that of Hinze only in the numerical constant.

Equation (7a) also applies to the stripping breakup as may be shown by assuming dV/dr in Eq. (4) to be positive and integrating under the condition V = 0 for r = 0. This provides for the situation that the maximum stress is exerted on the edges of the drop, as occurs in stripping breakup. Thus Eq. (7a) can be used for either bag or stripping breakup and there remains only to identify the stagnation pressure and effective surface tension pressure distributions and magnitudes in greater detail if one wishes to delineate further between the bag and stripping breakup mechanisms. Computation of breakup times by Eq. (7a) does not require this deliniation however.

Equation (7a) is valid except when the liquid is extremely viscous or is a solid. In these cases, Eq. (2a) must be used as written in integrating Eq. (3). Final results are given in Ref. 13. The kinetic energy term in Eq. (5) will usually be negligible in these cases. Thus, the present theory, with slight modification, could be used to estimate the mechanical erosion (breakup) of solid particles in aerodynamic flows.

The derivation of Eq. (7a) implied laminar, non-accelerated flow with negligible end-effects (Ref. 14). The assumption of non-accelerated flow may not be quite true, but photographs of the breakup process (II) suggest the acceleration to be very small, if any (after the initial drop deformation). The treatment also used the maximum liquid flow velocity rather than the average velocity. The latter implies a parabolic velocity distribution is established in the flowing liquid. However, the distances required to establish this distribution are very large compared to the size of a liquid drop (Ref. 12). Using the average velocity would increase the predicted breakup time slightly. The breakup criteria used (i.e. setting

the sheared liquid displacement equal to the drop diameter), was based on the fundamental fact that a separation of two molecular bond distances between molecules is usually sufficient to reduce the bond energy to essentially zero. However, photographs of the breakup process (II) show that the liquid is often displaced several drop diameters before breakup is initiated. The photographs also show that a finite time exists between when the liquid starts to break, and when breakup is essentially complete. This time is often comparable to the time required for the initiation of breakup. Thus there is latitude in defining an experimental breakup time for comparison with theory. For consistency the experimental breakup time (II) was taken to be the time between the air flow hitting the drop and the time at which breakup of the drop just begins. However, the total breakup time is larger. Comparison of Eq. (7a) with the experimental data (II) shows the theoretical breakup time is slightly greater than the experimental time to initiate the breakup, and is comparable to the time to breakup the drop completely. Hence, the breakup criteria used is reasonable for practical purposes. Related to breakup criteria are the values used for C_D and k in Eq. (8). The shape of the drop changes continuously throughout the breakup; hence it is only some average C_D and k that can be used. The experimental value of C_D changes from less than unity to greater than unity during the breakup process (II), and for most practical work can be taken to be unity. Rabin et. al. (Ref. 5) found the value to be essentially unity over a large range of conditions. k was evaluated from the experimental results (II) to have a value of about 2.

Equation (7a) will adequately predict breakup times for both the bag and stripping mechanism using a value for C_D and k of 1 and 2. To elucidate which mechanism is occurring under defined conditions, however, it is necessary to evaluate these parameters according to values of the individual pressure and frictional drag. Thus, two individual expressions of the form of Eq. (7a) may be written, with one containing the pressure drag stress in the pressure expression (Eq. 8), and the second containing the friction drag stress. Breakup of a drop will occur by the mechanism which takes place with the fastest rate, i.e., with the shortest breakup time. When the rates are comparable, the drop should exhibit both bag and stripping breakup behavior.

The effective stress distribution on a drop undergoing breakup is not known, but Tomotika and Aoi (Ref. 15) indicated that for a sphere the frictional drag is twice the pressure drag for all Reynolds numbers. We will assume this to be true for liquid drops undergoing breakup even though the shape deviates from that of a sphere. Total drag on the drop during breakup is $\rho_a U^2 C_D/2$, and hence for bag and stripping breakup the pressure expressions are:

$$P_b = (1/3)\,(\rho_a U^2 C_D/2) - k_b\sigma/d \qquad (10a)$$

$$P_s = (2/3)\,(\rho_a U^2 C_D/2) - k_s\sigma/d \qquad (10b)$$

k_b and k_s are constants which reflect the surface tension pressure tending to hold the drop together. This pressure is greater at the edges of the

drop (where the curvature is greater) than in the middle, and hence, $k_s > k_b$. The values of k_b and k_s were determined to be about 4 and 1 resp., by fitting the equations to the experimental data.

INITIAL DROPLET SIZES

Aerodynamic breakup of a drop through either a bag or stripping mechanism results from a shearing of the drop by a non-uniform pressure produced by the air flow. This shearing produces a liquid film which subsequently breaks to give the resultant droplets. The breakup time of the drop is controlled by the rate of formation of this film since the actual breaking of the film is a fast process. However, the geometry of this film, together with the manner in which the film breaks determine the resultant droplet sizes.

The model we consider to describe droplet formation during the breakup of a liquid drop is based primarily on stripping breakup, but essentially the same view may possibly be taken in describing the droplet sizes from bag breakup. The shear stress at the outer surface of the drop produces a boundary layer of flowing liquid of average thickness y. This liquid layer (sheet) upon leaving the drop experiences a small divergence (expansion), due to the pressure at the downwind end of the drop, which breaks the sheet laterally into individual strips of average width W. Simultaneous with the diverging ejection of the liquid boundary layer from the drop, the parallel gas flow along the surfaces of the layer induces instabilities (vibrations) in the layer in the horizontal direction. The optimum wavelength instability L grows most rapidly and breaks the layer into pieces of average size WyL. Surface tension forces then produce spherical drops with an average diameter D from these pieces; thus, $\pi D^3/6 = WyL$, or

$$D = (6\ WyL/\pi)^{1/3} \tag{11}$$

Photographs of the breakup process roughly support the proposed model.

The value of L was calculated by Squire (Ref. 16) who found:

$$L = 4\pi\sigma/\rho_a U^2 \tag{12}$$

y is calculated from the breakup model given previously. Shearing of the liquid follows Eq. (4). Breakup of the liquid film is assumed to occur when the sheared film traverses a distance equal to the drop diameter d. This produces a triangular shaped film thickness which varies from zero (at the tip) to y, or an average thickness of y/2. Thus, Eq. (4) becomes $d/(t)(y/2) = P_{xy}/\eta$. For simplicity consider liquids whose viscosity and surface tension forces are small compared to the aerodynamic flow forces involved. Then t is given by Eq. (9a), and the shear stress on the layer is approximately the stagnation pressure $(1/2)\rho_a U^2$. Hence:

$$y = 4\eta/\left[U(\rho_a \rho_l)^{0.5}\right] \tag{13}$$

W is estimated as follows. Consider an arc of length S in the plane of the liquid sheet leaving the liquid drop. $S = r\theta$, where r is the distance

to a point defining the radius of curvature of the arc, and θ is the angle subtended by the arc. The arc undergoes expansion due to the divergence of the film, i.e., $ds/dt = \theta\, dr/dt$. The derivative dr/dt is the velocity of the liquid sheet V, whereas ds/dt defines a critical velocity V_c for breakup of the sheet into strips. Thus, $V_c = \theta V$. The distance around the drop is 2π radians; hence the number of strips $N = 2\pi/\theta = 2\pi V/V_c$. The numerical distance around the drop is πd; hence $W = \pi d/N = dV_c/2V$. For liquids having low viscous and surface tension forces compared to the aerodynamic flow forces, $\rho_a U^2 = \rho_l V^2$. V_c is obtained from this expression and the conventional stability equation (Ref. 1) defining the critical aerodynamic velocity required for liquid breakup, i.e., $C_D \rho_a U^2/2 = 4\sigma/d$. Consider C_D to be unity. Neglecting the small variation of air density with air velocity gives:

$$W = (d/2U)\,(8\sigma/d\rho_a)^{1/2} \qquad (14)$$

Combining the above equations gives the average diameter of the droplets produced by the aerodynamic breakup of a liquid drop:

$$D = \left[\frac{136\,\eta\,\sigma^{1.5}\,d^{0.5}}{\rho_a^{2}\,\rho_l^{0.5}\,U^{4}}\right]^{1/3} \qquad (15)$$

Equation (15) was derived for conditions where the aerodynamic flow forces are much larger than the viscous and surface tension forces. This situation comprises most cases of practical interest. If the liquid viscosity is large, or if the flow velocity is low and the surface tension is high, then Eq. (15) as written may not be valid. In these cases the various approximations indicated in the derivation (e.g., the value used for t) should be replaced by the more exact expressions. Equation (15) predicts the average droplet size produced varies inversely as the 4/3 power of the relative velocity. The work of Weiss and Worsham with liquid jet stripping (Ref. 17) disclosed such a relationship, and the theory of Mayer (Ref. 10) also predicts this relationship. Thus, evidence is accumulating for the support of this velocity-droplet diameter relationship. Eq. (15) also predicts the droplet diameter varies directly as the 1/6 power of the initial droplet diameter, and the 1/3 power of the liquid viscosity. These precise relationships were also found experimentally by Weiss and Worsham. It will be shown in II that Eq. (15) is in reasonable agreement with the average droplet size data obtained on the present program. However, a fit to the data of Weiss and Worsham as well as to the data from similar studies by Brown (Ref. 18) suggests the value of the constant 136 in Eq. (15) should be larger by a factor of about two. Such a factor is obtained in Eq. (15) by considering the shear stress to be 2/3 the stagnation pressure, and the strength of the film leaving the drop to be $8\sigma/d$ (two surfaces are involved). Since the data of these investigators was not for single drop breakup, and in view of the experimental uncertainties, the best value to be taken for the constant in Eq. (15) is not presently known.

The breakup of a liquid drop produces a distribution of droplet sizes; whereas Eq. (15) predicts only the average size. A complete distribution of droplet sizes could possibly be derived by considering a distribution of surface instability wavelengths to produce the horizontal breakup, as discussed by Borodin and Dityakin (Ref. 19). Brown (Ref 18) has shown that a log normal distribution is a reasonable representation of the distribution of droplets produced by the stripping breakup of liquids.

REFERENCES

(1) Lane, W. R., Ind. Eng. Chem., 43, 1312 (1951)

(2) Magarvey, R. H. and Taylor, B. W., J. App. Phys., 27, 1129 (1956).

(3) Priem, R. J., Jet Propulsion, 27, 1084 (1957).

(4) Engel, O. G., J. Res. NBS, 60, 245 (1958).

(5) Rabin, E., Schallenmuler, A. R., and Lawhead, R. B., AFOSR TR 60-75, March 1960; AFOSR TN 59-129, March 1959.

(6) Hanson, A. R., Domich, F. G. and Adams, H. S., Phys. Fluids, 6, 1070 (1963).

(7) Morrell, G., NASA TN D-677, November 1960.

(8) Hinze, J. O., App. Sci. Res., A1, 253, 273 (1949).

(9) Gordon, G. D., J. App. Phys., 30, 1759 (1959).

(10) Mayer, E., ARS Journal, 31, 1783 (1961).

(11) Glasstone, S., Laidler, K. J., and Eyring, H., The Theory of Rate Processes, McGraw-Hill Book Co., New York, 1941.

(12) Prandtl, L. and Tietjens, O. G., Applied Hydro and Aeromechanics, Dover Publications, New York, 1937.

(13) Tobolsky, A., Powell, R. E., and Eyring, H., The Chemistry of Large Molecules, Interscience, New York, 1943, pp. 125-190.

(14) Partington, J. R., An Advanced Treatise on Physical Chemistry, Vol. 2, The Properties of Liquids, Longmans, Green & Co., New York, 1951.

(15) Tomotika, S. and Aoi, T., Quart. J. Mech. App. Math., 3, 140 (1950).

(16) Squire, H. B., Brit. J. App. Phys., 4, 167 (1953).

(17) Weiss, M. A., and Worsham, C. H., ARS Journal, 29, 252 (1959).

REFERENCES (Cont'd)

(18) Brown, R. E., "The Atomization of a Solution of 2, 4-Dihydroxybenzophenone in Bis (2-Ethylhexyl) Hydrogen Phosphite," Rept. 0395-04(20)SP, Aerojet-General Corp., Downey, Calif., 1964.

(19) Borodin, V. A., and Dityakin, Y. F., NACA Tech. Memo No. 1281, 1951.

BLANK PAGE

AERODYNAMIC BREAKUP OF LIQUID DROPS

II. EXPERIMENTAL

H. E. Wolfe and W. H. Andersen*
Aerojet-General Corporation
Downey, California

INTRODUCTION

This paper sumarizes an experimental investigation of the aerodynamic breakup of liquid drops, including breakup time, mechanism, and resultant droplet sizes. Previous studies (I, Ref. 1-6) have been concerned mainly with the (critical) conditions required for breakup from a pure stability (non-rate) point of view. This investigation has been described in greater detail in Ref. 1.

APPARATUS

The air flows used were produced in a shock tube. Theory and limitations of shock tube gas flows are available (e.g., Ref. 2,3). The shock tube was vertical (flow upward) and consisted of a 29 in. long steel pipe compression chamber (4-in. ID), a 55-in. long, 2-in. square cross section expansion chamber comprising a diaphram holder, a 24-in. long steel shock formation section, a 17-in. long steel test section containing glass viewing windows, and a 12-in. long end section made of plexiglas. The compression chamber contained a section to provide smooth flow transition to the expansion chamber. Compressed air was the driver gas. The expansion chamber was operated at atm. pressure and was open-ended, permitting the gas flow to exhaust to the atmosphere. Duration of constant flow conditions behind the shock front was about 3 millisec. The diaphram material was Mylar and was ruptured by an exploding wire technique.

Shock velocity was measured by monitoring the arrival-time of the shock front at two pressure transducers (Endevco Model 2501-500) mounted 14.25-in. apart in the test-section wall. Signals from the transducers were amplified by Shasta Wide-Band amplifiers and fed into a Beckman Model 7370 Counter. Independent measurements using an oscilloscope technique confirmed the data obtained by the counter.

*Presently employed at Shock Hydrodynamics, Inc., Sherman Oaks, California.

Breakup of a liquid drop by the gas flow was photographed by a Beckman Whitley Model 326-3 Dynafax Camera capable of framing rates up to 26,000 frames/sec. The light source used was a Beckman Whitley Model 357 Electronic Flash Unit. A Wollensak Raptar f/2.8, 3-in. Telephoto lens was used to obtain the desired magnification and field of view.

BREAKUP TIME STUDIES

Breakup time and mechanism of an individual liquid drop were studied by photographing the free-falling drop from the time of its interaction with the shock front of the gas flow until its breakup was essentially complete. The drop was released in the shock tube from a hypodermic needle and its fall was permitted to interrupt a beam of light focused on a photocell. This interruption triggered the camera light source and the explosion of the wire that burst the diaphram. Since the Dynafax camera required an intense source of light for adequate exposure at high framing rates, it was possible to open the camera shutter just prior to releasing the drop and obtain the pictures without film fogging. Drop size was determined by the diameter of the hypodermic needle. For drops smaller than 1.0 mm, a microburet similar to that used by Asset (Ref. 4) was fabricated.

Liquids used in the studies were water, mercury, bis, and three silicone fluids with widely different viscosities. These liquids encompass a wide variety of physical properties.

Liquid	Surface Tension (dynes/cm)	Viscosity (centipoise)	Density (gm/cc)
Water	72.0	0.89	1.00
Mercury	487.0	1.55	13.60
Bis	27.6	5.97	0.92
Silicone Fluids			
GESF (96) 0.65	17.5	0.47	0.76
GESF (96) 10	22.3	9.52	0.94
GESF (96) 200	23.4	169.5	0.97

Drop diameters used varied from 0.05 to 0.3 cm; the relative velocity between the gas flow and the liquid ranged from 50 to 450 ft/sec.

Figure 1 shows a typical film sequence of the bag breakup of a water drop. In agreement with previous studies (I, Ref. 3-6) the pictures show the breakup to be brought about by the gas flow behind the shock front, rather than by the front itself. The time required for the shock front to travel over the drop (of the order of 10 μ sec) is small compared with the time between shock arrival and the time the drop begins to shatter (500 μ sec and greater). Flattening begins on the downwind side of the drop and the lateral diameter subsequently increases from pressure on both faces until the drop assumes a shape similar to an oblate spheroid. Flattening is accompanied by slight surface disturbances. The drop is then blown out in a concave manner to form a hollow bag attached to a roughly circular ring. The bag then bursts to form droplets, followed by breakup of the ring.

Figure 2 shows the effect of relative velocity on the breakup of a water drop. At the lower velocities the drop breaks by a bag mechanism; whereas, at the higher velocities the drop breaks by a stripping mechanism. The surface disturbances are very pronounced in the latter mechanism, and probably related to the waves discussed by Mayer (I, Ref. 10). The solid diagonal lines between the sequences are roughly iso-time lines; they indicate the influence of gas velocity on the drop at comparable time periods. Increase in velocity increases both the rate of deformation and breakup of the drop. The liquid stripped from the periphery of the drop does not initially follow a path parallel to the general flow, but rather appears to diverge to form a cone-like cloud of droplets. This behavior was used in deriving the preceding model (I) for resultant droplet size.

Figure 3 shows the influence of viscosity on the breakup behavior. Increasing viscosity retards the deformation and breakup process. This could lead to a larger droplet size stripped off since it permits the drop to acquire a larger velocity (and thus reduces the relative velocity). In addition, the liquid stripped from the periphery of the drop leaves as larger sheets, ligaments, and droplets rather than smaller ones as occurs at low viscosities.

The above figures are illustrative of the pictures acquired. Reference 1 contains all of the film sequences for all of the liquids. Lack of space prohibits detailed discussion of these photos here but a further comment may be made. The photos showed that at low gas velocities the breakup always occurred by the bag breakup mechanism. As the relative velocity was increased slightly (other parameters remaining fixed) a re-entrant or Stamen portion of liquid formed at the center of a flattening drop on the downwind side. As the bag continued to form, the stamen elongated to form a ligament of liquid, centered within the bag rim. The usual rupture of the bag and rim then occurred and the stamen collapsed into a series of larger drops. As the relative velocity was increased further, more of the mass of the drop became concentrated in the stamen portion with less available to form the bag. This effect continued with increasing velocity until the majority of the drop mass was contained in the center stamen portion. At this point, the bag no longer formed and a lip formed around the drop periphery and was stripped off as a sheet which shattered into droplets. At higher velocities the stripping breakup mechanism always occurred. Thus it appears that there is a smooth transition in behavior in going from the bag to the stripping breakup mode. Physical properties of the drop also influenced the breakup mechanism but in a manner secondary to the relative gas velocity. These properties were generally not studied systematically.

Breakup times of the drops under various conditions were determined from the photo sequences. As discussed before (I), the experimental breakup time was taken as the interval of time between the first signs of drop deformation from the shock passage, and the initial breakup of the drop. The pictures show that the total breakup time is a small factor (usually 2 to 3) larger than the time to just initiate breakup. Comparison of the experimental breakup times with the times predicted by the equation

previously derived (I, Eq. 7) is shown in Figure 4. The length of the individual data points indicates the uncertainty in reading the times from the films. Agreement and correlation between experiment and theory is good although the experimental times generally are smaller than the theoretical times. However, since total breakup time is greater than the breakup initiation time by a small factor, the theoretical equation is reasonably valid for practical purposes. In applying the theory no differentiation was made between the bag and stripping mechanism, and the value of k (I, Eq. 8) was taken from a best fit of the data to be 2.

Figure 5 shows a comparison of the experimental breakup times with those predicted by the (slightly modified) breakup equation of Gordon (I, Ref. 9). The Gordon equation was derived for bag breakup but is apparently also applicable for stripping breakup. Gordon used a surface tension pressure that was too high to allow all of the data to be used (i.e., breakup was often predicted not to occur when it did occur). By decreasing this pressure by a factor of two or more most of the data could be used, and Figure 5 is using a factor of two. The Gordon breakup time equation is then:

$$t = \frac{2d\sqrt{\rho}^{0.5}}{(\rho_a U^2 - 8\sigma/d^{0.5}} + \frac{32\eta}{(\rho_a U^2 - 8\sigma/d)} \qquad (1)$$

Symbols used in this equation were defined before (I). Equation (1) is in good agreement with the data except for a small approximately constant factor.

The experimental data were also compared to the limiting expressions developed by Hinze (I, Ref. 8). Good agreement with all of the data was not found, nor was it expected, since not all of the liquids and conditions correspond to the limitations imposed by the equations. The theoretical times predicted were generally less than the experimental times for liquids and conditions where his equations should be valid.

The individual bag and stripping breakup data are compared in Figures 6 and 7 with the breakup equation (Eq. 7) of (I), using the individual pressure expressions, Eq. (10a) and (10b). k_b and k_s were determined to be about 4 and 1, resp., by best fit to the data. Agreement of theory with the stripping breakup times is good, but with bag breakup the agreement can be made better by adjusting the relative values used for the pressure and friction drag. This suggests that the explanation proposed for the dual breakup mechanism of liquid drops (bag and stripping) is reasonable.

A brief study was made of the drag coefficients of the deformed drops undergoing acceleration and breakup. A typical set of curves is shown in Figure 8. Distance, velocity, and acceleration were determined from the experimental data, and C_D was obtained from:

$$C_D = \frac{4\sqrt{\rho}\, d^3}{3\rho_a (U - V)^2 d_i^2} \frac{dV}{dt} \qquad (2)$$

d_1 is the lateral diameter of the deformed drop. The slight negative velocity is due to the initial free-fall of the drop. Breakup time was about 0.4 millisec and hence in this case the average value of C_D during the initiation to breakup was about unity. Values of C_D usually varied from less than, to greater than unity for most of the cases studied. It was concluded that an effective value of unity for C_D during breakup was reasonable, and Rabin et. al. (I, Ref. 5) previously found a value of unity for drops accelerated in a gas stream. The errors inherent in obtaining the acceleration for a deforming drop are large, however, and the shapes of the drag coefficient vs time curves were not consistent. Peak values for C_D varied from 0.9 to 4.4.

DROPLET SIZE STUDIES

A study was made of the sizes of the droplets produced by the breakup of a liquid drop. Bis was used as the test liquid because of its very low vapor pressure which reduces evaporation of the liquid. Also, previous experience had been gained on its behavior in aerosol form, typical spread factors for bis droplets on glass had been determined, and chemical assay techniques to determine the quantity of bis sampled had been worked out and tested. The shocktube was used in a horizontal position in these studies and the plexiglas end section of the expansion chamber was removed in some of the studies. The droplets produced by the breakup were collected on 12 standard microscope slides mounted in a holder, creating a 4-x-6-in. plane-sampling surface. The holder was mounted on a movable stand, with the center of the sampling surface concentric with the shocktube axis and the plane of the surface normal to the tube axis. The stand was positioned to place the sampling surface a predetermined distance from the open end of the expansion chamber. This distance was determined experimentally, and was the distance at which the droplet sizes were found to be roughly insensitive to distance. After a drop breakup test was conducted, the microscope slides were removed, and photomicrographs of the sampled material were taken at three locations along the centerline of the slide. To provide data from which the radical distribution of the sampled material could be determined, recordings were made of the coordinates of each of the photomicrographs on the slide surface. The sampled material was also washed from the slides and put into a solution, permitting assays to be made of the amount of material collected for material-balance calculations.

Studies were conducted at several relative velocities and for three drop sizes. Breakup mechanism included both bag and stripping breakup. Figure 9 shows a typical set of photomicrographs of the sampled material. The apparent measured diameters of the drops were multiplied by the experimentally determined spread factor (about 0.43) to give the true drop diameters. Figure 10 shows typical plots of cululative percent mass vs droplet diameter for both bag and stripping breakup. The droplet size distributions produced by the drop breakup are to good approximation log normal distribtuions (I, Ref. 18). Figure 11 shows the comparison between the experimental mass mean droplet diameters of all the data and the mean diameters predicted by the theory developed in I (Eq. 15). Agreement is reasonable, considering the relative scatter in the data. In view of this

scatter it is difficult to draw definite conclusions regarding the validity of Eq. (15). The data suggest the influence of droplet diameter and relative velocity may differ from that predicted by Eq. (15). However, the data of Weiss and Worsham (I, Ref. 17) are consistent with the variations predicted. Comparison of the data with the Mayer theory (I, Ref. 10) is given in Figure 12. The mean droplet diameter given by Mayer is:

$$D = 71.2B \left[\eta (\sigma/\rho_l)^{0.5} / \rho_a U^2 \right]^{2/3} \qquad (3)$$

B is an undetermined constant whose value must be determined by experiment. Its value from Figure 12 is about 0.18. However, the value of B is probably a weak function of drop diameter. Drop diameter is presently not a parameter in the Mayer equation. The discrepancy between experiment and the Mayer theory is due primarily to the relative velocity dependence, which is the same as in Eq. (15). Further experimental studies are required to test and refine the theoretical droplet size expressions.

ACKNOWLEDGMENTS

This work (Parts I and II) was supported by the U. S. Army Chemical Center. The authors would like to thank Dr. L. Zernow, K. N. Kreyenhagen, and G. W. Woffinden for their encouragement given to this work, and G. A. Ackerman and J. C. Colerich for their assistance in the experimental phases of the program.

REFERENCES

(1) Wolfe, H. E. and Andersen, W. H., "Kinetics, Mechanism, and Resultant Droplet Sizes of the Aerodynamic Breakup of Liquid Drops," Rept. No. 0395-04(18)SP, Aerojet-General Corp., Downey, April 1964.

(2) Glass, I. I., Martin, W. and Patterson, "A Theoretical and Experimental Study of the Shock Tube," UTIA Rept. No. 2, Univ. of Toronto, 1953.

(3) Greene, E. F. and Toennies, J. P., Chemical Reactions in Shock Waves, Academic Press, New York, 1964.

(4) Asset, G., Am. Ind. Hygiene Assoc. Jour., 20, 56 (1959).

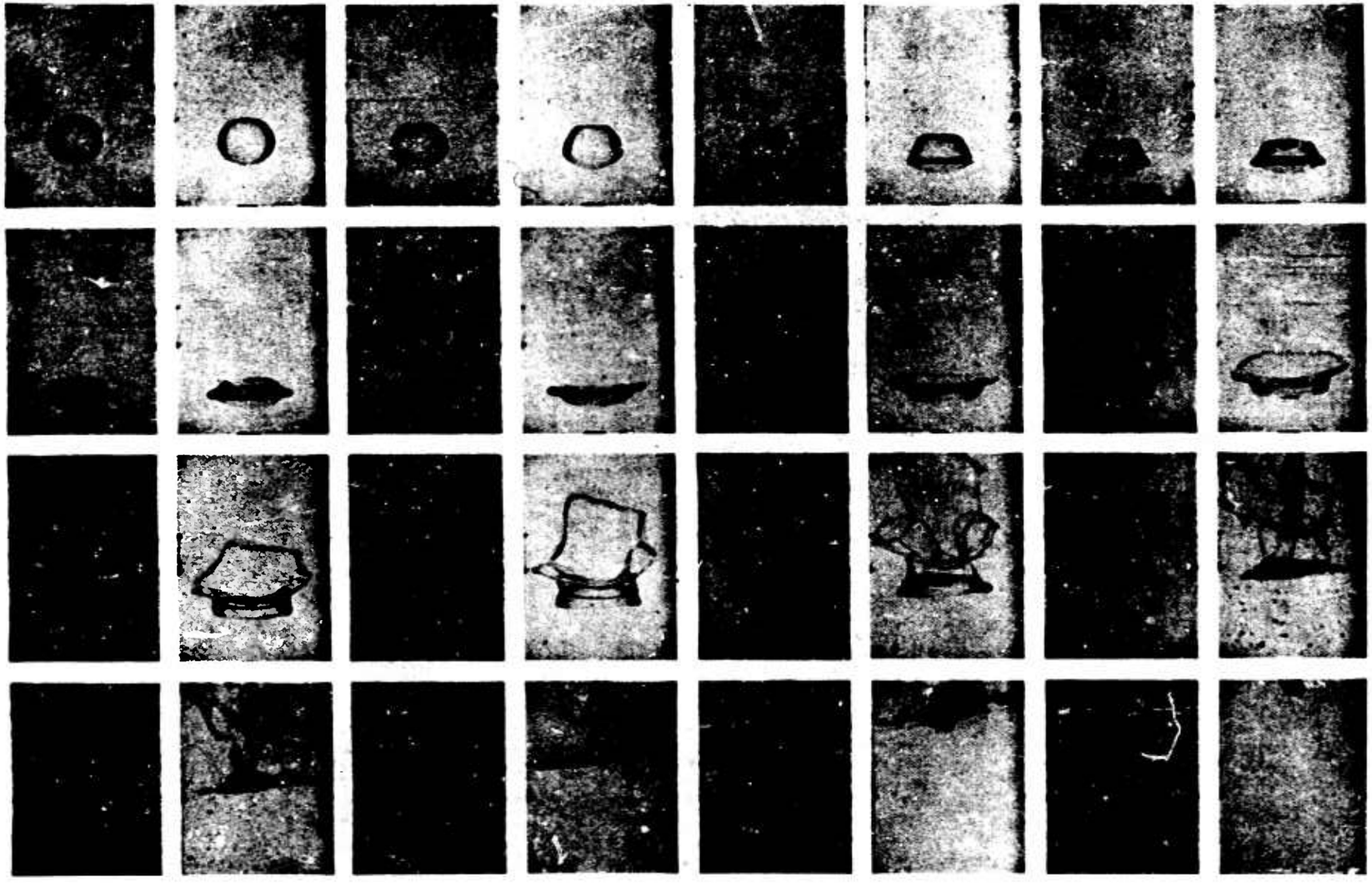


Figure 1. Breakup of a 1.9mm Water Drop at a Relative Velocity of 53 ft/sec. Time per frame 0.117 msec

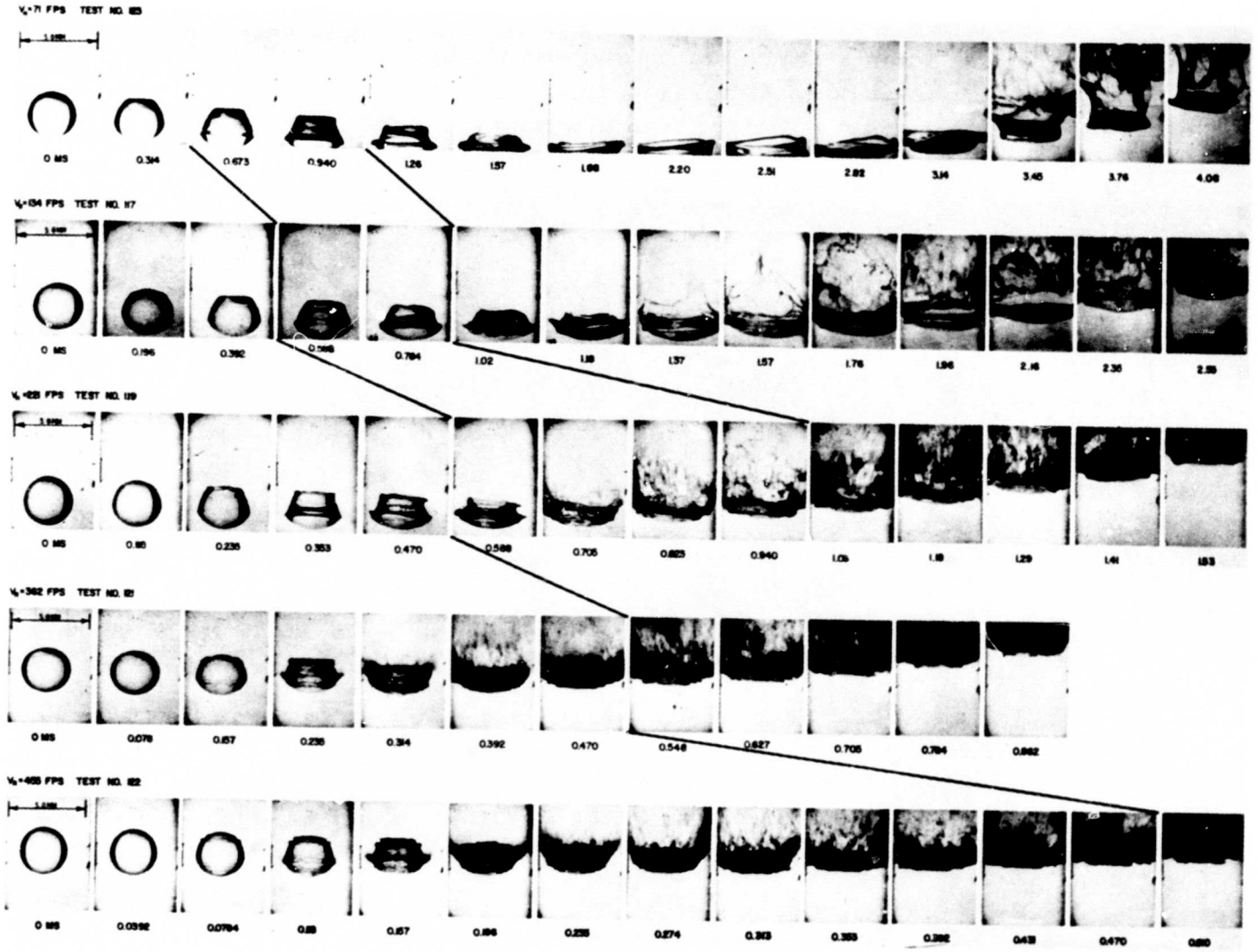


Figure 2. Effect of Relative Velocity on the Breakup of 3.0mm Water Drops.

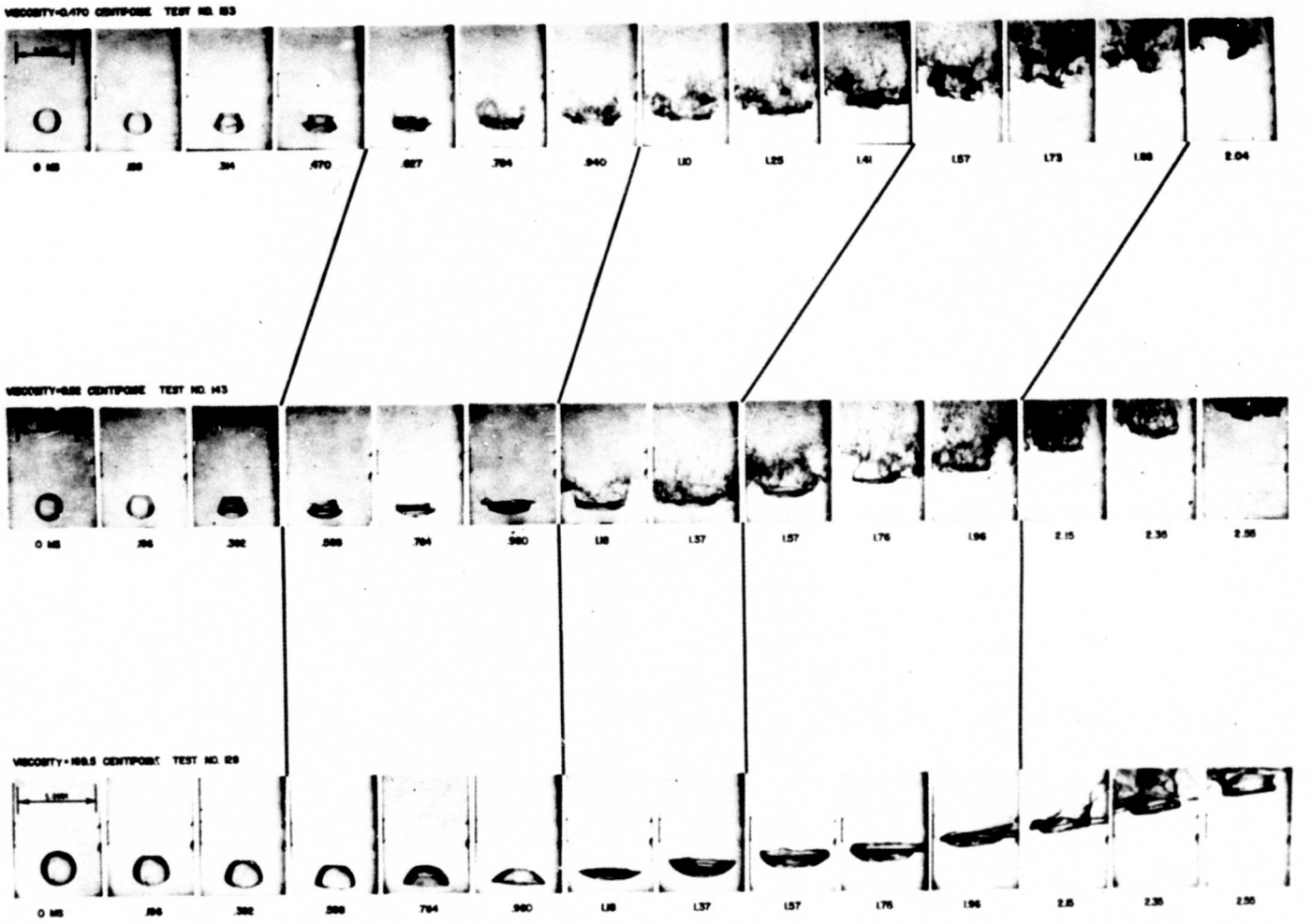


Figure 3. Effect of Viscosity on Breakup.
Drop Size: 2.1mm
Relative Velocity: 127 FPS

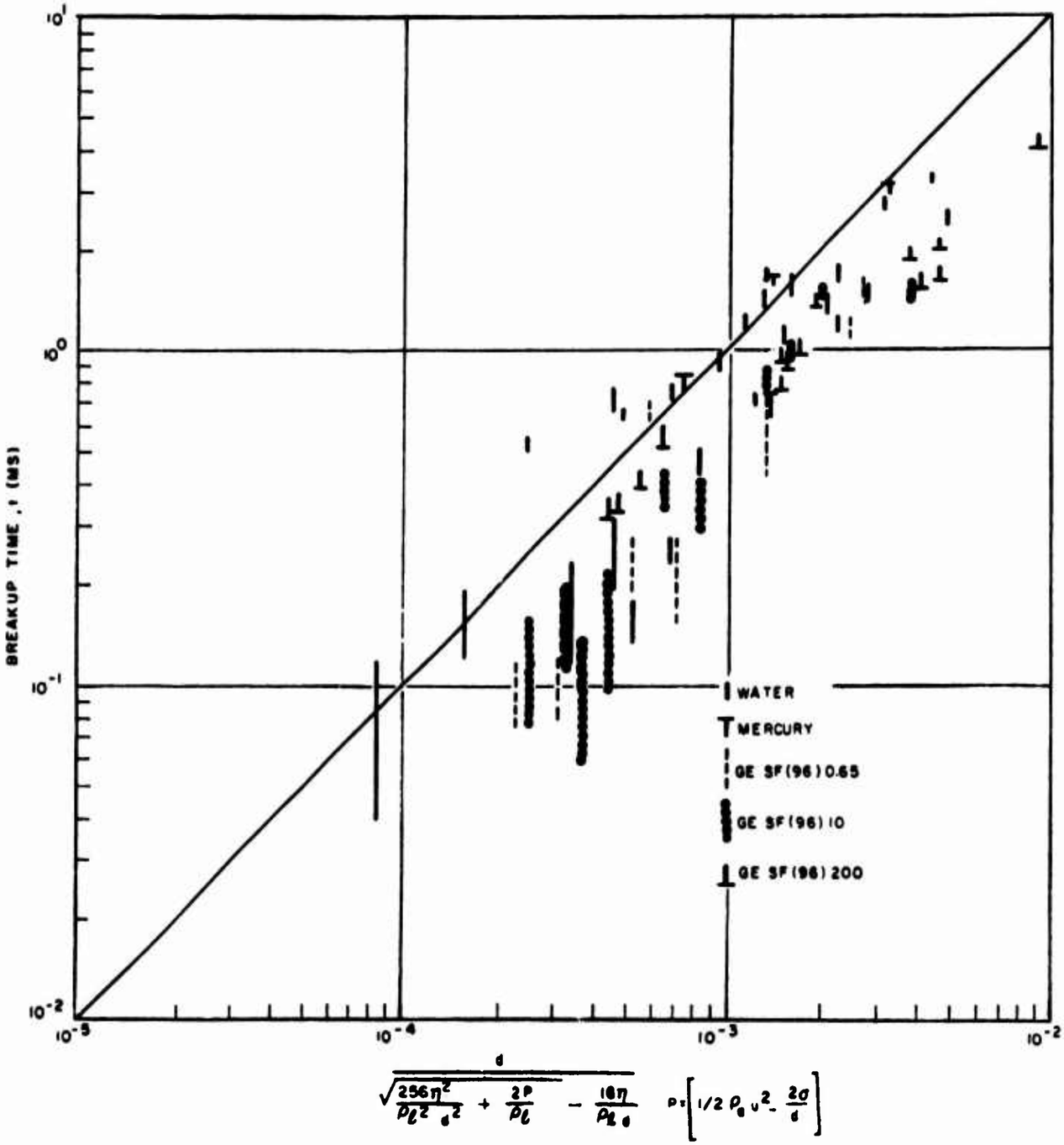


Figure 4. Comparison of Experimental Drop Breakup Times with the Andersen-Wolfe Equation.

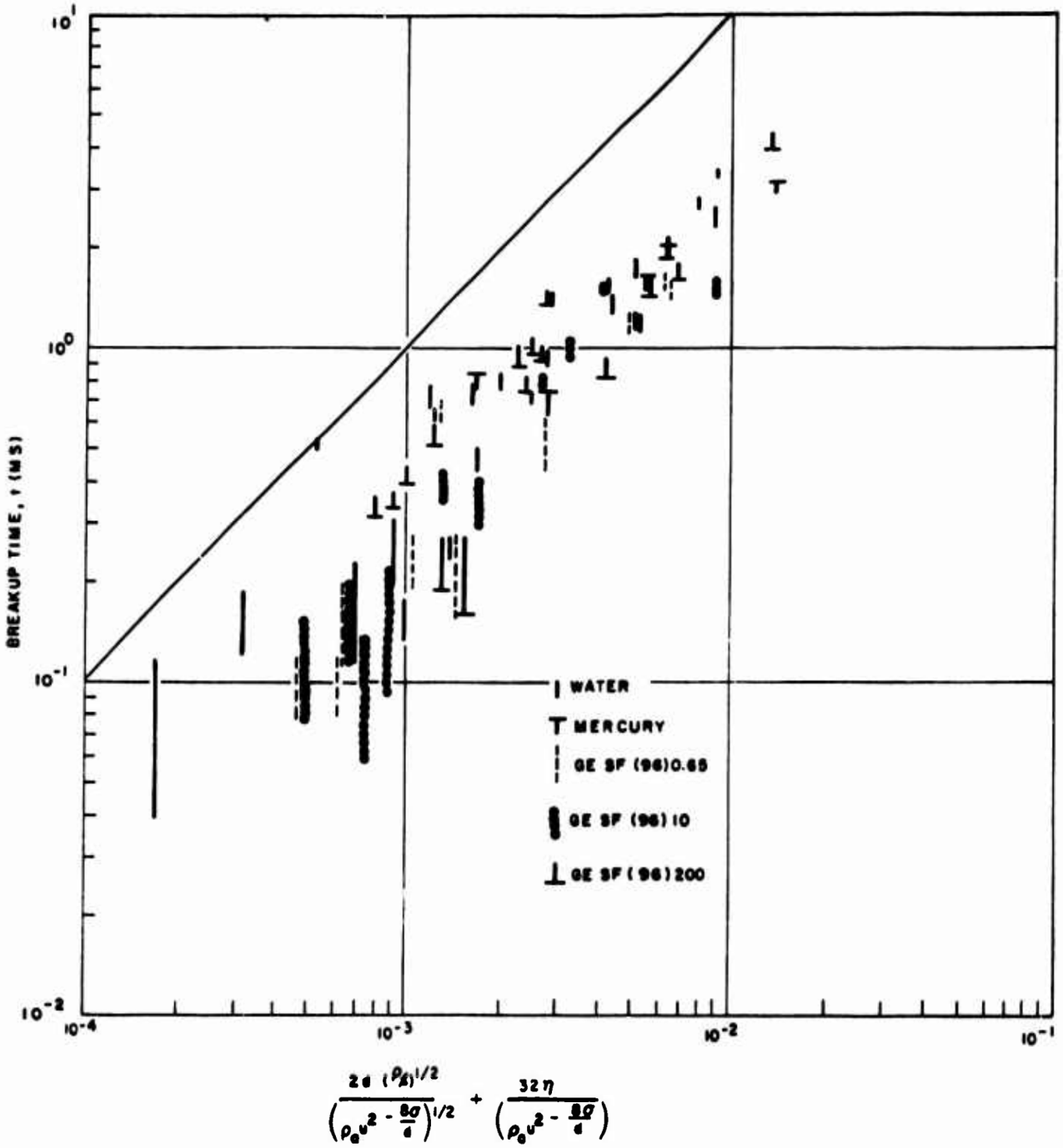
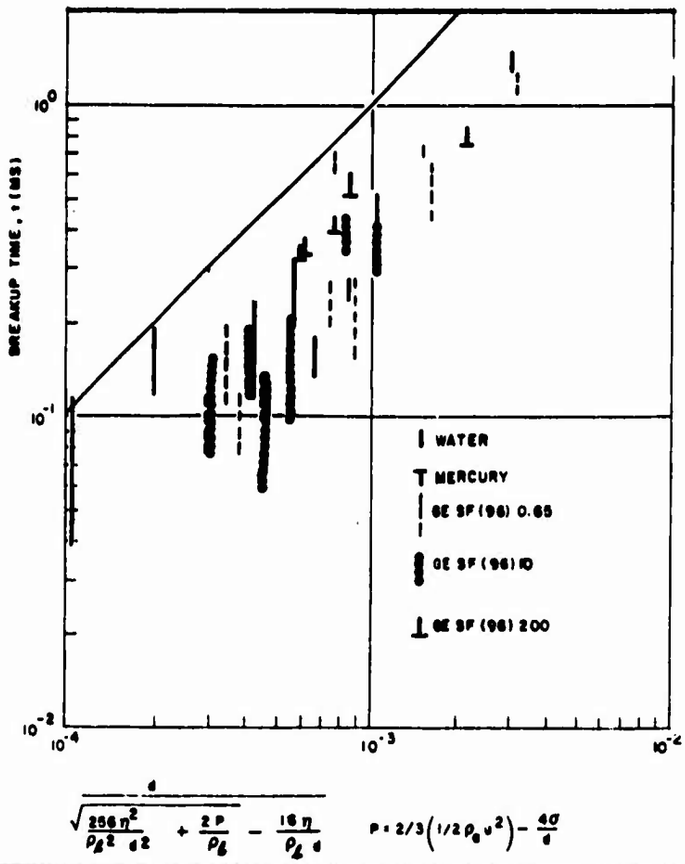
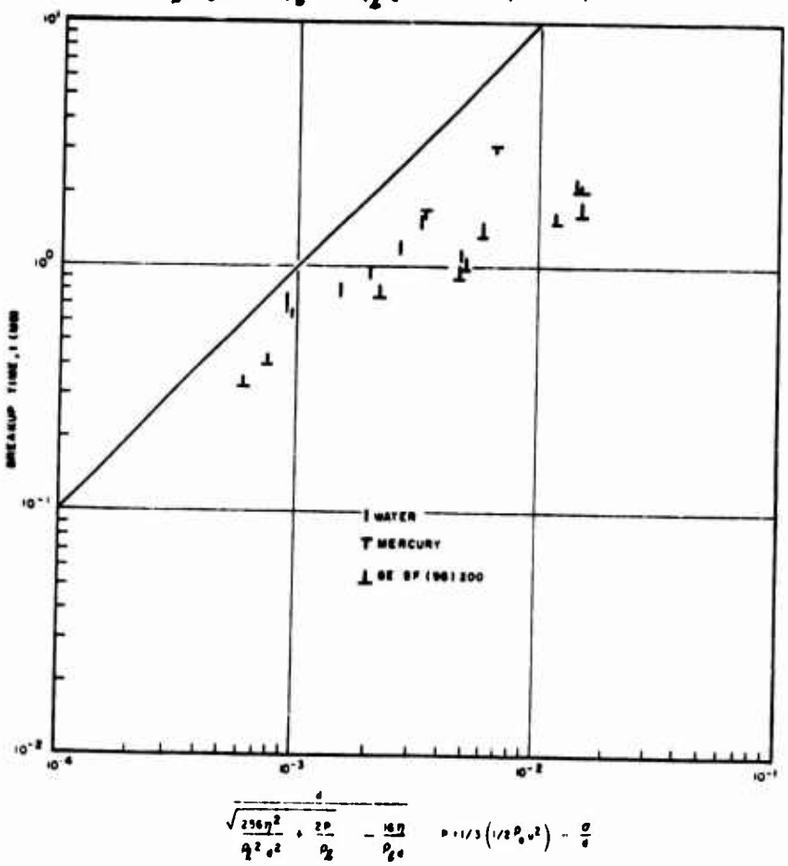


Figure 5. Comparison of Experimental Drop Breakup Times with Gordon Theory for Reduced Surface Tension Pressure.



$$\frac{d}{\sqrt{\frac{256\eta^2}{\rho_\ell^2 d^2} + \frac{2P}{\rho_\ell}} - \frac{16\eta}{\rho_\ell d}} \qquad P = 2/3\left(1/2\,\rho_g v^2\right) - \frac{4\sigma}{d}$$

Figure 6. Comparison of Experimental Stripping Breakup Times with Andersen-Wolfe Equation.



$$\frac{d}{\sqrt{\frac{256\eta^2}{\rho_\ell^2 d^2} + \frac{2P}{\rho_\ell}} - \frac{16\eta}{\rho_\ell d}} \qquad P = 1/3\left(1/2\,\rho_g v^2\right) - \frac{\sigma}{d}$$

Figure 7. Comparison of Experimental Bag Breakup Times with Andersen-Wolfe Equation.

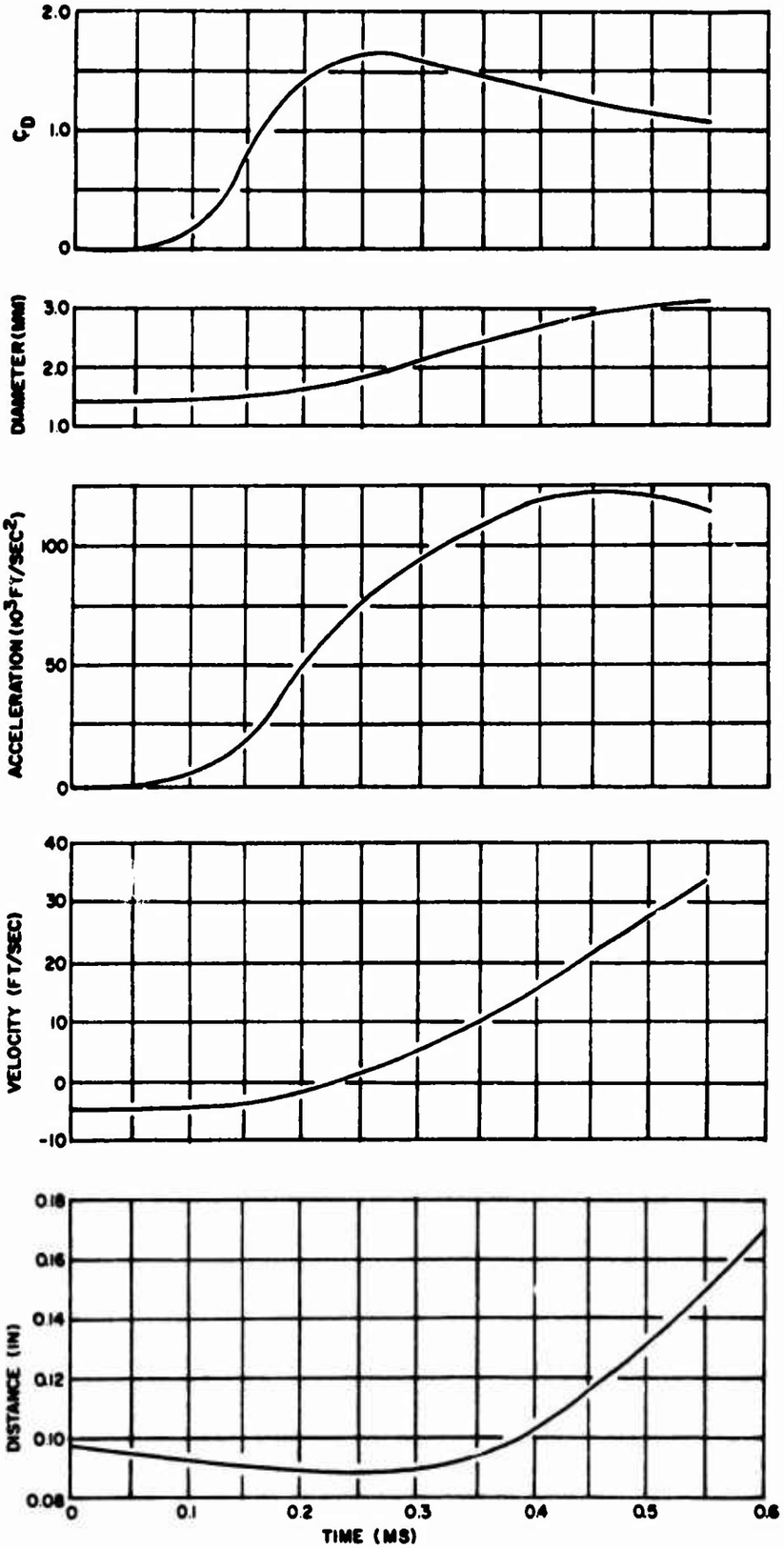


Figure 8. Motion of a 1.45mm Diameter Drop of G. E. SF(96)200 Silicone Fluid Subjected to an Airflow of 340 ft/sec.

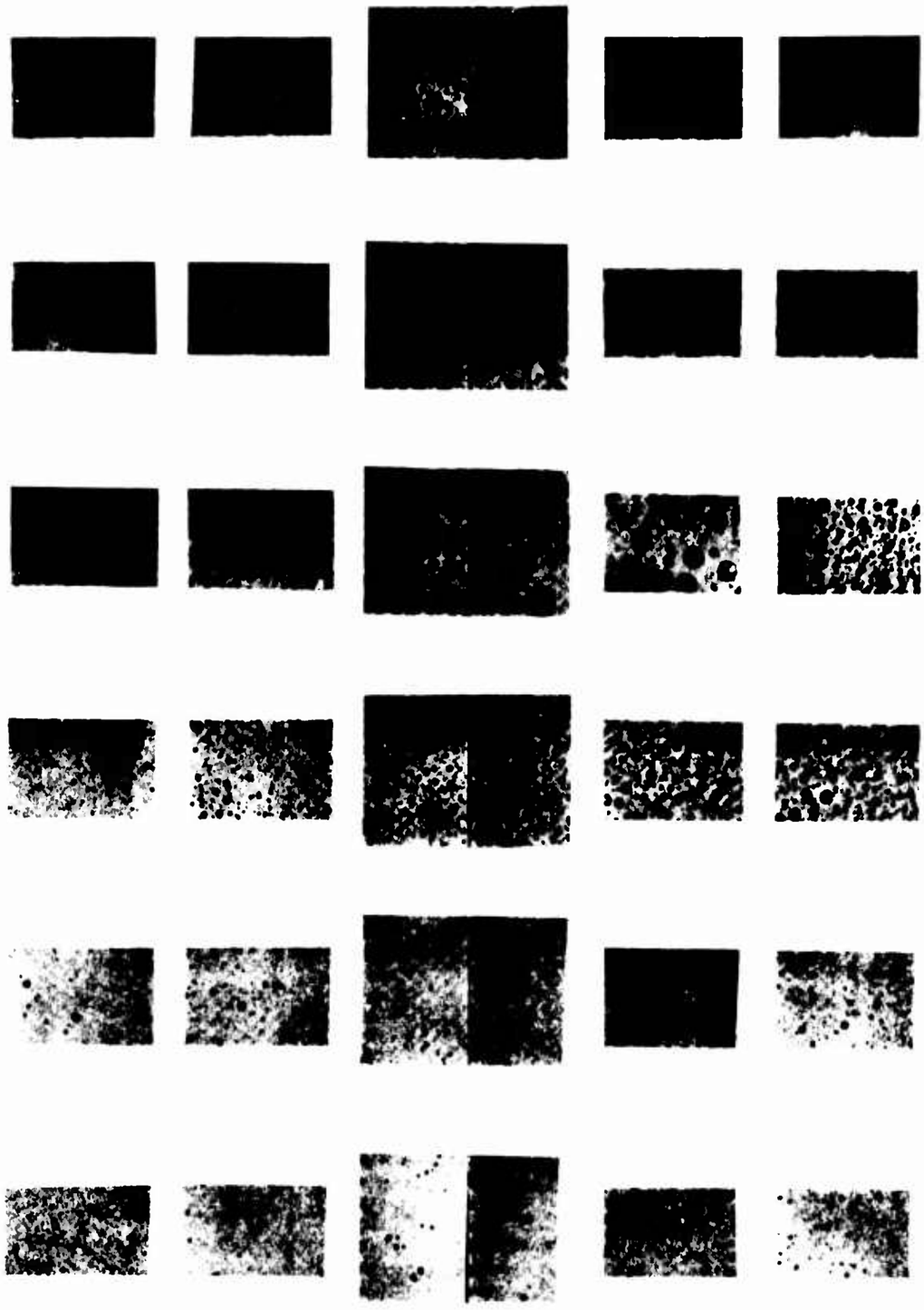


Figure 9. Photomicrographs of Typical Droplet Size Distribution Resulting from Breakup.
Drop Size: 2.7mm
Relative Velocity: 395 ft/sec
MMD 34 μ

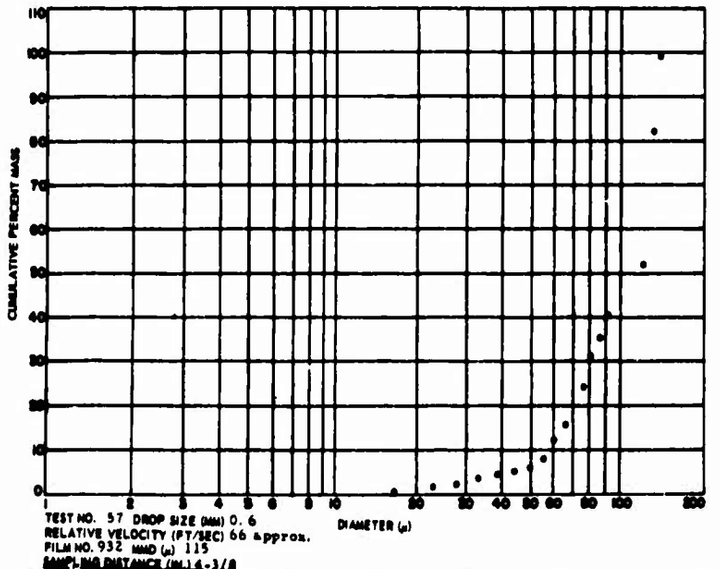


Figure 10(a). Cumulative Percent Mass vs Mass Median Diameter for Bag Breakup.

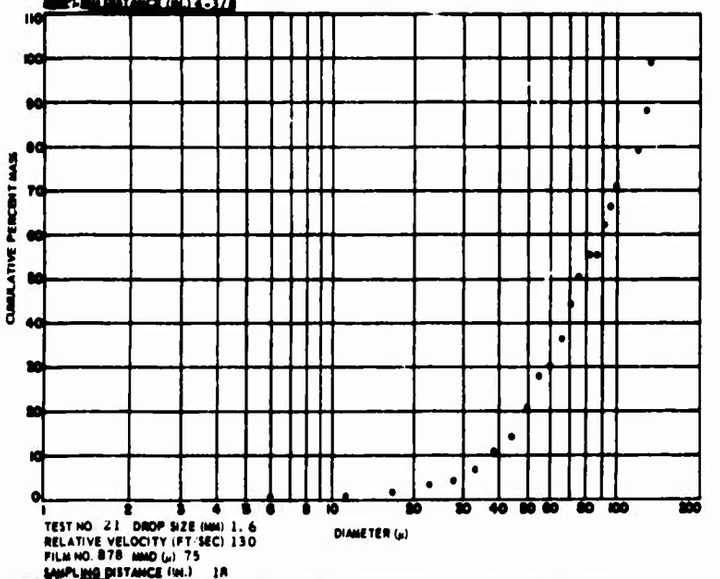


Figure 10(b). Cumulative Percent Mass vs Mass Median Diameter for Stripping Breakup at Low Velocity.

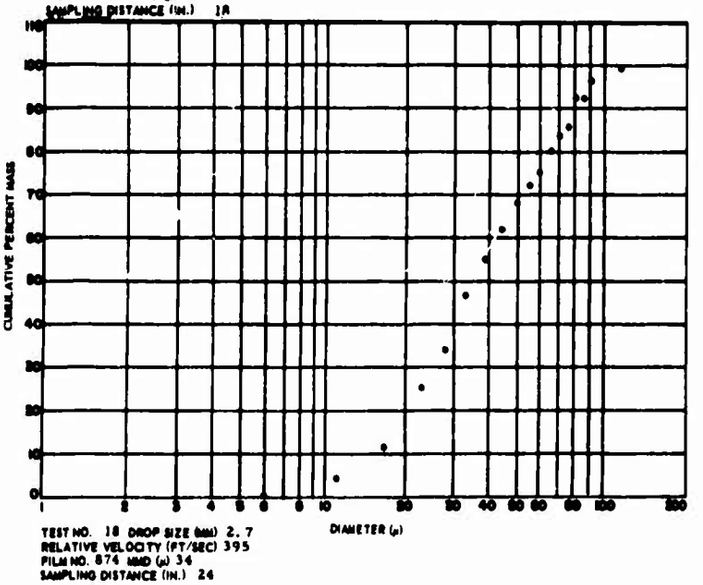


Figure 10(c). Cumulative Percent Mass vs Mass Median Diameter for Stripping Breakup at High Velocity.

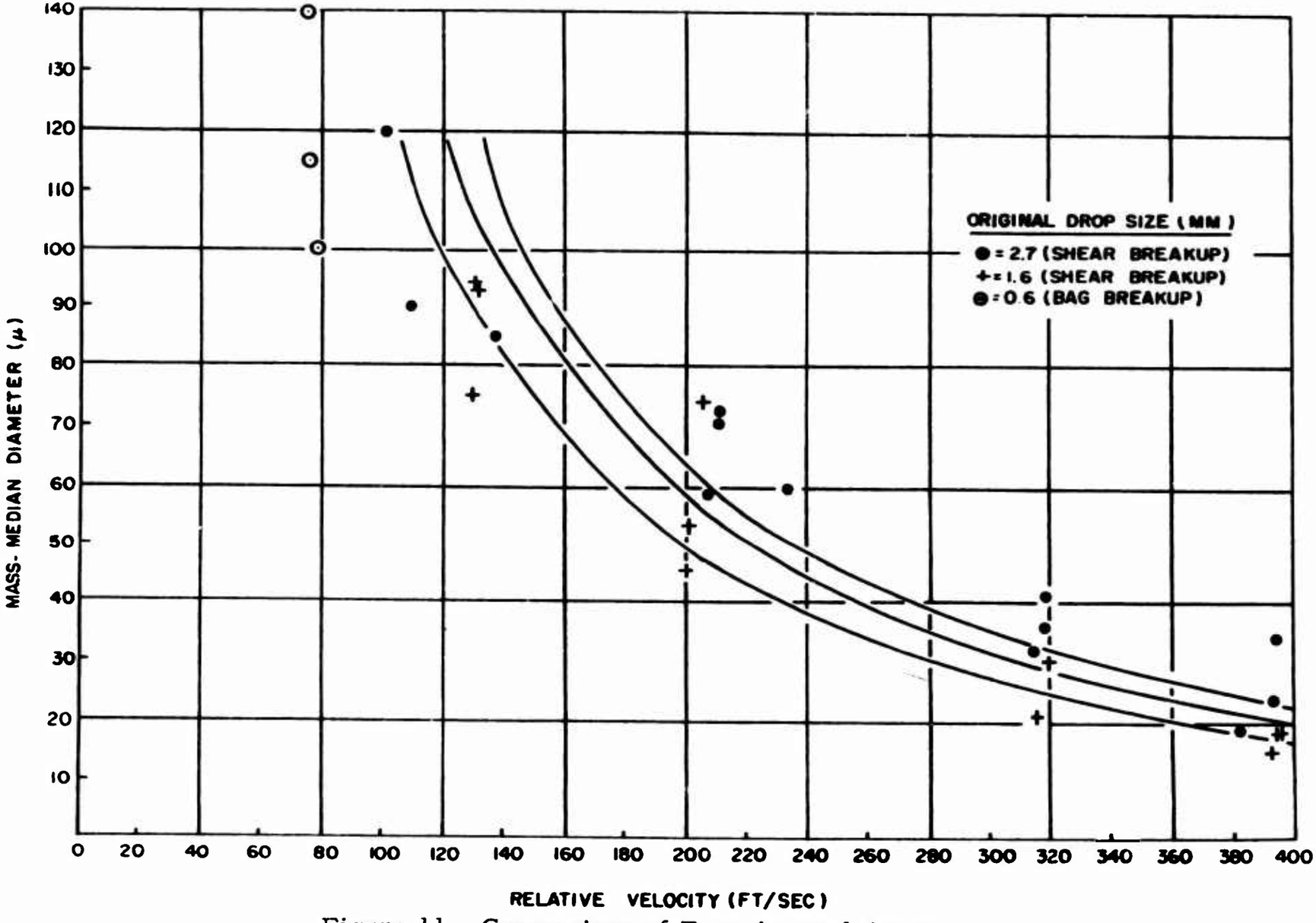
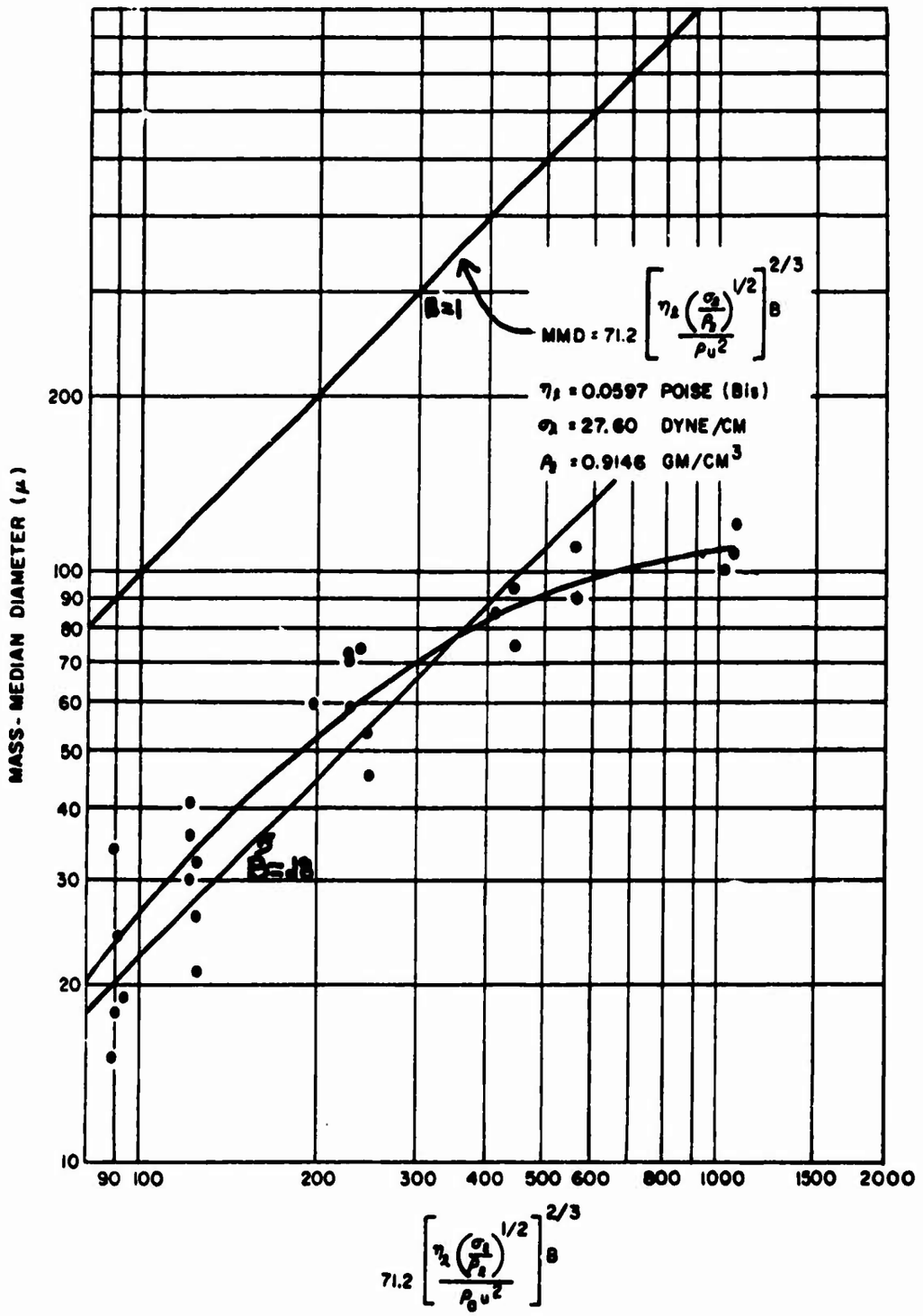


Figure 11. Comparison of Experimental Average Mass Droplet Sizes with Theory. (Ambrosen - Wolfe)



2020-30-1

Figure 12. Comparison of Experimental Average Mass Droplet Size with Mayer Theory

BLANK PAGE

ONBOARD SPECTRAL OBSERVATION TECHNIQUE FOR A MODEL IN A SHOCK TUBE

William M. Houghton
NASA Langley Research Center
Hampton, Virginia

INTRODUCTION

During spacecraft reentry, gas cap radiation plays a major role in heat transfer to the space vehicle. In simulating reentry by subjecting a spacecraft model to the flow of a shock tube it is important to measure the radiation emitted by this gas cap, particularly that which actually strikes the model. The usefulness of spectroscopic techniques for analyzing this radiation is well established. Such spectroscopic measurements are usually made by placing a window in the tube wall adjacent to the model and arranging the spectrograph to view the desired spatial region; figure 1 illustrates such a method. Several problems arise with this technique in the form of alinement difficulties, absorption by the free stream between the model and window, and the difficulty of transforming the two-dimensional side view into the true radiation characteristics about the model.

This paper discusses an "onboard" technique being investigated at Langley Research Center to alleviate these problems by the use of collecting optics located inside a hollow model-sting assembly. The general idea of this technique is to place windows in the model nose and use a suitable means for gathering the radiation passing through the window and conducting it to a spectrograph located outside the shock tube. Two approaches have been tried. The first involves a fiber optics bundle placed in the model as shown in figure 2. A second method being evaluated utilizes a mirror-relay system as shown in figure 3.

The "onboard" radiation measuring techniques reported to date have employed blackbody-type detectors or wide bandpass detectors to measure total radiative energy (refs. 1 and 2). In our measurements, however, both time and spatial resolution are required as well as the capability of observing various

wavelengths over a wide spectral range. If the complete time history of a wide spectral range, say several thousand angstroms, is required a separate drum camera-spectrograph should be used for each spatial point desired. In many experiments, however, it is adequate to record several wavelengths at each of several points. In this case a single stigmatic spectrograph fitted with multiple phototubes may be used to monitor several wavelengths at different points.

At present the "onboard" approach has been tested for a single point located at the stagnation point of a blunt-nose model. However, a contemplated system will employ multiple fiber bundles, or multiple images in the relay mirror case, to gather radiation from 5 or 6 points on the model surface.

INSTRUMENT DESCRIPTION AND MEASUREMENTS

Figure 4 shows the laboratory setup for the fiber optics tests. One fiber bundle was located inside the model behind a protective window and used to conduct the collected radiation to a vacuum feed-through window. A second fiber bundle gathered the radiation passing through the window and directed it onto the spectrograph slit. Approximately 90 percent of the radiation was lost at this vacuum feed through; coupled with the transmission of the fiber bundle, the overall efficiency of transfer from model to spectrograph was about 5 percent.

The spectrograph used for the fiber optics tests was a Hilger E-612 adapted to a 70-mm drum camera. The time resolution obtained was 10μ sec and the wavelength resolution variable from about 20 Å in the red to 5 Å in the blue. Figure 5 is a typical spectrogram obtained. It is evident that little data was recorded at the beginning of the run, that is, during the time of good flow. This is attributed to the large loss encountered in the vacuum feed-through coupling. In a bench setup using a flash lamp source, spectra made with one continuous fiber bundle showed well-exposed lines, while two bundles coupled across a glass window showed only a few faint lines. Thus it is concluded that elimination of the vacuum feed-through loss will make the fiber optics usable. An additional disadvantage of the fiber bundles is their transmission cutoff at 3800 Å. Improved fiber bundles have been recently made available which transmit well from 3400 Å to 14,000 Å and can be provided with a potted vacuum seal to eliminate the feed-through window. For time-resolved work or for stacking bundles on the slit of a stigmatic spectrograph, small-diameter bundles are desirable. For maximum efficiency the fiber bundles should be placed directly against the spectrograph slit since auxiliary optics cannot increase the steradiancy and will only contribute losses.

Figure 6 shows the shock tube setup for the mirror-relay system. Radiation entering through an aperture in the model nose was reflected by a

plane mirror through a vacuum seal window to a spherical mirror. The spherical mirror then directed the radiation to another plane mirror and then to a focus on the spectrograph slit. The off-axis angle has been kept as small as possible ($<10^{\circ}$) to minimize aberrations. This not only obtains maximum efficiency but for multipoint work will allow several points on the model nose to be formed as separate and distinct images on the spectrograph slit. Spectra of the mirror-relay tests were recorded with a custom spectrograph which incorporated either glass plates for time-integrated spectra or multiple phototubes for time-resolved data at several wavelengths. By replacing the glass plate with a thin metal plate containing machined slits, various wavelengths could be selected to be monitored by phototubes. From the time-integrated spectrogram a slit plate was fabricated to select the 3883 CN bandhead and the 3021 Fe line. Figures 7 and 8 show data obtained with this method. These records are part of a shock-tube-impurities study presently being conducted and here serve only to show the degree of success obtained with the "onboard" technique. To date spectra over the 2500 Å to 6500 Å region have been recorded, but extension to the vacuum UV is feasible. Figure 9 is a computed transmission curve from published reflectance data (ref. 3) to give an idea of the efficiency to be expected for a three-mirror system at short wavelengths.

COMMENTS

As was stated above, only single-point spectrograms have been made in the shock tube with the "onboard" approach. However the extension to multipoint is being studied in the laboratory to determine the best spatial resolution to be expected. Considering the mirror-relay system, it is possible to place two 1/16-inch-diameter holes 1/4 inch apart on the model nose and still resolve these as separate spectra at the film plane of the spectrograph. The next step in the laboratory study is to design and fabricate a model assembly to contain mirrors or prisms to gather light from the side regions of the model. The tentative goal for the onboard mirror system is to be able to record the time history of radiation from six points for two different wavelengths at each point.

Ellipsoidal mirrors seem desirable to use as the 45° mirror in the model. This would allow only one reflecting surface between the model nose and the spectrograph slit, a desirable feature for the vacuum UV. However, because of the expense of ellipsoidal mirrors a window should be used in the model nose to prevent damage to the mirror from the relatively large particles in the flow.

CONCLUSION

The "on board" technique works very effectively for the mirror-relay system for a single point. The extension to multipoint recording is currently being developed and looks entirely feasible. Due to the inefficiency of mirror coatings at short wavelengths, the three mirror system is limited to about 1200Å, either with or without a window.

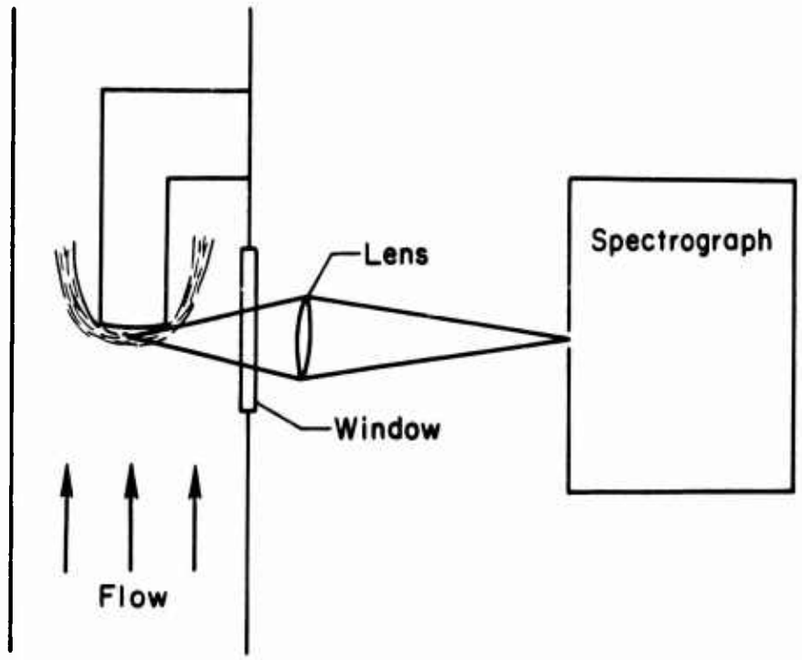
The fiber optics method is usable but hampered by the 95-percent losses described. Improved fiber bundles and vacuum feed-through techniques should make this method good over the 3400Å to 1.4μ region. Fiber bundles are simple to install in a model and eliminate alinement difficulties completely.

REFERENCES

(1) J. S. Gruszczynski, C. J. Harris, D. A. Rogers, W. R. Warren, Jr. "Fast Response Total Radiation Gauge for Measurement of Radiant Emission From High Temperature Gas" presented as a paper at IEEE Meeting in New York City, March 1963.

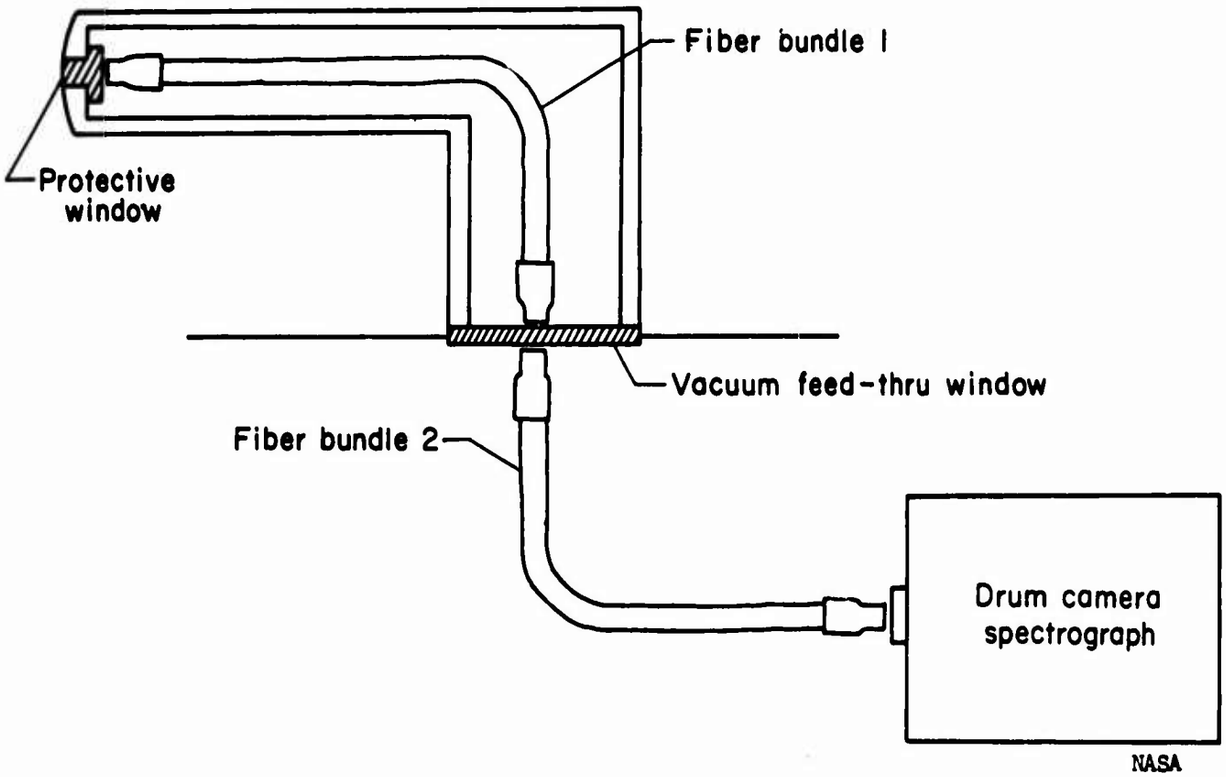
(2) J. C. Camm, B. Kivel, R. L. Taylor, J. D. Teare, Avco-Everett Research Report 93; Dec. 1959.

(3) R. K. Brehm and G. Benzie, Review of Scientific Instruments, 28, 552; 1957.



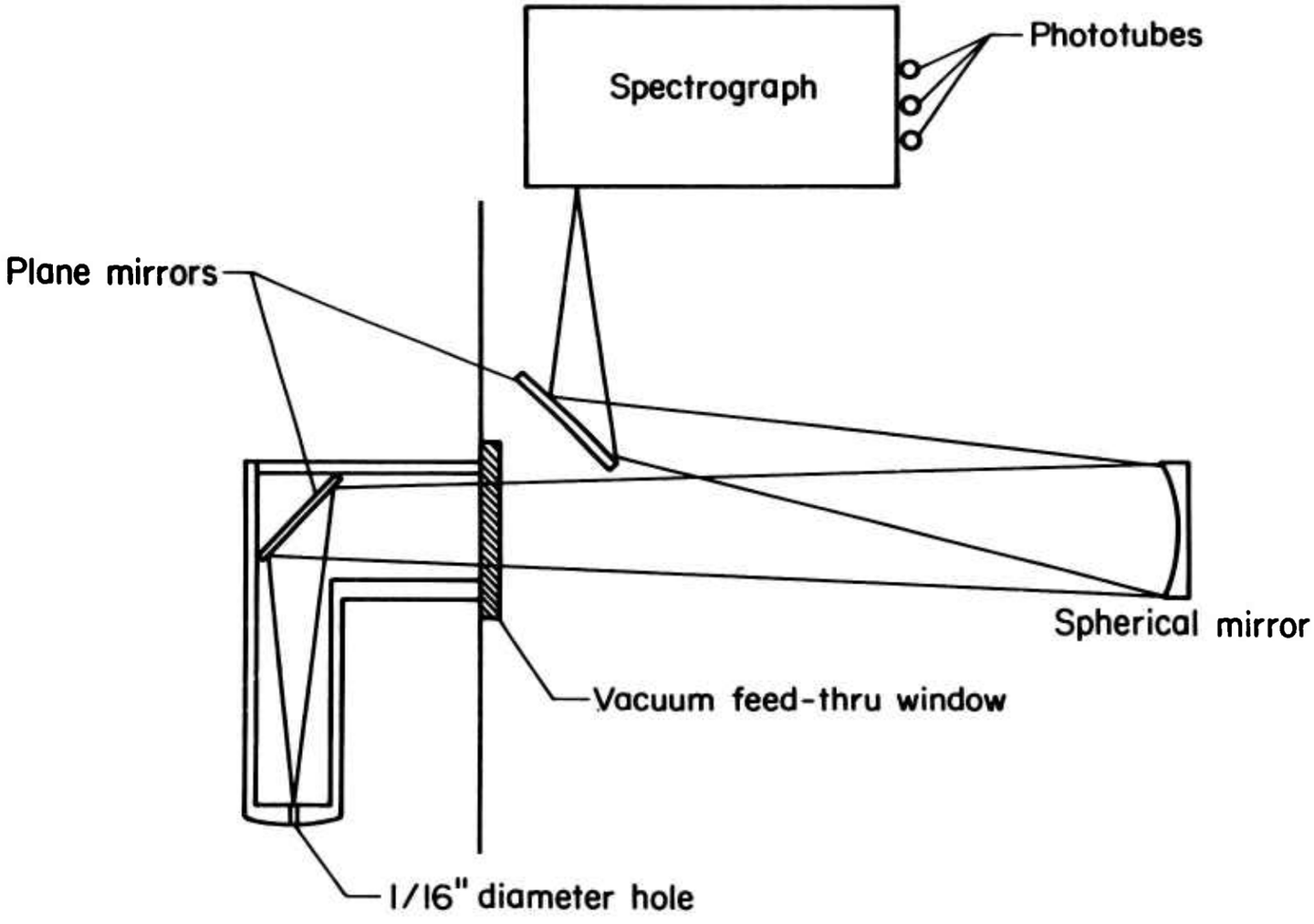
NASA

Figure 1.- Conventional approach for shock tube spectroscopy.



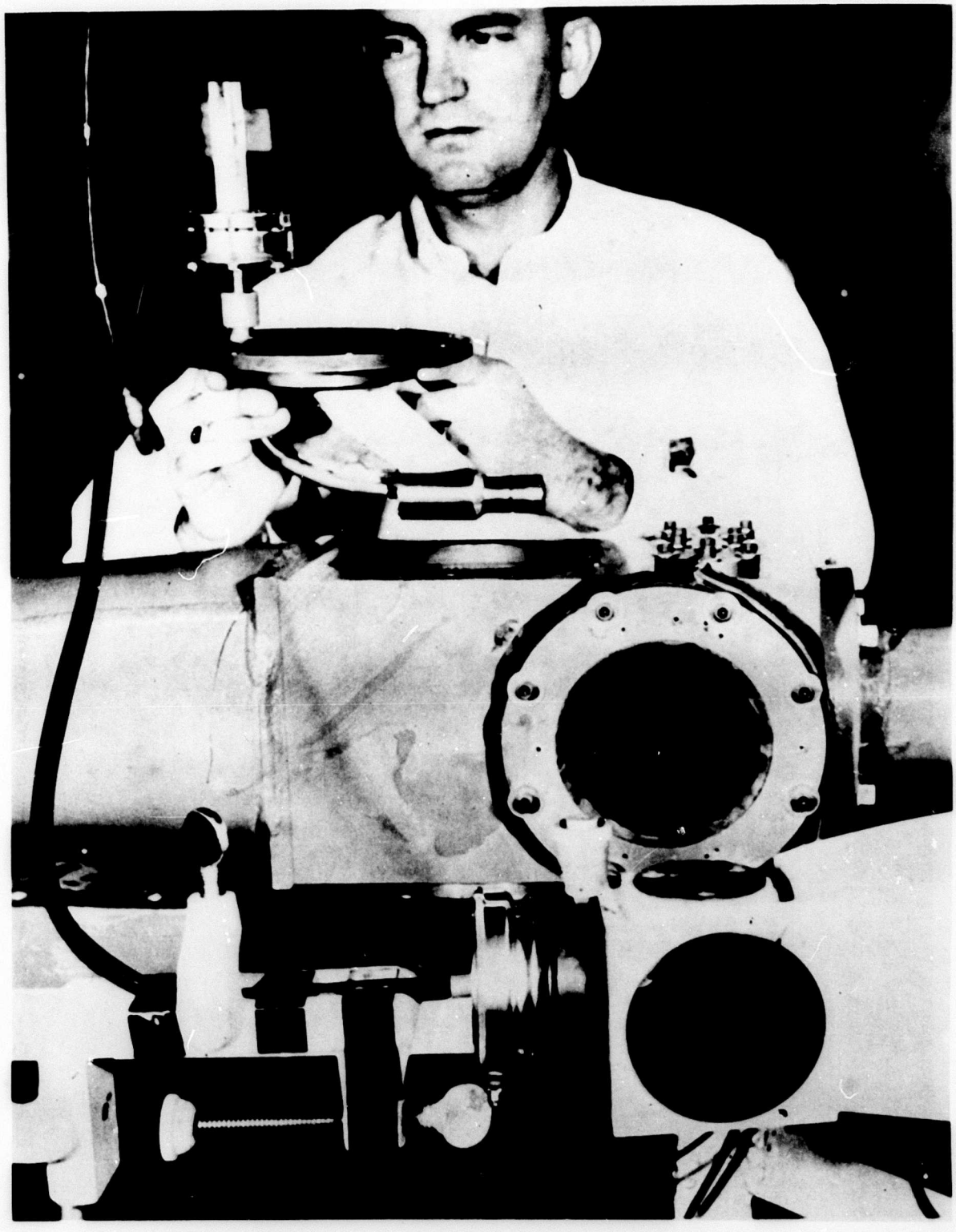
NASA

Figure 2.- Onboard fiber optics system.



NASA

Figure 3.- Mirror-relay system.



NASA

Figure 4.- Fiber optics setup for shock tube.

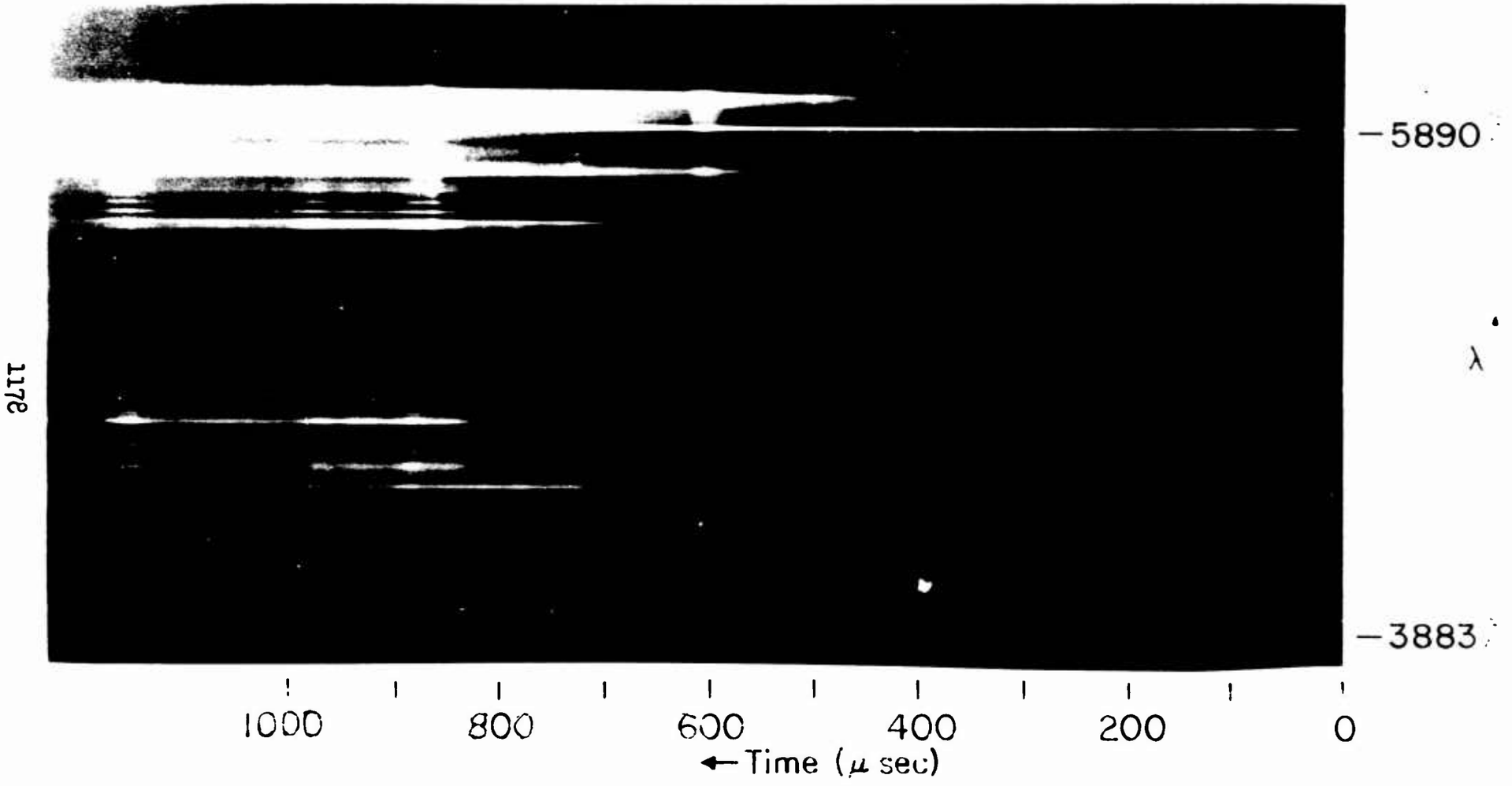
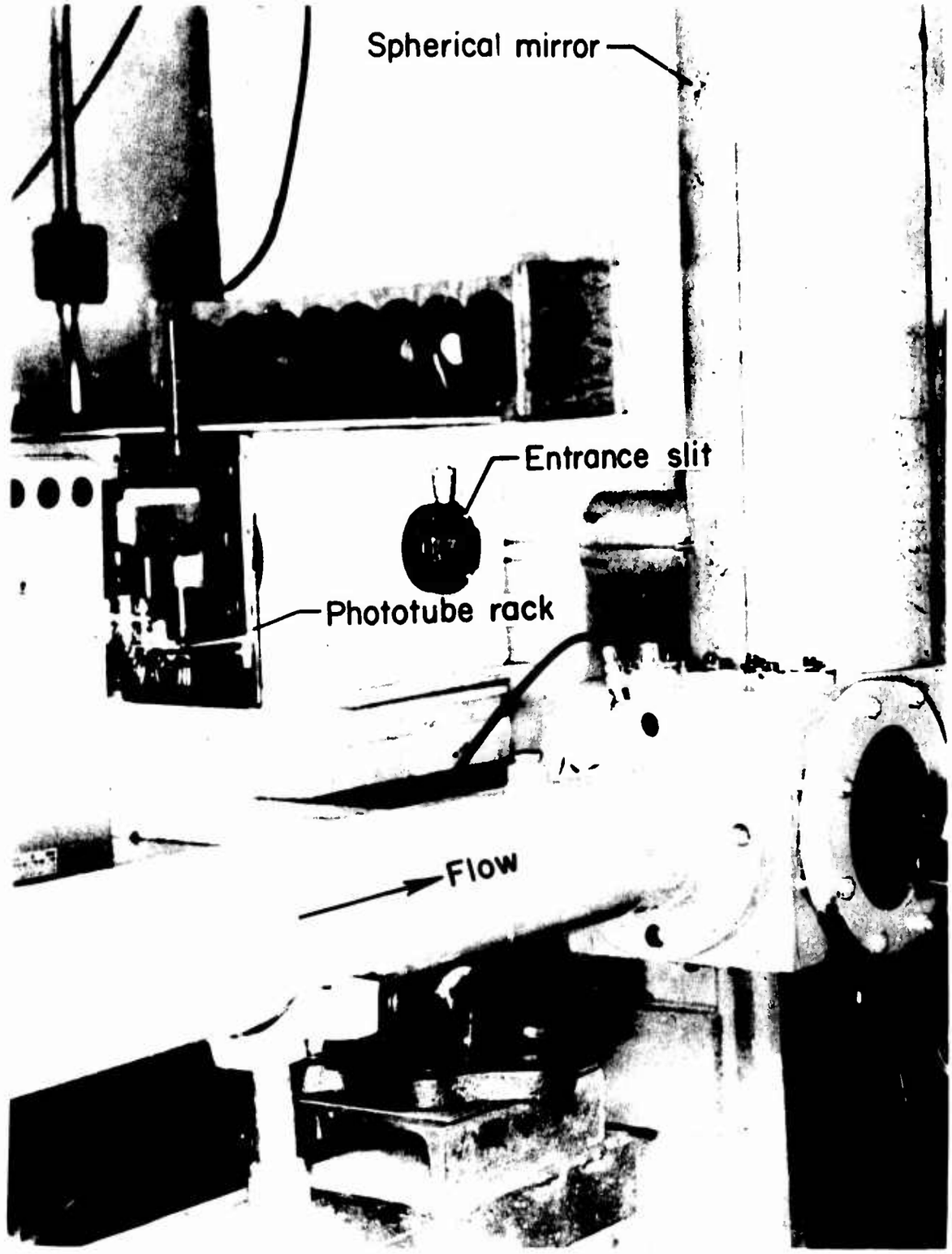


Figure 5.- Time-resolved spectrogram obtained with fiber optics system.



NASA

Figure 6.- Relay mirror setup for shock tube.

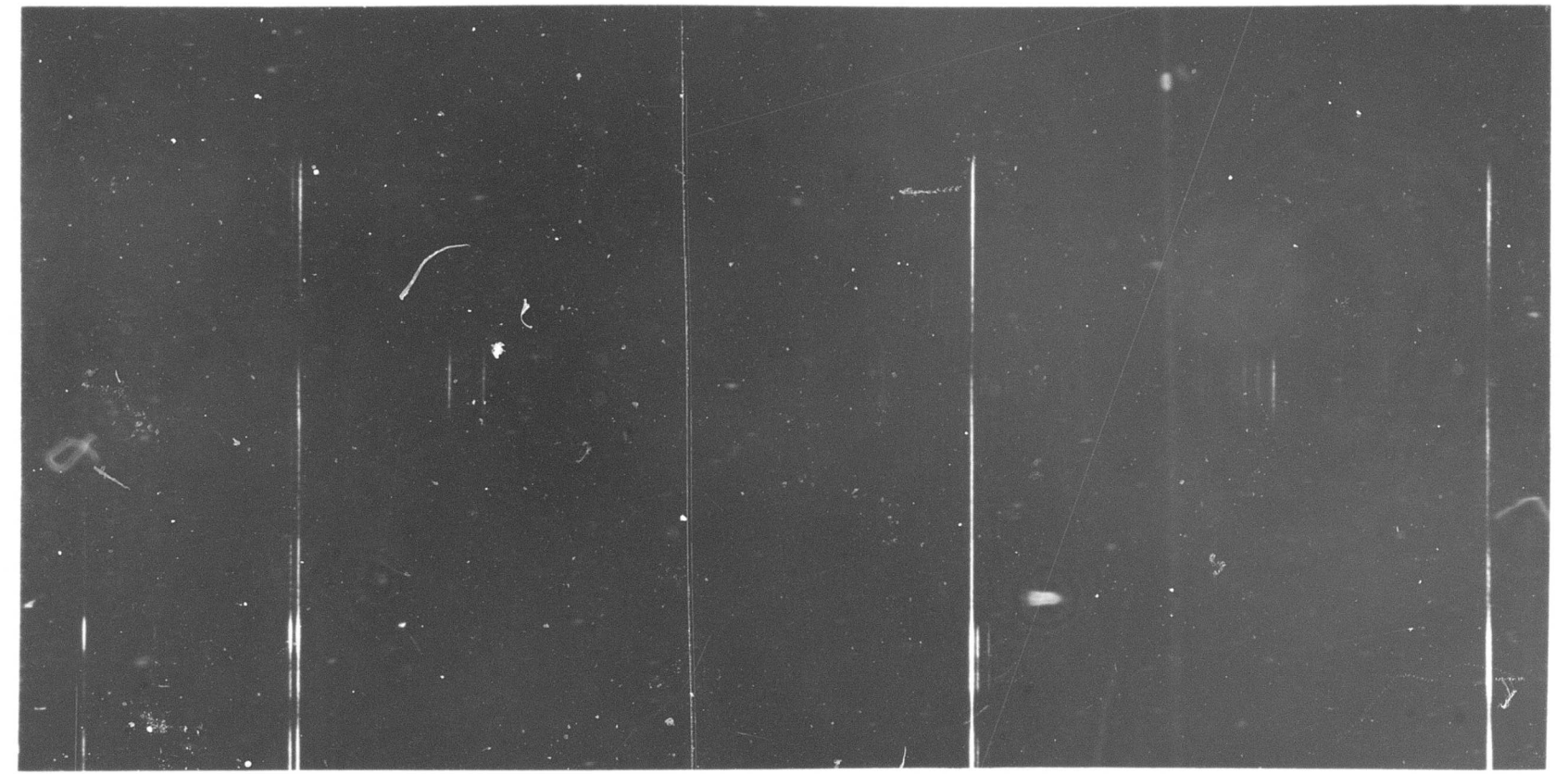
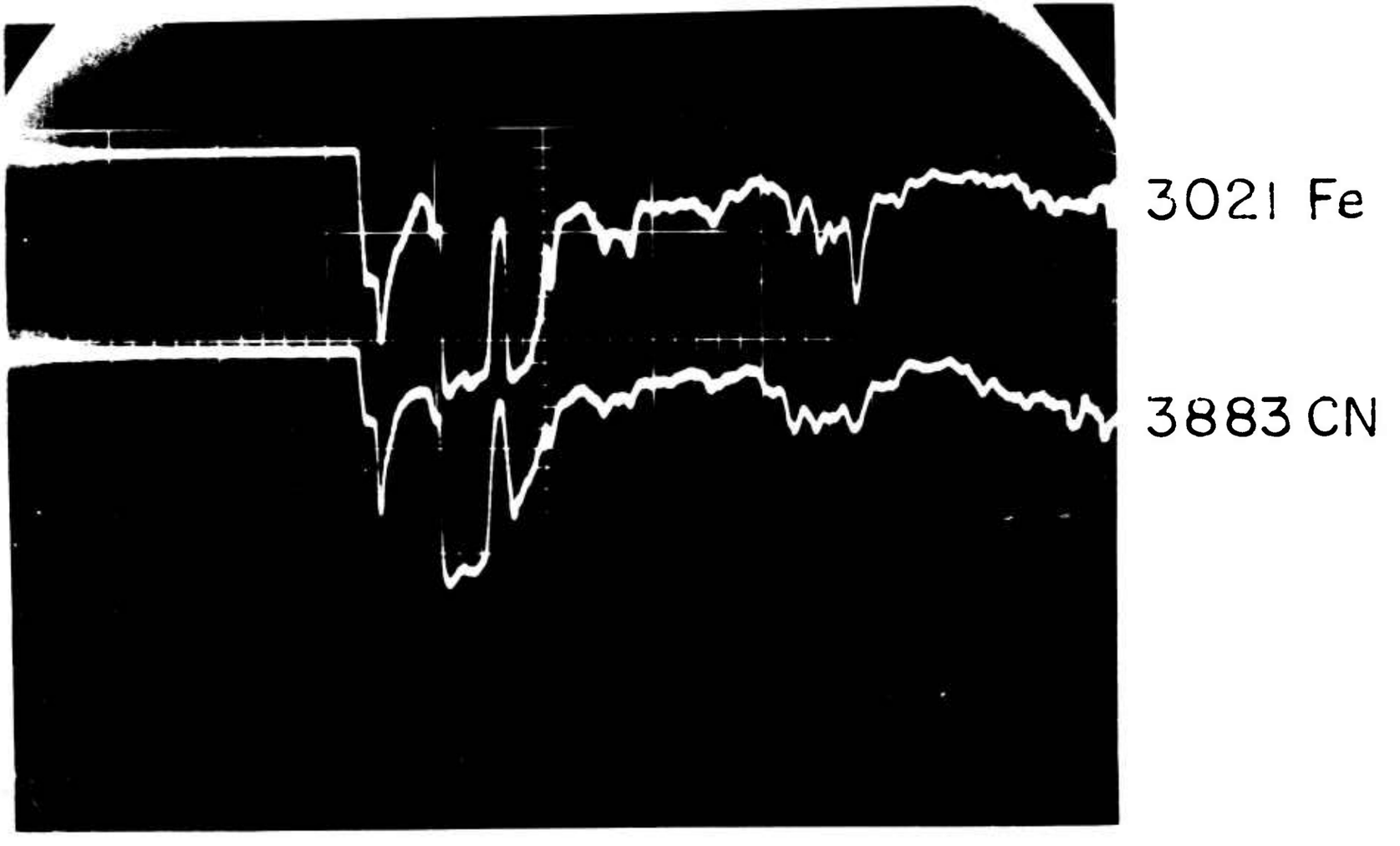
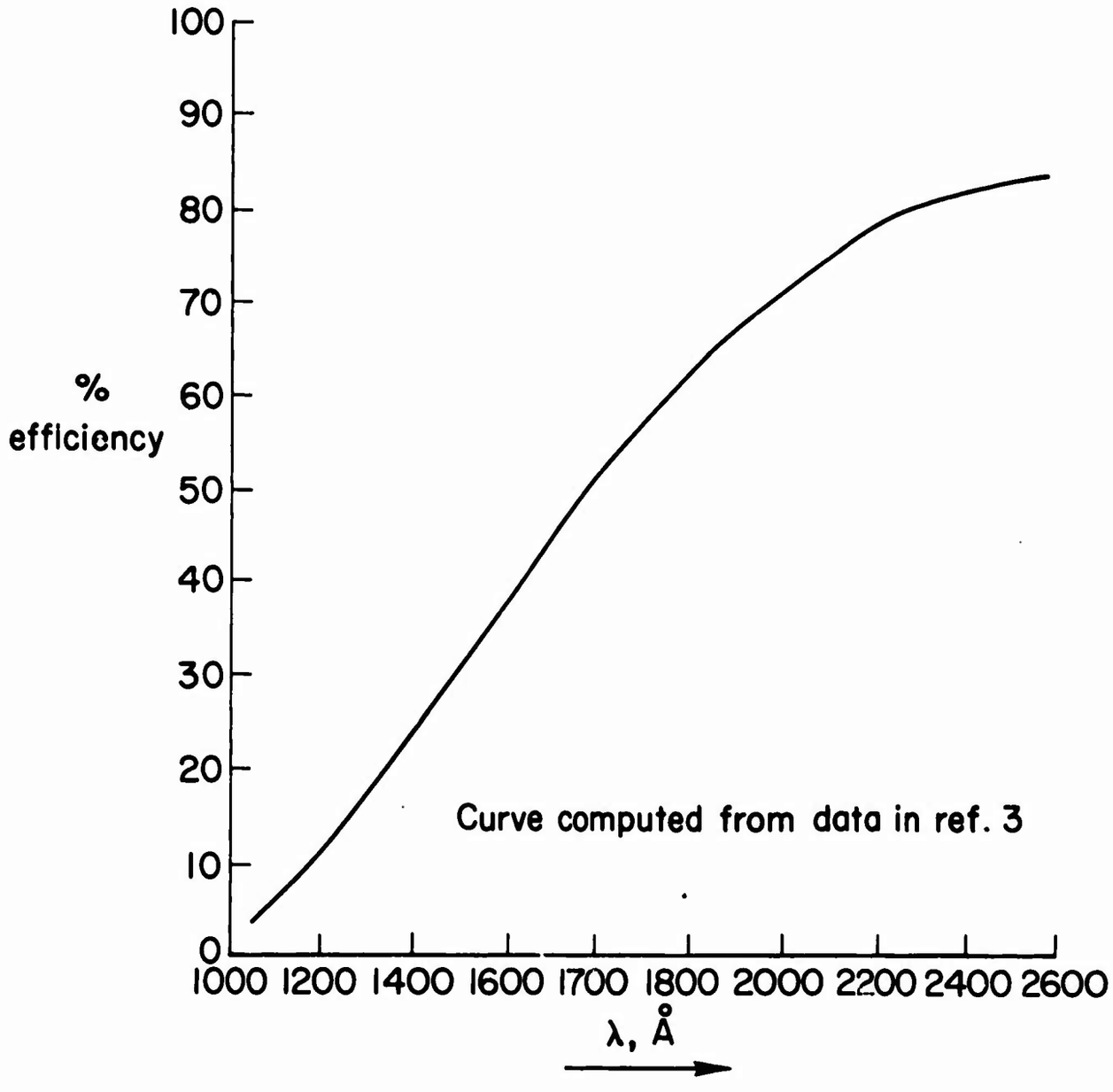


Figure 7.- Time-integrated spectrogram with mirror-relay system.



NASA

Figure 8.- Time histories of Fe and CN with mirror-relay system.



NASA

Figure 9.- Efficiency for three reflections from aluminum-coated mirrors.